PROCEEDINGS

of the 13th TSME International Conference
on Mechanical Engineering

12th – 15th December 2023 | Chiang Mai, Thailand

Co-organized by
Chiang Mai University (CMU)
and Thai Society of Mechanical Engineers (TSME)

ISBN (e-book) 978-616-398-916-1



Proceedings of the 13th TSME International Conference on Mechanical Engineering

TSME-ICoME 2023
12th–15th December 2023 | Chiang Mai, Thailand

Co-organized by
Chiang Mai University (CMU)
and Thai Society of Mechanical Engineers (TSME)

ISBN (e-book) 978-616-398-916-1

Proceedings of the 13th TSME International Conference on Mechanical Engineering
February 2024
1st Edition

Published by
Department of Mechanical Engineering, Faculty of Engineering, Chiang Mai University
239 Huay Kaew Rd., Suthep, Muang District, Chiang Mai, 50200 Thailand

ISBN (e-book) 978-616-398-916-1

Table of Contents

Message from President of Chiang Mai University (CMU)

Distinguished participants, ladies and gentlemen, on behalf of all my colleagues, it gives me a great pleasure to welcome you to Chiang Mai on the occasion of the 13th TSME International Conference on Mechanical Engineering (TSME-ICoME 2023).

Since its inception in 1987, the Thai Society of Mechanical Engineers (TSME) has played a pivotal role in fostering collaboration and knowledge exchange within the mechanical engineering community. The alliance with the American Society of Mechanical Engineers (ASME), the Japan Society of Mechanical Engineers (JSME), and the Korean Society of Mechanical Engineers (KSME) has further enriched this tradition, transforming the TSME International Conference into a truly global platform.

This year's conference is especially meaningful for Chiang Mai University, as we take great pride in being part of the organizing team for this prestigious event. Situated in the captivating city of Chiang Mai, we eagerly anticipate creating an inspiring environment for the exchange of ideas among scientists, academics, researchers, and industry representatives.

The TSME-ICoME 2023 conference is not merely a gathering; it is a forum for collaboration, networking, and profound discussions on the latest advancements in mechanical engineering and related disciplines. We believe that through this collective effort, we can drive research, extend the frontiers of science and technology, and contribute to the progress of our field.

As we embark on this intellectual journey, I encourage you to immerse yourself in the rich academic atmosphere, forge new connections, and engage in meaningful conversations that will undoubtedly shape the future of mechanical engineering.

On behalf of Chiang Mai University, I extend my sincere gratitude to the organizers, sponsors, and most importantly to each participant for making TSME-ICoME 2023 a reality. May this conference be a memorable and transformative experience for all.

Thank you.

Professor Pongruk Sribanditmongkol, M.D., Ph.D.
President of Chiang Mai University (CMU)

Message from Head of Mechanical Engineering Department Chiang Mai University (CMU)

I am very pleased to welcome you to Chiang Mai for the 13th TSME International Conference on Mechanical Engineering (TSME-ICoME 2023) that is co-organized by the Thai Society of Mechanical Engineers (TSME) and Chiang Mai University. It is an honor for us to collaborate with TSME to hold this international conference this year. I am also glad that researchers from academia and industry come to join the conference, presenting their contributions to advancing knowledge of mechanical engineering and related disciplines.

Taking place in one of the most attractive cities in the north of Thailand, the conference is aimed at bringing together all generations of researchers and industrialists from several countries to share their research findings and expertise. Presentations, discussions, and knowledge exchange would lead to expanding collaborations and enlarging research networks in our international community.

On behalf of the conference organizing team, I would like to thank the president of TSME, guests of honor, keynote speakers, invited speakers, technical committees, non-technical committees, reviewers, and members of TSME for their contributions and support in various aspects. I am grateful to our industrial partners, including sponsors, for coming to provide visions of cutting-edge technology in industry and demonstrate potential applications of such technology to the participants. I am also thankful to all the delegates for coming to share their valuable ideas and research results at our conference, which makes the conference worthwhile.

Last but not least, I wish you all success with your objectives for taking part in this conference. I also highly expect you to enjoy your time during your stay in Chiang Mai.

Thank you.

Assistant Professor Dr. Pinyo Puangmali
Head of Mechanical Engineering Department, CMU

Message from President of Thai Society of Mechanical Engineers (TSME)

The 13th International Conference on Mechanical Engineering, or ICoME 2023 is jointly hosted and organized by the Thai Society of Mechanical Engineers (TSME) and the Department of Mechanical Engineering, Faculty of Engineering, Chiang Mai University.

As usual, in this ICoME 2023, the TSME collaborates with the Japan Society of Mechanical Engineers (JSME), the Korean Society of Mechanical Engineers (KSME), and the American Society of Mechanical Engineers (ASME) to gather an international scholars, engineers, and researchers around the world. This is to learn and present their updated researches, new findings, technologies, and innovations. TSME has realized the importance of rapid changes and disruption in technologies, especially in the fields related to mechanical engineering. While, the energy efficiency, renewable energy technology, and global warming and environmental issues also become the major concerns.

The ICoME 2023 has received overwhelming interest from the mechanical engineering community, with keynote speakers and delegates from around the world. On behalf of the TSME committee, I would like to sincerely express my gratitude to the Department of Mechanical Engineering, Faculty of Engineering, Chiang Mai University, for their contribution and dedication to host this TSME–ICoME 2023.

Finally, I would like to welcome all participants to the TSME–ICoME 2023. I hope you enjoy the conference and gain the fruitful experience and opportunity to learn, to discuss or even to expand your research network in this conference. Also, I hope you have a pleasant stay and have a great time in Chiang Mai, where is one of the most attractive and beautiful cities of Thailand.

Thank you and best wishes.

Professor Dr. Kulachate Pianthong
President of Thai Society of Mechanical Engineers (TSME)

About the Conference

Since 1987, the Thai Society of Mechanical Engineers (TSME) has held annual conferences, aiming to gather scholars and practitioners in various fields of mechanical engineering to share expertise and create collaborative networks. In 2010, with collaboration from the American Society of Mechanical Engineers (ASME), the Japan Society of Mechanical Engineers (JSME), and the Korean Society of Mechanical Engineers (KSME), the TSME started to hold international conferences. Since then, "The TSME International Conference on Mechanical Engineering (TSME-ICoME)" has been held annually.

In 2023, the 13th TSME International Conference on Mechanical Engineering (TSME-ICoME 2023) is co-organized by the Thai Society of Mechanical Engineers (TSME) and Chiang Mai University. Taking place in Chiang Mai, one of the most attractive cities in Thailand, the conference will again bring together scientists, academics, researchers, and industry representatives to share knowledge and expertise in mechanical engineering and related disciplines.

As a forum for collaboration and networking among delegates, as well as in-depth discussions on research methodologies, findings, etc., the conference will drive research and extend science and technology frontiers. Papers accepted following peer review will be published in the conference proceedings or, optionally, in the Journal of Research and Applications in Mechanical Engineering (JRAME).

Members of Thai Society of Mechanical Engineers (TSME)

1) Chiang Mai University
2) Suranaree University of Technology
3) Burapha University
4) Chulalongkorn University
5) Prince of Songkla University
6) King Mongkut's Institute of Technology Ladkrabang
7) King Mongkut's University of Technology Thonburi
8) Silpakorn University
9) Mahasarakham University
10) Royal Thai Naval Academy
11) Thai-Nichi Institute of Technology
12) Mahidol University
13) Khon Kaen University
14) Rajamangala University of Technology Ratanakosin
15) Srinakharinwirot University Ongkharak Campus
16) Rajamangala University of Technology lsan
17) Ubon Ratchathani University
18) Mahonakorn University of Technology
19) Rangsit University
20) Thammasat University
21) Kasetsart University Sriracha Campus
22) Naresuan University
23) Chulachomklao Royal Military Academy
24) Navaminda Kasatriyadhiraj Royal Air Force Academy
25) Pathumthani University
26) Sripatum University
27) Kasetsart University Bangkhen Campus
28) King Mongkut's University of Technology North Bangkok
29) Rajamangala University of Technology Thanyaburi
30) Bangkokthonburi University
31) Southeast Asia University
32) Panyapiwat Institute of Management
33) Kasetsart University Kamphaeng Saen Campus
34) Walailak University

Lists of Committees

Honorary Chair

Prof. Dr. Kulachate Pianthong
President of Thai Society of Mechanical Engineers (TSME)

International Scientific Committee

Prof. Dr. Ashwani K. Gupta
University of Maryland, USA

Prof. Dr. Adrian Bejan
Duke University, USA

Prof. Dr. Nicholas Xuanlai Fang
MIT, USA

Prof. Dr. Narita Yoshihiro
Hokkaido University, JAPAN

Prof. Dr. Ning Zhu
Shizuoka Institute of Science and Technology, JAPAN

Prof.Dr. Katsunori Hanamura
Tokyo Institute of Technology, JAPAN

Prof. Dr. Jens Nørkær Sørensen
Technical University of Denmark, DENMARK

Prof. Dr. Ashim K. Datta
Cornell University, USA

Prof. Dr. Kambiz Vafai
University of California, USA

Assoc. Prof. Dr. Renkun Chen
University of California, USA

Prof. Dr. Yoshiharu Mutoh
Nagaoka University of Technology, JAPAN

Prof. Dr. Naoki Maruyama
Mie University, JAPAN

Prof. Dr. Takeshi Asai
University of Tsukuba, JAPAN

Prof. Dr. Arun S. Mujumdar
Hong Kong University of Science & Technology, HONG KONG

Prof. Dr. Seokwoo Jeon
KAIST, REPUBLIC OF KOREA

Assoc. Prof. Dr. Elmi Abu Bakar
Universiti Sains Malaysia, MALAYSIA

Prof. Dr. Pham Tuan Anh
Ho Chi Minh City University of Technology, VIETNAM

Assoc. Prof. Dr. lman K. Reksowardojo
Institute of Technology, Bandung, INDONESIA

Prof. Dr. Le Anh Tuan
Hanoi University of Science and Technology, VIETNAM

Prof. Dr. Ocktaeck Lim
University of Ulsan, REPUBLIC OF KOREA

Dr. Huynh Thanh Cong
Ho Chi Minh City University of Technology, VIETNAM

Prof. Dr. Hendri Syamsudin
Institut Teknologi Bandung, INDONESIA

Assoc. Prof. Dr. Pham Huu Tuyen
Hanoi University of Science and Technology, VIETNAM

Prof. Dr. Hironori Saitoh
Sojo University, JAPAN

Prof. Dr. Jau-Huai Lu
National Chung Hsing University, TAIWAN

Ybhg. Prof Ir. Dr. Mohd Khairol Anuar bin Mohd Ariffin
University Putra Malaysia, MALAYSIA

Dr. Ong Hwai Chyuan
University of Malaysia, MALAYSIA

Prof. Dr. Younho Cho
Pusan National University, REPUBLIC OF KOREA

Prof. Dr. Park, Chan IL
Gangneung-Wonju National University, REPUBLIC OF KOREA

Prof. Dr. Chisachi Kato
JSME, JAPAN

Prof. Dr. Shuichiro Hirai
Tokyo Institute of Technology, JAPAN

Local Scientific Committee

Prof. Dr. Sumrerng Jugjai
King Mongkut's University of Technology Thonburi - Alternative Energy and Combustion (AEC)

Gp. Capt. Prof. Dr. Prasatporn Wongkamchang
Navaminda Kasatriyadhiraj Royal Air Force Academy - Automotive, Aerospace and Marine Engineering (AME)

Assoc. Prof. Dr. Vitoon Uthaisangsuk
King Mongkut's University of Technology Thonburi - Applied Mechanics, Materials and Manufacturing (AMM)

Prof. Dr. Phadungsak Rattanadecho
Thammasat University - Computation and Simulation Techniques (CST)

Prof. Dr. Suwat Kuntanapreeda
King Mongkut's University of Technology North Bangkok - Dynamic Systems, Robotics and Controls (DRC)

Assoc. Prof. Dr. Jackrit Suthakorn
Mahidol University - Biomechanics and Bioengineering (BME)

Prof. Dr. Jaruwat Charoensuk
King Mongkut's Institute of Technology Ladkrabang - Energy Technology and Management (ETM)

Prof. Dr. Somchai Wongwises
King Mongkut's University of Technology Thonburi - Thermal System and Fluid Mechanic (TSF)

Prof. Dr. Kulachate Pianthong
Ubon Ratchathani University - Engineering Education (EDU)

Thai Society of Mechanical Engineers (TSME) Organizing Committee

Assoc. Prof. Dr. Worawut Wisutmethangoon	Senior Advisor
Assoc. Prof. Dr. Withaya Yongchareon	Senior Advisor
Prof. Dr. Sumrerng Jugjai	Senior Advisor
Asst. Prof. Dr. Chinda Charoenphonphanich	Senior Advisor
Prof. Dr. Phadungsak Rattanadecho	Senior Advisor
Manit Koothanapath	Advisor
Yuthana Charoenwong	Advisor
Dr. Payung Sukdasawit	Advisor
Apichit Lumlertpongpana	Advisor
Assoc. Prof. Dr. Yossapong Laoonual	Advisor
Assoc. Prof. Dr. Pongpan Kaewtatip	Advisor
Assoc. Prof. Dr. Perapong Tekasakul	Advisor
Jiraboon Vityakraisign	Advisor
Maj. Gen. Chukiat Chuaypetch	Advisor
Tinakon Pongluxna	Advisor
Dr. Samroeng Netpu	Advisor
Prof. Dr. Kulachate Pianthong	President
Prof. Dr. Jaruwat Charoensuk	Vice President
Prof. Dr. Smith Eiamsa-ard	Vice President
Asst. Prof. Dr. Pornthip Keangin	Secretary
Asst. Prof. Dr. Warakom Nerdnoi	Treasurer
Asst. Prof. Dr. Nattadon Pannucharoenwong	Receptionist
Assoc. Prof. Dr. Preechar Karin	Registrar
Dr. Montana Rungsiyopas	Public Relations
Assoc. Prof. Dr. Kanit Wattanavichien	Committee
A.M. Prof. Dr. Noppol Hanklar	Committee
Prof. Dr. Tanakorn Wongwuttanasatian	Committee
Assoc. Prof. Dr. Amornrat Kaewpradap	Committee
Dr. Taperit Thongshoob	Committee
Assoc. Prof. Dr. Anchasa Pramuanjaroenkij	Committee
Asst. Prof. Dr. Wirachai Roynarin	Committee
Dr. Nuwong Chollacoop	Committee
Asst. Dr. Sarawoot Watechagit	Committee
Asst. Dr. Pichet Ninduangdee	Committee
Sayan Pansang	Committee
Dr. Somsit Moonsatan	Committee

Local (Chiang Mai University) Organizing Committee

Asst. Prof. Dr. Pinyo Puangmali	Conference Chair
Prof. Dr. Matthew Owen Thomas Cole	Conference Advisor
Prof. Dr. Nakorn Tippayawong	Conference Advisor
Assoc. Prof. Dr. Niti Kammuang-lue	Conference Secretary
Prof. Dr. Pradit Terdtoon	Committee
Prof. Dr. Radom Pongvuthithum	Committee
Prof. Dr. Tanongkiat Kiatsiriroat	Committee
Assoc. Prof. Dr. Aree Achariyaviriya	Committee
Assoc. Prof. Dr. Attakorn Asanakham	Committee
Assoc. Prof. Dr. Ittichai Preechawuttipong	Committee
Assoc. Prof. Dr. James Christopher Moran	Committee
Assoc. Prof. Dr. Konlayutt Punyawudho	Committee
Assoc. Prof. Dr. Phrut Sakulchangsatjatai	Committee
Assoc. Prof. Dr. Siva Achariyaviriya	Committee
Assoc. Prof. Dr. Theeraphong Wongratanaphisan	Committee
Assoc. Prof. Dr. Thongchai Fongsamootr	Committee
Assoc. Prof. Dr. Thoranis Deethayat	Committee
Assoc. Prof. Dr. Watchapon Rojanaratanangkule	Committee
Assoc. Prof. Dr. Woradej Manosroi	Committee
Assoc. Prof. Wongkot Wongsapai	Committee
Asst. Prof. Dr. Anucha Promwungkwa	Committee
Asst. Prof. Dr. Anusan Permsuwan	Committee
Asst. Prof. Dr. Arpiruk Hokpunna	Committee
Asst. Prof. Dr. Chaiy Rungsiyakull	Committee
Asst. Prof. Dr. Chakkapong Chamroon	Committee
Asst. Prof. Dr. Chatchawan Chaichana	Committee
Asst. Prof. Dr. Damorn Bundhurat	Committee
Asst. Prof. Dr. Det Damrongsak	Committee
Asst. Prof. Dr. Kengkamon Wiratkasem	Committee
Asst. Prof. Dr. Kodkwan Namsanguan	Committee
Asst. Prof. Dr. Mana Saedan	Committee
Asst. Prof. Dr. Nat Vorayos	Committee
Asst. Prof. Dr. Natanee Vorayos	Committee
Asst. Prof. Dr. Nattawit Promma	Committee
Asst. Prof. Dr. Nattawut Neamsorn	Committee
Asst. Prof. Dr. Pana Suttakul	Committee
Asst. Prof. Dr. Patraporn Kamonpet	Committee
Asst. Prof. Dr. Pawarut Jongchansitto	Committee
Asst. Prof. Dr. Pruk Aggarangsi	Committee
Asst. Prof. Dr. Somchai Pattana	Committee
Asst. Prof. Dr. Wetchayan Rangsri	Committee
Asst. Prof. Dr. Viboon Changrue	Committee
Asst. Prof. Dr. Watcharapong Tachajapong	Committee
Asst. Prof. Dr. Yottana Khunatorn	Committee
Asst. Prof. Dr. Yuttana Mona	Committee
Dr. Kanya Rattanamongkhonkun	Committee
Dr. Krit Sujarittham	Committee
Dr. Faifan Tantakitti	Committee
Dr. Napassawan Khammayom	Committee
Dr. Ramnarong Wanison	Committee
Mr. Kajorndej Phimphilai	Committee

Keynote Speaker

Speaker: Emeritus Prof. Masanori Monde

Affiliation: Saga University, Japan

Title: Physical Model of Hydrogen Storage Tank During Fueling and Its Concerned Safety Standards

Abstract:

Hydrogen is attracting attention as a next-generation energy source from the perspective of global warming prevention. Hydrogen-powered vehicles, called fuel cell electric vehicles (FCEVs) has been rapidly developed by an improvement of fuel cell performance. For example, a small passenger car requires about 6 kg of hydrogen to drive 600 km.

In order to safely fill the 6-kg tank of FCEVs with hydrogen in about three minutes, we have to follow a safety regulation, called SAE 2601. According to the regulation, hydrogen is filled under the condition that a pressure and also a temperature for hydrogen in the tank should be not beyond 87.5 MPa and 85 degrees Celsius during the hydrogen filling. This regulation has been established based on a thermal analysis for the hydrogen as well as on the measured pressure and temperature during filling. This presentation deals with the concept and procedure of thermal analysis and explains the safe filling criteria.

The energy characteristics of electric vehicles (BEVs), fuel cell electric vehicles (FCEVs) and hybrid electric vehicles (HEVs) as a drive source for transportation vehicles are discussed from a thermal engineering viewpoint and the results are reported.

Biography:

1976, March	Graduate of doctor course of the University of Tokyo, Department of Mechanical Engineering
1989, April	Professor, Dept. of Mechanical Engineering, Saga University
2014, April	Emeritus Professor, Saga University
2014, April	Project Professor, Kyushu University
2015, October	Vice President, Saga University
2017, October	Project Professor, Saga University, and Guest Professor, Kyushu University
2007:	Head of Thermal Engineering Division in Japan Society of Mechanical Engineers
2009:	Scientific council member of International Center of Heat and Mass Transfer (ICHMT)
2008:	Associate Member of Science Council of Japan
2012:	President of Heat Transfer Society of Japan
2005, May	Scientific Paper Award from Japan Society of Refrigerating and Air Conditioning
1978, April	The Best Paper Award from Japan Society of Mechanical Engineers
2005, November	The 2005 Best Paper Award from Heat Transfer Division in ASME
2007, May	Scientific Paper Award from Heat Transfer Society of Japan
2009, May	Scientific Contribution Award from Japan Society of Mechanical Engineers
2016, May	Long-term Contribution Award from Japan Society of Mechanical Engineers

Keynote Speaker

Speaker: Prof. Dong-Gyu Ahn

Affiliation: Chosun University, Korea

Title: Remanufacturing Methodology of Mechanical Parts Using Metal Additive Manufacturing

Abstract:

Recently, interest on remanufacturing of end-of-life (EOL) products has greatly increased as green and circulation technologies to cope with environmental issues and resource depletion. A metal additive manufacturing (MAM) process has been widely used for remanufacturing of mechanical parts. The aim of this presentation is to investigate the remanufacturing methodology of mechanical parts using the MAM process. The design method of the substrate and the deposited region, including failure mode analysis of the damaged region, functional decomposition of the geometry, the control of the deposited volume, etc., is proposed for remanufacturing. Concerning particulars for the deposition and the post-processing are investigated to improve thermo-mechanical characteristics and quality of the remanufactured parts. Several case studies are performed for remanufacturing of mechanical parts. Finally, the applicability of the proposed methodology is discussed using the results of case studies.

Biography:

Dong-Gyu Ahn received his B.S. degree from the Pusan National University, Korea in 1992. He then received his M.S. and Ph.D. degrees from KAIST, Korea in 1994 and 2002, respectively. Prof. Ahn is currently a Professor at the Department of Mechanical Engineering, Chosun University, Korea. He is serving as he is serving as vice president of the KSME, vice president of the KSMPE, director of KSTP (Korean Society of Technology of Plasticity), associate member of CIRP (The International Academy for Production Engineering), chair of ICMDT2017 (International Conference on Machine Tool, Design & Tribology), chair of ICD3DP2023 (International Conference on Design for 3D Printing), etc. In addition, he is serving as senior editor of IJPEM-GT (International Journal of Precision Engineering and Manufacturing-Green Technology), editor in chief of JKSMPE (Journal of Korean Society of Manufacturing Process Engineers), editorial board of IJPEM (International Journal of Precision Engineering and Manufacturing), editor of TKSME (Transaction of The Korean Society of Mechanical Engineers), etc. Prof. Ahn's research interests include development and application of additive manufacturing technologies, rapid manufacturing, lightweight structure, forming technology, and mold & die.

Keynote Speaker

Speaker: Prof. Dr. Matthew O.T. Cole

Affiliation: Department of Mechanical Engineering,
Chiang Mai University, Thailand

Title: Electromagnetic Actuation: New Possibilities
Through Materials and Topologies

Abstract:

This presentation will examine some of the core challenges in the design and development of electromagnetic (EM) actuation systems for machine motion control. Continued growth in applications is driving research to improve power, efficiency, versatility, and precision of EM actuators. Starting from a review of basic operating principles, the fundamental roles of topology and material selection in EM actuator design will be explored. Examples will be shown from recent research, focusing mainly on active magnetic bearing design and applications. The talk will also examine some interesting new applications of smart materials to create electromagnetic actuators with unique properties.

Biography:

Matthew Cole graduated from the University of Cambridge, U.K. in 1994 with an M.A. degree in Natural Sciences. He then studied for M.Sc. and Ph.D. degrees in Mechanical Engineering at the University of Bath, U.K. In 2003 he joined the faculty of the Department of Mechanical Engineering at Chiang Mai University, becoming a full Professor in 2017. His research work started in the field of active magnetic bearings and rotor vibration control problems and has since expanded to consider various problems in the dynamics and control of machine systems, including rotating machinery, high precision robots, and smart vibration control systems. He has published over 100 peer-reviewed articles and conference papers on related topics. He is a twice recipient of the Thomas Bernard Hall Prize from the Institute of Mechanical Engineers (IMechE) for his research on active control of rotor vibration. He has served on the board of editors for the IMechE Journal of Systems and Control Engineering and currently acts as an Associate Editor.

Keynote Speaker

Speaker: Dr. Kirkpong Kiatpanichagij, D. Eng. (Mechatronics)

Affiliation: Research and Development Department, DEXON Technology Public Company Limited, Thailand

Title: The Development of Inline Inspection Tools (ILIs) in Thailand

Abstract:

Pipelines are the critical infrastructures in oil and gas transportation. To maintain their integrities, they regularly require inspection by equipment named inline inspection tools (ILIs). The ILIs use non-destructive testing techniques (NDT) to assess the pipelines status. Additionally, there are a number of engineering fields used for designing and constructing ILIs, i.e., electronics, firmware, software, mechanical design, industrial engineer, machining, and reliability testing.

Dexon technology PCL is a sole Thai company, who designs and produces the ILIs in Thailand and uses them to provide worldwide inspection services. The presentation will detail the development of ILIs in Thailand. It will introduce the ILIs, the NDT techniques deployed in each ILIs types, their use cases, and their limitations. Then, specific knowledge and resources for developing them will be provided. Finally, on-going research directions will be discussed.

Biography:

Dr. Kirkpong Kiatpanichagij is currently the director of research and development department at Dexon Technology Thailand. He leads development of inline inspection tools, i.e., ultra sonics testing (UT), magnetics flux leakages (MFL), Caliper, inertia measurement unit (IMU), and crack sizing (CS). He received a doctoral degree in mechatronics in 2009. During 2009-May 2012, he served in research role as a postdoctoral fellow in image analysis at Planetary and Space Science Centre, PASSC, Canada. He joined DEXON Technology Public Company Limited in May 2012.

Invited Presentation

Speaker:
Prof. Dr. Ashwani K. Gupta
Department of Mechanical Engineering, University of Maryland, College Park, USA

Title: Effect of Spent FCC Catalyst on CO2 Assisted Gasification of Pinewood

Abstract:

This research examines the synergistic effects of using CO_2, spent fluid cracking catalyst (sFCC), and pinewood wastes for energy and chemicals production. The effect of utilizing sFCC catalysts on syngas yield, quality, and energy is examined during pyrolysis and CO_2-assisted gasification of pine wood. In catalytic CO_2-assisted gasification, the influence of catalyst position (in-situ and quasi-situ catalytic modes) and temperature was also investigated. The results showed that the presence of spent sFCC catalysts increased the syngas and energy yields. Catalytic pyrolysis increased the overall syngas yield by 35% compared to non-catalytic pyrolysis. The CO_2-assisted gasification provided more syngas than pyrolysis. The CO_2-assisted gasification increased the overall syngas yield by 74% and 125% compared to catalytic and non-catalytic pyrolysis, respectively. A comparison of quasi-in-situ gasification to in-situ catalytic gasification showed that quasi-in-situ gasification increased syngas yield and energy yields by 21% and 22%, respectively, which implies that quasi-in-situ catalytic gasification is more efficient and effective at increasing the syngas yield and also provided energy recovery as high as 21.5 $MJ/kg_{feedstock}$.

Invited Presentation

Speakers:
Prof. Dr.-Ing. Heinz Peter Berg[1] and
Prof. Dr.-Ing. Roland Dückershoff[2]
[1]Brandenburg University of Technology Cottbus-Senftenberg, Germany
[2]University of Applied Sciences Mittelhessen, Germany

Title: Highly Effective Conversion of Green Ammonia to Electricity in TURBO Fuel Cell Systems (MGT-SOFC) for the Future Transportation Sector with a Focus on Marine Applications

Presented Paper: ETM0027

Abstract:

The term "TURBO Fuel Cell (TFC)" was used to describe a very compact and highly efficient MGT-SOFC hybrid system in 2017 (by Berg et.al.) and validated in further research projects. The system is a recuperated micro gas turbine (MGT) process with an embedded solid oxide fuel cell (SOFC) subsystem with high temperature (HEX) and redox heat exchanger. For the ammonia fuel supply, the redox heat exchanger consists of a post-oxidation module with integrated heat exchange to the cracker. In the oxidation module, the anode exhaust gas is reacted exothermically with the oxygen from the cathode exhaust gas of the SOFC. The heat from the fuel cell and from this after-reaction is used for the endothermic cracking process. Due to the high temperature, the catalyst and the nickel network on the anode side, there are ideal conditions for ammonia splitting. Furthermore, with the same design and the addition of a steam generator, carbon-based hydrogen derivatives (such as methane, methanol) can also be converted into electricity with the same high degree of efficiency. This presentation describes the high heat integration effect of the turbo fuel cell design and the thermodynamic background. Electrical efficiencies of over 70% and the high-power density clearly show the advantages of pressurized charging over atmospheric SOFC systems. Due to its very compact design, the TFC system can compete with conventional diesel engines in terms of size. The technology makes sense when using green ammonia and other green fuels. In addition, with further adaptation and weight reduction of the SOFC cells, TURBO Fuel Cell technology will be very important as a future alternative drive-in mobility.

Conference Program

12 December 2023

Time	Grand Nanta 1
14.00 – 17.00	Registration

13 December 2023

Time	Grand Nanta 1-2
08.00 – 09.00	Registration
09.00 – 09.15	Video Presentations and Introduction to TSME-ICoME 2023 Head of Mechanical Engineering Department, CMU
09.15 – 09.20	Welcoming Speech Vice President of Chiang Mai University (CMU)
09.20 – 09.35	Opening Remarks President of Thai Society of Mechanical Engineers (TSME) and Guests of Honor
09.35 – 09.40	Opening Ceremony and Photo Session
09.40 – 10.00	Coffee Break
10.00 – 10.30	Keynote Emeritus Prof. Masanori Monde
10.30 – 11.00	Keynote Prof. Dong-Gyu Ahn
11.00 – 11.30	Keynote Prof. Dr. Matthew O.T. Cole
11.30 – 12.00	Keynote Dr. Kirkpong Kiatpanichagij
12.00 – 13.30	Lunch
13.30 – 14.00	Invited Presentation Prof. Dr. Ashwani K. Gupta
14.00 – 14.30	Invited Presentation Prof. Dr.-Ing. Heinz Peter Berg and Prof. Dr.-Ing. Roland Dückershoff
14.30 – 14.50	Coffee Break

13 December 2023

Time	Grand Nanta 1-2	Grand Nanta 3	Grand Nanta 4	Mengrai 1	Mengrai 2	Mengrai 3
14.50 – 15.10	TSF0033	AEC0001	AME0001	ETM0006	AMM0008	CST0009
15.10 – 15.30	TSF0031	AEC0002	AME0010	ETM0005	AMM0021	CST0007
15.30 – 15.50	TSF0014	AEC0003	AME0007	ETM0004	AMM0010	CST0011
15.50 – 16.10	TSF0012	AEC0012	AME0005	ETM0001	AMM0006	CST0014
16.10 – 16.30	TSF0023	AEC0005	AME0011	ETM0011	AMM0005	CST0019
16.30 – 16.50	TSF0022	AEC0007		ETM0013	AMM0004	
16.50 – 17.00	Break					
17.00 – 18.00	TSME Committee Meeting					

14 December 2023

Time	Grand Nanta 1	Grand Nanta 2	Grand Nanta 3	Grand Nanta 4	Mengrai 1	Mengrai 2
09.00 – 09.20	TSF0010	AEC0006	AME0013	ETM0010	AMM0020	DRC0010
09.20 – 09.40	TSF0001	AEC0013	AME0003	ETM0021	AMM0019	DRC0008
09.40 – 10.00	TSF0026	AEC0011	AME0002	ETM0016	AMM0007	DRC0001
10.00 – 10.20	TSF0021	CST0015	AME0019	ETM0007	AMM0001	DRC0009
10.20 – 10.40	Coffee Break					
10.40 – 11.00	TSF0007	AEC0004	AME0020	ETM0018	AMM0014	DRC0004
11.00 – 11.20	TSF0013	AEC0008	AME0022	ETM0015	AMM0009	DRC0006
11.20 – 11.40	TSF0024	TSF0030	AME0017	CST0018	AMM0017	DRC0003
11.40 – 12.00	TSF0011	EDU0001	CST0012	CST0006	AMM0016	DRC0005
12.00 – 13.00	Lunch					
13.00 – 13.20	TSF0009	AEC0010	AME0009	ETM0012	AMM0011	BME0001
13.20 – 13.40	TSF0028	AEC0015	AME0008	ETM0017	AMM0012	BME0010
13.40 – 14.00	TSF0025	AEC0016	AME0021	ETM0002	AMM0013	BME0003
14.00 – 14.20	TSF0018	AEC0009	AME0004	ETM0025	AMM0018	BME0002
14.20 – 14.40	TSF0032	AEC0018	ETM0026	ETM0009		CST0002
14.40 – 15.00	Coffee Break					
15.00 – 15.20	TSF0004	TSF0016	AME0006	ETM0019	CST0008	BME0009
15.20 – 15.40	TSF0006	TSF0015	AME0016	ETM0020	CST0003	BME0008
15.40 – 16.00	TSF0005	TSF0027	AME0024	ETM0022	CST0004	BME0007
16.00 – 16.20	TSF0003	TSF0029	AME0014	ETM0023	CST0010	BME0004
16.20 – 16.40	TSF0017	TSF0008		ETM0024	CST0016	BME0006
16.40 – 17.00	Break					
17.00 – 18.00	TSME Meeting					
18.00 – 22.00	Conference Banquet					

15 December 2023

Time	Grand Nanta 1	Grand Nanta 2	Grand Nanta 3	Grand Nanta 4	Mengrai 1	Mengrai 2
09.00 – 09.20	TSF0002	AEC0019	AME0012	AMM0015	CST0005	DRC0002
09.20 – 09.40	TSF0019	AEC0017	AME0015	AMM0002	CST0001	DRC0007
09.40 – 10.00	TSF0020	AEC0014	AME0023	AMM0022	CST0013	BME0005
10.00 – 10.20	ETM0003					
10.20 – 10.40	ETM0014					
10.40 – 11.00	ETM0008					
11.00 – 11.20	Coffee Break					
Time	**Grand Nanta 1**					
11.20 – 12.00	Best Paper Awards and Closing Ceremony					
12.00 – 13.00	Lunch					

List of Presentations

Alternative Energy and Combustion (AEC)

AEC0001	Predicting Biocrude Oil Yields from Hydrothermal Liquefaction of an Energy Grass: Machine Learning Approach and Experimental Validation T Katongtung and N Tippayawong
AEC0002	Environmental Impact and Sustainable Solutions for Broiler Farming: A Case Study in Northern Thailand H M S Bandara and C Chaichana
AEC0003	Design, Make and Preliminary Testing of a High Throughput Ablative Pyrolysis Reactor for Biomass and Agro-Residues N Khuenkaeo and N Tippayawong
AEC0004	Densification of Water Hyacinth for Pellet Fuel Production P Prasertpong, N Chamhom, P Punnarapong, and P Sittisun
AEC0005	Experimental Study on the Explosion Intensity of Lithium-Ion Batteries in Air and Helium Environments G Phanomai, K Phanomai, K Tassananakajit, S Wongwises, and P Trinuruk
AEC0006	Experimental Investigation on the Optimal Frequency for Acoustic Fire Extinguishing in Different Duct Configurations F Awae, P Chareonmark, P Tapanapongpan, S Wongwises, and P Trinuruk
AEC0007	Biogas Purification Kit and Combustion Characteristic Study Results W Nawae, P Solod, T Petdee, T Naemsai, J Jareanjit, and W Suksuwan
AEC0008	Thermal Efficiency and Economic Analysis of Biomass Boiler Using Cylindrical Sawdust Stove as Heat Source P Tompat, K Pianthong, and J Dincherdchu
AEC0009	Enlargement of Inverse Diffusion Flame Burner with Thermal Analysis on Similarity Numerical Model C Chantang and A Kaewpradap
AEC0010	Development of Fuel Injection System for Low and Zero Carbon Fuels in the 1 MW 4-Stroke Marine Engine Y Woo, J Jang, A-H Ko, Y Jung, Y D Pyo, G Moon, D Kim, J Seo, and K Kim
AEC0011	In-Depth Analysis of Municipal Solid Waste's Higher Heating Value (HHV) for Green and Clean Renewable Energy in the context of Way of Live K Laohalidanond, T Wiangthong, and S Kerdsuwan
AEC0012	Fe-Co Bimetallic Electrocatalysts Atomically Dispersed on Zeolitic Imidazolate Framework (ZIFs) to Enhance Oxygen Reduction Reaction Activity N Jongmanwattana, Y-S Chen, and K Punyawudho
AEC0013	Experimental Investigation on Tar Generation from Softwood and Hardwood under Thermochemical Conversion Processes S S Hla, A Youngdee, C Chaichana, and D Roberts
AEC0014	Topology Optimization of Anode Catalyst Layer for Polymer Electrolyte Membrane Water Electrolyzers Considering Effect of Gas Coverage P Passakornjaras, P Orncompa, M Alizadeh, T Suzuki, S Tsushima, and P Charoen-amornkitt
AEC0015	Bio-diesel Fuel Synthesis using Clamshell as Ecofriendly Catalyst Y Jiang, J Liang, and N Zhu
AEC0016	Hydrogen Generation based on Sodium Borohydride and Citric Acid Reactions and Engine Applications Y Takeuchi, N Zhu, K Amano, and K Fukuda
AEC0017	Electric Car Conversion of Small Pickup Truck; Engineering Process and Test Results P Krachang and P Aggarangsi

AEC0018	Impact of Biodiesel Fuel on a Light-Duty Diesel Vehicle Particle Emissions and Thermal Efficiency S K J R Aung, W Phairote, P Karin, M Srilomsak, S Srimanosaowapak, H Kosaka, and C Charoenphonphanich
AEC0019	Impact of Partial-Flow Particulate Filter on Emissions from a Light-Duty Diesel Vehicle H Q Dang, P Karin, P T Cosh, P Thaeviriyakul, P Kummul, S Srimanosaowapak, H Kosaka, and M Srilomsak

Automotive, Aerospace, and Marine Engineering (AME)

AME0001	Vision-Assisted Multirotor Landing on a Moving Target J Pravitra, P Moonsri, Y Chaonafang, C Reunpakdan, and J Moudpoklang
AME0002	Flight Test Stall Analysis of a Light Amphibious Airplane with NACA 2412 Wing Airfoil S Chinvorarata, B Watjatrakul, P Nimdum, T Sangpet, and P Vallikule
AME0003	Fatigue Life Simulation of Automotive Aluminium Alloy Wheel Under Dynamic Cornering Load V Poungkom, U Pinsopon, and M Pimsarn
AME0004	Numerical Investigation on Vibration Characteristic for Composite Sandwich Structure with Bolted Joint Junction V Sripawadkul, M Suraratchai, and P Bunyawanichakul
AME0005	Study of Variable Operating Parameters Effect on PEMFC Performance P D Thao, V T Chau, N H Khan, S Mek, S Hirai, and L Visarn
AME0006	Effect of Debonding on Vibration Response of Honeycomb Sandwich Panel M Suraratchai, V Sripawadkul, and P Bunyawanichakul
AME0007	-
AME0008	Experimental Validation of Indoor Landing of Multicopter A Ruangwiset
AME0009	MRBDO of an Aircraft Wing Structure Using a Metaheuristic N Suratemeekul, N Kumkam, and S Sleesongsom
AME0010	Study on Vibration Characteristics of Airless Tire K Fujita, T Suzuki, T Okano, Y Washimi, K Sasaki, and T Tanimoto
AME0011	A Study on the Characteristics of Mixed Fuels in Diesel Engines J Jang, Y Woo, Y Shin, A Ko, Y Jung, C Cho, G Kim, and Y Pyo
AME0012	Efficiency Evaluation on Cooling Behaviour of Water-Cooling Jacket for Synchronous Reluctance Motor K H Nguyen, M Masomtob, B Kerdsup, S Karukanan, P Champa, T D Pham, S Hirai, C T Vo, P Kummool, and C Charoenphonphanich
AME0013	A Feasibility Study of Railway Power Swapping from Diesel-Electric Propulsion to Pure-Electric Propulsion in Urban Areas T Tantitamthiti and M Sooklamai
AME0014	Study Self-Cleaning Air Condition System in Toyota Vios 1.5E (2010) W Tinsuwan, T Boonset, N Pannucharoenwong, S Echaroj, S Vongpradubchai, S Hemathulin, and P Boontatao
AME0015	Rolling Resistance Evaluation of Non-pneumatic Tire with Linked Zig-zag Structure using Scale Model T Suzuki, T Okano, Y Washimi, K Sasaki, T Tanimoto, K Fujita, K Yokoyama, K Ushijima
AME0016	Efficiency and Control: Modelling and Validation of an Electric Fan Bus Cooling System A Kosin, A Kosiyanurak, T Sri-on, N Pothi, and J Srisertpol
AME0017	Design of Battery Pack Enclosure Structure for Electric Conversion Vehicle S Intathumma, P Jongpradist, and S Kongwat

AME0018	-
AME0019	A Study on the Effects of using Different Biodiesel Blending Fractions on Tailpipe Emissions of Two Euro 5 Pickup Trucks S Naing, P Saisirirat, M Srilomsak, P Niyomna, P-P Ewphun, and N Chollacoop
AME0020	Design and Analysis of Lightweight Freight Wagon Structures According to the Standard of the State Railway of Thailand R Sulaimarn and M Sooklamai
AME0021	Precision Landing with Computer Vision C Thipyopas, W Leelawutprasert, N Thongton, W Laitrakun, K Faidetch, and E Sathitwattanasan
AME0022	Development of an Injector Spark Plug for the Injection and Ignition of Gaseous Fuels in Internal Combustion Engines for Use in Conventional Systems H P Berg, R Dückershoff, S Hertrampf, A Kloshek, and A Himmelberg
AME0023	Effect of Injection Frequency on Actual Fuel Injection Rate of Piezoelectric Diesel Fuel Injector J Boonjun and N Kammuang-lue
AME0024	Mathematical Model and Trim Analysis of an X-Wing Spinning Drone in Hover Using Numerical Optimisation N Tanman, D Anderson, and D Thomson

Applied Mechanics, Materials, and Manufacturing (AMM)

AMM0001	The Effect of CSLB on the Creep Behaviour of 316L Austenitic Stainless Steel S Kwankaomeng, J Kaew-on, and P Kansuwan
AMM0002	Study of Rolling Contact Fatigue Mechanism of ER9 and R260 Wheel/Rail Materials A Sukhom, T Talingthaisong, S Sucharitpwatskul, A Manonukul, and P Kansuwan
AMM0003	-
AMM0004	Evaluation of the Relationship Between Machine Learning Methods and AE Waveform Classification Accuracy K Togami and T Matsuo
AMM0005	Development of a Method for Evaluating Corrosion Defect by Acoustic Emission Signals using Machine Learning K Yamamoto and T Matsuo
AMM0006	Evaluation of the Initiation and Propagation Mechanisms of Corrosion under Coating Films Using Digital Image Correlation and Acoustic Emission Methods M Nara and T Matsuo
AMM0007	Experimental Investigation of Optimal Pressure Achieved through Rubber Foam Extension in the Curing Process T Naemsai, W Suksuwan, T Wissamitanan, and T Petdee
AMM0008	Sintered Steels with Improved Ductility Produced from Diffusion-Alloyed Powders A Z Myo, M Srilomsak, M Morakotjinda, T Yotkaew, N Tosangthum, P Wila, R Tongsri, and K Inaba
AMM0009	Comparison of Mechanical Properties Between Natural Rubber and Commercial Dairy Cow Hoof Blocks T Wissamitanan, T Namsai, A Sawatdiraksa, C Supapong, and T Petdee
AMM0010	Performance Analysis of an Electromechanical Air Purifier for Particulate Matter Removal in Large Rooms J Sukoum, J Laokawee, W Boonyung, A Yawooti, T Katongtung, and N Tippayawong
AMM0011	Development of an Effective Method for Cleaning Probes Used to Measure Microstructures Using Supersonic Flow S Beppu, H Murakami, A Katsuki, and T Sajima
AMM0012	Tool Condition Monitoring in Milling Using Sensor Fusion and Machine Learning Techniques Y Iwashita, H Murakami, A Katsuki, T Sajima, T Matsuda, and T Yoshizumi

AMM0013	Unsupervised Tool Wear Prediction Method Based on One-Class Support Vector Machine T Matsuda, H Murakami, A Katsuki, T Sajima, Y Iwashita, and T Yoshizumi
AMM0014	Design and Analysis of Shear Pin of Lever Arm in Generator Circuit Breaker Using Finite Element Method K Jaiyen and W Rangsri
AMM0015	Non-Destructive Estimation of Three-Dimensional Plastic Strain via Nonlinear Inverse Analysis Using Displacement S Fujii and M Ogawa
AMM0016	Investigate Stress on the Components of the Bolted Rail Joint by Considering the Effects of Bolt Preloading S K Le and J Wongsa-Ngam
AMM0017	A Study on the Effects of Chromium and Niobium Additions in Super-Alloyed Steel K Jewsuwun and P Surin
AMM0018	Investigation of Evaluation Indices for Bonding Strength of Healed Areas in Self-Healing Ceramics Using the Acoustic Emission Method T Agata, K Hasegawa, M Hiratsuka, and T Yanaseko
AMM0019	Investigation of Polarization Conditions of Metal Matrix Piezoelectric Composite with Surface Oxidized Metal Electrodes R Shirai and T Yanaseko
AMM0020	Development of Bending Fatigue Testing System for Endodontic Files T Kessaro, S Hiran-us, P Singhatanadgid, and S Morakul
AMM0021	Mixed-Mode I/III Fracture Toughness of Epoxy Resin Under Loading and Thickness Effects: An Artificial Intelligence Prediction Approach A Timtong, A Wiangkham, P Aengchuan, and A Ariyarit
AMM0022	Preliminary Study on 3D-Printed NR Latex in Fluid Media K Chansoda, C Suvanjumrat, P Wiroonpochit, T Kaewprakob, and W Chookaew

Computation and Simulation Techniques (CST)

CST0001	Parametric Study of Caudal Fin Shapes for Vortex-Induced Vibration (VIV) Energy Harvesting K Aueaiithiporn, K Daoweerakul, N Ratisen, P Chompamon, S Songschon, S Saimek, K Septham, and T Kamnerdtong
CST0002	CFD Analysis on the Performance of a DPI R F Al-Waked and T Abu Dahab
CST0003	Numerical and Experimental Investigations of the Impact of Nozzle Geometry on Performance of Impulse Hydro Turbines K Sakulphan, K Sengpanich, and T Tongshoob
CST0004	In-Situ and Near-Real Time of Shear Stress Measurement of Multiple Shear Stress Lab-on-Chip for Osteoblast Cell Cultivation Using Image Analysis W Chancharoen, J Aswakool, H H Aung, S Phetcharat, P Pothipan, A Moonwiriyakit, R Phatthanakkun, and T Jiemsakul
CST0005	Aerodynamics and Flow Characteristics of NACA0012 and 4412 with Cut-in Sinusoidal Trailing Edge Shape P Rattanasiri
CST0006	Decomposed Quadrilateral Finite Element for 2D Heat Transfer Analysis C Bhothikhun, K Sirisomboon, S Wasananon, T Sangsawang, and P Arromdee
CST0007	Multi-Objective Optimization of Lightweight Inboard Bearing Design for High-Speed Railway Axle T Nwe, A Tantrapiwat, and M Pimsarn
CST0008	Preventive Work and Health Monitoring for Technology by Cracks of Concrete Surface Using IR Camera and Resin Sensor N Shimoi, Y Yamauchi, K Nakasho, and C Cuadra

CST0009	Numerical Prediction of Evaporation Time Under Different Air Pressure Conditions by Discrete Phase Model P Charoenkitkaset, P Setaphram, M Saedan, A Hokpunna, W Manosroi, and W Tachajapong
CST0010	A CFD Validation Study of TNT Blasting in Unconfined Large Pipe Using LS-Dyna Program: An Overpressure Comparison N Prasitpuriprecha, S Namchatha, T Phengpom, J Priyadumkol, A Topa, C Suvanjamrat, and M Promtong
CST0011	Numerical Study of Impinging Slot Jet on Heating Surface for Heat Transfer Enhancement K Prajuntaboribal and C Plengsa-ard
CST0012	Comparison of Disc Brake Squeal between Ordinary and Drilled Brake Discs Using Finite Element Method A Sodsong, C Suphawimol, and R Kittipichai
CST0013	Redesign of the Mini Hydro Turbine Structure using Finite Element Analysis to Solve Resonance Problem P Sreejai, A Promwungkwa, and K Ngamsanroaj
CST0014	Bluff Body Design for Vortex-Induced Vibration Energy Harvesting N Jankul, S Supatheerawong, S Yaiboontham, P Chompamon, S Songschon, S Saimek, K Septham, and T Kamnerdtong
CST0015	The Heat Distribution Modeling on Solar Panels to Develop Cooling Methods W Borisut, C Pedchote, P Kunyoo, S Keawleam, and P Thawonsatid
CST0016	Acoustic Noise Reduction Using a Set of Circular Arc Splitter Plates P Pagdisongkram, J Tunkeaw, and W Rojanaratanangkule
CST0017	-
CST0018	Numerical Study of the Influence of Rotational Speeds on Microwave Heating Process in Rotating Centella Asiatica Porous Domains Using Moving Mesh Technique P Chawengwanicha1, P Rattanadecho, and P Keangin
CST0019	Design of UV-C Disinfection in Minibus P Keangin, P Chawengwanicha, S Somya, K Kongsri, and P Thonghom

Dynamic Systems, Robotics, and Controls (DRC)

DRC0001	Development of Four-Wheel Drive Skid-Steered Mobile Robot for Automated Hammering Inspection G Lee, K Hirae, and C Li
DRC0002	Nonlinear Motion Analysis of New Electromagnetic Vibration Actuator H Yaguchi and R Sato
DRC0003	Semantic Mapping and Voice User Interface based on ORB-SLAM and YOLO for navigating visually impaired person Q Wang, Y Shikanai, K Mima, and K Tobita
DRC0004	Dynamic Stability Analysis and Experiments of Self-Excited Vibration in a Flow Dynamics Conveying Machine M Takeda, Y Sugawara, and M Watanabe
DRC0005	Autonomous Navigation Without Sway for Overhead Crane Through Warehouse Management System Integration T Chunang, N Paomongkhon, A Yimyeam, N Suksabai, and I Chuckpaiwong
DRC0006	System Parametric Study of Hunting Motion Stability of a Two-Axle Railway Bogie on Straight Track Via Hopf Bifurcation Analysis T Sritrakul, N Depaiwa, and M Pimsarn
DRC0007	Measurement of Natural Vibration of Multi-Degree-of-Freedom System with Large Damping by Multi-Point Excitation Using Local Feedback Control T Tanaka, H Nakao, and Y Oura

DRC0008	Investigating Adaptive CPG-based Control of a Snake Robot with Switch Signal Input for Maneuvering in Varying Environments P Ngamkajornwiwat and N Pothita
DRC0009	Improving Workspace Interactions: A New Approach for Displaying Robot Path Planning in Shared Environments S Ruito and M Daigo
DRC0010	Development of Force Feedback System for a Virtual Tank Driving Simulator K Yaovaja, A Somboonchairot, B Wongchai, S Damyot, and S Jitpakdeebodin

Biomechanics and Bioengineering (BME)

BME0001	Design of Dynamic Stabilization System with Stiffness Similar to Normal Discs by Topology Optimization N Lertviriyachit, P Tangpornprasert, and C Virulsri
BME0002	Virtual Reality-Based Rehabilitation for Children with Cerebral Palsy J Ma'touq, J Sweiss, N Alnuman, I Abuzer, and M Sabieleish
BME0003	Development of Dynamic Prosthetic Foot for Moderate Active Amputees Using Parametric Optimization P Piwat, P Tangpornprasert, and C Virulsri
BME0004	Double-Plate Arrayed EWOD Lab-on-a-Chip Platform for DNA Sequencing by LAMP Method A Sangketdee, N Sikongplee, C Dhanaporn, and W Wechsatol
BME0005	Effect of Curved Root Canal on Torsional Shear Stress of NiTi Rotary Files P Tomeboon, S Hiran-us, S Morakul, and P Singhatanadgid
BME0006	Vibration of Degraded Human Knee Joint: Model and Simulation N Ajavakom and P Varopichetsan
BME0007	The Effect of Porous Stemmed Hip Prosthesis on Thai Femur, Compared with General Stemmed Hip Prosthesis, Using Finite Element Analysis N Rattanapan, S Thongkom, K Aroonjarattham, P Aroonjarattham, and C Somtua
BME0008	Static Bending Test of a Carbon Fiber Posterior Leaf Spring Ankle Foot Orthoses (PLS-AFOs) P Akarasereenont and A Wisessint
BME0009	A Study of the Design Parameters of Supporting Rods for Posterior Leaf Spring Ankle Foot Orthosis (PLS-AFO) P Sirilaophaisal and A Wisessint
BME0010	Design and Development of Isokinetic Exercise Machines for the Elderly: Elliptical Recumbent N Mayang and B Rungroungdouyboon

Energy Technology and Management (ETM)

ETM0001	Thermo-Hydraulic Performance of Heat Exchanger Tube Inserted with Curved-Wing Tape Vortex Generators N Koolnapadol, P Promvonge, P Promthaisong, P Hoonpong, C Khanoknaiyakarn, S Gururatana, and S Skullong
ETM0002	Experiment and Model of PV Module with Evaporative Cooling for Hybrid Power Generation and Distilled Water Production T Chea, A Asanakham, T Deethayat, and T Kiatsiriroat
ETM0003	Energy Consumption of Climate Control System for Bamboo Moth Mating T Maneerat, Y Mona, C Chaichana, and N Borirak
ETM0004	Experimental and Evaluation of Local Air Temperature and Heat Transfer of a Serpentine Copper Pipe Heat Exchanger N Khammayom, N Maruyama, and C Chaichana

ETM0005	A Study of Microclimate Designation in Near Equatorial Climate Condition: A Case Study in University Building E Sangthammarat and C Chutakositkanon
ETM0006	Comparison Study of Building Energy Consumption in Near Equatorial Climate Condition: A Simulation Case E Sangthammarat and C Chutakositkanon
ETM0007	Leveraging Flow Battery Technology: A Sustainable Solution for Green Energy Storage in PTTEP T Thamma, S Anantasate, J Jaiyen, A Liangbenjaponkul, P Trinuruk, N Wongyao, P Charoen-amornkitt, P Jenyongsak, and M Makaramani
ETM0008	Comparative Analysis of Energy Consumption in Semi-Autonomous Vehicles: The Influence of Adaptive Cruise Control across Various Powertrains W Achariyaviriya, K Janpoom, R Wanison, Y Mona, W Wongsapai, N Kammuang-lue, and P Suttakul
ETM0009	Parametric Study of Induction Heating System for Hot-air Generator Application P Wongphetsakun, A Kaewpradap, and W Onreabrooy
ETM0010	Understanding of Biosolids Transformation under Pyrolysis and Gasification Conditions S S Hla, A Ilyushechkin, N Sujarittam, and C Chaichana
ETM0011	Controllable Particle Sizes of Spherical Carbon from Resorcinol-Formaldehyde as Supported Materials L Intakhuen, A Siyasukh, C-Y Chen, and K Punyawudho
ETM0012	An Alternative Approach for Determining Charge Storage Mechanisms of Supercapacitors Using Sinusoidal Potential Scan W Pholauyphon, K Nantasaksiri, T Suzuki, S Tsushima, and P Charoen-amornkitt
ETM0013	Powertrain Modeling and Implementation of Energy Management Strategy for Plug-in Hybrid Motorcycle S Lin, P Karin, M Yamakita, B Kerdsup, P Saisirirat, and M Masomtob
ETM0014	A Comparative Study of Lithium-Ion and Sodium-ion Batteries after Flash Cryogenic Freezing R Wanison, K Punyawudho, P Sakulchangsatjatai, N Kammuang-lue, P Terdtoon, C Chaichana, and P Suttakul
ETM0015	Numerical Analysis of the Dwelling Distance from Displacement Diffuser T Pratubwong and K Khaothong
ETM0016	Case Studies of Challenges in IoT Implementation in Thailand C Chaichana, A Panyafong, K Intakahm, Y Mona, N Khammayom, and P Suttakul
ETM0017	Investigation of Electrochemical Reaction and Transport Properties of a Rotating Cylinder Electrode with Surface Modification T Suzuki, P Charoen-amornkitt, T Suzuki, and S Tsushima
ETM0018	TURBO Fuel Cell as a Bridging Technology for Decentralised Power Generation Using Hythane R Dückershoff, H P Berg, M Kleissl, and A Himmelberg
ETM0019	Effect of Multiple V-Baffles on Thermal Enhancement Characteristics in a Channel P Samruaisin, P Kaewkosum, A Phila, S Eiamsa-ard, S Bhattacharyya, V Chuwattanakul, and C Thianpong
ETM0020	Experimental Investigation of Heat Transfer and Pressure Loss in a Channel Installed with Wave-Sine Shaped Baffles W Keaitnukul, M Phumkaew, A Phila, K Wongcharee, V Chuwattanakul, N Maruyama, M Hirota, S Eiamsa-ard, and K Buanak
ETM0021	Impact of Charging Time and Vehicle Range on Ridesharing Service: Case Study of Chulalongkorn University P Khatsri, S Narupiti, and A Sripakagorn

ETM0022	Experimental Investigation of Heat Transfer and Friction Loss in Two-pass Rectangular Channels with Ribbed Walls P Thapmanee, S Pingta, A Phila, K Srisathit, K Wongcharee, N Maruyama, M Hirota, and S Eiamsa-ard
ETM0023	Thermal Characteristics of Rectangular Channels with Inline/Staggered Notched Baffles A Phila, W Keaitnukul, M Phumkaew, S Jiragraivutidej, N Maruyama, M Hirota, S Eiamsa-ard, and K Buanak
ETM0024	Influence of Relative Baffle Heights on Heat Transfer Performance of Airflow in a Rectangular Channel with Discrete V-Pattern Baffles S Pingta, P Thapmanee, A Phila, K Wongcharee, N Maruyama, M Hirota, S Eiamsa-ard, and P Promvonge
ETM0025	Local Air Temperature Profile Around Serpentine Pattern Copper Pipe Heat Exchanger for Crop Cultivation T S Wai, N Khammayom, C Chaichana, N Maruyama, and M Hirota
ETM0026	Deep Learning-Based NSGA-II Method for Achieving the Optimal Spiral Fin Geometry in a Crimped Spiral Fin-and-Tube Heat Exchanger M Mesgarpour, T Kaewkamrop, S Goodarzi, O Mahian, M S Shadloo, S Gholami, and S Wongwises
ETM0027 Invited Presentation	Highly Effective Conversion of Green Ammonia to Electricity in TURBO Fuel Cell Systems (MGT-SOFC) for the Future Transportation Sector with a Focus on Marine Applications H P Berg, R Dückershoff, M Kleissl, F Mauss, A Himmelberg, K Blumenröder, and Chr Rex

Thermal System and Fluid Mechanics (TSF)

TSF0001	Effect of Inlet Condition on Flow Distribution in a Water-Cooling Plates of 18650 Li-ion Battery Pack R Nanthatanti, J Charoensuk, M Masomtob, and S Hirai
TSF0002	Evaluation of Single Stage Heat Pump Performance with Pure and Zeotropic Refrigerants by Modified Figure of Merit (FOM) S Srou, T Deethayat, and T Kiatsiriroat
TSF0003	Size Selection of In-Lined Tube Bank Heat Exchanger with Electric Field for Air Cooling of Air-Conditioner Condenser E Tang, T Kiatsiriroat, and A Asanakham
TSF0004	Flow Simulation of Noodle Pot Porous Cover P Phon, J Tawatchai, A Wiwat, P Tinnakorn, and K Preecha
TSF0005	Effect of Heat Transfer from Variation of Cross-Sectional Area in Helical Coil Heat Exchanger Manufacturing Process S Sukarin, M Janthong, and S Thongwik
TSF0006	Precooling of Air Entering Air-Conditioner Condenser by Cooling Water from an Open-Pond via Inline or Staggered Tube Bank Heat Exchanger V Heang, A Asanakham, and T Kiatsiriroat
TSF0007	Behavior of Plane Synthetic Jets Passing Over Two-Dimensional Flat Plates K Suzuki, K Nishibe, and K Sato
TSF0008	Effect of Conjugate Heat Transfer on Thermo-Hydraulic Characteristics for the Non-Newtonian Fluid Flow in a Wavy Solar Power Plant with Metallic Porous Blocks S K Mehta, P K Mondal, and S Wongwises
TSF0009	Airflow Analysis Based on the Location of Air Conditioning in Negative Pressure Room G M Oo, K Kotmool, and M Mongkolwongrojn

TSF0010	Operating Characteristics of a Miniature Swing Rotary Expander for a Rankine Cycle Regenerative System Using Waste Heat D Makino and T Otaka
TSF0011	A Numerical Investigation of Evaporation Process in a Minichannel of Printed Circuit Heat Exchanger N N Aye, W Hemsuwan, and C Thumthae
TSF0012	The Design of Refrigerated Box Using Phase Change Material for Food Delivery P Charoenvanich and A Tragangoon
TSF0013	Extrusion Flow of Concentrated Particle Suspensions in Abrupt Contraction Channel T Koshiba and T Yamamoto
TSF0014	Experimental Evaluation of Spray Humidifier in Evaporative Process P Setaphram, P charoenkitkaset, W Tachajapong, A Hokpunna, M Saedan, and W Manosroi
TSF0015	Fundamental Flow Characteristics of Impinging Synthetic Jets M Yasumiba, K Nishibe, D Kang, and K Sato
TSF0016	Numerical Study of Fluid Behaviors in Fibrous Porous Electrodes and Optimization of Electrode Structure Using Lattice Boltzmann Simulation D Tanaka, T Suzuki, and S Tsushima
TSF0017	Effect of Plane Walls on Flow Characteristics of Primary Jets Controlled by Secondary Flow H Tezuka, K Yabu, K Nishibe, D Kang, and K Sato
TSF0018	Analyzing the Impact of Porosity Distribution in Porous Electrodes on Cyclic Voltammetry Responses V Kiniman, C Kanokwhale, P Boonto, W Pholauyphon, K Nantasaksiri, P Charoen-amornkitt, T Suzuki, and S Tsushima
TSF0019	Influence of Reaction-Diffusion Parameters on Topologically Optimized Porosity Distribution in Reaction-Diffusion Systems Considering Temperature Dependence M Long, M Alizadeh, P Charoen-amornkitt, T Suzuki, and S Tsushima
TSF0020	Modeling of Polymer Electrolyte Fuel Cell Cathode for Investigating the Effects of Cracks in a Microporous Layer P Orncompa, A Jeyammuangpak, S Saikasem, K Nantasaksiri, P Charoen-amornkitt, T Suzuki, and S Tsushima
TSF0021	Flow Characteristics of Plane Jets Passing Over Two-Dimensional Flat Plates K Ishiwata, K Nishibe, and K Sato
TSF0022	Effect of Open Elliptical Reflector Shape on Pressure Gradient during Shock Wave Focusing M Taniguchi, T Nitta, H Fukuoka, A Suda, K Hiro, and K Nakagawa
TSF0023	Influence of the Phase of the Oscillating Velocity Distribution at Slot Exit on a Jet Flow M Takano, M Katano, K Nishibe, and K Sato
TSF0024	Evaluation of Sap Flow Rates in Tomato by Stem Heat Balance Method Using Infrared Thermography T Nishimae, H Fukuoka, A Suda, and K Iida
TSF0025	Physical Factors of Fabric Duct that Influence on Occupant Thermal Comfort S Boonpaijit, S Panjapisutsri, T Prunkyangyuen, and K Khaothong
TSF0026	Evaluation for Optimal Configuration of Twisted Fiber Bundle Wick Heat Pipe with Top Heat Mode J Simsiriwong, R Wanison, P Sakulchangsatjatai, P Terdtoon, and N Kammuang-lue
TSF0027	Dependence of Inlet Flow Condition on Heat Transfer around the Flat Plate in a Pulsating Duct Flow H Saitoh and R Katoh

TSF0028	Turbulent and Sub-Grid Scale Stress Statistics in Turbulent Lid-Driven Cavity Flow P Phermkorn, P Suttakul, P Osataporn, and A Hokpunna
TSF0029	Fluid-Structure-Acoustic Coupling Analysis for Articulation Process M Matsubara, H Hasegawa, T Yamamoto, and E Nomura
TSF0030	Experimental Measurements of a Simplified Thermal Model for Surface Temperature Prediction of a Single Pouch Cell Li-Ion Battery M T Oo, C Benyajati, J Soparat, and P Karin
TSF0031	Hybrid Thermal Management System for Cooling Commercial Electric Vehicle Batteries – An overview K Boonma, N Patimaporntap, Y Laoonual, S Manova, and S Wongwises
TSF0032	Visualization of Compressor Oil Behaviour and Its Influence on the Heat Transfer Characteristics of Evaporator in a CO_2 Refrigerator J Keeni, N Maruyama, K Takiguchi, and T Watanabe
TSF0033	Enhanced Grid Generation Method with Artificial Intelligent for Accurate Tracking of Nanoparticles Using Birth/Death Cells Around Spherical Particles M Mesgarpour, S Wongwises, A Hadjadj, A Jedi, L Amiri, and M S Shadloo

Engineering Education (EDU)

EDU0001	The Use of DWSIM to Analyze and Optimize Steam Cycles S Chantasiriwan and S Charoenvai

Presented Papers

AEC0002

Environmental Impact and Sustainable Solutions for Broiler Farming: A Case Study in Northern Thailand

H M S Bandara[1,2,4] and C Chaichana[2,3,*]

[1]Master's Degree Program in Energy Engineering, Department of Mechanical Engineering, Faculty of Engineering, Chiang Mai University, Chiang Mai 50200, Thailand
[2]Renewable Energy and Energy Conservation Laboratory, Department of Mechanical Engineering, Faculty of Engineering, Chiang Mai University, Chiang Mai 50200, Thailand
[3]Department of Mechanical Engineering, Faculty of Engineering, Chiang Mai University, Chiang Mai 50200, Thailand
[4] Division of Mechanical Engineering Technology, Institute of Technology, University of Moratuwa, Homagama, 10200, Sri Lanka

* Corresponding Author: chatchawan.c@cmu.ac.th

Abstract. This study examines the environmental impact and energy potential of broiler farming in Northern Thailand's Mae Tha District. Through comprehensive data collection and analysis, we estimate greenhouse gas (GHG) emissions using the GHG protocol's Scope 1 and Scope 2 framework. Our findings highlight that manure management accounts for 55.6% of total emissions, with electricity consumption contributing 40.8%. Stationary and mobile combustion sources constitute the remaining 3.2% and 0.4%, respectively. Beyond emissions, we explore the significant energy potential of broiler litter, demonstrating that thermochemical technologies, such as gasification, can generate electricity exceeding the farm's daily demand. This study not only underscores the need for targeted GHG mitigation strategies, particularly in manure management, but also emphasizes the opportunity to reduce reliance on external energy sources, resulting in cost savings and emissions reduction. Future studies can expand on these findings by enhancing manure management practices and investigating sustainable energy solutions, advancing our understanding of the environmental implications within broiler farming practices.

Keywords: Broiler farming, GHG emissions, Manure management, Gasification, Sustainable solutions.

1. Introduction

The global demand for poultry products, particularly broiler meat, has witnessed an unprecedented growth in recent decades, driven by population growth, urbanization, and changing dietary preferences [1]. In response to this increasing demand, the intensive production of broiler chickens has become a dominant agricultural practice worldwide. However, this significant expansion of broiler farming raised growing concerns about its adverse environmental impacts, notably regarding greenhouse gas (GHG) emissions and waste management. In addition to Carbon dioxide (CO_2), nitrous oxide (N_2O), and methane (CH_4) are two GHGs of special significance in agricultural activities [2]. N_2O is mostly emitted as a byproduct of nitrification and denitrification, as well as during the loss of volatile nitrogen [3], [4]. CH_4 is produced via the process of methanogenesis, which involves the anaerobic decomposition of organic carbon molecules [5]. These anaerobic conditions can be observed in several environments, such as soil, stored manure, and the gastrointestinal tract of animals during enteric fermentation [6].

The total GHG emissions, including CO_2, N_2O, and CH_4 emissions can be expressed in CO_2 equivalents ($CO_{2\text{-eq}}$). Global warming potential (GWP) values are used to calculate the $CO_{2\text{-eq}}$ values of non-CO_2 GHGs. The GWP estimates how much a given mass of GHG contributes to global warming in comparison to CO_2. According to the Intergovernmental Panel on Climate Change (IPCC)'s sixth assessment report published in 2021, the GWP values for CO_2, CH_4-non fossil, and N_2O over a100-year time horizon are 1, 27.2 and 273 $CO_{2\text{-eq}}$, respectively [7]. The majority of the GHG emissions generated from the poultry industry are attributable to feed production, fossil fuel combustion, and manure management [8]–[10]. GHG protocol’s Scope 1 and Scope 2 emissions guidelines can be used to calculate the GHG emissions from the activities that are under the control of the broiler chicken farmers. Scope 1 emissions are direct emissions from sources that are owned or controlled by the farm. These include emissions from stationary combustion, mobile combustion, and fugitive emissions. Scope 2 emissions are indirect emissions from the consumption of purchased electricity of the farm [11].

Thailand is a global leader in the production and exportation of broiler chicken meat [12]. As of the statistics from September 2022, there are approximately 7,800 chicken farms spread across the country, with a total of around 494 million chickens. Broiler farming has become an important source of income in Thailand, significantly boosting the regional agricultural output and rural livelihoods. The primary objective of this study is to estimate the GHG emissions from a selected broiler farm in the Mae Tha District and to identify key emission sources and implement sustainable solutions to mitigate these emissions. Furthermore, this study aims to provide valuable contributions towards the environmental sustainability of broiler farming in the Mae Tha District of Lamphun province, Northern Thailand. Through the identification and promotion of sustainable solutions, the authors hope to foster a more robust and environmentally accountable broiler farming sector that can serve as a model for other regions facing similar challenges. This will also help policymakers, researchers, and industry stakeholders develop evidence-based strategies that promote sustainable broiler waste management practices.

2. Materials and Methods

2.1. Data collection

The data collection of this study was centred on a single broiler chicken farm located in the Mae Tha District of the Lamphun province in Northern Thailand, shown in Figure 1. The farm owner willingly participated in the survey and provided vital information regarding their broiler farming practices and manure management procedures. This data included farm information and activity data, namely, the number of chicken houses, chicken house size, flock capacity, number of cycles per year, bedding material input, amount of broiler litter produces, fuel consumption of stationary and mobile sources, electricity consumption, and methods of broiler litter disposal etc. Some of the important data gathered has been presented in Table 1 for easy reference and comprehension.

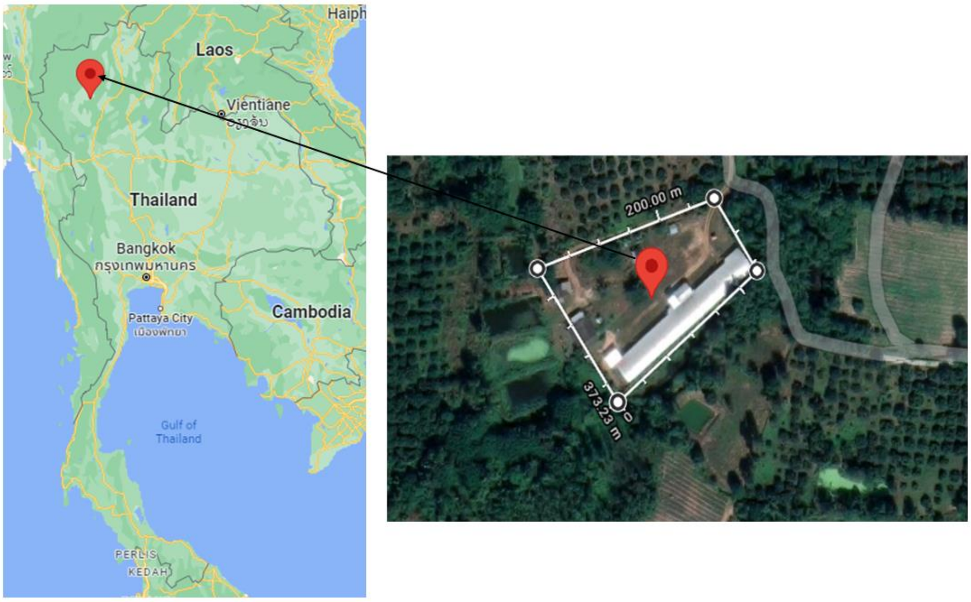

Figure 1. Chicken farm location.

Table 1. Key data collected from the farm.

Data	Value	Unit
Flock size	26000	birds per cycle
Production cycles	5	cycle/year
Cycle time	45	days/cycle
Diesel consumption– Mobile sources	20	l/cycle
Gasoline consumption – Mobile sources	10	l/cycle
LPG consumption- Stationary sources	4-5	tank[a]/ cycle
Electricity consumption	8000	kWh/month
Broiler litter collected	45000	kg/cycle

[a] 48 kg LPG tank.

Fuel consumption data was gathered in accordance with the Scope 1 emission guidelines provided by the GHG protocol. This farm has two diesel generators, and one LPG heater, which falls under stationary combustion sources. However, the farm owner did not record any fuel consumption data related to the diesel generators. The farm utilizes a diesel-powered truck, and a gasoline-powered motorcycle, which falls under the mobile combustion sources. Average monthly electricity consumption of the two broiler houses is around 8000 kWh, which is used to power 18 exhaust fans, 2 water pumps, and 95 LED lamps. Approximately 13500 kg of rice husk is used as the bedding layer of the broiler houses every cycle. About 45,000 kg of broiler litter, including manure, bedding, and waste feed, is collected at the end of every production cycle. These are collected, stored as shown in the Figure 2, and eventually sold to fertilizer companies, providing an additional income to the broiler farmer.

Figure 2. Manure storage of the farm.

2.2. Data analysis

2.2.1. GHG emissions from farm activities

The estimation of CO_2 emissions is performed by the multiplication of activity data and emission factors. Activity data is quantitative information on the activities that cause emissions, such as the amount of fuel burned or the number of animals in a livestock operation [13]. A significant amount of CO_2 is released to the atmosphere during fossil fuel combustion in farm activities, and the generation of purchased electricity. Country-specific emission factors of different fossil fuel sources, and electricity consumption were obtained by the Thailand Greenhouse Gas Management Organization (TGO) database. Emissions from manure management were calculated according to the IPCC guidelines. However, CH_4, and N_2O emission factors given in the IPCC worksheets are not derived for broiler manure with bedding material. Nonetheless, broiler farmers in Thailand use rice husk as the bedding material. Therefore, the emission factors for CH_4 emissions from enteric fermentation, CH_4 emissions from manure management, and direct N_2O emissions from manure management were acquired from a Taiwanese study that specifically utilized broiler manure with rice husk bedding as part of their research methodology [14]. When compared to the emission factors provided by the IPCC, it was clear that the CH_4 emission factors acquired from the Taiwanese study were much higher, although the N_2O emission factor was considerably lower (Table 2). This emphasizes the importance of including the emission factors with bedding material in the calculations.

Table 2. CH_4 and N_2O emission factors.

Emission factor	IPCC database	Taiwanese study	Unit
CH_4 from enteric fermentation	-	0.000148	kg CH_4/head/year
CH_4 from manure management	0.02	0.045	kg CH_4/head/year
N_2O from manure management (Direct)	0.001	0.000064	kg N_2O-N/kg N
N_2O emissions from volatilization (Indirect)	0.01	-	kg N_2O-N/kg N

2.2.2 Valorization of manure.

Although broiler farmers earn an additional income by selling broiler litter to fertilizer companies, more environmentally sustainable and economically profitable waste management alternatives are available. Combustion, pyrolysis, gasification, and hydrothermal liquefaction are some existing thermochemical conversion techniques for converting chicken litter into energy output and valuable byproducts [15], [16]. A case study in Netherlands has reported an electricity generation efficiency of 28% from combustion of poultry litter [17]. However, direct combustion of chicken manure is found to be less efficient than pyrolysis, and gasification with more adverse environmental effects [15]. Gasification presents the opportunity to not only generate electricity, but also produce biochar as a byproduct, that can be sold as a nutrient-rich soil additive [18]. Previous studies have shown that updraft gasification of poultry litter has an efficiency of approximately 26%, which is lower when compared to the high efficiency of nearly 60-80% achieved in fluidized bed gasification [19]. The following approach was used to explore if the broiler litter can be used to meet the electricity demand of the farm via combustion, and gasification.

Energy output can be calculated by the Equation (1) [20].

$$E = m \times LHV\ x\ \eta \tag{1}$$

where E is the energy output in MJ.
m is the mass of chicken litter in kg.
LHV is the Lower Heating Value of chicken litter in MJ/kg.
η is the electricity generation efficiency of thermochemical technology.

The moisture content of the collected manure sample was determined to be 9% on air dried basis through thermogravimetric analysis conducted in the laboratory according to the ASTM D7582. It is used to calculate the dry mass of the collected chicken litter sample. The ultimate analysis of the manure sample, performed using a CHNS/O elemental analyzer, determined that the broiler litter sample had a net heating value of 13 MJ/kg on air dried basis. These energy output values were used to estimate the electricity that can be generated through the combustion, and gasification processes from the broiler litter collected at the end of each production cycle.

3. Results and Discussion

This study aimed to estimate the GHG emissions linked to a broiler farm in the Mae Tha District of Lamphun province, located in Northern Thailand. By employing rigorous data collection and calculation methodologies, the authors were able to quantify the Scope 1 and Scope 2 emissions as defined by the GHG protocol.

According to the results, manure management was the most significant source of emissions (58.429 $tCO_{2\text{-}eq}$/year), accounting for 55.6% of total GHG emissions from the broiler farming operation. Electricity consumption was close behind (42.912 $tCO_{2\text{-}eq}$/year), accounting for 40.8% of emissions. Stationary combustion (3.362 $tCO_{2\text{-}eq}$/year) accounted for 3.2% of the total, with mobile combustion (0.386 $tCO_{2\text{-}eq}$/year) contributing 0.4% (Figure 3). The incomplete fuel purchase data provided by the farm owner may have lowered the stationary and mobile combustion emission estimates. Despite the potential underestimation, the study emphasizes the importance of manure management and the need for tailored strategies to mitigate emissions in broiler farming.

A previous study has highlighted that, factors such as feed type, feed conversion rate, and waste management influence the GHG emissions from broiler chicken farms [21]. Manure management alone contributes about 13% of GHG emissions for the global agricultural sector [22]. Litter amendment, reduced building stocking density, dietary supplementation enforced ventilation, and proper waste disposal within farms collectively contribute to the mitigation of greenhouse gases [21], [23].

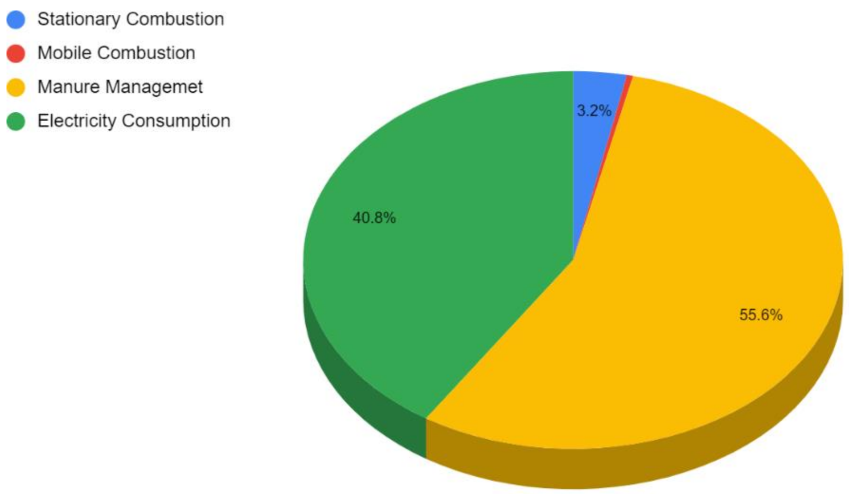

Figure 3. Percentage contribution of emission sources.

The daily electricity demand of the farm is approximately 260 kWh. Using the method described in the previous section, it was estimated that combustion of broiler litter can generate about 580 kWh/day with a low efficiency of 28%, while updraft gasification with a similar efficiency can produce nearly 540 kWh/day. Fluidized bed gasification having a much higher efficiency (60-80%) can generate 1240-1660 kWh/day (Table 3). It shows that these thermochemical technologies can produce more than twice as much as the electricity demand of this farm, using its own broiler waste. It is important to note that thermochemical conversion of chicken litter will not only reduce the waste volume, but also generate electricity, and nutrient-rich biochar as a byproduct that can be used as a soil amendment [24]. If these thermochemical technologies are implemented in the farm, it can reduce the need to purchase electricity from the grid, leading to a significant decrease in emissions associated with purchased electricity. It will also lower GHG emissions from manure management by drying, and thermally treating the waste, rather than storing the raw litter in a shed.

Utilizing broiler farm waste for electricity generation offers an effective means to lower GHG emissions while simultaneously delivering economic benefits. A case study conducted in Iran suggested promoting the adoption of high-efficiency equipment, substituting diesel-fuelled heaters with natural gas heaters, and implementing energy-efficient lighting solutions, all aimed at reducing electricity consumption in broiler farms [25]. According to a review, various technologies, including photovoltaic (PV), solar collectors, hybrid PV/Thermal systems, thermal energy storage, ground/water/air source heat pumps, as well as advanced lighting and radiant heating, can collectively achieve up to 85% energy savings [26].

Table 3. Electricity generation estimation.

Parameter	Value	Unit
Daily electricity demand	260	kWh
Estimated daily electricity generation from combustion (η = 28%)	580	kWh
Estimated daily electricity generation from updraft gasification (η = 26%)	540	kWh
Estimated daily electricity generation from fluidized bed gasification (η = 60-80%)	1240-1660	kWh

The operational dynamics of the studied broiler farm, where each cycle is followed by a 25-day gap, necessitate significant considerations for both storage and drying facilities. The intermittent availability of broiler litter demands storage capacities that can accommodate the litter accumulated over the 45-day cycle. This requirement highlights the need for substantial storage facilities to maintain a constant supply of feedstock for electricity generation from gasification. In addition, effective drying mechanisms are required to ensure that the feedstock is in suitable condition. These facilities play an essential role in preparing waste for energy conversion, highlighting the significance of well-designed infrastructure.

4. Conclusion

In this study, our primary objective was to estimate GHG emissions associated with a broiler farm in the Mae Tha District of Lamphun province, located in Northern Thailand. Employing rigorous data collection and calculation methodologies, we quantified the Scope 1 and Scope 2 emissions as defined by the GHG protocol. Our findings underscore the significance of manure management and electricity consumption as major sources of emissions in the broiler farming operation.

The study has unveiled critical insights into the emissions landscape of broiler farming operations. It has shown that manure management emerges as the primary contributor to GHG emissions, accounting for a substantial 55.6% of the total emissions at 58.429 $tCO_{2\text{-}eq}$/year. This finding places a spotlight on the need for targeted mitigation strategies within this area. Additionally, electricity consumption closely follows as another substantial source, representing 40.8% of emissions, equivalent to 42.912 $tCO_{2\text{-}eq}$/year. Furthermore, stationary combustion and mobile combustion contribute 3.2% and 0.4% of total emissions, respectively, adding to the overall emissions profile.

Moreover, our study has highlighted the significant energy potential of broiler litter. The daily electricity demand of the farm is approximately 260 kWh. Using the method described in the previous section, we estimated that combustion of broiler litter can generate about 580 kWh/day with a low efficiency of 28%, while updraft gasification with a similar efficiency can produce nearly 540 kWh/day. Additionally, fluidized bed gasification, with a much higher efficiency ranging from 60-80%, can generate 1240-1660 kWh/day. These findings indicate that thermochemical technologies can conveniently fulfil the electricity demand of this farm, utilizing its own broiler waste.

The significant level of manure management emissions suggests that interventions in this area hold promise for substantial environmental improvements. Furthermore, the efficient utilization of broiler waste for electricity generation highlights the potential for reducing reliance on external energy sources, which can lead to cost savings and decreased emissions.

Future research can capitalize on these findings by investigating and developing specific manure management methods and renewable energy solutions that align with the identified emission sources. These efforts may encompass optimizing waste-to-energy technologies, exploring alternative energy sources, and examining the broader economic and environmental implications of such initiatives.

5. Acknowledgments

Authors would like to extend our sincere gratitude to the broiler farm owner for providing essential data and cooperation throughout this research.

6. References

[1] S. Azarpajouh, S. L. Weimer, J. A. C. Díaz, and H. Taheri, “Smart Farming: A Review of Animal-Based Measuring Technologies for Broiler Welfare Assessment,” *CABI Rev.*, 2022, [Online].

[2] R. Maier, L. Hörtnagl, and N. Buchmann, “Greenhouse gas fluxes (CO2, N2O and CH4) of pea and maize during two cropping seasons: Drivers, budgets, and emission factors for nitrous oxide,” *Sci. Total Environ.*, vol. 849, p. 157541, 2022.

[3] N. C. Lawrence, C. G. Tenesaca, A. VanLoocke, and S. J. Hall, “Nitrous oxide emissions from agricultural soils challenge climate sustainability in the US Corn Belt,” *Proc. Natl. Acad. Sci. U. S. A.*, vol. 118, no. 46, 2021.

[4] M. U. Hassan *et al.*, “Management Strategies to Mitigate N(2)O Emissions in Agriculture.,” *Life (Basel,*

Switzerland), vol. 12, no. 3, Mar. 2022.
[5] V. Arelli, S. Juntupally, S. Begum, and G. R. Anupoju, "16 - Solid state anaerobic digestion of organic waste for the generation of biogas and bio manure," C. Hussain and S. B. T.-A. O. W. M. Hait, Eds. Elsevier, 2022, pp. 247–277.
[6] C. S. Dunkley, B. D. Fairchild, C. W. Ritz, B. H. Kiepper, and M. P. Lacy, "Carbon footprint of poultry production farms in South Georgia: A case study," *J. Appl. Poult. Res.*, vol. 24, no. 1, pp. 73–79, 2015.
[7] M. W. Jones *et al.*, "National contributions to climate change due to historical emissions of carbon dioxide, methane, and nitrous oxide since 1850," *Sci. Data*, vol. 10, no. 1, p. 155, 2023.
[8] C. Kayo, S. Tojo, M. Iwaoka, and T. Matsumoto, "Chapter 14 - Evaluation of Biomass Production and Utilization Systems," S. Tojo and T. B. T.-R. A. to S. B. S. Hirasawa, Eds. Boston: Academic Press, 2014, pp. 309–346.
[9] H. Tetteh *et al.*, "Carbon Footprint: The Case of Four Chicken Meat Products Sold on the Spanish Market," *Foods*, vol. 11, no. 22. 2022.
[10] R. Ibidhi, A. Y. Hoekstra, P. W. Gerbens-Leenes, and H. Chouchane, "Water, land and carbon footprints of sheep and chicken meat produced in Tunisia under different farming systems," *Ecol. Indic.*, vol. 77, pp. 304–313, 2017.
[11] F. Samara, S. Ibrahim, M. E. Yousuf, and R. Armour, "Carbon Footprint at a United Arab Emirates University: GHG Protocol," *Sustainability*, 2022.
[12] Emre Aydemir, Yasin Özel, and Erdener Altın, "World and Turkey over the past twenty years chicken examination of the production, consumption export and import," *World J. Adv. Res. Rev.*, vol. 11, no. 1, pp. 053–059, 2021.
[13] N. P. Cheremisinoff, "AP-42, Compilation of Air Pollutant Emission Factors," 2016, [Online]. Available: https://api.semanticscholar.org/CorpusID:133482340.
[14] S. Y. Wang, "Greenhouse gas and poultry production in Taiwan," no. March 2011, 2014.
[15] M. S. Hussein, K. G. Burra, R. S. Amano, and A. K. Gupta, "Temperature and gasifying media effects on chicken manure pyrolysis and gasification," *Fuel*, vol. 202, pp. 36–45, 2017.
[16] M. Guo, H. Li, B. Baldwin, and J. Morrison, "Thermochemical Processing of Animal Manure for Bioenergy and Biochar," *Anim. Manure Prod. Charact. Environ. Concerns, Manag.*, pp. 255–274, 2020.
[17] P. Billen, J. Costa, L. Van Der Aa, J. Van Caneghem, and C. Vandecasteele, "Electricity from poultry manure: A cleaner alternative to direct land application," *J. Clean. Prod.*, vol. 96, pp. 467–475, 2015.
[18] M. D. Manogaran, R. Shamsuddin, M. H. Mohd Yusoff, M. Lay, and A. A. Siyal, "A review on treatment processes of chicken manure," *Clean. Circ. Bioeconomy*, vol. 2, no. May, p. 100013, 2022.
[19] H. K. Jeswani, A. Whiting, A. Martin, and A. Azapagic, "Environmental and economic sustainability of poultry litter gasification for electricity and heat generation," *Waste Manag.*, vol. 95, pp. 182–191, 2019.
[20] V. Thongkhao, S. Sukpancharoen, and B. Prasartkaew, "Efficiency improvement of biomass gasifier using porous media heat recuperator," *Case Stud. Therm. Eng.*, vol. 48, no. February, p. 103143, 2023.
[21] A. H. E.-S. Mohammed *et al.*, "The Influence of Harmful Greenhouse Gases (GHG) Emission In-Door of Broiler Chickens' System on Their Health: 'Options of Prevention and Control,'" *Eur. J. Vasc. Endovasc. Surg.*, vol. 52, pp. 275–282, 2021.
[22] S. Fournel, F. Pelletier, S. Godbout, R. Lagacé, and J. Feddes, "Greenhouse gas emissions from three cage layer housing systems," *Animals*, vol. 2, no. 1, pp. 1–15, 2012.
[23] K. Kalus, D. Konkol, M. Korczyński, J. A. Koziel, and S. Opaliński, "Effect of Biochar Diet Supplementation on Chicken Broilers Performance, NH(3) and Odor Emissions and Meat Consumer Acceptance.," *Anim. an open access J. from MDPI*, vol. 10, no. 9, Sep. 2020.
[24] C. C. Tsai and Y. F. Chang, "Quality evaluation of poultry litter biochar produced at different pyrolysis temperatures as a sustainable management approach and its impact on soil carbon mineralization," *Agronomy*, vol. 11, no. 9, 2021.
[25] S. H. Pishgar-Komleh, A. Akram, A. Keyhani, and R. van Zelm, "Life cycle energy use, costs, and greenhouse gas emission of broiler farms in different production systems in Iran—a case study of Alborz province," *Environ. Sci. Pollut. Res.*, vol. 24, no. 19, pp. 16041–16049, 2017.
[26] Y. Cui, T. Elmer, T. Gurler, Y. Su, and S. Riffat, "A comprehensive review on renewable and sustainable heating systems for poultry farming," *Int. J. Low-Carbon Technol.*, vol. 15, Nov. 2019.

AEC0005

Experimental Study on the Explosion Intensity of Lithium-Ion Batteries in Air and Helium Environments

Gonrakarn Phanomai[1], Kidjakarn Phanomai[1], Karnpon Tassananakajit[1], Somchai Wongwises[1], and Piyatida Trinuruk[1,*]

[1]Department of Mechanical Engineering, King Mongkut's University of Technology Thonburi, 126 Pracha Uthit Road, Bang Mod, Thung Khru, Bangkok 10140, Thailand

* Corresponding Author: piyatida.tri@kmutt.ac.th

Abstract. Lithium-ion batteries are widely employed in electric vehicles. However, the batteries can generate heat during charging or discharging. Improper management of heat generation in the battery may cause thermal runaway and explosions. As a result, an efficient battery thermal management system (BTMS) is essential to reduce the risk of explosions. The purpose of this study was to investigate the thermal runaway characteristics of batteries at various states of charge (SOC) in both air and helium environments. Battery explosion in the controlled chamber was experimentally performed and analysed in this study. The influence of cloaking with air or helium and varying SOC on explosion intensity was examined. Surprisingly, the most intense thermal runaway, as represented by battery temperature, occurred in the battery with 75% SOC rather than the one with 100% SOC. This was because the battery with 100% SOC experienced considerable mass loss, leading to the dissipation of an enormous amount of heat into the chamber, resulted in a lower maximum battery temperature. The research also discovered that the surrounding environment significantly affected the severity and the explosion's characteristics. The use of helium gas achieved the reduction of thermal runway intensity, while using air resulted in more violent explosion compared to helium. This was due to the existence of oxygen, resulting in higher combustion temperatures.

Keywords: Explosion, Helium, Lithium-ion battery, State of charge, Thermal runaway.

1. Introduction

The burning of fossil fuels within internal combustion engines used in the transportation sector significantly contributes to the global warming crisis and the severity of climate change. Reducing emissions into the environment is vital because fossil fuels are finite resources and responsible for generating air pollution, which is the root cause of environmental issues. As a result, the adoption of alternative energy sources to replace the reliance on fossil fuels has become essential. Electric vehicles (EVs) and hybrid cars, both powered by lithium-ion batteries (LIBs), offer distinct advantages such as high power, high specific energy, low self-discharge, quick charging, and a long service life attributed to their value. It is important to highlight, however, that LIBs exhibit limited temperature stability, potentially leading to overheating or even fire explosions [1-2]. Thus, several studies on battery thermal management systems (BTMS) have been conducted to mitigate the possibility of injury to users [3-5].

Historically, incidents involving batteries have happened frequently, with over 60 thermal runaway (TR) events occurring in electrochemical energy storage plants worldwide [6]. Notably, on April 19th, 2019, the battery storage facility of Arizona Public Service Company (APS) at the McMicken substation in the United States experienced an accidental explosion due to internal battery defects, aggregation, and anomalous growth of lithium dendrites. The limitation of combustible gas emissions was reached. Similarly, on April 16th, 2021, battery explosion happened at the Dahongmen DC optical storage and charging integrated power station project in Beijing's Fengtai District, China. Two people were killed as a result of the accident. On July 30th, 2021, a Tesla Megapack energy storage system in Victoria, Australia, caught fire due to a leakage in the cooling system, triggering a short circuit and fire in the battery [7].

Mechanical, electrical, and thermal abuses are the three main categories that contribute to thermal runaway. Impaction and vibration are examples of mechanical abuse. Meanwhile, thermal abuse manifests through situations of overheating, whereas electrical abuse pertains to the potential impacts of overcharging and overdischarging [8-9]. The main parameter used to evaluate thermal runaway formation is the surface temperature of the battery. The explosive behaviour of a commercial 18650 Lithium Nickel Manganese Cobalt Oxide (NMC) cell was investigated in Extended Volume-Accelerating Rate Calorimetry (EV-ARC) by measuring the battery surface temperature [10]. While accounting for additional parameters such as gas productions, an enclosed cylindrical stainless steel chamber was utilized [11]. The result found that the propagation of fire significantly influenced the increase in thermal runaway intensity. The effect of various states of charge (SOCs) of LIBs 18650 on thermal runaway was examined by Zhang et al. [12]. It was discovered that LIBs with higher SOCs exhibited higher maximum temperatures and more explosive severity than batteries with lower SOC.

To improve safety performance, the use of inert gases has been recommended to mitigate battery explosions and fire propagation [4,13]. Torikai and Kudo [14] examined the ability of inert gas by employing inert gas-filled balloons to explore flame spread reduction. Inert gases can diminish the concentration of oxygen in the combustion area, limiting the spread of fire. Helium is an attractive inert gas for fire suppression because it has a thermal conductivity six times that of air at 27°C and does not chemically react with other substances [13-14]. However, the experiment to understand thermal runaway behaviour using LIBs exploding in a helium environment has never been done previously.

Therefore, the purpose of this study was to conduct an experiment with 18650 NMC LIBs in order to better understand the battery explosion. A 20.8-liter chamber with a 260 watt-heater coil was constructed to assess thermal runaway behaviour by measuring the battery surface and chamber temperatures, as well as chamber pressure. Additionally, the effect of varying SOCs, initial pressures, and diverse gas surrounds on the fire hazards associated with LIBs were also discussed in this study.

2. Battery Thermal Runaway

In general, lithium-ion batteries (LIBs) consist of some common components: cathode, anode, separator and electrolyte. The cathode material may be made from various compound materials. In this study, $LiNiMnCoO_2$ (NMC) battery is employed due to its outstanding characteristics for using in EV applications, such as higher energy density and being more appropriate for quick charging than other batteries. Graphite is used to form the anode material. The separator is made of micro-perforate plastic, which allows ions to pass through. Organic solvent and inorganic salt are used as the compound for producing the electrolyte [15].

When LIBs are subjected to abusive conditions, unanticipated heat can occur, causing the temperature of LIBs to approach the onset temperature of thermal runaway. This can happen if there is an unmanageable fire or explosion. The thermal runaway in LIBs is an exothermic reaction involving the decomposition of various components in battery such as solid electrolyte interphase (SEI), separator, binder, and so on [16], which generate a massive amount of heat released. Chombo and Laoonual [17] examined the thermal runaway formation of 18650 cylindrical cell LIBs. The burning steps were reported into six steps, as shown in Figure 1.

State 1: Thermal abuse:- LIBs were continuously heated without fire. SEI began to decompose and vaporize.
State 2: Safety vent cracked:- Gas generated inside the LIBs and triggered the safety valve to open. The electrolyte vapor and flammable gases were released.
State 3: Ignition:- When the battery temperature was sufficiently high upon reaching the onset temperature of thermal runaway, flammable gases ignited and occurring fire ignition.
State 4: Stable combustion:- The flame was reduced in size and sustained over time.
State 5: Mechanical rupture:- The increase of surface temperature attributed the collapse of the separator, resulting in a short circuit, consequently, heat induced thermal runaway.
State 6: Abatement:- The flame was gradually diminished until it was extinguished.

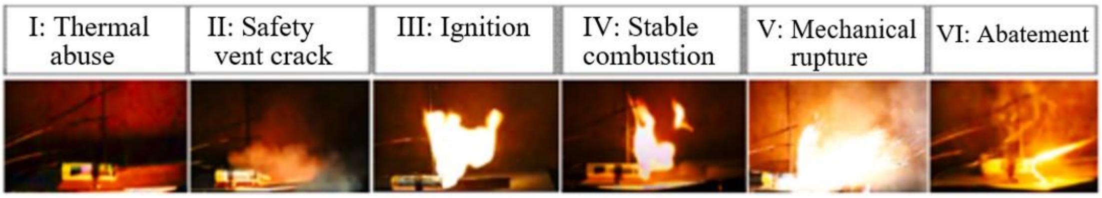

Figure 1. Burning stages of 18650 LIBs [17].

Feng et al. [18] used EV-ARC to tested 18650NMC LIBs and divided the thermal runaway formation into six stages, as illustrated in Figure .2SEI decomposition, anode reaction consumption of active material in anode, separator melting, separator breakup, and quick internal short circuit were all crucial events in thermal runaway.

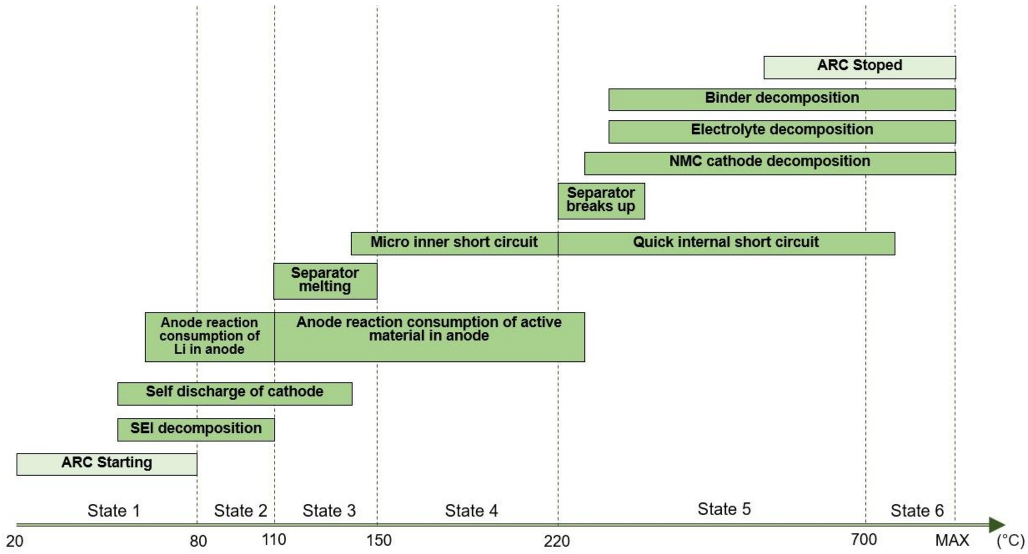

Figure 2. The stages of thermal runaway formation.

3. Methodology

3.1. Samples

LIB cells used in this study were commercial 18650 Samsung cylindrical LIBs with $LiNiMnCoO_2$ (NMC) cathode materials, as illustrated in Figure 3. Table 1 shows the battery specifications, such as the nominal voltage of 3.6 V and the capacity of 2500 mA. To activate and stabilize the chemical reactions inside the cell, the preconditioning process was essentially carried out before the battery was in regular use. All batteries were initially discharged at the 0.5C-rate and then charged using CCCV (constant current – constant voltage) at the 0.5C-rate, as specified by the specification. Consequently, LIBs were discharged to anticipatory SOCs and slept more than 2 hours until the voltage stabilized. It was then installed in the test chamber to investigate the fire hazard.

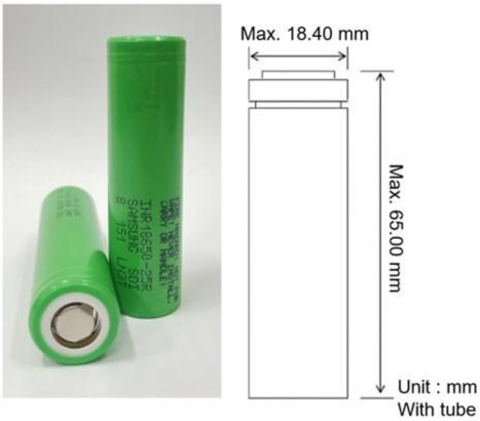

Figure 3. The dimension of 18650 Samsung NMC.

Table 1. Specifications of 18650 Samsung NMC used in the experiment.

Item	Specification
Standard discharge capacity (mAh)	2500 (at 1C)
Nominal voltage (V)	3.6
Standard charge	CCCV, 1.25A, 4.2V, 0.125A cut-off
Maximum continuous discharge (A)	20 (at 25°C)
Discharge cut-off voltage (V)	2.5
Cell diameter (mm)	18.4
Cell height (mm)	65
Cathode material	$LiNiMnCoO_2$ (NMC)
Anode material	Graphite

3.2. Apparatus

The experiment was performed in a closed chamber with a design capacity of 20.8 litters with very high safety. The system of test section consisted of four main parts: the heating part, the data recorder, the gas controller part, and the measurement parameters. A 260 W/220 V heater was installed to heat a battery cell, which was vertically placed inside the chamber. To force the development of thermal runaway in the battery, the heater was turned on at 90 W. The temperatures and pressure were continuously measured and recorded using National Instrument (NI). The front end of the chamber was equipped with a sight glass for visualizing the thermal runaway behaviour throughout the experiment. Figure 4(a) illustrates the gas controller section, which composed of a vacuum pump, manifold gauge, air compressor, and helium tank. To control the ambient condition in the chamber, the equipment of gas controller component was operated sequentially depending on the test circumstances.

Temperatures and pressure in the chamber were observed. Four thermocouples of type K were placed to measure the temperatures in various positions, as shown in Figure 4(b). T_o represented the heater temperature. The chamber and flame temperatures were denoted by T_1 and T_2, respectively. T_3 measured the temperature of cell battery. A pressure transducer was mounted at the back of the chamber to measure the pressure characteristic in the chamber during the test and thermal runaway.

3.3. Test conditions

The intensity of lithium-ion battery explosion under various environment conditions was investigated in this study. The environment, ambient pressure, available battery capacity or SOC, and other factors can have an impact on the intensity of battery explosion. Therefore, to achieve the objective of this study, a comparison study was determined under various test conditions.

The battery was encapsulated in two different surroundings: one covered by air, which inherently contained some oxygen, and one enveloped by helium gas to eliminated oxygen, which is a critical component of fire triangle. This study assessed the effect of various ambient pressures, 0 bar_g and 1 bar_g, as well as different SOCs, 0%, 50%, 75%, and 100% SOC, which represented the battery's capacity.

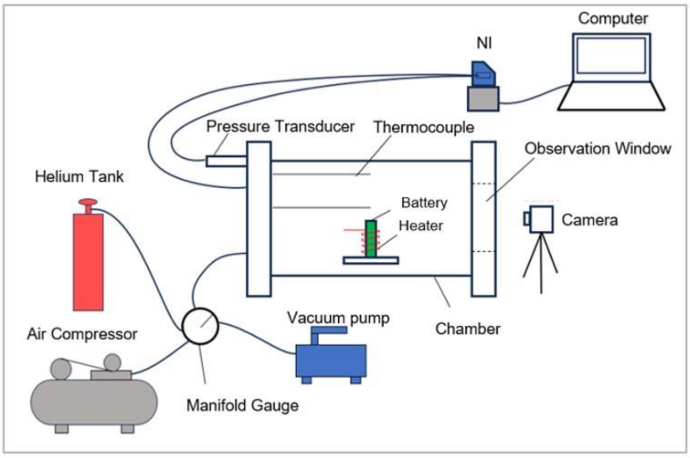

(a)

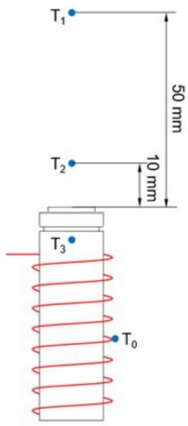

(b)

Figure 4. Experimental setup: (a) Schematic view of experiment, and (b) The placement of thermocouples

4. Results and Discussions

4.1. Effect of SOCs on thermal runaway

This section reported on the thermal runaway characteristics while the battery capacity was being in various SOCs in a controlled environment. The temperature profiles of battery at the same ambient pressure of 1 bar_g were demonstrated in Figure 5(a) for air and Figure 5(b) for helium. At the initial phase of heating, when the battery temperature was initially increased to a particular temperature, the electrodes, separator and electrolyte started to melt, decompose and evaporate into high-pressure gases inside the battery. When the battery's internal pressure reached the limit pressure of 2 - 2.6 MPa [10], the safety valve triggered and cracked, resulting in the released of electrolyte gases. Consequently, if heat was continuously supplied, the battery may ignite and the combustion reaction would occur, resulting in fire propagation and the release of combustion gases, hence increasing the severity of battery thermal runaway. This was because several battery's components were flammable, particularly the electrolyte, which had a boiling point of 100-150°C [13].

The results obviously show that the batteries with 50%, 75% and 100% SOCs can undergo ignition, as evidenced through an extreme increase in battery temperature when subjected to both air and helium environments. However, at 0% SOC, when the battery had minimum energy capacity, the cell did not have sufficient energy to initiate the catalytic process required for thermal runaway formation, resulting in its absence. The maximum temperature of thermal runaway formation was highest at 75% SOC and subsequently decreased at 50% and 100% SOC, respectively, as summarized in Table 2. Due to the tremendous explosion, which resulted in considerable mass loss and dissipated large amount of heat, the battery with 100% SOC surrounded by air could not experience the highest temperature, although having the largest capacity [19]. In the case of helium gas, 100% SOC also provided a lower maximum temperature than 75% and 50% SOC due to the oxygen consumption of 50% and 75% SOC in the adequate and proper combustion reaction. While in the case of 100% SOC, there was barely sufficient oxygen available, resulting in incomplete combustion. Nevertheless, the onset temperature of thermal runaway formation was lower for the battery with 100% SOC than for the battery with 75% and 50% SOC. In addition, it can detect a slight drop in battery temperature once the safety valve was opened.

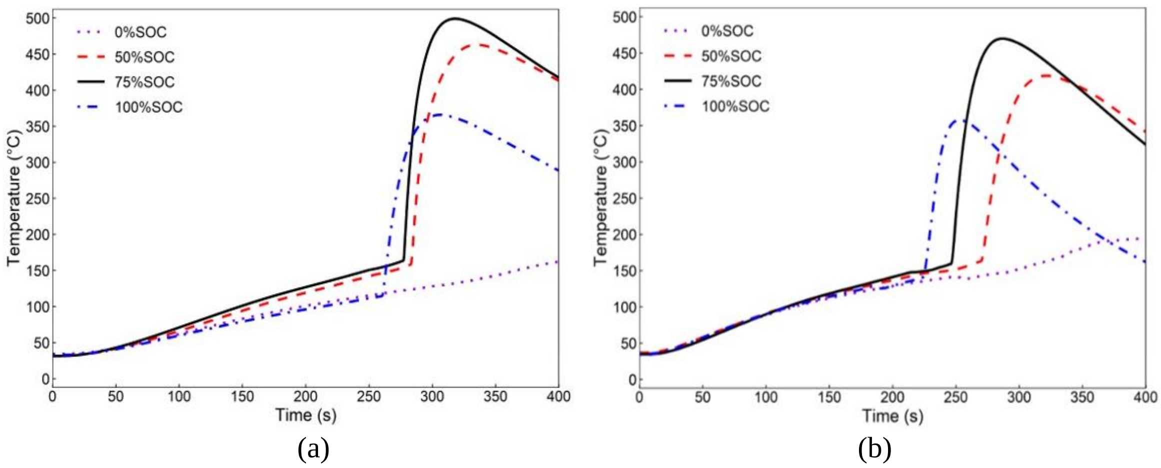

Figure 5. Temperature profiles of battery at 100%, 75%, 50%, and 0% SOC under the ambient pressure of 1 bar_g when (a) covered by air, and (b) covered by helium gas.

Table 2. Notable temperatures and times during thermal runaway in batteries with different SOCs.

SOC (%)	Ignition time (s)		Temperature of TR formation (°C)		Max. temperature (°C)	
	Air 1 bar_g	He 1 bar_g	Air 1 bar_g	He 1 bar_g	Air 1 bar_g	He 1 bar_g
0	-	-	-	-	162.27*	193.87*
50	283	269	158.52	162.57	462.68	418.65
75	277	245	163.58	158.72	498.95	469.78
100	261	223	119.47	140.58	365.52	357.62

Note: * cannot undergo ignition.

To better understand the thermal runaway formation, the photo visualization of a battery fire explosion was investigated, as seen in Figure 6. When the battery had reached the proper temperature and pressure, the safety vent valve was activated. The valve was opened, releasing some combustible gases into the environment. Consequently, the flame core of thermal runaway occurred, as shown in State 2. Lower SOC values, such as 50% SOC, resulted in a weaker fire explosion than 75% SOC. The presence of helium gas in the surroundings can potentially cause an oxygen shortage, but it can also notice a burning battery core. This was due to the battery's ability to generate oxygen on its own, which can trigger the chain reaction that happened in State 3 in the case of helium 1 bar_g. The intensity of the explosion in State 4 was more powerful in air than in helium, when compared at the same SOCs. In State 5, the flame weakened.

The summary of this section shows that increasing the SOC corresponded to an escalation in explosion intensity due to increased lithium intercalation in the negative electrode. This resulted in the venting of additional gas products, especially flammable gases, which had a significant impact on the severity of the thermal runaway [19].

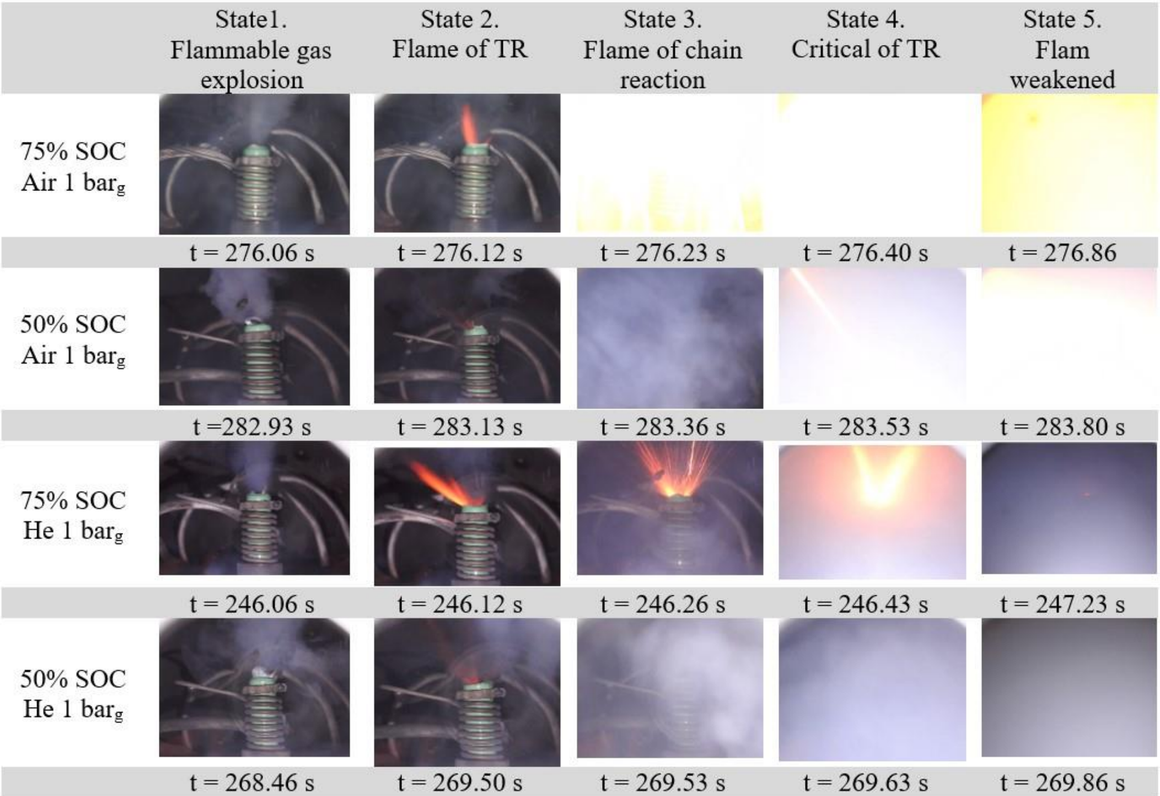

Figure 6. The thermal runaway processes of LIBs in different SOCs and various ambient conditions.

4.2. Effect of different surrounded gases

This section aimed to compare the effect of gas environments; without and with oxygen, on the thermal runaway formation. Because oxygen, fuel, and temperature are three basic elements of fire propagation that influence thermal runaway behaviour. Therefore, the environments of air and helium at the same ambient pressure were compared. Figure 7(a) shows that the thermal runaway intensity of the battery with 75% SOC in the air was stronger than that of the helium environment. The maximum battery surface temperature in an air environment was 498.95°C, which was greater than that in a helium atmosphere, which was 469.78°C.

Figure 7(b) exhibits the rate of temperature change in air and helium environments. Due to the difference in heat conductivity and density, a greater change in the rate of temperature in helium can be observed than in air during the initial heating phase. These factors can have a crucial impact on helium conduction and convection. The rate of temperature changes dropped suddenly when the safety valve was opened. At 150°C, the rate of temperature decreased distinctly in the helium atmosphere compared to the case of air. Higher energy released from the battery in a lower density gas environment had a direct impact on the momentum.

However, in a helium atmosphere, the LIB can occur a thermal runaway and undergo the explosion even when there was no oxygen in the environment. This was because LIB can generate oxygen on its own while being a chemical reaction when it was continually heated. Therefore, it was an oxygen-containing reaction, as given by Equation (1) [20].

$$(CH_2OCO_2Li)_2 \rightarrow Li_2CO_3 + C_2H_4 + CO_2 + \frac{1}{2} O_2 \tag{1}$$

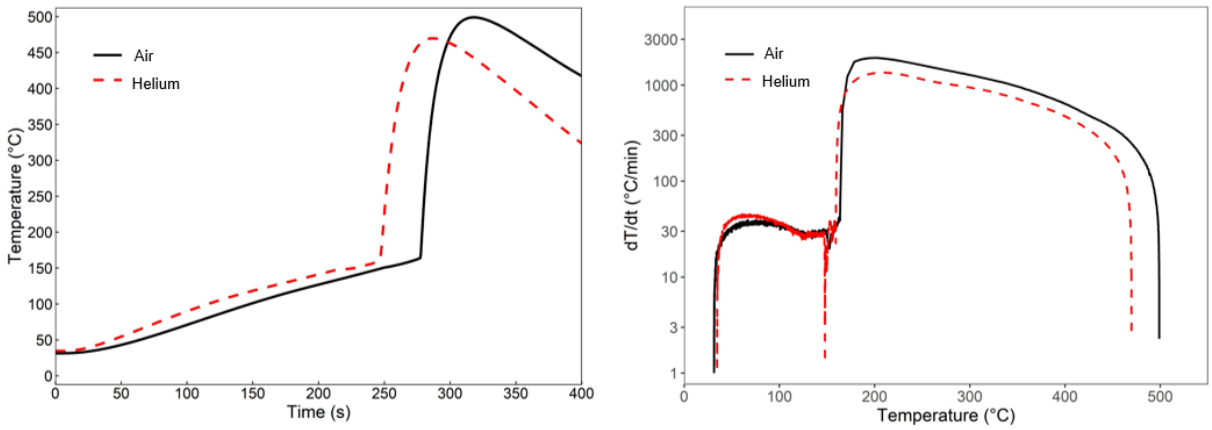

Figure 7. The results for the battery with 75% SOC in air and helium environments at the same initial pressure of 1 bar_g (a) The temperature profile, and (b) The rate of temperature change.

4.3. Effect of initial pressure on thermal runaway

The test conditions were set at various initial ambient pressures, 0 bar_g and 1 bar_g, to see the influence of external pressure on thermal runaway characteristics. Figure 8 shows that the presence of air as a gas environment caused a considerable increase in temperature and differential pressure. A higher initial pressure in air environment, 1 bar_g, persuaded a rise in oxygen concentration, which progressively promoted the chain reaction with more exothermic reactions and caused the development of an excessive pressure. Table 3 presents the differential pressure after the thermal runaway formation in various surroundings.

In helium environment, an increase in initial pressure caused an escalation in differential pressure, but the magnitude of the change was not proportional to the starting pressure. The difference in initial pressure had an impact on the operating pressure for safety valve opening. The increase in intracellular pressure caused by the cracking of the safety valve increased the velocity of the gas released during thermal runaway.

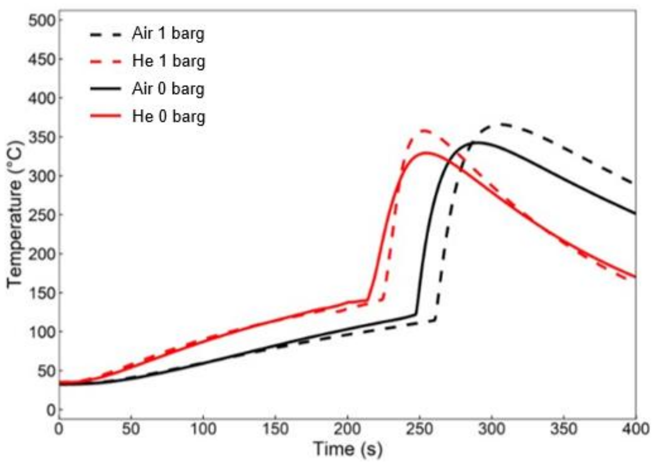

Figure 8. The temperatures of the battery with 100% SOC in air and helium environments at the different initial pressures

Table 3. The pressure rises during the thermal runaway

Gas environment	SOC (%)	Initial pressure (bar_g)	Differential pressure (bar)
Air	100	1	7.947
Air	100	0	3.399
Helium	100	1	1.977
Helium	100	0	1.309

5. Conclusions

Thermal runaway behaviour was investigated in this experiment using NMC LIBs 18650 at various SOCs. The temperatures and pressure for each air and helium environments at various initial pressures were major factors in the experiment to measure the severity of thermal runaway. The important issues can be summarized as follows:

- Batteries with 0% SOC cannot undergo thermal runaway, while batteries with 50%, 75%, and 100% SOC can. The intensity of thermal runaway increased with an increase in SOC, except for the battery with 100% SOC, where the dissipation of heat into the chamber from the considerable mass loss resulted in a lower maximum temperature.
- The use of inert gas, such as helium, can successfully decrease thermal runaway intensity because helium can inhibit chain reactions, causing incomplete combustion. In addition, the superior thermophysical characteristics of helium can persuade it to reject the heat from the battery through conduction and convection processes.
- The increase in initial ambient pressure significantly affected the rise in differential pressure during the thermal runaway formation. Due to the high outside pressure, a higher internal pressure was required to open the safety valve. This resulted in a higher temperature of the decomposed electrolyte and intense combustion in the case of 1 bar_g.
- An increase in air pressure resulted in an increase in oxygen concentration. This factor had a substantial impact on the rise of explosion pressure when thermal runaway occurred.

The relationship between the internal pressure and surface temperatures of LIBs would be further investigated in a future study, which might install a small thermocouple within the battery. Such research has the potential to improve the battery's safety.

6. Acknowledgements

The authors acknowledge the supported provided by National Science and Technology Development Agency (NSTDA) under the Research Chair Grant, Thailand Science Research and Innovation (TSRI) Basic Research Fund: Fiscal year 2023 (Program: Sustainable Mobility) and National Science, Research and Innovation Fund (NSRF) via the Program Management Unit for Human Resources & Institutional Development, Research and Innovation [grant number B40G660039].

7. References

[1] Wang, Q., Mao, B., Stoliarov, S. I., & Sun, J. (2019) A review of lithium ion battery failure mechanisms and fire prevention strategies. *Progress in Energy and Combustion Science*, 73, 95–131.

[2] Zhang, Y., Wang, H., Wang, Y., Li, C., Liu, Y., & Ouyang, M. (2021). Thermal abusive experimental research on the large-format lithium-ion battery using a buried dual-sensor. *Journal of Energy Storage*, 33, 102156.

[3] Malik, M., Dincer, I., Rosen, M. A., Mathew, M., & Fowler, M. (2018). Thermal and electrical performance evaluations of series connected Li-ion batteries in a pack with liquid cooling. *Applied Thermal Engineering*, 129, 472–481.

[4] Alipour, M., Hassanpouryouzband, A., & Kizilel, R. (2021). Investigation of the Applicability of Helium-Based Cooling System for Li-Ion Batteries. *Electrochem*, 2(1), Article 1.

[5] Lu, M., Zhang, X., Ji, J., Xu, X., & Zhang, Y. (2020). Research progress on power battery cooling technology for electric vehicles. *Journal of Energy Storage*, 27, 101155.
[6] Lai, X., Lai, X., Yao, J., Jin, C., Feng, X., Wang, H., Xu, C., & Zheng, Y. (2022). A Review of Lithium-Ion Battery Failure Hazards: Test Standards, Accident Analysis, and Safety Suggestions. *Batteries*, 8(11), Article 11.
[7] Hill, D. M. (2020). Battery Energy Storage System Event: Technical Analysis and Recommendations.
[8] Tran, M.-K., Tran, M.-K., Mevawalla, A., Aziz, A., Panchal, S., Xie, Y., & Fowler, M. (2022). A Review of Lithium-Ion Battery Thermal Runaway Modeling and Diagnosis Approaches. *Processes*, 10(6), Article 6.
[9] Duh, Y.-S., Sun, Y., Lin, X., Zheng, J., Wang, M., Wang, Y., Lin, X., Jiang, X., Zheng, Z., Zheng, S., & Yu, G. (2021). Characterization on thermal runaway of commercial 18650 lithium-ion batteries used in electric vehicles: A review. *Journal of Energy Storage*, 41, 102888.
[10] Zhao, C., Sun, J., & Wang, Q. (2020). Thermal runaway hazards investigation on 18650 lithium-ion battery using extended volume accelerating rate calorimeter. *Journal of Energy Storage*, 28, 101232.
[11] Zhao, J., Lu, S., Fu, Y., Ma, W., Cheng, Y., & Zhang, H. (2021). Experimental study on thermal runaway behaviors of 18650 li-ion battery under enclosed and ventilated conditions. *Fire Safety Journal*, 125, 103417.
[12] Zhang, Q., Niu, J., Zhao, Z., & Wang, Q. (2022). Research on the effect of thermal runaway gas components and explosion limits of lithium-ion batteries under different charge states. *Journal of Energy Storage*, 45, 103759.
[13] Boonkit, P., Petchsart, N., Apirakkitthworn, S. & Trinuruk, P., (2024) Improvement of cooling performance and mitigation of fire propagation in lithium-ion batteries using a novel gas-cooled thermal management system. *International Journal of Energy for a Clean Environment*, 25 (3), 13-31
[14] Torikai, H., & Kudo, S. (2021). Extinguishment of diffusion flames formed over a porous plate burner using rubber balloons filled with inert gases. *Progress in Scale Modeling, an International Journal*, 2, Article 4.
[15] Fu, Y., Lu, S., Li, K., Liu, C., Cheng, X., & Zhang, H. (2015). An experimental study on burning behaviors of 18650 lithium ion batteries using a cone calorimeter. *Journal of Power Sources*, 273, 216–222.
[16] Abada, S., Petit, M., Lecocq, A., Marlair, G., Sauvant-Moynot, V., & Huet, F. (2018). Combined experimental and modeling approaches of the thermal runaway of fresh and aged lithium-ion batteries. *Journal of Power Sources*, 399, 264–273.
[17] Chombo, P. V., & Laoonual, Y. (2022). Prediction of the onset of thermal runaway and its thermal hazards in 18650 lithium-ion battery abused by external heating. *Fire Safety Journal*, 129, 103560.
[18] Feng, X., Fang, M., He, X., Ouyang, M., Lu, L., Wang, H., & Zhang, M. (2014). Thermal runaway features of large format prismatic lithium ion battery using extended volume accelerating rate calorimetry. *Journal of Power Sources*, 255, 294–301.
[19] Liu, T., Tao, C., & Wang, X. (2020). Cooling control effect of water mist on thermal runaway propagation in lithium ion battery modules. *Applied Energy*, 267, 115087.
[20] Zou, K., He, K., & Lu, S. (2022). Venting composition and rate of large-format LiNi0.8Co0.1Mn0.1O2 pouch power battery during thermal runaway. *International Journal of Heat and Mass Transfer*, 195, 123133.

AEC0006

Experimental Investigation on the Optimal Frequency for Acoustic Fire Extinguishing in Different Duct Configurations

Fais Awae[1], Paranyu Chareonmark[1], Pattaphon Tapanapongpan[1], Somchai Wongwises[1], and Piyatida Trinuruk[1,*]

[1] Department of Mechanical Engineering, King Mongkut's University of Technology Thonburi, 126 Pracha Uthit Rd., Bang Mod, Thung Khru, Bangkok, 10140, Thailand

*Corresponding Author: piyatida.tri@kmutt.ac.th

Abstract. Fire is essential to humanity in all aspects, but it also poses a risk, especially in duct systems. Fire can spread throughout the building across the duct space, causing the entire building to burst into flames at the same moment. Most current fire extinguishers do not fit well in duct spaces, which have limited areas and numerous obstructions. To counter this problem, an innovative method of fire suppression, such as acoustic fire extinguishing, is needed. Therefore, this research aims to investigate the interaction between the acoustic wave and the fire in three different duct configurations. The Minimum Extinguish Power (MEP) and Sound Pressure Level (SPL), as well as airflow characteristics for fire extinguishing, were studied when the duct layouts were changed. The results show that the straight duct extinguished with the highest power. The elbow and zigzag configurations followed, which require equal extinguishing power due to turbulent airflow characteristics and SPL. It can be observed that the straight configuration was not complicated, resulting in lower turbulence on the flame. This made extinguishing fires more difficult and necessitated the employment of the highest power. In contrast, the elbow and zigzag ducts had multiple joints and so created more turbulence on the flame. The straight duct was effective in extinguishing until a frequency of 57.2 Hz, beyond this value it cannot extinguish any further. Similarly, the elbow and zigzag duct configurations reached their extinguishing limits at 65 Hz and 75 Hz, respectively. When the SPL of all three configurations was measured, it was uniformly observed that the straight configuration reliably demonstrated the lowest SPL in all instances where increased power was required for extinguishing. Additionally, the air velocity (AV) required to extinguish the fire was in the range of 0.30 to 0.50 m/s in all duct configurations. This can help to predict the necessary power adjustments required to achieve the desired velocity for extinguishing at frequencies that were not subject to this experiment.

Keywords: Acoustic wave; Diffraction characteristic; Duct space; Fire extinguishing; HVAC systems.

1. Introduction

Fire is essential to humanity in many aspects, for example, generating heat, cooking and more. Although fire has numerous benefits, it also carries a risk to our being. According to the statistics of public hazards in Thailand in 2022, fire accidents were the most common, accounting for 70.93% of all [1], while it had 54.31% of all incidents on the year 2021 [1]. Bangkok and Samut Prakan were ranked first and second suffering from fire incidences [1]. As human civilization progresses, more technology are implemented into daily life, increasing the frequency and danger of fire incidents. Heating, ventilation and air conditioning systems (HVAC) are one of those technologies. In the present time, HVAC system are become greater in number not only in commercial buildings, but also in households. Many residences in temperate climates install HVAC systems to provide heat and warm air during the winter season. Even though the likelihood of a fire in the ductwork is minimal, the consequences can be catastrophic. Fire can propagate throughout the building via the duct space, causing the entire building to catch in flame at the same moment. Nowadays, there are numerous innovative fire extinguishment solutions. Acoustic waves are one revolutionary technology being researched to extinguish fires. Even though this technology has been experimented for a while, the number of researches conducted has been limited.

In 2008, American Defense Advanced Research Projects Agency (DARPA) created a game-changing approach for extinguishing fires, employing sound waves as an alternate to traditional methods [2]. This new technology uses sound to accelerate air and distract flames, representing a significant change in fire prevention. Seth Robertson and Viet Tran [3] have applied the sound wave theory into a functional device. The finding shown that low-frequency acoustic waves had more effective for suppressing fires than high-frequency waves since it had greater impact on acoustic oscillation. Niegodajew et al [4] revealed that using lower frequencies need less speaker power and generated lower acoustic pressure for fire extinguishment than higher frequencies. Increasing the burner's power had minimal impact on the acoustic pressure, but much greater effect on the extinction power, especially when the distance between burner and acoustic source was enhanced. In addition, an acoustic screen was placed behind the fire source and moved to change the distance between fire source and waveguide to examine the profile of the extinction sound pressure level (ESPL). When the distance between the acoustic screen and the waveguide was shorter, a higher sound pressure level was required for fire suppression [5-6]. Not only the experiment, but the simulation results also confirmed that manipulating acoustic pressure and air velocity within a collimator can effectively extinguish flames [7]. Lower collimator exit diameter increased acoustic velocity, resulting in decreased pressure, similarly to fluid flow in a convergent pipe. The wave frequency range for flame suppression was around 92 Hz, with air velocity emerging as the primary extinguishing factor. Stawczyk and Wilk-Jakubowski [8] presented an extinguisher that generated from a speaker. The experimental results demonstrated the acoustic extinguisher's efficiency against flames. Notably, 14 Hz was the most economical frequency for extinguishment due to lower power consumption, whereas higher frequencies provided more benefits but necessitate more power.

Based on the information mentioned above, numerous studies on sound fire extinguishing have been carried out. However, very rare research related to extinguishing of duct fires has been conducted [10]. This is beneficial for researching the advantage of diffraction characteristic of sound wave to flow through narrow spaces. Therefore, the aim of this study is to conduct the experiment using sound wave extinguishing in three various ducts layouts. To fulfil this objective, the experiment was divided into three parts. The first part focused on investigating how loudspeakers suppress fires at various frequencies in each duct pattern. The term of minimum extinguishing power (MEP), extinction sound pressure level (ESPL), and extinguishing mean flow velocity were discussed. Second, the sound pressure level (SPL) at the candle's position was measured, followed by the mean flow velocity at the same location.

2. Fire and extinguisher

When discussing the subject of fire, the principle concept that leads to the occurrence of combustion involves a chemical interaction between a fuel source and oxygen. This reaction takes place within an environment characterized by exceptionally high temperatures. The consequence is the release of heat and light, accompanied with gas emissions. Understanding the origin of fire hinges on the flame tetrahedron concept, it comprises three essential components: fuel, oxygen, and heat, as illustrated in Figure 1. When the fuel reaches a critical temperature for ignition, mixing with some certain amount of oxygen. This triggers the breakdown of fuel molecules into smaller units, causing them to transition into a gaseous state. This transformation leads to the continuous emergence of a flame, commonly known as a "chain reaction".

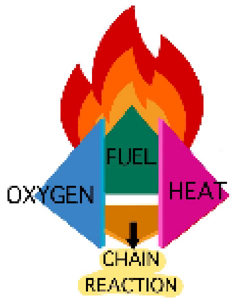

Figure 1. The concept of flame tetrahedron.

There are several techniques for fire extinction. Three mains strategies are outlined as follows: Foaming agents are widely employed in fire suppression, particularly in industrial applications and circumstances involving flammable liquid fires. The basic concept of agents is to establish a protective coating over the surface of fuel source, effectively inhibiting any prospects of re-ignition. Second, wet chemical solutions are often deployed as Class K fire extinguishers, notably in the food-related industries. These solutions react chemically with hot oils and fats, generating a foam layer that encompasses the burning oil. This strategic serves the dual purposes by preventing the emission of flammable vapours and obstructing the supply of oxygen required for combustion. Lastly, dry chemical powder is a versatile fire-suppressing agent, which are typically stored in portable fire extinguisher containers. The exterior layer of dry chemical powder functions as a thermal insulator, minimizing heat transfer between the fuel source and the fire, which can prevent the escalation of fires. However, the use of such chemical substances as foaming agents might have negative impacts on the surrounding and the living organisms [9]. Contemporary fire suppression methods may have unintended consequences in various situations. In particular, when fires occur in a confined space such as duct or pipe, the conventional usage of fire extinguishing agents could pose challenges owing to accessibility limitations. Moreover, employing water or chemicals for suppression may cause damage within these confined spaces. As a result, a concerted effort has been undertaken to explore and investigate acoustic wave technology as an alternative solution. This technology aims to navigate situations where access is restricted, without posing any detrimental effects on the environment.

3. Acoustic wave fire suppression

The use of acoustic waves for fire suppression expresses a highly effective technology, which is particularly appropriate for restricted location with limited access. Owing to challenges in accessing, a traditional fire suppression method such as water, gas, or chemical powders are impractical. Therefore, acoustic wave suppression emerges as an appealing alternative. This method minimizes the necessity for direct physical contact, making it harmless and safe for personnel involved.

The innovative concept of extinguishing fires with acoustic waves is to leverage the energy generated by speakers to induce fluctuations in air pressure, which disrupt the balance of fuel and oxygen at the flame's boundaries. This process behaves as a convective heat transfer mechanism in the flame region, thus effectively reducing the flame's average temperature. The fluctuations in air pressure induces the oscillations diminished the availability of oxygen for the flame, finally leading to inadequate oxygen levels required for combustion, resulting in flame extinguishment [7].

4. Experiment design

The significance of different duct configurations on the flame behavior within duct and their capability in acoustic wave fire extinguishing was the subject of this study. Three various duct patterns, including straight, elbow, and zigzag ducts, were designed by preserving the duct length constant at 100 cm and a collimator of 50 cm. The sound source was created by using a Tektronix AFG1062 function generator and Modify MA-13000 amplifier to increase signals from the function generator. The electrical qualities, including voltage, current and power, was measured by a power meter "YOKOGAWA WT310E". A JBL-GTO1214D 12-inch speaker with an RMS power of 350 W and a peak power rating of 1400 W was employed as a sound source and connected to the amplifier. A candle with a height of 3 cm and a wick of 1 cm was employed as a fire source and placed at the end of the duct. To visualize the behavior of candle flames, experimental videos were captured using a high-resolution camera, like the iPhone 11, with a 12-megapixel lens with an aperture of f/1.8. Figure 2 illustrates the schematic diagram of the experiment.

The experiments were divided into two parts:

i). Understand the acoustic wave characteristic of various duct designs and sound sources: A sound meter or a hot wire anemometer was equipped to measure the sound level or the mean flow velocity of air at the candle point in the duct. The experiment was carried out within a frequency range of 20-100 Hz, with 1 Hz increment. To observe how it affected the loudness as the frequency changed, the voltage RMS (Vrms) was set at 5.63 Vrms, 12.63 Vrms, and 19.65 Vrms, respectively. The data were collected for 5 seconds and the averaged value was calculated. The characteristic of sound wave in the ducts was represented via the terms of sound pressure level (SPL) and air velocity (AV).

ii). Investigate the minimum extinguishing power (MEP) for different duct layouts: The experiment started with a frequency of 25 Hz and gradually increased the power until the candle burned out. The frequency was then altered in 5-Hz increments. The experiment was terminated when the power was raised but the candle could not extinguish within 60 seconds or the maximum power exceeded 27.305 Vrms. These criteria were set to protect the speaker from the damage. Consequently, the frequency and power were recorded at each step, delivering the minimum extinguishing power (MEP).

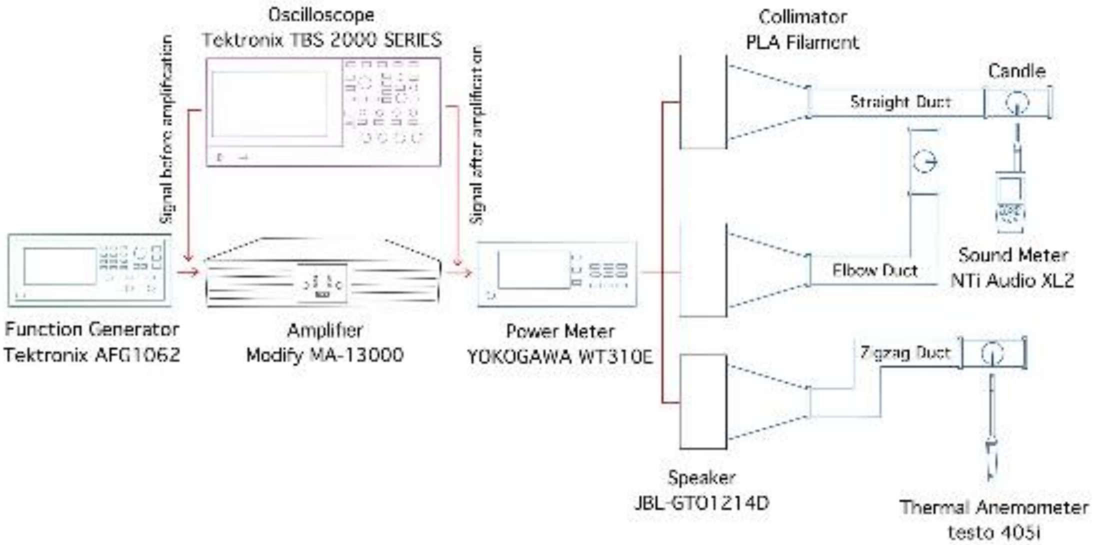

Figure 2. Schematic diagram of the experiment.

5. Results and Discussions

The experiment results were divided into two main parts. The first part, included Section 5.1 and 5.2, provided the detailed information regarding the characteristic of acoustic energy based on the duct designs and sources, which had not yet been related to their fire-fighting capabilities. The second part, which includes Section 5.3 and beyond, focused on the ability of acoustic fire extinguishers to suppress fires.

5.1. Sound pressure level characteristics

The sound pressure level (SPL) in each distinct duct design was measured by NTI XL2 sound level meter using A-weighting in an area where the fire source was located. The data was recorded continuously every second at a frequency range of 20 to 100 Hz, with 1-Hz increment per 5 seconds. Figures 3(a) and 3(b) depict the data and offer insight into how sound pressure and fire interacted. When sound travelled through a straight duct, as presented in Figure 3(a), the sound pressure level increased as the frequency increased. The sound with low-frequency tend to more fluctuate than high-frequency sounds. Additionally, it found that increasing the voltage input led to a corresponding increase in SPL while preserving similar characteristics.

Analysing the SPL characteristics of three different duct configurations was found that even the pattern of duct was differed, the SPL profiles were similar with difference in magnitude, as shown in Figure 3(b). The zigzag configuration had the potential to generate the highest SPL trend for every input voltage RMS, while the straight duct provided the lowest SPL trend among all three ducts. Furthermore, the SPL in the low-frequency range showed considerable variation among ducts, but the SPL in the high-frequency range was more uniform across all ducts.

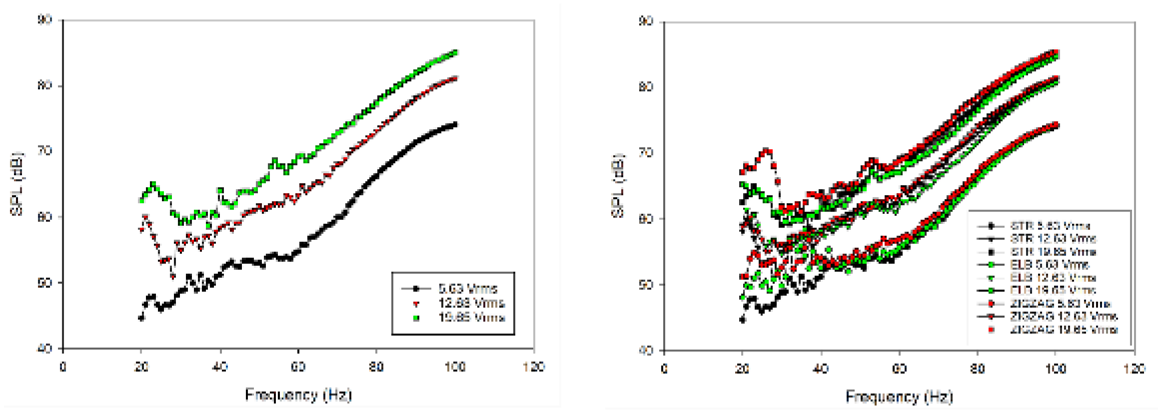

(a) (b)

Figure 3. Sound pressure level (SPL) as a function of frequency with different Vrms in (a) straight duct and (b) three distinct ducts: straight (STR), elbow (ELB), and zigzag.

As previously mentioned, the results show considerable fluctuations in low frequencies but barely minimal oscillations in high frequencies. This phenomenon can be explained through the occurrence of a resonance frequency between 30 and 40 Hz, when a sudden drop in SPL was detected. Resonance frequency also occurred at 60-70 Hz and 90-95 Hz due to it can observe severe shaking vibrations from the speaker at those frequencies throughout the testing. The impedance in the speaker reaching its local maximum point on the impedance curve (impedance vs frequency) generated the resonance. This resulted in a significant increase in vibration amplitude, which prevented the delivery power to the speaker and diminished the effectiveness and SPL in that resonance frequency range. Higher frequencies had lower local maxima, resulting in less violent vibrations than lower frequencies [7]. This was why the most acoustic fire extinguisher experiments avoid using frequencies where resonance had developed.

Although there was speculation regarding the occurrence of resonance frequency in this study, there was no solid evidence to confirm it. To observe and confirm this phenomenon with more concrete evidence, an impedance meter was needed to measure the impedance and plot the curve to identify the local maxima.

5.2. Air velocity characteristics

The purpose of this experiment was to determine the basic trend of air velocity (AV) across a range of frequencies while maintaining the same input voltage steady and comparing its trajectory at different voltage RMS inputs. Figure 4(a) depicts the air velocity profile of a straight duct at various voltage RMS. It is evident that the air velocity trend declined significantly between 20 and 60 Hz, after that it became more consistent and nearly constant. When approaching 90 Hz, the air velocity began to diminish again. The profiles resembled reverse exponential. Higher input voltage resulted in more power and enlarged air velocity. The velocity profiles at 19.65 Vrms and 12.63 Vrms were similar characteristics in that the velocity decreased gradually and became constant as the frequency reached 60 Hz. The air velocity stayed constantly at 0.22 m/s in the case of 19.65 Vrms, while it was 0.05 m/s inthe case of 12.63 Vrms. The 5.63 Vrms was less steep and reached zero velocity at the frequency of 49 Hz.

When three distinct duct designs were compared, as shown in Figure 7(b), there were only minimal differences in the air velocity profiles. However, the intriguing trendline was noticed in the zigzag and elbow ducts at 19.65 Vrms and 12.63 Vrms. The air velocity began to go up somewhat at approximately 70 Hz before descending again after 85 Hz. Whereas the trendlines of 5.63 Vrms gradually reduced and remained steady across all ducts. The appearance of fascinating trendline in zigzag and elbow ducts can indicate that this characteristic may potentially enhance the extinguishing ability of zigzag and elbow ducts at a high frequency as compared to straight duct. This agreed with the lowest SPL occurring in straight duct, as shown in Figure 6.

From these sections, if sound pressure level and air velocity had an impact on fire extinguishing ability, the straight duct could have the worst extinguishing ability. This contradicted the study's expectation that the straight duct could provide the best extinguishing capability due to its less complex configuration. This could make it easier for acoustic waves and air to pass through and interact with fire.

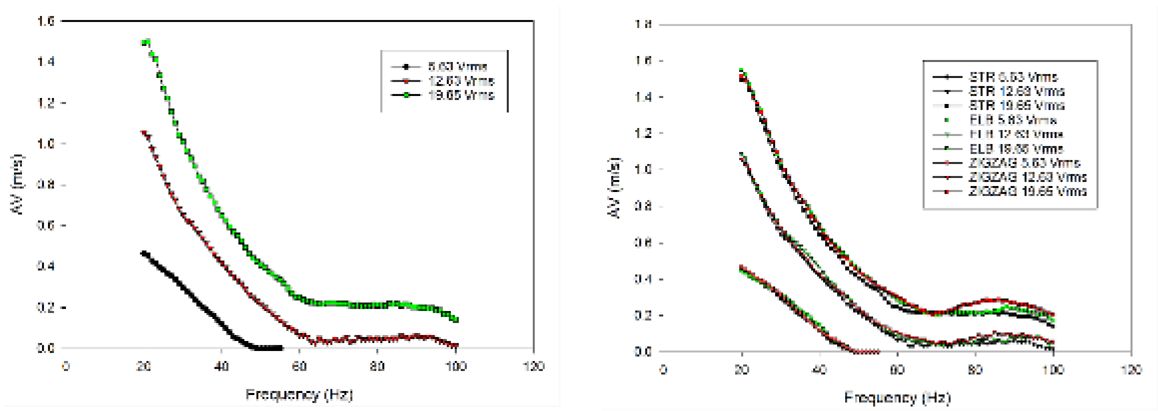

(a) (b)

Figure 4. The air velocity (AV) as a function of frequency with different Vrms in (a) straight duct and (b) three duct designs: straight (STR), elbow (ELB), and zigzag.

5.3. Minimum extinguishing power (MEP) characteristics

This section provides the experimental results on the minimum power required to extinguish a fire at various frequencies. Figure 5 shows the minimum extinguishing power (MEP) for fire extinguishment in three different duct configurations. At frequencies lower than 40 Hz, the deviation of MEP in all three ducts was not clearly noticeable. Following that, it found that the straight duct required the most power to extinguish fires when compared to the other two ducts. The MEP tendency in the elbow and zigzag ducts was identical. Furthermore, the zigzag duct exhibited a higher frequency of the extinguishment than the straight and elbow ducts. The maximum extinguishing frequency in the zigzag was 75 Hz, 65 Hz in elbow and 57.5 Hz in the straight duct.

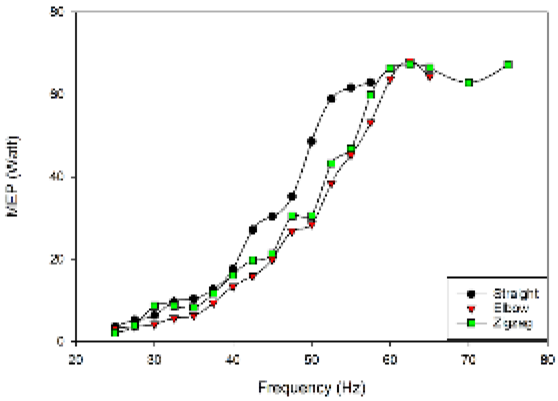

Figure 5. Minimum extinguishing power (MEP) in in three distinct ducts at various frequencies.

In previous sections, the lowest SPL and air velocity in a straight duct was discussed on its fire extinguishing capabilities, which corresponded to larger MEP required for fire extinguishing. It indicated a relationship between sound pressure, air velocity, and fire extinguishing abilities. The maximum extinguish frequency in straight duct was 57.5 Hz, the lowest frequency among all three ducts. This was due to the fact that the complex ducts, such as zigzag and elbow shapes, can generate the turbulent flow and increase the fire extinguishing ability, which did not occur in a straight duct. This can be observed by the movement of the candle flame, as illustrated in Figure 6. In straight duct, the candle flame burned consistently blown in a single direction for several seconds, but in the zigzag and elbow ducts, the flame oscillated more vigorously moving back and forth.

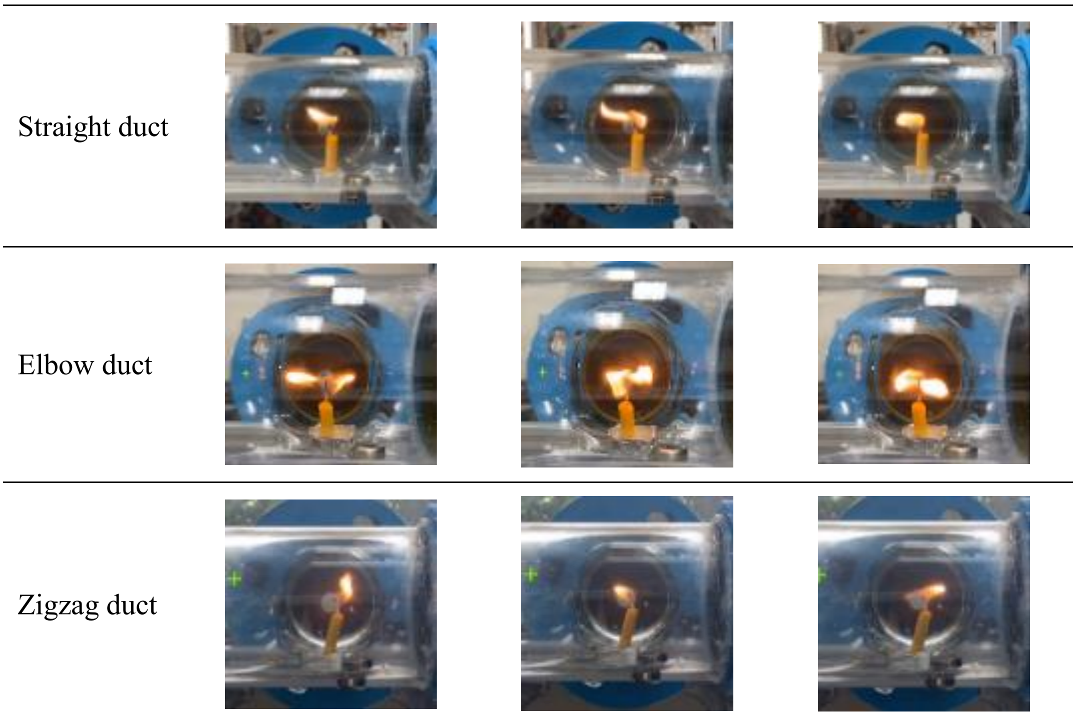

Figure 6. The behaviour of the candle flame in three different duct configurations.

5.4. Extinguishing sound pressure level (ESPL) and air velocity characteristics

This section describes the characteristics of extinguishing sound pressure level (ESPL) that are relevance to frequency and minimum extinguishing power (MEP). The ESPL was measured and recorded for 10 seconds, and the average value was examined. Figure 7(a) shows that the deviation in duct configurations cannot observe remarkable different on the ESPL, even if the extinguishing power at that frequency was varied. The findings corroborate the hypothesis of this study that the sound pressure level was related to extinguishing ability. Straight duct provided the lowest SPL, resulting in a larger demand of MEP to extinguish a fire to satisfy the minimum sound pressure level for extinguishing (ESPL).

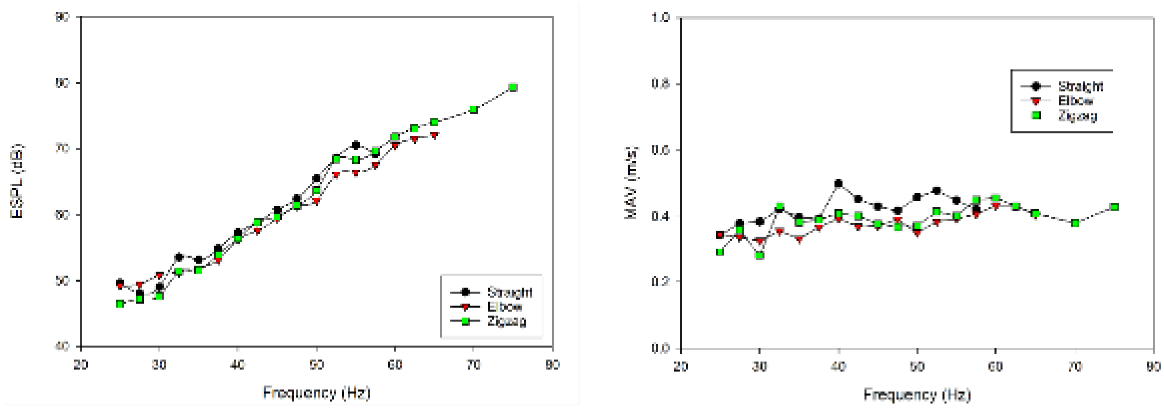

(a) (b)

Figure 7. The extinguish sound pressure level (ESPL) and minimum air velocity (MAV) characteristics for fire extinguishing in three different ducts (a) ESPL and (b) MAV.

The minimum extinguishing air velocity (MAV) is another factor in fire extinguishment. This parameter was also related to the minimum extinguishing power and its corresponding frequency. The air velocity was recorded for 10 seconds and averaged to determine the MAV needed to extinguish the fire. Figure 7(b) illustrates that complexities ducts with zigzag and elbow configurations required an air velocity range of 0.30 to 0.45 m/s to extinguish a fire. Straight ducts, on the other hand, required a greater air velocity for extinction flames of approximately 0.35 to 0.50 m/s. In addition, elbow duct is more stable, but the air velocity in zigzag duct presented more fluctuation. However, the trend of MAV appeared consistent across all ducts, with the straight duct standing out with a higher MAV, especially when the frequency was over 40 Hz. This indicates that the straight duct required higher airflow velocity to extinguish fires than the other ducts. This confirms a previous discussion that the straight duct encountered less turbulence, requiring higher air velocity and input voltage RMS to supply the extinguisher.

From this investigation, it can recognize that the air velocity threshold for fire extinguishing ranged from 0.30 to 0.50 m/s for these three duct configurations. When the air velocity threshold was highlighted on the straight duct's air velocity characteristic, as shown in Figure 8, it displayed the extinguishing boundary, which can predict the required input voltage RMS at a specified frequency or the necessary power for extinguishing flames. For instance, at 40 Hz, the needed input voltage RMS to extinguish a fire was roughly 12.63 Vrms.

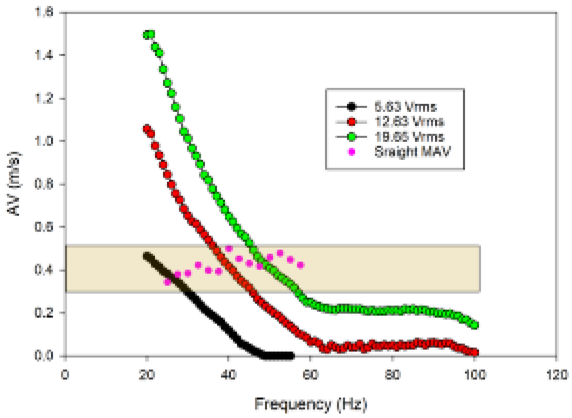

Figure 8. Air velocity characteristic and minimum extinguishing air velocity characteristic with and minimum extinguishing air velocity boundary.

Although the acoustic fire extinguisher offers an effective solution for extinguishing fires in small, narrow, and complex spaces such as ducts or electrical conduits, its mechanism is dependent on the speaker's ability to accelerate the flow of air particles, which is beneficial to fire suppression. In order to achieve this effect, the speaker must be large enough to interact with a substantial quantity of air particles in relative to the cross-sectional area of the space. This requirement makes the acoustic fire extinguisher system unsuitable for larger areas, since it would be costly and impractical for broad use. In such instances, traditional firefighting tactics would be a better choice and more cost-effective option.

6. Conclusion

The basic characteristics of an acoustic wave extinguisher and its ability to extinguish fires within different duct configurations were investigated in this study. To facilitate a comprehensive comparative analysis, several important parameters were considered, including minimum extinguishing power (MEP), minimum extinguishing air velocity (MAV), sound pressure level (SPL), and air velocity (AV).

The characteristics of sound pressure level and air velocity in a straight duct consistently delivered the lowest values for every input voltage RMS, followed by the elbow and zigzag ducts. In the low-frequency region, all ducts exhibited significant fluctuations and a drop in sound pressure level. While in the high-frequency region, all ducts showed a change of air velocity slope, with zigzag and elbow becoming upward but straight approach constant. The magnitude of sound pressure level needed to extinguish fire remained consistent across all duct designs, although higher frequencies necessitated greater sound pressure levels. The threshold air velocity required to suppress fire was in the range of 0.30 to 0.50 m/s. The effect of turbulent flow and duct complexity was also notable, which may explain why straight duct was the most difficult to extinguish fire and required the highest power supplied to the speaker.

In summary, the ability to flame extinguishment is dependent on the sound pressure level and air velocity. While these two factors are related to the input voltage RMS supplied to the extinguisher, which are not directly related with each other. Another crucial factor affecting the ability to extinguish flames within a duct is the available of turbulent flow. As a result of its intrinsic simplicity, straight duct provided the lowest extinguishing ability. For an optimal condition of fire extinguisher, it should operate at the lowest possible frequency. This requires less power while increasing air velocity and lowering sound pressure level to efficiently extinguish the fire.

7. Acknowledgements

The authors acknowledge the supported provided by National Science and Technology Development Agency (NSTDA) under the Research Chair Grant, Thailand Science Research and Innovation (TSRI) Basic Research Fund: Fiscal year 2023 (Program: Sustainable Mobility) and National Science, Research and Innovation Fund (NSRF) via the Program Management Unit for Human Resources & Institutional Development, Research and Innovation [grant number B40G660039].

8. References

[1] DPM Reporter. (2023, Sep 9) Statistic of Public Hazards in Thailand. https://dpmreporter.disaster.go.th/portal/disaster-statistics

[2] Anthony, S. (2012, July 16). DARPA creates sound-based fire extinguisher. *ExtremeTech.* https://www.extremetech.com/defense/132859-darpa-creates-sound-based-fire-extinguisher

[3] Interesting Engineering. (2017, January 13). Two Engineering Students Invent A Sonic Fire Extinguisher. Interesting Engineering. *Interesting Engineering*. https://interestingengineering.com/two-engineering-students-invent-a-sonic-fire-extinguisher

[4] Niegodajew, P., Łukasiak, K., Radomiak, H., Musial, D., Zajemska, M., Poskart, A., & Gruszka, K. (2018). Application of acoustic oscillations in quenching of gas burner flame. *Combustion and Flame*, 194, 245–249.

[5] Niegodajew, P., Gruszka, K., Gnatowska, R., & Šofer, M. (2018). Application of acoustic oscillations in flame extinction in a presence of obstacle. *In XXIII Fluid Mechanics Conference (KKMP 2018), IOP Conf. Series Journal of Physics*: *Conf. Series*, 1101, 012023.

[6] Gruszka, K., Durajski, A. P., Niegodajew, P., Wawrzyniak, A., Gnatowska, R., Beben, M., & Sofer, M. (2020). Studies of acoustic wave propagation when facing obstacle. *Acta Physica Polonica Series A*, 138(2), 280-282.

[7] Raavi, T. S., & Sharma, G. (2018). Sonic Fire Extinguisher. *Pramana Research Journal*, 8(11), 337-345.

[8] Stawczyk, P., & Wilk-Jakubowski, J. (2021). Non-invasive attempts to extinguish flames with the use of high-power acoustic extinguisher. *Open Engineering*, 11(1), 349–355.

[9] Gurbanova, M., Loboichenko, V., Leonova, N., & Strelets, V. (2020). Effect of inorganic components of fire foaming agents on the aquatic environment. *Journal of The Turkish Chemical Society Section A,* 7(3), 833-844.

[10] Kim, B., Bae, M., & Bae S. (2017). A study on a suitability of sound fire extinguisher in duct environment. *International Journal of Applied Engineering Research,* 12(24),15796-15800.

AEC0007

Biogas Purification Kit and Combustion Characteristic Study Results

Wannadear Nawae[1], Panadda Solod[1], Theerawat Petdee[2], Thanwit Naemsai[2], Jaruwat Jareanjit[2], and Wasu Suksuwan[2,*]

[1] Bachelor of Technology (Petroleum Technology), Faculty of Industrial Education and Technology, Rajamangala University of Technology Srivijaya, Songkhla, 90000, Thailand
[2] Department of Mechanical Engineering, Faculty of Engineering, Rajamangala University of Technology Srivijaya, Songkhla, 90000, Thailand

* Corresponding Author: wasu.s@rmutsv.ac.th

Abstract. This research investigates biogas purification methods to enhance biogas quality for sustainable energy use. The biogas purification system showcases stainless steel cylinders, illustrating user-friendly design. Our study explores purification approaches lime and water: Varying lime-to-water ratios enhance methane (CH_4) content by up to 5%. Steel Materials: Different steel types reduce carbon dioxide (CO_2) levels by up to 20%. Charcoal: Charcoal materials have limited impact on CO_2 and hydrogen sulfide (H_2S) content. Lime water purification shows potential for CH_4 enhancement, and steel types influence CO_2 reduction. Integration of lime water and mixed steel significantly improves biogas quality, with up to 20% lower CO_2 levels and increased combustion efficiency. These findings contribute to efficient and eco-friendly biogas utilization.

Keywords: Biogas Purification Kit, Biogas, combustion.

1. Introduction

Biogas stands as an impressive exemplar of renewable energy, poised to potentially replace conventional fossil fuels and waste natural gas, thereby contributing to an enhanced and more sustainable energy panorama [1, 2]. This eco-friendly energy source is created through the complex process of anaerobic digestion, involving various organic materials, from animal manure to a wide range of organic substances, all driven by microorganisms. The ensuing amalgamation of gases comprises methane (CH_4), carbon dioxide (CO_2), nitrogen (N_2), hydrogen (H_2), and hydrogen sulfide (H_2S), with methane overwhelmingly dominating this composition [3]. The presence of methane makes biogas flammable, making it essential for applications such as lighting and engine power in thermal energy.

Among the remarkable features of the anaerobic fermentation process that produces biogas, its simultaneous ability to reduce organic matter is particularly noteworthy. This transformation of organic matter leads to a decrease in both chemical oxygen demand (COD) and biological oxygen demand (BOD), highlighting the positive environmental impact of this process [4]. Importantly, the adoption of biogas technology shows the potential to significantly reduce organic matter content in fermentation agents, often by 50-70%. This substantial reduction presents a practical approach to address wastewater treatment and combat pollution.

In the biogas production process, the installation of biogas digesters, available in various sizes from small to medium, is a crucial step. These digesters serve a wide range of applications, including households and small to medium-sized industries. Once biogas is produced, it is immediately conveyed through pipelines for use. The standard setup involves connecting the biogas to a gas burner, as depicted in Figure 1.

However, direct combustion of biogas presents two significant challenges that require consideration. Firstly, the gas obtained may not meet required purity standards, potentially leading to equipment corrosion over time. Additionally, certain toxic gases are present in the biogas composition, making it impractical for use with intricate and sensitive equipment like engines. In cases where the application area is far from the gas fermentation tank, a common issue arises. The biogas pressure may be insufficient for seamless transportation over extended distances. Consequently, this pressure inadequacy hinders sustained and continuous biogas combustion, becoming a fundamental cause of instability in the fuel gas system.

Figure 1. Biogas digesters and the utilization of biogas.

From the gas that is used is not clean enough, it affects the corrosion of the equipment that is used. And there are some gases that are toxic. The research team has studied relevant research to solve the problem.

Atelge et al., [5] explores biogas as a promising renewable resource, highlighting its potential for waste-to-energy conversion. It examines biogas composition, purification techniques, and upgrading processes, with a focus on biomethane production. Biogas finds applications in CHP, fuel cells, and internal combustion engines, along with emerging prospects in chemical production.

Osorio et al., [6] Study on on optimizing the purification of biogas generated from anaerobic sludge digestion in wastewater treatment, with the aim of using it as a vehicle biofuel. The study emphasizes chemical desulfurization through scrubbing towers and activated carbon filters. Despite high initial H2S concentrations, the approach proves effective, yielding effluent biogas with H_2S levels under 1 ppm and negligible trace element presence among the analyzed elements.

Ray et al., [7] designing and developing a biogas production, purification, compression, and storage system for rural household cooking. Employing a floating drum digester, the system utilizes anaerobic digestion of kitchen waste and an elastic balloon for biogas collection. A foot lever compressor, silica gel container for water vapor removal, and a hydrogen sulfide scrubber are integrated. The prototype achieves around 4 bar pressure, compressing biogas within a 0.5m³ tank during a 30-minute operating cycle.

Nindhia et al. [8] study the process, which involves annealing the steel chips to remove residual stress and promote oxidation, yielding iron oxide. These iron oxide forms, Fe_2O_3 and $Fe(OH)_3$, effectively react with H_2S in biogas. However, sulfur precipitation as Fe_2S_3 on steel chips' surface reduces desulfurization efficiency. The research recovers effectiveness by reacting Fe_2S_3 with O_2 and H_2O, allowing for regenerative reuse of the desulfurizer.

Pertiwiningrum et al. [9] have advanced the use of chemically activated biochar-based rice husk as an alternative to fossil-fuel-derived activated carbon, aiming to adsorb carbon dioxide in biogas purification. By replacing 25% of natural zeolite, activated biochar effectively adsorbed carbon dioxide and enriched methane levels. Optimal results were achieved with a 30-minute purification, enhancing methane by 24%. This highlights activated biochar's potential as a biogas adsorbent, facilitated by chemical activation.

Jiang et al. [10] study the process, which involves ammonia removal through air stripping of digested dairy manure, addressing potential air and water quality concerns. Temperature and pH were identified as critical parameters. The optimized pH and lime dosage achieved 90% ammonia removal, and the stripped ammonia was converted to ammonium sulfate using sulfuric acid. The effluent's high pH was subsequently adjusted using biogas to both lower the pH and purify the biogas through H2S and CO_2 scrubbing. This method demonstrated feasibility and efficiency in ammonia removal from digested dairy manure.

Based on the initial studies discussed, it's evident that a predominant focus lies in the advancement of biogas purification techniques. These efforts primarily aim to mitigate polluting gases within biogas compositions by employing diverse materials such as lime, steel shavings, and charcoal. However, an unexplored realm pertains to the purification tailored for each specific biogas type, seeking the optimal utilization ratio. This particular aspect remains uncharted within the existing body of research.

Hence, this paper proposes an inventive approach to biogas purification. The developed purification design prioritizes simplicity of operation and minimal maintenance requirements, thereby addressing consumer concerns. Furthermore, this design demonstrates the capability to effectively separate pollutants from multiple biogas variants. To delve into the efficacy of removing carbon dioxide from biogas, the study embarks on constructing an innovative series of biogas purification. The research investigates optimal absorption materials for biogas purification, focusing on the removal of carbon dioxide and hydrogen sulfide pollutants from the biogas. Subsequently, the purified biogas is introduced into a combustion setting to assess its efficiency as a fuel source.

2. Methodology

Figure 2 showcases the 3D model and schematic representation of the biogas purification system, featuring a set of stainless steel biogas purification cylinders. These cylinders, each measuring 15 cm in diameter and 30 cm in height, are meticulously integrated with the stainless steel pipe inlet and outlet system. The outlet is thoughtfully equipped with a compressor designed to suction the treated biogas as it exits the system through the 2.5 cm diameter pipeline. The operational mechanism of the biogas purification kit involves the utilization of filtration materials within the purification device. These materials, strategically placed, target the capture of carbon dioxide (CO_2) and hydrogen sulfide (H_2S) gases from the biogas. The compressor pump actively facilitates the flow of biogas through this purification device, effectively eliminating these undesirable components. Importantly, the entire design emphasizes user-friendliness and ease of operation, aligning with the overarching design philosophy.

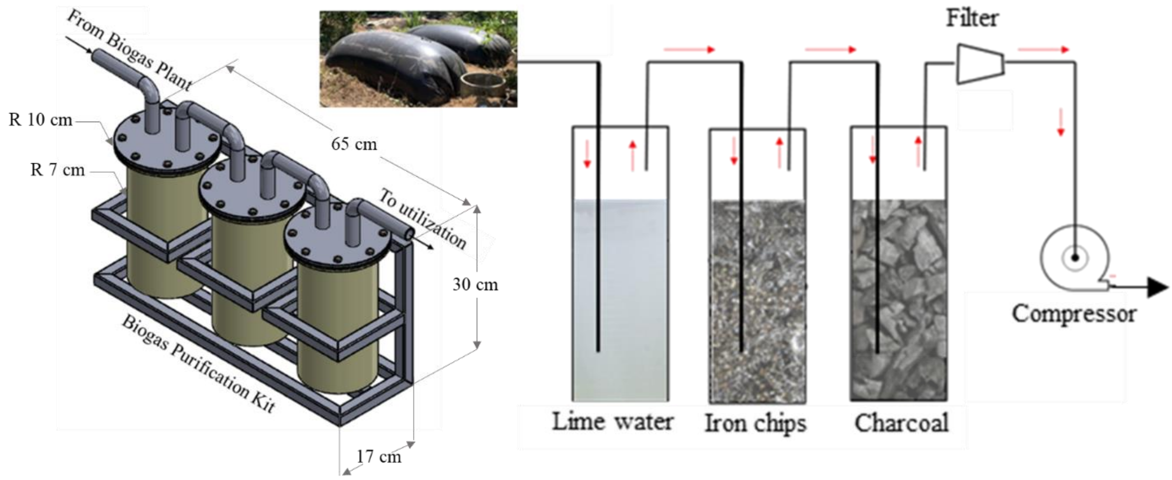

Figure 2. 3D model and schematic diagram of biogas purification kit.

In terms of the research methodology, the investigation commenced by assessing the elution potential of carbon dioxide (CO_2) and hydrogen sulfide gas (H_2S). This served as the foundation for studying the biogas elution conditions through three distinct composite filters.

(1) In the first group, lime and water were combined in varying proportions by mass: 0.5 kg of lime per 2.5 kg of water, 0.75 kg of lime per 2.5 kg of water, and 1 kg of lime per 2.5 kg of water.

(2) In the second group, the gas was directed through three types of steel materials (illustrated in figure 3(a)): 1 kg of steel chips, 1 kg of steel sheet, and 1 kg of mixed steel. Notably, elution occurred between 0.5 kg of steel powder and 0.5 kg of steel sheet.

(3) In the third group, biogas purification was executed using three distinct types of charcoal (depicted in figure 3(b)): 1 kg of charcoal powder, 1 kg of wood charcoal, and 1 kg of charcoal briquette.

Figure 3. Materials for composite filters.

Each of these groups encompassed various configurations to explore the effectiveness of composite filters in removing undesirable gas components from the biogas. This comprehensive approach allowed for a thorough evaluation of the purification capabilities of different materials and combinations. To ensure accurate measurements, the biogas was sampled every three trials, and data were collected at intervals of 2 minutes, 5 minutes, and 10 minutes, using a Biogas meter to precisely quantify the collected biogas volumes.

To analyze biogas composition, we used a portable gas detector (PONPE 322-C1, Thailand) as detailed in Table 1. Initially, the accuracy of the biogas analyzer was validated against established standards, including the in-house water and wastewater examination method (Part 2720 C. method) and ASTM D 1945 (Volume 05.06, 2015) at the Energy Research and Development Institute-Nakornping, Chiang Mai University

Table 1. Details of the instruments.

Parameter	Device	Accuracy
Biogas analyzer	Portable gas detector (PONPE 322-C1, Thailand)	CO_2: 0-100% Vol. ± 5% FS H_2S: 0-100 ppm ± 5% FS CH_4; 0-100% Vol. ± 5% FS O_2: 0-30% Vol. ± 5% FS Resolution: 0.01%, 1 ppm Repeatability Error ≤ 2%

The results, as depicted in Table 2, revealed remarkable similarity between the methane measurements obtained from both methods. However, slight discrepancies were noted in carbon monoxide and oxygen levels. This divergence could be attributed to the potential of ambient oxygen leakage during the process of collecting biogas in a gas collection bag. Despite this, the biogas analyzer demonstrated the capability to yield results akin to those generated by standard measuring instruments, especially when considering methane gas, which underscores its reliability in practical applications.

Table 2. Comparison of biogas analyzer and standard methods.

Gas detector	Inhouse method	gas detector portable	Unit
Methane (CH_4)	79.90	78.18	%vol.
Carbon dioxide (CO_2)	10.60	14.46	%vol.
Oxygen (O_2)	2.00	0.30	%vol.
Nitrogen (N_2)	7.50	-	%vol.
Hydrogen sulfide (H_2S)	-	< 100	ppm

3. Results and Discussions

In this study, we investigated the impact of lime water purification on the composition of biogas, focusing on methane (CH_4), hydrogen sulfide (H_2S), carbon dioxide (CO_2), and oxygen (O_2). Figure 4 illustrates the results obtained with varying lime-to-water ratios of 0.50:2.50, 0.75:2.50, and 1.00:2.50. The biogas composition before purification is represented by the red line in Figure 4(a) – 4(d).

Methane, a valuable component of biogas, showed a consistent increase in concentration following purification with lime water across all tested ratios. Notably, the highest methane concentration was observed with the 0.50:2.50 lime-to-water ratio. This finding suggests that lime water effectively enhances methane recovery, making it a promising method for improving biogas quality.

Hydrogen sulfide, an undesirable emission gas, exhibited a clear reduction in concentration as the lime-to-water ratio increased. The lime-to-water ratios of 0.75:2.50 and 1.00:0.25 were particularly effective, achieving purification levels below 20 ppm. Regarding the increase in CH_4 and the decrease in CO_2 and H_2S, this phenomenon can be attributed to biogas, determined by volume analyzed. When we effectively remove CO_2 and H_2S, it leads to higher CH_4 concentrations. These results indicate that lime water is a reliable means of mitigating hydrogen sulfide emissions in biogas production, contributing to a cleaner and safer working environment.

Carbon dioxide levels in biogas also decreased after purification with lime water, albeit with less pronounced differences among the tested ratios. While all ratios demonstrated some level of CO_2 reduction, the variations observed were not statistically significant. This suggests that lime water may be less effective at reducing carbon dioxide compared to other gases like hydrogen sulfide and methane. reduction.

Oxygen levels in biogas typically decrease over time due to biological processes within the tank. However, an interesting observation was made in the case of the 0.75:2.50 lime-to-water ratio, where oxygen levels were temporarily higher at 2 and 5 minutes after purification. This phenomenon can be attributed to initial residual oxygen within the tank, which had not yet been completely exhausted. Over a more extended period, oxygen levels in all cases decreased, aligning with the expected trend.

In summary, the results of this study demonstrate the potential of lime water purification in enhancing biogas quality and reducing emission gases, particularly methane and hydrogen sulfide. The 0.50:2.50 lime-to-water ratio showed the highest methane concentration, while the 0.75:2.50 and 1.00:0.25 ratios effectively reduced hydrogen sulfide levels below 20 ppm. Carbon dioxide reduction, although observed in all cases, was less substantial and not statistically significant.

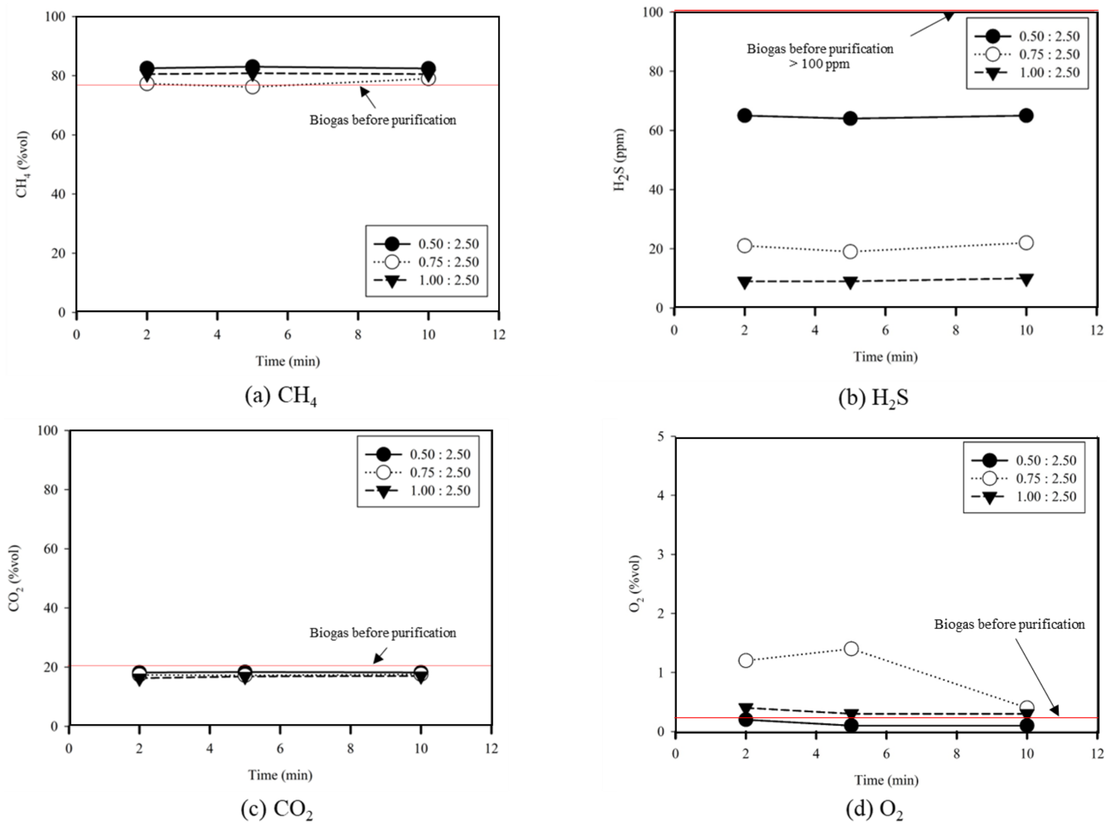

Figure 4. Investigating the changes in biogas composition through purification with lime water.

Figure 5 presents the results of gas composition analysis using different types of steel, consisting of steel chips (IC), steel sheet (IS), and mixed steel (MI). The study focused on the concentrations of methane (CH_4), hydrogen sulfide (H_2S), carbon dioxide (CO_2), and oxygen (O_2) to assess the effect of these steel types on biogas quality.

Figure 5(a) displays the methane composition results, showing that all types of steel steel positively influenced CH_4 concentration in biogas. Notably, the mixed steel (MI) configuration, which combined steel chips and steel sheets, exhibited the highest methane concentration among all cases. This finding suggests that the use of mixed steel can effectively enhance the recovery of CH_4 in biogas production processes. Increased methane concentration is desirable as it improves the energy content of biogas.

Figures 5(b) and 5(c) depict the concentrations of hydrogen sulfide (H_2S) and carbon dioxide (CO_2), two emission gases that need to be reduced to enhance biogas quality. The results indicate that all steel cases failed to reduce H_2S concentrations to levels below 100 ppm. This suggests that the selected steel types, including IC, IS, and MI, were not effective at mitigating hydrogen sulfide emissions. However, for carbon dioxide (CO_2), the steel cases demonstrated varying degrees of effectiveness in reducing its concentration. Notably, the MI configuration was the most efficient in reducing CO_2 levels, followed by IC and IS. This implies that the use of mixed steel can contribute to a significant reduction in carbon dioxide emissions from biogas. Figure 5(d) indicates that the MI configuration had the lowest O_2 levels, followed by IC and IS. Lower O_2 concentrations are desirable to enhance the safety and combustion efficiency of biogas.

The findings suggest that the choice of steel type, particularly the use of mixed steel, can play a crucial role in optimizing biogas production processes by increasing methane content and reducing carbon dioxide emissions.

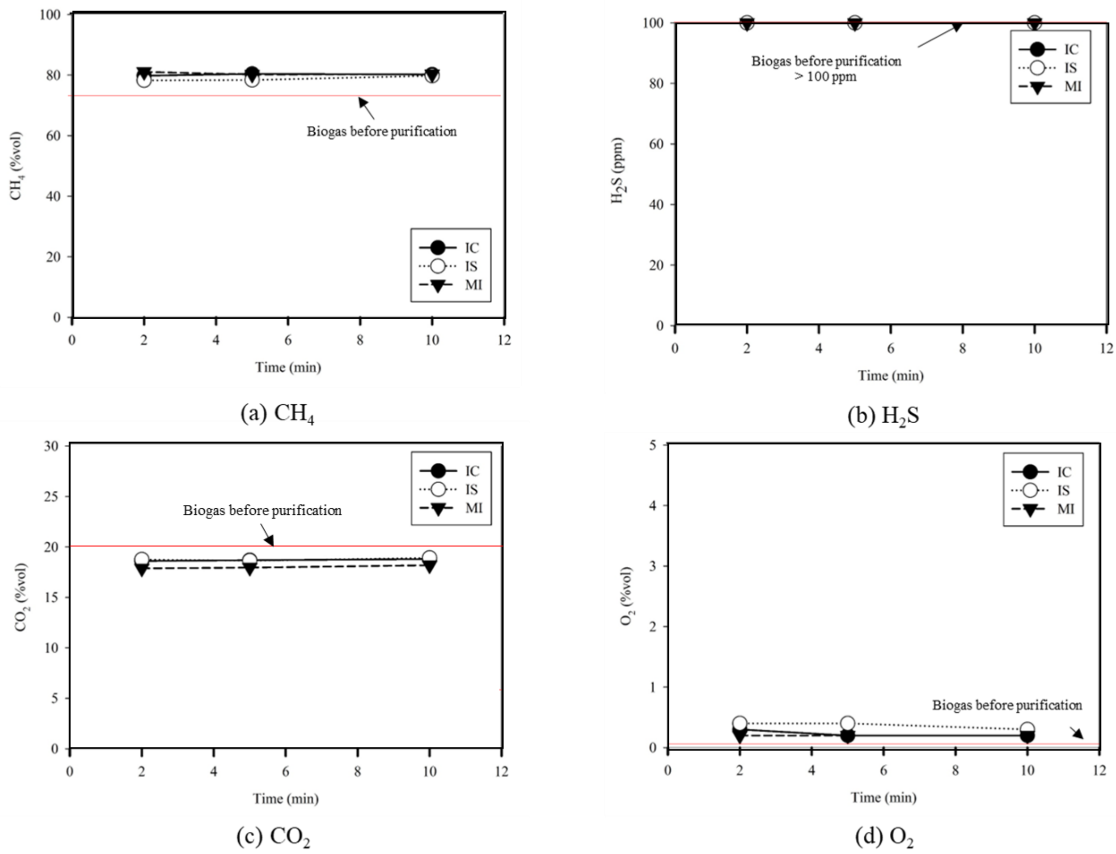

Figure 5. Investigating the changes in biogas composition through purification with steel.

Figure 6 presents the results of gas composition analysis after purification using three different types of charcoal: charcoal powder (WCP), wood charcoal (WC), and charcoal briquette (CB). The study aimed to assess the impact of these charcoal types on biogas composition, focusing on methane (CH_4), hydrogen sulfide (H_2S), carbon dioxide (CO_2), and oxygen (O_2).

In Figure 6(a), the results indicate that all three types of charcoal had a minimal impact on methane (CH_4) concentration in biogas. The CH_4 concentrations in all cases remained closely aligned with the biogas composition before purification. This suggests that charcoal did not significantly contribute to the purification of CH_4 from the biogas. It is apparent that other factors or purification methods may be more effective in enhancing CH_4 concentrations.

Figures 6(b) and 6(c) display the concentrations of hydrogen sulfide (H_2S) and carbon dioxide (CO_2), two emission gases that need to be reduced to improve biogas quality. Interestingly, the results show that the use of charcoal had no substantial effect on reducing the concentrations of H_2S and CO_2. These gases remained largely unchanged from the composition of biogas before purification. This indicates that charcoal, in the forms of WCP, WC, or CB, was not effective in mitigating hydrogen sulfide and carbon dioxide emissions.

The concentration of oxygen (O_2) in biogas is crucial, as higher levels can pose safety risks during combustion. Figure 6(d) reveals that the use of charcoal also had no significant effect on oxygen concentration. The O_2 levels after purification with charcoal were similar to those in the biogas before purification, indicating that charcoal did not contribute to reducing oxygen content.

In conclusion, the results of this study suggest that the use of charcoal, in the forms of charcoal powder (WCP), wood charcoal (WC), or charcoal briquette (CB), had minimal impact on gas composition during biogas purification. Specifically, there were no significant changes observed in methane (CH_4) concentration, hydrogen sulfide (H_2S), carbon dioxide (CO_2) emissions, or oxygen (O_2) content. Charcoal, in this context, appears to be ineffective for the purification of biogas components, such as CH_4, H_2S, and CO_2. Instead, it may primarily serve to reduce moisture content, which was not a focus of this study.

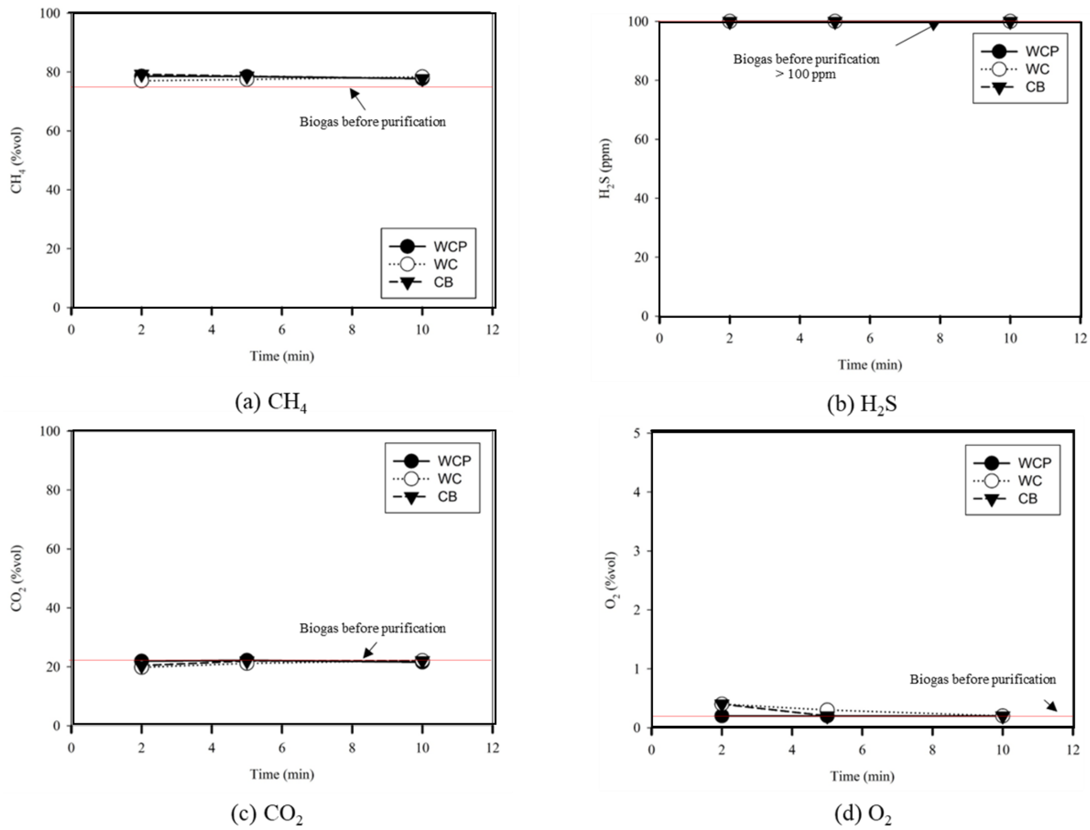

Figure 6. Investigating the changes in biogas composition through purification with charcoal.

In addition to the previously mentioned studies, this research explored the effectiveness of two selected purification materials: lime water with a ratio of 1.00:2.50 and mixed steel. The study aimed to determine the optimal purification materials for improving the composition of fuel gas by comparing biogas with and without purification. Charcoal was excluded from the study as it did not show significant effects on reducing biogas concentrations.

Lime water with a ratio of 1.00:2.50 and mixed steel were chosen as the purification materials to be integrated into purification kits. The impact of these materials on biogas composition was examined to assess their effectiveness in enhancing fuel gas quality. Table 2 presents a comparison of the composition of fuel gas between biogas without purification and biogas with purification using the selected materials. The result shown that the concentration of CO2 in biogas with purification was significantly lower than in biogas without purification. Specifically, CO2 levels were reduced by 0.51% through the purification process. This reduction is essential as lower CO2 content enhances the energy content of the biogas and reduces greenhouse gas emissions. In contrast to CO2, the concentration of O2 in biogas with purification was higher than in biogas without purification. This is attributed to the fact that biogas with purification is easier to burn, requiring less oxygen for combustion. The increase in O2 content further improves the combustion efficiency of the biogas.

The research also evaluated the combustion efficiency (C.E.) [11] of biogas with and without purification, as shown in Eq (1). Where $[CO_2]$ is volume concentration (dry) of CO_2, [CO] is volume concentration (dry) of CO. The results showed that biogas with purification exhibited a significantly higher combustion efficiency compared to biogas without purification, with a difference of 2.7971%. This improvement in combustion efficiency is a crucial factor as it enhances the energy utilization of biogas during combustion processes.

$$C.E. = \frac{[CO_2]}{[CO_2]+[CO]} \times 100\% \tag{1}$$

These findings emphasize the importance of selecting appropriate purification materials and methods to optimize the quality and energy content of biogas, making it a more environmentally friendly and efficient energy source.

Table 2. Comparison of fuel gas from biogas.

Gas detector	Biogas without Purification	Biogas with Purification	Unit
Carbon dioxide (CO_2)	2.4300	1.9200	%
Carbon monoxide (CO)*	0.0714	0.0011	%
Oxygen (O_2)	17.3000	18.7000	%
Combustion efficiency (C.E)	97.1456	99.9427	%

- Carbon monoxide was converted from parts per million (ppm) to a percentage (%) using the equation %CO = ppm/10,000.

4. Conclusion

This study investigated methods for improving biogas quality and energy content through purification and optimization techniques. We examined three key areas: lime water purification, the influence of different steel types, and the effectiveness of selected purification materials, specifically limestone and mixed steel.

Lime water purification demonstrated its potential to enhance methane (CH_4) recovery and reduce harmful emission gases. While all steel types increased CH_4 concentration, mixed steel (MI) showed the most promise. However, none of the steel types effectively reduced hydrogen sulfide (H_2S) concentrations.

The integration of lime water and mixed steel purification materials significantly enhanced biogas quality by lowering carbon dioxide (CO_2) levels and increasing combustion efficiency. These improvements have clear implications for cleaner energy production and reduced greenhouse emissions gas.

In conclusion, the choice of purification materials and methods is pivotal in optimizing biogas for sustainable energy applications. Our findings contribute to the development of more efficient and environmentally friendly biogas utilization. Future research should continue to refine and innovate purification techniques to unlock the full potential of biogas as a renewable energy source.

5. Acknowledgments

This work was financially supported by the Rajamangala University of Technology Srivijaya (RUTS).

6. References

[1] Kougias P.G. & Angelidaki, I. (2018). Biogas and its opportunities—A review. *Front. Environ. Sci. Eng, 14, https://doi.org/10.1007/s11783-018-1037-8*

[2] Khan, I. U., Othman, M. H. D., Hashim, H., Matsuura, T., Ismail, A. F., Rezaei-DashtArzhandi, M., & Wan Azelee, I. (2017). Biogas as a renewable energy fuel – A review of biogas upgrading, utilisation and storage. *Energy Conversion and Management*, 150, 277-294.

[3] Rasi, S., Veijanen, A., & Rintala, J. (2007). Trace compounds of biogas from different biogas production plants. *Energy*, 32, 1375-1380.

[4] Samudro, G., & Mangkoedihardjo, S. (Year). Review on BOD, COD and BOD/COD Ratio: A Triangle Zone for Toxic, Biodegradable and Stable Levels. *International Journal of Academic Research*, 2(4), 235-239.

[5] Atelge, M. R., Senol, H., Djaafri, M., Hansu, T. A., Krisa, D., Atabani, A., Eskicioglu, C., Muratçobanoˇ glu, H., Unalan, S., Kalloum, S., et al. (2021). A Critical Overview of the State-of-the-Art Methods for Biogas Purification and Utilization Processes. *Sustainability, 13, 11515*. https://doi.org/10.3390/su132011515.

[6] Osorio, F., & Torres, J.C. (2009). Biogas purification from anaerobic digestion in a wastewater treatment plant for biofuel production. *Renewable Energy, 34*, 2164-2171.

[7] Ray, N.H.S., Mohanty, M.K., & Mohanty, R.C. (2016). Biogas Compression and Storage System for Cooking Applications in Rural Households. *International Journal of Renewable Energy Research, 6(2).*593-598.

[8] Tirta Nindhia, T.G., Sucipta, I.M., Surata, I.W., Adiatmika, I.K., Putra Negara, D.N.K., & Trisna Negara, K.M. (2013). Processing of Steel Chips Waste for Regenerative Type of Biogas Desulfurizer. *International Journal of Renewable Energy Research, 3(1).*84-87

[9] Pertiwiningrum, A., Rhema, T., Wuri, M. A., Fitriyanto, N. A., & Tontowi, A. E. (2022). The Effect of Chemical Activation of Biochar on Biogas Purification. *IOP Conference Series: Earth and Environmental Science, 1108, 012032*. doi:10.1088/1755-1315/1108/1/012032.

[10] Anping Jiang, Tianxi Zhang, Quan-Bao Zhao, Xiujin Li, Shulin Chen, Craig S. Frear. (2014). Evaluation of an integrated ammonia stripping, recovery, and biogas scrubbing system for use with anaerobically digested dairy manure. Biosystems Engineering, 119, 117-126.

[11] Wu, K.-K., Chang, Y.-C., Chen, C.-H., & Chen, Y.-D. (2010). High-efficiency combustion of natural gas with 21–30% oxygen-enriched air. *Fuel, 89*, 2455–2462.

AEC0008

Thermal efficiency and economic analysis of biomass boiler using cylindrical sawdust stove as heat source

Pornpitak Tompat[1], Kulachate Pianthong[1,*], and Jing Dincherdchu[2]

[1] Department of Mechanical Engineering, Faculty of Engineering, Ubon Ratchathani University, 85 Satholmark road, Warinchamrap, Ubonratchathani , 34190
[2] Dhewada Power Limited Partnership, Muang district, Nakhon Phanom, 48000

* Corresponding Author: Kulachate.P@ubu.ac.th

Abstract. The purpose of this research is to investigate the thermal efficiency of the biomass boiler using a cylindrical sawdust stove as the heat source by using direct method. In this study, the biomass boiler is a small scale steam generator and custom fabricated to purposely utilize the cylindrical biomass stove using sawdust as fuel. This biomass boiler is a 4-turn fire tube, which fabricates in both vertical and horizontal configurations. It contains 230 liters of water, and the heat exchange area in the combustion chamber is 15.30 square meters fitted with four cylindrical biomass stoves using 15% humidity sawdust. The sawdust was packed in the biomass stove at different compression pressures, which are 60 bar, 80 bar, and 120 bar. Results showed that when the sawdust was packed at a pressure of 60 bar, the boiler can continuously produce the steam for 4 hours and gives a maximum efficiency of 29.52%. Similarly, when the sawdust was packed at a pressure of 80 bar, it also had a continuous steam generation for 4 hours, with a maximum efficiency of 29.47%. Furthermore, when the sawdust was packed at a pressure of 120 bar, it demonstrated a continuous steam production time of 5 hours, with the highest efficiency of 30.63%. Regarding the economic value of this biomass boilers, it was found that the cost of generating the steam was only 669.63 baht/ton of steam. This cost is much lower compared to using an LPG boiler, which incurs a cost of 1,867 baht/ton of steam. Furthermore, it is also more cost-effective than using a fuel oil boiler, which costs 1,430 baht/ton of steam. It is shown that this biomass boiler has a high potential technically and economically to apply in small or medium-sized industries.

Keywords: Biomass boiler, Thermal efficiency of biomass boiler, Economic value of biomass boiler, Biomass Stove.

1. Introduction

Thailand, sometimes, is considered as an agricultural country. In rural areas, there are many agricultural wastes such as bagasse, corncobs, sawdust, and longan husks. A study of their potential reveals that these waste materials can be utilized as energy sources, totaling at least 62 million tons per year [1]. Given the escalating cost of fossil fuels, these agricultural wastes have become a compelling prospect. They can serve as heat energy for households and small to medium enterprise (SME) industries. With a calorific value of 12-16 MJ/kg, they can be employed for various purposes such as electricity generation, boiler fuel, and producer gas. However, the utilization of these biomass resources as fuel comes with certain drawbacks, notably concerning the quality of the biomass fuel and its fluctuating prices. Hence, the development of biomass utilization technology becomes imperative to extract the maximum benefit from these resources.

A cylindrical biomass stove, also known as the "Dhevada stove," is a technology rooted in local wisdom. It involves the transformation of agricultural waste materials into compacted cylinders through crushing and compression [2]. This technology presents an intriguing alternative to traditional household cooking stoves, while also being suitable for development within the household industry sector. The distinguishing features of the cylindrical biomass stove include its cost-effectiveness in terms of fuel. Unused waste materials such as wood, sawdust, or rice husks are compressed into fuel rods. When utilizing a cylindrical biomass stove, it emits lower smoke and ash. Furthermore, it minimizes airborne dispersion, in contrast to conventional charcoal grills. It is easy to ignite, producing high-temperature flames, and can sustain operation for up to 4-7 hours per single fuel compression. The most remarkable aspect of the cylindrical biomass stove lies in its combustion behavior, manifesting in two forms: direct combustion and the generation of producer gas through an internal gasification process. In addition, cylindrical biomass stoves have been integrated with a biomass steam boiler, specifically a fire tube type boiler. Four cylindrical biomass stoves are employed as the primary fuel source for this boiler. It is a cost-efficient boiler in terms of steam production. This boiler is capable of generating steam at the pressure levels required by small and medium-sized enterprises (SMEs), typically ranging from 3-7 bar (or within a temperature range of 120-150˚C). For instance, it is used in applications such as animal feed factories and the Khanom Jeen factory, as illustrated in Figure 1.

Figure 1. Cylindrical biomass stove and biomass boiler.

Previous studies on biomass boiler efficiency have encompassed boiler characteristics and various biomass forms, with a predominant focus on the direct combustion of biomass. The method commonly used to assess the efficiency of biomass boilers is the Direct Method test. [3] C. Sanithai (2017) conducted a study evaluating the performance of a steam production system for manufacturing “khao cap” in the Yangkadai Tai Community Enterprise, Uttaradit Province. The test involved the utilization of longan wood as fuel for analyzing its thermal efficiency using the Direct Method. The results indicated that the thermal efficiency of the prototype steam production system fell within the range of 28.96-34.48%. In this research, the prototype system demonstrated a thermal efficiency approximately 14-20% higher than the traditional wood stoves used by the Yangkadai Tai Community Enterprise Group.

Since biomass boilers are already used in the SME industry, but in academics, this type of biomass boiler has not been widely tested and verified. Therefore, this project is to investigate the steam production capacity and the thermal efficiency of the biomass boiler using furnace. Biomass is the fuel to heat the boiler. and to study the cost of steam production compared to LPG and fuel oil.

2. Eexperimental method

2.1. Instruments and experimental equipment

2.1.1. Biomass boiler

Biomass boiler, including both vertical and horizontal fire tube configurations with 4 turns, feature a water capacity of 230 litre and encompass a heat exchange area of 15.30 m^2. These boilers are powered by cylindrical biomass stoves, serving as fuel to heat all four boilers, as visually illustrated in Figure 2.

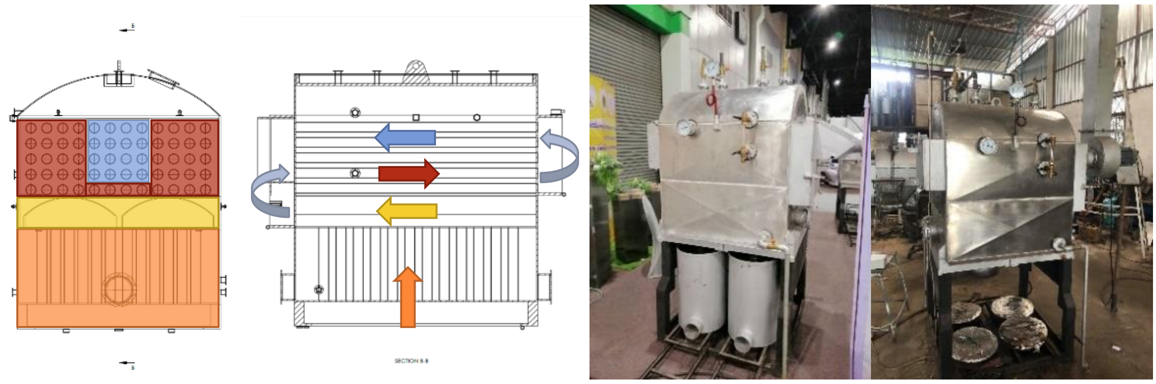

a) Section picture of the biomass boiler b) Biomass boiler and load cell installation to the boiler

Figure 2. Biomass boiler.

2.1.2. Cylindrical biomass stove

The cylindrical biomass stove is constructed using a 1 mm-thick steel sheet that is rolled into a cylinder shape. It has a diameter of 35 cm and stands at a height of 55 cm. The air inlet is 10 cm in diameter, and the flame outlet also has a diameter of 10 cm. Additionally, within the furnace, there are various components that serve as devices to ensure the biomass remains intact during combustion, thereby maintaining a stable combustion pattern. This arrangement is depicted in Figure 3.

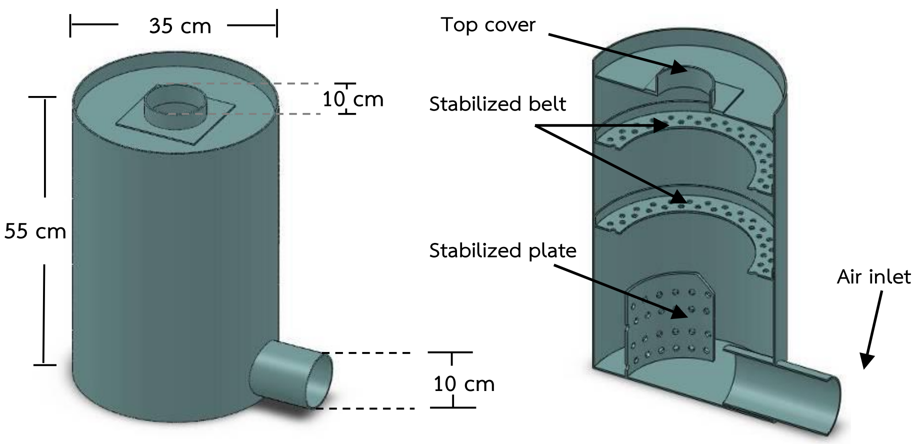

Figure 3. Dimensions of the cylindrical biomass furnace along with its internal structure.

2.1.3. Steam flow meter.

The steam flow meter is a Vortex type flow meter designed to measure steam flow. It has the following specifications: Flow Range: 300 kg/h, Maximum Temperature: 250°C, Accuracy: 1% This flow meter is utilized to precisely measure the rate of steam production within the boiler, serving a critical role in monitoring the system. as shown in Figure 4.

Figure 4. Steam flow meter.

2.1.4. Pressure gauge

A pressure gauge is a device used to measure the pressure of the steam in a boiler. The readings on the pressure gauge will tell bar (SI system) with PSI and lbf/in^2 [4-5].

2.1.5. Thermometer

The Thermometer Model TM-902C is a device based on the Thermocouple Type K cable. It is designed for temperature measurement and has the following specifications: Temperature Measurement Range: From -50°C to 1300°C, Temperature Reading Resolution: 1°C. This thermometer is specifically employed to measure the temperature of the feed water as it enters the boiler. It plays a crucial role in ensuring that the water entering the boiler is at the appropriate temperature for safe and efficient operation.

2.1.6. Load cell

A load cell is employed to gather data regarding the weight drop of the cylindrical biomass stove throughout the experimental process. In this setup, there are four load cells utilized, each with a weight capacity of 100 kg per load cell. The weight drop of the biomass stove will be recorded on an hourly basis. This data collection is aimed at determining the biomass utilization rate, which is demonstrated in Figure 5. The load cells enable precise monitoring of the changes in weight over time, allowing for accurate assessment of biomass consumption.

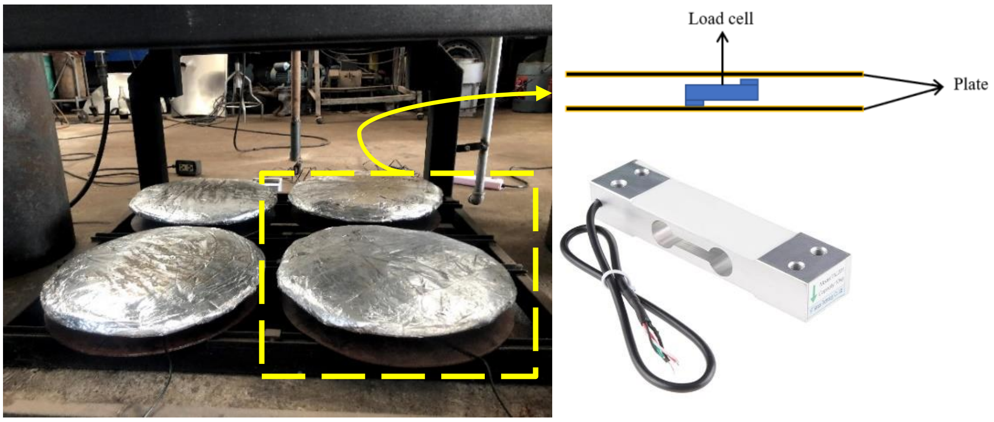

Figure 5. Load cell to measure the rate of biomass fuel consumption.

2.2. Experimental procedures and data collection

The test to determine the efficiency of this biomass boiler will employ the direct method. The measurements and analysis will be conducted under atmospheric pressure conditions (1 ATM) throughout the boiler's continuous operation, without any blow down within that range. The steps for conducting the survey and measurements are as follows:

2.2.1. Preparation of a cylindrical biomass stove

This biomass boiler utilizes four cylindrical biomass stoves as its fuel source. The biomass employed is sawdust with a moisture content of 15%. The compression of a cylindrical biomass stove is achieved using a hydraulic press, as depicted in Figure 6. During the compression process, sawdust is incrementally loaded into the cylindrical biomass burner and compressed gradually to meet the designated pressure. The resulting bulk density values for sawdust compressed at pressures of 60 bar, 80 bar, and 120 bar were determined to be 529.41 kg/m3, 571.77 kg/m3, and 592.94 kg/m3, respectively. All four furnaces are positioned on load cells to ascertain the rate of fuel consumption.

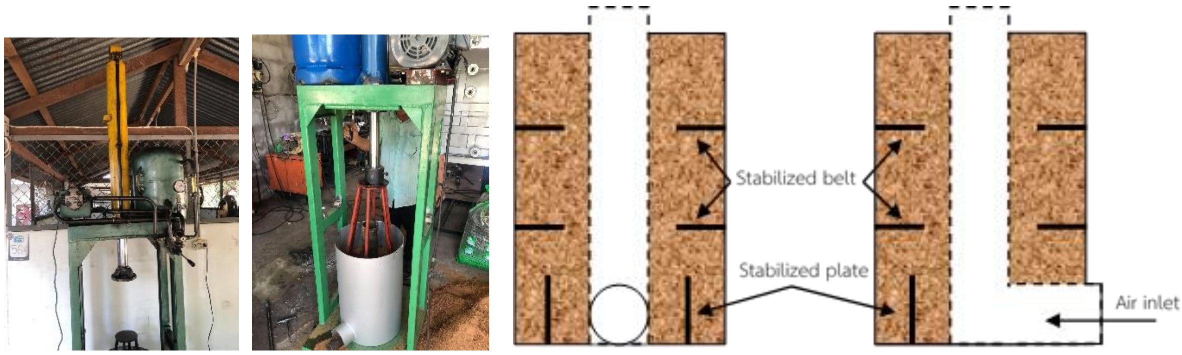

a) Hydraulic pressing machine

b) Characteristics of a cylindrical biomass stove with compressed sawdust.

Figure 6. Preparation of a cylindrical biomass stove.

2.2.2. Preparation of the biomass boiler.

Before conducting the experiment, ensure that the biomass boiler is prepared for testing. Take note of critical information such as the boiler's water level, feed water temperature, and the weight of the biomass used for fuel, among other relevant parameters.

2.2.3. Logging of Experimental Data.

During the experiment, data will be collected and recorded. This includes variables such as: Feed water flow rate (kg/h), Feed water temperature (°C), Steam flow rate (kg/h), Working pressure of steam (bar gage), Fuel consumption rate (kg/h) These data points will be utilized to calculate the efficiency of the biomass boiler using Equation (1) [6-9].

$$\eta_B = \frac{m_s(h_s - h_w)}{m_F . HV} \quad (1)$$

Where, η_B is boiler efficiency (%), m_s is steam flow rate (kg/h), m_F is fuel consumption rate (kg/h), h_s is enthalpy of steam (kJ/kg), h_w is enthalpy of feed water (kJ/kg), and HV is calorific value of fuel (kJ/kg).

2.2.4. Payback Period: PB

After gathering information about this biomass boiler, the acquired data will be analyzing the economic value of the boiler. This will be achieved through the calculation of the payback period, which represents the duration required for the income generated, minus operating expenses, to fully recover the initial investment. This metric is commonly expressed in terms of years. Investments with shorter payback periods are generally regarded as more favorable than those with longer periods. The payback period can be calculated using Equation (2).

$$\text{Payback period} = \frac{\text{TIC}}{\text{NCF}} \tag{2}$$

Where, TIC is total investment cost (Baht), NCF is net cash flow return per year (Baht/year)

2.2.5. Internal Rate of Return: IRR

The Internal Rate of Return (IRR) is the interest rate at which the Net Present Value (NPV) becomes zero. When the current loan interest rate exceeds the calculated project rate of return, it suggests that investing in such projects may not be advisable. Conversely, if the current loan interest rate is lower than the calculated project rate of return, it indicates a project with potential for higher returns. The Internal Rate of Return is calculated using Equation (3).

$$\text{NPV} = \sum_{n=1}^{N} \frac{\text{NCF}_n}{(1+i^*)^n} - \text{TIC} = 0 \tag{3}$$

Where i* is internal rate of return IRR (%), TIC is total investment cost (Baht), NCF_n is net cash flow in year n (baht/year), n is useful life (years)

3. Results and discussions

3.1. Biomass boiler efficiency

Based on the experiment conducted, the following observations were made: Upon starting the cylindrical biomass stove, the biomass boiler required 1 hour for steam generation. Steam flow rate measurements were taken at atmospheric pressure (1 ATM) with a steam temperature ranging from 102 to 106°C. The experiment indicated that the compression pressure for the biomass cylindrical stove at 60 bar. The biomass boiler displayed continuous steam production for a duration of 4 hours, achieving its highest efficiency of 29.52% during the third hour. When the biomass cylindrical furnace compression pressure was increased to 80 bar, the biomass steam boiler maintained a continuous steam generation time of 4 hours. The maximum efficiency reached was 29.47% during the third hour. Further increasing the compression pressure of the cylindrical biomass furnace to 120 bar led to the biomass steam boiler sustaining continuous steam generation for 5 hours. The peak efficiency of 30.63% was attained during the third hour. From the efficiency test of the biomass boiler, it is evident that each compression pressure applied to the cylindrical biomass stove yields similar efficiency values. However, the steam production duration varies, as higher compression pressures in the biomass stove result in longer burning times due to gasification effect and amount of biomass available. These findings provide a comprehensive understanding of the behavior and efficiency of the biomass boiler under different conditions, highlighting the impact of compression pressure on steam generation and overall performance. as shown in Figure 7.

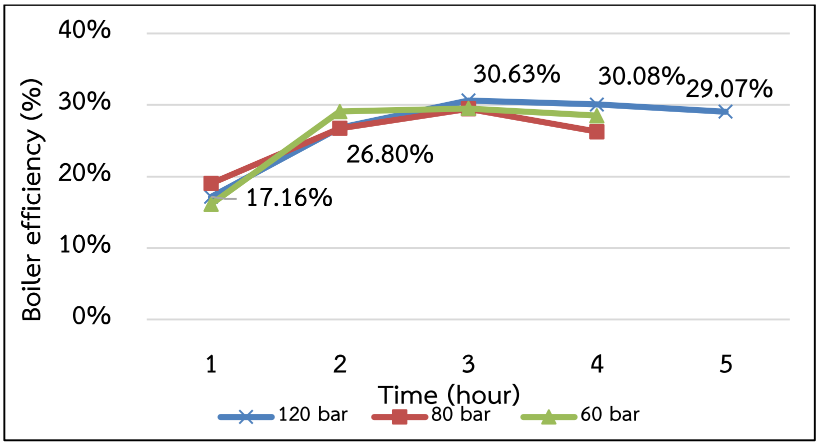

Figure 7. Biomass boiler efficiency at various compression pressure.

3.1.1. Testing at a cylindrical biomass stove compression pressure of 60 bar.

A cylindrical biomass stove was tested at a pressure of 60 bar with this biomass boiler. It was discovered that the stove exhibited continuous steam production over a 4-hour period, yielding a cumulative steam output of 248.44 kg. The highest steam generation, reaching 73.53 kg, was recorded during the second hour. The average steam production rate amounted to 62.11 kg/h. Moreover, the average fuel consumption rate was 27.21 kg/h. The resulted are plotted in Figure 8.

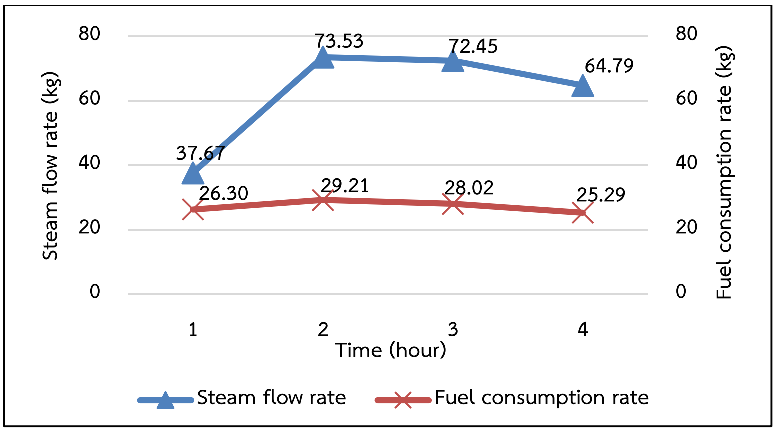

Figure 8. Steam flow rate and fuel consumption at compression pressure of 60 bar.

3.1.2. Testing at a cylindrical biomass stove compression pressure of 80 bar.

A cylindrical biomass stove was tested at a pressure of 80 bar with this biomass boiler. It was discovered that the stove exhibited continuous steam production over a 4-hour period, yielding a cumulative steam output of 237.22 kg. The highest steam generation, reaching 70.54 kg, was recorded during the third hour. The average steam production rate amounted to 59.30 kg/h. Moreover, the average fuel consumption rate was 27.82 kg/h. The resulted are plotted in Figure 9.

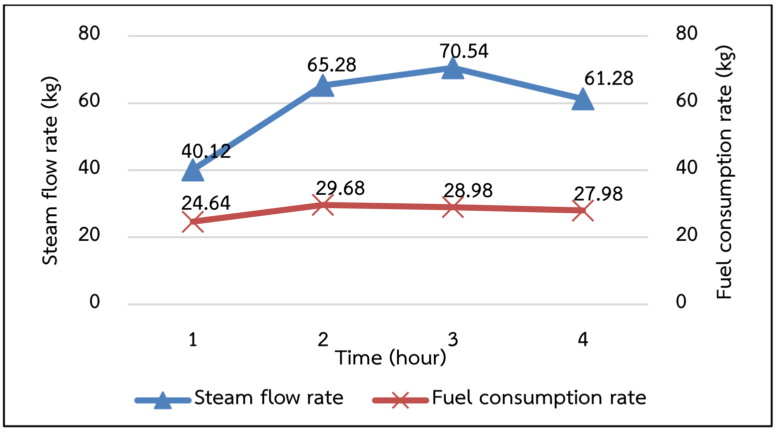

Figure 9. Steam flow rate and fuel consumption at compression pressure of 80 bar.

3.1.3. Testing at a cylindrical biomass stove compression pressure of 120 bar.
A cylindrical biomass stove was tested at a pressure of 120 bar with this biomass boiler. It was discovered that the stove exhibited continuous steam production over a 5-hour period, yielding a cumulative steam output of 290.48 kg. The highest steam generation, reaching 70.65 kg, was recorded during the third hour. The average steam production rate amounted to 58.09 kg/h. Moreover, the average fuel consumption rate was 24.95 kg/h. The resulted are plotted in Figure 10.

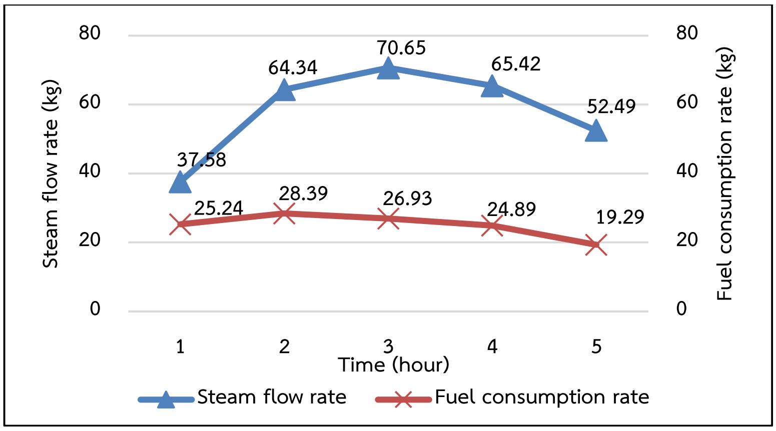

Figure 10. Steam flow rate and fuel consumption at compression pressure of 120 bar.

3.2. The economic value of the boiler.
The results of the biomass boiler experiment revealed an average steam production rate of 59.83 kg/hr, coupled with an average fuel consumption rate of 26.66 kg/hour. Consequently, when comparing this biomass boiler's performance in producing 1 ton of steam, it necessitates the use of 446.42 kg of fuel, which translates to a cost of 669.63 baht (considering a sawdust price of 1.5 baht/kg). In further comparison, when assessing the cost of generating 1 ton of steam using the boiler powered by LPG fuel and fuel oil, the following details emerge.

3.2.1. The economic value of the boiler compared to LPG.
The calculation of the cost to produce 1 ton of steam compared to LPG involves assessing the boiler's steam production under atmospheric pressure conditions. With a feed water temperature of 25°C, LPG is employed as the fuel source, boasting a heating value of 26,620 kJ/L. The boiler's efficiency is determined to be 80%. This calculation aims to ascertain the cost of generating 1 ton of steam, excluding

charges for electricity, chemicals, and related factors. The evaporation ratio calculation determined that the production of 1 ton of steam will require 66.36 kg of LPG fuel, corresponding to a cost of 1,867 baht. Referring to PTT's LPG price range of 1,274-1,455 baht per 48 kilograms (utilizing the median value of 1,350 baht per 48 kilograms) as of May 1, 2023, sourced from the Energy Policy and Planning Office (EPPO), Ministry of Energy.

3.2.2. The economic value of the boiler compared to fuel oil.

The calculation of the cost to produce 1 ton of steam compared to fuel oil involves the steam boiler's operation under atmospheric pressure conditions. The feed water temperature is set at 25°C. C grade fuel oil (FO 1500 (2) 2%SFO 1500 (2) 2%S) is employed as the fuel source, possessing a heat value of 38,174.47 kJ/L. The boiler's efficiency is determined to be 80%. The aim is to determine the cost of producing 1 ton of steam, excluding charges for electricity, chemicals, and related factors. The evaporation ratio calculation revealed that the production of 1 ton of steam will necessitate the utilization of 84.25 liters of fuel oil (fuel oil), corresponding to a cost of 1,430 baht. Referring to the price of fuel oil grade C, specifically FO 1500 (2), the retail price is recorded at 16.9736 baht per liter as of May 1, 2023, based on data sourced from the Energy Policy and Planning Office (EPPO), Ministry of Energy.

3.2.3. Payback Period: PB

The calculation of the payback period entails a simulation in which biomass boilers replace conventional boilers that utilize LPG and fuel oil. The specific requirements are presented in Table 1, and the payback period is computed using Equation (2). From the payback period calculation, it was determined that by substituting the existing LPG boiler with this biomass boiler, the payback period amounts to 2.78 years. Similarly, when replacing the current fuel oil boilers with the biomass boiler, the payback period is projected to be 4.38 years.

Table 1. Comparing the payback period of biomass boilers.

	Biomass	**LPG**	**Fuel oil**
Requirement: 100 kg/h of steam			
Assumption: The boiler works 5 hours a day, 300 days/year.			
Demand of steam in 1 year (ton/year)	150	150	150
Investment (TIC): The cost price of one biomass boiler is 250,000 baht *(from the experiment, one boiler produces average steam of 59.83 kg/h, so must replace 2 biomass boilers).	500,000	-	-
Cost of steam production per 1 ton (baht/ton)	669.63	1,867	1,430
Cost of steam production for 1 year (baht)	100,444.50	280,050	214,500
NCF	-	179,605.50	114,055.50
Payback Period (year)	-	2.78	4.38

3.2.4. Internal Rate of Return: IRR

The calculation of the internal rate of return entails a simulation in which biomass boilers replace conventional boilers that utilize LPG and fuel oil. The specific requirements are presented in Table 2, and the internal rate of return is computed using Equation (3). Based on the internal rate of return calculation, it was determined that the utilization of this biomass boiler to replace the existing LPG boiler yields an Internal Rate of Return (IRR) of 34%. On the other hand, substituting the current fuel oil boilers with the biomass boiler results in an Internal Rate of Return (IRR) of 18.70%.

Table 2. Comparing the internal rate of return of biomass boilers.

	Biomass	LPG	Fuel oil
Requirement: 100 kg/h of steam			
Assumption: The boiler works 5 hours a day, 300 days/year.			
The project's service life spans over a duration of 10 years. (n)			
Annual interest rate 10%			
Demand of steam in 1 year (ton/year)	150	150	150
Investment (TIC): The cost price of one biomass boiler is 250,000 baht *(from the experiment, one boiler produces average steam of 59.83 kg/h, so must replace 2 biomass boilers).	500,000	-	-
Cost of steam production 1 ton (baht/ton)	669.63	1,867	1,430
Cost of steam production for 1 year (baht)	100,444.50	280,050	214,500
Net cash flow remains constant every year. (NCF_n)	-	179,605.50	114,055.50
Internal Rate of Return: IRR		34%	18.70%

4. Concluding Remarks

Biomass boilers operating with a cylindrical biomass stove compression pressure of 60 bar and 80 bar exhibited identical steam generation times of 4 hours. Meanwhile, when the compression pressure of the cylindrical biomass furnace was increased to 120 bar, the steam generation duration extended to 5 hours. During each test scenario, the peak efficiency of the biomass boiler was achieved during the third hour of steam production. Specifically, the efficiencies recorded were 29.52%, 29.47%, and 30.63% for the compression pressures of 60 bar, 80 bar, and 120 bar, respectively. This is because the cylindrical biomass stove cannot adjust its heating power, thus, to maintain a consistent steam production in the boiler, it is necessary to add 5 liters of feed water every 5 minutes.

The cost of producing 1 ton of steam from biomass boilers is 669.63 baht, which is lower in comparison to both LPG and fuel oil. Specifically, the cost of generating 1 ton of steam is 1,867 baht for LPG and 1,430 baht for fuel oil.

When considering the investment in this biomass boiler for the SME industry, which already operates an existing boiler with a steam production rate of 100 kg/hr. The existing boiler operates for 5 hours each day, with operations occurring on 300 days/year. This biomass boiler serves as a replacement for both LPG-fired boilers and fuel oil boilers. When calculating the payback period, the resulting durations are 2.78 years and 4.38 years for LPG and fuel oil replacements, respectively. And when calculating the Internal Rate of Return over a 10-year project life at an annual interest rate of 10%, the rate of return is 34% compared to LPG fuel and the rate of return is 18.70% compared to fuel oil.

5. Acknowledgments

Thank you to the Department of Mechanical Engineering, Faculty of Engineering, Ubon Ratchathani University, for providing the research facility, and thank you to Dhewada Power Limited Partnership for offering guidance and support in the use of experimental tools.

6. References

[1] Department of Alternative Energy Development and Efficiency, Ministry of Energy. *Biomass Potential in Thailand*. Available: https://www.dede.go.th/ewt_news.php?nid=486

[2] S. Jodnok, (2010). Operating Characteristics Validation of a Novel Cylindrical Compression Biomass Stove, In *The 6th Conference on Energy Network of Thailand.* Bangkok.

[3] C. Sanitthai, (2017). Performance Assessment of Steam Generation System for Kao Kab Production For Yang Kadai Tai Community Enterprises, Uttaradit Province. In *The 13th Conference on Energy Network of Thailand, The Empress Chiang Mai.*

[4] Department of Industrial Works: Ministry of Industry, (2010).Sze, *Manual and maintenance of radiators, safety technology transfer project to enterprises: safety in the use of radiators.*

[5] The American Society of Mechanical Engineers, (1998).Sze, *Fired Steam Generators Performance Test Codes.* New York.

[6] Alan Carneiro et al., (2017). *Performance quantification of a cyclonic boiler using biomass sawdust,* Energy Procedia. 120: 403-409

[7] Yaojie Tu et al., (2019). *Effect of different operating conditions on the performance of 32 MW woodchip-fire grate boiler,* Energy Procedia. 158: 898-903

[8] Brundaban Patro (2015). *Efficiency studies of combination tube boilers*, Alexandria Engineering Journal. 55: 192-202

[9] R. Winit, (2009). *Thermal Performance of Small Scale Biomass Steam Boiler*. In The 23th Conference of Mechanical Engineering Network of Thailand, Chiang Mai.

AEC0009

Enlargement of Inverse Diffusion Flame Burner with Thermal Analysis on Similarity Numerical Model

C. Chantang[1] and A. Kaewpradap[1,*]

[1]Department of Mechanical Engineering, Faculty of Engineering,
King Mongkut's University of Technology Thonburi
126 Prachauthit Bangmod Thung Khru, Bangkok, 10140, Thailand

* Corresponding Author: amornrat.kae@kmutt.ac.th

Abstract. This research focuses on the enlarging the axial burner scale especially on inverse diffusion flame burner (IDF) with natural gas as the fuel by study of dimensional analysis, similarity, and numerical model. To analyses the similarity of difference burner scales by simulation study, the obtained simulation results were compared to the experimental previous study with around 8.5% of difference. In this study, there are four types of simulation results on firing rate for study of burner similarity, which consisted of the flame temperature, the temperature distribution, the flow distribution, and the average flow velocity. As the results, the burner dimension could be enlarged by the equation base on firing rate and the flame temperature predicting equation on firing rate 2.0 kW to 20.0 kW at equivalence ratio 1.0 with around 3.0% of difference. This research can be concluded that obtained dimensional analysis was appropriate method for enlarging the burner scale with similarity.

Keywords: Inverse diffusion flame burner, Thermal analysis, Similarity method, Numerical model, Combustion.

1. Introduction

Generally, there are many burner types applied for industrial application such as high velocity burner, regenerative burner, thermal radiation burner and burner for industrial boiler [1]. Especially, the burner in micro gas turbine or boiler applied for power generation are interesting to study and develop the burner technology due to growth of power energy demands [2]. Instead of high carbon fossil fuel, natural gas is the lowest carbon fuel consumed in power generation [3]. Comparison between other hydrocarbon fuel, low emission and more complete combustion are advantage from natural gas. The axial burner is most famous device applied with natural gas in boiler or gas turbine for power generation [4]. However, the premixed axial burners are a popular choice in various industrial applications due to their efficiency and clean combustion characteristics. The premixed combustion in axial burner come with certain safety concerns, primarily related to the risk of flashback flames. Flashback occurs when the flame travels back into the burner, reaching the mixing zone where the fuel and air are still premixed. This can lead to unstable and potentially dangerous combustion conditions [5]. Therefore, non-premixed burner has been developed to solve this problem. The previous research studied the two types of non-premixed axial burners: Normal Diffusion Flame (NDF) and Inverse Diffusion Flame (IDF) [6]. The better combustion characteristics of IDF axial than NDF axial burner was obtained. Moreover, the swirler was applied to improve the mixture for better [7]. In 2020, a fuel-port and an air-port of the IDF axial burner were designed for better mixing and combustion [8]. However, the experimental results were validated for only experimental scale burner which it had an error of combustion characteristics and precise dimension for industrial-scale burner [9]. Thus, it is important to study the process to find out the enlargement method from experimental-scale burner to industrial-scale burner. Not only the combustion experiment for burner improvement, but the burner model is also applied to investigated by simulation method [10]. Simulating and modeling axial burners before physical experimentation is indeed a crucial first step in the burner design process. Computational simulations provide valuable insights into the performance and combustion characteristics on axial burners under various operating conditions and help in selecting the most promising design configurations for further experimental testing. In order to apply the axial burner model for enlargement method, the validation of experimental result of referenced IDF axial burner in previous study is applied in this study [11]. The combustion characteristics and flame temperature of referenced burner (1313.7 °C) was observed at 2.0 kW of heat input or firing rate. Consequently, this study focuses on the enlargement method for industrial-scale burner during 2.0-20.0 kW of firing rate which the axial burner model is investigated to comply with the natural gas combustion characteristics and flame temperature from the referenced experimental results.

2. Methodology

2.1. Natural gas

Natural gas is a natural hydrocarbon fuel with methane as the main component. In this study, combustion of natural gas is investigated followed by natural gas composition referred in the previous study [4]. The main composition applied in this study is 89% of CH_4 and 11% of CO_2 by volume and lower heating value is between 36-46 MJ/m^3.

2.2. Stoichiometric combustion equation

The balancing of fuel-air chemical equations is fundamental to experiments because the quantities of fuel and air are used concerning the chemical equilibrium in the desired reaction. If there is enough oxygen, the hydrocarbon fuel can be burnt completely, thus the carbon in the fuel is converted to carbon dioxide (CO_2), the hydrogen is converted to water (H_2O), and the air still contains nitrogen. However, the product is at low temperatures, the nitrogen does not affect the reaction. Typical complete combustion for hydrocarbon fuels and airs can be shown as Eq. (1).

$$C_aH_b+\left(a+\frac{b}{4}\right)(O_2+3.76N_2)\rightarrow aCO_2+\left(\frac{b}{2}\right)H_2O+3.76\left(a+\frac{b}{4}\right)N_2 \tag{1}$$

2.3. Equivalence ratio

The equivalence ratio is a ratio between the air to fuel ratio in the actual combustion $(\dot{m}_f/\dot{m}_a)_{actual}$ and combustion theory $(\dot{m}_f/\dot{m}_a)_{stoi}$ as shown in Eq. (2). If air to fuel ratio in natural combustion is equal to combustion theory, it is called "Stoichiometry". Nevertheless, the combustion air to fuel ratio cannot equal the combustion theory, it is called "Lean Mixture" or "Rich Mixture" if an air-to-fuel ratio is less or more than combustion theory, respectively.

$$\boldsymbol{\Phi}=\frac{(\dot{m}_f/\dot{m}_a)_{actual}}{(\dot{m}_f/\dot{m}_a)_{stoi}} \tag{2}$$

2.4. Air and fuel flow rate

The calculation of the flow rate can be divided into two steps [6]. The first step is the calculation of the fuel flow rate ($\dot{m}_f$). It can be calculated with the firing rate (F.R.) and Low heating value of fuel (LHV) as represented in Eq. (3).

$$\dot{\boldsymbol{m}}_{\boldsymbol{f}} = {}^{\boldsymbol{F.R.}}\!/_{\boldsymbol{LHV}} \tag{3}$$

The airflow rate ($\dot{m}_a$) can be calculated by the equivalence ratio (Φ) and fuel to air ratio in the combustion theory as represented in Eq. (4).

$$\dot{\boldsymbol{m}}_{\boldsymbol{a}} = {}^{\dot{\boldsymbol{m}}_{\boldsymbol{f}}}\!\Big/_{(\dot{\boldsymbol{m}}_{\boldsymbol{f}}/\dot{\boldsymbol{m}}_{\boldsymbol{a}})_{\boldsymbol{stoi}}} \tag{4}$$

2.5. Dimensional analysis and similarity

Dimensional analysis and similarity are powerful tools used in fluid mechanics and other fields of science and engineering to simplify complex problems and experiments. This appliance can reduce the parameters, simplify the experimental setup, analysis and making it more manageable and cost-effective. It also helps in understanding the dominant factors that influence the behaviour of the system. The dimensionless parameters have amounts equal to the primary dimension of mass (M), length (L), and temperature (T). Dimensional Analysis has many benefits for fluid due to saving the cost and time of doing many experiments and helping to create the experimental plans, write the equation for the experiment results, and separate the non-effecting parameters to the experiment.

3. Simulation Study

3.1. Simulation model

Design the 3D part of the burner using the SolidWork2020 that can adjust the burner's characteristics and dimensions. The simulation model has only the burner's upper air tube and upper fuel tube for increasing mesh resolution, simulation precession and reducing time for calculation. The burner model applied in this study as shown in Figure 1.

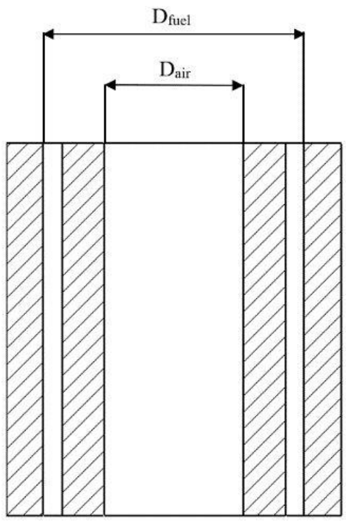

Figure 1. Dimension of IDF axial burner.

3.2 Simulation study

The simulation study used the Ansys Fluent program version 2021R1. The conditions are referenced from the previous study [10]. The simulation results and the experimental results have 8.53%. of difference. The mesh independence has been conducted and the optimized 500,000 mesh elements were obtained and applied for enlargement investigation model. The viscosity, radiation, and non-premixed combustion were simulated by transition SST model, the discrete ordinate model, and the species model with methane 89% and carbon dioxide 11% as a fuel, and the inlet of air and fuel are mass flow inlet with initial temperature is 26.85 °C. In the simulation post-process, the simulation results are side view of temperature distribution and maximum flame temperature at the same height ratio as the thermocouple in the experiment, and the average flow velocity at the burner trip.

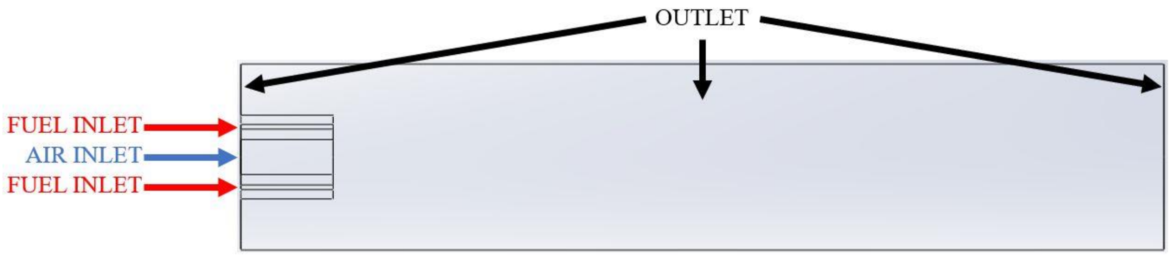

Figure 2. Position of the air inlet, fuel inlet, and outlet form axial burner model.

4. Result and discussion

4.1. Dimensional analysis

The dimensional analysis has five parameters used in the dimensionless equations written in Table 1. As the applied parameters can be written by three dimensionless equations as shown in Eq. (5)-(7). Following Eq. (6), the primary dimension parameters of fuel-port (D_f) and air-port diameter (D_a) are set up. Following Eq. (8), equal density (ρ), the lower heating value (LHV) for variation of firing rates between 2.0-20.0 kW and referenced firing rate (F.R.) at 2.0 kW are conducted to apply with Eq. (5) and Eq. (6) as the primary parameters.

Table 1. Example of changing the parameters into the primary dimension parameters.

Parameters	Dimension	Primary Dimension (MLT)
Firing rate, F.R.	kW	ML^2T^{-3}
Flow rate, $\dot{m}$	kg/s	MT^{-1}
LHV	kJ/kg	L^2T^{-2}
Density, ρ	kg/m^3	ML^{-3}
Diameter, D	mm	L

$$\pi_1 = \frac{\dot{m}}{(F.R.)^{\frac{1}{3}}\rho^{\frac{2}{3}}D^{\frac{4}{3}}} \tag{5}$$

$$\pi_2 = \frac{D_f}{D_a} \tag{6}$$

$$\pi_3 = \frac{\rho^{\frac{2}{3}}{D_a}^{\frac{4}{3}}(LHV)}{(F.R.)^{\frac{2}{3}}} \tag{7}$$

4.2. Similarity analysis

As the similarity analysis, the practical diameter (D_p) or enlarged diameter is calculated by the relation between the referenced diameter (D_m) and practical firing rate ($F.R._p$) as shown in Eq. (8). Then, the enlargement equation is shown in Eq. (9). Figure 3 shows the dimension of IDF axial burner which consist of fuel-port and air-port diameter. Following Eq. (8), the relation between higher firing rate at Φ = 1.0 with increase of fuel-port and air-port diameter are illustrated in Figure 4. When dividing the mass flow of air and fuel in different firing rates with the mass flow of air and fuel for referenced case (2.0 kW). The results are the number of times the air and fuel flow rate (m*), as followed in Figure 5. The equation from the relationship in Figure 5 is shown in Eq. (10).

$$D_p = \sqrt{\frac{\rho_m \times F.R._p}{\rho_p \times F.R._m}} \times \sqrt[4]{\frac{LHV_m{}^3}{LHV_p{}^3}} \times D_m \tag{8}$$

$$D_p = \sqrt{\frac{F.R._p}{2}} D_m \tag{9}$$

$$\dot{m}_{p*} = 0.5(F.R.)_p \tag{10}$$

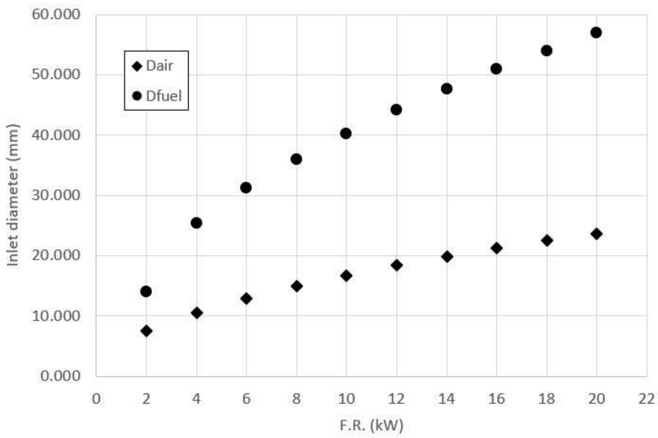

Figure 3. The relation between firing rate at Φ = 1.0 with fuel-port and air-port diameter by enlargement equation.

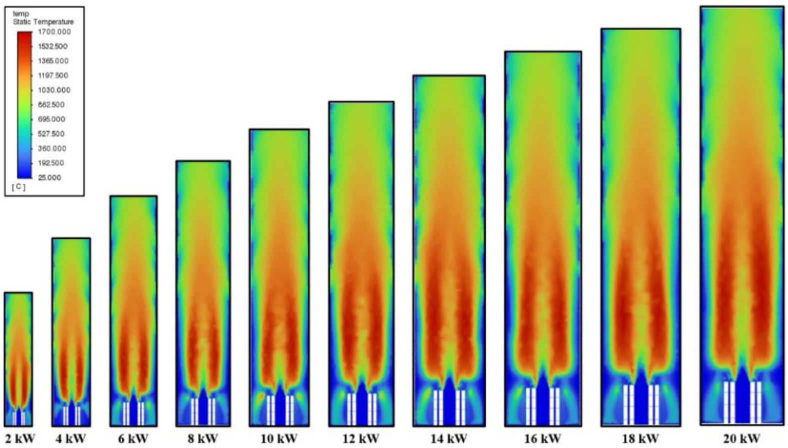

Figure 4. Temperature distribution in different firing rates.

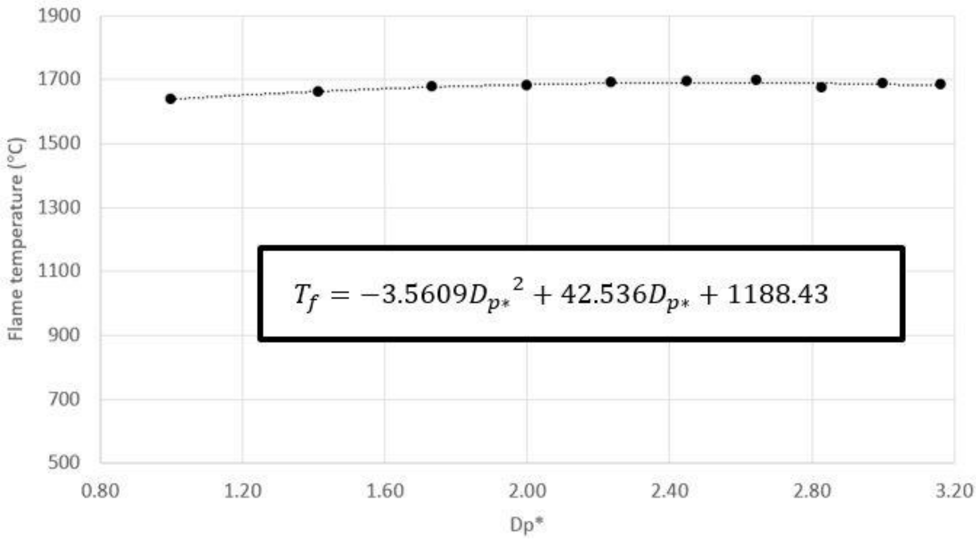

Figure 5. The relation between different scaling ratios and flame temperature.

4.3. Flame temperature in different firing rate at $\Phi = 1.00$

The temperature distribution in Figure 4 found that the ratio and positions of the temperature colour of every firing rate are like the reference case (2.0 kW). However, the bottom of the flames has a few different arcs. The flame temperature measuring is measured at the same height ratio as the experiment. Flame temperature results are shown in Figure 4. The relation between the flame temperature and the scaling ratio, D_{p*} as shown in Figure 5 and Eq. (11).

$$T_f = -3.5609 D_{p*}^2 + 42.536 D_{p*} + 1188.4 \tag{11}$$

The flame temperature results are measured at the same height ratio as the experiment as shown in Figure 5. The flame temperature result of the linearly scaling ratio is not close to the reference and more error is obtained at higher firing rate. The linear relation at F.R.= 10.0 kW, the error percentage of flame temperature is 22.1%, and the error percentage of average velocity is 92.74%.

4.4. Average velocity and Flow distribution of air and fuel at $\Phi = 1.00$

Following the simulation result of enlargement IDF burner model, the average velocity of the air and fuel flow at the burner tip was obtained. All average velocity results in different firing rates are closely equal to the reference (2.0 kW), and Figure 6 shows each burner's flow distribution of air and fuel at different firing rates. All burners have similar flow distribution. The average velocity and flow distribution results represent the similarity of each burner on different scales.

4.5. Comparison between the dimensional analysis scaling and linearly scaling at $\Phi = 1.00$

To study the effect of the dimensional analysis scaling. Therefore, dimensional analysis scaling needs to be compared with linearly scaling to show the accuracy and precision of changing IDF axial burner size. Figure 7 shows the trend of both scaling is clearly different. The trend of linearly scaling ratio is linearly increase but the trend of dimensional analysis scaling ratio is increased with a gradual decreasing differential. The comparison between temperature distribution of the dimensional analysis scaling ratio, and the temperature distribution of the linearly scaling ratio are shown in Figure 8. At the higher firing rate, the linearly scaling ratio temperature distribution has more dissimilarity to reference (2.0 kW). Figure 9 shows the average velocity results are measured at the tip of the burner. The average velocity result of the linearly scaling ratio is hugely different from the reference. It has more errors than the error of flame temperature results when the firing rate increases.

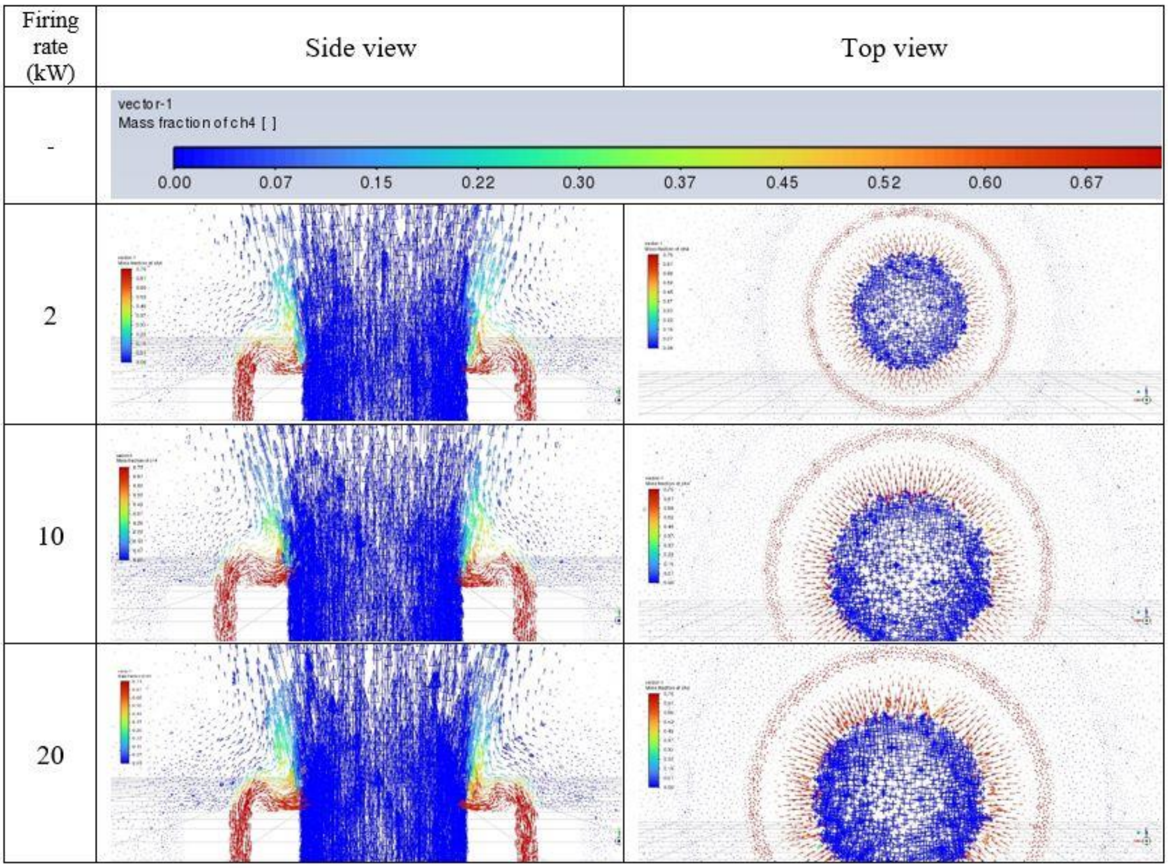

Figure 6. Flow distribution of air and fuel of burners at different firing rates.

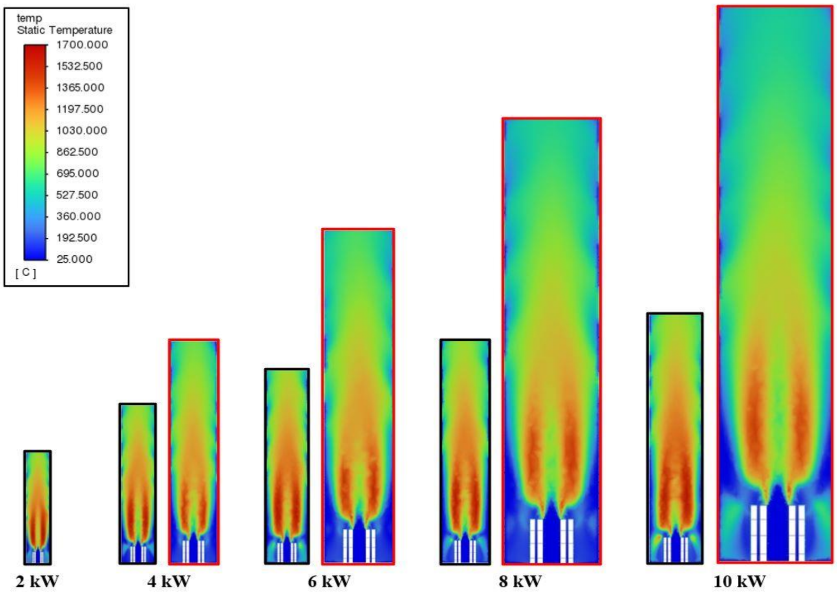

Figure 7. Comparison of temperature distribution in different scaling and different firing rates.

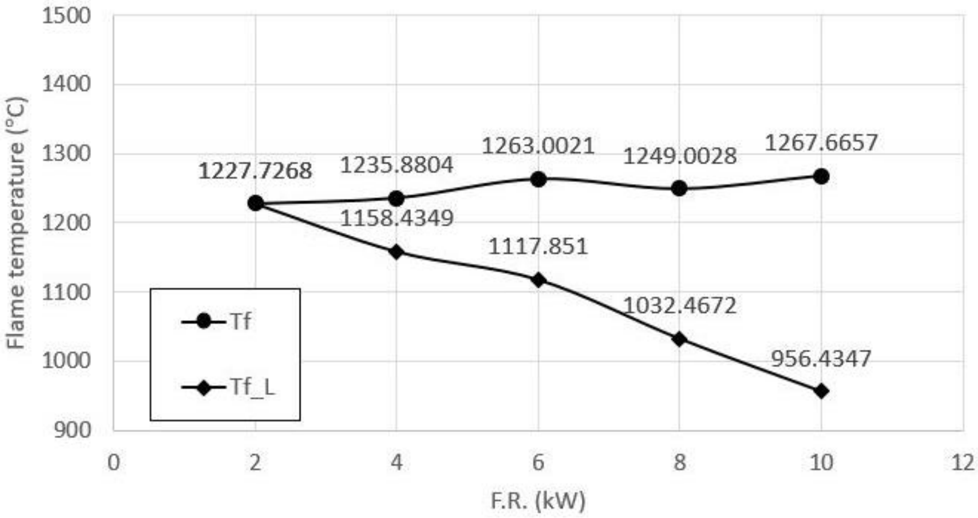

Figure 8. Comparison of flame temperature in different scaling ratios and firing rates.

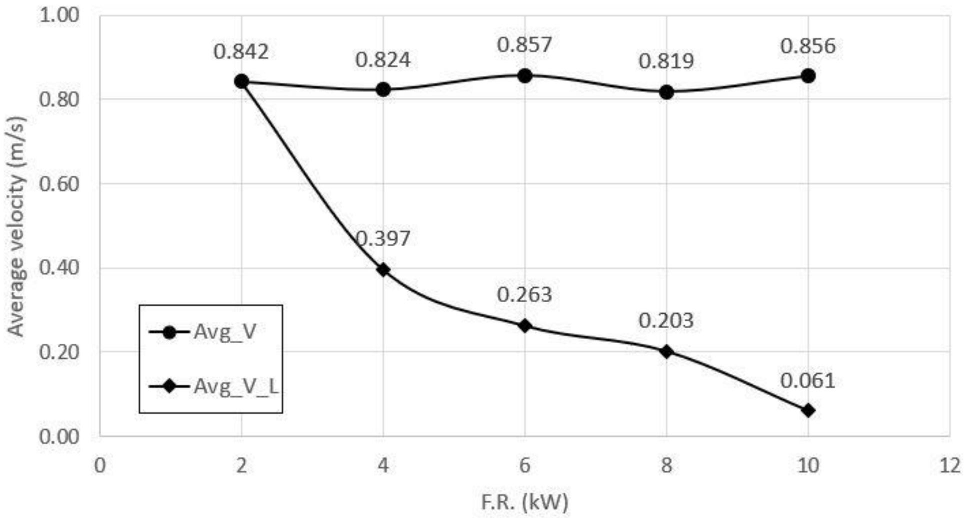

Figure 9. Comparison between firing rates and average velocity at burner tip in different scaling ratios.

5. Conclusion

In this study, the flame temperature, the temperature distribution, flow distribution, and average flow velocity could be comparable at enlarging or shrinking scale. As the results, the burner dimension could be enlarged by the equation base on firing rate and the flame temperature predicting equation on firing rate 2.0 kW to 20.0 kW at Φ=1.0 with around 3.0% of difference. Moreover, the linear relation at F.R.= 10.0 kW, the error percentage of flame temperature is 22.1%, and the error percentage of average velocity is 92.74%. This research can be concluded that obtained dimensional analysis was appropriate method for enlarging the burner scale with similarity.

6. Acknowledgments

The authors thank to Department of Mechanical Engineering, Faculty of Engineering, King Mongkut's University of Technology Thonburi for financial support and experimental facility, respectively. This research project is supported by Thailand Science Research and Innovation (TSRI): Basic Research Fund: Fiscal year 2023 under project number FRB660073/0164.

7. References

[1] Charles E. Baukal, (2003), Industrial Combustion Series, CRC Press LLC, pp. 561-578.

[2] Department of Alternative Energy Development and Efficiency [Internet]. Thailand: Combustion theory; [cited 2021 Jul 18]. Available from: http://www2.dede.go.th/bhrd/old/file_handbook.html.

[3] Natural Gas Separation Plant, Rayong Province, (2020), "General properties of natural gas", PTT Public Company Limited [Online], Available: https://dscng.pttplc.com [2020, October 2]

[4] Keawpradap A. and Jugjai S., (2019), "Improvement of IDF Burner Effects on Lean Non- Premixed Synthetic Thai Natural Gas Flames", Earth and Environment Science, Vol. 265, No. 2, pp. 1-7.

[5] Chantang, C., and Thuwongkawat, T., (2020), Improvement of synthetic natural gas combustion on IDF axial burner, Bachelor of Engineering Thesis, Mechanical Engineering, Faculty of Engineering, King Mongkut's University of Technology Thonburi, pp. 1-70.\

[6] Jassin FritzMartin KrönerThomas SattelmayerThomas Sattelmayer, (2004), Flashback in a Swirl Burner with Cylindrical Premixing Zone, Journal of Engineering for Gas Turbines and Power, Vol.126, No.2.

[7] Loss calculation of Contraction / Enlargement, www.maplesoft.com, [Online], Available: file:///C:/Users/amorn/Downloads/loss%20calculation%20of%20contraction%20and%20enlargement.flow.pdf [2023, May]

[8] Sasiwimonphan, S., and team, (2004), "Burner Adjustment Guide", Department of Alternative Energy Development and conserve energy Ministry of Energy, pp. 1-1 – 1-3.

[9] Jugjai S., (2004), Combustion, Printing House of Chulalongkorn University, Bangkok, pp.13-17.

[10] Chantang C., et al., (2022), "Investigation of Natural Gas Flame Temperature influenced Spiral Port on Axial Burner", Alternative Energy and Combustion, The 16th Asian Symposium on Visualization, June 7–10, Bangkok, Thailand, pp. 95-102.

[11] Amornrat Kaewpradap and Sumrerng Jugjai, (2019), Experimental Study of Flame Stability Enhancement on Lean Premixed Combustion of a Synthetic Natural Gas in Thailand", *Journal of Energy*, Vol.188, pp.116029, DOI: 10.1016/j.energy.2019.116029.

AEC0010

Development of fuel injection system for low and zero carbon fuels in the 1 MW 4-stroke marine engine

Y Woo[1,*], J Jang[1], A-H Ko[1], Y Jung[1], YD Pyo[1], G Moon[2], D Kim[3], J Seo[4], and K Kim[4]
[1]Korea Institute of Energy Research, 152 Gajeong-ro ,Yuseong-gu, Daejeon, 34129, Korea
[2]Korean register, 36 Myeongji ocean city 9-ro Gangseo, Busan, 46762, Korea
[3]HD Hyundai Heavy Industry, 1000 Bangeojinsunhwandoro, Dong-gu, Ulsan, 44032, Korea
[4]HD Korea shipbuilding and offshore engineering, GRC 19F, 477 Bundangsuseo-ro Bundang-gu Seongnam Gyeonggi-do, 13553, Korea

* Corresponding Author: ywoo@kier.re.kr

Abstract. As International Maritime Organization announced carbon net-zero strategy by 2050, alternative fuels are widely investigated to substitute conventional marine fuels to lead lower GHG emission in the marine engines. Not only natural gas but also a variety of low flash point fuels such as LPG, DME, hydrogen are among the candidates. In this study, high pressure fuel pump and injectors for low flash point fuels are designed to have sufficient power output and better emissions. As a result, a prototype fuel injection system was successfully developed and tested more than 400 hours in the target engine application. Compared to heavy fuel oil, the combustion of low flash point fuel showed better emission results in terms of total hydrocarbon, nitric oxides, and sulphuric oxides which are reduced by 14.5%, 45.3%, and 91%, respectively.

Keywords: Low flash point fuel, Green-house-gas, Internal combustion engine, Low carbon fuel, Zero carbon fuel.

1. Introduction

After IMO (International Maritime Organization) announced a drastic strategy on the reduction of GHG emissions in the international shipping which says net zero carbon emission is considered to be placed for both new building and existing ships as shown in Table 1, a lot of technical alternatives were suggested [1]. For example, Speed limitation, decrease in engine power output, LPG/LNG fuel adoption, batteries and fuel cells were suggested and each of them are under investigation to have feasible solution to mitigate the global warming.

Table 1. Initial IMO strategy on reduction of GHG emissions from ships.

Year	*2020*	*2025*	*2030*	*2040*	*2050*
CO_2 ***reduction***	*-20%*	*-30%*	*-40%*	*-70%*	*-100%*
Note	*For both new building & existing ships*				

The strategy is based on the year 2008's CO_2 as 940 Mt of CO_2 and all of them should be reduced by 2050. Due to this radical strategy, a variety of low carbon fuels are now under consideration to replace current heavy fuel oils. Since the strategy includes the existing ships and they are hard to be modified to adopt lighter fuel, a huge fuel transition is anticipated for newly building ships, and ammonia as well as hydrogen, which are called together as zero carbon fuel, are spotlighted to have an important role in the upcoming transition [2-4].

To meet this IMO strategy, global engine makers are trying to diversify the fuel options for their engine model line-ups. It is MAN-ES that is on the foremost frontier for the low flash point fuel adoption. After the success of so-called ME-GI engine, they developed ME-LGIP for LPG fuel and currently they are working on ammonia fuel option. For 4-stroke engines, Wartsila already built a methanol fueled vessel called Stena Line and announced W32LG fueled with LPG and then moved to develop ammonia dedicated marine engine as well. Aligned with these global technical trends, HD Hyundai Heavy Industry are planning to add more fuel options for their 4-stroke engine line-up to adopt LPG, ammonia, and hydrogen to afford the fuel flexibility.

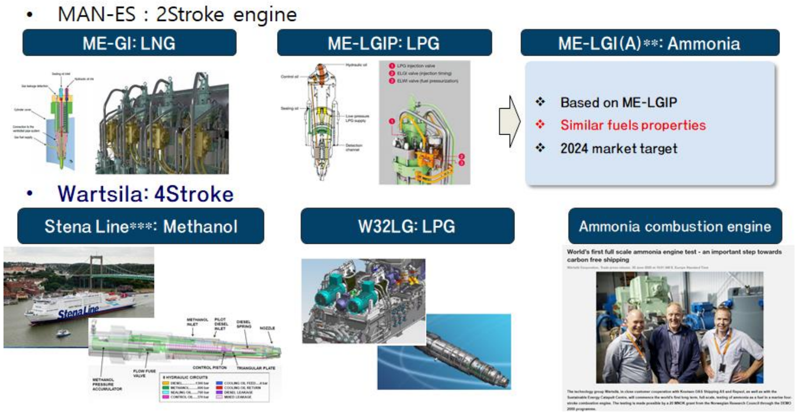

Figure 1. Global engine market trend.

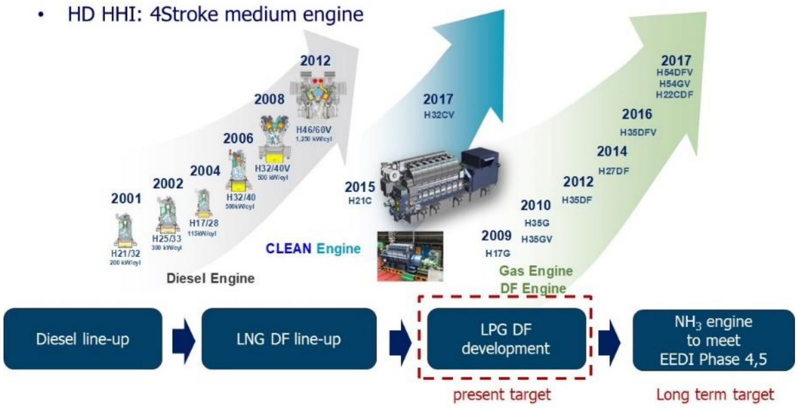

Figure 2. 4-stroke marine engine line-up of HD HHI.

2. Flow and combustion calculations

The research aims to develop of fuel injection system for low flash point fuels in the 1MW 4-stroke marine engine. LPG, methanol, and ethanol were selected to be checked the applicability into the target fuel injection equipment. After the development of the prototype to adapt to the new fuel, it was installed into the target engine to ensure its proper operation.

The fuel injection equipment comprise of fuel cam, fuel pump, high pressure fuel line, and fuel injection valve. The fuel pump is mechanically driven from the fuel cam which determines the timing and duration as well as the stroke of the injection event. To this purpose, analyses on the fuel flow and combustion calculation were conducted and the main design was completed through the integration of the produced data during them.

Table 2. Specifications of the injection nozzle geometry.

Case	Nozzle hole size (mm)	Nozzle hole number	Nozzle hole area (mm^3)
1	0.45	10	1.59
2	0.5		1.96
3	0.55		2.38
4	0.6		2.83
5	0.5	9	1.77
6	0.5	11	2.16

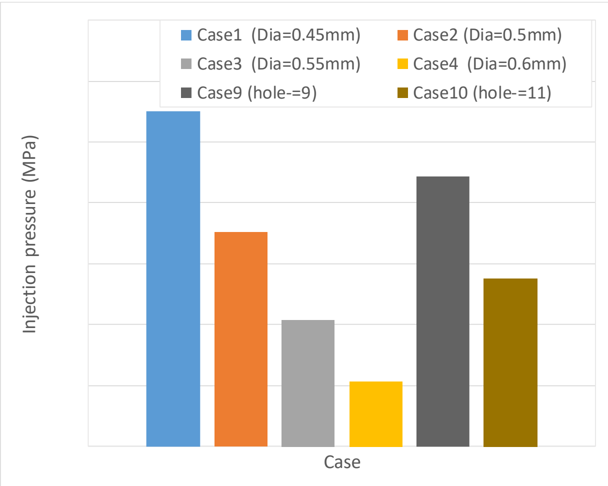

Figure 3. Injection pressure with regard to the nozzle geometries.

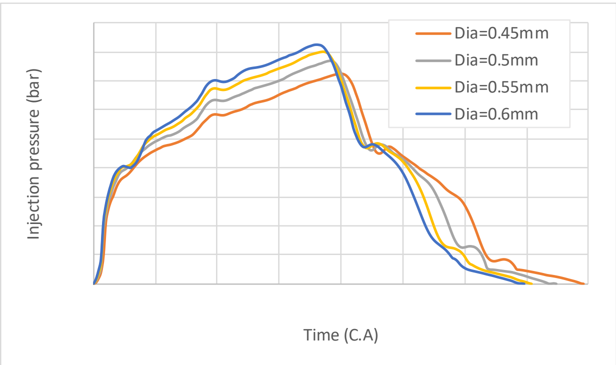

Figure 4. Fuel injection rate according to the different nozzle geometries.

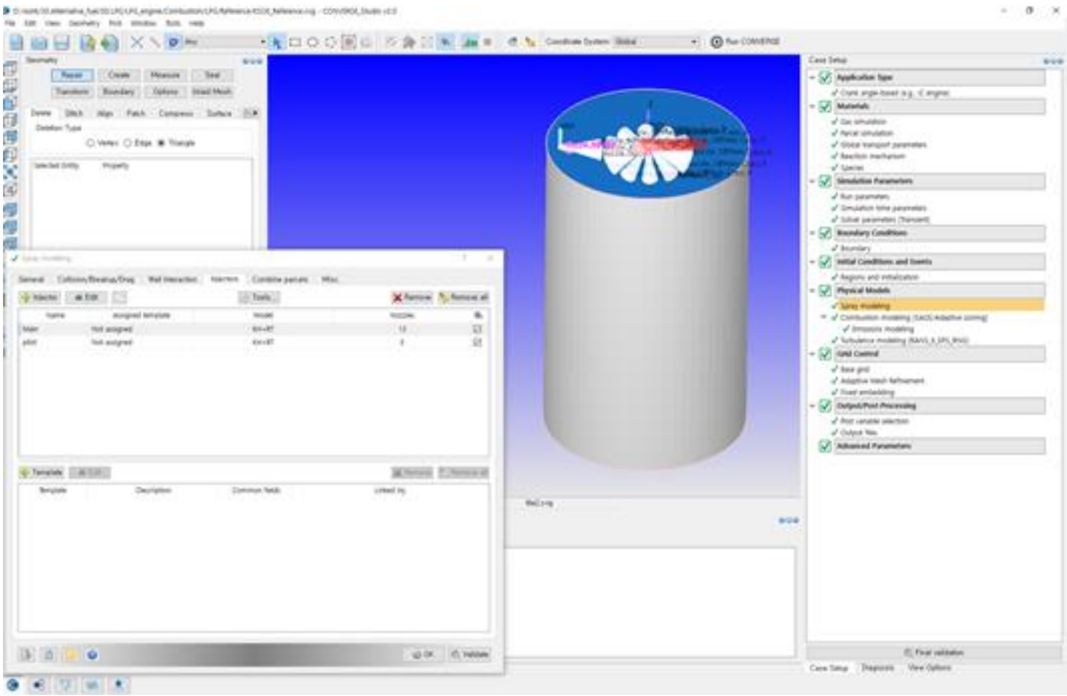

Figure 5. Engine model for the combustion calculation.

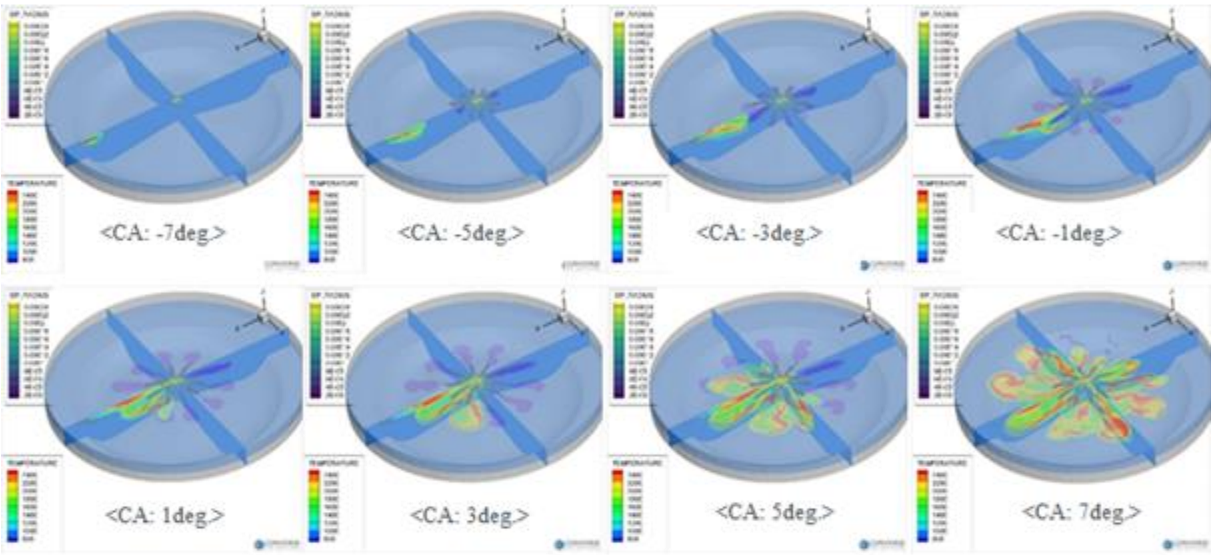

Figure 6. Calculated LPG combustion with the assist of micro-pilot diesel injection.

3. Prototype design and manufacturing

After the final design of the injection equipment was completed as shown in Fig. 7 based upon the data of flow and combustion analyses, the prototype of injection pump and valve were manufactured as shown in Fig. 8.

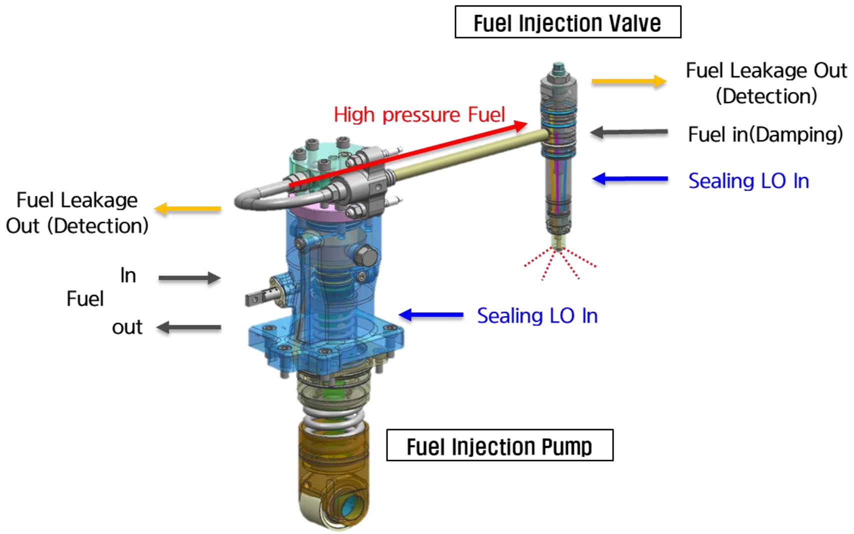

Figure 7. Final design layout of the target fuel injection system for low flash point fuels.

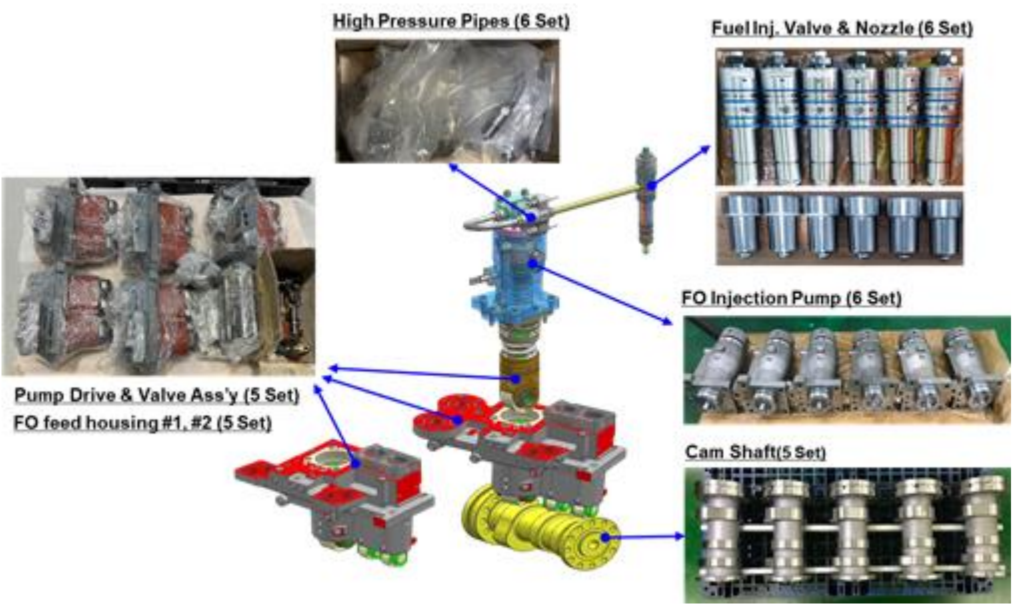

Figure 8. Preparation of the FIE components for the target 1MW engine operation with LPG fuel.

4. Prototype verification

After manufactured, the developed fuel injection system was verified in the purpose-built test rig shown in Fig. 9. The test rig run fuel cam with a rated speed with electric motor and fuel pump and injection valve are operated according to the cam motion. A fuel flow meter and injection rate meter are installed along the fuel line and after injector, respectively for fuel quantity measurement. The result showed that fuel was controlled well to show sufficient pressure, flow rates with respect to the control rack positions.

After test rig verification, 5 set of the injection systems loaded into the target engine and 200 hours endurance test was conducted. After the test emissions were measured and compared the one run with diesel before the modification of the fuel systems in the target engine which showed 14.5%, 91%, and 45.3% reduction in the THC, SO_2, and NO_x, respectively.

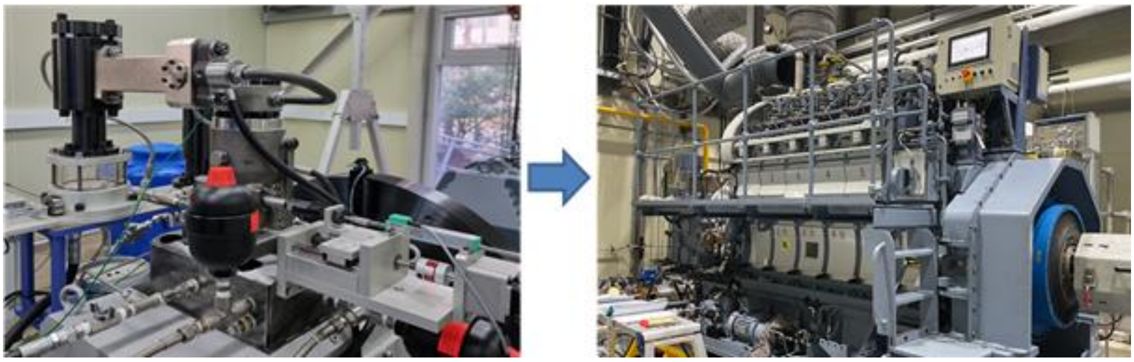

Figure 9. Purpose built FIE test rig and 1 MW target engine.

Table 3. Engine out mission reduction rate of LPG compared to diesel.

Load / Item	Diesel (Bunker-A)				LPG			
	25%	50%	75%	100%	25%	50%	75%	100%
THC [ppm]	245.6	148.3	153.2	142.8	173.9	137.5	121.4	141.6
SO_2 [ppm]	41.1	55.2	57.6	64.5	4.0	4.8	5.0	5.6
NOx [g/kWh]	6.92				3.79			

5. Conclusion

In this study, a new fuel injection system was designed and prototyped to be prepared for 1MW 4-stroke marine engine to mitigate GHG emission and the results can be summarized as follows:

1. A prototype LPG injection equipment was developed and which showed sufficient pressure and flow rate to run the target engine with producing comparable power outputs.
2. By replacing the conventional diesel fuel into LPG, the emissions showed better performance to show 14.5%, 91%, and 45.3% reduction in the THC, SO2, and NOx, respectively.
3. The developed system can be a basis to adopt zero carbon fuel, ammonia which is considered to reduce GHG emission further.

6. Acknowledgments

This work was supported by Technology Innovation Program funded by the Ministry of Trade, Industry and Energy (MOTIE, Korea) [Project No.: 20013146 and 20024387].

7. References

[1] IMO, RESOLUTION MEPC.377(80), “2023 IMO STRATEGY ON REDUCTION OF GHG EMISSIONS FROM SHIPS,” 2023

[2] Myung, C. L., Lee, H., Choi, K., Lee, Y. J. and Park, S. S. “Effects of gasoline, diesel, LPG and low-carbon fuels and various certification modes on nanoparticle emission characteristics in light-duty vehicles”. Int. J. Automotive Technology 10,5, pp.537-544. 2009
[3] DNV-GL, Maritime Forecast to 2050(Engergy transition outlook 2019), 2019
[4] Korean Register, “Forecasting the Alternative Marine Fuel : Ammonia,” 2019

The 13th TSME International Conference on Mechanical Engineering
12th – 15th December 2023
Chiang Mai, Thailand

AEC0013

Experimental Investigation on Tar Generation from Softwood and Hardwood under Thermochemical Conversion Processes

San Shwe Hla[1,*], Axel Youngdee[2], Chatchawan Chaichana[2], and Daniel Roberts[1]

[1]Energy Business Unit, Commonwealth Scientific and Industrial Research Organisation, 1 Technology Court, Pullenvale, Brisbane, Queensland 4069, Australia
[2]Department of Mechanical Engineering, Faculty of Engineering, Chiang Mai University, 239 Huay Kaew Rd., Muang District, Chiang Mai, Thailand 50200

* Corresponding Author: san.hla@csiro.au

Abstract. Among thermochemical conversion processes, gasification is gaining increasing attention due to its flexibility to produce a wide range of end products, extending beyond just heat and power, and its ability to scale to suit a range of feedstock scenarios. Until now, gasification has found application on a small scale, enabling remote power generation using biomass or agricultural waste streams. Despite the numerous advantages it offers, the utilization of biomass gasification for large-scale applications to produce hydrogen, fuels, and chemicals is still constrained by several challenges, with the formation and presence of tars in the syngas being the most prominent. Although there exists extensive research exploring the influence of different gasifier types, operating parameters, and catalyst compositions on tar formation and reduction in syngas derived from biomass gasification, there remains a significant gap in understanding the impact of biomass properties, specifically the effects of commercially available woody biomass varieties, on tar formation.

This study aimed to quantify the formation of tars at varying operating temperatures (300−900°C). To achieve this, a horizontal tube furnace was utilized, focusing on two of the most predominant wood species commercially produced in Australia: softwood (Pinus radiata) and hardwood (Eucalyptus). The collection, sampling, and analysis of tar in this study were performed following the standardised tar protocol established by the European Committee for Standardization. While both samples of softwood and hardwood exhibited a comparable level of volatile matter at approximately 84% on a dry basis, it was observed that the generation of tars from softwood was prominently greater than that from hardwood across all tested temperatures. In the case of hardwood, the generation of tars stabilised beyond 400°C. However, for the softwood sample, a significant increase in tars generation was observed up to 500°C, and the generation continued to gradually rise beyond 600°C until it reached its maximum tar generation at 800°C.

Keywords: tars in syngas, hardwood and softwood, biomass gasification, pyrolysis.

1. Introduction

Among thermochemical conversion technologies, direct combustion is the dominant method for utilising biomass on an industrial scale to produce either heat, electricity, or both. The use of combustion-based energy generation for biomass is a proven technology, and there are no significant technological obstacles to its implementation. This is exemplified by the Drax power station, situated in North Yorkshire, England, which is the largest power plant that generates electricity from biomass via combustion: it has a current capacity of 2,600 MW which can utilise wood pellets as feedstock [1].

Biomass gasification has great potential as a thermochemical conversion option due to its high overall efficiency and flexibility to produce various end products. However, unlike combustion, biomass gasification is not widely adopted for syngas production in industrial scale indicating the existence of barriers for its deployment. Recent studies and overviews have identified several issues, including challenges in managing the biomass supply chain, pre-treatment requirements for biomass gasification, gas conditioning and conversion technology, government policies, and the utilization of syngas for heat and power [2-4]. Most of these issues, such as pre-treatment, gas cleaning and economic feasibility, are somehow related to the formation and presence of tars in syngas which is considered to be the one of the biggest obstacles for biomass gasification to penetrate into commercial markets [5].

Extensive research spanning three decades has focused on deepening our understanding of the fundamental mechanisms underlying tar generation and cracking [6-9]. Furthermore, various approaches have been explored to reduce and eliminate tars in syngas, including the modification of conventional fixed bed gasifier systems [10-12], the implementation of catalytic tar cracking techniques [13-16], the integration of distinct thermochemical conversion processes in separate reactors [17-20], and the utilization of conventional auxiliary systems like scrubbers and electrostatic precipitators [21, 22]. Although the abundance of research conducted on the effects of various gasifier types, operating parameters (such as temperature, pressure, and gas velocity), and different catalyst compositions on tar formation and reduction in syngas produced via biomass gasification, the impact of biomass properties, particularly the impact of various types of commercially available woody biomass, on tar formation during thermochemical conversion processes remains relatively unexplored.

Australia encompasses two significant forest regions, with one situated in the western and southern parts of the country, while the other, known as the "green triangle," can be found in the southeastern region [23]. Australia's commercial plantation is composed of softwood species, primarily radiata pine, as well as predominantly native hardwood species, predominantly blue gum eucalypts. During the period ending in May 2022, Australia recorded a total of 5.719 million bdmt (bone dry metric tonnes) in combined annual exports of hardwood and softwood woodchips. Hardwood chips accounted for a significant portion, reaching 4.684 million bdmt, which represented approximately 82% of the total woodchip exports. Meanwhile, the exports of softwood woodchips amounted to 1.035 million bdmt, constituting roughly 18% of the total woodchip exports [24].

Australia is witnessing the emergence of a notable industry focused on wood pellet production. Presently, several prominent Australian companies specialise in manufacturing high-quality wood pellets primarily for export to countries such as Japan, Korea, and various European nations including the UK, the Netherlands, and Denmark. These wood pellets are used for co-firing in power stations, assisting these countries in meeting their emission reduction targets. Notable examples include Plantation Energy Australia (PEA) based in Western Australia and Altus Renewables based in Queensland. Together, these companies produce over 250,000 tons of wood pellets annually. Since there is no domestic market for wood pellets, their business operations are solely reliant on the international export market. Altus Renewables is also preparing for a project in Mount Gambier, situated in southern Australia, with plans to produce 500,000 tonnes of wood pellets annually [23]. These pellets will be exported from Portland Harbour to Europe and Asia, further expanding their presence in global markets. Blue gum woodchips, traditionally produced for pulp and paper customers. In general, wood chips have been used as solid fuel for space heating or in energy plants to generate electric power from renewable energy. Recently in Australia, the increased focus on utilising biomass for creating value-added products, coupled with the global decline in paper demand, has prompted the exploration of alternative markets for woody biomass products. This shift reflects the need to adapt and find new ways to maximise the value of woody resources in response to changing market dynamics and sustainability considerations.

While gasification is recognized as the optimal thermochemical conversion technology for generating value-added products such as liquid fuels, SAF (Sustainable Aviation Fuel), SNG (Synthetic Natural Gas), and hydrogen from woody biomass, there is a notable gap in understanding the impact of different wood types on gasification performance, particularly concerning tar formation. This study, therefore, aims to examine the formation of tar across a broad range of operating temperatures by utilising samples of Australian hardwood and softwood as feedstocks.

2. Experimental

2.1. Sample collection and preparation

For this study, two distinct types of wood samples were used: gum tree woodchips, which belong to the hardwood category (Eucalyptus), and wood pellets, classified as softwood (Pinus radiata). The gum tree woodchips were procured from a local landscaping shop, while the wood pellets were provided by Altus Renewables Limited. Altus's wood pellets are exclusively produced from pure pine sawdust, ensuring a composition of 100%. These pellets are specifically manufactured to meet the standards of the industrial sector.

A substantial quantity of samples exceeding 1 kg were dried using a laboratory oven, to measure the moisture content according to European Standard method ISO 18134-3:2015, which requires the oven temperature to be maintained at 105°C [25]. To ensure complete drying, the samples were initially left in the oven for a period exceeding 48 hours. Once dried, trays containing the samples were placed inside a large desiccator to cool down to room temperature. Immediate weighing of the samples was conducted to prevent moisture absorption from the surrounding atmosphere. The heating, drying, cooling, and weighing procedures were repeated until a total weight change of less than 0.2% was achieved. The moisture contents of the wood samples (on a wet basis) were then determined by calculating the difference in measured sample weight before and after the drying process.

Dry wood samples were then manually ground using a laboratory milling machine. The milling process was carried out systematically, employing various mesh screens with sizes of 5 mm, 3 mm, and 1 mm. Subsequently, when the wood particles reached a sufficiently reduced size, were then sieved to obtain a uniform size range between 425 μm and 1mm. Once the samples were sized, they were deemed suitable for conducting pyrolysis experiments. These samples were sent to the laboratory for comprehensive chemical analysis, including proximate and ultimate analyses, as well as energy content.

2.2. Pyrolysis rig (horizontal tube furnace) and pyrolysis procedure

The wood samples, prepared as previously mentioned, were placed into two laboratory ceramic crucibles. These crucibles were then loaded into an oven and subjected to overnight drying at a temperature of approximately 105°C. This step ensured the removal of any moisture that may have been absorbed by the samples during handling, especially during the grinding and sizing processes.

The pyrolysis experiments involving wood samples were carried out by using a horizontal tube furnace (HTF), capable of achieving temperatures as high as 1100°C. The two crucibles, each containing the dried wood samples, were carefully positioned inside the HTF, as illustrated in Figure 1. Approximately 7 g of wood samples can be loaded into each crucible. The reactor was then electrically heated from ambient temperature to the desired temperature range of 300–900°C at a heating rate of 3°C per minute. Once the targeted temperature was reached, it was maintained for a duration of 1 hour to ensure complete removal of devolatilization products from the wood samples. The entire process was carried out under a continuous flow of nitrogen at atmospheric pressure, maintaining a flow rate of 1 L per minute. Figure 1 illustrates the placement of two K-type thermocouples in the middle-top region of each crucible inside the horizontal tube furnace (HTF) to ensure uniform temperature distribution. After maintaining the targeted pyrolysis temperature for 1 hour, the reactor was cooled down, and the final weight of the solid remaining in the crucibles was measured.

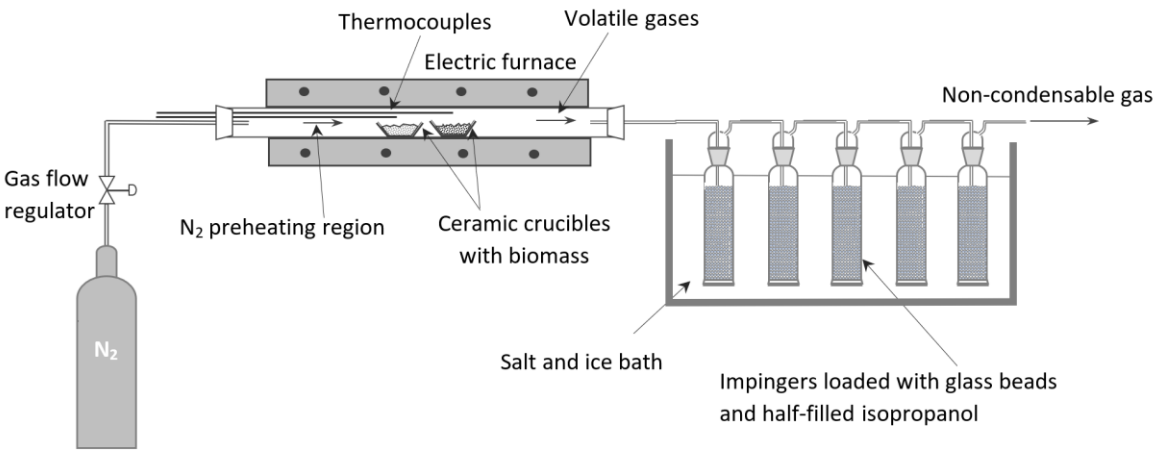

Figure 1. Schematic diagram of experimental set up for pyrolysis tests using a horizontal tube furnace.

The volatile gases generated during the pyrolysis experiments were transported through a quartz tube and a series of five interconnected impingers. These impingers were filled with glass beads and a minimum of 150 mL of isopropanol to effectively capture the condensable tar, as demonstrated in Figure 1. To facilitate the condensation of volatile components, the impingers were immersed in a mixture of ice and salt. This setup was derived from the tar protocol established by the European Committee for Standardization between 2003 and 2005 [26].

Following each experimental run, the solvent-condensate mixture obtained from all impingers was rinsed with additional solvent and combined in a single container. Due to the absence of heat maintenance facilities at the outlet of the quartz reactor, it was observed that certain volatile gas components condensed before reaching the series of impingers designed to capture the tars. For that reason, after each experiment, both the quartz tube reactor and the connecting line between the reactor and impingers were thoroughly rinsed and cleaned using isopropanol. The resulting cleaning solution was then added to the above-mentioned container. The experiments were repeated three times for each experimental condition to ensure the accuracy of the results.

2.3. Procedure for measurement of gravimetric tar and non-condensable gases

The collected mixture of condensable tar and solvents was transferred into a round bottom flask, which was weighed. The flask was subsequently placed on a rotary evaporator to separate the isopropanol solvent through evaporation under a moderate vacuum of approximately 10 kPa (abs). This process was conducted at a controlled temperature of 55°C, following the step-by-step procedures outlined in the tar protocol [26].

Once the complete separation of the solvent from the mixture was achieved, the flask was placed in a desiccator to cool down. The gravimetric tar left in the flask was then determined by calculating the difference between the measured weights of the empty flask and the flask after solvent evaporation. To calculate the total amount of non-condensable gases released during the pyrolysis experiment, the measured solid yield and tar yield were used as equation.

$$\textit{non-condensable gases} = \textit{weight of dry samples} - \textit{solid yield} - \textit{tar yield} \tag{1}$$

3. Results and discussion

3.1. Chemical and physical properties of hardwood and softwood

The chemical and physical of wood samples, which were prepared following the procedure outlined in the preceding section, were analysed using the standard methods specified in Table 1. According to Table 1, the proximate analysis indicated that the hardwood chip (as received) had more than three times the moisture content of the softwood pellet sample (as received). Additionally, the hardwood chip had a slightly lower volatile matter content and a slightly higher ash content compared to the softwood pellet sample. Based on the ultimate analysis, it is evident that softwood contains slightly higher carbon and hydrogen contents, while having lower oxygen content compared to hardwood. This difference is reflected in the energy content of the two samples, with softwood having slightly higher energy content than hardwood.

Table 1. Chemical analyses of softwood and hardwood samples on a dry basis, dry as free basis.

Analysis	Parameter	Softwood (wood pellet)	Hardwood (wood chip)	Analysis standard method
Proximate	Total moisture (wt% wb)	6.6	21.5	EN 14774-3: 2009
	Volatile matter (wt% db)	85.4	83.75	ISO 18123: 2015
	Fixed carbon (wt% db)	14.2	15.72	ISO 18123: 2015
	Ash (wt% db)	0.41	0.53	EN 14775: 2009
Ultimate	Carbon (wt% daf)	52.72	50.15	ISO 16948:2015
	Hydrogen (wt% daf)	6.33	5.83	ISO 16948:2015
	Nitrogen (wt% daf)	0.13	0.08	ISO 16948:2015
	Oxygen (wt% daf)	40.81	43.93	Balance
	Sulfur (wt% daf)	0.02	0.01	ISO 16994:2016 by ICP-OES
Energy Content	LHV (MJ/kg, db)	18.50	18.15	EN 14918:2009
	LHV (MJ/kg, wb)	17.12	13.60	EN 14918:2009
Density	Bulk Density (kg, wb/m3)	675	261	
Energy density	Energy Density (GJ/m3)	11.56	3.55	
Ash analysis	Na_2O (wt%)	3.74	2.72	NQ797 - Analysis of Materials - Fused bead XRF
	MgO (wt%)	15.50	8.20	
	Al_2O_3 (wt%)	1.56	1.68	
	SiO_2 (wt%)	6.00	10.20	
	P_2O_5 (wt%)	7.20	2.09	
	K_2O_3 (wt%)	13.06	6.34	
	CaO (wt%)	30.00	49.30	
	TiO_2 (wt%)	0.08	0.17	
	Mn_3O_4 (wt%)	1.20	0.98	
	Fe_2O_3 (wt%)	0.79	0.95	
	Other (wt%)	20.87	17.37	

When the energy contents of two wood samples are compared on a wet basis, a significant difference emerged the hardwood chips had a notably higher moisture content as discussed above. As expected, softwood pellets have over 2 and half times higher bulk density compared to hardwood chip due to high pressure compaction during pelletising. That makes softwood pellets over three times higher energy than hardwood chips as shown in Table 1.

Both wood samples were ashed at 580°C, and their respective ash compositions were analysed using standard methods and the results are listed in Table 1. The ash samples from both wood types exhibit significantly high calcium content, comprising almost half of the ash in hardwood and approximately one-third in softwood. Additionally, hardwood ash shows higher silicon content compared to softwood ash. On the other hand, softwood ash contains higher levels of magnesium (Mg), phosphorus (P), and potassium (K) compared to hardwood ash. However, the remaining mineral matter composition, including sodium (Na), aluminium (Al), manganese (Mn), and iron (Fe), appears to be similar between the ash samples of the two different woods. It's important to highlight that, when examining the composition of mineral matter, ash samples were generated in an oxidized environment while exposed to air. Our prior research revealed distinctions in mineral phase compositions and trace element contents between ash samples generated through combustion and those produced under gasification (reduction) conditions [27].

The biomass composition can be expressed in relation to its primary lignocellulosic fractions, namely hemicellulose, cellulose, and lignin contents. Nevertheless, the conventional method for determining these fractions in biomass samples is time-consuming and costly, involving complex procedures and the use of multiple chemical reagents [28]. In this project, we did not directly measure the lignocellulosic fractions of hardwood and softwood samples. However, existing literature suggests that hardwood typically contains a higher proportion of hemicellulose and lower levels of lignin and cellulose compared to softwood [28-30]. Moreover, it is worth noting that the hemicellulose and lignin present in softwood and hardwood consist of different types of compounds: softwood (pinewood) hemicellulose is composed of galactoglucomannans, along with mannose and galactose units while hardwood (eucalyptus) hemicellulose consists of glucuronoxylan, xylan, and acetyl groups [31-33]. According to Chan et al [33], these variations in hemicellulose compounds between softwood and hardwood plays significant a significant role in their distinct decomposition behaviour during pyrolysis, a significant finding in the context of this study.

3.2. Pyrolysis behaviour of hardwood and softwood

Among thermochemical conversions process of biomass, pyrolysis takes precedence as the initial stage and significantly influences product distribution. This study is focused on pyrolysis condition under slow heating rates, moderate post-pyrolysis residence times (e.g. up to 5 sec at 900°C). Within this context, it could indicate the potential for additional cracking and/or condensation of volatile gases. To a certain extent, these conditions could represent operational scenarios within pyrolysis zone of a fixed gasifier. This section focuses on presenting the yield of pyrolysis products from two distinct types of woods under various operating temperatures. Figure 2 illustrates the release of volatile matter and char yield from both types of wood samples as a function of temperature during the pyrolysis process. Up to 500°C, there is a significant increase in volatile matter release for both softwood and hardwood. Beyond 500°C, the release rate shows a gradual rise, reaching its peak at 900°C.

It should be noted that the amount of volatile matter tested in this series of experiments is lower than that reported by the results obtained using the standard method (ISO 18123:2015) as described in Table 1. The ISO 18123:2015 standard method for measuring volatile matter employs a high heating rate, with the sample being rapidly heated to the test temperature, completing the entire procedure in about 7 minutes. In contrast, our experiment utilised a slow heating rate (3°C per minute), taking hours to reach the target pyrolysis temperature. The disparity in the amount of volatile matter between the ISO standard method and our experimental data appears to be largely attributed to the significantly different heating rates employed in each experimental procedure.

Notably, at relatively lower pyrolysis temperatures, softwood produced higher amount of volatile matter being released compared to hardwood. Cellulose undergoes thermal devolatilization at a modest pyrolysis temperature around 230°C, progressing until 400°C [30]. Subsequently, the breakdown of lignin occurs at elevated temperatures spanning 400°C to 750°C [34]. This phenomenon explains why, when considering that softwood generally contains a greater proportion of cellulose compared to hardwood, softwood tends to initiate the devolatilisation process at lower pyrolysis temperatures than hardwood. However, as the operating temperature increases, the differences in volatile matter yield between the two wood types diminish. In contrast, the char yield demonstrates an opposite trend during the pyrolysis of softwood and hardwood, as shown in Figure 2.

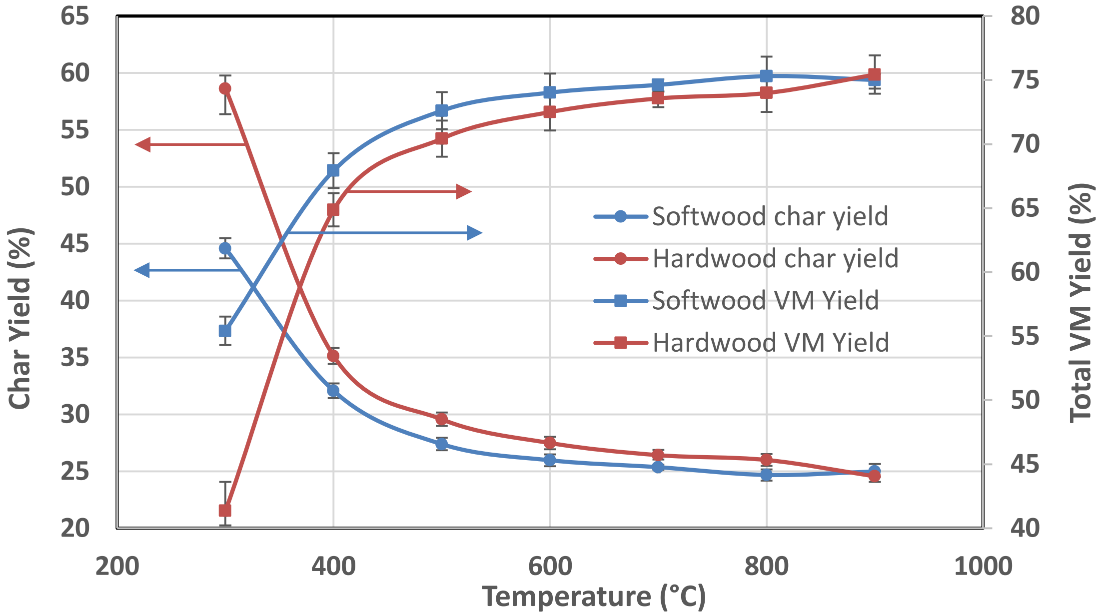

Figure 2. Char yields and total volatile yield of soft wood and hardwood under a range of pyrolysis temperature.

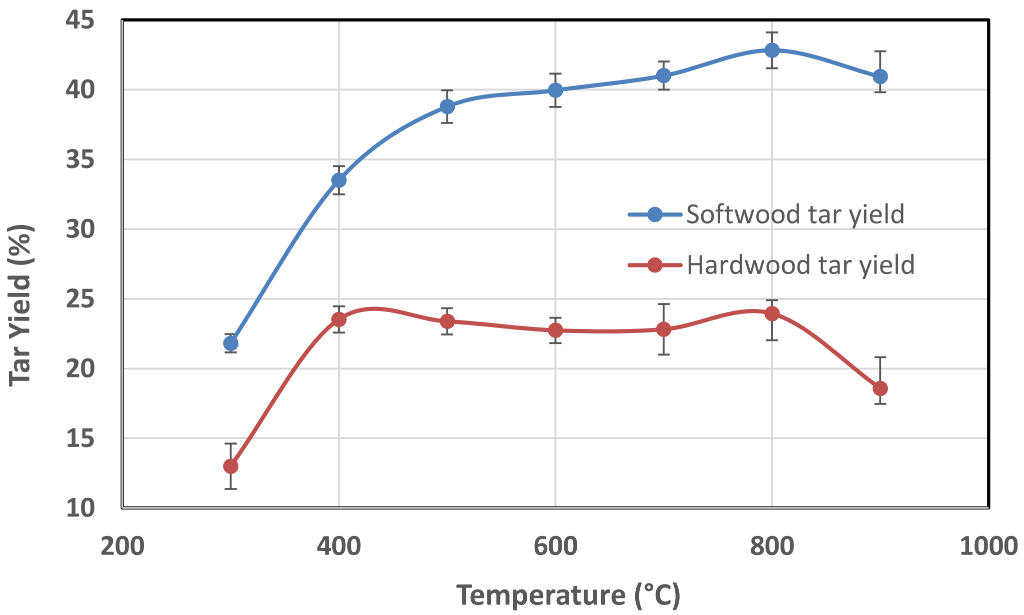

Figure 3. Tars (condensable volatile matter) yield of soft wood and hardwood under a range of pyrolysis temperature.

Volatile matter generated during the pyrolysis process can be primarily categorized into two groups: gases (referred to as non-condensable volatile matter) and tars (the condensable fractions of volatile matter). Our experimental analysis distinctly demonstrated that the gravimetric tars content originating from softwood significantly exceeds the tar released from hardwood across all pyrolysis temperatures examined in our study, as illustrated in Figure 3. Based on an extensive review of tar formation and evolution, it is evident that oxygenated compounds (referred to as primary tars) predominantly emerge when cellulose and lignin undergo pyrolysis at temperatures up to 700°C and secondary tars form at pyrolysis temperatures reaching up to 850°C [35]. These types of tars particularly oxygenated compounds form at elevated temperatures and exhibit high condensability at lower temperatures. This phenomenon could explain why softwood produce a greater quantity of condensable tars compared to hardwood as softwood is recognized for its higher proportion of lignocellulosic components. In addition, this is likely attributed to the hemicellulose content in softwood, predominantly composed of galactoglucomannans.

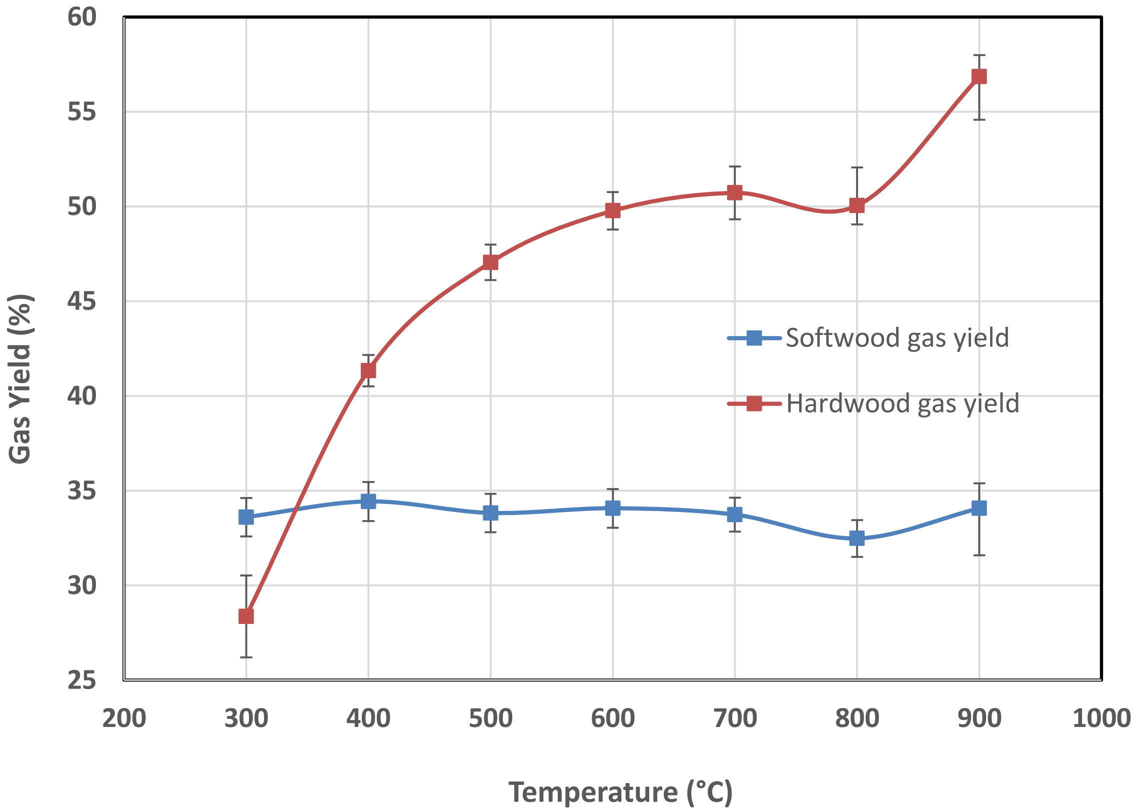

Figure 4. Gases (non-condensable volatile matter) yield of soft wood and hardwood under a range of pyrolysis temperature.

At the higher pyrolysis temperature, it was found that tar content from softwood is two times higher than that from hardwood. At elevated pyrolysis temperatures above 700°C, it was observed that the tar content generated from softwood was twice as substantial as the quantity released from hardwood. An interesting phenomenon to note is that at pyrolysis temperatures exceeding 800°C, there is a reduction in tar contents from both softwood and hardwood, attributed to the transformation of some of the tars into gases through a process of cracking at these elevated temperatures. Due to the relatively smaller quantity of tars (condensable volatile matter) in hardwood, a higher quantity of non-condensable gases was detected in the pyrolysis of hardwood compared to that released from softwood, as illustrated in Figure 4.

4. Conclusion and recommendation

This study focuses on the pyrolysis characteristics of Australian hardwood and softwood using a horizontal tube furnace. A key outcome of the study is the significant differences in gravimetric tar production between softwood and hardwood across all examined pyrolysis temperatures. Given that tars present a significant challenge in biomass gasification, undertaking precautions and careful attention becomes essential when engaging in softwood gasification. This might involve modification of gasification process for minimisation for tar generation and deploying larger gas cleaning facilities. It's important to note that these experimental tests were conducted exclusively within a pyrolysis environment. Therefore, a comprehensive series of gasification trials, conducted at either a laboratory-scale or within a pilot-scale gasifier, using both softwood and hardwood as feedstocks, would be required to validate the findings of this study.

5. References

[1] Drax. (2023). *Drax Power Station: The UK's largest renewable power station*. Retrieved June 2023 from https://www.drax.com/about-us/our-sites-and-businesses/drax-power-station/

[2] Pereira, E. G., da Silva, J. N., de Oliveira, J. L., & Machado, C. S. (2012). Sustainable energy: A review of gasification technologies. *Renewable and Sustainable Energy Reviews*, *16*(7), 4753-4762.

[3] Ruiz, J. A., Juárez, M. C., Morales, M. P., Muñoz, P., & Mendívil, M. A. (2013). Biomass gasification for electricity generation: Review of current technology barriers. *Renewable and Sustainable Energy Reviews*, *18*, 174-183.

[4] Sansaniwal, S. K., Rosen, M. A., & Tyagi, S. K. (2017). Global challenges in the sustainable development of biomass gasification: An overview. *Renewable and Sustainable Energy Reviews*, *80*, 23-43.

[5] Reed, T. B., & Gaur, S. (1998). *Survey of biomass gasification: Gasifier Project and Manufacturers around the World* (Vol. 1). Golden, CO: The National Renewable Energy Laboratory and The Biomass Energy Foundation, Inc.

[6] Liden, A. G., Berruti, F., & Scott, D. S. (1988). A KINETIC MODEL FOR THE PRODUCTION OF LIQUIDS FROM THE FLASH PYROLYSIS OF BIOMASS. *Chemical Engineering Communications*, *65*(1), 207-221.

[7] Boroson, M. L., Howard, J. B., Longwell, J. P., & Peters, W. A. (1989). Product yields and kinetics from the vapor phase cracking of wood pyrolysis tars [Article]. *AIChE Journal*, *35*(1), 120-128.

[8] Fagbemi, L., Khezami, L., & Capart, R. (2001). Pyrolysis products from different biomasses: application to the thermal cracking of tar. *Applied Energy*, *69*(4), 293-306.

[9] Rath, J., & Staudinger, G. (2001). Cracking reactions of tar from pyrolysis of spruce wood. *Fuel*, *80*(10), 1379-1389. https://doi.org/https://doi.org/10.1016/S0016-2361(01)00016-3

[10] Hla, S. S., Aye, L., Stewart, D. F., Connor, M. A., Fung, P., & Ng, S. H. (2004). *Tar levels in a stratified downdraft gasifier* Science in Thermal and Chemical Biomass Conversion, Victoria, BC, Canada, August 2004.

[11] Bhattacharya, S. C., Shwe Hla, S., & Pham, H.-L. (2001). A study on a multi-stage hybrid gasifier-engine system. *Biomass and Bioenergy*, *21*(6), 445-460.

[12] Reed, T. B., Walt, R., Ellis, S., Das, A., & Deutsch, S. (1999). Superficial velocity - the key to downdraft gasification.*Biomass. A growth opportunity in green energy and value-added products. Volume 2* Fourth Biomass Conference of the Americas, 29 Aug - 2 Sep 1999, Oakland, CA, USA.

[13] Abu El-Rub, Z., Bramer, E. A., & Brem, G. (2008). Experimental comparison of biomass chars with other catalysts for tar reduction. *Fuel*, *87*(10), 2243-2252.

[14] Zhang, S., Zhu, S., Zhang, H., Liu, X., & Xiong, Y. (2019). High quality H2-rich syngas production from pyrolysis-gasification of biomass and plastic wastes by Ni–Fe@Nanofibers/Porous carbon catalyst. *International Journal of Hydrogen Energy*, *44*(48), 26193-26203.

[15] Fredriksson, H. O. A., Lancee, R. J., Thüne, P. C., Veringa, H. J., & Niemantsverdriet, J. W. (2013). Olivine as tar removal catalyst in biomass gasification: Catalyst dynamics under model conditions. *Applied Catalysis B: Environmental*, *130-131*, 168-177.

[16] Pio, D. T., Tarelho, L. A. C., Pinto, R. G., Matos, M. A. A., Frade, J. R., Yaremchenko, A., Mishra, G. S., & Pinto, P. C. R. (2018). Low-cost catalysts for in-situ improvement of producer gas quality during direct gasification of biomass. *Energy*, *165*, 442-454.

[17] Henriksen, U., Ahrenfeldt, J., Jensen, T. K., Gøbel, B., Bentzen, J. D., Hindsgaul, C., & Sørensen, L. H. (2006). The design, construction and operation of a 75kW two-stage gasifier. *Energy*, *31*(10), 1542-1553. https://doi.org/https://doi.org/10.1016/j.energy.2005.05.031

[18] Gómez-Barea, A., Leckner, B., Villanueva Perales, A., Nilsson, S., & Fuentes Cano, D. (2013). Improving the performance of fluidized bed biomass/waste gasifiers for distributed electricity: A new three-stage gasification system. *Applied Thermal Engineering*, *50*(2), 1453-1462. https://doi.org/https://doi.org/10.1016/j.applthermaleng.2011.12.025

[19] Vogels, J. (2010, 16–20 May 2010). Industrial scale hydrogen production from biomass via Choren's unique Carbo-V-process. 18th World Hydrogen Energy Conference, Essen, Germany

[20] Wilk, V., & Hofbauer, H. (2013). Conversion of mixed plastic wastes in a dual fluidized bed steam gasifier. *Fuel*, *107*, 787-799.

[21] Zwart, R. W. R., Van der Drift, A., Bos, A., Visser, H. J. M., Cieplik, M. K., & Könemann, H. W. J. (2009). Oil-based gas washing—Flexible tar removal for high-efficient production of clean heat and power as well as sustainable fuels and chemicals. *Environmental Progress & Sustainable Energy*, *28*(3), 324-335.

[22] Chen, H., Namioka, T., & Yoshikawa, K. (2011). Characteristics of tar, NOx precursors and their absorption performance with different scrubbing solvents during the pyrolysis of sewage sludge. *Applied Energy*, *88*(12), 5032-5041.

[23] GEMCO Energy. (2023). *Wood pellets industry and market in Australia*. http://www.pellet-making.com/blog/wood-pellets-australia.html

[24] Forest & Wood Products Australia. (2022). *Annual woodchip exports totalled 5.719 Mbdmt year-ended May 2022*. https://fwpa.com.au/annual-woodchip-exports-totalled-5-719-mbdmt-year-ended-may-2022/

[25] ISO. (2015). *ISO 18134-3:2015 Solid biofuels — Determination of moisture content —Oven dry method — Part 3: Moisture in general analysis sample*. https://www.iso.org/standard/61637.html/

[26] Good, J., Ventress, L., Knoef, H., Zielke, U., Hansen, P. L., Kamp, W. v. d., Wild, P. d., Coda, B., Paasen, S. v., Kiel, J., Sjöström, K., Liliedahl, T., Unger, C., Neeft, J., Suomalainen, M., & P. Simell. (2005). *Sampling and analysis of tar and particles in biomass producer gases, Technical Report prepared under CEN BT/TF 143 "Organic contaminants ("tar") in biomass producer gases"*.

[27] Ilyushechkin, A., He, C., Hla, S.S. (2020). Characteristics of inorganic matter from Australian municipal solid waste processed under combustion and gasification conditions. *Waste Management & Research*, *39*(7), 928-936.

[28] Díez, D., Urueña, A., Piñero, R., Barrio, A., & Tamminen, T. (2020). Determination of Hemicellulose, Cellulose, and Lignin Content in Different Types of Biomasses by Thermogravimetric Analysis and Pseudocomponent Kinetic Model (TGA-PKM Method). *Processes*, *8*(9).

[29] Asmadi, M., Kawamoto, H., & Saka, S. (2017). Characteristics of softwood and hardwood pyrolysis in an ampoule reactor. *Journal of Analytical and Applied Pyrolysis*, *124*, 523-535.

[30] Tsalidis, G. A., Di Marcello, M., Spinelli, G., de Jong, W., & Kiel, J. H. A. (2017). The effect of torrefaction on the process performance of oxygen-steam blown CFB gasification of hardwood and softwood. *Biomass and Bioenergy*, *106*, 155-165.

[31] Koch, G. (2008). Raw Material for Pulp. In *Handbook of Pulp* (Vol. 1, pp. 21-68).

[32] Reyes, P., Teixeira Mendonca, R., Rodriguez, J., Fardim, P., & Vega, B. (2013). Characterization of the hemicellulosic fraction obtained after pre-hydrolysis of Pinus Radiata wood chips with hot water at different initial PH. *Journal of the Chilean Chemical Society, 58*, 1614-1618.

[33] Chan, F. L., & Tanksale, A. (2016). Catalytic steam gasification of pinewood and eucalyptus sawdust using reactive flash volatilization. *Applied Catalysis B: Environmental*, *187*, 310-327.

[34] Joffres, B., Laurenti, D., Charon, N., Daudin, A., Quignard, A., & Geantet, C. (2013). Thermochemical Conversion of Lignin for Fuels and Chemicals: A Review. *Oil & Gas Science and Technology – Rev. IFP Energies nouvelles*, *68*(4), 753-763

[35] Font Palma, C. (2013). Modelling of tar formation and evolution for biomass gasification: A review. *Applied Energy, 111*, 129-141.

AEC0017

Electric Car Conversion of Small Pickup Truck; Engineering Process and Test Results

Punyapat Krachang[1] and Pruk Aggarangsi[1,*]

[1]Department of Mechanical Engineering, Faculty of Engineering, Chiang Mai University 239, Muang District, Chiang Mai, 50200, Thailand

* Corresponding Author: pruk.a@cmu.ac.th

Abstract. The 1-ton truck is a highly popular vehicle in Thailand and several regions worldwide, with an accumulated quantity in Thailand exceeding seven million units. Almost all these trucks are powered by internal combustion engines. Transition towards electric mobility policy creates opportunity in electric conversion of existing trucks to accelerate number of electric vehicles share. This research presents an engineering process and Thailand regulations related to the conversion of 1-ton trucks with internal combustion engines into electric vehicles. The aim of this transcript is to summarize the important design aspects, technical equipment, and relevant documentation required for registration and legal compliance. Additionally, the research highlights the essential additional components that need to be designed, along with the performance testing of a modified truck. Test result reveals that the converted electric trucks can generate 111.69 horsepower and 348.17 N-m torque at the wheels. They have undergone road testing for a distance of 250 kilometres without any operational issues and can be legally registered as modified electric vehicles with Thailand Department of Land Transport. Consequently, this study provides guidelines for future engineering endeavouring in the field of electric truck conversions.

Keywords: EV conversion, pickup truck, electrical vehicle.

1. Introduction

Thailand has a consistently rising energy demand due to economic expansion and population growth. The industrial sector relies heavily on land transportation. As a result, 1-ton trucks have become dominant vehicles in Thailand, thanks to their versatility in community settings. Their ability to meet both commercial and personal passenger requirements demonstrates their adaptability to a wide range of user preferences. These vehicles significantly contribute to the transportation sector's advancement due to their inherent operational convenience. Additionally, their operational ease underscores their essential role in driving the country's transportation dynamics and, as a result, promoting national economic growth. The number of registered vehicles in this category has increased significantly in recent years. As of 2022, the cumulative registrations totaled 7,085,910. In that year, there was an additional 241,340 new registrations, representing a 3% increase over previous counts [1]. In 2021, the National EV Policy Committee announced its "30@30" policy, which aims to promote the widespread use of zero-emission vehicles (ZEVs). By 2030, this initiative proposes that at least 30% of newly manufactured vehicles be ZEVs. This strategy includes a production target of 725,000 electric passenger cars and pickups, 675,000 motorcycles, and 34,000 buses and trucks. It also promotes the use of 440,000 electric passenger cars and pickups, 650,000 motorcycles, and 33,000 buses and trucks. Additionally, strategic measures have been developed to promote the advancement of ZEVs in a variety of sectors [2]. In addition, Thailand government has announced the 13th National Economic and Social Development Plan (2023-2027). For promoted the next-generation automotive industry by emphasizing an expansion of the current industry onto more advanced technology and innovation together with determining key supportive measures for EVs, such as promoting the conversion of existing internal combustions cars into EVs to stimulate investment in the automotive industry's ecosystem and the transfer of EV technology. As a result, the number of conversions to EVs will be no less than 40,000 vehicles by 2027 [3]. While electric vehicles (EVs) are undoubtedly appealing, their high market prices and limited versatility pose obstacles to their widespread adoption. An in-depth assessment, particularly in the Thai context, highlights the significant impact of electric vehicle technological advancement on the relevant manufacturing sectors. The Thai automotive sector, which is largely made up of compact trucks and personal-use vehicles, is expected to transition to electric propulsion systems at a significantly slower pace. Given this gradual shift, manufacturers who focus on these vehicle categories and their essential components may only experience minor operational disruptions [4].

However, given the potential to convert 1-ton trucks, which have a service life of 7 to 15 years and a total of more than 2 million units, to an electric system, there is an opportunity to accelerate the country's transition to EVs, aligning with national policy objectives and expediting the achievement of goals. This approach not only alleviates the financial burden of purchasing a new vehicle, but it also provides an appealing alternative for those who are interested in adopting electric mobility. Given its cost-effectiveness, the performance of such converted vehicles is comparable to that of commercially available electric cars, and they can be customized to meet specific design preferences.

This study presents a technical design process for the modification of electric vehicles, as well as the introduction of standardized equipment and installation in accordance with electric vehicle modification service standards. This ensures that operations comply with relevant regulations, allowing for the lawful use of retrofitted electric vehicles.

2. Experimental Design and Methodology

2.1. Vehicle Selection Criteria for Conversion

This study sourced data on 1-ton truck volumes based on vehicle types registered with Thailand Department of Land Transport. To ensure data integrity and avoid potential duplication, only the database of initially registered vehicles was utilized.

Trucks in the 1-ton category that have been operational for a period ranging from 7 to 12 years are deemed suitable for electric conversion. The vehicle targeted for modification has been operational for a maximum of 15 years, considering the general usability of most cars spans 20 to 25 years. As well as in value aspects, pick-up trucks value generally fall below 50% of newly purchased price after 7 years [5]. As such, data on initial registrations from 2011 to 2016 were extracted from the Department of Land Transport's first registration statistics database to determine potential conversion candidates. The total count amounted to 1,667,154 vehicles. This is subdivided into personal trucks, with 1,666,617 vehicles, as defined by the Road Traffic Act of 1979, and a smaller segment of 537 trucks registered under the Land Transport Act of 1979. Comprehensive details are presented in Table 1.

Table 1. Number of 1-ton Trucks Eligible for Electric Conversion.

	Number of Vehicles Suitable for Modification						
Van & Pick-Up	2011	2012	2013	2014	2015	2016	Total
By Road Traffic Act, B.E. 1979	275,324	331,489	336,064	268,646	232,968	222,126	1,666,617
By Land Transport Act, B.E. 1979	144	119	133	110	26	5	537
Total	275,468	331,608	336,197	268,756	232,994	222,131	1,667,154

2.2. Power estimation model

According to the fundamental theory of vehicle dynamics [6,7], we know that EV's instantaneous power is determined by vehicle speed, acceleration and roadway grade is shown in Figure 1.

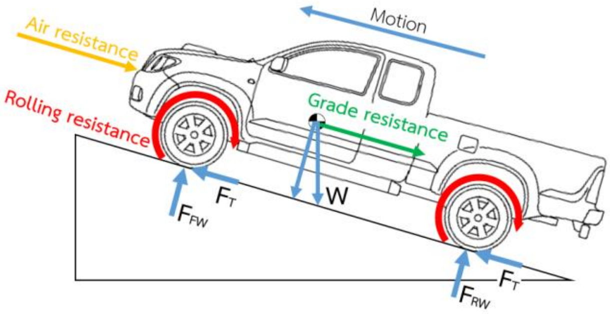

Figure 1. Forces acting on a vehicle when driving on a gradient condition.

Therefore, the proposed model essentially is an analytic description of the relationship among EVs' power, velocity, acceleration, and grade. First, according to basic physics, the required tractive effort for a vehicle driving on certain conditions is determined by three major resistances as described by the following equation:

$$F_{w(net)} = m_e a + R_a + R_r + R_g \tag{1}$$

Where $F_{w(net)}$ is tractive effort (N); m_e is Equivalent vehicle mass (kg); a is acceleration (m/s^2), and R_a, R_r, and R_g are aerodynamic, rolling, and grade resistances respectively (N).

Given that vehicle velocity is v (m/s) and roadway grade is θ (degree) R_a, R_r, and R_g can be calculated by the following equation (2) – (4), respectively

$$R_a = k_a v^2 = \frac{1}{2}\rho c_d A v^2 \tag{2}$$

$$R_r = f_{rl} mg cos\theta \tag{3}$$

$$R_g = mg sin\theta \tag{4}$$

where k_a is aerodynamic resistance constant, which is determined by air density ρ (kg/m^3), frontal area of the vehicle A (m^2), and coefficient of drag c_d (no unit); f_{rl} is rolling resistance constant (no unit); and g is gravity acceleration (g = 9.81 m/s^2). Combining Eqs. (1) and (2-4), we can get:

$$F_{w(net)} = m_e a + \frac{1}{2}\rho c_d A v^2 + f_{rl} mg cos\theta + mg sin\theta \tag{5}$$

The Eq. (5) can be applied for ICE and electric vehicles. To generate above tractive force, the required power (P_v, watt) for a vehicle traveling at vehicle velocity (v) can be estimated using the following equation:

$$P_v = F_{w(net)} \bullet v \tag{6}$$

P_v is actually output power, which is provided by the input power (P, watt). For ICE vehicles, P is generated by combustion of the fuel; but for EVs, P is generated by an electric motor. EVs are much more efficient than ICE vehicles because electrical power losses for an electric motor are small [8,9]. If we assume the motor efficiency or efficiency of transmission in ICE is η_t, we have the following relationship between the input power and output power. The equation could be written as follows:

$$P = \frac{P_v}{\eta_t} = F_{w(net)} \bullet \frac{v}{\eta_t} = \left(m_e a + \frac{1}{2}\rho c_d A v^2 + f_{rl} mg cos\theta + mg sin\theta \right) \bullet \frac{v}{\eta_t} \tag{7}$$

2.3. Vehicle Performance Evaluation

This study assesses the alterations in vehicle performance after the integration of electric drivetrain modifications, juxtaposing this with the vehicle's pre-modification performance. The objective is to discern whether the modified performance aligns with, or is commensurate to, the original standards and specifications. For this purpose, the vehicle test bench was anchored on a MAHA chassis dynamometer (LPS 3000). Performance parameters, such as maximum engine or motor power, wheel power, torque, and maximum speed, were gauged using this apparatus. Additionally, an on-board diagnostic (OBD) system, interfaced with the engine control unit (ECU), logged all pertinent engine data, including emissions, mileage, and speed. The MAHA chassis dynamometer software (LPS 3000 beta) facilitated the acquisition of engine torque and speed under the stipulated test conditions. A visual documentation of the performance measurement process is presented in Figure 2.

Figure 2. Visual Documentation of Vehicle Performance Measurement.

2.4. Apparatus Selection for Electric Vehicle Retrofitting

After extensive research into the automotive preferences of the Thai market, it became evident that the Toyota brand, especially the Toyota Hilux Vigo Smart Cab, held a significant place in consumer choice. Consequently, this model was selected for adaptation. Detailed specifications are provided in Table 2. The initial phase of the conversion predominantly involves mechanical alterations. All components associated with the car's internal combustion process, ranging from the fuel tank, fuel tract, engine, and transmission, must be removed. However, the original electrical wiring remains intact, serving the vehicle's lighting, signal lights, and other ancillary systems. While the core electrical system remains to support the installations on the vehicle, some refinements might be necessary to retain its original functionality.

Table 2. Technical Specifications of the Toyota Hilux Vigo Smart Cab.

Length Width Height	5,135 x 1,760 x 1,735 mm.	Engine	2,694 cc, 4 stroke, 4 cylinder
Wheelbase	3,085 mm.	Fuel supply	EFI Gasoline; 76 litter fuel tank
Tread Front / Rear	1,510 / 1,510 mm.	Maximum power	118 kW /5,200 rpm
Kerb weight	1,540 kg.	Maximum torque	241 Nm /3,800 rpm
power steering	Rack & Pinion	Transmission	Clutch, 5-speed manual
Front suspension	Double wishbone	Front brake	Ventilated disc
Rear suspension	Rigid type and leaf spring	Rear brake	Drum LTS
Tires	Steel wheel 215/65 R16C	Cooling system	Water cooled

In determining the appropriate motor size, it's crucial to align it with the necessary driving force and torque. At a minimum, the motor's power should adhere to the standards set by the Department of Land Transport. This determination leverages data acquired from engine and motor manufacturers to facilitate a comparative analysis between conventional engine-driven cars and those modified to employ electric motors. Table 3 provides a detailed comparison.

Table 3. Comparative Analysis of Conventional Engine and Electric Motor Specifications.

	Motor TZ290XS	Engine 2TR-FE
Maximum Power	110 kW / 4,000 RPM	118 kW /5,200 RPM
Rated Power	65 kW / 1,900 RPM	-
Maximum Torque	700 Nm / 4,000 RPM	241 Nm /3,800 RPM
Rated Torque	327 Nm / 1,900 RPM	-
Weight	445 kg (Motor & Battery)	200 Kg (Engine & Gear)

The selection of the driving motor must be designed appropriately to suit the motion equation of the vehicle, considering a total weight close to the maximum value specified by the car manufacturer at 1-ton. This entails the consideration of the power and torque of the motor to adequately counteract resistance from aerodynamic resistance, rolling resistance, and grade resistance. All three resistances must be calculated in conjunction with the road gradient specified by the Department of Highways, which defines the road gradient not exceeding percentages of 4, 6, 8, and 12, respectively. Additionally, the driving motor should be capable of effectively substituting the engine along with the power transmission system, catering to all usage scenarios.

To comprehensively understand the performance of traditionally motorized vehicles versus those modified to utilize electric motors—specifically concerning wheel torque, wheel power, and vehicle speed—it's crucial to ascertain whether such modifications are coherent and apt. Data from Table 3 were been synthesized to generate Figure 3, which presents a comparative analysis of wheel torque (in Nm), wheel power (in kW), and vehicle speed performance.

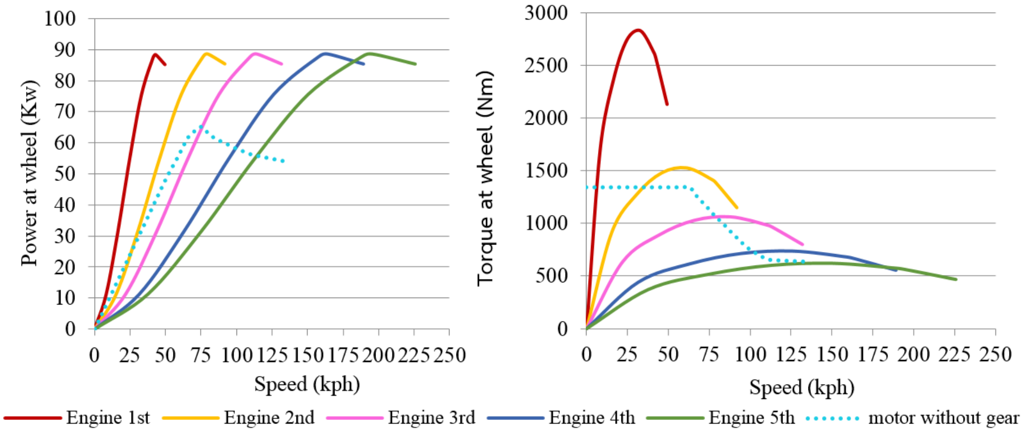

Figure 3. Comparative Analysis of Wheel Torque and Wheel Power against Vehicle Speed Performance.

The drive motor, rated at 1 1 0 kW / 7 0 0 Nm, along with its mounting brackets, is specifically designed to seamlessly integrate with the pre-existing mounts of the engine and gearbox. Three positions are allocated on the front chassis. Two Lithium-Polymer batteries are held together by thick steel plates to prevent damage, are strategically positioned in the under-chassis compartment of the vehicle. Control equipment pertinent to propulsion, as well as ancillary devices, are placed in the engine compartment at the front chassis. This arrangement not only facilitates easier inspection and maintenance but also capitalizes on the available space in the engine compartment. Refer to Figure 4 for a visual representation. Subsequent to these modifications, the vehicle's overall weight escalated from 1,540 kg to 1,900 kg. To accommodate this weight increase and to safeguard the battery pack situated beneath, the suspension has been elevated beyond the height of standard springs.

Figure 4. Depiction of Motor, Battery, and Associated Electrical Components Installation.

Moreover, the newly designed drive shaft was conceived as a two-piece driveline, comprising two shafts and an intermediate support bearing. This intermediate support bearing can be affixed to the original chassis without modifications, while the secondary shaft aligns with the rear-axle final drive seamlessly. The detailed design and fabrication process of the drive shaft is depicted in Figure 5.

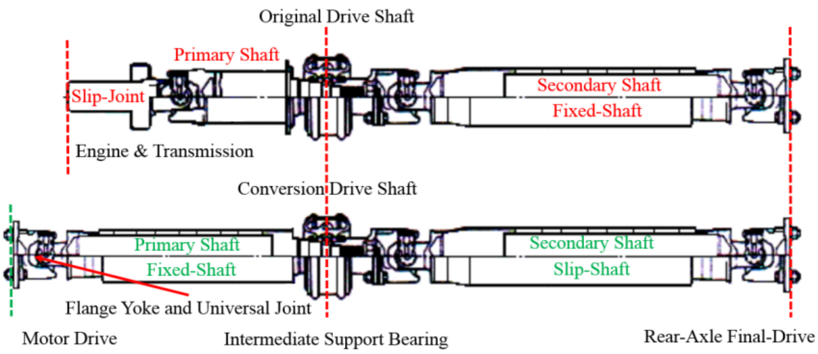

Figure 5. Schematic Representation of the Driven Shaft Design and Construction Process.

3. Results and discussion

3.1. Comparative Analysis of Vehicle Performance Pre- and Post-Modification

Traditionally, testing machinery for vehicles requires detailed information about the vehicle's systems, such as the engine type, compressed air type, and transmission system. This information is typically provided through the OBD port. However, when a vehicle is modified to have an electric drive system, it is not possible to provide this information in the same way. Additionally, the OBD port may not be available or accessible.

To circumnavigate these obstacles and glean accurate performance metrics, the investigator harnessed a hybrid method. By integrating the data sourced from a testing device and conducting inverse calculations, they could determine pivotal performance indicators like the rotational speed of the motor and its torque. The specific calculations or methods used are detailed in the following equation:

$$N_m = \frac{v*60}{\pi*D_w*i_t} \tag{8}$$

Where N_m is motor rotational speed (rpm), D_w is overall wheel diameter (m) and i_t is total transmission ratio (no unit)

Given that motor torque is T_m (Nm) and wheel power is P_w (kW) motor torque can be calculated by the following equation.

$$T_m = \frac{P_w * 60 * 1000}{2 * \pi * N_m} = \frac{P_w * 9549}{N_m} \tag{9}$$

In assessing vehicle performance, we juxtaposed the metrics prior to modification with those post-conversion to an electric drive system. This analysis utilized data sourced both from the chassis dynamometer and from reverse calculations. Differences in performance values were also examined. The comparative results are presented in Table 4.

Table 4. Comparative Analysis of Vehicle Performance Pre- and Post-Modification

Parameter	Before conversion (After used engine)	After conversion (New electric motor)	Variant
Maximum input power	110.2 kW /5,180 RPM	83.29 kW /2,460 RPM	Decrease 26.91 kW
Maximum wheel power	84.6 kW /5,180 RPM	83.29 kW /2,460 RPM	Decrease 1.31 kW
Maximum torque	226.0 Nm /3,950 RPM	348.17 Nm /2,188 RPM	Increase 122.17 Nm
Maximum speed	156.8 km/h /5,240 RPM	115.67 km/h /3,668 RPM	Decrease 41.13 km/h

3.2. Testing in Real-world Scenarios

For the preliminary real-world evaluation, a designated driving route was established between Chiang Mai and Lamphun. This selected route encompasses a round trip distance of approximately 250 km, beginning and concluding at the university.

To emulate authentic driving conditions, the car was tested on routes typically used by conventional vehicles. This specific route was chosen because it offers varied speed opportunities and provides a representation of generally moderate traffic density over the test distance. Additionally, sections of the route feature varied terrain with alternating ascents and descents. Some stretches also pass through areas with heavier traffic congestion. For the test, the vehicle's battery was fully charged to its maximum capacity of 54.6 kWh during non-peak hours, and the evaluation was conducted with two testers present.

During the road test designed to simulate real-world conditions, the vehicle's speed varied in response to prevailing traffic situations. This test route subjected the vehicle to natural accelerations, decelerations, and stops based on traffic signals. Unlike controlled tests, the vehicle's internal environment was also variable the air conditioning system's temperature and fan speed settings were not fixed but adjusted as required by the tester. From a full battery charge, the vehicle successfully traversed a total distance of 250 kilometers until the battery was unable to further power the motor. The test is visual documentation is available in Figure 6.

Figure 6. Route utilized for real-world testing and associated images from the evaluation.

Post-test, the vehicle's battery was recharged to full capacity, a process taking approximately 6 hours and consuming 34.828 kWh of electrical energy from the grid (Grid to Wheel: GTW). During the real-world evaluation, the vehicle exhibited an energy consumption rate of 139.31 Wh/km or 7.1 km/kWh. While the energy consumption rate per unit of energy for diesel engine 1-ton trucks in Thailand averages 13.40 km/liter, it is also equivalent to 755 Wh/km or 1.325 km/kWh [10].

3.3. The results of procuring equipment for modification and equipment installation operation

Drive motor: The chosen drive motor is of the AC Motor type, specifically a Permanent Magnet Synchronous Motor, with specifications of 65/110 kW, 327/700 Nm, and 367 Vdc. It is water-cooled. The motor mount has been designed to be compatible with the original three-point engine mount located at the front chassis.

Battery: The selected battery is a lithium-polymer cell, configured in a 56P102S-type connection. Its total specifications are DC 367.2 V and 148.8 Ah, with an air-cooled mechanism and a storage capacity of 54.6 kWh. The battery unit is designed for placement within the vehicle's chassis structure, situated on both sides. The positioning does not exceed the wheelbase's length, and it is secured with steel plates flanking both sides of the vehicle's structural frame.

New Drive Shaft: The newly designed drive shaft is segmented into two sections. It's crafted to ensure the bearing set's mounting point, or shaft doll, aligns with the original chassis region. Concurrently, its design allows for the mobility of the rear mid-axle. Adhering to the ASME code standards [11], the shaft exhibits a diameter of 60 mm.

Equipment Installation Design for Driving and Electrical System Control: The placement of driving-associated apparatuses and electrical system controls has been meticulously planned. These components are mounted on a specialized platform, crafted from dual-layered box steel, which provides foundational support for secure installation. This platform is furnished with designated mounting points, allowing for optimal positioning within the front chassis, directly above the motor's mounting site. The strategic locale of each device is influenced by its functional synergy with related equipment. Additionally, design considerations factored in the vehicle's original equipment layout, such as the juxtaposition of the electric power steering pump with the steering rack, the electric compressor's alignment with the condensing unit and evaporator, and the coordination of the electric vacuum pump with the brake master cylinder and booster body, among other arrangements.

Battery Charger: Selection and Positioning: The chosen charger is an on-board, DC-DC variant with a high voltage capacity of 6,600 W and a low voltage of 98 W, complemented by an AC Type 2 Charger. The charging interface has been strategically positioned at the vehicle's original refuelling point, situated on the left side.

Upon completing the procurement and installation of modification equipment for the 1-ton truck, it was observed that the electric-powered variant is approximately 360 kilograms heavier than the manufacturer's original unloaded weight. To accommodate this weight increase and to safeguard the battery pack situated beneath, the suspension has been elevated beyond the height of standard springs. Concerning battery charging, utilizing a standard charging method necessitates approximately six hours to elevate the battery from its minimum level to full capacity.

3.4 Documentation Necessary for Registration and Regulatory Compliance

To register an electrically modified vehicle at the Provincial Transport Office in Thailand, two main steps must be followed:

1. Document Preparation Process

The Department of Land Transport provides a guideline handbook for assessing vehicle conditions when replacing traditional engines with electric motors [12]. The required documentation illustrate in Figure 7.

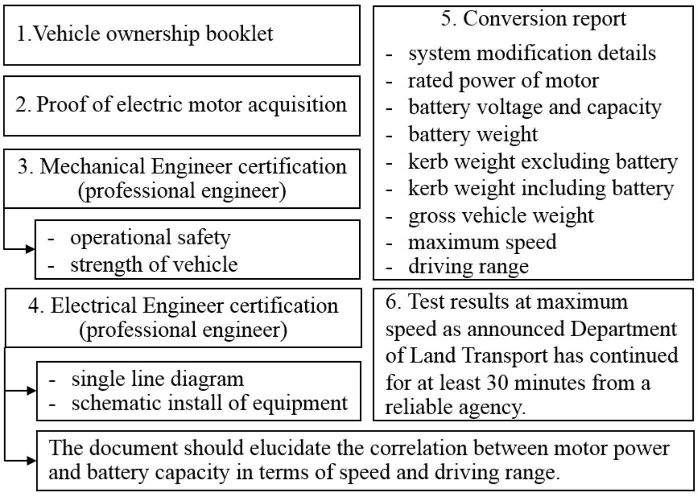

Figure 7. The required documentation for registration.

In alignment with the motor power for 1-ton truck category, it must conform to the specifications set out by the Department of Land Transport as per the Automobile Act B.E. 2020 [13]. The electric motor should possess a power of no less than 15 kilowatts and be capable of propelling the vehicle at a maximum speed of no less than 90 kilometers per hour. An “e” mark should be affixed to the rear of the vehicle.

2. Procedures for Document Submission and Vehicle Inspection at the Transport Office

2.1 Submit the requisite documents for review at the designated document inspection point.

2.2 Present the modified vehicle for a thorough inspection at the Vehicle Inspection Department.

2.3 Upon successful inspection, collect the required documents to proceed with change notification.

2.4 Settle any associated fees required for change notification.

2.5 Await the issuance of the updated registration manual that reflects the documented changes.

4. Conclusion

In the quest to convert 1-ton trucks with internal combustion engines into electric vehicles, it is paramount that one first meticulously reviews pertinent legislation. Subsequently, a thorough evaluation of the motor's efficiency is essential to ensure that its performance does not deviate negatively from the original specifications. Another crucial factor to consider is the intended driving range, as this is directly contingent upon battery capacity. This emphasis on battery capacity is underscored by the fact that the battery, being the most expensive component, represents over half of the total modification cost.

During the equipment modification and installation phase, it was discerned that modern car models predominantly employ the CAN bus system for inter-device communication. This system enables efficient data exchange between various devices and control units. One significant implication of this observation is that certain original equipment in the vehicle can be harmoniously integrated with electric drive systems, including the Accelerator Pedal, Brake Pedal, Power Switch, Shift Collar, among others. Moreover, several pre-existing systems, specifically those already configured as electrical systems like electric steering, air conditioning, and electric cooling systems, can be assimilated without any significant alterations. This compatibility has the potential to considerably mitigate both the complexity and costs of the modification process.

After comprehensive testing, both via a chassis dynamometer and real-world on-road evaluations, the modified electric drive system was found to be compliant with the Department of Land Transport's stipulations. The electric motor, with its rated power of 83.29 kW (111.69 hp) and torque of 348.17 N-m, allows the vehicle to achieve speeds of up to 115.67 kilometers per hour. Moreover, the vehicle can sustain a speed of 90 kilometers per hour for durations exceeding 30 minutes, aligning with the legal benchmarks set for electrically modified vehicles. Furthermore, during empirical assessments, the vehicle displayed an energy consumption metric of 139.31 Wh/km.

It is of paramount importance for future endeavors to utilize precise energy consumption models. Instituting standard criteria for the pricing and modification of electric vehicle equipment is recommended. The integration of such standards into inspection and testing protocols, especially regarding the structural soundness and safety of modified vehicles, can be transformative. Securing endorsements from government agencies for these standards will undoubtedly enhance the confidence of electric vehicle modification enthusiasts and simplify the overall authorization process, thus catalysing increased interest in these modifications.

5. Acknowledgments

This work dedicated to people who want to convert their vehicle from fuel to electric vehicle. The authors would like to thankful for Energy Research and Development Institute-Nakornping, Chiang Mai University and department of mechanical engineering, faculty of engineering, Chiang Mai University and to all which cannot named here.

6. References

[1] Department of Land Transport, Transportation Statistics Report 2022
[2] EPPO, Guidelines for promoting electric vehicles [Online], available:https://www.eppo.go.th/index.php/en/component/k2/item/17415-ev-charging-221064-04 [31/8/2023]
[3] Office of the National Economic and Social Development Council, The Thirteenth National Economic and Social Development Plan (2023-2027), [Online], available: https://www.nesdc.go.th/article_attach/article_file_20230615134223.pdf [25/10/2023]
[4] NSTDA, Assessment of Electric Vehicle Technology Development and Its Implication in Thailand [Online], available:http://waa.inter.nstda.or.th/stks/pub/2015/20151222-electric-vehicle.pdf [31/8/2023]
[5] Rueanthip K,[Online], available:https://www.the101.world/used-car-prices/ [31/8/2023]
[6] Gillespie T, Fundamentals of Vehicle Dynamics, Society of Automotive Engineers, 1992, Pages 79-124.
[7] Bonnick A, Vehicle dynamics: Tractive resistance. Automotive Science and Mathematics. Butterworth-Heinemann. 2008. p. 123-126
[8] Xinkai W, David F, Alfredo C, William A. Kitch, 2015, Electric vehicles' energy consumption measurement and estimation, Transportation Research Part D 34 (2015) 52–67
[9] Duangsrikaew B, Mongkoltanatas J, Benyajati C, Karin P, and Hanamura K. 2019, Battery Sizing for Electric Vehicles Based on Real Driving Patterns in Thailand, World Electric Vehicle Journal, Vol.10, No. 43
[10] Pongswang M.,[Online], available: https://www.headlightmag.com/2023-08-23-preview-acce-fuel-isuzu-dmax-19-x-speed-6mt/ [20/10/2023]
[11] Richard G. Budynas and J. Keith Nisbett Shigley's Mechanical Engineering Design, McGraw-Hill, 9th edition, 2011
[12] Department of Land Transport, Guideline handbook for assessing vehicle conditions when replacing traditional engines with electric motors,[Online], available:https://www.dlt-inspection.info/dlt/cl/pdf uploads/2022_06_16_10_54_06.pdf [31/8/2023]
[13] Department of Land Transport, The determination of the power of an electric motor as per the Motor Vehicle Act B.E. 2020 ,[Online], available:https://www.dlt-inspection.info/dlt/cl/pdf uploads/2022_03_17_08_52_57.pdf [31/8/2023]

AEC0018

Impact of Biodiesel Fuel on a Light-Duty Diesel Vehicle Particle Emissions and Thermal Efficiency

Sone Khar Jar Ring Aung[1], Watanyoo Phairote[1,*], Preechar Karin[1], Mek Srilomsak[1], Sompong Srimanosaowapak[2], Hidenori Kosaka[3], and Chinda Charoenphonphanich[1]

[1]School of Engineering, King Mongkut's Institute of Technology Ladkrabang, Bangkok 10520, Thailand
[2]National Energy Technology Centre, National Science and Technology Development Agency, Pathum Thani 12120, Thailand
[3]School of Engineering, Tokyo Institute of Technology, Tokyo 152- 8552, Japan

* Corresponding Author: watanyoo.ph@kmitl.ac.th

Abstract.

The usage of diesel vehicles is high in daily life around worldwide, which can result in the release of particle emissions into the environment. As part of this research, particle emissions and thermal efficiency were carried out on a 2.5-liter 4-cylinder common rail direct injection light-duty diesel vehicle using B7 fuel (7% vol biodiesel and 93% vol diesel) and B100 fuel (100 % vol biodiesel). The vehicle was operated at three constant engine speeds of 1500 rpm, 2000 rpm, and 2500 rpm along with four different constant engine torques of 84 Nm, 112 Nm, 140 Nm, and 160 Nm. The exhaust emissions and thermal efficiency of the vehicle were examined by comparing different volume percentages of biodiesel in the fuel. The result showed a significant 12% increase in fuel consumption when using B100 fuel compared to B7 fuel. Furthermore, the investigation demonstrated the reduction of smoke intensity and exhaust temperature by 62% and 4% respectively by utilizing B100 fuel.

Keywords: Diesel Engine, Particle Emissions, Thermal Efficiency, B7, B100.

1. Introduction

The daily usage of diesel vehicles in various sectors, including transportation, agriculture, and heavy industry applications, is the main source of air pollution. While diesel engines can deliver high power output, there is one downside that cannot be ignored. Emitting high levels of particle and NOx emissions is the disadvantage of diesel vehicles and 72% of PM 2.5 emission is from them [6]. Using biodiesels is one of the solutions to reduce particle emissions by their elemental compositions. Iman K. et al., [2] investigated that the utilization of biodiesel can reduce particulate matter up to 83% compared to conventional diesel fuel. Diesel fuel is mainly composed of hydrocarbons with carbon and hydrogen atoms while biodiesel fuel is primarily composed of carbon, hydrogen, and oxygen. Biodiesel is also called as Fatty Acid Methyl Ester (FAME) and produced from crude palm oil (CPO) by the esterification process in Thailand [4].

Nanjundaswamy Harsha et al., [8] demonstrated different fuel properties effect on diesel's engine emissions and performance by using four petroleum based and one biodiesel with cetane number ranging from 26 to 72. The fuel with high cetane number can deliver higher thermal efficiency under most conditions due to their inherent low ignition delay. Biodiesel fuel can provide greater thermal efficiency and less smoke due to its low rich combustion zones, but it has higher brake specific fuel consumption than other fuels because of its lower calorific value. Applying biodiesel in vehicles leads to more benefits than the burning of fossil fuel because it is produced from renewable sources of energy such as vegetable oils, animal fats, or waste cooking oil [1,4].

The study of Luis et al., [1] used biofuel that was obtained through the esterification of used cooked oils (UCO). The result also showed the fuel with a higher cetane number that is being oxygenated enhances the combustion quality, reduces CO_2 (carbon dioxide) emission. However, it consumed more fuel to produce the same energy available in combustion because of having lower calorific value. The work of Iman K. et al., [2] demonstrated the study of high-ratio biodiesel and pure biodiesel FAME. This study expressed NOx emissions for the urban cycle increased in the same way of the ratio of biodiesel increased but this was within the restriction that is imposed by the Euro4 emissions standard. This is a clue suggesting that usage of biodiesel promotes more complete combustion. Conversely, biodiesel emitted lower CO (carbon monoxide), HC (hydrocarbon) and particle emissions.

The purpose of the present research is to investigate the impact of biodiesel fuel on a light-duty diesel vehicle particle emissions and thermal efficiency. In previous studies, vehicle thermal efficiency was mentioned and explained less frequently in relation to particle emissions. The current study is designed to examine vehicle thermal efficiency in connection with particle emissions. In thermal efficiency, fuel consumption, energy input, brake specific fuel consumption, brake specific energy consumption and brake thermal efficiency were studied. For particle emissions, CO_2, NO, and smoke intensity were examined. The research was carried out on a 2.5-liter 4-cylinder common rail direct injection light-duty diesel vehicle using B7 and B100 fuels. The engine was driven at three constant engine speeds of 1500 rpm, 2000 rpm, and 2500 rpm with four different constant engine torques of 84 Nm, 112 Nm, 140 Nm, and 160 Nm. The study found that biodiesel can reduce particle emissions while providing higher brake thermal efficiency compared to commercial diesel.

2. Research and Methodology

2.1. Vehicle Specifications and Fuel Properties

A light-duty diesel vehicle, four-cylinder, direct injection four-stroke common rail was applied for this study, and the specification of engine is listed in Table 1. The engine of used vehicle can operate the maximum power of 75 kW at 3600 rpm and the maximum torque of 260 Nm at 1600-2400 rpm. The vehicle that was used in the experiment can meet up to the Euro4 emission standard.

Table 1. Vehicle Specifications.

Items	Specifications
Model	D4D
Engine Type	2KD-FTV, 4 Cylinder In-line
Fuel System	Direct Injection 4-Stroke Common Rail
Displacement Volume	2494 cc
Bore x Stroke	92 x 93.8 mm
Compression Ratio	18.5:1
Vehicle Mass	1590 kg
Maximum Power	75 kW @ 3600 rpm
Maximum Torque	260 Nm @ 1600-2400 rpm

In this study, two different fuels were used. The fuels are B7 (7% vol biodiesel and 93 % vol diesel) and B100 (100 % vol biodiesel). B7 is commercial diesel fuel that can be found at most of the fuel station in Thailand and B100 is pure biodiesel. Biodiesel is obtained from crude palm oil by using refined bleached and deodorized palm oil (RBDPO) [4]. The test method and properties of fuel including density, viscosity, calorific value, heat of vaporization, carbon content, hydrogen content, oxygen content, auto ignition temperature, stoichiometric air fuel ratio, and distillation are listed in Table 2. The carbon content of B7 is higher, and the oxygen content is lower than that of B100. The former studies showed the exhaust emissions of B100 is lower than B7 due to higher oxygen content supports more complete combustion. The calorific value of B100 is 14% lower than B7. In the case of calorific value, a fuel with a lower number can result in higher fuel consumption to produce the same output power as a fuel with a higher calorific value. According to the chemical formula, B7 lacks oxygen molecules while B100 contains them. Therefore, these two fuels were chosen to investigate the vehicle's emissions and thermal efficiency.

Table 2. Fuel Properties.

Fuel Properties	Test Method	B7	B100
Chemical Formula	-	$C_{12}H_{28}$	$C_{14.9}H_{29.9}O_{1.9}$
Carbon (% mass)	ASTM D 5291	85.1	74.5
Hydrogen (% mass)	ASTM D 5291	14.0	12.5
Oxygen (% mass)	ASTM D 5291	0.9	13.0
Auto ignition temperature (°C)		288	294
Calorific Value (kJ/kg)	ASTM D 240	46,180	39,525
Heat of vaporization (kJ/kg)		250	300
Viscosity at 40°C (mm^2/s)	ASTM D 445	3.0	4.5
Density at 25°C (kg/m^3)	ASTM D 1298	844.8	875.3
Stoichiometric air fuel ratio	-	14.7	12.3
Distillation (°C)	ASTM D 86- 11b		
T10		214.3	336.2
T30		250.3	339.7
T50		281.5	341.4
T70		312.5	345.4
T90		352.3	351.2

2.2. Experimental Set Up and Test Conditions

The experiment was conducted on a chassis dynamometer (450DS 2WD single retarder dyno) that can run in the act of on-road driving conditions. The chassis dynamometer is a 2WD single retarder ready dyno that can simulate a driving environment by controlling the load of vehicle. The chassis dyno controller allowed for precise of the testing conditions that covered all driving situations. A 2.5-liter 4-cylinder common rail direct injection light-duty diesel vehicle was used in the investigation and operated under three constant engine speeds of 1500 rpm, 2000 rpm, and 2500 rpm with four different constant engine loads of 84 Nm, 112 Nm, 140 Nm, and 160 Nm. The data is collected once the vehicle has stabilized at a constant speed and load. The research targeted biodiesel on emissions reduction and vehicle performance on fuel consumption and thermal efficiency. The schematic diagram of the experimental set up is shown in Figure 1. The pump transferred fuel from the separate tank to the common rail for weighing fuel consumption. The fuel consumption was measured with a weight scale and the measuring accuracy is ± 0.15g. The emissions of the vehicle were measured by the AVL exhaust gas analyzer (DITEST Gas 1000) at the end of the exhaust gas tail pipe. The acuteness of the gas analyzer is ±0.002% vol for O_2, ± 0.3% vol for CO_2, and ± 5 ppm for NO respectively. Carman Scan On-Board Diagnosis I (OBD II) was used to display engine conditions in all test situations. The concentration of particulate matter or smoke was measured by using smoke intensity meter. BOSCH smoke intensity meter used the light reflection technique to obtain the smoke density that was captured on a paper filter and the measuring accuracy is ± 3%.

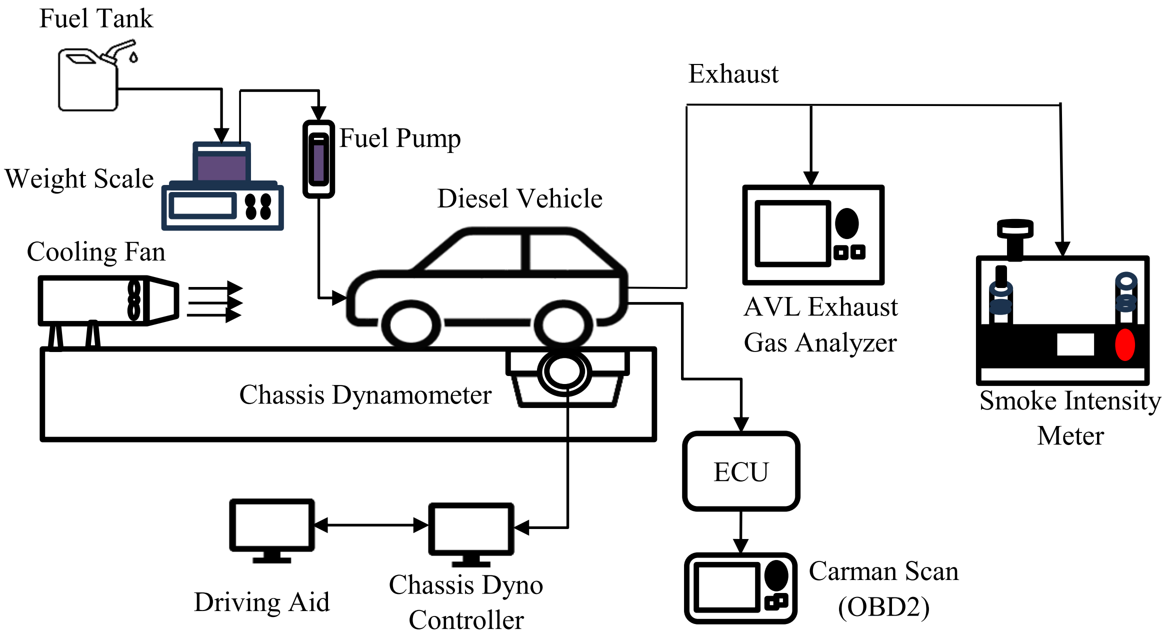

Figure 1. Schematic Diagram of Experimental Setup.

3. Calculation Method

3.1. Vehicle Brake Thermal Efficiency

The engine performance is expressed as energy input (Q^{o}_{in}), brake specific fuel consumption (BSFC), brake specific energy consumption (BSEC), and brake thermal efficiency (BTE). These parameters are calculated by the below equations. The input energy is the fuel consumption rate to the calorific value of the fuel. It is expressed in kW. BSFC is the rate of fuel consumption rate to the power output by an engine. It is measured in kg/kWh. BSEC is the rate of energy consumption to the power output by an engine. It is measured in kJ/kWh. BTE is the amount of power output by an engine to the heat energy given to a system. It is described in percentage.

$$\mathring{Q}_{in} = \mathring{m}_f \, . \, Q_{LHV} \tag{1}$$

$$\text{Brake Specific Fuel Consumption (BSFC)} = \frac{\text{Fuel Consumption Rate}}{\text{Brake Power}} = \frac{\mathring{m}_f}{4\pi\tau . \frac{N}{60} \frac{1}{2}} \tag{2}$$

$$\text{Brake Specific Energy Consumption (BSEC)} = \text{BSFC} \, . \, Q_{LHV} \tag{3}$$

$$\text{Brake Thermal Efficiency (BTE)} = \frac{\text{Brake Power}}{\text{Energy Input}} = \frac{4\pi\tau \, . \, \frac{N}{60} \, . \, \frac{1}{2}}{\mathring{Q}_{in}} \tag{4}$$

Where;

τ = engine load (Nm)
N = engine speed (rev/min)
$\mathring{m}_f$ = mass of fuel consumption rate (g/s)
Q_{LHV} = lower heating value (kJ/g)
Q^{o}_{in} = energy input (kW)

4. Results and Discussions

4.1. Vehicle Performance

The engine performance features are expressed as brake specific fuel consumption (BSFC, kg/kWh), brake specific energy consumption (BSEC, kJ/kWh), and brake thermal efficiency (BTE, %). fuel consumption as m^o_f was measured by a weight scale. BSFC, BSEC and BTE were calculated from fuel consumption, engine speed, torque, energy input to the system, and brake power output. The comparisons of fuel consumption, energy input, BSFC, BSEC and BTE are shown in Figure 2. The fuel consumption rate of B100 is higher than B7 in all conditions as shown in Figure 2(a) and it is the same trend as the former studies. B100 consumes more fuel to deliver the same amount of energy from combustion because of its lower calorific value. Q^o_{in} of B7 is higher at low-speed (1500 and 2000 rpm) and lower at high-speed (2500 rpm) than B100. B100 can give nearly the same energy input as B7 under tested conditions because of its higher oxygen content that can boost more complete combustion although lower calorific value as shown in Figure 2(b). Figure 2(c) describes B100 resulting more brake specific fuel consumption while taking consideration of the same quantity of brake power and the calculation method is described in Equation (2). In Figure 2(d), at low-speed of 1500 rpm, brake specific energy consumption (BSEC) of B100 is lower than B7 because it had more time for chemical reaction of fuel and air to deliver energy. At high-speed of 2500 rpm, BSEC of B100 is higher because of its larger molecular structure, higher cetane number and higher viscosity and the calculation method is shown in Equation (3).

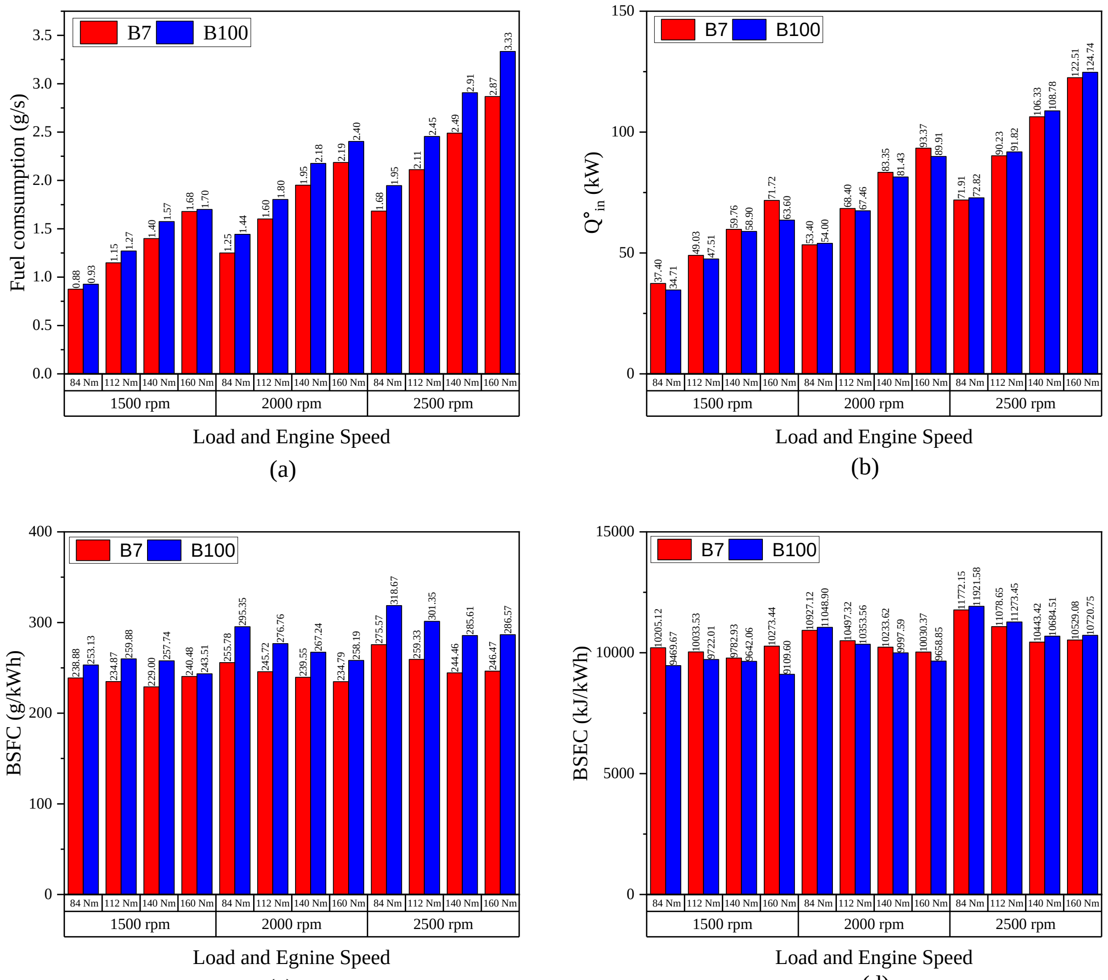

(a) (b) (c) (d)

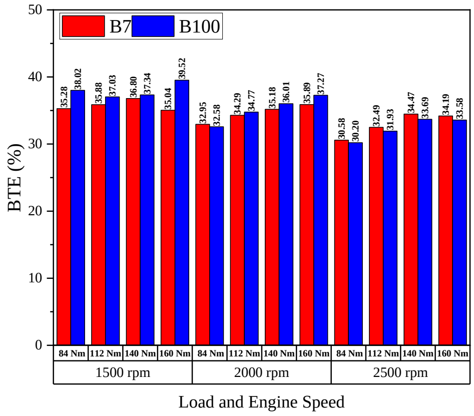

(e)

Figure 2. Comparison of (a) Fuel Consumption, (b) Q^o_{in}, (c) BSFC, (d) BSEC, and (e) BTE.

The brake thermal efficiency (BTE) comparison is expressed in Figure 2(e) and calculation method can be explored in Equation (4). The overall BTE of B100 is higher than B7 under examined conditions. This can make an impact in more complete combustion promoting by higher oxygenate content in the fuel.

4.2. Exhaust Emissions

The exhaust emissions were measured by smoke intensity meter and AVL gas analyzer, and the comparisons are expressed in Figure 3 involving smoke intensity (%), NO (ppm), CO_2 (% Vol) and O_2 (% Vol) records. The smoke intensity meter was used to measure the density of smoke that came out from the exhaust tailpipe. The smoke intensity of B100 is lower than B7 at all test conditions attributes to more oxygen content in B100 which enhances complete combustion [5]. As the outcome result, the smoke intensity can be reduced by more than 60% than B7 as shown in Figure 3(a). The investigation of CO_2 evaluated by gas analyzer is expressed in Figure 3(b). CO_2 emissions of both B7 and B100 increased in the same way as increasing engine loads in all engine speed conditions because of increasing fuel injection to overcome the raising engine loads. The release O_2 gas of B100 is slightly higher than B7 owing to the higher oxygenated content in the B100 as shown in Figure 3(c).

The comparison of exhaust temperature is expressed in Figure 3(d). The exhaust temperature of B7 is higher than B100 in almost all conditions resulting higher NOx emission, and therefore usage of B100 can contribute to global warming reduction. The presence of NOx in the atmosphere can lead to respiratory problems, acid rain, and detriments to photosynthesis. Therefore, the emissions of NOx are significantly affected to both human health levels and environment [1]. The observation of nitrogen oxide was measured by gas analyzer and is displayed in Figure 3(e). According to the result, the emission of nitrogen oxide from B100 is lower than from B7.

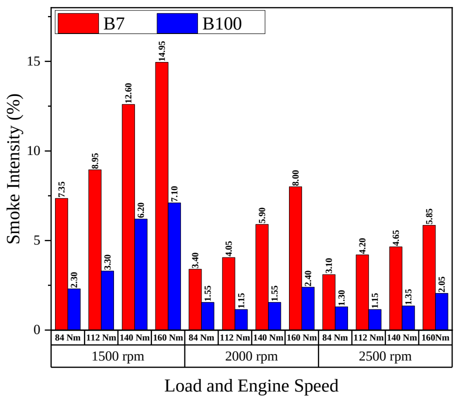

(a)

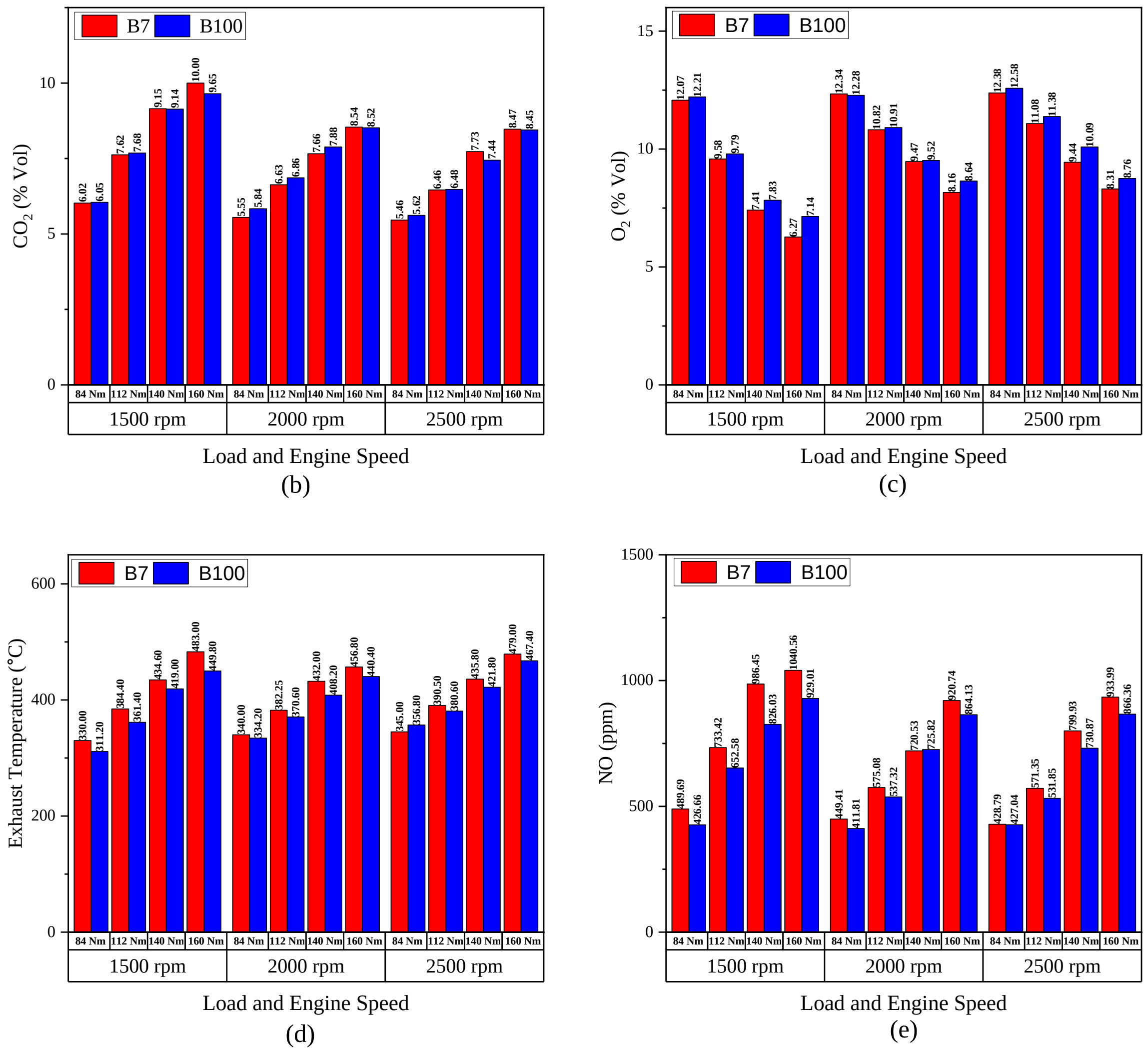

Figure 3. Comparison of Exhaust Emissions (a) Smoke Intensity, (b) Carbon Dioxide, (c) Oxygen, (d) Exhaust Temperature, and (e) Nitrogen Oxide.

5. Conclusion

The present research investigated the impact of biodiesel fuel on a 2.5-liter 4-cylinder common rail direct injection light-duty diesel vehicle particle emissions and thermal efficiency on a chassis dynamometer that can simulate the real-road condition. The vehicle was operated at three constant engine speeds of 1500 rpm, 2000 rpm, and 2500 rpm with four different constant engine loads of 84 Nm, 112 Nm, 140 Nm, and 160 Nm. The two fuels of B7 (7% vol biodiesel and 93% vol diesel) and B100 fuel (100 % vol biodiesel) were applied to investigate the results. The fuel consumption and brake specific fuel consumption of B100 is higher than those of B7. On the other hand, B100 can reduce smoke intensity up to 60%. The results of brake specific energy consumption and brake thermal efficiency of B100 are superior at low-speed of 1500 rpm compared to B7, while those of B7 are greater at high-speed of 2500 rpm, even though fuel consumption of B7 is lower than B100. The harmful gas, NO emission of B100 is lower than B7. The variations of CO_2 emission and O_2 of both fuels are in the same trend. The above outcomes demonstrate that B100 can be one of the alternative ways to reduce particle emissions from the transportation sector to the environment.

6. Acknowledgements

The authors would like to thank National Research Council of Thailand (NRCT), National Science and Technology Development Agency (NSTDA), King Mongkut's Institute of Technology Ladkrabang (KMITL) for their support.

7. References

[1] Luis Serrano, Barbara Santana, Nuno Pires, Cristina Correia, "Performance, Emissions, and Efficiency of Biodiesel versus Hydrotreated Vegetable Oils (HVO), Considering Different Driving Cycles Sensitivity Analysis (NEDC and WLTP)", Fuels 2021, 2, 448–470. https://doi.org/10.3390/fuels2040026

[2] Iman K. Reksowardojo, Hari Setiapraja, Mokhtar, Siti Yubaidah, Dieni Mansur, Agnes K. Putri, "A Study on Utilization of High-Ratio Biodiesel and Pure Biodiesel in Advanced Vehicle Technologies", Energies 2023, 16, 718. https:// doi.org/10.3390/en16020718

[3] Nanjundaswamy, H., Tatur, M., Tomazic, D., Koerfer, T. et al., "Fuel Property Effects on Emissions and Performance of a Light-Duty Diesel Engine," SAE Technical Paper 2009-01-0488, 2009, https://doi.org/10.4271/2009-01-0488

[4] Phobkrit Kanokkhanarat, Preechar Karin, Nattawoot Depaiwa, Veerayut Wongpattharaworakul, Chadchai Srisurangkul, Masaki Yamakita, "Influence of ethanol biodiesel blends on a diesel engine's efficiency and exhaust emission characteristics", https://doi.org/10.1016/j.matpr.2022.06.532 2214-7853

[5] Phobkrit Kanokkhanarat, Nattawoot Depaiwa, Preechar Karin, Veerayut Wongpattharaworakul, Chadchai Srisurangkul, Masaki Yamakita, "Investigation of the Impact Bioethanol Blends into Biodiesel on Combustion Characteristics, Engine Performance, and Emissions of Diesel Engine", ICERE-2022, doi:10.1088/1755-1315/1121/1/012014

[6] 6 Sources of PM2.5 Emissions by vehicle modes (Source: U.S. EPA) | Download Scientific Diagram (researchgate.net)

[7] Preechar Karin, Aphichai Tripatara, Phyo Wai, Ban-Seok Oh, Chinda Charoenphonphanich, Nuwong Chollacoop, Hidenori Kosaka, "Influence of ethanol-biodiesel blends on diesel engines combustion behavior and particulate matter physicochemical characteristics", https://doi.org/10.1016/j.cscee.2022.100249

[8] Nanjundaswamy, H., Tatur, M., Tomazic, D., Koerfer, T. et al., "Fuel Property Effects on Emissions and Performance of a Light-Duty Diesel Engine," SAE Technical Paper 2009-01-0488, 2009, https://doi.org/10.4271/2009-01-0488

AEC0019

Impact of Partial-Flow Particulate Filter on Emissions from a Light-Duty Diesel Vehicle

Huy Quang Dang[1,2], Preechar Karin[1,*], Plan Teekatasn Cosh[1], Poonnut Thaeviriyakul[1], Pongsak Kummul[1], Sompong Srimanosaowapak[3], Hidenori Kosaka[4], and Mek Srilomsak[1]

[1]School of Engineering, King Mongkut's Institute of Technology Ladkrabang, Bangkok 10520, Thailand
[2]College of Engineering, Can Tho University, Can Tho, Vietnam
[3]National Metal and Materials Technology Center, National Science and Technology Development Agency, Pathum Thani 12120, Thailand
[4]School of Engineering, Tokyo Institute of Technology, Tokyo 152-8552, Japan

* Corresponding Author: preechar.ka@kmitl.ac.th

Abstract. This study examines particle and gaseous emissions from a light-duty diesel vehicle equipped with a partial-flow catalyzed diesel particulate filter (P-CDPF). The vehicle underwent testing on a chassis dynamometer following the new European driving cycle. The results show a significant reduction in total hydrocarbon (THC) and carbon monoxide (CO) when employing P-CDPF. Specifically, catalytic coating successfully converted 48% of THC and 66% of CO into carbon dioxide (CO_2). This resulted in a 6% increment in CO_2 emissions after the driving cycles. Nitrogen oxides (NOx) increased after P-CDPF because of elevated in-cylinder temperature due to backpressure. Additionally, the integration of P-CDPF resulted in a 45% reduction in particulate number (PN) and a 60% reduction in particulate mass (PM). The findings of this study propose a feasible solution for controlling harmful substances, thereby contributing significantly to practical initiatives aimed at reducing harmful emissions emitted by untreated diesel vehicles.

Keywords: Diesel Emission, Particulate Matter, Partial Flow Diesel Particulate Filter, New European Driving Cycle.

1. Introduction

Diesel engine has been widely used in various fields of road transportation, agriculture, and industry due to its high efficiency [1]. However, it releases highly toxic gases that directly affect human health and the environment [2-4]. The ideal products of diesel combustion are CO_2 and water. However, by-products, including unburnt HC, CO, NOx, and particulate matters, are practically produced due to incomplete combustion. Although polluted emissions constitute only 1% of the total composition of diesel exhaust [5], the large number of diesel vehicles on the roads worldwide has turned it into a critical issue. Numerous solutions have been applied to reduce harmful substances focusing on pre-combustion, combustion, post-combustion. In pre-combustion stage, biodiesels made from palm, soybean, and sunflower are commonly used as practical solutions for advanced combustion due to their high oxygen content and high cetane number [6]. Exhaust gas recirculation system for NOx control and common rail direct injection system for combustion efficiency are essential methods in the combustion stage. Although these technologies have enhanced combustion and reduced soot fractions, the increasingly stringent regulations on emissions necessitate the use of after-treatment devices to eliminate the aforementioned emissions. Diesel oxidation catalyst (DOC) is utilized to reduce gaseous emissions such as HC and CO by converting them into CO_2 and water [7]. Meanwhile, diesel particulate filter (DPF) is efficiently employed to trap and oxidize PM through regeneration process. DPFs can be categorized as wall-flow or full-flow DPF (F-DPF) and partial-flow DPF (P-DPF). Due to its wall-flow mechanism, F-DPF exhibits higher filtration efficiency compared to P-DPF, generally above 90%. However, the increasing soot accumulated within F-DPF must be oxidized to prevent a backpressure in the combustion chamber. Elevated backpressure is the primary cause of reduced engine performance, leading to increased fuel consumption and reduced thermal efficiency [8,9]. Thus, an external heat source such as fuel injection is applied to raise temperature within the filter for soot oxidation, known as active regeneration process. On the other hand, P-DPF is a flow-through filter that partially traps and oxidizes soot through passive regeneration process. Due to its working principle, P-DPF is a non-blocking particulate filter, causing lower backpressure compared to F-DPF. Its filtration efficiency ranges from 50% to 70%, without the need for additional thermal treatment system for the filter regeneration. As the number of untreated diesel vehicles continues to escalate in developing countries, stringent emission regulations are set to be applied in the near future. Consequently, installing P-DPF can be an effective solution for retrofitting and reducing gaseous and particle emissions.

Several studies have investigated the application of P-DPF to eliminate unwanted substances emitted from diesel engine. Lefort et al. examined the potential of using uncoated P-DPF to support F-DPF in reducing the necessity for active regeneration events that lead to increased fuel consumption [10]. The results showed that over 25% of PM was reduced across various engine conditions. Moreover, introducing P-DPF led to a gradual and consistent pressure increase over the loading period. This reduced the frequency of active regeneration process within F-DPF, thus reducing fuel consumption. In a comprehensive overview, Görsmann et al. detailed the application of catalytic coatings in diesel particulate filter systems, aimed at facilitating filter regeneration through soot oxidation using nitrogen dioxide (NO_2) and oxygen (O_2) [11]. The temperature required for soot oxidation with O_2 was reported to be between 400^0C-550°C, whereas when using NO_2, this temperature lowered to 250°C. Jacobs et al. employed DOC and P-DPF system to mitigate particulate matters and gaseous emissions from heavy-duty diesel vehicles [12]. The outcomes revealed a substantial 74% reduction in particulate matters for the new system and 63% for the aged system. Moreover, the drop exceeded 90% for carbon monoxide (CO) and hydrocarbon (HC) emissions. Notably, consistent backpressure across various model-year vehicles with differing exhaust temperature profiles demonstrated the system's robust durability. Mon Phyo et al. [13] implemented a combined system consisting of DOC and uncoated P-DPF on diesel engines under various conditions. The integration resulted in a slight increase in fuel consumption and decreased thermal efficiency under some conditions. However, the installation did not significantly affect the overall results due to the low backpressure. The passive regeneration process of metallic P-DPF was observed by Oh Bs. et al. [14] through the investigation of particle nanostructure and exhaust gas measurement before and after P-DPF. By comparing these analysis results, the authors suggested that PM is trapped and oxidized passively with NO_2 and O_2.

To further investigate the effects of P-DPF on diesel vehicle emissions during actual driving conditions. This study employs a P-CDPF installed in a light-duty diesel vehicle following the new European driving cycle (NEDC) using fuel B10. The study thoroughly examines regulated emissions, including HC, CO, NOx, and CO_2. Particle emission characteristics, comprising particulate number (PN) and particulate mass (PM), are also discussed. The highlight of this study is underscored by the prevailing challenge posed by untreated aging diesel vehicles, which continue to operate beyond expected lifespans in developing countries. The findings offer a potential solution for emission control strategies, contributing to practical efforts aimed at reducing undesirable substances from diesel vehicles.

2. Material and Method

2.1. Vehicle specifications and fuel properties

This study was carried out in a commercial diesel-powered light-duty vehicle, the properties of which are described in Table 1. This vehicle is employed with a 2.5-liter common rail diesel engine. Its maximum engine output power is 75 kW obtained at 3600 rpm, and the maximum engine torque is 260 Nm from the range 1600 rpm to 2400 rpm.

Table 1. Vehicle specifications.

Parameters	Details
Vehicle type	Light-duty vehicle
Vehicle mass	1590 kg
Engine model	2KD-FTV, 4 cylinder In-line
Fuel system	Common rail direct injection
Air intake system	Turbocharged
Displacement volume	2.5L
Bore x Stroke	92.0 mm x 93.8 mm
Compression ratio	18.5:1
Maximum power	75 kW @ 3600 rpm
Maximum torque	260 Nm @ 1600 - 2400 rpm

Biodiesel blends provide the advanced benefit of an oxygenated fuel, enhancing combustion efficiency and reducing emission release. This study employed commercial B10 fuel, comprising 10% biodiesel and 90% diesel fuel. The fuel properties and their standards are detailed in Table 2. The elevated oxygen content and cetane number found in fuel B10 create favorable conditions for advanced combustion, consequently reducing harmful emissions [15].

Table 2. Fuel properties.

Properties	Standard	Values
Carbon (wt %)	ASTM D5291	84.66
Hydrogen (wt %)	ASTM D5291	13.56
Oxygen (wt %)	ASTM D5291	1.78
Cetane index	ASTM D976	54.9
Calorific value (MJ/kg)	ASTM D240	45.63
Density @ 15^0C (kg/m^3)	ASTM D4052	835
Viscosity @ 40^0C (mm^2/s)	ASTM D445	3.0

2.2. After-treatment system

The after-treatment system used in this study is a commercial metallic P-CDPF coated with platinum, the parameters are detailed in Table 3. As shown in Figure 1, P-CDPF structure consists of metal guide foil and metal filter media stacked inside it. The metal foil acts as a shovel, guiding a portion of the exhaust from the inlet and redirecting it toward the fibrous filter media to trap particulate matters. The rest of the exhaust flows to the other outlet end of the filter without being filtered. Due to the flow-through characteristics, exceeded soot beyond filter capacity is not collected in the filter. As a result, the exhaust gas can continue to flow without significantly increasing backpressure. Apart from the primary function of capturing PM, P-CDPF can also considerably reduce a fraction of the harmful substances from the exhaust, such as CO and HC from the exhaust gas by converting them into CO_2 and water.

Another crucial effect of P-CDPF is its contribution to the production of NO_2 from NOx, aiding in the soot oxidation process [11].

Table 3. Parameters of metallic P-CDPF.

Parameters	Details
Type of catalyst	Platinum
Cell density (CPSI)	200
Length (mm)	200
Diameter (mm)	144
Porosity (%)	85

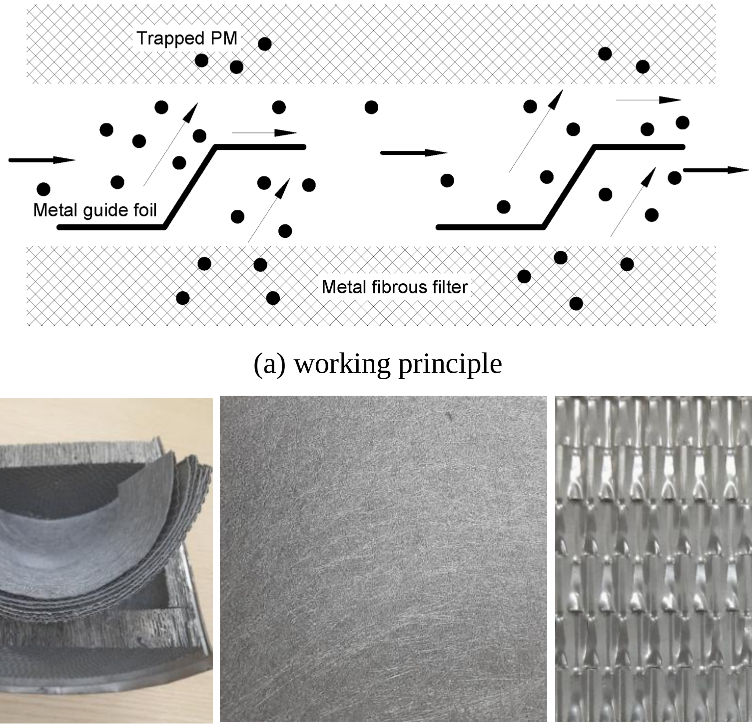

(a) working principle

(b) layers inside P-CDPF (c) metal fibrous filter (d) metal guide foil

Figure 1. Metallic P-CDPF (a) working principle (b) various layers of (c) metal fibrous filter and (d) metal guide foil.

2.3. Experiment setup

Exhaust gas emitted from the light-duty diesel vehicle using commercial B10 fuel was collected and analyzed to investigate particulate and gaseous emissions in the case of with and without P-CDPF under the NEDC. The experiment was conducted at the Automotive Emission Laboratory within the Pollution Control Department in Thailand, where the testing system adheres to the international standard ISO/IEC 17025. As shown in Figure 2, the experiment setup involved positioning the vehicle on a single roller chassis dynamometer (Schenck Komeg EMDY 48). The dynamometer was linked to a cooling fan to replicate realistic wind conditions. Surrounding humidity and temperature in the test room were controlled complying with the standard to prevent any effects on the measurements. An external fuel tank was used to diminish the impact of impurities from the main tank. Vehicle speed was controlled by a driver to operate under NEDC conditions aided by a driver-aid screen with no more than 2% error. NEDC consists of two successive phases: the urban driving cycle (UDC) and the extra-urban driving cycle (EUDC). The UDC includes four elementary cycles with a total duration of 780 seconds, covering

4 kilometers, featuring an average vehicle speed of 19 kilometers per hour (km/h). This phase represents driving conditions on the city road with frequent start-stop events. In contrast, the driving conditions under EUDC simulate the highway road with an average speed of 63 km/h, covering 7 kilometers within 400 seconds.

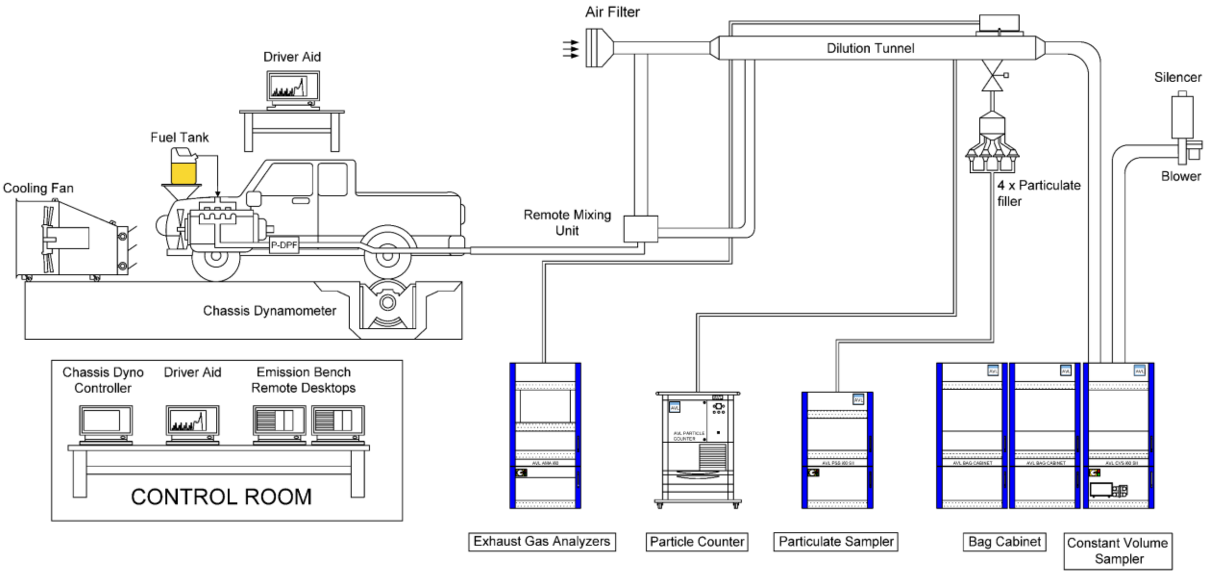

Figure 2. Particle and gaseous emissions testing setup.

At the beginning of the experiment, exhaust gas from the vehicle was diluted with the known quantity of surrounding air in dilution tunnel using a constant volume sampling system. This aims to lower its temperature, prevent condensation, and describe its actual behavior when exposed to the atmosphere. Upon dilution, a portion of diluted exhaust was drawn into gas analyzers to measure the real-time concentration of specific pollutants in parts per million (ppm). Simultaneously, diluted exhaust gas sample was collected in sampling bags, enabling the measurement of concentration in different phases. This study examines regulated gaseous emissions, including CO, THC, NOx, and CO_2, using gas analyzer (AVL AMA i60). Flame ionization and chemiluminescence detectors were respectively used to analyze THC and NOx, while CO and CO_2 were analyzed by non-dispersive infrared technique. Emission factor (in g/km) for each phase was calculated based on the concentration and density of pollutant, volume of the diluted exhaust and the covered distance. Additionally, particulate matters from diluted exhaust were collected on a filter during test phase using device AVL PSS i60 SII. At the beginning and the end of test phase, the filter was weighed and emission factor of PM was calculated. PN concentration from diluted exhaust was measured by particle number counter using the light-scattering technique, expressed in particles per cubic centimeter (#/cm^3). The PN emission factor (#/km) was then derived from the concentration and density of particulate matter, volume of the diluted exhaust and the covered distance. The exhaust gas temperatures (EGT) and pressure drops when employing P-CDPF were investigated in a transient test with various engine conditions. Thermocouples type K and pressure sensors (MPX5050DP) were inserted at positions before and after P-CDPF to measure EGTs and pressure drops at three engine speeds of 1500, 2000, and 2500 rpm and four engine loads of 84, 112, 140, and 160 Nm. The signals were then linked to the Arduino board and analyzed to get the results.

3. Results and Discussions

3.1. Pressure drops and exhaust gas temperatures

The pressure drops across P-CDPF were observed during the transient test conducted under various engine speed and load conditions. The minimum pressure drop was recorded at the engine speed of 1500 rpm and engine load of 84 Nm, while the maximum level was observed at 2500 rpm and 160 Nm, measuring 1.7 kPa and 8.3 kPa, respectively. A similar observation was also noticed in EGT, where higher loads led to increased EGT due to the greater quantity of injected fuel. EGT ranges from 317^0C to 489^0C in all tested conditions, with a slight increase observed when P-CDPF was installed, measuring from 318^0C to 498^0C. This increase can be attributed to the high kinetic energy of residual exhaust molecules due to exhaust backpressure. It is suggested that the observed EGT ranges are suitable for soot oxidation by O_2 and NO_2, reducing the effect of backpressure through filter passive regeneration.

3.2. Gaseous emissions

Figure 3 shows the instantaneous concentration of gaseous emissions versus vehicle speed under NEDC. As shown in Figure 3(a) and 3(b), higher levels of THC and CO were observed under UDC phase (first 780 seconds along the horizontal axis) compared to that during the EUDC phase (from 780 to 1180 seconds along the horizontal axis). The difference can be attributed to the frequent start-stop operating condition in UDC where the engine frequently worked in cold start state. During cold starts, fuel failed to vaporize and atomize properly due to its higher viscosity at lower temperatures, leading to incomplete combustion. This issue can also be attributed to the low engine speed and the relatively slower movement of the piston. Consequently, there was more time for heat loss through the cylinder wall surface during each combustion cycle, resulting in a decrease in in-cylinder temperature. In contrast, the average vehicle speed of 63 km/h in the EUDC led to reduced emissions. This improvement was due to the enhanced fuel atomization and proper mixing at higher engine speeds. This led to fewer fuel-rich regions, promoting higher combustion efficiency. Moreover, the higher engine speed means less time for heat loss through the cylinder wall surface in each combustion cycle, leading to an increase in in-cylinder temperature. Furthermore, a notable disparity becomes evident between the acceleration and deceleration periods. Emission level exhibited an increase during acceleration compared to the decrease during deceleration. This originated from scenario in which the combustion chamber received a heightened influx of fuel to rapidly overcome the instant load during acceleration. Conversely, the deceleration period witnessed fewer amounts of injected fuel due to the activation of the cut-off function, leading to lower emission levels.

As shown in Figure 3(c), CO_2 experienced lower concentration through UDC compared to EUDC phase. The maximum concentration observed in UDC is 15000 ppm, while that of EUDC is approximately 35000 ppm. The disparity can be attributed to the accelerated fuel injection rate into the combustion chamber to generate more power under EUDC. As mentioned earlier, the vehicle operated under optimal configurations during EUDC, facilitating more complete combustion and resulting in higher CO_2 levels. A similar trend was also observed with NOx emissions, as depicted in Figure 3(d). A noticeable increase in NOx emissions can be seen during the EUDC. Specifically, the maximum concentration was around 100 ppm for all cases during the UDC, while that was 280 ppm with EUDC. This is due to higher vehicle speed, where more fuel was injected, resulting in elevated flame temperatures within the combustion chamber. The heightened flame temperature was the primary factor behind the increased NOx emissions [16].

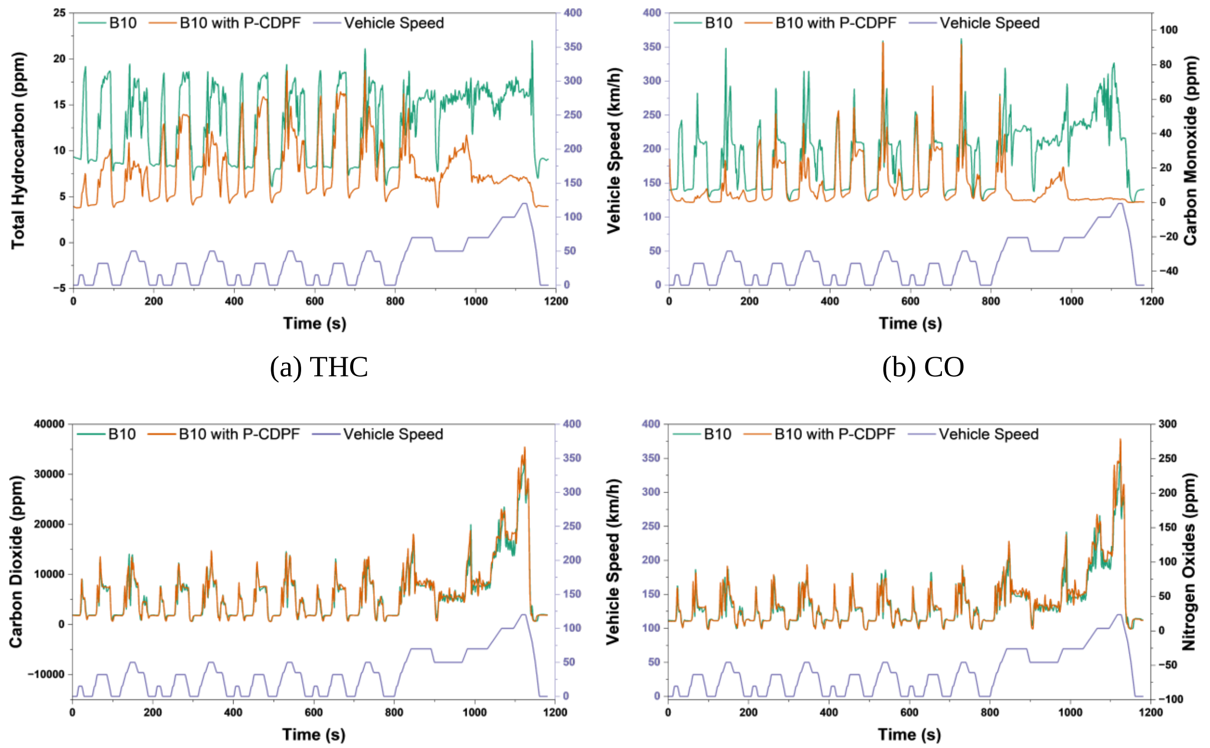

(a) THC

(b) CO

(c) CO_2

(d) NOx

Figure 3. Instantaneous concentration of gaseous emissions under NEDC.
(a) total hydrocarbon, (b) carbon monoxide, (c) carbon dioxide, and (d) nitrogen oxides

Figure 4 shows emission factors of pollutants in grams per kilometer (g/km) under NEDC using fuel B10, with and without the P-CDPF installation. In UDC phase, when the engine operated under normal temperature, THC exhibited the highest emission level at 0.163 g/km while CO also followed a similar pattern, with a recorded value of 0.838 g/km. These pollutants dropped to 0.061 g/km and 0.404 g/km respectively when vehicle ran under EUDC. Upon the installation of the P-CDPF, the results exhibited significant reduction as 40% THC and 49% CO were eliminated. The decline was attributed to Pt catalyst activities, which aid in the conversion of CO and THC into CO_2 and water [17]. Moreover, P-CDPF showed higher performance as seen in EUDC, with 59% and 86% of THC and CO reduction. It is suggested that the higher vehicle speed in EUDC resulted in increased EGT, leading to superior conversion efficiency. After the whole NEDC, there were 48% THC and 66% CO removed by P-CDPF. The results significantly highlight the conversion performance of P-CDPF which not only traps PM but also eliminates harmful emissions. However, introducing the P-CDPF resulted in the increased CO_2 and NOx emissions. Specifically, a 6% increase in NOx emissions was recorded after the integration of P-CDPF, which stemmed from the impact of backpressure. Exhaust backpressure hampers the efficient expulsion of exhaust gas, resulting in remaining residual exhaust gas. The high kinetic energy of residual gas molecules can be attributed to increased in-cylinder temperature. The higher in-cylinder temperature when employing P-CDPF is the primary factor accounting for higher NOx emissions. In terms of CO_2 emissions, the combination with P-CDPF led to increased CO_2 levels because of Pt catalyst activities, as previously mentioned. It is essential to note that CO_2 levels were dominant compared to THC and CO. Therefore, as a hypothetical analysis, the 6% increase in CO_2 emissions when employing P-CDPF could also originate from the oxidation of PM into CO_2.

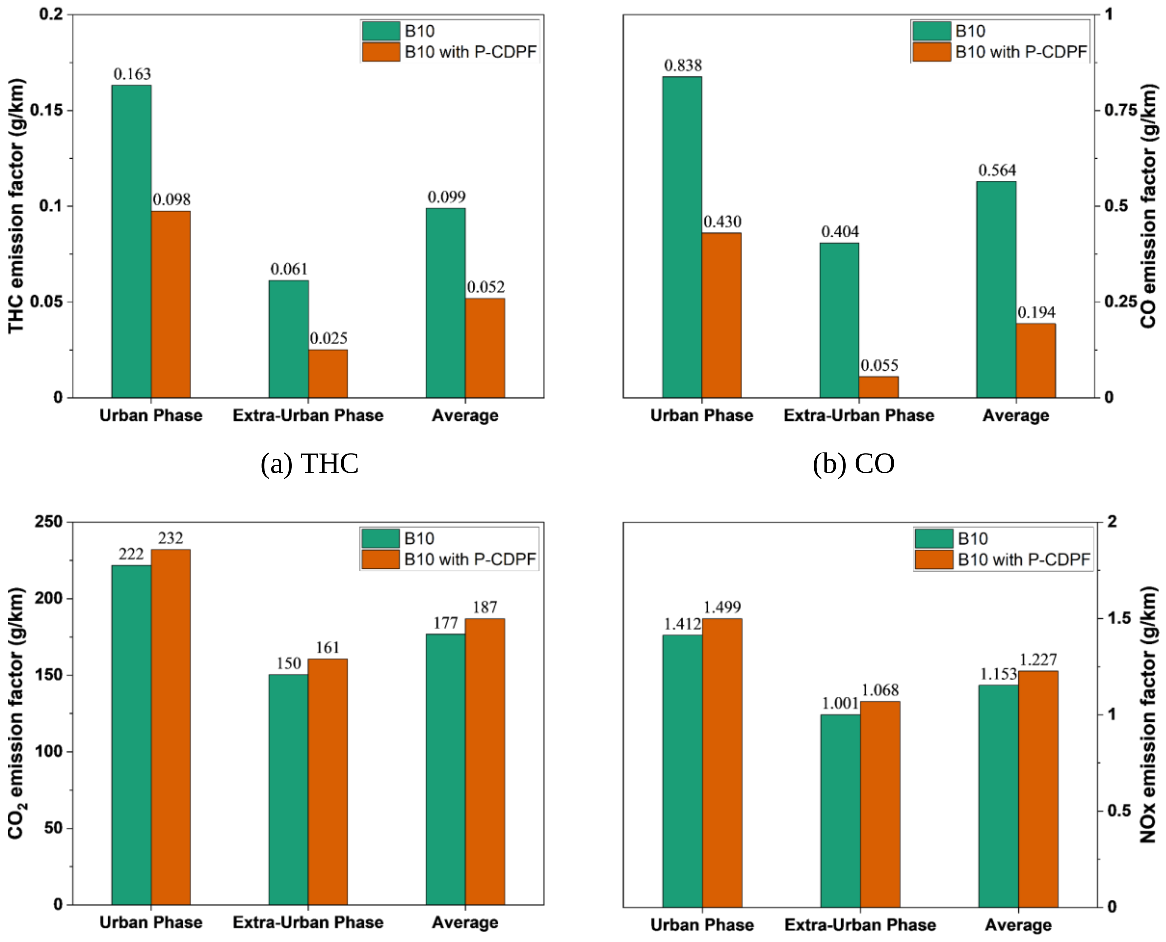

(a) THC (b) CO

(c) CO_2 (d) NOx

Figure 4. Distribution of gas emissions by phase during NEDC conditions.
(a) total hydrocarbon, (b) carbon monoxide, (c) carbon dioxide, and (d) nitrogen oxides

3.3. Particulate matters

Figure 5 illustrates the particulate emission characteristics of a light-duty diesel vehicle during the NEDC when utilizing fuel B10, both in the presence and absence of a P-CDPF. The evolution of PN concentration, as shown in Figure 5(a), was significantly influenced by the cold start feature inherent to the UDC phase. Specifically, PN reached its peak concentration of 8.08×10^6 #/cm^3 during the UDC in the absence of a P-CDPF since engine did not reach its optimal temperature when initially starting. The low engine temperature affected fuel viscosity because it is a temperature-dependent parameter. Higher viscosity results from lower temperature in UDC leading to improper fuel vaporization and atomization. This involves fuel-air mixing and as a result, leads to incomplete combustion. However, a noticeable reduction in PN concentration was recorded in the EUDC at an average vehicle speed of 63 km/h. The peak PN concentration in the absence of a P-CDPF was 6.86×10^6 #/cm^3. This reduction was attributed to the increased in-cylinder temperature due to low heat loss and proper fuel-air mixing at high engine speed.

The significant reductions of PN emission factors under both phases of NEDC were observed in Figure 5(b). When P-CDPF was employed in UDC, the emission rate decreased from 1.7×10^{14} #/km to 9.5×10^{13} #/km. While in EUDC, the rate dropped from 7.6×10^{13} #/km to 4.2×10^{13} #/km. The results indicated an unchanged 45% reduction in PN emissions after the implementation of P-CDPF in both UDC and EUDC, leading to consistent reduced levels under NEDC. Regarding PM emission factor, as shown in Figure 5(c), the installation of P-CDPF resulted in a 60% reduction under NEDC, with a recorded level of 0.013 g/km. These significant reductions underscore the effectiveness of P-CDPF in trapping particulate matters. Additionally, the catalytic coating promotes the conversion of NO into NO_2. The chemical reactions of NO_2 and O_2 with carbon convert PM into CO_2 and NO, supporting the observed increase in CO_2 levels after P-CDPF installation, as discussed earlier.

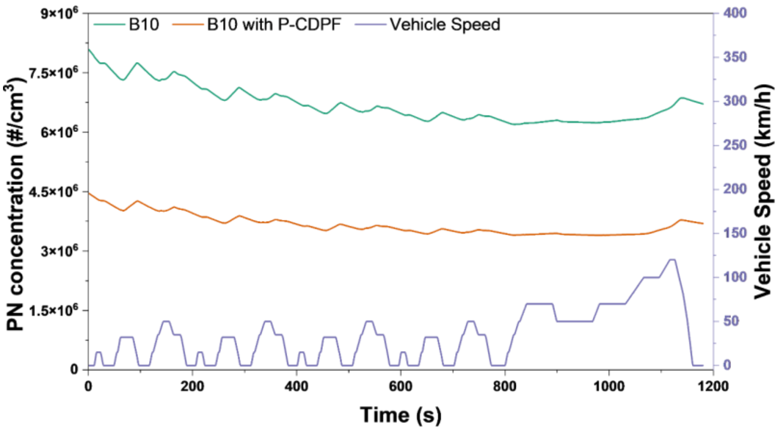

(a) Real-time of PN concentration

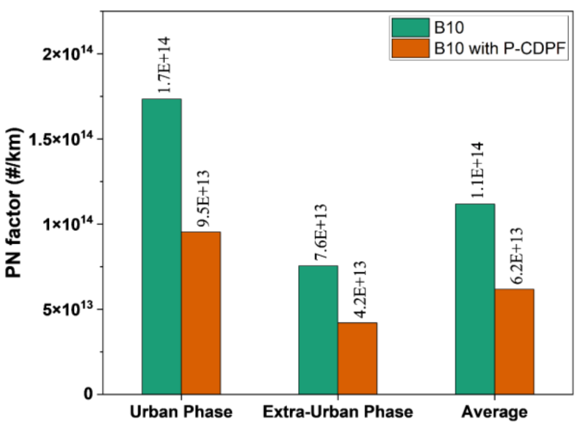

(b) PN factor

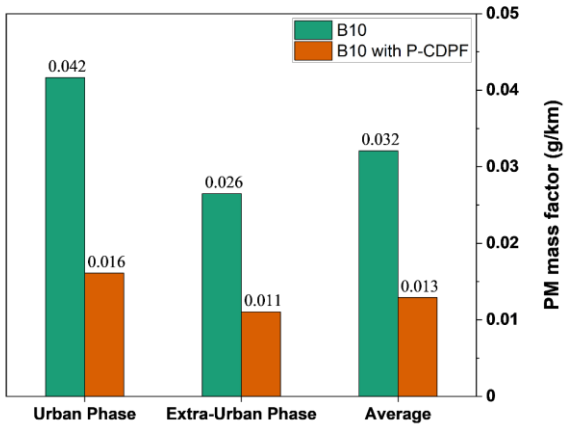

(c) PM mass factor

Figure 5. Particulate emissions during NEDC
(a) real-time of PN concentration (b) PN factor and (c) PM mass factor

4. Conclusion

This study examined particle and gaseous emissions from a light-duty diesel vehicle following NEDC using fuel B10 in cases with and without the installation of P-CDPF. The results showed the effectiveness of catalytic coating on converting THC and CO into CO_2 and water, with 48% and 66% reduction, respectively. Meanwhile, because of the abovementioned mechanism, CO_2 increased by 6%. NOx exhibited a 6% increment after P-CDPF because of elevated temperature due to backpressure. The measurement of exhaust gas temperature under varied engine conditions confirmed favorable conditions for soot oxidation, while pressure drops remained within acceptable ranges. The integration of P-CDPF showed its efficacy in trapping and oxidizing particulate matters. Specifically, 60% of PM and 45% of PN were eliminated. The findings indicate a viable emission control strategy, contributing to practical efforts aimed at reducing harmful substances from untreated diesel vehicles.

5. Acknowledgment
The authors would like to thank National Research Council of Thailand (NRCT), National Science and Technology Development Agency (NSTDA), and Pollution Control Department (PCD). This work was financially supported by King Mongkut's Institute of Technology Ladkrabang [2566-02-01-056].

6. References
[1] Heywood, J. B. (2019). *Internal Combustion Engine Fundamentals*. McGraw-Hill.

[2] Kagawa, J. (2002). Health effects of diesel exhaust emissions—a mixture of air pollutants of worldwide concern. *Toxicology*.

[3] R. Prasad, V. R. B. (2010). A Review on Diesel Soot Emission, its Effect and Control. *Bulletin of Chemical Reaction Engineering & Catalysis*.

[4] Lloyd, A. C., & Cackette, T. A. (2001). Diesel engines: environmental impact and control. *J Air Waste Manag Assoc*, 51(6), 809-847.

[5] W. Addy Majewski, M. K. K. (2006). *Diesel Emissions and Their Control*. SAE International.

[6] Karmakar, A., Karmakar, S., & Mukherjee, S. (2010). Properties of various plants and animals feedstocks for biodiesel production. *Bioresour Technol*, 101(19), 7201-7210.

[7] Russell, A., & Epling, W. S. (2011). Diesel Oxidation Catalysts. *Catalysis Reviews*, 53(4), 337-423.

[8] Ebrahimnataj, M. R., Tiji, A. E., Eisapour, M., Ali, H. M., Talebizadehsardari, P., Ehteram, M. A., & Abdolmaleki, S. (2021). The effect of soot accumulation and backpressure of an integrated after-treatment system on diesel engine performance. *Journal of Thermal Analysis and Calorimetry*, 147(15), 8435-8443.

[9] Ingo Mikulic, R. Z., Scott Eakle. (2010). Dependence of Fuel Consumption on Engine Backpressure Generated by a DPF. *SAE Technical Paper 2010-01-0535*.

[10] Lefort Isaline, Herreros Jose, & Athanasios, T. (2014). The Use of a Partial Flow Filter to Assist the Diesel Particulate Filter and Reduce Active Regeneration Events. *SAE International Journal of Engines*, 7(4), 1953-1960.

[11] Görsmann, C. (2005). Catalytic Coatings for Active and Passive Diesel Particulate Filter Regeneration. *Monatshefte für Chemie*, 136(1), 91-105.

[12] Jacobs, T., Chatterjee, S., Conway, R., Walker, A., Kramer, J., & Mueller-Haas, K. (2006). Development of Partial Filter Technology for HDD Retrofit. *SAE*.

[13] Mon Phyo, M. Z., Wai, P., Thin, M. H., Oh, B.-S., Phairote, W., Srilomsak, M., Charoenphonphanich, C., Masomtob, M., Srimanosaowapak, S., Kosaka, H., & Karin, P. (2023). Experimental investigation of metallic partial-flow particulate filter on a diesel engine's combustion pressure and particle emission. *Case Studies in Thermal Engineering*, 49.

[14] Oh, B.-s., Thaeviriyakul, P., Phairote, W., Srilomsak, M., Charoenphonphanich, C., Po-ngaen, W., Srimanosaowapak, S., Hanamura, K., & Karin, P. (2023). Effect of Metallic Microfiber Flow Through Diesel Particulate Filter System on Diesel Engine's Particle Emission Physicochemical Characteristics. *Emission Control Science and Technology*, 9(1), 47-65.

[15] Jain, S., & Sharma, M. P. (2010). Prospects of biodiesel from Jatropha in India: A review. *Renewable and Sustainable Energy Reviews*, 14(2), 763-771.

[16] Al-Shemmeri, T. T., & Oberweis, S. (2011). Correlation of the NOx emission and exhaust gas temperature for biodiesel. *Applied Thermal Engineering*, 31(10), 1682-1688.

[17] Reşitoğlu, İ. A., Altinişik, K., & Keskin, A. (2014). The pollutant emissions from diesel-engine vehicles and exhaust aftertreatment systems. *Clean Technologies and Environmental Policy*, 17(1), 15-27.

AME0001

Vision-Assisted Multirotor Landing on a Moving Target

J Pravitra, P Moonsri, Y Chaonafang, C Reunpakdan, and J Moudpoklang*

Navaminda Kasatriyadhiraj Royal Air Force Academy,
999 Moo 9 National Highway 2224, Mittraphap, Muak Lek, Saraburi, 18180,Thailand

* Corresponding Author: moudpoklang@windowslive.com

Abstract. This paper presents a multirotor unmanned aircraft system capable of semi-autonomous landing on a moving target. The target consists of concentric circles of multiple colors. Color segmentation and shape comparison are used to identify the target. The global position of the target is estimated using Extended Kalman Filter. Trajectory command is then sent to a commercial off-the-shelf flight control hardware. Our semi-autonomous landing capability was validated via flight tests.

Keywords: Autonomous Landing, Extended Kalman Filter, Multirotor, UAV.

1. Introduction

Recent advances in computation, sensing, and automation have enabled engineers to explore and develop new capabilities for Unmanned Aircraft Systems (UASs). Of one particular interest is the ability to autonomously land a UAS on a moving platform. Naval and maritime law enforcement operations can greatly benefit from this capability. Maritime UAS applications include (but are not limited to) intelligence, surveillance, and reconnaissance (ISR), fire control support, anti-submarine warfare, search and rescue, anti-piracy, drug and migrant interdiction. There have been several research works related to maritime UAS operations including flight testing and landing with parallelized optimal algorithm [1], linear trajectory optimization and dynamic inversion control [2], and nonlinear trajectory optimization [3-6]. However, most implementations of shipboard UAS operations require shipboard sensors—which infer high cost and require ship states to be uplinked to the aircraft.

Vision-based methods offer an attractive alternative since they do not require shipboard sensing. However, they introduce other challenges. Particularly, they require a rather involved target state estimation algorithm. Vision-based landing on a moving platform has been studied extensively in [7-8], and the progress was greatly accelerated during the Mohamed Bin Zayed International Robotics Challenge 2017 [9-11].

The contribution of this paper is to provide a low-cost solution for semi-autonomous landing on a moving platform—and to serve as a pilot project for undergraduate research at Navaminda Kasatriyadhiraj Royal Air Force Academy (NKRAFA). This paper is organized as follows. We first present both software and hardware architecture where simulation was greatly utilized during the development process. We then discuss implementation of target detection, target state estimation, and trajectory generation. We then conclude the paper with a flight test result.

2. Architecture

2.1. Flight Test Architecture

This section describes the hardware architecture for our system. Onboard the multirotor aircraft, Cube Orange is used as the primary flight controller. The aircraft also carries an Nvidia Jetson Xavier NX. The camera is connected to the Jetson. Our custom software runs solely on Jetson, and there is no need to modify Ardupilot codebase on the Cube. Two ground control station (GCS) computers are required to operate the system. The first computer is a Windows machine that runs Mission Planner GCS. This GCS is mainly for monitoring the aircraft (via an interface that is familiar to the users). The second computer is a Linux machine which runs our custom GCS software. This GCS is an "engineering" GCS written using Qt library. The GCS displays video feed, plots, and the current mode of the aircraft. It can also send custom commands to the aircraft. The first GCS is connected to the Cube via a wireless serial link while the second GCS is connected to the Jetson via a WiFi link. The hardware architecture is summarized in Figure 1.

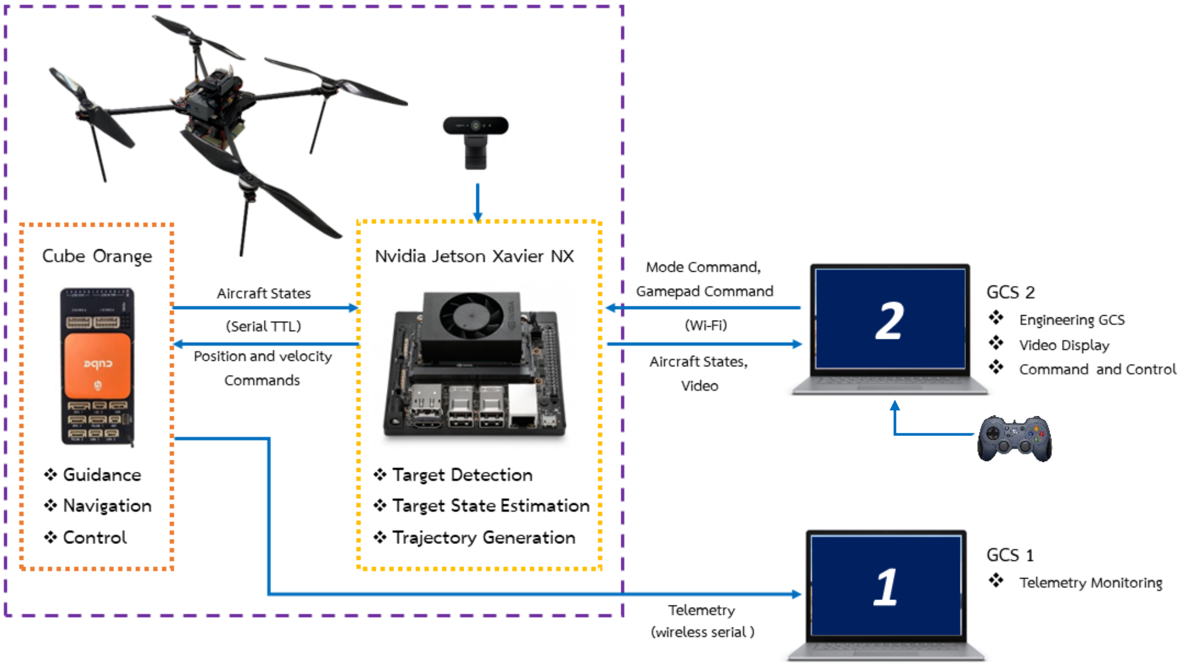

Figure 1. Flight test architecture.

2.2. Simulation Architecture

Much like any research involving flight tests, software error that we might unknowingly introduced may result in catastrophic consequences. It is thus imperative that our software is thoroughly tested in simulation before we ever attempt a flight test. We developed an architecture where software (both onboard and GCS) can be reconfigured to compile as a single Linux executable with no modification in the source code. Thus, the same code that runs during the flight test also runs in simulation. We utilize Ardupilot software-in-the-loop feature and Gazebo simulation environment—enabling the entire testing setup to be run in one single Linux computer. The simulation architecture shown in Figure 2. Note the similarity between flight test architecture (Figure 1) and the simulation architecture (Figure 2).

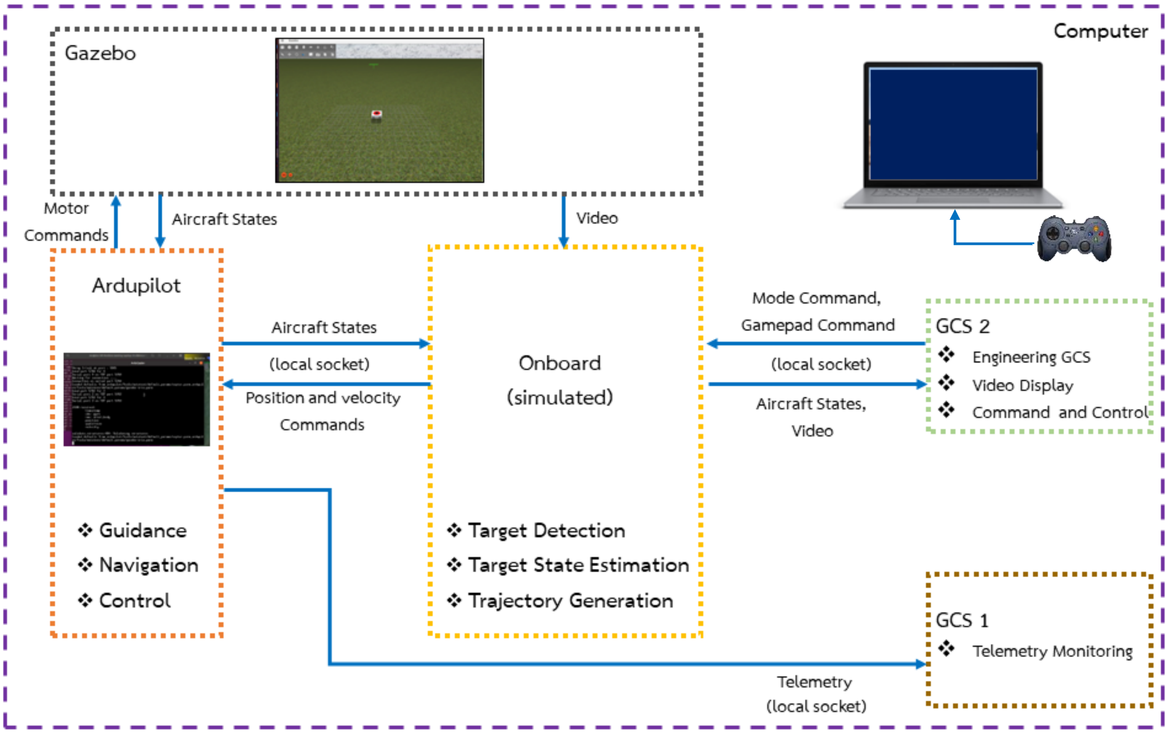

Figure 2. Simulation architecture.

3. Target Detection

This section describes the vision pipeline. The section outlines how the centroid and the area of the target (in pixels) are determined through several OpenCV operations. Starting from a video frame (which is already corrected for lens distortion), the RGB image is converted to the HSV space, and then binarized using a specified threshold. "Open" and "close" morphological operations are then applied to remove small pixel patches. The contours are then detected, and the largest contour is selected for further processing. Since the target is a circle and the camera is mounted at a downward-facing attitude, a simple way to verify that the largest contour is indeed a circle is to compare the area of the contour against the area of the smallest circle enclosing the contour. If the difference is below a certain threshold, then a valid circle has been detected. The centroid and the area of the circle are then published to the target state estimation algorithm. The vision pipeline is summarized in Figure 3. The thresholding result and the detected contour are shown in Figure 4.

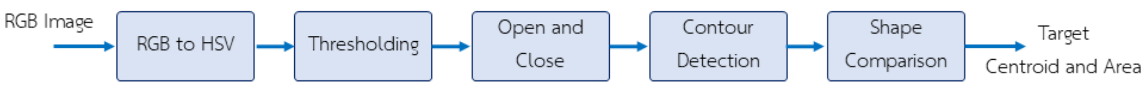

Figure 3. Image processing pipeline to obtain the target centroid and area.

Figure 4. Image after thresholding, the detected contour, and the pinhole camera model.

4. Target State Estimation

4.1. Extended Kalman Filter

In this work, Extended Kalman Filter (EKF) is utilized for target state estimation. We opt for the standard EKF formulation with the prediction equations.

$$\dot{\hat{\boldsymbol{x}}} = \boldsymbol{f}(\hat{\boldsymbol{x}}) \qquad\qquad \dot{\boldsymbol{P}} = \boldsymbol{A}\boldsymbol{P} + \boldsymbol{P}\,\boldsymbol{A}^T + \boldsymbol{Q} \tag{1}$$

where $\hat{\boldsymbol{x}}$ is the estimated states, $\boldsymbol{f}(\hat{\boldsymbol{x}})$ is the dynamics model with $\boldsymbol{A} = \frac{\partial f}{\partial x}|_{\hat{x}}$, $\boldsymbol{P}$ is the covariance matrix, and $\boldsymbol{Q}$ is the (tunable) expected process noise. The update equations follow the form

$$\boldsymbol{K} = \boldsymbol{P}^{-}\,\boldsymbol{C}^T\,(\boldsymbol{C}\boldsymbol{P}^{-}\boldsymbol{C}^T + \boldsymbol{R})^{-1} \qquad \hat{\boldsymbol{x}} = \hat{\boldsymbol{x}}^{-} + \boldsymbol{K}(\boldsymbol{z} - \boldsymbol{h}(\hat{\boldsymbol{x}}^{-})) \qquad \boldsymbol{P} = (\boldsymbol{I} - \boldsymbol{K}\,\boldsymbol{C})\boldsymbol{P}^{-} \tag{2}$$

where $\boldsymbol{h}(\hat{\boldsymbol{x}})$ is the measurement model with $\boldsymbol{C} = \frac{\partial h}{\partial x}|_{\hat{x}^-}$. $\hat{\boldsymbol{x}}^{-}$ are $\boldsymbol{P}^{-}$ are the pre-updated state and covariance. $\boldsymbol{z}$ is the measurement. $\boldsymbol{K}$ is the Kalman gain, and $\mathbf{R}$ is the (tunable) expected measurement noise.

4.2. Process Model

The target dynamics is modeled as a simple 6-states integrator. The states are the position and velocity of the target in an Earth-fixed North-East-Down frame: $\hat{\boldsymbol{x}} = \begin{bmatrix}\hat{p}_{xt} & \hat{p}_{yt} & \hat{p}_{zt} & \hat{v}_{xt} & \hat{v}_{yt} & \hat{v}_{zt}\end{bmatrix}^T$. Hence, the target dynamics is

$$\begin{bmatrix}\dot{\hat{p}}_{xt} & \dot{\hat{p}}_{yt} & \dot{\hat{p}}_{zt} & \dot{\hat{v}}_{xt} & \dot{\hat{v}}_{yt} & \dot{\hat{v}}_{zt}\end{bmatrix}^T = \begin{bmatrix}\hat{v}_{xt} & \hat{v}_{yt} & \hat{v}_{zt} & 0 & 0 & 0\end{bmatrix}^T \tag{3}$$

4.3. Measurement Model

4.3.1. Position Vision Update

Let $\boldsymbol{p} = \begin{bmatrix}p_x & p_y & p_z\end{bmatrix}^T$ be the current position of the aircraft and let ϕ, θ, and ψ be the Euler angles of the aircraft. Both the position and the Euler angles are obtained from the aircraft's navigation filter (from Ardupilot). The position of the target written in the camera frame can be expressed as

$$\hat{\boldsymbol{l}} = \begin{bmatrix}\hat{l}_x \\ \hat{l}_y \\ \hat{l}_z\end{bmatrix} = \boldsymbol{R}_2(\alpha)\left(\boldsymbol{R}_1(\phi)\boldsymbol{R}_2(\theta)\boldsymbol{R}_3(\psi)\left(\begin{bmatrix}\hat{p}_{xt} \\ \hat{p}_{yt} \\ \hat{p}_{zt}\end{bmatrix} - \begin{bmatrix}p_x \\ p_y \\ p_z\end{bmatrix}\right) + \boldsymbol{e}\right) \tag{4}$$

where $\boldsymbol{e}$ is the relative position between the body frame and the camera frame written in the body frame, and α is the elevation angle of the camera relative to the aircraft's xy plane. The matrices $\boldsymbol{R}_1(\cdot)$, $\boldsymbol{R}_2(\cdot)$, and $\boldsymbol{R}_3(\cdot)$ are the standard rotation matrices. From the pinhole camera model (Figure 4), the relationship between the expected target centroid $\begin{bmatrix}\hat{b} & \hat{c}\end{bmatrix}^T$ (in pixels) and $\hat{\boldsymbol{l}}$ can be written as

$$\begin{bmatrix}\hat{b} \\ \hat{c}\end{bmatrix} = \frac{f}{\hat{l}_x}\begin{bmatrix}\hat{l}_y \\ \hat{l}_z\end{bmatrix} \tag{5}$$

where f is the focal length of the camera.

For this target estimator, note that we have determined experimentally that the time between image input and the measurement update is typically less than 0.1 s. This time delay is small enough that we do not need to implement time delay compensation in the estimator.

4.3.2. Area Update

Utilizing the fact that the actual target area is known, the accuracy of the vertical position estimate can be improved by comparing the expected projected area against the area observed by the camera. The expected projected area (in pixel^2) is

$$\hat{A} = \left(\frac{f}{i_x}\right)^2 \pi R^2 \left| [\boldsymbol{R}_2(\alpha)\boldsymbol{R}_1(\phi)\boldsymbol{R}_2(\theta)\boldsymbol{R}_3(\psi)]_{(3,3)} \right| \tag{6}$$

where R is the actual (known) radius of the target. The operation $[\cdot]_{(3,3)}$ is the operation that extracts the third row and the third column entry of the matrix.

4.3.3. Zero Vertical Velocity Update

Furthermore, utilizing the fact that the target is not moving vertically, zero vertical velocity can be artificially injected in equations (2) by setting $z = 0$ and

$$\boldsymbol{h}(\widehat{\boldsymbol{x}}) = [0 \quad 0 \quad 0 \quad 0 \quad 0 \quad 1]\,\widehat{\boldsymbol{x}} \tag{7}$$

In summary, the EKF update (equations (2)) are ran using three different sources: pixel position, pixel area, and artificial zero vertical velocity.

5. Trajectory Command Generation

This section describes the position, velocity, and heading commands generation. Recall that in our architecture (Figure 1), we deliberately choose not to implement our own position/velocity controller, but rather rely on a well-proven Ardupilot position controller. The estimated horizontal position and velocity from Section 4 can be directly injected to Ardupilot because of the following reasons.

1) The horizonal position and velocity are already kinematically consistent as part of the EKF dynamics model.
2) The position and velocity are already smooth, assuming that the process noise and the measurement noise matrices are properly tuned. An explicit command filter is not necessary.
3) Ardupilot internally imposes velocity, acceleration, and jerk limits—thus automatically prevents extreme maneuvers.

The vertical position and velocity estimates are not as reliable when compared to the horizontal estimates. Their accuracy is not sufficient for autonomous landing. We therefore restrict ourselves to semi-autonomous landing. The horizontal commands are fully automated while the vertical velocity command is manipulated by an operator via a gamepad. The vertical velocity command is integrated to obtain the vertical position command.

For heading, a simple method is employed. The vehicle will maintain a constant heading, which is the heading at the instant when the target tracking mode is initially turned on.

Additional protections are also imposed in order to prevent unsafe operations. Specifically, a stop (zero velocity) command will be sent if one of the following criteria occur

1) The horizontal position covariance (P_{11} or P_{22}) exceeds a certain limit.
2) The horizontal distance between the aircraft and the target $\sqrt{(\hat{p}_{xt} - p_x)^2 + (\hat{p}_{yt} - p_y)^2}$ exceeds a certain limit.
3) Gamepad command timeout (if the onboard computer has not received the gamepad command for longer than a certain time limit)
4) When any of the command is not a finite number

6. Flight Test Results

We validated our system thoroughly in simulation. Once the result was satisfactory, we then validated our system in flight. A photo from a flight test is shown in Figure 5. The GCS screenshot and the plots from the flight test are shown in Figures 6 and 7. The target was pulled by hand, and the aircraft was able to automatically track the horizontal position of the moving target. The aircraft also correctly responded to the commanded vertical speed (inputted by the operator). The target was continuously pulled while the GCS operator carefully injected the vertical speed commands. Semi-autonomous landing was then successfully achieved. The video from the flight test can be viewed at https://www.youtube.com/watch?v=NkWTiSi0OjA.

Figure 5. Flight validation at Navaminda Kasatriyadhiraj Royal Air Force Academy.

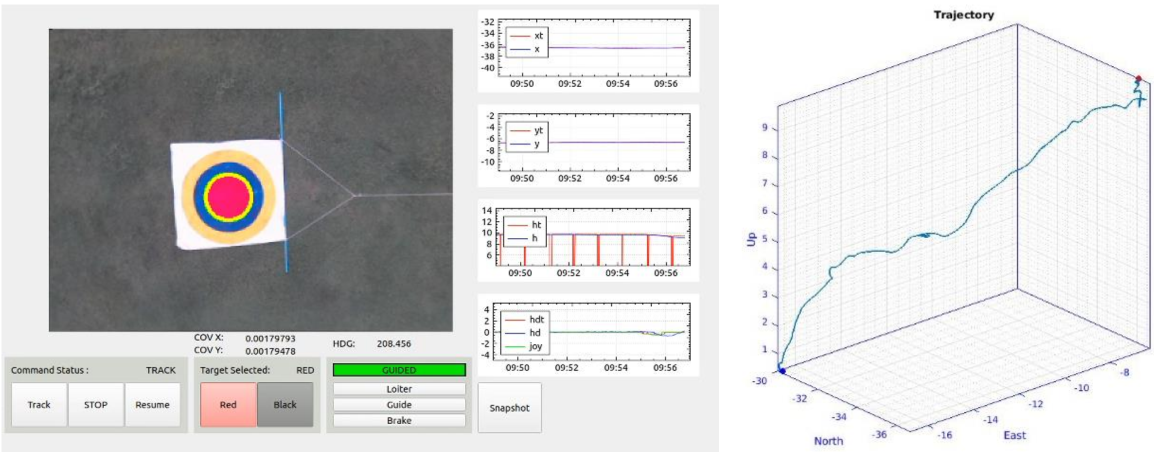

Figure 6. GCS Screenshot during the flight test and the trajectory of the flight test.

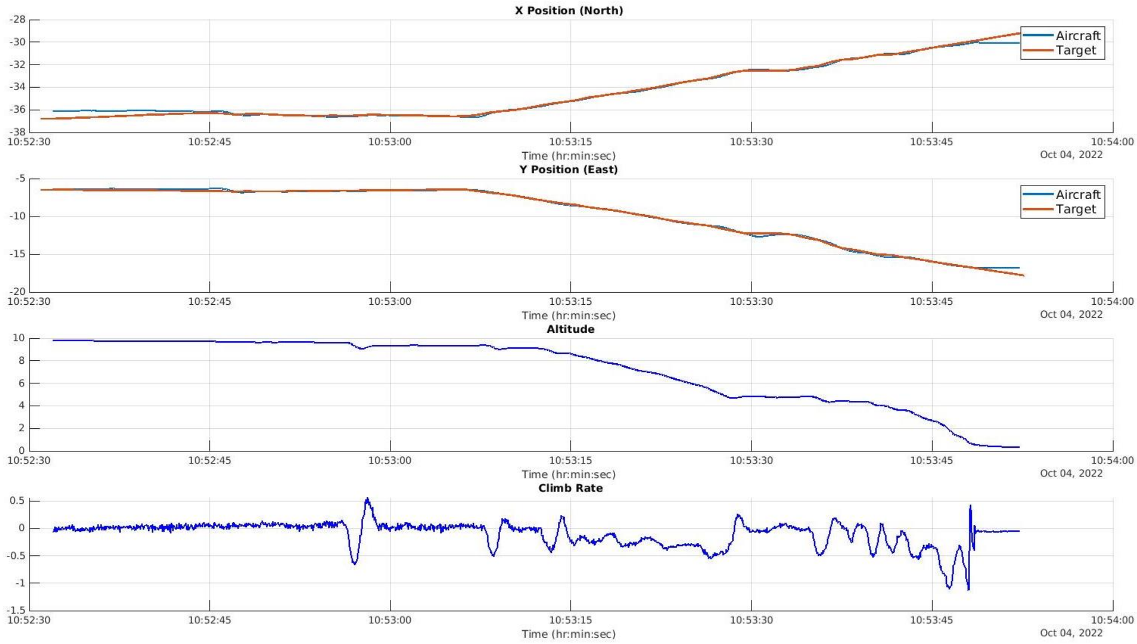

Figure 7. Position and climb rate during the flight test.

7. Conclusion

This paper presented a multirotor UAS capable of semi-autonomous landing. Horizontal position tracking is fully automated while a GCS operator manipulates the vertical speed. Target detection was achieved through color segmentation and shape comparison. Extended Kalman Filter was used for target state estimation. Practical aspects for the command generation process were also discussed. The flight test result showed that semi-autonomous landing was successfully achieved.

8. Acknowledgments

The authors would like to thank the members of Griffin and M Solar-X UAV research team at Navaminda Kasatriyadhiraj Royal Air Force Academy (NKRAFA) especially Tharit Hanggasee and Suttipong Takampang for their help with the hardware. We also would like to thank the faculty and staff at the Department of Mechanical Engineering and the Academic Division at NKRAFA for their valuable comments and their administrative support.

9. References

[1] Pravitra J 2021 "Shipboard UAS Operations with Optimized Landing Trajectory" *PhD thesis, Pennsylvania State University*

[2] Yang J 2018 "Autonomous Control Modes and Optimized Path Guidance for Shipboard Landing in High Sea States" *PhD thesis, Pennsylvania State University*

[3] Nakamura T, Haviland S, Bershadsky D and Johnson E 2016 "Vision-based Optimal Landing on a Moving Platform" *72nd American Helicopter Society International Annual Forum* p 3331-3341

[4] Watanabe T and Johnson E 2017 "Automatic Landing on a Moving Platform Using Deep Neural Network Estimation" *7th AHS Technical Meeting on VTOL Unmanned Aircraft Systems and Autonomy*

[5] Zhao D, Mishra S and Gandhi F 2019 "Real-time Path Planning for Time-optimal Helicopter Shipboard Landing via Trajectory Parametrization"

[6] Comandur V, Walters R and Prasad J 2019 "MPPI Parallel Trajectory Optimization for Guidance in Rotorcraft Shipboard Landing" *Vertical Flight Society 75th Annual Forum and Technology Display*

[7] Lee H, Jung S and Shim D 2016 “Vision-based UAV Landing on the Moving Vehicle. *International Conference on Unmanned Aircraft Systems (ICUAS 2016)* p 1-7

[8] Lange S, Sünderhauf N and Protzel P 2008 “Autonomous Landing for a Multirotor UAV using Vision" *International Conference on Simulation, Modeling, and Programming for Autonomous Robots (SIMPAR 2008) p 482-491*

[9] Beul M, Houben S, Nieuwenhuisen M and Behnke S 2017 “Fast Autonomous Landing on a Moving Target at MBZIRC” *European Conference on Mobile Robots (ECMR)* p 1–6

[10] Falanga D, Zanchettin A, Simovic A, Delmerico J and Scaramuzza D 2017 “Vision-based autonomous quadrotor landing on a moving platform” *IEEE International Symposium on Safety, Security and Rescue Robotics (SSRR)* p 200-207

[11] Baca T, Stepan P, Spurny V, Hert D, Penicka D, Saska M, Thomas J, Loianno G and Kumar V 2019 “Autonomous Landing on a Moving Vehicle with an Unmanned Aerial Vehicle,” *Journal of Field Robotics* p 874–891

AME0004

Numerical Investigation on Vibration Characteristic for Composite Sandwich Structure with Bolted Joint Junction

V Sripawadkul, M Suraratchai, and P Bunyawanichakul*

Department of Aerospace Engineering, Faculty of Engineering, Kasetsart University, 50 Ngam Wong Wan Rd., Lat Yao, Chatuchak, Bangkok, 10900, Thailand

* Corresponding Author: phacharaporn.b@ku.ac.th

Abstract. A composite sandwich structure possesses outstanding characteristics in providing flexural stiffness to weight ratio. This advantage makes this kind of structure widely used in several applications such as automotive, aeronautics, space, sports goods, and so on. This paper focuses on a sandwich panel used as a part of the solar panel structure with a dimension of 740 mm by 840 mm for the TSC-1 satellite. The structure must be designed to resist the average and fluctuating accelerations of the launch in order to avoid resonance. It is susceptible to failure at connections due to the weakness of the core material. This paper presents a numerical investigation of the vibration characteristics of five different groups of in-line bolts. The result can be used as a guideline for satellite design to withstand vibrations while transporting to the expected altitude in low-earth orbit.

Keywords: Junction, Bolted Joint, Vibration Characteristic, Mode Shape, Sandwich Structure.

1. Introduction

Through cutting-edge research and development, space exploration brings multiple benefits and promotes breakthrough technology. The human race's attempt is to send humans or unmanned spacecraft outside the Earth's atmosphere for centuries. Weight reduction for spacecraft can directly convert into the ability to carry additional propellant, allowing satellites to operate for longer periods of time [1]. Having this competitive advantage is the most crucial goal for space applications. Due to their specific strength and rigidity, composite sandwich constructions have significant weight-saving advantages over conventional materials such as metals. Sandwich panels are used in satellite construction to provide such high-performance features. These designs demand the junction of the panel to the structure or sub-structures in order to maintain the structural integrity of the satellite throughout all missions. Bolted joint junctions are unavoidable in a satellite sandwich panel. Every satellite is regarded as a payload to be carried by a launch vehicle. They must be developed to ensure that their initial mission of overall flight environment from the Earth's surface to their final orbit is successful. Before launching, it is critical to evaluate the vibration characteristics of the entire structure [2].

Theoretical calculation of the vibration characteristic of a sandwich structure is difficult because it depends on a number of factors, such as the shape and physical properties of junction materials, bolt type and material, bolt patterns, materials and number of washers, joint aperture strength, load types, contact configuration, environmental conditions, and so on. There is no single correct solution or method to all circumstances. It can be approached using a simple finite element model all the way up to a completely nonlinear three-dimensional finite element model with geometric nonlinearities and frictional contact [3-7]. In some circumstances, the load can be predicted using an analytical method first [8-9], followed by a numerical examination using a finite element model.

2. Problem Description

This paper focuses on the vibration characteristics of a solar panel with five in-line bolted patterns attached to the primary structure of the Thai Space Consortium-1 or TSC-1 satellite [10-11]. The TSC-1 satellite is classified as a small one (weighing less than 100 kg). When ridesharing to the launcher, its entire envelope is 740 mm x 840 mm x 900 mm. The honeycomb core sandwich serves as the satellite's main panels. The core is made of aluminum 3003-H18, with hexagonal cells of 9.5 mm and foil thickness of 0.5 mm. The primary structure's skin is made of aluminum 5005-H22, and the solar panel is made of CFRP M18/M55J.

The studied solar panel has a total thickness of 20 mm. It has an 8-ply laminate skin with a stacking sequence of $[45°/-45°/0°/90°]_s$. A lamina has a nominal thickness of 0.13 mm and a fiber volume fraction of 60%. The solar panels are 740 mm x 840 mm in dimension. It must be designed to reserve a middle area for solar cells with top and bottom margins of 70 mm and left and right margins of 30 mm, as shown in Figure 1(left). The top margin region is set aside for torsion hinge placement when installing the solar panel. The bottom margin area is reserved for holes to install burn-wire in the center and stoppers on both sides.

A hexagonal-head aluminum bolt M4 x 0.7 is planned as the recommended pitch and edge distance for the solar panel, with a safety factor larger than 2 [12]. The pattern on the bottom border region remains the same. The top margin area was analyzed for five in-line bolt patterns, which were termed Pattern I, II, III, IV, and V, as illustrated in Figure 1(right). A pair of bolts with 50 mm pitch and 25 mm edge distance are joined to a torsion hinge. Torsion hinges on solar panels are represented by flat plates measuring 25 mm x 50 mm x 2 mm. A pair of holes are drilled to attach the bolt to the primary structure. The stopper is the same size as the plate of the torsion hinge. The five patterns use one to three torsion hinges: only Pattern I uses one, Patterns II and III use two, and the remaining patterns use three. All patterns are symmetric to the panel's center line.

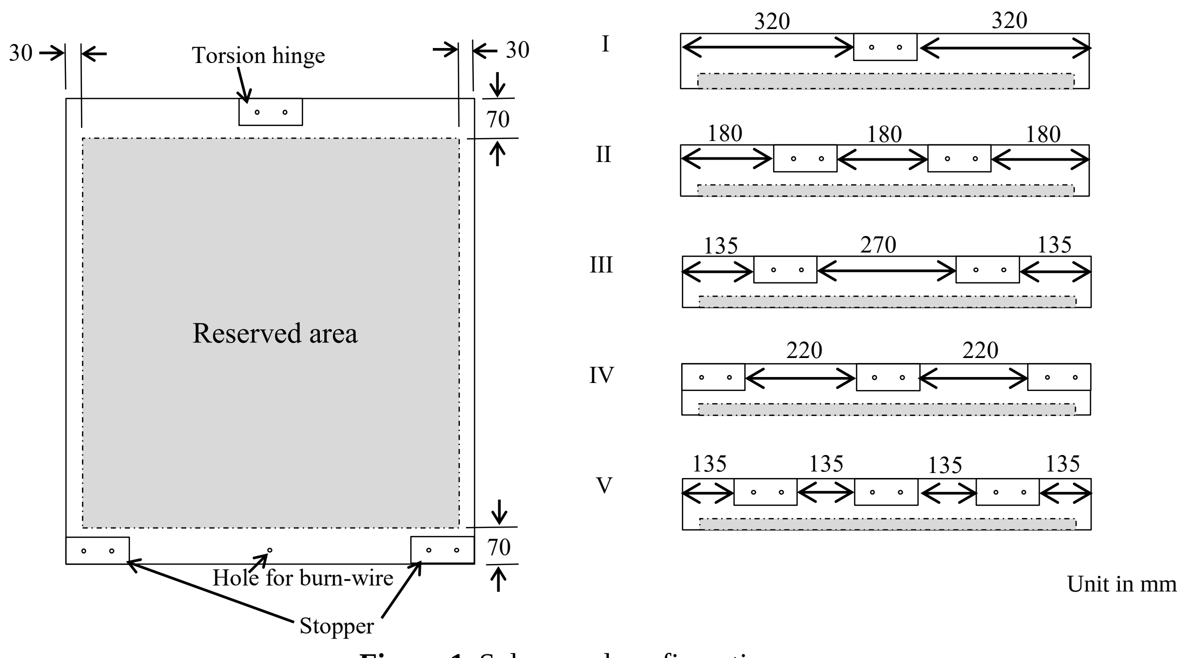

Figure 1. Solar panel configuration.

A solar panel is made up of several materials, with the core being more prone to failure at connections due to its lower stiffness than the skins. It is essential to strengthen the core by using inserts instead of the honeycomb core, which is weaker material. Composite potted inserts must be inserted after the sandwich panel is manufactured to prevent local stress concentration through the connection [13-14]. The through-the-thickness insert type CM607-M4-N24AM was chosen with the locking torque suggestion into the finite element model [14].

3. FE Modelling

Due to the high level of detail and the numerous joints, it is exceedingly challenging to include detailed bolted joint models in a FE modeling of the entire satellite. Three-dimensional CAD models of the sandwich panel were constructed, as previously described. All insert-related components were simplified by representing them as axisymmetric skins, inserts, and potting elements for assembly with the sandwich panel. By placing a plate at the corresponding bolt pattern, the five patterns intended for the construction of torque hinges were represented. Clamping pressure was applied straight from 1.2 Nm locking torque to represent the bolts. The surface is subjected to 96 MPa, which is 1.5 times the nominal diameter [8]. Aluminum was used to make all of the inserts, bolts, torsion hinges, and stopper plates.

3.1. Plate assembly and insert-related components

This section contains the first example of the five patterns, Pattern I, as well as its component elements. The model in Figure 2 represents Pattern I and other insert-related elements. The assembly models for the remaining patterns were created using the same manner. All assembly models were created using the commercial software SolidWorks.

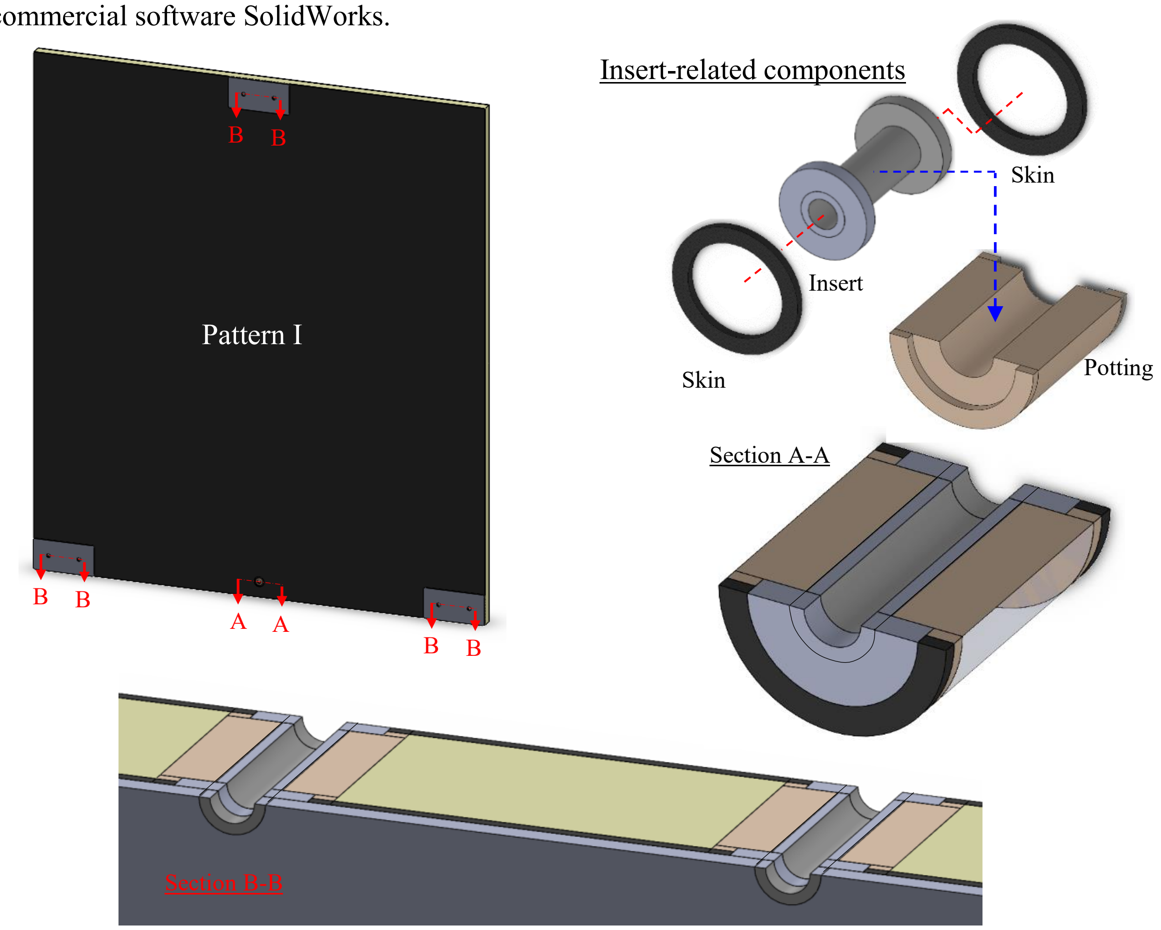

Figure 2. Final assembly of Pattern I and insert-related components.

All dimensions of insert-related components were established using the market's commercial insert, which was represented as axisymmetric for ease of simulation [14]. The top and bottom flanges of the insert models were made with a thickness of 1 mm and a diameter of 12 mm. Its entire thickness corresponds to the sandwich panel's total thickness of 20 mm. At a diameter of 6 mm, the insert's strut was designed to take pressure from preload into consideration. Due to the fact that inserts frequently fail under a pull-out stress, potting material with a 16 mm diameter must be used to increase this resistance. Figure 3 shows two in-line bolts in the cutting section, which corresponds to section B-B in Figure 2, spaced 50 mm apart. The colors of the bolted joint assembly display the different materials.

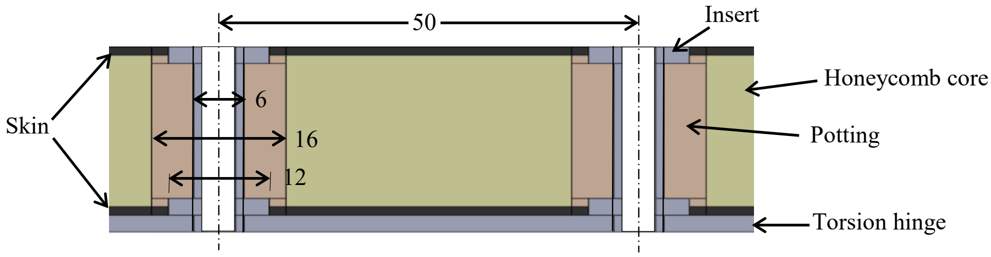

Figure 3. Cutting section of a pair of bolted joint assemblies, dimension in mm.

3.2. Material Assignment

Four material characteristics were taken from the satellite panel itself and implemented into the models. Analytical and numerical methods were used to determine the material properties of CFRP M18/M55J skins and honeycomb core, respectively. Potting and aluminum that are purchased from the manufacturer have isotropic material characteristics. The elastic modulus of aluminum employed in the model is 70 GPa, the Poisson's ratio is 0.33, and the density is 2,770 kg/m^3. The model's potting Araldite material has the following characteristics: a density of 936 kg/m^3, a Poisson's ratio of 0.3, and an elastic modulus of 315 MPa. Based on the lamina properties listed in Table 1, the laminate properties of the skins were calculated using the classical lamination theory [1]. Table 2 shows laminate properties of the lay-up [45°/-45°/0°/90°]$_s$. This is an orthotropic material that has the same material behavior as the core. The ANSYS honeycomb creator extension was used to determine the properties of the core referred to in [10], which are shown in Table 3.

Table 1. Unidirectional mechanical properties for a CFRP M18/M55J lamina [15].

V_f	ρ (kg/m^3)	E11 (GPa)	E22 = E33 (GPa)	G12 = G13 (GPa)	G23 (GPa)	ν12 = ν13	ν23
0.6	1,600	301	5.9	4.6	3.17	0.27	0.4

Table 2. Laminate mechanical properties for CFRP skins.

ρ (kg/m^3)	Exx = Eyy (GPa)	Ezz (GPa)	Gxy (GPa)	Gyz = Gxz (GPa)	νxy	νyz= νxz
1,600	106	5.9	2.31	2.5	0.06	0.37

Table 3. Honeycomb AL3003-H18 mechanical properties [10].

ρ (kg/m^3)	Exx=Eyy (MPa)	Ezz (MPa)	Gxy (MPa)	Gyz (GPa)	Gxz (GPa)	νxy	νyz= νxz
45.41	100	1,150	1	165	244	0.49	0.01

3.3. Boundary Conditions

Five patterns for all three-dimensional models were transferred to the ANSYS program for analysis. Figure 4 exhibits a detailed model of the Pattern I panel, including a torsion hinge in an aluminum plate on the top area attached to the primary structure of the TSC-1 satellite. A hole in the bottom reserved area and two aluminum stoppers are also included in the model. Every hole has an insert to reinforce the panel. The area surrounding the hole, which has an inner and outer diameter of 4 mm and 6 mm, respectively, in the bottom reserved area, was restrained or blocked in z-translation. Again, the bolt was not explicitly represented in the model; instead, the preload was applied as pressure over the insert's strut as previously mentioned. Solid elements with a quadratic element order were used to model each component. Torsion hinge aluminum plates had their top surfaces fixed, signifying their connection to the primary structure. As seen in Figure 5, all of the subsequent models were modified from Pattern I. To attach to the torsion hinge, as previously described, the remaining patterns were adjusted in the top area. The model's boundary conditions were all added using the same technique.

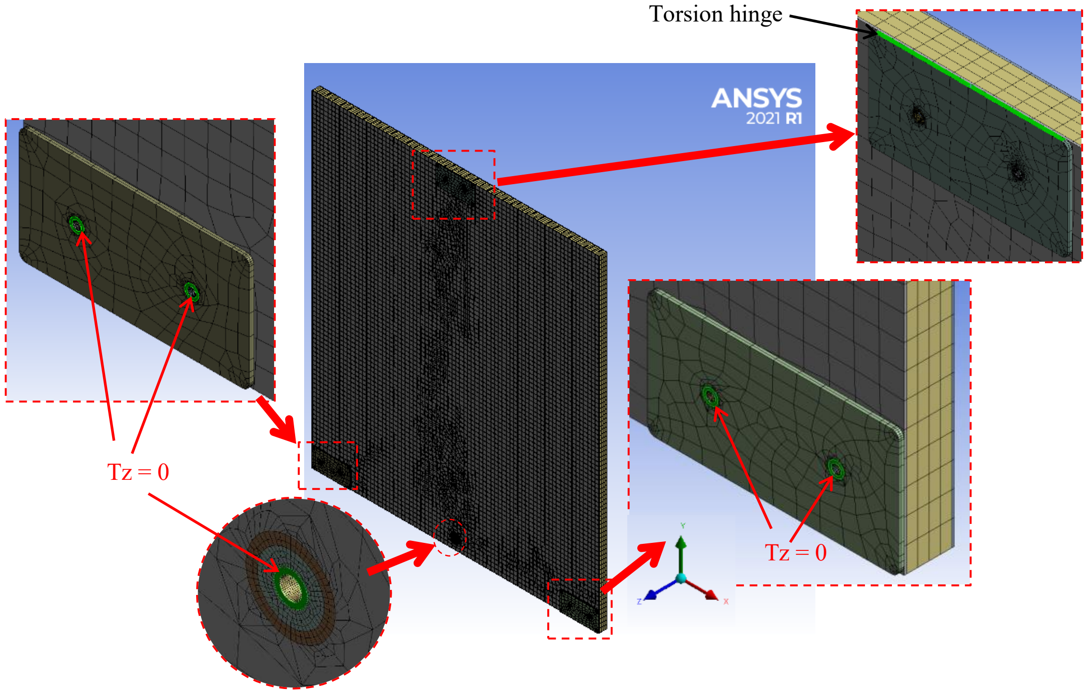

Figure 4. Boundary conditions of the Pattern I.

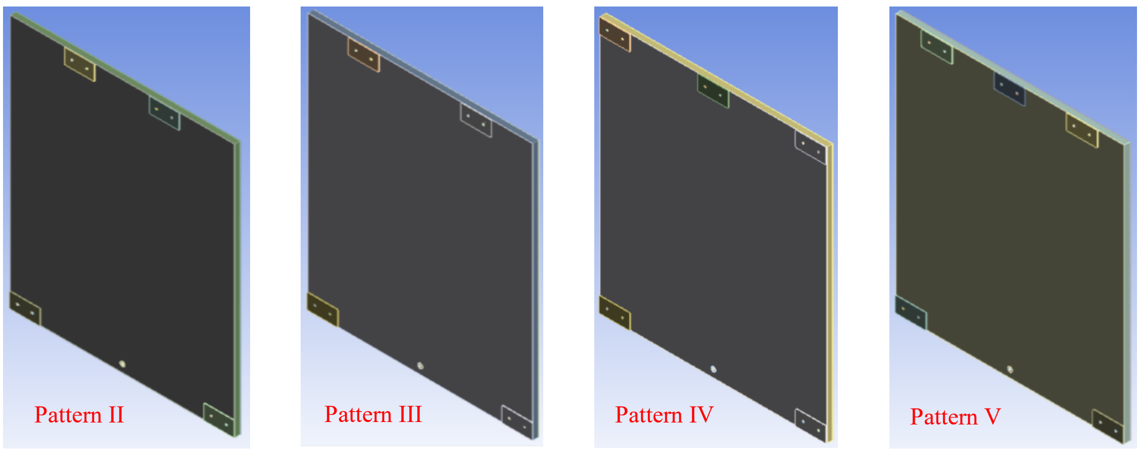

Figure 5. Four models of the remaining patterns.

4. Results and Discussion

In this paper, the Finite Element Method was used as the major investigation technique. The static analysis findings show preload around each bolt, as shown in Figure 6 (a). Under static loading, the stress fields are local, presenting roughly 20% less than applied pressure while remaining safe for the corresponding torsion. Natural frequencies are examined using modal analysis tools by ANSYS software.

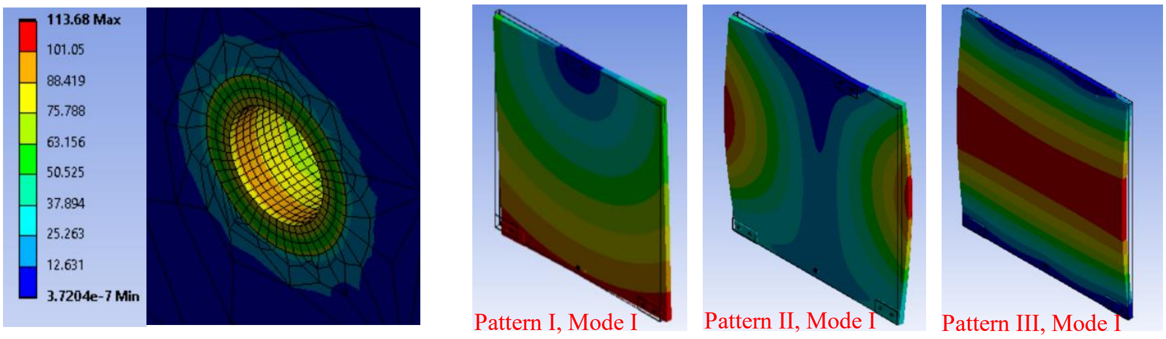

(a) (b)

Figure 6. (a) Local stress around a hole and (b) Typical mode shape of the 1st vibration mode.

Table 4 and 5 summarize the results of the first six vibration modes. Only one torsion hinge (Pattern I) has a substantial influence in the lowest eigen-frequency mode, but the other patterns provide a 2.5 times larger value. The first vibration mode is unaffected by the panel's use of more torsion hinges, which is determined by 152.86 - 159.58 Hz for Pattern II-V. Because only one torsion hinge joint will likely be to perform side-sway action, in-plane mode shape is more essential than out-of-plane vibration pattern, as demonstrated in Figure 6 (b). The mode shape of the lowest vibration mode identified is altered to out-of-plane deformation by adding one more torsion hinge.

Table 4. First six modes for five patterns.

Mode \ Pattern	I	II	III	IV	V
1	61.71[a]	152.86[b]	156.89[b]	159.15[b]	159.58[b]
2	84.66[b]	153.43[b]	163.99[b]	173.23[b]	170.06[b]
3	133.98[b]	196.78[a]	226.24[a]	292.58[a]	256.73[a]
4	272.64[b]	408.45[b]	457.90[b]	470.16[b]	466.12[b]
5	311.72[b]	422.45[b]	481.76[b]	504.07[b]	510.92[b]
6	461.69[b]	473.75[b]	490.77[b]	538.22[b]	528.20[b]

[a] Side-sway (in-plane) mode shape is more critical than an out-of-plane one.
[b] Out-of-plane mode shape is more critical than a side-sway (in-plane) one.

When Pattern II and III are compared, the spacing between torsion hinges has only a slight impact on the frequency of the first vibration mode but has a substantial impact on the side-sway mode shape in the third modal frequency. When comparing the torsion hinge spacing for Patterns IV and V at the third modal frequency, the same tendency can be seen. This could lead to a decision on a bolted joint junction for a solar panel. Two torsion hinges are sufficient for ridesharing with the launcher. The spacing between each torsion hinge could effect on the pattern of vibration. Three of them may be stiffer, with no additional impact other than increased weight and reduced reserved area for the solar cell.

Table 5. Mode shapes of the first six modes for five patterns.

Mode	Pattern I	Pattern II	Pattern III	Pattern IV	Pattern V
1	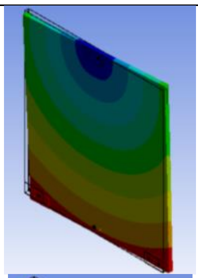	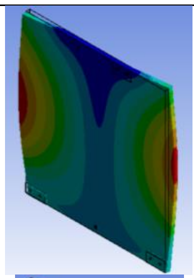	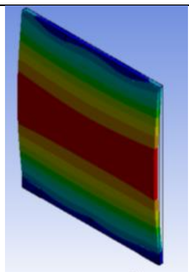	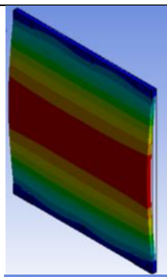	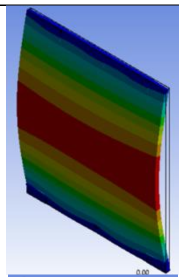
2	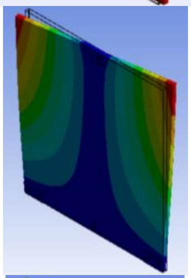	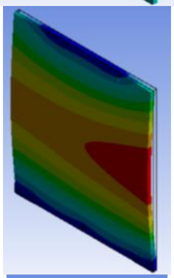	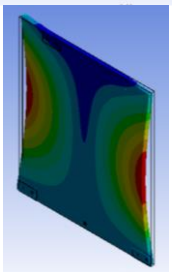	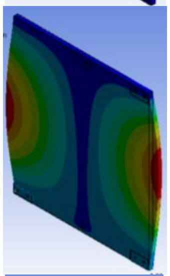	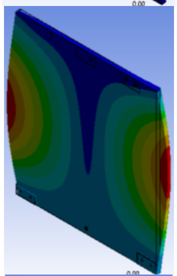
3	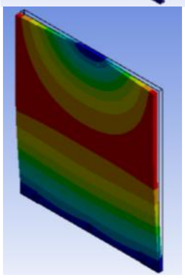	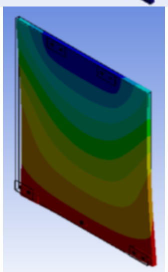	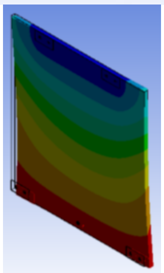	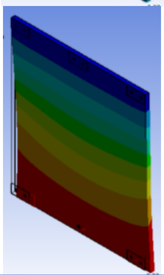	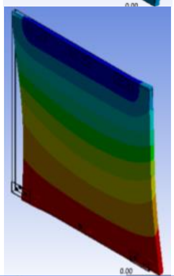
4	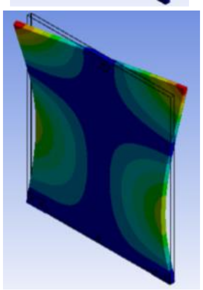	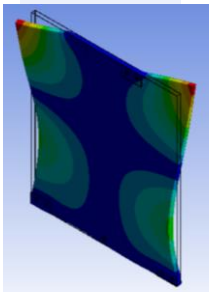	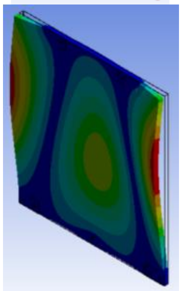	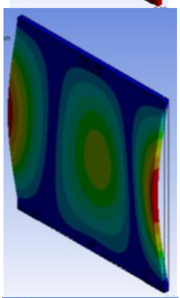	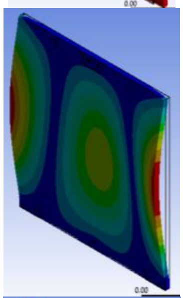
5	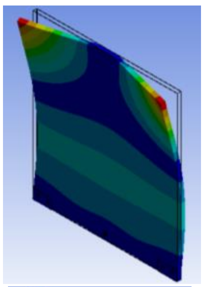	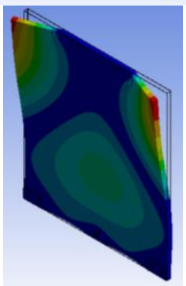	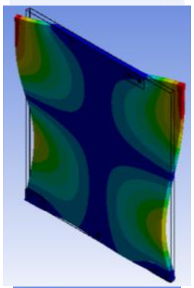	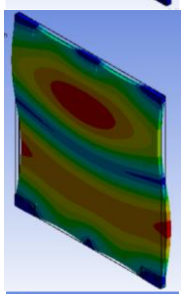	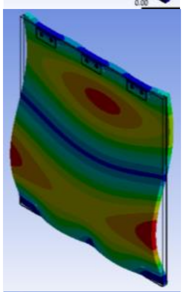
6	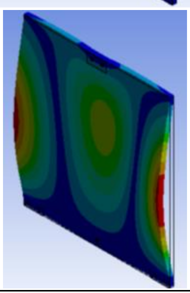	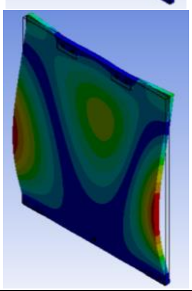	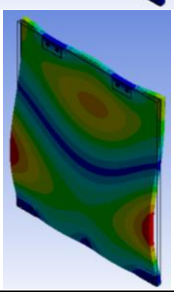	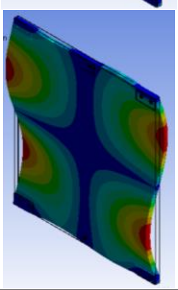	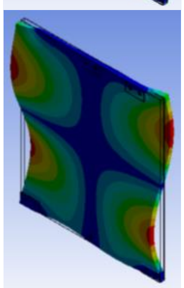

5. Conclusion

There is a lot of satellite structure on bolted joint junction. Many analytical and numerical bolted joint models have been investigated under static and dynamic loading. This work presents a numerical evaluation of the vibration characteristics of the most optimal bolted joint junction arrangement. Another bolt pattern design that could be used instead of in-line is two rows, although that is beyond the scope of this study. Honeycomb core modeling, on the other hand, might be more detailed by replacing solid elements with shell elements that correspond to the physics of the aluminum sheet. Instead of defining the bolted joint junction as a function of preload, the results avoid contact between the bolt strut and the hole surface. Indeed, numerical results alone may not be adequate to cover all aspects of the loading requirements that have been addressed. Further research is required to put up the test to validate the model. More study is being conducted on the TSC-1 satellite's overall construction, including all launch environment components.

6. Acknowledgments

The authors wish to acknowledge assistance in providing initial information from the National Astronomical Research Institute of Thailand (Public Organization).

7. References

[1] Jones, R. M. (1999). Introduction to composite materials. *Mechanics of composite materials*, 1-53.
[2] *SpaceX* (2022). *Rideshare payload user's guide*. Space Exploration Technologies Corp.
[3] Sen, F., Pakdil, M., Sayman, O., & Benli, S. (2008). Experimantal failure analysis of mechanically fastened joints with clearance in composite laminates under preload. *Materials and Design*, 29, 1159-1169.
[4] Coman, C.-D. (2018). Numerical analysis for the influence of the geometrical and mechanical parameters on the stiffness and strength of the compostie bolted joints. *INCAS Bulletin*, 10(4), 21-33.
[5] Coman, C.-D. (2018). Static and dynamic design methods for hybrid bolted joints in a satellite structure. *INCAS Bulletin*, 10(2), 185-197.
[6] Broughton, W. R., Crocker, L E., & Gower, M. R. L.(2002). *Design requirements for boned and bolted composite structures*. NPL report MATC (A) 65. Crown.
[7] Chutima, S., & Blackie, A. P. (1995). Effect of pitch distance, row spacing, end distance and bolt diameter on muti-fastened composite joints. *Composite Part A*, 27A(2), 105-110.
[8] Budynas, R. G., & Nisbett, J. K. (2011). *Shigley's mechanical engineering design*. McGraw-Hill.
[9] Brown, K. H., Morrow, C., Durbin, S., & Baca, A. (2008). *Guideline for bolted joint design and analysis: version 1.0*. Sandia National Laboratories.
[10] Mongkolves, S., Sangthon, A., Torteeka, P., Meenakand, P. & Saisutjarit, P. (2021). Structural analysis of Thai Space Consortium-1 satellite based on Falcon 9 launch vehicle vibration profile. In *the 2nd Innovation Aviation and Aerospace Industry, International Academy of Aviation Industry (IAAI)* (Vol. 1, p. 28-30).
[11] Phichayophas, C., Suratatchai, M., Sripawadkul, V., Bunyawanichakul, P., Mongkolves, S., & Sangthon, A. (2022). Vibration characteristics of honeycomb sandwich panel for Thai Space Consortium-1 satellite. In *the 6th Southeast Asia Workshop on Aerospace Engineering* (Vol. 1, p. 84-92).
[12] Gay, D., Hoa, S. V., & Tsai, S. W. (2003). *Composite materials: Design and applications*, CRC Press.
[13] Shur-lok (1996). *Shur-lok design manual: Fasteners for sandwich structure.* Shur-lok Corporation.
[14] Clarendon (2021). *Potted inserts: product catalogue.* Clarendon: Specialty fasteners.
[15] European Cooperation for Space Standardization (2011). *ECSS-E-HB-32-20 Part 1A.* ESA Requirements and Standard Division.

AME0005

Study of Variable Operating Parameters Effect on PEMFC Performance

P D Thao[1], V T Chau[2], N H Khan[1], S Mek[1], S Hirai[3], and L Visarn[4,*]

[1]Department of Mechanical Engineering, School of Engineering, King Mongkut's Institute of Technology Ladkrabang, 1 Chalong Krung 1 Alley, Lat Krabang, Khet Lat Krabang, Krung Thep Maha Nakhon 10520, Thailand
[2]Faculty of Automotive Engineering Technology, Industrial University of Ho Chi Minh City, Go Vap District, Ho Chi Minh City, 727900, Vietnam
[3]School of Engineering, Tokyo Institute of Technology, Meguro City, Tokyo, 152-8550, Japan
[4]National Energy Technology Center (ENTEC), National Science and Technology Development Agency, Pathum Thani, Bangkok, 12120, Thailand

* Corresponding Author: visarn.lil@entec.or.th

Abstract. The Proton Exchange Membrane Fuel Cell (PEMFC) is considered as the main fuel cell candidate technology for light-duty and heavy-duty transportation applications with high power densities generating. Studies in improving PEMFC performance help reduce the powertrain size and weight of fuel cell electric vehicles (FCEVs). Relative humidity (RH) and operating temperature (OT) are the key operating parameters contributing to PEMFC characteristics. In this study, the effects of RH and OT on the PEMFC performance were investigated by varying RH from 50% to 70% and OT from 60°C to 80°C. The experiments were conducted on a single PEMFC cell with an active area of 25 cm^2. Polarization curves and power graphs were used to study the effects of OT and RH on PEMFC performance. The impacts of OT and RH were examined based on the range analysis method. The experiment results show that, the OT has more influence on PEMFC performance than RH. Besides that, individual effects of OT and RH changed when taking both parameters into study the combined effects. Furthermore, the group of appropriate combined operating parameters of the fuel cell was defined to maximize the PEMFC performance.

Keywords: PEMFC, Performance, Temperature, Humidity.

1. Introduction

The soaring reliance on fossil fuels for the automotive industry and their environmental impacts have attracted researchers to explore alternative solutions for internal combustion engine vehicles (ICEVs). Fuel cell electric vehicles and battery electric vehicles (BEVs) are the main candidates to be successors [1]. Among them, FCEVs provide a longer range, shorter refueling time within two minutes, better tolerance of cold weather, and lighter weight compared to BEVs in light-duty transportation applications [2]. The PEMFC is usually used for FCVEs due to its wide range of power density (1×10^{-3}~250 kW), high efficiency at the energy conversion and its friendly user operating conditions [1-3]. In comparison of efficiency for transportation, PEMFCs performed at 40–50% while the current efficiency of ICEs is 20–35% [4]. The normal electrochemical reactions in a PEMFC are represented in Equations (1) to (3) [5]:

Anode side: $$H_2 \rightarrow 2H^+ + 2e^- \quad (1)$$

Cathode side: $$\frac{1}{2}O_2 + 2H^+ + 2e^- \rightarrow H_2O \quad (2)$$

Overall reaction: $$H_2 + \frac{1}{2}O_2 \rightarrow H_2O \quad (3)$$

However, one of the primary drawbacks of FCEVs is carrying a fuel cell system consumes plenty of weight and space [4]. Efforts to enhance PEMFC performance can help to reduce the size, weight, and cost of the fuel cell stack, the inverter and the motor [6]. Several two- and three-dimensional models on PEMFC characteristics of transport in membrane, catalyst layers, gas diffusion layers, and channels were developed for improving transport in membrane, catalyst layers, gas diffusion layers, and channel; and performance of PEMFCs [7]. A large number of research focus on the development of new materials (e.g., $La_{1-x}Sr_xGa_{1-y}Mg_yO_3$ oxide ion conductors) as well as new processing techniques (e.g., electrocatalyst-layer deposition for polymer electrolyte fuel cells) achieved a rise in power densities [5]. Besides that, the design of test systems using PID, Fuzzy, even machine learning control logics were conducted for examination [8-10], evaluation [9, 11], and optimization [9, 12] of operating parameters on PEMFC performance and efficiency. On one hand, the typical value of OT (°C) and RH (%) were (60, 70, 80) [3, 8, 9, 13-22] and (50, 60, 70) [3, 9, 16-21, 23, 24], respectively. On another hand, many studies of individual operating conditions effects on PEMFC performance using hydrogen with air or oxygen were carried out. Then, they came up with different optimal values of hydrogen stoichiometry ratio (HSR), air stoichiometry ratio (ASR), OT, and RH such as: (HSR 1.2, ASR 1.5, OT 60°C, 50RH %) , (HSR 1.5, ASR 2.0, OT 65°C, RH anode 100 %, RH cathode 80 %) [22], (HSR 1.5, ASR 2.0, OT 90°C, RH anode 90%, RH cathode 50%) [24], and (HSR 1.5, ASR 2.0, pressure 3 bar, OT 60°C, RH 100%) [25]. These differences are the driver to study the operating parameters of fuel cells. Unfortunately, the cell size is small, and the combined effects of several operating parameters simultaneously are the barriers withstanding the investigation of these factors. Therefore, understanding the individual and combined effects of operating parameters on PEMFC performance is essential to the development of high-performance PEMFCs. In accordance with the Nernst equation and the exchange rate, the OT, gas inlet pressure, air RH and ASR of cell are known to influence the performance of PEMFC, which are expressed in Equation (4) and Equation (5) [3, 5, 18, 26].

Nernst equation $$\mathrm{E} = \mathrm{E}_0 - \frac{\mathrm{RT}}{2\mathrm{F}} \ln \frac{1}{\mathrm{p}_{\mathrm{H}_2}\, \mathrm{p}_{\mathrm{O}_2}^{\frac{1}{2}}} \quad (4)$$

The exchange rate between reactants and products under balanced state can help to improve the performance of fuel cells by increasing the concentration of reactants [1].

$$\mathrm{J}_0 = \mathrm{nFC}_{\mathrm{R}}^{*}\mathrm{f}_1 \mathrm{e}^{-\frac{\Delta \mathrm{G}_1^{\dagger}}{\mathrm{RT}}} \quad (5)$$

Several studies applied orthogonal experimental design and range analysis to optimize the parameters of PEMFC under steady working conditions. With the help of four factors (OT, gas inlet pressure, RH, and ASR) and three levels orthogonal table, Shixiang Xia et al. showed the results that the effect of ASR and gas inlet pressure on PEMFC performance are the largest under the conditions of medium-high and low current densities, respectively, while the OT and air RH have little impact on the performance of PEMFC [4]. Besides that, Dengcheng Liu et al. concluded the impact of ASR and OT on the output voltage of the stack was obviously higher than that of RH and backpressure regardless of the change of load conditions [18]. These studies performed the thought of full factorial. However, they showed the conflicts impact of OT on PEMFC performance. Part of the reason is that they neglected many cases owing to orthogonal experimental design, which helps to save time and effort of conducting experiments, so this method cannot achieve a comprehensive evaluation of parameter effects. Moreover, in the viewpoint of FCEVs design, the large weight and size of the humidification system and heat dissipation are technical barriers that need to be resolved [2]. Additionally, RH has a greater impact on conductivity than OT, conductivity drops dramatically due to dehydration [5]. Efforts to eliminate the fuel cell subsystem as a humidification system are consequential to make the FCEVs best design [26]. In this paper, the effects of typical OT range (60-80°C) and medium range RH (50-70%) on PEMFC performance over the raise of current density were investigated based on the polarization curve and the range analysis method. Furthermore, the individual and combined effects of OT and RH were evaluated and compared to each other to highlight the difference between them.

2. Experimental

2.1. Experimental setup

2.1.1. PEMFC components

A PEMFC single cell with 25cm^2 of active area was used throughout this study, which was produced by Fuel Cell Technologies Incorporated and shown in Figure 1. The proton exchange membrane used in the study is a Nafion ©112 with a thickness of 50 µm. The platinum loading on both anode catalyst layer and cathode catalyst layer is 0.3 mg/cm^2. The microporous layer (MPL) was attached to the gas diffusion layer (GDL). The flow fields on both sides had a triple serpentine channel configuration that led gases into the cell under co-flow direction. The current collectors were made of copper coated gold and the aluminum coated gold was applied to the two endplates.

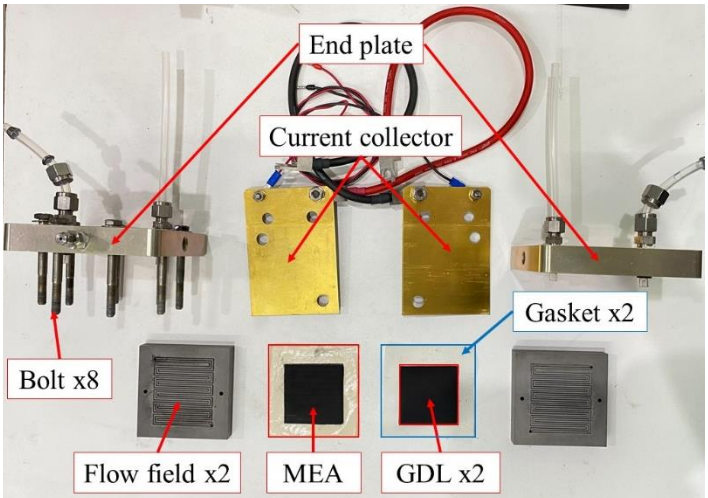

Figure 1. PEMFC components.

Besides that, two heating rods were installed in the anode and cathode endplates and a thermocouple in the cathode endplate was used to inspect the OT of cell. Then, the single cell was assembled by eight bolts at 5 Nm torque and checked with liquid leak detector to ensure there is no gases leaking out the cell during experiments.

2.1.2. Test system schematic diagram

In this study, all the experiments were performed by a self-design test system which is demonstrated in Figure 2. This work used compressed gases from stored tanks with hydrogen (99.5%) as a reducer and air as an oxidant. The gases pressure was controlled by the regulators before coming in the volume flow controllers. After that, the flow was kept at a constant at each operating condition and then they were humidified with deionized (DI) water by humidifiers. Pre-heaters were used to heat up the connecting tubes to ensure there was no condensation on the tube wall before humidified gases flow into the cell.

The test system could regulate (1) the reactant gas flow or the reading value (RD) with full scale (FS) of mass flow rate from 51 smL/min to 20 sL/min and flow accuracy ± (0.5%RD ± 0.2%FS); (2) correctly load up to 120V, 30A, and 150W at constant voltage (CV), constant current (CC), and constant power mode (CP), respectively; (3) relative humidity of the inlet gases from 0 to 100%; (4) OT range is 0 - 400°C with resolution of 0.1°C and accuracy ±0.5%FS.

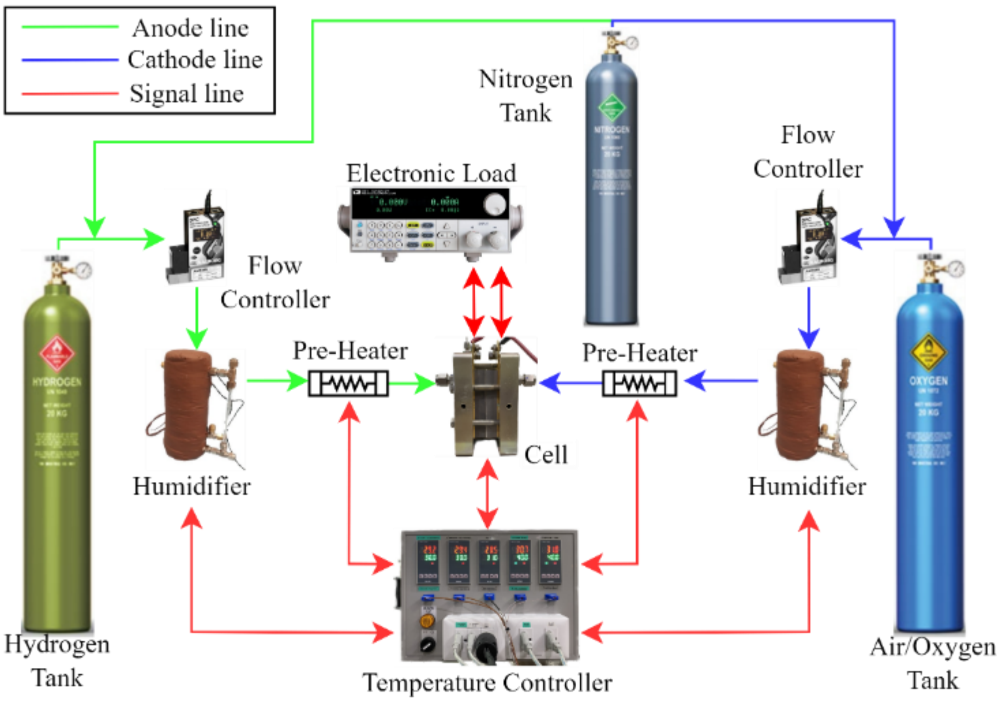

Figure 2. System schematic diagram.

2.2. Experimental procedures

2.2.1. MEA activation

After the cell was assembled and connected the test system, the activation process was conducted before the cell was put into formal experiments. As a result of the MEA and stack manufacturing process, the catalyst layer contained impurities hindering the PEMFC performance. Therefore, a period of operation was needed to remove impurities and help the cell reach incubation phase to improve its performance [27]. In addition, the new proton exchange membrane was initially dry and required to be hydrated to establish transport channels for hydrogen protons [18, 28].

The activation conditions were set at 70°C OT, 80% RH, and 150 smL/min gases flow rate on both sides. To begin with nitrogen at open circuit voltage (OCV) in an hour. After that, hydrogen and air were fed into the cell at OCV in 30 minutes. Then, the CC load was applied at 0.1A/cm^2 in five hours. Finally, the cell output voltage seemed unchanged and had no longer raise, which indicated the activation was complete.

2.2.2. The cell output voltage testing and performance characterization of PEMFC

The levels of OT and RH were determined by selecting some typical values of parameters, three levels of OT (°C) and RH (%) were (60, 70, 80) and (50, 60, 70), respectively. The nine operating conditions composed of two factors and three levels are shown in Table 1.

Before conducting each specific operating conditions, the cell was purged with N_2 at 200 smL/min in 5 minutes both sides to remove water droplets, and/or film in the flow channels, also the gases come from the air and/or remained from the previous experiment. In accordance with Table 1, the nine polarization curves were contrasted with the nine groups of operating condition results and the performance changes were also performed in different current densities. In order to draw polarization curves, the current density was held at 12 points: 0, 0.016, 0.032, 0.05, 0.1, 0.15, 0.2, 0.25, 0.3, 0.375, and 0.4 A/cm^2. After changing the operating parameters (such as OT, RH, and CC load), the cell output voltage was recorded after 15 minutes at each point to reach the steady state reading. During these experiments, the HSR and ASR were kept stable at 1.5 and 2.0, respectively. At the meantime, the back pressure was kept at ambient pressure and the flow rate of gases was calculated due to CC load value while the minimum hydrogen flow rate was always remained at 100 smL/min to prevent starvation at the anodic electrode resulting in carbon support degradation of the catalytic layer which is considered to be the most hazardous [29].

Table 1. The operating conditions table with two factors and three levels.

Experiment Number	Factor	
	OT (°C)	RH (%)
1	60	50
2	60	60
3	60	70
4	70	50
5	70	60
6	70	70
7	80	50
8	80	60
9	80	70

The range analysis, which was applied to define the influence degree of OT and RH from nine experiment results, was a statistical method to determine the factors sensitivity to the experimental result [30]. The calculation process of range analysis is shown in Equation (6) and Equation (7) [31].
Difference between the average value of experimental results which contain factor X with m levels ($\overline{I_{Xm}}$) and the average value of all results (Y):

$$\delta_{Xm} = \overline{I_{Xm}} - Y \tag{6}$$

The influence degree of the factor X:

$$T_X = R_{Xmax} - R_{Xmin} \tag{7}$$

Where
$$R_{Xmax} = \max(\delta_{X1}, \delta_{X2}, \dots, \delta_{Xm})$$
$$R_{Xmin} = \min(\delta_{X1}, \delta_{X2}, \dots, \delta_{Xm})$$

Range is defined as the distance between the extreme values of the data. The greater the range is, the more sensitive the factor is [30].

3. Results and discussion

In practice, the output voltage of PEMFC is lower than reversible voltage (E_0) according to irreversibilities such as activation, ohmic, and concentration losses, which are active throughout the entire polarization curve [2]. Therefore, in this study, the current density was separated into three ranges including low current density (0-0.05 A/cm^2), medium current density (0.05-0.3 A/cm^2), and high current density (0.3-0.4 A/cm^2) to observe the different impacts of OT and RH on PEMFC performance. The polarization curve, in combination with the power curve, is usually used to determine optimum operation points in terms of voltage, current, and power [2]. Besides that, the changes in polarization curve would lead to the changes of cell power considering the same current density range.

3.1. *Effect of operating temperature*

The operating temperature has direct effect on the ion conductivity of the membrane, electrode kinetics, and mass transfer of the reactants [32]. Hence, fuel cell OT was an impactful parameter, and was selected to examine its effect on PEMFC performance. The effects of OT on PEMFC performance under various RH values were demonstrated in the polarization curves together with power curves shown in Figure 3. It was obvious that OT had small impact on PEMFC performance at the low current density range under varying RH conditions. Its influence was considerable at medium current density range, and dramatic at the high current density range.

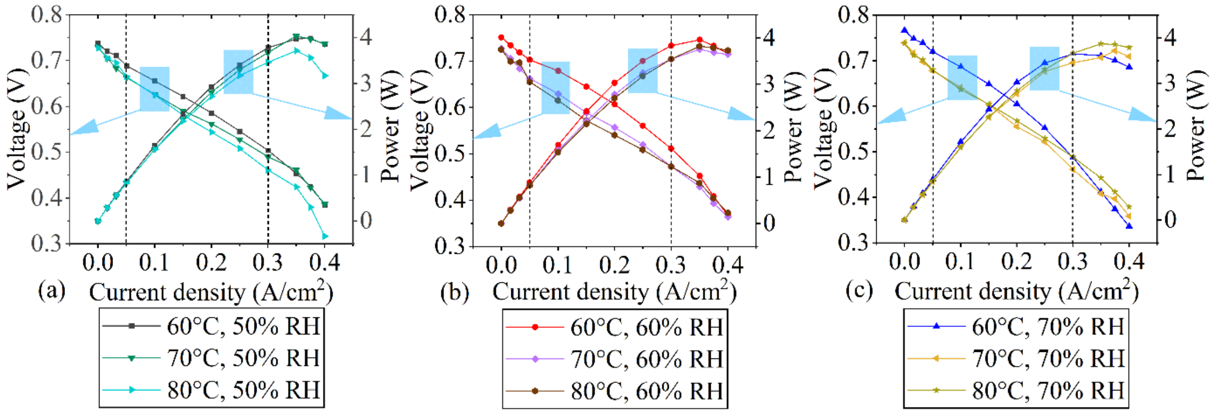

Figure 3. Effect of various OT on PEMFC performance at (a) 50% RH, (b) 60% RH, and (c) 70% RH.

3.1.1. *Effect of OT at 50% RH*

It could be observed in Figure 3 (a) that the cell output voltage dropped according to the rise of OT, and it generated the maximum power at 60°C. At the medium range of current density, the cell output voltage trendline was enhanced at 60°C. Especially, at the high current density range, the lower OTs had a positive impact on the cell voltage while the high OT (80°C) led to the plummeting of cell potential because the membrane inside the fuel cell lost its moisture, and the ion transportability was reduced [22].

3.1.2. *Effect of OT at 60% RH*

At 60% RH, the cell output voltage seemed to be upward trend due to the increase of OT as demonstrated in Figure 3 (b). The cell voltage raises remarkably at 80°C OT compared to the lower ones at low and medium current density ranges because an adequate temperature helped to reduce the need of activation energy in the catalyst layer and improved the reaction rate achieved in enhanced PEMFC performance [13, 22]. However, the effect of OT at high current density was narrowed down, resulting in converging of cell potentials at 0.4 A/cm^2.

3.1.3. *Effect of OT at 70% RH*

Among three levels of RH, the combination of 70% RH and 60°C OT performed the best cell potential at medium ranges of current density, shown in Figure 3 (c). Besides that, the cell output voltage at 70°C and 80°C seemed unchanged throughout these ranges. Though, at the high current density range, the PEMFC cell generated the highest voltage at 80°C instead of 60°C, even when it touched the trough of cell potential due to flooding when operating at 60°C at 0.4 A/cm^2.

Generally, the effects of OT on PEMFC performance are inconsistent at different RH values. At the low and medium ranges of current density, 60°C OT is consider as optimal operating condition due to less amount of saturated water vapor is supplied to the fuel cell resulting in less water created. Thus the inlet region is less humidified, and the outlet region is less flooded [25]. However, at high current density range, 80°C OT generated good performance of PEMFC. Because the elevated temperature can simply remove water from inside the cell, potentially causing the membrane to lose its moisture [22].

3.2. Effect of relative humidity

In accordance with the OT effects, the RH also has direct influences on fuel cell reaction kinetics, mass tranfer, membrane resistance, and thus PEMFC performance [24, 32]. The effect of various RHs on PEMFC performance under different OTs are demonstrated in Figure 4. At low current density range, the RH had little effect on PEMFC performance, though its impact was evident at medium and significant at high current density ranges.

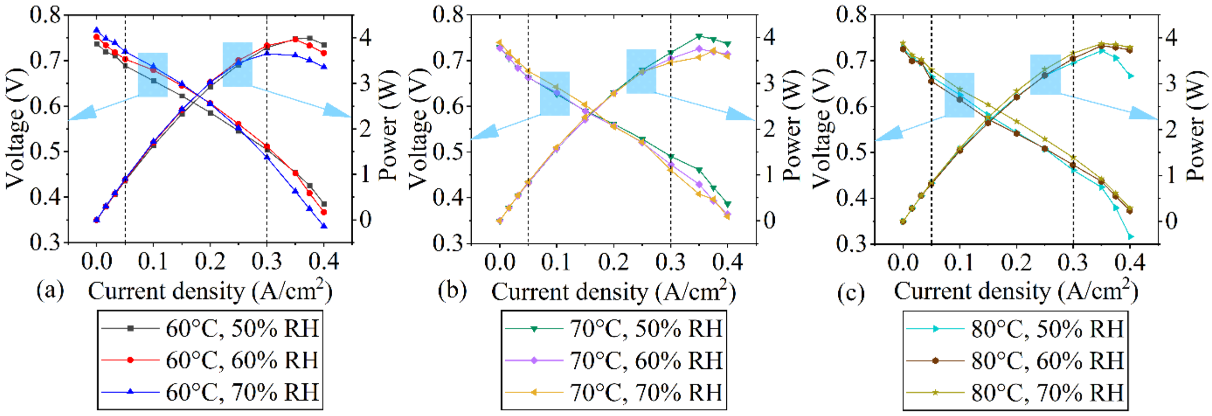

Figure 4. Effect of various RH on PEMFC performance at (a) 60°C, (b) 70°C, and (c) 80°C.

3.2.1. Effect of RH at 60°C OT

When PEMFC runs at low OT (60°C), the RH rise caused the decline of PEMFC power. Because at the high current density range, raising the RH leads to more water accumulation and flooding inside the flow channels [14]. As a results, the electrode reactions are hindered by reduced reactants concentration at reaction sites [2]. It was obvious that flooding started to occur from medium range of current density illustrated in Figure 4 (a). Remarkably, the gases of higher RH fed into the cell, the larger cell performance drop. The low RH condition was suited to the high current density due to the increased water generated [24].

3.2.2. Effect of RH at 70°C OT

At medium OT (70°C), the cell served the best potential at 50% RH, and was moderately influenced by the change in RH, resulting in the tiny gaps of output voltage lines within the medium range of current density in Figure 4 (b). In contrast, the rise of RH substantially enhanced the cell performance at the high current density range. Where the cell potential was maximized at 70% RH due to the rise of 70°C OT compared to 60°C OT, on account of water content in the membrane moved forward and transmission impedance falls with increasing relative humidity, which enhanced the proton conductivity [14, 22].

3.2.3. Effect of RH at 80°C OT

Figure 4 (c) clearly illustrated the rise of RH led to the increase of the cell output voltage at high OT (80°C). The high temperature of the cell contributed to internal water removal and promotes the water contained in membrane leading to high membrane conductivity [22]. The cell performance was optimal at 70% RH. During medium current density operation, the cell potential touched the trough at 60% RH, but it was improved at the high range while 50% RH deteriorated dramatically the cell performance. According to high OT, the membrane lost its moisture, and the ion transportability went down. The dryness of the membrane resulted in the elevation of impedance and the ohmic losses [22].

Throughout the RH experiments, it is judged that at the high current density range and 70% RH condition, the PEMFC faces more difficulties in water transport [24], so the 50% RH is the optimal condition for low OT (60°C) while the cell performance is maximized with 70% RH within medium and high 70-80°C OT.

3.3. Results and analysis of nine groups of combination parameters

The polarization curve shows the voltage of the PEMFC at different current densities. By measuring the polarization curves, the influences of the operating parameters such as OT and RH on the performance of PEMFCs can be characterized. [14]. The nine polarization curves and performances under different current densities of the desired experiments are shown in Figure 5.

In light of the prior individual analysis about effects of OT and RH on PEMFC performance, the optimal operating parameters of (1) OT was 60°C at the low and medium current density ranges, (2) OT was 80°C at the high current density range, (3) RH at low OT (60°C) was 50% RH, and (4) RH at medium and high OT (70-80°C) was 70%. However, when taking both OT and RH into combination study, the PEMFC voltage and overall power of three combinations (60°C and 50% RH), (60°C and 60% RH), and (70°C and 50% RH) were better than others. In which, the combined condition (60°C and 60% RH) did not perform great performance throughout the individual effect examinations.

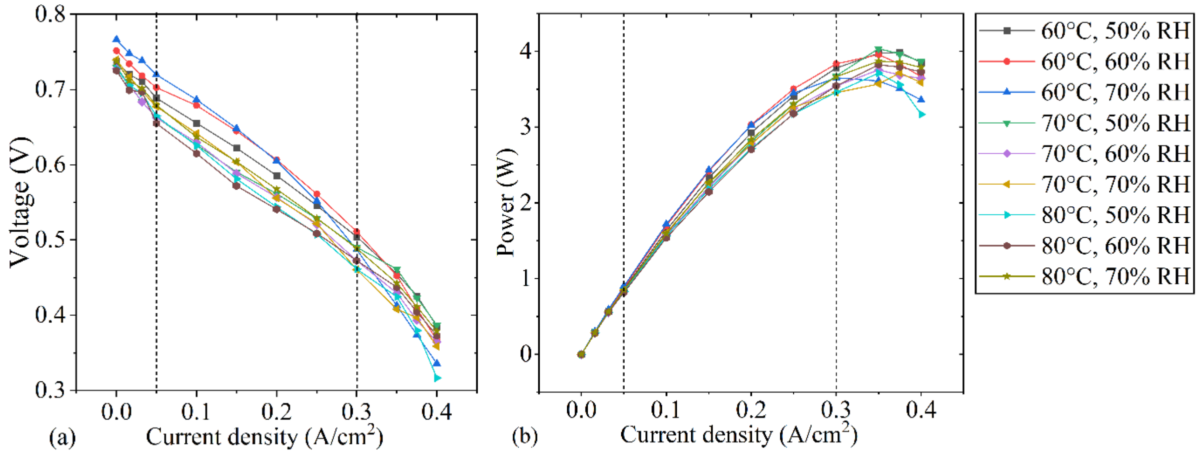

Figure 5. (a) Polarization curves and (b) Power curves of nine group tests.

Besides that, the PEMFC generated stable power within the low and medium current density ranges. At the high current density range, the operating parameters affected the PEMFC characteristic significantly, which resulted in substantial changes of power trend lines. Most of the power lines reached the peaks around 0.35 A/cm^2 and then voltage dropped sharply. Moreover, the worst overall power come from three combinations (70°C and 70% RH), (80°C and 50% RH), and (80°C and 60% RH) as a result of too high OT or RH effects on PEMFC performance.

3.4. Range analysis of nine group tests

The desired experiments were performed at different current densities. Using the range analysis method, the influence degrees of OT and RH on overall PEMFC power were calculated under 0.4 A/cm^2 and shown in Table 2. Figure 6 illustrated the influence degree of parameters to observe the parameters impact changes under different current densities.

Table 2. Calculation results of range analysis under 0.4 A/m^2.

Influence degree	Current density (A/cm^2)										
	0.000	0.016	0.032	0.050	0.100	0.150	0.200	0.250	0.300	0.375	0.400
OT	0.022	0.028	0.034	0.037	0.048	0.053	0.048	0.038	0.027	0.007	0.006
RH	0.016	0.015	0.016	0.020	0.019	0.021	0.012	0.007	0.007	0.026	0.016

Table 2 and Figure 6 show that OT has more impact on PEMFC performance than RH at the low and medium ranges of current density, which is demonstrated in the gap between influence degree of OT and RH approximately to 2-2.5 times.

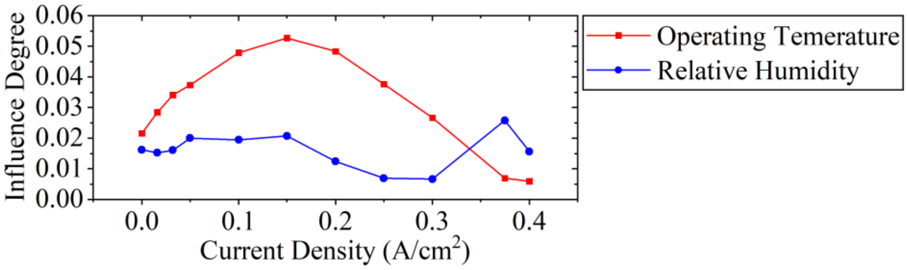

Figure 6. Influence degree of parameters on PEMFC performance.

The impact of OT is the largest at medium range of current density with the peak of influence degree at 0.15 A/cm^2 while the RH has a slight impact on PEMFC performance at low and medium current densities. When the PEMFC almost reach the peak of performance at 0.35 A/cm^2, the contributions of OT and RH on PEMFC performance look nearly equal. During these current densities range, the rise of OT is proportional to the increasing of overall cell performance. However, the roles of OT and RH have switched since the cell started to operate at high current density resulting in dropping dramatically of OT influence degree and tripling of RH influence degree. After the RH impact reaching the peak and causing the flood, it plummets at 0.375-0.4 A/cm^2 range due to flooding taking place inside the cell, which results in the major PEMFC power drop occurring in this range as shown in Figure 5 (b).

4. Conclusion

In this study, the output voltage and performance of a single PEMFC under varied operating temperatures and relative humidities were investigated experimentally. The individual and combined effects of the OT and RH on PEMFC performance were studied based on polarization curves, power curves, and range analysis. The main conclusions are summarized as follows:

(1) The OT contributed a small impact on PEMFC performance at the low current density range and its impact raised over the increase of current density. Within the medium current density range, the PEMFC power moved forward due to the rise of OT at 60% RH, but it dropped gradually according to the increase of OT at 50% and 70% RH. At higher current density, the OT tended to be optimal at high temperature (80°C).

(2) At the low current density range, the RH also had little influence on PEMFC performance. At the medium current density range, the RH impact was minimized especially when PEMFC operated at 70°C OT. However, the RH played decisive role at the high current density range. At low OT, the smaller RH (50%) is better, but the rise of RH (70%) is essential to PEMFC performance when the OT is high (70-80°C).

(3) Even the individual effects of OT and RH indicated the optimal operating conditions with a couple values of OT (60°C and 80°C) and RH (50% and 70%), the combination effects showed the maximum PEMFC overall performances at (60°C, 50%), (60°C, 60%), and (70°C, 50%). Thus, it is crucial to examine all the operating parameters for evaluation and optimization of PEMFC performance instead of individual parameters investigation.

(4) The OT had far larger impact than RH at low and medium ranges of current density. But at the high current density range, the RH would play more important role than OT. Moreover, they both contribute nearly equal impacts on PEMFC performance when its power is maximum.

5. Acknowledgments

The authors gratefully acknowledge the financial support from National Energy Technology Center (ENTEC) Thailand, the motivation and consulting from King Mongkut's Institute of Technology Ladkrabang, and Tokyo Institute of Technology.

6. References

[1] K. S. C. Yun Wang, Jeffrey Mishler, Sung Chan Cho, Xavier Cordobes Adroher. (2011). A review of polymer electrolyte membrane fuel cells: Technology, applications, and needs on fundamental research. *Applied Energy*, 88, 981–1007.

[2] M. F. O. Omar Z. Sharaf. (2014). An overview of fuel cell technology: Fundamentals and applications. *Renewable and Sustainable Energy Reviews*, 32, 810–853.

[3] R. L. Shixiang Xia, Xin Cui, & Jing Shan. (2016). The application of orthogonal test method in the parameters optimization of PEMFC under steady working condition. *International Journal of Hydrogen Energy*, 41(26), 11380-11390.

[4] C. Song. (2002). Fuel processing for low-temperature and high-temperature fuel cells. Challenges, and opportunities for sustainable development in the 21st century. *Catalysis Today*, 77, 17–49.

[5] S. M. Haile. (2003). Fuel cell materials and components. *Acta Materialia* 51, 5981–6000.

[6] J. B. W.P. Teagan, & B. Barnett. (1998). Cost reductions of fuel cells for transport applications: fuel processing options. *Journal of Power Sources* 71, 80–85.

[7] H.-W. Wu. (2016). A review of recent development: Transport and performance modeling of PEM fuel cells. *Applied Energy*, 165, 81-106.

[8] H. L. Yuzhen Xia, Xiaojun Wu, Guilin Hu, Hao Pan, & Baizeng Fang. (2023). Design of New Test System for Proton Exchange Membrane Fuel Cell. *Energies*, 16(2).

[9] D. Q. Heng Shaoa, Linfa Penga, Peiyun Yia, & Xinmin Laia. (2019). In-situ measurement of temperature and humidity distribution in gas channels for commercial-size proton exchange membrane fuel cells. *Journal of Power Sources*, 412, 717–724.

[10] J. G. Z. Y D Zhan, & Y G Guo. (2015). Development of Advanced Hardware and Software for Proton Exchange Membrane Fuel Cell Test Systems. *Australian Journal of Electrical and Electronics Engineering*, 3(3), 201-209.

[11] T. Z. Quangang Xia, Zhifei Sun, Yuan Gao. (2023). Design and optimization of thermal strategy to improve the thermal management of proton exchange membrane fuel cells. *Applied Thermal Engineering*, 222.

[12] Y. L. Jiawen Li, and Tao Yu. (2021). Temperature Control of Proton Exchange Membrane Fuel Cell Based on Machine Learning. *Frontiers in Energy Research*, 9.

[13] K. J. Prem Kumar Thiyagarajan, & Manoj Kumar P. (2022). Combination studies of operating cell, inlet-line, and humidification temperatures on performance of proton exchange membrane fuel cell. *Fuel Cells*, 22(3), 71-84.

[14] Z. T. Junjie Zhao, & Siew Hwa Chan. (2022). In-situ measurement of humidity distribution and its effect on the performance of a proton exchange membrane fuel cell. *Energy*, 239.

[15] Y. Y. Sanying Hou, Shijun Liao, Jianwei Ren, Hongqing Wang, Pengfei Yang, Kejie Du, Jiexin Li, & Haining Peng. (2020). Enhanced low-humidity performance in a proton exchange membrane fuel cell by developing a novel hydrophilic gas diffusion layer. *International Journal of Hydrogen Energy*, 45(1), 937-944.

[16] R. R. Munazza Mohsin, M. Mohsin-ul-Mulk, Abida Yousaf, & Viktor Hacker. (2020). Electrochemical characterization of polymer electrolyte membrane fuel cells and polarization curve analysis. *International Journal of Hydrogen Energy*, 45(45), 24093-24107.

[17] R. L. Bohan Wang, Dengcheng Liu, Ji Xu, & Bowen Feng. (2019). Investigation of the effect of humidity at both electrode on the performance of PEMFC using orthogonal test method. *International Journal of Hydrogen Energy*, 44(26), 13737-13743.

[18] S. X. Dengcheng Liu, Houwen Tang, Di Zhong, Bohan Wang, Xin Cai, & Rui Lin. (2018). Parameter optimization of PEMFC stack under steady working condition using orthogonal experimental design. *Wiley Energy Research*, 43(7), 2571-2582.

[19] R. S. K. Ruksawong, V. Monyakul, N. A. David, P. C. Sui, & N. Djilalid. (2017). Investigation of PEMFC under Static Magnetic Field: Temperature, Relative Humidity and Performance. *Journal of The Electrochemical Society*, 164(2), F1-F8.

[20] R. L. Qian Zhang, Ludovic Techer, & Xin Cui. (2016). Experimental study of variable operating parameters effects on overall PEMFC performance and spatial performance distribution. *Energy*, 115, 550-560.

[21] I. G. Fabio V. Matera, Assunta Patti, & Enza Passalacqua. (2016). Fuel cell performance assessment for closed-loop renewable energy systems. *Journal of Energy Chemistry*, 25, 531–538.

[22] B.-H. S. Tien-Fu Yang, Mohammad Ghalambaz, & Wei-Mon Yan. (2020). Effects of operating parameters and load mode on dynamic cell performance of proton exchange membrane fuel cell. *International Journal of Energy Research*, 45(2), 2474-2487.

[23] C. Z. Tao Zeng, Zhiyu Huang, Mengxiao Li, Siew Hwa Chan, Qian Li, Xuesong Wu. (2019). Experimental investigation on the mechanism of variable fan speed control in Open cathode PEM fuel cell. *International Journal of Hydrogen Energy*, 44(43), 24017-24027.
[24] G. C. Yiming Xu, Jienan Zhang, Yuyang Li, & Sichuan Xu. (2021). Investigation of Inlet Gas Relative Humidity on Performance Characteristics of PEMFC Operating at Elevated Temperature. *World Electric Vehicle Journal*, (12).
[25] D. K. K. Young Sang Kim, Kook Young Ahn, & Min Soo Kim*. (2020). Parametric study on the local current distribution of polymer electrolyte membrane fuel cell with counter flow channel under pressurized condition. *Journal of Mechanical Science and Technology* 34(5), 2189-2198.
[26] S. R. S.J. Peighambardoust, & M. Amjadi. (2010). Review of the proton exchange membranes for fuel cell applications. *International Journal of Hydrogen Energy*, 35, 9349-9384.
[27] S. M. M. Zhiani, & M. M. Taghiabadi. (2013). Comparative Study of On-Line Membrane Electrode Assembly Activation Procedures in Proton Exchange Membrane Fuel Cell. *Fuel Cells*, 13(5), 946–955.
[28] S. Z. Xiao-Zi Yuan, Jian Colin Sun, & Haijiang Wang. (2011). A review of accelerated conditioning for a polymer electrolyte membrane fuel cell. *Journal of Power Sources*, 196(22), 9097-9106.
[29] X. Z. Huicui Chena, Tong Zhang, & Pucheng Pei. (2019). The reactant starvation of the proton exchange membrane fuel cells for vehicular applications: A review. *Energy Conversion and Management*, 182, 282-298.
[30] Z. Y. GAO Xiangsheng, ZHANG Hongwei, & WU Qiong. (2012). Effects of Machine Tool Configuration on Its Dynamics Based on Orthogonal Experiment Method. *Chinese Journal of Aeronautics*, 25(2), 285-291.
[31] F. D. Jinyong Peng, Qiwei Xu, Youwei Xu, Yan Qi,XuHan, Lina Xu, Guorong Fan, Kexin Liu (2006). Orthogonal test design for optimization of supercritical fluid extraction of daphnoretin, 7-methoxy-daphnoretin and 1,5-diphenyl-1-pentanone from Stellera chamaejasme L. and subsequent isolation by high-speed counter-current chromatography. *Journal of Chromatography A*, 1135(2), 151-157.
[32] H. Z. Jianlu Zhang, Jinfeng Wu, & Jiujun Zhang. (2013). *Pem Fuel Cell Testing and Diagnosis*. Elsevier.

AME0006

Effect of debonding on vibration response of honeycomb sandwich panel

M Suraratchai*, V Sripawadkul, and P Bunyawanichakul

Department of Aerospace Engineering, Faculty of Engineering, Kasetsart University, 50 Ngam Wong Wan Rd., Lat Yao, Chatuchak, Bangkok, 10900, Thailand

* Corresponding Author: monchai.s@ku.th

Abstract. The aim of this study is to evaluate the effect of debonding on the vibration characteristics of the sandwich panel. The studies were carried out on rectangular flat sandwich panels made of thin aluminum sheets and a honeycomb core. The effect on natural frequencies and the mode shapes of the debonding at different sizes were numerically investigated by the finite element model. The results show that the debonding reduces the natural frequencies of the sandwich panels, however, a small debonding region has little effect, especially on the lowest mode of vibration. The decreasing of the natural frequencies increases disproportionately when the debonding size extends beyond the critical value. The results can be helpful for assessing the effects of debonding and can be used for non-destructive evaluations of the damage to sandwich panels from vibration characteristics.

Keywords: Sandwich Panel, Vibration Characteristics, Natural Frequency.

1. Introduction

Sandwich structures consist of two relatively thin parallel sheets of skin boned on a relatively thick and lightweight core of honeycomb or foam. They have high bending strength-to-weight and bending stiffness-to-weight ratios. The honeycomb structure is widely used for aviation, naval/marine, automotive, civil structures, and space applications. It gives the advantage in terms of vibration and noise absorption and low thermal conductivity.

Bonding of skin to the honeycomb core process is difficult, and it is the factor determining the strength of the sandwich structure. The imperfect fit, the unclean surface, or missing adhesive bond during the manufacturing process may cause a partial disbond between the skin face and the honeycomb core, which is also known as core-to-face sheet debonding. The disbond may also result from an in-service experience [1-3].

Debonding impact to the strength of the sandwich structure, e.g. the load bearing capacity [3]. Dynamic parameters such as natural frequencies, mode shapes, and frequency response functions are also affected by the debonding. This can be used for vibration-based damage identification techniques as a non-destructive method for detection and quantification of invisible defects [4,5]. Therefore, understanding debonding effects on dynamic responses of sandwich structures is an important engineering task. The dynamic analysis of a delaminated composite beam and debonded sandwich plate were studied by using a linear spring model in interfacial region [6,7]. The vibration response of a delaminated composite sandwich beam was studied by using 2-D FE model using soft element along a delaminated region in [8]. An analytical method using the split sandwich beam model and the equation of motion to assess the impact of the degree of debonding on the flexural stiffness and the natural frequency was researched in [9].

2. Problem Description

The case study of this research is based on a sandwich panel used in the basic construction of the Thai Space Consortium-1, or TSC-1 satellite [10, 11]. The TSC-1 satellite is a small satellite which weighs less than 100 kg. The entire envelope of this satellite is 740 mm x 840 mm x 900 mm. The sandwich panel was selected in the construction of satellite structures due to its lightweight, high stiffness to weight ratios, and especially vibration-damping properties that suit the launching environments. The honeycomb core sandwich serves as the satellite's main panels is selected for study. The study panel has a total thickness of 20 mm, formed by two layers of surface with a 0.8 mm thickness of aluminum 5005-H22 and a hexagonal-shape honeycomb core with a 0.5 mm foil thickness and 9.5 mm cell size of aluminum 3003-H18. The main structure of the TSC-1 satellite must withstand vibrations while transporting satellites to the expected altitude in low earth orbit.

One of the most common damage mechanisms in sandwich panels is debonding at the skin/core interface. It can happen and go unnoticed by the human eye if there is a manufacturing flaw or any tools fall on the panel. Debonding may have an impact on the failure mechanism and strength behavior of the panel. This work presents the influence of debonding size on the dynamic characteristics of the sandwich panel. FE modeling of free vibrations of sandwich plates with honeycomb cores containing an embedded debonding between the core and the face sheet is investigated.

3. Numerical Study

The change of the natural frequencies and corresponding vibration modes with changing size of the delamination were calculated using the ANSYS finite element code.

3.1. Material Properties

The honeycomb core material theoretically establishes orthotropic material behavior, and a numerical method was used to determine the material properties listed in Table 1. The AL5005-H22 was selected as skin material and has the following characteristics: a density of 2,700 kg/m^3, a Poisson’s ratio of 0.33, and an elastic modulus of 68 GPa.

Table 1. Honeycomb AL3003-H18 mechanical properties [1].

ρ (kg/m^3)	$E_{xx} = E_{yy}$ (MPa)	E_{zz} (MPa)	G_{xy} (MPa)	G_{yz} (GPa)	G_{xz} (GPa)	ν_{xy}	$\nu_{yz} = \nu_{xz}$
45.41	100	1,150	1	165	244	0.49	0.01

3.2. Geometries and boundary conditions

The honeycomb sandwich panel for the primary structure of the TSC-1 satellite [10] was selected to investigate the vibration characteristics of a debonding panel. The panel has a total thickness of 20 mm, formed by two layers of surface with a 0.8 mm thickness of aluminum 5005-H22 and a hexagonal-shape honeycomb core with hexagonal cells of 9.5 mm and foil thickness of 0.5 mm of aluminum 3003-H18. The panel dimensions were a length of 840 mm and a width of 740 mm, corresponding to directions x and z, respectively as shown in Figure 1. The sandwich panel was modeled as a plate with simply supported boundary conditions. At the center of the structure, the penny-shape debonding area was model between skin and honeycomb. The debonding area is selected as a parameter in this work, and the circular diameter was varied as a factor of the plate area between 0.5% to 10%.

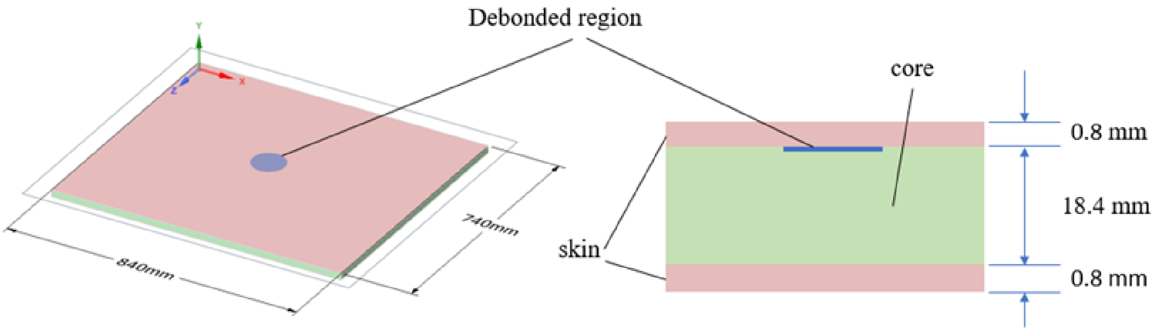

Figure 1. Model of the sandwich panel with honeycomb core.

3.3. FE Modelling

The sandwich panel is modeled into 5 layers: Top skin, Top interface, Core, Bottom interface, and Bottom skin. The top skin and the bottom skin are formed by layers of a 0.8 mm thickness of aluminum 5005-H22, and they are represented by solid elements. The interface layers of 0.01 mm thickness are inserted between the skin and the core. These layers are represented by shell elements. The material properties of aluminum 3003-H18, which was used in the honeycomb core, are used for the interface layers, except the debonding area. The core is formed with an 18.38 mm thickness of AL3003-H18 honeycomb, and it is represented by solid elements. All contacts between each layer are bonded. The finite element model is shown in Figure 2.

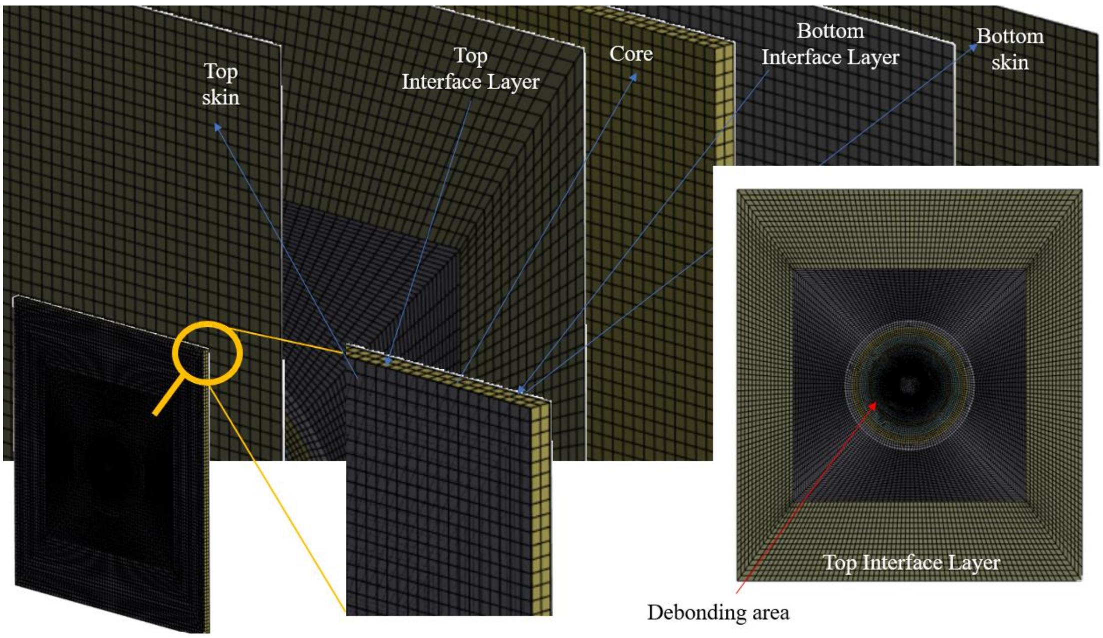

Figure 2. Finite element model of the sandwich panel.

A finite element mesh sensitivity study was performed to ensure that the finite element meshes were fine enough to give satisfactory results. The result of study was shown in Figure 3, and finally, an element size of 10 mm with a total of 181,586 nodes utilized in this study. The soft elements were used in the debonding region to represent the local debonding. Optimization studies were conducted to determine the suitable value of the elastic modulus (E) of the soft element, and the best value was determined as 1 kPa.

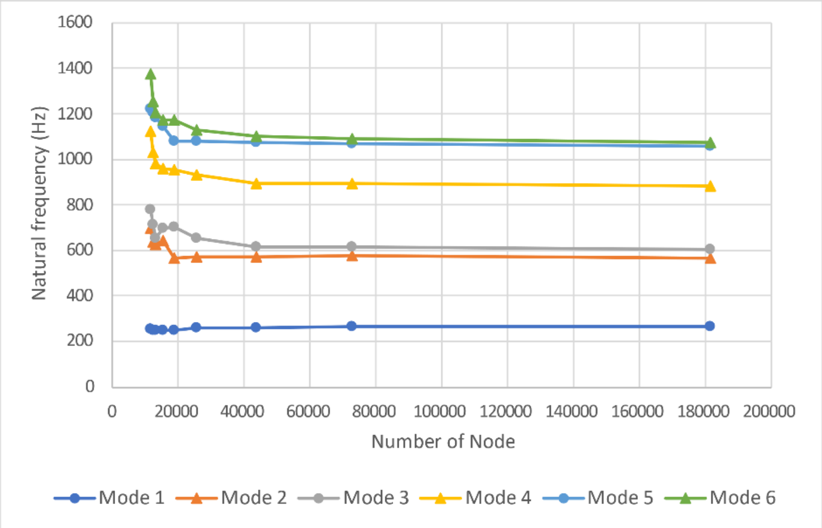

Figure 3. Convergence study of the first six natural frequencies of sandwich panel.

4. Results and Discussion

Effects of debonding on vibration responses of sandwich panels were evaluated by comparing the finite element results of free vibration analysis between intact panels and debonding panels.

4.1. Natural frequency over a debonding area

The skin and the honeycomb core of sandwich structures were separated, when debonding occur. As, the skin of panel over the debonding area is freely vibrate, then it was considered as flat plate with fixed support. The natural frequency of this skin was calculated by finite elements method and compared to the following expression [12]:

$$\omega = \frac{\alpha}{D^2}\sqrt{\left(\frac{Eh^3}{12(1-\nu^2)}\right) \times \left(\frac{1}{\rho h}\right)}$$

where α denotes a frequency constant, ω is the natural frequency of vibration, D is circular diameter, h is the thickness, and ρ is the density. The computational results of the natural frequencies of the circular debonding areas with different sizes are shown in Figure 4, it is observed that for a given mode, the natural frequency decreases as the debonding size increases. For the small debonding area, the natural frequency changes very rapidly as debonding size becomes smaller. On the other hand, for large debonding size, the natural frequency difference decreases as debonding become larger.

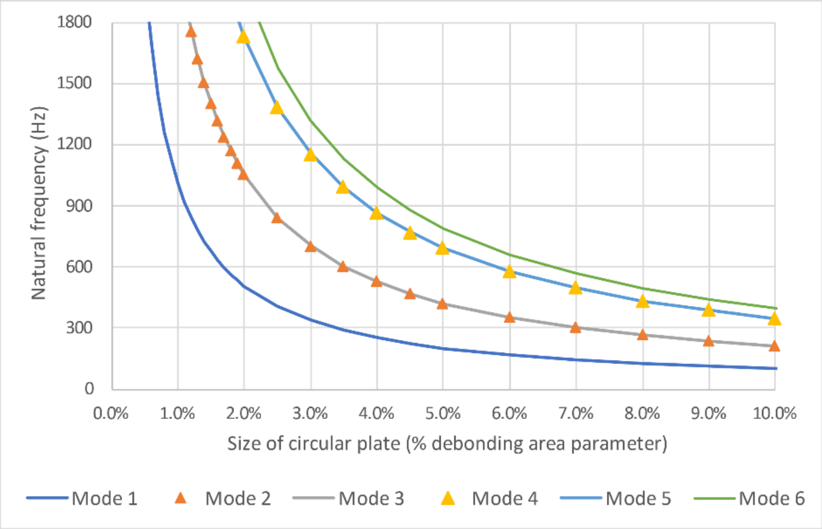

Figure 4. Natural frequencies versus the difference debonding sizes.

4.2. Natural frequency of debonding sandwich panels

Natural frequencies of sandwich panels are examined using modal analysis in ANSYS. Table 2 summarize the results of the first six vibration modes of difference debonding area sizes.

Table 2. The first six natural frequencies of sandwich panels with a circular debonding.

Mode	Debonding area parameter						
	0% No debonding	0.5% (dia. 62.9 mm)	2.0% (dia. 125.8 mm)	4.0% (dia. 177.9 mm)	6.0% (dia. 217.9 mm)	8.0% (dia. 251.6 mm)	10.0% (dia. 281.3 mm)
1	263.88	263.85	263.25	260.36	252.66	236.53	211.09
2	567.84	567.10	560.27	499.98	414.79	362.38	334.27
3	605.03	603.22	591.38	542.71	497.11	433.69	377.71
4	882.61	882.50	702.67	565.17	504.89	435.68	380.79
5	1056.80	1056.10	881.26	706.93	574.89	537.42	492.53
6	1076.30	1075.30	1060.20	708.10	587.01	552.66	495.89

Table 3 presents the mode shape results of the first six vibration modes. For an intact plate and a plate with a debonding area is less than 2%, Mode 1 presents the normal mode, and the antisymmetric mode of the plate occurs in Mode 2 and Mode 3. The debonding open mode is observed when the debonding area is more than 4% in Mode 1 and Mode 2. The higher mode shapes, the debonding open mode is observed although the debonding area is small.

Table 3. Mode shapes of the first six modes.

Mode	Debonding area parameter					
	No debonding	0.5%	2.0%	4.0%	6.0%	10.0%
1	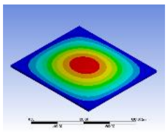	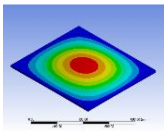	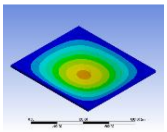	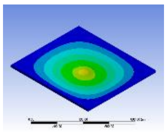	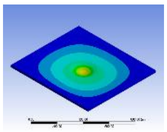	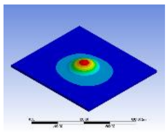
2	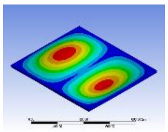	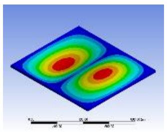	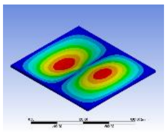	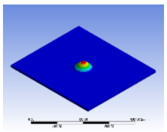	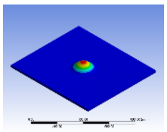	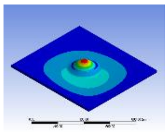
3	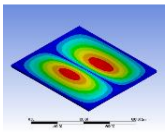	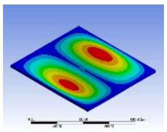	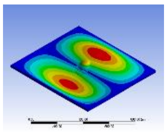	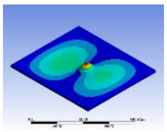	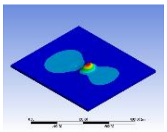	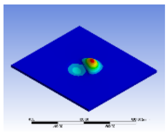
4	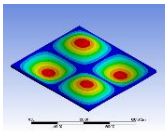	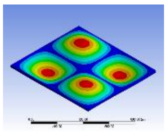	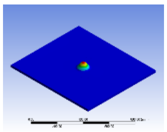	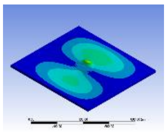	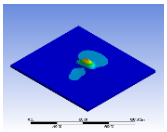	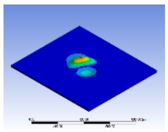
5	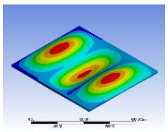	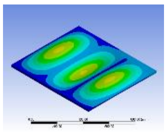	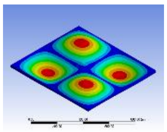	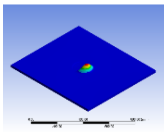	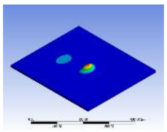	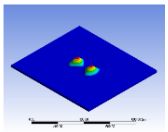
6	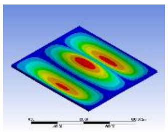	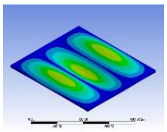	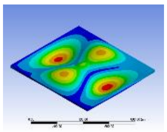	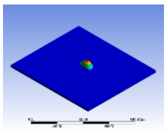	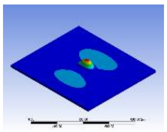	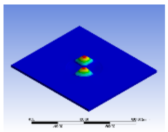

Figure 5 presents the natural frequency ratio normalized by the natural frequency of the intact sandwich plate; it shows that the natural frequencies were slightly decreasing with the presence of debonding. This is caused by the debonding reduced the stiffness of the overall plate. For the small debonding area, the effect of debonding to the natural frequency of the first vibration mode is very small. However, the natural frequency increases significantly when the size of the debonding area becomes larger. It also notices that the decrease in natural frequency is more noticeable for higher mode natural frequencies.

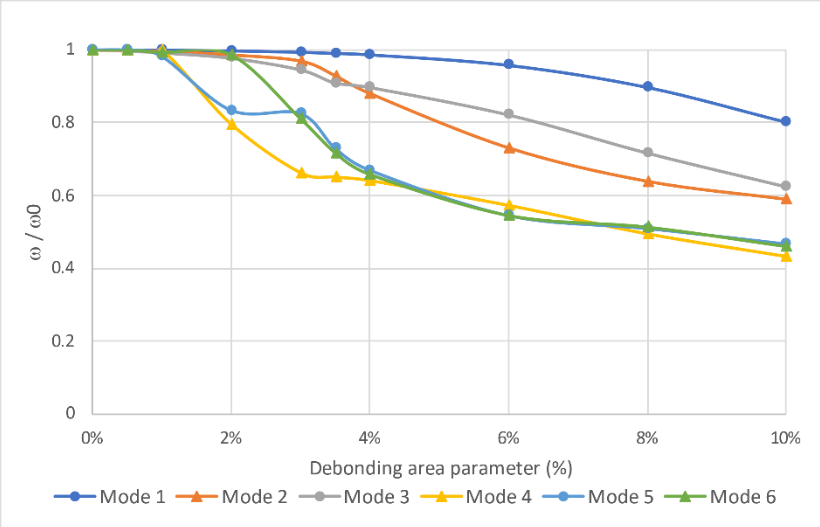

Figure 5. Normalized natural frequencies degradation of the debonding panel for various debonding sizes.

In Figure 6, the natural frequencies of debonding sandwich panels are plotted by solid lines, and the natural frequencies of circular debonding areas are plotted by dash lines. It shows that the natural frequencies of each mode were significantly changed when the natural frequencies of debonding sandwich panels (solid lines) intersected with the natural frequencies of circular debonding areas (dash lines). The effect is more noticeable for the higher modes of vibration. This represents that there is a critical debonding, to which extent beyond this limit the decreasing of the natural frequencies increases rapidly and this critical limit was related to the natural frequencies of the circular skin plate located at the debonding region.

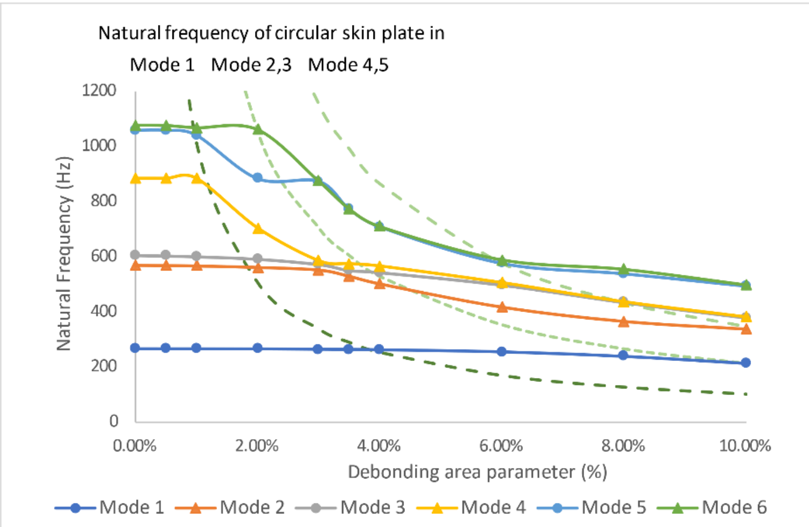

Figure 6. Natural frequencies degradation of the debonding panel for various debonding sizes.

5. Conclusion

This work presents a numerical evaluation of the vibration characteristics of a symmetric sandwich panel consisting of isotropic face sheets and an orthotropic honeycomb core using the finite element method. The results were obtained by the commercial software ANSYS. A solid model of the panel was developed to investigate the natural frequency for the first six modes under simply support conditions. Debonding reduces the stiffness as well as the natural frequencies of the sandwich panels, however a small debonding region has little effect especially on the lowest mode of vibration. The mode shapes contain a local deformation in debonding area. The higher natural frequencies and mode shapes are more sensitive to the debonding present. Large debonding regions introduce additional vibration frequencies, the associate mode shape of which show a disbond opening in vibration. There is a critical debonding extent beyond which the decreasing of the natural frequencies increases disproportionately. Further studies require experimental testing to compare and validate the model.

6. Acknowledgments

The authors wish to acknowledge assistance in providing initial information from the National Astronomical Research Institute of Thailand (Public Organization).

7. References

[1] Triantafillou, T. C., & Gibson, L. J. (1987). Failure mode maps for foam core sandwich beams. Materials Science and Engineering, 95, 37–53.

[2] Triantafillou, T. C., & Gibson, L. J. (1989). Debonding in foam-core sandwich panels. Materials and Structures, 22(1), 64–69.

[3] Falk, L. (1994). Foam core sandwich panels with interface disbonds. Composite Structures, 28(4), 481–490.

[4] Wei Fan, & Pizhong Qiao. (2010). Vibration-based Damage Identification Methods: A Review and Comparative Study. Structural Health Monitoring: An International Journal, 10(1), 83–111.

[5] Zhu, K., Chen, M., Lu, Q., Wang, B., & Fang, D. (2014). Debonding detection of honeycomb sandwich structures using frequency response functions. Journal of Sound and Vibration, 333(21), 5299–5311.

[6] Luo, H., & Hanagud, S. (2000). Dynamics of delaminated beams. International Journal of Solids and Structures, 37(10), 1501–1519.

[7] Chakrabarti, A., & Sheikh, A. H. (2009). Vibration and Buckling of Sandwich Laminates having Interfacial Imperfections. Journal of Sandwich Structures & Materials, 11(4), 313–328.

[8] Baba, B. O., & Gibson, R. F. (2007). The Vibration Response of Composite Sandwich Beam with Delamination. Advanced Composites Letters, 16(2), 65-74.

[9] Kim, H.-Y., & Hwang, W. (2002). Effect of debonding on natural frequencies and frequency response functions of honeycomb sandwich beams. Composite Structures, 55(1), 51–62.

[10] Phichayophas, C., Suratatchai, M., Sripawadkul, V., Bunyawanichakul, P., Mongkolves, S., & Sangthon, A. (2022). Vibration characteristics of honeycomb sandwich panel for Thai Space Consortium-1 satellite. In *the 6th Southeast Asia Workshop on Aerospace Engineering* (Vol. 1, p. 84-92).

[11] Mongkolves, S., Sangthon, A., Torteeka, P., Meenakand, P. & Saisutjarit, P. (2021). Structural analysis of Thai Space Consortium-1 satellite based on Falcon 9 launch vehicle vibration profile. In *the 2nd Innovation Aviation and Aerospace Industry, International Academy of Aviation Industry (IAAI)* (Vol. 1, p. 28-30).

[12] Liew, K. M., & Lim, C. S. (1997). Analysis of dynamic responses of delaminated honeycomb panels. Composite Structures, 39(1-2), 111–121.

AME0008

Experimental Validation of Indoor Landing of Multicopter

Annop Ruangwiset*

Department of Mechanical Engineering,
King Mongkut's University of Technology Thonburi,
126 Pracha Uthit Rd., Bang Mod, Thung Khru, Bangkok, 10140, Thailand

* Corresponding Author: annop.rua@kmutt.ac.th

Abstract. Even though the autonomous multicopters are widely used and generally accepted on this day, such as in a field of photographing, surveying, and agriculture, they are mainly used in the outdoor that GPS system is available. One of the major issues for the autonomous indoor multicopter is the positioning system. And for indoor landing, several works used vision-based method with artificial marker. But in some building the illumination may interfere the marker. In this work a commercial ultrasonic-based indoor positioning system is selected. The precision landing control was developed by dividing overall process into simple task control states. The flight test results demonstrated the capability and the repeatability of developed program to land precisely within decided 10 cm radius from the target landing point.

Keywords: multicopter, precision landing, indoor flight.

1. Introduction

An unmanned aerial vehicle (UAV) which is commonly known as drone nowadays is widely used in also military and non-military purposes. The applications, for example, are reconnaissance, mapping, photography, farming, and so on. And the multicopter typed UAV is often used because of its capability of hovering at a desired point and compactness. These applications are done at an outdoor open space which the satellite-based GPS is available for acquiring the position of UAV to perform an autonomous navigation flight. However, the indoor applications of multicopter such as warehouse monitoring, light part delivery [1, 2] have been proposed in recent years from the point of view of avoiding heavy traffic on ground and flexible adjustment of transportation path. But inside a building is generally cannot receive the GPS satellites signal then the indoor localization techniques have been studied in several works, for example, Light Detection and Ranging (LiDAR) [3], Received Signal Strength Indication (RSSI) [4], computer vision [5], and so on.

On the other hand, the multicopters consume plenty of energy from the battery for rotating the rotors to produce enough lift. The multicopters for indoor application usually have to be small enough to pass a corridor or a space between storage shelves. Therefore, these multicopters cannot carry a large battery and as a result their flight time are often a few minutes. In order to prolong their service time, the idea of battery charging or swapping station has been proposed [6, 7]. In that case, the multicopter has to land more precisely and accurately than landing on a broad and flat ground. The vision-based methods with the use of artificial marker such as ArUco are widely studied [8] and used of commercial products. But the reflection of light effects the position recognition of marker and cannot used in dark area.

Thus, the goal of our work is to develop the autonomous system of multicopter for indoor application. And this paper focuses on the precision landing. The ultrasonic-based indoor positioning system from Marvelmind robotics [9] is used. The landing control program is developed according to the control states that were considered in this work and verified by flight test. In the rest of this paper, experimental setup, control states during landing, results, and discussion are presented sequentially.

2. Experimental Equipment

2.1. Multicopter

For ease of hardware modification and repairing, this work used a 650 mm flame wheel, X-frame, laboratory built aluminum frame quadcopter as shown in Figure 1. The Pixhawk 4 Mini was selected as the flight control unit for its compactness. The Raspberry Pi computer board was used to communicate between the Pixhawk 4 Mini and the indoor positioning system, and perform the calculation of precision landing control. The main specifications of the experimental quadcopter were shown in Table 1.

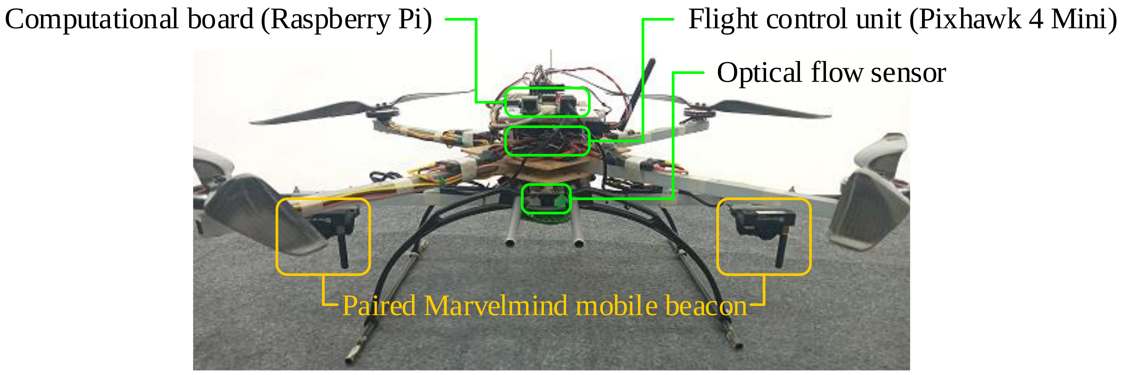

Figure 1. The experimental quadcopter.

Table 1. Main specifications of the experimental quadcopter.

Size of flame wheel		650 mm	Battery	Li-Po 14.8 V 3000 mAh
Propulsion unit	Motor	Brushless motor 5010 – 360 KV	Flight control unit	Pixhawk 4 Mini
	Propeller	16” x 5.5”	Take-off weight	2.1 kg

2.2. Indoor Positioning System

This work aimed to avoid the interference of an artificial marker from a light while landing precisely on a decided point such as a charging station. However, the development of an indoor positioning system was not the objective of this work. Hence several commercial indoor positioning systems were considered. Finally, from the point of view of high precision and easy setup, the Marvelmind robotics' indoor positioning system was selected. The system consists of the network of stationary beacon interconnected by wireless communication and the mobile beacon mounted on the moving target. The position of the mobile beacon is calculated based on a propagation delay of an ultrasonic pulses between stationary and mobile beacons. To simulate a landing area, 4 stationary beacons were used and placed as shown in Figure 2. The decided landing point was the center of those 4 stationary beacons.

Moreover, besides the lack of GPS signal, another problem in indoor flight is the interference between the steel structure of building and the magnetometer which is generally used for acquiring the heading direction of multicopter. In this work 2 mobile beacons were used in pairing mode to get the direction where these paired mobile beacons are facing. And this direction of paired mobile beacons was used instead of the yaw angle from Pixhawk 4 Mini in the heading direction control of the experimental quadcopter. The paired mobile beacons were mounted to the right and left sides of the experimental quadcopter as shown in Figure 1.

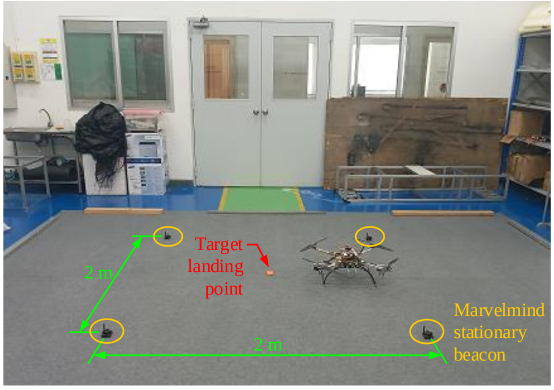

Figure 2. Setup of the indoor positioning system to simulate a landing area.

3. Precision Landing Control

For the inner loop control of stabilization and position holding, the Pixhawk 4 Mini flight control unit used in this work was installed PX4 [10] which is an open-source flight control software and was used in position mode by using optical flow sensor. In the position mode of PX4, when the neutral command is sent to roll, pitch, yaw, and throttle control, the multicopter will level and hold heading and position in 3D space at that time. But in this position mode, if the multicopter are disturbed, the control will only attempt to stabilize the multicopter and it will be leveled and stopped at a new position. Hence, the outer loop control to land precisely was developed in this work as in the below description.

3.1. Control state

In order to land precisely on the decided point, the landing process was considered to be divided into 7 control states as in the following.

Control state 1: Yaw to landing point

When the multicopter came back near the landing area, the multicopter will be yawed heading to the landing point while leveling and maintaining its current altitude.

Control state 2: Approach to landing point

The multicopter will be pitched to move forward to the landing point while heading to the landing point, horizontally holding the rolling movement, and maintaining the altitude until the multicopter came within a given horizontal radius from the landing point. This work set this horizontal radius to be 0.5 m according to the rough size of frame wheel of the experimental quadcopter.

Control state 3: Align heading with the direction of landing station

In case of landing on a charging station, the multicopter has to land with heading aligns with the direction of the station. Therefore, in this work, the multicopter will be yawed to align its heading with the y axis of the indoor positioning system. In this control state, the rolling and pitching movement are leveled and the current altitude is still maintained.

Control state 4: Move close to the landing point

While aligning the heading with the direction of landing station and maintaining the current altitude, the rolling and pitching movement will be controlled to move close to the landing point until the multicopter came within a given horizontal radius from the landing point. This work set this horizontal radius to be 0.25 m according to the half of the radius in control state 2.

Control state 5: Descend

The altitude will be lowered, and at the same time the heading is controlled to be align with the direction of landing station, and the rolling and pitching movement are controlled to move to the landing point.

Control state 6: Finely adjust position

When descended to a given altitude close to the ground, the multicopter will be controlled to maintain the altitude again. The rolling and pitching movement will be controlled to move until the multicopter came within a radius of decided precision landing. This work set the altitude in this control state to the altitude that the skid of experimental quadcopter was 0.05 m above ground. And the decided precision landing is set to be 10 cm radius from the landing point that is generally precise enough for landing on a certain point of charging station.

Control state 7: Cut the throttle and land

When the multicopter came within the radius of decided precision landing, the control will cut the throttle immediately to land on ground at that position.

However, the control states can be jumped over or back during the landing process if the conditions of that state are met.

3.2. Feedback control

By dividing the landing process into 7 control states as described, the necessary outer loop feedback controls were yaw angle control, position control in horizontal plane, and altitude control. The block diagram of these outer loop feedback controls was shown in Figure 3.

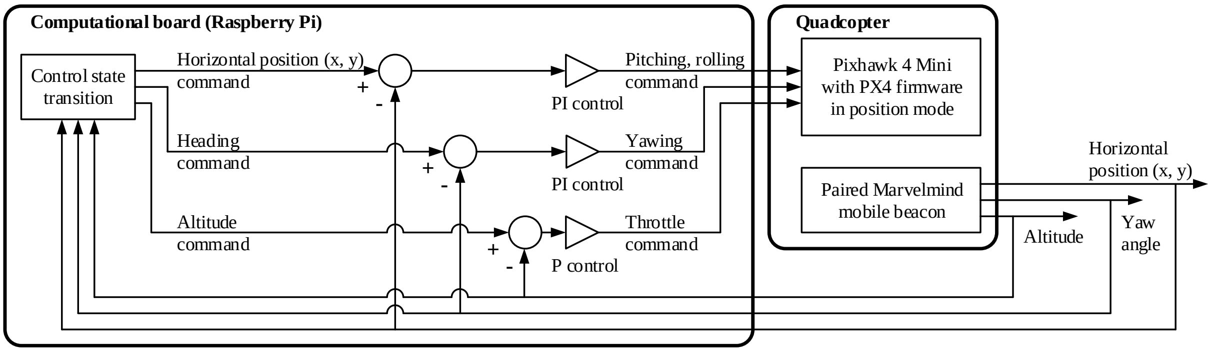

Figure 3. Block diagram of the precision landing control.

To obtain precise movement, the feedback controllers were designed to get calm response. Therefore, a small value of the proportional gain of feedback controller was selected to prevent large overshoot and oscillation. But the smaller proportional gain, the larger steady-state error will usually be remained. Therefore, the integral controller was adopted into the yaw angle control and the position control in horizontal plane in order to reduce the steady-state error to be within decided precision. But the altitude will be decreased gradually during landing process, not essential to hold precisely at an altitude, then only the proportional controller was adopted into the altitude control.

4. Results

Several flight tests have been performed to validate the proposed precision landing control, and the results are presented in this section. Firstly, the results of the main feedback controls, i.e. yaw angle control and horizontal position control, are presented separately. After that, the results of the overall landing process are presented.

4.1. Yaw angle control

In this test, the experimental quadcopter was commanded to yaw to a decided heading direction also from left and right sides. Figure 4 shows the results of yaw angle control in case of heading to 45 deg. The results indicate the stability and settle in ±5 deg of steady-state error.

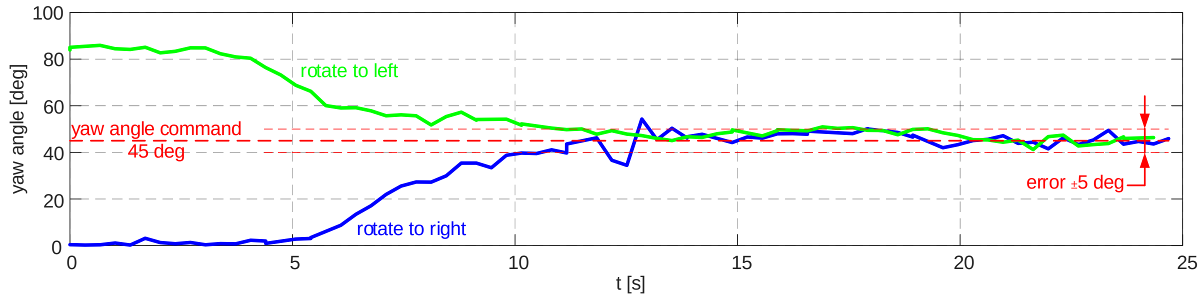

Figure 4. Yaw angle control results.

4.2. Horizontal position control

In this test, the experimental quadcopter was commanded to fly to a target point and hover over that point. Figure 5 shows the result of commanding to the target point coordinate (1, 1) m in the indoor positioning system fixed axes. Figure 5 (a) is the time-series data of position in x axis and y axis, and (b) is the flight trajectory in xy plane. Although the response has overshoot approximately 0.7 m, it oscillates only a little bit and settles in ±0.1 m of steady-state error.

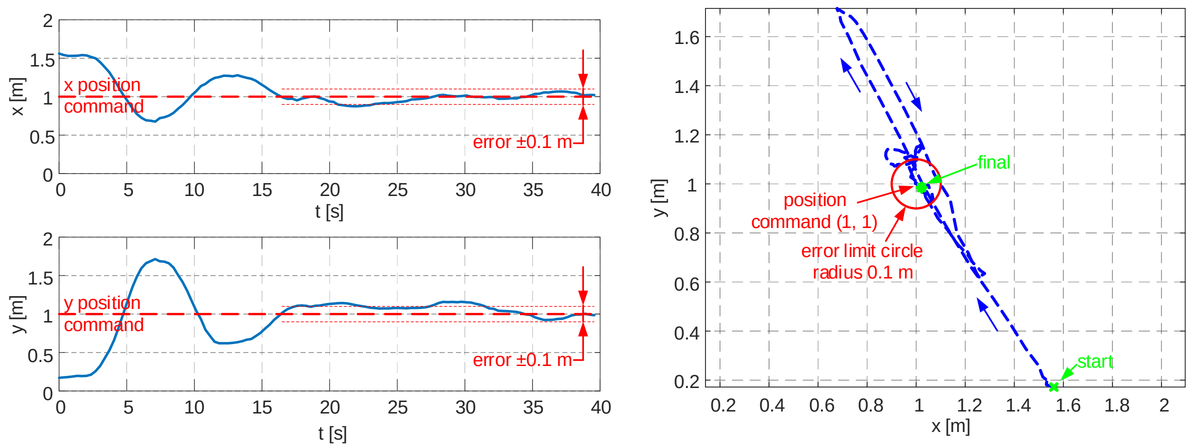

(a) time-series (b) trajectory in xy plane

Figure 5. Horizontal position control results.

4.3. Precision Landing control

The test of overall landing process started from hovering the experimental quadcopter at a point away from the target point, then shifted to the automatic precision landing process. The program developed in this work will control all movement, i.e. rolling, pitching, yawing, and altitude, according to the control state as described in section 3.1 until the quadcopter completely landed on the ground. The flight trajectories of the representative flight tests are shown in Figure 6. And the deviations of final landed point and heading direction from 20 flight tests are tabulated in Table 2 in descending order from the largest distance from the target landing point. These results indicate the repeatability of precision landing results. In fact, the flight test was conducted much more times with random starting point and heading direction. The developed program could land the experimental quadcopter within the decided precision of 10 cm radius from the target landing point all flights.

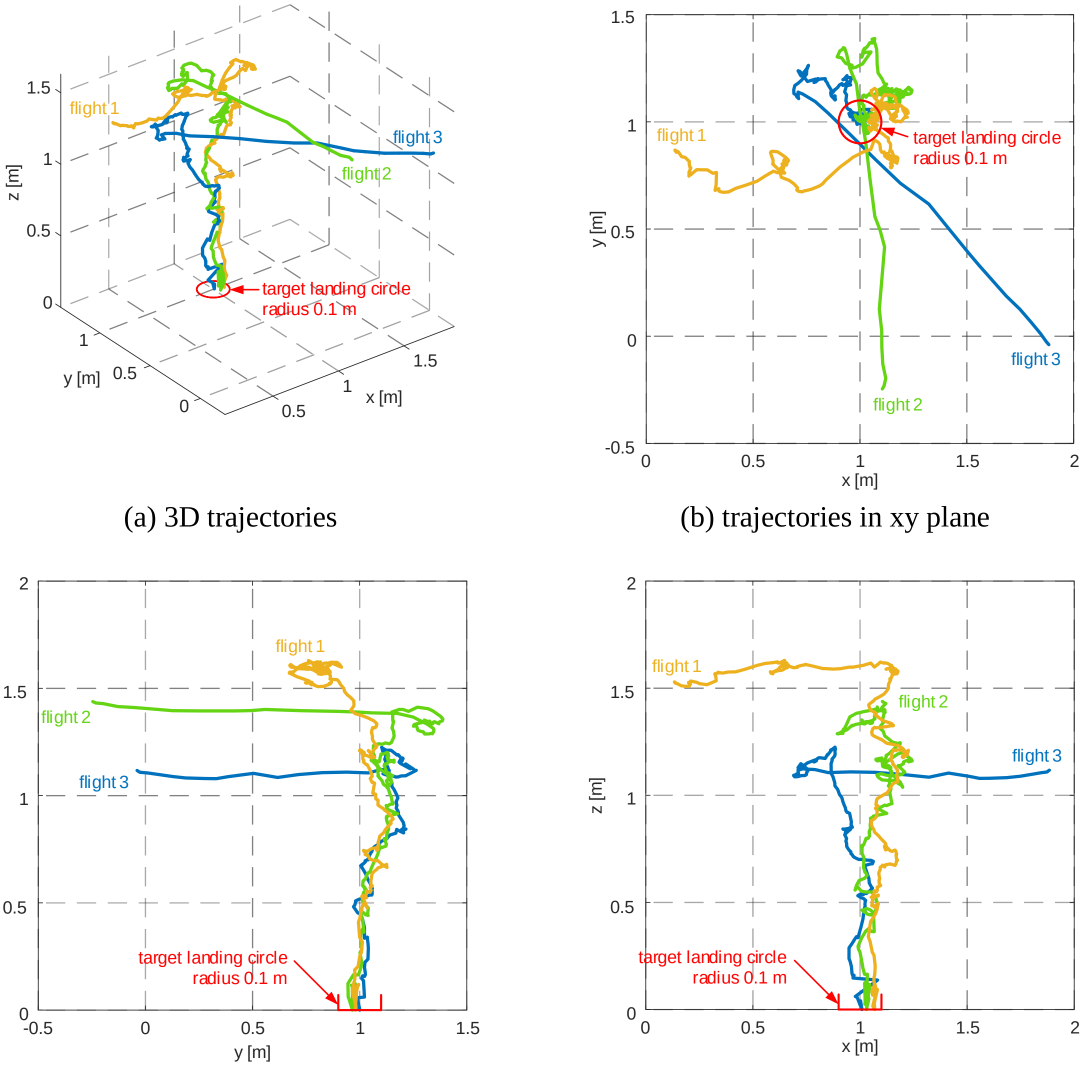

(a) 3D trajectories (b) trajectories in xy plane

(c) trajectories in yz plane (d) trajectories in xz plane

Figure 6. Flight trajectories during precision landing control.

Table 2. Final landed point and heading direction results.

No.	Deviation x (cm)	Deviation y (cm)	Deviation Heading (deg)	Deviation Distance (cm)
1	2.6	8.1	-2.0	8.5
2	3.9	7.3	2.7	8.3
3	-1.7	7.7	0.6	7.8
4	-7.5	1.5	2.4	7.7
5	-6.9	3.1	2.1	7.6
6	-2.7	6.7	-2.5	7.2
7	6.7	-0.4	2.0	6.7
8	-5.9	-1.8	3.9	6.2
9	-6.1	0.4	2.8	6.1
10	3.9	4.2	-0.3	5.7
11	4.6	0.1	1.4	4.6
12	-4.0	2.2	1.6	4.5
13	4.3	1.2	5.2	4.5
14	4.0	-0.4	1.8	4.0
15	-3.9	-0.6	0.7	3.9
16	3.8	1.1	4.1	3.9
17	-3.4	0.9	0.2	3.5
18	-0.1	-1.9	3.9	1.9
19	-0.8	-1.7	4.7	1.8
20	-1.2	0.0	1.5	1.2

5. Conclusion

In this paper, the indoor precision control was developed and the flight tests were performed. This work divided the landing process into 7 control states and adopted proportional integral controllers in yaw angle control and position control. The proportional controllers were tuned to move the experimental quadcopter gently, and the integral controllers were introduced to reduce the steady-state error. All of the flight test results demonstrated the capability and the repeatability that the experimental quadcopter was landed within decided precision of 10 cm radius from the target landing point. Although this work focused on the indoor flight and the commercial ultrasonic-based positioning system was used to solve the problem of light interference in vision-based method and to be able for using in dark places, but the proposed control can be applied to outdoor flight or use with the vision-based positioning method.

6. Acknowledgment

This research project is supported by Thailand Science Research and Innovation (TSRI). Basic Research Fund: Fiscal year 2022 under project number FRB650048/0164.

7. References

[1] Perez-Grau, Francisco J., et al. (2021). Introducing autonomous aerial robots in industrial manufacturing. *Journal of Manufacturing Systems*, 60 (2021), 312-324.

[2] Orgeira-Crespo, Pedro, et al. (2020). Methodology for indoor positioning and landing of an unmanned aerial vehicle in a smart manufacturing plant for light part delivery. *Electronics*, 9 (10), 1680.

[3] Shahrin, M. R., et al. (2018). 3D indoor mapping system using 2D LiDAR sensor for drones. *International Journal of Engineering & Technology*, 7 (4.11), 179-183.

[4] Lagmay, J. M. S., et al. (2018). Automated indoor drone flight with collision prevention. In *TENCON 2018-2018 IEEE Region 10 Conference* (p. 1762-1767).

[5] Gonzalez-Castano, F. J., et al. (2020). Self-corrective sensor fusion for drone positioning in indoor facilities. *IEEE Access*, 9 (2020), 2415-2427.

[6] Voznesenskii, E. A. (2021). Automated battery charging system for multi-rotor aerial vehicles. In *2021 Wave Electronics and its Application in Information and Telecommunication Systems (WECONF)* (p. 1-4).

[7] Lee, D., Zhou, J., & Lin, W. T. (2015). Autonomous battery swapping system for quadcopter. In *2015 International conference on unmanned aircraft systems (ICUAS)* (p. 118-124).

[8] Khazetdinov, A., et al. (2021). Embedded ArUco: a novel approach for high precision UAV landing. In *2021 International Siberian conference on control and communications (SIBCON)* (p. 1-6).

[9] https://marvelmind.com [Accessed: 2023, Aug 31].

[10] https://px4.io [Accessed: 2023, Aug 31].

AME0009

MRBDO of an Aircraft Wing Structure Using a Metaheuristic

N. Suratemeekul, N. Kumkam, and S. Sleesongsom*

Department of Aeronautical Engineering, International Academy of Aviation Industry, King Mongkut's Institute of Technology Ladkrabang, Bangkok, 10520, Thailand

* Corresponding Author: suwin.se@kmitl.ac.th

Abstract: The objective of this research is to develop a multiobjective reliability-based design optimization (MRBDO) method using probabilistic techniques for designing aircraft wing structures. The design problem aims to minimize structural stress and mass while maximizing the buckling factor due to aerodynamic loads, accounting for uncertainties in material properties. The design variables include the thicknesses of various components of the aircraft wing structure, such as ribs, spars, and skins. It is well-known that material property uncertainties can hinder the feasibility of optimization outcomes. To address this issue, uncertainty quantification techniques based on probabilistic methods are employed. However, combining these techniques with optimization and dealing with the structural complexity in modeling can lead to a double-looped nested problem and computational time constraints. To mitigate these complexities in the design process, a two-step MRBDO approach and the utilization of metaheuristics (MHs) are explored as alternatives. The results demonstrate that the two-step MRBDO method, in conjunction with Latin Hypercube Sampling (LHS) and MHs, is an efficient and successful approach for designing aircraft wing structures under uncertain conditions.

Keywords: Multiobjective reliability-based design optimization, Aircraft wing structure, LHS, MHs.

1. Introduction

In general, uncertainty can be encountered in all phases of aircraft design, which often results in unfeasible design outcomes. Reliability-Based Design Optimization (RBDO) has been employed to address uncertainties within a single-objective optimization framework through an iterative process [2]. This iterative optimization and uncertainty quantification process is known as a double-looped nested problem, leading to increased computational complexity. Uncertainty quantification is utilized to assess the reliability or failure probability arising from inherent uncertainties within the system. The primary choice for quantification typically involves probabilistic techniques. An alternative option is non-probabilistic techniques, which aim to address the limitations of probabilistic methods. Probabilistic techniques demand more precise calculations, which can result in inefficient computations. One well-known technique within the probabilistic group is Monte Carlo simulation (MCS). However, MCS is associated with computational time consumption. To mitigate this issue, adaptive techniques have been developed, including the first-order and the second moment (FOSM), the first-order reliability method (FORM), and the second-order reliability methods (SORM) [3].

Additionally, a direct variant to MCS, such as Projection Pursuit Multivariate Transform (PPMT), has been proposed, which has been demonstrated to outperform other methods like Latin Hypercube Sampling (LHS) [4]. Several enhancements to LHS, such as maximin Latin hypercube sampling (MLHS) and Latin hypercube sampling with multidimensional uniformity (LHSMDU), have demonstrated improved performance [4]. More recently, the focus has shifted from single-objective optimization to multi-objective optimization, incorporating a two-step approach to address the challenging task of reliability-based design optimization for truss structures [5]. The two-step multi-objective reliability-based design optimization (MORBDO) of aircraft wing structures using fuzzy set theory has been proposed [6]. Additionally, the same approach for aircraft wing structure design, transitioning from non-probabilistic to probabilistic techniques, has been explored as an alternative [7]. From a review of the existing literature, it becomes evident that the two-step approach warrants further attention in the design of aircraft wing structures. The expectation is that this new approach can enhance performance in locating a set of reliable solutions.

2. Multiobjective Reliability-based Design Optimization with Two-step Approach

This study serves as an extension of previous research [6-7, 8] and is built upon the idea of the relationship between Multiobjective Design Optimization (MODO) results and Reliability-Based Design Optimization (RBDO). The relationship was initially validated by the work in [8], which showed that the MODO solution set closely aligns with the RBDO solution. Consequently, solving MODO in the first step and subsequently addressing RBDO using the initial solutions from the previous step can significantly reduce the time required for solving RBDO problems. In prior work, [5] addressed RBDO by solving it for each initial solution from the second step.

This relationship has been reaffirmed in very recent work employing non-probabilistic techniques to generate a Multiobjective Reliability-Based Design Optimization (MORBDO) solution set from the initial solutions of the first step [8]. In the present work, we aim to expand upon the recent research by using probabilistic techniques to generate MORBDO solution sets. The first step still involves generating a solution set using MODO with a sufficient number of iterations. This set is then employed to search for MRBDO solutions with only a few additional iterations. The general process for this new technique is outlined as follows:

A two-step approach:

1. Perform MODO to identify the solution set.
2. Execute MORBDO to discover reliability-based solutions, using the initial solution set from the previous step.

This technique reduces both time consumption and complexity in addressing MORBDO problems, particularly when numerical experiments employ the finite element method (FEM). Combining reliability analysis with FEM is known to increase computational demands significantly. Computational resource consumption is particularly high when conducting reliability analysis from an initial state. The proposed technique helps reduce computation time in the first step by exclusively addressing MODO problems rather than MORBDO and saving MORBDO for the remaining iterations in the second step. An advantage of this new technique is its ease of integration with other uncertainty quantification methods, whether probabilistic [7] or non-probabilistic [8]. The proposed technique will be employed in synthesizing the aircraft wing model [7].

3. Design demonstration example

3.1. Aircraft wing model

A design demonstration in this study involves the design of a Goland wing with a semi-span of 6.096 m, a chord of 1.216 m, and a thickness of 0.0508 m. The entire aircraft wing is constructed from aluminum, with material properties detailed in Table 1 (Figure 1).

The design process employs a two-step approach for the Goland wing structure. However, the primary challenge lies in the finite element analysis and the aerodynamic load calculations necessary for sizing the component thickness, as these tasks are computationally time-consuming. In this study, the aircraft wing operates at a 5° angle of attack, resulting in applied aerodynamic loads due to the free-stream velocity acting upon it. The aerodynamic load is determined using a vortex ring method with coding developed in MATLAB. Subsequently, this load is applied to the aircraft wing structure for structural analysis, encompassing stress (σ) and buckling, using finite element analysis (FEA) techniques. For a more comprehensive overview of the general analysis, additional information is available in reference [7].

In aircraft design, the primary objective is to minimize mass, as it significantly impacts energy consumption. Therefore, the sizing design of the Goland wing structure is modeled as a multi-objective deterministic design problem with three conflicting objectives: minimizing stress and mass while maximizing the buckling factor. The multi-objective deterministic (MODO) problem is formulated as follows.

$$\text{Min } \{\sigma, \text{M}, -\lambda\} \tag{1}$$

$$\text{Subject to} \quad \lambda \geq 1$$

$$\sigma \leq 0.5\sigma_y$$

$$0.0001 \leq t_i \leq 0.002 \text{ m.}$$

In this context, σ represents the maximum equivalent stress across the entire aircraft wing structure, M signifies the structural mass, λ denotes the buckling factor, and σ_y stands for the yield stress. The thickness of the entire structure shown in Figure 1 can be divided into 92 design variables. To address the computational demands of this task, a combination of metaheuristics (MHs), commercial finite element analysis (FEA) software, and an aerodynamic code is employed, all managed through MATLAB. The flow diagram for this process is illustrated in reference [7].

The in-house optimizer for the Multi-Objective Deterministic Design (MODO) problem, as presented in reference [6], has demonstrated its performance in searching for the optimum solution set. This optimizer is known as the Multi-Objective Opposite-Based Population-Based Incremental Learning (MOPBIL).

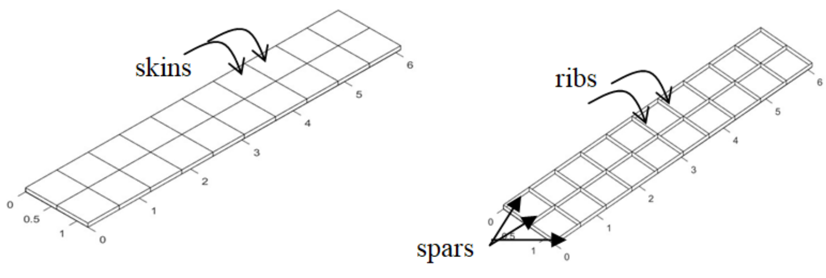

Figure 1. Geometry model of a Goland wing.

Table 1. Material properties of aluminium.

Properties	Value	Unit
Young's modulus (*E*)	70×10^9	Pa
Poisson's ratio (*v*)	0.3	-
Density (ρ)	2700	kg/m^3

3.2. Uncertainty quantification

Uncertainty quantification using a group of probability-based methods such as Monte Carlo Simulation (MCS), Latin Hypercube Sampling (LHS), and Orthogonal Latin Hypercube Sampling (OLHS) has been employed for generating random variables related to mechanical components [9]. The study revealed that LHS is a favorable choice for uncertainty quantification, as it is less time-consuming while delivering adequate performance. LHS enhances computational efficiency over MCS by utilizing stratified random sampling, thereby reducing spurious correlations [10] and eliminating unnecessary random sampling in MCS.

The process of uncertainty quantification involves three essential steps: sampling of all random variables, conducting numerical experiments, and performing statistical analysis. The ultimate goal is to determine the probability of failure (p_f) and reliability. In this study, the formulation for reliability and probability of failure is presented as follows:

The reliability index (β) of the problem is computed by

$$\beta_j(\boldsymbol{x}, \boldsymbol{y}) = \frac{mean(g_j(\mathbf{x}, \mathbf{y}))}{std(g_j(\mathbf{x}, \mathbf{y}))}, \text{ j} = 1, \ldots, \text{n} \tag{2}$$

where $mean(g_j(\mathbf{x}, \mathbf{y}))$ is the mean value of each constraint j, $std(g_j(\mathbf{x}, \mathbf{y}))$ is the standard deviation (STD) values of the constraint $g_j(\boldsymbol{x})$, $\boldsymbol{x}$ is the design variable vector, and $\boldsymbol{y}$ is the random variable vector.

Then the probability of failure can compute as follow:

$$p_f = 0.5\left(1 + erf\left(\frac{\beta}{\sqrt{2}}\right)\right) \tag{3}$$

where erf is an error function.

Finally, the reliability value (R) of the system can be expressed.

$$R = \text{Prb}[g(X) < 0] = 1 - p_f \tag{4}$$

3.3. MORBO problem

With the uncertainty quantify technique in the previous section, a general MODO of aircraft wing structure in (1) can be changed to MORBDO problem:

$$\text{Min } \{\sigma, \text{M}, -\lambda\} \tag{5}$$

$$\text{Subject to} \quad \lambda \geq 1$$

$$\sigma \leq 0.5\sigma_y$$

$$R = \text{Prb}[g(X) < 0] = 1 - p_f > 0.998$$

$$0.0001 \leq t_i \leq 0.002 \text{ m.}$$

4. Numerical Experiment

In this study, the experiment consists of numerical simulations using in-house computer code and commercial software, which is a combination of MATLAB R2023 and finite element analysis (FEA) software. The Multi-Objective Deterministic Design (MODO) process involves the search for an optimum structure using the MOPBIL algorithm, with function evaluations conducted through FEA to assess stress, mass, and buckling factor. Additionally, an in-house MATLAB code is employed for calculating aerodynamic loads using the vortex ring method.

For the flight conditions in this study, the wing is subjected to static aerodynamic loads at cruise speed, and stress and buckling constraints due to these applied loads are taken into consideration. The aerodynamic force is calculated based on air density (ρ_{air} = 1.2 kg/m^3), free-stream velocity (v = 40 m/s), and a wing angle of attack (AoA) of 5 degrees, which is applied over the wing's surface. The MODO problem (1) is solved in the first step with a sufficient number of iterations.

The second step, MORBDO can accomplish by using LHS to quantify uncertainties due to the material properties are Young's modulus (E), Poisson's ratio (ν), and yield stress (σ_y) with adequate iteration. Reliability analysis in the second step, the mean value and the variance of the random variable can be assigned as (μ_E, σ_E) = (70, 19.799) GPa, (μ_ν, σ_ν) = (0.3, 0.023), and ($\mu_{\sigma y}$, $\sigma_{\sigma y}$) = (100, 24.495) MPa.

The specifications of the personal computer used for testing the design problem include an AMD Ryzen 5 4600H processor with Radeon Graphics running at 3.00 GHz, 8.00 GB of RAM, and a 64-bit Windows 10 operating system.For the optimizer's initial values, a population size of 30, a Pareto archive size of 30, and a number of iterations set at 400 are used for the first step, except for the last step, which runs for only 30 iterations. In the second step, Latin Hypercube Sampling (LHS) is employed to generate random variables, and 1000 samplings are performed.

5. Results and Discussion

The design results are divided into two steps according to our technique. The Pareto frontier for the first step and some related values are presented in Figure 2 and Table 2, respectively. The figure displays the Pareto fronts, showing a range of stress from 780,670 to 3,802,100 Pa for solutions No. 1 and No. 24, respectively. Mass reduction leads to energy savings, with a range of 23.6856 to 52.8643 kg for solutions No. 5 and No. 3, respectively. To address serious failures due to buckling, the range of buckling factors obtained is 1.0579 to 10.3640 for solutions No. 5 and No. 4. These usable solutions meet the constraints. To elaborate further, solution No. 1 represents the minimum stress, solution No. 5 demonstrates the minimum structural mass, and solution No. 4 exhibits the maximum wing buckling factor. In the same Table (5th-7th column), the statistical of the system is tested for calculating p_f, β, and R using Equations (2), (3), and (4) of some solutions, respectively. From the Figure 2 shows some of Pareto solutions get higher reliability more than 0.998, except the solution No. 1, 2, 5-6,9-11, 14-15, 22 and 30, implying that there are less reliable (red circle).

In the second step, Multi-Objective Robust Design Optimization (MORBDO) begins with the initial solution set from the first step and runs for 30 iterations. The results are presented in Figure 3 and Table 3. It's worth noting that the Pareto fronts in Figure 2 and Figure 3 are closely related, as mentioned in the previous study [8]. The MODO solution set can updated the solution getting lesser $p_f \leq 0.002$ or R ≥ 0.998, except the solution No. 1, 2, 5, 8, 9, and 11 as presented in Figure 3 (red circle). The results (Table 3) show that the Pareto fronts obtained the range of stress as 780,670 – 3,802,100 Pa at the solution No. 1, and No. 16, respectively. Mass reduction has resulted in energy savings, with values ranging from 23.6230 to 52.8643 kg for solutions No. 26 and No. 3, respectively. Regarding concerns about serious failures due to buckling, the range of buckling factors obtained is 1.0579 to 10.4130 for solutions No. 5 and No. 19. These usable solutions meet the constraints. To provide further insight, solution No. 1 represents the minimum stress, solution No. 26 demonstrates the minimum structural mass, and solution No. 19 exhibits the maximum wing buckling factor. In the same Table, 5th-7th column presented the statistical testing such that p_f, β, and R of some solutions, respectively.

From the results, we can draw the following conclusions:

(1) The proposed technique can efficiently update the solution set of the Multi-Objective Deterministic Design Optimization (MODO) problem to the Multi-Objective Robust Design Optimization (MORBDO) problem with only a few iterations, saving significant time in solving reliability-based design.

(2) The reliability solutions closely align with the MODO solutions.

Additionally, some selected aircraft wing structures from both the first step and the second step are presented in Figure 4 and Figure 5, respectively. These selected structures exhibit a related design evolution, as they are upgraded from the MODO solutions to achieve better reliability for the MORBDO solutions. The improvement in reliability is a result of the reconfiguration of certain members within the aircraft wing structure.

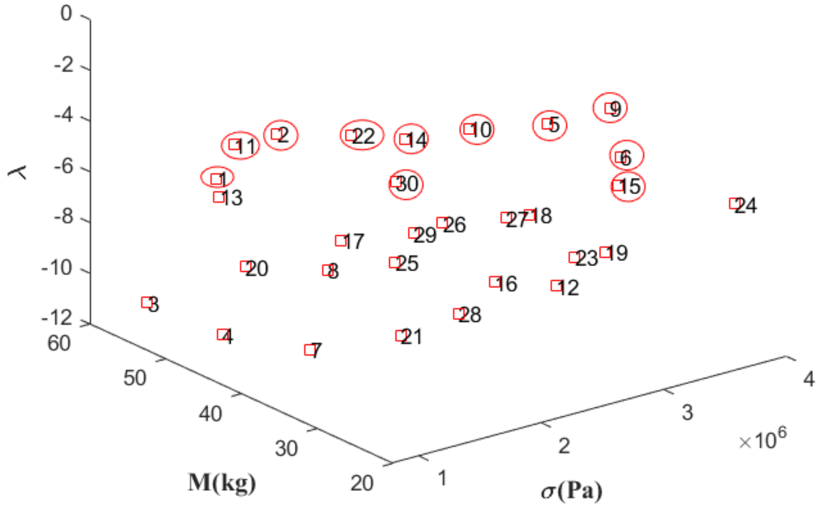

Figure 2. Pareto frontier from the first step.

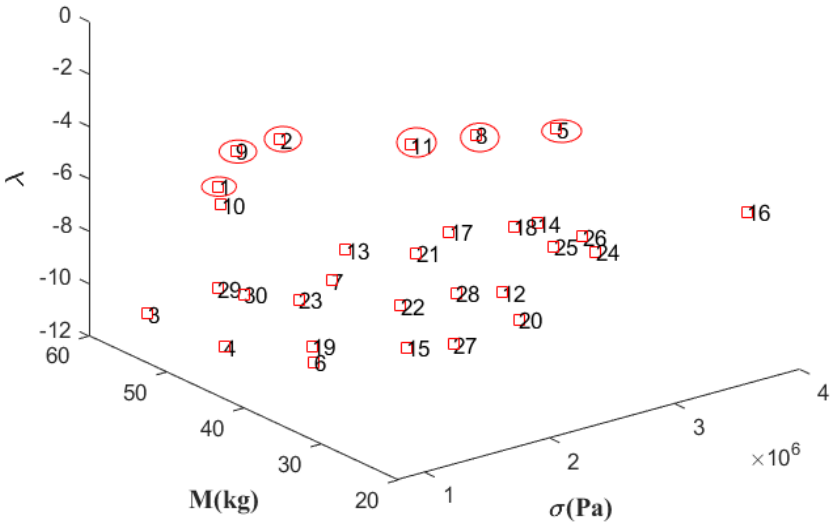

Figure 3. Pareto frontier from the second step.

Table 2. Objective value and Reliability test of some Pareto solution set from the first step.

Pareto Front No.	Stress (Pa)	Mass (kg)	Buckling (-)	Reliability Index (β)	Probabilistic of Failure (p_f)	Reliability Value (R)
1	780670.0	43.2708	-3.9858	2.6815	0.0037	0.9963
3	808400.0	52.8643	-10.205	3.2326	0.0006	0.9994
4	881450.0	44.0974	-10.364	3.2379	0.0006	0.9994
5	2278500.0	23.6856	-1.0579	0.2007	0.4205	0.5795
14	1515500.0	30.2791	-1.583	1.3235	0.0928	0.9072
15	2892400.0	24.4059	-4.4008	2.7635	0.0029	0.9971
24	3802100.0	23.7076	-6.2397	3.0033	0.0013	0.9987

Table 3. Objective value and Reliability test of some Pareto solution set from the second step.

Pareto Front No.	Stress (Pa)	Mass (kg)	Buckling (-)	Reliability Index (β)	Probabilistic of Failure (p_f)	Reliability Value (R)
1	780670.0	43.2708	-3.9858	2.6815	0.0037	0.9963
3	808400.0	52.8643	-10.205	3.2326	0.0006	0.9994
5	2278500.0	23.6856	-1.0579	0.2007	0.4205	0.5795
14	2210100.0	25.1022	-4.7712	2.8340	0.0023	0.9977
15	1689200.0	33.5971	-10.0	3.2257	0.0006	0.9994
16	3802100.0	23.7076	-6.2397	3.0033	0.0013	0.9987
19	1342300.0	40.229	-10.413	3.2393	0.0006	0.9994
26	2482800.0	23.623	-5.4367	2.9217	0.0017	0.9983

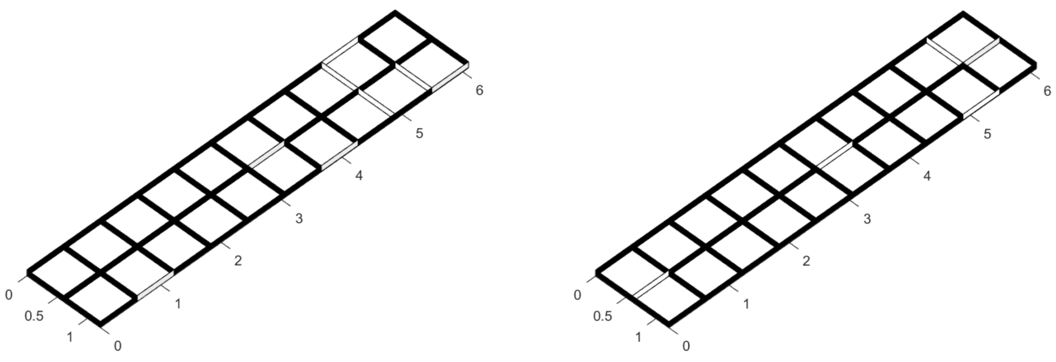

(a) (b)

Figure 4. Some internal aircraft wing structure from first step (a) sol. 14 and (b) sol. 15.

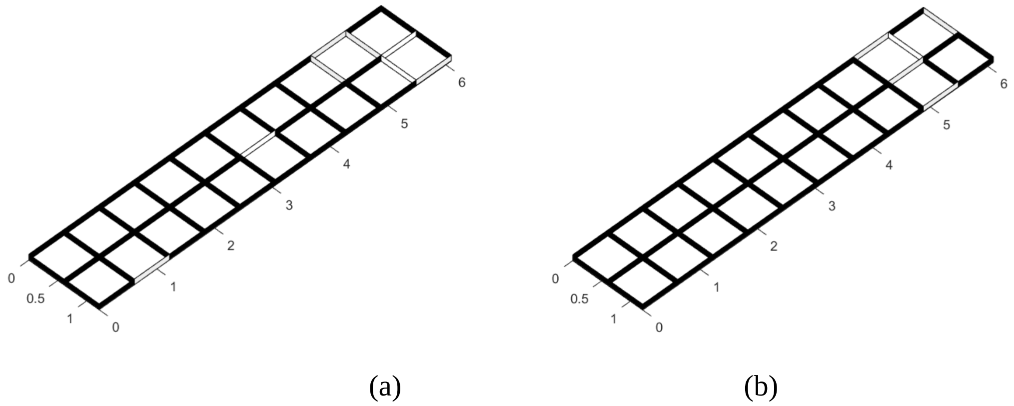

Figure 5. Some internal aircraft wing structure from second step (a) sol. 14 and (b) sol. 15.

6. Conclusions

This research introduces a new approach to Multi-Objective Reliability-based Design Optimization (MORBDO) using a two-step method, demonstrated through the design of a Goland wing. The process commences with multi-objective optimization (MODO) of the wing structure and is followed by a few iterations to enhance its reliability using probabilistic techniques. Recognizing that the deterministic optimal aircraft structure design is impractical in practice due to the presence of uncertainties, this study accounts for these uncertainties in the design problem. The LHS technique is employed to generate random variables to address material property uncertainties. The results suggest that the proposed technique can efficiently update the solution set of the MODO problem to the MORBDO problem with only a few iterations, leading to time savings in solving reliability-based design challenges. Moreover, the reliability solutions closely align with the MODO solutions. However, it's important to note that the assignment of R values cannot be defined at an initial stage; the normal constraint method could provide improvement in future studies.

7. Acknowledgments

The authors express their gratitude for the program and the financial support provided by King Mongkut's Institute of Technology Ladkrabang.

8. References

[1] L´opez, C.,Baldomir, A.,&Hern´andez, S.:The relevance of reliability-based topology optimization in early deign stages of aircraft structures. *Structural and Multidisciplinary Optimization*vol. 55(3), pp. 1121–1141 (2017).

[2] D' Ippolito, R., Donders, S., Hack, M., Van Der Linden, G.,& Vandepitte, D.: Reliability-based design optimization of composite and steel aerospace structures. In: *Proceeding of 47th AIAA/ ASME/ ASCE/AHS/ASC structures, structural dynamics and materials conference*, pp. 6621–6633. Newport, RI, United States (2006).

[3] Elishakoff, I., &Colombi, P.: Combination of probabilistic and convex models of uncertainty when scarce knowledge is present on acoustic excitation parameters.*Computer methods in applied mechanics and engineering* vol. 104, pp. 187–209 (1993).

[4] Erten, O., Pereira, F.P.L., & Deutsch, C.V.: Projection Pursuit Multivariate Sampling of Parameter Uncertainty. *Appl. Sci.*vol. 12, 9668 (2022).

[5] Ho-Huu, V., Duong-Gia, D., Vo-Duy, T., Le-Duc, T.,& Nguyen-Thoi, T.: An efficient combination of multi-objective evolutionary optimization and reliability analysis for reliability-based design optimization of truss structures. *Expert Systems with Applications* vol. 102, pp. 262–272 (2018).

[6] Sleesongsom, S., Winyangkul, S. &Bureerat, S.:Reliability-based design of an aircraft wing using a fuzzy-based metaheuristic. In: *Proceedings of the ASME 2021 International Mechanical Engineering Congress*

*and Exposition*vol. *13: Safety Engineering, Risk, and Reliability Analysis; Research Posters.* Virtual, Online. November. pp. 1–5, V013T14A016. ASME (2021).

[7] Chanu, S., Wattanathorn, A., Senpong, M.,&Sleesongsom, S. Reliability-Based Design Optimization of a Goland Wing with a Two-Step Approach. In: Tan, Y., Shi, Y., Niu, B. (eds) Advances in Swarm Intelligence. ICSI 2022. *Lect. Notes Comput. Sci.* vol. *13345*, 399–410 (2022).

[8] Sleesongsom, S., Kumar, S., & Bureerat, S. Two-Step Multi-Objective Reliability-Based Design Optimization of Aircraft Wing Structures. *Symmetry*, vol. 14, 2125 (2022).

[9] Chanu, S., Wattanathorn, A., Senpong, M., &Sleesongsom, S. Reliability analysis in design of mechanical components. *AIP Conference Proceedings*, Vol. 2601, 020030 (2023).

[10] McKay M.D., Conover, WJ, & Beckman RJ. A comparison of three methods for selecting values of input variables in the analysis of output from a computer code. *Techno metrics*, Vol. 21(2) 239–45 (1979).

AME0010

Study on Vibration Characteristics of Airless Tire

K Fujita[1,*], T Suzuki[2], T Okano[2], Y Washimi[2], K Sasaki[2], and T Tanimoto[2]

[1] Department of Mechanical Engineering, National Institute of Technology, Ube College, 2-14-1 Tokiwadai, Ube, 755-8555, Japan
[2] EV System Laboratory, Research Division, Nissan Motor Co.,Ltd., 1-1 Morinosatoaoyama, Atsugi, 243-0123, Japan

* Corresponding Author: katuhide@ube-k.ac.jp

Abstract. In recent years, the research on airless tire (Non-pneumatic tire, NPT) for passenger cars is getting attention. The background to this is the development of automatic driving technology. Autonomous driving of Level 4 and above is unmanned driving, so it is more important to reduce the frequency of maintenance due to accidental failures, and punctureless airless tires are expected as tires for autonomous driving vehicles. In this research, the vibration characteristics of an airless tire is investigated using scale model of an airless tire. Natural frequencies and mode shapes of a non-rotating airless tire are evaluated by the experimental modal analysis method with ground contact boundary condition. Based on the obtained results, we compared and examined the vibration characteristics of airless tire and conventional pneumatic tire.

Keywords: Airless tire, Vibration characteristic, Experimental modal analysis.

1. Introduction

In recent years, research on airless tires for passenger cars has attracted attention [1,2]. The background to this research is the development of automatic driving technology. The efforts related to automatic driving technology in Japan began earnestly in 2013. At that time, targets were set for 2020. Since those targets were almost reached, the next goal was to implement autonomous driving transport services at 40 locations in society by 2025.

Automatic driving technology is defined in six levels, from 0 to 5. Automatic driving at level 4 or higher is unmanned driving, so it is more important to reduce the frequency of maintenance due to accidental failures. Therefore, punctureless airless tires are expected. The airless tire is considered to have the same potential as the steel radial tire, which is the greatest invention in the history of tire technology. However, it has been pointed out the worse for rolling resistance, wind noise caused by the spoke structure and axle vibration. The rolling resistance of tires is a very important characteristic for tire development, and the reduction of rolling resistance is becoming more important because it is closely related to fuel efficiency. The purpose of this study is to clarify the factors contributing to the rolling resistance of airless tires experimentally.

In this research, as a preliminary step, the vibration characteristics of airless tire has been investigated. As for vibration characteristics, natural frequencies and natural mode shapes of a non-rotating airless tire are evaluated by the experimental modal analysis method with ground contact boundary condition. Based on the obtained results, we compared and examined the vibration characteristics of airless tire and conventional pneumatic tire.

2. Excitation Test

2.1. Experimental equipment

In the experiment, a scale model that simulates the structure of a full-size airless tire is used. Figure 1 shows the appearance of the scale model used in this experiment, and Table 1 shows its specifications. It consists of wheels, spokes and tread rings, and has an outer diameter of 200mm and a width of 50mm.

The wheel is made of aluminum alloy, and the spokes and tread ring are made of urethane resin prototyped by vacuum casting. The wheel and spokes are mechanically joined, and the spokes and tread ring are joined by two-color molding. The tread ring is made of a harder resin than the spokes, and the blending ratio of the materials is adjusted to achieve the material hardness shown in Table 1.

Figure 1. Airless tire

Table 1. Specifications of scale model.

Dimension	Diameter	200[mm]
	Width	50[mm]
	Thickness of Tread ring	5[mm]
Material	Wheel	Aluminum alloy (A6063)
	Spoke	Urethane resin UPX8400(Sika Japan Ltd.) Compounding ratio A:B:C=100:100:35 Shore A hardness: 83
	Tread ring	Urethane resin UP5690(Sika Japan Ltd.) Compounding ratio A:B:C=100:100:97 Shore D hardness: 90
Manufacturing	Wheel	Sanjyu Co., Ltd
	Spoke, Tread ring	Plamerry design Co., Ltd. (Vacuum injection)

Figure 2. Experimental equipment for rolling test.

Figure 2 shows the experimental equipment for rolling test to measure rolling resistance. The airless tire is fixed to a cantilevered tire shaft and is pressed against the drum with a pressing load. In this state, the tire rotates passively by rotating the drum with the drive motor. In rolling test, the rolling resistance can be measured by 6-component force transducers equipped with the tire shaft.

2.2. Experimental procedure

Figure 3 shows the experimental setup of the excitation test. The tire is pressed against the drum with a preload of 300 N, and an impact hammer was used to excite the impact force. The excitation point was fixed, and the force excitation was performed in three directions as shown in Figure 4 in order to excite all vibration modes. The induced acceleration responses in radial, circumferential and lateral directions were measured. The measurement positions were the center of the tread where the tire was divided into 12 equal parts in the circumferential direction, and the measurement points were 11 points excluding contact point⑦ as shown in Figure 5. The excitation was repeated five times at each point, and the resulting data was averaged to improve accuracy. The impact force and acceleration response signals were amplified and applied to a signal analyzer. The frequency response function (i.e. accelerance) was obtained using ME'scope software. The natural frequency and natural mode shape were identified from the accelerance.

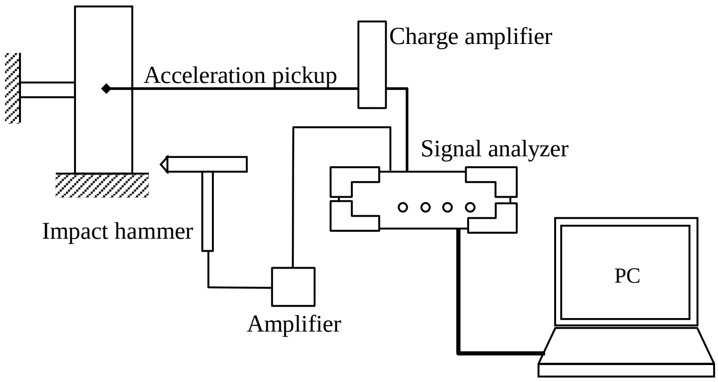

Figure 3. Experimental setup of excitation test.

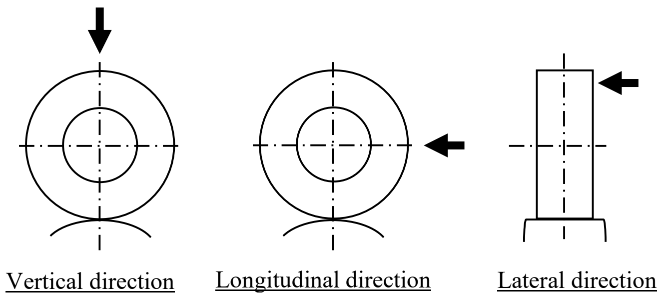

Figure 4. Excitation direction.

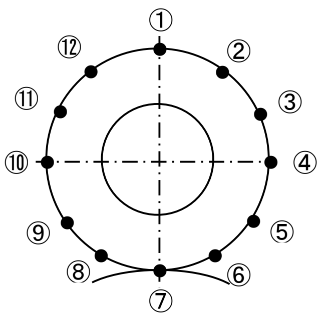

Figure 5. Measurement points.

2.3. Experimental results

The natural frequency can be determined from the resonance peak of accelerance. Since 11 accelerances were obtained in this impact test, the natural frequency was determined by overlapping them. Figure 6 shows the superimposed accelerance.

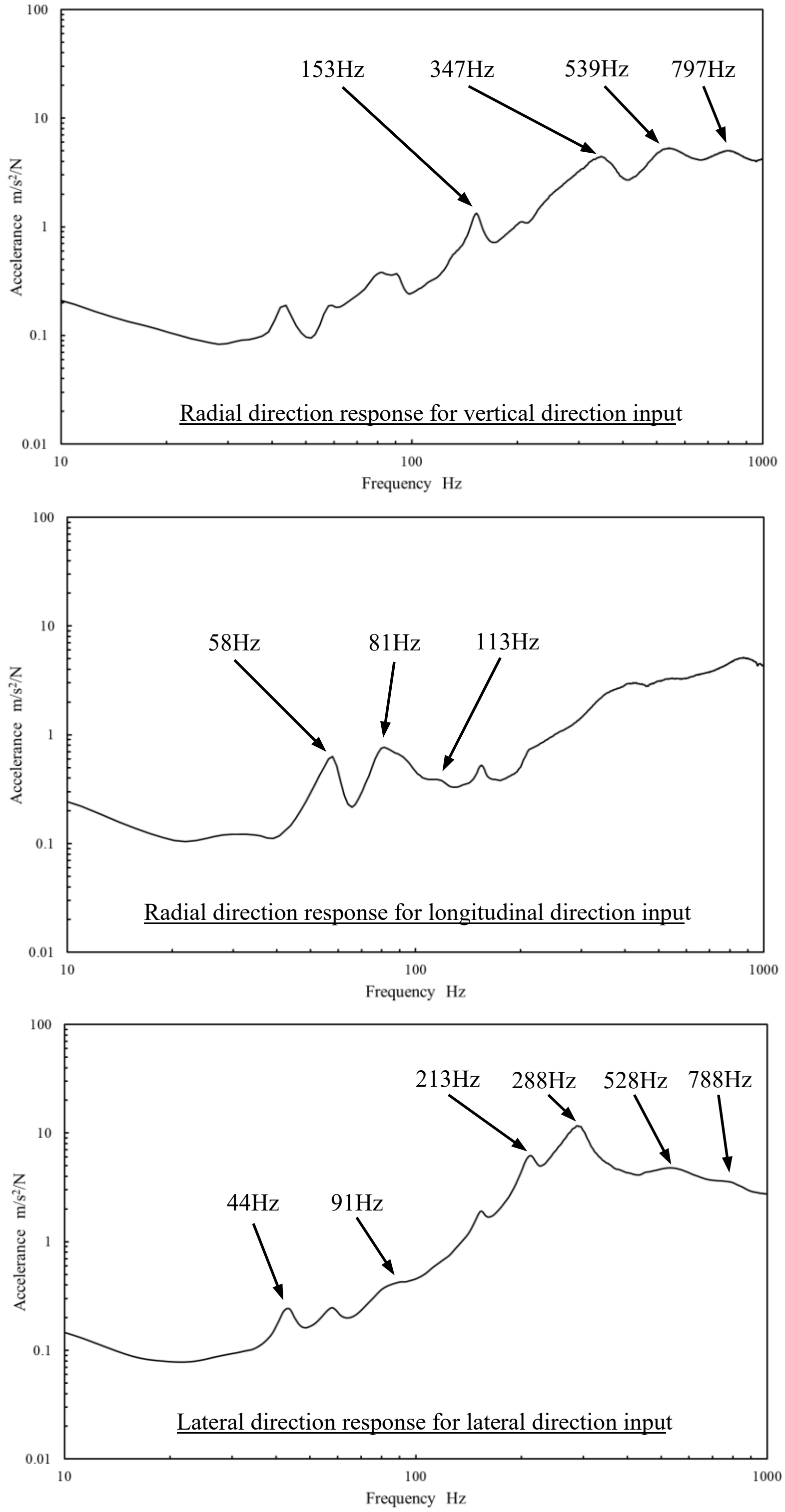

Figure 6. Superimposed accelerance.

It was confirmed that the four resonance peaks (153Hz, 347Hz,539Hz and 797Hz) correspond to the vibrational modes in the vertical direction from the accelerance excited in the vertical direction. In addition, it was confirmed that the three resonance peaks (58Hz, 81Hz and 113Hz) correspond to the vibration modes in the longitudinal direction from the accelerance excited in the longitudinal direction. Furthermore, it was confirmed that six resonance peaks (44Hz, 91Hz, 213Hz, 288Hz, 528Hz and 788 Hz) correspond to the axial vibration mode from the axially excited accelerance.

The vibrational modes of pneumatic tire are researched through modal analysis of the tire wheel system with axel fixed and tire loaded on the drum by Pacejka, H. B. and Zegelaar, P. W. A. [3,4]. The calculated vibrational modes are also shown as general mode shape in Table 2 and Table 3. The mode shapes were identified by comparing the obtained mode shapes with general mode shapes. Although no lateral elastic mode has been reported for pneumatic tire, it is predicted that 288Hz corresponds to the 1.5th order, 528Hz to the 2.5th order, and 788Hz to the 3.5th order of lateral elastic mode from the mode shapes.

Table 2. Natural frequencies and natural vibration modes (In plane).

Freq.	58Hz	81Hz	113Hz	153Hz	347Hz	539Hz	797Hz
Experimental result	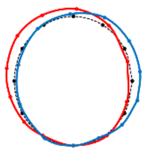	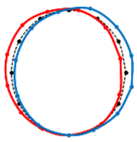	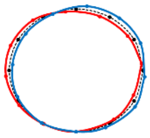	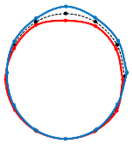	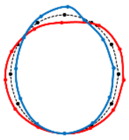	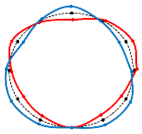	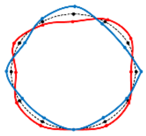
General mode shape [3,4]	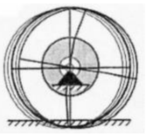 Rotational (in-phase)	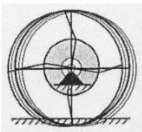 Rotational (anti-phase)	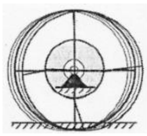 Longitudinal	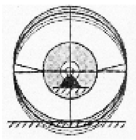 Vertical	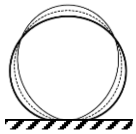 Vertical (n = 1.5)	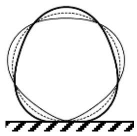 Vertical (n = 2.5)	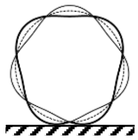 Vertical (n = 3.5)
	Rigid mode				Elastic mode		

Table 3. Natural frequencies and natural vibration modes (Out of plane).

Freq.	44Hz	91Hz	213Hz	288Hz	528Hz	788Hz
Experimental result	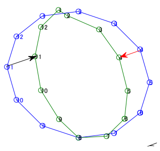	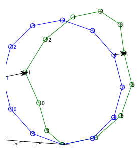	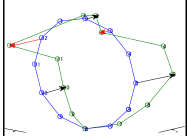	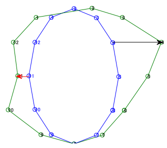	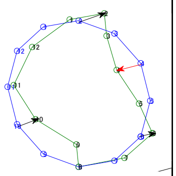	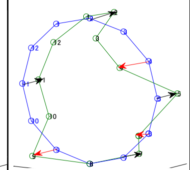
General mode shape [3,4]	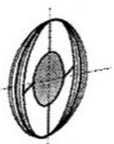 Yaw	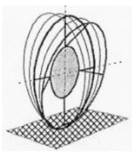 Camber	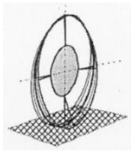 Lateral	Lateral (n = 1.5)	Lateral (n = 2.5)	Lateral (n = 3.5)
	Rigid mode			Elastic mode		

3. Consideration

Compared with the vibration characteristics of conventional pneumatic tire, the natural frequency of the airless tire is extremely high, and multiple natural vibration modes were confirmed in the frequency range of 40 to 800zHz. Regarding the vibration mode shape, basically the mode shapes corresponding to the vibration mode of conventional pneumatic tire were confirmed. However, as for out of plane vibration mode, multiple lateral elastic modes that have not been confirmed in pneumatic tires were confirmed.

4. Conclusion

In this study, natural frequencies and natural mode shapes of a non-rotating airless tire are evaluated by the experimental modal analysis method with ground contact boundary condition. The following results have been clarified.

(1) As the vibration characteristics of the airless tire, 13 natural frequencies were confirmed in the frequency range of 40 to 800Hz, 7 in plane vibration modes and 6 out of plane vibration modes were confirmed. Four rigid modes and three elastic modes were confirmed for in plane vibration modes. As for out of plane vibration modes, three rigid modes and three elastic modes were confirmed.

(2) It was confirmed that the natural frequency of airless tire is much higher than that of pneumatic tire. This is thought to be due to the smaller size of the airless tire used in this experiment, and the higher rigidity due to the difference in structure from pneumatic tire.

(3) It was confirmed that the natural mode shape of airless tire is basically corresponding to that of pneumatic tire. However, as for out of plane natural mode, multiple lateral elastic modes that have not been confirmed in pneumatic tire were confirmed.

5. References

[1] Deng, Y., Wang, Z., Shen, H., Gong, J. & Xiao, Z.(2023). A comprehensive review on non-pneumatic tyre research. *Materials & Design*, 227.

[2] Nakajima, Y.(2020). The picture of future tire, *Journal of the Society of Rubber Science and Technology*, Vol.93,No.9.(in Japanese)

[3] Pacejka, H. B.(2006). *Tyre and Vehicle Dynamics*. Elsevier.

[4] Zegelaar, P. W. A.(1998). *The dynamic response of tyres to brake torque variations and road unevennesses*. PhD thesis, Delft University of Technology.

AME0011

A study on the characteristics of mixed fuels in diesel engines

J Jang[1], Y Woo[1], Y Shin[1], A Ko[1], Y Jung[1], C Cho[1], G Kim[1], and Y Pyo [1,*]

[1]Korea Institute of Energy Research, 152 Gajeong-ro ,Yuseong-gu, Daejeon, 34129, Korea

* Corresponding Author: ydpyo@kier.re.kr

Abstract. A lot of research is being conducted to use high-efficiency equipment and low-carbon / carbon-free fuel to solve the problem of global warming. In the engine sector, interest in high-efficiency diesel engines has been high, but direct combustion of fossil fuels has limitations in reducing greenhouse gas emissions. Research is ongoing. Recently, there is a high interest in e-Fuel as an alternative fuel, such as hydrogen, ammonia, methane, methanol, and ethanol DME. LPG is known as a fuel that can be produced as an e-Fuel. When such an e-Fuel is used in a diesel engine, it is possible to achieve high efficiency due to the high compression ratio of a diesel engine and to achieve a much lower level of harmful exhaust gas concentration than a diesel engine. However, problems due to fuel-slip may occur. In this study, a system capable of supplying CNG (Compressed Natural Gas), LPG (Liquified Petroleum Gas), NH3, etc. was applied for co-combustion, and each performance was confirmed. The engine used in the experiment is a 3.9-liter four-cylinder CRDI engine and is equipped with a turbocharger. When each fuel was used for mixed firing, maximum output was secured. However, in the exhaust gas, HC and NH3-slip increased. In the case of NOx, there was also a decrease, which is judged to be due to interference with combustion by the fuel used for co-firing.

Keywords: Engine, Dual-fuel, Diesel, Combustion.

1. Introduction

In order to raise interest in global warming and resolve it, much research is being conducted to use high-efficiency devices and low-carbon/non-carbon fuels. In the engine sector, there has been a lot of interest in highly efficient diesel engines, but since they burn fossil fuels directly, there are limitations in reducing greenhouse gas emissions, and due to the problem of exhaust emissions, the use of alternative fuels or a combination of low-carbon and non-carbon fuels has been doing in progress [1]. Alternative fuels that can be used in diesel engines are broadly divided into two types. It is a fuel that has a high cetane number and can be used as an alternative to diesel fuel, and a gaseous fuel that has a low cetane number and high octane number and must be ignited through pilot injection. It is a fuel that helps reduce exhaust emissions. In the former case, the representative fuel is DME [2], and in the latter case, most gasoline alternative fuels can be used, including CNG (Compressed Natural Gas), LPG (Liquified Petroleum Gas), and NH3. CNG and LPG are low-carbon fuels, and NH3 is a carbon-free fuel [3, 4]. Therefore, when compared under the same conditions, it is possible to reduce CO2 emissions compared to the case of using gasoline and diesel fuel.

In order to reduce carbon dioxide emitted from internal combustion engines, the distribution of electric vehicles is expanding, but the driving range of electric vehicles is shorter than that of existing internal combustion engine vehicles. Additionally, there is a shortage of charging stations to charge batteries. If the battery is used up without a charging facility nearby, you will need to tow the vehicle or bring a portable charging device to recharge it. Most mobile charging devices use precharged batteries, but in this case, the number of vehicles that can be charged using the mobile charging device is inevitably small. Therefore, in order to compensate for these shortcomings, there are cases where a mobile charging device using an internal combustion engine generator is used. The motive of this study is to reduce carbon dioxide emissions while maintaining the high efficiency of diesel engines by co-firing low-carbon/non-carbon fuels in diesel engines to overcome the irony of using internal combustion engines to charge electric vehicles.

In this study, CNG, LPG, and NH3 were supplied to the engine using MFC at the front of the intake port for co-combustion, and the performance of each was confirmed. The engine used in the experiment is a 3.9-liter four-cylinder CRDI engine and is equipped with a turbocharger. Through this, we aim to understand the characteristics of co-firing engines according to fuel.

2. Experimental setup and conditions

For the mixed combustion engine experiment, a 4-liter, 4-cylinder CRDI diesel engine was used as a base engine, as shown in Fig. 1 and Table 1. CNG, LPG, and NH3 could be supplied from the front of the intake port, and the amount of fuel supplied was controlled through the MFC. Exhaust gas was measured using MEXA-9100D and MEXA-1400. The engine load was controlled using an eddy current type dynamometer.

As shown in Table 2, the experimental conditions were tested at 1600 rpm and the load was changed to 25, 50, 75, and 100%. Under each condition, CNG, LPG, and NH3 were co-fired according to the diesel substitute rate and the exhaust gas characteristics were investigated.

Table 1. Engine specifications.

Items	Value
Displacement volume (L)	3.99
Number of cylinders	4
Bore size (mm)	103
Stroke length (mm)	118
Compression ratio	17
Turbocharger	WGT

Table 2. Test conditions.

Engine speed (rpm)	Load condition (%)	Substitute rate (%)
1600	25, 50, 75, 100	15 ~ 75

Figure 1. Picture of test engine

3. Result and discussion

Each figure should have a brief caption describing it and, if necessary, a key to interpret the various lines and symbols on the figure.

3.1. Power results

Diesel fuel was replaced using CNG, LPG, and NH3 at full load conditions of 25, 50, 75, and 100% at 1600 rpm. Fig. 2 compares the output according to each fuel, load condition, and replacement rate. The 0% replacement rate is the result of using diesel alone. When replacing diesel fuel with CNG, LPG, or NH3, it can be seen that most outputs are almost the same as when using diesel alone. However, when the load is low, the diesel replacement rate may be low or no replacement may be possible. In particular, in the case of ammonia, CNG and LPG could replace diesel by 50% under 25% load conditions, but combustion of ammonia was unstable, so experiments were not possible, and the output did not increase even if the amount of ammonia supplied was increased.

In the case of CNG, it was possible to replace diesel by up to 87.5% under 100% load conditions. However, in the case of LPG and NH3, it was possible to test up to 50% replacement rate, but this was due to the insufficient performance of the heat exchanger used in the experiment, that is, the heat exchanger installed to vaporize liquid LPG and NH3, causing liquid LPG and NH3 to enter the engine irregularly. This is because the engine's output suddenly fluctuated as it was supplied, making it impossible to properly proceed with the experiment. In this regard, we plan to conduct additional experiments by replacing the heat exchanger in the future.

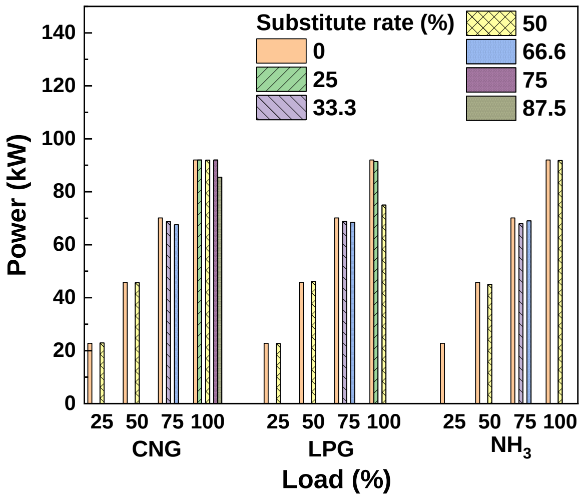

Figure 2. Power at 25, 50, 75, 100 % load condition using CNG, LPG, NH3 substitute rate.

3.2. THC and NH3 results

Fig. 3 compares the THC emission concentration according to each fuel, load condition, and replacement rate. The 0% replacement rate is the result of using diesel alone. In the case of CNG and LPG, emissions are increasing as diesel is replaced, and emission concentration appears to be decreasing as engine load increases. Additionally, the higher the replacement rate, the higher the THC emission concentration. This is believed to be the result of unburned fuel due to the use of hydrocarbon-based CNG and LPG gas fuel, and CNG and LPG supplied through the MFC at the front of the intake manifold being discharged as is during the intake and exhaust process.

When replacing with ammonia, there is no significant change in THC emission concentration compared to CNG and LPG, because ammonia fuel is not measured as THC even if it is unburned or slips. As a result of measurement using an exhaust gas analyser, all measurement results were measured above 5000 ppm, which is the measurement limit of the instrument. Ammonia is known to be a precursor that causes secondary fine dust, so it is necessary to manage emissions, and for this, a post-processing device such as AOC (Ammonia Oxidation Catalyst) will be needed.

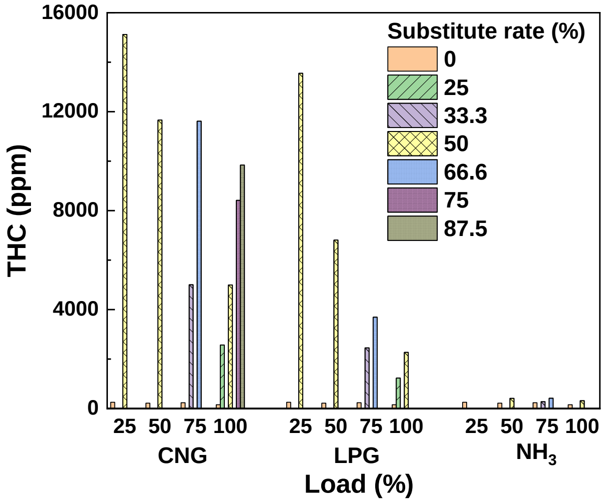

Figure 3. THC at 25, 50, 75, 100 % load condition using CNG, LPG, NH3 substitute rate.

3.3. NOx result

Fig. 4 compares NOx emission concentration according to each fuel, load condition, and replacement rate. The 0% replacement rate is the result of using diesel alone. In all experimental conditions, NOx emissions were reduced when co-firing compared to diesel combustion alone. This is because diffusion combustion, which is the basis of diesel combustion, has decreased and premixed burn in lean conditions has increased. The air-fuel ratio of a diesel engine is always a lean condition, and this also applies to co-fired engines. CNG, LPG, and NH3 fuel are supplied in gaseous form at the front of the intake port and exist in the cylinder as a premixed mixture.

Even when NH3 is used, it can be seen that the amount of NOx generated is reduced. When burning NH3, NOx is created during the combustion process due to the nitrogen atoms contained in the fuel, which may increase the emission concentration, but did not show an increase in this experiment.

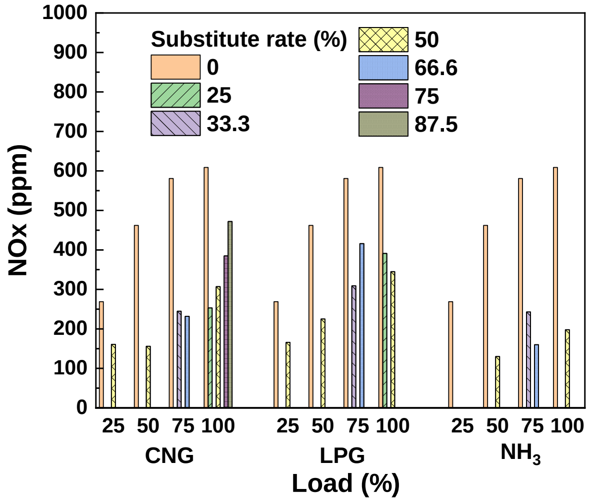

Figure 4. NOx at 25, 50, 75, 100 % load condition using CNG, LPG, NH3 substitute rate.

3.4. CO2 result

Fig. 5 compares CO2 emission concentration according to each fuel, load condition, and replacement rate. The 0% replacement rate is the result of using diesel alone. Looking at the carbon dioxide emission concentration results from co-combustion of CNG and LPG fuel, emissions are generally similar to those of diesel alone combustion, or lower emission concentration results are shown under some conditions. If the combustion efficiency is the same, lower CO2 emission concentration is shown when using low-carbon fuels CNG and LPG. However, in the results of this experiment, there are cases where higher CO2 emission concentration is shown even when low-carbon fuel is used. This is believed to be due to problems with combustion efficiency when using CNG and LPG.

When ammonia is used, since it is a carbon-free fuel, the CO2 emission concentration decreases in proportion to the amount of ammonia fuel used.

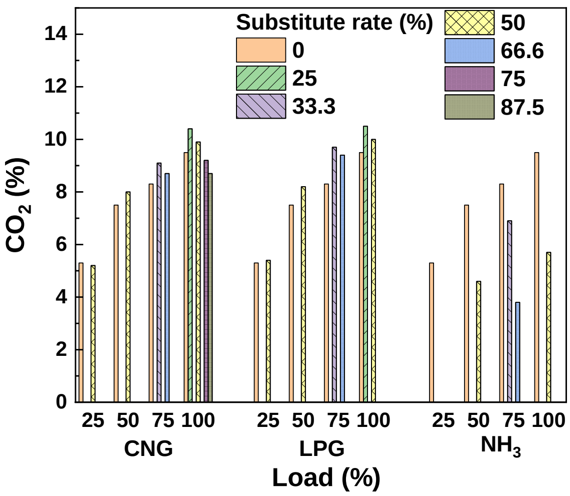

Figure 5. CO2 at 25, 50, 75, 100 % load condition using CNG, LPG, NH3 substitute rate.

4. Conclusion

This study is the result of basic research on the characteristics of co-firing by applying CNG, LPG, and NH3 to diesel engines for engine generators using low-carbon/zero-carbon fuels for mobile charging devices that can charge electric vehicles in emergency situations. am. CNG, LPG, and NH3 were supplied in gaseous form to the MFC at the front of the intake port while controlling the fuel amount. The experimental results are as follows.

1. Even when co-firing by applying CNG, LPG, and NH3 to a diesel engine, output performance equivalent to that of a diesel engine was obtained. In the case of CNG, 87.5% of diesel replacement was possible at 100% load.
2. Regarding THC emissions, the concentration of THC emissions increased significantly when using CNG and LPG due to unburned fuel and fuel slip. When ammonia was used, the THC concentration was similar to diesel combustion alone, but the ammonia emission concentration increased significantly.
3. NOx emissions showed a decrease even when using CNG, LPG, and NH3, and it is believed that the NOx emission concentration decreased due to a decrease in combustion temperature due to an increase in lean premixed burn.
4. CNG and LPG are low-carbon fuels, and NH3 is a non-carbon fuel, so CO2 emission concentration was expected to decrease under all conditions, but when CNG and LPG were used, there was an increase compared to diesel combustion alone. This is believed to be related to combustion efficiency.

In the future, we plan to change the fuel supply method and supply location to determine the limits of diesel fuel replacement rate and study ways to minimize exhaust gas concentration.

5. Acknowledgments

This research was supported by Project (20024387) of the Ministry of Trade, Industry and Energy, Korea.

6. References

[1] Korean Register 2019, *친환경 미래 선박 연료 전망*

[2] Arcoumanis, C., Bae, C., Crookes, R., & Kinishita E., (2008). The potential of di-methyl ether (DME) as an alternative fuel for compression-ignition engines: A review. *Fuel*, 87(7), 1014-1030.

[3] Bae, C., & Kim J., (2017). Alternative fuels for internal combustion engines. *Proceedings of the Combustion Institute*, 36(3), 3389-3413.

[4] Xu, L., Xu, S., Bai, X., Repo, J., Hautala, S., & Hyvonen, J., (2023). Performance and emission characteristics of an ammonia/diesel dual-fuel marine engine. *Renewable and Sustaninable Energy Reviews*, 185, 113631.

AME0013

A feasibility study of railway power swapping from diesel-electric propulsion to pure-electric propulsion in urban areas

Thirawat Tantitamthiti[1] and Manon Sooklamai[1,*]

[1]Division of Mechanical Technology Education, Faculty of Industrial Education and Technology, King Mongkut's University of Technology Thonburi,
126 Pracha Uthit Rd., Bang Mod, Thung Khru, Bangkok 10140, Thailand.

* Corresponding Author: manon.san@kmutt.ac.th

Abstract. This research is a feasibility study of railway power swapping from diesel-electric propulsion to pure-electric propulsion in urban areas, The benefits are the cost of energy saving and lower tailpipe emissions. The numerical models and mathematics simulation scenarios have been made for considering the net energy-consuming and differences. The rail vehicles of the State Railway of Thailand namely Alsthom for the locomotive type, and NKF for the diesel multiple unit (DMU) type, were considered. There are eight types of modifications, there were battery-electric shunting locomotive (BESL), battery electric locomotive (BEL), overhead catenary system electric shunting locomotive (OCSESL), overhead catenary system electric locomotive (OCSEL), battery electric shunting multiple unit (BESMU), battery electric multiple unit (BEMU), overhead catenary system electric shunting multiple unit (OCSESMU) and overhead catenary system electric multiple unit (OCSEMU). Two train routes were considered as short and long routes as follows. The short route of 30.3 km with 11 stations from Bangkok station to Phra-Chom-Klao station for investigating in case of shunting locomotive and shunting DMU. The long route of 61.4 km with 19 stations from Bangkok station to Chum-Thang-Chachoengsao station for investigating in case of diesel-electric locomotives and DMU. The results show that electrification by using the overhead catenary system offers the most cost-effective travel option.

Keywords: Battery-electric, Diesel-electric, Overhead catenary system, Railway, Power swapping.

1. Introduction

Bangkok's railway system currently serves as a hub for various vehicles, leading to significant air pollution within the city. The types of transportation causing air pollution include passenger motorcycles, passenger cars, passenger vans, passenger buses, and passenger trains.

Specifically, diesel locomotives have been used for over 50 years [1] with multiple generations and caused air pollution problems due to their long-lasting internal diesel engines. As mentioned, Bangkok and its surrounding metropolitan areas are facing severe air pollution issues. Air quality often exceeds normal levels, posing risks to human health, animals, plants, and properties. The region's primary sources of air pollution are emissions from vehicle exhaust. Mainly from diesel-powered vehicles, particularly in congested areas and near roads [2]. Diesel engines are widely used in various vehicles in

Bangkok, including cars, pickup trucks, buses, diesel locomotives, and diesel-powered trains. In response to global environmental challenges such as global warming and air pollution, many countries governments have been supporting the transition to cleaner energy sources to reduce greenhouse gas emissions. One of the strategies involves shifting towards electric vehicles (EVs) and hydrogen-powered vehicles [3]. Nowadays, the energy transition trends indicate that efforts are being made and that it is possible to transition power from the use of internal combustion engines into electrified locomotives [4] because it is more efficient in energy conversion and has lower emissions.

Therefore, this research has studied the feasibility of converting a diesel locomotive to a pure-electric propulsion system while running in urban areas. The train routes were from Bangkok Station to Phra Chom Klao Station, 30.3 kilometers, 11 stations for the case of short distance route. And from Bangkok Station to Chum-Thang-Chachoengsao station, 61.4 kilometers, with 19 stations for the case of long-distance routes. The focus is the rate of energy consumption in each modified locomotive and diesel multiple-unit train.

2. Related principles and theories

2.1. Diesel-electric locomotive

A diesel-electric locomotive is a type of locomotive that employs the method of power transmission using electricity [5]. It consists of a diesel engine, a generator, and traction motors for wheel rotation. Within the diesel-electric locomotive, the following main components are shown in Figure 1.

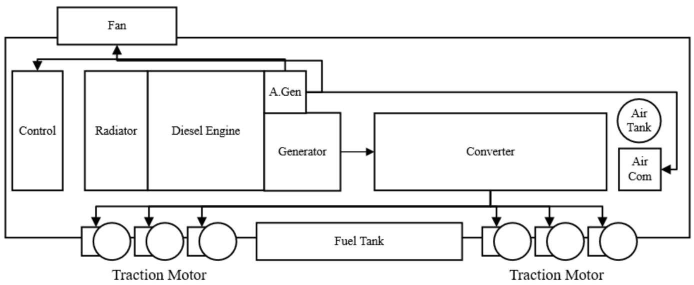

Figure 1. The component of a diesel-electric locomotive [5].

2.2. Diesel multiple unit (DMU)

Diesel multiple unit (DMU) [6] is a type of passenger train that is self-propelled by its diesel engine and is equipped with a driver's compartment or control room onboard. It doesn't require a separate locomotive to pull the train. The main components used for propulsion are shown in Figure 2.

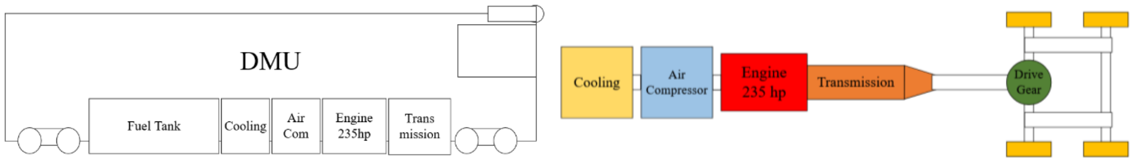

Figure 2. The component of a Diesel Multiple Unit (DMU) [6]

2.3. Overhead catenary system (OCS)

The commonly used alternating current electric train system has a voltage of 25,000 volts. The electric power supplied to the train through the overhead system passes through a catenary, which is a steel wire hung from the overhead line [7]. Trains powered by electricity are equipped with a pantograph that lifts the catenary to allow the electric current to flow into the propulsion system.

2.4. Railway rolling resistance.

The total resistance consists of the resistance at a constant speed (v = const.) and the resistance from acceleration. The resistance to movement is divided into running resistance and track resistance, which arises from gradients and the curvature radius of the track. The running resistance originates from air resistance and additional opposing forces [8]. Various other resistances are depicted in Figure 3.

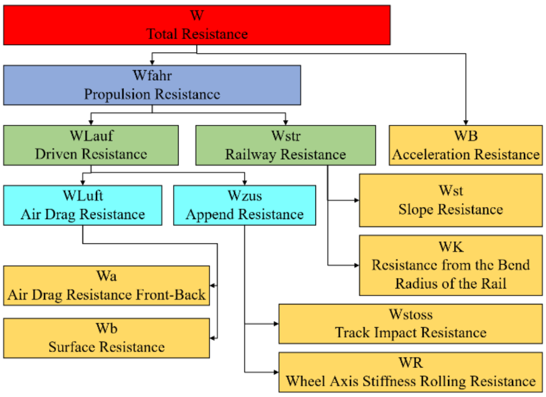

Figure 3. The overall rolling resistance diagram of the railway system. [8].

2.4.1. Air drag resistance according to the Hannover formula.

the air drag resistance, the Hannover formula can also be used in the same way and is a formula that applies to road vehicles. The air resistance of a train composition can be calculated as an equation as follows [8].

$$W_{Luft} = \left[c_{W,L} + c_{W,W1} + (n-2)\cdot c_{W,Wm} + c_{W,Wn}\right]\cdot\left[(1+K_W)\cdot\frac{\rho}{2}\cdot A\cdot v^2\right] \tag{1}$$

Where W_{Luft} is the air drag resistance (N), $c_{W,L}$ is the aerodynamic resistance coefficient of the locomotive head (with a value of 0.26), $c_{W,W1}$ is the aerodynamic resistance coefficient of the car immediately following the locomotive (with a value of 0.13), $c_{W,Wm}$ is the aerodynamic resistance coefficient of the cars in the middle of the train (with a value of 0.10), $c_{W,Wn}$ is the aerodynamic resistance coefficient of the cars at the end of the train (with a value of 0.23), K_W is the aerodynamic resistance coefficient for the airflow angle, ρ is the air density (kg/m³), A is the cross-sectional area (m²), v is the velocity (m/s) and n is the number of passenger cars.

2.4.2. Append resistance.

The Append resistance from Figure 4 consists of wheel axis stiffness rolling resistance (W_R) and track impact resistance (W_{Stoss}), which varies according to the weight of the railway vehicle [8]. Wheel axis stiffness rolling resistance (W_R) can be described by the following equation:

$$W_R = f_R \cdot m \cdot g \tag{2}$$

Where W_R is the wheel rolling resistance (kN), f_R is the coefficient of wheel rolling resistance, (with a value of 0.0015), m is the mass of the vehicle (kg), and g is the acceleration due to gravity (m/s²).

The track impact resistance (W_{Stoss}) can be described as [8].

$$W_{Stoss} = c_d \cdot m \cdot v \tag{3}$$

Where W_{Stoss} is the track impact resistance (kN), m is the mass of the vehicle (ton), v is the velocity (km/h), and c_d is the coefficient of impact with the rail [8] which can be expressed as

$$c_d \approx 0.025\left[\frac{N}{ton \cdot km / h}\right] \tag{4}$$

2.4.3. Railway resistance

Due to the long distances and routes investigated, there is minimal gradient resistance and curvature resistance, thus these factors were not included in the analysis.

2.4.4. Acceleration resistance

When increasing the running speed, acceleration involves both linear and rotational mass acceleration. For the rotational mass acceleration, besides the wheel mass and the moment of inertia of the wheel, the rolling rate of the wheelset also plays a role. A higher rolling rate and higher moment of inertia of the wheel result in higher acceleration resistance. To simplify, the rotational mass is combined with the linear mass using the added mass factor λ. The acceleration resistance equation is as follows [8]:

$$W_B = 1000 \cdot m \cdot b \cdot \lambda \tag{5}$$

Where W_B is the acceleration resistance (kN), b is the acceleration (m/s²), m is the mass of the vehicle (kg), and λ is the added mass factor (with a value of 1.2).

2.4.5. Total resistance.

The total resistance for this research can be obtained using the following equation [8]:

$$W = W_{Luft} + W_R + W_{Stoss} + W_B \tag{6}$$

Where W is the total resistance (kN), W_{Luft} is the air drag resistance (kN), W_R is the wheel rolling resistance (kN), W_{Stoss} is the track impact resistance (kN), and W_B is the acceleration resistance (kN).

2.5. Energy storage system (ESS)

In this research study, the Nickel Manganese Cobalt Oxide (NMC) type of lithium-ion battery [9] was chosen for the electrical energy storage system. The details are nominal capacity 280 Ah, average voltage 3.7 VDC, specific energy 240 Wh/kg, and weight 4.25 ± 0.05 kg.

2.6. Kinetic energy

Energy is the energy that arises within an object in motion [10]. It is utilized in this research to determine the amount of energy lost during the period when the train is moving with varying speeds and changing weights. The equation for kinetic energy is given by:

$$KE = \frac{1}{2}mv^2 \tag{7}$$

Where KE is the kinetic energy (J), m is the mass (kg), and v is the velocity (m/s).

3. Methodology

3.1. Research tools

In the data collection process, a GPS device and stopwatch were employed as tools for tracking movement related to the time along the route that the trains were operated. The route from Bangkok Station to Chum Thang Chachoengsao Station was selected for this research for both departure and return trips. After that, the collected data will be analyzed and formulated as the mathematical model for calculating the energy consumption for each type of train propulsion system.

3.2. Short-distance route (Shunting Locomotive and Shunting DMU)

The short-distance route of 30.3 km with 11 stations is from Bangkok station to Phra-Chom-Klao station. The train is initially propelled by electric shunting for urban areas and switched to diesel-powered for the remaining distance of the journey, see Figure 4.

3.3. Long-distance route (Locomotive and DMU)

The long-distance route of 61.4 km with 19 stations is from Bangkok station to Chum-Thang-Chachoengsao station. The train is initially propelled by a pure electric locomotive for urban areas.

From Phra Chom Klao Station to Khlong Bang Phra Station is powered by diesel engines for driving. From Khlong Bang Phra Station to Chum Thang Chachoengsao Station is then powered by pure electric propulsion again. The scenarios are shown in Figure 4.

Figure 4. Train route and propulsion scenarios.

3.4. Types of locomotives analysis

Polrut Boonme et al. [11] have examined the Alsthom diesel-electric locomotive model details include a 2400 hp engine, a locomotive weight of 82.50 tons (during operation), and a specific fuel consumption value of 389 g/kWh. The information on the details of the NKF diesel multiple units model including a 235 hp engine, a weight of 35.32 tons (during operation), and a specific fuel consumption value of 213 g/kWh [12]. The locomotives analyzed in this study are classified into two models: Alsthom and NKF.

These models are categorized into two types based on their power sources: battery-electric and overhead catenary systems. When considering the previously defined routes, these locomotive models can be transformed into eight distinct configurations: Battery-electric shunting locomotive (BESL), Battery electric locomotive (BEL), Overhead catenary system electric shunting locomotive (OCSESL), Overhead catenary system electric locomotive (OCSEL), Battery electric shunting multiple unit (BESMU), Battery electric multiple unit (BEMU), Overhead catenary system electric shunting multiple unit (OCSESMU) and Overhead catenary system electric multiple unit (OCSEMU) of the 8 modifications above, the design characteristics are shown in Figure 5.

3.5. Propulsion systems and component efficiency

The efficiency of the equipment inside the diesel-electric locomotive affects the energy input and output of the locomotive system [13], Certainly, here are the divisions of the modified formats for Diesel Locomotive and DMU, arranged in sentences:

For the diesel locomotive, there are three energy source options OCS, battery, and diesel engine, as shown in the efficiency values of the equipment in Figure 6(a).

For the diesel multiple units, there are also three energy source options OCS, battery, and diesel engine, as shown in the efficiency values of the equipment in Figure 6(b).

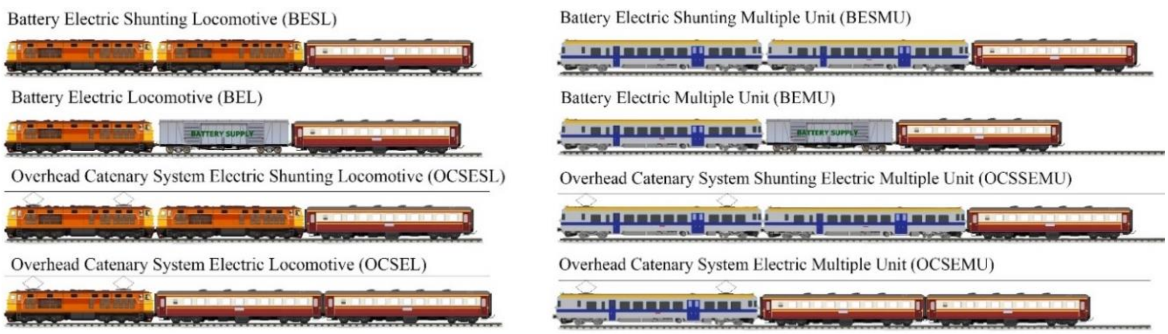

Figure 5. Train types are categorized by propulsion systems.

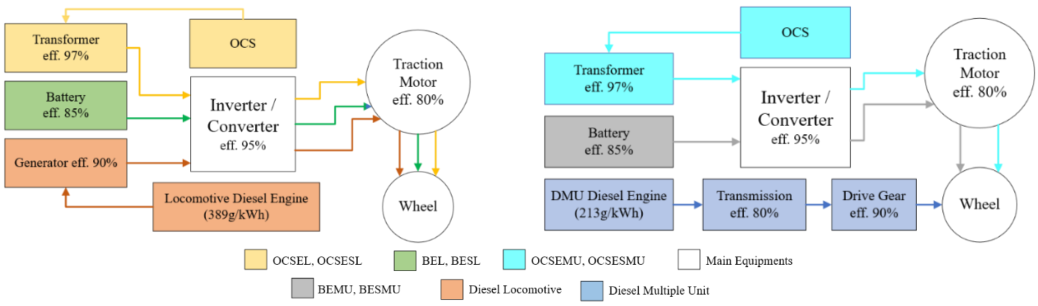

(a) (b)

Figure 6. Propulsion systems and component efficiency of each train type, (a) Locomotive (b) DMU.

3.6. The equation of fuel and energy consumption

David Norton [14] The power usage of a train can be determined by multiplying the total resistance of the train by the efficiency of the system from Figure 6., resulting in equations (8) and (9).

$$P_{eng} = W \times v \times \eta_{engsys} \quad (8)$$

$$P_{elec} = W \times v \times \eta_{elecsys} \quad (9)$$

Where P_{eng} is the engine power (kW), P_{elec} is the electric power (kW), W is the total resistance (kN), v is the velocity (m/s), η_{engsys} is an engine efficiency system, and $\eta_{elecsys}$ is an electric efficiency system.

For the fuel consumption during train operation, the following equation can be applied.

$$F_c = \frac{P_{eng} \cdot SFC \cdot \Delta t_{range}}{1000 \cdot \rho_{diesel}} \quad (10)$$

Where F_c is the fuel consumption (L), SFC is the specific fuel consumption (g/kWh), Δt_{range} is the time when there is a change in distance (hr.) and ρ_{diesel} is density of diesel fuel (kg/L).

Comparing the engine power and electrical power over time to study the energy consumption values during train movement, using Equations (11) and (12).

$$ENC = P_{eng} \times t \quad (11)$$

$$ELC = P_{elec} \times t \quad (12)$$

Where ENC is the engine consumption (kWh), ELC is the electricity consumption (kWh), and t is the time (h).

4. Results and Discussions

4.1. Data collection from locomotive and DMU

Train movement data collection from the locomotive and the DMU speed profiles by recording both departure and return trips. The data includes the total of the instances for each of the two models, and the velocity along the train route either departure and return trips. The collected data is then averaged for analysis, as depicted in the following shown in Figure 7.

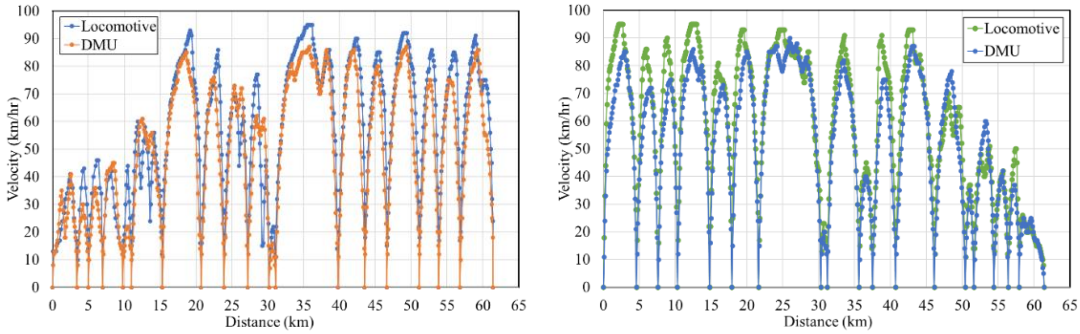

(a) (b)

Figure 7. The speed per distance from the movement of trains of both types, for (a) departure trip and (b) return trip.

From Figure 7. both (a) and (b) provided, the speed per distance for the train's motion on the departure trip. For the Locomotive, the average speed is 56.1 km/h, with a maximum speed of 95 km/h. The DMU has an average speed of 48.8 km/h, with a maximum speed of 87 km/h. On the return trip, for the Locomotive, the average speed is 56.8 km/h, with a maximum speed of 95 km/h. The DMU has an average speed of 51.6 km/h, with a maximum speed of 90 km/h. It can be observed that during urban transit, speeds do not exceed 60 km/h.

4.2. Analyzed traction power and kinetic energy of the trains

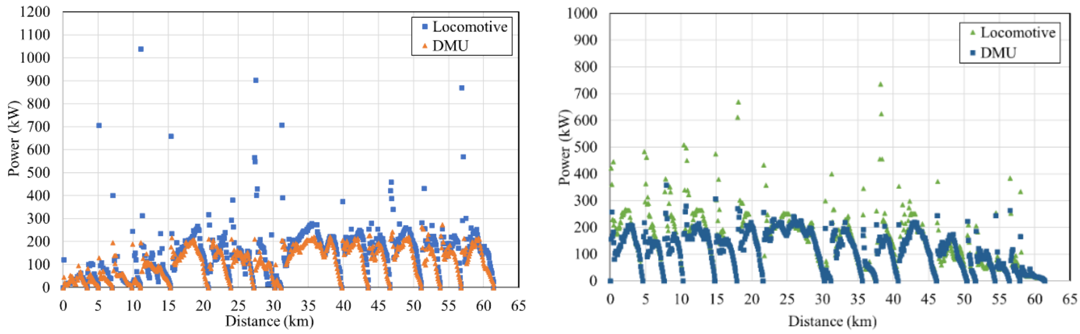

(a) (b)

Figure 8. The traction power of the trains along the routes, (a) departure trip and (b) return trip.

From Figure 8. both (a) and (b) provided, the power per distance for the train's motion on the departure trip. For the Locomotive, it has a maximum power of 1,243.2 kW, and the DMU has a maximum power of 273.8 kW. On the return trip, the Locomotive had a maximum power of 1,102.0 kW, and the DMU had a maximum power of 357.6 kW. It can be observed from the results that during the acceleration phase, there is a maximum power output, which then decreases as the train reaches a constant speed. This behavior is influenced by the size of the engine and the weight of the train.

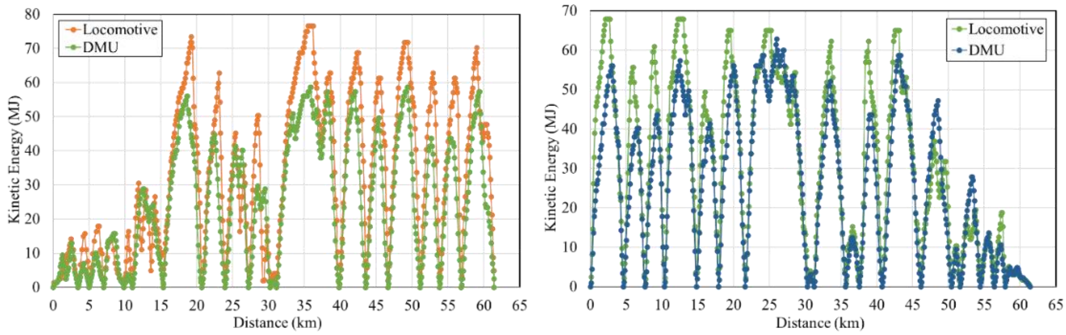

(a) (b)

Figure 9. The kinetic energy of train motion along the route, (a) departure trip and (b) return trip.

From Figure 9. both (a) and (b), the kinetic energy along the route distance for the train's motion on both the departure and return trips. It can be observed that the kinetic energy increases when the train is moving at higher speeds, noted that it should be compared together with the velocity profile in Figure 7. This has an impact on the ability to use regenerative braking, where the energy can be recovered from braking, which can then be used to supply to other systems or stored by battery for future use. However, when the train is operating at lower speeds, especially within the city, the energy recovered from braking may be insufficient for effective regenerative braking and energy storage.

4.3. Analysis of energy consumption from the electrical modification model.

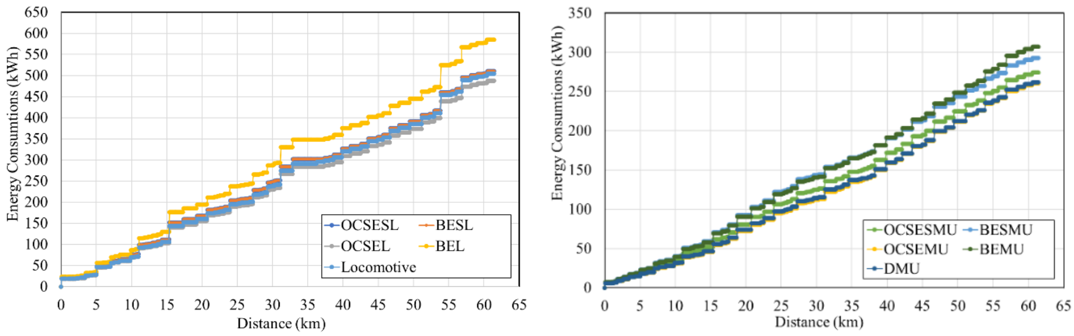

(a) (b)

Figure 10. The energy consumption per distance from the result of train modifications for departure trip, (a) Locomotive, and (b) DMU.

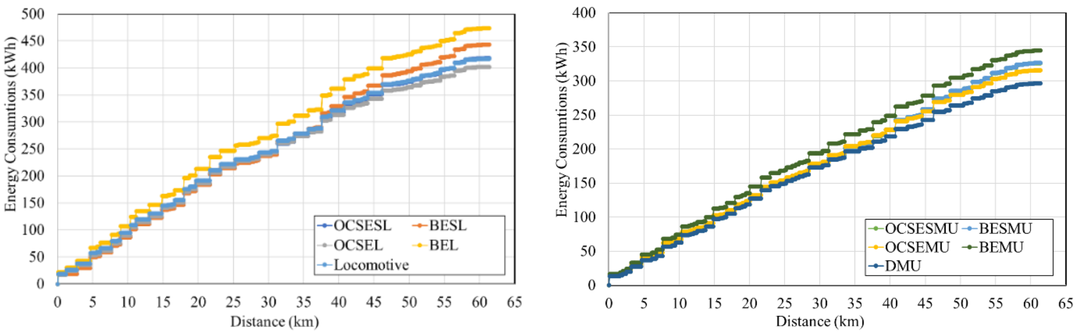

(a) (b)

Figure 11. The energy consumption per distance from the result of train modifications for the return trip, (a) Locomotive, and (b) DMU.

From Figure 10, it is apparent that for the Locomotive models, different formats exhibit energy consumption levels that are approximately similar, at around 500 kWh. However, in the case of the BEL format, the energy consumption is higher, standing at 585 kWh, as shown in Figure 10 (a). Regarding the DMU models, various formats have energy consumption levels that are relatively close to each other, ranging from approximately 260 kWh to 310 kWh, as depicted in Figure 10 (b).

From Figure 11, it's evident that for the Locomotive models, various formats have energy consumption levels that are close to each other, ranging from approximately 400 kWh to 475 kWh. The BEL format consistently has the highest energy consumption among all formats, as indicated in Figure 11(a). In the case of the DMU models, different formats exhibit energy consumption levels that are relatively similar, ranging from approximately 275 kWh to 350 kWh, as depicted in Figure 11(b). Notably, the BEMU format consistently has the highest energy consumption among all DMU formats, as shown in Figure 11(b).

4.4. Analyzed energy consumption and cost of each modified train model.

Firstly, let's consider a price assumption of 32 Baht/Liter for diesel fuel and an electricity cost of 5.25 Baht/kWh. Additionally, a total of 5 passenger cars trains were involved in this analysis, as shown in Table 1 to Table 2.

Table 1. Results of locomotive and DMU model modified for departure trip.

Data	Modified Models									
	Locomotive	BEL	OCSEL	BESL	OCSESL	DMU	BEMU	OCSE MU	BES MU	OCSES MU
Total weight (Ton)	220.0	246.8	220.5	241.8	240.5	201.0	226.8	201.5	232.8	231.5
Capacity ESS (kWh)	-	605.7	84.0	333.1	84.0	-	314.3	84.0	172.8	84.0
Engine energy (kWh)	504.7	183.6	168.7	262.9	262.9	261.9	123.3	113.6	149.2	149.0
Electric energy (kWh)	0	401.9	320.0	284.2	249.1	0	183.8	146.8	143.4	125.1
Fuel cons. (Liter)	231.8	69.9	64.8	107.7	107.9	65.8	3.9	28.5	37.4	37.4
Fuel cost (Baht)	7,417.4	2,238.2	2,074.5	3,446.3	3,453.3	2,104.5	987.7	911.9	1,195.5	1,195.5
Electricity cost (Baht)	0	2,109.7	1,680.2	1,492.2	1,307.7	0	808.6	645.8	631.0	550.3
Total cost (Baht)	7,417.4	4,347.9	3,754.7	4,938.5	4,761.4	2,104.5	1,796.4	1,557.7	1,826.5	1,745.8

Table 2. Results of locomotive and DMU model modified for the return trip.

Data	Modified Models									
	Locomotive	BEL	OCSEL	BESL	OCSESL	DMU	BEMU	OCSE MU	BES MU	OCSES MU
Total weight (Ton)	195.0	220.8	195.5	225.9	225.5	201.0	226.8	201.5	231.9	231.5
Capacity ESS (kWh)	-	505.5	84.0	275.3	84.0	-	355.8	84.0	195.7	84.0
Engine energy (kWh)	417.1	197.3	181.66	239.9	239.9	296.5	144.9	133.5	176.1	176.1
Electric energy (kWh)	0	276.6	220.35	203.6	178.18	0	199.9	182.2	150.3	150.1
Fuel cons. (Liter)	174.1	91.0	83.7	109.5	109.5	67.4	36.3	33.4	44.0	44.0
Fuel cost (Baht)	5,570.5	2,912.1	2,679.1	3,505.1	3,505.1	2,156.9	1,160.5	1,069.4	1,407.4	1,407.4
Electricity cost (Baht)	0	1,217.3	969.5	896.1	784.0	0	879.4	801.9	661.3	660.3
Total cost (Baht)	5,570.5	4,129.4	3,648.7	4,401.2	4,289.1	2,156.9	2,039.9	1,871.3	2,068.7	2,067.7

From Table 1, for the locomotive modified case, it is shown that the OCSEL model has the lowest expenditure of 3,754.7 baht/trip of operation. Following this, in ascending order, the BEL, OCSESL, BESL, and original locomotive models, respectively. In the case of DMU, the OCSEMU model has the lowest expenditure of 1,557.7 baht/trip of operation. Following this, in ascending order, the OCSESMU, BEMU, BESMU, and original DMU models, respectively. These results indicate that the train's weight and the electricity consumption rate have an impact on the cost of operation for each modified model.

From Table 2, there are expenditures on the return trip similar to that of the departure trip. The OCSEL model has the lowest expenditure in the case of modified locomotive case. The OCSEMU model has the lowest expenditure in the case of modified DMU case. The weight of the train and the electricity consumption rate have an impact on the operating cost of each modified train model.

5. Conclusion

The analysis of modified train formats, utilizing electric energy from two types of trains, Locomotive and DMU, on the route from Bangkok station to Chum-Thang-Chachoengsao station, covering a distance of 61.4 km, reveals that the highest energy demand occurs during the acceleration phase of the train. Regarding the energy consumption cost for all eight modified models without considering infrastructure investment, it has been found that the format utilizing energy from the Overhead Catenary System (OCS) offers the most cost-effective travel option, varying from 35 – 97% saver than using diesel engine in operation. Furthermore, the modified battery-electric locomotive and modified battery-electric DMU have the potential to do so. However, the total investment including infrastructure, O&M, and many more factors needs to be considered much more in detail for a final decision.

6. References

[1] State Railway of Thailand. *History of the State Railway of Thailand*. [online]. Available: https://www.railway.co.th/AboutUs/ [2023, August 1].

[2] Committee on Natural Resources and Environment, Senate. (2020). *The problem of dust particles no larger than 2.5 microns (PM2.5) in Bangkok Metropolitan Region*. The Secretariat of the Senate.

[3] Cedric De Cauwer, Joeri Van Mierlo and Thierry Coosemans. (2015**)** *Energy Consumption Prediction for Electric Vehicles Based on Real-World Data,* Vrije Universiteit Brussel, pp. 2-20.

[4] The Business Research Company. (2023). *Electric Locomotives Global Market Report 2023*. [online]. Available: https://www.reportlinker.com/p06277717/Electric-Locomotives-Global-Market-Report.html?utm_source=PRN [2023, August 2].

[5] Caio Guilherme da Silva Moraes, Student Member, Sergio Luis Brockveld Junior , Marcelo Lobo Heldwein , Senior Member, Andre Stanzani Franca´, Anderson Silva Vaccari, and Gierri Waltrich. (2020). *Power Conversion Technologies for a Hybrid Energy Storage System in Diesel-Electric Locomotives*. EEE Transactions on Industrial Electronics. pp.1-2.

[6] Stuart Mackay. *DMU Technology - The Basics*. [online]. Available: https://railcar.co.uk/technology/the-basics. [2023, August 1].

[7] Nakhon Chantrasorn. (2012). *Railway Engineer with extensive knowledge in railway engineering*. The national science and technology development agency. pp.229-250.

[8] Bunleng Soranin, Nisai Feuangwerachotisakul, Somnuk Watthanasuriyakul, Monta Phudchawi, Kampol Siritawatin, Chayakorn Netmai, and Apichat Wangyai Chaim. (2021). *Railway Vehicle Technology (Schienen-fahrzeugtechnik)*. 1st Edition. Rungsangthong Printing Co., Ltd.

[9] Shezhen XiHo Energy Tecnology. *CATL 280Ah 3.7V NMC Prismatic Rechargeable Lithium Ion Battery*. [online]. Available: https://www.xihobattery.com/products/catl-280ah-37v-nmc-prismatic-rechargeable-lithium-ion-battery. [2023, August 2].

[10] Carlos Armenta-Déu and Hernán Cortés. (2023). *Analysis of Kinetic Energy Recovery Systems in Electric Vehicles*. Energies. MDPI.

[11] Polrut Boonme, Supachai Lakkam and Phusit Chotswasd. (2016). *An Investigation of Brake Specific Fuel Consumption and Pollution of Locomotive Engines*. RMUTTO Research Journal.

[12] EB Machinery. *Cummins 6CTA8.3-G2 (163KW).* [online]. Available: https://www.cumminsengine.net/cummins-6cta8-3-g2.html [2023, August 3]

[13] Miguel Angel Rodriguez-Cabal, Diego Alejandro Herrera-Jaramillo, Juan David Bastidas-Rodriguez, Juan Pablo Villegas-Ceballos, and Kevin Smit Montes-Villa. (2022). *Methodology for the Estimation of Electrical Power Consumed by Locomotives on Undocumented Railroad Tracks*. Energies. MDPI.

[14] David Norton. (2012). *Power Converter Efficiency: Formulas and Calculations.* [online]. Available: https://www.edn.com/efficiency-calculations-for-power-converters. [2023, August 3].

AME0017

Design of Battery Pack Enclosure Structure for Electric Conversion Vehicle

S Intathumma[1], P Jongpradist[1, 2], and S Kongwat[1, 2, *]

[1]Department of Mechanical Engineering, Faculty of Engineering, King Mongkut's University of Technology Thonburi, Bangkok, 10140, Thailand
[2]Future Automotive Structure Research Group (FASt), Mobility and Vehicle Technology Research Center, King Mongkut's University of Technology Thonburi, Bangkok, 10140, Thailand

* Corresponding Author: suphanut.kon@kmutt.ac.th

Abstract. Electric conversion vehicles are an alternative transportation solution, effectively reducing greenhouse gas emissions. The battery, serving as the primary energy storage component, is safeguarded within a battery pack enclosure to protect it from potentially contaminated road debris. The efficient design of battery pack enclosures is a crucial concern for ensuring the safety of electric vehicles. Therefore, this study aims to utilize topography, topology and size optimization techniques to enhance the design of the battery pack enclosure by considering normal operating conditions, natural frequency, and impact loading from road debris contamination. A finite element model is implemented to analyze structural strength under the desired loading conditions using HyperWorks. A preliminary analysis of the battery pack enclosure indicated that the impact loading scenario is the most severe condition and requires particular attention in the design process. Topography optimization techniques were employed to design the beading of the outer component. The layout of the internal member was determined through topology optimization, aiming to minimize structural displacement. The results demonstrated that the optimized battery pack enclosure successfully met all structural requirements and achieved a 73.2% reduction in displacement compared to the baseline model despite a slight increase in structural weight.

Keywords: Battery Pack Enclosure, Electric Conversion Vehicle, Ground Impact, Topology Optimization, Topography Optimization.

1. Introduction

The transportation sector plays a significant role in the global emission of greenhouse gases and is notable for its rapid growth [1]. Consequently, electric vehicles have gained considerable interest. One emerging concept gaining popularity in certain circles is the conversion of internal combustion vehicles into electric vehicles, primarily due to cost considerations. One of the critical components that distinguishes an electric vehicle from a combustion vehicle is its battery [2]. The battery is typically located beneath the vehicle within a battery enclosure.

In recent years, some studies have been conducted on designing a battery pack enclosure, which found that steel is suitable for use as a material in automotive applications because it is reasonably priced and environmentally sustainable [3]. However, it is crucial to incorporate measures in the battery pack enclosure design is to mitigate resonance with the vibrations experienced during the car's operation. These vibrations can induce stress, change the shape of the battery pack enclosure, and, in some cases, even result in excessive heat generation that could lead to a fire hazard [4, 5]. The vibrational frequencies of electric vehicles during regular operation typically fall within the range of 7-200 Hz. It is advisable to aim for a standard frequency of 70 Hz or higher to avoid resonance issues [6]. Additionally, it is essential to design the battery pack enclosure to endure typical operational conditions like left turn, right turn, and braking. These actions can generate damping forces because of the battery's weight [7, 8]. Another critical scenario to consider is the possibility of rock debris on the road surface colliding with the underside of the vehicle during normal driving, which can potentially cause danger. If the deformation of the battery exceeds 3 mm, there is a risk of a potential explosion [9]. Therefore, designing a battery pack enclosure to meet these desired conditions is imperative.

Numerous researchers have investigated the strength of the battery pack enclosure to prevent damage from operating conditions and rock debris [10]. Structural optimization was also utilized in designing the battery pack enclosure, considering various factors, such as safety factors and structural strength under specified load conditions [11]. Various optimization techniques, such as topology, topography, and size optimization, aim to shape the material's surface to enhance strength while maintaining consistent thickness [12]. On the other hand, topology optimization seeks to determine the appropriate structural design for specific conditions [13].

This study focuses on designing a stainless-steel battery pack enclosure for an electric conversion vehicle, within the constraints of limited space, with the goal to enhance performance through finite element analysis using HyperWorks. Topography and topology optimization techniques are employed to seek the optimal shape of the structure, while size optimization is then utilized to find the optimal thickness. The design criteria include the ability to withstand normal operation conditions without experiencing permanent deformation, the required natural frequency of the structure, and the loading conditions resulting from potential ground impacts. Finally, the strength of the optimized model battery is also examined.

2. Preliminary analysis of the baseline model

2.1. Finite element model

The battery pack enclosure comprises two main structural components: the outer and inner structures. The outer structure's role is to safeguard the batteries and electronic circuits. It is attached to the vehicle frame with three points on each side, totaling six connection points. These connections are achieved using nuts and bolts. The inner structure provides support for the battery, as illustrated in Figure 1. The battery pack enclosure houses a total of 48 batteries, each weighing 1.98 kg. The battery pack enclosure's model is created using shell elements with an element size of 6 mm. The finite element model consists of 60,615 nodes and 114,972 elements. The thicknesses of outer and inner structures are 2 mm. The material properties of both components are assigned as SS400, in which the mechanical properties are shown in Figure 2. The battery pack enclosure in this study is used for the internal combustion vehicle that is switched to electric power and must provide strength without permanent deformation under normal operating conditions, can prevent damage caused by natural frequencies, and support impact from rock debris under the car without damaging the battery.

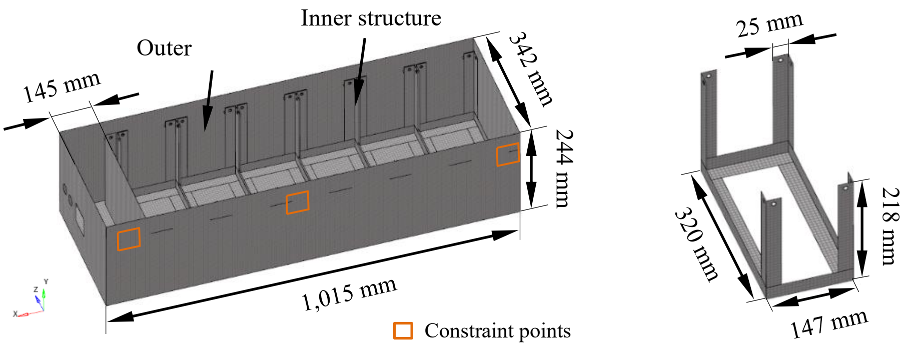

(a) (b)

Figure 1. (a) Battery pack enclosure model (b) Inner structure.

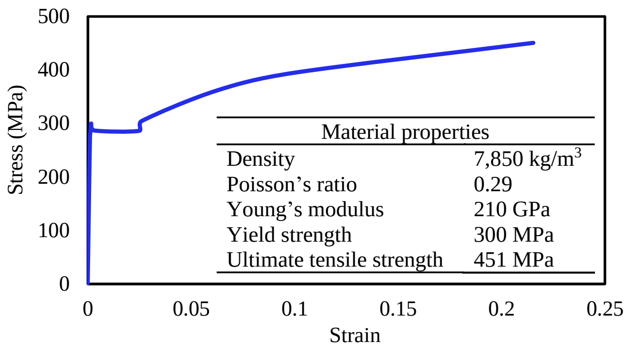

Figure 2. Stress-strain curve of SS400 steel.

2.2. Finite element analysis

The baseline model of the battery pack enclosure is examined under three primary scenarios: normal operation, natural frequency, and impact conditions. The boundary conditions involve constraining translation in the x- and y-directions, as well as rotation in the x- and z-directions at three constraint points on each side of the battery pack enclosure are applied to analyze all scenarios, representing the points where the battery pack enclosure is attached to the vehicle frame, as illustrated in Figure 1a. Normal operating conditions encompass four distinct load cases, including scenarios involving battery weight, turning, braking, and movement. In these cases, forces are applied to the model as listed in Table 1, with an example of the position of the applied force depicted in Figures 3a and 3b. The structure frequencies are explored by examining the first ten modes in a modal analysis. An impactor with a conical shape and a tip radius of 20 mm is utilized for the impact condition, having a mass of 0.45 kg, as shown in Figure 3c. The impactor is initiated with an initial velocity of 50 kph (13.89 m/s) in the y-direction, the point where the impactor begins is positioned 4 mm away from the bottom of the battery pack enclosure, targeting the lower plate of the battery pack enclosure. This setup is representative of potential road debris impacts. The analyses for normal operating conditions and impact scenarios are executed using linear-static and nonlinear-dynamic calculations in HyperWorks.

The strength requirements for the battery pack enclosure dictate that the safety factor must be at least 2.0 under normal operating conditions. Additionally, the natural frequency of the structure should surpass 70 Hz. The results from the finite element analysis under normal operating conditions are presented in Table 2, showing that all load cases meet the requirements. The first structural mode of the structure exhibits a natural frequency of 94.6 Hz, which also exceeds the specified threshold. During the impact condition, the bottom part of the structure experiences a maximum displacement of 9.2 mm. This situation raises concerns as the deformation should not surpass 3 mm to prevent potential battery explosion. Therefore, the impact scenario represents the most critical condition in the battery pack enclosure design, while the other cases involve a certain degree of overdesign. However, it is important to note that while the FE results have been meticulously examined and interpreted, conducting future research that involves validating the FE simulations through experiments, such as impact tests, would further bolster the reliability and trustworthiness of the results.

Table 1. Magnitude and directions of forces for each normal condition load.

Load cases	Force directions		
	X	Y	Z
Battery weight	-	-155.4 N	-
Forward movement	-54.4 N	-	-
Brake	155.4 N	-	-
Left turning	-	-	116.5 N
Right turning	-	-	-116.5 N

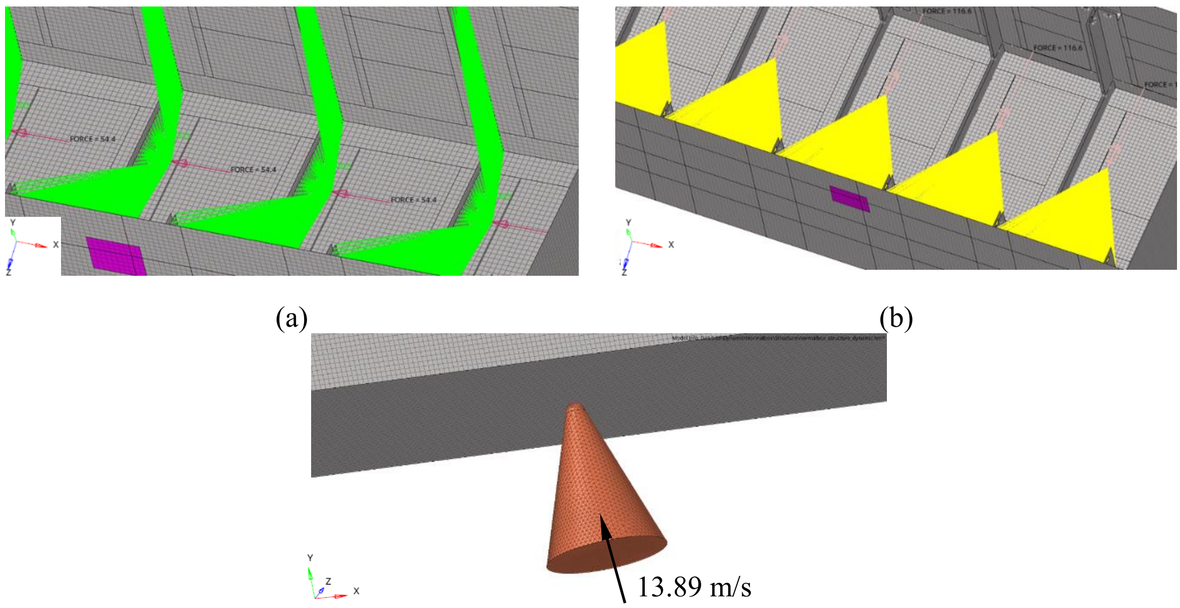

(a) (b) (c)

Figure 3. Loading conditions (a) Forward movement case (b) Turning left case (c) Impact case.

Table 2. Results of normal conditions.

Load cases	Maximum stress (MPa)	Safety Factor	Criteria
Battery weight	15.84	15.5	Pass
Forward movement	15.35	16.0	Pass
Brake	26.04	9.41	Pass
Left turning	46.49	5.27	Pass
Right turning	47.73	5.13	Pass

According to the analysis results of the baseline model, it is evident that the battery pack enclosure needs to undergo an optimization process to ensure its structural integrity under impact conditions. To achieve this, various structural optimization techniques will be employed. These techniques include topography optimization for refining the design of the outer structure, topology optimization for enhancing the design of the inner structure, and size optimization to optimize the thickness of components.

3. Optimization

The optimization of the battery pack enclosure is divided into three processes: topography, topology, and size optimization (Figure 4). Topography optimization is utilized to define the specific shape of the outer structure's bead. This shape is stamped into the structure to enhance its structural strength without altering its thickness. Topology optimization, in which the element densities are assigned as design variables, is then employed to seek an optimal layout of the inner structure. Finally, size optimization involves determining the appropriate thickness of all structural components of the battery pack enclosure. These optimization processes are geared towards enhancing the structural performance of the battery pack enclosure under desired conditions, including impact loading. A summary of the optimization problems for each procedure is provided in Table 3.

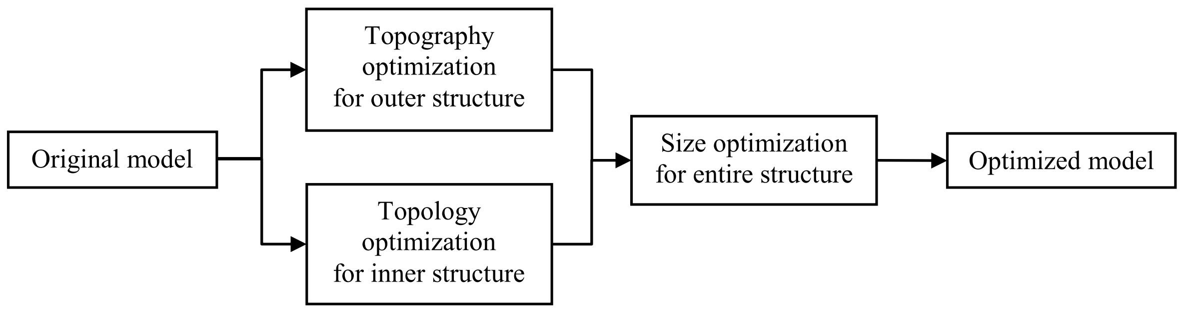

Figure 4. Optimization process.

Table 3. Optimization problem.

Optimization		Conditions
Topography	Objective	Minimize compliance
	Constraints	Stress < 150 MPa Displacement < 3 mm Frequency > 70 Hz Pattern grouping: 2-plane symmetry
	Design variables	Bead parameter -Draw angle = 60 degree -Width ≥ 30 mm -Draw height = 10 mm
Topology	Objective	Minimize displacement
	Constraints	Volume fraction < 0.3 Pattern grouping: 2-plane symmetry
	Design variables	15 mm ≤ Dimension ≤ 60 mm Member gap ≥ 60 mm
Size	Objective	Minimize mass
	Constraints	Stress < 150 MPa Displacement < 3 mm
	Design variables	1.2 mm ≤ Thickness ≤ 4 mm

The results of both topography and topology optimization are depicted in Figure 5a, showcasing the creation of beads on the outer structure and the search for an optimal layout for the inner structure, respectively. Based on these results, it is observed that the maximum stress reached 37.87 MPa during right-turning cases, passing the safety requirements for normal operation conditions and natural frequency. Unfortunately, under impact conditions, the optimized model from topography optimization alone exhibited a maximum displacement of 7.22 mm, whereas the model resulting from combined topography and topology optimization accomplished to reduce the maximum displacement to 5.9 mm. This clearly indicates that the optimized model resulting from topography and topology optimization falls short in safeguarding the battery against impact loading. Size optimization is then implemented to enhance structural performance by determining the appropriate thickness for various components. As a result, the optimized model reveals a thickness of 1.2 mm for the side of the outer structure, while other components have a thickness of 4 mm. Furthermore, the results of the finite element analysis indicate that, under impact loading conditions, the maximum displacement measures 2.46 mm (Figure 5b). The factor of safety and natural frequency also adhere to the specified criteria. Therefore, the optimized model resulting from topography, topology, and size optimization successfully fulfills all the required criteria.

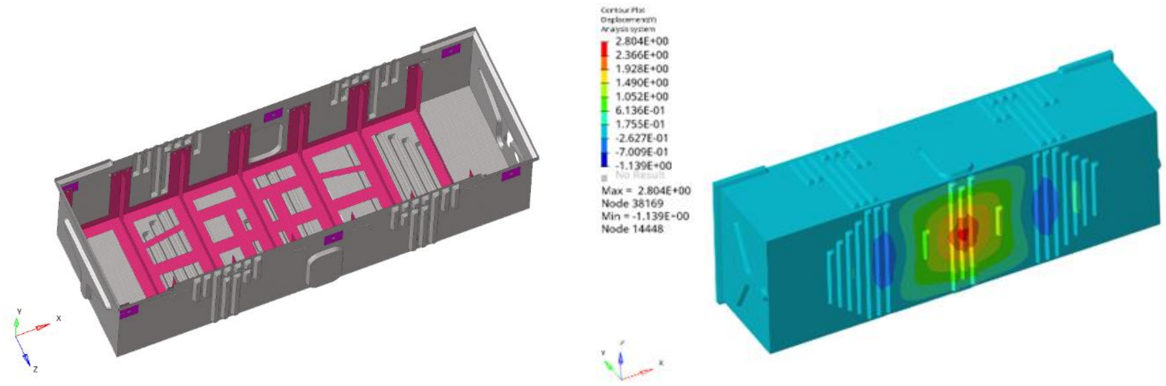

(a) (b)

Figure 5. Optimization result (a) Optimized battery pack enclosure (b) Deformation of the optimized model.

The results obtained from impact analysis on the optimized battery pack enclosure can be compared with other models, as depicted in Figure 6. This comparison highlights that the optimized model effectively satisfies the displacement criteria, thereby ensuring the battery's protection against collisions with rock debris. Specifically, the optimization achieved through size optimization technique results in a remarkable 73.2% reduction in maximum displacement compared to the baseline model, with a corresponding 13.4% increase in structural weight. Furthermore, the structural components of the optimized model demonstrate the ability to absorb 100% of the impact energy. Conversely, the topography and topography-with-topology-optimized models can absorb up to 48% and 69% of the impact energy, respectively, with a slight change in weight compared to the baseline model. However, the results emphasize that the maximum displacement still exceeds 3 mm, a factor deemed unacceptable in the design process. The topography optimization results indicated suitable locations for creating beads on outer structure, while the optimal layout of the inner structure was obtained through topology optimization. Both techniques contributed to enhancing the overall stiffness of the structures, leading to a slight reduction in displacement compared to the baseline model. Therefore, the size optimization process remains indispensable to ensure that the battery pack enclosure maintains the requisite strength to withstand diverse scenarios without compromising the battery's integrity. The optimized model resulting from size optimization also indicated that the displacement still surpassed the specified constraint by 16.7%.

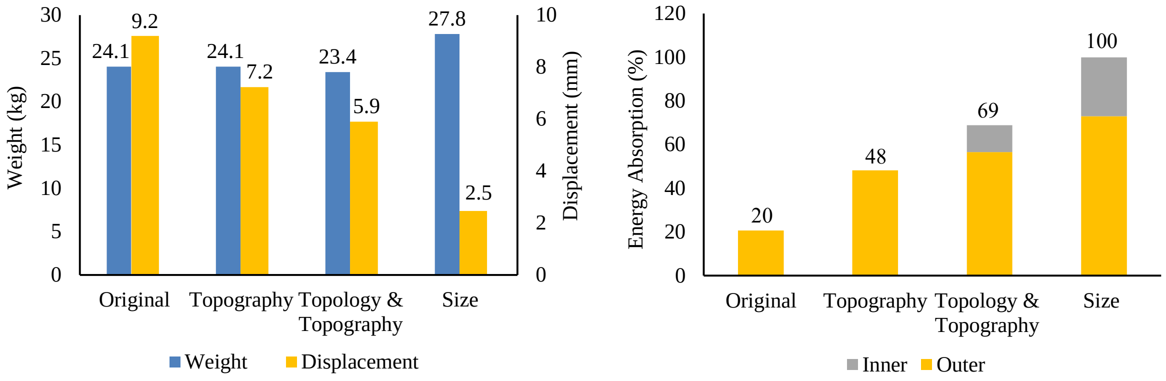

(a) (b)

Figure 6. Comparison result of the difference process (a) Weight and displacement (b) Energy absorption.

4. Conclusion

This paper presents the design of a battery pack enclosure intended for electric vehicles converted from internal combustion vehicles. Through optimization processes, it was ensured that the enclosure can withstand normal operating conditions without incurring permanent deformation, maintain natural frequencies higher than the required value, and endure impact scenarios rock debris colliding from the vehicle's underside. The results demonstrate that the optimized battery pack enclosure, following topography, topology and size optimization, successfully meets the requirements for maximum displacement after impact, albeit with a slight increase in weight.

5. Acknowledgement

This research has received funding support from the National Science, Research and Innovation Fund (NSRF) via the Program Management Unit for Human Resources & Institutional Development, Research and Innovation [grant number B40G660039] and Thailand Science Research and Innovation (TSRI) Basic Research Fund: Fiscal year 2024 (Program Sustainable Mobility).

6. References

[1] Bhowmik, R., Rahut, D. B., & Syed, Q. R. (2022). Investigating the impact of climate change mitigation technology on the transport sector CO2 Emissions: Evidence from panel quantile regression. *Frontiers in Environmental Science*, 10, 916356.

[2] Hoeft, F. (2021). Internal combustion engine to electric vehicle retrofitting: Potential customer's needs, public perception and business model implications. *Transportation Research Interdisciplinary Perspectives*, 9, 100330.

[3] Bala, A., & Chaitanya Kamaraju, M. (2020). Design and Optimization of Battery Housing in Electric Cars.

[4] Hooper, J. M., & Marco, J. (2014). Characterising the in-vehicle vibration inputs to the high voltage battery of an electric vehicle. *Journal of power sources*, 245, 510-519.

[5] Hooper, J. M., & Marco, J. (2015). Experimental modal analysis of lithium-ion pouch cells. *Journal of Power Sources*, 285, 247-259.

[6] Pal, S. K., Singh, S., Singh, H., Le Phung, M. L., Yooyen, S., & Sleesongsom, S. (2020). Intelligent design optimization of battery pack enclosure for electric vehicle by considering cold-spraying as an additive manufacturing technology. *Energy Storage*, 2(3), e148.

[7] Lu, W., Xiao-kai, C., & Qing-hai, Z. (2016). Muti-objective topology optimization of an electric vehicle's traction battery enclosure. *Energy Procedia*, 88, 874-880.

[8] Wang, T., Chen, X., Chen, G., Ji, H., Li, L., Yuan, Q., ... & Ji, Y. (2021). Investigation of mechanical integrity of prismatic lithium-ion batteries with various state of charge. *Journal of Electrochemical Energy Conversion and Storage*, 18(3), 031002.

[9] Kermani, G., Dixon, B., & Sahraei, E. (2019). Elliptical lithium-ion batteries: transverse and axial loadings under wet/dry conditions. *Energy Science & Engineering*, 7(3), 890-898.
[10] Yang, N., Fang, R., Li, H., & Xie, H. (2019, November). Dynamic and static analysis of the battery box structure of an electric vehicle. In *IOP Conference Series: Materials Science and Engineering* (Vol. 688, No. 3, p. 033082). IOP Publishing.
[11] Klarbring, A., & Christensen, P. W. (2009). An introduction to structural optimization. Solid Mechanics and its Applications. *Springer Science+ Business Media BV*.
[12] Kong, Y. S., Abdullah, S. H. A. H. R. U. M., Omar, M. Z., & Haris, S. M. (2016). Topological and topographical optimization of automotive spring lower seat. *Latin American Journal of Solids and Structures*, 13, 1388-1405.
[13] Bendsoe, M. P., & Sigmund, O. (2003). *Topology optimization: theory, methods, and applications*. Springer Science & Business Media.

AME0019

A Study on the Effects of using Different Biodiesel Blending Fractions on Tailpipe Emissions of Two Euro 5 Pickup Trucks

Sitt Naing[1], Peerawat Saisirirat[2], Mek Srilomsak[1,*], Phumanan Niyomna[2], Pop-Paul Ewphun[2], and Nuwong Chollacoop[2]

[1]School of Engineering, King Mongkut's institute of Technology Ladkrabang (KMITL), 1 Chalong Krung Rd., Lat Krabang, Bangkok, 10520, THAILAND
[2]National Energy Technology Center (ENTEC), National Science and Technology Development Agency (NSTDA), 114 Thailand Science Park, Pahonyothin Rd., Khlong Nueng, Khlong Luang, Pathum Thani, 12120, THAILAND

* Corresponding Author: mek.sr@kmitl.ac.th

Abstract. The impacts of using different biodiesel fractions on the DPF active regeneration intervals, levels of regulated emissions, and analyzed results of particle size distribution were experimentally explored in this study. The certified Euro-5 quality diesel fuels with different biodiesel fractions with B7, B10, and B20 were tested in two Euro-5 light-duty pickup trucks (with 2.8L and 2.4L engine sizes), represented the largest portion of on-road vehicles in Thailand. The vehicle tailpipe emissions were analyzed for both test vehicles according to the ECE-R83 Rev.4 (Euro-5) method, and the instantaneous emission analysis of soot concentrations and PM size distribution were also carried out in real-time throughout the NEDC driving cycle to track the distribution of peak PM emissions in various operating conditions. The results showed that using different biodiesel blending fractions has no significant difference in the tailpipe emissions and particle size distribution. For the analysis of active DPF regeneration intervals, the results showed compliance with the PM emissions output. Furthermore, the lowest particulate emissions resulted in longer regeneration intervals as observed in the 2.4L vehicle using B20 diesel fuel.

Keywords: Biofuel blended fuels, Regulated emissions, PM size distribution analysis, Active DPF regeneration intervals.

1. Introduction

The diesel engine as an internal combustion engine can be widely applied in many sectors such as transport, industry, and agriculture because of its high efficiency and low fuel consumption. Unfortunately, their main drawback is the emissions of Particulate Matter (PM) which are related to smoke emission, Nitrogen Oxides (NO), and Carbon Monoxide (CO) which are the main air pollutants affecting human health conditions and environment. In addition, the fossil diesel fuel used in diesel engines is not renewable and have many negative impacts on both living things and the global warming. Due to the pressing need to replace fossil fuels and reduce the Greenhouse Gas (GHG) emissions, biodiesel fuel has been becoming popular as an alternative renewable fuel that can be blended with fossil fuels to reduce usage of fossil fuel and its pollution impacts. As of 2021, Thailand accounted for 3.8% of the global total palm oil production [1] (Chaiwat Sowcharoensuk, 2022). There are approximately 390,000 Palm Oil farm households across the country and large farmers tend to invest in their own crude palm oil mills. As Thailand has many reliable sources of palm oil production, using palm oil as a biodiesel blend should be a reasonable approach to contribute to the reduction of fossil fuel usage and help tackle its related pollution problems and benefit the agricultural income.

However, the transport fuel consumption has been expanding due to growing of economic activities, so reducing the usage of fossil fuels alone is not enough to mitigate the climate change crisis and improve air quality. Therefore, automotive emission standards are being raised throughout the world to help negate these pollution problems. This is also happening in Thailand where the Euro-5 automotive emission standard will be implemented together with fuel quality improvement [2]. The new diesel-certified fuel will be used by all new generation vehicles sold after January 1st, 2024, and the existing predecessor vehicles which will still be a major portion of on-road vehicles in Thailand for a while. This government action is expected to play a major role in improving air pollution quality, especially in reducing emissions produced by the automotive sector.

In addition, the fractions of biofuels were reported to be able to improve quality of vehicle exhaust gas. Moreover, using biofuels will also reduce Greenhouse Gas emissions that cause climate change crises. In (2016), Jung et al. analyzed the impacts of biodiesel blended fraction on the exhaust emission by using a single-cylinder common-rail diesel engine [3]. The biodiesel of Fatty-Acid Methyl Ester (FAME) was derived from waste-cooking oil. In this study, Jung et al. analyzed the exhaust particulate emissions using three methods, e.g., Thermo-Gravimetric Analysis (TGA), Elemental analysis, and Transmission Electron Microscopy (TEM). They discovered that the increasing of biodiesel proportion reduced the molecular complexity of the soot precursor particles which also have more hydrogen- and oxygen- contents. These observed particulate components can be easily oxidized and will be able to decompose before becoming the PM emission in the exhaust gas. The microscopic analysis has been investigated by Y. Songsaengchan, et al. in (2011) and they concluded that the impact on particulate emission is related to the increase of fuel oxygen content [4].

As mentioned before, this study aims to explore the impacts of biodiesel blending fractions on improving vehicle exhaust composition, regulated emission levels, and DPF regeneration intervals. The tested vehicles were two LDVs, one is a 2.8L automatic transmission (AT) pickup truck and the other is a 2.4L manual transmission (MT) pickup truck.

2. Experimental Methodology

To make sure that the test fuels are Euro-5 certified quality, the test fuels were blended from based diesel fossil fuel (B0) with Euro-5 certified quality and the neat biodiesel (B100). The based diesel fossil fuel (B0) was purchased through special approval from the Department of Energy Business (DOEB) while the neat biodiesel (B100) was supported by certified biodiesel manufacturers. Then the test fuels were mixed at the desired fraction of 7,10 and 20 in percent (as B7, B10, and B20 fuels). The properties of tested diesel fuels are shown in Table 1.

In the case of the test vehicles, two LDVs, certified Euro-5 vehicle emission standards vehicles, and still not available in the current Thailand automotive market, were supported by the automotive company (Toyota Motor Thailand). Both vehicles are pickup trucks which represent the largest segment of diesel vehicles in Thailand. The specifications of both test vehicles are shown in Table 2. These two vehicles are in brand-new condition to be used solely for research purposes. The experiments were performed in both vehicles for all three biodiesel fuels.

All the experimental tests were performed under the UN ECE Regulation No.83 Rev.4-5 [5,6], and the Euro-5 emission regulations are shown in Table 3. The test vehicles were equipped with a certified chassis dynamometer and the automotive tailpipe emissions were also analyzed by the AVL full-flow dilution system – Constant Volume Sampler (CVS), modeled PSS i60 single dilution (SD). The considered tailpipe pollutions in exhaust gas were analyzed by standard apparatus of exhaust-gas analyzing machine used for type approved tests, including the gravimetric particulate matter (AVL smart

Sampler SPC-472) for measuring the PM emission, AVL Particle Counter for the particle number concentration which must be measured after volatile particle remover system, the Flame Ionization Detector (FID) for total unburned hydrocarbon (THC) and methane (CH_4), the Chemiluminescence Detector (CLD) for oxides of nitrogen (NO, NO_2, and NO_x), the Paramagnetic oxygen detector (PMD) to measure oxygen (O_2). The exhaust-gas analyzing machines were calibrated to meet linearity criteria of 2.5%. In addition, the Micro Soot Sensor (MSS) and the Engine Exhaust Particle Sizer (EEPS) Spectrometer were also equipped to monitor real-time soot concentration (in g/m^3 or mg/m^3) and apply size distribution analysis. The MSS can measure PM emission in a range of 0.001 – 50 mg/m^3 with a resolution of 0.01 mg/m^3 and a maximum frequency of 100 Hz. The MSS is more suitable for analyzing tailpipe emissions from high-emission standard vehicles with light soot content. The EEPS can monitor the size distribution of particulate emission ranging between 5.6 - 560 nm which can cover particle size from 'Nucleation mode' (< 0.1µm) and small-to-middle 'Accumulation mode' (0.1 – 2.0 µm), according to the definition of atmospheric particulate emission (Air Quality Expert Group, 2005)[7]. The tailpipe exhaust gas emissions were analyzed along the test protocol consisting of the New European Driving Cycle (NEDC, cold-started). The velocity profile during NEDC standard driving cycle is shown in Figure 1. In addition, both test vehicles were always monitored to not activate an active DPF-regeneration process during the test cycle to avoid abnormal exhaust gas emissions. The vehicle load factors were considered according to the vehicle weight for each test vehicle.

For the analysis of active DPF regeneration intervals based on all three test fuels, both vehicles were equipped with temperature sensors installed on the inlet and outlet of the DPF to monitor the DPF regeneration events. Pressure sensors were also installed inside the DPF to monitor real-time pressure buildup inside the DPF. Both vehicles were driven a total distance of 90,000 km to get enough consistent data to track regeneration intervals using all three fuels and fuel changing between B10, B20, and B7 was performed every 30,000 km interval. GPS tracking devices were also installed on the test vehicles to track the traffic condition along the road test.

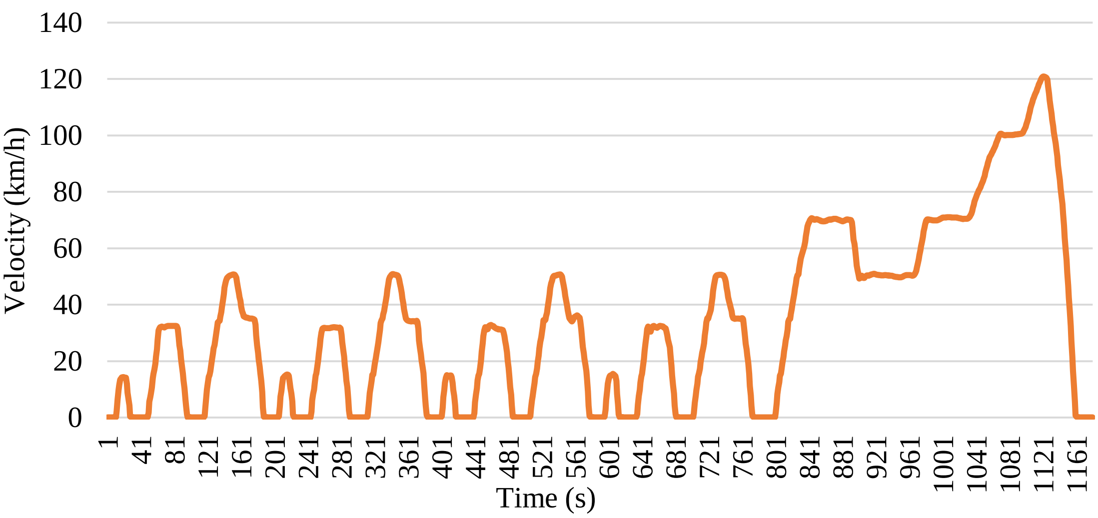

Figure 1. Velocity Pattern during NEDC standard driving cycle.

Table 1. Properties of tested fuels.

Name	Fuel 1 Commercial Euro-5 B7	Fuel 2 Commercial Euro-5 B10	Fuel 3 Commercial Euro-5 B20	
Certified		Euro-5 fuel		Test method
Color	Yellow	Yellow	Yellow	Visual inspection
Density (g/cm^3)	0.8272	0.8302	0.8333	ASTM D4052
Initial Boiling Point (˚C)	170.1	167.7	174.6	ASTM D86
90%vol. recovered temperature (˚C)	352.9	344.9	351.6	ASTM D86
Flash Point (˚C)	65.0	66.0	72.0	ASTM D93
Pour Point	< -6	< -6	-3	ASTM D97
Gross Heat of Combustion (MJ/kg)	45.89	45.85	45.80	ASTM D4868
Sulfur Content (mg/kg)	4	10	6	ASTM D5453
Water Content (mg/kg)	75	101	106	ASTM D6304
Biodiesel (FAME) content (%vol)	6.6	11.2	23.4	EN 14078
Cetane Number	59.8	60	59.4	ASTM D976

Table 2. Specifications of test vehicles.

Name	Euro-5 Pickup truck	Euro-5 Pickup truck
Brand	TOYOTA	TOYOTA
Vehicle type	Extended cab pickup truck	4-doors pickup truck
Model	Hilux Revo	Hilux Revo
Pollution level	Euro-5	Euro-5
Power transmission	Automatic	Manual
Engine code	1GD-FTV	2GD-FTV
Engine capacity (cm^3)	2,755	2,393
Engine type	DOHC Inline 4	DOHC Inline 4
Bore x Stroke (mm)	92 mm x 103.6 mm	92 mm x 90 mm
Compression ratio	15.6	16.8
Maximum torque (Nm @ engine speed)	500 Nm @ 1,600 - 2,800 rpm	400 Nm @ 1,600 - 2,000 rpm
Maximum power (kW @ engine speed)	150 kW @ 3,400 rpm	110 kW @ 3,400 rpm

Table 3. Euro-5 emission standards

Category	Unit	Values
Particulate Matter (PM)	mg/km	5
Particle Number (PN)	[#/km] x 10^9	600
CO	mg/km	740
NO_X	mg/km	280
NO_X + THC	mg/km	350

3. Results and Discussions

3.1. Accumulative Exhaust Gas Emission during Standard Test Cycle

This section shows a comparison between tailpipe emissions of both Euro-5 standard test vehicles when using test fuels with different biodiesel fractions of B7, B10, and B20. The results of regulated emissions are shown for Particulate matter (PM, Figure 2), Particulate Number (PN, Figure 3), Carbon monoxide (CO, Figure 4), Oxides of Nitrogen (NO_X, Figure 5), and Sum of Nitrogen Oxides (NO_X) and total Unburned Hydrocarbon (NO_X and THC, Figure 6). In both test vehicles, the stock exhaust treatment system can treat almost all the regulated emissions to very low levels. The effect of biodiesel blending fractions on the exhaust gas emission composition can be observed in the following figures.

As for the results, the exhaust treatment system on both test vehicles can treat the emissions to an extent that could not be significantly distinguished by legislated Euro-5 emission standards. The 2.8L automatic transmission pickup truck has very low PM and PN when compared to those of the 2.4L manual transmission pickup truck. This may be due to the load factors during the test carried out according to the standard test cycle. The 2.8L truck was an extended pickup truck while the 2.4L truck was a double cab and when their power-to-weight ratios were compared, the 2.8L one had the higher power-to-weight ratio. This led to the 2.4L truck emitting higher levels of particulate matter and number during similar test cycles. Furthermore, as for the CO emissions, the results showed a good relation between the oxygen content of biodiesel fuels and CO emission levels. As the CO is fundamentally formed only in the rich fuel zone, higher oxygen content in B20 showed the least CO emissions in both test vehicles. For the NO_X emissions, the biodiesel blending fractions showed no significant effect on the emission levels in both vehicles.

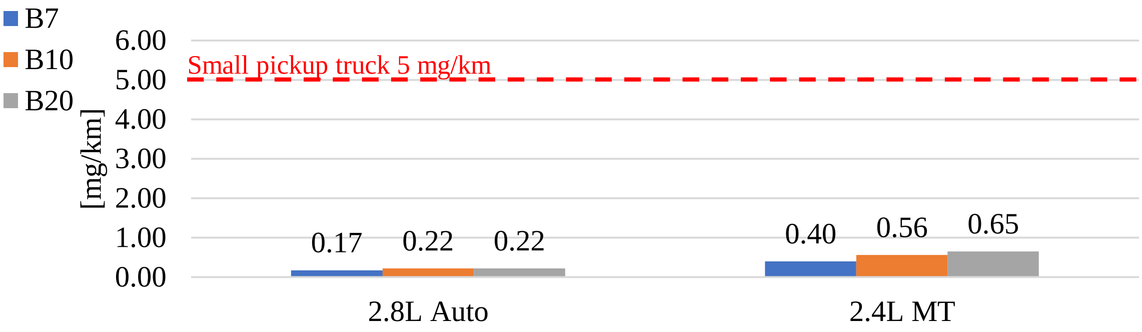

Figure 2. Accumulative Particulate Matter (PM) emission of the standard test cycle.

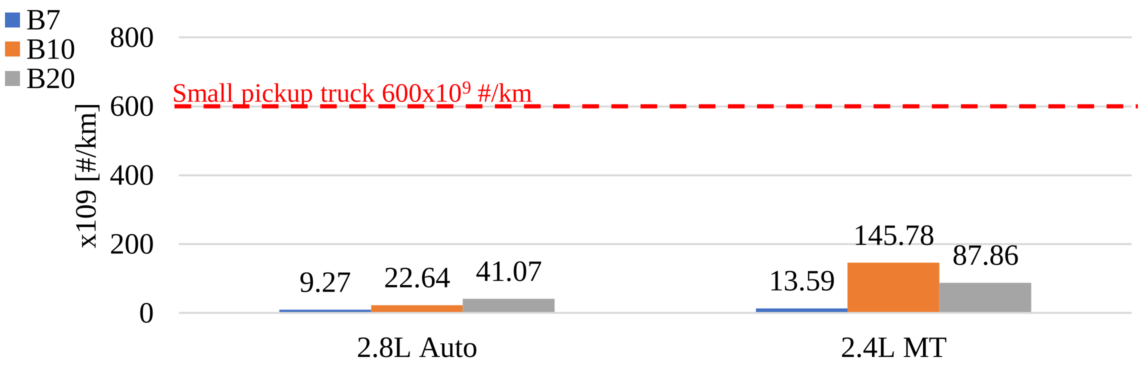

Figure 3. Accumulative Particulate Number (PN) of the standard test cycle.

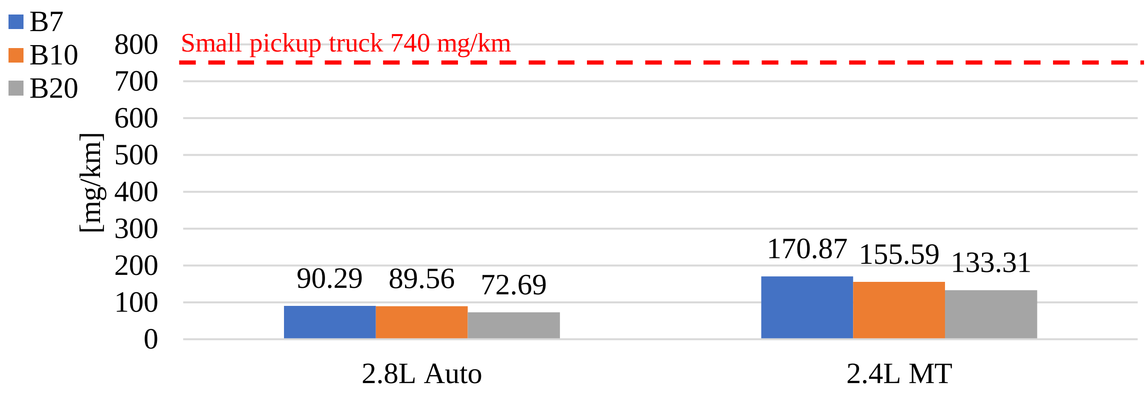

Figure 4. Accumulative Carbon Monoxide (CO) of the standard test cycle.

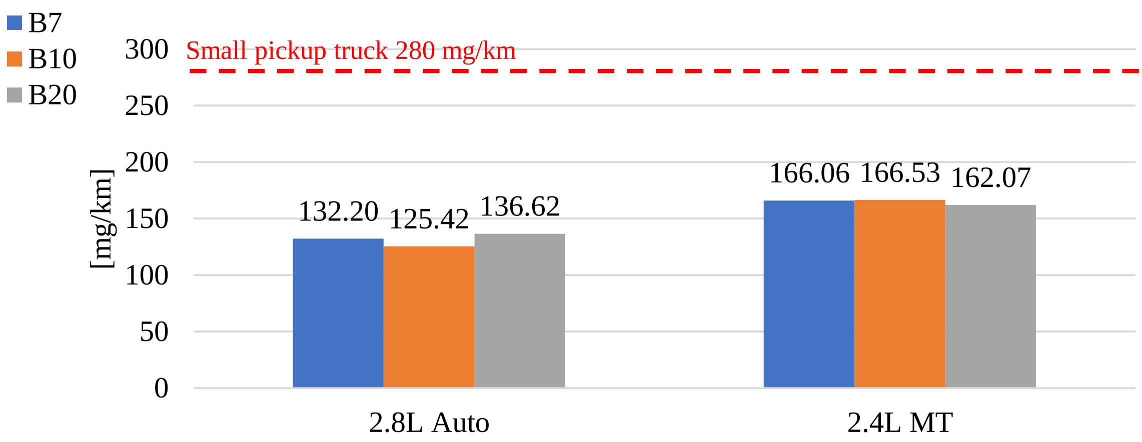

Figure 5. Accumulative Oxides of Nitrogen (NO_X) of the standard test cycle.

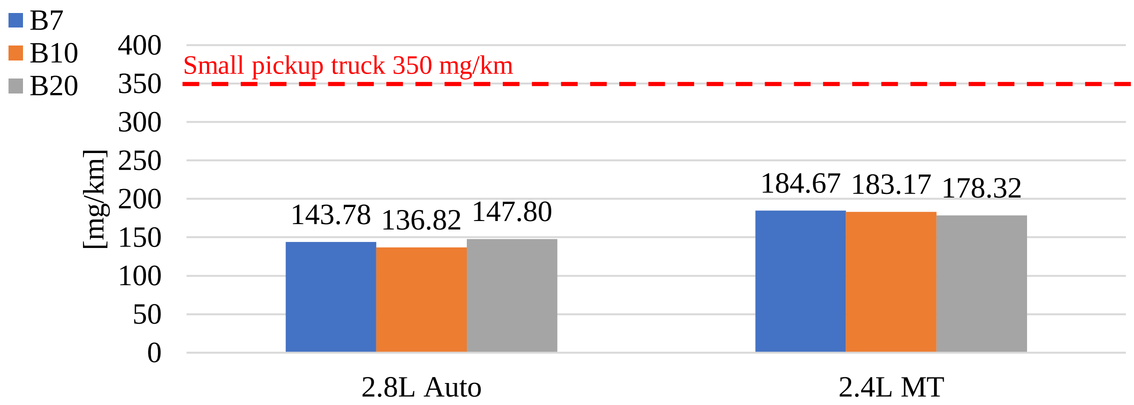

Figure 6. Accumulative Sum of Nitrogen Oxides (NO_X) and total Unburned Hydrocarbon (THC) of the standard test cycle.

3.2. Impacts of Biodiesel Blending Fractions on Size Distribution of Particulate Emission

The impacts of biodiesel fraction in both vehicles were explored by applying size distribution analysis in this section. There were two periods of PM peaks in the NEDC driving cycle, one was observed between UDC (0 – 800 s) and the other between EUDC (800 – 1200 s). The size distribution results of PM peaks for test vehicles between these two driving cycles for test fuels commercial Euro-5 B7, B10, and B20 are shown in Figure 8, and Figure 9 respectively.

The results showed that both Euro-5 Pickup trucks emitted particulate emission in nucleation mode (< 0.1 µm) and accumulation mode (0.1 – 2.0 µm) during the standard NEDC driving cycle, and most of the particulate emissions were in nucleation mode for all test conditions. Euro-5 B7 fuel can reduce observed maximum particle count to smaller ranges compared to that of the commercial Euro-5 B10, and B20 in both vehicles during the standard NEDC driving cycle. The 2.8L automatic transmission truck showed lower PM and PN counts than the 2.4L manual transmission truck in all three fuels, and for the 2.4L truck, using B10 showed a significant particle number peak in UDC when compared to the rest of the test fuels. This may be due to the load factors during the standard NEDC driving cycle as the 2.4L truck was on higher load factor than the 2.8L truck.

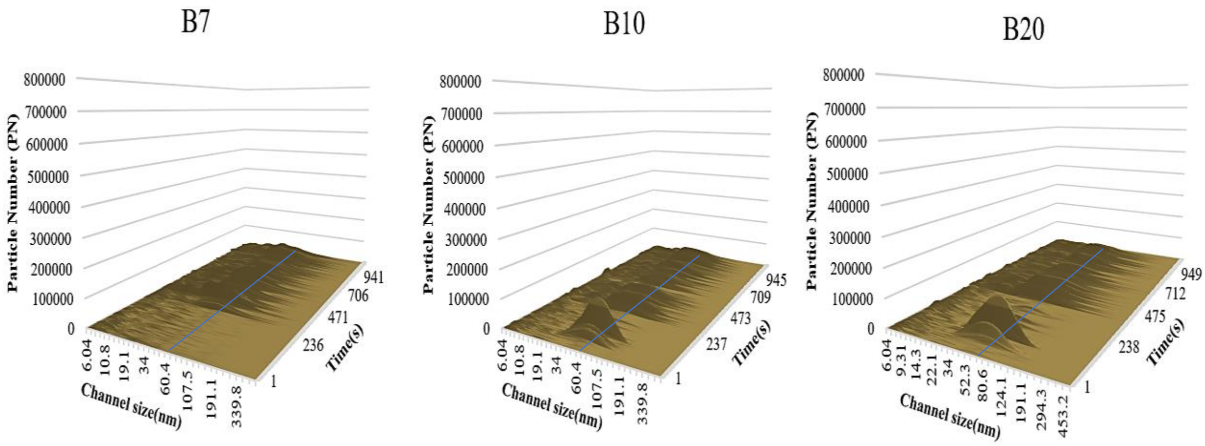

Figure 8. Particulate size distribution of test Euro-5 fuels in Euro-5 2.8 L Pickup Truck.

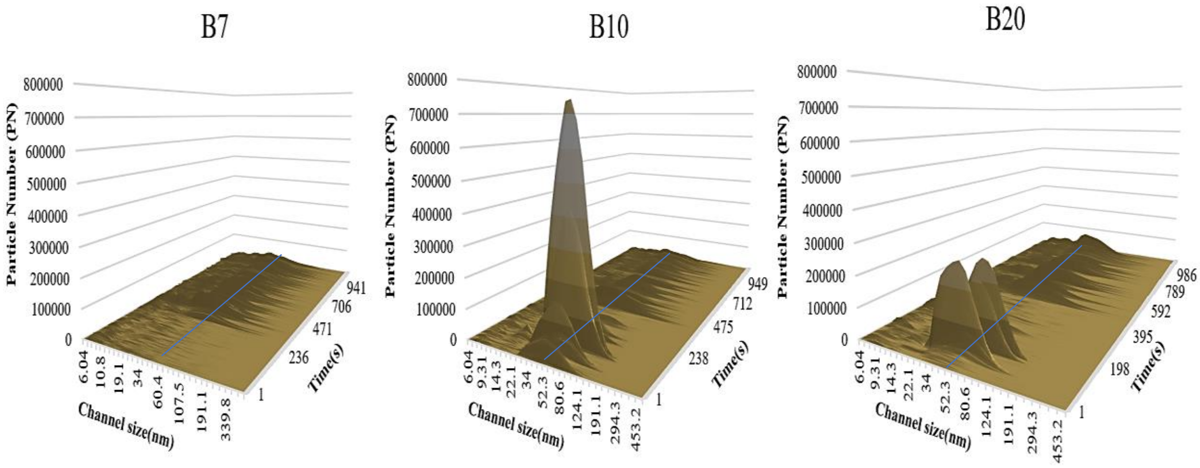

Figure 9. Particulate size distribution of test Euro-5 fuels in Euro-5 2.4 L Pickup Truck.

3.3. Active Regeneration Intervals during Real-World Driving Conditions

This section shows a comparison between active DPF regeneration intervals of both test vehicles using commercial Euro-5 B7, B10, and B20. The overall active regeneration intervals of urban, extra-urban, and average are shown in Figure 11 and Figure 12.

The results showed that using different biofuel blends exhibits significant differences in the active DPF regeneration intervals only in the 2.4L pickup truck. From the observed results, the 2.8L pickup truck with Automatic Transmission has not shown a significant difference in active DPF regeneration intervals when running on B7, B10, and B20. Besides, the 2.4L pickup truck with Manual Transmission shows the longest DPF regeneration intervals when using B20 diesel fuel in all three categories; city, province, and average.

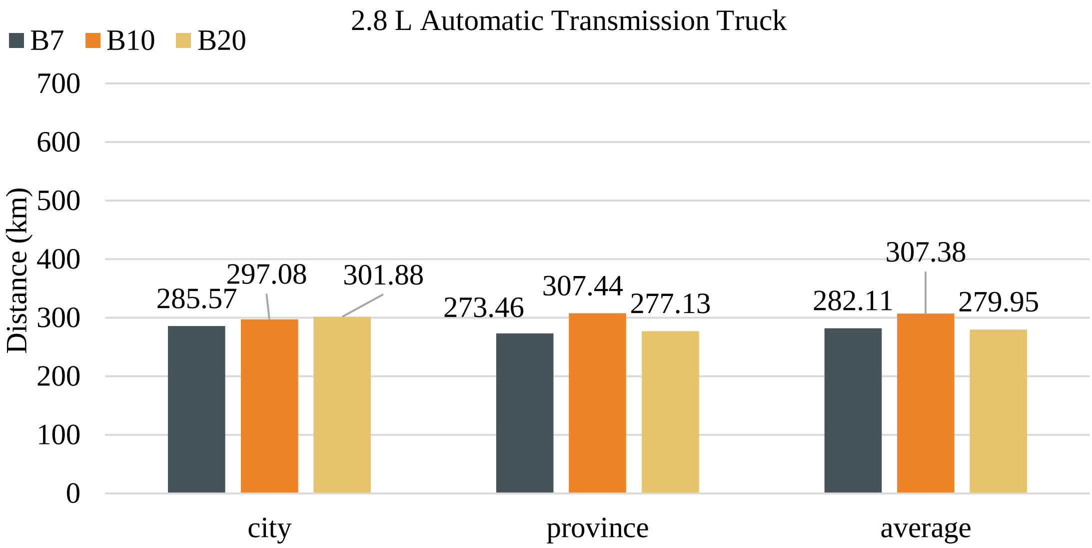

Figure 11. Active Regeneration Intervals of 2.8L pickup truck.

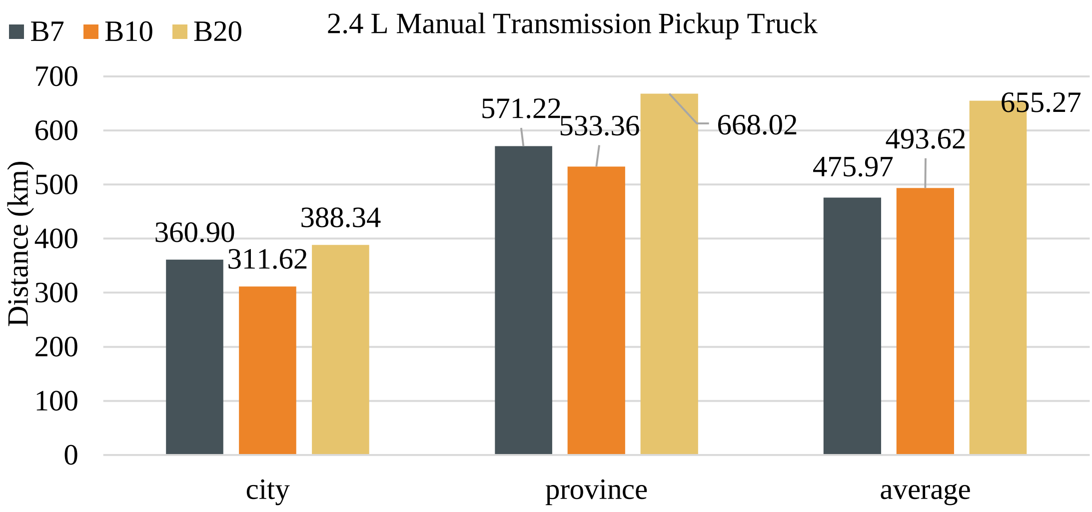

Figure 12. Active Regeneration Intervals of 2.4L pickup truck.

4. Conclusions

The impacts of biodiesel fraction on tailpipe emissions have been explored in this work. Three different fuels were experimentally tested on two different engine-size vehicles and transmission layouts with the same Euro-5 emission standard. The observed results were summarized as follows:

- The Euro-5 standard vehicles can help reduce all the regulated pollution in the tailpipe exhaust gas from their brand-new condition to a certain vehicle age. The regulated pollutants can be treated until they cannot be distinguished on the timeline of standard test pattern except for the NO_X emission which had quite significant amounts but still under the Euro-5 emission standards.
- In both test vehicles, the results showed some evidence of CO emissions decreasing with increasing biodiesel blending fractions. However, the definitive results need further in-depth study.
- The size-distribution analysis showed no significant relationship between PM and PN with all test fuels as the stock exhaust systems on both vehicles can treat the particle emissions to very low levels when compared with the Euro-5 emission standards.
- For the active regeneration intervals, all three test fuels on the 2.4 L truck had the longest regeneration intervals than the 2.8 L truck during real-world driving tests although it had a lower power-to-weight ratio.

5. Acknowledgments

This work was supported by the National Energy Technology Center (ENTEC), the National Science and Technology Development Agency (NSDTA), and Toyota Motor Thailand.

6. References

[1] Chaiwat Sowcharoensuk 2022. *Industry Outlook 2022-2024: Palm Oil Industry*. https://www.krungsri.com/en/research/industry/industry-outlook/agriculture/palm-oil/io/oil-palm-industry-2022-2024

[2] Department of Energy Business 2022 “Characteristics and Quality of Diesel Fuel”, Thailand Government Gazette. **137** 2020, 9 June http://elaw.doeb.go.th/document_doeb/TH/699TH_0001.pdf

[3] Jung Y Hwang J and Bae C 2016 Fuel. **165** 413 https://doi.org/10.1016/j.fuel.2015.10.076

[4] Songsaengchan Y Chareonphonphanich C Karin P Chollacoop N Tongroon M and Hanamura K 2011 *The Second TSME Int. Conf. on Mechanical Engineering* Oct 19-21 Krabi, Thailand.

[5] United Nations 2015 Agreement Concerning the Adoption of Uniform Technical Prescriptions for Wheeled Vehicles, Equipment and Parts which can be Fitted and/or be Used on Wheeled Vehicles and the Conditions for Reciprocal Recognition of Approvals Granted based on these Prescriptions (Geneva: United Nations)

[6] PTT Inl’s Analytical and Testing Services AEM005 Gasoline and Diesel Vehicle Emission Test, Tailpipe https://www.pttplc.com/th/Products/Ourbusinessbypttplc/Technologyandengineeringunit/Technologyandengineering/Productanalysis.aspx

[7] Department for Environment, Food and Rural Affairs 2005 *Particulate Matter in the United Kingdom* (London: Defra Publications) ISBN 0-85521-143-1

AME0020

Design and analysis of lightweight freight wagon structures according to the standard of the State Railway of Thailand

Rungsalit Sulaimarn[1] and Manon Sooklamai[1,*]
[1]Division of Mechanical Technology Education, Faculty of Industrial Education and Technology, King Mongkut's University of Technology Thonburi,
126 Pracha Uthit Rd., Bang Mod, Thung Khru, Bangkok 10140, Thailand.

* Corresponding Author: manon.san@kmutt.ac.th

Abstract. This study is focused on the design of a novel lightweight freight wagon and the subsequent structural analysis in accordance with the State Railway of Thailand's freight wagon standards. Three-dimensional representations of three underframe wagon structures were generated using computer-aided design software. The primary objective is to create a lighter-weight freight wagon that adheres to the State Railway of Thailand's acceptable standards. These 3-D models of freight wagons are designed based on the actual dimensions of real wagons capable to carry two of 20-foot-long containers. The variations in the designed wagon models primarily involve the connection patterns of structural members and the minimization of material usage. Following the creation of these 3-D models, a computer simulation employing the finite element method is conducted to assess the structural strength of the wagons. The original wagon model is validated by comparing it with a real, in-service wagon in terms of damage points and deformations. Subsequent models are then developed based on simulation results, aiming to meet the reference standards. As a result, the final freight wagon model achieves a 15.11% reduction in weight compared to the original model, while maintaining a safety factor for the entire wagon structure that exceeds the 1.3 threshold set by the State Railway of Thailand.

Keywords: Computer simulation, Lightweight, Standard, Underframe freight wagon.

1. Introduction

The railway transportation system currently holds a significant role in the lives of people, whether utilized for personal travel or commercial endeavors. This evolution signals a promising trajectory, especially within the railway sector. The economic growth agenda prioritizes enhancing competitiveness, with a focus on advancing the transportation infrastructure [1]. Railway transportation stands as a pivotal pillar in infrastructure development, enjoying global recognition for its unmatched cost-efficiency per unit of conveyance [2]. Given the utilization of relatively simple technology in the production of freight wagons and the capacity for domestic manufacturing, it can serve as a foundational step for Thailand's burgeoning railway industry. Regarding the available boxcar wagons, they have the potential to contribute significantly to the growth of rail cargo transportation, aligning with government directives. Currently, there is a notable surge in demand from entrepreneurs for rail cargo transportation, and this demand is anticipated to rise even further [3]. The expansion of the national railway transportation system aims to adapt to evolving needs and reduce the resources required for altering freight train structures. The adjustment of existing frame configurations adheres to established standards, such as those outlined in the State Railway of Thailand's SRT Spec. No. SF-26/2552 for 308 Complete Bogie Container Flat Wagons designed for Meter Gauge Track [4], as well as the EN 12663-2:2010 standard [5]. These standards encompass various safety factors. The working guidelines emphasize studying and developing different structural forms of the freight transport train Bogie Container Flat Wagon (BCF) using simulation methods. These forms are characterized by a maximum empty weight of no more than 14.80 tons. and a maximum load weight not exceeding 45.20 tons. Subsequently, a finite element analysis will be conducted to assess the structural strength of each form under similar applied forces. The study results will provide a comparative analysis of the structural strength, serving as a reference for designing modifications to the frame structure of the freight transport train (BCF). The wagon structure can be constructed using thinner profiles and beams, contributing to weight reduction and an increase in maximum payload capacity [6]. Consequently, enhancing the bearing structures of hopper wagons is essential for their profitability, expanding the range of goods they can transport, and facilitating their use not only on main lines but also in international combined shipments [7]. Conversely, reducing the vehicle structure's mass through lightweight design approaches is a viable solution to decrease the power required during operation, which, in turn, can help mitigate pollutant emissions into the atmosphere [8].

2. Methodology

2.1. Original underframe of a freight wagon

The way to create highly reliable and authentically realistic models using computer programs begins with the application of the well-established SRT operational structural framework, commonly referred to as the original underframe of a freight wagon. This original underframe plays a crucial role in refining, enhancing, and crafting diverse models. From this point forward, we shall refer to it as “Model 1”.

Figure 1. The original underframe of a freight wagon.

Table 1. Specification of the original underframe (Model 1).

Weight [including fittings]	7526	kg
Weight [not including fittings]	6534.6	kg
Width	2450	mm
Length [Over headstocks]	14000	mm
Max. axle load on rail	16	Ton/Axle
Material	SS400	-
Density	7860	kg/m^3
Tensile Yield Strength	275	MPa
Compressive Yield Strength	250	MPa
Tensile Ultimate Strength	510	MPa
Young’s Modulus	200	GPa
Poisson’s Ratio	0.3	-

2.2. Finite Element Analysis

Finite Element Analysis (FEA) serves as a versatile and indispensable engineering tool for the design and evaluation of mechanical components and structures. It entails the meticulous creation of a 3D model that closely mirrors the real-world product and takes into account vital factors such as geometry, materials, and properties. The precision and reliability of FEA findings hinge significantly on the quality of the Mesh, an intricate lattice of elements that divides and dissects the model. Employing a finer Mesh subdivides the structure into smaller elements, furnishing more nuanced insights into its behavior under various conditions. The results derived from FEA are often conveyed through color-coded representations, a visual aid that simplifies the comprehension of crucial parameters like stress and deformation. This predictive capability empowers engineers to anticipate how components will respond when subjected to diverse loads. Consequently, it streamlines the process of design refinement and ensures that the end product complies with the stringent safety and performance standards essential for modern engineering. FEA is undoubtedly a cornerstone of contemporary engineering, offering a reliable and efficient approach to product design. Its iterative process encompasses essential stages such as model creation, Mesh generation, the specification of boundary and loading conditions, and the thorough analysis of findings. In this research work, the finite element analysis has been performed by using Ansys software.[9]

2.2.1. Safety Factor (SF)

2.2.2.1. Static Load

In line with Thai State Railway specifications, the Safety Factor (*SF*) is determined using allowable stress and maximum Von-Mises stress. This equation evaluates safety factor, which indicates safety when it's equal to or greater than 1, and a lack of safety when less than 1. It is a standard approach in engineering to ensure the safety of structures under various conditions.[10]

$$Safety\ Factor\ (SF) = \frac{Allowable\ Stress}{Maximum\ Von-Mises\ Stress} \tag{1}$$

The Mohr-Coulomb Stress formula in Ansys is a vital tool in engineering and materials science, assessing structural safety and integrity to meet established standards. It considers parameters like maximum tensile stress (σ_1), minimum compressive stress (σ_3), and stress limits. A Safety Factor above 1 signifies compliance with safety standards, while below 1 implies risk. This formula is fundamental to ensure materials and structures adhere to safety requirements, a crucial aspect of engineering.[11]

$$F_s = \left[\frac{\sigma_1}{S_{tensile\ limit}} + \frac{\sigma_3}{S_{compressive\ limit}} \right]^{-1} \tag{2}$$

2.2.2.2. Variable Load

The Goodman Equation is vital in mechanical engineering for ensuring component safety and reliability under alternating and mean stresses. It helps predict fatigue failure accurately in components subjected to various loads, thereby enhancing reliability. The equation calculates the Safety Factor (*SF*) by determining equivalent alternating stress (S_a) and mean stress (S_m), using the Goodman diagram for safety assessment. A Safety Factor above 1 signifies safety, safeguarding design integrity. This equation is critical for assessing component safety and reliability, ensuring endurance under variable loads, and preventing failures [11].

$$\frac{1}{SF} = \frac{1}{S_e} + \frac{1}{S_a} + \frac{1}{S_m} \tag{3}$$

2.3. Validation

In order to ensure the reliability of the design, it is essential to incorporate a verification process for the obtained results by comparing real-world scenarios with those simulated in the computer program. This involves a step-by-step procedure to evaluate the congruence between the actual structural framework and the outcomes produced by the computer simulation. Details of finite element for Model 1: Element Order Program Controlled, Element size 50.0 mm, Bounding Box Diagonal 14,232 mm, Nodes 498070, Element 242712, load application 68,670 N, applied by surface effect, structural weight is not considered. The following outlines the steps involved in this verification process.

2.3.1. Start by measuring the deflection distance of the actual structural framework before placing two containers, each weighing 3,500 kg or 68,670 N on the underframe structure.

2.3.2. Position the containers on the designated spots of the structural framework and measure the deflection distance of the framework caused by placing the containers.

2.3.3. Employ a laser level, A PUMPKIN green beam self-leveling laser model PTT-LSG5L28259 was used for underframe height measurement. The brief specifications are as follows: Laser Class II, vertical accuracy range of 2 mm to 5 mm, spot accuracy of 1 mm to 3 mm, measuring range of up to 20 m, self-leveling range of ±3 degrees, and a light projection angle of 120 degrees. It was used for measuring the height of the underframe from a reference level before and after the containers were placed on the underframe structure to determine the deflection values.

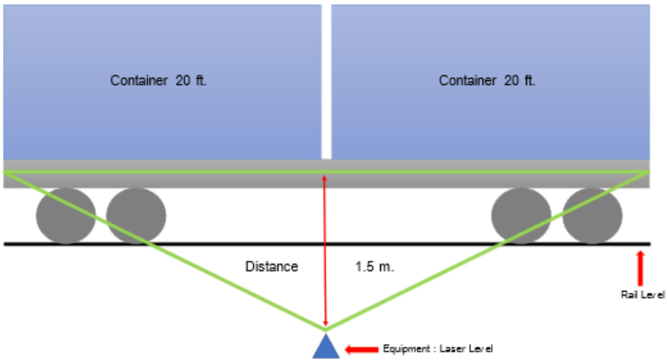

Figure 2. Level and position measurement setup.

2.3.4. Subsequently, compare the obtained values with the computer-generated results. For this comparison, assume the conditions are consistent in one direction and the weight used is the same, utilizing a three-dimensional model

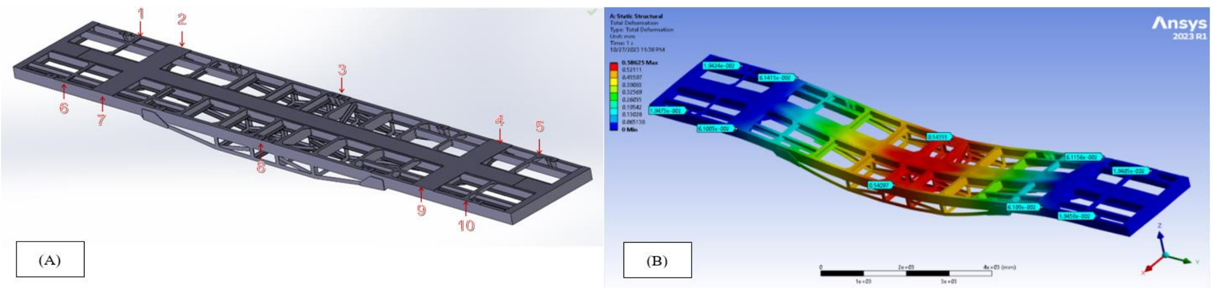

Figure 3. The positions where the forces act on the underframe structure, and the simulation result. (A) Measured values from the real structure. (B) Simulated values from the software.

Table 2. Validation data of the original underframe (Model 1) between measurement and simulation.

Measuring Point	The height of the underframe at unload (mm) (1)	The height of the underframe with a load of 68,670 N					Computer simulation	Different
		1st Loading (mm) (2)	2nd Loading (mm) (3)	3rd Loading (mm) (4)	Average height (mm) (5)	Different height (mm) │(1)-(5)│	Deflection value (mm)	Measurement vs. simulation (mm)
1	865.0	865.0	865.0	865.0	865.0	0.00	0.019	0.019
2	869.5	869.5	869.5	869.5	869.5	0.00	0.061	0.061
3	875.0	874.5	875.0	874.0	874.5	0.50	0.543	0.043
4	865.0	865.0	865.0	865.0	865.0	0.00	0.061	0.061
5	865.0	865.0	865.0	865.0	865.0	0.00	0.019	0.019
6	865.0	865.0	865.0	865.0	865.0	0.00	0.019	0.019
7	869.5	869.5	869.5	869.5	869.5	0.00	0.061	0.061
8	875.0	874.5	874.5	874.5	874.5	0.50	0.540	0.040
9	865.0	865.0	864.5	865.5	865.0	0.00	0.061	0.061
10	865.0	865.0	865.0	865.0	865.0	0.00	0.019	0.019

2.4. Design Models of Underframes

The original underframe is constructed with three prominent components: the center sill, side sill, and end sill. The center sill and side sill extend continuously along the entire length without any joints. Additional structural elements are welded to the center sill and side sill to fortify their structural integrity.

The design of Model 2 and Model 3 utilized the same material as specified in the Material Table for Model 1, as depicted in Table 1. This approach was taken to ensure the engineering simulation closely resembled reality. Model 2 was designed with a reduced weight of 6139.9 kg, while Model 3 was further lightened to weigh 5549.9 kg

Due to the relatively complex and heavy nature of the underframe in Model 1, new underframe structures were designed to be simpler and lighter in weight, while still maintaining the required strength according to SRT standards. As a result, two new underframe structures, known as Model 2 and Model 3, were created using computer software.

The modifications in Model 2 still preserve the three main components: the center sill, side sill, and end sill. Notably, we have reduced the supplementary structural elements that were initially added to enhance strength. Instead, we have enlarged and widened the center sill in the central section to augment its structural robustness, thereby replacing the reduced structural elements.

In the case of Model 3, we have diminished the presence of the side sill to reduce the overall weight of the structure. Concurrently, we have amplified the structural strength of the center sill to compensate for the eliminated elements. The end sill has been completely excluded, and a flat top surface is employed in the front and rear sections to evenly distribute the applied loads. This ensures that Model 3 continues to adhere to the prescribed strength standards as stipulated by the State Railway of Thailand.

The details of the finite element analysis for Model 2 are as follows: Element Order Program Controlled, Element size 50.0 mm, Bounding Box Diagonal 14,224 mm, Nodes 314,732, Elements 155,023.

The details of the finite element analysis for Model 3 are as follows: Element Order Program Controlled, Element size 50.0 mm, Bounding Box Diagonal 14,226 mm, Nodes 307,287, Elements 155,505.

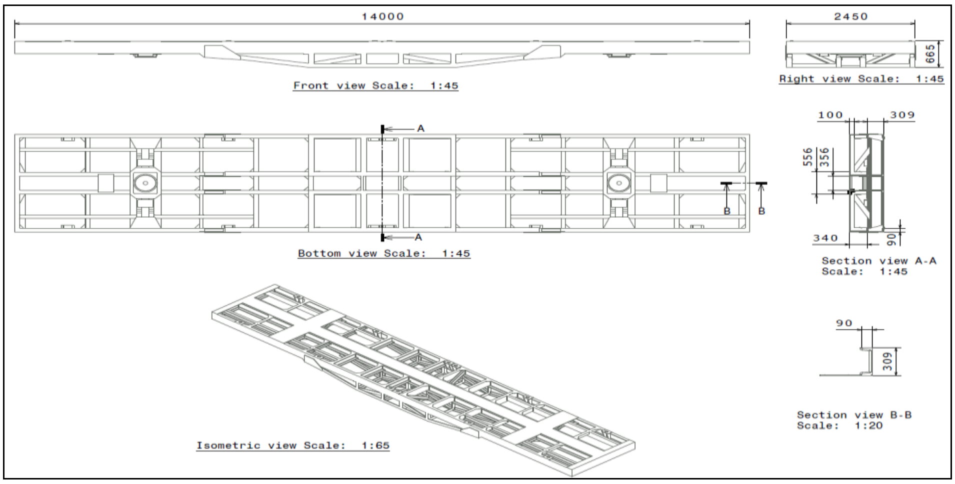

Figure 4. Model of the original underframe of a freight wagon.

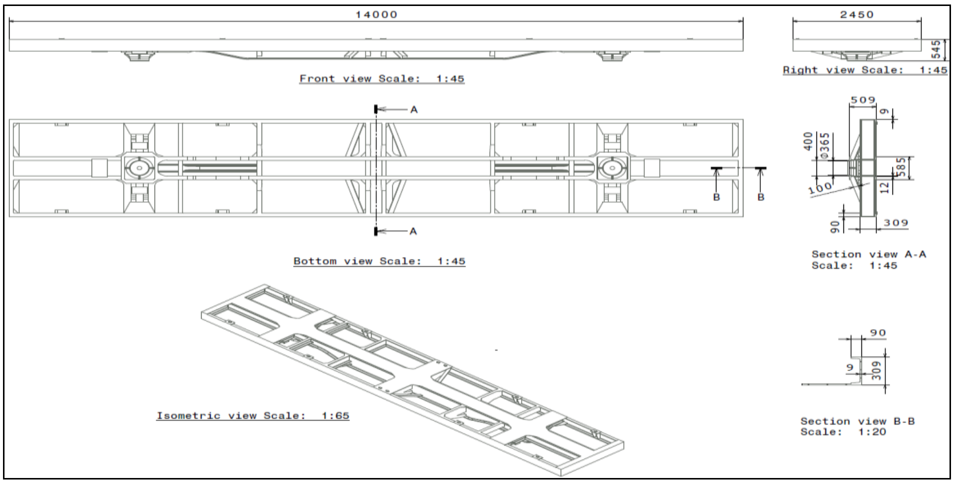

Figure 5. Design of Model 2.

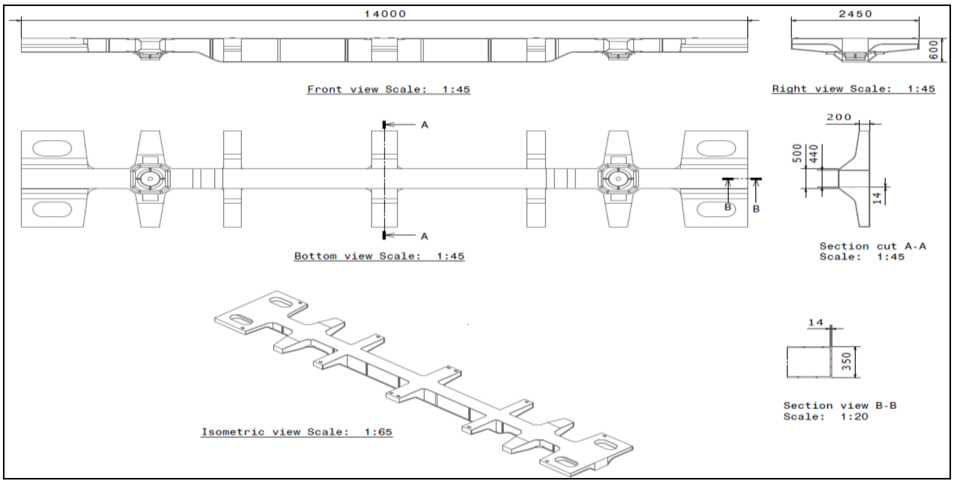

Figure 6. Design of Model 3.

3. Results and Discussion

To validate this hypothesis, a uniformly distributed load of 443,000 N was applied onto the underframe structure by surface effect, to simulate the loading of two units of a 20-foot container with a total weight as specified by SRT, which does not exceed 14.8 tons for the structure, and 45.2 tons for the cargo.

3.1. Result

3.1.1. Model 1

The simulation has been performed for displacement, Von-Mises stress, and safety factor, and presented in Figures 7 and 8. In Figure 7, the deformation analysis reveals a maximum displacement of 2.54 mm, while the stress analysis in Figure 8 indicates a maximum Von-Mises stress of 47.478 MPa. These results ensure structural strength and reliability under the load. Notably, the minimum safety factors are 4.29 for static load, and 1.81 for variable load, as illustrated in Figure 7.

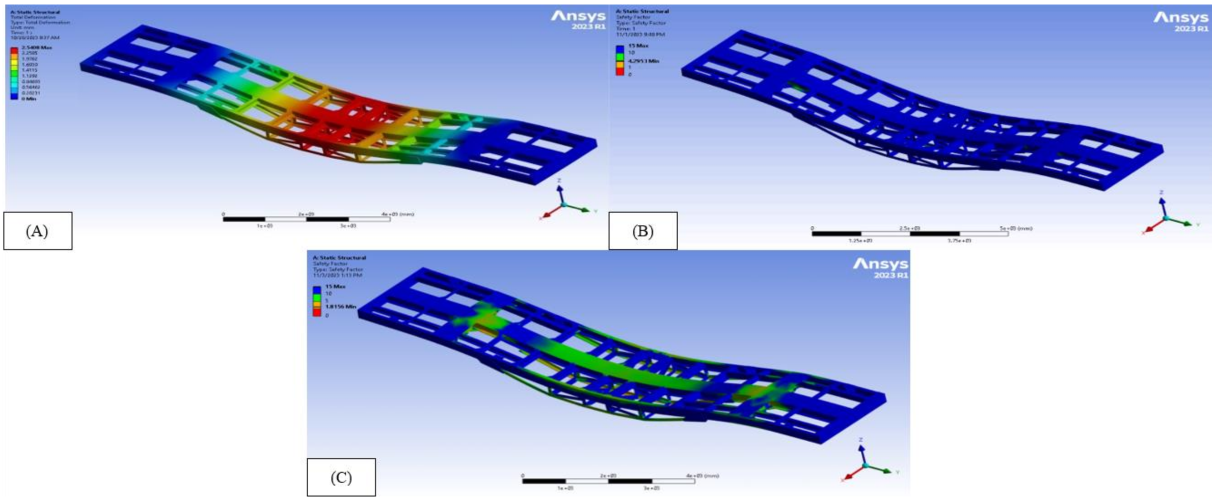

Figure 7. Model 1 Deformation and Lowest Safety Factor Position Under Load.
(A) Deformation (B) Safety Factor by Mohr-Coulomb (C) Safety Factor by Goodman

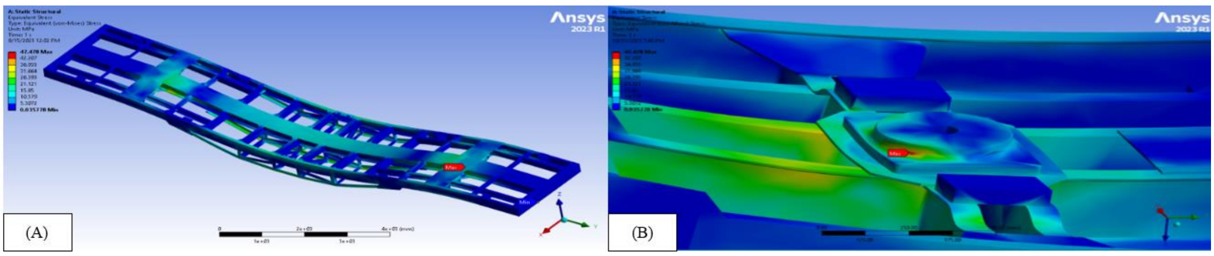

Figure 8. The maximum Von-Mises stress position and images showing critical points.
(A) Max Von-Mises Stress (B) Stress Hotspot

3.1.2. Model 2

Figures 9 and 10 provide the results of deformation, Von-Mises stress, and safety factor. The maximum deformation reaches 4.65 mm, showing structural flexibility. The Von-Mises stress peaks at 63.49 MPa in specific areas, and the average Von-Mises stress is 10.06 MPa, assessing overall stress levels. The safety factor drops to a minimum of 3.67 for static load, while 1.35 for variable load.

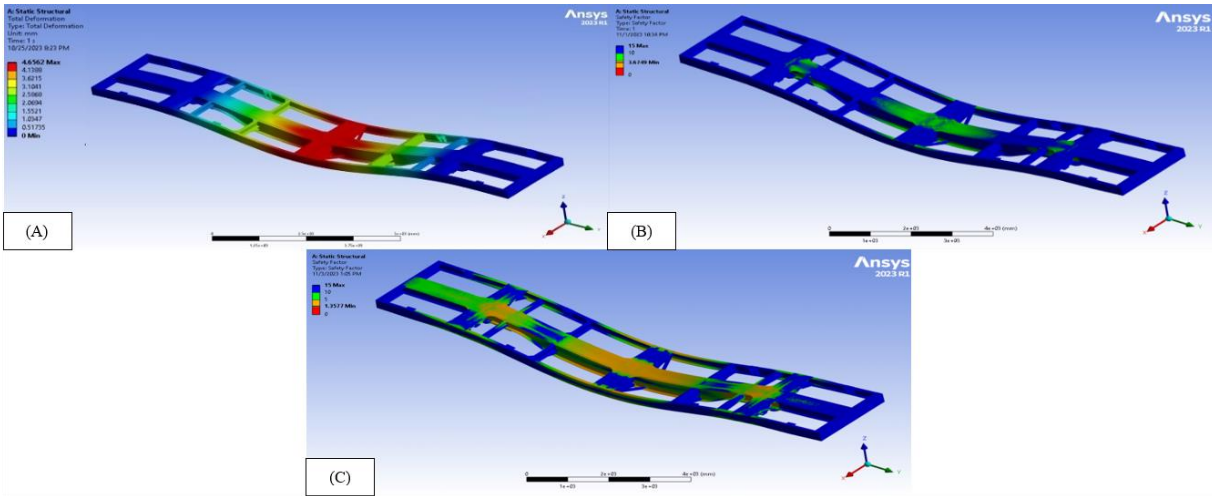

Figure 9. Model 2 Deformation and Lowest Safety Factor Position Under Load.
(A) Deformation (B) Safety Factor by Mohr-Coulomb (C) Safety Factor by Goodman

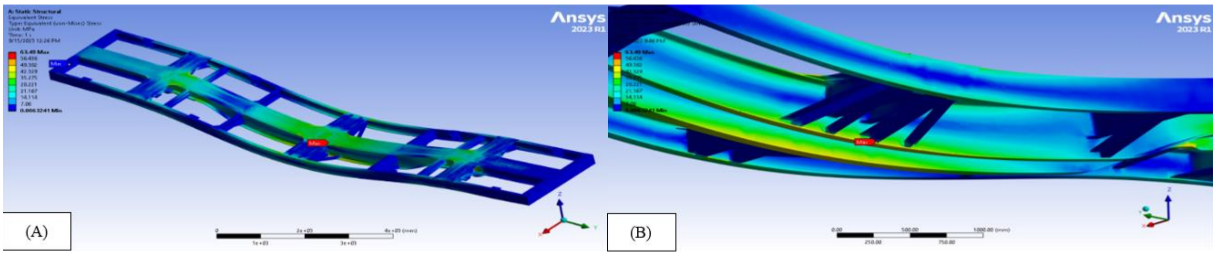

Figure 10. The maximum Von-Mises stress and images highlighting critical points for Model 2.
(A) Max Von-Mises Stress (B) Stress Hotspot

3.1.3. Model 3

The deformation analysis illustrated in Figure 11 shows a maximum displacement of 3.59 mm with an average value of 1.15 mm across the structure. In Figure 12, the Von-Mises stress values reach a peak of 62.97 MPa. The minimum safety factor is 3.49 for static load, and 1.36 for variable load.

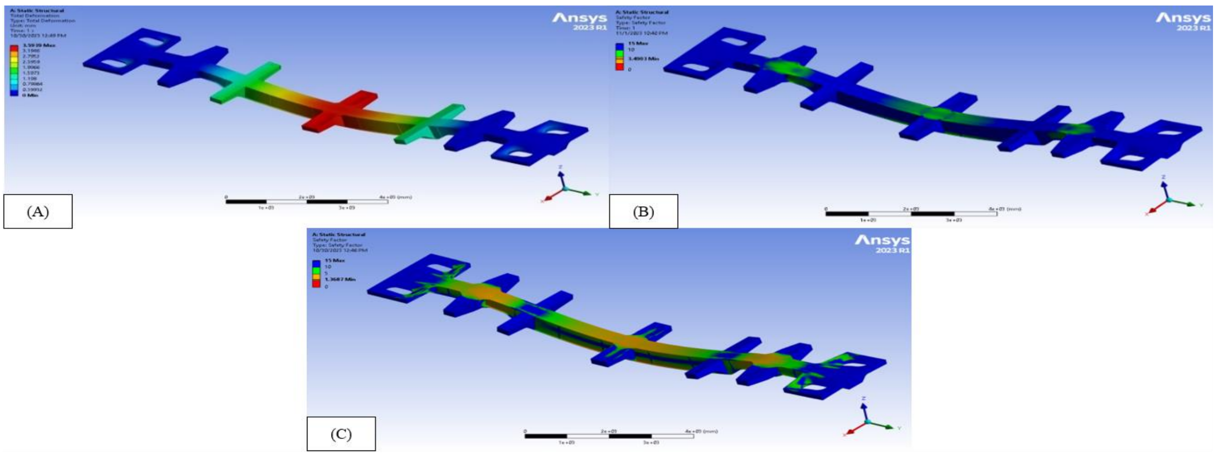

Figure 11. Model 3 Deformation and Lowest Safety Factor Position Under Load.
(A) Deformation (B) Safety Factor by Mohr-Coulomb (C) Safety Factor by Goodman

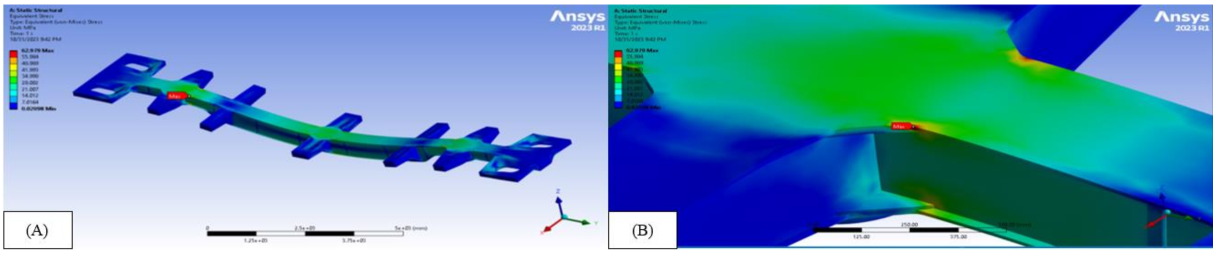

Figure 12. The maximum Von-Mises stress position and images showing critical points for Model 3. (A) Max Von-Mises Stress (B) Stress Hotspot

3.2. Discussion

Maximum stress and maximum deformation do not always occur at the same location in a structure, and this phenomenon can be explained by various engineering factors. Different material properties, non-uniform force distribution, geometric effects, boundary conditions, material anomalies, and nonlinear material behavior can all contribute to this disparity. Understanding these factors is essential in engineering design to predict and address stress concentrations, deformation patterns, and potential failure points, ensuring the reliability and safety of structures.

The details of finite elements for Model 1, 2, and 3, as discussed in Section 2.2 for Model 1 and Section 2.4 for Models 2 and 3, involved the conditions of force distribution that are applied in the same direction, as mentioned in Section 3. The maximum Von-Mises stress that occurred in Model 1 is located in the region between the Underframe and the Bogie interconnecting. In Model 2, the point of maximum Von-Mises stress is at the lower part of the reinforced structure design to accommodate forces between the center sill and side sill. In Model 3, with the improvements made, the maximum Von-Mises stress occurred on the reinforced steel plate on the center sill, closed to the point where it supports the Bogie.

The structural enhancements exhibit the capacity to reduce the weight of the underframe structure in 2 demonstrated in section 2.4. Similarly, Model 3 exhibits a weight reduction of around 987.4 kg, as indicated in section 2.4.

4. Conclusion

Table 3. Standard values by the State Railway of Thailand and Ansys software simulations.

Model	Allowable displacement value by SRT. (mm)	Maximum displacement by simulation (mm)	Allowable stress value by SRT. (MPa)	Maximum Von-Mises stress by simulation (MPa)	Safety Factor using Equation (1)	Safety Factor by Ansys using Equation (2)	Safety Factor by Ansys using Equation (3)	Tare weight by simulation (kg)
Model 1	16.00	2.54	206.25	47.478	4.34	4.29	1.81	6534.6
Model 2	16.00	4.65	206.25	63.49	3.24	3.67	1.35	6139.9
Model 3	16.00	3.59	206.25	62.97	3.27	3.49	1.36	5549.9

The design of this freight train structure adheres to the safety standards outlined by the State Railway of Thailand [4] and EN 12663-2:2010 [5], which is the standard for railway applications - structural requirements of railway vehicle bodies - Part 2: Freight wagons. It is based on a model previously employed in Thai railway operations and has been further developed through computer-aided simulations, ensuring the reliability of the obtained data. The primary focus of this design is to explore innovative structural models capable of reducing the structure's weight, thereby increasing its cargo capacity while simultaneously reducing energy consumption during transportation. Furthermore, it could reduce track damage and deterioration due to the operation of heavy rail vehicle structures.

In particular, Model 3, as depicted in Figure 6, was used for simulating full-load conditions with a payload of 443,000 N. The analysis revealed a maximum deformation of 3.59 mm. The von Mises stress reached a maximum of 62.97 MPa, which is below the yield strength of the material that specified criteria by SRT. Similarly, Model 2 exhibited maximum von Mises stress of 63.49 MPa, which is also below the criteria that limited to 75% of the material's yield strength at 275 MPa. However, Model 3 can achieve a maximum weight reduction of 987.4 kg or approximately 15.11% when compared to the original (Model 1). Therefore, Model 3 is then promoted to be the high-potential underframe structure design for weight reduction and structural strength, leading to enhancement in cargo capacity and energy efficiency during operation, all within the prescribed safety standards. Hence, it can be inferred that Model 3 represents the most promising design for a lightweight freight wagon underframe that complies with SRT standards.

5. References

[1] KongSiri, P., Narong, S. (2020). Study and Analysis of the Structural Strength of Light Rail Vehicle Passenger Car Bodies. In *Thailand Mechanical Engineering Network Conference* (Vol.34, p. 509-513).

[2] Pongskorn, P., Songsak, S., & Ratthapoom, P. (2021). Analysis and Design of Passenger Railway Car Body Structures for 1.0-Meter Gauge Tracks in Thailand. In *Proceedings of the National Civil Engineering Conference* (Vol. 26, p. 01-08).

[3] Nopphawhan, T. (2022). thebangkokinsight [Online], Available: *https://www.thebangkokinsight.com/news/business/economics/238404/*

[4] INTERNATIONAL BID NO. ICB-1102 (2011).*308 Complete Bogie Container Flat Wagons for Meter Gauge Track,* PART II GENERAL SPECIFICATIONS

[5] EN 12663-2:2010 *Railway applications - Structural requirements of railway vehicle bodies - Part 2: Freight wagons*

[6] Stoilov, V., Simić, G., Purgić, S., Milković, D., Slavchev, S.,Radulović, S. & Maznichki, V. (2019). Comparative analysis of the results of theoretical and experimental studies of freight wagon Sdggmrss-twin. In *IOP Conf. Series: Materials Science and Engineering* (Vol. 664, p. 01-08).

[7] Vatulia, G., Gerlici, J., Fomin, O., Lovska, A., Fomina, Y., & Kravchenko, K. (2023). Analysis of the Strength of the Supporting Structure of a Two-Section Hopper Wagon under Operating Loading Conditions. *Journal of Switzerland Appl. Sci.*, 13, 859, pp. 01-17.

[8] Cascino, A., Meli, E., & Rindi, A. (2023). A strategy for lightweight designing of a railway vehicle car body including composite material and dynamic structural optimization. *Journal of Railway Engineering Science*. 1-11.

[9] Burnett, David S. (1991). *Finite Element Analysis: From Concepts to Applications*

[10] Beer, Ferdinand, Johnston, Jr., E. Russell, Dewolf, John, Mazurek, David (2011). *Mechanics of Materials*,

[11] J.S. Shigley, C.R. Mischke, and R.G. Budynas (2008). *Mechanical Engineering Design*, 8th ed.

[12] Wacharagorn, P., Artporn, W. (2022). Analysis for stress distribution in underframe of a bogie container flat wagon using FEM. In *Academic Conference of Kasetsart University* (Vol. 57, p. 313-319).

[13] Thadhuangnuen, K., Narapipatkul, N., Hatthasupha, A., & Kanjanomai, C. S. (2019). Impact of Residual Stress on the Critical Crack Size in Rail Weld Toe of Railway Track. In *Thailand Mechanical Engineering Network Conference* (Vol. 35, p. 266-271).

[14] Inthratul, B. *(*1996*). Carriage and Wagon Inspection Technical Manual.* Center for Railway Engineering and Vehicle Technology, State Railway of Thailand.

[15] Stoilov, V., Slavchev, S., Maznichki, V., & Purgic, S. (2019). Analysis of some problems in the theoretical wagon strength studies due to the imperfection of the European legislation, In *IOP Conference Series: Materials Science and Engineering* (Vol. 618).

AME0021

Precision Landing with computer vision

Chinnapat Thipyopas[1,*], Wisarut Leelawutprasert[1], Noppanut Thongton[1], Woranop Laitrakun[1], Kittipon Faidetch[1], and Ekarat Sathitwattanasan[1]

[1]Faculty of Engineering Kasetsart University, Bangkok

* Corresponding Author: fengcpt@ku.ac.th

Abstract. Unmanned aerial vehicles (UAVs) are used in various fields, and the most important aspect of UAVs' automatic operation is landing. Currently, most UAVs use only data or signals received from satellites for automatic landing. However, using satellite data can be quite inaccurate, especially if the UAV is landing in an area where satellite signals are unstable. Therefore, most users of UAVs prefer to use the infrared light landing method, which involves using a camera with a lens that can detect infrared light on the UAV and a device that emits infrared light placed at the landing pad. This method provides less error than using satellite data, but the equipment is relatively expensive and has other limitations such as light. In this research, we chose to use computer vision for automatic landing. This involves placing a camera on the UAV and placing 6 AprilTags on the landing pad. This allows the UAV to land accurately even if not all AprilTags are visible. Through testing, this method resulted in an average error of only 0.1175 meters when all AprilTags were visible.

Keywords: Unmanned aerial vehicles, computer vision, AprilTags.

1. Introduction

Unmanned Aerial Vehicles (UAVs) are a technology that has been widely used in various sectors, not only in the military sector for security purposes. With UAVs, we can carry out missions more safely without risking human lives and control them from afar. This technology has been applied in civilian sectors, ranging from leisure activities, aerial photography, search and rescue, to business, such as agriculture and delivery services. Nowadays, UAVs are developed to be more automated, using data and signals from satellites to calculate their position, speed, and other important information for take-off, mission, and landing. However, using satellite signals has its limitations, and in some cases, UAVs may need to land in areas without stable signals, which may cause inaccuracies in their movements. Therefore, the purpose of this research is to develop a more accurate landing system for UAVs, so that they can land precisely in desired locations, such as on a charging station for recure mission in fields or for mapping and survey to extend searching range. In the present, there are various research studies that investigate and test automatic landing techniques using different methods. The popular approach is to use special visual markers. Goeller, L. [2] uses computer vision with a 3-color circle symbol to help with landing accuracy, achieving a landing accuracy of 5 centimeters. Wubben et al. [9] uses computer vision with ArUco symbols to achieve a landing accuracy of 11 centimeters. Moreira et al. [7] uses computer vision with a triangular arrangement of 6 dots forming a triangle and an ArUco symbol in the center to achieve a landing accuracy of 1 centimeter. Another approach is to use infrared light. In [6] uses infrared light to achieve a landing accuracy of 19 centimeters. Hayajneh et al. [8] also uses infrared light to achieve a landing accuracy of 20 centimeters. Kalinov et al. [3] uses infrared light on a mobile robot on the ground to achieve a landing accuracy of 2.5 to 1.25 centimeters. Aboumrad et al. [1] also uses infrared light to assist in landing with an accuracy of 3 centimeters. The approach also used for precision landing is to use RTK system. Kownacki et al. [4] utilizes satellite or GNSS for automatic landing. In this research work two types of aircraft are used namely vertical takeoff and landing aircraft and a quadcopter type unmanned aerial vehicle with four rotors. The landing accuracy is 43.8 and 40.2 centimeters, respectively. Because of infrared method and RTK method have a high price for equipment, so the aim of this work is to develop a precision landing system by using a fiducial marker, AprilTag, because Kalaitzakis et al. [5] shown that AprilTag has detection rate more than another fiducial marker that will make the precision landing system using AprilTag can work smoothly.

2. Experiments equipment

In this section we explain our choice of equipment for the experiment.

3.1. A Custom UAV

Tarot FY650 TL65B01 was used for the frame of UAV. The autopilot runs on the Pixhawk flight controller. The drone also features on-board Raspberry pi (RPi) model B, which communicated with the autopilot via the MAVLink protocol. Under the custom UAV, Logitech C922 USB Camera was installed downwards used for AprilTag detection.

Figure 5. A Custom UAV used in the experiment.

3.2. Landing Pad

The landing pad was divided into 2 parts. The first part is for the Big Tag only. The Big Tag has a length of 74.9 cm. the second part is for the Bundle Tag and the Small Tag. The Bundle Tags are the tags that are placed around the rectangle conner, and the Small Tag is the tag that is placed on the center of landing tag. These Tag have the same size, a length of 10 cm.

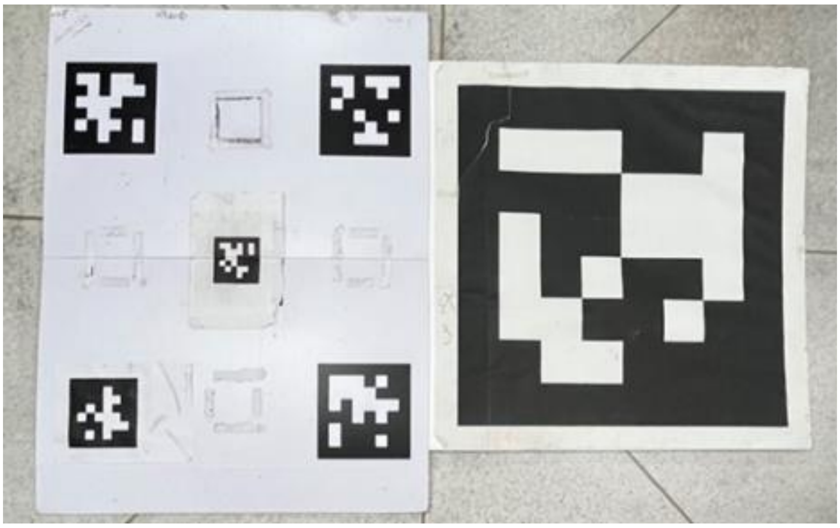

Figure 6. A simulation of the AprilTag symbol and the layout of the tags to be placed at the landing spot.

3. Methodology

In designing an automated landing system, it is necessary to be able to precisely guide the UAVs to the landing spot. This requires designing both the system and the symbols that will be placed on the landing pad. In an emergency where the aircraft is unable to see or only partially see some tags, the system must be able to safely command the UAVs to operate and land.

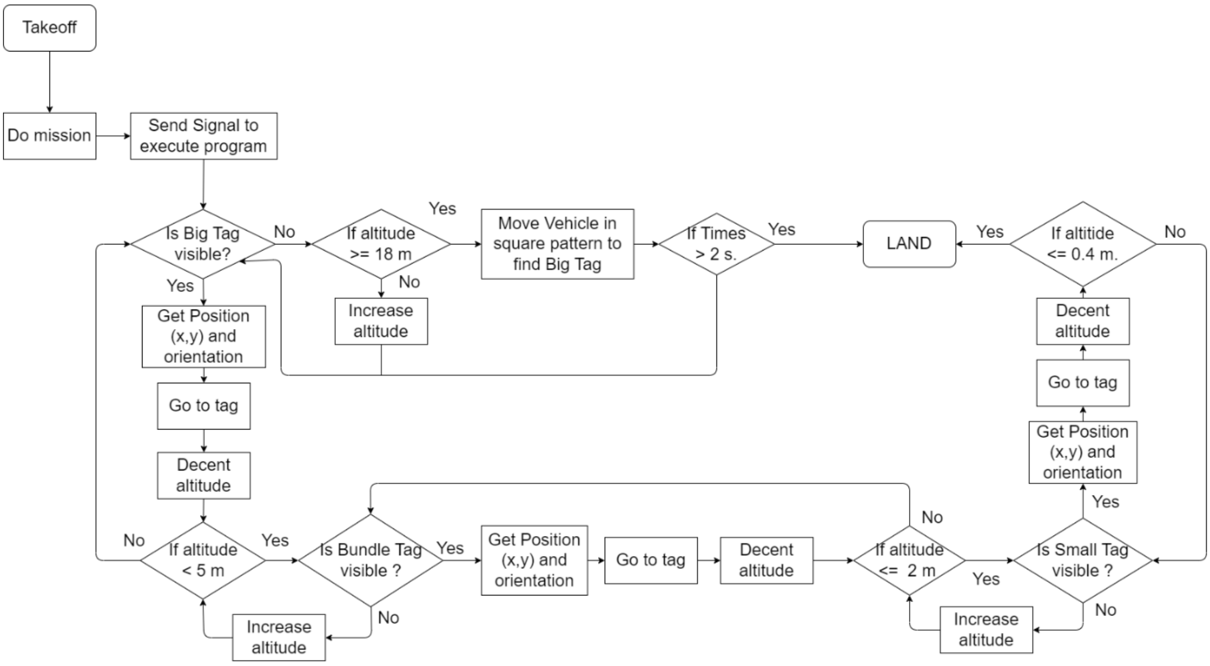

Figure 7. Autonomous Landing method.

The principle of an automatic landing system is that when UAVs take off and completes its mission and is ready to land, UAVs will send a signal to the system to start working. The system will then divide into 3 sections.

1. When the system starts working, it will check whether the UAVs see the big tag or not. The system will divide the working process into 2 conditions:

1.1 If cannot see it, the system will further divide the working conditions into 2 conditions:

   1) Check if the height is higher than 18 meters. If it is, the system will command the UAVs to move in a rectangle to search for the big tag. If it has searched more than twice and still cannot find it, the system will command the aircraft to land using data from GPS.
   2) If the height is less than 18 meters, the system will command the UAVs to increase its height and check whether it sees the big tag or not. If it still cannot see it, the system will command the UAVs to increase its height again until the height is higher than 18 meters, and then follow condition 1.

1.2 If the big tag is visible, the system will command the UAVs to move to the tag using the x and y coordinates read from the tag and reduce its height. When the height is lowered to less than 5 meters, the system will switch to working in section 2.

2. The system will check whether the UAVs see the bundle tags or not. The system will divide the working process into 2 conditions:

2.1 If it cannot see it, the system will command the UAVs to increase its height and check whether it sees the bundle tags or not. If it still cannot see it, the system will command the UAVs to increase its height again until the height is higher than 5 meters, the system will switch to working in section 1.

2.2 If the bundle tags are visible, the system will command the UAVs to move to the tag using the x and y coordinates read from the tag and reduce its height. When the height is lowered to less than 2 meters, the system will switch to working in section 3.

3. The system will check whether the UAVs see the small tag or not. The system will divide the working process into 2 conditions:

3.1 If it cannot see it, the system will command the UAVs to increase its height and check whether it sees the small tag or not. If it still cannot see it, the system will command the UAVs to increase its height again until the height is higher than 2 meters, the system will switch to working in section 2.

3.2 If the bundle tags are visible, the system will command the UAVs to move to the tag using the x and y coordinates read from the tag and reduce its height. When the height is lowered to less than 0.4 meters, the system will command the UAVs to land and use 6 AprilTags placed next to each other at the landing pad.

4. Results

In our experiment, we test in 3 cases. First, an autonomous landing using GPS data. Second, a precision landing using AprilTag that can see all of tags in landing pad. And last, a precision landing using AprilTag that cannot see some of tags in Bundle Tags, tags where are placed around rectangle corner. Flight testing and collecting accuracy of automatic landing systems will repeat the test and collect several times and average the landing in each case.

Table 1. A table summarizing the results of landing using data from satellites and designed automatic landing systems.

Method	GPS data	Full tags	Cannot see 1 tag	Cannot see 2 tags	Cannot see 3 tags	Cannot see 4 tags
Average error (meter)	1.835	0.1175	0.204	0.210	0.194	0.213

From the test flight and collecting the error data, it can be seen that the automatic landing with satellite data (GPS) has an average deviation of up to 1.835 meters, so it is not suitable for use in the automatic landing at requires a lot of precision. And using AprilTags placed next to each other, landing is very accurate. The error is only 0.1175 meters, and in an emergency causing the tag to not be visible at all, it can still land automatically quite accurately.

5. Discussion

In this work, the process that is used for control UAVs does not check if the position UAVs moved is the same as position that program commanded. If UAVs land in environments such as windy, the UAVs landing position will have more error distance. To reduce this error distance, we designed a system to check the position every time the UAVs decent altitude. Even it can land more accurately but it needs more time to land compare with landing by using GPS. If the UAVs detect AprilTags when have roll or pitch angle, the relative position the system calculated will have some error. We designed the system to not trust the relative position calculated when the UAVs have roll or pitch angle more than 5 degrees to reduced error that occurs from roll or pitch angle.

6. Conclusion

Achieving accurate landing of multirotor UAVs remains a challenging issue, as GPS-based landing procedures are associated with errors of a few meters even under ideal satellite reception conditions, performing worse in many cases. In addition, GPS-assisted landing is not an option for indoor operations. To address this issue, in this work a vision-based landing solution that relies on AprilTag markers is presented. This approach has been shown to be effective, consistent, and more accurate than GPS-only landing approaches. These markers allow the UAV to detect the exact landing position from a high altitude, paving the way for sophisticated applications including automated package retrieval or the landing of large UAV swarms in a very restricted area, among others.

As future work, it is planned to improve the overall efficiency of the protocol. This can be done by decreasing the landing time even further, the accuracy can be increased. Finally, the algorithm can be further optimized so that the UAV is able to land under less favorable weather conditions.

7. References

[1] Aboumrad, A., Haun, J., Alexander, M., & Nansong, W. (2020). An Automatic Platform for Landing and Charging of UAVs to Extend UAV Operations.

[2] Goeller, L. (2018). Drone Precision Landing using computer vision.

[3] Kalinov, I., Safronov, E., Agishev, R., Kurenkov, M., & Tsetserukou, D. (2019). High-Precision UAV Localization System for Landing on a Mobile Collaborative Robot Based on an IR Marker Pattern Recognition.

[4] Kownacki, C., Ambroziak, L., Ciezkowski, M., Wolniakowski, A., Romaniuk, S., Bozko, A., & Ołdziej, D. (2023). Precision Landing Tests of Tethered Multicopter and VTOL UAV on Moving Landing Pad on a Lake.

[5] M. Kalaitzakis, S. Carroll, A. Ambrosi, C. Whitehead and N. Vitzilaios, "Experimental Comparison of Fiducial Markers for Pose Estimation," *2020 International Conference on Unmanned Aircraft Systems (ICUAS)*, Athens, Greece, 2020, pp. 781-789, doi: 10.1109/ICUAS48674.2020.9213977.

[6] Mondal, M., Shidlovskiy, S., Shashev, D., & Okunsky, M. (2021). Autonomous Infrared Guided Landing System for Unmanned Aerial Vehicles.

[7] Moreira, M., Azevedo, F., Ferreira, A., Pedro, D., Matos-Carvalho, J., Ramos, Á., Campos, L. (2021). Precision Landing for Low-Maintenance Remote Operations with UAVs.
[8] R. Hayajneh, M., & E. Badawi, A. R. (2019). Automatic UAV Wireless Charging over Solar Vehicle to Enable Frequent Flight Missions.
[9] Wubben, J.; Fabra, F.; Calafate, C.T.; Krzeszowski, T.; Marquez-Barja, J.M.; Cano, J.-C.; Manzoni, P. Accurate Landing of Unmanned Aerial Vehicles Using Ground Pattern Recognition. Electronics 2019, 8, 1532. https://doi.org/10.3390/electronics8121532

AME0024

Mathematical model and trim analysis of an X-wing spinning drone in hover using numerical optimisation

N Tanman[1,*], D Anderson[1], and D Thomson[1]

[1]James Watt School of Engineering, College of Science & Engineering, University of Glasgow, Glasgow, G12 8QQ, the United Kingdom

* Corresponding Author: n.tanman.1@research.gla.ac.uk

Abstract. Currently, several designs have been proposed in order to deal with the limitations of conventional Unmanned Aerial Vehicles (UAVs). Unlike conventional quadcopters, an X-wing spinning drone can possibly provide an increase in hovering efficiency by adding four wings and a tilting mechanism as it might require less power consumption in spinning hover at specific wing pitch angles. This paper seeks to examine a simplified nonlinear mathematical model of the X-wing spinning drone as well as a trim analysis of the vehicle in a hovering flight mode. To simply model this unconventional vehicle, the blade element momentum theory (BEMT) was utilised to evaluate wing aerodynamics based on the local flow conditions and the thrust and torque estimation models were employed to calculate the thrusts and torques generated by the motors. In addition, the optimisation process was used to investigate the vehicle trim. In order to gain insight into the behaviour of the vehicle, numerical simulations were performed. The simulation results were in accord with the other spinning vehicle models as well as the helicopter theory. When the wing blade angle began to decrease from 90 degrees, the vehicle initially lost altitude due to a loss of the vertical thrust from the motors. After the drone started to spin, it gained lift forces from the wings to increase the altitude. In the trim condition, the drone could maintain its altitude by appropriately optimising the motor speeds although it changed the wing blade angle to different degrees. The simpler models developed in this work represent a possibility to apply these models to design other intelligence vehicles.

Keywords: Mathematical model, Trim analysis, Spinning drone, Unconventional UAV.

1. Introduction

Nowadays, Unmanned Aerial Vehicles (UAVs) have been extensively utilised in a number of civilian applications. However, there are some limitations to the use of conventional UAVs. For example, conventional quadcopters are designed to be able to fly vertically and horizontally. Nonetheless, these quadcopters may have the limitation of the hover time and also the range in forward flight. Precisely, this limits the use of the vehicle in a task that requires longer operating times, as well as larger operation areas. Therefore, increasing UAV capabilities is likely one of the most challenging in the development of UAVs.

Several designs have been proposed in order to deal with the limitations of conventional UAVs, especially manoeuvrability [1-2]. The manoeuvrability of UAVs can be simply increased by additional configuration, such as adding a tilting mechanism or increasing the number of rotors [3]. A conventional quadcopter can lose altitude and fall down if the vehicle starts to spin in any case. However, with additional proper design, the quadcopter may be able to hover longer and also fly further in forward flight. Thus, it is possible that a conventional quadcopter can be developed by adding four wings into the vehicle arms in order to deal with a loss of the vertical thrust of the rotors while the vehicle spins. Additionally, the vehicle can be equipped with a tilting mechanism in order to perform hover, transition and forward flight by using the differential thrust of the propellers. This unconventional quadcopter can be analysed as part of a fixed-wing and rotary-wing vehicle. It is likely that this spinning drone has not been identified. Therefore, in this paper, this vehicle will be simply called an X-wing spinning drone.

The question to be asked here is how can this novel electric UAV based on both fixed and rotary wing vehicles be modelled while it spins. Therefore, this paper attempts to provide an overview of a simplified nonlinear mathematical model of the X-wing spinning drone as well as a trim analysis of the vehicle. However, this work does not engage with the transition and forward flight modes. The main contribution of this paper is to design a novel unconventional UAV using simpler models.

2. Mathematical Model

2.1 Coordinate frame definition

The position of a vehicle can be described in the inertial frame, whereas the total forces and moments acting on the vehicle can be described in the body frame. That means, a couple of coordinate frames will be involved in describing the motion of the vehicle. Figure 1 shows the coordinate frames used in this report and a free-body diagram of the X-wing spinning drone in hover flight mode.

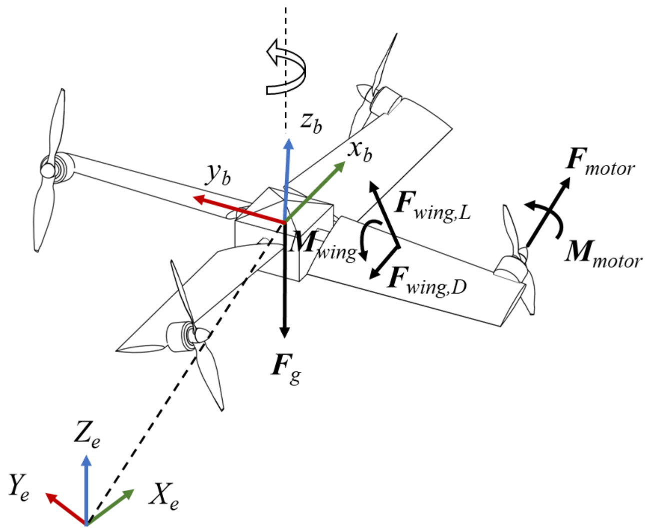

Figure 1. Reference frames and free body diagram of the X-wing spinning drone.

In the numerical simulation, 12 state variables were used, which are the position and Euler angles of the vehicle in the inertial frame, the velocity and angular rates of the vehicle in the body frame, and angular rates, to describe the system.

2.2 Kinematic and dynamic equations

The motion of the X-wing quadcopter drone that is treated as a rigid body can be described by kinematic and dynamic equations. At a given time step, dynamic and kinematic equations can be solved using MATLAB/Simulink. The kinematic equations can be expressed as follows:

$$\dot{\mathbf{p}} = \mathbf{R}^{ib}\mathbf{v} \tag{1}$$

$$\begin{bmatrix} \dot{\phi} \\ \dot{\theta} \\ \dot{\varphi} \end{bmatrix} = \begin{bmatrix} 1 & \sin\phi\tan\theta & \cos\phi\tan\theta \\ 0 & \cos\phi & -\sin\phi \\ 0 & \sin\phi\sec\theta & \cos\phi\sec\theta \end{bmatrix} \boldsymbol{\omega} \tag{2}$$

where $\mathbf{p}$ is the position of the vehicle, $\mathbf{R}^{ib}$ is the rotation matrix transforming the vector expressed in the body frame into a vector expressed in the inertial frame, and $\mathbf{v}$ and $\boldsymbol{\omega}$ the translational and rotational velocities of the vehicle. Additionally, the dynamic equations can be formulated as follows:

$$\dot{\mathbf{v}} = \frac{1}{m}\left(\sum \mathbf{F}^b - \boldsymbol{\omega} \times (m\mathbf{v})\right) \tag{3}$$

$$\dot{\boldsymbol{\omega}} = \mathbf{I}^{-1}\left(\sum \mathbf{M}^b - \boldsymbol{\omega} \times (I\boldsymbol{\omega}) - \tau_{gyro}\right) \tag{4}$$

where $\mathbf{F}^b$ and $\mathbf{M}^b$ are the resultant force and moment acting on the vehicle expressed in the body frame, m is the total mass of the vehicle, and $\mathbf{I}$ is the inertia matrix of the vehicle. For simplicity, this work considers the inertia matrix as a constant matrix. It should be noted that gyroscopic precession τ_{gyro} needs to be accounted in Equation (4) as there is a change in angular momentum from pitching each propeller [4, 5].

2.3 Forces and moments

Body forces which are the forces acting on the X-wing in spinning hover are the sum of the gravitational force, the thrust forces from the motors, and the aerodynamic forces produced by the wings of the vehicle. Each wing and motor are summed from an i^{th} motor/wing. The resultant force vector in the body frame can be written as:

$$\mathbf{F}^b = \mathbf{F}_g^b + \sum_{i=1}^{4} \mathbf{F}_{motor_i}^b + \sum_{i=1}^{4} \mathbf{F}_{wing_i}^b \tag{5}$$

Similarly, the moments acting on the X-wing in spinning hover flight mode are the sum of the motor moments and the wing moments. The resultant moment vector in the body frame can be stated as:

$$\mathbf{M}^b = \sum_{i=1}^{4}\left(\mathbf{r}_{motor_i} \times \mathbf{F}_{motor_i}^b + \mathbf{M}_{motor,M_i}^b\right) + \sum_{i=1}^{4}\left(\mathbf{r}_{wing_i} \times \mathbf{F}_i + \mathbf{M}_{wing,AC_i}^b\right) \tag{6}$$

One should be aware that the moments from the motors are the torques from the effect of the spinning propellers $\mathbf{M}_{motor,M}^b$ and the moment from the thrusts and the motor moment arms $\mathbf{r}_{motor}$. Likewise, there are two wing moments which are the pitching moments of each wing $\mathbf{M}_{wing,AC}^b$ and the moments from the resultant forces and the wing moment arms $\mathbf{r}_{wing}$.

2.3.1 Gravitational force model

For the effects of gravity on the body frame, the gravitational force of the vehicle can be modelled as:

$$\mathbf{F}_g^b = m\mathbf{R}^{bi}\mathbf{g} \tag{7}$$

where $\mathbf{F}_g^b$ is the gravitational force of the vehicle, $\mathbf{R}^{bi}$ is the rotation matrix transforming the vector expressed in the inertial frame into a vector expressed in the body frame, and $\mathbf{g}$ is the gravitational acceleration vector with respect to the inertial frame.

2.3.2 Motor force and moment models

The total motor force expressed in the body frame is the sum of the thrust generated by each motor. Comparably, the total motor moment with respect to the body frame is the sum of the torques generated by each motor and the cross-product terms from each motor. The thrust and the torque generated by a single propeller can be estimated using Equations (8) and (9), respectively.

$$F_{m,i} = k_T \omega_i^2 \tag{8}$$

$$M_{m,i} = k_Q \omega_i^2 \tag{9}$$

where $k_T = C_T(J)\rho A R^2$ is the lumped rotor thrust coefficient, $k_Q = C_Q(J)\rho A R^3$ is the lumped rotor torque coefficient which both C_T and C_Q are functions of advance ratio J, and ω is the angular velocity of the motor. An important point to remember is that both k_T and k_Q can generally be obtained from experiments. Advanced Precision Composites (APC) provides the propeller performance data files on the website [6], which can simply be used to acquire both k_T and k_Q values. The APC propeller 9.0 × 4.5 propeller was used in the numerical simulations.

2.3.3 Wing aerodynamic models

Figure 2 shows a sketch of the dimensions and blade element on one wing of the X-wing spinning drone. In this study, c_0 and c_R are defined as the root and tip chord lengths, respectively. The terms r_0, r_R, and l refer to the root cut-out, blade spanwise and blade radius. x refers to the absolute position from a rotation axis.

Figure 3 defines the relative angles, velocities, and forces of the wing section in the spinning hover flight mode. The aerodynamic angle of attack of the wing is α which is the angle between the wing chord and the resultant velocity U. The inflow angle β is the angle between the free stream velocity and the body frame. The pitch angle γ is the angle between the wing chord and the body frame. Lift $F_{wing,L}$ and $F_{wing,D}$ drag forces are produced from the airflow at the wing section. These two forces are normal to and parallel to the freestream velocity, respectively. Therefore, the resultant force acting on the wings expressed in the body frame is $F^b_{wing,i} = F^b_{wing,L} + F^b_{wing,D}$.

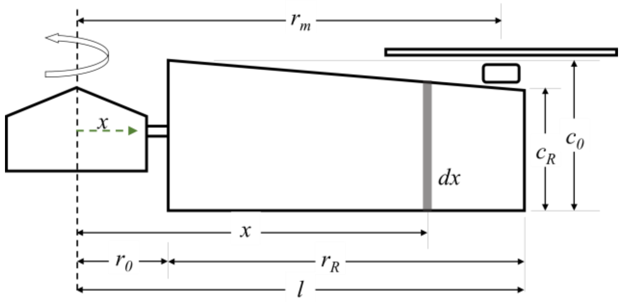

Figure 2. Dimensions and blade element of a wing.

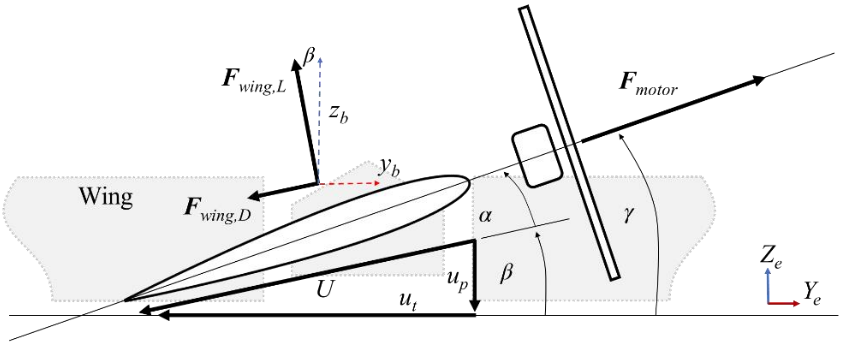

Figure 3. The wing relative angles α, β, and γ in the spinning hover flight mode.

Since the pitch angle will vary between 0 to 90 degrees, it needs to investigate the relationships of the lift and drag coefficients, and the angle of attack within this range. Figure 4 shows the coefficients of the aerofoil NACA0012 at Reynold's number of 500,000. The relationships can be found in [7].

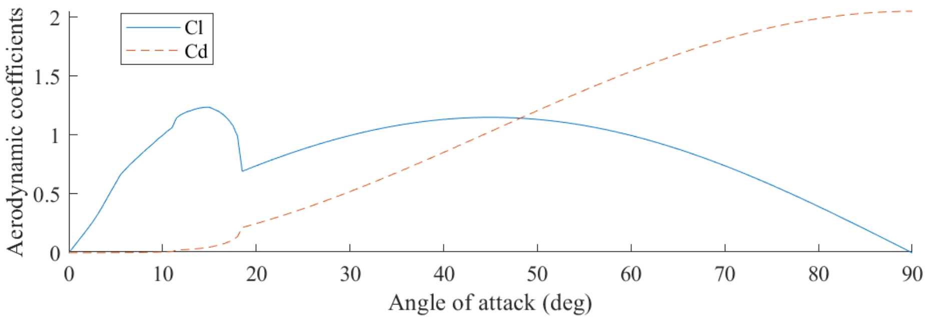

Figure 4. Lift and drag coefficients with respect to the angle of attack from 0 to 90 degrees.

The blade element theory (BET) has been discussed in the analysis of helicopter rotors extensively in the literature [8, 9]. Once the vehicle starts spinning, the wing blades which are treated as rigid will act as helicopter rotors. Therefore, the blade element theory can be a useful tool to examine the wing aerodynamic model. The resultant velocity at the blade element can be expressed as $U = \sqrt{U_T^2 + U_p^2}$, where $U_p = V_c + \upsilon_i$ is the out-of-plane velocity normal to the rotor disc plane, and $U_T = \Omega x$ is the in-plane velocity parallel to the rotor disc plane. Therefore, the relative inflow angle at the blade element which is the angle between the local airflow velocity and the body frame can be defined as $\beta = \arctan(U_p / U_T)$. Also, if the pitch angle at the blade element is γ, the effective angle of attack α can be expressed as $\alpha = \gamma - \beta$. The total lift and drag forces for each wing are determined using BET. The aerodynamic forces for each element are modelled as follows:

$$dL = \frac{1}{2}\rho U^2 c_n C_l dx \tag{10}$$

$$dD = \frac{1}{2}\rho U^2 c_n C_d dx \tag{11}$$

$$dM = \frac{1}{2}\rho U^2 c_n C_m \bar{c} dx \tag{12}$$

where c_n is the local wing chord expressed as a function of the spanwise distance, dx is the blade-element width, U is the resultant local airflow velocity, C_l, C_d, and C_m are lift, drag, and moment coefficients, the lift dL and drag dD forces act perpendicular and parallel to the resultant airflow, and dM is the pitching moment.

From the blade element momentum theory (BEMT) for axial flight, the inflow ratio can be expressed in closed form as can be seen in [8]. Considering the hovering condition, the inflow ratio equation can be simplified by defining the climb inflow ratio $\lambda_c = 0$. The inflow ratio can be modified with Prandtl's tip-loss function F_p to deal with the loss of lift near the tips. Thus, the inflow ratio with the tip-loss factor in hovering condition can be given by:

$$\lambda_h = \frac{\sigma C_{l_\alpha}}{16F_P}\left(\sqrt{1+\frac{32F_P}{\sigma C_{l_\alpha}}\gamma r} - 1\right) \tag{13}$$

where σ is the wing blade solidity and C_{l_α} is the lift-curve slope of the aerofoil section comprising the rotor. It is unfortunate that this current study is limited by the absence of the prop wash effect at the wingtip. Prandtl's tip-loss function accounts for the loss of the lift near the wingtip due to air vortices. It can be written as follows:

$$F_P = \frac{2}{\pi}\arccos\left(\exp\left(-\left[\frac{N_b(1-r)}{r\sin\beta}\right]\right)\right) \tag{14}$$

where N_b is the number of rotor blades and *r* is the relative position of the blade element.

3. Numerical Simulation Results and Discussion

In order to gain insight into the nature of the vehicle, two case study numerical simulations are presented and discussed. The first section of this topic examines the wing aerodynamic quantity distribution. Then, the linear and angular velocities are presented. For simplicity, it is assumed that the motor speeds were all set as 590 rad/s for all simulations. It should be noted that this is the motor speed for conventional hover mode. For each simulation run, the wing pitch angle is fixed at a given angle.

3.1 Wing aerodynamic quantity distribution

Assuming the wing aerofoil of NACA 0012, at given control variable states which were all the motor speeds of 590 rad/s and the blade pitch angle of 15 degrees, wing aerodynamic quantity distribution along the wingspan can be plotted. As can be seen from Figure 5, in general, the lift and drag forces increase with increasing distance from the spinning axis. However, Prandtl's tip-loss function was also used to account for the effects due to air vortices. This results in the loss of the lift and drag at the wingtip. The vertices cause an increase in the locally induced velocities at the wingtip. Also, these vertices decrease the local angle of attack near the wing tip. Since the wingspan has a cut-out area, it leads to the absence of various aerodynamic quantities from the centre of gravity of the vehicle to the wing root. The obtained simulation results regarding wing aerodynamic distribution are in accord with the predictions based on helicopter theory [8], and also other spinning aircraft models [10, 11].

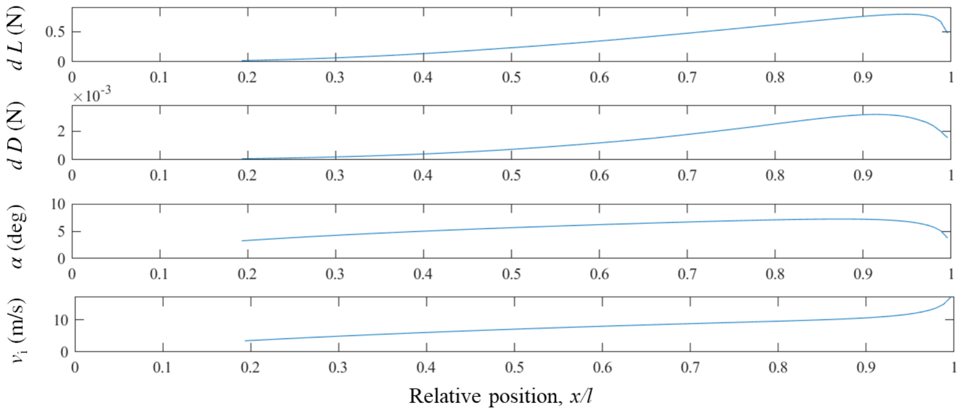

Figure 5. Wing aerodynamic quantity distribution along the wingspan.

3.2 Displacement and velocities

The wing blades of the spinning drone are perpendicular to the ground at the beginning. When the wing blade angle is not 90 degrees, the vehicle will lose altitude due to a loss of vertical thrust from the motors. After the drone starts to spin, it will gain the lift forces from the wings to increase the altitude. As shown in Figure 6, the angular and linear velocities of the vehicle were plotted to examine the behaviour of the drone regarding the z-axis. Although the vehicle was designed to be able to change the wing blade angle from 90 to 0 degrees, it is convenient to select only three different angles to represent high, medium, and low pitch angles. The selected angles were 85, 45, and 15 degrees at the same motor speed of 590 rad/s for all cases, respectively. At the given state, the vehicle tends to reach a higher value of the angular velocity at a steady state when the blade pitch angle is lower. The z-axis linear velocity tends to decrease at first and then increase to reach a steady state.

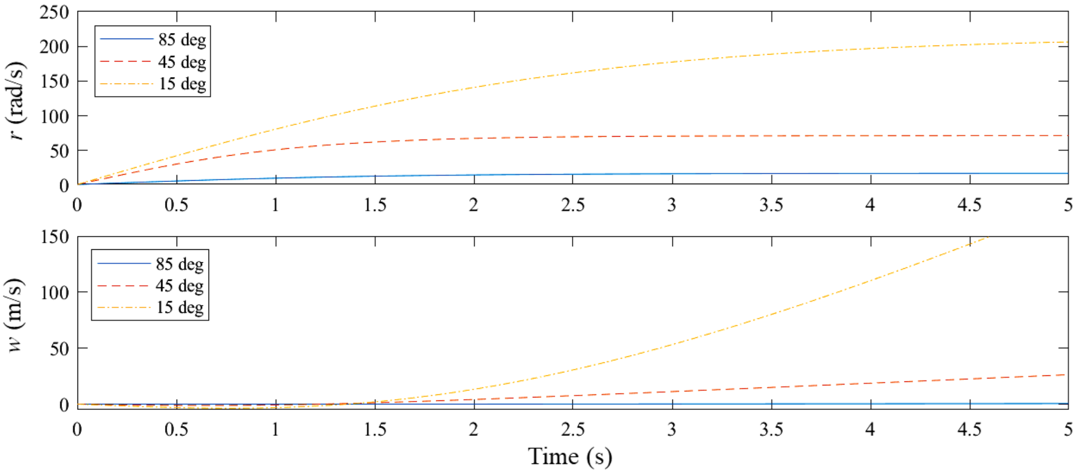

Figure 6. Vehicle displacement with respect to the inertial frame
and vehicle angular and linear velocities with respect to the body frame.

4. Trim Analysis

Trim analysis can be used to describe the mechanics of a spinning drone. The trim problem examines the equilibrium point that is required to hold the vehicle in a steady state. In the trim problem for spinning hover, the X-wing spinning drone may be increasing the yaw angle, but the three translational velocities and all accelerations are equal to zero.

This topic presents a trim optimisation problem to examine the equilibrium point in the spinning flight mode for the various blade pitch angles. The problem statement describes how to formulate an entire problem. The algorithm used in this problem and the design variables are revealed as well. The last section presents the results and discussion.

4.1 Problem statement

This problem shows how to maintain altitude in the spinning hover flight mode at various blade pitch angles by changing the motor speeds at the given vehicle characteristics. The state variables and control inputs at an equilibrium point were examined. In the trim, the general nonlinear equations of motion can then be modified as $\mathbf{x} = f(x_e, u_e)$. The general trim problem for this problem can be considered as the acceleration vector is uniformly zero. Therefore, the governing equation of the trim optimisation problem can be written as $\mathbf{x} = [u \ \upsilon \ w \ p \ q \ r]^T = 0$. The control inputs were chosen to be the design variables to maintain an altitude at a specific blade pitch angle. As the motor speeds will be adjusted for each blade pitch angle, four design variables in the optimisation problem are the four motor speeds given by $\mathbf{u} = [\omega_1 \ \omega_2 \ \omega_3 \ \omega_4]^T$. The design variables are a design vector that each variable is to be determined by the optimiser on the feasible region. Typically, Optimisation Toolbox solvers provide functions to minimise or maximise objectives while satisfying constraints. The solvers can be used to find a local optimum and this local optimum can be a global optimum [12]. Thus, it seems possible that the results are due to the good initial guess values. Also, it is needed to set the lower and upper boundaries in order to execute MATLAB Optimisation solvers. The present study employed *fmincon* to solve this optimisation problem as it is suitable for finding a minimum of constrained nonlinear functions.

The vehicle is meant to be able to maintain its altitude while spinning. The six accelerations squared were selected as the objective function for the optimisation problem to ensure that the function values are getting close to zero. Therefore, the entire optimisation problem can be expressed as follows:

$$\begin{aligned} &\text{minimise} && \dot{u}^2 + \dot{v}^2 + \dot{w}^2 + \dot{p}^2 + \dot{q}^2 + \dot{r}^2 \\ &\text{with respect to} && \omega_1, \omega_2, \omega_3, \omega_4 \end{aligned} \tag{15}$$

where $\omega_1, \omega_2, \omega_3, \omega_4$ are the design variables which are bound by lower and upper bounds of 100 and 1,000 rad/s, respectively. In this study, an altitude and velocities were set as equality constraints.

4.2 Trim results and discussion

The wing blades of a spinning drone can change the pitch angle from 90 degrees vertical to 0 degrees horizontal. The different pitch angles cause the vehicle to rotate at different angular speeds. When the vehicle changes from the conventional hover mode to spinning mode, the altitude will drop a little. In order to maintain altitude, the drone has to adjust its motor speeds to match the forces generated by the drone's rotation. The model can determine the optimal results from the initial and control inputs. Optimised values of the objective function, state variables, and decision variables for three different wing blade pitch angles are presented in Table 1. All objective functions which were the sums of accelerations are very close to zero. Although these accelerations are not identically zero, the vehicle can still maintain an altitude of about 10 m. In other words, the drone is in trim for these different angles. In order to avoid redundancy, some trim result values are not shown in the table. That is, the obtained results of the translational velocities u, υ, and w and angular rates p and q were all zero. Additionally, each motor speed was the same after trimming. Therefore, it is indicated as ω without any subscript.

Table 1. Optimised values for three different wing blade pitch angles.

Objective function, state variables and decision variables	85 degrees	45 degrees	15 degrees
Objective function	7.64×10^{-11}	3.92×10^{-11}	1.10×10^{-11}
r (rad/s)	14.8	48.3	67.3
ω (rad/s)	586.8	445.5	199.9

Figure 7 shows the vehicle displacement from a trimming optimisation problem at three different blade pitch angles. After putting the state variables and the motor speeds from the trim optimisation problems into the equations of motion as initial values, the vehicle can maintain the altitude as well as the vehicle's angular velocity while spinning in the specified period.

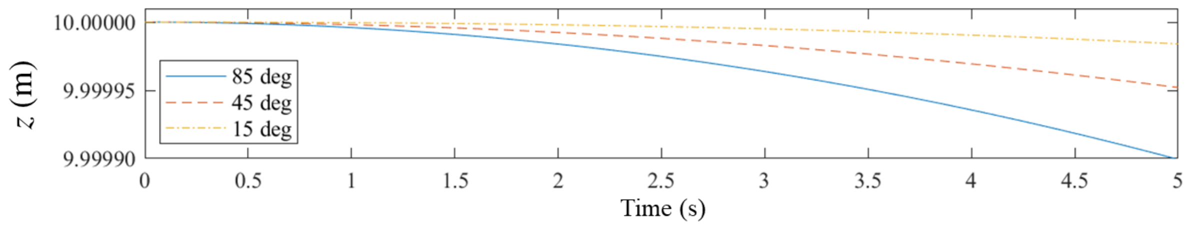

Figure 7. Vehicle displacement after trimming.

From a spinning hover optimisation problem, the results for the motor speed and the vehicle angular velocity versus the wing blade pitch angle can be plotted. Figure 8 shows the variations in the motor speed and the angular velocity with the pitch angle, respectively. To conventionally hover for a given spinning drone specification, the vehicle needs to have all motor speeds of around 590 rad/s or 5,630 RPM. When the wings are not vertical, the vehicle is able to spin. To spinning hover, the vehicle decreases the motor speeds, while the angular velocity increases exponentially. At the lower pitch angles, the vehicle is able to spin faster as the wings can produce higher lift and lower drag forces according to the characteristics of the aerofoil NACA0012. It is worth mentioning that the blade pitch angle varied from 90 to 5 degrees in this study. It appears that at the wing pitch angle of 0 degrees or all the wings are horizontal, the vehicle cannot be trimmed to spinning hover. This might be explained by the fact that there are no vertical thrusts to hover from both the motors and wings.

The most interesting aspect of these figures is that each trend seems to be smooth when varying the pitch angle from 90 degrees down to 35 degrees, and then they have a little change in the trends after that. A possible explanation for this might be related to the wing forces around those wing pitch angles. In other words, there is a huge drop of the total wing forces around the pitch angle of 30 degrees which is in accord with the lift and drag coefficient characteristics of the designated aerofoil. It is worth noting that although the wing blade pitch angle is set to be 30 degrees, the local angles of attack along the wingspan are between 10-18 degrees where there is a huge drop happening in the lift coefficient profile of NACA0012.

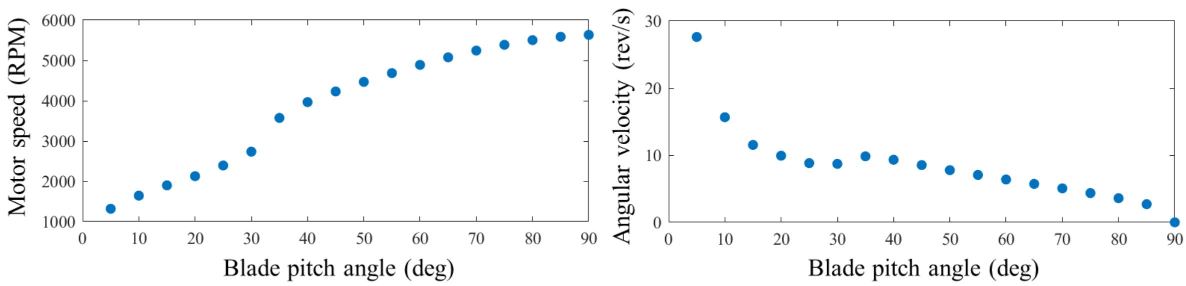

Figure 8. Variations in motor speed and vehicle angular velocity with blade pitch angle.

4.3 Power comparison in hover

In order to evaluate the effectiveness of adding four wings, the power required in hover was employed. The obtained results from the trim optimisation problem were utilised to estimate the power required and time in spinning hover. Some researchers have proposed closed-form equations to estimate the endurance of battery-powered rotary-wing UAVs. The endurance equation of an electric aircraft can be written in the general formula of Peukert's equation as [13, 14]:

$$E = t = Rt^{1-n}\left[\frac{VC}{P_{req}}\right]^n \tag{16}$$

where t is the estimated flight time, Rt is the battery hour rate, n is the discharge rate, V is the battery voltage, C is the battery capacity, and P_{req} is the power required. The total power required for hovering flight is the sum of the wing blade power and the motor/propeller power and can be calculated as the following equation:

$$P_{req} = P_i + P_o + P_r \tag{17}$$

where P_i is the induced power to hover, P_o is the profile power to overcome the profile drag of the wing blades, and P_r is the power for the motor/propeller. The power of the auxiliary systems such as a tilting mechanism, and the power losses will not be considered here.

With a specific battery, the power consumption and hover time of the vehicle can be estimated. A sample of LiPo 3S 2,200 mAh batteries and the total mass of the vehicle of 1.48 kg were chosen to conduct this case study. Figure 9 shows the estimated power required and time in hover. As expected, the power required to hover in spinning mode is less than in conventional mode, especially at lower pitch angles. Likewise, the estimated hover times from spinning hover are greater than regular hover. To be more precise, as the vehicle spins faster while using the lower motor speeds, it therefore requires less power required and also gives more hover times. It is important to realise that by varying the blade pitch angles from 90 to 30 degrees, the estimated times are slightly increasing and then rise up exponentially after 30 degrees due to a change in the total wing forces as stated earlier. However, there are no results regarding the power required and hover time at the wing pitch angle of 0 degrees as mentioned previously.

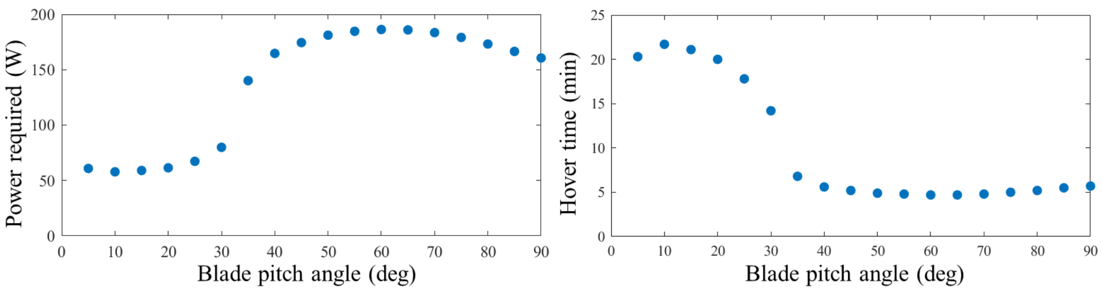

Figure 9. Variations in estimated power required and hover time with blade pitch angle.

5. Conclusion

The purpose of this paper was to develop a simplified mathematical model for the X-wing spinning drone and also to determine the trim analysis of the vehicle in hover flight modes. In order to simply model this unconventional vehicle, the BEMT was utilised to evaluate aerodynamics for the wing blades, whereas thrust and torque estimation models were used as a quadcopter. Also, the optimisation process was used to examine the vehicle trim. The obtained results of the numerical simulation study indicated that the findings were qualitatively according to the results of other spinning models as well as the predictions based on helicopter theory. The investigation of the vehicle trimming showed that the drone can maintain altitude after changing the wing blade angle to various degrees by optimising the motor speeds appropriately.

The mathematical model proposed in this study can easily be developed further to design other unconventional drones similar to this one. The reliability of the numerical simulations can be improved by developing some models, such as other inflow models, aerofoils, or drag models. Further work on the forward flight modes needs to be done to fully understand the mechanics of the vehicle.

6. References

[1] Ang, K.Z.Y., Cui, J.Q., Pang, T., Li, K., Wang, K., Ke, Y., Chen, B.M. (2015). Design and Implementation of a Thrust-Vectored Unmanned Tail-Sitter with Reconfigurable Wings. *Unmanned Systems*, Vol. 3:143–162.

[2] Chen, Z.J., Stol, K.A., Richards, P.J. (2019). Preliminary design of multirotor UAVs with tilted-rotors for improved disturbance rejection capability. *Aerospace Science and Technology*, Vol. 92:635–643

[3] Junaid, A. B., Sanchez, A.D.D.C., Bosch, J.B., Vitzilaios, N., Zweiri, Y. (2018). Design and implementation of a dual-axis tilting quadcopter. *Robotics*, Vol. 7:1–20

[4] Low, J.E., Sufiyan, D., Win, L.S.T., Soh, G.S., Foong, S. (2019). Design of a Hybrid Aerial Robot with Multi-Mode Structural Efficiency and Optimized Mid-Air Transition. *Unmanned Systems*, Vol. 7:195–213

[5] Dharmawan, A., Ashari, A., Putra, A.E. (2017). Mathematical Modelling of Translation and Rotation Movement in Quad Tiltrotor.

[6] Advanced Precision Composites (APC) (2022). Performance data. (cited: 1 August 2023). Available from: https://www.apcprop.com/technical-information/performance-data/.

[7] Prouty, R.W. (1990). *Helicopter Performance Stability and control*. PWS Publishers.

[8] Leishman, J.D. (2006). *Principles of helicopter aerodynamics*. Cambridge University Press.

[9] Johnson, W. (2013). *Rotorcraft aeromechanics.* Cambridge University Press.

[10] Matiè, G., Topiè, M., Jankovec, M. (2015). Mathematical model of a monocopter based on unsteady blade-element momentum theory. *Journal of Aircraft*. Vol. 52:1905–1913.

[11] Low, J.E., Pheh, Y.H., Foong, S. (2016). Analysis of wing twist effects on hover flight dynamics of a single rotor aerial craft. *In: IEEE/ASME International Conference on Advanced Intelligent Mechatronics*, AIM. Institute of Electrical and Electronics Engineers Inc., pp 323–328.

[12] MathWorks. (2021). *Optimization Toolbox User's Guide*. The MathWorks, Inc.

[13] Gatti, M. (2017). Complete Preliminary Design Methodology for Electric Multirotor. *Journal of Aerospace Engineering.* https://doi.org/10.1061/(ASCE)AS.1943-5525.0000752.

[14] Biczyski, M., Sehab, R., Whidborne, J.F., Krebs, G., Luk, P. (2020). Multirotor Sizing Methodology with Flight Time Estimation. *Journal of Advanced Transportation.*

AMM0001

The effect of CSLB on the creep behaviour of 316L austenitic stainless steel

Sutapat Kwankaomeng, Jatuporn Kaew-on, and Panya Kansuwan*

Department of Mechanical Engineering, School of Engineering, King Mongkut's Institute of Technology Ladkrabang, Bangkok, 10520, Thailand

* Corresponding Author: panya.ka@kmitl.ac.th

Abstract. This research aims to study the creep behaviour of structurally modified 316L austenitic stainless steel samples at different percentages of coincidence-site-lattice boundaries (CSLBs) with approximately the same average grain sizes of 60 μm. The controlled microstructure is attained using thermomechanical processes, i.e., single-step and iterative recrystallization. The samples obtained are low % CSLB test pieces with 32.3% CSLB and high % CSLB test pieces with 42.3 % CSLB. A series of creep tests are performed at 650°C for three different stress levels at 220, 260, and 290 MPa for three different temperatures at 600, 625, and 650°C. The results show that creep rupture life is strongly related to CSLB fractions with control grain sizes of the samples. Rupture life increases with the fractions of CSLBs. With the exact creep mechanism as specified by test stresses and temperatures, activation energy values calculated from the tests explain the lower creep rate of high % CSLB samples and; thus, the longer rupture life.

Keywords: Creep, Grain boundary engineer, Activation energy, Coincidence-site-lattice.

1. Introduction

Due to its high corrosion resistance of austenitic stainless steel, a steel grade of 316L is widely used in various corrosive applications in petrochemicals, refineries, power plants, pipelines, or plant equipment. However, some drawbacks exist. Stainless steel becomes more vulnerable at elevated operating temperatures to environmentally induced damages, such as intergranular corrosion, stress corrosion cracking, pitting corrosion, etc. [1, 2]. Service engineers require steels that provide more strength and microstructural stability to extend their structural applications within the temperature range from 260 to 1200°C. Approaches to improve the elevated-temperature characteristics of the steel are alloying and thermomechanical processes that yield various grades of steel [3, 4]. One of the main objectives is achieving specific phases that distribute optimally across the base materials. Other than average grain size, the methods can be applied to increase the fraction of particular grain boundaries (GBs) within. Even though GBs occupy a tiny portion of bulk materials, it is well-accepted that GBs play a critical role in controlling some macroscopic phenomena of bulk materials [5-9].

As a result of different grain misorientation, a GB occurs as a planar defect that can be classified as high-angle GBs, low-angle GBs, or special low-energy GBs. Instead of the misorientation of the two adjacent grains, their disorientation defines the boundary's free volume and energy. Of the specific disorientations, some lattices of two neighboring grains occupy the same sites, known as coincident site lattices (CSL). If the sites frequently repeat, the atomistic structure at the boundary becomes tighter and denser, approaching the perfect crystal inside the grains. The reciprocal density of the coincident sites designates an n-number within the sigma notation, i.e. Σn [10-12]. The unique low-energy GBs with low free volume at the boundaries are $\Sigma 3$, $\Sigma 9$, $\Sigma 27$. Using the molecular dynamic calculation, the energy levels of the GBs decrease sharply [9]. The special microscopic characters stand out in the macroscopic phenomena, such as intergranular corrosion [6], intergranular fracture strength [5], and creep behaviors [13]. Furthermore, the surface structure of a Ni alloy dictated by crystallographic orientation impacts the carbon nanostructure formation rate [7].

Creep is a permanent deformation occurring when a metal is exposed to high-stress levels at an elevated temperature for an extended period of time. The deformation occurs slowly until the material fails to bear load or deforms excessively due to a dominant damage mechanism. The usages of the metal operating in creep range are ubiquitous in piping systems in industrial plants, thermal resistant parts in jet engines, etc. If the metals are engineered to counter the relevant mechanism, a longer service life of the metal components is probable. As a result, there would be a significant impact on depreciation reduction to the overall industrial economy. A generic creep deformation map of 2.25Cr-1Mo [14] demonstrates two primary damage mechanisms in the creep range: power law creep dominated at relatively high-normalized stress levels and diffusion creep at relatively low-normalized stress levels. Each of them can be subdivided into two minor mechanisms at relatively low and high homologous temperatures. The four creep damage mechanisms are dislocation core diffusion, lattice diffusion, Coble creep, and Nabarro-Herring creep.

Many attempts to improve creep behaviors of metals aim to eliminate diffusional paths, the weak links. The preferred structure is the single crystal. For polycrystalline materials, columnar grain and larger grain size structures perform better than small grain size structures at higher severe conditions. Others applied grain boundary engineering (GBE), including iterative recrystallization, one-step recrystallization, iterative strain annealing, and one-step strain annealing to alter the fraction of GB types [7, 15-18]. Particularly to the creep deformation, S. Spigarelli [19] found the beneficial influence of a large proportion of low-$\sum$ GBs to the creep response of AISI 304L steel. It was found that the nature of the special GBs suppressed the intergranular precipitated carbide. However, the former research does not report the grain size's influence. Different GBE, the subset of thermomechanical processes, results in different grain sizes and creep behavior. Thus, this research attempts to control the initial grain size for all test pieces to be the same. The experimental setup allows us to study only a parameter (the fraction of low-$\sum$ GBs) that affects their creep behaviors. Following the GBE processes in [16], we reproduced three structurally modified 316L austenitic stainless steel samples at different percentages of coincidence-site-lattice boundaries (CSLBs) with approximately the same average grain sizes of 60 μms. The samples are an as-received test piece at 23.4% CSLB, a low % CSLB test piece at 32.3% CSLB, and a high % CSLB test piece at 42.3% CSLB.

2. Theory

Creep is the time-dependent strain that occurs after a force is applied to a metallic component at an elevated temperature. Engineers usually perform a series of creep tests at different stresses and temperatures to study the creep behaviors. The relationship between strain and time can be mathematically represented mathematically by combining Maxwell and Kelvin-Voigt bodies [20]. One of the standards that state the test procedure is ASTM E139 [21], starting from creep test apparatus, sample preparation, test piece size and dimension, test piece preparation, calibration, and testing procedures. There are two types of tests. The creep-rupture test is the test that aims to measure rupture time, while the other test is the creep test, which aims to measure creep and creep rate with time. Three different creep ranges from the creep test can be identified by creep rate: primary, secondary, and tertiary (Figure 1). Upon loading, the sample instantaneous deforms to an initial elastic strain before slowly deforming at a decreasing strain rate. In the primary creep, the hardening rate, such as strain hardening, is higher than the softening rate, such as recovery and recrystallization. When the strain rate becomes steady, the creep behavior enters secondary creep or steady-state creep, in which a minimum creep rate is defined. During the steady-state creep, the materials deform slowly with a dominant mechanism relevant to the level of stress and temperature. Engineers use the steady state creep rate to predict the expected service life of a part when given operating load cases. In tertiary creep, the material degradation rate inducing microstructure instability makes the material lose load-bearing capability, and the strain rate increases exponentially until rupture.

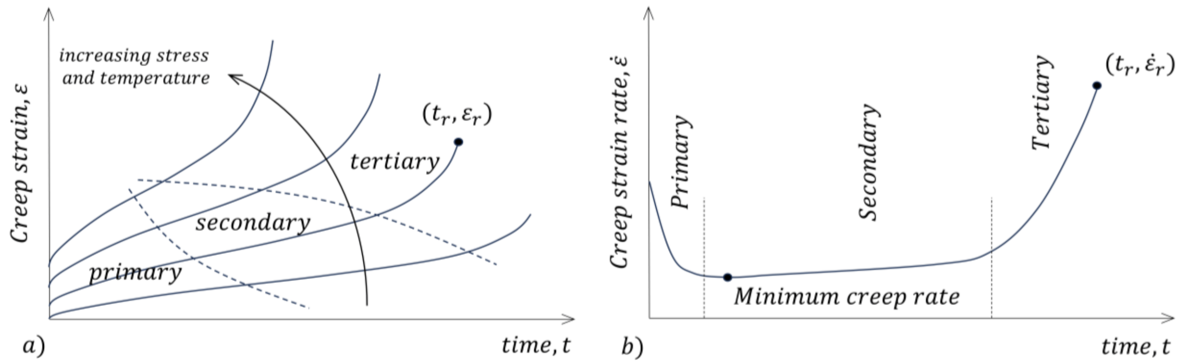

Figure 1. a) Different creep test by increasing stress and temperature b) A corresponding creep rate.

The complex creep mechanism in the secondary creep is usually mathematically modeled by a rate equation, as in Equation (1) [22], expressing the relationship among minimum creep rate, applied stress, and temperature.

$$\dot{\varepsilon}_{min} = \dot{\varepsilon}_o \left(\frac{\sigma}{E}\right)^n D \quad (1)$$

in which $\dot{\varepsilon}_o$ is materials constants, n is stress exponent, D is diffusion coefficient in Arrhenius-type thermal dependence as in Equation (2).

$$D = exp\left(\frac{-Q_a}{kT}\right) \quad (2)$$

in which Q_a is the activation energy, k is the Boltzmann's constant, and T is the temperature.

To determine the value of Q_a and n, one has to perform a series of creep tests at different stresses and temperatures specified by using an experimental design. The relationship of the major parameters, i.e., applied stress, minimum creep rate, and temperature, are analyzed to fit a mathematical model according to Equations (1) and (2). The attained values of Q_a and n are used to construct a creep deformation map of the materials (Figure 2). There are two distinctive deformation mechanisms. Diffusion creep is the creep-controlling mechanism operating in relatively low stress due to atomic diffusion with vacancy enhancement. In this regime, the value of n is about one. Coble creep compensates permanent deformation by GB diffusion while Naberro-Herring operates through both GB and volume diffusion. The calculated values of Q_a distinct the mechanism zones. Generally, Coble creep dominates at relatively low homologous temperatures, but Naberro-Herring occurs at relatively higher homologous temperatures. Power law creep activates the deformation at higher stress values by dislocation motion. Thermally activated glide is the rate-controlled parameter at lower temperatures than recovery-controlled creep when the dislocation climbing enhances the creep process [22-24].

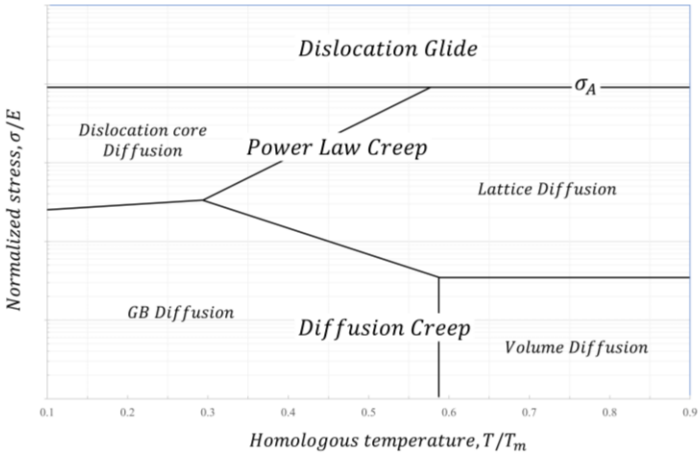

Figure 2. Creep deformation mechanism map [14].

3. Experimental procedure

This research aims to study the effect of CSLBs on the creep behavior of 316L austenitic stainless steels. Samples with approximately the same grain size but different percentages of CSLBs are grain boundary-engineered (GBEed) by thermomechanical processes accomplished in [16]. The procedures are repeated to prepare creep samples used in this work. The first step of the procedure on the as-received specimen is a solution heat treatment in which initial carbide phases are dissolved by soaking the samples at 1200°C for 1 hour to unify their microstructure for usage as an initial microstructural phase. The step is followed by air-cooling to room temperature to obtain the microstructure (Figure 3a). All the solution heat-treated cylindrical shafts with 1-inch diameter are then machined to tensile test pieces at 7.5 mm diameter in reduced sections. The GBE processes introduce elastic strain energy by 40% elongation by reducing the diameter from 7.2 to 4.8 mm. We anneal the samples at 1100 °C for 10 minutes to obtain recrystallized specimens with an average grain size of 60 µm (Figure 3b). The process is named the "Single-step recrystallization process." The other set of the solution heat-treated samples is plastic-strained to 40% elongation and then annealed at 1125°C for 10 minutes, resulting in recrystallized specimens with an average grain size of 80 µm (Figure 4a). The samples are tensile plastic strained a second time by 40% elongation and then annealed at 1130°C for 10 minutes to obtain samples with an average grain size of 60 µm (Figure 4b). The second process is the "Iterative recrystallization process," which further decreases the diameter of the reduced section from 4.8 to 3 mm as required for the creep tests.

To evaluate grain boundary characteristic distribution (GBCD) in a fraction of CSLBs, we performed the standard metallographic procedures to prepare the samples for evaluation in an SEM, Hitachi model S3400N. The SEM is equipped with EDAX for Orientation image microscopy (OIM) from the Kikuchi pattern and index using embedded software version 5.3.2. The GBCD is determined based on Brandon's criterion, as stated in Equation (3) [25]. The results are shown in Table 1 and Figure 5.

$$\Delta\theta_{max} = 15\Sigma^{-1/2} \tag{3}$$

Table 1. The measured fraction of special grain boundaries of each sample [16].

Item	Sample Name	Process	Average grain size (µm)	%CSLB
1	As-received	As-received	100	23.4
2	Low % CSLB	Single-step recrystallized	60	33.7
3	High % CSLB	Iterative recrystallized	60	42.2

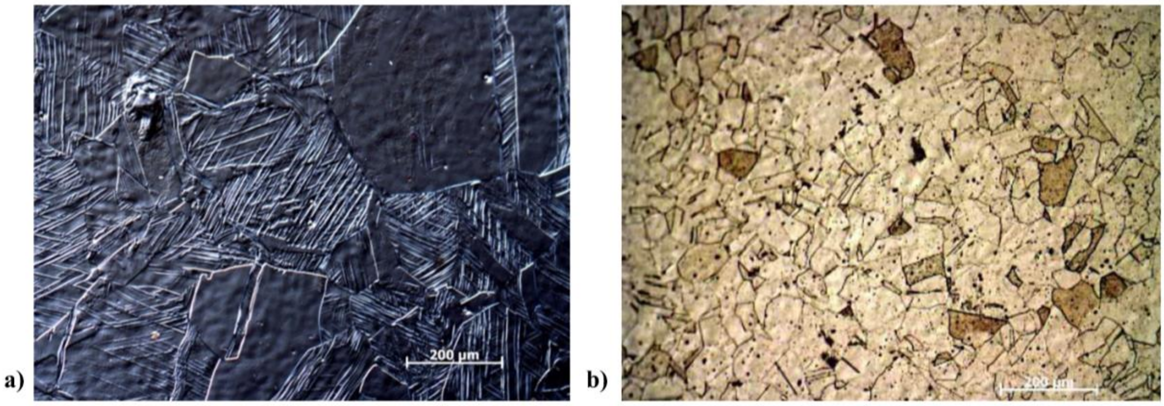

Figure 3. a) As-received b) Single-step recrystallized with an average grain size of 60 µm [16].

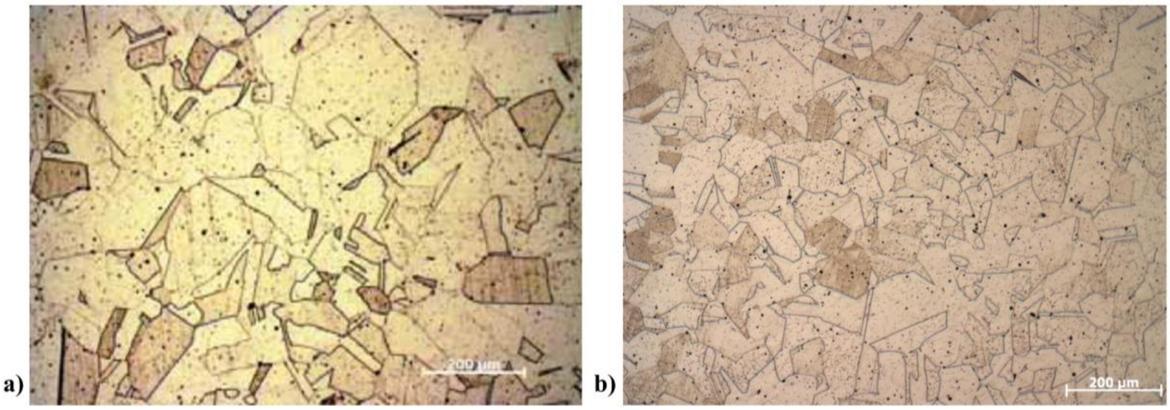

Figure 4. a) Single-step recrystallized with an average grain size of 80 µm b) Iterative recrystallized with an average grain size of 60 µm [16].

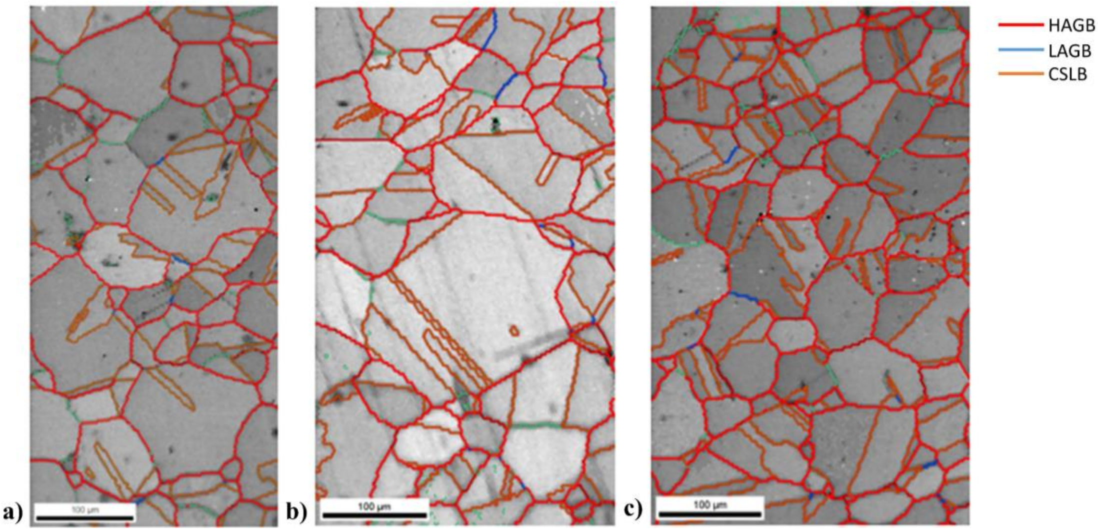

Figure 5. The special GB classification as a result of Kikuchi pattern and index a) Single-step recrystallized 60 µm b) Single-step recrystallized 80 µm c) Iterative recrystallized 60 µm [16].

Table 2. Creep test conditions.

Condition	Temp. (°C)	Stress (MPa)
1	650	220, 260, 290
2	625, 600	290

All test specimens are prepared to the standard creep test specimens with a diameter of 3 mm. Table 2 indicates the test conditions performed on SATEC Model M3 (Figure 6).

a)  b) 

Figure 6. Creep test machine SATEC Model M3.

4. Result and Discussion

Creep test conditions are constant temperature and constant load cases on as-received, High % CSL, and Low % CSL samples. The tests are performed at 650 ºC but different stress values at 220, 260, and 290 MPa for the constant temperature cases. The creep test curve for each constant temperature results in Figure 7. The stress is at 290 MPa for constant stress load cases, but the temperatures are 600, 625, and 650ºC. The results in creep test curves are demonstrated in Figure 8. Table 3 concludes the evaluated creep parameters, rupture time, and minimum creep rate.

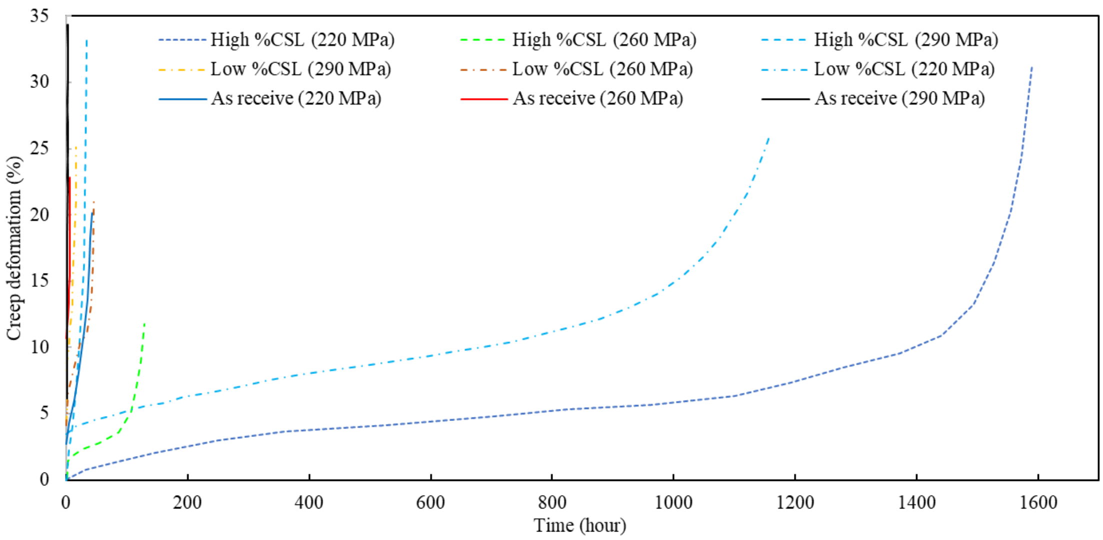

Figure 7. The creep test curve of each sample for constant temperature at 650ºC.

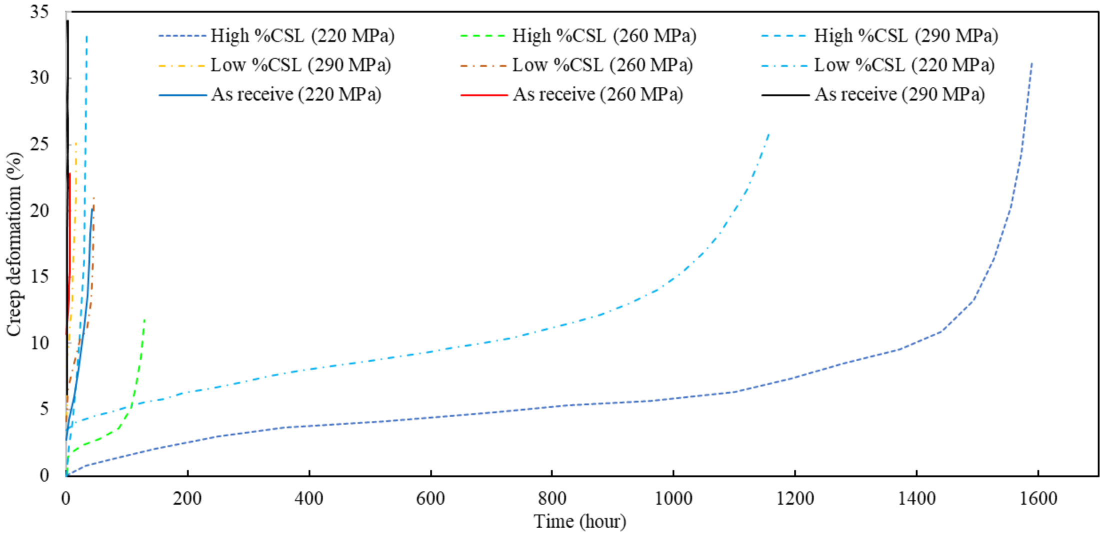

Figure 8. The creep test curve of each sample for constant applied stress at 290 MPa.

Table 3. Derived experimental parameters for each load case.

Temperature (°C)	Stress (MPa)	As-received		Low % CSL		High % CSL	
		Rupture time (hr)	Min. Creep rate (s^{-1})	Rupture time (hr)	Min. Creep rate (s^{-1})	Rupture time (hr)	Min. Creep rate (s^{-1})
650	220	42	1.46E-08	1177	5.81E-10	1611	2.43E-10
	260	6	1.76E-07	46	1.33E-08	130	2.33E-09
	290	3	4.92E-07	15	5.53E-08	34	1.38E-08
625		22	2.64E-08	34	2.31E-08	45	1.23E-09
600		45	1.37E-08	1096	1.79E-09	1214	3.08E-11

Obviously, the High % CSL samples express longer rupture time and lower minimum creep rate than those of Low % CSL samples. We could interpret the behavior from the values of n and Q_c in which n implies the creep mechanism and Q_c limits the rate of the relevant thermal activated mechanism. From Table 3, the parameters can be derived from Equation (1) and (2). Table 4 shows the evaluated values for Low % CSL and High % CSL

Table 4. Values of n and Q_c.

Sample identification	Low % CSL	High % CSL
Fraction of CSL	32.4%	42.3%
Stress exponent, n	2.16	2.55
Activation energy, Q_c	280.3 kJ/mol	396.8 kJ/mol

Typically, stress exponent (n) and Activation energy (Q_c) determine the dominant creep mechanism. Due to the stress exponents in both cases not changing significantly, the atomic diffusion compensating for creep deformation uses the same diffusing path. The value of n is in the range of 2 and 3, which is greater than one that specifies the creep in the Coble creep regime but less than three if the creep mechanism is in the High-temperature diffusion region. Only the activation energy in the High % CSL case increases significantly. We expect the major creep mechanism is the Coble creep, in which the diffusion path is along GBs. When the percentage of the special GBs increases, the diffusion path is still along the GBs, but the activation energy increment reduces the deformation rate. Conversely, the increase in % CSL could shift the diffusion path to other mechanisms but with higher activation energy. The higher activation energy diffusing path is diffusing along the dislocation core creep. However, the typical value of the stress exponent is about 3 to 7, depending on the active dimension of the nature of the paths. The second hypothesis is improbable. We must perform more creep tests to create the system's complete creep deformation map. The approach will verify the assumption.

5. Conclusion

5.1. Creep rates depend on two major loading parameters: stress and temperature. Furthermore, the parameters will determine the creep deformation mechanism specified in the materials' creep deformation map. Creep deformation should be constructed and consulted to impose encounter measures to extend the creep service life of the material.

5.2. It is evident from the results that the creep rate significantly reduces when the fraction of special GBs (low-CSLBs) increases. This effect is due to the increment of the relevant activation energy.

5.3. The significant reduction of creep rate is a result of the increment of the activation energy increases from 280.3 to 396.8 kJ/mole. The energy change is the ramification upon the increment of %CSLB from 32.4% to 42.3%.

5.4. It is inconclusive if the Coble creep is still active before and after GBE. If this is the case, the activation energy upon the increment of the fraction of the special GBs is the thermal activation energy of the CSLB diffusion mechanism. However, if the previous dominant mechanism differs from the later creep mechanism, the activation energy evaluated after GBE is the next lower active activation energy for the creep to operate.

5.5. A creep deformation map is necessary to specify the creep mechanism in the creep range of materials' operation.

6. Acknowledgment

This work was financially supported by King Mongkut's Institute of Technology Ladkrabang [KREF015607]

7. References

[1] Kumar, M.S., Sujata, M., Venkataswamy, M.A. and Bhaumik, S.K., (2008), Failure analysis of a stainless steel pipeline. *Engineering Failure Analysis*. 15(5): p. 497-504.

[2] Ibrahim, M.A.M., Rehim, S.S.A.E. and Hamza, M.M., (2009), Corrosion behavior of some austenitic stainless steels in chloride environments. *Materials Chemistry and Physics*. 115(1): p. 80-85.

[3] *ASM Specialty Handbook : Heat Resistant Materials*, ed. J.R. Davis. 1997: ASM International.

[4] *ASM Specialty Handbook : Stainless steels*, ed. J.R. Davis. 1999: ASM International.

[5] Watanabe, T., (1984), An Approach to Grain Boundary Design for Strong and Ductile Polycrystals. *Res Mechanica*. 11: p. 47-84.

[6] Palumbo, G., King, P.J., Aust, K.T., Erb, U. and Lichtenberger, P.C., (1991), Grain boundary design and control for intergranular stress-corrosion resistance. *Scripta Metallurgica et Materialia*. 25: p. 1775-80. DOI: http://dx.doi.org/10.1016/0956-716X(91)90303-I.

[7] Chamnan-arsa, S., Santawitee, O., Manonukul, A., Wongwiriyapan, W. and Kansuwan, P. *The effect of CSL Grain boundary on Carbon Nanostructure Synthesis*. in *the 8th International Conference on Materials Science and Technology (MSAT-8)*. 2014. Bangkok, Thailand.

[8] Kobayashi, S., Tsurekawa, S. and Watanabe, T., (2016), A new approach to grain boundary engineering for nanocrystalline materials. *Beilstein Journal of Nanotechnology*. 7: p. 1829-49.

[9] Chiba, R. and Kansuwan, P., (2022), Grain boundary plane rotation analysis for FCC bicrystal structures using MD simulation. *International Journal of Computational Materials Science and Engineering*. 11(1). DOI: https://doi.org/10.1142/S2047684121500299.

[10] Randle, V., *The measurement of grain boundary geometry*. 1993, London: IOP Publishing Ltd.
[11] Randle, V. and Horton, D., (1994), Grain growth phenomena in Nickel. *Scripta Metallugica et Materialia*. 31: p. 891-895.
[12] Brandon, D.G., (1966), The structure of high-angle grain boundary. *Acta Metallurgica et Materialia*. 14: p. 1479-1484. DOI: http://dx.doi.org/10.1016/0001-6160(66)90168-4.
[13] Lehockey, E.M. and Palumbo, G., (1997), On the creep behavior of grain boundary engineered Nickel. *Materials Science and Engineering: A*. 237(2): p. 168-172.
[14] Maruyama, K., Sawada, K., Koike, J., Sato, H. and Yagi, K., (1997), Examination of deformation mechanism maps in 2.25Cr—1Mo steel by creep tests at strain rates of 10−11 to 10−6 s−1. *Materials Science and Engineering: A*. 224(1): p. 166-172. DOI: https://doi.org/10.1016/S0921-5093(96)10566-9.
[15] Randle, V., (2010), Grain boundary engineering: an overview after 25 years. *Materials Science and Technology*. 26: p. 253-61.
[16] มงคล แหยมทองคำ, ปัญญา ขันธ์สุวรรณ. ขบวนการเพิ่มสัดส่วน *CSL* โดยควบคุมขนาดเกรนในเหล็กกล้าไร้สนิม *316L* in การประชุมวิชาการเครือข่ายวิศวกรรมเครื่องกลแห่งประเทศไทย ครั้งที่ *31* 2560. จังหวัดนครนายก.
[17] Wintawong, T., Santawitee, O. and Kansuwan, P. *Grain boundary engineering in 316L austenitic stainless steel*. in *The 4th TSME International Conference on Mechanical Engineering*. 2013. Pattaya, Chonburi, Thailand.
[18] อัญชลี บุญเลิศ, อรอุมา สันตวิธี, กรรณชัย กัลยาศิริ, ปัญญา ขันธ์สุวรรณ, (2559), กระบวนการอบอ่อนหลังความเครียดต่ำ-หนึ่งขั้น สาหรับการเพิ่มสัดส่วนขอบเกรนแบบ low-Sigma CSLB ในเหล็กกล้าไร้สนิม 316L Single-Step Small Strain Annealing for Low-Sigma CSLB Fraction Enhancement in 316L Austenitic Stainless Steels. วิศวสารลาดกระบัง. 33.
[19] Spigarelli, S., Cabibbo, M., Evangelista, E. and Palumbo, G., (2003), Analysis of the creep strength of a low-carbon AISI 304 steel with low-Σ grain boundaries. *Materials Science and Engineering: A*. 352(1): p. 93-99. DOI: https://doi.org/10.1016/S0921-5093(02)00903-6.
[20] ผู้ช่วยศาสตรจารย์ ดร.ปัญญา ขันธ์สุวรรณ, การวิเคราะห์ความแข็งแรงและอายุความล้าด้วยระเบียบวิธีไฟไนต์เอลิเมนต์: Structural and Fatigue Life Analysis using Finite Element Method. 2023: ศูนย์จำหน่ายตำรา คณะวิศวกรรมศาสตร์.
[21] *ASTM E139-11 Standard Test Methods for Conducting Creep, Creep-Rupture, and Stress-Rupture Tests of Metallic Materials*. 2011, ASTM International: West Conshohocken, PA, USA.
[22] Josef Betten, *Creep Mechanics*. 2008: Springer-Verlag Berlin Heidelberg.
[23] Coble, R.L., (1963), A Model for Boundary Diffusion Controlled Creep in Polycrystalline Materials. *Journal of Applied Physics*. 34(6): p. 1679-1682. DOI: 10.1063/1.1702656.
[24] Herring, C., (1950), Diffusional Viscosity of a Polycrystalline Solid. *Journal of Applied Physics*. 21: p. 437-445.
[25] Brandon, D.G., (1966), The structure of high-angle grain boundaries. *Acta Metallurgica*. 14(11): p. 1479-1484. DOI: https://doi.org/10.1016/0001-6160(66)90168-4.

AMM0004

Evaluation of the relationship between machine learning methods and AE waveform classification accuracy

Keito Togami[1,*] and Takuma MATSUO[1]

[1]School of Science and Technology, Meiji University, 1-1-1 Higashi-mita Tama-ku, Kawasaki-shi, Kanagawa, 214-8571, Japan

* Corresponding Author: ce232068@meiji.ac.jp

Abstract. The acoustic emission (AE) method is used for non-destructive inspection of machines and structures because it can detect small cracks inside materials and minute deformations before fracture. The AE method can also use the characteristics of the detected waveforms to estimate the phenomena occurring inside the material and the fracture mode. However, the analysis of AE waveforms has the problem that the accuracy varies depending on the skill of the engineer. Therefore, the purpose of this study is to develop a method for analysing AE waveforms using machine learning. Different types of machine learning methods were used to classify AE waveforms, and the relationship between AE waveform characteristics and classification accuracy was evaluated. Defects of different depths were placed on steel plates by end milling, and artificial AE signals from the defects and AE of rust fracture caused by corrosion were excited. These signals were classified using supervised and unsupervised learning methods, and the results showed that the classification was high accurate for supervised learning, but low accurate for unsupervised learning. Thus, it is necessary to select an effective machine learning method according to the characteristics of the waveforms to be classified.

Keywords: Acoustic Emission, Corrosion Defect, Atmospheric Corrosion, Nondestructive Inspection, Machine learning, Deep learning.

1. Introduction

Visual inspection and ultrasonic testing are conventionally used as nondestructive inspection methods for corrosion of steel members. However, these inspections are time-consuming and costly [1]. In this study, the acoustic emission (AE) method, a non-destructive inspection method, is used as a solution to these problems. The acoustic emission (AE) method is a non-destructive inspection method that detects acoustic signals emitted when cracks or other damage occurs in the inspected object, enabling real-time monitoring of the object [2]. Applications are currently being developed in various fields such as materials research and in industrial application [1]. In previous study about corrosion monitoring by AE method, corrosion-induced damages of materials, such as corrosion of tank bottom [3] and soil corrosion of underground steel pipes [4] has been evaluated using the AE method. However, long-term measurements are required to evaluate corrosion conditions using these methods. Moreover, many AE signals are detected during long-term AE monitoring. Therefore, manual waveform analysis is difficult. Another problem is that the accuracy of AE waveform analysis varies depending on the ability of the engineer performing the work. Therefore, machine learning methods are expected to be used to automatically analyze many AE signals. However, it is not clear what kind of machine learning methods are effective in analyzing AE signals. In this study, the corrosion propagation of steel plates was evaluated by AE method using machine learning. two types of methods, CNN (supervised learning) and k-means (unsupervised learning), were used for classification, and the classification accuracy was investigated to determine the optimal machine learning method.

2. Lamb wave AE signals and machine learning method

AE generated by atmospheric corrosion of steel plates used for classification in this study propagates as Lamb waves, which are waves that propagate through the plates. the Lamb wave is divided into symmetric mode (S-mode) and asymmetric mode (A-mode), and the velocity of each depends on frequency. Figure 1 shows the group velocity dispersion curve of the fundamental mode of a Lamb wave propagating through a 5 mm steel plate. It has been found that the S_0 mode of AE waves generated in a plate is more strongly excited when the generation position is near the center of the plate thickness. The AE signal generated at deeper defect depths due to corrosion tends to have a higher S_0 mode intensity, and the progress of corrosion can be evaluated based on the characteristics of the AE waves [5].

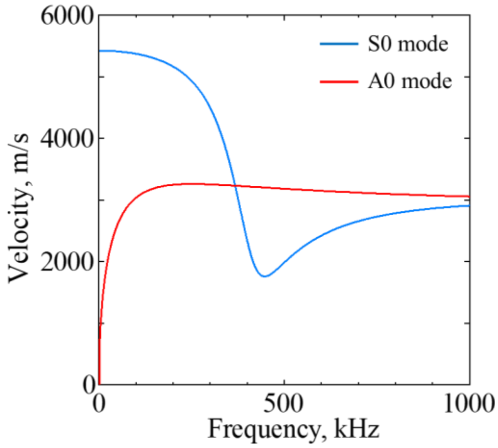

Figure 1. Group velocity dispersion curve S_0 and A_0 mode in steel plate of thickness 5 mm.

AE signals with this feature were classified using two types of machine learning methods: Convolutional Neural Network (CNN : supervised learning) [6] and k-means (unsupervised learning) [7]. CNN is a network that can capture spatial features and is suitable for image classification. The k-means method is used to divide the given data into k clusters.

3. Accelerated Corrosion Test

Figure 2 shows a diagram of the experimental setup for an accelerated corrosion test to monitor AE signals. Defects of 1, 2, and 3 mm were created on a 5 mm thick steel plate using an end mill to simulate wall thinning due to corrosion. Approximately 0.5 ml of 5 % NaCl solution was dropped into each defect (2,3,4) and no defect area (1) 6 days a week for 30 days to perform the corrosion acceleration test. The AE monitoring was performed by installing an AE sensor (PAC, R15α) at 40 mm from each defect and measuring the AE signal generated during the corrosion acceleration test. The AE signal was increased by 40 dB using a preamplifier and measured using a digitizer. The sampling interval was 50 ns and the number of sampling points was 8192, respective. The threshold value was set at 10 mV. The detected waveforms were classified as AE signals generated from which defects based on the arrival time to each sensor. Wavelet contourmap of waveform was used for classification. In images used for machine learning, we aimed for discrimination accuracy by using Lamb wave characteristics to reduce information unnecessary for discrimination. Therefore, we applied pre-processing to the AE waveform

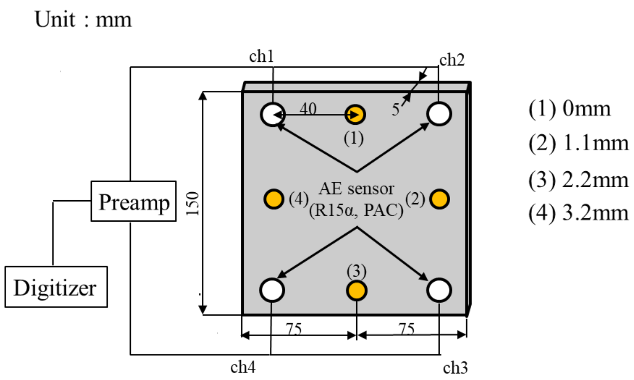

Figure 2. Experimental setup for monitoring AE signals from rust fracture.

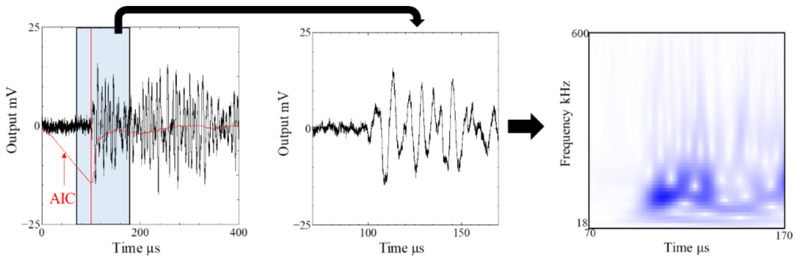

Figure 3. Pre-process for making classification data.

before wavelet transform, and attempted to improve the discrimination accuracy by setting the required range of wavelet transform to 18 kHz to 600 kHz this time. Figure 3 shows an overview of the preprocessing method.

1. Detect the first motion part of the waveform using the AIC (Akaike Information Criterion).
2. Extract the waveform during the period from 30 µs before the initial motion of the waveform to approximately 100 µs.
3. Continuous wavelet transform of the extracted waveform.

Figure 4 shows representative and extracted AE waveforms and their wavelet transform results at each corrosion depth using the above procedure. The circled areas in the figure are the S_0 and A_0 mode packets. It can be seen that the amplitude of the S_0 mode increases as the defect reaches near the center.

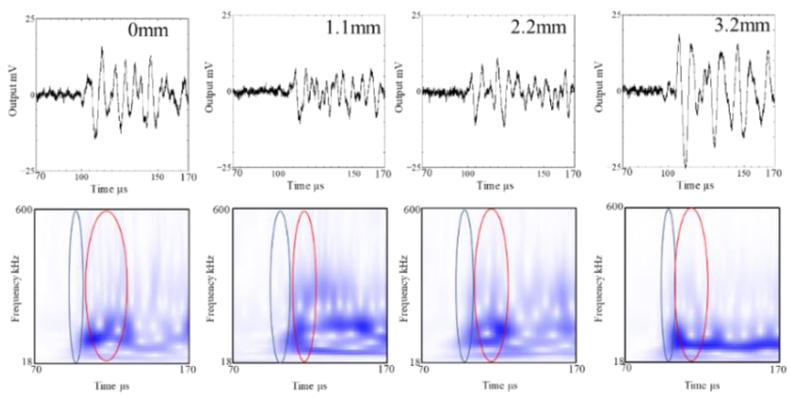

Figure 4. AE waveforms (Upper) and their wavelet contourmaps (Lower) from four corroded area.

4. AE Classification by supervised learning

Machine learning with CNN was performed. Figure 5 shows a schematic diagram of a CNN, a type of supervised learning. The input is a grayscale wavelet transformed image of size 128x128x1. The output is set to 4 because four types of defect depth are simulated in the accelerated corrosion test. The pooling layer was performed using 2 × 2 size maximum value pooling, and the overall structure of the CNN consists of four layers of convolution and pooling layers, followed by four layers of total coupling. The activation function used was a sigmoid function for the last all-coupling layer (32→4), while ReLU was used for the rest.

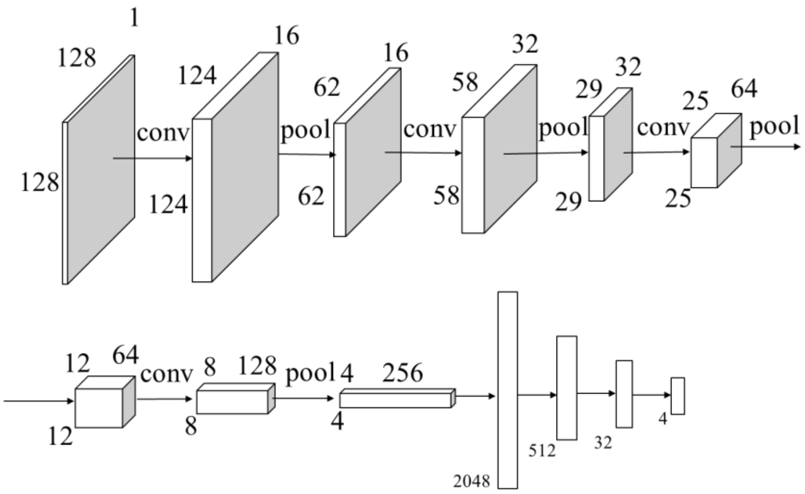

Figure 5. A Schematic diagram of CNN.

For classification, waveforms from two of the four sensors closest to the AE source were used. For the AE signals generated from each corrosion defect area, 11000 events were used as training data and 3600 events were classified. Figure 6 shows a typical example of a classified waveform. The waveforms have the same characteristics as those shown in Figure 4, and it can be confirmed that they are correctly classified.

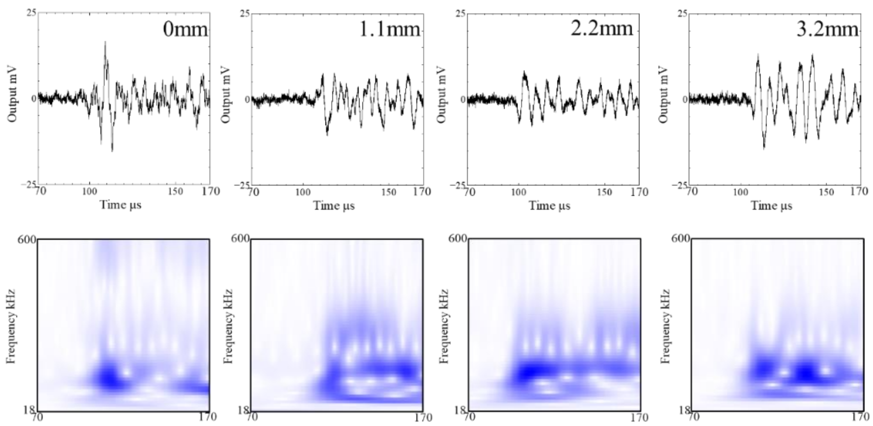

Figure 6. A typical example of classified waveforms by using CNN.

Table 1 shows the results of classifying AE waveforms caused by corrosion with different defect depth using CNN. The overall classification accuracy was approximately 96.4%, indicating that the AE waveforms due to different corrosion simulating defect depth could be classified with high accuracy by the CNN. The CNN is considered to be suitable for identifying AE waveforms caused by corrosion with different of defect depth, as it can automatically extract and identify features from the wavelet transformed image.

Table 1. The classification result by using deep learning.

AE source depth, mm	Clustering result				
	Cluster1	Cluster2	Cluster3	Cluster4	Accuracy, %
0	3517	17	29	37	97.7
1	27	3453	101	19	95.9
2	12	46	3501	41	97.3
3	55	29	103	3413	94.8

5. AE Classification by unsupervised learning

We next performed clustering of AE waveforms with different defect depth using the k-means, a type of unsupervised learning. The input is a grayscale wavelet transformed image of size 128x128x1. The number of clusters for the k-means method was set to 4, which is the same as the number of defect depths. The number of data used for clustering is the same as for CNN classification data. Table 2 shows the classification results. Table 2 shows that the classification accuracy was lower. Figure 7 shows a typical classified waveform. As shown in Figure 4, there is no correlation between the intensity of the S_0 mode and the classification results. The reason for the low clustering accuracy in this study can be considered to be the small difference in the feature values among the AE waveforms in this study in the present results. The wavelet contourmaps in Figure 7 shows cluster1 is generally lighter in intensity, cluster 2 has a darker shading in the initial motion part, cluster 3 has a darker shading in the low frequency part, and cluster4 does not have as dark an initial motion part as cluster 2.

Table 2. The result of clustering by using k-means.

AE source depth, mm	Clustering result				
	Cluster1	Cluster2	Cluster3	Cluster4	Accuracy, %
0	1447	1203	272	678	40.2
1	1245	703	823	829	19.5
2	513	901	1367	819	38.0
3	656	969	921	1054	29.3

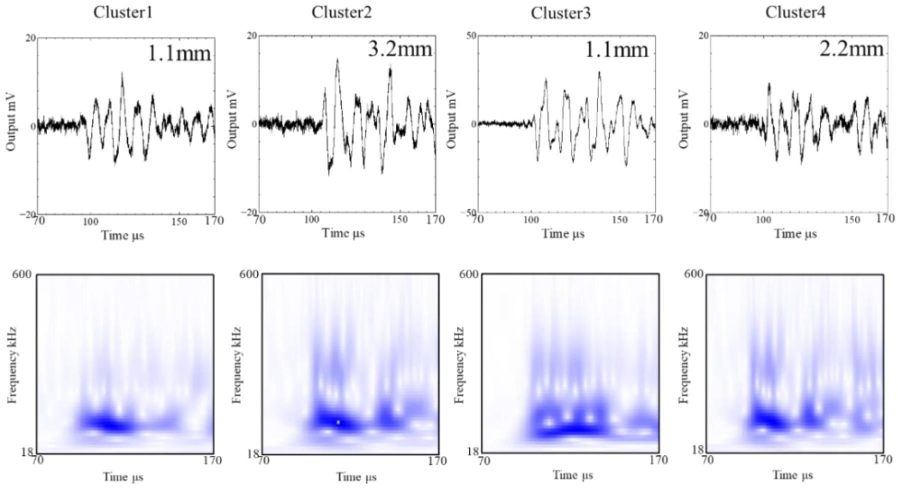

Figure 7. A typical example of classified waveforms by using k-means.

6. Conclusion

In this study, AE monitoring in accelerated corrosion tests was conducted to investigate whether supervised or unsupervised learning could be used to estimate defects by using AE waveforms caused by corrosion with defects of four depths. In the case of CNN with supervised learning, the overall discrimination accuracy exceeded 90 %. In the case of k-means with unsupervised learning, the overall discrimination accuracy did not exceed 50 %. These results indicate that the CNN captured the desired characteristics of each AE, while the k-means method failed to capture the desired characteristics of each AE waveform, resulting in a loss of discrimination accuracy. These results indicate that machine learning may be effective in identifying AE waveforms by considering the type of machine learning and the format of the data according to the AE waveform data.

7. Acknowledgments

A part of this work was supported by JSPS KAKENHI Grant Number 21K03777.

8. References

[1] Raman S, Baldev R, U. Kamachi MudaliPrabhakar S. (2019). Non - Destructive Evaluation of Corrosion and Corrosion - assisted Cracking. WILEY.

[2] Japan Non-Destructive Inspection Association (2016). Practical Acoustic Emission Testing. Springer.

[3] Li Z,Yuyama S,Yamada M,Sekine K,Kitsukawa S,Maruyama H,Konno S. (2005). Investigation on AE Signal/Noise Processing in Corrosion Damage Evaluation of Tank Bottom. Journal of Acoustic Emission. 23, 233-242.

[4] Cho H, Takemoto M. (2007). AE Monitoring of Soil Corrosion of Buried Pipe. Journal of Acoustic Emission. 25, 267-275.

[5] Kurihara T, Matsuo T, Kono T, Numata T. (2019). Development of Corrosion Depth Evaluation Method in Steel by Acoustic Emission Method. Proc. Int. Conf. On Mechanical Engneering (Pattaya) Thailand: 10th TSME International Conference on Mechanical Engineering, 106-111.

[6] Christof A, Tanel P, Leopold P, Oliver S. (2016). Deep learning for computational biology. Molecular Systems Biology, 12(878), 1-16.

[7] J.A.Hartigan, M.A.Wong. (1979). Algorithm AS 136: A K-Means Clustering Algorithm. Journal of the Royal Statistical Society. Series C, 28 (1), 100-108..

The 13th TSME International Conference on Mechanical Engineering
12th – 15th December 2023
Chiang Mai, Thailand

AMM0005

Development of a Method for Evaluating Corrosion Defect by Acoustic Emission Signals using Machine Learning

Keisuke Yamamoto[1,*] and Takuma Matsuo[1]

[1]School of Science and Technology, Meiji University, 1-1-1 Higashi-mita Tama-ku, Kawasaki-shi, Kanagawa, 214-8571, Japan

* Corresponding Author: ce222090@meiji.ac.jp

Abstract. Since the steel pipe has a risk of leaking the contents due to corrosion, it is necessary to evaluate the soundness regularly. A conventional non-destructive inspection method has the problem that it requires a lot of cost to inspect a large area. Therefore, the acoustic emission (AE) method, which enables real-time monitoring of corrosion conditions, is the preferred method. The AE method can evaluate damage conditions based on waveform parameters, however, changes in AE parameters due to differences in damage conditions are small. Therefore, visual identification requires a lot of time for identification, and the accuracy varies depending on the skill of the engineer. In this study, it aims at development of the method to evaluate corrosion defect by AE signals using machine learning. At first, nine pipes which was subjected to thickness reduction with different depths was corroded. A 5% NaCl solution was dropped periodically in the pores to accelerate corrosion. Each steel pipe was conducted a 100-minute thermal cycle test to generate AE by short term measurement. Next, wavelet transforms were applied to AE waveforms to extract the wavelet coefficient of specific frequency, and the intensity ratio of the L(0, 1)-modes and F(1, 1)-modes, which are the fundamental modes of cylindrical waves were used as features for supervised learning. As a result, it was possible to classify corrosion defect with high accuracy when the damage level is divided into 3 groups.

Keywords: Acoustic Emission, Corrosion, Cylindrical wave, Machine Learning.

1. Introduction

Steel pipes used for transporting water and gas have a problem of leaking due to corrosion. Therefore, health-monitoring techniques to prevent aging-related leakage of pipes are required [1]. Currently, visual and hammering inspection are generally used for monitoring infrastructures; however, the results vary significantly depending on the experience and ability of the operator and it is difficult to determine conditions in real time [2]. In addition, it is difficult to evaluate corrosion defect depth in quantitatively. Also, ultrasonic testing is one of the techniques for pipe-line inspection. This method can detect defects with reflective surfaces perpendicular to the direction of propagation and can estimate the defect depth. However, the directivity changes depending on the shape of the defect, and the defect depth may not be accurately determined in a real environment. It also requires extensive scanning, which takes a lot of time and cost [3]. Therefore, in this study we focused on Acoustic emission (AE) method. Acoustic emission testing is a tool for monitoring damage in real time [4]. AE testing is a method for detecting the elastic wave excited by the micro cracks in the atmospheric rusting of pipes; however, it is difficult to evaluate the amount of corrosion defect because the corrosion defect is not a direct parameter of AE [4]. In the previous study on corrosion monitoring applying AE testing, such as corrosion of tank bottom [5] and soil corrosion of underground steel pipes [6] has been evaluated. However, large amount of data needs to be detected by long-term AE monitoring. Therefore, in our previous study, we developed a method for actively generating rust fractures using thermal shock [7]. Hence, AE waves can be detected by short time measurement. Additionally, from the change of the intensity ratio of the cylindrical wave mode for each corrosion depth, the possibility of evaluating corrosion depth by using the value of the wavelet coefficient of AE signals was shown. Furthermore, machine learning (ML)-based approaches have the potential to automatically estimate the amount of corrosion defect depth from AE waveforms without relying on the skills of an operator. Therefore, this study aims at development of a method to evaluate corrosion defect depth of steel pipes by AE signals using machine learning.

2. Evaluation of corrosion defect depth using changes in AE propagation mode

2.1. Theoretical relationship between corrosion defect depth and change in AE propagation mode

A guided wave propagating through a cylindrical object is called a cylindrical wave [8]. Therefore, AE waves propagating in a cylinder can be regarded as cylindrical waves. Cylindrical waves can be classified into three types: longitudinal mode (L-mode), flexural mode (F-mode), and torsional mode (T-mode) [8]. Figure 1 shows the L and F modes, which are most strongly detected by an AE sensor. Although, L-mode is an axially symmetric mode in which the out-of-plane displacement is the same in the circumferential direction, F-mode is a non-axially symmetric mode in which the out-of-plane displacement is different in the circumferential direction. Additionally, cylindrical waves can be treated as Lamb waves, when the outer diameter of the pipe is longer than 8 times the thickness [9]. In this study, the theoretical velocity dispersion curves were calculated by considering the steel pipes used as steel plates of the same wall thickness. Figure 1 shows the group velocity dispersion of the L-mode and F-mode of cylindrical waves propagating in a steel pipe which outer diameter is 110 mm and thickness 7 mm.

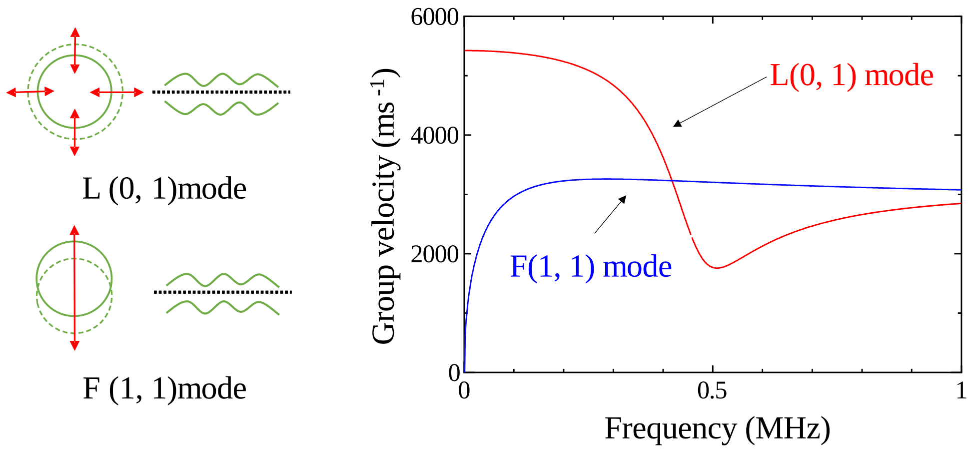

Figure 1. Guided wave in Cylinder (left) and Group velocity curves of cylindrical waves (right).

2.2. Experimental setup

At first, AE monitoring was performed for actual corrosion, and mode intensity ratio were evaluated manually. Figure 2 shows the experimental setup. Nine steel pipes with different holes of corrosion defect were installed and the accelerated-corrosion tests were performed. The wall thickness of the steel pipe was 3.8 mm. Holes simulating corrosion defect depth at 0%, 5%, 10%, 15%, 25%, 35%, 50%, 60%, 75% of the wall thickness were made using an end mill. Then, the holes were periodically sprayed with 5% NaCl solution to progress corrosion. The corrosion period was approximately one month. An AE sensor (PAC, R15α) having the resonance frequency of 150kHz was installed at 300 mm from each hole to detect AE signal. To generate AE signals in short term, the specimens after corrosion tests were thermally cycled by irradiating infrared lamps. Thermal cycling test was performed using a voltage regulator controlled by thermocouples and the heating temperature by infrared lamps was kept constant. The thermal cycle consisted of heating for 30 minutes and cooling for 60 minutes to generate rust expansion and compression. The temperature displacement was recorded by a data logger (Pico Technology, TC-08) using thermocouples.

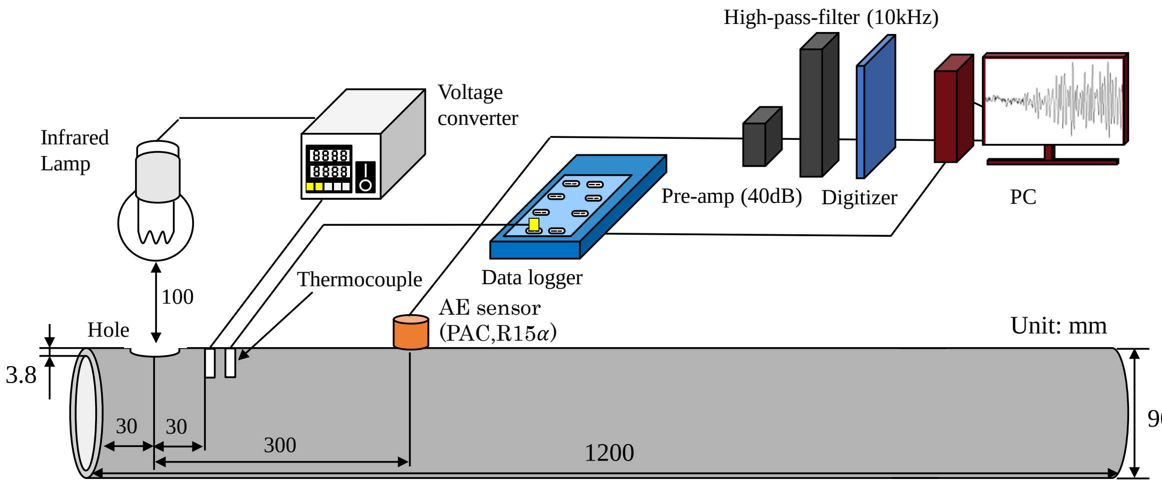

Figure 2. Experimental setup for AE monitoring in accelerated corrosion and thermal cycle test.

2.3. Accelerated corrosion test by thermal cycling test

Figure 3 depicts typical AE waveforms generated at each hole and the time-dependent change of the WT coefficient at 150kHz of the time-frequency analysis results by WT for the obtained waveform. The red circle in the waveform denotes the arrival waveform of the packet of L(0, 1) mode of the cylindrical wave and the blue circle denotes the arrival waveform of the packet of F(1, 1) mode. The theoretical arrival times of L(0, 1) and F(1, 1) modes are depicted by red and blue lines. Here, the wavelet coefficient takes the value of the peak of the wave that intersects the theoretical arrival time of each mode. Figure 4 shows box plots of the data for wavelet coefficient ratio for the different corrosion defect depth. The black dots in the figure represent outliers beyond the interquartile range. The result showed that the wavelet coefficient ratio increases quadratically as the depth of the AE source from the outer surface of the steel pipe approaches the center of the pipe’s thickness. Therefore, it is possible to estimate the amount of corrosion defect depth of the steel pipe by comparing wavelet coefficient of each cylindrical wave mode of the AE waves; however, wavelet coefficient of each corrosion defect depth has a large variation, and it is difficult to identify the correct defect depth by visual. In addition, there are various depths of corrosion defect in real environments, and it is necessary to acquire a large amount of data to find the accurate defect depth. Therefore, machine learning should be used to accurately evaluate the corrosion defect depth.

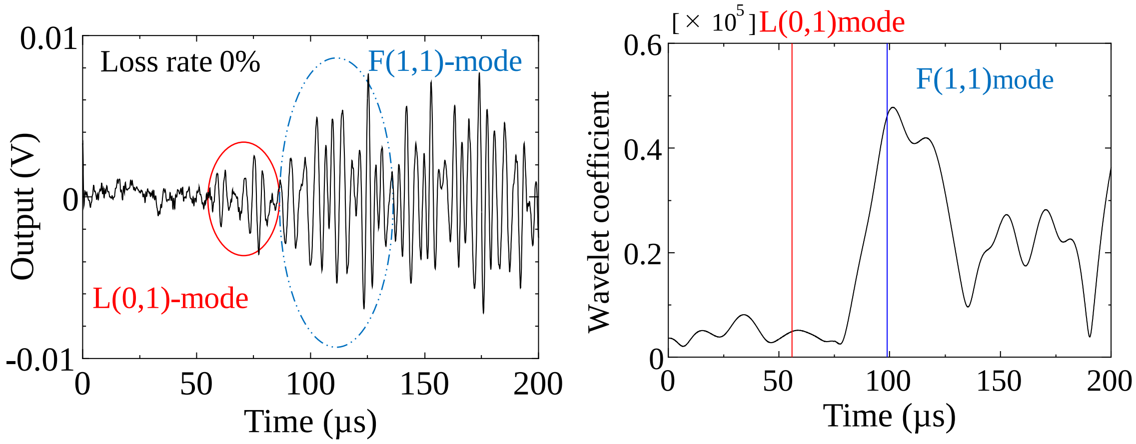

Figure 3. AE waveforms (left) and the wavelet coefficient at 150 kHz (right).

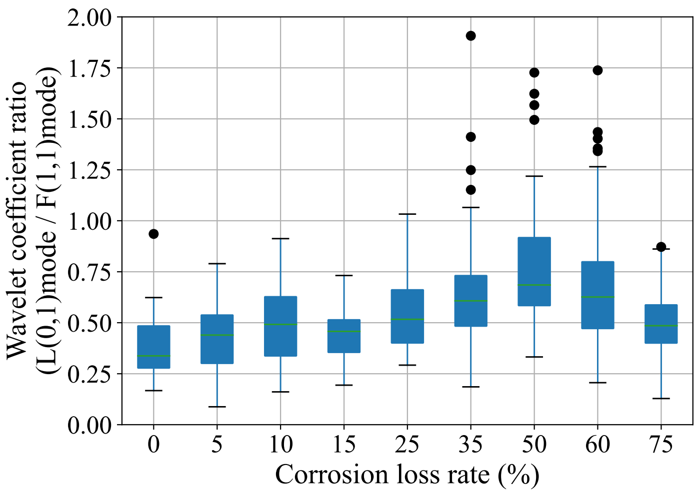

Figure 4. Relationship between the wavelet coefficient ratio and corrosion loss rate from steel pipe.

3. Machine learning algorithm for evaluating corrosion defect depth

3.1 Machine learning algorithm

AE monitoring results can be used for training the machine learning model to classify corrosion defect depth automatically. In this study, multiple logistic regression analysis was used to classify defect depth. This machine learning model establishes a linear relationship between input and output by minimizing error using training data set. We used this model because, the model reduces the risk of overtraining due to the relatively low complexity compared to other models. Table 1 shows the cumulative AE events obtained from each steel pipe. It showed a variation in the number of AE generated from each steel pipe. Therefore, it will cause a problem that the unbalanced classes are biased toward the majority class, and it can contribute significantly to lower accuracy. To solve this problem, Synthetic Minority Over-Sampling Technique (SMOTE) was applied to increase the data for each corrosion defect depth and create balanced datasets [10]. This oversampling algorithm is a method of creating new points by interpolation from points in the neighborhood of minority data.

Table 1. Cumulative AE events of each steel pipe.

Hole depth (mm)	Corrosion loss rate (%)	Cumulative AE events
0	0	20
0.19	5	79
0.38	10	30
0.57	15	38
0.95	25	180
1.33	35	101
1.9	50	71
2.28	60	151
2.85	75	158

3.2 Feature extraction and learning process

As per the method shown in Section 2.3, wavelet coefficients of L(0, 1) and F(1, 1) modes at the resonance frequency of 150 kHz for the cylindrical waves were extracted from AE waveforms. At first, we attempted to classify 8 pipes; however, the accuracy was very low. Therefore, we used two datasets and aimed to classify them in two ways. Table 2 provides the detail of the first dataset. This dataset was created for the purpose of classifying steel pipes using three steel pipes, the corrosion loss rate of 0%, 25%, and 50% were used. In the table, original data indicates the number of AE events detected by AE monitoring, and oversampled data indicates the number of data oversampled using SMOTE. Next, we attempted to classify the corrosion defect depth into 3 groups. Table 3 shows the dataset after dividing into 3 groups. Group 1 is a relatively small damage group with corrosion loss rate of 0%~10%, group 2 is a group with progressive damage with corrosion loss rate of 15%~35%, group 3 is a highly damaged group with corrosion loss rate of 40%~50%. After oversampling the data using SMOTE, both datasets are divided into two parts, training data and testing data with 70:30 ratios. In this study, the machine learning results were evaluated using typical evaluation methods such as confusion matrix, accuracy, precision, recall, F1-score.

Table 2. Details of datasets for 3 pipes classification.

Corrosion loss rate (%)	Original data	Oversampled data	All data
0	20	160	180
25	180	0	180
50	71	109	180

Table 3. Details of datasets for 3 groups classification.

Corrosion loss rate (%)	Original data	Oversampled data	All data
Group1 : 0, 5, 10	129	190	319
Group2 : 15, 25, 35	319	0	319
Group3 : 40, 50	222	97	319

4. Results and discussions

Table 4 shows the confusion matrix that was used for representing the result for 3pipes classification. It also shows the average value of wavelet coefficient ratio of collect data for each label. In this matrix, the horizontal scale showed the predicted result, and the vertical scale displayed the true result of each data. As indicated by the yellow boxes, the number of cases where prediction label and true label match is the highest for each steel pipe, indicating that the prediction model recognizes the difference in corrosion loss rate. Additionally, the average value of wavelet coefficient ratio of collect data increased significantly as the depth of the AE source from the outer surface of the steel pipe approaches the center of the pipe's wall thickness. It indicates that the wavelet coefficient of L(0, 1) and F(1, 1) modes used as the feature of machine learning behave theoretically. Table 5 shows the machine learning results obtained for 3 pipes classification. The accuracy for classifying 3 pipes was 70.1%, which means that most data were discriminated into the correct classification. Additionally, in the other three evaluation method, most values exceeded 0.7, which indicates that this prediction model perform relatively well. However, the result with a corrosion loss rate 25% has low accuracy compared to other steel pipe and the result is scattered to 0% and 50%. This is because the wavelet coefficient of L(0, 1) and F(1, 1) modes are highly variable, and the features extracted from the 25% steel pipe is likely to be misidentified by both the 0% and 50%.

Table 4. Confusion matrix and wavelet coefficient ratio of each steel pipe.

		Prediction label (%)			Average Wavelet coefficient ratio of collect data
		0	25	50	
True label (%)	0	50	2	2	0.34
	25	17	26	11	0.49
	50	8	8	38	0.85

Table 5. Result for 3 pipes classification.

Corrosion loss rate (%)	Accuracy (%)	Recall	Precision	F1 Score
0		0.93	0.67	0.78
25	70.1	0.48	0.72	0.58
50		0.7	0.75	0.72

Table 6 shows the confusion matrix that was used for representing the result for 3groups classification and the average value of wavelet coefficient ratio of collect data for each group. As indicated by the yellow boxes, the number of cases where prediction label and true label match is the highest for each steel pipe, indicating that the prediction model recognizes the difference in corrosion loss rate. Additionally, the average value of wavelet coefficient ratio of collect data increased significantly as theoretically. Table 7 shows the machine learning results obtained for 3 groups classification. The accuracy for classifying 3 groups was 54.1%, which means that the accuracy is low, and it can not be said that the classification model is not practical. The other three evaluation method did not exceeded 0.7, and it indicated that the prediction model's performance is not well.

Table 6. Confusion matrix and wavelet coefficient ratio of each steel pipe.

		Prediction label (%)			Average Wavelet coefficient ratio of collect data
		1	2	3	
True label (%)	1	55	31	10	0.29
	2	28	44	24	0.52
	3	20	19	57	0.87

Table 7. Result for 3 groups classification.

Corrosion loss rate (%)	Accuracy (%)	Recall	Precision	F1 Score
Group1 : 0, 5, 10		0.57	0.53	0.55
Group2 : 15, 25, 35	54.1	0.46	0.47	0.46
Group3 : 40, 50		0.59	0.63	0.61

To summarize the results of the two classifications, the classification of three steel pipes was able to classify with a certain degree of accuracy: however, the classification of the three groups of damage resulted in low accuracy. This difference is because this dataset has a data in which the difference in corrosion loss rate between classes is smaller than the difference in corrosion loss rate in each group. Although, there is a variation in the value of wavelet coefficient of L(0, 1) and F(1, 1) modes in each steel pipe shown in Figure 4, it can be attributed to the fact that the actual AE source and the corrosion defect depth do not always coincide as shown. Figure 5 shows the case which the actual AE source and the corrosion defect depth do not match. Therefore, it can be assumed that such AE has resulted in lower accuracy of the training data and reduced the accuracy of machine learning. In order to improve this problem, training data could be generated using simulated waveforms. In addition, it is important to have a large number of test data to improve the reliability of machine learning and to detect AEs in highly damaged condition. Based on the above results, the effectiveness of using machine learning to evaluate corrosion defect depth has shown; however, to improve the accuracy, the training method of machine learning model and the waveforms used for the training data should be considered in the future research. In addition, it is also showed the effectiveness of using the relationship between corrosion defect depth and change in AE propagation mode as feature of machine learning.

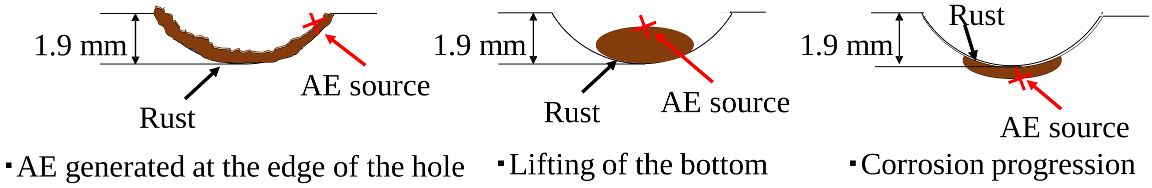

Figure 5. Examples of AE generation locations which cause errors in classification results.

5. Conclusion

In this study, we proposed a method to automatically classify AE waveforms with different corrosion defect depth by machine learning. It was shown that the wavelet coefficient of the L (0, 1)-mode and F (1, 1)-mode, which are the fundamental modes of cylindrical waves, is effective as a feature of machine learning. The results showed that AE waveforms could be classified with high accuracy when the difference in corrosion loss rate was 25%. Furthermore, even using a small dataset obtained from a short-time measurement, the possibility of evaluating the differences in AE waveforms with different corrosion defect depth was also shown.

6. References

[1] Gery W., Denny S., Prabhat K., Braian L Strite, & David R. (2000). *Nucl. Eng. Des,* **195** 149.

[2] Susan S., & Edwin T. (2022). *Abdulkadir Hussein.Materials,* **15** 4.

[3] Raman S, Baldev R, U. Kamachi MudaliPrabhakar S. (2019). *Non-Destructive Evaluation of Corrosion and Corrosion-assisted Cracking*. WILEY.

[4] Cho H., & Takemoto M. (2007). *J.Acoust. Emiss,* **25** 321.

[5] Li Z,Yuyama S,Yamada M,Sekine K,Kitsukawa S,Maruyama H,Konno S. (2005). Investigation on AE Signal/Noise Processing in Corrosion Damage Evaluation of Tank Bottom. *Journal of Acoustic Emission*. 23, 233-242.

[6] Cho H, Takemoto M. (2007). AE Monitoring of Soil Corrosion of Buried Pipe. *Journal of Acoustic Emission*. 25, 267-275.

[7] Kurihara T., Matsuo T., Kono T., & Numata T. (2019) Development of corrosion depth evaluation method in steel by acoustic emission method. In *The 10th TSME International Conference on Mechanical Engineering* (106-111).

[8] Joseph L R. (2004). Ultrasonic Waves in Solid Media. *Cambridge University Press,* 154-176.

[9] Jian L., & Joseph L R. (2006). IEEE Trans. *Ultrason.Ferr.Freq.Control,* **44** 35.

[10] Nitesh V., Kevin W., Lawrence O., & W. Philip K. (2002). SMOTE: Synthetic Minority Over- sampling Technique. *Journal of Artificial Intelligence Research 16,* 321-357.

AMM0006

Evaluation of the Initiation and Propagation Mechanisms of Corrosion under Coating Films Using Digital Image Correlation and Acoustic Emission Methods

Masaya Nara[1,*] and Takuma Matsuo[1]

[1]School of Science and Technology, Meiji University, 1-1-1 Higashi-mita Tama-ku, Kawasaki-shi, Kanagawa, 214-8571, Japan

* Corresponding Author: ce222055@meiji.ac.jp

Abstract. Steel machinery and structures are typically protected from corrosion by coating, but corrosion can still occur under the coating. Evaluating the initiation and progression of corrosion under the coating through visual inspection is challenging, and corrosion often remains undetected until it has advanced. Therefore, this study aims to evaluate the initiation and progression mechanism of corrosion under the coating using Digital Image Correlation (DIC) and Acoustic Emission (AE) methods, and to develop early detection techniques for corrosion under the coating. Corrosion acceleration tests were conducted using coated steel plate, and the occurrence of corrosion under the coating was assessed using DIC and AE methods. The result revealed that corrosion under the coating generates AE signals due to the self-destruction of rust under the coating during its initiation and progression, accompanied by minor swelling and discoloration in the coating. Subsequently, the surface changes of the coated steel plate due to the progression of corrosion under the coating were evaluated using Scanning Electron Microscopy (SEM) and Energy-Dispersive X-ray Spectroscopy (EDS) analysis. The results revealed that, during the progression of corrosion under the coating, minor damages occur in the coating, allowing internal components of the substrate to seep out, leading to discoloration of the coating. In conclusion, the study showed that corrosion under the coating involves rust self-destruction and coating discoloration during initiation and progression, making AE and DIC methods applicable for early detection of corrosion under the coating.

Keywords: Acoustic Emission, Digital Image Correlation, Atmospheric Corrosion, Corrosion Under Coating.

1. Introduction

Deterioration caused by corrosion is a problem for steel structures such as bridges and plants. Therefore, many structures are coated for corrosion protection. However, corrosion under the coating, which occurs at the interface between the coating and the metal, is a problem. Corrosion under the coating is difficult to detect visually and often cannot be detected until corrosion has developed. Therefore, it is difficult to evaluate the initiation and progression mechanisms of corrosion, and the development of evaluation methods is required. In previous research on corrosion of coated steel plate, Katayama et al. have reported the evaluation of paint degradation using surface potential measurements, allowing the detection of corrosion under the coating and coating deterioration [1]. Additionally, Sakagami has utilized pulse heating infrared thermography to diagnose coating degradation based on temperature distribution on the coating surface, detecting potential blisters not visible through visual inspection [2]. However, these conventional studies have not assessed the phenomena occurring in the early stages of corrosion under the coating development. To facilitate the early detection of corrosion under the coating, it is essential to comprehensively understand and discuss the phenomena occurring in the initial stages of corrosion under the coating. In our previous studies [3][4], it was confirmed that the position and condition of corrosion under the coating can be evaluated by analyzing the surface images of the specimen before and after the change using the digital image correlation (DIC) method [5], because the apparent in-plane displacement of the coating appears due to the generation of corrosion products under the coating. Additionally, we verified that the Acoustic Emission (AE) method [6] can be used to detect AE waves associated with the progression of corrosion on coated steel plate. We found that AE waves resulting from rust cracking are of high frequency (around 150kHz), while AE waves from coating damage are of low frequency (around 40kHz) when conventional AE sensor with resonant frequency of 150 kHz was used. In this study, DIC and AE methods are used to evaluate the initiation and progression mechanisms of corrosion under the coating, and their suitability as early detection methods for corrosion under the coatings is studied.

2. Evaluation of the Initiation and Propagation of Corrosion under the Coating Using DIC and AE

2.1. Detection of Corrosion under the coating using DIC and AE Methods

To evaluate the mechanism of corrosion under the coating, accelerated corrosion tests were conducted on coated steel plate and corrosion progress was monitored using the DIC and AE methods. Figure 1 shows the experimental setup used in this study. The test specimens are carbon steel (JIS S45C, 150W x 60L x 2T). The specimens were surface polished with #120, #400, #600, and #800 grit abrasive paper and coated with white acrylic spray. A random pattern was also applied with black acrylic spray for DIC analysis. AE sensors (PAC, R15α, resonance frequency 150 kHz) were placed at the four corners of the specimens to monitor AE during the corrosion test; AE signals were amplified by a preamplifier by 40 dB and then A/D converted by a digitizer. After capturing the microscopic surface image of the test specimen, which served as the reference image for DIC, using an Olympus SZX9 stereoscopic light microscope with a CCD Camera, daily accelerated corrosion tests were conducted by dripping a 5% NaCl aqueous solution (≒40 μL) onto the specimen. The deposited salts were then removed with purified water, and surface images were taken daily under a microscope to measure the surface deformation of the coating due to DIC. Here, images were captured with a camera at a distance of 76 mm from the test specimen, covering an area of approximately 25 mm x 21.5 mm. The DIC analysis conditions were set to use a reference image taken under a microscope prior to the accelerated corrosion test (5320 x 4600 pixels), and subsequently, daily captured surface images were used as comparison images. The analysis was conducted over a measurement range of 5000x4500 (X x Y) pixels, utilizing a subset size of 31x31 pixels and a subset shift of 5 pixels, with bilinear interpolation applied for the analysis. AE was continuously monitored during corrosion tests.

Figure 2 shows enlarged images of the DIC change detection points on the specimen surface taken by a microscope camera on days 3, 5, and 7 after the start of the experiment (Upper) and the results of DIC analysis calculating displacement from the reference image (Lower). The displacement values obtained through DIC analysis are displayed using a color scale. On the day 3 after the experiment began, significant surface displacement was detected in the areas shown in Figure 2, and it was observed to gradually expand over time. Subsequently, on the day 9, corrosion was visually confirmed at the site of this displacement. Therefore, it is believed that the surface displacement detected by DIC analysis indicated corrosion under the coating. However, this displacement is believed to be a result of the growth of rust under the coating, leading to damage to the coating from within, causing rust to seep through and result in discoloration on the surface of the test specimen, rather than being triggered by the swelling of the coating.

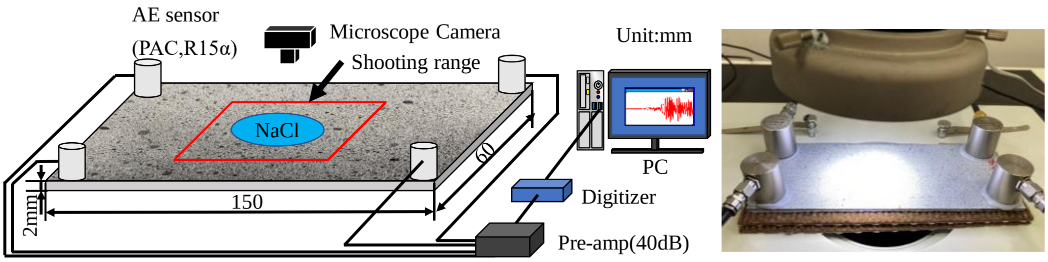

Figure 1. Experimental set up for monitoring corrosion initiation under the coating by using DIC and AE methods.

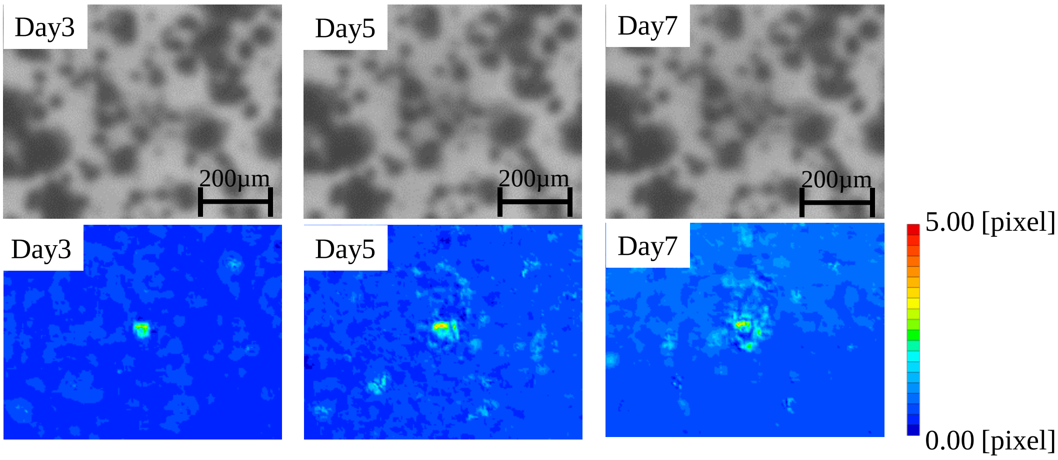

Figure 2. Images of corrosion progression on the test specimen's surface, taken with a microscope on days 3, 5, and 7 after the start of the experiment (Upper), and the results of DIC analysis calculating the displacement from reference images for corrosion progression (Lower).

Figure 3 shows a typical AE waveform (left) and its frequency spectrum (right) detected 3 days after the start of the experiment. The vertical axis setting during AE measurements was configured with a maximum amplitude of 200 mV and a threshold of 8 mV. The horizontal axis was set with a sampling interval of 50 ns, a pre-trigger of 2048, and a total of 8192 data points. The AE waveform was measured on the third day from the start of the experiment, aligning with the same day as the detection of coating displacement using DIC. The detected AE exhibits a peak frequency of 158 kHz, while previous research [3] has indicated that AE resulting from rust self-destruction typically has a peak frequency around 150 kHz. Therefore, the AE in Figure 3 is believed to be a result of rust self-destruction. From the above results, it has been determined that during the onset of corrosion under the coating, AE signals are generated through the self-destructive behavior of rust under the coating.

2.2. Characterization of corrosion propagation under the coating

To evaluate the mechanism of corrosion propagation under the coating, changes in the surface of the coating were observed using a scanning electron microscope (SEM, JEOL JCM-7000 NeoScopeTM). Experiments were conducted under the same conditions as in 2.1. The same locations were observed by SEM while observing the surface deformation with DIC, and component analysis of the photographed locations was performed using EDS. Figure 4 shows the images taken by microscope on day 11, 21, and 31 after the start of the experiment, and the DIC measurements of the surface deformation of the coating

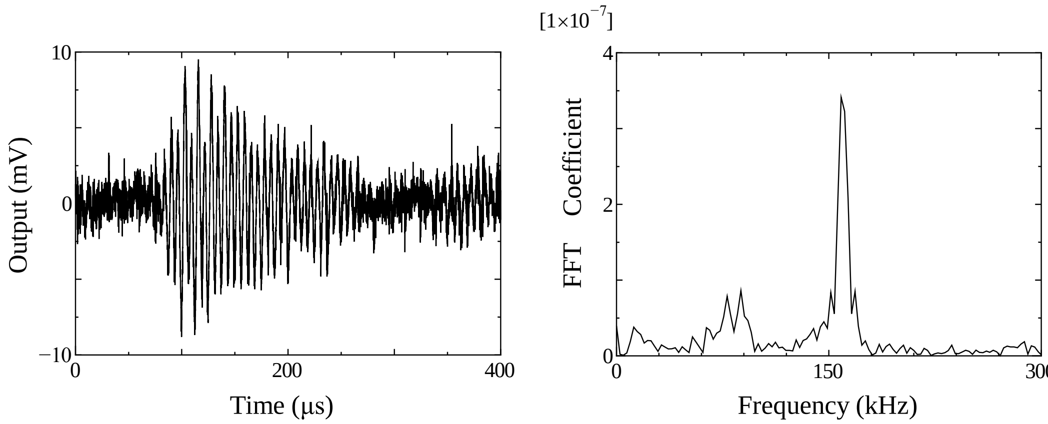

Figure 3. An example of AE waveform (left) and its frequency spectrum (right) detected during the test.

on the same days. Figure 5 is an SEM image of the same location as Figure 4. In this experiment, surface changes due to DIC were first detected on day 11, while surface cracks were detected by SEM on day 21. It is believed that surface changes occurred before cracks were detected by SEM because cracks of smaller size than the SEM's observation range had formed prior to the day 21, and corrosion occurred as NaCl solution was absorbed into the corrosion layer beneath the coating.

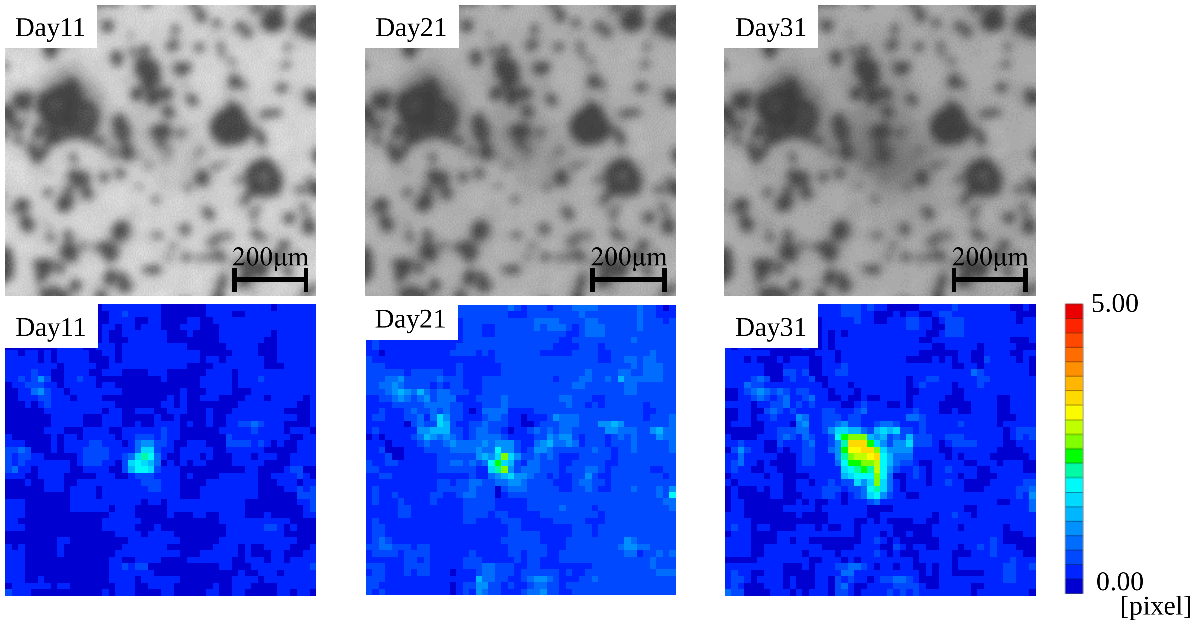

Figure 4. Micrographs of the specimen surface at 11,21 and 31 days after the start of the experiment (Upper) and the results of deformation measurement by the DIC methods (Lower).

Figure 6 shows the change over time of the results of component analysis by EDS. Since carbon was present in the black portion of the coating, it is considered to have gradually decreased with the discoloration of the coating due to the seepage of the internal components. On the other hand, iron oxide and silicon dioxide increased with the occurrence of cracks. This is considered to be due to the exposure of the internal steel portions by the opening of the cracks. Moreover, the increase in titanium dioxide is believed to be due to the oxidation of Ti present in the white portion of the coating. Based on the above, it is presumed that during the process of corrosion under the coating, microscopic damage occurs in the

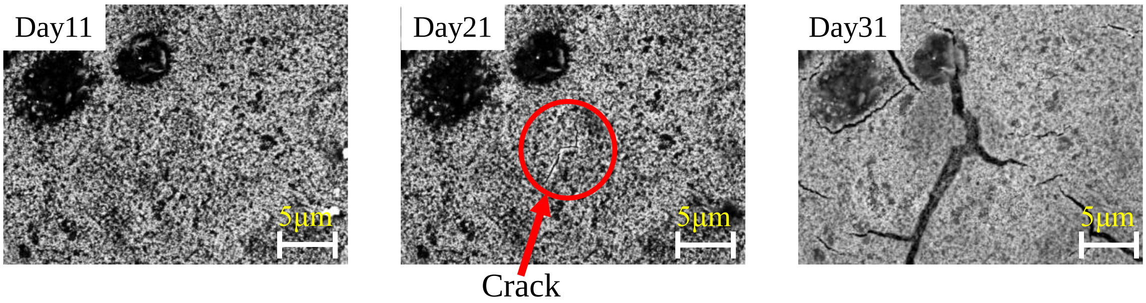

Figure 5. Change in surface crack propagation process using SEM at 11, 21 and 31 days.

coating, from which internal components of the substrate seep out, causing the discoloration of the coating. It is also estimated that moisture enters the steel section through the cracks and corrosion propagates.

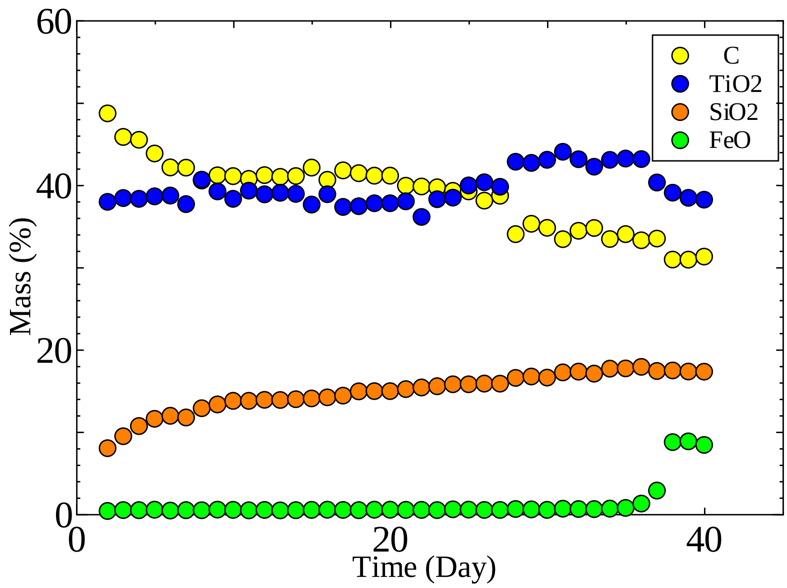

Figure 6. Change in the results of EDS analysis of specimen surfaces.

These results demonstrate the usefulness of the present method as an early detection method for corrosion under the coating layer of actual steel structures. While there are still challenges to be addressed when conducting measurements in real environmental conditions, the long-term vision involves the installation of AE sensors on actual structures such as bridges, enabling the immediate detection of corrosion under the coating using the AE method. Additionally, the use of drones or robots equipped with cameras to capture photos of different sections of the inspected object and subsequently stitching together the DIC analysis results would eventually make it possible to inspect the entire object using the DIC method.

3. Conclusion

In this study, corrosion acceleration tests were conducted on coated steel plate to evaluate the occurrence and progression mechanism of corrosion under the coating. After investigating how corrosion develops under the coating using the AE and DIC methods, the surface changes of the specimens were observed from a more microscopic point of view using SEM and EDS analysis to see what phenomena were actually occurring. The results revealed that during the initiation and progression of corrosion under the coating, AE signals were generated due to coating damage and self-destruction of rust, leading to subtle discoloration of the coating. Additionally, through SEM observations and EDS analysis, it was determined that fine coating damage occurred during the advancement of corrosion under the coating, allowing internal substrate components to seep out and causing discoloration of the coating. Based on the above, it has been demonstrated that corrosion under the coating involves rust self-destruction and coating discoloration during its initiation and progression, thereby illustrating the applicability of AE and DIC methods as early detection techniques for corrosion under the coating.

4. Acknowledgements

The microscope images used in this study were obtained from a sensor kit loaned by Sony Semiconductor Solutions Corporation.

5. References

[1] H.Katayama, K.Seki, I.Shitanda, M.Itagaki, H.Masuda, “Non-destructive Evaluation of Deteriorated Organic Coated Steels Using Surface Potential Measurement”, J. Jpn. Soc. Colour Mater., 85[6],235-239 (2012)
[2] T.Sakagami, Journal of the Japan Society of Marine Engineering, Vol. 41, No. 5, (2006), pp. 34 - 41
[3] T. Kagami et al, 2017 Proc. Int. Conf. on Mechanical Engineering (Bangkok) vol 8 (Thailand: The 10th TSME International Conference on Mechanical Engineers) p 78
[4] Y. Miyazaki, T.Matsuo, JSCE Materials and Environments, 68, pp.53-56 (2021).
[5] Bing Pan, Kai Li, “A fast digital image correlation method for deformation measurement”, Optics and Lasers in Engineering 49 (2011), pp 841 – 847
[6] Yoshihiro Mizutani: “Practical Acoustic Emission Testing”, The Japanese Society for Non-Destructive Inspection, Springer Japan, Tokyo, (2016).

AMM0008

Sintered steels with improved ductility produced from diffusion-alloyed powders

A Z Myo[1,*], M Srilomsak[1], M Morakotjinda[2], T Yotkaew[2], N Tosangthum[2], P Wila[2], R Tongsri[2], and K Inaba[3]

[1]School of Engineering, King Mongkut's Institute of Technology Ladkrabang, Chalongkrung Road, Ladkrabang, Bangkok 10520, Thailand
[2]Particulate Materials Processing Technology (PMPT), National Metal and Materials Technology Center, 114 Paholyothin Road, Khlong Nueng, Khlong Luang, Pathumthani 12120, Thailand
[3]Department of Transdisciplinary Science and Engineering, Tokyo Institute of Technology, 2-12-1-I6-5 Ookayama, Meguro-ku, Tokyo, 152-8550, Japan

* Corresponding Author: ruangdt@mtec.or.th

Abstract. Conventional sintered steels have low ductility due to the presence of porosity, inherited from voids at powder particle corners in a green compact. The porosity level can be reduced by using novel processing methods, such as warm compaction, high velocity compaction, and double compaction and double sintering. However, the application of these processes can lead to higher cost of production. A new concept for producing a sintered steel with high strength and improved ductility is proposed to be based on sintered steel matrix modification and porosity reduction. In this work, the addition of 4.0 wt% silicon carbide, instead of graphite, to different diffusion bonded powders, such as Distaloy SA (with composition of Fe-0.50Mo- 1.50Cu-1.75Ni), Distaloy AE (with composition of Fe-0.50Mo-1.50Cu-4.00Ni), Distaloy DH (with composition of Fe-1.47Mo-2.0Cu), and Distaloy DC1 (with composition of 1.50Mo-2.0Ni), led the formation of pore filling particles, known as black particles, and the formation of ausferrite in sintered steel matrix. The pore filling and the presence of ausferrite matrix led to promising tensile strengths with low yield ratios and elongation values of over 5.0 %.

Keywords: Sintering, silicon carbide, austempered ductile iron microstructure, ausferrite, and tensile properties.

1. Introduction

A conventional 'press and sinter process' has been being widely applied for fabricating automotive parts because its productivity is considered as economy-scale and sintered parts require minimal or without machining [1, 2]. However, conventional sintered steels have low ductility due to the presence of porosity, inherited from voids at powder particle corners in a green compact. The porosity level can be reduced by using novel processing methods, such as warm compaction [3], high velocity compaction [4], double compaction and double sintering [5], high isostatic pressing [6]. However, the applications of these processes can lead to higher cost of production.

The recent discovery of a new approach by tailoring sintered steel chemistry sheds light on enhancement of both strength and ductility of sintered steels. In previous works, it was reported that silicon carbide (SiC) additions with contents of 4.0 to 5.0 wt% to iron (Fe) or Fe-based powders could lead to the formation of ductile iron-like microstructure, whose feature comprised a black particle embedded in ferrite-pearlite matrix [7, 8]. The change of base powder chemistry by increasing molybdenum (Mo) content in Fe-Mo powders led to the formation of novel ductile iron-like microstructure, whose feature comprised a black particle embedded in ferrite, pearlite, and ausferrite matrix [9]. The modification of sintered alloy produced from Fe-0.85Mo + 4.0 wt% SiC mixture by copper (Cu) powder additions also led to the formation of novel austempered ductile iron microstructure, whose feature comprised a black particle embedded in ferrite-ausferrite matrix [10]. When varied alloying nickel (Ni) element contents were employed, novel austempered ductile iron microstructure, whose feature comprised a black particle embedded in ferrite, ausferrite, and martensite matrix was obtained [11]. The results given above provide the assumptions that the use of judicious SiC powder content instead of graphite can lead to the formation of ductile iron family microstructure and the combination of alloying Mo, Cu, Ni, Si and C elements can lead to the formation of as-sintered austempered ductile iron microstructure. To prove such hypothesis, different diffusion bonded powders with compositions given in Table 1 were used in this work.

Table 1. Compositions of Distaloy powders used for this work.

Metal powder	Compositions (wt%)			
	Mo	Cu	Ni	Fe
Distaloy DH	1.47	2.00	-	Balance
Distaloy DC1	1.50	-	2.00	Balance
Distaloy SA	0.50	1.50	1.75	Balance
Distaloy AE	0.50	1.50	4.00	Balance

2. Experimental procedure

The base metal powders employed in this work are given in Table 1. The names of sintered steels were the same as the names of base metal powders. The base metal powders were admixed with 4.0 wt% SiC powder. The powder mixtures were added with 1 wt.% zinc stearate as a lubricant. The powder mixtures were compacted into green tensile test bars with green density of 6.5 g/cm^3. The green tensile test bars were sintered at 1250 ºC for 45 minutes in a vacuum furnace, Schmetz of Germany, at pressure of $1.28x10^{-5}$ MPa. After sintering, specimens were slowly cooled at the cooling rate of 0.1 °C/s. Specimens for optical microscopy (OM) were prepared according to a standard procedure, including cutting, mounting, grinding (180 to 1200 grit silicon carbide papers), polishing (6, 3, and 1 μm diamond pastes), and etching. The etchants employed in this work was 2 % Nital in ethanol. To understand the effect of alloying elements on microstructural development, the chemical distribution was determined by using electron probe microanalyzer (EPMA) machine (Shimadzu EPMA8050G). Phase identification was carried out by using the X-ray diffraction (XRD) technique. The polished specimens were employed for XRD characterization. XRD was performed by using Rigaku TTRAX III X-ray diffractometer with copper source (wavelength of 1.54 Å) and conditions including step size of 0.2°, time 0.5 s/step and angle of 30-100°. Macrohardness test was carried out on un-etched specimens using 100 kgf load (HRB) with 15 indentations per a specimen. Tensile property of the sintered materials was carried out at room temperature using Instron Universal Instrument.

3. Results and Discussion

3.1. Characterization of experimental sintered steels

The microstructural feature of sintered Distaloy DH (Figure 1a) and Distaloy DC1 (Figure 1c) steels comprised a black particle embedded in the matrix consisting of ferrite halo, ausferrite and pearlite. The XRD patterns of sintered Distaloy DH (Figure 1b) and Distaloy DC1 (Figure 1d) steels showed strong peaks of face-centered cubic (fcc) crystal structure of γ-austenite, moderate peaks of body-centered cubic (bcc) crystal structure of α-ferrite, and weak peaks of orthorhombic crystal structure of M_3C carbide. The XRD peaks of γ-austenite and α-ferrite confirm the presence of ausferrite, which comprises bainitic ferrite and austenite plates. The XRD peaks of M_3C carbide confirm the presence of pearlite colonies. The matrices of both sintered Distaloy DH and Distaloy DC1 steels, consisting of ferrite halo, pearlite, and ausferrite, indicate that 3 different phase transformations occurr during slow post sintered cooling. They include stable eutectoid transformation of austenite to ferrite halo, metastable eutectoid transformation of austenite to pearlite and austempering transformation of austenite to ausferrite. The formation of ferrite halo by stable eutectoid transformation and that of pearlite by metastable eutectoid transformation in sintered Fe + 5.0% SiC alloy [7], sintered Fe-0.85Mo + 4.0 wt% SiC alloy [8], and sintered Distaloy DH and Distaloy DC1 steels (this work) can follow the mechanisms given for as-cast ferritic-pearlitic ductile irons [12]. However, the formation of ausferrite, as the major microstructural component of sintered Distaloy DH and Distaloy DC1 steels under slow and continuous cooling is the novel phenomenon. The ausferrite formation is strongly dependent on austenite stability because of two reasons. The first one is that the austinite plate, one component of ausferrite, remains stable at room temperature. The second is that the typical ausferrite in an austempered ductile iron forms under isothermal heat treatment in temperature range between pearlite and martensite transformation temperatures or roughly about 300-450 °C [13]. The austenite stability, as indicated by the presence of ausferrite, is related to the combined effect of alloying Mo, Si and C elements in sintered Fe-Mo-Mn- Si-C composites [9]. The presence of Cu, as an austenite stabilizer, in sintered Distaloy DH steel or that of Ni, as an austenite stabilizer, in sintered Distaloy DC1 steel would enhance the austenite stability. Therefore, the ausferrite becomes the dominant microstructural component of the matrices of both sintered Distaloy DH and Distaloy DC1 steels. The microstructural feature of sintered Distaloy SA steel comprised a black particle embedded in the matrix consisting of ferrite halo and ausferrite (Figure 1e). The XRD pattern of this sintered steel showed strong peaks of γ-austenite and α-ferrite (Figure 1f). The microstructural feature of sintered Distaloy AE steel comprised a black particle embedded in the matrix consisting of bainitic ferrite and martensite plates (Figure 1g). The XRD pattern of this sintered steel showed strong peaks of γ-austenite and α- ferrite (Figure 1h). Since the XRD peaks of α-ferrite and α′ martensite overlap, only peaks of α-ferrite are labelled in Figure 1h.

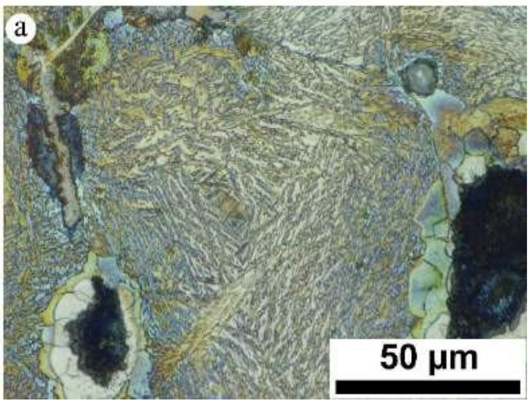

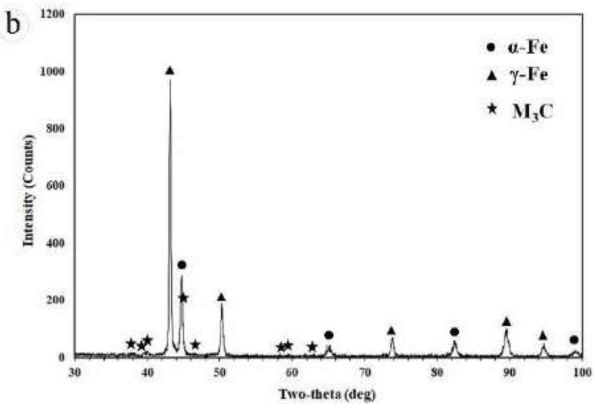

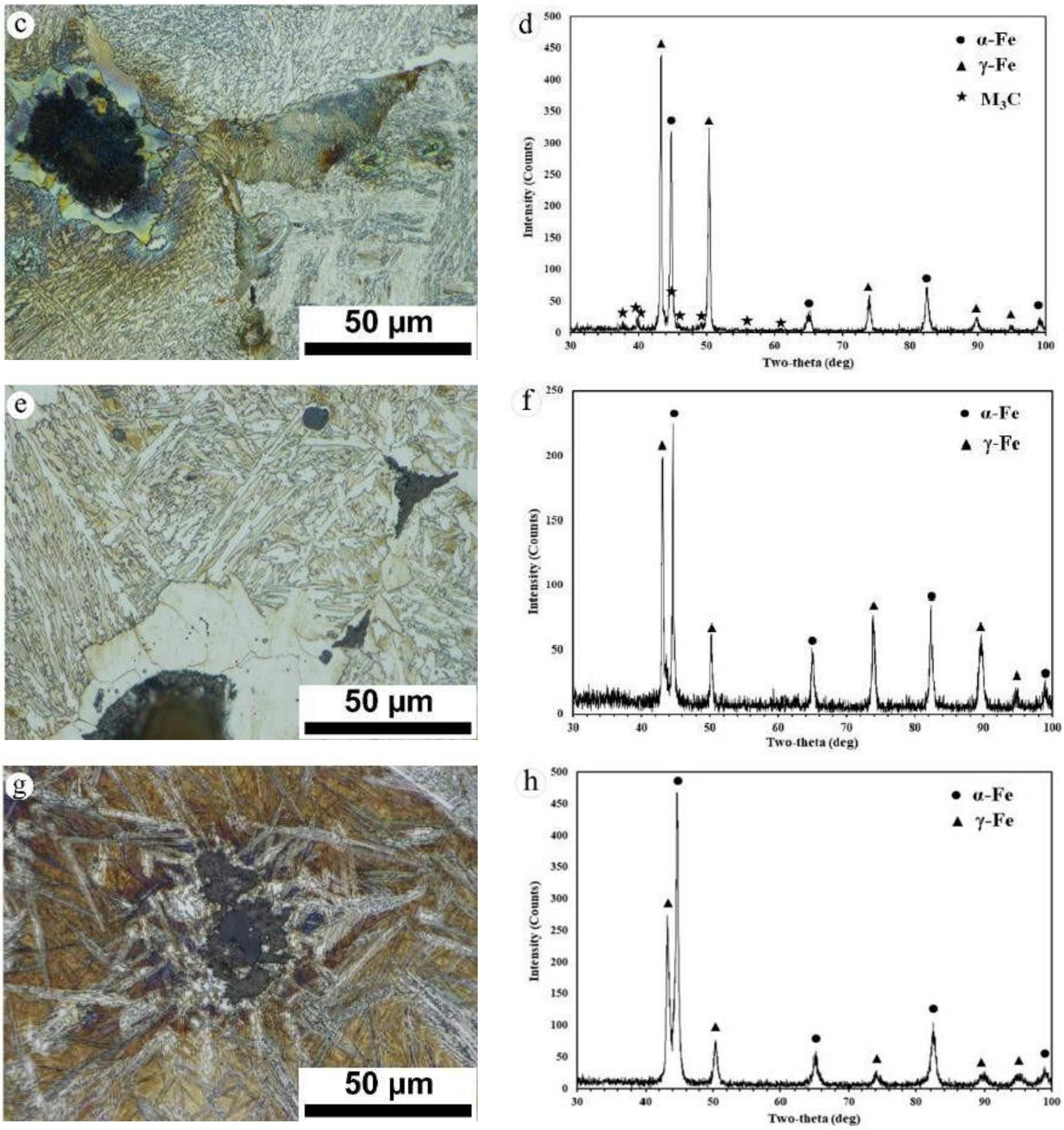

Figure 1. Optical images and XRD patterns of experimental sintered steels; (a, b) Distaloy DH, (c, d) Distaloy DC1, (e, f) Distaloy SA, and (g, h) Distaloy AE.

The microstructure of sintered Distaloy SA steel shows that the combined effect of alloying Mo, Cu, Ni, Si and C elements leads to the total replacement of pearlite by ausferrite. Since the microstructural feature has a black particle embedded in the matrix consisting of ferrite halo and ausferrite, the sintered Distaloy SA steel microstructure can be identified as that of a dual phase austempered ductile iron [14]. The microstructure of sintered Distaloy SA steel consisting of a black particle embedded in the matrix consisting of bainitic ferrite and martensite plates indicates that the stable and metastable eutectoid transformations are totally suppressed. The coexistence of bainitic ferrite and martensite constituents in sintered Distaloy SA steel indicates that its austenite has strong stability due to high Ni content of 4.0 wt%, leading to low temperature bainitic and martensitic phase transformations. When a low-carbon steel is isothermally heat-treated at low temperatures the coexistence of bainitic ferrite and martensite laths is commonly observed [15-17]. When a high-carbon steel is isothermally heat-treated at low temperatures the bainitic ferrite laths distributed in martensite matrix is commonly observed [18, 19]. The matrix microstructure of sintered Distaloy SA steel resembles that of a high-carbon steel isothermally heat-treated at low temperatures.

3.2 Chemical distribution in experimental sintered steels

EPMA elemental distribution maps were determined in an area around pearlite colonies in sintered Distaloy DH steel (Figure 2). It was found that pearlite colonies had high concentrations of C, Mo and Cu but low concentrations of Fe and Si, compared to surrounding ausferrite. All C, Cu, Fe, Mo, and Si elements showed homogeneous distribution in ausferrite regions. In sintered Distaloy DC1 steel (Figure 3), it was found that pearlite colonies had high C concentration and low Fe and Si concentrations, compared to surrounding ausferrite. Alloying Mo and Ni showed considerably homogenous distribution in both pearlite and ausferrite. Due to the elemental distribution maps given above, it can be implied that pearlite formation required low Si concentration. It is commonly known that judicious Si content can suppress carbide precipitation from austenite [20]. The reason for carbide precipitation inhibition by Si is that the precipitation of para- equilibrium carbide from austenite becomes impossible because of a lack of a driving force for precipitation. The carbide can then only form with the partitioning of silicon, which may take an inordinately long time [21]. The precipitation of M_3C carbide lamellae of pearlite colonies in both sintered Distaloy DH and Distaloy DC1 steels is also attributed to high C concentration in austenite, that leads to carbide precipitation because of a large driving force for the reaction even for para-equilibrium precipitation.

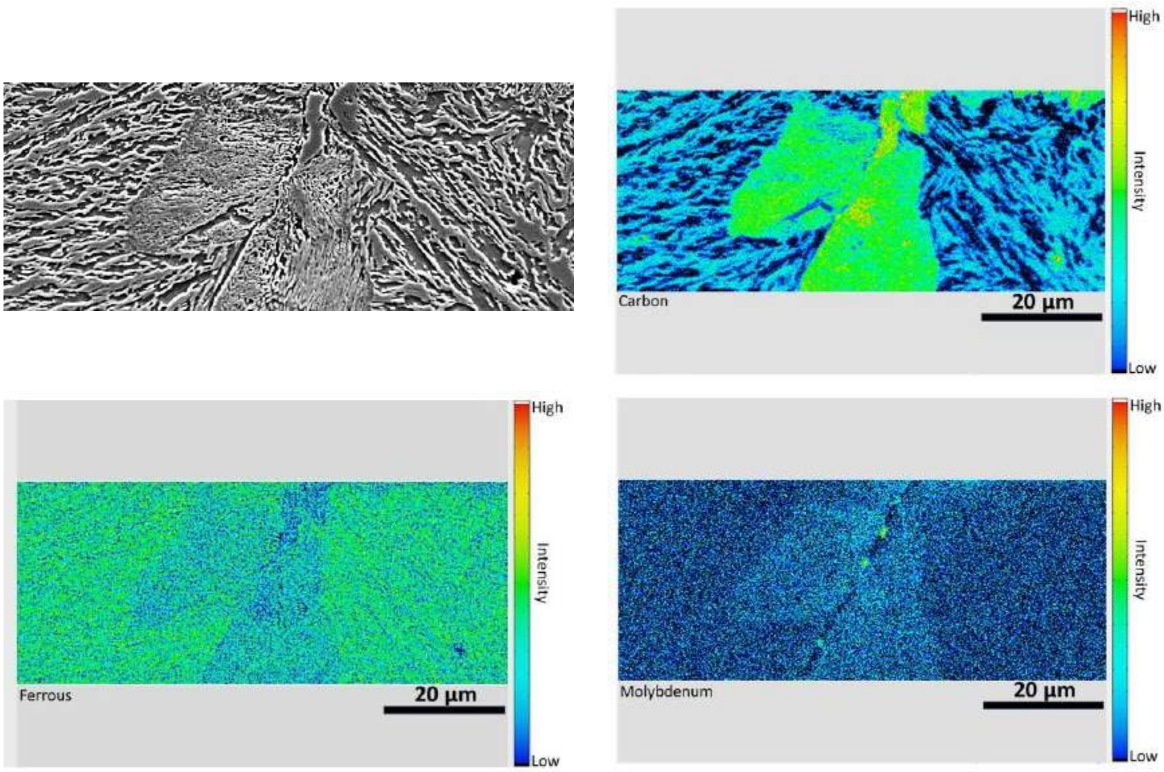

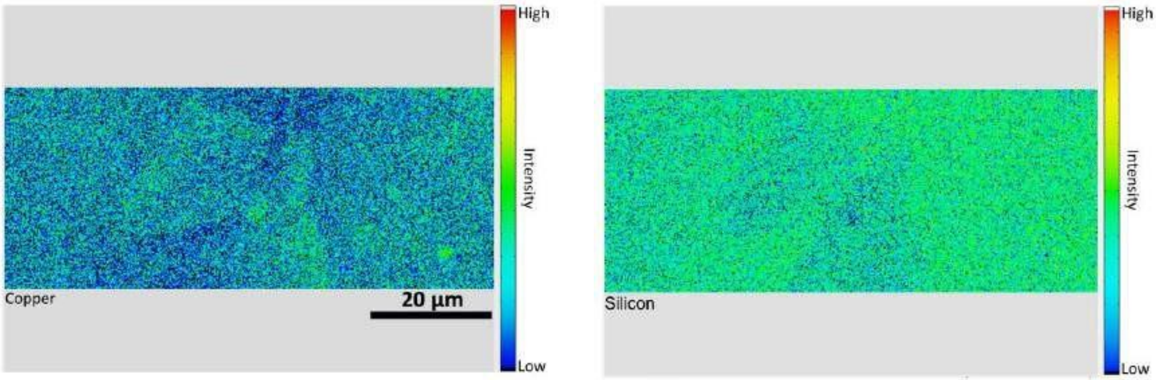

Figure 2. EPMA elemental distribution maps in sintered Distaloy DH steel.

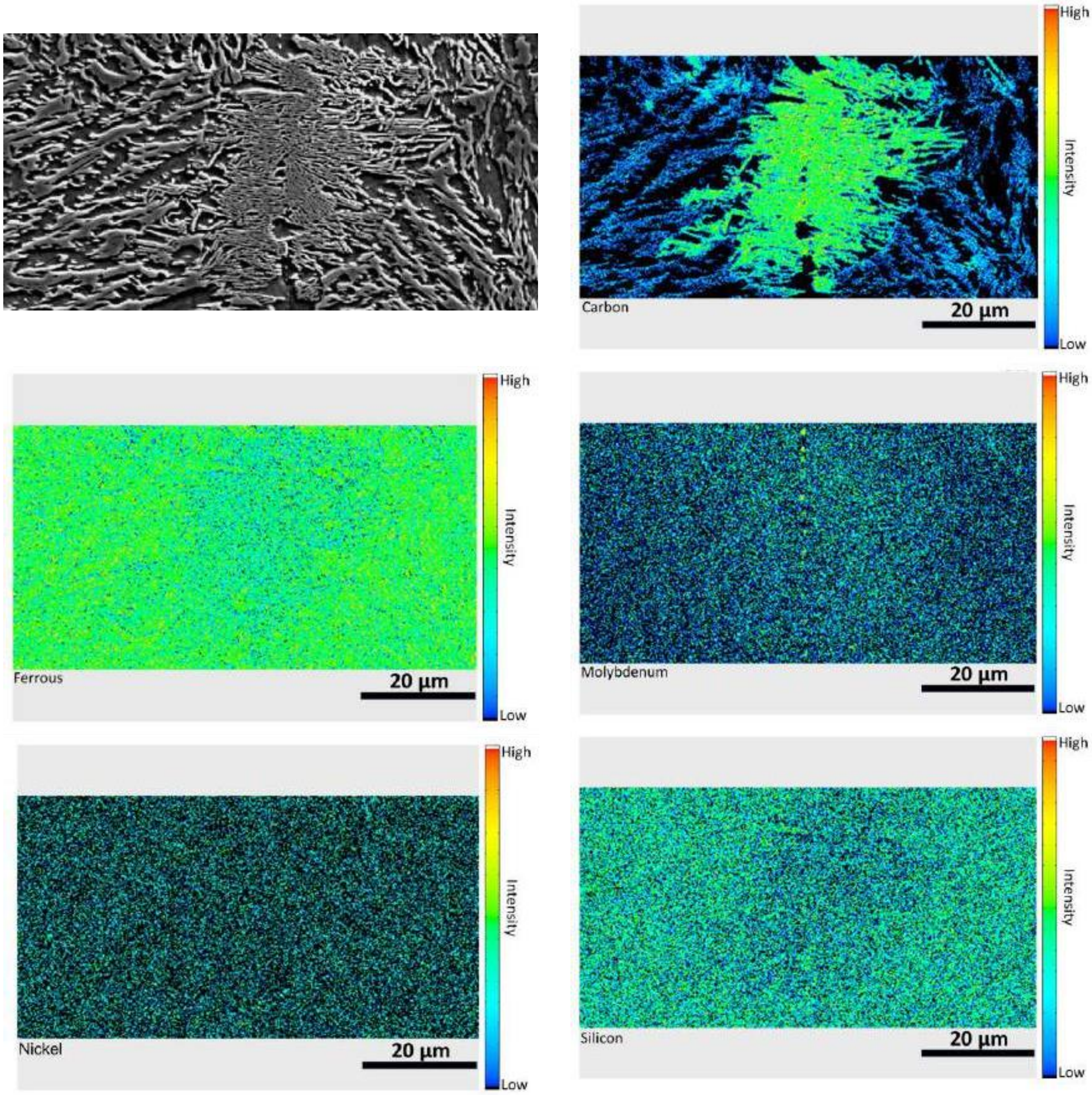

Figure 3. EPMA elemental distribution maps in sintered Distaloy DC1 steel.

3.3 Mechanical property

All experimental sintered steels showed promising mechanical properties, such as ultimate tensile strength (UTS) values of > 700 MPa, yield strength (YS) values of > 250 MPa, elongation values of >5.0 %, and hardness values of > 80 HRB (Figure 4). When tensile strength and elongation are considered, it is found that the increasing order of tensile strength value in experimental sintered steels is that sintered SA < sintered DC1 < sintered DH < sintered AE while the increasing order of elongation value is that sintered DC1 < sintered SA < sintered DH < sintered AE. This indicates that experimental sintered steels have synergy between strength and ductility. In general, a material with high strength suffers low ductility, known strength-ductility trade off dilemma. There are several approaches for evading of strength-ductility trade off dilemma in materials, such as, the dual-phase lamellar microstructure [22], core-shell microstructure [23], nano twinning [24], dual heterogeneous structure [25], heterogeneous structure [26], metastability- engineering strategy [27], and micro-banding and the accumulation of a high density of dislocations in single-phase high-entropy alloys (HEAs) [28]. When the microstructural feature of sintered Distaloy DH, Distaloy DC1, and Distaloy SA steels are considered, the dual-phase lamellar microstructure, alternating bainitic ferrite and austenite plates, seems to be the mechanism for evading of strength- ductility trade off dilemma. However, when compared to the microstructures of the materials having ability to overcome strength- ductility trade off dilemma, as given in references [22-28] the microstructural feature of sintered Distaloy AE steel seems to be the novel microstructural feature showing ability to evade the strength- ductility trade off dilemma.

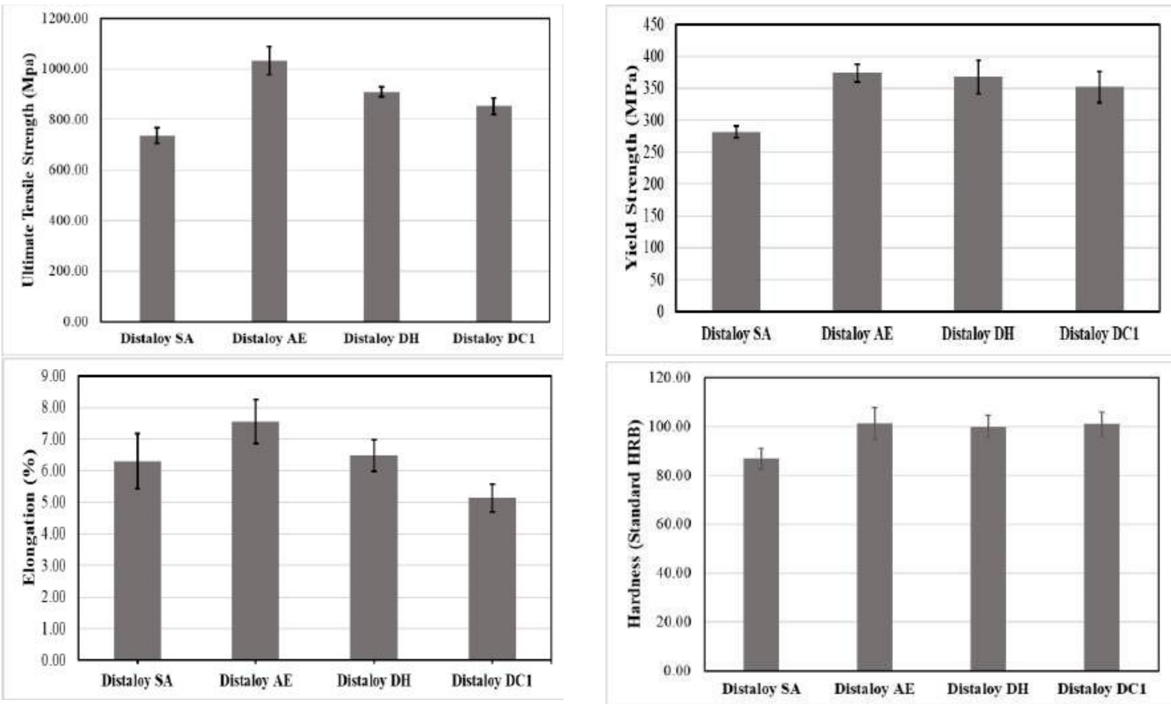

Figure 4. Mechanical properties of experimental sintered steels.

4. Conclusions

The concluding remarks could be drawn from the experimental results as given below.

(1) Slowly cooled sintered steels produced from 4 diffusion bonded powders, such as Distaloy SA (with composition of Fe-0.50Mo-1.50Cu-1.75Ni), Distaloy AE (with composition of Fe-0.50Mo-1.50Cu-4.00Ni), Distaloy DH (with composition of Fe-1.47Mo-2.0Cu), and Distaloy DC1 (with composition of 1.50Mo-2.0Ni) powders, mixed with 4.0 wt % SiC powder had microstructures consisting of black particle, ferrite halo, pearlite, ausferrite and martensite, depending on chemistry

of diffusion bonded powders.

(2) These sintered steels exhibited promising mechanical properties with synergy of strength and ductility.

5. Acknowledgements

The first author (A. Z. Myo) is grateful for financial support from National Science and Technology Development Agency (NSTDA) TAIST scholarships. This work is financially supported via the project 'Design and manufacturing of replacement parts for railway applications (P1951261)' under NSTDA, Pathum Thani, Thailand. Technical supports are obtained from National Metal and Materials Technology Center (MTEC), Pathum Thani, Thailand.

6. References

[1] Fujiki, A. (2001). Present state and future prospects of powder metallurgy parts for automotive applications. *Materials Chemistry and Physics, 67,* 298-306.

[2] Tan, Z. Q., Zhang, Q., Guo, X.Y., Zhao, W.J., Zhou, C. S., Liu, Y. (2020) New development of powder metallurgy in automotive industry. *Journal of Central South University, 27,* 1611-1623.

[3] Rahman, M. M., Ariffin, A. K., Nor S. S. M. (2009). Development of a finite element model of metal powder compaction process at elevated temperature. *Applied Mathematical Modelling, 33,* 4031-4048.

[4] Bai, Y., Li, L., Fu, L., Wang, Q. (2021). A review on high velocity compaction mechanism of powder metallurgy. *Science Progress, 104*(2), 1-20.

[5] Hammes, G., Schroeder, R., Binder, C., Klein, A. N., de Mello, J. D. B. (2014). Effect of double pressing/double sintering on the sliding wear of self-lubricating sintered composites. *Tribology International, 70,* 119-127.

[6] Atkinson, H. V., Davies, S. (2000). Fundamental aspects of hot isostatic pressing: An overview. *Metallurgical and Materials Transactions A, 31*, 2981-3000.

[7] Chakthin, S., Poolthong, N., Tongsri, R. (2008). Effect of reaction between Fe and carbide particles on mechanical properties of Fe-base composite. *Advanced Materials Research, 55-57,* 357-360.

[8] Ruangchai, K., Wiengmoon, A., Morakotjinda, M., Krataitong, R., Tanprayoon, D., Yotkaew, T., Tosangthum, N., Patakham, U., Tongsri, R. (2017). Microstructure, hardness and wear properties of sintered Fe-Mo-Si-C steels with spheroidal graphite iron/compacted graphite iron-like. *Key Engineering Materials, 751*, 47-52.

[9] Nithimethakul, T., Karin, P., Ohtake, N., Wila, P., Yodkaew, T., Vetayanugul, B., Morakotjinda, M., Tongsri, R. (2021). The effect of molybdenum on the microstructure and mechanical behaviour of the sintered Fe-Mo-Mn-Si-C composite. *IOP Conf. Series: Materials Science and Engineering, 1137,* 012028.

[10] Morakotjinda, M., Yotkaew, T., Vetayanugul, B., Wanalerkngam, A., Tongsri, R. (2023). Promotion of ausferrite formation in as-sintered Fe-Mo-Si-C-(Cu) composites due to Cu addition. *Materials Chemistry and Physics, 296*, 127226.

[11] Kaewkam, T., Kansuwan, P., Ohtake, N., Wila, P., Krataithong, R., Tosangthum, N., Yotkaew, T., Tongsri, R. (2021). Sintered Fe-Ni-Si-C alloys. *IOP Conf. Series: Materials Science and Engineering, 1137,* 012035.

[12] Lacaze, J., Sertucha, J., Åberg, L. M. (2016). Microstructure of as-cast ferritic-pearlitic nodular cast irons. *ISIJ International, 56,* 1606-1615.

[13] Kim, Y. J., Shin, H., Park, H., Lim, J. D. (2008). Investigation into mechanical properties of austempered ductile cast iron (ADI) in accordance with austempering temperature. *Materials Letters, 62,* 357-360.

[14] Basso, A., Caldera, M., Massone, J. (2015). Development of high silicon dual phase austempered ductile iron. *ISIJ International, 55,* 1106-1113.

[15] Samanta, S., Biswas, P., Giri, S., Singh, S. B., Kundu, S. (2016). Formation of bainite below the MS temperature: Kinetics and crystallography. *Acta Materialia, 105,* 390-403.

[16] Rampelberg, C., Allain, S. Y. P., Geandier, G., Teixeira, J., Lebel, F., Sourmail, T. (2021). Carbide- free bainite transformations above and below martensite start temperature investigated by in-situ high- energy X-Ray diffraction. *JOM, 73*, 3181-3194.

[17] Łukaszewicz, G., Szczygieł, M., Węsierska-Hinca, M., Chmielarz, K., Wierzbicka, E., Wasiak, K. (2023). Interrupted quenching and bainitising below Ms temperature of EN X37CrMoV5-1 hot-work tool steel: Bainitic transformation kinetics, microstructure and mechanical properties. *Materials Science and Engineering*

A, 869, 144740.
[18] Sajjadi, S. A., Zebarjad, S. M. (2007). Isothermal transformation of austenite to bainite in high carbon steels. *Journal of Materials Processing Technology, 189*, 107-113.
[19] Toji, Y., Matsuda, H., Raabe, D. (2016). Effect of Si on the acceleration of bainite transformation by preexisting martensite. *Acta Materialia, 116*, 250-262.
[20] Caballero, F. G., Santofimia, M. J., Capdevila, C., García-Mateo, C., de Andrés, C. G. (2006). Design of advanced bainitic steels by optimisation of TTT diagrams and T_0 curves. *ISIJ International, 46*, 1479-1488.
[21] E. Kozeschnik, E., Bhadeshia, H.K.D.H. (2008). Influence of silicon on cementite precipitation in steels. *Materials Science and Technology, 24*, 343-347.
[22] Gao, Y. F., Zhang, W., Shi, P. J., Ren, W. L., Zhong, Y. B. (2020). A mechanistic interpretation of the strength-ductility trade-off and synergy in lamellar microstructures. *Materials Today Advances, 8*, 100103.
[23] Srivastava, A. K., Patel, N. K., Kumar, B. R., Sharma, A., Ahn, B. (2020). Strength-ductility trade- off in dual-phase steel tailored via controlled phase transformation. *Journal of Materials Engineering and Performance, 29*, 2783-2791.
[24] Wei, Y., Li, Y., Zhu, L., Liu, Y., Lei, X., Wang, G., Wu, Y., Mi, Z., Liu, J., Wang, H., Gao, H. (2014). Evading the strength-ductility trade-off dilemma in steel through gradient hierarchical nanotwins. *Nature Communications, 5*, 3580.
[25] Du, X. H., Li, W. P., Chang, H. T., Yang, T., Duan, G. S., Wu, B. L., Huang, J.C., Chen, F. R., Liu, C. T., Chuang, W. S., Lu, Y., Sui, M. L., Huang, E.W. (2020). Dual heterogeneous structures lead to ultrahigh strength and uniform ductility in a Co-Cr-Ni medium-entropy alloy. *Nature Communications, 11*, 2390.
[26] Wu, S. W., Wang, G., Wang, Q., Jia, Y. D., Yi, J., Zhai, Q. J., Liu, J. B., Sun, B. A., Chu, H. J., Shen, J., Liaw, P. K., Liu, C. T., Zhang, T.Y. (2019). Enhancement of strength-ductility trade-off in a high-entropy alloy through a heterogeneous structure. *Acta Materialia, 165*, 444-458.
[27] Li, Z., Pradeep, K. G., Deng, Y., Raabe, D., Tasan, C. C. (2016). Metastable high-entropy dual- phase alloys overcome the strength-ductility trade-off. Nature 534 (2016) 227-230.
[28] Guo, W., Su, J., Lu, W., Liebscher, C. H., Kirchlechner, C., Ikeda, Y., Körmann, F., Liu, X., Xue, Y., Dehm, G. (2020). Dislocation-induced breakthrough of strength and ductility trade-offin a non- equiatomic high-entropy alloy. *Acta Materialia, 185*, 45-54.

AMM0009

Comparison of Mechanical Properties between Natural Rubber and Commercial Dairy Cow Hoof Blocks

T Wissamitanan[1], T Namsai[2], A Sawatdiraksa[3], C Supapong[4], and T Petdee[2,*]

[1]Department of Industrial, Rattaphum College, Rajamangala University of Technology Srivijaya, Rattaphum, Songkhla 90180, Thailand.
[2]Department of Mechanical Engineering, Faculty of Engineering, Rajamangala University of Technology Srivijaya, 1 Ratchadamnoennok Rd. Boyang Sub-district Muang District, Songkhla, 90000, Thailand
[3]Department of Applied Agriculture Faculty of Agriculture Rajamangala University of Technology Srivijaya, 109 Moo 2, Tamyai, Thungsong, Nakhon Si Thammarat, 80110, Thailand
[4]Department of Animal Science Faculty of Agriculture Rajamangala University of Technology Srivijaya, 133 Moo 5, Thung Yai Sub-district, Thung Yai District, Nakhon Si Thammarat 80240, Thailand

* Corresponding Author: Theerawat.p@rmutsv.ac.th

Abstract. The objective of this study was to compare the mechanical properties of natural rubber versus three types of commercial dairy cow hoof blocks, including wood, commercial rubber, and ethylene vinyl acetate (EVA). The mechanical properties were tested to evaluate compressive strength, compression set, coefficient of friction, water absorption, and energy absorption according to standardized testing protocols. The experimental results indicated that the dairy cow hoof blocks made from natural rubber had superior compressive resistance, permanent restoration, and slip resistance values compared to the commercial dairy cow hoof blocks. However, there are still disadvantages in terms of water absorption and energy absorption. In the future, it will be necessary to enhance the mechanical properties of the natural rubber hoof block for dairy cows to test, implement, and use them on dairy cows during the clinical phase.

Keywords: Dairy cow hoof block, Natural rubber, and Mechanical properties.

1. Introduction

The global dairy industry faces various dynamics, including a modest annual increase of 0.9 percent in dairy production, contributing to 1.34 percent of the world's agricultural output. India leads the world in dairy farming, boasting 58.50 million dairy cows, followed by the European Union with 23.30 million and Brazil with 17.95 million. Historically, raw milk production grew at a rate of 1.39 percent per year, totaling 513.93 million tons, reflecting a 2.21 percent increase from the prior period. The European Union dominates unprocessed milk production with 155.55 million liters [1–2]. The global demand for milk increases annually by 0.89 percent, reaching 183.98 million tons. In Thailand, dairy cows play a pivotal role in the economy, with a focus on increasing milk production, achieving 1.62 percent annual growth to 1.23 million tons, driven by government policies and quality improvement initiatives [3].

However, challenges persist, including rising production costs due to government standards and health concerns, leading to the need for improved farm management and disease control measures. Foot-and-mouth disease outbreaks can disrupt milk sales, causing financial losses for producers despite preventive efforts. Despite these difficulties, there is potential for growth and higher levels of quality in the global dairy industry [4]. The welfare of dairy cows holds paramount significance in ensuring the consistent and efficient production of raw milk [5]. Among the various health concerns, they may face, one of the most prevalent is foot pain, primarily in the hoof region. This frequently gives rise to hoof inflammation, ultimately increasing the risk of disease [6]. The two forms of hoof disease are non-infectious and infectious. Typically, the infectious form is found on the hoof floor, hoof flesh, hoof heel, and hoof mite. Typical symptoms include leg pain and difficulty walking and standing [7]. Treatment typically consists of hoof dressings to remove debris and hoof coverings to distribute weight. The infectious type is usually found in the crevices between the hoofs and is severely painful and unable to put weight on the legs. Dairy cows are sick with lethargy, pain, and swelling in their legs. Treatment may involve bandaging the wound along with medicine to relieve pain and inflammation, along with antibiotics, which may have side effects on the quality of the milk.

Currently, the use of hoof blocks or blocks for dairy cows to help heal wounds around the hoof is widely used in foreign countries. Hoof blocks are made from a variety of materials, including wood [8], hard plastic, foam, and rubber [9]. In most cases, they use adhesives to attach to dairy cow hooves. The blocks serve to elevate the hooves so that the wounded hooves don't encounter dirt and speed up the healing of the hoof wound. To analyze the mechanical qualities, there has been a great deal of study that has been built on the mechanical characteristics of rubber and synthetic materials for usage in many sectors in terms of the creation of commercial block materials [10–14]. In addition, the mechanical properties that characterize wearing comfort are energy diffusion and absorption [15], which affect hoof comfort and a cow's walking posture, including the effects on milk production. However, there are still few studies in this area. Therefore, it is an interesting issue in this study.

This research has seen the problem of lameness in dairy cows, so the idea was to assess dairy cow hoof blocks made from natural rubber from previous research [4] to reduce cow hoof injuries from various diseases. The objective of this study was to compare the mechanical properties of natural rubber versus three types of commercial dairy cow hoof blocks. The mechanical properties were tested to evaluate and compare compressive strength, compression set, coefficient of friction [16], water absorption, and energy absorption according to standardized testing. To assess the strengths and weaknesses of the developed dairy cow hoof blocks and compare their advantages with commercially available hoof blocks. The main properties used in testing and comparing include compressive resistance; with the cow's body weight being transmitted to all four legs, the front legs will bear more weight than the hind legs. 10% of total body weight, permanent recovery -when installed on a dairy cow's hoof, the block will support the body weight of the dairy cow all the time while standing or walking, causing it to collapse and recover while the dairy cow sits or lies down; slip resistance—most of the pen floor is wet, making it difficult to balance while walking; energy absorption (affects walking comfort); and resistance to water absorption (damages the block).

2. Theory and methodology

2.1. Dairy cow hoof blocks

A dairy cow hoof block is a specialized device used in the management of hoof-related issues and lameness in dairy cows. It serves a purpose comparable to that of a horse's hoof block but is designed to accommodate the distinct hoof anatomy and is suitable for the dairy cow. Typically, dairy cow hoof blocks are manufactured from inflexible and nonslip materials, such as wood, hard plastic, and rigid and synthetic rubber. These blocks are attached to strong claws on the uninjured side of the hoof. This will help support and relieve injuries to cows' hooves that have wounds and make the wound heal faster. The hoof block is attached directly to a healthy hoof and relieves pressure from the injured hoof, making it suitable for alleviating lameness and hoof issues in livestock. Furthermore, a hoof block is simple and fast to install on a healthy hoof and is secured with an adhesive that dries rapidly, as shown in Figure 1.

The dairy cow hoof blocks used for mechanical properties testing in this research, as shown in Figure 2, encompassed two distinct categories: those crafted from natural rubber from previous research [4] and commercially available dairy cow hoof blocks. The first category, as shown in Figure 2(D), was a dairy cow hoof block made from natural rubber by a vulcanized process. The second category was commercially available dairy cow hoof blocks, including dairy cow hoof blocks made from wood (as seen in Figure 2(A)), commercial rubber (as seen in Figure 2(B)), and EVA (as seen in Figure 2(C)).

Figure 1. The position of dairy cow hoof block.

Figure 2. The materials of dairy cow hoof blocks: (A) wood, (B) commercial rubber, (C) EVA, and (D) natural rubber from previous research [4].

Table 1. The characteristics of four dairy cow hoof blocks.

Hoof block	Materials	Weight (g)	Max. Dimension		Thickness (mm)	Prices (Baht)
			Length (mm)	Width (mm)		
A	wood	64.1	112	53.2	20	70
B	Commercial rubber	188.4	108	54.5	20	500
C	EVA	20.5	120	52	20	100
D	Natural rubber	93.1	117.8	51.2	20	100

2.2. Mechanical properties

Compressive strength is one of the important mechanical properties of materials in supporting the weight of dairy cows because it is a property commonly used to determine product standards or quality. In the actual use condition, most rubber products tend to receive more pressure than forces caused by other behaviors, especially rubber products that were used in engineering, which were tested according to ASTM D 575-91 by preparing a workpiece with a diameter of 28.5 mm, a thickness of 12.5 mm, a pressing speed of 10 mm/min, and a pressing distance of 50% strain. The calculation of the relationship can be calculated from Equations (1) and (2), respectively, finding the relationship between stress (σ) and strain (ε) values under uniaxial compression.

$$\sigma = \frac{F}{A_0} \tag{1}$$

$$\varepsilon = \frac{\Delta L}{L_0} = \frac{L - L_0}{L_0} \tag{2}$$

where F is the compressive force (N), A_0 is the cross-sectional area of the test specimen while there is no force applied (mm^2), ΔL is the height change (mm), L is the height (mm) while subjected to a compressive force, and L_0 is the original height (mm) of the test specimen without force.

The compression set test was carried out on cylindrical specimens using a continuous compressive strain of 25% for 22 hours, as recommended by ASTM D395-03 (Test Method B). The specimens were tested at room temperature of 25 °C with five replications and had a thickness of 12.5 mm and a diameter of 28.5 mm. Furthermore, the compression set's percentage was computed using Equation (3).

$$Compression\,set\,(\%) = \frac{t_o - t_i}{t_o - t_n} x100 \tag{3}$$

where % of the compression set is represented as a percentage of the original deflection, t_o is the original thickness, t_i is the final thickness, and t_n is the thickness of the spacer bar employed.

The hysteresis loop test is performed on circular sample specimens in accordance with ASTM D 575-91. The sample of each dairy cow hoof block was pressed using the universal mechanical testing equipment at a compression speed of 10 mm/min by compressing the rubber to shrink by load control at 160 kg and then backward, repeating three cycles. Since the first and second cycles were for conditioning the specimens, known as Mullin's effect, the third cycle of compressive testing for the specimens is provided, and it may be determined as the area difference under a force-elongation curve when the specimen is loaded vs. unloaded. The hysteresis loop for finding the energy absorbed is calculated according to Equation (4).

$$Energy\,absorbed = \oint CurveAdx - \oint CurveBdx \tag{4}$$

where *Energy absorbed* is hysteresis loss (J), a fitting curve conveys *curves A and B* to find the equation in the Excel plot. The integral method is determined by the graph area.

The coefficient of static friction [16] of the foam composites was determined using the sliding angle friction method in accordance with ASTM D 202. This method is used to determine static friction, also known as the force that holds an object in place. In the test, the test specimens were installed with an optional sliding block with 3 mm-thick blocks. The specimens were raised at the specified incline angle at a rate of 1.5° ±0.5°/s for 10 seconds. The lifting of the specimens was stopped when the movement of the specimens occurred, and then the angle was recorded to the nearest 0.5°. The coefficient of static friction was calculated according to Equation (5).

$$\mu_s = \tan\theta \tag{5}$$

where μ_s was the coefficient of static friction and θ was the angle of testing (degree).

For the water absorption test following ASTM D 570, the specimens are dried in an oven for a specified time and temperature and then placed in a desiccator to cool (*Dry weight (g)*). Immediately upon cooling, the specimens are weighed. The material is then immersed in water at agreed-upon conditions, often 23°C for 24 hours or until equilibrium. The specimens are removed, patted dry with a lint-free cloth, and weighed (*Wet weight (g)*). Water absorption is expressed as an increase in weight percent that was calculated according to Equation (6).

$$Percent\,water\,absorption(\%) = \frac{Wet\,weight - Dry\ weight}{Dry\ weight} x100 \tag{6}$$

2.3. Tools and testing

This work tested the mechanical properties relevant to the use of dairy cow hoof blocks (as shown in Figure 3), consisting of compressive strength, compression set, coefficient of friction, water absorption, and energy absorbed. The universal testing machines of the Instron brand were used to test compression resistance and energy loss from hysteresis loop properties. The grip was made from resin, modeled after a real dairy cow's foot, and molded in plaster. The slide angle friction was used to measure hoof blocks, which determined the angle of inclination, and its specification had an angle range of 0 to 80 degrees. This feature is an indicator of the stability of dairy cows while in use. As for the compression set test, the steel sheet pressed onto the workpiece is pressed down according to the standard distance. The water absorption test uses a plastic container filled with water and places the dairy cow's hoof blocks in it to soak according to the conditions of the test standards mentioned above. Each experiment was repeated five times, and the mean and standard deviation were calculated.

Figure 3. Experimental testing.

3. Results and discussions

3.1. Compressive strength

The graph (as shown in Figure 4) displayed the relationship between stress and strain for each type of dairy cow hoof block in this research. The result presented was that the dairy cow hoof block made from natural rubber had the maximum stress (3.04±0.21 MPa), followed by wood (2.59±0.42 MPa), commercial rubber (1.62±0.2 MPa), and EVA (0.75±0.12 MPa), respectively. During the compression test at 50% strain, it was found that the wood cracked at only 10% strain and therefore could not be tested further. The part of natural rubber that had the greatest ability [4, 10, 11] to resist compression compared to others. This is a vital property for supporting the weight of dairy cows with a body weight of up to 680 kg, which is the weight standard for adult cow mothers in Thailand.

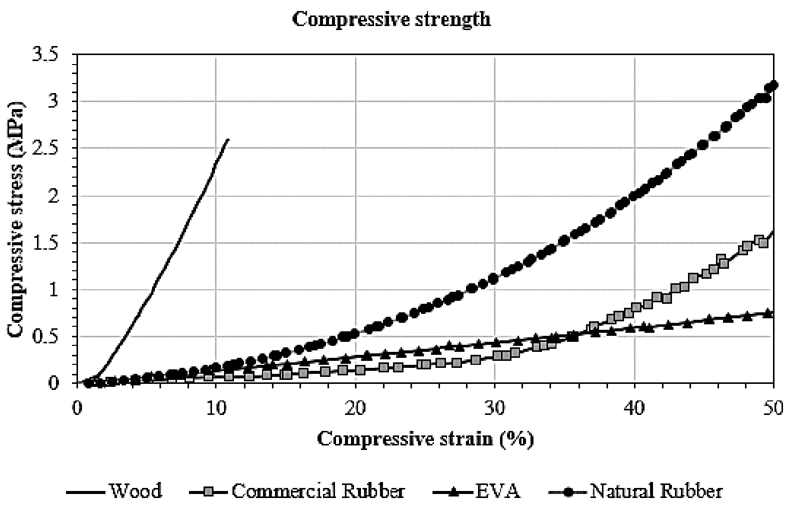

Figure 4. The result of compressive strength of four dairy cow hoof blocks.

3.2. Compression set

Figure 5 shows the result of the compression set (%) of each dairy cow hoof block. This mechanical property was one of the properties for the usability of a dairy cow hoof block because of the large body weight of dairy cows and standing for long periods of time, which causes the hoof blocks to collapse. The graph shows the percentage of permanent collapse due to exposure to compression for a long time

[4, 11]. The experimental results discovered that the dairy bovine hoof blocks from previous research had a low percentage of compression set value and had a similar value to commercial rubber because natural rubber has excellent properties of restoring shape from supporting pressure. In contrast, the percentage of wooden and EVA dairy cow hoof blocks had higher compression set values than commercial rubber and natural rubber, indicating a slower return to its original shape.

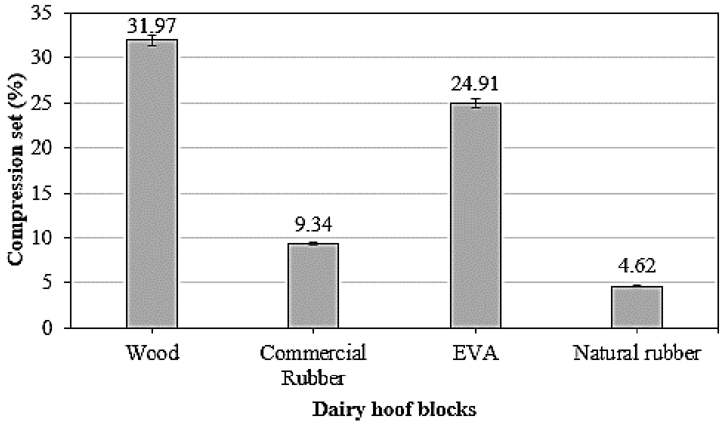

Figure 5. The result of compression set of four dairy cow hoof blocks.

3.3. Coefficient of friction

The bar graph in Figure 6 shows properties of resistance to slipping because when cow hoof blocks are installed on the hooves while dairy cows walk, they will cause slipping because most farms consist of cement, mud, and dirt, which makes it difficult for dairy cows to balance while walking. The experimental result indicated that dairy cow hoof blocks made from natural rubber had a higher coefficient of friction than others. The coefficient of friction indicated resistance to slipping [13, 14, 16].

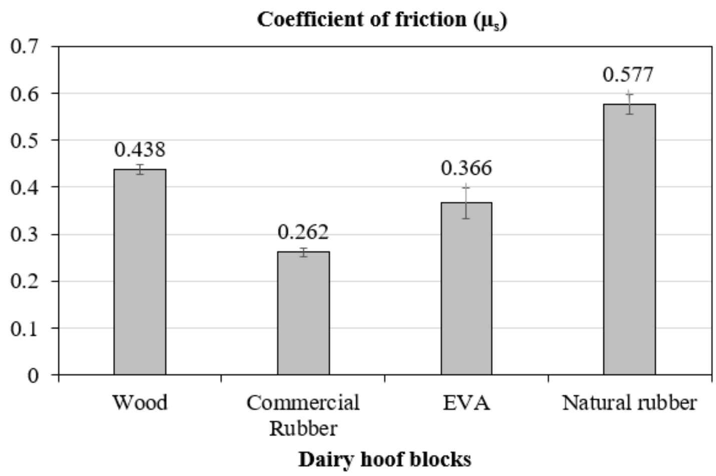

Figure 6. The result of coefficient of friction of four dairy cow hoof blocks.

3.4. Water absorption

Most dairy farms use water to clean the animal pens, which may cause water to pool in some areas. When a dairy cow walks, the cow's hoof blocks encounter water. The material developed must also have good water-absorption properties [12]. The graph, as shown in Figure 7, showed the result of the water absorption of four dairy cow hoof blocks. The experimental result showed that wood had the highest water absorption value compared to other materials. Meanwhile, natural rubber, EVA, and commercial rubber have low water absorption values, respectively, meaning that materials with low water absorption are suitable for development into dairy cow hoof blocks due to the environment in the farm area.

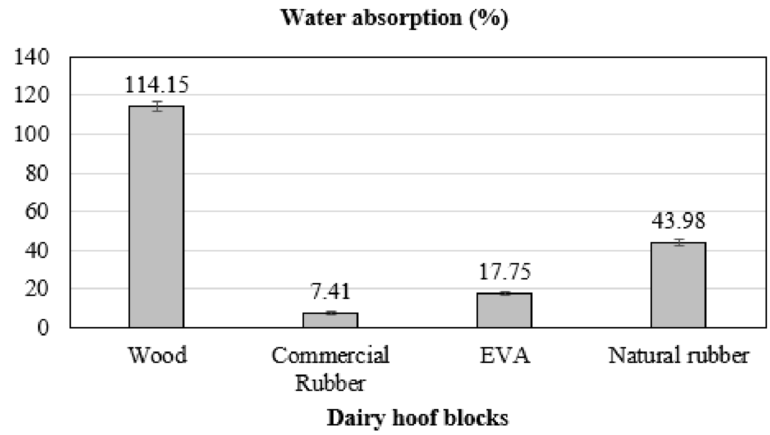

Figure 7. The result of water absorption of four dairy cow hoof blocks.

3.5. Energy absorbed

The result of the energy absorption property (as shown in Figure 8) was important for walking comfort and weight support in dairy cows. In property testing, hysteresis cycles are a common method for testing flexible materials. The results were shown in the graph, as shown in Figure 8(a). All dairy cow hoof blocks are pressed with artificial dairy cow hoof (made from resin) under constant load control at 160 kg per hoof (load) and released (unload) in three cycles. The first cycle will be used to calculate the absorption energy using Equation 4, and the obtained values are shown in Figure 8(b).

The results of the hysteresis cycle show the energy loss or energy absorbed trend of each material in the dairy cow hoof blocks. EVA has the largest circumferential area, followed by rubber, natural rubber, and wood, respectively. However, if we look at the quick recovery of the material, natural rubber is better at restoring its shape than other materials. This feature will affect the balance of dairy cows while walking and hitting their feet [10, 11, 15].

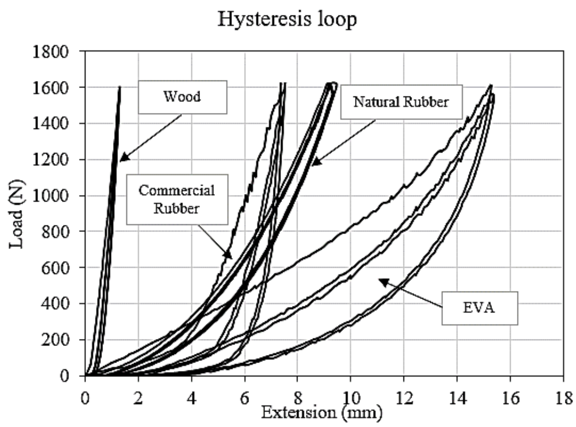

(a)

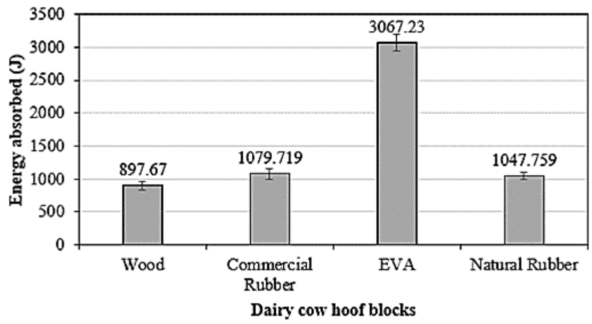

(b)

Figure 8. The results of hysteresis loops (a) and energy absorbed (b) of four dairy cow hoof blocks.

4. Conclusion

This study found that the dairy cow hoof blocks developed from natural rubber had some mechanical properties that were superior to commercial dairy cow hoof blocks, including pressure resistance, permanent restoration, and resistance to slipping. However, several attributes remain weak spots, such as resistance to water absorption and energy absorption. All of the aforementioned features are characteristics of the usage of dairy cow hoof blocks. To test, implement, and employ natural rubber hoof blocks on dairy cows in the clinical phase, it will be required to improve the mechanical properties of their susceptible places in the future.

5. Acknowledgments

Thank you for funding from the fiscal year 2023 revenue budget and the Mechanical Engineering Department, Faculty of Engineering, Rajamangala University of Technology Srivijaya for allowing use of the experimental location.

6. References

[1] Howden, M., & Zammit, K. (2019). *Analysis of United States and Australian agriculture–a comparison*.

[2] Shamsuddoha, M., Nasir, T., & Hossain, N. U. I. (2023). *A Sustainable Supply Chain Framework for Dairy Farming Operations: A System Dynamics Approach. Sustainability*, 15(10), 8417.

[3] Dairy: *World Markets and Trade*, *United States Department of Agriculture, Foreign Agricultural Service*, Dec 2019

[4] Sawatdiruksa, A., Supapong, C., Thongsrinual C., & Petdee, T., (2023). Development of cattle hoof blocks from natural rubber. *In Proceeding of the 37th ME-NETT Conference (Songkla).-Thailand* (Vol. 37, p. 388-394).

[5] Neculai-Valeanu, A. S., & Ariton, A. M. (2022). *Udder health monitoring for prevention of bovine mastitis and improvement of milk quality*. Bioengineering, 9(11), 608.

[6] Langova, L., Novotna, I., Nemcova, P., Machacek, M., Havlicek, Z., Zemanova, M., & Chrast, V. (2020). *Impact of nutrients on the hoof health in cattle. Animals*, 10(10), 1824.

[7] Sadiq, M. B., Ramanoon, S. Z., Mossadeq, W. S., Mansor, R., & Syed-Hussain, S. S. (2021). *Prevalence and risk factors for hoof lesions in dairy cows in Peninsular Malaysia. Livestock Science*, 245, 104404.

[8] Ranjbar, S., Rabiee, A. R., Reynolds, M. W., Mohler, V. L., & House, J. K. (2021). *Wooden hoof blocks: are we using the right wood?. New Zealand veterinary journal*, 69(3), 158-164.

[9] Müller, K. R., Laven, R. A., & Laven, L. J. (2023). *Persistence of orthopaedic hoof blocks for the treatment of lame cattle kept permanently at pasture. New Zealand Veterinary Journal, (just-accepted)*, 1-15.

[10] Petdee, T., Naemsai, T., Pianhanuruk, E., Boonchouytan, W., & Homkhiew, C. (2022). Effects of blowing agents and curing temperatures on physical and mechanical properties of natural rubber foam for laminated floor tiles. *Polymers and Polymer Composites, 30, 09673911221106684.*

[11] Srewaradachpisal, S., Dechwayukul, C., Chatpun, S., Spontak, R. J., & Thongruang, W. (2020). Optimization of the rubber formulation for footwear applications from the response surface method. *Polymers*, 12(9), 2032.

[12] Thirumal, M., Khastgir, D., Singha, N. K., Manjunath, B. S., & Naik, Y. P. (2008). Effect of foam density on the properties of water blown rigid polyurethane foam. *Journal of applied polymer science*, 108(3), 1810-1817.

[13] Derieux, J. B. (1935). The coefficient of friction of rubber. Rubber Chemistry and Technology, 8(3), 441-442.

[14] Yamaguchi, T., Sugawara, T., Takahashi, M., Shibata, K., Moriyasu, K., Nishiwaki, T., & Hokkirigawa, K. (2017). Dry sliding friction of ethylene vinyl acetate blocks: Effect of the porosity. *Tribology International*, 116, 264-271.

[15] Tomin, M., & Kmetty, A. (2022). Polymer foams as advanced energy absorbing materials for sports applications—A review. *Journal of Applied Polymer Science*, 139(9), 51714.

[16] Petdee, T., Naemsai, T., Homkhiew, C., & Pianhanuruk, E. (2023). Multiple response optimization of wood sawdust/natural rubber foam composites for stair tread covers. *Industrial Crops and Products*, 204, 117312.

AMM0011

Development of an effective method for cleaning probes used to measure microstructures using supersonic flow

S Beppu[1], H Murakami[1,*], A Katsuki[2], and T Sajima[2]

[1]The University of Kitakyushu, 1-1 Hibikino, Wakamatsu-ku, Kitakyushu, Fukuoka, 808-0135, Japan
[2]Kyushu University, 744 Motooka, Nishi-ku, Fukuoka, 819-0395, Japan

* Corresponding Author: murakami@kitakyu-u.ac.jp

Abstract. With recent advances in microfabrication technology, the importance of measuring microstructures has been increasing. We have therefore developed a measurement system that uses small-diameter optical fiber probe. However, before and after measurement, fine foreign substances may adhere to the probe tip. If a probe with foreign substances adhering to it is used for measurement, a measurement error occurs due to the thickness of the foreign substance when it is positioned between the probe tip and the measured surface. Although ultrasonic cleaners are generally used for cleaning, they cannot remove foreign particles from micro-probe. In this study, we describe the results of performance evaluation tests of cleaning after designing and fabricating a nozzle shape, with the aim of removing foreign substances efficiently and without damage by using supersonic flow. As a result, it was confirmed that the nozzle with a diameter of 2.5 mm was able to remove almost all foreign substances without breaking at stylus installation locations z = 0 mm or less.

Keywords: Microstructure measurement, optical fiber probe, cleaning, supersonic flow.

1. Introduction

With the development of processing technology in recent years, there has been an increase in the number of three-dimensional microstructure shapes, such as micro-diameter holes in various nozzles [1], Through Silicon Via (TSV) [2], Micro Electro Mechanical System (MEMS), micro parts in micromachines, optical communication devices, medical devices, and so on. The importance and need for precise measurement of microstructure is increasing, as the advancement of microfabrication technology cannot be realized without the development of these measurement technologies.

Although several methods have been studied and proposed for measuring microstructures using flexure-based probes [3, 4], vibrating probes [5, 6], fiber probes [7, 8], optical trapping probes [9], tunneling effect probes [10] and three-dimensional atomic force microscopy (3D AFM) probes [11, 12]. for last decade, no measurement technology for micro 3D shapes has been established to meet the requirements [2], especially for shapes with deep holes and grooves. One of the key technologies for microstructure measurement is how to fabricate a micro probe and detect contact with the measured object.

We have therefore developed a measurement system that uses an optical fiber stylus [13-17]. However, fine foreign substances may adhere to the stylus tip. Although no foreign substances adhere to the stylus tip immediately after fabrication of stylus, foreign substances from air or measured surface may adhere to the stylus tip during its transport or measurement. If a stylus with foreign substances is used for measurement, a measurement error will be increased by the thickness of the foreign substance if it is positioned between the stylus tip and the measured surface. In this study, we describe the results of performance evaluation tests of cleaning after designing and fabricating a nozzle shape, with the aim of removing foreign substances efficiently and without damage by using supersonic flow.

2. Principle of measurement

Figure 1 shows the schematic diagram of the measurement system. A focused laser beam is irradiated toward the stylus shaft from the X direction. The laser beam is reflected upward through a prism and irradiated onto the stylus shaft. The light transmitted through the stylus shaft is received by two pairs of dual-element photodiodes placed on opposite sides with the stylus between them. Here, the stylus shaft is used as a rod lens to magnify the displacement of the stylus shaft caused by contact of the stylus tip with the measured surface. When the stylus tip contacts the measured surface and the stylus shaft deflects and displaces, a difference is generated in the light intensity of the light received by each of the two dual-element photodiodes, allowing the direction of contact to be detected.

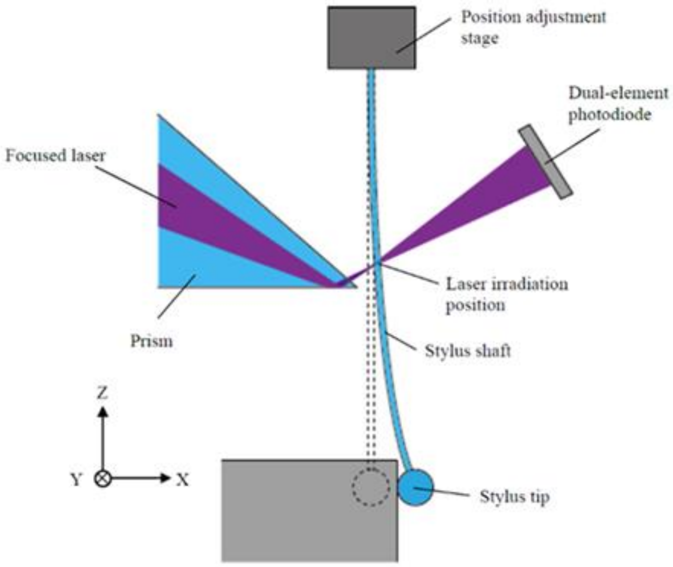

Figure 1. Schematic diagram of the measurement system.

3. Influence of foreign substance adhesion on the stylus

We have developed a measurement system that uses a small-diameter optical fiber as a stylus. However, fine foreign substances may adhere to the stylus tip. As shown in Figure 2, no foreign substance adheres to the stylus immediately after its fabrication, but foreign substances from the air or measured surface may adhere to the stylus during its transport or measurement (Figure 3). When a stylus with foreign substances is used for measurement, a measurement error occurs due to the thickness of the foreign substance if the foreign substance is positioned between the stylus tip and the measured surface. Although Ultrasonic cleaners are generally used for cleaning, the previous experiments by our group have failed to remove foreign substances from the stylus. In this study, we propose the cleaning method using supersonic flow.

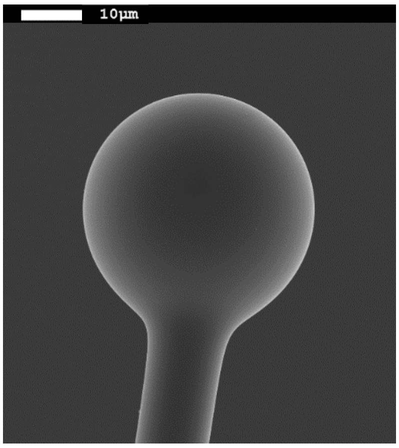

Figure 2. Stylus immediately after production.

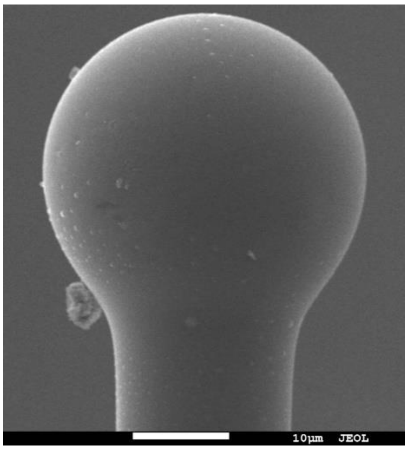

Figure 3. Stylus with foreign substances.

4. Cleaning method using supersonic flow

4.1. Design and fabrication of supersonic nozzles

When the diameter of foreign substance is less than several tens of micrometers, the influence of surface forces such as van der Waals force, electrostatic force, and liquid bridge force becomes greater, and these surface forces become larger than gravity. When foreign substance is smaller than this size, it adheres easily to the stylus. The surface force is affected by environmental factors such as humidity and the roughness of the measured surface. To remove foreign substances from the stylus in supersonic flow, it is first necessary to know the magnitude of the adhesion force due to surface forces [18]. Figure 4 shows the relationship between the lifting force generated by supersonic flow and the pulling (surface) force.

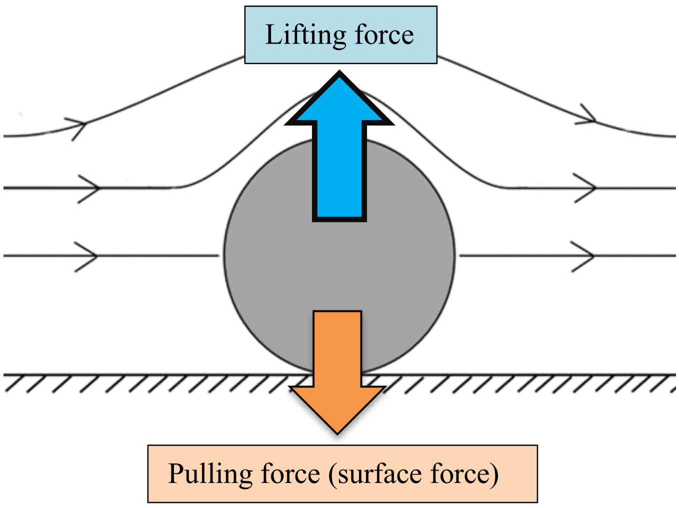

Figure 4. Schematic of lifting and pulling (surface) force.

Next, we consider the force required to pull the foreign substances away from the stylus. For simplicity, we consider the case of a spherical foreign substance and a flat measured surface. The lifting force can be calculated from Bernoulli's theorem [19]. At flow velocities of 300 m/s or greater, the lifting force acting on foreign substance with a diameter of 10 nm or larger is greater than the pulling (surface) force, and foreign substances 10 nm in diameter or greater could be separated from the stylus. Since the repeatability of the measurement system is approximately 30 nm, the research goal is set to remove foreign substances with diameters of 10 nm or greater. Therefore, a supersonic nozzle with a flow velocity of 400 m/s or higher was designed to remove foreign substances with a diameter of 6 nm or greater, allowing for a margin of error. Figure 5 shows the shape of the fabricated nozzle. The nozzle geometry was calculated using the characteristics method. In this study, two types of nozzles with nozzle throat with diameters of 2.5 mm and 5 mm were fabricated and investigated in the experiments.

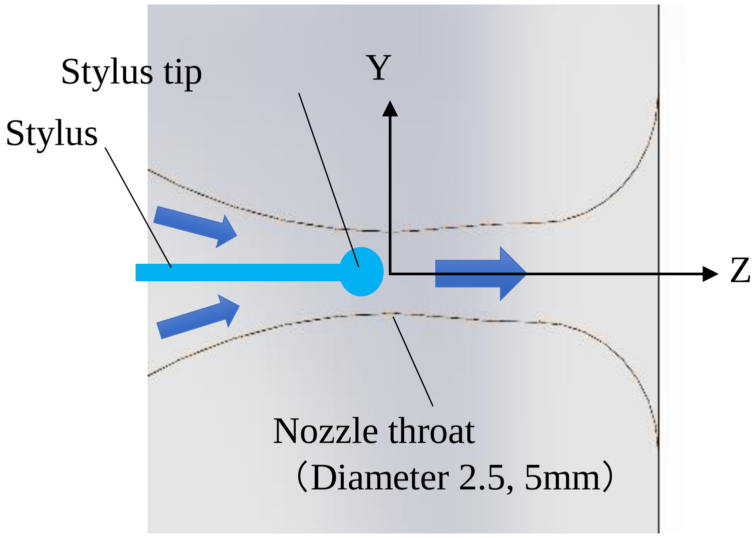

Figure 5. Shape of fabricated nozzle.

4.2. Cleaning method

Next, the stylus tip with a diameter of 30 μm was fixed as shown in Figure 5, and the cleaning effect of the stylus was investigated after air flow at maximum velocity for 5 seconds. Silica particles with a diameter of 2 μm were manually attached to the stylus. The stylus after cleaning was then observed using Scanning Electron Microscope (SEM) to evaluate the cleaning effect.

4.3. Results of cleaning experiment and discussion

In this experiment, styli were first cleaned using a nozzle with a diameter of 5 mm. Table 1 shows the results of cleaning experiment using styli with foreign substances with a diameter of 2 μm. The tips of styli were placed at z = -2, 0, and 2. As shown in Table 1, the styli were all broken. This suggests that the stylus may have been broken due to excitation by the flow inside the nozzle.

Next, a nozzle with a diameter of 2.5 mm was fabricated to reduce the flow rate by narrowing the diameter of the nozzle throat, and cleaning was performed. The results are shown in Table 2. Table 2 shows that the stylus cleaned at z = 0 mm or less was able to remove almost all foreign substances without breaking. However, in some cases, the stylus tip ball was damaged. This may have been caused by the stylus swinging and hitting the nozzle wall during cleaning, which may have damaged the stylus tip. In terms of cleaning effectiveness, it was confirmed that nozzles with a diameter of 2.5 mm can clean the stylus without breaking at z = 0 mm or less. These results indicate that the optimal nozzle throat width for this system is currently 2.5 mm in diameter.

Table 1. Results of cleaning using a nozzle with a diameter of 5 mm.

Cleaning position	Before cleaning	After cleaning
Z=-2	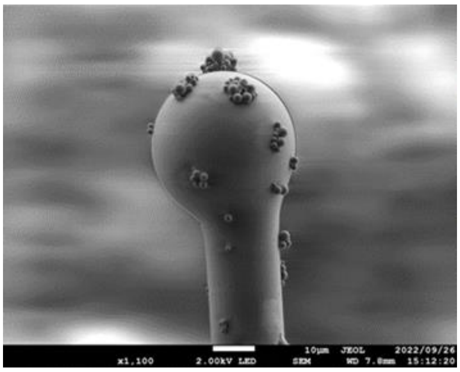	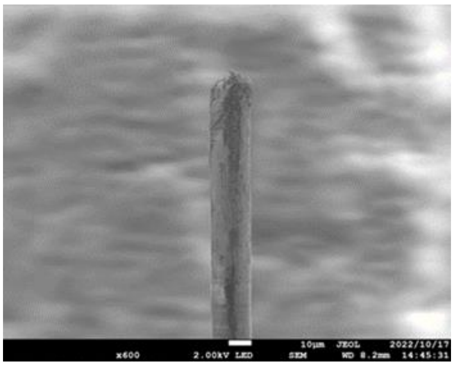
Z=0	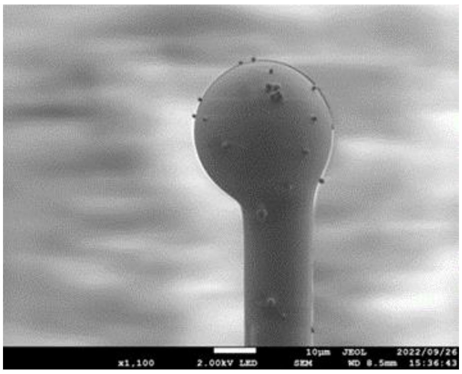	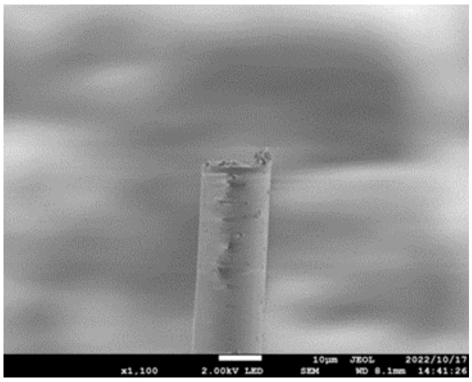
Z=2	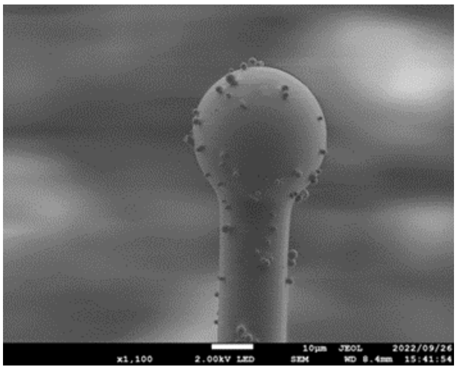	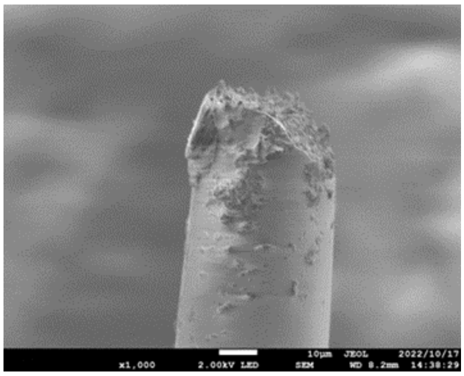

Table 2. Results of cleaning using a nozzle with a diameter of 2.5 mm.

Cleaning position	Before cleaning	After cleaning
Z=-4	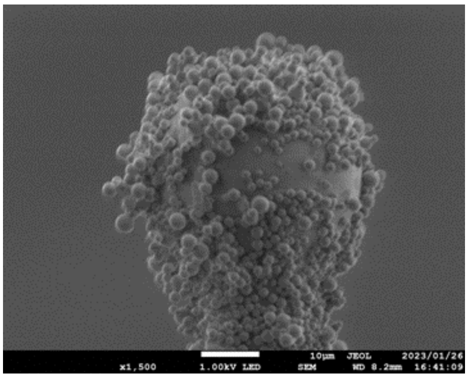	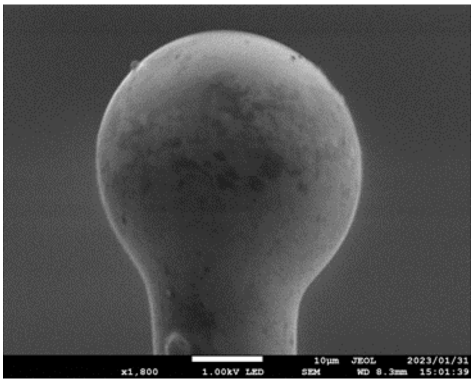
Z=0	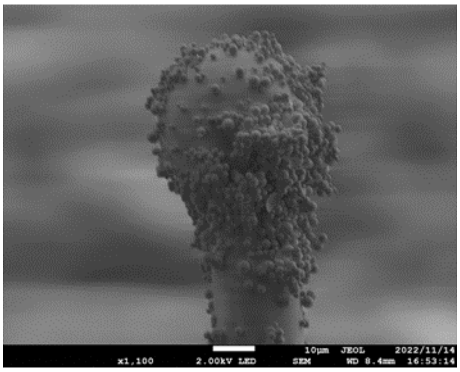	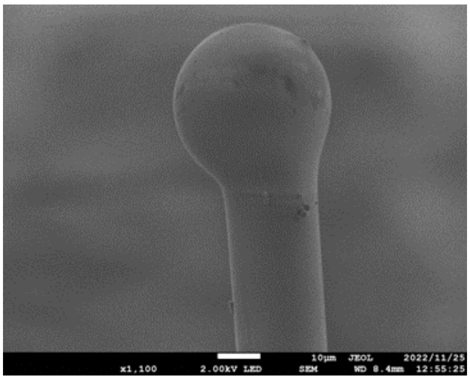
Z=2	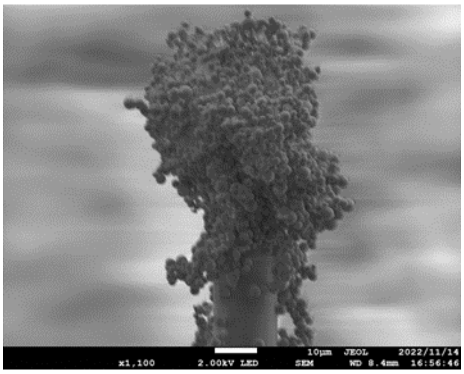	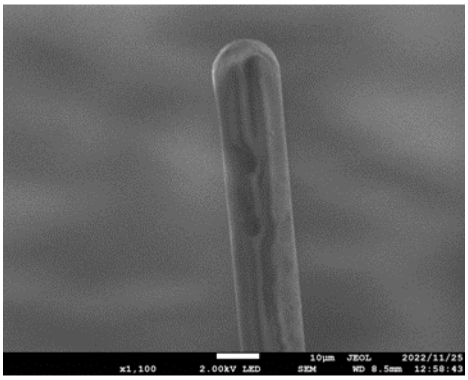

5. Conclusion

In this study, we proposed a stylus cleaning method using supersonic flow. The nozzles with a diameter of 5 mm and 2.5 mm were designed and fabricated, and the cleaning evaluation experiments were conducted. As a result, it was confirmed that the nozzle with a diameter of 2.5 mm was able to remove almost all foreign substances without breaking at stylus installation locations z = 0 mm or less. However, damage to the stylus was observed in some cases. This is thought to be caused by the supersonic flow vibrating the stylus and causing the tip to impact the nozzle wall. Future studies are needed to reduce this damage.

6. Acknowledgements

This study was partly supported by a research grant from the JSPS KAKENHI Grant Number 26420392 and the mitsui foundation for the advancement of tool and die technology.

7. References

[1] Laboratory NP. Dimensional metrology for high-aspect-ratio micronozzles. The European Metrology Programme for Innovation and Research. 2014;SRT-i06:1-3.

[2] Iff WA, Hugonin JP, Sauvan C, Besbes M, Chavel P, Vienne G, et al. Electromagnetic analysis for optical coherence tomography based through silicon vias metrology. Appl Opt. 2019;58:7472-88.

[3] D Metz SJ, K Kniel and A Dietzel. Integration of an isotropic microprobe and a microenvironment into a conventional CMM. Measurement Science and Technology. 2019;30:115007(15pp).

[4] Alblalaihid K, Lawes S, Kinnell P. Variable stiffness probing systems for micro-coordinate measuring machines. Precision Engineering. 2016;43:262-9.

[5] Ren Z, Wang D, Jing W, Wang S, Jiang Z, Ren J, et al. A probe-type high-precision micro-force sensor based on quartz DETF resonator. Measurement Science and Technology. 2021;32.

[6] Ito S, Shima Y, Kato D, Matsumoto K, Kamiya K. Development of a Microprobing System for Side Wall Detection Based on Local Surface Interaction Force Detection. International Journal of Automation Technology. 2020;14:91-8.

[7] Feng K, Cui J, Sun X, Dang H, Shi T, Niu Y, et al. Investigation of a Three-Dimensional Micro-Scale Sensing System Based on a Tapered Self-Assembly Four-Cores Fiber Bragg Grating Probe. Sensors (Basel). 2018;18.

[8] Zou L, Ni H, Zhang P, Ding X. Assembled Cantilever Fiber Touch Trigger Probe for Three-Dimensional Measurement of Microstructures. Sensors (Basel). 2017;17.

[9] Michihata M, Takaya Y, Hayashi T. Improvement of Laser Trapping Based Microprobe in Laser Shaded Condition. Journal of Advanced Mechanical Design, Systems, and Manufacturing. 2012;6:764-70.

[10] Schuler A, Hausotte T, Sun Z. Micro- and nanocoordinate measurements of micro-parts with 3-D tunnelling current probing. Journal of Sensors and Sensor Systems. 2015;4:199-208.

[11] Zhang R, Wu S, Liu L, Lu N-H, Fu X, Gao S-T, Hu X-D. A CD probe with a tailored cantilever for 3D-AFM measurement. Measurement Science and Technology. 2018;29.

[12] Dai G, Häßler-Grohne W, Hüser D, Wolff H, Danzebrink H-U, Koenders L, Bosse H. Development of a 3D-AFM for true 3D measurements of nanostructures. Measurement Science and Technology. 2011;22.

[13] Murakami H, Murakami H, Katsuki A, Sajima T, Uchiyama K. Development of a two-step stylus with elastic hinge for microstructure measurement to improve sensitivity and vibration characteristics. Precision Engineering. 2023;80:72-81.

[14] Uchiyama K, Murakami H, Katsuki A, Sajima T. Development of a Sharp-Tipped L-Shaped Stylus for Measurement of Nanoscale Sidewall Features. International Journal of Automation Technology. 2022;16:489-96.

[15] Murakami H, Katsuki A, Sajima T, Uchiyama K, Yoshida I, Hamano Y, Honda H. Development of measurement system for microstructures using an optical fiber probe: improvement of measurable region and depth. Measurement Science and Technology. 2020;31.

[16] Murakami H, Katsuki A, Sajima T, Uchiyama K. Fabrication of Ultra-Small-Diameter Optical-Fiber Probe Using Acid-Etch Technique and CO2 Laser for 3D-Micro Metrology. International Journal of Automation Technology. 2017;11:699-706.

[17] Murakami H, Katsuki A, Sajima T, Suematsu T. Study of a vibrating fiber probing system for 3-D micro-structures: performance improvement. Measurement Science and Technology. 2014;25.

[18] Murakami H, Katsuki A, Sajima T, Fukuda M. Reduction of Liquid Bridge Force for 3D Microstructure Measurements. Appl Sci-Basel. 2016;6:11.

[19] Uwe Schlosser TB, Eckhard Schollmeyer. Some Remarks on the Removal of Adhered Particles by Oscillating Air Flows. Journal of Adhesion Science and Technology. 2009;23:787-98.

AMM0012

Tool condition monitoring in milling using sensor fusion and machine learning techniques

Y Iwashita[1], H Murakami[1,*], A Katsuki[2], T Sajima[2], T Matsuda[1], and T Yoshizumi[1]

[1]The University of Kitakyushu, 1-1 Hibikino, Wakamatsu-ku, Kitakyushu, Fukuoka, 808-0135, Japan
[2]Kyushu University, 744 Motooka, Nishi-ku, Fukuoka, 819-0395, Japan

* Corresponding Author: murakami@kitakyu-u.ac.jp

Abstract. The purpose of the study is to estimate the tool wear from the sensor information using sensor fusion technology and machine learning algorithms that utilize multiple sensor information. First, the features related to tool wear were extracted. Machine learning algorithms were then used to predict the tool wear. Finally, the prediction performance of each model was compared. Comparison results confirm that Gradient Boosting Decision Tree and Deep Learning have relatively high prediction performance.

Keywords: tool condition monitoring, sensor fusion, machine learning.

1. Introduction

In recent years, as the transition to smart factories has progressed in the industrial world, there has been growing interest in technologies for detecting and predicting abnormalities during machining [1-3]. Automation of the machining process is one of the key issues in the construction of a smart factory when automating the entire production process. In particular, the spindle and tool condition monitoring technology contributes to reduced tool costs by changing tool at an appropriate time, improved surface quality, and increased productivity through reduced machine tool downtime. When tools are changed at the manufacturing site, tools are often replaced after machining a certain number of pieces or after machining for a certain period, and tools that can still be used are often discarded. Since the progression of tool wear varies greatly even under the same machining conditions, tools, and workpiece, tools are often replaced with considerable safety precautions, and the effective utilization rate of tools is currently not high. Therefore, it is important to construct a tool condition monitoring system that monitors the condition of cutting tools during machining and to replace cutting tools at the appropriate time to improve productivity and machined surface quality. In addition to productivity improvement and cost reduction, predictive maintenance can be expected to prevent machine breakage, failure, and deterioration of consumable parts. Therefore, we have been developing a spindle with a built-in AE sensor to monitor the tool during machining [4]. However, it is difficult to reliably predict tool wear conditions with a single sensor because AE signals and cutting forces change not only with tool wear but also with changes in depth of cut and cutting speed. Therefore, this study reports the results of an investigation of a method for predicting tool wear at a given point in time from sensor information using sensor fusion techniques and machine learning algorithms based on multiple sensor signals.

2. Experimental data acquisition method

Machining experiments were conducted by attaching multiple sensors to machine tools, and the acquired data was used to predict tool wear using the signal processing technique and machine learning model. The dynamometer was installed on the linear motor stage, and the workpiece was bolted to the top of the dynamometer. The dynamometer is used to measure cutting resistance in the X, Y and Z directions during machining. The high-sensitivity AE sensor was mounted on the side of the dynamometer to acquire AE waves generated during cutting. A 3-axis accelerometer was mounted on the spindle housing to measure the vibration of the spindle in the X, Y and Z directions. The microphone is mounted using a magnetic base and directed toward the tool tip to record the sound produced by the cutting process. Each sensor signal was acquired at a sampling frequency of 1 MHz. The torque, motor current, spindle torque, and spindle power consumption signals of the XYZ axis drive motor were obtained from the NC controller at a sampling frequency of 1 kHz. The workpiece materials were C45 and SKD11, and machining was performed with a two-flute square endmill. Its diameter is 3 mm. The radial and axial depth of cut were 0.1 and 3 mm. The endmill was fed to perform cutting downward. The width of the workpiece is 120 mm, and cutting over this width is defined as one cutting pass. When measuring tool wear, the machine tool was temporarily stopped and the flank wear width at 1.5 mm from the tool tip was measured from the microscope image. The photograph of the experimental apparatus used in this study is shown in Figure 1, and the machining conditions of the experiment are shown in Table 1.

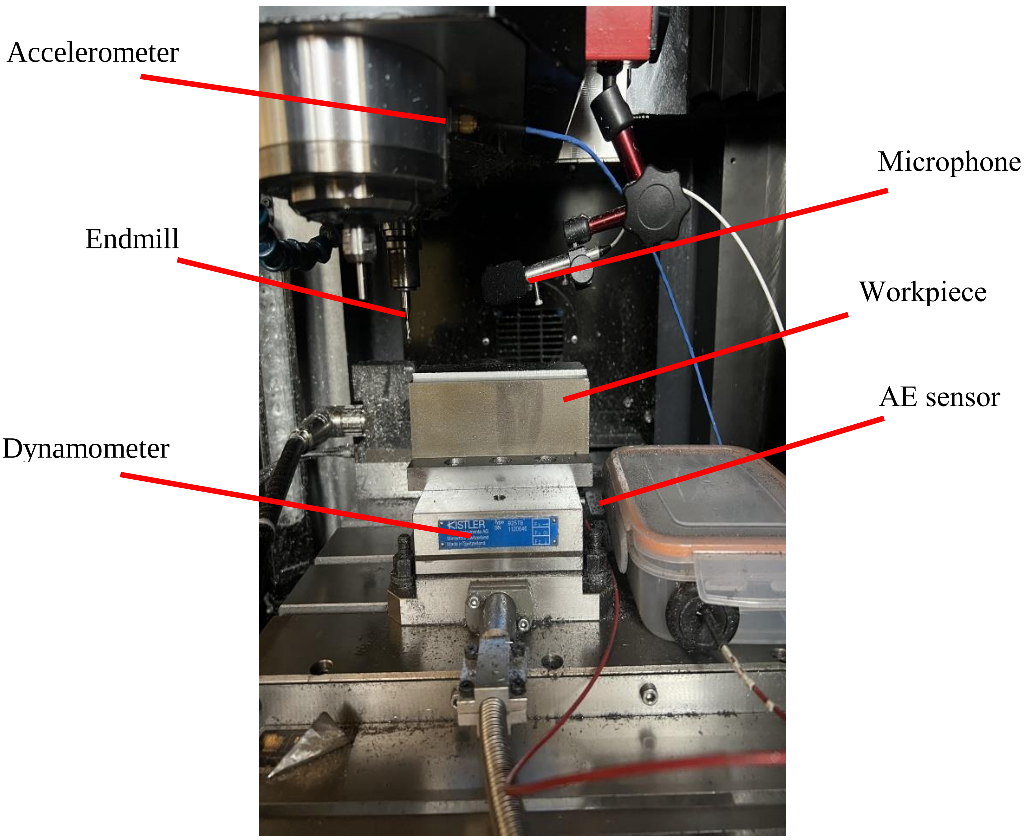

Figure 1. Experimental apparatus.

Table 1. Machining conditions.

Experimental number	Workpiece	Rotational speed (rpm)	Cutting speed (m/min)	Feed rate (mm/min)	Depth of cut per tooth (mm)
1	C45	2800	26.4	200	0.036
2	C45	2800	26.4	200	0.036
3	C45	2800	26.4	200	0.036
4	SKD11	1400	13.2	45	0.016
5	SKD11	1400	13.2	45	0.016
6	SKD11	1400	13.2	45	0.016
7	SKD11	1400	13.2	90	0.032
8	SKD11	1400	13.2	90	0.032
9	SKD11	1400	13.2	90	0.032

3. Feature extraction

In order to predict the tool wear accurately using machine learning, it is important to extract and select information that is highly correlated with tool wear from the raw data. In this study, features were obtained from both the time and the frequency domain. 9 time-domain features were obtained from the raw data, and 21 frequency-domain features were obtained from the frequency spectrum obtained by FFT. Table 2 shows the 30 features used in this study.

For each of the above 16 sensor signals, 30 features were calculated, for a total of 480 features. Ten features of cutting condition and mechanical property of workpiece were added to the 480 features to obtain a total of 490 features. From these 490 features, 50 features of high importance were selected for training using gradient boosting decision trees. Tool wear was also predicted when all the features were used for comparison.

Table 2. Features.

Time domain	Mean, Root Mean Square, Variance, Standard deviation, Kurtosis, Skewness, Shape Factor, Peak to Peak value, Crest factor
Frequency domain	Spectral mean, Spectral RMS, Spectral variance, Spectral standard deviation, Spectral kurtosis, Spectral skewness, Spectral shape factor, Spectral Peak to Peak value, Spectral crest factor, FFT(0kHz), FFT(1-50kHz), FFT(51-100kHz), FFT(101-150kHz), FFT(151-200kHz), FFT(201-250kHz), FFT(251-300kHz), FFT(301-350kHz), FFT(351-400kHz), FFT(401-450kHz), FFT(451-500kHz), FFT(90-100Hz)
Cutting condition	Rotational speed, Cutting speed, Feed rate, Feed per tooth
Mechanical property of workpiece	Vickers Hardness, Tensile Strength, Thermal Conductivity, Specific Cutting Force

4. Comparison of machine learning models

In this study, we used four methods to predict tool flank wear width: Random Forest (RF), Gradient Boosting Decision Tree (GBDT), Support Vector Regression (SVR), and Deep Learning (DL) to compare each learning model. Random Forest is a one of the ensembles learning that combines multiple decision trees to improve generalization capability, and is used for classification and regression. Decision trees are created in parallel, and the average of the output results of each decision tree is calculated to make a prediction. Gradient Boosting Decision Trees is a machine learning technique that combines gradient descent, ensemble learning, and decision trees. Support Vector Machines can perform classification and regression by determining a boundary or hyperplane that would partition the two classes of data groups. Deep Learning is based on neural networks, which are systems that mimic the structure of neurons in the brain and can learn features by building multiple layers of networks. The loss function was evaluated using MSE.

Figures 2 and 3 show the results of the prediction using the 50 important features mentioned above. Figure 2 shows the results of the prediction using the experimental number 4 as test data and the other data as training data. The GBDT have the highest prediction accuracy and was able to predict the tool flank wear width with an RMSE of 25.8 µm. (RF: 28.9 µm, GBDT: 25.8 µm, SVR: 35.6 µm, DL: 28.7 µm). Figure 3 shows the results of the prediction using the experimental number 3 as test data and the other data as training data. Compared to the case where the experimental number 4 was used for the test data, all of them are more accurate. Especially DL has the highest prediction accuracy. The tool flank wear width could be predicted with an RMSE of 7.8 µm (RF:12.1 µm, GBDT: 9.3 µm, SVR: 20.1 µm, DL: 7.8 µm). Each hyperparameter set by trial and error in the algorithm used is shown in Table 3.

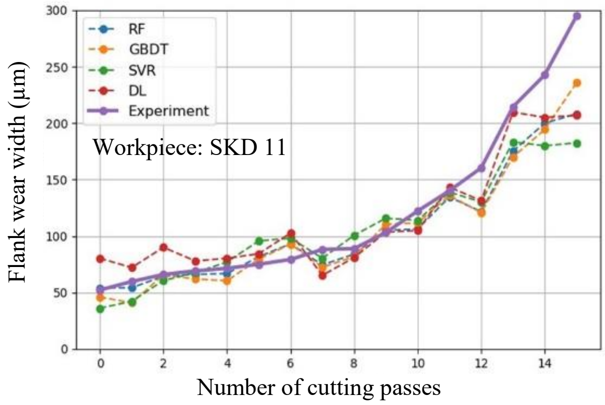

Figure 2. Prediction results for each model

(Exp. 4: 50 features are used).

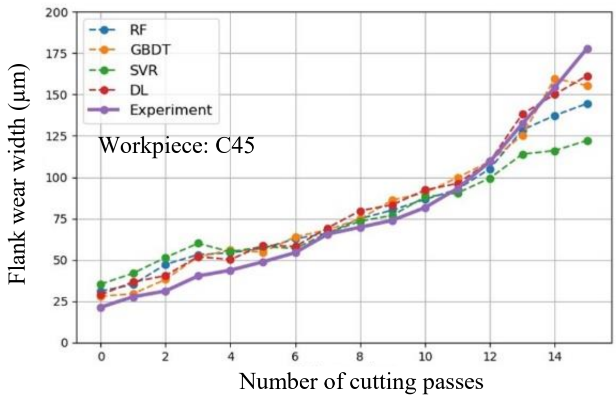

Figure 3 Prediction results for each model

(Exp. 3: 50 features are used).

Table 3. Hyperparameters.

RF		GBDT		SVR		DL	
n_estimators	9500	n_estimators	100	C	0.38	Hidden layer 1	128
Max_features	0.05	learning_rate	0.11	gamma	0.01	Hidden layer 2	64
criterion	squared_mean_error	max_features	5	epsilon	0.001	Hidden layer 3	64
max_depth	10					batch_size	72
						epochs	88

The results of the prediction using all the features are shown in Figures 4 and 5. Figure 4 shows the results of the prediction using the experimental number 4 as test data and the other data as training data. The GBDT has the highest prediction accuracy and can predict the tool flank wear width with an RMSE of 22 μm. (RF : 29.8 μm, GBDT : 22 μm, SVM : 37.1 μm, DL : 34.7 μm). This is as accurate as when 50 features are used. Figure 5 shows the results of the prediction using the experimental number 3 as test data and the other data as training data. SVM has the highest prediction accuracy and can predict the tool flank wear width with an RMSE of 8.0 μm. (RF : 12.0 μm, GBDT : 12.4 μm, SVM : 8.0 μm, DL : 8.8 μm). It was found that 50 features were able to predict with better accuracy. Table 4 shows a comparison of the results when 50 features are used and when all features are used. These results confirm that GBDT and DL have relatively high prediction performance.

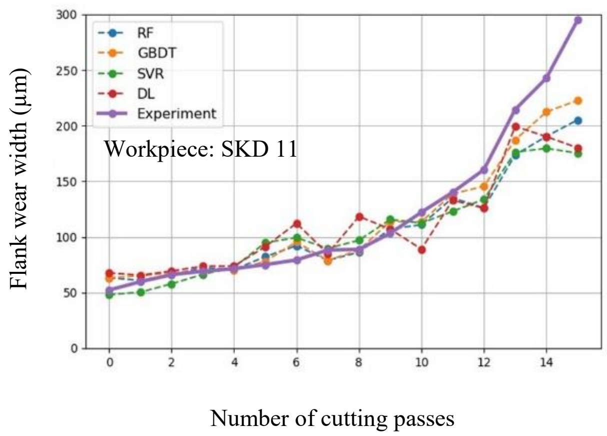

Figure 4. Prediction results for each model

(Exp. 4: all the features are used).

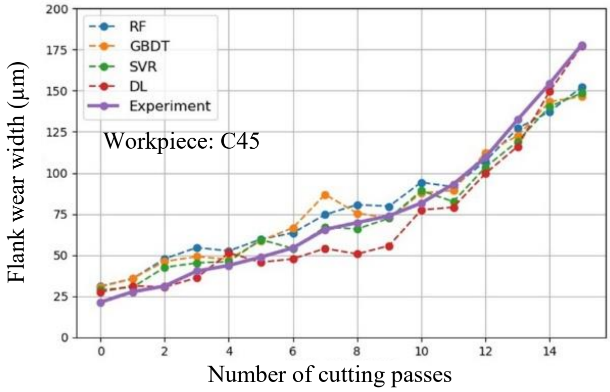

Figure 5. Prediction results for each model

(Exp. 3: all the features are used).

Table 4. comparison of RMSE of each prediction results.

Test data	RF	GBDT	SVR	DL
4 (50 features)	28.9	25.8	35.6	28.7
4 (All features)	29.8	22.0	37.1	34.7
3 (50 features)	12.1	9.3	20.1	7.8
3 (All features)	12.0	12.4	8.0	8.8

5. Conclusion

In this study, multiple sensors (dynamometer, accelerometer, AE sensor, microphone, and signals obtained from the NC controller) were used to predict tool flank wear. Machine learning models were trained with 50 features of high importance and all features as a comparison. As a result, when the experimental number 3 was used for the test data, the prediction was highly accurate. However, when experiment number 4 was used for the test data, the results were not satisfactory. This may be due to the difficulty in predicting the steep gradient where the wear exceeds 150 µm for the case of the experimental number 4. It is also considered that the amount of training data in the study was not sufficient. When all the features are used, the prediction using the experimental number 4 as test data is as accurate as the prediction using 50 features. On the other hand, the prediction using all features was less accurate than the prediction using 50 features when the experimental number 3 was used as test data. Comparison of various machine learning methods confirms that GBDT and DL have relatively high prediction performance.

Future issues include the need to improve the accuracy of prediction by devising a better selection method for feature values. In addition, it is necessary to collect more training data to enable prediction under more machining conditions.

6. References

[1] Teti R, Mourtzis D, D'Addona DM, Caggiano A. Process monitoring of machining. CIRP Annals. 2022;71:529-52.

[2] Ntemi M, Paraschos S, Karakostas A, Gialampoukidis I, Vrochidis S, Kompatsiaris I. Infrastructure monitoring and quality diagnosis in CNC machining: A review. Cirp J Manuf Sci Tec. 2022;38:631-49.

[3] Li X, Liu X, Yue C, Liang SY, Wang L. Systematic review on tool breakage monitoring techniques in machining operations. International Journal of Machine Tools and Manufacture. 2022;176.
[4] Murakami H, Katsuki A, Sajima T, Uchiyama K, Houda K, Sugihara Y. Spindle with built-in acoustic emission sensor to realize contact detection. Precision Engineering. 2021;70:26-33.

AMM0013

Unsupervised tool wear prediction method based on one-class Support Vector Machine

T Matsuda[1], H Murakami[1,*], A Katsuki[2], T Sajima[2], Y Iwashita[1], and T Yoshizumi[1]

[1]The University of Kitakyushu, 1-1 Hibikino, Wakamatsu-ku, Kitakyushu, Fukuoka, 808-0135, Japan
[2]Kyushu University, 744 Motooka, Nishi-ku, Fukuoka, 819-0395, Japan

* Corresponding Author: murakami@kitakyu-u.ac.jp

Abstract. The development of condition monitoring for machine tool is very important to improve production efficiency and reduce costs. In recent years, many machining condition monitoring methods have been developed using machine learning, but most of them use supervised learning methods. Supervised learning methods require a large amount of experimental data, but collecting this data is time-consuming and costly. Therefore, we have been investigating a method that can predict tool wear without learning by using sensor data collected during machining. In this study, we describe the prediction accuracy of one-class Support Vector Machine (SVM) when machining workpieces of multiple materials using tool. As a result, comparing the results of prediction using all features with those using 5 features from the sensor and 20 features from the NC controller, the latter was confirmed to have higher prediction accuracy.

Keywords: tool wear prediction, unsupervised learning, one-class Support Vector Machine.

1. Introduction

In recent years, as represented by Industry 4.0 and Digital Transformation (DX), the use of digital technology in industry has been advancing, and the importance of technologies to utilize various types of sensor data has been increasing. In the machining process, tools are gradually worn during machining. When tool wear exceeds the standard value, it not only significantly affects the machining quality of the workpiece but can also lead to tool breakage and machine tool failure. When a machine tool breaks down, the production process must be stopped, resulting in increased downtime.

As for the total downtime during the machining process, the largest portion of downtime is due to problems caused by tool life, with approximately 20% of downtime caused by broken tools. In addition, continued machining with worn tools also affects the surface quality of the workpiece. Care should be taken regarding the timing of tool change because premature tool change can lead to lower productivity and higher costs. In actual manufacturing sites, tools are often replaced after processing a certain number of parts or a certain amount of time has elapsed, and tools that can still be used are discarded. Therefore, it is important to develop a tool condition monitoring system that monitors the wear condition of cutting tools during machining and to replace cutting tools at the appropriate time to improve productivity and machining quality [1-3]. In addition to productivity improvement and cost reduction, predictive maintenance can be expected to prevent machine damage and deterioration of consumable parts. Various methods have been proposed for predicting tool wear using machine learning [4], but these methods require a large number of machining experiments because of the need for training data. Therefore, we propose a method for estimating tool wear using a one-class Support Vector Machine (SVM) [5] that does not require prior learning. One-class SVM are trained using only data from the early stages of machining, and outliers are calculated using sensor data from the progression of wear. This outlier and information on each cutting condition, tool and workpiece material, etc. are used to estimate tool wear.

2. Experimental data acquisition method

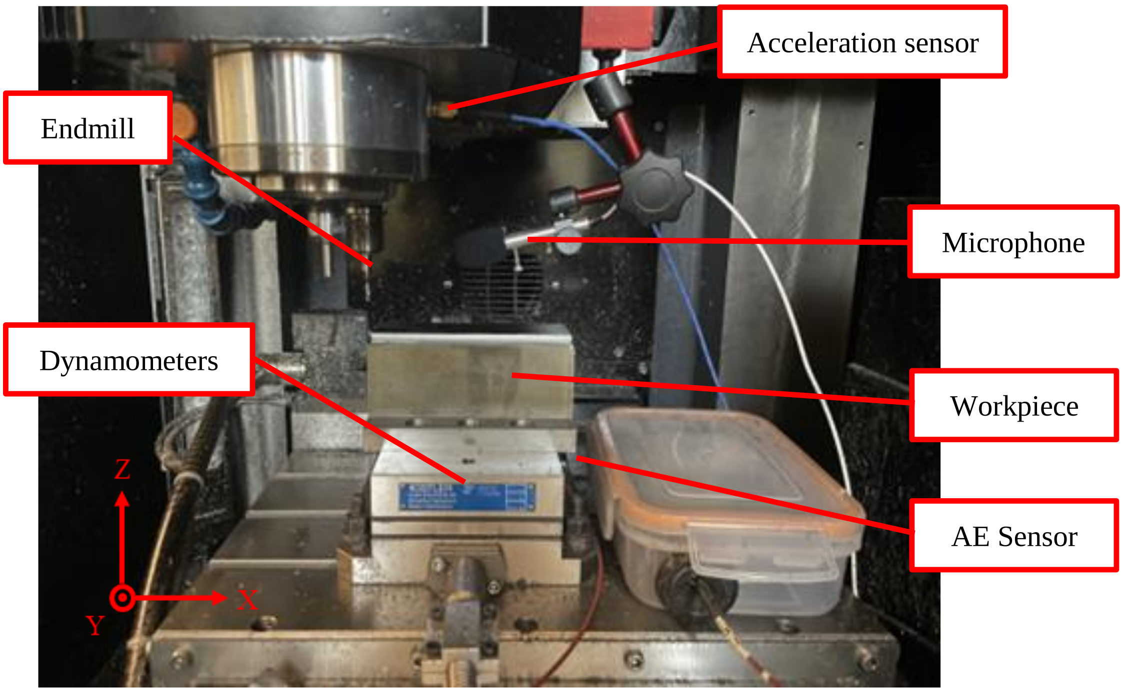

Figure 1. Experimental apparatus.

Figure 1 shows the experimental apparatus. Machining experiments were conducted by attaching multiple sensors to machine tools, and the data was used to develop signal processing techniques and machine learning models. A multi-component dynamometer was installed on the linear motor stage, and the workpiece was bolted to the top of the dynamometer. The dynamometer is used to measure cutting resistance in the X, Y and Z directions during machining. A high-sensitivity AE sensor is mounted on the side of the top plate of the dynamometer to acquire AE waves generated by friction and plastic deformation of the workpiece during cutting. A 3-axis accelerometer is mounted on the spindle housing to measure the vibration of the spindle in the X, Y and Z directions. The microphone is mounted using a magnetic base and directed toward the tool tip to record the sound produced by the cutting process. Each sensor signal was acquired at a sampling frequency of 1 MHz. The torque and motor current of the XYZ linear motor stage, spindle torque, and spindle power consumption signals were obtained from the NC controller at a sampling frequency of 1 kHz.

The workpiece materials are C45 and SKD11, and machining was performed with a two-flute square endmill. Its diameter is 3 mm. Endmill side cutting experiments were conducted with a radial depth of cut of 0.1 mm, an axial depth of cut of 3 mm. The endmill was fed to perform cutting downward. The width of the workpiece is 120 mm, and cutting over this width is defined as one cutting pass. The flank wear width was measured from the microscope image. A two-flute end mill made of high-speed steel was used in the machining experiments. In the case of C45 workpiece, the workpiece was machined at a rotational speed of 2800 rpm and a feed rate of 200 mm/min. In the case of SKD11 workpiece, the workpiece was cut under two conditions: a rotational speed of 1400 rpm and a feed rate of 45 mm/min, and a rotational speed of 1400 rpm and a feed rate of 90 mm/min. Three cutting experiments were conducted for each condition, for a total of nine data sets.

3. Feature extraction

In order to make highly accurate predictions using machine learning, it is important to extract and select information from the raw data that is highly correlated with tool wear. In this study, features were obtained from both the time domain and the frequency domain. A total of 30 features were obtained: 9 time-domain features from the raw data and 21 frequency-domain features from the frequency spectrum obtained by FFT. Table 1 shows a list of the features.

For each of the above 16 sensor signals and NC controllers, 30 features shown in Table 1 were calculated, yielding a total of 480 features. Ten features of tool and workpiece material properties and machining conditions were added to the 480 features to obtain a total of 490 features. In addition, the importance of the features was calculated by the gradient boosting decision tree from 490 features. Five features obtained from each sensor and 20 features obtained from the NC controller were used, starting with the most important ones. In addition, 10 features of mechanical property of workpiece and cutting condition are used for all predictions.

Table 1. List of features.

Time domain	RMS, Variance, Standard deviation, Kurtosis, Skewness, Shape Factor, Peak to Peak value, Crest Factor
Frequency domain	Spectral mean, Spectral RMS, Spectral Variance, Spectral Standard deviation, Spectral Kurtosis, Spectral Skewness, Spectral Shape Factor, Spectral Peak to Peak value, Spectral Crest Factor, FFT0(dc), FFT(1-50kHz), FFT (50-100kHz), FFT (100-150kHz), FFT (150-200kHz), FFT (200-250kHz), FFT (250-300kHz), FFT (300-350kHz), FFT (350-400kHz), FFT (400-450kHz), FFT (450-500kHz), FFT (90-100Hz)
Mechanical property of workpiece	Vickers Hardness, Tensile Strength, Thermal Conductivity, Specific Cutting Force
Cutting condition	Rotational speed, Cutting speed, Feed rate, Feed per tooth

4. One-class SVM

One-class SVM is an outlier detection method using Support Vector Machine [5]. One-class SVM creates a boundary around normal data and calculates the distance from this boundary as the degree of abnormality. In this study, only the first data feature of each experiment was used to create model bounds. Using this model, we calculated the degree of abnormality a obtained during the machining experiment. Figure 2 shows the degree of abnormality calculated by One-class SVM using all features for a workpiece material of C45. The hyperparameters of the One-class SVM were set to nu = 0.01 and gamma = 0.00001, which was the most accurate through trial and error simulation. As shown in Figure 2, the degree of abnormality appears as a negative value, with the greater the degree of abnormality, the closer it is to -1. Therefore, to estimate the flank wear width, the degree of abnormality a is multiplied by a negative coefficient k and fitted to the experimentally obtained wear curve using the least-squares method. The flank wear width V_{Bk} wear is then predicted using equation (1).

$$V_{Bk} = ka \tag{1}$$

In this study, the coefficient k was identified using the C45 data. Figures 3 and 4 show a comparison of the wear widths estimated using equation (1) and those obtained from experiments. Table 2 shows the RMSE values calculated using the coefficient of C45. Comparing Figures 3 and 4, it can be seen that the error in the SKD11 results in Figure 4 increases considerably when the number of cutting passes exceeds 20. This may be due to the fact that the equation (1) does not include parameters related to cutting conditions and workpiece material. Therefore, we propose the following method to enable prediction even for different workpiece materials and cutting conditions. If the parameters are defined as the coefficient of the tool and workpiece combination w, the cutting speed v, the cutting speed index n_1, the feed f, the feed index n_2, the depth of cut t, and the depth of cut index n_3, then tool wear is proportional to the cutting-related parameters $w\left(\frac{1}{v^{\frac{1}{n_1}}}\right)\left(\frac{1}{f^{\frac{1}{n_2}}}\right)\left(\frac{1}{t^{\frac{1}{n_3}}}\right)$ [6]. Therefore, as shown in equation (2), the value obtained by multiplying the degree of abnormality by the above parameter is used as an estimate of tool flank wear V_{Bw}. Identify the parameters n_1, n_2, and n_3 using one experimental data set of C45 workpiece.

$$V_{Bw} = aw\left(\frac{1}{v^{\frac{1}{n_1}}}\right)\left(\frac{1}{f^{\frac{1}{n_2}}}\right)\left(\frac{1}{t^{\frac{1}{n_3}}}\right) \tag{2}$$

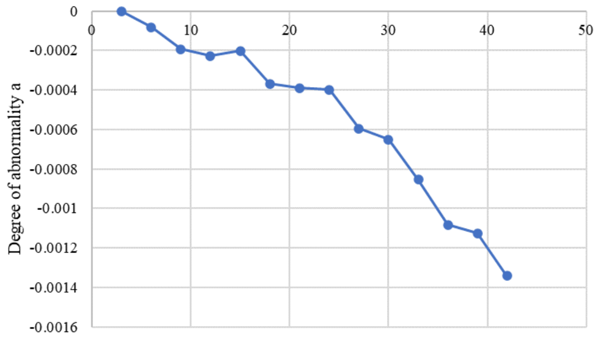

Figure 2. Degree of abnormality calculated using all features.

(C45, 2800 rpm, 200 mm/min)

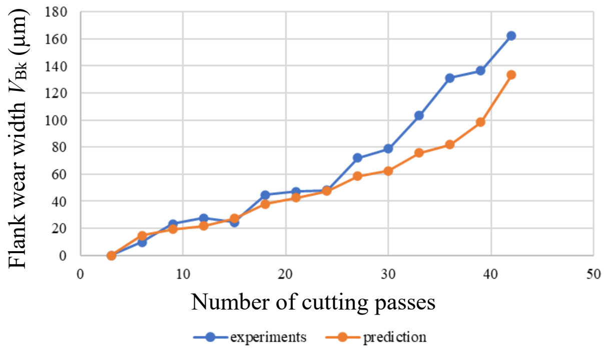

Figure 3. Comparison of predicted and experimental wear of C45.

(C45, 2800 rpm, 200 mm/min)

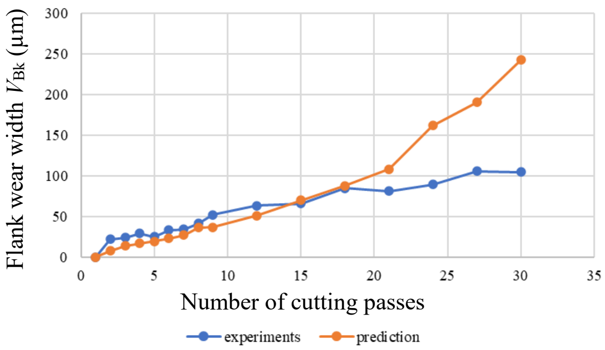

Figure 4. Comparison of predicted and experimental wear of SKD11.

(SKD11, 1400 rpm, 45 mm/min)

Table 2. RMSE calculated using the coefficient of C45.

Workpiece	RMSE
C45	19.3
SKD11	79.7

5. Prediction of tool wear using one-class SVM

Using the features selected in the previous section, the degree of abnormality is calculated from the one-class SVM, and the tool flank wear width V_{Bw} is predicted using equation (2). The degree of abnormality was calculated using the features shown in Table 3, and the wear width was estimated using equation (2). Table 3 shows the Root Mean Squared Error (RMSE) values of the predicted results. A comparison of the experimentally measured and estimated wear widths is shown in Figures 5 to 10. Figures 5, 7, and 9, the degree of abnormality for the three experimental conditions were calculated using five sensor features and 20 NC controller features, and the wear width was predicted using equation (2). Figures 6, 8, and 10 predicted the wear width by calculating the degree of abnormality for the three experimental conditions using all features. When all the features are used and predicted, the prediction for the workpiece material SKD11 with a feed rate of 45 mm/min deviates significantly. The cause of this is currently unknown, but it is conceivable that overlearning may be occurring due to the large number of features. If the workpiece material and tool combination changes in this method, it is necessary to conduct at least one machining experiment to obtain data and determine the coefficient w in equation (2). It was confirmed that once the coefficients between the workpiece material and the tool were determined, the flank wear width could be predicted appropriately even if the cutting conditions changed.

Table 3. RMSE comparison by selected features.

Features	C45 (2800rpm,200mm/min)	SKD11 (1400rpm,45mm/min)	SKD11 (1400rpm,90mm/min)
All features	7.4	34.8	9.7
NC-10	15.2	13.1	11.2
Sensor-10	24.1	30.3	16.0
Sensor-5, NC-5	21.5	16.9	13.2
Sensor-5, NC-20	14.0	16.3	8.4
Sensor-10, NC-10	17.6	19.4	12.6
Sensor-10, NC-20	13.7	18.4	9.5

*Features are calculated by gradient boosting decision tree and selected in order of importance.

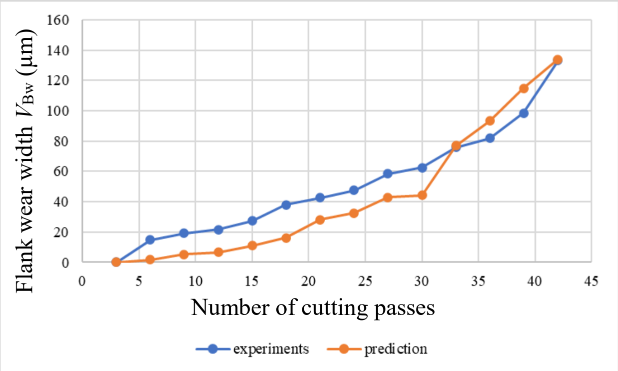

Figure 5. Uses 5 sensors and 20 NC features.
(C45, 2800 rpm, 200 mm/min)

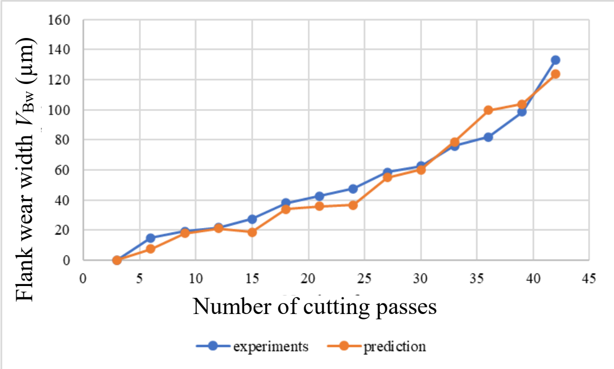

Figure 6. All features used.
(C45, 2800 rpm, 200 mm/min)

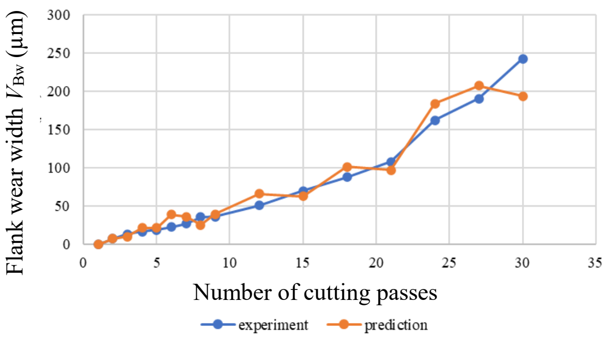

Figure 7. Uses 5 sensors and 20 NC features.
(SKD11, 1400 rpm, 45 mm/min)

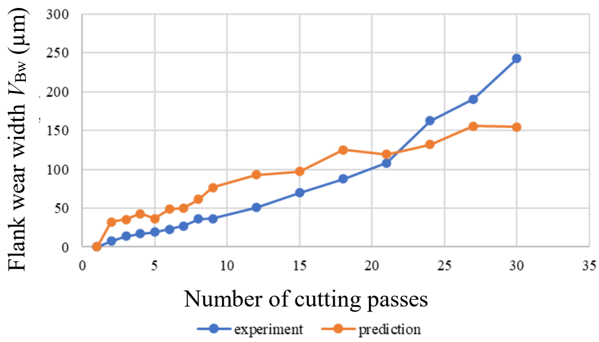

Figure 8. All features used.
(SKD11, 1400 rpm, 45 mm/min)

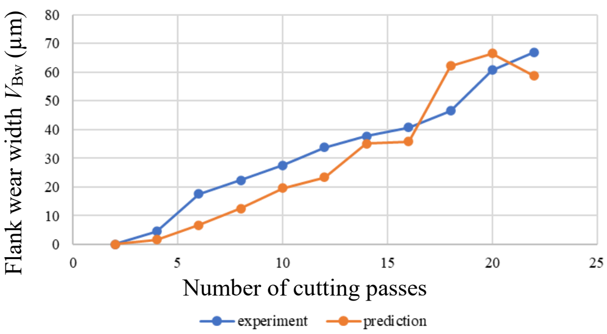

Figure 9. Uses 5 sensors and 20 NC features.
(SKD11, 1400 rpm, 90 mm/min)

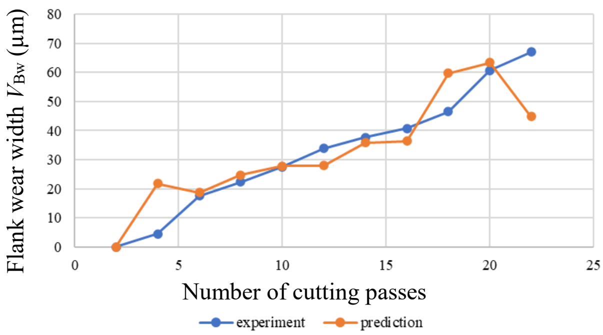

Figure 10. All features used.
(SKD11, 1400 rpm, 90 mm/min)

6. Conclusion

In this study, we used a one-class SVM to predict the flank wear width in unsupervised learning. The following are conclusions from this study. Comparing the results of prediction using all features with those using 5 features from the sensor and 20 features from the NC controller, the latter was confirmed to have higher prediction accuracy. In the future, we plan to investigate ways to predict without any learning or obtaining coefficients in machining experiments.

7. References

[1] Li X, Liu X, Yue C, Liang SY, Wang L. Systematic review on tool breakage monitoring techniques in machining operations. International Journal of Machine Tools and Manufacture. 2022;176.

[2] Teti R, Mourtzis D, D'Addona DM, Caggiano A. Process monitoring of machining. CIRP Annals. 2022;71:529-52.

[3] Ntemi M, Paraschos S, Karakostas A, Gialampoukidis I, Vrochidis S, Kompatsiaris I. Infrastructure monitoring and quality diagnosis in CNC machining: A review. Cirp J Manuf Sci Tec. 2022;38:631-49.

[4] Xiao W, Huang J, Wang B, Ji H. A systematic review of artificial intelligence in the detection of cutting tool breakage in machining operations. Measurement. 2022;190.

[5] Manevitz LM, Yousef, M. One-class svms for document classification. Journal of Machine Learning Research. 2002;2:139-54.

[6] Okuyama S, Une, A.., Yui, A., Suzuki, H. Fundamentals of Machining Technology. Corona Publishing Co LTD. 2013.

AMM0016

Investigate Stress on the Components of the Bolted Rail Joint by Considering the Effects of Bolt Preloading

Sai Kham Le[1] and Jittraporn Wongsa-Ngam[1,*]

[1]Department of Mechanical Engineering, School of Engineering, King Mongkut's Institute of Technology Ladkrabang, Bangkok 10520, Thailand.

* Corresponding Author: jittraporn.wo@kmitl.ac.th

Abstract. The bolted rail joint is used to line up the two rail ends for smooth running of the train wheel. The bolted joint consists of many important components including rail, fishplate, bolt, and nut. Due to the rail joint assembled with many components, complex interaction happens between the components under the repeated wheel load. Consequently, the components will damage and fail. In this study, the bolted rail joint components are modeled as a 3D model in Abaqus CAE. The finite element numerical simulation is carried out for the bolted rail joint under the static wheel load. The von Misses stress on each component is investigated when the bolt is tightened in different preloading conditions (loosened, normal, and overtightened). The results show that the higher stress magnitude occurs on the rail upper fillet and rail-end bolt, on the top of the fishplate, and on the bolt head-to-shank when the bolt preloading condition is loosened.

Keywords: Rail, Fishplates, Bolt, Von Mises stress.

1. Introduction

The bolted rail joint is used to connect the two rail ends with two fishplates on both sides and tightened by the bolt. It is widely used in rail transit, crossing, switches, and for temporary usage. The bolted joint is the weakest element in the railway structure due to its imperfection and gap between two rail ends, resulting in the development of higher stress. Then, the rail upper fillet, rail-end bolt hole, fishplate, and bolt will crack and fail under the static and dynamic loads [1, 2]. As a consequence of being defective, it may cause derailment of the carriages.

In relation to the rail damage, Mandal [3] said, the wheel-rail contact impact behavior was the source of railhead defect, wear, and rail end battering in the rail joint. Wen et al. [4] carried out the finite element analysis of the bolted rail joint by considering the effect of axle load and train speed. They found that the higher axle load declined the steel material on the railhead at the rail end due to it accelerating the higher stress and strain, while the train speed has a weak effect on the rail under dynamic load. While the wheel passes over the discontinuous rail joint, the wheel jumps and lands on the railhead even near the end or not, the battering and bending of the rail ends occurs [5]. Moreover, Zhu et al. [6] considered the wheel load to apply on different positions on the rail joint under static wheel load. One is applied on the rail-end bolt hole, while the other is applied on the rail end. They also simulated the rail joint with different cases of fishplates and crossties configurations by using finite element analysis. Their analysis reported that the stresses on the rail-end bolt hole and the upper fillet were increased when the load was applied on the rail end and decreased in the support crosstie. Le and Wongsa-Ngam [7] studied the effect of rail-end bolt hole positions and investigated the stress on the rail upper fillet and rail-end bolt hole at the rail joint. It can be assumed that the applied wheel load position on the rail end is a critical factor in seeing the maximum stress and strain of the rail joint components.

Furthermore, Kataoka et al. [8, 9] studied the effect of different bolt preloading at the rail joint with the applied load on the rail end. They validated the results from the finite element analysis and field test to measure the stresses around the rail bolt holes. Zhu et al. [2] used the rail joint with six and eight bolts tightening, to study the effect of bolt preloading conditions (loosened, standard, and overtightened) in the numerical simulation. They examined the stress distribution in the rail upper fillet, and rail-end bolt hole. The effect of bolt preloading as loosened condition, the stress on the rail upper fillet and the rail-end bolt hole increased. Samantaray et al. [10] also used finite element analysis and considered the effect of bolt preloading as loosened conditions for two bolts at the rail joint under static wheel load. Their study analyzed the stress and deformation on the rail, fishplate, and bolt. The stress increased in the rail-end bolt hole, the middle of the fishplate, and the bolt near to the rail end.

The rail joint with four bolts is widely used in Thailand; however, the stress analysis on the components of the bolted rail joint in cases of with the effect of bolt preloading is limited in recent works. In this present study, the effect of bolt preloading conditions on the bolted rail joint are considered to determine the stress on the components. The bolted rail joint structure is modelled based on the reference data from the State Railway of Thailand (SRT) using 3D finite element models in Abaqus CAE. The finite element analysis (FEA) is performed to study the bolted joint under the static load. The numerical simulation results will present von Mises stress on the rail, fishplate, and bolt as details.

2. FEA Modelling and Methodology

In this study, a 3D finite element Analysis (FEA) was carried out to simulate the bolted rail joint structure. It is based on the existing design of the State of Railway Thailand (SRT). SRT design used four bolts for the assembly of the rail joint components. It comprises BS 100 rail, fishplate, M27 bolt, and concrete sleeper for the rail joint structure. It has a 6 mm gap between two rail ends. The distance between the adjacent sleepers from center to center is 600 mm. The position of the bolted joint is placed between two adjacent sleepers which is called the suspended joint. The length of the rail joint 12 m appropriate for the rail joint analysis in FE simulation [11]. However, the full rail model was considered in this study. The components of the rail, fishplate, bolt, and sleeper were modeled as a 3D solid model in Abaqus CAE. Then, the components of the 3D FE model were assembled as the realistic situation that is now used in SRT. The assembly of 3D bolted rail joint structure is shown in Figure 1(a). All the components material is steel except for the sleeper, which is made of concrete. The mechanical properties of the components of the bolted rail joint are listed in Table 1 [12].

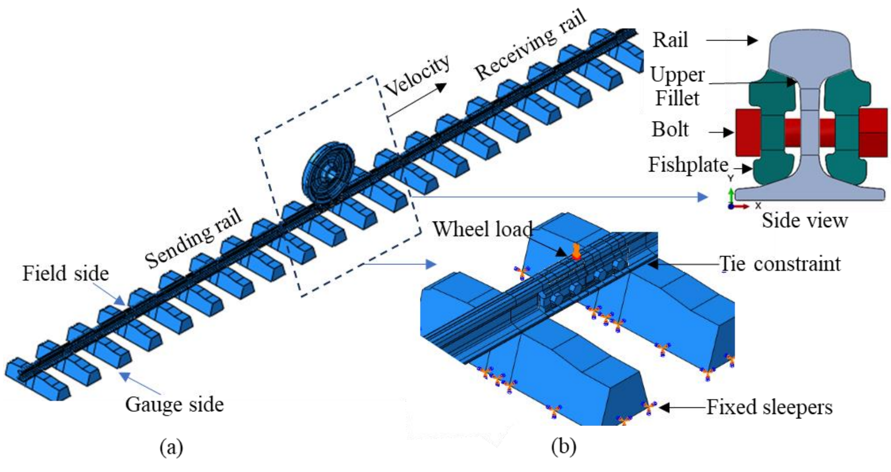

Figure 1. 3D bolted rail joint structure.

Table 1. Mechanical Properties of the Components.

Parts	Young's Modulus (GPa)	Yield Strength (MPa)	Poisson's ratio	Density (kg/m^3)
Rail (BS 100A)	207	640	0.3	7800
Joint bar	207	640	0.3	7800
Nut and bolt	207	640	0.3	7800
Sleeper	40	46.6	0.18	1265

In the load module, two steps of loads were applied to the bolted joint analysis. The bolt preloading equation (1) is considered in step 1 of the numerical simulation [10,11,13]. The bolt preload is

$$P_b = \frac{T}{K_b D} \tag{1}$$

where P_b, T, D, and K_b are the bolt preload, the bolt torque, the bolt diameter, and the bolt coefficient K_b (K_b = 0.19-0.25). The parameters of T, D and K_b were applied to 498 N·m, 25.4 mm, and 0.2, respectively. Finally, the bolt preloading value equals 97.9 kN which is in the range of (89.0-133.4 kN) of AREMA in Chapter 5, Section 5.5 [14]. According to the purpose of this study is to investigate the stress on the components based on the effect of bolt preloading conditions. The torques of 136 N·m and 791 N·m are also added to joint for the analysis, while the other parameters are still the same. All the bolt preloading conditions are listed in Table 2. In each condition analysis, the bolt load is applied to each bolt axially in the finite element numerical simulation.

Table 2. Bolt Preloading.

Bolt preloading conditions	
Loosened	26.7 kN
Normal	97.9 kN
Overtightened	155.7 kN

The static wheel load is considered in step 2 of the numerical simulation. The wheel load is 20 tons per axial of the existing design of SRT. Due to the symmetry of the railroad, only half of a straight railroad was considered in this study. Therefore, the total wheel load for a single rail is 10 tons and increased by a dynamic factor of 1.3 [8]. Then, the wheel load is transformed into a wheel pressure load according to the Hertz wheel-rail contact patch [3]. The wheel pressure load is applied on the sending rail end as shown in Figure 1(b).

For the FE simulation, the contact interaction between the bolted joint components were used the surface-to-surface contact standard in the default system. The contact friction of 0.3 is applied. The boundary conditions of the bolted rail joint simulation are displayed in Figure 1(b). Here, tie constraint was used between the rail and rail-pad. The constraint of the rail is fixed in X (lateral) and Z (longitudinal) directions at the rail end away from the joint to prevent solid model motions and considered free movement in Y (vertical) direction at the joint to know the rail joint performance effect to stress. The solid mesh model used an eight-node fully integrated trilinear brick element, C3D8. The advantage of this element is that it does not suffer from volumetric locking and has no problem with rail incompressibility [3]. The mesh model of the bolted rail joint is shown in Figure 2. The mesh size in the applied load location is considered as a high mesh density for accurate results. However, the mesh size at the contact between the rail and the fishplate is created as a fine mesh. Furthermore, the mesh size away from the rail joint region is considered as a coarse mesh. The total elements and nodes of the models are 1776470 and 1956866, respectively. The successful analysis of all the numerical simulations is discussed in the following sections.

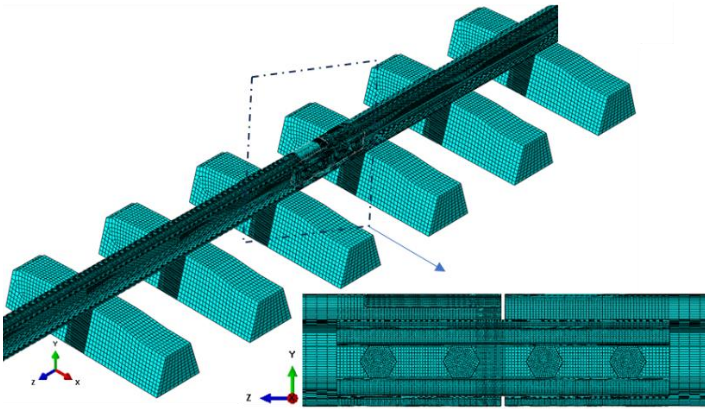

Figure 2. A mesh model of the bolted rail joint.

3. Finite Element Analysis Results and Discussion

The von Misses stresses of the rail, fishplate, and bolt influenced by three different preloading of loosened, normal, and overtightened conditions are performed by using 3D finite element analysis. The stress distributions on the individual components of the bolted rail joint are discussed in the following subsections.

3.1. Stress of the rail

The stress distributions on the sending rail with different preloading conditions of loosened, normal and overtightened are shown in Figure 3. The results show that higher stress occurs around the holes, especially at the rail-end bolt hole for all three preloading conditions. However, the values of stress are different with different preloading conditions in which the highest stress values are found in the case of loosened. For detail inspection, the values are recorded along two directions of 0° and 45° as same as the previous work by Kataoka et al [7]. It is found that the maximum stress on the rail-end bolt hole is 380 MPa (at the edge of 0°) and 157 MPa (at the edge of 45°) for loosened, 218 MPa (at the edge of 0°) and 105 MPa (at the edge of 45°) for normal, and 354 MPa (at the edge of 0°) and 146 MPa (at the edge of 45°) for overtightened. The stress distributions around the hole of the sending rail have the same tendency as presented by Kataoka et al [7]. They found that the maximum stress on the rail-end bolt hole was 235 MPa at the edge of 0° and 145 MPa at the edge of 45° for normal preloading conditions.

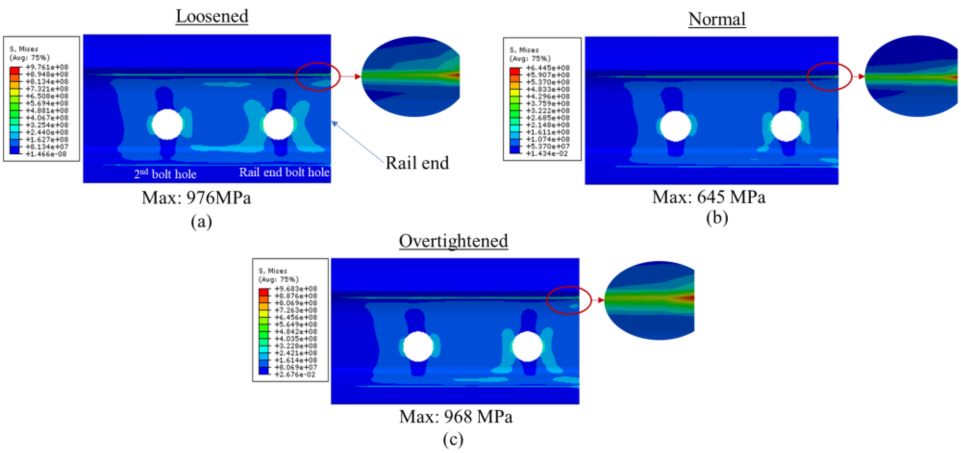

Figure 3. The distributions of Von Mises stress on the sending rail with different preloading conditions (a) loosened, (b) normal, and (c) overtightened.

Another critical stress area is on the upper fillet of the rail end as shown in Figure 3 indicated by red circles. The higher stress values are due to the contact load between the rail end edge and fishplate during the load applied over the rail end. The maximum stress on the upper fillet rail end is 976 MPa for loosened, 645 MPa for normal, and 968 MPa for overtightened, respectively. The maximum stress location may initiate the fatigue crack of the rail [4].

3.2. Stress of the fishplate

The stress distribution on the fishplate under different bolt preloading conditions is presented in Figure 4. The stress is higher at the contact regions between the rail and the fishplate, and between the fishplate and the bolt. The maximum stress occurs on the top of the fishplate where the rail end edge was contacted to it under the wheel load. The maximum stress on the top of the fishplate is 831 MPa for loosened, 430 MPa for normal, and 660 MPa for overtightened, respectively. The maximum stress is situated on the top of the fishplate which is related to the Gallou et al. work [13].

3.3. Stress of the bolt

The stress distribution on the bolt under different preloading conditions is shown in Figure 5. This is the bolt that nearer to the rail gap. The larger stress occurs at the bolt head-to-shank where is the contact edge between the bolt hole and the fishplate. The stress distribution regions and the larger stress location is related to [10,15] works. The maximum stress of that area is 585 MPa for loosened, 364 MPa for normal, and 581 MPa for overtightened, respectively.

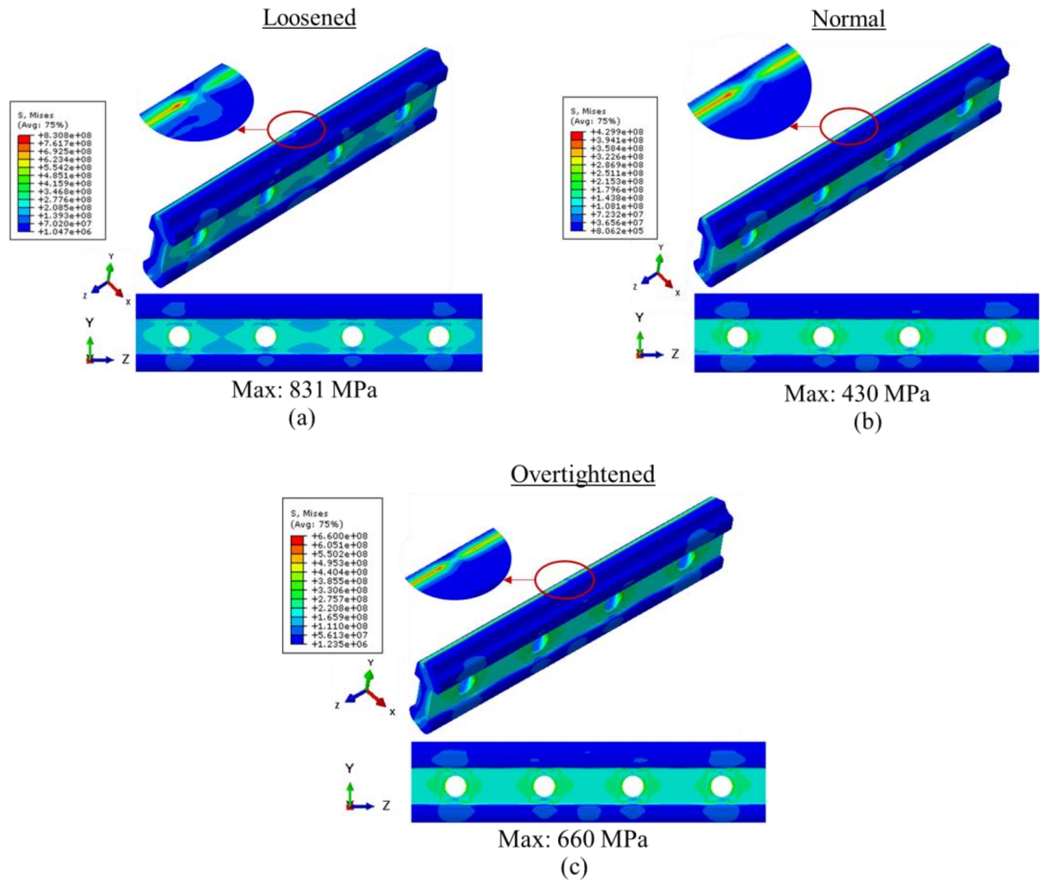

Figure 4. Von Mises stress of the fishplate (a) loosened, (b) normal, and (c) overtightened.

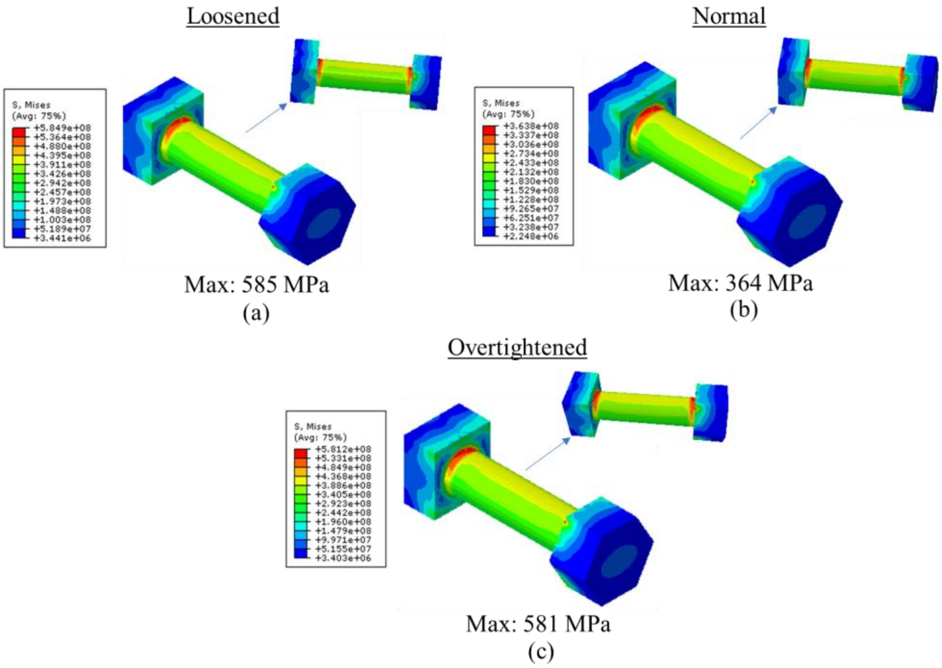

Figure 5. Von Mises stress of the bolt (a) loosened, (b) normal, and (c) overtightened.

The analysis of von Mises stress on the components of the bolted rail joint based on the effect of different bolt preloading conditions is summarized in Table 3. This table purposes to highlight the maximum stress from findings in each component. Table 3 presents the highest stress of the bolt is 585 MPa which is located on the bolt head to shank in loosened condition. Furthermore, the highest stress of the fishplate is 831 MPa. This stress is on the top of the fishplate, where it is in contact with the rail end edge in a loosened condition. In addition, the analysis also found that the higher stress on the rail-end bolt hole and the upper fillet is 380 MPa and 976 MPa when the study was simulated as a loosened bolt preloading condition. Overall, when analyzing the bolted rail joint components, the maximum stress occurs in the upper fillet rail end in the loosened condition. Because the rail joint reduces the stiffness in the loosened state of the bolt. This leads to the slippage of the fasteners or failure of the bolt strength, which negatively affects the main structure under the loads. As a result, the stresses on the components of the rail joint structure in the contact area are increased. While the other preloading conditions, the bolted rail joint is good in stiffness. Therefore, it was known that the effect of preload for the bolt is also very important for the components of the rail joint under the loads.

Table 3. Maximum Stress on the Components.

Components	Higher Stress	Location	Conditions
Rail	976 MPa	At the upper fillet	Loosened
	380 MPa	At the rail-end bolt hole edge of 0°	Loosened
Fishplate	831 MPa	At the top of the fishplate, where is in contact with the rail end edge	Loosened
Bolt	585 MPa	At the bolt head to shank	Loosened

4. Results Validation

The von Mises stresses of the bolted rail joint components under different preloading conditions of the bolt in the finite element simulation are compared with the model recently developed by Samantaray et al. [10]. When the bolt was tightened as normal condition, the stresses on the fishplate (430 MPa) and bolt (364 MPa) agree well with those of Samantaray et al. [10]. In this condition, the stress is in the region of the confined yield strength, as shown in Table 1. On the other hand, if the bolt was tightened under the other two conditions, the stresses on the rail-end bolt hole and the bolt are under the yield strength, but the stresses on the upper fillet and the top of the fishplate are over the yield strength. This fact relates to Miao et al. [16], "Loosening or overtightening of a bolt can lead to connector slippage or failure of bolt strength, both are harmful to the main structure."

5. Conclusion

Finite element numerical simulation of the bolted rail joint has been successfully done. The effect of bolt preloading conditions was considered to the bolt for the bolted rail joint study under static wheel load. In post-processing of analysis, the FE numerical simulation results were studied the von Mises stress on the components such as rail, fishplate, and bolt of the bolted rail joint. In this finite element analysis, the main results are drawn as follows:

(1) The von Mises stress on the rail-end bolt hole and the upper fillet was increased when the bolt preloading was loosened. Furthermore, the stress on the top of the fishplate and the bolt also increased. The stress of the individual components was decreased when the bolt was tightened as normal conditions.

(2) By considering the bolt overtightened, it raised the stress on the contact components of the rail joint, but the stress magnitude was not reached to the level of loosened condition. The occurring maximum stress location for every component is possible to cause fatigue crack.

The future work will study the effect of bolt preloading on the bolted rail joint under transient conditions by using finite element analysis. The main finding will be studied the stress on the rail head near the gap, the upper fillet and the rail-end bolt hole where was found the crack problem in many recent works to enhance the lifetime of the rail.

6. Acknowledgments

This work was supported by King Mongkut's Institute of Technology Ladkrabang (KMITL).

7. References

[1] Zhu, K., Edwards, R., Qian, Y., & Andrawes, B. O. (2016). Fatigue analysis of rail-head-to-web fillet at bolted rail joint under various impact wheel load factors and support configurations. *Proc. of the 2016 joint rail Conf. (JRC2016).*

[2] Zhu, K., Edwards, J. R., Qian, Y., & Andrawes, B. (2016). Finite element analysis of the effects of bolt condition on bolted rail joint stresses. *Journal of Transportation Research Board. No. 2545.* 36-45.

[3] Mandal, N. K. (2016). Ratchetting damage of railhead material of gapped rail joints with reference to free rail end effects. *Journal of Rail and Rapid Transit, 0*(0), 1-15.

[4] Wen, Z., Jin, X., & Zhang, W. (2003). Contact-impact stress analysis of rail joint region using the dynamic finite method. *Wear, 258*(2005), 1301-1309.

[5] Keshavarzian, H., & Nesari, T. (2017), Reliability analysis for cyclic fatigue life prediction in railroad bolt hole. International Journal of Civil, Environmental, Structural, Construction and Architectural Engineering. (Vol. 11, p. 1173-1178).

[6] Zhu, K., Qian, Y., Edwards, J. R., & Andrawes, B. O. (2017). Finite element analysis of rail-end bolt hole and fillet stress on bolted rail joints. *Journal of Transportation Research Board. No. 2607.* 33-42.

[7] Le, S. K., & Wongsa-Ngam, J. (2021). Stress analysis in the rail upper fillet and rail-end bolt hole at the rail joint. *IOP Conf. Ser.: Mater. Sci. Eng. 1137*(2021), 012050.

[8] Kataoka, H., ABE, N., & Wakatsuki, O. (2002). Evaluation of service life of jointed rails. *QR of RTRI* (Vol. 43, p. 101-106).

[9] Kataoka, H., Oikawa, Y., & Wakatsuki, O. (2005). Dynamic analysis of stresses and evaluation of service life of jointed rails. *QR of RTRI* (Vol. 46, p. 250-255).

[10] Samantaray, S. K., Mittal, S. K., Mahapatra, P., & Kumar, S. (2019). Assessing the flexion behavior of bolted rail joint using finite element analysis. *Journal of Engineering Failure Analysis, 104*(2019), 1002-1013.

[11] Mandal, N. K., & Dhanasekar, M. (2013). Sub-modelling for the ratchetting failure of insulated rail joints. *International Journal of Mechanical Sciences, 75*(2013), 110-122.
[12] Wondimu, A. Alemu, N., & Sivaprakasam, P. (2020). Study on effect of dynamic load on rail joint bar by finite element method (FEM). In Taylor & Francis Proc. *Advances in Materials and Processing Technologies*.
[13] Lanham, M. (2005). American railway engineering and Maintenance-of-way association (AREMA).
[14] Gallou, M., Frost, M., EI-Hamalawi., & Hardwick, C. (2019). Assessing the deflection behavior of mechanical and insulated rail joints through finite element analysis.
[15] Ding, K., & Dhanasekar, M. (2006). Flexural behavior of bonded-bolted butt joints due to bolt looseness. *Journal of Advances in Engineering Software*, *38*(2007), 596-606.
[16] Miao, R., Shen, R., Zhang, S., & Xue, S. (2020). A review of bolt tightening force measurement and loosening detection. *Journal of Sensors*, 20 (2020), 3165.

AMM0017

A study on the effects of chromium and niobium additions in super-alloyed steel

Kawin Jewsuwun[1,*] and Prayoon Surin[2]

[1]Department of Advanced Manufacturing Technology, Faculty of Engineering, Pathumwan Institute of Technology, Bangkok, Thailand
[2]Department of Industrial Engineering, Faculty of Engineering, Pathumwan Institute of Technology, Bangkok, Thailand

* Corresponding Author: kawin.jew@gmail.com, prayoon99@gmail.com

Abstract. The research aims to analyze the effects of adding chromium (Cr) and niobium (Nb) on the microstructure and mechanical properties of super-alloyed steel. The investigation of the grain structure of these super-alloyed steels commences with the introduction of chromium and niobium to the test specimens. Subsequently, the specimens are annealed at temperatures of 900°C and 1000°C for durations of 1, 2, 3, and 4 hours. Following the heat treatment process, the specimens undergo micro-hardness testing and are evaluated using scanning electron microscopy (SEM). The outcomes of the research reveal a notable increase in directional stiffness spanning the entire casting area, contributing to a corresponding rise in hardness values. This augmentation in hardness concurrently leads to enhancements in the material's mechanical properties. These improvements and alterations in the material's properties confer increased versatility upon super-alloyed steels.

Keywords: Chromium (Cr), Niobium (Nb), Niobium (Nb), Micro-hardness, Scanning electron microscopy, Microstructure, Mechanical properties.

1. Introduction

Super alloyed steels are extensively utilized in applications requiring high mechanical performance and the ability to withstand wear and elevated temperatures. The mechanical properties of such materials are directly influenced by their microstructure and the incorporation of alloying elements [1]. The development of the microstructure involves the introduction of key alloying elements like Cr, Mn, B, Nb, and Er into super alloyed steel [2-4]. For instance, niobium is often introduced to enhance microstructural stability at elevated temperatures. The larger atomic size of niobium, compared to iron, leads to a delay in recrystallization [5]. This phenomenon promotes recrystallization at higher temperatures due to the presence of precipitated niobium, which retards the phase transition to a lower temperature range. Consequently, the mechanical properties of super alloyed steel are improved [6-8].

In a study by J. Opapaiboon et al. [9], the impact of chromium content on the heat treatment behavior of multi-alloyed white cast iron was investigated. Varying the Cr content from 3% to 9%, the specimens were subjected to hardening within the austenitic temperature range of 1323 to 1373 K. Subsequent annealing led to an increase in hardness, peaking at 5% Cr content, and gradually diminishing as Cr content increased. The highest hardness was achieved through tempering between 773 and 798 K, favoring the lower temperature range. Higher Cr contents (above 6%) resulted in increased hardness when hardened from elevated austenitization temperatures.

M. Ali et al. [10] examined the influence of boron and the combined addition of boron and niobium on phase transition behavior, resultant microstructure, and mechanical properties of low carbon steels. The findings revealed that the incorporation of boron, either alone or in combination with niobium, elevated the critical transition temperature across the critical range. The addition of boron alongside niobium lowered the initial transition temperature of bainite, whereas the addition of boron alone had marginal or negligible effects. While the hardness value remained relatively unaffected by the addition of boron alone, it led to higher tensile strength (UTS), yield strength (YS), and elongation to rupture strength. The inclusion of boron alongside niobium marginally increased ultimate tensile strength and strength. Generally, both boron and the combined boron-niobium addition resulted in reduced impact strength.

In another study by W. Sckudlarek et al. [11], the effect of niobium doping on austempering temperature was explored in ductile cast iron, analyzing its microstructure and mechanical properties. The cast iron underwent austempering at two different temperatures: 320°C and 360°C for durations of 15, 30, 60, and 90 minutes. The graphite distribution exhibited homogeneity, maintaining over 90% globularization, and contributed to an increased volume fraction of pearlite. This led to the formation of niobium carbide clusters dispersed within the matrix and graphite. Additionally, this promoted enhanced strength, tensile strength, and decreased elongation rate.

The objective of this research was to enhance the microstructure and mechanical properties of super-alloyed steel. By selectively introducing chromium (Cr) and niobium (Nb) and subsequently subjecting the material to baking at 900°C and 1000°C for 1, 2, 3, and 4 hours respectively, this study provides insights that could potentially find application in future industrial endeavors.

2. Experiment

2.1. Material

The super- alloyed steels used in the experiments contained chemical compounds as shown in Table 1. The specimens' structures were subsequently heat-treated at 1500 °C for 4 hours and allowed to cool in air. Following this, they were annealed at 900 °C and 1000 °C for 1, 2, 3, and 4 hours, and then allowed to cool in air. The specimens were first rough-polished using 120, 200, 400, 700 and 1000 grit sandpaper, followed by polishing with 8, 4.5 and 1-micron diamond powder. Subsequently, the specimen surfaces were etching the surface of the workpiece with 2 solutions: 50 ml of hydrochloric acid solution mixed with 10 g of sodium meta- bisulfite in 100 ml of distilled water. to reveal the microstructure of the workpiece. The microstructures of the specimens were then analyzed using scanning electron microscopy. Vickers overall hardness tests were conducted on specimens that had not undergone the surface etching process. A diamond indenter with a load of 30 kgf was applied for 15 seconds, utilizing 9 compression points per specimen. The obtained values were averaged to determine the microhardness through the Vickers test. On the other hand, specimens that had undergone the surface etching process were used for the hardness tests. A diamond indenter with a load of 100 gf was applied for 15 seconds, using 9 compression points per specimen. The obtained values were averaged to determine the microhardness as well.

Table 1. Chemical composition of the super-alloyed steels used in the experiment.

Element		**Element**	
C	2.9242	**Ni**	0.2611
Si	1.8013	**Cr**	21.1092
Mn	0.3417	**Mo**	1.5024
P	0.0443	**Cu**	0.6227
S	0.0149	**Nb**	2.8856

3. Result and Discussions

3.1. Hardness

From the comprehensive hardness testing of the restructured super-alloy steel, it was observed that implementing a heat treatment to modify the structure led to an increase in overall hardness. This increase in overall hardness was particularly noticeable when comparing the results obtained at 1000°C and 900°C, as illustrated in Figure 1. Additionally, there was a rise in micro-hardness at 900°C., the micro-hardness was found to be at its highest during the 3-hour and 4-hour tempering periods, with niobium (Nb) exhibiting the greatest hardness, as depicted in Figure 2. On the other hand, at 1000°C during the 3 h tempering period, both chromium (Cr) and niobium (Nb) had the highest hardness as shown in Figure 3. However, it's noteworthy that at a temperature of 1000°C, extending the tempering time beyond 3 hours resulted in a decrease in the hardness of the super-alloy steel. From the experimental results, it was found that when the tempering periods was longer, the hardness increased slightly. Because the tempering time is too short, it produces a small amount of carbide.

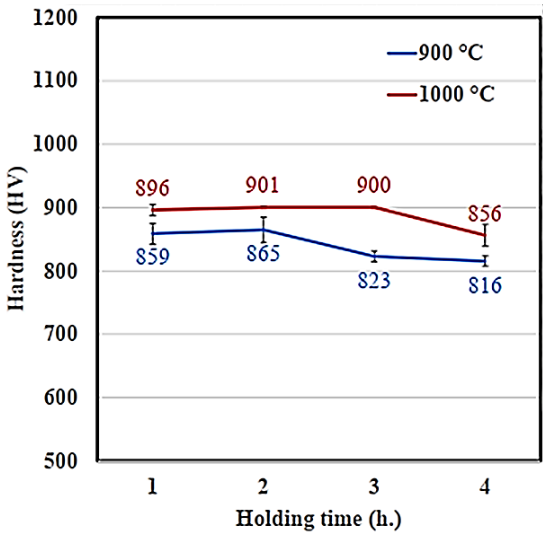

Figure 1. Comparing hardness values of specimens at 900°C and 1000°C.

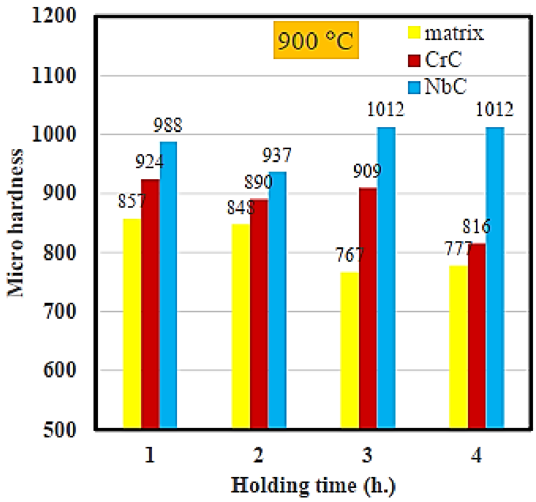

Figure 2. Tempering at 900 ^{o}C

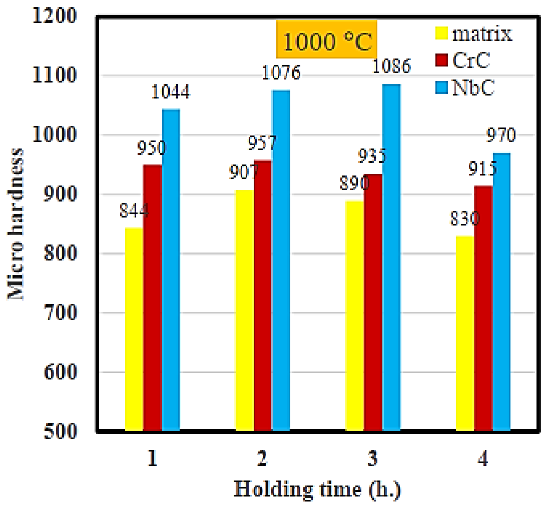

Figure 3. Tempering at 1000 ^{o}C

3.2. Micro-structure

Upon examining the microstructure using scanning electron microscopy, it was observed that the structure of the modified super-alloy steel exhibited a large branching pattern. The microstructure of the super- alloy steel before heat treatment is shown in Figure 4a. It can be observed that the improved microstructure appears as white bars distributed in the super-alloy steel. Figure 4b shows the SEM image of the microstructure of the modified super- alloy steel at 1000x magnification. Subsequent to undergoing the heat treatment process, the structure of the super-alloyed steel at 900°C, with a tempering time of 2 hours, began to transform into smaller branches over a span of 4 hours as shown in Figure 5. However, when subjected to a temperature of 1000°C, an extended tempering time resulted in a higher solubilization of Niobium as shown in Figure 6. Consequently, the hardness of the super- alloy steel increased proportionately. Nonetheless, the hardness exhibited a decline when the tempering time exceeded 3 hours. After improving the structure at 900 ^{o}C, it was found that the chromium element had less dispersion but still retained the highest hardness after tempering at 3 h. At 1000 ^{o}C, a crystalline structure of chromium was formed resulting in the structure being the hardest at 3 h after tempering.

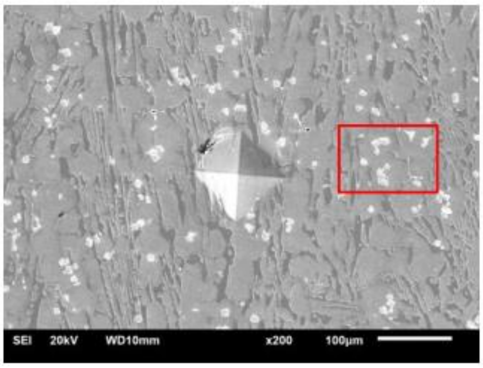

(a)

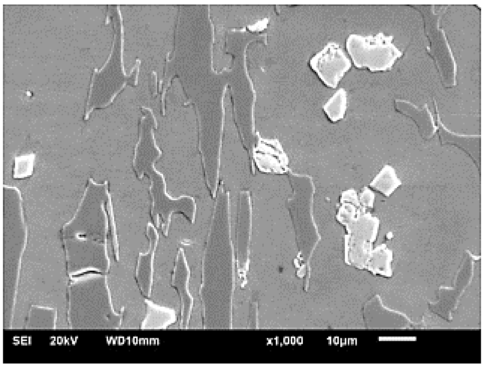

(b)

Figure 4. SEM images showing the microstructure of modified super-alloy steel with magnification (a) 200x (b) 1000x.

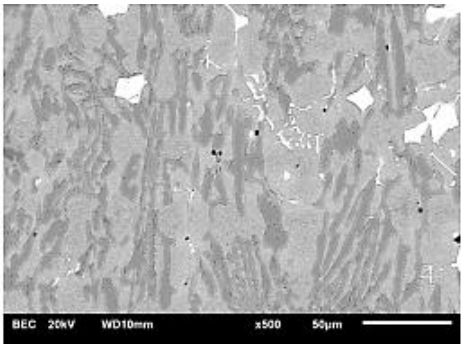

(a)

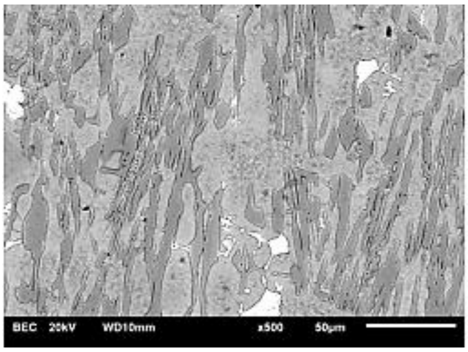

(b)

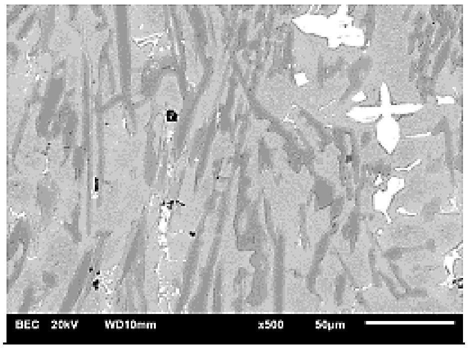

(c)

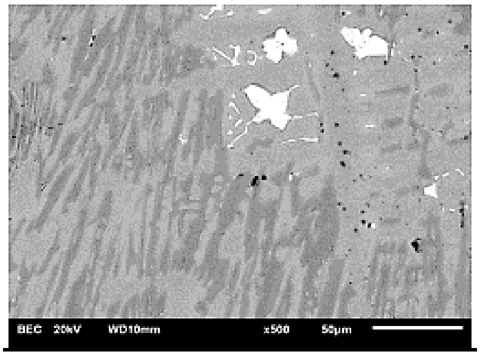

(d)

Figure 5. SEM photographs show the microstructure of super-alloyed steel after tempering at 900°C for (a) 1 hour, (b) 2 hours, (c) 3 hours, and (d) 4 hours.

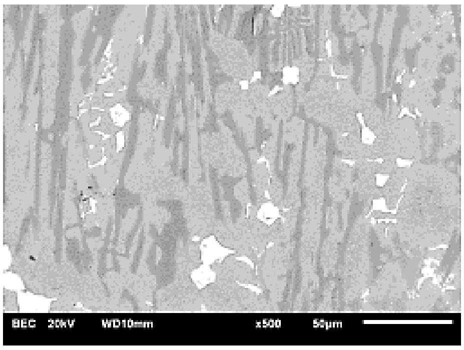

(a)

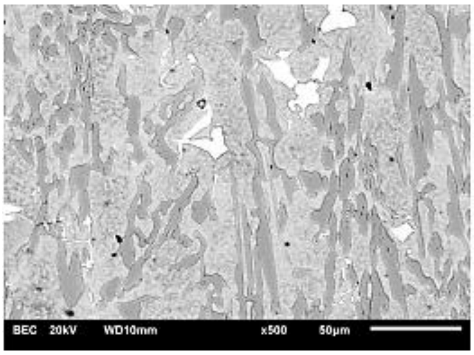

(b)

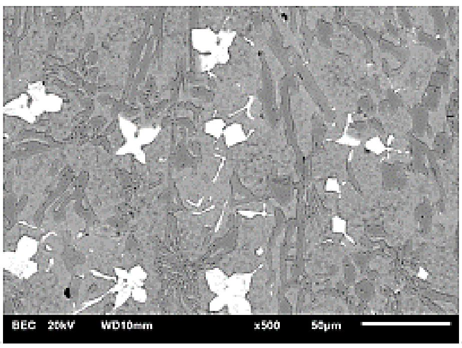

(c)

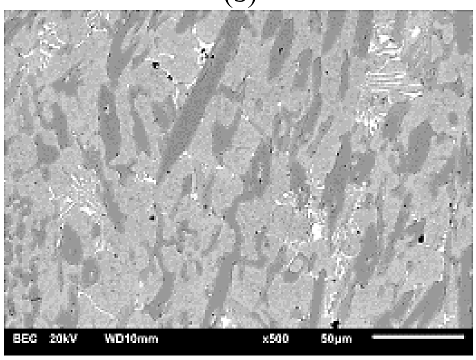

(d)

Figure 6. SEM photographs show the microstructure of super-alloyed steel after tempering at 1000°C for (a) 1 hour, (b) 2 hours, (c) 3 hours, and (d) 4 hours.

4. Conclusion

1. The improved structural super-alloy steel exhibits enhanced overall hardness, with the hardness at 1000°C being higher than that at 900°C.

2. The micro-hardness of the restructured super-alloy steel has been increased. At 900°C, the niobium-dispersed sites displayed the highest hardness after a tempering time of 3h, followed by 4h > 1h, 2h. At 1000°C, the niobium-dispersed sites exhibited the highest hardness during a tempering time of 3h > 2h > 1h > 4h, while the chromium-dispersed sites showed the highest hardness for a tempering time of 1h, 2h > 3h > 4h.

3. Microstructure: After improving the structure, it was found that at a temperature of 900 ºC, as time increased, the hardness during the period when chromium was distributed in the super-alloyed steel decreased. At a temperature of 1000 ºC, as time increases, the hardness value increases and decreases when the tempering time is more than 3 hours, and this results in crystallization of places where chromium is distributed in the super-alloyed steel.

4. The SEM imaging results show that niobium is distributed in the super-alloyed steel over a range of temperatures and tempering times.

5. References

[1] KARL-HEINZ ZUM GAHR. (1987). MICROSTRUCTURE AND WEAR OF MATERIALS, ELSEVIER SCIENCEP PUBLISHERS B.V. (Vol.10, p.1-562).

[2] P.S.BANDYOPADHYAY, SK GHOSH, S.K. GHOSH, S.KUNDU, and S.CHATTERJEE (2011). Evolution of Microstructure and Mechanical properties of Thermomechanically Processed Ultrahigh-Strength Steel. METALLURGICAL AND MATERIALS TRANSACTIONS A. (Vol.42A,p 2742 -2752).

[3] H.J. Jun, J.S. Kang, D.H. Seo, K.B.Kang and C.G. Park. (2005). Effects of deformation and boron on microstructure and continuous cooling transformation in low carbon HSLA steels. Materials Science and Engineering A 422. (p.157 – 162).

[4] Mohammed Ali. (2020). Influence of Chromium Content on the Microstructure and Mechanical Properties of Thermomechanically Hot-Rolled Low- Carbon Bainitic Steels Containing Niobium. Applied Sciences MDPI. (p.1 -13).

[5] M.G. AKBEN, I. WEISS and J. J. JONAS. (1980). DYNAMIC PRECIPITATION ANDSOLUTE HARDENING IN A V MICROALLOYED STEEL AND TWO Nb STEELS CONTAINING HIGH LEVELS OF Mn, Acta Metallurgica (Vol.29, p 111 – 121) .

[6] G. -Y.. Qiao, Y.B. Cao, B. Liao and F.-R. Xiao. (2017). Effect of hot deformation and precipitation on continouous cooling transformation of a high- Nb steel, Ironmaking & Steelmaking, (p.1 – 9).

[7] Milosav Beres, Thomas E.Weirich, Klaus Hulka and Joachim Mayer.(2004), TEM Investigatins of Fine Niobium Precipitates in HSLA Steel, Materials Technology – Microalloyed Steels.(Vol.11, p.753 – 758).

[8] Yan Chen, Dantian Zhang, Yongchang Liu, Huijun Li and Dakun Xu.(2013). Effect of dissolution and precipitation of Nb on the formation of acicular ferrite/bainite ferrite in low-carbon HSLA steels. MATERIALS CHARACTERIZATION 84 (p.232-239).

[9] Jatupon Opapaiboon and Yasuhiro Matsbara.(2019),Effect of Chromium Conternt on Heat Treatment Behavior of Multi – Alloyed White Cast Iron for Abrasive Wear Resistance, Materals Transactions.(Vol.2,p.346 – 354).

[10] Mohammed Ali and Jukka Komi. (2021), Incompatible effects of B and B+Nb additions and inclusions´ characteristics on the microstructures and mechanical properties of low-carbon steels. MATERIALS SCIENCE & ENGIEERING. (p.1-26).

[11] Wilson Sckudlarek, and Cesar E. Da Costa. (2021). Effect of austempering temperature on microstructure and mechanical properties of ductile cast iron modified by niobium. (Vol.21,p2414 – 2425).

AMM0018

Investigation of Evaluation Indices for Bonding Strength of Healed Areas in Self-Healing Ceramics Using the Acoustic Emission Method

Toyoki AGATA[1], Koji HASEGAWA[2], Masaki HIRATSUKA[2], and Tetsuro YANASEKO[2,*]

[1] Graduate School of Kogakuin University, 2665-1, Nakano-machi, Hachioji-shi, Tokyo,192-0015 Japan

[2] Kogakuin University, 2665-1, Nakano-machi, Hachioji-shi, Tokyo,192-0015 Japan

* Corresponding Author: yanaseko@cc.kogakuin.ac.jp

Abstract. The purpose of this study is to establish a method for evaluating the bonding strength of self-healing ceramics in the healed region, which are candidate turbine materials for next generation jet engines. To achieve this objective, four types of specimens of SiC/Al_2O_3 composite, a typical self-healing ceramic, were prepared in the standard, damaged, incompletely healed and completely healed states. Three-point bending tests were performed and the amplitude of the sudden acoustic emissions (AE) signals, the accumulated energy and the AE spectrum were analysed. The results showed a stepwise increase in the abrupt AE signal to failure for the reference and fully healed specimens, and the AE spectrum peaked on the high frequency side. For the damaged and incompletely healed specimens, a small amount of sudden AE occurred, but the amount of energy was small and the AE spectrum peaked on the low frequency side.

Keywords: Self-healing Ceramics, Acoustic Emission, Three-point Bending, Crack Initiate, Bonding strength.

1. Introduction

In recent years, the impact of CO_2 on global warming has received increasing attention. The transport sector is responsible for 25% of the world's energy-related CO_2 emissions, and the CO_2 emissions per passenger in aircraft are estimated to be 15 to 20 times higher than in trains, making aircraft a very large source of CO_2 emissions. In addition, the increase in CO_2 emissions from aircraft due to the increase in the number of flights as a result of globalization has become an issue. According to the Aviation Environment Protection Council of the International Civil Aviation Organization, if no further action is taken, CO_2 emissions from the sector are expected to triple by 2040 compared to 2020[1].

One of the measures mentioned as a possible solution to this problem is to improve the fuel efficiency of aircraft. There are several ways to improve the fuel efficiency of aircraft, including increasing the combustion temperature of engines and improving the heat resistance of turbine blades [2]. Measures to increase the combustion temperature of engines have been studied for some time.

Measures to increase the combustion temperature of engines have been studied for some time, and the current combustion temperature has been improved to 1600°C [3]. However, the current material of turbine blades is not suitable for the combustion temperature of engines because of its high heat resistance. However, the melting point of Ni-based alloys, the current material used for turbine blades, is about 1450°C, and raising the temperature above 1500°C increases the formation of harmful nitrogen oxides (NOx)[4]. One strategy that has attracted attention is the use of ceramics instead of Ni-based alloys as turbine blade materials. Ceramics are lightweight, heat-resistant, and oxidation-resistant, making it possible to achieve lighter and uncooled turbines by changing materials. It is estimated that these effects can improve the fuel efficiency of jet engines by up to 14.8% and reduce CO_2 emissions by approximately 600 million tons [1]. However, ceramics have the disadvantage of being more prone to foreign object damage (FOD) caused by soot and dust generated by combustion in jet engines than metals.

To overcome this weakness, self-healing ceramics are being developed [5]. The optimum self-healing temperature for self-healing ceramics varies depending on the self-healing agent used in the formulation. Therefore, the appropriate self-healing agent for use in turbines must be selected for different temperature ranges depending on the position. Although the selection criteria such as the volume expansion coefficient of the oxidation products and the healing temperature and time have been investigated, the bonding strength between the oxidation products and the matrix, which is one of the selection criteria, has not been evaluated in detail [6][7]. In this study, three-point bending tests of self-healing ceramics are performed before and after healing, and the acoustic emissions (AE) generated during the tests are recorded and analysed to search for indicators that can evaluate the self-healing state and bonding strength. Completion of this index will allow comparison of self-healing ceramics using different self-healing agents and will allow selection of the appropriate self-healing agent for the temperature range in which it will be used.

2. Experimental Method

2.1. Materials

Al_2O_3 powder (Taimeikron, TM-DAR, average particle size 0.14 µm) and SiC powder (Shin-Etsu Chemical, SER-06, average particle size 0.6 µm) were used as specimens.

2.2. Fabrication of SiC30vol.%/Al_2O_3 ceramics

Al_2O_3 powder and SiC powder were wet-mixed in a ball mill at a volume ratio of 7:3, dried, ground and finally sieved to 106 µm. 30 vol.% SiC/Al_2O_3 powder was sintered in a hot press (FVPHP-R-5, Fuji Radio Industry Co). Sintering was performed in an Ar atmosphere of 0.2 MPa, followed by holding at 2023 K for 3.6 ks and cooling. A uniaxial pressure of 15 MPa was applied during heating and holding. After sintering, the density was measured by the Archimedes method and specimens with a relative density of 98% or higher were formed into specimens. The test specimens were machined from the above sintered specimens to 3 ± 0.1 mm × 4 ± 0.1 mm × 36 to 45 mm with a surface roughness of $Ra \leq 0.2$ µm according to JIS R 1601: 2008 (Room temperature flexural strength test method for fine ceramics) [8]. The specimens were divided into three types: "standard specimen", which is the standard for the original strength of the specimen; "damaged specimen", which was pre-cracked using a Vickers indenter at a load of 2 kgf to reduce its strength; and "healed specimen", which was healed at 1373 K using a tabletop muffle furnace (Advantech Toyo Corporation, KM-280) to regain its strength. The damaged specimen was healed at 1373 K in a bench top muffle furnace (Advantech Toyo Corporation, KM-280) to regain its strength. The healed specimens were prepared with an incomplete healing time of 5 h and the fully healed specimens were prepared with a healing time of 24 h in order to measure the AE associated with fracture due to exfoliation of oxidation products during incomplete healing.

2.3. Three-point bending test

For each specimen, a three-point bending test was performed according to JIS R1601 using a Tensilon-type universal material testing machine (A&D Corporation, RTG-1310) to evaluate the flexural stress of each specimen and to obtain AE signals. To facilitate the acquisition of AE between multiple specimens, a broadband AE sensor (NF CORPORATION, Ltd., AE-900S-WB) was installed on the fixture side of the three-point bending machine to perform the test without changing the sensor position, and the three-point bending test and AE measurements were performed until the load that indicated significant specimen failure decreased. The sampling rate was 10 MHz, and the signal was amplified by a +40 dB preamplifier for AE (NF Circuit Design Block Co., Ltd., 9913) and acquired on a PC via a high-pass filter (cutoff frequency: 50 kHz, Thorlab, EF125) and a high-speed A/D converter (Spectrum, M2i.4032-exp) to eliminate mechanical vibration noise from the testing machine.

2.4. AE analysis

The amplitude of the AE signal exceeding the threshold was taken as the AE energy, and the AE energy was accumulated every microsecond as the cumulative AE energy. In addition, time-frequency analysis using STFT (Short-Time Fourier Transfer) was performed on the AE waveform to measure the peak frequency specific to sudden-type signals associated with small crack initiation, and the AE signal that occurred earliest after the start of the test was assumed to be due to a crack occurring at the weakest part, and a comparison was made for each specimen.

3. Results and Discussion

3.1. AE analysis

Using the AE observations of the specimens, the amplitude and cumulative energy of the AE generated to each fracture are shown in Figure 1. Damaged, incompletely healed, and completely healed materials are classified as follows: damaged material is pre-cracked and not healed; incompletely healed material has recovered bending stress above the reference material and is fractured from the pre-crack; and completely healed material has recovered bending stress above the reference material and is fractured from outside the pre-crack. Figures 1(a) and 1(d) show that the standard specimen and the fully healed specimen had a large AE signal once before fracture, indicating that the cracks progressed cumulatively. Figures 1(b) and 1(c) show that the damaged and incompletely healed specimens have small cracks, but the amount of energy is small, indicating that the cumulative energy to fracture is small. This indicates that as complete healing progresses and strength is restored, the cracks are cumulative to fracture and the cumulative energy is large.

Figure 2 shows the results of comparing the spectrum of AE that first occurred in each specimen at the initial stage of each specimen with different healing conditions. The AE frequencies observed in the standard specimens were widely distributed from low to high frequencies, while those in the damaged and incompletely healed specimens were concentrated on the low frequency side. This indicates that low frequency AE occurs when a crack starts in the damaged area and high frequency AE occurs when a new crack starts in the base metal. The high AE frequencies observed in the damaged and incompletely healed specimens are thought to be due to the fact that the cracks are larger in area than those in the standard and fully healed specimens because they are unhealed or incompletely healed, as shown in 3.1, and are broken from the pre-cracks. The high frequency component observed in the fully healed specimens compared to the damaged and incompletely healed specimens is probably due to the fact that the healing process was sufficiently advanced to dissipate the stress, resulting in the formation of more small area cracks.

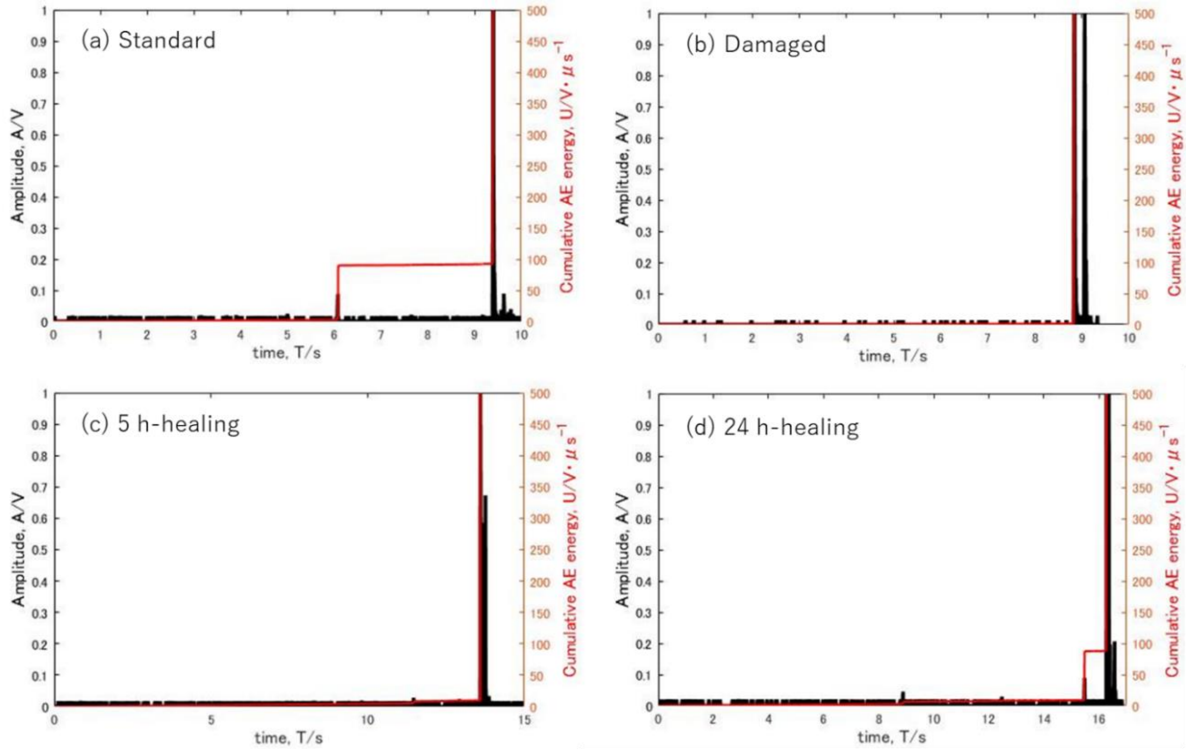

Figure 1. AE amplitude and accumulated energy of (a) Standard, (b) Damaged, (c) Incompletely healed and (d) Completely healed specimen.

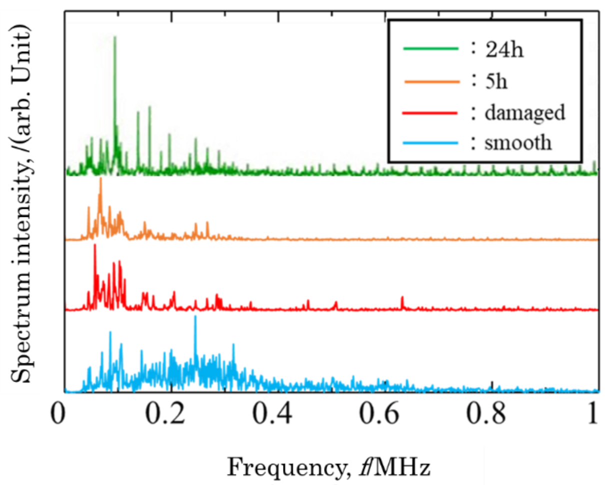

Figure 2. Comparison of AE spectrum of each specimen.

4. Conclusion

In order to establish an index for evaluating the healing state of self-healing ceramics and the bond strength between self-healing agents and base metal, the fracture behaviour of self-healing ceramics before and after healing was investigated by the AE method in parallel with a three-point bending test. By analysing the AE signals of specimens with different healing conditions, it was found that the cumulative energy to failure of damaged and incompletely healed specimens was lower than that of standard specimens, and the AE spectrum had a peak at a lower frequency. The AE spectrum peaked at high frequencies for the fully healed specimen. These results suggest that the frequency spectrum of AE generated in the initial stage and the stress at that time, obtained by time-frequency analysis of AE signals, can be used as an indicator of bonding strength in the healed area and may be used for appropriate selection of self-healing agents.

5. References

[1] Ministry of Land, Infrastructure, Transport and Tourism of Japan." Status of Efforts to Reduce CO_2 in the Aviation Field." https://www.mlit.go.jp/common/001403136.pdf , accessed July 28 , 2023 .

[2] Takayuki TAKAHASHI, Multi-materials technology for aircraft structure, The Japan Institute of Light Metals Vol. 72 No. 4 (2022) 151–158.

[3] MORIAI, Hideki and MIYAKE, Yoshiaki(2008). Aircraft Engine and Spray Combustion Technology. Journal of the Combustion Society of Japan Vol.50 No.153 (2008) 225-234

[4] Haruki MATSUSHITA, Naomichi FUKUDA, Kazuteru KAWATA and Nobuhiro OHSHITA, Analysis of NOx formation behavior in waste combustion ～Development of three-dimensional analysis with detailed reaction mechanism～, Nippon Steel Engineering Technical Report Vol. 11 (2020).

[5] Wataru Nakao. Prospects and significance of self-healing materials research. Japan Society of Mechanical Engineers 2012 Annual Conference, J044073 -1.

[6] Toshio Osada Hara Toru(2020). Self-healing by design: universal kinetic model of strength recovery in self-healing ceramics .Science and Technology of Advanced Materials 21 pp.599.

[7] Peter Greil. Self-Healing Engineering Ceramics with Oxidation-Induced Crack Repair. pp.1-8.

[8] Japanese Industrial Standard, JIS R 1601, "Testing Method for Flexural Strength of Fine Ceramics at Room Temperature" (2008)

AMM0019

Investigation of Polarization Conditions of Metal Matrix Piezoelectric Composite with Surface Oxidized Metal Electrodes

Ryo SHIRAI[1,*] and Tetsuro YANASEKO[2]

[1]Graduate School of Kogakuin University, 2665-1, Nakano-machi Hachioji-shi, Tokyo, 192-0015, Japan
[2]Kogakuin University, 2665-1, Nakano-machi Hachioji-shi, Tokyo, 192-0015, Japan

* Corresponding Author: am22033@g.kogakuin.jp

Abstract. Metal matrix piezoelectric composites have been developed to improve strength of piezoelectric ceramics. This composite is fabricated by embedding piezoelectric ceramics with surface-oxidized metal-core in metal matrix. However, when composites are polarized, the oxide film on the metal-core absorbs the electric field, which lowers the electric field applied to the piezoelectric ceramics and inhibits polarization. In addition, there is a possibility of dielectric breakdown of the oxide film of the metal-core when an electric field is applied. The breakdown electric field and permittivity of the oxide film were measured, and the obtained data were applied to a series capacitor model to optimize the polarization conditions. Measurements of oxide film data for Ni and Ti, the candidate materials for the metal-core, revealed that the average values of the breakdown electric field and permittivity were 16.88 kV/mm and 9.637 for nickel and 2.610 kV/mm and 85.49 for titanium, respectively. The obtained data were applied to series capacitors model, however it was not possible to obtain a polarized electric field above 0.3 kV/cm and below the breakdown electric field of the oxide film. Therefore, it proved difficult to optimize the polarization conditions by optimizing the Ni and Ti oxide films.

Keywords: Structural Health Monitoring, Piezoelectric Sensor, Metal Matrix Composite, Oxide Film, Polarization.

1. Introduction

In recent years, structural health monitoring (SHM) has been attracting attention as a technology to ensure safety and security in Japan, where disasters occur frequently. This technology involves installing sensors on structures to be monitored and using the information obtained to determine the health of the monitored structure [1-4]. Acceleration sensors are commonly used in SHM techniques [1-4], therefore, this study focuses on piezoelectric sensors which typically used as acceleration sensor.

The piezoelectric sensors are based on piezoelectric ceramics [5-9], which have a piezoelectric effect, and have the advantages of not requiring a power supply for the sensor and being inexpensive and compact [5-9]. On the other hand, the disadvantage of piezoelectric sensors is that they are very fragile and cannot handle large loads, such as earthquakes, which is an issue in SHM.

To overcome this problem, metal matrix piezoelectric composite (MMPC) has been developed [10]. This composite is fabricated by embedded Pb(Ti, Zr)O_3 (lead zirconate titanate, PZT) which typically piezoelectric ceramics in a metal matrix that has excellent mechanical strength, thereby improving strength and expanding the range of applications. The composite material has a larger strain range usable as a sensor than PZT alone, however, its performance as a sensor was low because the polarization treatment of the piezoelectric ceramics was not optimized.

In the previous study [10], the oxide film is relevant to the optimization of the polarization treatment. Polarization treatment is a process to give piezoelectricity to piezoelectric ceramics by aligning the direction of spontaneous polarization through the application of an electric field. In the polarization treatment of this composite material, the applied electric field is distributed to PZT and the oxide film due to its structure, and the polarization electric field tends to be large because it is necessary to compensate for the electric field distributed to the oxide film. Therefore, it is necessary to achieve good polarization without causing dielectric breakdown of the oxide film, which requires optimization of the oxide film thickness.

In the previous study [12], the dielectric strength and dielectric constant of Ni and Ti oxide films were obtained, and an optimization method was developed by applying the series capacitor model for PZT and oxide films shown in Equation (1) to the obtained oxide film data. Where d_{PZT}: thickness of piezoelectric ceramic, d_{oxide}: thickness of oxide film, ε_{PZT}: permittivity of PZT, and ε_{oxide}: permittivity of oxide film. Two constraints for optimization were set: the polarization electric field V_p/d_{PZT} was greater than 3 KV/cm [11], which is sufficient to polarize PZT, and V/d_{oxide} was less than the breakdown electric field. Polarization condition optimization was performed by searching for values of d_{PZT}, d_{oxide}, and V such that V_p/d_{PZT} could be optimized to meet the constraints.

$$\frac{V_p}{d_{PZT}} = \frac{1}{d_{PZT} + \frac{\varepsilon_{PZT} d_{oxide}}{\varepsilon_{oxide}}} V \tag{1}$$

Although the optimization results did not yield a polarization field that satisfied the constraint, it was found that the higher the permittivity and breakdown electric field of the oxide film, the closer the value of the polarization field to the constraint. However, since this is an analytical optimization, it is not clear what trend will emerge when the polarization process is actually performed. Therefore, the objective of this study was to confirm how the output voltage changes during the actual fabrication and polarization of MMPC.

2. Experimental methods

2.1. Materials

PZT powder (Hayashi Chemical Industry, MPT, average particle diameter less than 0.1 µm), pure water, polyvinyl alcohol, (Japan Vinyl Acetate & Popal Corporation, JF-17), ethanol (Imazu Pharmaceutical Industries, purity 99.5%), glycerin (Hayashi Chemical Industry) were used as materials for the preparation of PZT sintered bodies. Ni fibers (Niraco Corporation, 0.5 mm diameter, purity of 99.9% or higher) and Ti fibers (Niraco Corporation, 0.5 mm diameter, purity of 99.9% or higher) were used as electrodes. In addition, pure aluminum plates (A1050, 2.5 mm and 1 mm thick) were used as the base metal and lid. The 2.5 mm thick aluminum plate was machined for use as the matrix. 30 mm × 30 mm × 2.5 mm, and then grooved on the surface with dimensions of 20.1 mm × 2.1 mm × 2.1 mm. The 1 mm thick aluminum plate was machined to 30 mm × 30 mm × 1 mm for use as a lid. Copper foil (30 mm × 30 mm × 0.02 mm thick, C1220) as the insert material.

2.2. Fabrication of MMPC

Oxide films were applied to Ni fibers. Using the results of a previous study [11], an oxide film with a thickness of 22.71 µm was deposited by heat treatment at an oxidation temperature of 1423 K and a holding time of 36.0 ks. Similarly, an oxide film with a thickness of 97.00 μm was deposited on Ti by heat treatment at an oxidation temperature of 1273 K and a holding time of 3.6 ks.

The PZT powder was then mixed with a PVA solution at a weight ratio of 1:1, dried in a muffle furnace, crushed, and sieved to obtain a particle size of less than 100 μm. In the compression molding process, 2 g of PZT powder was first placed into a die, then, pressed by 100 MPa. After that, surface oxidized metal fiber was inserted into the die, 2 g of powder was added, and pressed by 100 MPa again. The obtained compact was debindered and sintered in a muffle furnace. The temperature was raised to 623 K at a rate of 1 K/min, held for 18.0 ks, and then raised to 1323 K and held for 7.2 ks to produce a sintered compact. The PZT portion of the sintered compact was then cut and polished to 18 mm × 2 mm × 2 mm. The sintered body was placed into the groove of metal matrix, covered with copper foil as an insert material, and covered with an aluminum plate with 1 mm thickness. The sintered PZT and matrix were then composited by hot pressing. The conditions were pressure of 4.4 MPa, temperature of 873 K, and holding time of 2.4 ks.

2.3. Polarization treatment

From the optimization graph of the previous study (Figure 1) [11], it is thought that the higher the applied voltage, the more the polarization field increases and the higher the output power. In this section, polarization treatment is performed on the composite materials prepared above to investigate what trends are observed in output. The polarization treatment used the polarization system shown in Figure 2. The MMPC was placed in silicon oil filled in an oil bath. The silicon oil was then heated to 373 K in the oil bath, and after reaching the set temperature, voltage was applied to the composite material with a holding time of 1.8 ks for polarization treatment. After the holding time, the heater was turned off, the silicon oil was allowed to cool naturally, and the voltage was turned off when the temperature reached around 373 K. The applied voltage ranged from 100 V to 50 V. The applied voltage was increased in 50 V increments from 100 V. After the polarization treatment was completed under each condition, the following drop weight test was performed, and the polarization treatment was performed again after the drop weight test. This process was repeated until the oxide film broke down.

2.4. Drop-weight test

Drop-weight test was conducted on the polarized MMPC to confirm the output voltage. The test was conducted using the equipment shown in Figure 3. First, a vise for fixing the MMPC was fixed to an optical surface plate. Next, the composite material was fixed to the vise, and the + terminal of the oscilloscope was connected to the electrode and the - terminal to the base material. A steel ball was then free-fallen through the pipe from a height of 300 mm and impacted on the MMPC. The output voltage generated by the impact on the MMPC was measured using an oscilloscope.

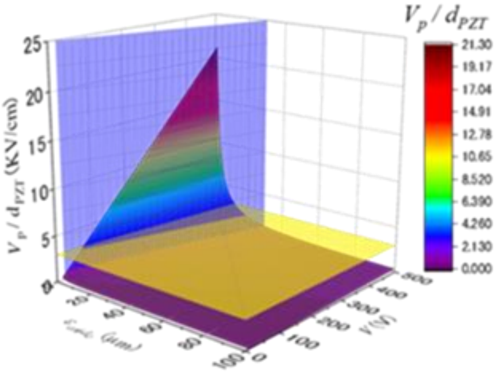

Figure 1. Effect of applied voltage and thickness of Ni oxide film on poling electric field.

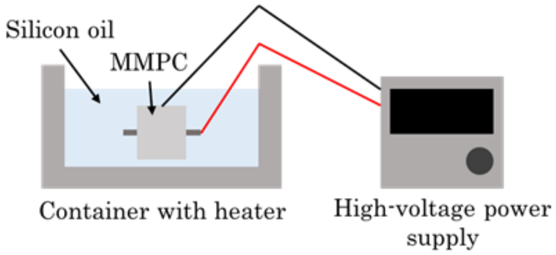

Figure 2. Schematic diagram of the polarization treatment system.

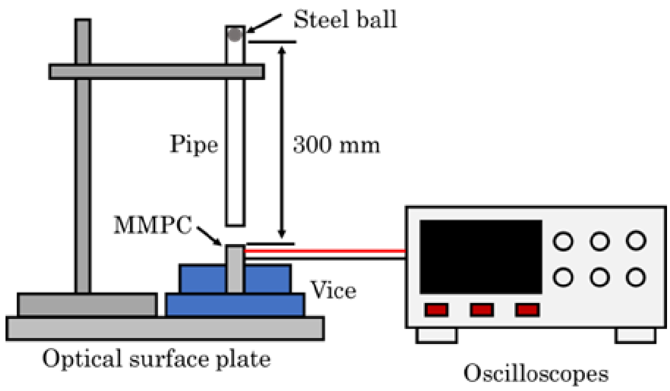

Figure 3. Schematic diagram of falling weight test sytem.

3. Experimental results and discussion

Polarization treatment resulted in breakdown of the Ni oxide film at an applied voltage of 250 V. This breakdown occurred at a lower voltage than the original dielectric breakdown voltage of 470 V. The relatively high oxidation temperature of 1423 K and the extremely long holding time of 36.0 ks are considered to have caused the breakdown due to the formation of brittle portions in the oxide film. On the other hand, the Ti oxide film did not function as an electrode because the Ti fibers were embrittled by oxidation during the PZT sintered body fabrication stage.

For the drop-weight test, output voltages at applied voltages of 100, 150, and 200 V were obtained in the Ni oxide film. This confirmed that the polarization process was successful. An example of the waveform of the output voltage measured with an oscilloscope is shown in Figure 4. As a result, the output voltage was 0.056V, 0.12V, and 0.31V at 100V, 150V, and 200V, respectively. Figure 5 shows the relationship between output voltage and calculated polarization electric field. The polarization electric field was calculated using Equation 1 of the series capacitor model. The polarization field V_p/d_{PZT} was calculated for each value of d_{PZT}: 0.75 mm, d_{oxide}: 21.71 µm, ε_{PZT}: 1300, ε_{oxide}: 6.503, and V: applied voltage. The graph shows that the output voltage increases as the calculated polarization field increases. This confirms that as the applied voltage increases, the actual polarization field increases as well as the calculated one. Since this trend follows the equation of the series capacitor model, the usefulness of the optimization method was confirmed by experiment. However, the calculated value of the polarization electric field is clearly smaller than the target value of V_p/d_{PZT} = 3 kV/cm. This may be due to the low dielectric constant of the oxide film, which causes the electric field to be absorbed by the oxide film, resulting in a very small electric field applied to the PZT.

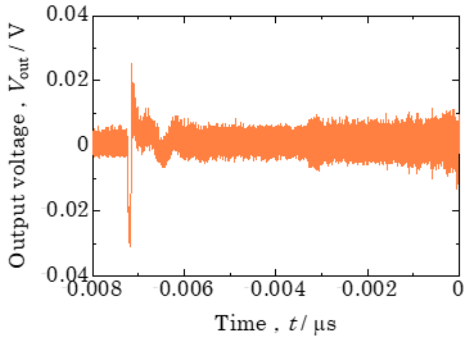

Figure 4. Waveform of output voltage (Applid voltage : 100 V)

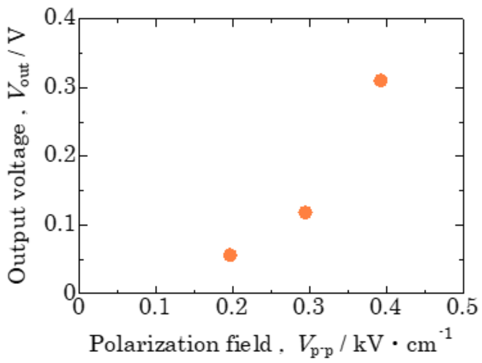

Figure 5. Relationship between polarization electric field and output voltage.
The output voltage is the peak-to-peak value in the waveform.

4. Conclusion

In this study, MMPC were fabricated, polarized, and drop-weight tested to investigate the output power. The results showed that the output voltage increased with increasing applied voltage. This indicates that the actual polarization field increases with increasing applied voltage as well as the calculated value. And this result confirms the usefulness of the optimization method. However, the polarization electric field was very small due to the low dielectric constant of the Ni oxide film, and a polarization electric field of V_p/d_{PZT} = 3 kV/cm, which is sufficient to polarize PZT, was not obtained. Future prospects include the development of MMPC with a PZT film around the electrodes and improved power output by optimizing the polarization conditions in such composites.

5. References

[1] Okada, K., and Shiraishi M., Structural health monitoring of buildings, Japan Construction Mechanization Association (2009), p.58.

[2] Tajima, M., Matsumoto, S., Hkukunaga, H., Impact Load Identification of CFRP Laminates by PZT Piezoelectric Sensor (2nd Report, Experimental Verification), Transactions of the Japan Society of Mechanical Engineers (2004), pp. 81-88.

[3] Takeda, N., Research and development of structural health monitoring technology, The Japan Society for Aeronautical and Space Sciences (2003), p142.

[4] Mita, A., and Nagai, N., Optimal Design and Lifetime Estimation of FBG Accelerometers for Structural Health Monitoring, Architectural Institute of Japan (2001), p.79.

[5] Ando, A., Technical development of piezoelectric ceramic materials, J. Jpn. Soc. Powder Powder Metallurgy, 67 (2020), pp. 455-463.

[6] Asano, M., Effect of Mechanical Damage on Piezoelectric Properties of Piezoelectric Ceramics, Kochi University of Technology (2016).
[7] Tajitsu, Y., Yoneda, T., Development and application of fluorinated organic piezoelectric materials, VALQUA Technical Journal (2014), p.12.
[8] Uetsuji, Y., Nakamura, Y., Ueda, S., Nakamachi, E., Evaluation of ferroelectric properties of piezoelectric ceramics based on crystal homogenization method, J. Soc. Mat. Sci., Japan (2003), pp.1116-1121.
[9] Shirakihara, K., Tanaka, K., Akiniwa, Y., Mizuno, K., Effect of Polarization on Deformation and Fracture of Piezoelectric Ceramics, J. Soc. Mat. Sci., Japan (2002), Vol.51, No.7, pp. 736-742.
[10] Horikiri, K., Yanaseko, T., Kuboki, I., Sato, H., Asanuma, H., Development of surface oxidized metal fiber/ piezoelectric ceramics/aluminum composite, Mechanical Engineering Journal, 6, (2019), 18-00556.
[11] Cartmell, S. H., Thurstan, S., Gittings, J. P., Griffiths, S., Bowen, C. R., Turner, I. G., Polarization of porous hydroxyapatite scaffolds: Influence on osteoblastcell proliferation and extracellular matrix production, Society For Biomaterials (2013), pp.1047-1052
[12] Shirai, R., Yanaseko, T., Optimization of polarization conditions of Metal Matrix Piezoelectric Composite based on breakdown electric field and permittivity of oxide film of metal-core within piezoelectric ceramics, Proceedings of International Conference on Materials and Processing 2022, (2022), Th-2C-3

AMM0020

Development of Bending Fatigue Testing System for Endodontic Files

Teeramate Kessaro[1,*], Sirawut Hiran-us[2], Pairod Singhatanadgid[1], and Sarita Morakul[1]

[1]Department of Mechanical Engineering, Faculty of Engineering, Chulalongkorn University, Bangkok, 10330, Thailand
[2]Department of Operative Dentistry, Faculty of Dentistry, Chulalongkorn University, Bangkok, 10330, Thailand

* Corresponding Author: teeramate.kessaro@gmail.com

Abstract. Root canal treatment in dental applications poses a risk of fatigue failure for endodontic files because these files are continuously subjected to cyclic bending loads within curved root canals. In order to prevent a risk of failure during operations, dentists must understand and be able to evaluate the number of cycles to failure (NCF) of each file's condition. Therefore, this paper aims to design and develop a novel bending fatigue testing system for endodontic files by which the NCF of the files can be evaluated and monitored. In the testing system, modifications were made to the motor control unit to extract both the calibrated encoder signals and current signals. These signals were utilized to track the motor's completed cycles and monitor file breakage time, respectively, allowing for the accurate determination of the NCF for the tested files. To validate the proposed bending fatigue testing system, twenty endodontic files were carried out and rotated in an artificial root canal until they fractured, and the NCF of each file was then assessed. The files were categorized into four subgroups, each undergoing rotation in an artificial root canal with a 5 mm radius of curvature. The subgroups included angles of curvature of 30°, 45°, and 60° at body temperature, as well as an angle of 45° at room temperature. All tests were conducted in temperature-controlled distilled water in a container. The findings of this study demonstrated concordance with those of earlier research, specifically revealing a decrement in the NCF of the files as the angle of curvature of the artificial root canal increased and as the ambient temperature rose. Moreover, all files that underwent testing within this system exhibited visible indications of bending fatigue fractures. By virtue of these results, the efficacy of the proposed testing system in conducting bending fatigue tests for endodontic files is substantiated.

Keywords: endodontic file, bending fatigue, testing system, NCF monitoring.

1. Introduction

Endodontic files are crucial surgical instruments used by dentists during root canal treatments. Their primary function centers on the cleansing and shaping of the root canal. Nowadays, most endodontic files available in the market are made of Nickel-Titanium alloy (NiTi). This alloy is recognized for its high flexibility and low stiffness. Such characteristic renders NiTi files a more appropriate option for utilization within curved root canals, as compared to files made from conventional materials such as carbon steel and stainless-steel files [1-3]. Furthermore, NiTi also offers superior corrosion resistance compared to these metals. This makes NiTi files well-suited for root canal treatments in which the files usually come into contact with fluids, including irrigation fluid within the root canal and steam during sterilization.

Despite the NiTi file possessing appropriate mechanical and chemical properties for root canal treatment, NiTi file fractures remain inevitable and frequently happen during the endodontic operations [4-5]. Such file failures during root canal treatment can result in significant patient distress and may necessitate urgent endodontic surgery. In general, endodontic files primarily fail in two main ways: through bending fatigue failure or torsional failure [6-7]. Bending fatigue failure originates from the file's continual rotation within a curved root canal. To elucidate, as the file rotates within the curved canal, each point of the file in the curved section undergoes alternating tensile stress, while situated on the outer half of the curve, and compressive stress, while located on the inner half. This repetitive stress cycle causes material fatigue, eventually leading to the file's fracture. The file's cross-section most susceptible to this type of failure is the one at the point of maximum flexure or, in simpler terms, the middle of the canal's curved section [8-9]. Torsional failure, on the contrary, arises when a file's tip or another segment becomes jammed in a canal, yet the shank keeps rotating by the motor. This leads to increasing shear stress in the file's cross-section. If the shear stress in a specific cross section exceeds the metal's ultimate strength in shear, the file unavoidably breaks. Instruments that fracture due to torsional failure often show indications such as plastic deformation or distortion [6]. While dental files might encounter both torsional and bending fatigue loads during clinical operation, previous studies emphasized that material fatigue played a pivotal role in endodontic file breakage [10-11]. Cheung et al. [11] clarified that this was owing to the considerably higher fatigue crack growth rates observed in NiTi compared to other metals with comparable strength. Consequently, the rapid propagation of a microcrack can lead to potentially disastrous fracture once initiated. Accordingly, investigations into the bending fatigue life of endodontic files have been crucial. They enable dentists to specifically select safe and appropriate files for treating each individual patient in endodontic operations, while also aiding researchers and manufacturers in enhancing various aspects of endodontic file development.

Bending fatigue life studies require a testing system to assess the number of cycles to failure (NCF) of tested files under different testing conditions. The studies indicated that several parameters influence the NCF of files. These included aspects like file shape and size, file material properties, root canal dimensions, and ambient temperature. For example, root canals with lower radius of curvature and higher angle of curvature can potentially lead to lower NCF of inserted files in comparison to those with higher radius and lower angle [4, 12-14]. In addition, as the temperature increased from room temperature to body temperature, the NCF of the file tended to decrease [15-16].

The majority of prior research on file bending fatigue life utilized a testing system designed to evaluate the NCF of the file by multiplying the file's fracture time (recorded via video recording or timer) with its rotational speed. This method used to assess NCF relied on the premise that the file's rotational speed remained constant. However, this assumption may not hold true in real operations. Hence, calculating the NCF using this method may not be accurate. Moreover, inaccuracies in time measurement, whether through video recording or a timer, could also introduce errors in the calculated NCF value for the file.

Building upon the research gap highlighted earlier, this paper, therefore, aims to design and develop a novel bending fatigue testing system for endodontic files by which the NCF of the files can be directly evaluated and monitored.

2. Design of the Bending Fatigue Testing System for Endodontic Files

2.1. Overview of the testing system

As shown in Figure 1, there are many units in the testing system: the artificial root canal unit, temperature control unit, vertical stage unit, motor control and monitoring unit, and visual monitoring unit. The artificial root canal unit contains an artificial root canal block (ARC block) which is a block that has simulated-root-canal grooves called artificial root canals on its faces. The ARC block is locked in place by the hole of a locking block. The whole artificial root canal unit is located in an acrylic bath filled with temperature-controlled water. To insert an endodontic file into the artificial root canal, the vertical stage unit which grips a handpiece with the file at one end is moved down. The rotational speed of the file can be controlled by a motor controller. During the bending fatigue test, the encoder signal and current signal from the motor can be extracted and used to count the number of cycles the motor actually completes and to monitor when the file is broken respectively. Thus, the number of cycles to failure (NCF) of the file can be easily monitored and evaluated. Besides motor signal monitoring, a digital microscope is used to visually monitor the breakage of the file.

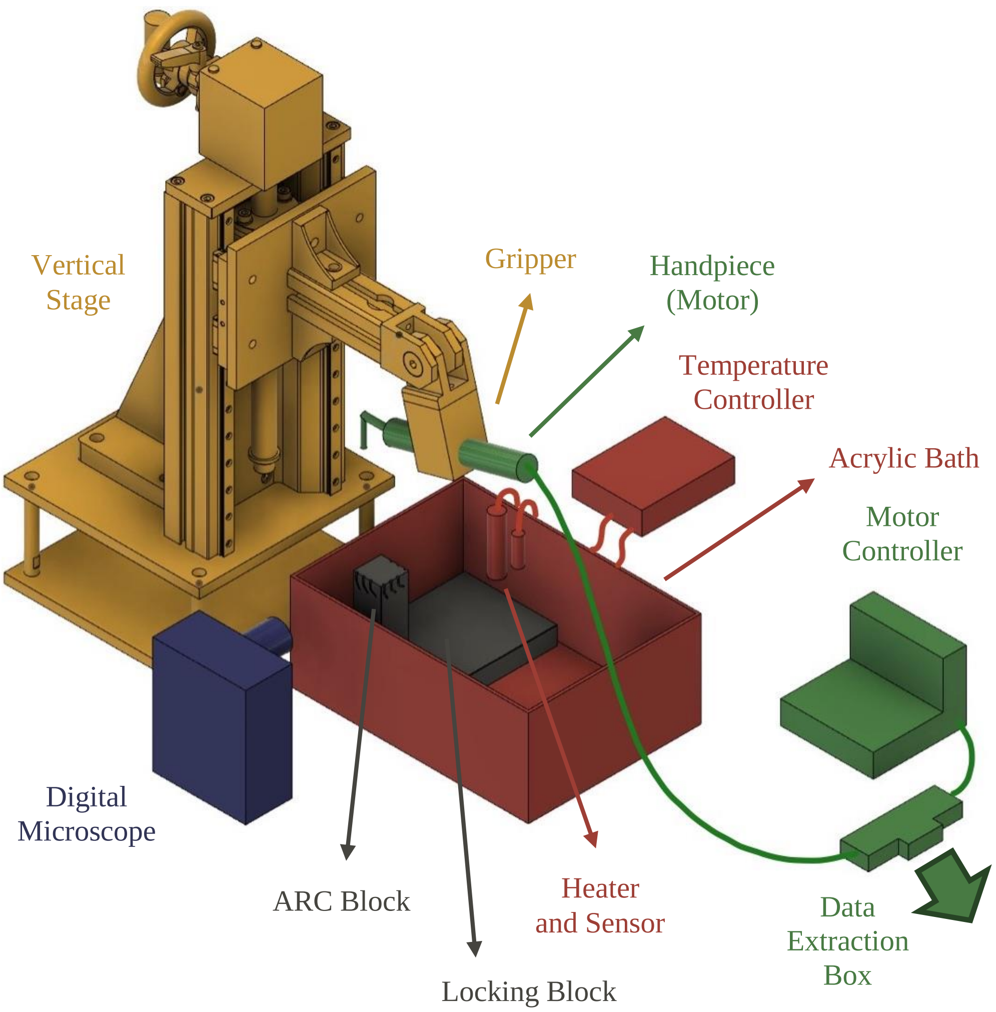

Figure 1. Illustration of bending fatigue testing system and its components: the artificial root canal unit (grey), temperature control unit (red), vertical stage unit (orange), motor control and monitoring unit (green), and visual monitoring unit (blue).

2.2. Artificial Root Canal Unit

The ARC block in the artificial root canal unit is made of hardened SKD11 steel which is a high-carbon steel possessing high hardness and high wear resistance. As a result, an artificial root canal wall will experience minimal wear during the test, thereby enhancing the reproducibility of the performed test. The artificial root canals, featuring a radius of curvature of 2 mm, 5 mm, and 8 mm along with an angle of curvature of 30°, 45°, and 60°, are machined onto the surfaces of the ARC block. These curvature attributes, namely the radius and angle, are based on the characterization by Pruett et al. [4] for describing the curvature of any root canal. All artificial root canals possess identical centerline lengths. To ensure consistent loading conditions, the midpoint of the curved section in all artificial root canals is situated 7 mm away from its tip along the canal's centerline. This guarantees that even though the tested files don't go through the same artificial root canal, they experience the most challenging stress on the identical cross-sectional area. Each artificial root canal is custom-designed to precisely match the taper of the tested file, ensuring an accurate and reproducible file trajectory. If the artificial root canal differs from the file in terms of shape, the file will not conform to the intended parameters, resulting in a reduced curvature during testing. This discrepancy can significantly impact bending fatigue test outcomes. In addition, this standardization enables logical comparisons among files that exhibit differences in shape and size, or origin from different file systems. Located at the base of the ARC block, there is a square shaft designed to fit into its corresponding hole on the locking block to properly place the ARC block in the specified position and to mitigate any potential vibrations of the ARC block that may arise while testing. In order to reduce the susceptibility of the locking block to corrosion, aluminum is selected as the material for the locking block due to the propensity of aluminum oxide to form upon exposure to air and water, therefore serving as a protective barrier against ongoing corrosion of the metal.

2.3. Temperature Control Unit

This unit includes an acrylic bath filled with water of which temperature is controlled. The artificial root canal unit is placed within this bath. To ensure the water remains within the desired temperature range, a temperature controller, heater, and temperature sensor are employed. The activation of the heater is regulated by the temperature controller. Specifically, when the sensor detects that the water temperature falls below the acceptable range, the controller activates the heater. Conversely, when the water temperature exceeds the designated range, the controller deactivates the heater immediately.

2.4. Motor Control and Monitoring Unit

The motor control and monitoring unit comprises three principal elements: the motor (handpiece), the motor controller, and the data extraction box. The motor controller receives inputs of specified rotational speeds and the motor's maximum torque from users. Subsequently, it transmits an actuating signal to the motor via their interconnection. This signal serves to set the motor into motion according to the provided input parameters. To establish a comprehensive feedback control loop, the motor then initiates the transmission of a feedback signal to the controller. This feedback signal can be retrieved from the connection using a data extraction box positioned within the connection pathway. Key instances of such signals encompass the current signal and the encoder signal. The current signal can show the amount of electrical current the motor utilizes to create an internal torque that gets it rotating over time. Also, this signal can equivalently denote an external torque applied to the motor. This equivalence stems from the fact that heightened (or diminished) external torque prompts a corresponding increase (or decrease) in internal torque within the motor. This internal torque adjustment is necessary to counterbalance the external torque, thereby maintaining a net torque of zero and enabling the motor to sustain a consistent rotational speed. To put it simply, when the external torque increases, the value of the current signal also increases, and vice versa. This connection can be utilized to identify when the file breaks. This is because when the file fractures, the path of the file inside the simulated root canal takes a sudden alteration. As a result, the point or area where the file comes into contact with the simulated root canal changes. This alteration leads to a shift in the amount of frictional force at that point or area of contact, thus shifting the file's external torque. Consequently, the external torque—applied to the file and impacting the current signal as well—sharply changes at the moment the file fractures. Apart from the current signal, the encoder signal, derived from an encoder—a sensing apparatus capable of converting motion into an electrical signal—serves the purpose of ascertaining attributes like position, count, speed, or direction as time progresses. When the file's fracture time is determined through current signal analysis, it becomes possible to correlate this time with the encoder signal to obtain the NCF of the file. To elaborate, the number of revolutions the motor goes through at the exact moment the file breaks represents the NCF of the file.

3. Validation of the Bending Fatigue Testing System for Endodontic Files

Zenflex, a newly heat-treated NiTi endodontic file system, was used to validate the testing system. Twenty files were examined using an optical microscope to ensure the absence of any visible defects. Should any file exhibit defects, it was promptly substituted with a new defect-free file. The files were tested under four different conditions, where the experimental temperature and angle of curvature of the artificial root canal were varied. These conditions included body temperature (37 ± 1°C) with curve angles of 30°, 45°, and 60°, as well as room temperature (20 ± 1°C) with a curve angle of 45°. Hence, the tested files were divided into four groups, each comprising five files for testing under the respective conditions. In all situations, the artificial root canal had the same radius of curvature of 5 mm. The tested file was precisely placed within the artificial root canal, positioning the end of the cutting segment level with the canal's coronal point. This procedure was followed to guarantee uniformity in the path and loading conditions for all tested files across each experimental condition. The files were set to be rotated at 1000 rpm. Once a file broke, its number of cycles to failure (NCF) was determined using two methods to make a comparison. The conventional approach involved multiplying the recorded fracture time, captured by a digital microscope, with the file's rotational speed. The proposed method, on the other hand, assessed NCF using analysis of both the extracted encoder signal, which was calibrated, and the current signal. Moreover, the NCF values were subsequently compared among various experimental conditions, and their correspondence with findings from prior research was assessed. To verify the capacity of the proposed testing system in generating bending fatigue loads on the file, broken files were examined from a lateral perspective using an optical microscope. Additionally, some fractured files were randomly chosen from each group for a detailed analysis of their fractured surfaces using the microscope.

4. Result and Discussion

To make certain that the tested files experienced only cyclic bending load without any significant torsional load, and to clarify that all fractures were due exclusively to bending fatigue, optical microscopy was employed for the examination of the tested files, as illustrated in Figure 2 and Figure 3. The absence of distortion around the fracture site in Figure 2 served to confirm that the proposed testing system did not generate substantial torsional load during testing, and thereby the files did not break because of excessive shear stress. In addition, the presence of a sharp break at the fracture area possibly suggested fatigue as the cause of the breakage. Figure 3, displaying the fracture surface of the tested files, reveals that fracture surfaces lack directional features like circular or swirl lines, which typically arose from twisting load. This suggested that torsional load was not a factor in the fracture of the tested files. Additionally, the flat nature of the fracture surfaces implied the influence of cyclic bending load in causing file fracture.

As depicted in Figure 4, the fatigue life (measured as the number of cycles to failure, NCF) of the tested samples differed between the conventional and proposed approaches. The proposed method was carefully calibrated to accurately measure the motor's revolution count. The discrepancy between NCF determined from the conventional and proposed method may primarily stem from the assumption drawn in the conventional method. This assumption, which assumed a consistent rotational speed for calculating the motor's cycles within a specific time, may not hold true due to real-world operational variations. Factors such as changes in mechanical load, power supply fluctuations, and friction can cause fluctuations in the motor's actual performance, deviating from the intended rotational speed setting. Using the conventional method for NCF calculation, consequently, might lead to less accurate results than the proposed NCF evaluation. Furthermore, inaccuracies in the methods used to measure the time of file failure, whether via video recording or timers, could introduce additional errors to the conventionally calculated NCF value for each sample.

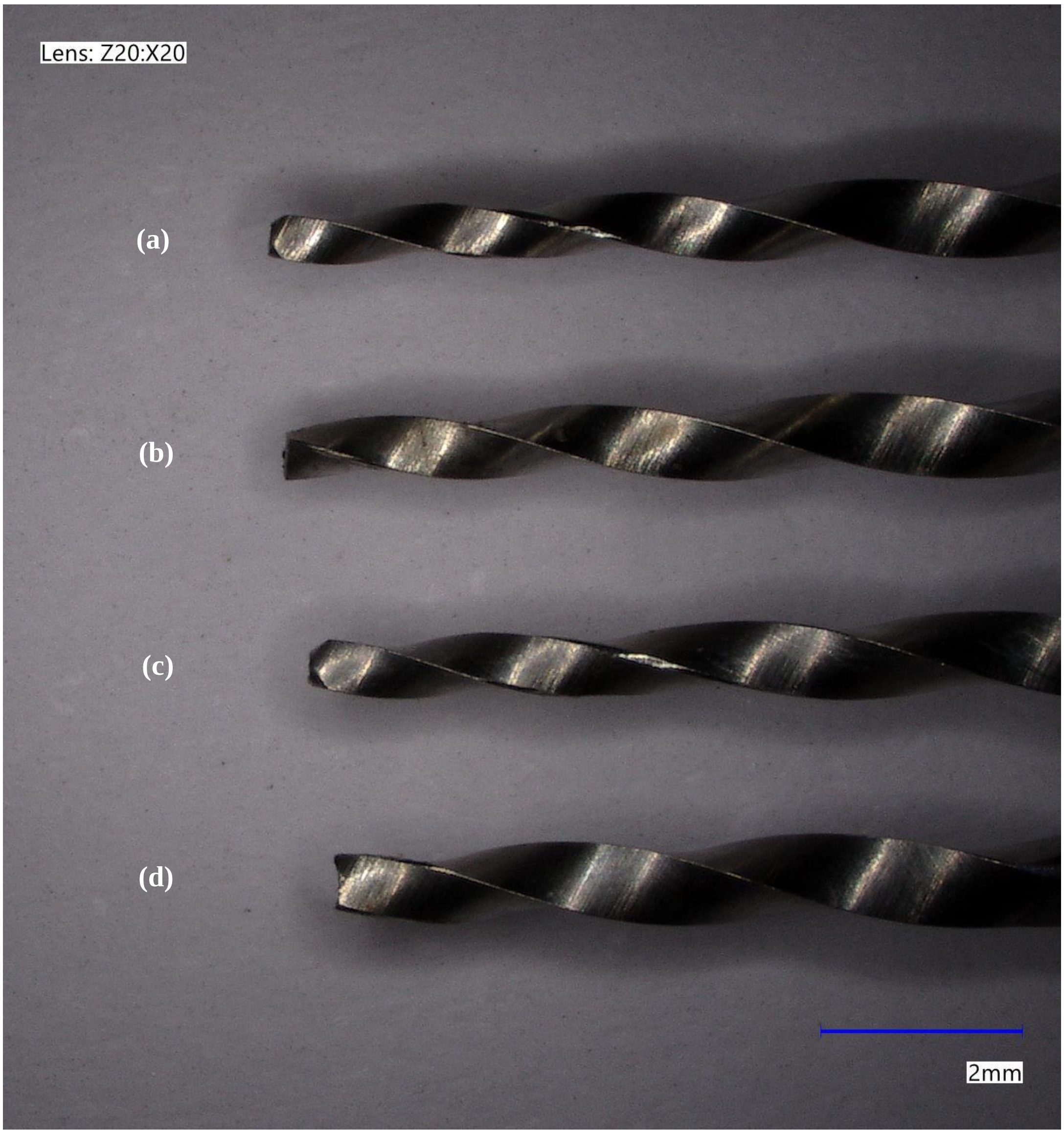

Figure 2. Side view, using an optical microscope, of fractured files from all testing conditions: (a) 45° angle of curvature at room temperature, (b) 30° angle of curvature at body temperature, (c) 45° angle of curvature at body temperature, and (d) 60° angle of curvature at body temperature.

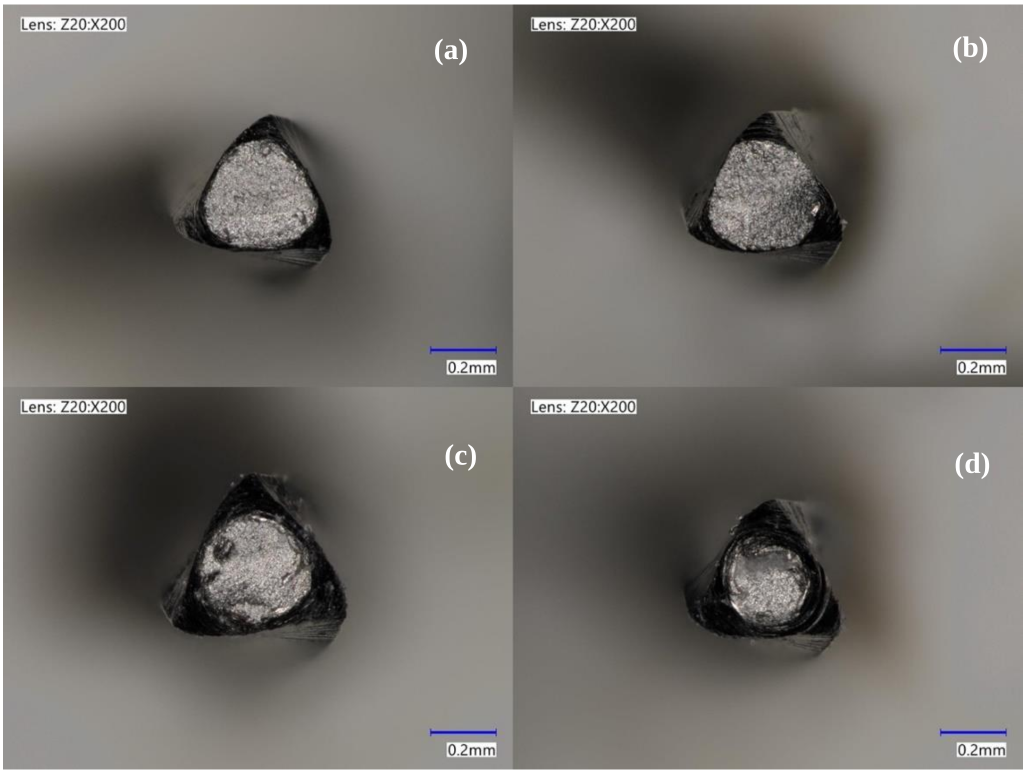

Figure 3. Fractured surface, using an optical microscope, of broken files from all testing conditions: (a) 45° angle of curvature at room temperature, (b) 30° angle of curvature at body temperature, (c) 45° angle of curvature at body temperature, and (d) 60° angle of curvature at body temperature.

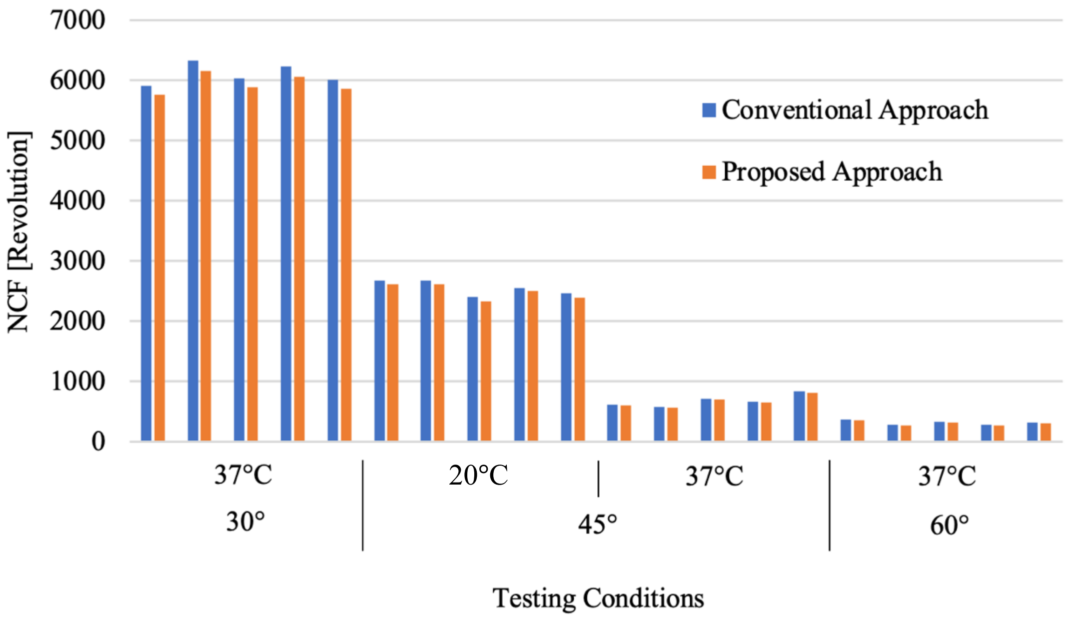

Figure 4. Variation in the number of cycles to failure (NCF) for all tested files under different testing conditions involving varying angles of curvature and temperatures. NCF values were obtained from two distinct methods.

Beyond the disparity in NCF from different methods, Figure 4 also shows two trends: First, as the curvature angle increased with a constant test temperature, NCF decreased. Second, with a fixed angle of curvature, NCF decreased as temperature rose. The initial trend aligned with previous research findings, regardless of whether the sample used in those studies was Zenflex or not [4, 12-14]. This trend could be attributed to the fact that as the file was inserted into a root canal with a greater curvature angle, it experienced heightened stress, particularly at the curved part. This increased stress likely resulted in a shorter bending fatigue life for the file. Conversely, a less severe curvature angle might lead to reduced stress and an extended bending fatigue life for the file. The second trend also corresponded to prior studies about temperature effects on the NCF of the files [15-16]. This tendency may stem from the interconnection between the mechanical properties of the file and its phase composition, which, in turn, mainly hinged on the surrounding temperature and the method of temperature alteration (via cooling or heating) [17]. When the temperature surpassed the austenitic finishing temperature, the alloy transitioned to the austenitic phase, characterized by high stiffness or a high elastic modulus. On the contrary, when the temperature fell below the martensitic finishing temperature, the NiTi adopted the martensitic phase, leading to good deformability or a lower elastic modulus, and consequently leading to enhancement of the file's bending fatigue resistance [18]. This implied that a higher martensitic phase composition in the file could lead to an increased NCF. In addition to the influence of temperature, the phase of NiTi can also be altered through mechanical stress. To elaborate, subjecting austenitic NiTi to mechanical loads can induce a gradual shift in its phase composition towards the martensitic phase. Upon unloading, the phase reverted back to the austenitic state. Nevertheless, it was unnecessary to consider the impact of mechanical stress on the file's phase transformation in this study, as the mechanical load was carefully managed through controlled factors, such as the curvature of the artificial root canal and the file's insertion depth, during the temperature-varied testing conditions. The phase transformation temperature of Zenflex was evaluated using differential scanning calorimetry analysis by Zanza et al. [19]. The martensitic and austenitic finishing temperatures of Zenflex were determined to be around 24°C and 31°C, respectively. Therefore, at room temperature, it was likely that the file would have a relatively high martensitic phase composition, attributed to the temperature falling below the martensitic finishing temperature, thus giving rise to the NCF. In contrast, when exposed to body temperature, the file's martensitic phase composition might be lower, owing to the temperature exceeding the austenitic finishing temperature, subsequently resulting in a lowered NCF.

5. Conclusion

In this research, a new bending fatigue testing system for evaluating and monitoring the number of cycles to failure (NCF) of endodontic files is designed and developed. The accuracy of this testing system in measuring the revolutions completed by the motor, and consequently NCF, is established through the calibration of encoder signals. The testing system simplifies NCF measurement by automatically extracting current and encoder signals, eliminating the need to manually record the file's fracture time and multiply it by the motor's rotational speed to calculate NCF. Moreover, all files subjected to testing within this system demonstrate clear signs of bending fatigue fractures. This underscores that the developed testing system is capable of applying cyclic bending loads to the tested files with minimal torsional load influence. The observed NCF trends of the tested files also align with prior research, indicating the reliability of the proposed testing system for conducting bending fatigue tests for endodontic files. Considering these advantages, the testing system can be applied to more advanced or more clinical-related bending fatigue tests for endodontic files. For example, it can be used in situations where files are tested in closed root canals, where visual access to check for file breakage is impossible. This overcomes the limitations of conventional methods that rely on recording the fracture time of the file.

6. References

[1] Gao, Y., Gutmann, J. L., Wilkinson, K., Maxwell, R., & Ammon, D. (2012). Evaluation of the impact of raw materials on the fatigue and mechanical properties of ProFile Vortex rotary instruments. Journal of endodontics, 38(3), 398–401.

[2] Piasecki, L., Al-Sudani, D., Rubini, A. G., Sannino, G., Bossù, M., Testarelli, L., Di Giorgio, R., da Silva-Neto, U. X., Brandão, C. G., & Gambarini, G. (2014). Mechanical resistance of carbon and stainless steel hand instruments used in a reciprocating handpiece. Annali di stomatologia, 4(3-4), 259–262.

[3] Kuzekanani M. (2018). Nickel-Titanium Rotary Instruments: Development of the Single-File Systems. Journal of International Society of Preventive & Community Dentistry, 8(5), 386–390.

[4] Pruett, J. P., Clement, D. J., & Carnes, D. L., Jr (1997). Cyclic fatigue testing of nickel-titanium endodontic instruments. Journal of endodontics, 23(2), 77–85.

[5] Bergmans, L., Van Cleynenbreugel, J., Wevers, M., & Lambrechts, P. (2001). Mechanical root canal preparation with NiTi rotary instruments: rationale, performance and safety. Status report for the American Journal of Dentistry. American journal of dentistry, 14(5), 324–333.

[6] Sattapan, B., Nervo, G. J., Palamara, J. E., & Messer, H. H. (2000). Defects in rotary nickel-titanium files after clinical use. Journal of endodontics, 26(3), 161–165.

[7] Ullmann, C. J., & Peters, O. A. (2005). Effect of cyclic fatigue on static fracture loads in ProTaper nickel-titanium rotary instruments. Journal of endodontics, 31(3), 183–186.

[8] Peters O. A. (2004). Current challenges and concepts in the preparation of root canal systems: a review. Journal of endodontics, 30(8), 559–567.

[9] Parashos, P., Gordon, I., & Messer, H. H. (2004). Factors influencing defects of rotary nickel-titanium endodontic instruments after clinical use. Journal of endodontics, 30(10), 722–725.

[10] Peng, B., Shen, Y., Cheung, G. S., & Xia, T. J. (2005). Defects in ProTaper S1 instruments after clinical use: longitudinal examination. International endodontic journal, 38(8), 550–557.

[11] Cheung, G. S., Peng, B., Bian, Z., Shen, Y., & Darvell, B. W. (2005). Defects in ProTaper S1 instruments after clinical use: fractographic examination. International endodontic journal, 38(11), 802–809.

[12] Keskin, N. B., & Inan, U. (2019). Cyclic fatigue resistance of rotary NiTi instruments produced with four different manufacturing methods. Microscopy research and technique, 82(10), 1642–1648.

[13] Lee, M. H., Versluis, A., Kim, B. M., Lee, C. J., Hur, B., & Kim, H. C. (2011). Correlation between experimental cyclic fatigue resistance and numerical stress analysis for nickel-titanium rotary files. Journal of endodontics, 37(8), 1152–1157.

[14] Anantula, K., & Vankayala, B. (2021). A comparative evaluation of cyclic fatigue resistance of ProTaper Gold, Dia-X, and ZenFlex nickel–titanium rotary files in the canals with different angles of curvature. Endodontology, 33(4), 212-215.

[15] Grande, N. M., Plotino, G., Silla, E., Pedullà, E., DeDeus, G., Gambarini, G., & Somma, F. (2017). Environmental Temperature Drastically Affects Flexural Fatigue Resistance of Nickel-titanium Rotary Files. Journal of endodontics, 43(7), 1157–1160.

[16] Hiran-Us, S., & Morakul, S. (2023). Effect of Temperatures on Cyclic Fatigue Resistance of 3 Different Ni-Ti Alloy Files. International dental journal, S0020-6539(23)00099-0. Advance online publication.

[17] Zupanc, J., Vahdat-Pajouh, N., & Schäfer, E. (2018). New thermomechanically treated NiTi alloys - a review. International endodontic journal, 51(10), 1088–1103.

[18] Figueiredo, A. M., Modenesi, P., & Buono, V. (2009). Low-cycle fatigue life of superelastic NiTi wires. International Journal of Fatigue, 31, 751-758.

[19] Zanza, A., Russo, P., Reda, R., Di Matteo, P., Donfrancesco, O., Ausiello, P., & Testarelli, L. (2022). Mechanical and Metallurgical Evaluation of 3 Different Nickel-Titanium Rotary Instruments: An In Vitro and In Laboratory Study. Bioengineering (Basel, Switzerland), 9(5), 221.

CST0001

Parametric study of caudal fin shapes for vortex-induced vibration (VIV) energy harvesting

K. Aueaiithiporn, K. Daoweerakul, N. Ratisen, P. Chompamon, S. Songschon, S. Saimek, K. Septham, and T. Kamnerdtong*

Department of Mechanical Engineering, King Mongkut's University of Technology Thonburi, 126 Pracha Uthit Rd., Bang Mod, Thung Khru, Bangkok 10140, Thailand

* Corresponding Author: thoatsanope.kam@kmutt.ac.th

Abstract. Renewable energy from water has gained popularity due to its ease of conversion into mechanical energy. When water flows around a circular cylinder with a Reynolds number ranging from 300 to 300,000, it generates a phenomenon known as the Kármán vortex street, which can be utilized in the design of energy harvesting devices. One such device that utilizes vortex energy is a piezoelectric system attached to a flexible beam, where the power of the harvested energy is directly related to the deflection of the beam. The biomimicry of caudal fins is applied to the end of flexible beam to improve the efficiency of the device. The fork types of caudal fin are investigated based on four kinds of fish: Bluefin Trevally, Bigeye Trevally, Humpback Snapper, and Great Barracuda. In this research, surface area, length, height, aspect ratio, mass, and center of mass are controlled to avoid any advantageous influences on the shapes. A Reynolds number of 32,500 and a free stream velocity of 0.5 m/s are used. The simulation is based on Computational fluid dynamics (CFD) and the Finite Element Method (FEM) to investigate the Fluid-Structure Interaction (FSI) using Altair HyperWorks softwares. The results show that the Bluefin Trevally gives the highest equivalent power and beam displacement at the same monitoring point, with 87.92 % improvement in displacement and 261.40% improvement in equivalent power compared to the normal rectangular shape of the beam.

Keywords: Biomimicry, Caudal Fin, Computational fluid dynamics (CFD), Vortex-induced vibration (VIV), Fluid-Structure Interaction (FSI), Energy harvesting.

1. Introduction

According to the world's human population growth, many countries tend to consume more energy. However, the reliance on fossil fuels for energy production has detrimental effects on the environment. Thus, renewable energy is naturally replenished and has a minimal impact on the environment and provides a cleaner and more sustainable alternative for meeting our future energy needs [1]. However, renewable energy technology nowadays needs to develop more for demand of using renewable energy. This research study is about the energy harvesting from natural phenomena named “Kármán vortex street”. As the fluid flows around the object, it creates alternating areas of low-pressure and high-pressure regions. These pressure differences induce the formation of vortices, which are swirling patterns of fluid motion. In the case of Kármán vortex street, the vortices are shed alternately from each side of the object, forming a distinctive pattern resembling a series of swirling eddies. This phenomenon will induce the object to vibrate, known as Vortex-induced vibration (VIV) [2].

In a study conducted by Xinyu An et al. The effects of plate length and flow velocity on wake structure were explored through two-dimensional computational fluid dynamics (CFD) simulations. The findings indicated that the optimal plate length for maximizing energy harvesting efficiency lies within the range of 1.5 times to 2.5 times the plate's cylinder diameters [3]. In an experiment conducted by Emmanuel Mbondo Binyet et al. The focus was on investigating the use of a flexible plate in the wake of a square cylinder for piezoelectric energy harvesting. The research findings indicated that the selection of geometric parameters should align with the desired range of incoming flow velocities. Moreover, it was observed that longer plates yield higher power output, although they exhibit lower conversion efficiencies [4]. Ou Xie et al. simulation and experiment study fishtail motion response in two scenarios: close to the ground and with different areas. Horizontally positioned fishtails were found more effective near the ground, while the height of vertically placed fishtails had minimal impact on efficiency. Increasing fishtail area (dv=4C0) improved effectiveness for both vertical and transverse configurations [5].

The present study aims to investigate the shape parameters influencing energy harvesting. This will be achieved through practical fluid structure interaction (P-FSI) modeling, employing OptiStruct and AcuSolve solvers. The investigation will encompass simulations involving various shapes of forked fish tails while maintaining consistent conditions such as plate length, flow velocity, aspect ratio, mass, and center of mass. The objective is to ascertain the extent to which shape parameters influence energy harvesting efficiency.

2. Methodology

2.1. Model design

The main structure of the simulation model consists of two main components: a bluff body serving as a vortex generator and a beam connected to the caudal fin shapes. This configuration consists of a cylinder with a diameter of 65 mm, specifically designed to operate at a Reynolds number of 32,500 with a flow rate of 0.5 m/s to induced vortex generation. The beam has dimensions of 80 mm in length, 15 mm in height, and 1 mm thickness. Additionally, a caudal fin with a length of 30 mm is included, as illustrated in Figure 1. Table 1 provides an overview of the material properties utilized in the model's construction, as referenced in prior works [6-7].

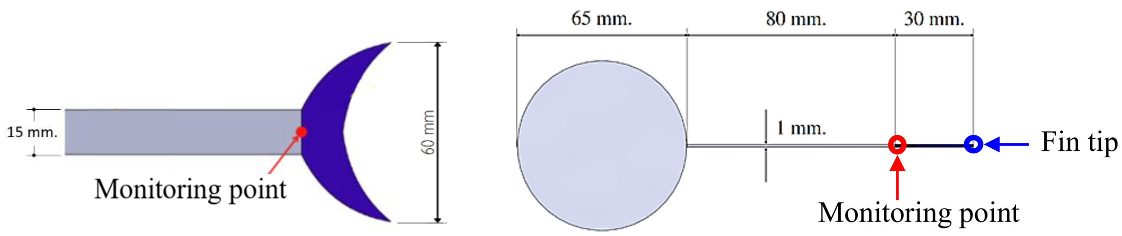

Figure 1. The dimension of the model.

Table 1. Material properties of fluid and structure.

Properties	Value	Unit
Beam and Caudal fin		
- Density, ρ	1300	kg/m^3
- Poisson's Ratio, ν	0.4	
- Elastic Modulus, E	1800	MPa

The caudal fins design is divided into two sets: SET 1, consisting of biomimicry-inspired shapes, and SET 2, involving parameter-based designs focusing on leading angle and curvature which are improved from the best model of SET1. The control parameters for these designs are detailed in Table 1.

Table 1. The controlled parameters of caudal fins.

Parameters	Value	units
Fin height (h)	60	mm
Mass (m)	0.94	g
Caudal fin surface area (A)	1450	mm^2
Aspect ratio (h^2/A)	2.48	-
Center of mass	(11.62,0,0)	-

2.1.1. Design of Biomimicry- inspired shapes

The biomimicry-inspired shapes were carefully selected as part of the simulated model to represent a range of swimming characteristics. Notably, all of the caudal fins in both sets are of the forked type. Figure 2 shows four distinct shapes of caudal fins from four different species: Bluefin Trevally, Bigeye Trevally, Humpback Snapper, and Great Barracuda. These species exhibit diverse feeding habits that are closely related to their respective caudal fin shapes.

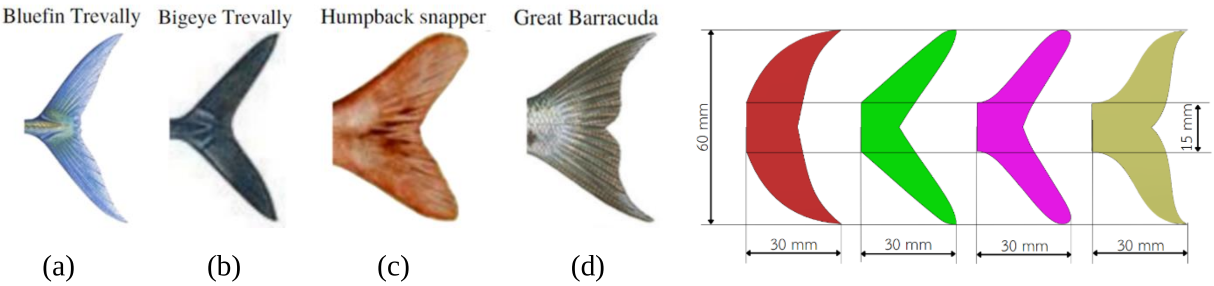

Figure 2. The shapes and dimensions of caudal fin SET1 Models (1.1-1.4).

2.1.2. Parameter-based designs

The SET 2 models are investigated from the SET 1 model, specifically the Bluefin Trevally shape shown in Figure 2(a), which exhibits the maximum displacement amplitude. In SET 2, these shapes undergo modifications to their leading angles and curvature, as illustrated in Figure 3.

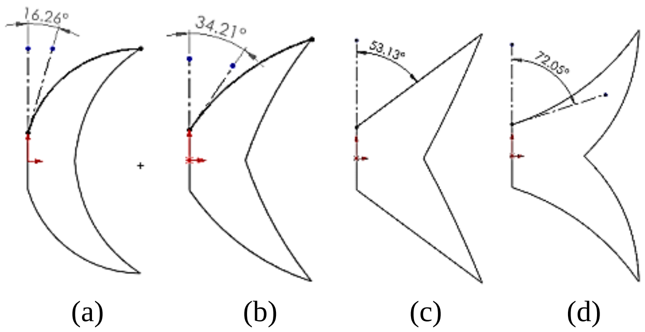

Figure 3. Caudal fin SET 2 models (2.1-2.4) : The shape design by curvature and leading angle.

The varied leading angles and curvature are shown in Table 2. These designs have increased the curvature to transition from a convex to a concave fin as shown in Figure 3.

Table 2. Parameters of SET 2.

Model	Curvature (mm.)	Leading angle (degree)
2.1	R31.25	16.26
2.2	R57.81	34.21
2.3	R0	53.13
2.4	R-57.81	72.05

2.2. Simulation Process

The simulations are performed by using Altair 2023, OptiStruct and AcuSolve solver to calculate the P-FSI approach. The mesh generation is discretized by SimLab. Figure 4 is the dimension of computational fluid domain which use in the simulation.

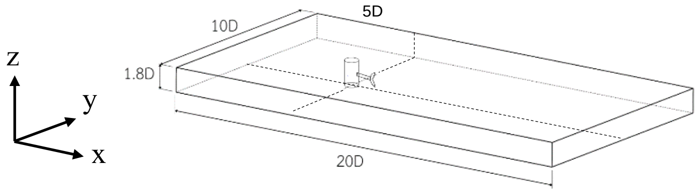

Figure 4. The computational fluid domain.

In P-FSI method, the modal analysis of the beam and caudal fin also performed to analyse the dynamics behaviour of the structure. The hexahedron elements are applied to the structure as shown in Figure 5(a). The computational domain is meshed using unstructured tetrahedron elements (Tet4) and creating inflation layers with prism as in Figure 5(b). The total number of elements is about 500,000.

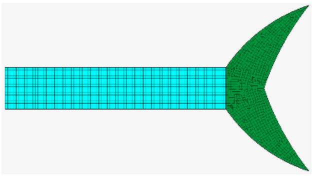

(a)

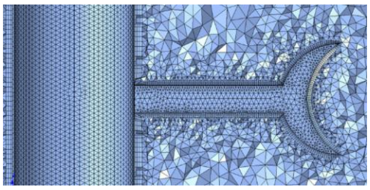

(b)

Figure 5. (a) Mesh generation of the beam and caudal fin, (b) computational domain.

Incompressible water at 25 °C with an inlet velocity of 0.5 m/s and a static pressure of 0 Pa at the outlet is set as the boundary condition for the computational domain. The structure is constructed with symmetry on the top and bottom sides, as illustrated in Figure 7. The time step is 0.001 second, controlled under the CFL < 1 condition [8], with a desired y+ of 30 [9]. Computational Fluid Dynamics (CFD) techniques are applied to investigate the problem. The Spalart-Allmaras [10] turbulent model is used, computed with a moving mesh to predict adverse pressure gradients due to shedding vortices.

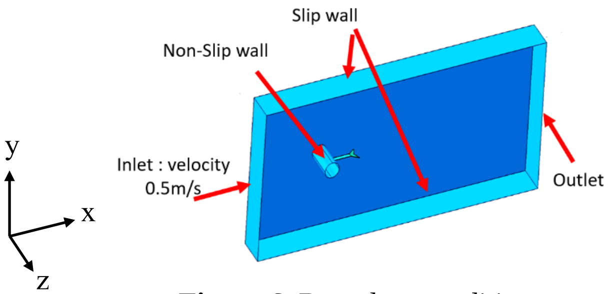

Figure 6. Boundary conditions.

2.3. Simplified power calculation
To compare the performance of various caudal fin shapes, the equivalent power is used and determined by calculating the equivalent force from the deflection of cantilever beam at the monitoring point in Figure 7 for half period shown in Figure 8. Therefore, the strain energy per cycle of the beam can be obtained.

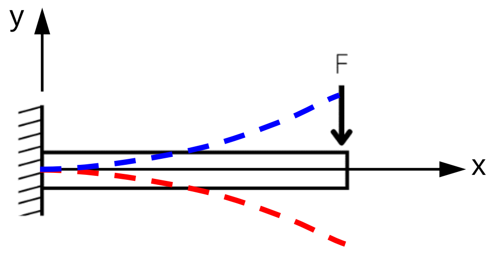

Figure 7. Simplified load on cantilever beam.

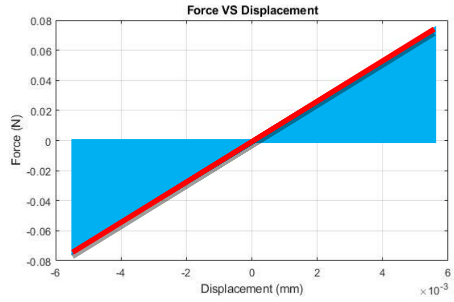

Figure 8. Equivalent force vs displacement.

3. Results

3.1. Displacement and equivalent power of caudal fins set 1 and 2

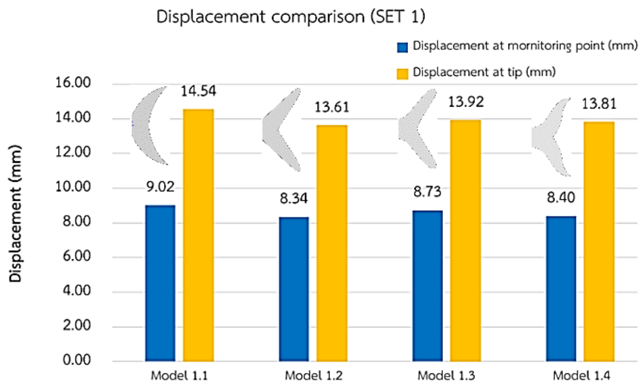

Figure 9. Amplitude displacement (SET 1).

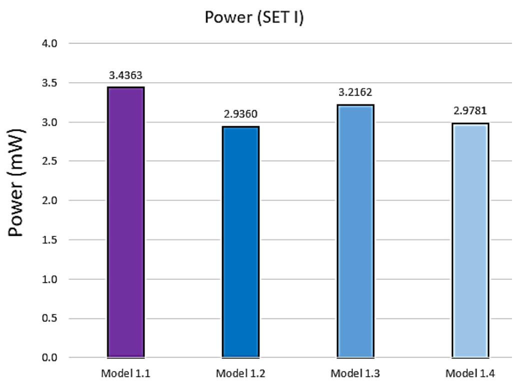

Figure 10. Equivalent Power (SET 1).

In SET 1, Figure 9 shows the displacement of each shape at monitoring points and the fin tip, indicating that Model 1.1, Bluefin Trevally, has the highest displacement of 9.02 mm and generates 3.4363 mW of power, as shown in Figure 10. Moreover, the vibration frequencies are 1.6018 Hz, 1.6009 Hz, 1.6005 Hz, and 1.6251 Hz, respectively. The displacement of the caudal fin is a key parameter that affects power generation.

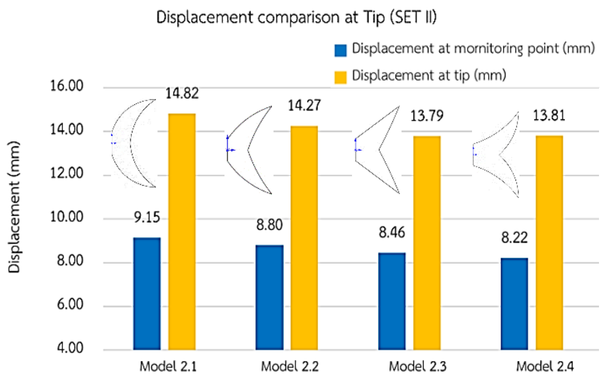

Figure 11. Amplitude displacement (SET 2).

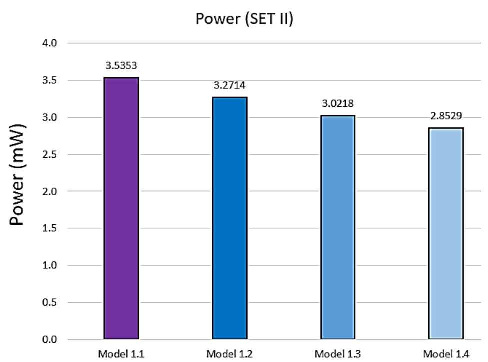

Figure 12. Equivalent Power (SET 2).

The designs in SET 2 are based on models from the model 1.1 of SET 1 that generates the highest power. They involve variations in leading angles and curvature to investigate their effects. Figure 11 shows the displacement of SET 2 after changing curvature and leading angle of caudal fins from model 1.1 of SET1. It is found that Model 2.1 achieves the highest displacement at 9.15 mm at the monitoring point and generates 3.5353 mW power which is better than all of models. The vibration frequencies are 1.6015, 1.6022, 1.6013, and 1.6013 Hz, respectively. This means that the best fin model for harvesting energy from vortex should be in a crescent shape. Meanwhile, the equivalent power of each model of SET2 is also shown in Figure 12.

3.2. Transverse pressure contour (y-direction)

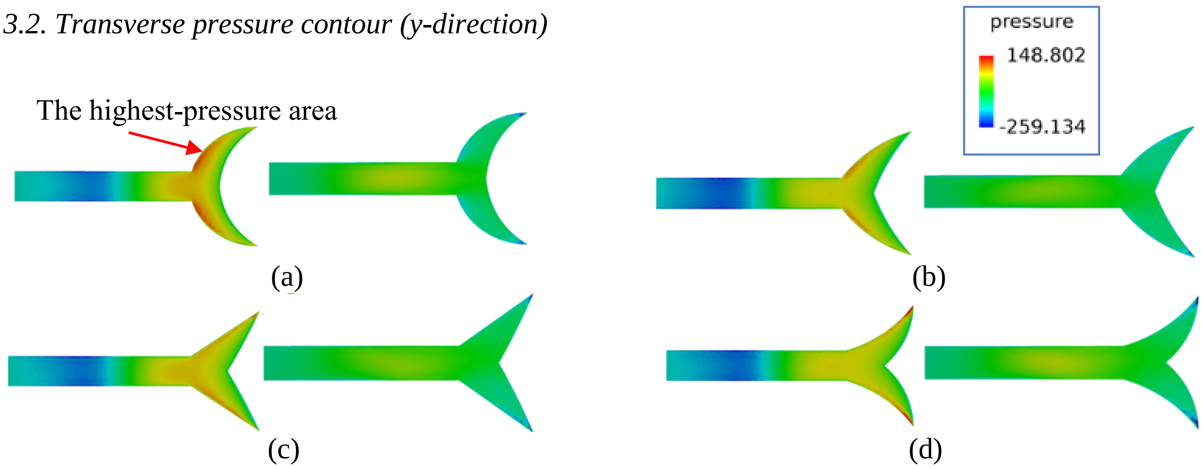

Figure 13. Pressure contours on upper and lower surface of tails (SET 2).

The high-pressure region occurs around the leading edge of the caudal fin and the low-pressure region occurs on the middle of the beam. Especially, Model 2.1 shows a remarkably bigger high-pressure area, which induces the tail to oscillate with the highest amplitude displacement, as depicted in Figure 13.

3.3. Longitudinal fluid pressure contour

Longitudinal fluid pressure contours are examined in a steady flow simulation with only fins, under the same flow conditions to see the effect of the leading and tailing edges.

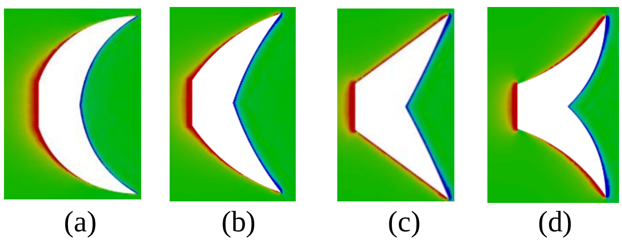

Figure 14. Longitudinal pressure contours (SET 2).

Model 2.4 produces a bigger high- and low-pressure region at the fin tip compared to other models due to its large leading angle and curvature radius, creating a greater pressure difference zone. This results in higher resistance than the other models. In contrast, Model 2.1 has the smallest high- and low-pressure region due to its small leading angle and curvature radius facilitating the flow and preventing pressure accumulation. Consequently, the pressure difference in this model is minimized, as shown in Figure 14.

3.4. Drag and lift coefficients

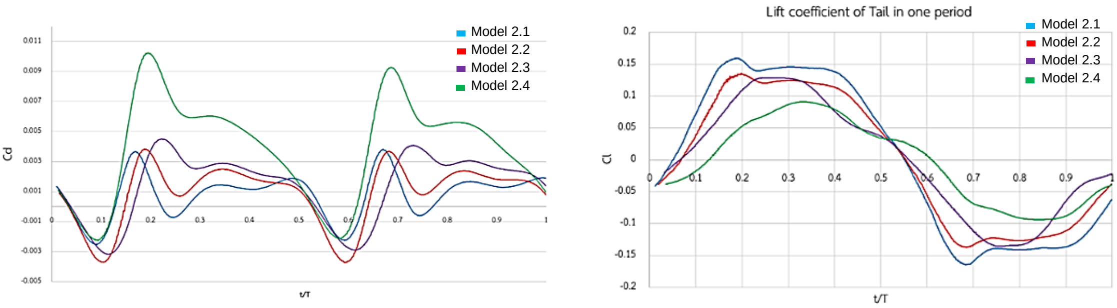

(a) (b)

Figure 15. Drag and lift coefficients of tails (SET 2**)** within one period**.**

According to Figure 15(a), the characteristics of loads on the beams and caudal fins during one period are presented in terms of drag coefficients. The drag can be ranked from the highest to the lowest model: 2.4, 2.3, 2.2, and 2.1, respectively. These drag coefficient behaviors are inversely related to the lift coefficients in Figure 15(b) which are ranked from model 2.1 to 2.4, respectively.

Considering both drag and lift coefficients provides insights into the overall force acting on the beam and fin. This force is derived from the pressure difference induced by eddy currents, leading to the creation of low-pressure areas. Furthermore, the effect of the force corresponds to the resulting amplitude. Hence, it can be concluded that a larger drag coefficient results in a decrease in amplitude, while a higher lift coefficient leads to an increase in amplitude.

3.5. The x-velocity, vorticity, and fluid pressure contours of water during the tail moving down.

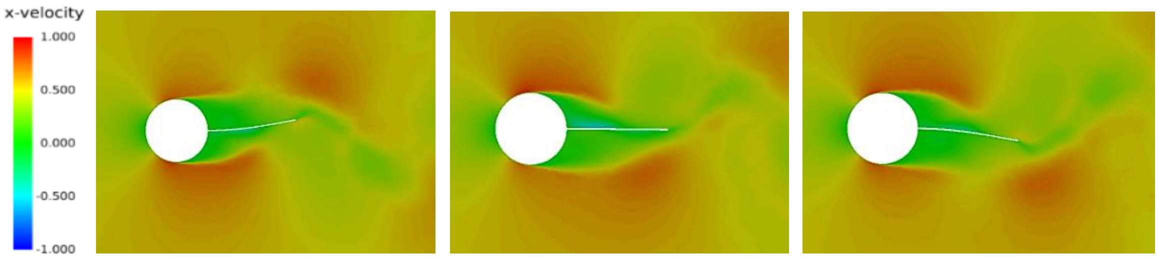

Figure 16. The x-velocity of the flow while moving down.

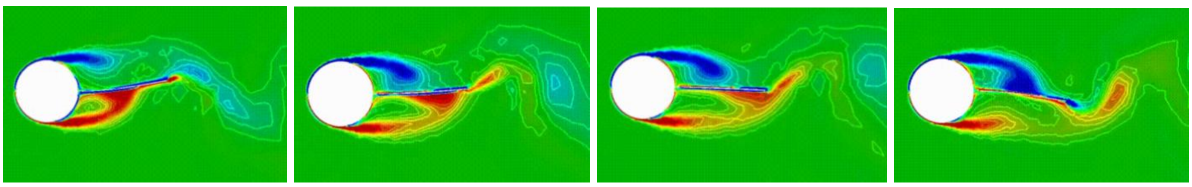

Figure 17. The effect of vorticity to the caudal fin while moving down.

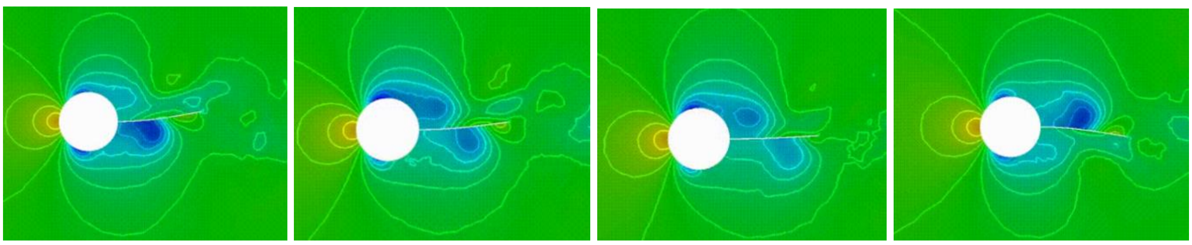

Figure 18. The effect of fluid pressure to the caudal fin while moving down.

When considering the velocity in the direction of water flow while the tail is moving down, the tail tends to move into the direction of high-velocity region as shown in Figure 16. The vorticity also performs at the bottom of tail and moves from left to right and then followed by the vorticity at the top of tail in the same manner after the first process finished, shown in Figure 17, which induces low pressure at that region and generates pressure difference causing the tail moving down shown in Figure 18. This behavior occurs and causes the tail to flap back and forth continuously.

3.6. Comparison of maximum drag and lift coefficients

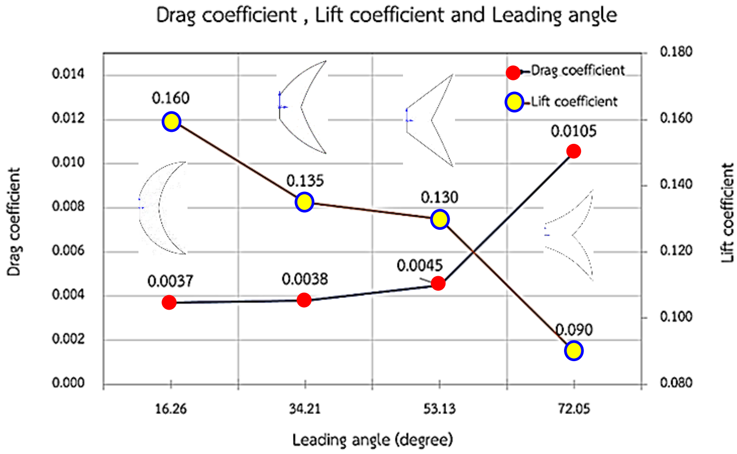

Figure 19. Comparison of drag and lift coefficients vs leading angles.

Figure 19 illustrates the relationship between the maximum drag and lift coefficients within a single period and four SET2 models, each characterized by distinct leading angles. Specifically, the tail model (referred to as beam-fin) exhibits a higher lift coefficient and a lower drag coefficient simultaneously, leading to a substantial increase in the deflection of the beam.

3.7. Power improvement with different fins

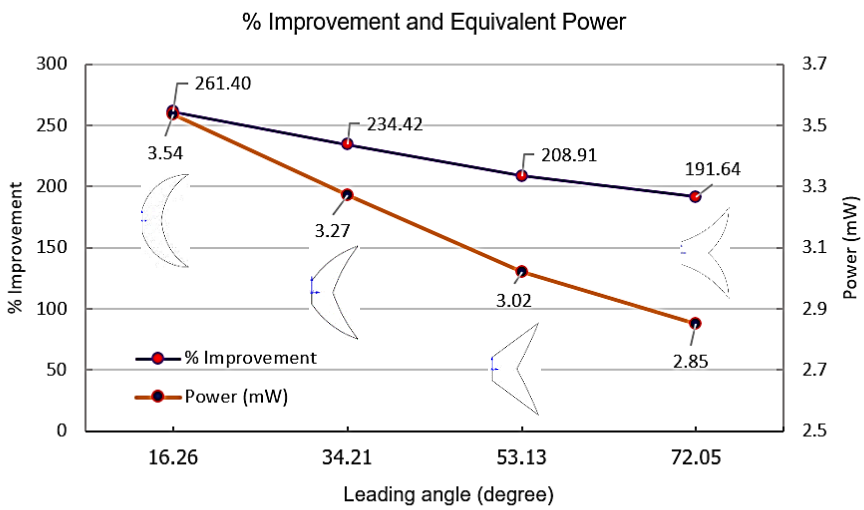

Figure 20. Improvement of SET2 models.

In Figure 20, all models generate more power than the rectangular shape. Model 2.1 produces the highest power, reaching 3.54 mW, which is 261.40% higher than the normal rectangular shape.

4. Conclusion

According to the results, the study results indicate that the factors influencing the oscillation amplitude can be described as follows:

1. The fin's physical characteristics, such as leading angle and curvature radius in contact with the fluid, strongly influence pressure distribution around the fin. A smaller leading angle and increased fin convexity create higher-pressure region compared to other models, leading to the greatest pressure difference in the transverse direction. Conversely, models with a larger leading angle and higher fin concavity generate a lower-pressure region, causing the greatest pressure difference in the longitudinal direction. The best caudal fin shape in this work should be a crescent shape.

2. Differences in pressure around the fin affect both the drag and lift coefficients. Transverse pressure differences increase the lift coefficient, while longitudinal differences elevate the drag coefficient. Displacement amplitude depends on these coefficients. The drag coefficient varies inversely with displacement amplitude, while the lift coefficient shows a direct relationship. A higher drag coefficient increases resistance and reduces amplitude, while a higher lift coefficient enhances amplitude.

3. Power generation depends on both displacement amplitude and vibration frequency. However, in this simulation, the frequencies among all models did not significantly differ. Therefore, displacement amplitude emerges as the primary factor for calculating mechanical power. Models designed for the highest amplitude yield the greatest power output. In summary, the best model in this study is model 2.1, which achieves a displacement amplitude of 9.15 mm at the monitoring point and 14.82 mm at the tail tip, resulting in a power output of 3.54 mW, a remarkable 261.40% improvement over the normal rectangular fin shape.

This finding has the potential for future applications in the design of energy-harvesting devices, utilizing electric generators like piezoelectric plates.

5. References

[1] Demirbaş, A. (2006). Global renewable energy resources. *Energy sources*, *28*(8), 779-792.

[2] Kawai, H. (1993). Vortex induced vibration of circular cylinder. *Journal of Wind Engineering and Industrial Aerodynamics*, *46*, 605-610.

[3] An, X., Song, B., Tian, W., & Ma, C. (2018). Design and CFD simulations of a vortex-induced piezoelectric energy converter (VIPEC) for underwater environment. *Energies*, *11*(2), 330.

[4] Binyet, E. M., Chang, J. Y., & Huang, C. Y. (2020). Flexible plate in the wake of a square cylinder for piezoelectric energy harvesting—Parametric study using fluid–structure interaction modeling. *Energies*, *13*(10), 2645.

[5] Xie, O., Yao, J., Fan, X., Shen, C., & Zhang, C. (2022). Numerical and experimental study on the hydrodynamics of a three-dimensional flapping caudal fin in ground effect. *Ocean Engineering*, *260*, 112049.

[6] Chompamon, P., Tiansiri, R., Chularak, T., Kotwongsa, R., Songschon, S., Saimek, S., Septham, K., & Kamnerdtong, T. (2022). Performance improvement of caudal fin shapes for vortex-induced vibration energy harvesting. In *Proc. Int. Conf. of The 16th Asian Symposium on Visualization* (p 1-6).

[7] Chompamon, P., Tiansiri, R., Chularak, T., Kotwongsa, R., Songschon, S., Saimek, S Septham, K., Kamnerdtong, T. (2022). Performance evaluation of caudal fin shapes for vortex-induced vibration energy harvesting. In *Proc. Int. Conf. of The 12th TSME International Conference on Mechanical Engineering* (p 1-7)

[8] Li, S., & Sun, Z. (2015). Harvesting vortex energy in the cylinder wake with a pivoting vane. *Energy*, *88*, 783-792.

[9] George, W. K. (2013). *Lectures in Turbulence for the 21st Century*. Chalmers University of Technology.

[10] Tarafder, M. S., & Bipul, M. S. I. (2023). Numerical Simulation of Turbulent Flow around Hydrofoil by Spalart-Allmaras Model, In *Proc. Int. Conf. of The 13th International Conference on Marine Technology* (pp. 7)

The 13th TSME International Conference on Mechanical Engineering
12th – 15th December 2023
Chiang Mai, Thailand

CST0002

CFD Analysis on the Performance of a DPI

R F Al-Waked[1,*] and T Abu Dahab[1]

[1]Department of Mechanical and Maintenance Engineering, German Jordanian University, Amman 11180, Jordan

* Corresponding Author: rafat.alwaked@gju.edu.jo

Abstract. Effects of inhalation flow rate, mouthpiece length and mouthpiece shape on the performance of the dry powder inhaler (DPI) were investigated. Initial quantification of flow turbulence levels and flow fields generated within the were examined using computational fluid dynamics (CFD) approach. The CFD model was validated against available published works in literature. Results showed that the length of the mouthpiece determines the level of flow development through the mouthpiece itself and does not affect the flow at the base of the inhaler. Also, as the length of the mouthpiece decreases a non-uniform behaviour existed at the outlet of the inhaler where regions of high velocity were presented thus an overall decrease in the performance of the inhaler. As the inhalation flow rate increases the level of turbulence in the device increases and reaching a maximum at the grid. This study showed that the geometry of a dry powder inhaler mouthpiece could have a significant effect on the amount of throat deposition produced and the flow development when using the device by controlling the exit air flow velocity.

Keywords: DPI, CFD, Human Lungs, Inhalation Drug Delivery.

1. Introduction

Respiratory drug delivery devices are used to assist in curing respiratory system diseases as they are dependable on the unique physical characteristics of respiratory tract and lung: There are less digestive enzyme in the lung than in the digestive tract and the hydrolytic enzymes show less activities, both of which are helpful to enhance bioavailability of the Active Pharmaceutical Ingredient (API) [1]. The respiratory tract and lung have a huge surface area where plenty of capillary vessels exist and carry huge blood flow. Additionally, alveolar epithelial cells are arranged by a monolayer structure which would greatly improve the rate and extent of the API absorption. The API is absorbed into systemic circulation directly, avoiding the hepatic first-pass effect [2]. For respiratory disease, inhalation drug delivery could decrease the drug quantity by enhancing therapy efficiency, and decreasing systemic side effect by direct action on target cells. Therefore, the respiratory drug delivery mechanism has been widely used to treat respiratory disease by topical therapy and other disease by systemic therapy [3].

Pressurized meter-dose inhalers (pMDIs) could be considered as the main source of drug delivery to the lungs as they represent more than 80% of the global market [4]. However, this type of inhalers has a number of shortcomings in effectiveness and usability. Most prescribed pMDIs are inefficient as they deliver only one third of the amount of drug to the lungs. Moreover, there were environmental concerns of the propellant used in the pMDIs, chlorofluorocarbon (CFC) was contributing to irreparable damage to the ozone layer in the environment [5]. As a result, there has been an interest in developing alternatives to the pMDI. This is when the concept of the breath actuated dry-powder inhaler (DPI) came to life.

The pressurized metered-dose inhaler and DPI are medical aerosol delivery devices that combine a device with a specific formulation and dose of drug. Each actuation of the inhaler is associated with a single inspiration of the patient. An ideal inhaler has been characterized in literature as accurate and consistent in effective drug delivery, easy and convenient to use, easy to teach, learn and remember how to use correctly, capable of delivering a range of drugs, accurate dose counter, patient feedback of dose taken, convenient to carry, robust; visually appealing to the patient, easily identifiable in terms of the drug/strength contained in the inhaler, and propellant-free [4]. The main aim when designing a DPI is to provide an environment where the drug can maintain its physiochemical stability and produce reproducible drug dosing. DPIs should be designed to deliver high fine particle fraction (FPF) of the drugs from the formulations. Devices with higher resistance need higher inspiratory force by the patients to achieve desired air flow, which could be difficult for patients with severe asthma and for children and infants [6, 7]. This means that device design is also an important factor in deciding its efficiency because the dimensions and internal anatomy of the device introduce resistance to airflow. Generally, the performance of an inhaler is governed by three main factors: drug formulations, design of the inhaler and patients inspiratory flow rate [8]. A number of studies have recently been performed to investigate the dependency of DPI performance on these factors [9].

Computational fluid dynamics (CFD) modelling has been utilised to study effects of patients' inspiratory flow rates and certain design aspects such as grid structure, mouthpiece geometry, and size of the air inlet on the performance of the inhaler [10]. Coates et. al. [10] studied the effect of modifying the design of dry powder inhalers on the inhaler performance and also studied which design features affect the overall performance of the inhaler using CFD tools. It was concluded that as the grid voidage increased the amount of powder retained in the inhaler doubled. This was because of the increase of tangential flow of the particles in the inhaler mouth piece. The length of the mouthpiece was also studied by Coates et. al [10], due to its importance in determining the level of development of the flow inside the mouthpiece. The length of the mouthpiece was found to not affect the inhaler performance since the flow generated in the device in not greatly affected by the length of the mouthpiece. Zhou et al. [11] investigated the air flow pattern and particle impaction. It was concluded that there is no significant difference in the aerosolization behaviour between the original and 1/3 mouthpiece length devices. The air inlet size and grid structure of a single capsule dry powder inhaler was found to affect the aerosolization of the carrier-based powder.

Undeveloped flow contains areas of high velocity that results in an increase in throat impaction when the patient is inhaling through the inhaler. It is believed that the larger the level of flow development in the mouthpiece the more uniform the flow profile is at the device exit. Uniform flow profile results in a reduced area or region of high velocity, potentially reducing throat impaction and improving overall inhaler performance.

The current study aims at investigating effects of: inhalation flow rate, mouthpiece length, and mouthpiece shape on the performance of the DPI and to provide an initial quantification of flow turbulence levels and flow fields generated within the DPI device and outlets. Furthermore, the aim is to investigate effects of flowrates on the deposition inside the lung tracks. CFD analysis based on Ansys package was performed to determine how flow fields generated within the inhaler varies with different inhalation flow rates, mouthpiece lengths and geometries. The Discrete Phase Model (DPM) of Fluent-Ansys was used to study the dispersion of the dry powder in the inhaler. The computational model was validated by research available in literature. CFD analysis was also performed to determine how the inhalation flowrates affects the deposition within the lung tracks.

2. Methodology

2.1. Governing Equations

The motion of a fluid is governed by the Navies-Stokes equations in an Eulerian-framework. CFD approach was used to solve the Navier-Stokes equations based on the following equations:

$$\frac{\partial \alpha_f \rho_f}{\partial t} + \nabla.\left(\alpha_f \rho_f u_f\right) = 0 \tag{1}$$

$$\frac{\partial \alpha_f \rho_f}{\partial t} + \nabla.\left(\alpha_f \rho_f u_f\right) = -\alpha_f \nabla \mathrm{p} - F_{fp} + \nabla.\left(\alpha_f \tau\right) + \alpha_f \rho_f g \tag{2}$$

The first equation above is the continuity equation of the fluid, where α_f is the volumetric fraction, ρ_f is the density and u_f is the velocity of the fluid. The second equation is the momentum conservation equation, where ∇p is the pressure difference, F_{fp} is the fluid-particle interaction force, $\nabla.(\alpha_f \tau)$ is the viscous stress tensor and the last term $\alpha_f \rho_f g$) is the gravitational force. The fluid-particle interaction force F_{fp} is the sum of the fluid-particle interaction forces of all particles.

Fluid flow must satisfy the law of conservation of mass where the mass of the system must remain constant over time, as the system mass cannot change quantity if it is not added or removed. This could be expressed as:

$$\frac{\partial \rho}{\partial t} + \frac{\partial (\rho u_x)}{\partial x} + \frac{\partial (\rho u_y)}{\partial y} + \frac{\partial (\rho u_z)}{\partial z} = 0 \tag{3}$$

In DPM, the motion of the particle is modelled with respect to newton's laws of motion of an individual particle. Fluid flow is modelled as a continuum phase with respect to the local averaged Navier-Stokes equations on a computational cell scale. Both of particle and fluid phases are able to have mutual interactions such as momentum, heat and mass transfer. Using DPM to generate particle deposition relationships is considered an important approach for validating the model and for assessing predicted particle impingement behaviour during studying the performance of device. Lagrange particle tracking method treats the fluid flow field as being comprised of a large number of finite sized fluid particles which have mass, momentum, internal energy, and other properties. Mathematical laws could then be written for each fluid particle. The trajectories are calculated by integrating the particle force balance equation:

$$\frac{\partial u_p}{\partial t} = F_D + F_G \tag{4}$$

where F_D is the drag force per unit particle mass and F_G the gravitational force on particle.

2.2. Boundary Conditions and Simulation Parameters

The Standard k-ω model with low Reynolds number (LRN) was adopted for the turbulent flow of air as fluid. All transport equations were discretized to be at least second order accuracy in space. A Second-order upwind scheme was used to discretize the pressure equations. Rosin-Rammler logarithmic diameter distribution of inert particles, injected using face normal direction, was used as input for Fluent's DPM. It was assumed that particles behave in such way that when contact with the wall they stay “trapped” and the particles that reach the outlet surface “escape” the device domain. The flow rates that were studied were 10, 28.3, 45, 60, and 90 L/min. The utilized boundary conditions are listed in Table 1.

2.3. Computational Models

In order to analyse the efficiency of the inhaler, it is important to analyse the fluid domain inside the inhaler where the air will flow. As for the lungs model, it was built on solidworks® using the dimension given in literature [12]. The fluid domain was drawn on Solidworks®; in Ansys® the inlets, outlet and the walls were defined. After importing the model from Solidworks®, the mesh for the fluid domain of the inhaler was made using Ansys® software. The lungs were was meshed with tetrahedral cells due to their better adaptation to complex geometries. The mesh was finer near the walls, compared to the rest of the computational domain, with a 0.5 mm element size was used as shown by Figure 1, in order to ensure capturing all of the phenomena governing particle deposition onto the internal surfaces due to higher velocity and pressure gradients.

Table 1. Boundary conditions utilised for the simulation process.

Type	Value	Unit
Element Size	0.5	mm
Gravity	9.81	m/s^2
Flow rate	Variable	L/min
Mass flow rate at inlet	Variable	kg/s
Number of Particles	200	-
Density of Particles	1670	kg/m^3
Air density	1.225	kg/m^3

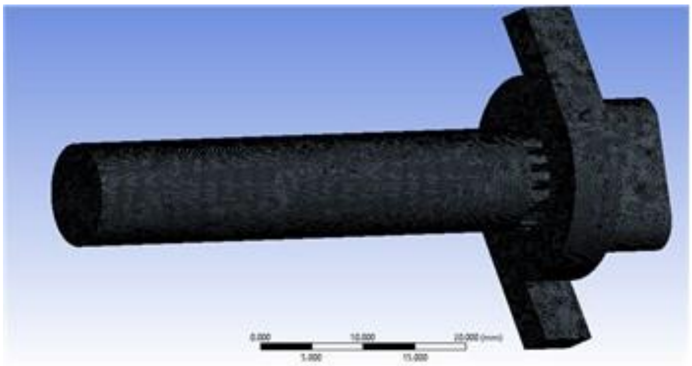

(a)

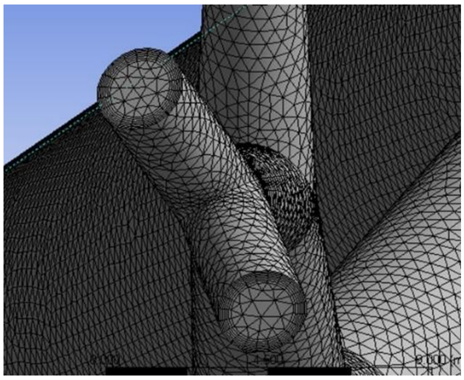

(b)

Figure 1. Mesh of the fluid domain of (a) the inhaler and (b) the Lung track..

It was assumed that particles behave in such a way that when in contact with wall they stay "trapped", and the particles that reach the outlet surface "escape" the fluid domain. Under this assumption, it was possible to calculate how many particles were set at the beginning of the calculation, and how many particles went out of the device. This data was then taken and used as an input to simulate the deposition of the particles inside the human lungs.

3. Results and Discussion

After successfully completing the mesh analysis it was found that the results obtained are correspondent with those published in the literature [13]. Table 2 shows the mesh analysis done to decide which element size is to be used during the simulation. All the meshes show similar pattern with an asymmetric flow field where the flows near wall regions in the mouthpiece have relatively higher velocity than central area. It was concluded that the 0.5 mm element size was the most appropriate as the percentage difference between the maximum velocity achieved in the validation model and the efficiency of the inhaler in both models are close. Moreover, the current work was validated against Tong et al. [14] work and the percentage difference between the models was found to be around 4%. Such difference could be explained by the nature of the model built by Tong et al. [14] where coupling was done between the CFD simulation and DPM and the existence of a capsule in the model adopted. It is worth mentioning that, V is the velocity achieved in the simulation, V_1 is the validation velocity based on literature [13] and V_2 is the validation velocity based on literature [14]. Eff. is the achieved efficiency in the simulation whereas Eff. 1 is the efficiency in literature [13]. Moreover, the velocity at the inlet was found to be 11.79 m/s whereas in the simulation it was found to be 11.38 m/s which gives almost a 3% difference as shown by Figure 2.

Table 2. Mesh analysis and validation study.

Size (mm)	10	5	3	1	0.7	0.5
Mesh #	70514	69847	73841	267840	572875	1210769
V (m/s)	37.4	40.2	39.4	41.4	44.2	46.9
V_1 (m/s)	47.5	47.5	47.5	47.5	47.5	47.5
V_2 (m/s)	45.0	45.0	45.0	45.0	45.0	45.0
[V_1] (%)	21.4	15.5	17.1	12.9	7.1	1.4
[V_2] (%)	20.5	12.1	14.2	8.6	1.9	4.1
Eff. (%)	73.0	54.5	59.5	71.5	61.5	68.0
Eff. 1 (%)	69.0	69.0	69.0	69.0	69.0	69.0
(%)	5.8	21.0	13.8	3.6	10.9	1.5

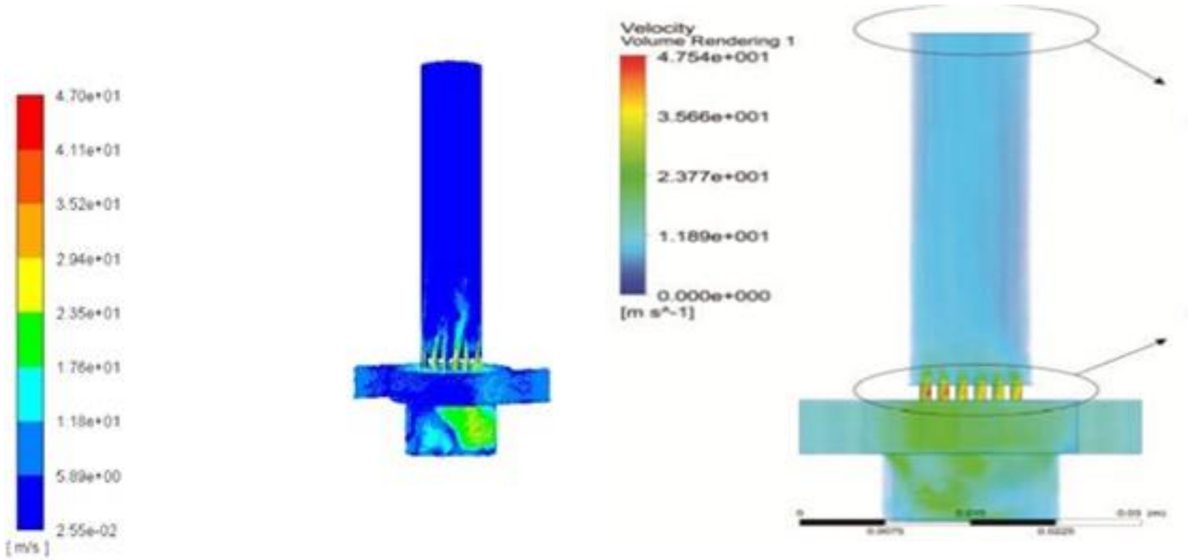

(a) (b)

Figure 2. Comparison of velocity contours (a) Current CFD work, (b) Published work [13].

3.1. Mouthpiece Length

The length of the mouthpiece was studied due to its importance in determining the level of flow development through it. Undeveloped flow could contain regions of high velocity that could enhance throat impaction upon inhalation. It is believed that the more developed the flow is, the more uniform the flow profile at the device exit is. This uniform profile reduces the regions of high velocity, potentially reducing throat impaction and improving overall inhaler performance. In general, identical flow patterns were observed at the base of the inhaler. The flow fields generated in the mouthpiece at different flowrates were also identical up to the exit of each mouthpiece.

Figure 3 shows the flow field and velocity at the exit for the 20 mm mouthpiece length. For the inhaler with the 75 mm length mouthpiece, a well distributed velocity profile occurred at the inhaler exit exhibiting a small velocity difference. The velocity differences at the exit for the 20 mm and 36 mm mouthpiece length cases were slightly greater than those of 48 mm and 75 mm mouthpiece cases. As the mouthpiece length is reduced, a nonuniform flow profile occurred where two regions of high velocity were observed together with regions of lower velocity. The flow patterns in the base of the inhaler were almost identical. This is due to the fact that the flow was not developed and there are regions of high velocity that will increase throat deposition and reduce the inhaler performance. Nonuniform behaviour could be explained by the level of turbulence kinetic energy present in the body. Therefore, it is important to know the level of turbulence that is required to be present in the device to enhance its performance.

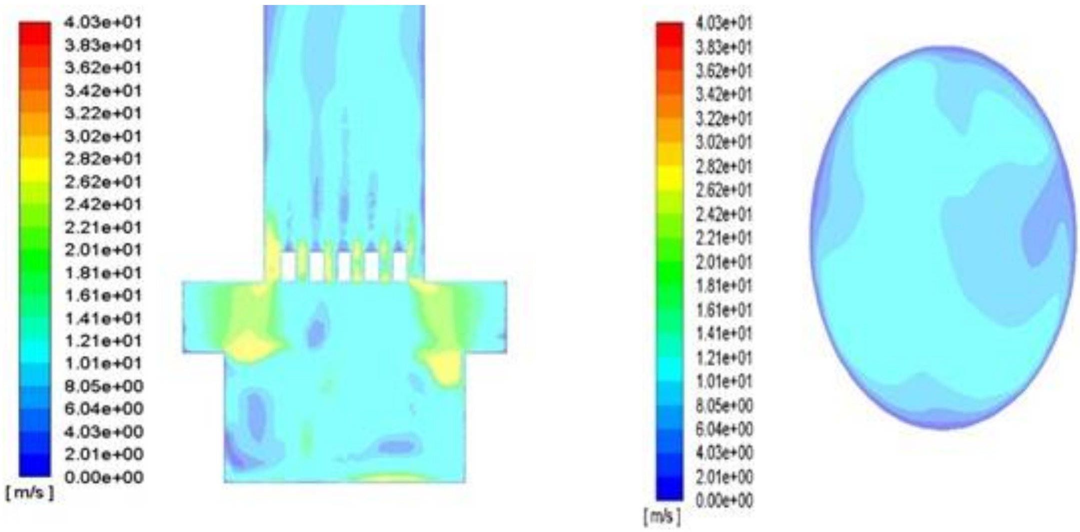

(a) (b)

Figure 3. Velocity magnitude for the 20 mm length: (a) centre cross section, (b) Exit.

Table 3 shows the variations in the efficiency and the values of the turbulent kinetic energy (TKE) across the inhaler. The TKE is a measure of the absolute turbulence level generated within the device. As the mouthpiece length increases the level of turbulence increases to a level and then decreases again. Therefore, it is of vital importance to know the level of turbulence that is required to be present in the device to enhance the deagglomeration process. Also, the efficiency increases to a level with increasing mouthpiece length. Coates et al. [10] stated that the length of the mouthpiece does not have a great effect on the efficiency of the inhaler, however it greatly affects throat deposition.

Table 3. Variation in efficiency and TKE with respect to mouthpiece length.

Mouthpiece length	TKE (m^2/s^2)	Efficiency (%)
20 mm	3.58	60.5
36 mm	3.26	65.5
48 mm	3.85	68
75 mm	2.06	51

3.2. Inhalation flow rate

Effects of air flow on the overall performance of a DPI and the corresponding flow turbulence levels that maximized the inhaler performance were examined. Increasing the air flow inhaled through a DPI could change the device flow field and the TKE and ISSR within the device which affects the inhaler performance. The inhalation flow rate could also affect the deagglomeration process within the device. The deagglomeration potential is a term used to assess the ability of a device flow field to disperse drug agglomerates, taking into account particle interaction with the turbulent flow field and particle impactions with the device walls and neighbouring particles. The scope of this study did not allow a determination into the intensity of particle-particle impactions. Consequently, this mechanism is no longer discussed and should be reviewed in further research. Table 4 shows the TKE and the integral scale strain rates (ISSR) at different flow rates. ISSR is a measure of the velocity gradient across the integral scale eddies. These parameters are important as they help in understanding how particles move through the inhaler. The highest values of TKE and ISSR were achieved at the wall grid which highlights the grid importance in studying the dispersion of the inhaler. As the flow rate increased, the TKE and ISSR increased which increased drug retention within the device at higher flow rates and increased in throat deposition due to non-uniform flow at the exit of the mouthpiece. Therefore, increasing the device flow rate results in higher velocity at the exit, which caused the increased throat deposition.

Table 4. TKE and ISSR under different inhale flow rates.

Flow rate (L/min)	TKE (m^2/s^2)	ISSR (m^2/s)	Efficiency (%)
10	0.59	571.84	66
28.3	3.85	1519.29	68
45	9.77	2268.5	64
60	16.54	2891.33	56
90	38.5	4122.05	50

3.3. Mouthpiece Geometry

The geometry of the mouthpiece could affect the amount of throat deposition and the device retention produced when using the inhaler. Table 5 shows the TKE, ISSR and the efficiency for different mouthpiece shapes. It can be seen that there are no major differences in the values of the TKE and ISSR for different mouthpiece shapes. However, the efficiency differs. The square configuration as well as the 16 mm Diameter configuration had the lowest efficiencies due to the device retention. Furthermore, the geometry of a DPI mouthpiece could have significant effects on the amount of throat deposition produced and the flow development when controlling the exit air flow velocity. It is concluded that the mouthpiece geometry does not affect the flow in the base of the inhaler however it affects the flow development exiting the inhaler, thus throat deposition.

Table 5. TKE and ISSR for different mouthpiece geometries.

Mouthpiece Shape	TKE (m^2/s^2)	ISSR (m^2/s)	Efficiency (%)
10 mm Diameter Circle	3.58	1474.34	60.5
16 mm Diameter Circle	3.28	1493.29	53.5
21 mm Diameter Circle	3.09	1483.23	70
Oval	3.25	1486.92	66.5
Square	3.51	1504.64	51

3.4. Lungs Simulation

The inhaler output of the inhaler models was used as an input to the lungs model. Table 6 lists the outlet flow rates obtained for the inhalers which were used as the input flow rate boundary conditions for the lungs. The velocity of injected particles was calculated after running an air flow simulation for the lungs as the inlet flow rate is set. It was found that as the flow rate increases the velocity at the inlet of the lungs increases. The velocity at the inlet was then calculated and set as the velocity at which the particles will be injected at. Then the discrete phase simulation was done to track the particles. It was also found that as the inhalation flow rate increases the values of the TKE increases.

Table 6. TKE and injection velocities at different flow rates.

Case	Flow rate (g/s)	Flow rate (L/min)	Velocity of injection (m/s)	TKE (m^2/s^2)
1	0.204	10	1.474	0.0370
2	0.580	28.3	4.193	0.213
3	0.920	45	6.650	0.684
4	1.224	60	8.844	1.126
5	1.824	90	13.180	2.189

As the flow rate increases the values of the particles deposed in the throat rejoint increases. Figure 4 shows the percentages of particles trapped in the throat region as the flow rate increases. This is due to the fact that the non-uniform from velocity profile is present at the inhaler outlet as the flow rate increases. As the particles travel down the lungs from generation to generation, the percentage of particles trapped at lower generations is higher than the percentage of particles trapped at higher generation even at different flow rates. As the particles travel to lower generations the diameter and length of the generation decreases so more particles were trapped there. A great percentage of the particles were trapped at first in the throat region then moving down the generations the percentage increases.

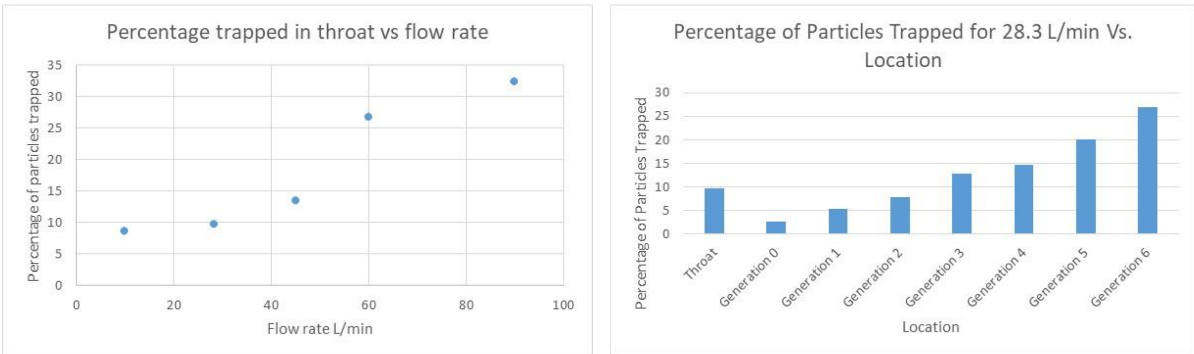

(a) (b)

Figure 4. Percentage of particles trapped based on (a) flow rate, (b) location.

Figure 5 shows the velocity tracks along the lungs geometry and the branches of the lungs for the 10 L/min flow rate. The velocity increases after the throat region due to the decreasing track diameter. Moreover, the velocity increases at the end of the branches due to the diameter decreasing. An increase in the velocity as flowing down through the branches resulted in an increase in turbulence which means that flowing from generation to generation the deposition in each generation increases. There is a total number of 64 outlets inside the lungs model until the 6th generation. In general, as the flow rate increases the velocity at each corresponding outlet increases which resulted in higher depositions. Moreover, the velocity values at each outlet were not the same due to the unsymmetric geometry of the lung.

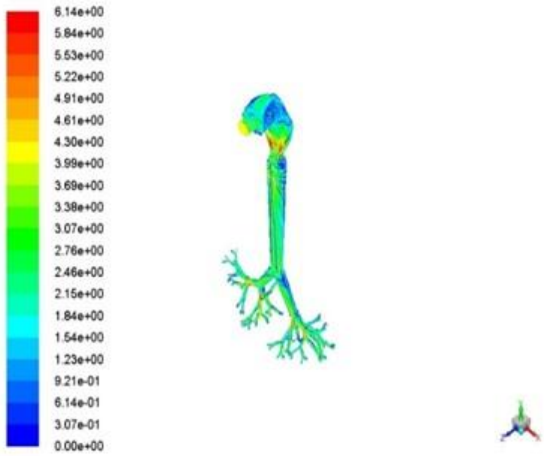

Figure 5. Contours of velocity at lungs track and branches at 10 L/min.

Table 6. TKE and injection velocities at different flow rates.

Flow Rate (L/min)	Max Velocity (m/s)	Min Velocity (m/s)	Max Pressure (Pa)	Min Pressure (Pa)	TKE (m^2/s^2)
10	6.14	0	42.6	-5.15	0.2134
28.3	6.4	0	48.6	-5.14	0.2758
45	9.71	0	107.82	-13.66	0.6379
60	12.74	0	161.46	-29.804	1.158
90	19.72	0	364.64	-80	2.326

4. Conclusion

CFD analysis was performed to study how flow field generated in the inhaler varies with different inhalation flow rates, mouthpiece lengths and geometries and how the inhalation flow rate affects particles deposition inside the lungs system. DPM was used to study the dispersion of the dry powder in the inhaler. The computational model was validated against published research. It is concluded that:

- The length of the mouthpiece determines the level of flow development through the mouthpiece itself. The length of the mouthpiece did not affect the flow at the base of the inhaler but at the exit. As the length of the mouthpiece decreased, a non-uniform behaviour did exist at the outlet of the inhaler. Regions of high velocity did present which increased throat particles deposition. Consequently, an overall decrease in the performance of the inhaler.
- As high inhalation flowrates increased the level of turbulence in the device which caused the velocity at the exit and the throat deposition to increase.
- The geometry of a dry powder inhaler mouthpiece showed significant effects on the amount of throat particle deposition and flow development when controlling the exit air flow velocity of the device.
- As the flow rate through the lounges increased, the velocity at the inlet of the lungs was increased and the value of the TKE was increased causing an increase in the number of particles trapped. As the particles travelled down the lungs from one generation to a lower generation,

the percentage of particles trapped at the lower generation was higher than the percentage of particles trapped at the higher generation for all investigated flow rates.

5. Acknowledgments

The support provided by the Deanship of Scientific Research of the German Jordanian University (GJU), Jordan is gratefully acknowledged. The current work has utilized equipment that was supported by the German Jordanian University Seed Grant Number (SATS 06/2018).

6. References

[1] Scherließ, R., Bock, S., Bungert, N., Neustock, A., & Valentin, L. (2022). Particle engineering in dry powders for inhalation. European Journal of Pharmaceutical Sciences, 172, 106158. https://doi.org/https://doi.org/10.1016/j.ejps.2022.106158

[2] J. Yu, & Y.W. Chien. (1997). Pulmonary drug delivery: Physiological and mechanistic aspects. Crit Rev Ther Drug Carrier Syst, 14(4), 395-453.

[3] Gengenbach, T. (2012). Numerical Simulation of Particle Deposition in the Human Lungs

[4] O'Connor, B. J. (2004). The ideal inhaler: design and characteristics to improve outcomes. Respir Med, 98 Suppl A, S10-16. https://doi.org/10.1016/j.rmed.2004.02.006

[5] Lavorini, F., Pistolesi, M., & Usmani, O. S. (2017). Recent advances in capsule-based dry powder inhaler technology. Multidisciplinary Respiratory Medicine, 12(1), 11. https://doi.org/10.1186/s40248-017-0092-5

[6] de Boer, A. H., Hagedoorn, P., & Grasmeijer, F. (2022). Dry powder inhalation, part 2: the present and future. Expert Opinion on Drug Delivery, 19(9), 1045-1059. https://doi.org/10.1080/17425247.2022.2112570

[7] de Boer, A. H., Hagedoorn, P., Hoppentocht, M., Buttini, F., Grasmeijer, F., & Frijlink, H. W. (2017). Dry powder inhalation: past, present and future. Expert Opinion on Drug Delivery, 14(4), 499-512. https://doi.org/10.1080/17425247.2016.1224846

[8] Jones, M. D., & Price, R. (2006). The Influence of Fine Excipient Particles on the Performance of Carrier-Based Dry Powder Inhalation Formulations. Pharmaceutical Research, 23(8), 1665-1674. https://doi.org/10.1007/s11095-006-9012-7

[9] Wong, W., Fletcher, D. F., Traini, D., Chan, H.-K., & Young, P. M. (2012). The use of computational approaches in inhaler development. Advanced Drug Delivery Reviews, 64(4), 312-322. https://doi.org/https://doi.org/10.1016/j.addr.2011.10.004

[10] Coates, M. S., Fletcher, D. F., Chan, H.-K., & Raper, J. A. (2004). Effect of Design on the Performance of a Dry Powder Inhaler Using Computational Fluid Dynamics. Part 1: Grid Structure and Mouthpiece Length. Journal of Pharmaceutical Sciences, 93(11), 2863-2876. https://doi.org/https://doi.org/10.1002/jps.20201

[11] Zhou, Q. T., Tong, Z., Tang, P., Citterio, M., Yang, R., & Chan, H.-K. (2013). Effect of Device Design on the Aerosolization of a Carrier-Based Dry Powder Inhaler—a Case Study on Aerolizer® Foradile®. The AAPS Journal, 15(2), 511-522. https://doi.org/10.1208/s12248-013-9458-6

[12] Groneberg, D. A., Witt, C., Wagner, U., Chung, K. F., & Fischer, A. (2003). Fundamentals of pulmonary drug delivery. Respiratory Medicine, 97(4), 382-387. https://doi.org/https://doi.org/10.1053/rmed.2002.1457

[13] Šušteršič, T., Vulović, A., Cvijić, S., Ibrić S., & Filipović, N. (1997). Aerosol Particle Deposition in Dry Powder Inhaler Aerolizer®. IPSI Transactions on Advanced Research, 13(2), P9.

[14] Tong, Z. B., Zheng, B., Yang, R. Y., Yu, A. B., & Chan, H. K. (2013). CFD-DEM investigation of the dispersion mechanisms in commercial dry powder inhalers. Powder Technology, 240, 19-24. https://doi.org/https://doi.org/10.1016/j.powtec.2012.07.012

CST0003

Numerical and Experimental investigations of the impact of nozzle geometry on performance of impulse hydro turbines

K. Sakulphan[1,*], K. Sengpanich[2], and T. Tongshoob[3]

[1,3] Department of Mechanical Engineering, School of Engineering, Sripatum University, Jatujak, Bangkok, 10900, Thailand
[2] Department of Mechanical Engineering, School of Engineering, Kasetsart University Sriracha Campus, Chon Buri, 20230, Thailand

* Corresponding Author: Kiattisak.sa@spu.ac.th

Abstract. The spear valve is an important flow control device for Pelton and Turgo hydro turbines. This research studies the effect of nozzle geometry on jet dispersion, efficiency, and impact force on the turbine blade. Also, the effect of the offset distance between the spear valve and turbine blade is investigated and optimized. 3D multiphase free surface flow CFD is used to analyses the different geometries and determine the best performance of spear valve and offset distance. An experimental setup was designed to validate the CFD results. It was found that from the above parameters the geometry of nozzle holder and spear tip were of little influence on the performance. The large angles of the spear tip produced smaller losses and changed the flow rate faster than the other geometry. Moreover, the offset distance had a lot of influence on efficiency and jet force more than the shape parameters. As the results, the optimum offset distance was found to be 8 times of the jet diameter and produced jet losses of less than seven percent in the hydraulic energy.

Keywords: Impulse turbine injector, Spear valve design, Free-surface jet, Jet dispersion, Jet deviation, Nozzle angle, and spear valve angle.

1. Introduction

The main characteristic of impulse turbine is to convert the high and medium pressure energy in the penstock into kinetic energy in the water jet. This happens in the nozzle and spear valve. The configuration design must be considered for improving the impulse turbine performance. The water jet velocity is fixed by the pressure energy and the flow rate is controlled by moving the spear valve to adjust the power production. There are some studies available that investigate the kinetic energy losses in the nozzle valve. The losses depend on the spear tip stroke, short stroke caused a higher head loss inside nozzle than long spear tip stroke [1, 15]. The water jet dispersion depends on the water pressure with an increased external thickness of mixed air-water flow and the friction with the air produces the velocity decay [3, 4]. Moreover, the flow visualization was used to investigate the real case of water jet dispersion, increased jet dispersion at high pressure causes decreased efficiency [5]. Numerical simulation tools such as multi-phase free surface flow has been used to investigate the losses for different spear tip stroke and angles, the larger spear tip angles result in a better performance, while the smaller angles have the same effect for the large spear tip stroke [6, 11]. Also, the effect of different water jet shape was investigated; the circular jet provides higher efficiency than square, triangular, and elliptical jet shape [7].

The industry standard of nozzle holder angle and spear tip angles was investigated to improve the hydraulic efficiency by using computational numerical simulation. The optimal design with the nozzle holder and spear tip angles of 110-degree and 70-degree improves the efficiency by 0.7 percent from the industry standard design of 90-degree and 50-degree nozzle and spear tip angles [8, 9]. The experiment was created for investigating three cases of nozzle holder and spear tip angles with the Pelton and Turgo turbine. The nozzle holder and spear tip angles of 110 degree and 70 degrees (NA110SA70) can improve the turbine efficiency less than one percent when compared to the standard design (NA80SA55) and large nozzle holder and spear tip angles (NA150SA90) [11, 12]. However, in the authors previous study, the spear tip angle of 55-degree couple with nozzle holder of 90 degree was designed for use with the impulse Turgo turbine of 90kW. It found that, losses in the water jet at the design flow rate are caused by the water jet divergence and high turbulence inside the nozzle, which reduced the turbine efficiency more than 10 percent [14]. It can be concluded that the kinetic energy loss inside nozzle depends on the nozzle geometry and spear tip stroke, affecting the performance of impulse turbine. While the offset distance between the spear valve and turbine blade also has an important influence on the loss of entrance energy. Therefore, this study is dedicated to investigating the effect of the nozzle holders and spear tip shapes on jet dispersion, jet loss, impact force and offset distance by using the numerical simulation CFD tools and experimental test.

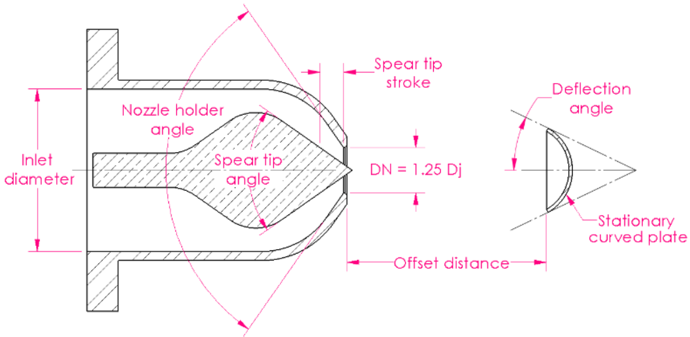

Figure 1. Description of spear valve.

Table 1. Details of nozzle holder and spear tip angles used in the experiment.

Flow rate	Nozzle holder angle	Spear tip angle	Offset distance
0.25 Q_D	90°	50°	8.5 *Dj*
0.50 Q_D	110°	60°	17.0 *Dj*
0.75 Q_D		70°	25.5 *Dj*
1.00 Q_D		80°	34.0 *Dj*

2. Geometric parameter design of spear valve

Spear valve are designed to give minimum losses, and to produce a good, coherent jet. A spear valve consists of a nozzle holder with spear tip at the center. The spear tip is moved in and out to vary the flow rate. Figure 1 show that the spear valve geometric parameters, *Nozzle Diameter (DN)*, needs to be larger than design jet diameter, because the jet emerging from nozzle first contracts down to a narrow point called the vena contracta, and the jet size is calculated at this point. It is made 25 percent larger to ensure that the correct jet size can be achieved [2]. In this study, the nozzle and spear valve have been designed based on the design flow rate (Q_D) of 1.5 liter per second and net head (H) of 10 meters. This parameter was used to calculate the jet velocity (V_j) of 14m/s and jet diameter (D_j) of 11.68 mm. including the size of inlet diameter of nozzle holder. The average water velocity at the inlet nozzle holder was design of 0.5 m/s. This is sufficient to avoid excessive fluid turbulence. Two angles of 90 and 110 degrees paired with four angles of the spear tip angle of 50, 60,70, and 80 degrees were used to investigate the jet force, jet dispersion and jet deviation by different four offset distance as shown in table 1.

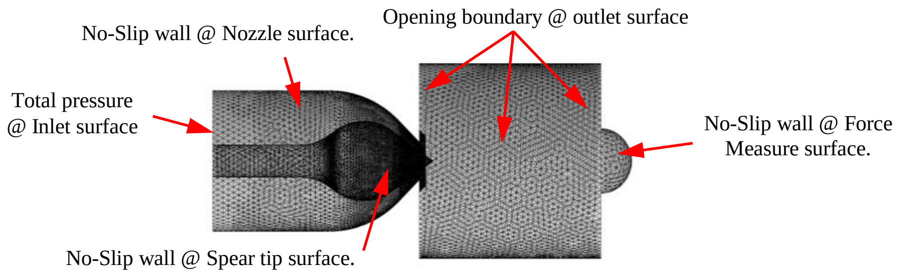

Figure 2. Computational domain grid and boundary condition setting.

3. Numerical simulation investigation

Based on published research available in this area, Computational Fluid Dynamics (CFD) is a recognized tool for analysis of the most complex flow phenomena such as the flow between the high-speed jet and the turbine runner geometry. In this study, ANSYS CFX simulations were used. The k-ω Shear Stress Transport (SST) turbulence model with free-surface for multiphase modeling will be used to model the high-speed jet flow phenomena. Figure 2 shows the computational domain grid of the spear valve. The boundary conditions on the computational domain were discretized using a high-resolution scheme. A second order backward Euler scheme was used for the transient terms. As the convergence criteria, the simulations were stopped when the mass residuals were lower than 10^{-6}. The turbulence was considered by using a k-ω based SST turbulence model with automatic near wall treatment. As the boundary conditions, the total pressure (stable) is defined at the inlet boundary, while the opening boundary condition with the average atmospheric static pressure is arranged at the surrounding of the opening surface. At the surfaces no-slip wall condition and smooth roughness wall were applied on the nozzle, spear tip, and force measure surface. The initial volume fraction conditions of air are one and of water zero. That is solved by a second order, using a sufficiency small timestep 2×10^{-4} sec. The computational mesh is consisting of ~400,000 nodes and ~ 2,200,000 tetrahedral elements.

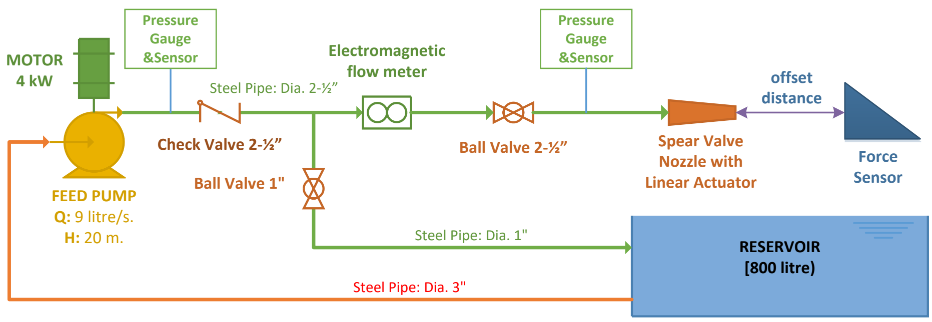

Figure 3. Schematic of experimental setup.

4. Experimental setup

Figure 3 shows the experimental setup, the working fluid for performance testing circulates in the closed loop. A feed pump was installed to supply pressure and water flow rate as required for experimental setup. The inlet pressure is controlled by increasing or decreasing the speed of the feed pump by using an inverter. The nozzle pressure value was obtained using pressure transmitters and checked again with the pressure gauge. The water flow rate value was measured by an electromagnetic flow meter. The bypass valve was used for maintaining the pressure value of 1 bar. Then, the force sensor was installed to measure the jet force value along the axial at different offset distances, as shown in Figure 4. A linear actuator was used to control the spear tip stroke.

Figure 4. Experimental setup and nozzle holder & spear tip used for experimental tests.

5. Validation and discussion

5.1. Numerical simulation results

The potential energy of water is converted into kinetic energy by using spear valve. The spear tip travel changes the cross-sectional area so that the flow rate of the nozzle valve can be controlled and hence the power. Comparisons are presented in Figure 5, the relationship between the actual flow and the design flow with different spear tip strokes for various spear valve geometries. It is clear from the CFD simulation results that the nozzle holder angle of 90 degrees coupled with the spear tip angle of 80 degree (NA90SA80), at the design flow rate value, it had a shorter stroke than any other spear valve shapes. On the other hand, the nozzle holder angle of 110 degree coupled with spear tip angle of 50 degree (NA110SA50) will have need a longer stroke to get the same flow rate value as with other shapes. Comparing the two nozzle holder angles at the same spear tip stroke of various spear tip angles, the nozzle holder angle of 90 degree had a greater flow rate than the nozzle holder angle of 110 degree.

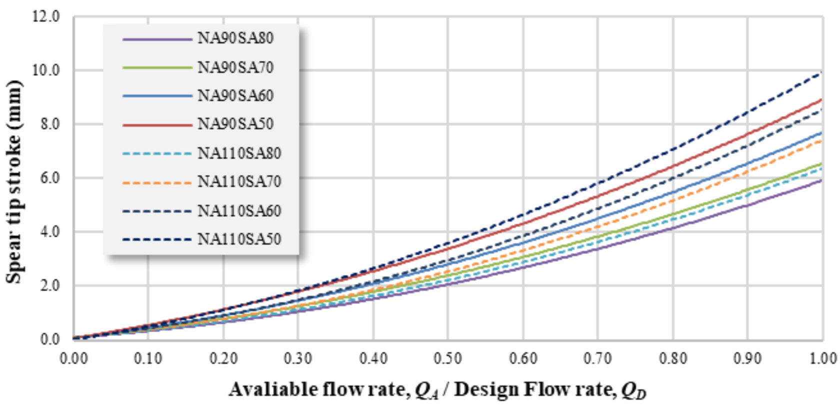

Figure 5. Comparison of the spear tip stroke and flow rate variation of various spear valve geometries.

The jet force functioning as the offset distance for various spear valve shapes and varying the flow rates of 25%, 50%, 75% and 100%, increasing the offset distance will result in decrease jet force.

While increasing the proportion of flow rates in term of percentage, the jet force increases, and the curve pattern obtained by are quite similar (practically coinciding). It clearly shows that friction loss with the air produces jet velocity decay at the longer offset distance and is not influenced by the spear valve shapes.

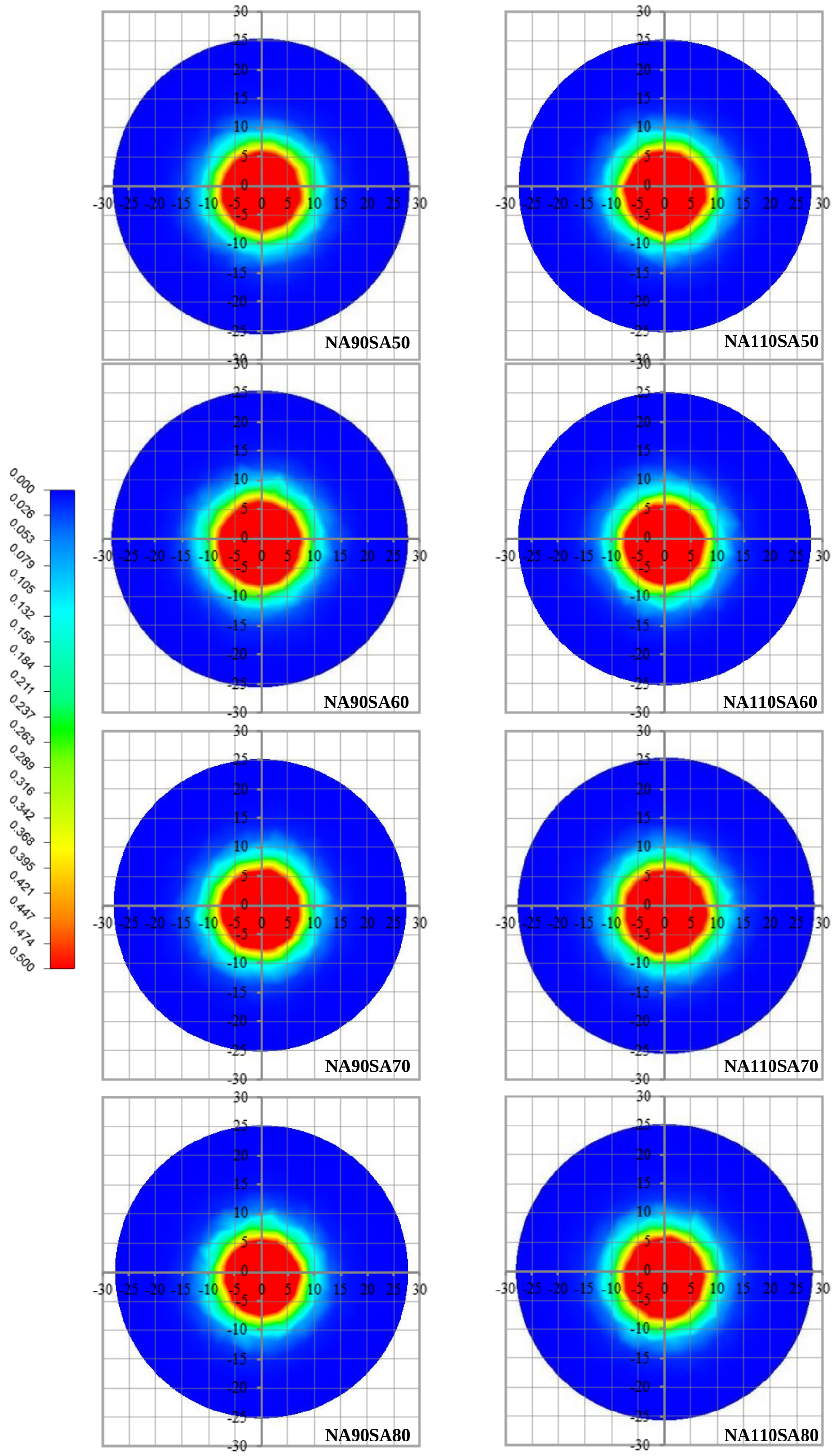

Figure 6. Comparison the jet dispersion of various spear valves with offset distance of 8.5 D_j.

5.2. Analysis of the jet dispersion and jet deviation

To investigate the dispersion of the water jet, a cutting plane in the numerical simulation software was created. The cutting plane offset from the spear valve is 8.5 times jet diameter. The cutting plane displays a water volume fraction contour plot for the jet dispersion as shown in Figure 6. The red color area of contour plot at the center region correspondence with the 100 percent phase of water volume fraction, which gradually decreases with the water jet mixed with the air surrounding jet diameter and the rest blue color area of contour plot shows 100 percent phase of air. Comparing the jet dispersion with the difference spear valve geometries at the same flow rate and offset distance, the dispersion of the jet in for each shape is quite similar. The red color region is close to the design value of jet diameter. It is approximately 12 millimeters. According to the results, the effect of the nozzle holder and spear tip angle on the jet dispersion is not significant. The jet dispersion depends on the flow rate and water pressure.

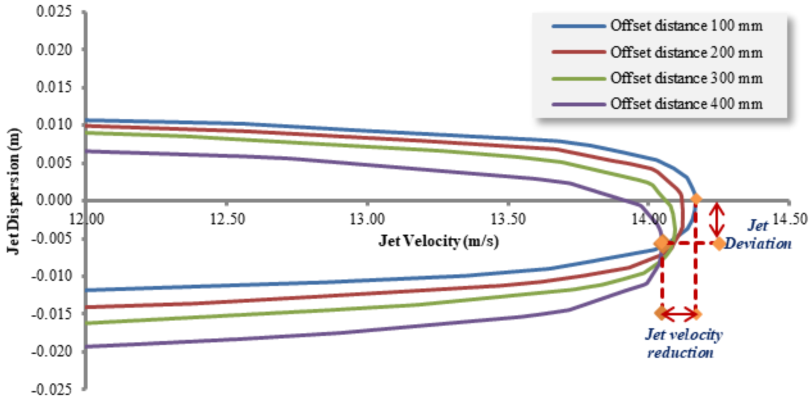

Figure 7. The relationship between jet deviation and jet velocity reduction of the NA90SA80.

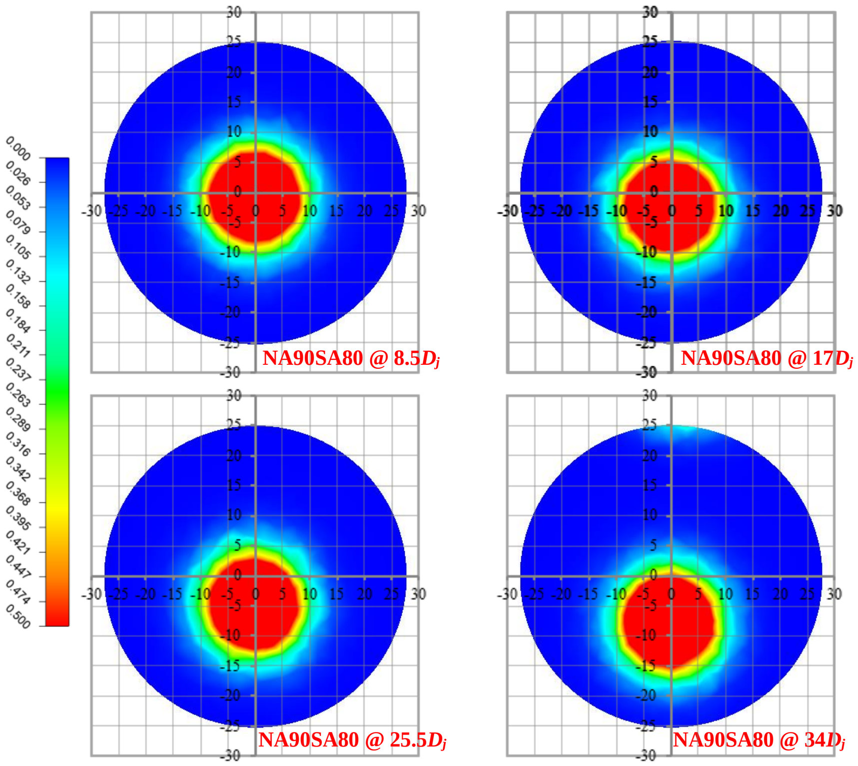

Figure 8. Jet deviations at various offset distance of NA90SA80.

Based on the results, the spear valve shape of NA90SA80 uses the shortest stroke to control the flow rate. It was used to analyze jet deviation. Figure 7 presents the relationship between jet velocities of NA90SA80 with four positions of offset distance. The jet velocity curve clearly shows the effect of the offset distance. The jet velocity was reduced due to air friction and deviated from the horizontal direction due to gravity. The axial jet velocity distributed in the cross section is non-uniform at each offset position. The center of jet flow drops down from the axis design point. It is called jet deviation. The change in the axial jet velocity decreases with each offset distance, it is called jet losses. Therefore, the distance between the design point at turbine blade and nozzle valve has a direct impact on the performance of the impulse turbine system. The nozzle valve position should be compensated on the vertical axis for reducing this impact on the design. According to the results, Figure 8, the position of the jet diameter (red contour) has the downward direction along the Y axis by gravity. It can be confirmed from Figure 7 that the offset distance of nozzle valve assembly directly affects the turbine shaft power. It also causes loss due to misalignment of the design point.

5.3. Experimental results

The experimental spear tip stroke curve results for different flow rate were quite similar to the numerical simulation results. The maximum deviation value occurs at the spear valve shape NA90SA80 is approximately 21 percent, while the minimum deviation value is around 0.2 percent that occurs at the spear valve shape NA110SA50. Comparing the results of experiments with numerical simulation results of NA90SA80 as shown in Figure 9, the slope and trend of the jet force curve are similar. The jet force deviation value of not more than 5 percent means that the value of the numerical simulation is quite reliable. This value is close to the actual value measured by the experimental under the boundary conditions of the same problem set. Moreover, the water jet force values at the difference offset distance of 8.5D_j, 17D_j, 25.5D_j, and 34D_j, the values are close to those obtained from the numerical simulation.

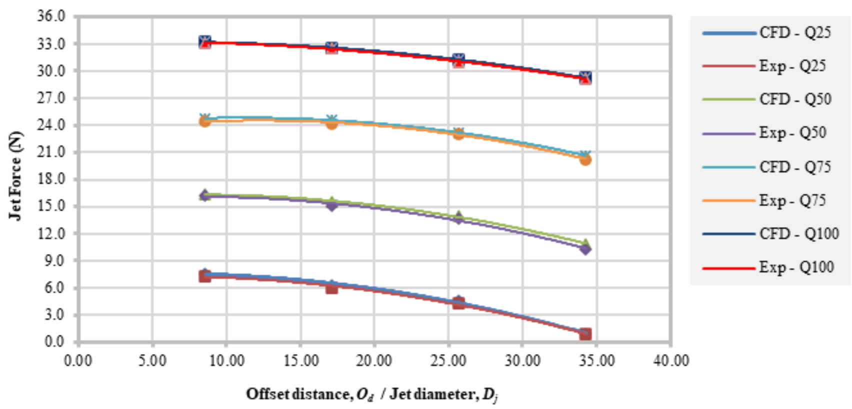

Figure 9. Comparison of the jet force of NA90SA80 obtained by experimental and numerical results.

The visual inspection in the actual test of the jet dispersion is quite difficult. High speed cameras need to be used to capture and measure and could not be done. However, the comparing CFD prediction and experimental results demonstrates that the flow rate and jet force was predicted accurately. The injection diameter will contract until it is constant and the actual flow rate equal to design flow rate as shown in Figure 10. The spread of the injection will increase over long distances because of friction from the air, which will reduce the jet velocity.

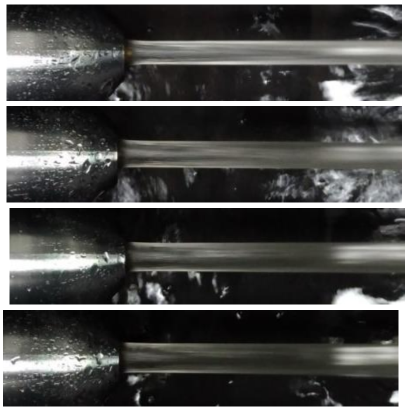

NA90SA80-Q25

NA90SA80-Q50

NA90SA80-Q75

NA90SA80-Q100

Figure 10. The actual jet dispersion of different flow rate of NA90SA80.

5.4. Results discussion

Based on the results of the CFD program and experimental test, it was found that the relationship of the nozzle holder and spear tip angle compared with the jet dispersion are quite small effects. The difference between the nozzle holder and the spear tip shapes does not directly affect the distribution of water jet, but it changes the injection area to control the flow rate. Although, the large angle of nozzle holder and spear tip will give minimal losses inside of spear valve. The jet deviation from the axis was increasing with the offset distance but is mainly due to gravity and can be compensated for. The air resistance causes the jet velocity and force to decrease.

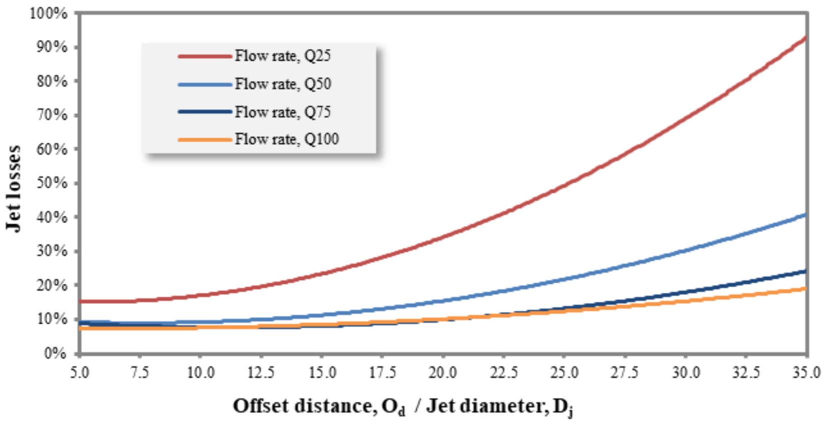

Figure 11. Water jet loss variations by offset distance.

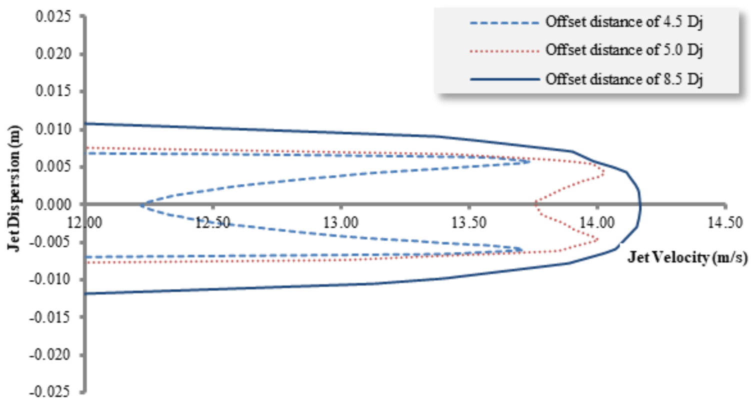

Figure 12. Velocity profiles variation of NA90SA80 obtained by CFD prediction.

The variation of the water jet losses and offset distance is shown in Figure 11, it clearly shows that the air resistance has more influence than the spear valve shape. The long offset distance has reduced the jet force and increased the jet dispersion. These energy losses are found to be about 15 percent for the offset distance of 35 times of jet diameter at design flow rate value ($1.0Q_D$). On the other hand, the very close offset distance value lower than 10 times of jet diameter, the velocity profile of the injector is unstable, resulting in lower core jet velocities as shown in Figure 12.Therefore, it can be concluded that, the optimum spacing of the spear valve combinations with the dispersion and the minimum deviation of the water jet with jet losses about 7 percent when the offset distance is equal to 8 times of jet diameter.

6. Conclusions

The effect of spear valve geometry on water jet dispersion and the influence of the offset distance between the spear valve and turbine blade is investigated and optimized. 3D multiphase free surface flow CFD is used to analyze the flow behavior of different geometries and determine the best performance of spear valve shapes and offset distance. An experimental setup was designed to validate the CFD results. The conclusions are summarized as follows:

1) Large angles of the nozzle holder and spear tip resulted in minimal kinetic energy losses of 0.15 percent and change the flow rate faster due to the smaller total stroke than the any other geometry. But increase the jet dispersion.

2) The largest part of the energy losses occurs between the spear valve outlet and the blade. The larger the flow rate the higher the losses. The jet losses increase about 1.5 percent for each addition offset of 8.5 times the jet diameter as shown in figure 13. A maximum jet dispersion of 30 percent diffusion of the designed jet diameter was observed.

3) The optimum offset distance between spear valve and the blade is equal to 8 times the jet diameter. The optimal nozzle holder angle of 90 degree combined with spear tip angle of 80 degree gives best performance.

7. Acknowledgements

The authors would like to thank the department of research fund and technology development, Provincial Electricity Authority (PEA), Thailand for funding of the experimental testing.

8. References

[1] H.B. Matthias, J. Prost, and C. Rossegger, *Investigation of the flow in Pelton turbines and the influence of the casing*, International Journal of Rotating Machinery, Vol. 3(4), (1997) 239-247

[2] J. Thake, *The micro-hydro Pelton turbine manual, Design, Manufacture and installation for small scale hydropower*, London: ITDG Publishing, ISBN: 978-1-85339-4607, (2000)

[3] A. Catanase, M. Bargazan, and C. Hora, *Numerical simulation of a free jet in Pelton turbine*, Proceeding of the 6th International conference on hydraulic machinery and hydrodynamics, 21-24 October 2004

[4] M. Peron, E. Parkinson, L. Geppert, and T. Staubli, *Importance of jet quality on Pelton efficiency and cavitation*, Proceedings of the 7th International conference on hydraulic efficiency measurements (IGHEM2008), 3-6 September 2008

[5] T. Staubli, A. Abgottspon, P. Weibel, C. Bissel, E. Parkinson, J. Leduc, and F. Leboeuf, *Jet quality and Pelton efficiency*, Conference paper, Hydro 2009

[6] V.N. Athanasios, E.P. Dimitrios, and J.S. Anagnostopoulos, *Numerical study of the effect of spear valve design on the free jet flow characteristics in impulse hydroturbines*, 7th GRACM International congress on computational mechanics in Athens (Greece), 30 June – 2 July 2011

[7] V. Gupta, V. Prasad, and R. Khare, *Effect of jet shape on flow and torque characteristics of Pelton turbine runner*, Journal of Engineering Research and Applications, Vol. 4(1), (2014) 318-323

[8] D. Benzon, A. Zidonis, A. Panagiotopoulos, G.A. Aggidis, J.S. Anagnostopoulos, and D.E. Papantonis, *Impulse turbine injector design improvement using computational fluid dynamics*, Journal of Fluids Engineering, Vol. 137(4), (2015) pp. 041106
[9] D. Benzon, A. Zidonis, A. Panagiotopoulos, G.A. Aggidis, J.S. Agnostopoulos, and D.E. Papantonis, *Numerical investigation of the spear valve configuration on the performance of Pelton and Turgo turbine injectors and runners*, Journal of Fluids Engineering, Vol. 137(11), (2015) pp. 111201
[10] A. Zidonis, D. Benzon, and G.A. Aggids, *Development of impulse turbines and new opportunities*, Renewable and Sustainable Energy Reviews, Vol. 51 (2015)1624-1635
[11] Z. Chongji, X. Yexiang, X. Wei, W. Tao, Z. Jin, W. Zhengwei, and L. Yongyao, *Numerical analysis of Pelton nozzle jet flow behavior considering elbow pipe*, Proceeding of the 28th IAHR symposium on hydraulic machinery and systems, 022005, (2016)
[12] A. Zidonis, S. Petley, G.A. Aggidis, D.S. Benzon, A. Panagiotopoulos, J.S. Anagnostopoulos, and D.E. Papantonis, *Experimental investigation and analysis of the spear valve deign on the performance f Pelton turbines: three case studies*, Hydro 2017 International Conference and Exhibition in Seville (Spain) from October 9th to 11th, 2017
[13] D. Benzon, A. Zidonis, A. Panagiotopoulos, J.S. Anagnostopoulos, and D.E. Papantonis, *Experimental investigation and analysis of the spear valve design on the performance of Turgo turbine*, Hydro 2017 International Conference and Exhibition in Seville (Spain) from October 9th to 11th, 2017
[14] S. Kiattisak, *A new optimal selection method, geometry design and validation for hydro turbine type and size of micro hydropower plant in Thailand, dissertation*, School of Engineering and Technology, Asian Institute and Technology, Thailand, August semester 2017
[15] J. Heungsu, J.H. Park, S. Youhwan, and C. Minsuk, *Friction loss and energy recovery of a Pelton turbine for different spear positions*, Journal of Renewable Energy, 123 (2018) 273-280

CST0004

In-Situ and Near-Real Time of Shear Stress Measurement of Multiple Shear Stress Lab-on-Chip for Osteoblast Cell Cultivation using Image Analysis

Wares Chancharoen, Ph.D.[1,*], Jirasin Aswakool[1], Hein Htet Aung[1], Sirilak Phetcharat[1], Phattarin Pothipan[2], Aekkacha Moonwiriyakit, Ph.D.[2], Rungreang Phatthanakkun, Ph.D.[3], and Thanakorn Jiemsakul[4]

[1]Princess Srisavangavadhana College of Medicine, Chulabhorn Royal Academy, 906 Kampangpetch 6 Rd., Talat Bang Khen, Lak Si, Bangkok, 10210, Thailand
[2]Chakri Naruebodindra Medical Institute, Faculty of Medicine Ramathibodi Hospital, Mahidol University, 111 Suwannabhumi Canal Rd, Bang Pla, Bang Phli District, Samut Prakan, 10540, Thailand
[3]Synchrotron Light Research Institute, 111 University Avenue, Muang District, Nakhon Ratchasima, 30000, Thailand
[4]National Nanotechnology Center, National Science and Technology Development Agency, 111 Thailand Science Park, Phahon Yothin Rd, Klong Nueng Klong Luang Pathum Thani 12120, Thailand

* Corresponding Author: wares.cha@cra.ac.th

Abstract. Microfluidic devices are widely used in engineering and medical fields for researching topics such as cell cultivation and innovations in the pharmaceutical industry. However, microfluidic devices pose challenges for directly evaluating the mechanical and rheological properties, such as shear stress and viscosity and in real-time or *in-situ* measurements. In this study, we proposed an image processing algorithm based on optical flow that analyses fluid flow videos captured by a digital camera and microscope to estimate fluid velocity, velocity gradient, and wall shear stress. The videos were captured from 5 areas of interest from 3 similar microfluidic chips designed to generate specific shear stress conditions. Consequently, shear stress was estimated from the image processing method and validated with the computational fluid dynamics (CFD) results obtained *in-silico* using COMSOL multiphysics. With further developments, the method presented in this study could be a platform for making near real-time measurements for lab-on-chip cellular study and to better understand the effect of shear stress, a mechanical stimulus, on osteoblast cell cultivation.

Keywords: Farneback, image processing, optical flow, osteoblast cell, shear stress measurement.

1. Introduction

The domain of microfluidic technology has gained popularity and acceptance across multiple industry sectors, paving the way for many innovations. Microfluidics have emerged as the latest research solutions across industries, from healthcare diagnostics to chemical synthesis [1]. The recent surge in the adoption of microfluidic devices is attributed to their responsiveness, accuracy, increased yield, and resource efficiency. Nowadays, Polydimethylsiloxane (PDMS) is renowned for its versatility, and it is extensively employed in the fabrication of microfluidic devices. PDMS is highly suitable as a substrate material for cell cultivation modules due to its inherent properties, such as biocompatibility, transparency, and ease of design and fabrication. With the help of advanced fabrication techniques, the intricate microenvironments created using this material can accurately mimic the in vivo conditions. Consequently, PDMS-based microfluidic platforms provide an optimal environment for observing cell behaviour under controlled flow conditions [2].

A major challenge in microfluidics research is the precision required, especially to make accurate measurements at the micrometre scale. The physical characteristics of fluids at this scale routinely defy conventional measurement techniques, requiring the use of sophisticated methodologies for understanding the relationship between fluid dynamics and living cell behaviours. Although the physical properties inside the microfluidic are possible to be directly measured by biosensor or micro-mechanism, such devices may disrupt the physical, chemical, or biological properties. Such disruptions will compromise the results of the experiment [3]. Simulations and modelling are often used to estimate the measurable values. However, solely relying on computed values does not accurately reflect the real conditions. The measurement taken non-invasively at micrometre is critical for understanding the relationship between biological behaviours and the environment.

Moreover, different cell types require unique conditions for successful culturing, including nutrient provision, spatial constraints, fluidic flow rates, and medium viscosity [4]. Only when the cells are cultured correctly their optimal functions can be observed. The Osteoblast cells, responsible for secreting the proteins that makeup bone, have a critical requirement for optimal cultivation of elevated wall shear stress. Osteoblast cell behaviour is yet to be fully understood, as traditional experimental techniques cannot control micro-environmental conditions [5]. Osteoblasts prefer environments with appropriate wall shear stress, showing increased cell density and differentiation compared to static or no wall shear stress conditions [6]. Thus, accurate measurement of wall shear stress is essential for understanding osteoblast function and behaviour. Quantifying the wall shear stress on a PDMS-based microfluidic device can significantly improve the comprehension of osteoblast and, consequently, the cultivation process.

Most cellular-biological studies employ a full-blown Particle Image velocimetry (PIV) technique to track fluid movement using tracer particles. Comparative studies such as Vig et al. [7] showed that optical-flow-based velocimetry can outperform the results of a PIV. As it is the more accessible solution, the optical flow tool in MATLAB was chosen for implementation in this study. This study uses computer vision analysis on the video from light microscopy to estimate the velocity of the flow. When inducing a controlled fluid flow within microchannels, it is possible to observe the movements of pigment particles within the fluid. When combined with optical flow analysis, these observations facilitate the identification of velocity gradients, enabling the derivation of wall shear stress profiles. The integration of imaging and analysis enhances understanding of the relationship between fluid dynamics and osteoblast behaviour [8].

2. Materials and method

In this study, the method of using microscopy images and computer vision analysis to measure wall shear stress inside a microfluidic chip designed for osteoblast cell cultivation. Video recordings of a testing fluid flowing inside the microfluidic chip chamber were taken with a digital camera and a microscope. The videos were analysed using MATLAB software to calculate the fluid flow at different points in the video frame, constructing a velocity profile. The wall shear stress at various areas within the microfluidic chip was calculated by using the velocity gradient. Since the primary measurement outputted by the optical flow algorithm was the fluid velocity at different locations in the video (in pixel/frame), the velocity from microfluidic chip CFD analysis for verification. After confirming that the velocity could be accurately measured, the wall shear stress was calculated by using velocity gradient from the video. Consequently, the wall shear stress was then compared with the results from simulation.

2.1. The Design of microfluidic chip

The first stage of the study required fabricating a microfluidic chip for culturing osteoblast cells under the influence of high wall shear stress and, consequently, a constant flow condition in the chip. A new microfluidic chip for studying osteoblast cell growth has been developed using a combination of mathematical modelling and fabrication techniques. This will be explained on this section. A CFD analysis in COMSOL Multiphysics software was used to optimise the design of the chip to obtain the optimal flow rate and shear stress conditions required for osteoblast culturing. Secondly, a manufacturing method is required to fabricate the newly designed chip with multi-wall shear stress values.

2.1.1. CFD analysis

The Three-Dimensional models of the chips were created in the SOLIDWORKS and were then imported to COMSOL Multiphysics for fluid flow analysis as shown in Figure 1. The CFD analysis included the material properties of the chip and the fluid to obtain the flow rate and shear stress at 5 different points in the chip as shown in Figure 2. Prior to final design selection for osteoblast cultivation, the simulation serves to choose the most appropriate design with desired shear stress on the cell. After the design has been selected for fabrication, A specific condition is performed to be later reproduced in a physical experiment. [9].

The input flow rate of the fluid was set to 50 μL/min. The dynamic viscosity of 9.3×10^{-4} Pa·s and fluid density of 998.2 kg/m^3 were set. The pressure at the output was set to 0 (zero) Pa. After the simulation, the velocity at different points in the chamber and the wall shear stress were calculated. An extremely fine mesh was set in the simulation to obtain the velocity values at positions very close to the wall. Moreover, a particular fabrication process is required to replicate the chip design from the computer-aided model. The following section provides a brief overview of the process.

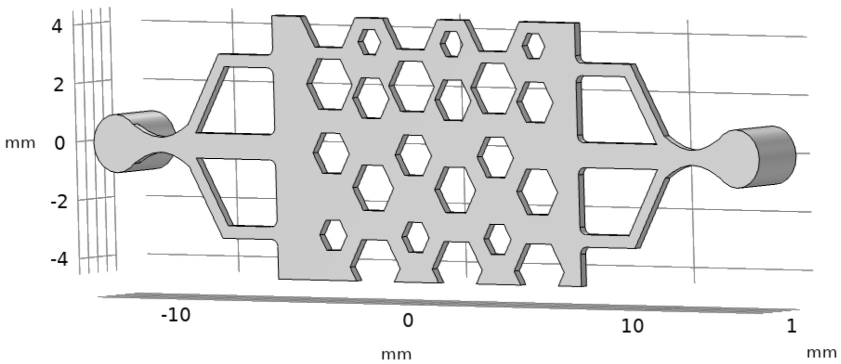

Figure 1. Multi-wall shear stress microfluidic chip 3D model in COMSOL Multiphysics.

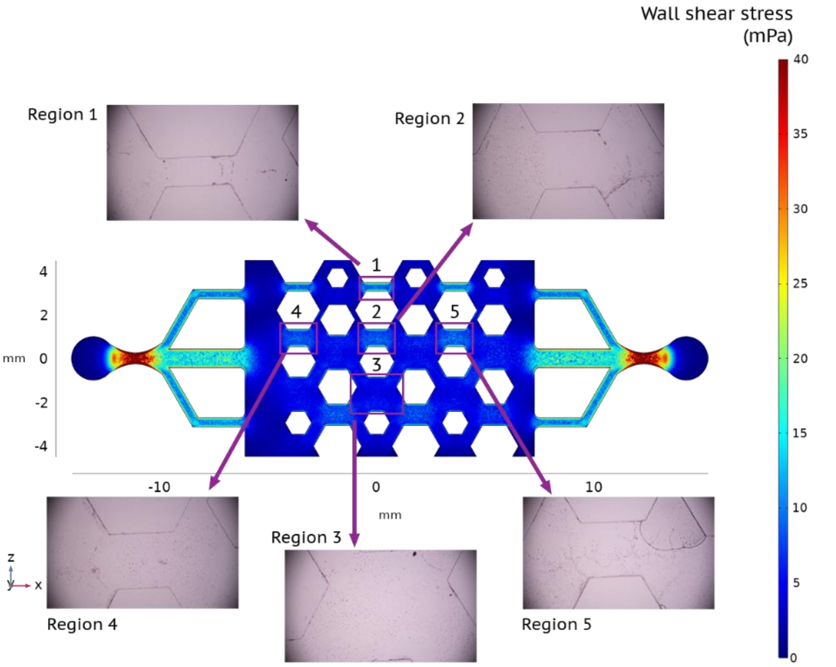

Figure 2. The microscope images (10X) of 5 regions as an AOI compared with the model in COMSOL Multiphysics.

2.1.2. Fabrication of microfluidic chip

The microscale channel was produced via a procedure known as a soft lithography. Soft lithography, a versatile method, can generate micro- and nanoscale features on a wide range of materials. The microfluidic chip was fabricated as follows. Initially, a photomask was fashioned to exhibit the desired pattern for the microfluidic chip. The layer of polydimethylsiloxane (PDMS) was cast onto a glass slide. And the photomask was situated on top of the PDMS and subjected to ultraviolet light (UV). Afterwards, the unexposed PDMS was extracted. Finally, the PDMS was separated from the glass slide and diced into individual chips. The fabricated chips are used to record the flow of testing fluid to perform the shear stress analysis using the testing fluid. The following section describes the detailed setup of the experiment.

2.2. The experiment setup

This stage of the study involved a meticulous design of laboratory setup to record video of the fluid flow within microchannels for subsequent optical flow analysis, as shown in Figure 3(a) and the setup in experiment are show in Figure 3(b). To perform the microscopy and imaging of the experiment, an Olympus CX23 light microscope equipped with a Canon EOS 6D camera connected by EF lens to C mount adapter was used as shown in Figure 3(c). Equipped with a 10x objective lens and 10x eyepiece lens, the microscope allowed the imaging of the interior of the microfluidic channels. The experiment used deionized water and Sigma-Aldrich 42922 microparticle 3-micrometre based on polystyrene pigments dispersed within the fluid to visualise the flow. The pigment was diluted at one microliter per one millilitre (1:100) and introduced into the microfluidic channels. A constant flow rate of 50 microliters per minute was achieved using a LongerPump (LSP01-1C) as shown in Figure 3(a). Video of the fluid flow was recorded by the Canon EOS 6D camera positioned on top of the microscope. The videos are captured in MOV format at 720p resolution, with a frame rate of 59.94 per second (fps) as shown in Figure 3(c). The experimental sequence involves recording each area of interest (AOI) in the microfluidic chip for 3 minutes. This approach guarantees a thorough examination of fluid flow dynamics in the microchannels. Consequently, the experiment is followed by calculating wall shear stress in the microchannel of the fabricated chip in multiple locations using an optical flow algorithm in

MATLAB. To experiment with complex fluid flow measurement, 5 regions of AOI were selected as mentioned in Figure 2.

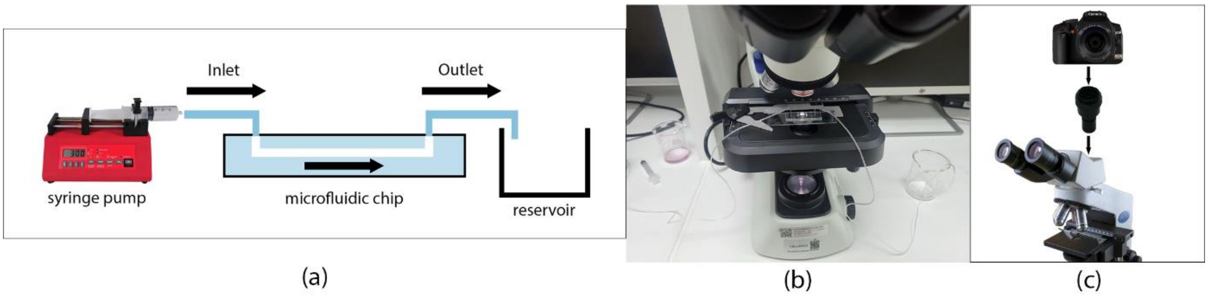

Figure 3. (a) The experimental setup with syringe pump and microfluidic chip. (b) The setup of a microfluidic chip on the Olympus CX23 microscope. (c) The diagram picture of recording system. Mouthing the Canon EOS 6D on top of Olympus CX23 by connecting with an EF-C mouth adapter to record the video.

2.3. Algorithm development in MATLAB for image analysis

The final stage of this research is devoted to developing an accurate MATLAB-based algorithm that has been rigorously tested to extract the flow velocity data from the microchannel images. The pre-processing stage of the algorithms primarily involves performing the crucial operations of rotation and crop of the AOI of the video frame, thereby ensuring that it is aligned and straightened on the frame. The AOI comprehensively covers the whole width of the tube, enabling the measurement of the wall-to-wall velocity profile. Optical flow algorithms break down the velocity of the pixels in x and y components and horizontal and vertical directions in the video frame, respectively. Our method only uses the velocity in the x-axis or horizontal direction for calculating the velocity gradient with respect to the distance from the wall. The crop and rotation steps are seen in Figure 4.

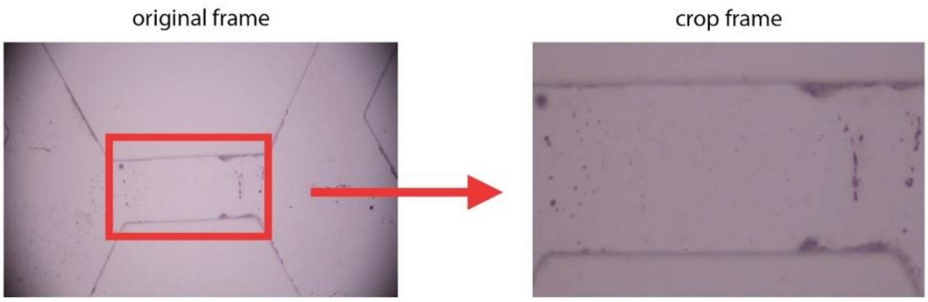

Figure 4. The pre-processing state, crop, and rotating the video frame in AOI.

To convert the pixel-based values outputted by the algorithm to physical distances and velocities, formula (1) was used. This conversion enables us to get estimates and calculated values in the same units as the CFD analysis for comparison.

$$c = \frac{d_{\text{physical}}}{d_{\text{pixel}}} \quad (1)$$

Where the c is the Conversion Factor in unit metre per pixel, d_{physical} is the reference on physical distance in unit metre scale and, d_{pixel} is the reference on computer pixel distance in unit pixels.

This study included conducting a comprehensive assessment of optical flow functions, namely "opticalFlowFarneback" to determine the most suitable option for employment in this scenario. All the optical flow methods use the same equation— to compare differences between 2 consecutive images derived from the brightness constancy assumption on the formula (2) [10].

$$I_x u + I_y v + I_t = 0 \quad (2)$$

Where the I_x, I_y, and I_t are the spatiotemporal image brightness derivatives, u is the horizontal (x-direction) component of the flow velocity, and v is the vertical (y-direction) component of the flow velocity.

After performing a test using a video of a synthetic flow with known flow velocimetry, the algorithm most sensitive to velocities and velocity gradients of the flow near the wall shall be selected for validation against the CFD analysis results. Once the algorithm has been validated, the wall shear stress is computed by using the formula equation (3). Subsequently, it is necessary to construct a graph of the wall shear stress scale and compare the ensuing results to those obtained from the CFD analysis.

$$\tau = \mu \frac{du}{dy} \quad (3)$$

where the τ is the wall shear stress (Pa), μ is the dynamic viscosity of the water at 0.93×10^{-3} Pa·s, and $\frac{du}{dy}$ are the velocity gradient perpendicular to the surface, indicating how quickly the velocity changes with respect to the distance from the surface.

3. Result and discussion

3.1. CFD analysis and experiment results

The CFD analysis result shows the shear stress as a contour map inside the microfluidic chip as shown in Figure 5. and the video frame samples from the recording experiment is shown in Figure 6. Complementing the quantitative analysis, the patterns of pigment movement captured in the recorded videos were visually examined. It is worth noting that a series of images were extracted from the videos, effectively showcasing the movement of pigmented particles as they flowed from right to left within the microchannel (black arrow in Figure 6). These images provide a vivid illustration of the characteristic laminar flow patterns, where layers of fluid move in parallel streams with minimal intermixing. This observation is consistent with the expectations for controlled microfluidic environments, establishing a tangible connection between experimental outcomes and fluid dynamics theory.

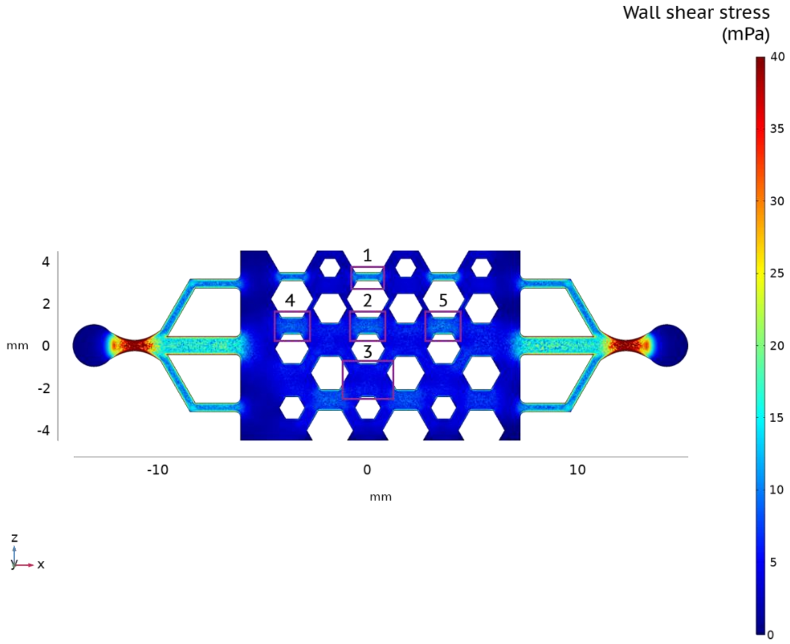

Figure 5. The wall shear stress result of 5 AOI regions from CFD analysis of microfluidic chip.

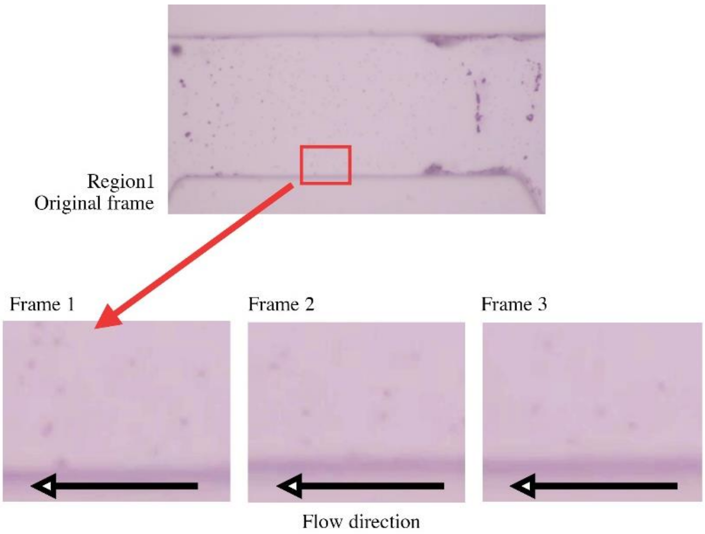

Figure 6. The video recording experiment in the microfluidic chip with black arrows showed the flow movement from the right to left. The Frame 1 is the first exposure and the Frame 2 & 3 are the second and third exposures, respectively.

3.2. Optical flow algorithm

The Farneback method has demonstrated its sensitivity in capturing the near-wall velocity profile for synthetic flow video. Optical flow algorithms, specifically designed to detect slight changes in pixel intensity, were employed in our experiment. Nevertheless, the fast-changing regions of flow, which are farther from the wall, cannot be precisely estimated. A precise wall-to-wall velocity profile can be generated with enhanced spatial and temporal resolution. However, an accurate velocity gradient in the vicinity of the wall is sufficient to compute the wall shear stress.

The analysis produced encouraging results, establishing the precision and suitability of the MATLAB optical flow-driven velocity estimation technique yields results very close to the CFD analysis output. The study yielded promising outcomes, demonstrating the accuracy and appropriateness of the velocity estimation technique driven by MATLAB optical flow. The results obtained were in close proximity to the CFD analysis output. The results in region four were not as satisfactory as expected, possibly due to issues with the cleanliness of the microchannel, which may have had an impact on fluid flow and led to a slower flow rate than the CFD analysis. Alternatively, there may be other factors affecting the outcome that are not yet known.

According to Figure 7, the comparisons between CFD analysis outputs and results from optical flow-based estimations show a close alignment, with discrepancies only spanning an order of magnitude. Applying logical analysis to determine the outliers and set of valuable estimates shows that a rudimentary algorithm can be used to calculate the shear stress inside of a microfluidic channel. That evidence provides supportive evidence for near-real-time shear stress calculation that can be implemented using optical flow.

The optical flow results indicate inaccurately in the velocity and shear stress values near the boundary layer region. These inaccuracies can be attributed to the missing data in the boundary layer area, which subsequently affects the raw data analysis. Some of the solution idea to solve the missing data on the near of the boundary layer are increase the number of the pigment diluting in the liquid and use the higher frame rate speed of the camera system to capture the moment of flow.

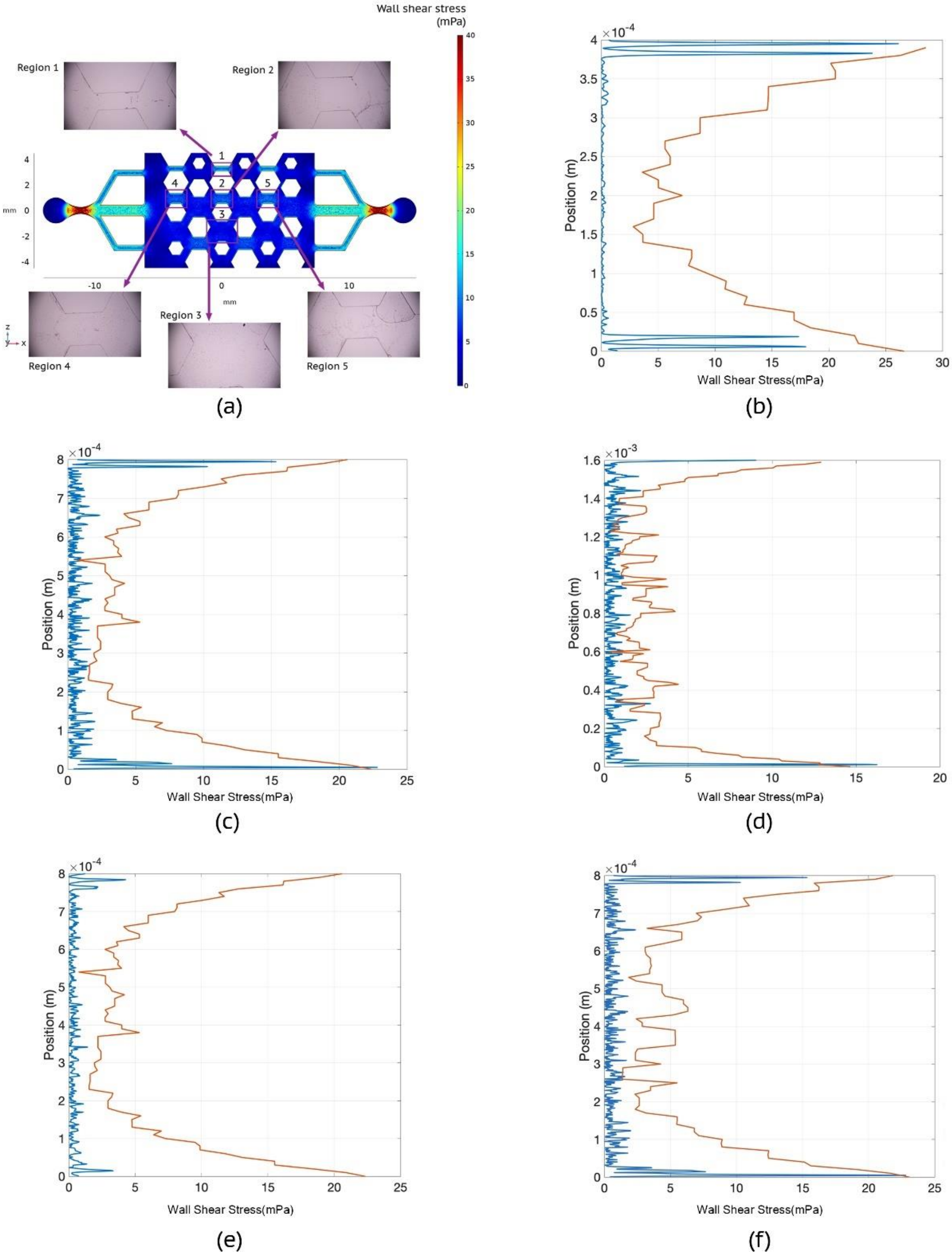

Figure 7. The wall shear stress profile compares the result of optical flow detection (blue line) and the CFD analysis (orange line), (a) 5 AOI regions on chip, (b) result of region 1, (c) result of region 2, (d) result of region 3, (e) result of region 4, and (f) result of region 5.

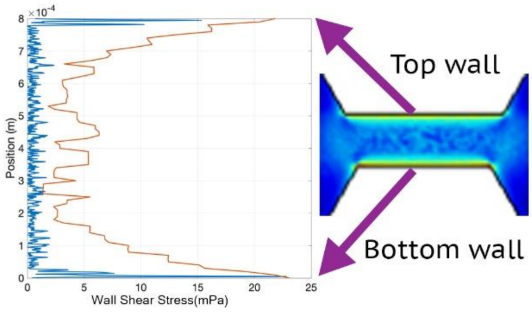

Figure 8. The wall location on the microfluidic chip compared to experimental result graph.

Table 1. The comparison of wall shear stress results from the CFD analysis and experiment with MATLAB optical flow in 5 regions of AOI.

Region	Wall location in microchannel	Wall Shear Stress		
		CFD analysis (mPa)	Experiment (mPa)	% of difference
1	Bottom	26.61	27.02	+ 1.51 %
	Top	28.52	19.93	- 30.14 %
2	Bottom	20.60	16.85	- 18.22 %
	Top	22.34	24.63	+ 10.22 %
3	Bottom	12.92	9.67	- 25.15 %
	Top	14.66	17.28	+ 17.83 %
4	Bottom	21.48	5.00	- 76.72 %
	Top	20.76	3.51	- 83.09 %
5	Bottom	21.83	16.84	- 22.87 %
	Top	23.09	24.63	+ 6.65 %
absolute average				± 29.24 %

The measured and compared the CFD analysis with the detection on observation in experiment of the wall shear stress is shown in Figure 8, where focus is given to the important edges of the microchannel. More specifically, the upper edge is labelled as the "Top wall," while the lower edge is called the "Bottom wall." By matching the diameters of the microchannel on the Y-axis of the graph with the actual of the microchannel, a direct comparison is made between the results of the CFD analysis, and the outcomes obtained from the experiments.

Table 1 presented provides a comparison of wall shear stress values derived from CFD analysis and observation, including the corresponding percentage increase of difference. The overall percent difference is estimated to be around 29.24 %. There may be errors in certain parameters of the experiment, such as the cleanliness of the microchannel, the video frame rate, or the video file format, which could affect the results; nevertheless, it is worth noting that despite the influence of certain parameters and the complex of microfluidic fluid dynamic system, the observed trend of values closely approximates the CFD analysis results, thereby indicating a satisfactory agreement between the two datasets. The MATLAB optical flow tool can identify and observe fluid flow in order to compute the wall shear stress of boundary layers within the fluid. The outcome is comparable to that of the CFD analysis. The trend of the wall shear stress values is generally similar to that of the CFD analysis. It is reasonable to depend on this method and use it to measure the real conditions in microfluidic and other microfluidic channel systems.

4. Conclusion

While the indication that "opticalFlowFarneback" performs reliably and consistently is a positive result, it is also important to do further study. A deeper investigation into the specific parts of the algorithm that contribute to its success can provide valuable insights that help improve this methodology. Additionally, there are potential ways to make the optical flow algorithm better and improve the quality of images, which could lead to the better accuracy and reduce deviations. Recording videos with higher clarity and more frames per second can provide more information of the fast-moving part in the channel.

It should compare the results and how well the current method works with more advanced optical flow algorithms like Liteflownet [11]. For textures that are not very detailed, like our diluted pigments, using an event-based optical flow estimation might give better results [12]. Despite its limitations, this study showed a possible way to calculate wall shear stress in a microfluidic channel with reasonable accuracy, providing measurements in nearly real-time.

5. Acknowledgments

This research project is supported by Chulabhorn Royal Academy (Fundamental Fund: fiscal year 2023 by National Science Research and Innovation Fund (FRB660044/0240 Project code 180851)).

6. References

[1] Whitesides, George M. "The origins and the future of microfluidics." nature 442, no. 7101 (2006): 368-373.

[2] Faustino, Vera, Susana O. Catarino, Rui Lima, and Graça Minas. "Biomedical microfluidic devices by using low-cost fabrication techniques: A review." Journal of biomechanics 49, no. 11 (2016): 2280-2292.

[3] Schoenitz, M., L. Grundemann, W. Augustin, and S. J. C. C. Scholl. "Fouling in microstructured devices: a review." Chemical communications 51, no. 39 (2015): 8213-8228.

[4] Burova, Iva, Ivan Wall, and Rebecca J. Shipley. "Mathematical and computational models for bone tissue engineering in bioreactor systems." Journal of tissue engineering 10 (2019): 2041731419827922.

[5] Mansoorifar, Amin, Ryan Gordon, Raymond C. Bergan, and Luiz E. Bertassoni. "Bone-on-a-chip: microfluidic technologies and microphysiologic models of bone tissue." Advanced functional materials 31, no. 6 (2021): 2006796.

[6] Guo, Pan, Yi Zhou, Ziyang Jin, Yan Zhou, and Wen-song Tan. "Fluid shear stress promotes osteogenesis of bone mesenchymal stem cells at early matrix maturity phase through Lamin A/METTL3 signal axis." Biochemical Engineering Journal 188 (2022): 108685.

[7] Vig, Dhruv K., Alex E. Hamby, and Charles W. Wolgemuth. "On the quantification of cellular velocity fields." Biophysical journal 110, no. 7 (2016): 1469-1475.

[8] Jin, Jianfeng, Richard T. Jaspers, Gang Wu, Joannes AM Korfage, Jenneke Klein-Nulend, and Astrid D. Bakker. "Shear stress modulates osteoblast cell and nucleus morphology and volume." International Journal of Molecular Sciences 21, no. 21 (2020): 8361.

[9] Bahmaee, H., Owen, R., Boyle, L., Perrault, C. M., Garcia-Granada, A. A., Reilly, G. C., & Claeyssens, F. (2020). Design and evaluation of an osteogenesis-on-a-chip microfluidic device incorporating 3D cell culture. *Frontiers in Bioengineering and Biotechnology, 8*. https://doi.org/10.3389/fbioe.2020.557111

[10] Fleet, David, and Yair Weiss. "Optical flow estimation." In the Handbook of mathematical models in computer vision, pp. 237-257. Boston, MA: Springer US, 2006.

[11] Hui, Tak-Wai, Xiaoou Tang, and Chen Change Loy. "Liteflownet: A lightweight convolutional neural network for optical flow estimation." In Proceedings of the IEEE conference on computer vision and pattern recognition, pp. 8981-8989. 2018.

[12] Benosman, Ryad, Sio-Hoi Ieng, Charles Clercq, Chiara Bartolozzi, and Mandyam Srinivasan. "Asynchronous frameless event-based optical flow." Neural Networks 27 (2012): 32-37.

CST0005

Aerodynamics and flow characteristics of NACA0012 and 4412 with cut-in sinusoidal trailing edge shape

P Rattanasiri[1,*]

[1]Department of Mechanical Engineering, Faculty of Engineering, Burapha University, Chonburi Campus, Chonburi, 20130, Thailand

* Corresponding Author: pareecha@eng.buu.ac.th

Abstract. This paper presents the influence of the cut-in sinusoidal trailing edge shape on the wake flow behaviour of symmetric NACA0012 and asymmetric NACA4412. A wavelength of 0.5*c* with three amplitudes of sinusoidal curve (*h*) of 0.025*c*, 0.050*c* and 0.075*c* are used to model the cut-in trailing edge shape, where *c* is the chord length. The flow is simulated at Reynolds number 10^6 at angle of attack 5 degree. The structured C-grid of the computational fluid domain is modelled using the open-source *Salome*. Unsteady Reynolds-Average Navier-Stokes (RANS) technique and k-ω *SST* turbulence model with the log law wall function are selected to solve the problem using the open-source *Code_Saturne*. The results of aerodynamics performance, drag and lift, are analysed to describe the airfoil characteristics. The pressure distribution, pressure contour and velocity contour are illustrated for selected planes.

Keywords: NACA 0012, NACA 4412, URANS, sinusoidal trailing edge.

1. Introduction

Recently, wind turbine technology has been developed rapidly, consequently, it is possible to produce electricity efficiently for wind potential in Thailand. Lately, there are many wind power plants launched around Thailand. It is known that the downwind area of the plant can experience the noise problem caused by the turbine blade. Modified blade shapes such as leading edge and trailing edge have been proposed to reduce the blade noise [1-2]. A general objective of this study is to analyze the effect of such trailing edge modification on the aerodynamic performances and flow characteristics behind the blade.

Recently, the author published the results of flow past NACA profiles; 0015, 4415, 4615, 6415 and 6815 with the cut-in sinusoidal trailing edge (TE) shape. The simulation has been done by using the Unsteady Reynolds-average Navier-Stokes (URANS) technique at a high Re=10^6 at the of attack 5° in [3-6]. The summary of results are as follows: firstly, the wavelength of the cut-in curve has no effect on the performances for any given airfoil profiles. Secondly, the amplitude of the cut-in curve has an effect on performances of airfoils with blunt TE and cut-in TE. Lastly, lift and drag of some profiles with cut-in TE are increased when compared with its baseline TE.

The results in [6] showed that the camber of an airfoil can generate a higher suction on upper surface and high pressure appears on the lower surface compared with pressure distribution of the symmetric airfoil. It results in higher lift for the asymmetric airfoil than that of the symmetric airfoil. By cutting the TE removes the small overpressure around it, it also explains the increase of lift. In most cases, by cutting the TE, the low pressure is also observed on the blunt TE, it explains the increase of drag.

The study has been done for 0012 with cut-in sinusoidal trailing edge (cut-in TE) shape by using Direct Numerical Simulation (DNS) simulation at the Reynolds number *Re*=5000 and the angle of attack 5°. The results showed that the lift of airfoil with modified TE increased by 10% compared with the baseline TE shape, however, it also showed an increase of the drag by 2.5% [7].

The comparison results of 4412 and 4415 with cut-in TE at a selected amplitude [3] showed that, firstly, the wavelength of the sinusoidal curve had no effect on the performance. Secondly, the comparison of C_L/C_D between 4412 and 4415 with the same TE showed that 4412 was found to provide better performance than that of 4415.

Therefore, the aim of this paper is to study the influence of the amplitude of cut-in sinusoidal curve on the aerodynamic performances and wake flow behavior downstream of 0012 and 4412 profiles. A wavelength with different three amplitudes of sinusoidal curve (*h*) are used to model the cut-in TE shape. Due to the limitation of the computer performance, the simulation is simplified to use the Unsteady Reynolds-average Navier-Stokes (URANS) technique at a high *Re*=10^6 at the of attack 5°.

2. Theorical Approach

The overall CFD simulation process are pre-processing, processing and post-processing. Firstly, for pre-processing, the airfoil geometry and fluid domain are modelled and the meshes are generated in the open-source program *Salome*. Then, the open-source *Code_Saturne* is used to setup fluid property, boundary conditions, initial conditions and solver algorithm. Finally, the results are analysed in the post-processing. The mesh convergence is also checked to validate the results.

2.1. NACA geometry profiles and trailing edge modelling

The cross-sectional profiles of NACA, 0012 and 4412, are shown in Figure 1. The sinusoidal parameters described in Figure 2 are used in Equation (1) for the cut-in TE:

$$\bar{x}(z) = c - h\left\{1 - cos\left(\frac{2\pi}{\lambda}z\right)\right\} \quad (1)$$

where $\bar{x}(z)$ is the chord coordinate, z is the spanwise coordinate, and c is the chord length. The wavelength λ is 0.5*c*. There are three amplitudes of sinusoidal curve (*h*) of 0.025*c*, 0.050*c* and 0.075*c*. The 3D geometry of airfoils with baseline TE, blunt TE and cut-in TE are shown in Figure 3(a), 3(b) and 3(c), respectively.

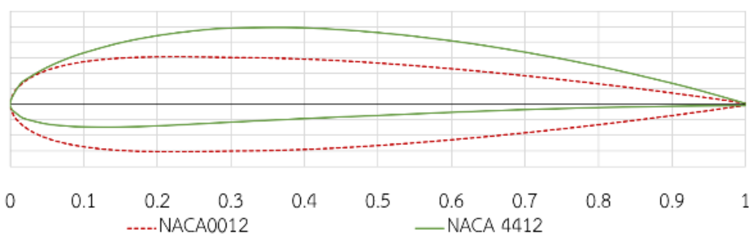

Figure 1. NACA0012 and 4412.

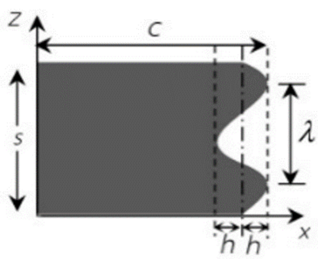

Figure 2. Sinusoidal Parameter [5].

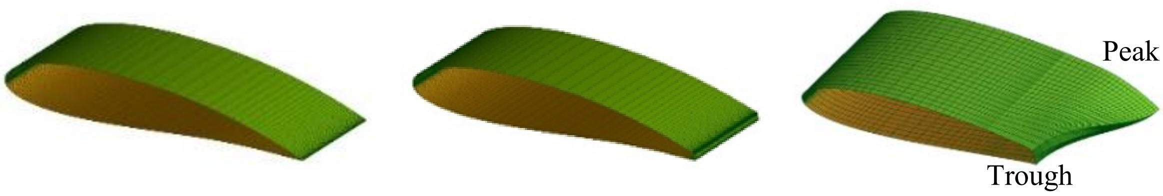

(a) baseline TE (b) blunt TE (c) cut-in TE

Figure 3. Airfoils with (a) baseline TE, (b) blunt TE and (c) cut-in TE [5].

2.2. Fluid far-field, boundary condition, mesh strategy and solver set up

A C-grid type is selected with 20*c* in both upstream and downstream *x*-direction, as shown in Figure 4. Related fluid properties and boundary conditions are set as shown in Table 1. Figure 5 shows an isometric view of the mesh on the trough plane. To capture the flow, the appropriate local refinement around the airfoil and in the wake region are used with $y^+ \approx 30$ at the walls in agreement with the "2 scales (log law) wall function" implemented in the solver *Code_Saturne*. Table 2 shows the detail of the set-up of the solver.

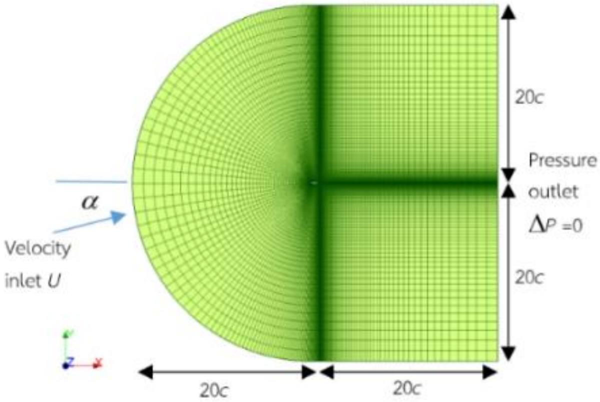

Figure 4. Far-field and boundary conditions [5].

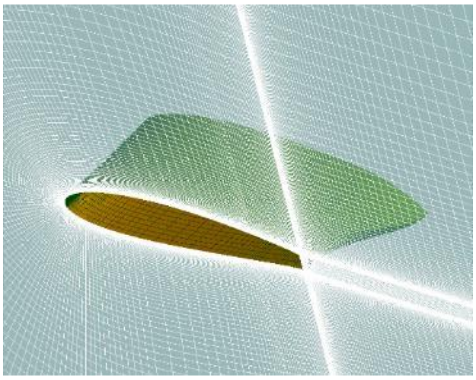

Figure 5. Trough plane structure mesh [5].

Table 1. Set up fluid property

List	Set up
The inlet velocity (U)	1 m/s
Outlet	ΔP_{outlet}=0
Angle of attack (α)	5°
Turbulent intensity	1%
The dynamic viscosity (μ)	10^{-6} Pa.s
The density (ρ)	1 kg/m^3
Peak/Trough plane boundaries	Symmetry

Table 2. Simulation set up

List	Set up
Model	URANS
Approach	FVM and SIMPLEC
Scheme	A Second Order Linear Upwind (SOLU)
Turbulent model	k-ω SST
Time step	0.01
RMS	<10^{-8}

2.3. Aerodynamics force calculation

The lift and drag coefficients, C_L and C_D, respectively, are calculated as shown in Equation (2). The $\%C_L$ and $\%C_D$ are calculated using Equations (3) and (4), respectively,

$$C_L = \frac{\text{Total lift}}{\frac{1}{2}\rho\, U^2 s c'} \quad \text{and} \quad C_D = \frac{\text{Total drag}}{\frac{1}{2}\rho\, U^2 s c'} \tag{2}$$

$$\%C_L = \frac{C_{L,modified\,TE} - C_{L,baseline}}{C_{L,baseline}} \times 100\% \tag{3}$$

$$\%C_D = \frac{C_{D,modified\,TE} - C_{D,baseline}}{C_{D,baseline}} \times 100\% \tag{4}$$

where s is the spanwise-length (λ/2) and c' is the physical chord length of airfoils, c, $c-h$ and $c-2h$ for baseline TE (peak), cut-in TE and blunt TE (trough), respectively.

The total lift and total drag forces are estimated from the pressure and skin friction forces. The related pressure coefficients C_P and the friction coefficients C_F are calculated by Equation (5).

$$C_P = \frac{P - P_0}{\frac{1}{2}\rho\, U^2} \quad \text{and} \quad C_f = \frac{\tau_W}{\frac{1}{2}\rho\, U^2} \tag{5}$$

where P is the pressure at the point at which C_P is determined. P_0 and U are the pressure and velocity in the free-stream. τ_w is the wall shear-stress.

3. Mesh convergence

In the process of numerical simulation, checking mesh convergence is one measure of accuracy. Assessment of the results for the mesh convergence for baseline TE of 0012 and 4412 were done in [3]. The number of cells in *x*-*y* plane were tested for 50k, 100k, 150k and 200k. It is shown that the convergence for C_L and C_D can be obtained and 100k-cells is selected to model the baseline TE and blunt TE. Assessment of the results for the baseline TE was also done using a comparison with viscous analysis by the XFoil program [3].

For the airfoil with cut-in TE, the 10 and 20 mesh layers are selected for shaping the TE in *z*-direction. Due to the simplicity of structured mesh, the mesh convergence from coarse (1.1M), medium (1.7M), medium-fine (2.1M) to the fine mesh (2.3M) can be obtained for C_L and C_D. The results of lift, drag, velocity contour and pressure contour are observed. Figure 6 and 7 show the velocity contour and the pressure contour at the trough plane of 4412 with cut-in TE at h=0.075, respectively. Figure 6(a) and 7(a) show the contours obtained using the coarse mesh (1.1M cells) and Figure 6(b) and 7(b) show those obtained using the fine mesh (2.3M cells). It can be seen that only minor differences in the wake are visible. Figure 8 shows the result of 3D mesh convergence of 4412 with cut-in TE at h=0.050. From accuracy and time consumption prospect, therefore, the coarse mesh (1.1M) is selected in this study.

(a) Velocity contour 1.1M meshes

(b) Velocity contour 2.3M meshes

Figure 6. Velocity contour at the trough plane of 4412 with cut-in TE at h=0.075.

(a) Pressure contour 1.1M meshes

(b) Pressure contour 2.3M meshes

Figure 7. Pressure contour at the trough plane of 4412 with cut-in TE at h=0.075.

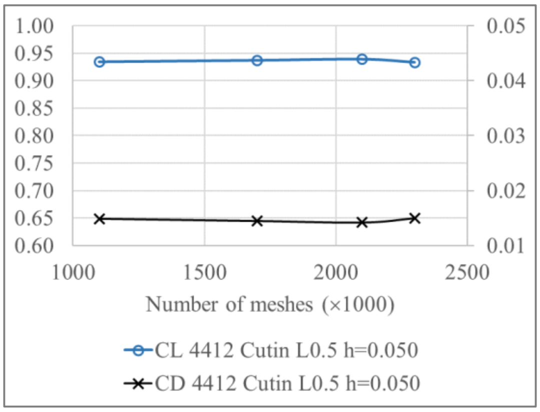

Figure 8. Mesh convergence C_L and C_D of 4412 with cut-in TE.

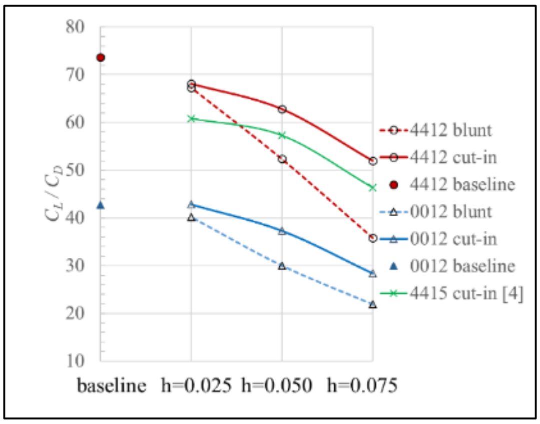

Figure 9. The lift to drag ratio (C_L/C_D)

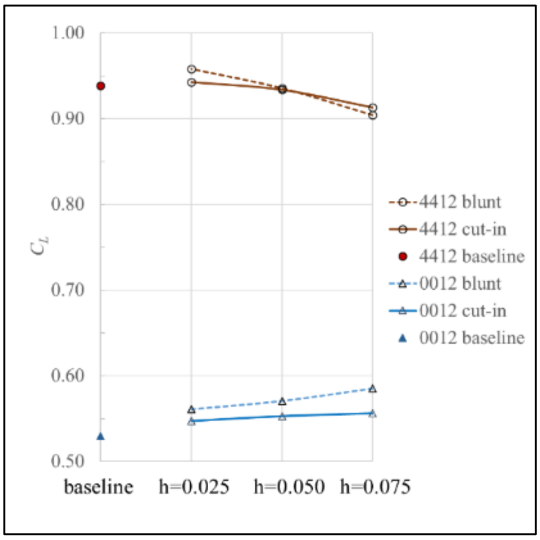

Figure 10. Lift coefficient (C_L)

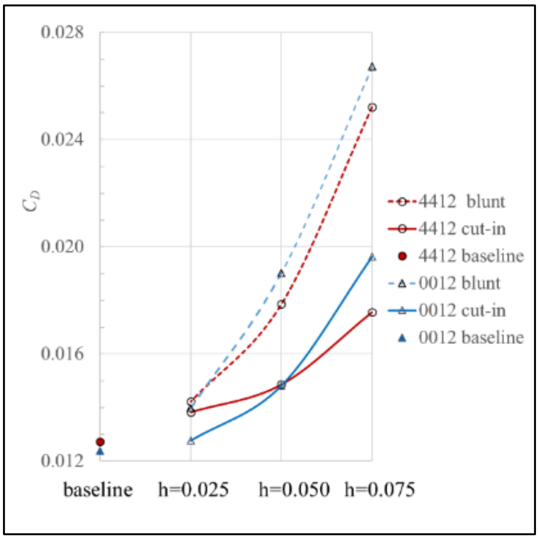

Figure 11. Drag coefficient (C_D)

Table 3. C_L, C_D, $\%C_L$ and $\%C_D$ of 0012 and 4412 with modified TE and $\%C_L$ and $\%C_D$ of 4415 from ref [4] for comparison.

		C_L		C_D		$\%C_L$			$\%C_D$		
TE	*h/c*	0012	4412	0012	4412	0012	4412	4415	0012	4412	4415
Blunt TE	0.025	0.5608	0.9579	0.0140	0.0142	5.9	2.1	7.6	12.8	11.8	12.0
	0.050	0.5707	0.9356	0.0190	0.0179	7.8	-0.3	8.3	53.6	40.3	40.5
	0.075	0.5854	0.9045	0.0267	0.0252	10.5	-3.6	5.3	115.6	98.1	112.3
Cut-in	0.025	0.5473	0.9428	0.0128	0.0138	3.3	0.5	3.8	3.0	8.6	4.5
λ/c=0.50	0.050	05528	0.9339	0.0148	0.0149	4.4	-0.5	4.1	19.6	16.7	11.4
	0.075	0.5561	0.9133	0.0196	0.0176	5.0	-2.7	4.3	58.4	37.9	37.9
Baseline TE		0.5296	0.9384	0.0124	0.0127						

Note: ‘Minus’ sign means the decreasing of force when compared with baseline TE.

4. Results

4.1. Influence of amplitude to the aerodynamic performances

The physical chord length c', as defined in section 2.3, is used to scale the C_L and C_D. Figure 9 shows the lift to drag ratio (C_L/C_D). The results of C_L and C_D are shown in Figure 10 and 11, respectively. The $\%C_L$ and $\%C_D$ of the modified TE airfoil compared with the baseline TE airfoil are presented in Table 3. The results of 4415 with modified TE from [4] is included in this table and Figure 9 to compare with the results of 4412.

4.1.1. C_L/C_D

From Figure 9, by observing the group of blue curves (0012) and red curves (4412), and also a green curve (4415), the effect of TE is similar. The airfoil with cut-in TE (continuous line) provides higher C_L/C_D than the airfoil with blunt TE (dash line). Considering each TE type, 4412 provides better performances (C_L/C_D) than 0012 and 4415.

4412 with the baseline TE obtains the highest C_L/C_D of all airfoils in this study. 4412 with the cut-in TE at h=0.025 is the highest C_L/C_D of all modified TE airfoils.

0012 with blunt TE at h=0.075 shows the lowest C_L/C_D because of the significant increase of drag by 115.6% (see Table 3). 4412 with blunt TE at h=0.075 shows the lowest C_L/C_D of all 4412 profiles, as a result of 3.6% of lift reduction and 98.1% of drag increment.

Concerning the amplitude of the modified TE (h), for blunt and cut-in TE profiles, similar results are observed. The shallow cut-in TE (h=0.025) shows the highest C_L/C_D, and the deep cut-in TE at h=0.075 results in the lowest C_L/C_D. Similar trend is observed for blunt TE. It is found that these results are similar to the results shown in [4-5] for NACA xx15.

4.1.2. Lift and drag

From results in Figure 10 and 11 and Table 3, the comparison of all modified TE profiles shows, firstly, 4412 with the blunt TE at h=0.025 and 0012 the cut-in TE at h=0.025 provide the highest and the lowest C_L, respectively. Secondly, 0012 with the cut-in TE at h=0.025 and 0012 with the blunt TE at h=0.075 provide the lowest and the highest C_D, respectively.

The effect of the TE shows a significant difference of C_L between the symmetric airfoil (0012) and the asymmetric airfoil (4412). For 0012, the lift is increased with the deeper cut. On the other hand, 4412 shows a decrease of lift with the deeper cut.

By comparing the cut-in TE with baseline TE, the results of 0012 reveal that at h=0.025, the $\%C_L$ and $\%C_D$ are increased by 3.3% and 3.0%, respectively. Whilst at h=0.075, the $\%C_L$ is increased by 5.0% and $\%C_D$ is increased by 58.4%. The results of 4412 reveal that at h=0.025, the $\%C_L$ and $\%C_D$ are increased by 0.5% and 8.6%, respectively. Whilst at h=0.075, the $\%C_L$ is decreased by 2.7% and the $\%C_D$ is increased by 37.9%.

The effect of the cut is significant concerning $\%C_D$. Shallow cut-in at h=0.025 shows the results in additional drag of 3.0% compared with baseline TE and the deeper cut-in at h=0.075 shows an additional drag of 115.6%.

4.2. The pressure distribution

Figure 12 presents the corresponding C_P and C_f of airfoils with cut-in TE at h=0.075 versus the chord station. The pressure distribution around 0012, 4412 and 4415 with cut-in TE, at the peak and trough plane are shown in Figure 13 and 14, respectively.

Considering the pressure distribution around 0012 with cut-in TE for h=0.025 at peak plane, Figure 13(a), and its trough plane, Figure 14(a), it appears that the cutting TE has no significant effect on the upstream pressure distribution around the airfoil. Similar results are also observed for the other profiles. The pressure distribution at the peak plane and trough plane are similar to that obtained for the baseline and blunt profiles, respectively.

4.2.1. Peak plane

On Figure 13, all profiles on the peak plane show an intense overpressure in the region of the stagnation point, and suction on the upper surface of the wing. These actions are the origin of an airfoil's lift.

As shown in Figure 13(c-d), the camber of airfoil generates a higher suction on upper surface and high pressure appears on the lower surface, when compared with pressure distribution of the symmetric airfoil shown in Figure 13(a-b). It results in higher lift for asymmetric 4412 profile than that of the symmetric 0012 profile (Table 3).

Figure 12 (left column) shows C_P curve of each profiles. The summation of the area between the upper and lower surface of C_P curve is the lift force. The results confirm and explain the higher lift of 0012 compared with 4412 profiles with the same cut-in TE.

4.2.2. Trough plane

Comparing Figure 13(a) and 14(a), cutting the TE removes the small overpressure around it. This resulting cut blunt TE leads to the low pressure and the presence of a wake downstream (Figure 15). It explains the increase of pressure drag, which increases the total drag indicated in Table 3.

4.3. The velocity contours

Velocity contours of airfoil with cut-in TE for various amplitudes (*h*) are shown in Figure 16. The side-views are selected at the peak plane (*z*=0) and trough plane (*z*=0.25). The blue zone downstream of the airfoil highlights the low velocity wake. The peak plane shows a small disturbed flow similar to the result of baseline TE. The trough plane shows an unsteady wake flow similar to the result of blunt TE.

Figure 16(c) and (d) show average velocity profile of the wake downstream of 4412 at peak and trough planes. It shows a steady wake downstream of 4412 at the peak plane. At the trough plane, there is an unsteady wake downstream of 4412 with cut-in at *h*=0.025 which is narrower than the wake for *h*=0.075. It explains the smaller C_D of 4412 cut-in at *h*=0.025 compared with *h*=0.075 (the drop of the red line in Figure 9).

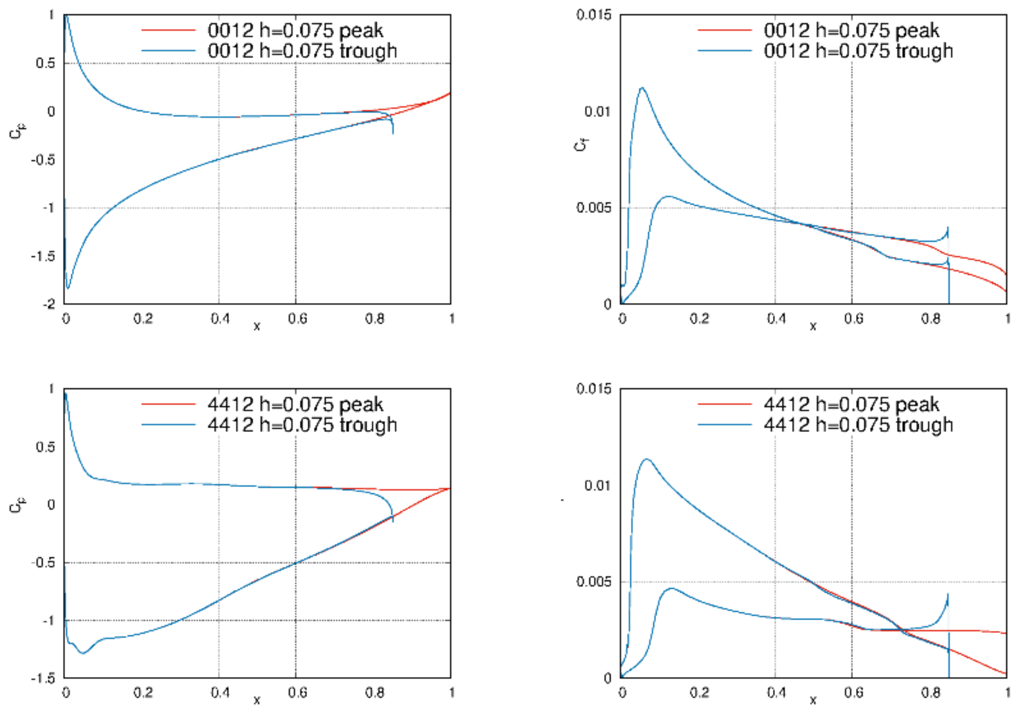

Figure 12. C_P (left column) and C_f (right column) of airfoils with cut-in TE at *h*=0.075 versus the chord station (*x*).

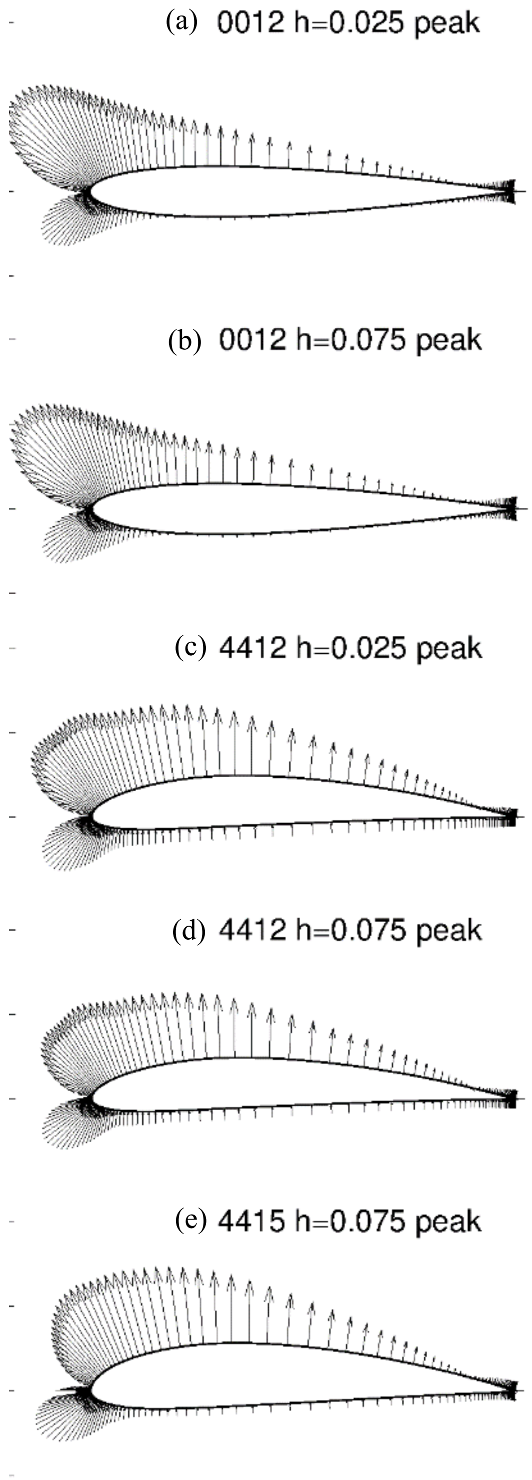

Figure 13. Pressure distribution of the airfoils with cut-in TE at the peak plane.

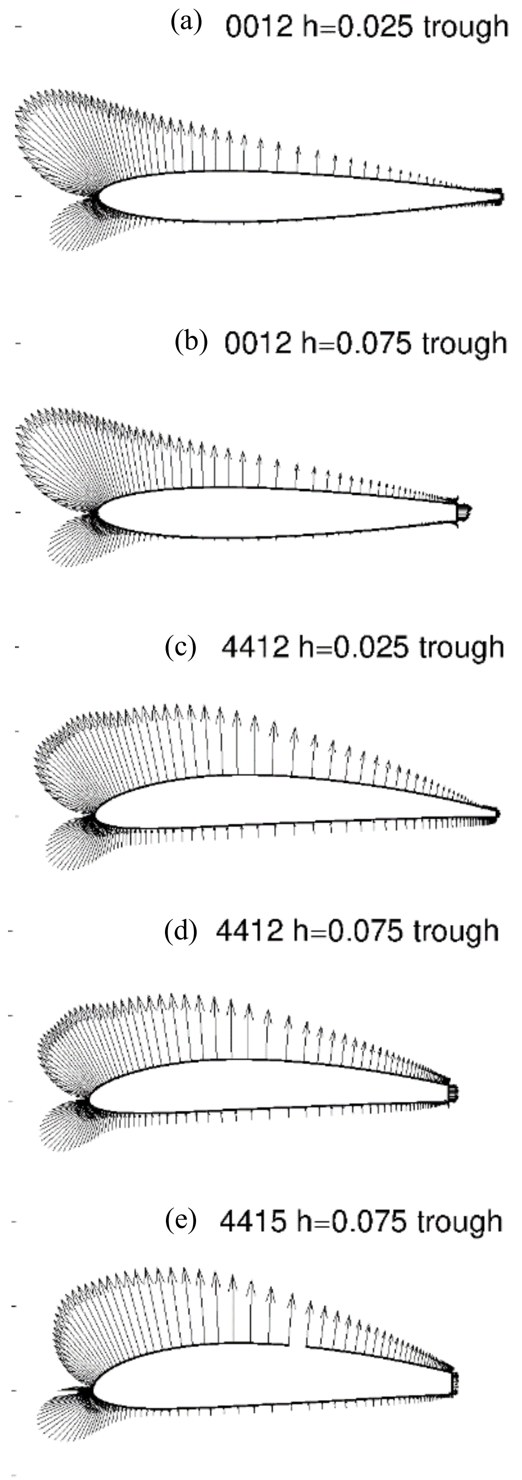

Figure 14. Pressure distribution of the airfoils with cut-in TE at the trough plane.

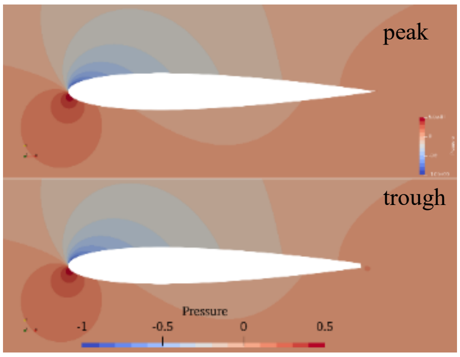

(a) 0012 h=0.025

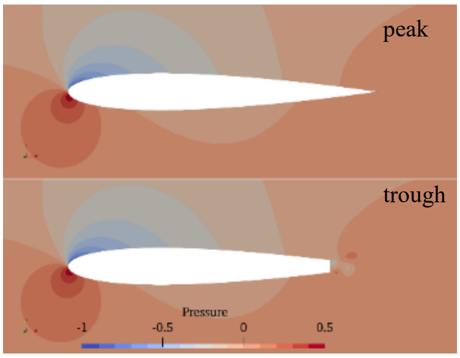

(b) 0012 h=0.075

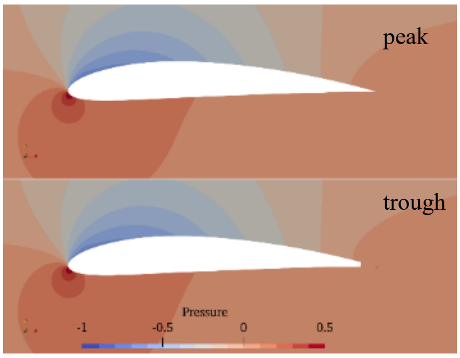

(c) 4412 h=0.025

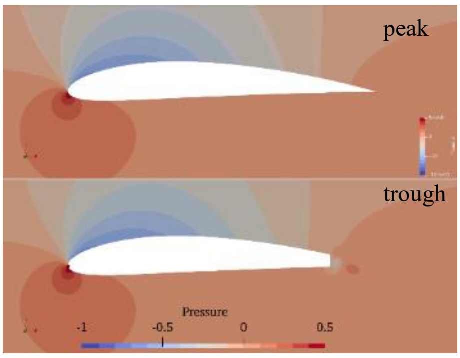

(d) 4412 h=0.075

Figure 15. Pressure contour of the airfoils with cut-in TE at the peak and trough plane.

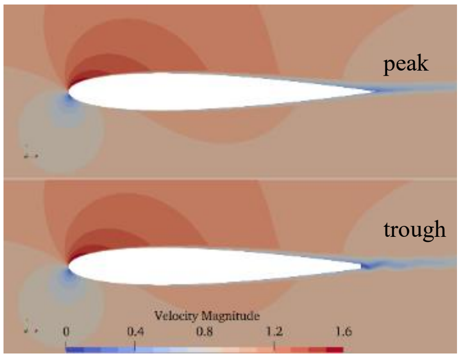

(a) 0012 h=0.025

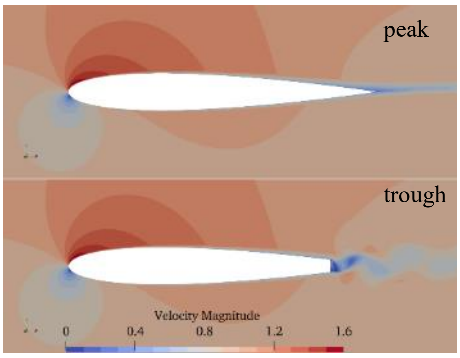

(b) 0012 h=0.075

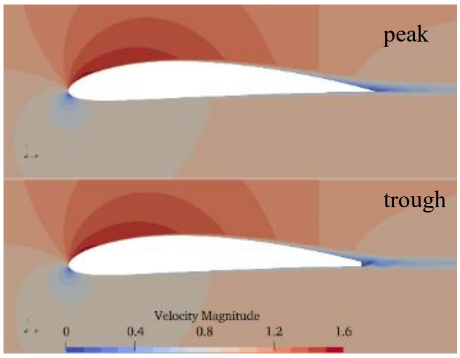

(c) 4412 h=0.025

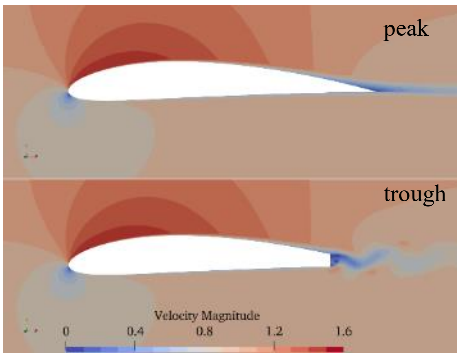

(d) 4412 h=0.075

Figure 16. Velocity contour of the airfoils with cut-in TE at the peak and trough plane.

5. Conclusion

The geometries of NACA 0012 and 4412 airfoils with a zero thickness trailing edge is selected as a baseline TE profile. The cut-in sinusoidal TE profile with three sinusoidal amplitudes h at 0.025, 0.050 and 0.075 with 0.50 wavelength are selected as the cut-in TE profile. The blunt TE profile is a cut-off TE for $2h$.

The unsteady RANS simulations using the open-source code *Code_Saturne* are selected to estimate the aerodynamic forces. The flow is simulated at high Re = 10^6 for angle of attack 5 degree. The results of cut-in TE are compared with the benchmark baseline and blunt TE shape.

In summary, the results show that the amplitude has an effect on C_L/C_D of airfoils with the blunt and cut-in TE. For modified TE airfoils, 4412 with cut-in TE at h=0.025, provides the best performance. The velocity and pressure contours, as well as the C_P and C_f distributions on the airfoils with modified TE were investigated to explain the loss of lift and the increase of drag.

6. Acknowledgments

Author wishes to acknowledge Faculty of Engineering, Burapha Univeristy to provide a funding of this project. Part of the computations was also performed on the high performance computer funded by the National Science and Technology Development Agency (NSTDA), contract no. JRA-CO-2563-13102-TH.

7. References

[1] Rogers, A. L., Manwell, J. F., and Wright, S. (2002). Renewable Energy Research Laboratory: Wind turbine acoustic noise issues, Department of Mechanical and Industrial Engineering, University of Massachusetts at Amherst.

[2] Wagne, S., Bareiss, R. and Guidati, G. (1996). Wind turbine noise, Springer Berlin, Heidelberg.

[3] Rattanasiri, P. and Perrin, R. (2020). Influence of the Wavelength of Cut-In Sinusoidal Trailing Edge Shape to the Aerodynamic Characteristic of the Airfoil, in the IOP Conference Series: Materials Science and Engineering 886 (1), 012020.

[4] Rattanasiri, P. (2021). Influence of the amplitude of cut-in sinusoidal trailing edge shape to the aerodynamic characteristics of airfoils, in the 35th Conference of the Mechanical Engineering Network of Thailand, Nakhon Pathom, Thailand. (p.564-568) (in Thai)

[5] Rattanasiri, P. (2022). Influence of the cut-in sinusoidal trailing edge shape on the aerodynamic characteristics of NACA6415 and 6815 at angle of attack 5 degree, in the 36th Conference of the Mechanical Engineering Network of Thailand, Prachuap Khiri Khan, Thailand. (p.615-621) (in Thai)

[6] Rattanasiri, P. (2022) Influence of the cut-in sinusoidal trailing edge shape on the aerodynamic characteristics of NACA profiles at various angle of attack, in the 36th Conference of the Mechanical Engineering Network of Thailand, Prachuap Khiri Khan, Thailand. (p.622-629) (in Thai)

[7] Rattanasiri, P. (2023). Flow characteristics behind NACA0015, 6415 and 6815 with the cut-in sinusoidal trailing edge shape, in the 37th Conference of the Mechanical Engineering Network of Thailand, Song khla, Thailand. (p.630-637) (in Thai)

[8] Rattanasiri, P. and Perrin, R. (2018). Direct Numerical Simulation Study of the Aerodynamic Performance of NACA0012 with Sinusoidal Tailing Edge Shape, the 9th Thai Society of Mechanical Engineers International Conference on Mechanical Engineering, Phuket, Thailand. (p.712-718)

CST0006

Decomposed Quadrilateral Finite Element for 2D Heat Transfer Analysis

C. Bhothikhun*, K. Sirisomboon, S. Wasananon, T. Sangsawang, and P. Arromdee

Department of Mechanical Engineering, Faculty of Engineering and Industrial Technology, Silpakorn University, Sanam Chandra Palace Campus, Nakhon Pathom, 73000, Thailand

* Corresponding Author: Bhothikhun_c@su.ac.th

Abstract. This study proposed the decomposed quadrilateral element for analyzing two-dimensional heat transfer problems by using finite element method. Each four-node quadrilateral element is subdivided into four sub-triangles and the finite element formulation can be derived without using numerical integration. While using the general isoparametric quadrilateral element, four-point numerical integration and isoparametric coordinate transformation are needed to perform. Some numerical examples in heat transfer problems are used to validate the proposed element. It is found that the decomposed quadrilateral element can provide good solution accuracy in solving heat transfer problems.

Keywords: Decomposed quadrilateral element, Finite element method, Heat transfer.

1. Introduction

In general engineering work, some structures or parts normally experience such thermal loads. As ensuring the safety of these is important, therefore it is necessary to have a good understanding of the thermal response through heat transfer analysis. Analytical method is proved to be effective for some problems in obtaining exact thermal responses. However, when dealing with such complex geometry or boundary conditions, the exact solutions can be difficult to find. As a result, numerical technique, especially the finite element method (FEM), is therefore commonly used in such analysis [1].

In the past few decades, various numerical approaches have been developed to address heat transfer issues [2]. Among these methods, the finite element method (FEM) is considered an outstanding tool for thermal analysis in engineering. Within the realm of FEM analysis, the quadrilateral isoparametric element holds significant importance due to its accuracy and stability. Nonetheless, this traditional quadrilateral element has some drawbacks. Firstly, the presence of numerical integration with four points in each element during the construction of the finite element matrices increases the computational cost, especially for large-scale problems. Additionally, ensuring the quality of the mesh is important as the isoparametric coordinate transformation is a necessity in numerical calculations, especially during finite element matrices formulation. Severe distortions in elements can cause the determinant of the Jacobian matrix to be negative, leading to failure in numerical analysis [3,4].

To overcome these limitations, researchers have explored some new approaches. One such endeavor involves the development of the reduced integration technique to mitigate computational efforts associated with the quadrilateral element. This technique strategically employs only one integration point, effectively reducing computational costs [5]. However, its stability is not consistently guaranteed. Subsequent studies have aimed at enhancing the stability of the one-point integration technique. For example, Liu and Belytschko introduced the orthogonal hourglass control method to address stability and extended it to solve thermal problems [6]. Belytschko and Bachrach proposed mixed methods to stabilize the one-point numerical integration, offering highly accurate solutions [7]. Unfortunately, these stabilization approaches are constrained to mapped quadrilateral elements. The other work of stabilization one-point integration includes that given by Koh and Belytschko [8,9].

To overcome those limitations, the smoothed finite element method (SFEM) was proposed by Liu et al. [10,11] by combining with the strain smoothing operation [12]. The SFEM method separates the elements into smoothing cells, and the Green's divergence theorem has been applied along the edges. Accordingly, no coordinate transformation is required in computing the finite element stiffness matrix, and the element shape can be arbitrary. The SFEM also provides good performance for distortion meshes compared with the traditional quadrilateral element in solid mechanics problems. This method is also employed for other types of problems, such as vibration analysis [13] and plate and shell analysis [14,15]. However, such method cannot reduce the computation cost compared with the traditional quadrilateral finite element.

Cui et al. [16] proposed another way to avoid the numerical integration technique. The quadrilateral elements were subdivided into sub-triangles and only one integration point is needed in construction the finite element matrices. The decomposed quadrilateral element was used to obtain solutions for statics and free vibration problems. The element provided high solution accuracy and required lower computation cost than the conventional quadrilateral isoparametric element. However, such a method has not yet been used for solving heat transfer problems. Therefore, in this research, the decomposed quadrilateral element is presented to analyze two-dimensional heat transfer problems. The corresponding finite element equations are derived and presented. Some numerical examples in heat transfer problems are used to validate the proposed element. Such solutions are also compared with the exact solution.

2. Governing equations

For two-dimensional heat transfer analysis in the x-y coordinate system, the governing differential equation for steady-state conduction heat transfer is,

$$\frac{\partial}{\partial x}\left(k_x \frac{\partial T}{\partial x}\right)+\left(k_y \frac{\partial T}{\partial y}\right)+Q=0 \tag{1}$$

where T represents the temperature, Q is the internal heat generation, k_x and k_y are the thermal conductivity coefficients in x and y directions.

The boundary conditions may consist of specified temperature (T_s), specified surface heating (q_s), specified surface convection or surface radiation along the edges.

3. Finite element equation

The finite element formulation of the decomposed quadrilateral element for heat transfer problem will be presented in this section. First, the problem domain in the analysis is discretized into a set of quadrilateral elements. Then each quadrilateral element is further subdivided into four sub-triangles (Δ1, Δ2, Δ3 and Δ4) as shown in Fig.1. The coordinate of central point (x_c,y_c) can be given as,

$$x_c=\frac{1}{4}\left(x_1+x_2+x_3+x_4\right) \tag{2}$$

$$y_c=\frac{1}{4}\left(y_1+y_2+y_3+y_4\right) \tag{3}$$

And the temperature at central point can also be defined as,

$$T_c = \frac{1}{4}\left(T_1 + T_2 + T_3 + T_4\right) \tag{4}$$

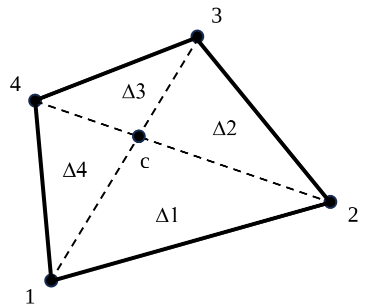

Figure 1. A quadrilateral element that is divided into four sub-triangles.

For each sub-triangular element, the temperature distribution can be defined with linear interpolation function for triangular element [17]. For example, in sub-triangular element Δ1, the temperature field can be written as,

$$T_{\Delta 1} = N_1 T_1 + N_2 T_2 + N_3 T_c \tag{5}$$

where N_i is the conventional linear interpolation function of triangular element which is,

$$N_i = \frac{1}{2A_{\Delta 1}}\left(a_i + b_i x + c_i y\right) \tag{6}$$

and

$$a_i = x_j y_k - x_k y_j\,; \quad b_i = y_j - y_k\,; \quad c_i = x_k - x_j \tag{7}$$

where i, j, k are cyclic permutation of 1, 2, c (corresponding to the node number of triangle) and $A_{\Delta 1}$ is the area of triangle Δ1 which can be calculated by,

$$A_{\Delta 1} = \frac{1}{2}\left[x_2\left(y_c - y_1\right) + x_1\left(y_2 - y_c\right) + x_c\left(y_1 - y_2\right)\right] \tag{8}$$

The temperature field of other sub-triangular elements by changing the cyclic permutation to 2, 3, c; 3, 4, c and 4, 1, c, respectively. The temperature field of the quadrilateral element can be obtained by weighted average of the temperature field from sub-triangles as,

$$T = \left(\frac{A_{\Delta 1}}{A}\right)T_{\Delta 1} + \left(\frac{A_{\Delta 2}}{A}\right)T_{\Delta 2} + \left(\frac{A_{\Delta 3}}{A}\right)T_{\Delta 3} + \left(\frac{A_{\Delta 4}}{A}\right)T_{\Delta 4} \tag{9}$$

where A is the total area of quadrilateral element. This leads to

$$T = N_1^* T_1 + N_2^* T_2 + N_3^* T_3 + N_4^* T_4 \tag{10}$$

where $N_1^*, N_2^*, N_3^*, N_4^*$ are interpolation functions of the decomposed quadrilateral element which are,

$$N_1^* = \left(\frac{A_{\Delta 1}}{A}\right)\left(N_1 + \frac{1}{4}N_3\right)_{\Delta 1} + \left(\frac{A_{\Delta 2}}{A}\right)\left(\frac{1}{4}N_3\right)_{\Delta 2} + \left(\frac{A_{\Delta 3}}{A}\right)\left(\frac{1}{4}N_3\right)_{\Delta 3} + \left(\frac{A_{\Delta 4}}{A}\right)\left(N_2 + \frac{1}{4}N_3\right)_{\Delta 4} \tag{11}$$

$$N_2^* = \left(\frac{A_{\Delta 1}}{A}\right)\left(N_2 + \frac{1}{4}N_3\right)_{\Delta 1} + \left(\frac{A_{\Delta 2}}{A}\right)\left(N_1 + \frac{1}{4}N_3\right)_{\Delta 2} + \left(\frac{A_{\Delta 3}}{A}\right)\left(\frac{1}{4}N_3\right)_{\Delta 3} + \left(\frac{A_{\Delta 4}}{A}\right)\left(\frac{1}{4}N_3\right)_{\Delta 4} \quad (12)$$

$$N_3^* = \left(\frac{A_{\Delta 1}}{A}\right)\left(\frac{1}{4}N_3\right)_{\Delta 1} + \left(\frac{A_{\Delta 2}}{A}\right)\left(N_2 + \frac{1}{4}N_3\right)_{\Delta 2} + \left(\frac{A_{\Delta 3}}{A}\right)\left(N_1 + \frac{1}{4}N_3\right)_{\Delta 3} + \left(\frac{A_{\Delta 4}}{A}\right)\left(\frac{1}{4}N_3\right)_{\Delta 4} \quad (13)$$

$$N_4^* = \left(\frac{A_{\Delta 1}}{A}\right)\left(\frac{1}{4}N_3\right)_{\Delta 1} + \left(\frac{A_{\Delta 2}}{A}\right)\left(\frac{1}{4}N_3\right)_{\Delta 2} + \left(\frac{A_{\Delta 3}}{A}\right)\left(N_2 + \frac{1}{4}N_3\right)_{\Delta 3} + \left(\frac{A_{\Delta 4}}{A}\right)\left(N_1 + \frac{1}{4}N_3\right)_{\Delta 4} \quad (14)$$

Temperature gradient of the quadrilateral element can be written as,

$$\begin{Bmatrix} \dfrac{\partial T}{\partial x} \\ \dfrac{\partial T}{\partial y} \end{Bmatrix} = \begin{bmatrix} \dfrac{\partial N_1^*}{\partial x} & \dfrac{\partial N_2^*}{\partial x} & \dfrac{\partial N_3^*}{\partial x} & \dfrac{\partial N_4^*}{\partial x} \\ \dfrac{\partial N_1^*}{\partial y} & \dfrac{\partial N_2^*}{\partial y} & \dfrac{\partial N_3^*}{\partial y} & \dfrac{\partial N_4^*}{\partial y} \end{bmatrix} \begin{Bmatrix} T_1 \\ T_2 \\ T_3 \\ T_4 \end{Bmatrix} = [B] \begin{Bmatrix} T_1 \\ T_2 \\ T_3 \\ T_4 \end{Bmatrix} \quad (15)$$

where each term in [B] can be derived as,

$$B_{11} = \frac{1}{8A}\left[\left(4b_1 + b_3\right)_{\Delta 1} + \left(b_3\right)_{\Delta 2} + \left(b_3\right)_{\Delta 3} + \left(4b_2 + b_3\right)_{\Delta 4}\right] \quad (16)$$

$$B_{12} = \frac{1}{8A}\left[\left(4b_2 + b_3\right)_{\Delta 1} + \left(4b_1 + b_3\right)_{\Delta 2} + \left(b_3\right)_{\Delta 3} + \left(b_3\right)_{\Delta 4}\right] \quad (17)$$

$$B_{13} = \frac{1}{8A}\left[\left(b_3\right)_{\Delta 1} + \left(4b_2 + b_3\right)_{\Delta 2} + \left(4b_1 + b_3\right)_{\Delta 3} + \left(b_3\right)_{\Delta 4}\right] \quad (18)$$

$$B_{14} = \frac{1}{8A}\left[\left(b_3\right)_{\Delta 1} + \left(b_3\right)_{\Delta 2} + \left(4b_2 + b_3\right)_{\Delta 3} + \left(4b_1 + b_3\right)_{\Delta 4}\right] \quad (19)$$

$$B_{21} = \frac{1}{8A}\left[\left(4c_1 + c_3\right)_{\Delta 1} + \left(c_3\right)_{\Delta 2} + \left(c_3\right)_{\Delta 3} + \left(4c_2 + c_3\right)_{\Delta 4}\right] \quad (20)$$

$$B_{22} = \frac{1}{8A}\left[\left(4c_2 + b_3\right)_{\Delta 1} + \left(4c_1 + c_3\right)_{\Delta 2} + \left(c_3\right)_{\Delta 3} + \left(c_3\right)_{\Delta 4}\right] \quad (21)$$

$$B_{23} = \frac{1}{8A}\left[\left(c_3\right)_{\Delta 1} + \left(4c_2 + c_3\right)_{\Delta 2} + \left(4c_1 + c_3\right)_{\Delta 3} + \left(c_3\right)_{\Delta 4}\right] \quad (22)$$

$$B_{24} = \frac{1}{8A}\left[\left(c_3\right)_{\Delta 1} + \left(c_3\right)_{\Delta 2} + \left(4c_2 + c_3\right)_{\Delta 3} + \left(4c_1 + c_3\right)_{\Delta 4}\right] \quad (23)$$

The typical conduction stiffness finite element matrix is given by [1],

$$K_c^{ij} = \int_\Omega \left(k_x \frac{\partial N_i}{\partial x}\frac{\partial N_j}{\partial x} + k_y \frac{\partial N_i}{\partial y}\frac{\partial N_j}{\partial y} \right) d\Omega \quad (24)$$

For isotropic conduction coefficient material, the conduction stiffness finite element matrix can be integrated directly and leads to closed form of conduction stiffness matrix as,

$$\left[K_c\right] = ktA\left[B\right]^T\left[B\right] \quad (25)$$

4. Results and discussion

Two examples are presented to evaluate the performance of the decomposed quadrilateral element for heat transfer analysis. These problems consist of: (1) rectangular plate with specified temperatures along four edges, (2) rectangular plate with specified temperatures and insulated along the edges. Such solutions are also compared with the exact solutions.

4.1. Rectangular plate with specified temperatures along four edges

A 2m x1m rectangular plate has the thermal conductivity coefficient of k = 1 w/m-°C. The thickness of the plate is 0.1 m. The plate has specified temperatures along the four edges as shown in Fig.2. The exact solution of the temperature distribution is given in Ref. [1] as,

$$T(x,y) = \frac{\sin(\pi x/2)\sinh(\pi y/2)}{\sinh(\pi/2)} \tag{26}$$

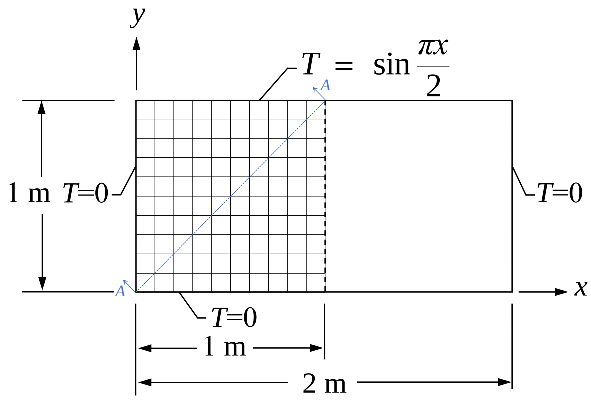

Figure 2. Rectangular plate with specified edge temperatures.

Due to its symmetry, only half left of the plate in Fig.2 is modeled and analyzed. The model is discretized into uniform square meshes of 4x4, 8x8 and 10×10 intervals (25, 81 and 121 nodes). From the problem statement, the plate tends to have highest temperature at top edge center of the plate. The temperature along the diagonal line of the model (line A-A) that is obtained from the proposed method will be compared with the exact solution as shown in Fig. 3. The results obtained from the decomposed quadrilateral element converge to the exact solution as the meshes are refined. Figure 4 shows the temperature contour of the results from mesh 10×10. It can be seen that the results obtained from the decomposed quadrilateral element closely match the exact solution.

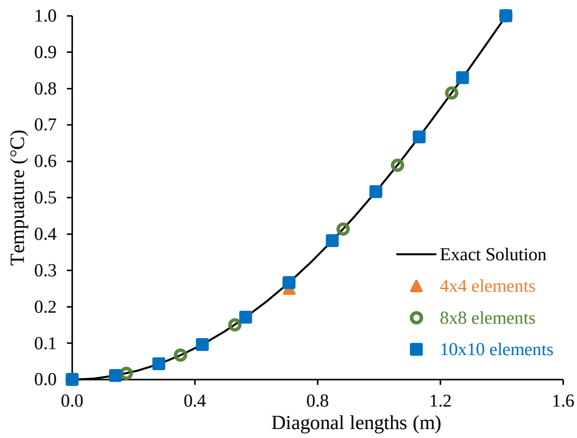

Figure 3. Comparative temperature along the diagonal line.

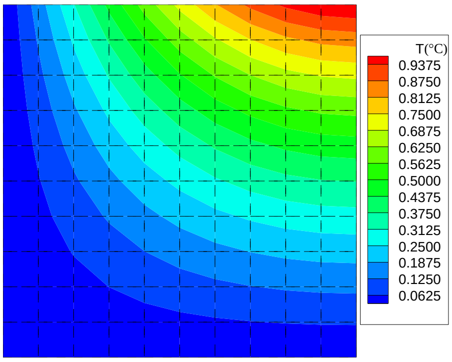

Figure 4. Temperature contour obtained from 10x10 elements.

4.2. Rectangular plate with specified temperatures and insulated along the edges

A 4m x4m rectangular plate has the thermal conductivity coefficient of k = 1 w/m-°C. The thickness of the plate is 0.1 m. The plate has specified temperatures set to be insulated along some edges as shown in Fig.5. The exact solution of the temperature distribution is given in Ref. [1] as,

$$T(x,y) = \frac{\cosh(\pi y/4)\cos(\pi x/4)}{\cosh(\pi/4)} \tag{27}$$

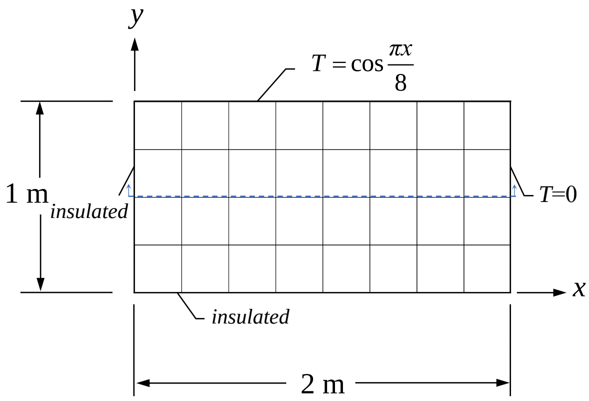

Figure 5. Rectangular plate with specified temperatures and insulated edges.

The problem domain is discretized into uniform meshes of 4x2 and 8x4 intervals (15 and 45 nodes). Figure 6 shows the temperature contour of the results from mesh 8x4. The temperature along the center line (dash line at y=0.5) of the model from the proposed method will be compared with the exact solution as shown in Fig. 7. The results obtained from the decomposed quadrilateral element converge to the exact solution as the meshes are refined. It is obvious that the results obtained from the decomposed quadrilateral element really correspond to the exact solution.

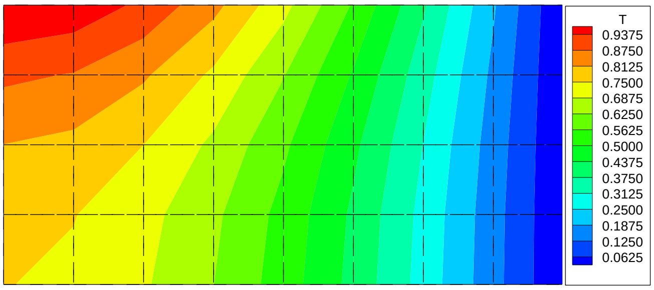

Figure 6. Temperature contour obtained from 8x4 elements.

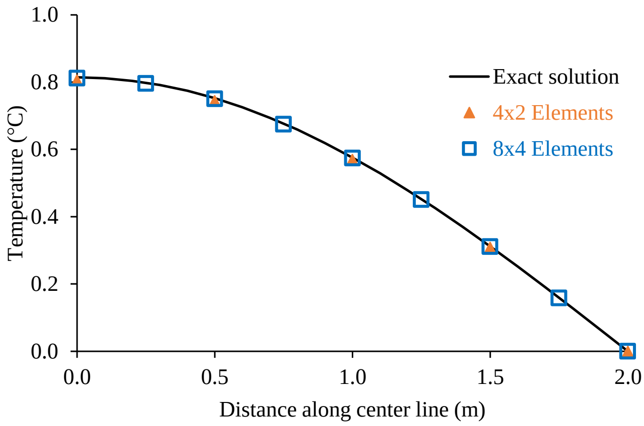

Figure 7. Comparative temperature along the center line.

5. Conclusion

The decomposed quadrilateral element for analyzing two-dimensional heat transfer problems by using finite element method was presented. The corresponding closed form of finite element formulation was derived and presented herein without using numerical integration. While the conventional isoparametric quadrilateral element needed four-point numerical integration and isoparametric coordinate transformation. The proposed method was preliminary evaluated by analyzing some heat transfer problems of which exact solution can be found. The results showed that the decomposed quadrilateral element provided good solution accuracy and converged to the exact solution as the meshes are refined. It is obvious that the results obtained from the decomposed quadrilateral element assuredly correspond to the exact solution. Further research should investigate more complex heat transfer problems and delve into the impact of mesh distortion.

6. References

[1] Dechaumphai, P. (2010). *Finite Element Method: Fundamentals and Applications*. Alpha Science International.

[2] Dechaumphai, P. (1995). Adaptive Finite Element Technique for Heat Transfer Problems. *Journal of Energy, Heat and Mass Transfer*, 17(1), 87–94.

[3] Zienkiewicz, O.C., & Taylor, R.L. (2000). *The Finite Element Method*. Oxford: Butterworth Heinemann, 5th ed.

[4] Liu, G.R., & Quek, S.S. (2003). *The Finite Element Method: A Practical Course.* Oxford: Butterworth Heinemann.

[5] Malkus, D.S., & Hughes, T.J.R. (1978). Mixed finite element methods-reduced and selective integration techniques: A unification of concepts. *Computer Methods in Applied Mechanics and Engineering*, 15(1), 63–81.

[6] Liu, W.K., & Belytschko, T. (1984). Efficient linear and nonlinear heat conduction with a quadrilateral element, *International Journal for Numerical Methods in Engineering*, 20(5), 931–948.

[7] Belytschko, T., & Bachrach, W.E. (1986). Efficient implementation of quadrilaterals with high coarse-mesh accuracy, *Computer Methods in Applied Mechanics and Engineering*, 54(3), 279–301.

[8] Koh, B.C., & Kikuchi, N. (1987). New improved hourglass control for bilinear and trilinear elements in anisotropic linear elasticity., *Computer Methods in Applied Mechanics and Engineering*, 65(1), 1–46.

[9] Belytschko, T., & Bindeman, L.P. (1991). Assumed strain stabilization of the 4-node quadrilateral with 1-point quadrature for nonlinear problems, *Computer Methods in Applied Mechanics and Engineering*, 88(3), 311–340.

[10] Liu, G.R., Dai, K.Y., & Nguyen, T.T. (2007). A smoothed finite element method for mechanics problems. *Computational Mechanics*, 39(6), 859–877.

[11] Dai, K.Y., Liu, G.R., & Nguyen, T.T. (2007). An n-sided polygonal smoothed finite element method (nSFEM) for solid mechanics. *Finite Elements in Analysis and Design*, 43(11-12), 847–860.

[12] Chen, J.S., Wu, C.T., Yoon, S., & You, Y. (2001). A stabilized conforming nodal integration for Galerkin mesh-free methods. *International Journal for Numerical Methods in Engineering*, 50(20), 435–466.

[13] Dai, K.Y., & Liu, G.R. (2007). Free and forced vibration analysis using the smoothed finite element method. *Journal of Sound and Vibration*, 301(3-5), 803–820.

[14] Nguyen-Xuan, H., Rabczuk, T., Bordas, S., & Debongnie, J.F. (2008). A smoothed finite element method for plate analysis. *Computer Methods in Applied Mechanics and Engineering*, 197(13-16), 1184–1203.

[15] Nguyen-Thanh, N., Rabczuk, T., Nguyen-Xuan, H., & Bordas, S.P.A. (2008). A smoothed finite element method for shell analysis. *Computer Methods in Applied Mechanics and Engineering*, 2008, 198(2), 165–177.

[16] Cui, X.Y., Liu, P.W., & Li, G.Y. (2015). An element decomposition method with variance strain stabilization. *Science China Physics, Mechanics & Astronomy*, 58 (7), 1–10.

[17] Logan, D.L. (2015). *A First Course in the Finite Element Method*. Cengage Learning, sixth edition.

CST0008

Preventive Work and Health Monitoring for Technology by Cracks of Concrete Surface Using IR Camera and Resin Sensor

N Shimoi[1,*], Y Yamauchi[1], K Nakasho[2], and C Cuadra[1]

[1]Faculty of Systems Science and Technology, Akita Prefectural University, Yurihonjo, 015-0055, Japan

[2]Graduate School of Sciences & Technology for Innovation, Yamaguchi University, Ube,755-8611, Japan

* Corresponding Author: shimoi@akita-pu.ac.jp

Abstract. Safety inspections of infrastructure rely on visual inspections and hammering inspections by inspectors. However, there is a problem that inspection results vary because of differences in the technical level of inspectors. In order to solve these problems, we propose an inspection method and preventive work using coating type resin sensor and an infrared camera. The non-destructive evaluation technique by thermography is increasingly being used as a tool for the maintenance of concrete structures. In most applications, the evaluation of only the location and shape of defects on planes is expected, therefore, no method has been developed for evaluating the depth of defects. After the application of infrared reactive resin, the target area, and thermos graphics are taken sequentially. Then, analyses the temperature curves obtained at each pixel during cooling defect states in different parts of the temperature distribution by Fourier transform. This particular temperature change is related to the size of the defect. Approximately 10% of aluminium powder is mixed in the applied gel resin, and this aluminium powder has the property of concentrating due to its specific gravity in areas damaged by compression failure or floating. In this paper, we report on the technology related to the identification and size measurement of defects in infrared reactive resin, and the effect of preventive work to prevent the scattering and collapse of defects caused by destruction.

Keywords: Infrared thermography, Non-destructive inspection, Spalling prediction, Reinforcement.

1. Introduction

In Japan, many infrastructurally important structures such as bridges and tunnels have been produced for more than 50 years [1]. However, in real life, bridges that have already reached the end of their useful life must continue to be used. It therefore becomes necessary to detect dangerous conditions such as the collapse of these structures as soon as possible. It is important to monitor deterioration and structural changes constantly over the long term, because those changes play a major role in building a safe and secure society. Realizing such monitoring can be supported by the study of measurement and evaluation methods after fully understanding the usage environment, such as the characteristics of the structure to be measured and its years of use. In 20 years, 65% of bridges and 45% of tunnels are expected to be over 50 years old. Monitoring technology to check the soundness of structures is very important to constantly monitor deterioration and structural changes under long-term monitoring. I think that it plays an important role in constructing the system. In the past, safety inspections of infrastructure structures were targeted within 50 years after construction, when safety was guaranteed. The development of new monitoring technology is urgently required. In order to realize such soundness monitoring, it is desirable to fully understand the characteristics of the structure to be measured and the usage environment such as the number of years of use, and then consider the measurement method and evaluation method before implementing it. In order to reliably maintain the soundness of infrastructure structures, it is necessary to accurately evaluate the state of structures by judging the presence, frequency, and location of damage from survey and inspection data. Specifically, we will quantify empirical evaluation methods such as "visual inspection" and "hammering inspection" and further improve the efficiency of "non-destructive inspection" such as X-ray inspection and magnetic flaw detection (standardization and cost reduction, etc.) and high performance (improvement of accuracy, automatic data judgment, etc.) are important [2] .

Therefore, the authors have developed a method that can measure the soundness of concrete piers of bridges, inner walls of tunnels, tiled walls of high-rise buildings, etc. in a simple, long-term, inexpensive manner, such as concrete cracks, defects, and wall floats. A technical method was examined. As a result, it was thought that the problem could be solved by using the original infrared reactive resin and image analysis technology that enables passive measurement with a long-wave infrared camera. This technology is mainly based on active measurement such as heating and pre-cooling due to the temperature change of the measurement object, which is usually measured by an infrared camera. In order to enable passive measurement at room temperature, we mixed aluminium powder into the gel resin and applied it to the concrete to be treated. When a crack occurs on the concrete wall surface shown in Figure 1 (a) or a float shown in Figure 1 (b) occurs, the aluminium powder in the gel resin flows and concentrates on the defect. Therefore, when the wall is heat-retained by sunlight, the missing part is emphasized by the temperature difference between the infrared radiation and the atmosphere. In addition, even if there is no heat radiation from the sunlight from the wall surface, it is possible to detect defects, etc. from the temperature difference between the wall surface and the wall surface due to the radiative cooling effect from the aluminium powder in the gel resin due to the difference in materials. It was confirmed that, in addition, the coated gel resin for this measurement has a repair effect because it flows into cracks and defects due to the difference in specific gravity between resin and metal. Therefore, this measurement method is considered to be a measurement technology that serves both as a measure of defects in concrete walls and as a preventive measure. It has been reported that rainwater that flows into the concrete structure from the defective part flows into the room and causes rain leakage, accelerating deterioration [3].

(a) (b)

Figure 1. The concrete flaking occurs and cracks in concrete surface.

2. Preventive work and measurement technology using infrared reactive coating type resin sensor

In recent years, it has been used to measure “float” and “surface cracks” related to reinforcing steel corrosion in concrete using an external camera. However, the radiant energy of infrared rays is proportional to the temperature. An infrared camera detects the infrared energy and converts it into a pseudo-temperature image. The detection wavelength of infrared rays is thought to be around the middle infrared wavelength. It is expected that the density of heat energy will increase as it decreases.

2.1. Comparison with Conventional Technology

Various methods are used for quantitative evaluation of soundness for the purpose of disaster prevention and mitigation of structures. As a sensor system for measuring displacement and vibration due to static load, there is a method of measuring displacement using a laser displacement meter or a contact-type displacement meter, and a method of measuring natural vibration with a micro vibration meter and analysing the fracture state and stress concentration by FEM analyses. There are methods to identify locations [4,5]. In addition, X-ray analysis using FEM is useful as a non-destructive and quantitative evaluation method for residual stress in structures, but it is difficult to analysed crack growth with this method. Among these methods, microtremor vibration measurement obtains the Fourier spectrum ratio of vertical and horizontal motion components, normalizes the horizontal vibration to the vertical vibration, and determines the amplification characteristics and natural period of the structure. There are other methods to obtain it. The measurement system consists of a microtremor meter, a data logger, and a PC. The laser doppler velocimeter (LDV) method [6] detects the velocity from the phase difference due to the doppler effect between the irradiated light and the reflected light when the object is irradiated with laser light. This measurement system consists of two LDV devices, a data logger, a PC, and a digital displacement gauge, and costs about 4.5 to 6 million yen per measurement unit. In addition, X-ray non-destructive equipment can be installed for monitoring limited areas, but it is not practical for long-term measurement because it requires equipment costs of about 8 to 10 million yen and power supply. On the other hand, in the wall inspection technology of structures using an infrared camera, the thermography method, which utilizes the temperature difference due to the sunlight on the outer wall of the building, uses the difference in the conductivity of the wall material to measure the difference that occurs in the defective part. There is varies depending on the size, depth and condition of the crack [7]. In addition, we have also developed a technique to study an image filter processing method that emphasizes the damaged area from an infrared thermal image. We are challenged with a statistical establishment method for estimating the probability of damage prediction as an index of the degree of damage in the temperature change [7]. They are a method of extracting a defective part based on the feature amount of a processed image. On the other hand, Nakamura et al. of Kyoto University used infrared thermography to measure specimens at each damage stage in a reinforcement corrosion expansion pressure simulation test for the purpose of quantitatively evaluating the risk of spalling. The degree of risk of spalling is calculated as an index that can evaluate the degree of deterioration without considering the form [9-11]. In order to evaluate the safety and soundness of concrete structures, long-term monitoring of more than 20 years is considered necessary. However, there is a problem that a measuring device that can guarantee the required monitoring period and a smart sensing method that enables danger prediction do not exist at present [12-13]. Table 1 shows the specifications of the infrared camera used in the measurement, and Figure 2 shows the outline drawing of the camera used in the test.

2.2. Issues related to structure monitoring

As a method to measure the deterioration of structures mainly due to secular change, the measurement of “strain” and “deflection”, which accompany the deterioration of structure strength due to corrosion and concrete failure, is considered for soundness evaluation. However, it is difficult to accumulate and evaluate long-term measurement results over a period of 10 to 20 years due to the difficulty of reproducibility due to the passage of time in fixed-point observations, and the accumulation of quantitative observation data due to the influence of atmospheric conditions due to weather conditions. In addition, the effect of “unevenness” due to changes in the temperature around the measurement in the structure, the thermal effect due to uneven thickness of the concrete wall, and the occurrence of erroneous detection due to the adhesion of relics to the surface can be considered. In addition, if the image analysis by the infrared camera is completed and the part evaluated as a defective part is different from the part evaluated as a defective part by the hammering inspection at a later date, the final judgment is made by X-ray image analysis or magnetic inspection. There is also concern about the complexity of even if these test results are accumulated, if a long period of time passes, it is thought that the evaluation method will progress greatly due to improvements in measurement methods and data image analysis software, etc., and there is a possibility that it will be wasted. However, considering the 50-year replacement period of infrastructure structures, we must consider the method and necessity of storing these images as digital data.

Table 1. Specifications of infrared camera specs.

Model	InfRec R450
Detector	Two-dimensional non-cooling method
Measurement temperature range	-40 to 1500 degrees
Measurement wavelength	8 to 14 μm
Number of pixels	480 × 360
Measurement field of view	24 degrees × 18 degrees
Standard lens	10 cm to ∞
Weight	3.8 kg

Figure 2. IR Camera.

2.3. Principle of infrared thermography

Objects that exist at room temperature emit energy by infrared radiation. Planck's law of radiation is expressed in equation (1), which states that all objects emit energy proportional to the fourth power of their absolute temperature. Boltzmann's law is shown in equation (2) [14].

$$E(\lambda b) = \frac{2hc^2}{\lambda^5}\frac{1}{e^{hc/\lambda KT}-1} \qquad 〔\mathrm{W / m^2 \mu m}〕 \tag{1}$$

Eλb : Black body spectral radiant emittance at wavelength λ

c : Speed of light 3×10^{8} (m/sec)

h : Planck's constant (6.6×10^{-27} Js)

K : Boltzmann constant (1.38×10^{-16} J/k)

T : Absolute temperature of blackbody (K)

Λ : Wavelength (m)

$$Wb = \sigma t^4 \qquad 〔\mathrm{W / m^2}〕 \tag{2}$$

Wb : Integrating the wavelength from λ = O to λ = ∞ from Planck's formula

Black body spectral radiance −82

σ : Boltzmann constant (5.7×10 W/m)

t : Absolute temperature of blackbody (K)

$$\lambda_{max} = 2897/T \qquad 〔\mu\mathrm{m}〕 \tag{3}$$

When the measurement target is 40°C (absolute temperature $T = 273 + 40 = 313$ K), wavelength λ is 2897 ÷ 313 = approximately 9.2 μm from equation (3).

2.4. Infrared thermal radiation relational expression

Figure 3 portrays an image acquired using infrared thermal radiation. The infrared rays emitted from the measurement target are propagated by equations (1)- (3). From the principle of the infrared thermography method, when measured with an infrared camera indoors, if no difference exists between the outside temperature in the air and the temperature of the test object, then the heating of the test object must also be considered. We compare changes in the infrared thermal images with and without preheating. Moreover, we measure the effects of applying gel resin under similar conditions [15-17].

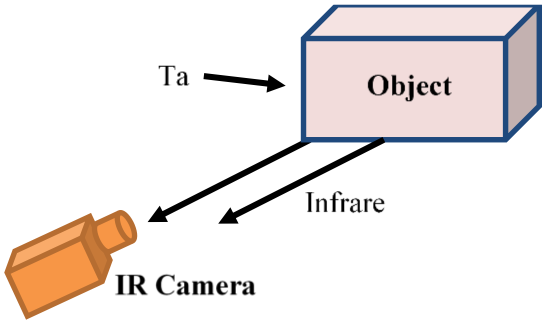

Figure 3. Image acquisition by infrared thermal radiation.

3. Measurement Method and Performance Evaluation of Infrared Reactive Coating Resin

3.1. Image analysis using an infrared reactive coated resin sensor

From the principle of the infrared thermography, when measuring with an infrared camera indoors, if no difference exists between the outside temperature in the atmosphere and the temperature of the test object, then one can forcibly heat the surface, perhaps using a halogen lamp, to heat the interior of the test object. A method of measuring cracks and floats based on the temperature difference between the surface and interior can be used. However, the use of such a method requires that the measurement conditions always be established and implemented under favorable conditions, with due consideration devoted to the influence of the outside air temperature, the measurement target material and color, the spectral reflectance, and the measurement distance. Actual practical measurements are expected to be difficult. Figure 4 portrays the influence of the loading tester of the specimen A and the reinforcement arrangement of the specimen B. A test specimen is prepared using ordinary concrete with a 2 mm cover thickness on this reinforcing bar. For this study, to improve the measurement level considering the problems caused by these thermal image characteristics, specimen A was an RC post with a φ65 hole drilled 235 mm below the center on the left side of the lower part of the specimen A. Specimen B is an RC post with a φ65 hole drilled 235 mm above the center on the right side of the specimen. Hole of φ65 was artificially machined to imitate the defect of a concrete support column. It was conducted to measure the strength effects on the upper and lower parts. However, to ascertain the measurement effects of the infrared camera by resin coating and the result of preventive work in the fracture situation, gel resin (CY52-276; Dow Corning Toray Co. Ltd.) was applied to the entire lower surface of each test specimen A, B, except for the upper 300 mm. A coating film containing 10 % aluminum powder with particles of 10-20 μm was applied to about 0.1 mm thickness. The material properties of this resin include resistance to ultraviolet rays, lack of hardening over time in the coating film, and maintenance of a gel-like property. Moreover, it does not retain water. It takes about 1 hour to harden after mixing No.1 liquid and No.2 liquid equally. The price is 1,000 yen per kilogram.

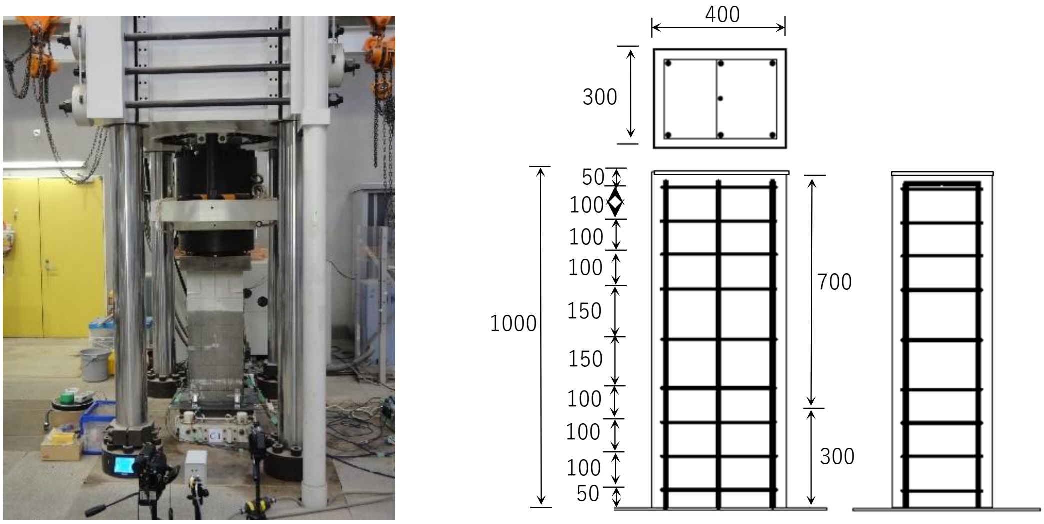

(a) (b)

Figure 4. Experiment of equipment and specimen.

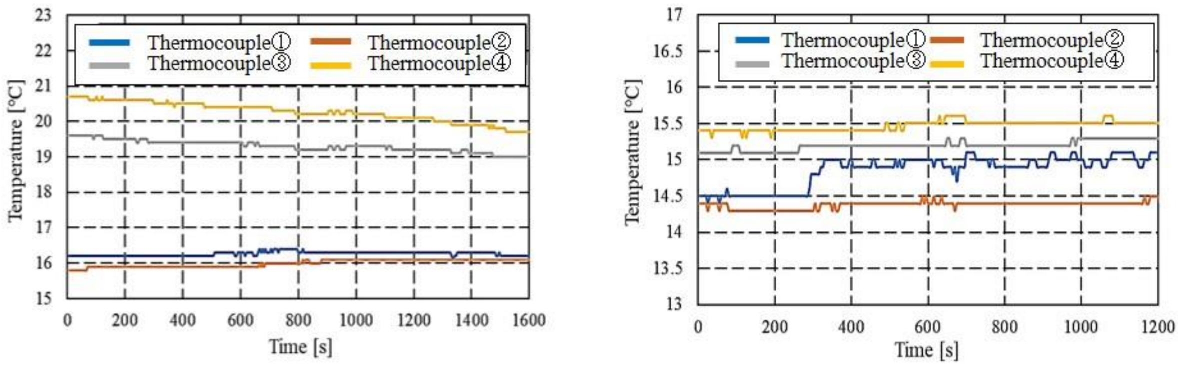

(a) (b)

Figure 5. Relation of temperature difference in specimens A and B to the temperature change of the specimens.

3.2. Infrared imaging using resin coating

3.2.1. Examination of thermal image analysis by passive measurement

To compare the effects of thermal imaging with and without surface overheating, specimen A was heated from the back side for about 20 min using a carbon heater (900 W; Yamazen Corp.). Because the thermal conductivity of concrete is 1.6, about 61.05 times higher than the thermal conductivity of air, which is 0.026, we predicted that the surface temperature would rise after about 30 min. Therefore, after another 30 min had passed, we conducted a destructive test. Figure 5 presents temperature changes of specimens A and B. Panel (a) shows a temperature comparison of specimen A by measurement with overheating. Panel (b) presents the measurement results found for specimen B measured at room temperature (21°C) without overheating by passive measurement. The temperature difference on the surface of the specimen from the start to the end of the test was 4°C for A and 0.6°C for B. Figure 6 portrays details of the position and shape of the through-holes made in specimens A and B.

3.2.2. Construction evaluation of preventive work

On specimens A and B, the gel resin (CY52-276; Dow Corning Toray Co., Ltd.) was applied to the entire lower surface, except for the upper 300 mm at about 0.1 mm thickness. We observed the damage and the state of falling fragments after the destructive testing of the parts coated with this resin and parts not coated with this resin. Figure 7 presents specimen B after completion of the destructive test. Destruction is generated by the shearing force generated obliquely from the right side of the screen and compressive force applied from the top. Particularly, it seems that infrared measurement was able to confirm the effects of suppressing the scattering and collapse of concrete fragments because of compression failure and the "floating" situation indicated by the arrow, which is difficult to detect using a visible light camera. Panel (a) depicts a thermal image of specimen B taken using an infrared camera. Panel (b) portrays an image taken using a visible light camera. In both cases, the elapsed times of force application were equal.

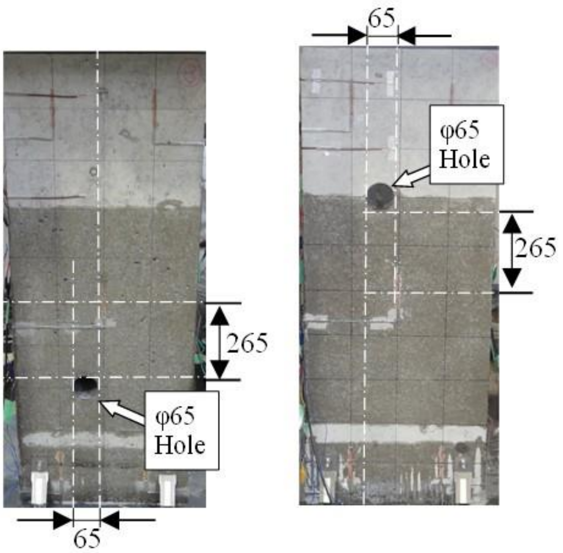

(a) (b)

Figure 6. Specimen A and Specimen B (Size 300 × 400 × 1000 mm).

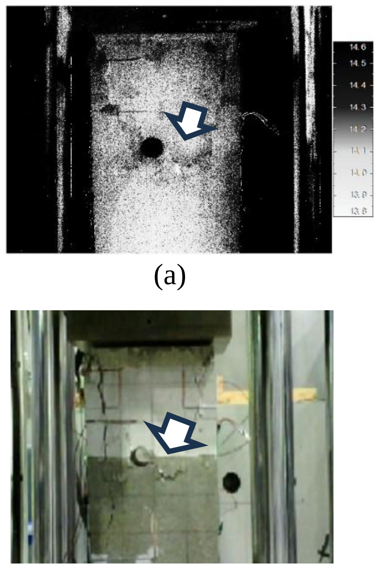

(a)

(b)

Figure 7. Infrared camera image and visible light camera image.

4. Measurement Results and Discussion

Figure 8 presents results obtained from the destructive tests conducted on specimens with upper and lower defects. Panel (a) presents a comparison of (i) an infrared thermal image and (ii) a visible light image at the time of maximum load, (iii) an infrared thermal image and (iv) a visible light image at the end of loading, for the specimen in Figure 6 (a) with preheating. Panel (b) presents a comparison of (i) an infrared thermal image and (ii) a visible light image under the maximum load, and (iii) an infrared thermal image and (iv) a visible light image after the end of the load at room temperature of 21°C without any preheating, for the specimen in Figure 6 (b). Panel (c) shows (i) an infrared thermal image at maximum load and (ii) a visual comparison of the visible light image with the optical image, and (iii) the infrared thermal image at the end of loading.

In panel (a), the test was started 30 min after heating the test piece with a carbon heater for 20 min. As shown in Figure 8, the temperature was measured and recorded (i) at the center 50 mm from the top of the surface, (ii) at the center 250 mm from the top of the surface, (iii) at the center 50 mm from the top of the back, and (iv) at the center 250 mm from the top of the back. The infrared thermal image reproduces a state in which the upper temperature is high and the lower temperature is low. In the visible light image, the state of damage caused by the load applied to the test object is recognized only on the surface, but in the infrared thermal image, the damage state of the surroundings directly affected by the applied force in the deep part is also recognized. Our findings demonstrated the possibility of observing invisible parts in contrast to visible light images. The temperature difference of the specimen was confirmed as matching the theory-based prediction, the residual heat strongly affected the external thermal image of the specimen surface after a certain period of time. In the infrared thermal image, as Table 2 shows, the temperature difference of the specimen is only 0.6°C, but it is recorded in a state that is comparable to the image after heating shown in (a). This finding is attributable to the effects of the resin applied to the specimen surface. The resin has effect of a poultice and maintains the difference between the temperature of the specimen surface and room temperature, making it possible to obtain clear infrared thermal images [18-20].

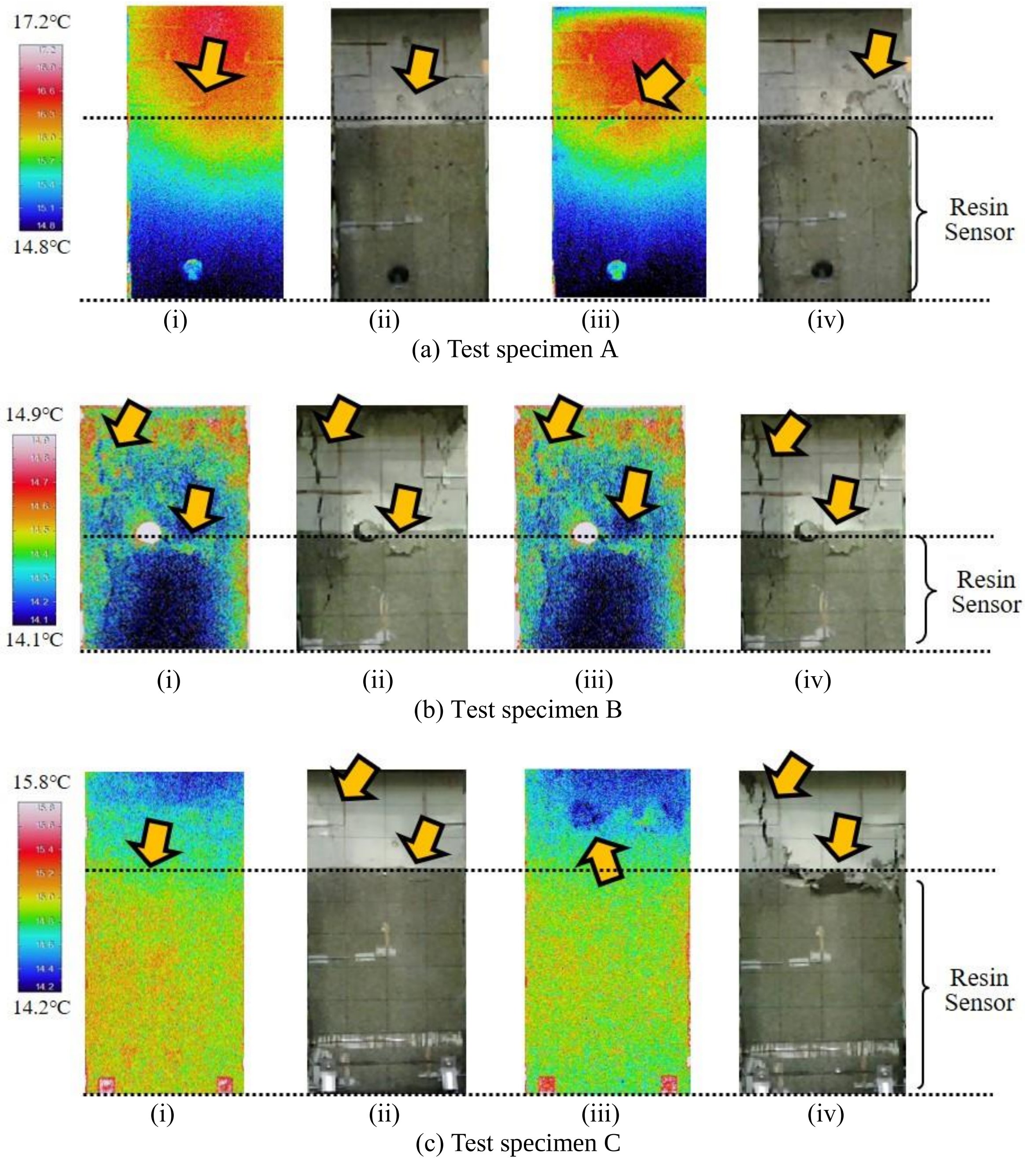

Figure 8. The results of the destructive test on specimens with upper and lower defects and non-defects.

Table 2. Comparison of measurement surface temperature gap by specimens A, B and C.

No.	Test specimen A (°C)	Test specimen B (°C)	Test specimen C (°C)
T1	16.3	14.9	14.5
T2	16.0	14.4	15.0
T3	19.3	15.2	15.2
T4	20.3	15.5	15.3
Temperature gap	4.0	0.6	0.8

5. Conclusion

Using this measurement technology, this study produced the following findings.

1) Improving the resolution of infrared thermal images necessitates increasing the temperature difference from the outside air. We obtained clear thermal images while maintaining a large difference in radiant heat from the fracture site. In this case, it was more effective than measurement by heat generation from the outside.

2) Observing the mechanism by which a shear fracture occurs first in the fracture of the test specimen was not possible because of compression. Left and right bulges occur in the central part because of expansion. It was possible to visualize parts that are invisible to the naked eye.

3) The gel-resin-coated sensor improved thermal image acquisition during passive measurement and yielded results that were suitable for measuring "peeling" and "floating".

4) The resin coating effect can be useful as a construction method to prevent the progress of shearing and peeling at the time of destruction. Moreover, it can prevent falling from the top and collapsing.

5) Application of this resin is thought to prevent rainwater intrusion, metal corrosion, and deterioration.

6) The surface coating effect of this resin was found to be effective at reducing swelling and surface peeling caused by reinforced concrete column deformation during loading.

6. Acknowledgments

This research was partially supported by JSPS Kakenhi Grant No. 20H00290, for which we express our appreciation.

7. References

[1] Ministry of Land, Infrastructure, & Transport. Infrastructure maintenance information. Available from <https://www.mlit.go.jp/sogoseisaku/maintenance/02research/02_01_01.html> (2020). (in Japanese)

[2] Matsuoka, H., Hirose, Y., Kurahashi, T., Murakami, Y., Toyama, S., Ikeda, H., Iyama, T., & Ihara, I. (2018). Application of a joint variable method for high accurate numerical evaluation of defect based on hammering test. *Journal of the Society of Materials Science*, *67*(9), 869-876. (in Japanese).

[3] Ueda, H., Ushijima, S., & Shyutto, K. (2007). Properties and deterioration prediction of acid attacked concrete. *Japan Society of Civil Engineers*, *63*(1), 27-41. (in Japanese).

[4] Tamai, H. (2003). Elasto Plastic Analysis Method for frame with exposed-type column base considering influence of variable axial force. *Journal of Structural and Construction Engineering*, *68*(571), 127-135. (in Japanese).

[5] Shimoi, N., Nishida, T., Obata, A., Nakasho, K., Madokoro, H., & Cuadra, C. (2016). Comparison of displacement measurements in exposed type column base using piezoelectric dynamic sensors and static sensors. *American Journal of Remote Sensing*, *4*(5), 23-32. (in Japanese).

[6] Miyashita, T., Ishii, H., Fujino, Y., Shoji, T., & Seki, M. (2007). Understanding of high-speed train induced local vibration of a railway steel bridge using laser measurement and its effect by train speed. *Japan Society of Civil Engineering A*, *63*(2), 277-296. (in Japanese).

[7] Michimura, K. (2008). Deterioration diagnosis technology by infrared method. *Material Life Society*, *20*(1), 21-26. (in Japanese).

[8] Hayashi, H., Hashimoto, K., & Akashi, Y. (2013). Improving detection accuracy of concrete damage by infrared thermography. *Japan Concrete Institute, 35*(1), 1813-1818. (in Japanese).

[9] Nakamura, M. (2002). Health monitoring of building structures. *Society of Instrument and Control Engineers,*

41(11), 819-824. (in Japanese).
[10] Shimoi, N. (2001). The technology of personal mine detecting for humanitarian demining. *Transactions of the Society of Instrument and Control Engineers, 37*(6), 577-583. (in Japanese).
[11] Ono, K. (2003). Study on technology for extending the life of existing structures, New urban society technology fusion research. *The Second New Urban Social Technology Seminar*, 11-23. (in Japanese).
[12] Biscarini, C., Catapano, I., Cavalagli, N., Ludeno, G., Pepe, F. A., & Ubertini, F. (2020). UAV photogrammetry, infrared thermography and GPR for enhancing structural and material degradation evaluation of the Roman masonry bridge of Ponte Lucano in Italy, NDT and E International, 115, 102287.
[13] Kumagai, K., Nakamura, H., & Kobayashi, H. (1999). Computer aided nondestructive evaluation method of welding residual stresses by removing reinforcement of weld. *Transactions of the Japan Society of Mechanical Engineers, Series A, 65*(629), 133-140. (in Japanese).
[14] Shimizu, K. (1987). The latest technology for far-infrared use. *Industrial Technology Association*, 6-24. (in Japanese)
[15] Maldague, X. (2002). Introduction to NDT by active infrared thermography. *Materials Evaluation*, 1-22.
[16] Xu, Y., Hwang, S., Wang, Q., Kim, D., Luo, C., Yang, J., & Sohn, H. (2020). Laser active thermography for debonding detection in FRP retrofitted concrete structures. *NDT & E International*, 114, 102285.
[17] Xu, J., Wang, H., Duan, Y., He, Y., Chen, S., & Zhang, Z. (2020). Terahertz imaging vibro-thermography for impact response in carbon fiber reinforced plastics. *Infrared Physics & Technology*, *109,* 103413.
[18] Ourinson, D., Emanuel, G., Csordàs, A., Dammaß, G., Müller, H., Sternkiker, C., Clement, F., & Glunz, S. W. (2019). In-Situ Wafer Temperature Measurement During Firing Process via Inline Infrared Thermography. *AIP Conference Proceedings*. 2156, 020013.
[19] Sakagami, T., Mizokami, Y., Shiozawa, D., Fujimoto, T., Izumi, Y., Hanai, T., & Moriyama, A. (2017). Verification of the repair effect for fatigue cracks in members of steel bridges based on thermoelastic stress measurement. *Engineering Fracture Mechanics*, 183, 1-12.
[20] Kohashi, M., Ohta, Y., & Watanabe, T. (1998). Non-thermal Effect of a Ceramics Radiation on a Yeast Glucose-6-phosphate dehydrogenase, *Bioscience, Biotechnology, and Biochemistry, 62*(2), 297-301.

CST0009

Numerical Prediction of Evaporation Time Under Different Air Pressure Conditions by Discrete Phase Model

Pongwarin Charoenkitkaset, Pimphram Setaphram , Mana Saedan, Apiruk Hokpunna, Woradej Manosroi, and Watcharapong Tachajapong*

Department of Mechanical Engineering Faculty of Engineering, Chiang Mai University Chiang Mai, Thailand

* Corresponding Author: watcharapong.t@cmu.ac.th

Abstract. Evaporation processes of water droplets is influenced by many factors such as pressure, temperature, velocity, diameter of droplets, and vapor diffusion coefficient especially, pressure which is an important factor affecting the evaporation time of liquid droplets. The evaporation of liquid droplets has been extensively studied both numerically and experimentally. Numerical simulation provides a cost-effective and reliable tool. Several studies have shown the benefit of using Computational Fluid Dynamics (CFD) is a tool to predict the evaporation processes. In this research, evaporation of water droplets in tubes under different pressure conditions (-1bar, -0.75bar, -0.5bar, -0.25bar, and atmosphere pressure) was studied through CFD simulations using Ansys Fluent software. The computational model is a droplet evaporation simulation by discrete phase model (DPM) and species transport model to examine, the evaporation in the cylindrical tube with a diameter of 0.4 m and a length of 3 m. Water droplets of 20 micron were injected into the tube at different internal pressures to study the effect of pressure on the evaporation time. The simulation results show that there is a clear relationship between pressure and evaporation time of water droplets. The evaporation time of the water droplets in the tube at different pressure conditions (-1bar, -0.75bar, -0.5bar, -0.25bar, and atmosphere pressure) are 0.158s-0.177s, 0.189s-0.192s, 0.202s-0.231s, 0.261s-0.314s, 0.376s-0.436s respectively. It was clear that the evaporation time is shorter at low pressure conditions.

Keywords: Computational Fluid Dynamics (CFD), evaporation of water, droplets, discrete phase model (DPM).

1. Introduction

Study of liquid droplets evaporation processes in flow stream is very important in engineering applications. The liquid droplets evaporation processes have been studied immensely both numerically and experimentally. Especially numerical simulation provides a cost-effective and reliable tool. Several research have shown the usefulness of using Computational Fluid Dynamics (CFD) as a tool to predict the evaporation processes.

According to numerous evaporation processes studies, it was found that there are many factors effecting to evaporation processes in flow stream. The main factors are pressure, temperature, velocity, diameter of droplets, and vapor diffusion coefficient [1]. Pressure was found to be an important factor affecting the evaporation process with less evaporation observed at high pressures [2].

In this study, the computational model for continuous phase flows, 3D steady RANS equations for conservation of mass, momentum and energy were solved in combination with the realizable k-Ɛ turbulence model [3]. Lagrangian trajectory simulations of droplets evaporation was simulated by discrete phase model (DPM) and species transport model. The discrete phase interacts with the continuous phase, and the discrete phase model source terms were updated after each continuous phase iteration. A model was made of the cylindrical tube with a diameter of 0.4 m and a length of 3.0 m. Water droplets evaporation in tube under different pressure conditions (-1bar, -0.75bar, -0.5bar, -0.25bar and atmosphere pressure) were simulated.

2. Numerical Modelling

2.1. Governing Equations

The CFD model used in this study is 3D using the Lagrangian-Eulerian approach. Air with water droplets was considered incompressible, steady flow in which the realizable k–Ɛ turbulence model is capable to simulate. In the Lagrangian-Eulerian approach, the continuity and momentum equations are solved in the standard form as follow.

2.1.1. Continuity Equations

$$\frac{\partial \rho}{\partial t} + \nabla.(\rho \vec{v}) = S_m \tag{1}$$

Equation (1) is the general form of the continuity equation and is valid for incompressible flow. The source (S_m) is the mass added to the continuous phase (due to vaporization of water droplets). For an incompressible fluid, the density (ρ) is constant.

$$\frac{\partial u}{\partial x} + \frac{\partial v}{\partial y} + \frac{\partial w}{\partial z} = S_m$$

2.1.2. Momentum Equations

$$\frac{\partial}{\partial t}(\rho \vec{v}) + \nabla.(\rho \vec{v}\vec{v}) = -\nabla p + \rho \vec{g} + \vec{F} \tag{2}$$

Where p is static pressure, $\rho \vec{g}$ and $\vec{F}$ are the gravitational body force and external body force (that arise from interaction with the dispersed phase) respectively.

2.1.3. Energy Equations

$$\frac{\partial}{\partial t}(\rho E) + \nabla.\big(\vec{v}(\rho E + p)\big) = -\nabla.\left(\sum_j h_j J_j\right) + S_h \tag{3}$$

2.1.4. Species Transport Equations

$$\frac{\partial}{\partial t}(\rho Y_i) + \nabla.(\rho \vec{v} Y_i) = -\nabla.\vec{J}_i + R_i + S_i \tag{4}$$

The source terms (S_m, F, S_h, and S_i) are used to include the contributions of the water droplet evaporating species, water droplet forces, and evaporation energy from the dispersed phase (water droplets). During evaporation, water droplets diffuse and convect into the surrounding air through the species transport equation.

2.1.5. Discrete Phase Model (Water Droplets)

Discrete Phase Model (DPM) exchange mass, momentum, energy, species with the continuous phase and can be solved by Navier-Stokes equations. Lagrangian trajectory simulations are performed for the discrete phase. The discrete phase interacts with the continuous phase, and the discrete phase model source terms are updated after each continuous phase iteration. To solve the equations of motion for the droplets, the droplets are tracked by Lagrangian method by applying Newton's 2nd Law with the following equation of motion (Eq.5).

This occurs when the discrete phase, even with a large mass, has a much smaller volume (less than 10%) than the continuous phase. After each iteration of the continuous phase calculations, the particle paths are calculated and determined separately.

$$m_p \frac{dV_p}{dt} = \sum F = F_D + F_g + F_{th} + F_s \tag{5}$$

where m_p is the water droplet mass, and v_p is the water droplet velocity vector. The right-hand side is the combined force acting on the water droplets, including drag force (F_D) gravity and buoyancy force (F_g) Saffman lift force (F_s) and thermophoretic force (F_{th}) (for more details see [4]).

The droplet temperature change depends on convection, evaporation, and radiation .The energy equation for water droplets is as follow.

$$m_p c_p \frac{dT}{dt} = \pi d^2 h(T_\infty - T) + \frac{dm_p}{dt} h_{fg} + Radiation \tag{6}$$

where h_{fg} is the latent heat .The radiation heat transfer term can be reasonably neglected because the range of temperatures is low in this study.

The convective heat transfer coefficient (h) can be obtained with an empirical correlation [6-7] as shown in Equation (7)

$$Nu_d = \frac{hd}{\lambda} = 2.0 + 0.6 Re_p^{0.5} Pr^{0.33} \tag{7}$$

where Nu is the Nusselt number, and Pr is the Prandtl number.

The evaporated mass is calculated by two modes i.e., evaporating and boiling. The evaporated mass change rate or vaporization rate is affected by the relative humidity in the air shown in Equation (8) which is controlled by the concentration difference between droplet surface and the air stream.

$$-\frac{dm_P}{dt} = \pi d^2 k_c (C_s - C_\infty) \tag{8}$$

where k_c is the mass transfer coefficient and C_s is the vapor concentration at the droplet surface, which is evaluated by assuming that the flow over the surface is saturated. $C\infty$ is the vapor concentration of the bulk flow, which is obtained by solving the transport equation in the computational cell. The value of kc can be given from a correlation similar to Equation (7) as follows:

$$Sh_d = \frac{k_c d}{D} = 2.0 + 0.6 Re_p^{0.5} Sc^{0.33} \tag{9}$$

where Sh is the Sherwood number, Sc is the Schmidt number (defined as ν/D), and D is the mass diffusion coefficient of the water vapor in the bulk flow.

When the droplet temperature reaches the boiling point, the following equation can be used to evaluate its evaporation rate.

$$-\frac{dm_P}{dt} = \pi d^2 \left(\frac{\lambda}{d}\right)(2.0 + 0.46 Re_d^{0.5}) + ln\big(1 + C_p(T_\infty - T)/h_{fg}\big)/C_p \tag{10}$$

where λ is the gas/air heat conductivity and cp is the specific heat of the bulk flow. Theoretically, evaporation processes can occur at two stages:

(Stage1) when the temperature is higher than the saturation temperature (based on local water vapor concentration), water evaporates according to Equation (8), and the evaporation is controlled by the water vapor partial pressure until 100% relative humidity is achieved;

(Stage2) when the boiling temperature (determined by the air-water mixture pressure) is reached, water continues to evaporate according to Equation (10). After the droplet evaporates due to either high temperature or low moisture partial pressure, the water vapor is transported away due to convection and diffusion as described in the water vapor species transport (Eq. 4).

2.1.6. Turbulence model

The realizable k-Ɛ turbulence model was used for simulating Particle-Laden Flows in this study. Initial studies have shown that the realizable model provides the best performance of all the k-Ɛ model versions for several validations of Particle-Laden Flows [9]. The realizable k-Ɛ turbulence model is a two-equation model based on the Boussinesq assumption, with transport equations for turbulent kinetic energy k and its dissipation rate Ɛ[5]. It predicts the spreading rate of both plane and round jets accurately. It is also likely to provide superior performance for flows involving rotation, boundary layers under strong adverse pressure gradients, separation and recirculation [6].

The effects of the turbulence models (standard k- Ɛ model, RNG k−Ɛ model, realizable k-Ɛ model, standard k-ω models, Reynolds stress model) on the results of evaporative cooling were studied. With water spraying [7], it was found that no turbulence model was considered superior to other models. However, realizable k-Ɛ model was used as the main model for analyzing the results because it was more suitable for further development by improving the constants used in the k and ε equations.

The modeled transport equations for k and Ɛ in the realizable k−Ɛ model are

$$\frac{\partial}{\partial t}(\rho k)+\frac{\partial}{\partial t}(\rho k u_j)=\frac{\partial}{\partial x_j}\left[\left(\mu+\frac{\mu_t}{\sigma_k}\right)\frac{\partial k}{\partial x_j}\right]+G_k+G_b-\rho\mathcal{E}-Y_M+S_k \tag{11}$$

and

$$\frac{\partial}{\partial t}(\rho\mathcal{E})+\frac{\partial}{\partial x_j}(\rho\mathcal{E}u_j)=\frac{\partial}{\partial x_j}\left[\left(\mu+\frac{\mu_t}{\sigma_{\mathcal{E}}}\right)\frac{\partial k}{\partial x_j}\right]+\rho C_1 S_{\mathcal{E}}-\rho C_2\frac{\mathcal{E}^2}{k+\sqrt{\nu\mathcal{E}}}+C_{1\mathcal{E}}\frac{\mathcal{E}}{k}C_{3\mathcal{E}}G_b+S_{\mathcal{E}} \tag{12}$$

where

$$C_1=\max\left[0.43\frac{\eta}{\eta+5}\right],\qquad \eta=S\frac{k}{\mathcal{E}},\qquad S=\sqrt{2S_{ij}S_{ij}}$$

The eddy viscosity is computed from

$$\mu_t=\rho C_\mu\frac{k^2}{\mathcal{E}} \tag{13}$$

C_μ is computed from

$$C_\mu=\frac{1}{A_0+A_s\frac{kU^*}{\mathcal{E}}} \tag{14}$$

where

$$U^*=\sqrt{S_{ij}S_{ij}+\tilde{\Omega}_{ij}\tilde{\Omega}_{ij}} \tag{15}$$

and

$$\tilde{\Omega}_{ij}=\Omega_{ij}-2\mathcal{E}_{ijk}\omega_k$$

$$\Omega_{ij}=\overline{\Omega_{ij}}-\mathcal{E}_{ijk}\omega_k$$

where $\overline{\Omega_{ij}}$ is the mean rate of rotation tensor viewed in a rotating reference frame with the angular velocity ω_k. The model constants A_0 and A_s are given by

$$A_0 = 4.04, \qquad A_s = \sqrt{6}\cos\phi$$

where
$$\phi = \frac{1}{3}\cos^{-1}\left(\sqrt{6}W\right), \quad W=\frac{S_{ij}S_{jk}S_{ki}}{\tilde{S}^3}, \quad \tilde{S} = \sqrt{S_{ij}S_{ij}}\,, \quad S_{ij} = \frac{1}{2}\left(\frac{\partial u_j}{\partial x_i} + \frac{\partial u_i}{\partial x_j}\right)$$

The realizable k–Ɛ turbulence model constants are

$$C_{1\varepsilon} = 1.44,\ C_2 = 1.9\,,\ \sigma_k = 1.0\,,\ \sigma_\varepsilon = 1.2$$

2.1.7. Evaporation time of water droplet in the base case

The base case parameter is followed Reda Ragab (2012) [4]. The inlet condition of the domain was specified by a flow velocity. The outlet condition was set at the constant atmospheric pressure, and the sides of the domain were taken as periodic.

Regarding the discrete phase, a mono-disperse spray composed of 4 streams injected at the inlet of the duct. According to typical droplet evaporation values, the base case parameters are shown in Table1.

Table 1. The base case parameter

Parameter	Base Case Value
Inlet air Temperature	310 K
Inlet air Velocity	1 m/s
Droplet Inlet Velocity	3 m/s
Droplet Diameter	20 μm
Droplet Mass	$4.18\text{x}10^{-12}$ kg
Droplet Temperature	300 K
Relative Humidity	60%

From base case parameter that shows in Table 1, Reda Ragab (2012) [4] found that the evaporation time of the 20 micrometer water droplets was around 0.407s and the variation in diameter also conforms with the d^2-law of droplet evaporation time.

2.2. CFD simulation

In this research, a computational model of the 3D cylindrical tube with a diameter of 0.4 m and a length of 3.0 m was setup. Water droplets evaporation in tube under different pressure conditions was simulated. Overview of the solution method was defined as shown in Figure 1.

2.2.1. Computational geometry and grid

According to base case, the 3D cylindrical tube computational domain was created with a diameter of 0.4m and length of 3.0m. Geometry and mesh generation were performed with the Ansys fluent design modeler, resulting in a mesh with 6,627,759 polyhedral mesh (Figure 2). The grid resolution resulted from a mesh Independence Study that will be outlined in Figure 2.

A mesh independence study was performed to provide a solution that is independence of mesh accurately capturing the pressure inside the tube [8]. The changes in the average pressure due to the change in the mesh resolution taken at middle of the tube. The mesh independence study shows at least 6,627,759 mesh elements are needed for the solution to be an independence of mesh and appropriate for this computational model as shown in Figure 3.

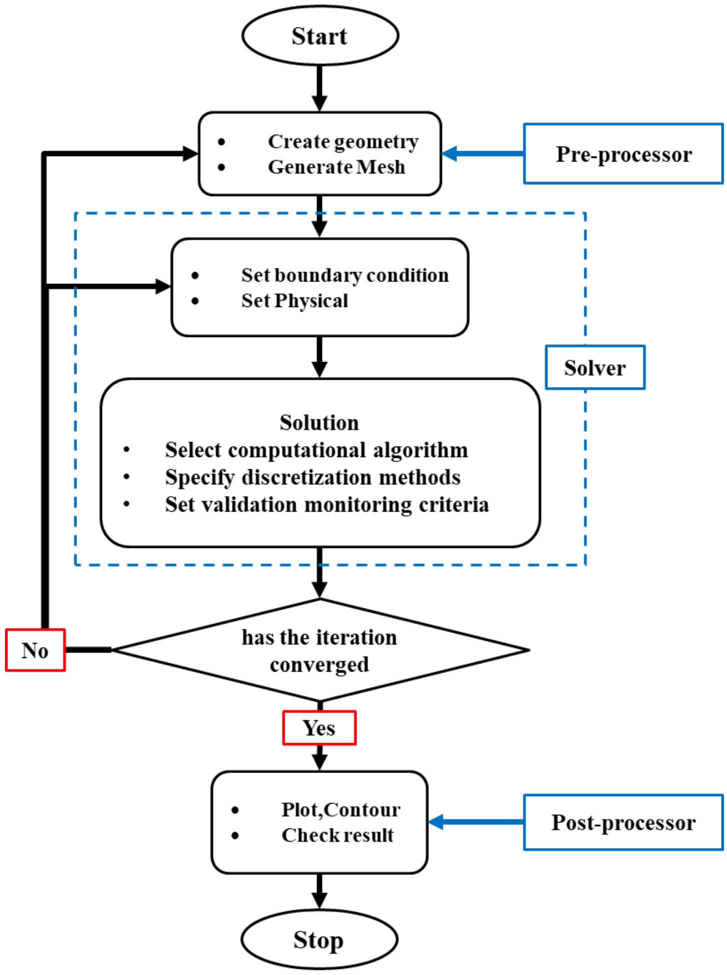

Figure 1. Overview of the solution method.

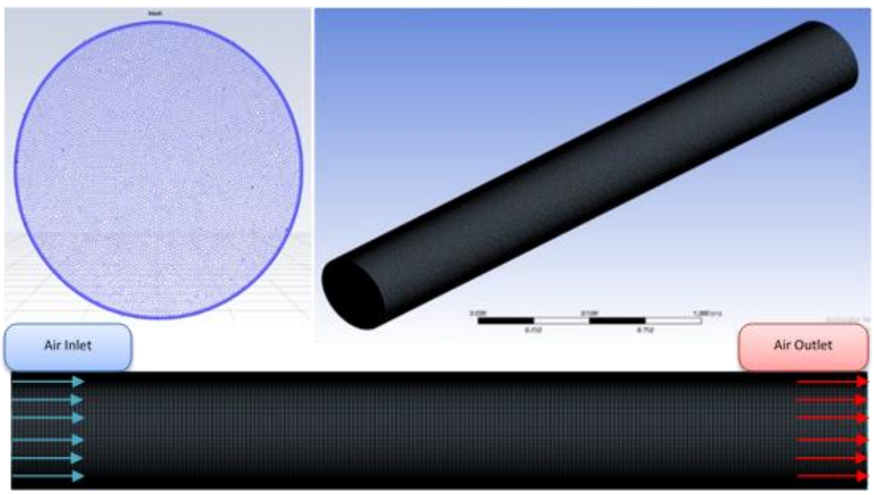

Figure 2. Geometry and polyhedral mesh generation.

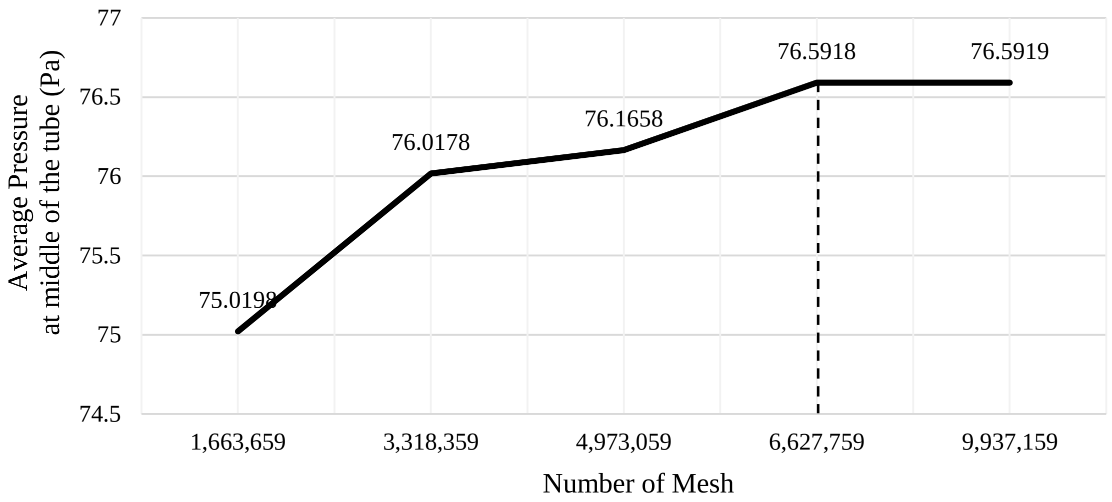

Figure 3. Mesh independence study.

2.2.2. Boundary conditions

The inlet boundary condition of the domain is specified by temperature and pressure. The air flow velocity and temperature condition at the inlet were a constant at 1m/s and 310K respectively. The inlet air pressure condition were -1bar, -0.75bar, -0.5bar, -0.25bar, and atmosphere pressure. The sides of the domain were taken as periodic. Regarding to the discrete phase, a mono-disperse spray composed of 1,000 streams was injected at the center of the inlet. According to typical droplet evaporation values, the base case parameters are shown in Table 1.

2.2.3. Spray nozzle characteristics

The cone spray model provided by Ansys Fluent 2022 was used. The water droplets (20 micrometer) were injected into the computational domain from a nozzle with 90 degree cone angle, and 1 mm diameter positioned in the middle of the inlet plane of the computational domain and oriented horizontally in downstream direction as shown in Figure 4.

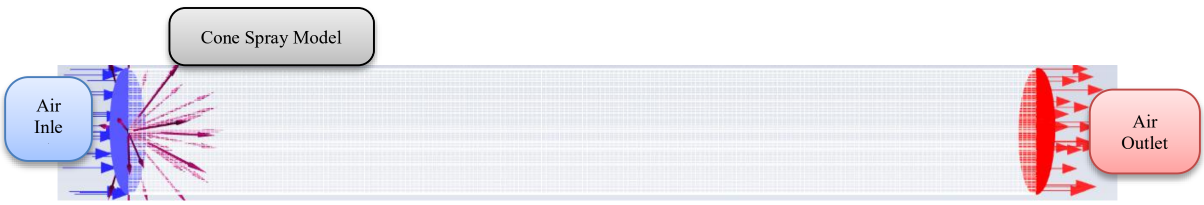

Figure 4. Cone Spray Model provided by Ansys Fluent 2022.

2.2.4 Solver settings

The PISO algorithm was used for pressure-velocity coupling. Pressure interpolation was second order and second-order discretization schemes. It was used for both the convection terms and the viscous terms of the equations. It was assumed that the solution is converged when the normalized residual for each conservation equation was less than or equal to 10^{-6}.

3. Result and Discussion

The CFD model was simulation by discrete phase model (DPM) and species transport model to predict the evaporation processes of water droplets in tube under different pressure. Water droplets of 20 micron were injected into the tube at different internal pressures to study the effect of pressure on the evaporation time. From the Figure 5, the results show that the water droplets residence time was near to the base case value at atmosphere pressure. The results of the different air pressure simulation are displayed according to the following topics.

3.1. Residence time of water droplets at different air pressure

The simulation results show that there is a clear relationship between pressure and evaporation time of water droplets. The evaporation time of the water droplets in the tube at different pressure conditions (-1bar, -0.75bar, -0.5bar, -0.25bar, and atmosphere pressure) were 0.158s-0.177s, 0.189s-0.192s, 0.202s-0.231s, 0.261s-0.314s, 0.376s-0.436s, respectively.

From the simulation results, it can be seen that the residence time of water droplets change according to the pressure conditions. The less residence time of water droplets was observed in low air pressure values. Moreover, the range of maximum-minimum residence time was lower when the air pressure decreased. It means that the water droplets take approximately the same time to evaporate.

This relationship was represented with the Figure 5.

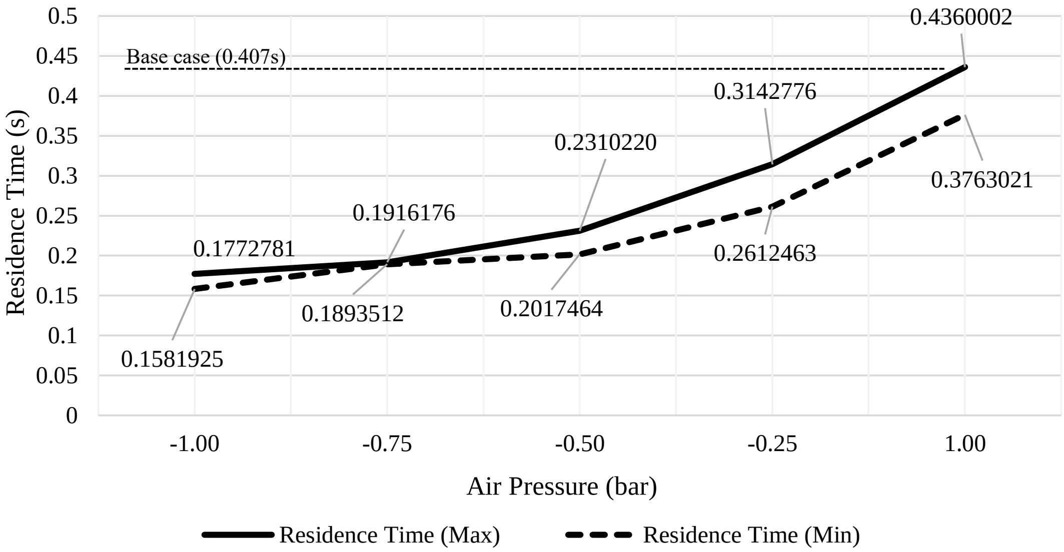

Figure 5. Relationship between water droplets residence time and air pressure.

3.2. Devolatilization of water droplets at different pressure

To analyze the evaporation time of water droplets at different pressure ranges, devolatilization of water droplets should be considered. The simulation results show that pressure conditions effected the devolatilization of water droplets. The devolatilization of water droplets increased when the air pressure reduced. This relationship was represented with the Figure 6.

From Figure 6, the maximum and average devolatilization of water droplets values increase when air pressure decreased. However, the difference between the maximum and average values increased when the air pressure decreased. It means that when the air pressure reduced, there was a large volumes of evaporation process occurred in a short period of time and then decreased until completely evaporation process, as shown in Figure 7.

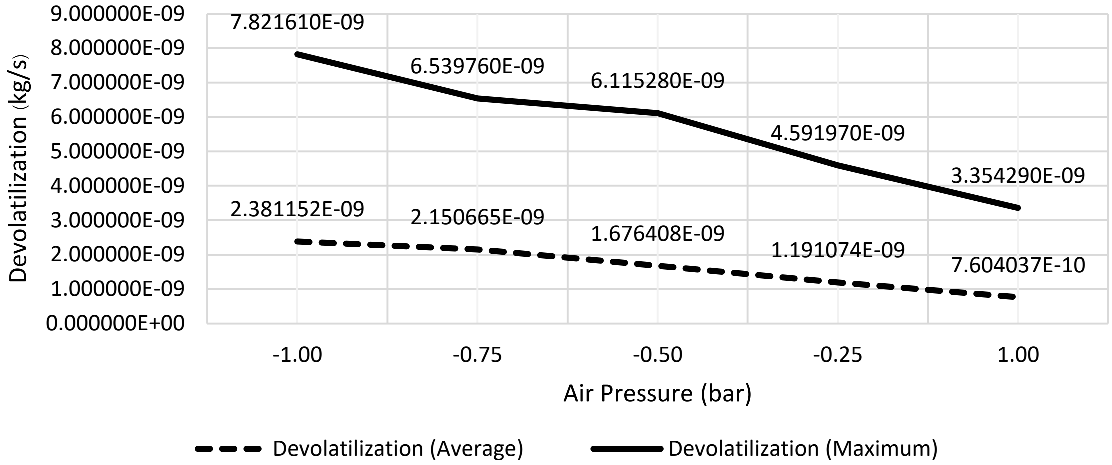

Figure 6. Relationship between devolatilization of water droplets and air pressure.

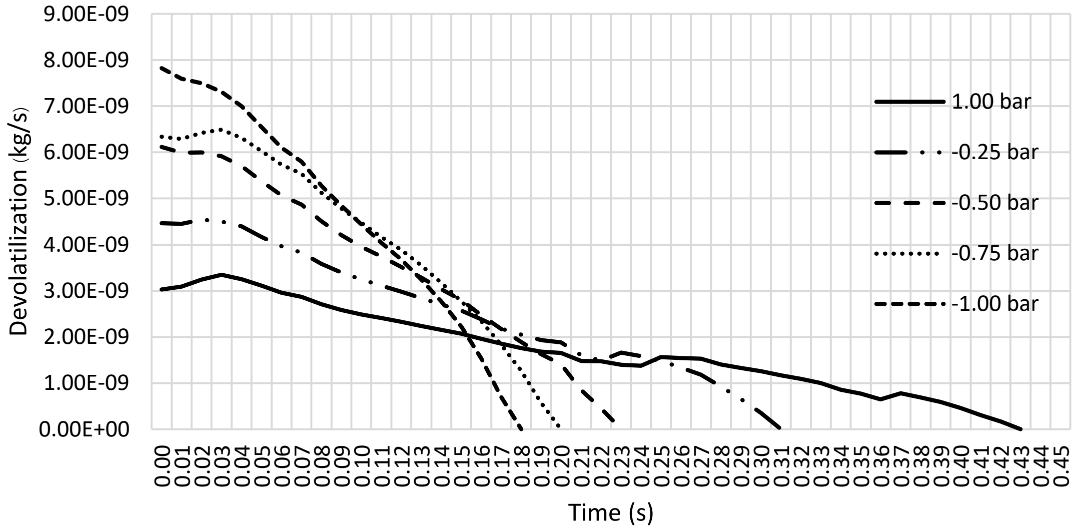

Figure 7. Relationship between water droplets devolatilization and evaporation time.

3.3. Water droplets mass and evaporation time at different pressure

According to Figure 8, evaporation of water droplets was occurred rapidly especially when air pressure reduced. The devolatilization was high at the initial of evaporation process than at the end. The initial mass of a 20 micrometer water droplet was 4.18×10^{-12} kg. Water droplets mass decreased rapidly at the beginning because they had a large surface area, which promotes evaporation. It was found that the droplet mass decreased significantly when the air pressure was decreased.

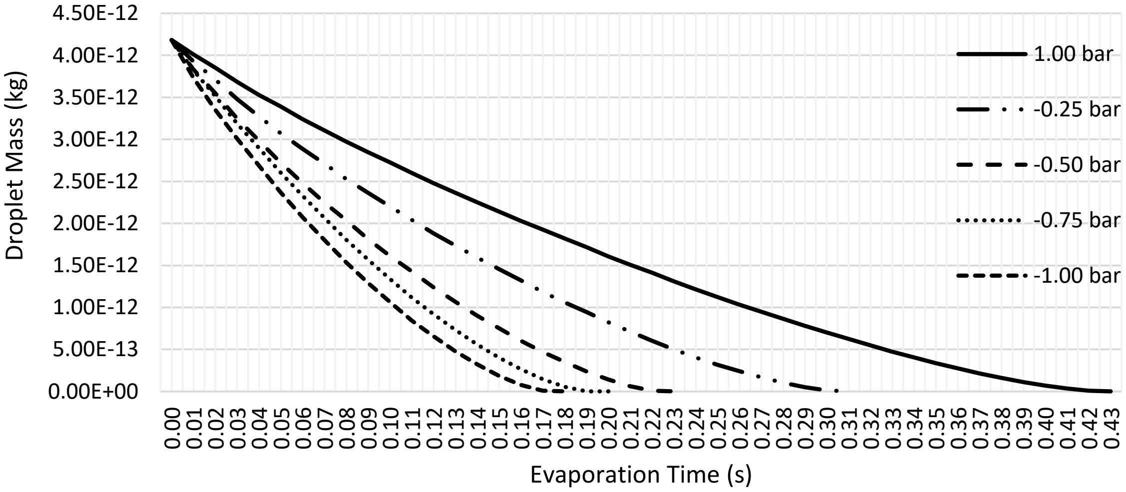

Figure 8. Relationship between water droplets mass and evaporation time.

3.4. Water droplets diameter and evaporation time at different pressure

In contrast to the droplets mass, the droplets diameter slowly decreased at the beginning of evaporation process because the initial evaporation occurs across the entire large surface area. However, reducing the air pressure effected to decreasing substantially as seen on Figure 9.

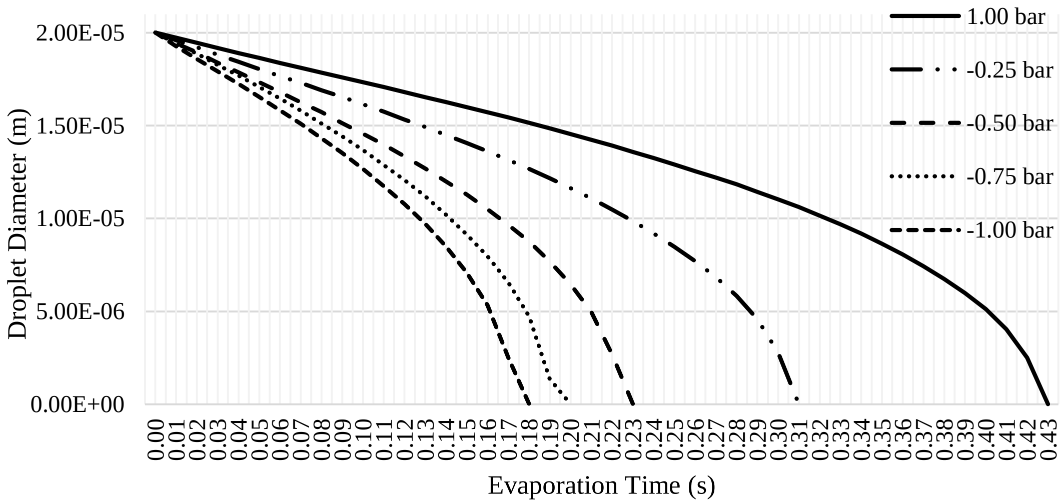

Figure 9. Relationship between water droplets diameter and evaporation time.

4. Conclusion

This study represents that CFD simulation of evaporation by using the Lagrangian-Eulerian (3D steady RANS) approach can accurately predict and tracking water droplets evaporation behaviour with an acceptable accuracy. The evaporation of water droplets was influenced by many factors. Pressure was an important factor affecting the evaporation process of water droplets. It was found that there is a clear relationship between pressure and evaporation time. A strong relationship pressure and devolatilization of water droplets was also found. It can be said that the residence time of the water droplets was shorter at low pressure conditions and reducing the air pressure results in a high level of devolatilization of water droplets.

5. Acknowledgments

The authors would like to thank Chiang Mai University for financial supports and Computational Fluid Dynamics (CFD) Simulation Software of this research.

6. References

[1] Jay Kumar, Jaspreet Singh, Harsh Kansal, Gursimran Singh Narula, Prabhjot Singh, (2014).CFD Analysis of Flow Through Venturi, International Journal of Research in Mechanical Engineering & Technology, 4(2), pp.214-217.

[2] Evren Özgür, Prof. Dr. Kasım Koçak (2015). The Effects of the Atmospheric Pressure on Evaporation, Acta Geobalcanica (Vol.1,p. 17-24)

[3] Giulio Lorenzini, Alessandra Conti, Daniele De Wrachien(2012), Computational Fluid Dynamics (CFD) Picture of Water Droplet Evaporation in Air, Irrigation & Drainage Systems Engineering,1(1)

[4] Reda Ragab and Ting Wang (2012). An Investigation of Liquid Droplet Evaporation Model Used in Multiphase Flow Simulation. ASME International Mechanical Engineering Congress & Exposition (Vol.7, p.485-497).

[5] Tony Persson. (2013). Eulerian-Lagrangian Modeling of Multicomponent Spray for Aseptic Treatment of Carton Bottles in the Food Process and Packaging Industry. Chalmers university of technology.

[6] ANSYS Inc. Release 18.0 (2017). ANSYS Fluent Tutorial Guide. ANSYS Europe, Ltd.

[7] H.Montazeri, B.Blocken, J.L.M. Hensen (2014). Evaporative cooling by water spray systems: CFD simulation, experimental validation and sensitivity analysis. Building and Environment (Vol.83, p.129-141).

[8] M.A.Abd Halim, N.A.R. Nik Mohd, M. N. Mohd Nasir and M. N. Dahalan (2018). The Evaluation of k-ε and k-ω Turbulence Models in Modelling Flows and Performance of S-shaped Diffuser. International Journal of Automotive and Mechanical Engineering,15(2), 5161-5177

CST0010

A CFD Validation Study of TNT Blasting in Unconfined Large Pipe Using LS-Dyna Program: An Overpressure Comparison

Nuttapoom Prasitpuriprecha[1,5], Sirawit Namchatha[1,5], Tinnapob Phengpom[2,5], Jetsadaporn Priyadumkol[1,5], Ameen Topa[3], Chakrit Suvanjamrat[1,4], and Machimontorn Promtong[1,5,*]

[1] Department of Mechanical Engineering, Faculty of Engineering, Mahidol University, Nakhon Pathom, 73170, Thailand
[2] Institute for Innovative Learning (IL), Mahidol University,Nakhon Pathom, 73170, Thailand
[3] Faculty of Ocean Engineering Technology and Informatics, Universiti Malaysia Terengganu, Malaysia
[4] Laboratory of Computer Mechanics for Design (LCMD), Mahidol University, Nakhon Pathom 73170, Thailand
[5] CFD & Energy Research Group, Mahidol University, Nakhon Pathom, 73170, Thailand

* Corresponding Author: machimontorn.pro@mahidol.edu

Abstract. This paper presents the validation study to benchmark the computational fluid dynamics (CFD) results with experimental data of the blasting in an unconfined large pipe. In order to assess the numerical accuracy and reliability of the LS-DYNA program, especially in terms of capturing overpressure during the explosion in the pipe, two case studies with varied TNT sizes (0.25-0.50 lbs) were investigated. It should be noted that a large-diameter steel pipe with both ends open was adopted and created as the 3D model to simulate TNT blast loads and monitor the consequence effects. After comparing the transient pressure, it was found that the LS-Prepost software produced a good agreement with the experimental data. For instance, the experimental peak pressure for 0.25 lbs and 0.5 lbs TNT charges in unconfined tests were approximately 83.69 MPa and 101.16 MPa, which were close to the predicted results at around 78.87 MPa and 99.16 MPa, respectively. It should be noted that the frequency at which the simulations collected the pressure was 100 Hz, while the experiments were at 1,000 Hz. Overall, the trend of the reflected pressure inside the unconfined pipe was the same as in the experiment and took about 0.20 - 0.40 seconds to equal the ambient pressure gradually. Overall, the simulation cases could provide details of overpressure distribution along the length of the pipe during the explosion, hence contributing to a deeper understanding of pressure contours under blast loads. Further investigation will be conducted to gain insights into the dynamic response under the different sizes of TNT and semi-confined and confined pipe blasting scenarios. Hopefully, this research will contribute to developing engineering practices in blast-resistant design and risk assessment, benefiting professionals in blast engineering and bolstering the safety and resilience of structures exposed to explosive events.

Keywords: Numerical Validation, Computational Fluid Dynamics (CFD), Blast Loading, Unconfined Pipe, Pressure Contour Analysis.

1. Introduction

Different shockwave, heat, and gas release scenarios can result from explosive circumstances. To establish a numerical validity, it is necessary to perform experimental investigations to gain a thorough understanding of shock waves. Due to the need to avoid structural damage, the effects of blast loadings on structures are a useful research issue. The development of the blast modelling for in-depth analysis of global and local behavior will lead to the recommendation of a protective design standard for public structures. During the consequent reaction of burning, particle flying, and noise emission, highly reliable devices will be introduced for capturing the rapid motions of substances [1]. Highly dependable equipment for capturing the swift motions of substances will be introduced during the response of burning, particle flying, and noise emission. Highly dependable equipment for capturing the swift motions of substances will be introduced during the response of burning, particle flying, and noise emission. For a fire evacuation plan to meet safety requirements, it is necessary to understand the ASET and RSET parameters, which can be discovered through simulation[2]. To save money and time, the CFD technique can also be used as the promising tool to redesign the building's current components.

Numerous numerical research studies have been conducted over the years to enhance the properties of the materials and the buildings so they can absorb the energy released during explosions and withstand the associated blast loads [3-7]. The numerical work can be valid when the validation stage has been conducted, eventually the consequences of explosive reactions could be examined [8-10]. In-depth research into the dispersion and ventilation of poisonous gases and smoke particles, particularly concerning occupant safety in various contexts, is required because this blasting process produces high-temperature flames and hazardous particles propelling from the detonation point [6, 11]. As is well known, multi-physics programming enables engineers to realistically model diverse buildings and test the impact as many times as necessary to comprehend potential phenomena fully. Building designs are frequently optimized using simulation tools like LS-Dyna, Autodyne, and Explicit Dynamic to guard against anticipated and unforeseen explosion risks. However, there is some debate over whether the numerical prediction was accurate [12-14].

Recent research has examined the performance of several modern materials and a new strengthening technique for blast mitigation to improve the structural performance against blast loading. For instance[15], concentrated on testing the RC structure and tracking the blast resistance due to its enormous mass, reasonable price, and application in various construction shapes. As previously indicated, even though the RC structure's reinforcing steel bar can withstand blasts by primarily resisting tensile force, widespread flying debris cannot be prevented, which reduces the structure's stiffness and sectional capacity [16-19]. made an effort to make major structural components more ductile to stop structures from collapsing. A full-scale experiment on bridge decks made of Ultra High Strength Fiber Reinforced Concrete (UHPFRC) was carried out by[20]. As discovered, adding a layer of basalt mesh to the concrete cover at the specimen's soffit could increase blast resistance compared to conventional UHPFRC. As a result, the basalt mesh added to the UHPFRC slab enhances the blast performance, as evidenced by spalling and flying debris [21], used to strengthen techniques with fiber-reinforced polymer (FRP) to increase structural flexibility, reduce debris spalling from the core structure, and dramatically improve blast resistance to buildings. Additionally, many researchers contributed to the development of numerical models that were used to forecast how structural components strengthened with FRC or FRP would behave when subjected to blast loading [22].Therefore, proposing blast mitigation using FRC material and FRP strengthening by modelling the entire structures under blast impaction through numerical analysis is an alternative technique to grasp their performance and behaviors fully.

In this paper, the validation study of TNT blasting in unconfined pipes is presented. It should be noted that the work presented is a CFD study using the LS-DYNA software to predict the pressure in the pipe after the explosion. As expected, assessing the reliability and accuracy of the numerical approach by benchmarking with the experimental data is given. Two cases with different sizes of TNT will be introduced for validation investigation, and the transient pressure at the monitored distance will be compared with our experimental works. Hopefully, the numerical accuracy and the validation study could be established for further work focused on elucidating the blasting phenomena in migrating containers, and the crucial keys in terms of the design to resist the blast consequence could eventually be established.

2. Governing Equations

In order to capture the dynamic response of nonlinear structural mechanics in explosion and failure scenarios, researchers commonly use the CFD Transient structural technique. This approach typically involves formulating partial differential equations that govern mass, momentum, and energy within the Lagrangian mechanics framework.

The structural system is discretized using the finite element method, with initial conditions specifying material properties, applied loads, and constraints. As a consequence of the computing, the parameters like deformation, nodal forces, acceleration, and velocity. Additionally, the FSI tool can capture critical data related to structural failure, including factors like strain rates and stresses, and tracks motions at various points within the structure [23]. Furthermore, the mesh can be adjusted accordingly when transient loads deform the material model. The material's mass is calculated according to conservation criteria [24]. The updated volume of material is determined using density and the initial material mass, as shown in Equation (1).

$$\frac{\rho_0 V_o}{V} = \frac{m}{V} \tag{1}$$

Evaluating the deformation of materials following explosive events holds immense significance in ensuring safety and structural robustness. It is necessary to utilize sophisticated methodologies encompassing numerical simulations. By comparing the experiments, some insights can be gained and making reliable predictions, especially the explosive forces on structures and geological formations. When subjected to external loads, materials undergo deformation, transforming internal energy, some of which may convert into kinetic energy.

Supposing that the material exhibits elasticity, in that case, this energy transformation can be described through an equation known as the elastic-strain energy equation. As known, the applied stresses induce material deformation, as seen in Equation (2).

$$e = \frac{1}{\rho}\left(\sigma_{xx}\epsilon_{xx} + \sigma_{yy}\epsilon_{yy} + \sigma_{zz}\epsilon_{zz} + 2\sigma_{xy}\epsilon_{xy} + 2\sigma_{yz}\epsilon_{yz} + 2\sigma_{zx}\epsilon_{zx}\right) \tag{2}$$

Generally speaking, the simulation process for each element involves solving mass, momentum, and energy equations explicitly, with results from the previous time step informing new calculations. Precise control of time increments is pivotal for calculation stability and accuracy[25]. Energy calculations are consistently monitored for conservatism. The ALE Multi-Material method is employed to simulate air and TNT, with air characterized by specific properties and TNT's mass density drawn from prior research.

To expedite computational solutions, the complex JWL equation of state governing explosive behaviours is simplified into a more manageable ideal gas state equation. The JWL equation of state, a fundamental component in studying explosive behaviour, offers valuable insights into the relationships between various parameters. The JWL equation of state (Jones-Wilkins-Lee) (Equation (3)) is applied to estimate pressure numerically for the TNT charge detonation product[26].

$$p = A\left(1-\frac{\omega}{R_1 V}\right)e^{-R_1 V} + B\left(1-\frac{\omega}{R_2 V}\right)e^{-R_2 V} + \frac{\omega E}{V} \tag{3}$$

In this context, V denotes the specific volume, and E represents the internal energy per unit mass. The equation encompasses various specific constants of explosive charge type, including A, B, R_1, R_2, and others. Within the overpressure context, the equation is partitioned into distinct terms, each with its own significance. The first term on the right side of the equation holds paramount importance in the medium-pressure region, while the second term assumes critical relevance in the low-pressure zone, as elucidated by the third term. Importantly, the influence of the first and second terms within the equation diminishes significantly as the detonation product expansion progresses to later stages.

3. Experimental Description

3.1. Experimental Set-up

The experimental configuration can be seen in Fig. 1. The research team initiated a controlled detonation involving 0.25 to 0.5 lbs of TNT within the central region of a carbon steel pipe. The detonation was systematically placed in an unconfined condition. Two high-precision pressure sensors were strategically placed opposite near the pipe ends to measure and monitor the pressure variations. The pressure sensors were carefully calibrated, synchronized with precision, and synchronized for simultaneous and precise data acquisition, with exceptional accuracy down to the microsecond. This dual-sensor setup ensured data reliability, redundancy, and a comprehensive assessment of pressure wave dynamics during the experiment's various blasting scenarios.

(a) (b) (c)

Figure 1. (a) Experimental set-up of unconfined blast test, (b) Detonate position, (c) Pressure sensor position.

As mentioned earlier, the primary objective was to elucidate the pressure contours along the pipe's longitudinal axis from its endpoints. The data will be introduced to perform a crucial validation study and analyze the blast wave profiles during an explosion. As aimed, it could give us a comprehensive understanding of dynamic responses to blast wave propagation.

3.2. Details of the benchmarking data

The experimental phase was concluded successfully, and a pivotal aspect of this research lies in upcoming numerical simulations to validate and complement empirical observations. These simulations are crucial in our approach to comprehensively studying pipe blasting phenomena. At the present work, we aim to refine our understanding of the underlying physics, and gain deeper insights into system dynamics through the numerical modelling.

This synthesis of experimental and numerical approaches promises to enhance the accuracy and depth of our analysis, contributing to a more robust comprehension of pipe blasting intricacies. The experiment involved two TNT charge sizes (0.25 and 0.5 lbs) (see Table 1). It encompassed unconfined conditions within a 50 cm diameter, 2 m long carbon steel pipe, providing diverse results and valuable insights into blasting dynamics within such a conduit. The recorded pressure within the millisecond time scale was discussed in detail about the characterization of blast dynamics within the pipe, facilitating a comprehensive understanding of transient pressure phenomena during blasting experiments.

Figure 2. Unconfined condition blast test with 0.25 lbs TNT charge size (Side View).

Table 1. The defined cases for the numerical investigations.

Case Study	Explosive Weight	Initial Condition
1	0.25 lbs	Unconfined
2	0.5 lbs	Unconfined

4. Numerical Details

4.1. Geometry and Mesh

The geometry was created with a 3D Computer-Aided Design application and then imported into the LS-Prepost. In contrast, a maximum mesh size of 5×10^{-3} m for the pipe and 2×10^{-3} m for the TNT model were used. The simulation developed for the pipeline structure precisely studied the sensitive deformation using a Lagrangian solver. Due to its ultra-fast deformation, the bomb employs Eulerian (virtual) techniques to capture the blast's start and the consequent scenarios.

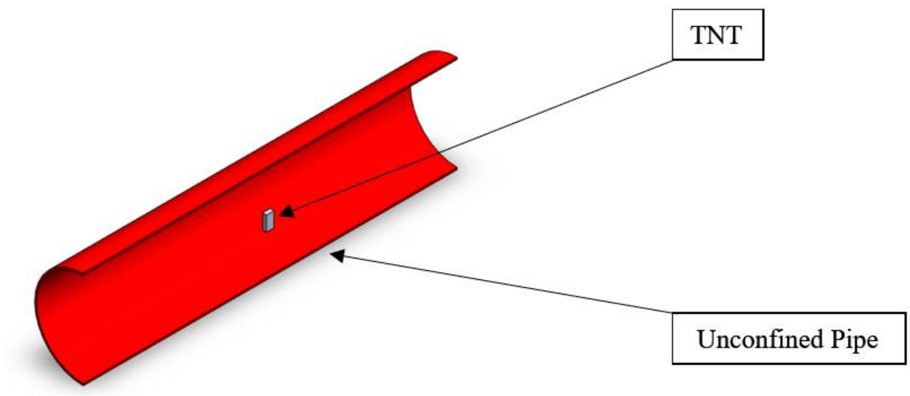

Figure 3. A cross section 3D model of the 2 m Carbon Steel pipe and TNT location (Center).

4.2. Descriptions of the Numerical Set-up

In this computational investigation, the utilization of the LS-DYNA software, integrated within the ANSYS environment, was implemented to comprehensively model the intricacies of the localized blast phenomenon. Further information on material properties and the specific models employed can be found in Table 2. For this simulation, the structural calculations were conducted using the Johnson-Cook model, chosen due to its aptitude for addressing the distinctive characteristics of blast testing and the material properties entailed in the study [27].

5. Results and Discussion

5.1. The overpressure comparison

This investigation conducted a comparative analysis of experimental and numerical investigations, focusing on different blast pipe scenarios with two TNT sizes (0.25 lb and 0.50 lb) as seen in Fig. 4 and **5**. Tracking shockwave propagation within the 2-meter pipe length, we observed radial emergence of shockwaves about 1 ms after ignition, closely followed by the flame front. Larger TNT sizes led to higher overpressure, with unconfined cases showing shockwave distances nearly doubling those of the blast.

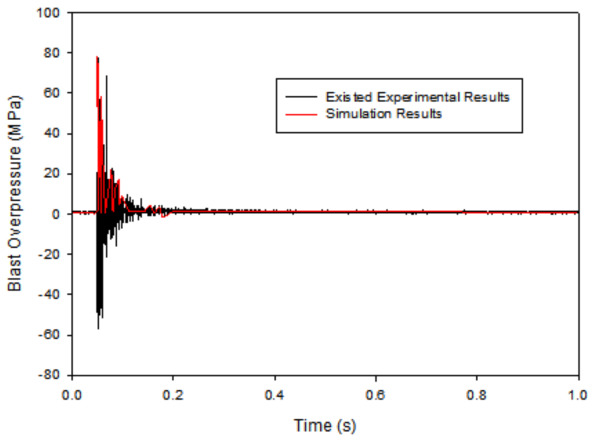

Figure 4. A comparison chart of pressure results between existed experiment and LS-DYNA simulation of unconfined case with 0.25 lbs TNT.

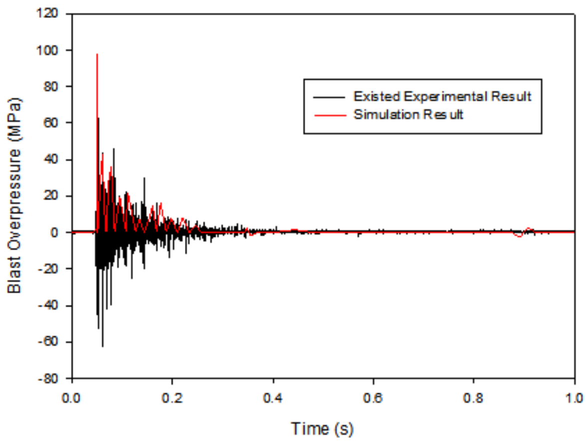

Figure 5. A comparison chart of pressure results between existed experiment and LS-DYNA simulation of unconfined case with 0.5 lbs TNT.

In Fig. 4 and Fig. 5, experimental and simulation results show strong agreement in peak pressure and time values, affirming the accuracy of our computational models. For instance, experimental peak pressures for 0.25 lbs and 0.5 lbs TNT charges closely align with simulations at approximately 78.87 MPa and 99.16 MPa, respectively. This robust match reinforces our confidence in the reliability of our models."

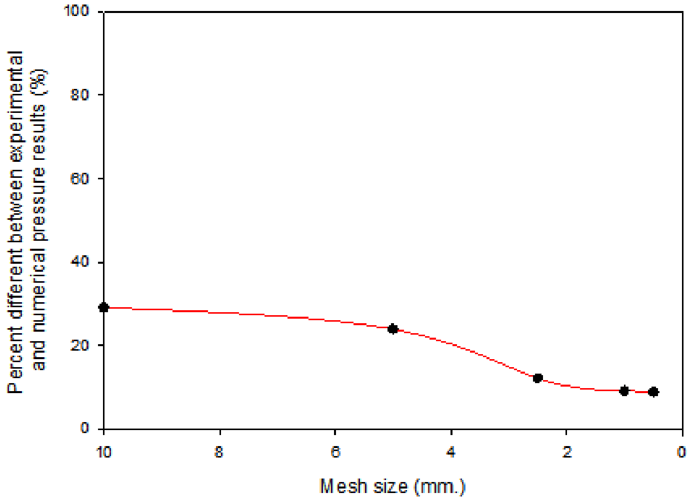

Figure 6. The percent different between experimental and numerical pressure results.

In this study, we implemented a mesh independence chart to assess the potential impact of mesh size on pressure results. This analysis was crucial to ensuring the reliability of our simulations. According to the chart, we found that using an environment air mesh size ranging between 1.5-0.5 mm is appropriate for our study. The percentage difference between numerical and experimental results falls below 10% for the same volume in this range. This indicates that our simulations are accurate and reliable within these mesh sizes. Therefore, we recommend utilizing mesh sizes within this range for similar studies, ensuring both computational efficiency and precise results

5.2. Tracking the pressure (shockwave) motions and its velocity

With the same initial conditions and setup as earlier, the simulations illuminate the blast dynamics in unconfined pipes. These simulations mirror the experimental details, including TNT charges (0.25 lb and 0.50 lb) and the carbon steel pipe dimensions (50 cm diameter, 2 meters length). Advanced numerical modelling precisely assesses wave-front and overpressure-front through travel distances and velocities within these blast phenomena.

Figure 7. Blast wave front using CFD approach by LS-DYNA Program.

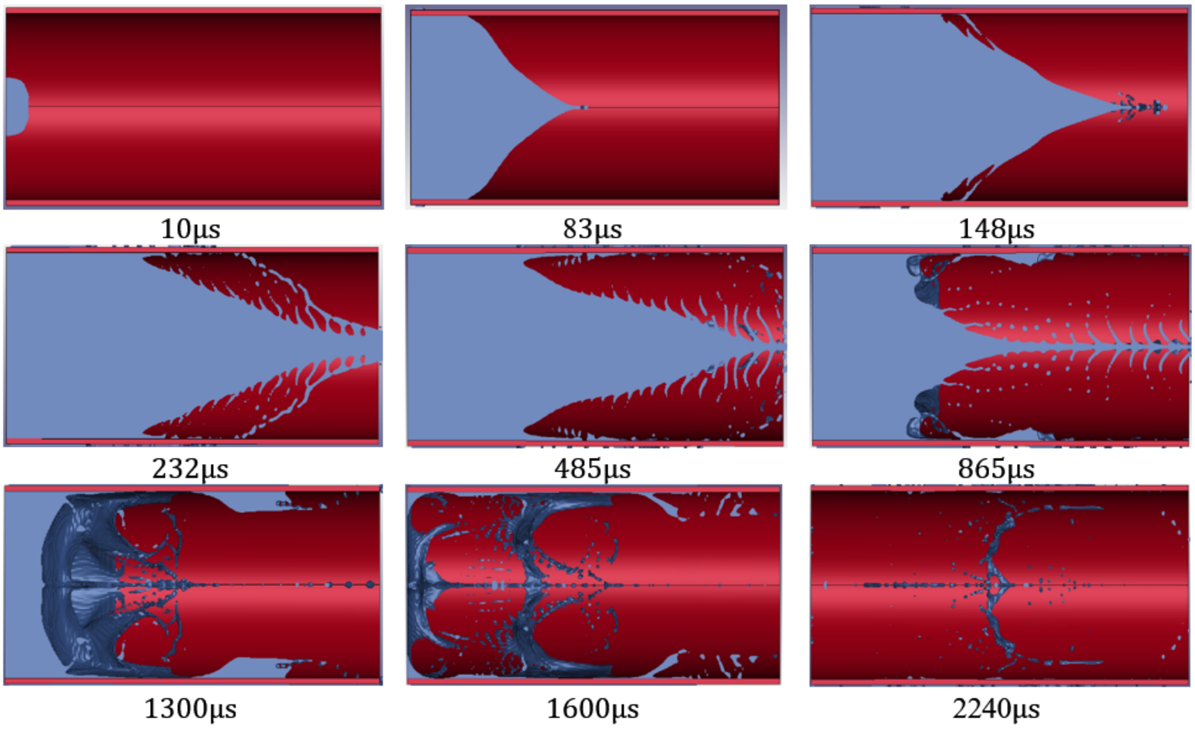

Figure 8. Cross section of TNT 0.25 lbs charge size blast contour in unconfine pipe at several times using CFD technique approach by LS-DYNA Program.

The simulation results reveal distinct characteristics for unconfined conditions. These results provide valuable insights into the behaviour of blast contour to pressure and flame flows, offering a comprehensive understanding of how these critical parameters evolve. By comparing the simulation results to the empirical data obtained from the experiments, researchers can validate the accuracy and reliability of the numerical models, thus enhancing the overall understanding of the complex blast dynamics within these pipe configurations.

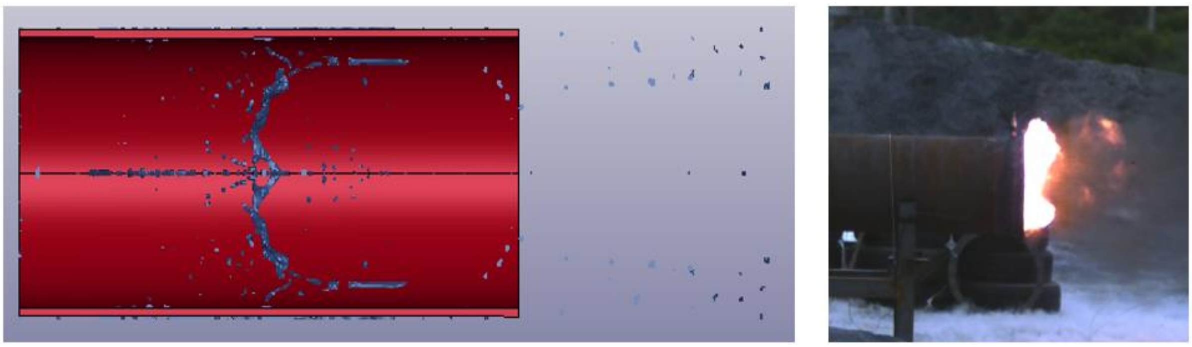

(a) (b)

Figure 9. (a) Cross section of TNT 0.25 lbs charge size blast contour at 3100 µs using CFD technique approach by LS-DYNA program compare with (b) experimental results of the same case.

Fig. 8 provides a striking visual representation of simulation results, faithfully reproducing blast wave dynamics like those observed in the unconfined pipe during the experiment. This computational analysis serves to elucidate the nuanced characteristics of blast phenomena comprehensively. The vivid depiction of the blast contour vividly illustrates the blast front wave emanating from the unconfined pipe, dynamically capturing pressure fluctuations in the surrounding environment. In the simulations, we can identify a peak pressure of a designated location, solidifying the precision and reliability of our computational models.

6. Conclusion

The investigation explored shockwave characteristics while highlighting blast overpressure distribution in the unconfined pipe by examining peak pressures and their dependence on TNT size and blast boundary shape. The study documented explosive outcomes, including wave-front pressure, for comparative analysis between our experimental and simulation results.

- The validation process has firmly established the reliability of utilizing the CFD approach with the LS-DYNA program for blast analysis, given the remarkable agreement between overpressure values in blast simulations and peak pressure measurements and their closely matched dispersion rates. Additionally, the pressure distribution contour for the blast was created using the CFD approach, and the simulation outcomes closely align with the experimental results.
- The research validates the CFD approach in simulating unconfined pipe blast scenarios accurately. While the study primarily focused on unconfined conditions, future research may explore its applicability in semi-confined and fully confined blast scenarios, expanding our insights into blast dynamics across diverse conditions.

In addition, the analysis indicates a heightened risk associated with internal explosions, prompting a further study of fragment motion, flame-front and wave-front velocities change over time, and temperature contours in the other scenarios, with potential applications in structural design and safety measures. Overall, this validation extends our confidence in numerical modelling for in-depth explorations of unconfined blast dynamics, highlighting its crucial role in understanding and predicting such complex phenomena.

7. Acknowledgments

This research has received funding support from the NSRF via the Program Management Unit for Human Resources & Institutional Development, Research, and Innovation [Grant number B16F640102]. Many thanks to the Mechanical Engineering Department, Faculty of Engineering, Mahidol University, for allowing us to use of their laboratory. Thanks to CADFEM SEA Pte. Ltd. - A certified Elite Channel Partner to ANSYS - for providing support and access to the CFD program named ANSYS Fluent 2022 R1.

8. References

[1] Li, Y., et al., *Dynamic response of stiffened plate under internal blast: Experimental and numerical investigation.* Marine structures, 2021. **77**: p. 102957.

[2] Tiwari, R., T. Chakraborty, and V. Matsagar, *Dynamic analysis of tunnel in soil subjected to internal blast loading.* Geotechnical and Geological Engineering, 2017. **35**: p. 1491-1512.

[3] Hu, Y., et al., *Blast loading model of the RC column under close-in explosion induced by the double-end-initiation explosive cylinder.* Engineering Structures, 2018. **175**: p. 304-321.

[4] Hao, Y., et al., *Field testing of fence type blast wall for blast load mitigation.* International Journal of Structural Stability and Dynamics, 2017. **17**(09): p. 1750099.

[5] Mkrtychev, O. and A. Savenkov, *Modeling of blast effects on underground structure.* International Journal for Computational Civil and Structural Engineering, 2019. **15**(4): p. 111-122.

[6] Gebbeken, N. and T. Döge, *Explosion protection—architectural design, urban planning and landscape planning.* International Journal of Protective Structures, 2010. **1**(1): p. 1-21.

[7] Abdollahzadeh, G., H. Faghihmaleki, and M. Avazeh, *Progressive collapse risk and reliability of buildings encountering limited gas–pipe explosion after moderate earthquakes.* SN Applied Sciences, 2020. **2**(4): p. 1-13.

[8] Xiao, W., M. Andrae, and N. Gebbeken, *Effect of charge shape and initiation configuration of explosive cylinders detonating in free air on blast-resistant design.* Journal of Structural Engineering, 2020. **146**(8): p. 04020146.

[9] Lidner, M. and Z. Szcześniak, *Numerical analysis of blast load from explosive materials using finite volume method.* Key Engineering Materials, 2017. **723**: p. 789-794.

[10] Liang, S.-M., J.-L. Hsu, and J.-S. Wang, *Numerical study of cylindrical blast-wave propagation and reflection.* AIAA journal, 2001. **39**(6): p. 1152-1158.

[11] Nguyen, H. and X.-N. Bui, *Predicting blast-induced air overpressure: a robust artificial intelligence system based on artificial neural networks and random forest.* Natural Resources Research, 2019. **28**(3): p. 893-907.

[12] Zhang, X.L., et al. *Study on the dynamic behaviors of X70 pipeline steel by numerical simulation*. in *Advanced Materials Research*. 2010. Trans Tech Publ.

[13] Chafi, M.S., G. Karami, and M. Ziejewski, *Numerical analysis of blast-induced wave propagation using FSI and ALEmulti-material formulations.* International Journal of Impact Engineering, 2009. **36**(10-11): p. 1269-1275.

[14] Tan, H., et al. *Validation of Computational Fluid Structure Interaction Models For Shape Optimization Under Blast Impact*. in *International Design Engineering Technical Conferences and Computers and Information in Engineering Conference*. 2010.

[15] Shi, Y., H. Hao, and Z.-X. Li, *Numerical simulation of blast wave interaction with structure columns.* Shock Waves, 2007. **17**(1): p. 113-133.

[16] Remennikov, A., et al., *Experimental investigation and simplified modeling of response of steel plates subjected to close-in blast loading from spherical liquid explosive charges.* International journal of impact engineering, 2017. **101**: p. 78-89.

[17] Yin, H. and Y. Ouyang, *Experimental and Numerical Study on Steel Fiber Concrete under Blast Loading.* Buildings, 2022. **12**(12): p. 2119.

[18] Wang, C.-h., et al., *Pressure load characteristics of explosions in an adjacent chamber.* Shock and Vibration, 2021. **2021**.

[19] Zhang, C., G. Gholipour, and A.A. Mousavi, *Nonlinear dynamic behavior of simply-supported RC beams subjected to combined impact-blast loading.* Engineering Structures, 2019. **181**: p. 124-142.

[20] HOLÝ, S., et al., *EXPERIMENTAL EVALUATION OF MATERIAL PARAMETERS FOR HIGH-RATE PHENOMENA SIMULATIONS WITH RESPECTS TO JOHNSON-COOK PLASTICITY.* 2011.

[21] Xu, K. and Y. Lu, *Debris velocity of concrete structures subjected to explosive loading.* International Journal for numerical and analytical methods in geomechanics, 2006. **30**(9): p. 917-926.

[22] Hu, Y., et al., *Characteristics of confined blast loading in unvented structures.* International Journal of Protective Structures, 2011. **2**(1): p. 21-43.

[23] Han, Y. and H. Liu, *Finite element simulation of medium-range blast loading using LS-DYNA.* Shock and Vibration, 2015. **2015**.

[24] Alonso, F.D., et al., *Characteristic overpressure–impulse–distance curves for vapour cloud explosions using the TNO Multi-Energy model.* Journal of hazardous materials, 2006. **137**(2): p. 734-741.

[25] Noh, G. and K.-J. Bathe, *An explicit time integration scheme for the analysis of wave propagations.* Computers & structures, 2013. **129**: p. 178-193.

[26] Lee, E., M. Finger, and W. Collins, *JWL equation of state coefficients for high explosives*. 1973, Lawrence Livermore National Lab.(LLNL), Livermore, CA (United States).

[27] Johnson, G.R. and W.H. Cook, *Fracture characteristics of three metals subjected to various strains, strain rates, temperatures and pressures.* Engineering fracture mechanics, 1985. **21**(1): p. 31-48.

CST0011

Numerical Study of Impinging Slot Jet on Heating Surface for Heat Transfer Enhancement

Kanakarn Prajuntaboribal[1] and Chalermpol Plengsa-ard[1,*]

[1]Department of Mechanical Engineering, Faculty of Engineering, Kasetsart University, Bangkok, 10900, Thailand.

* Corresponding Author: fengcpp@ku.ac.th

Abstract. This study explores the impinging slot jet phenomenon and its characterization using different turbulent models. A constant surface temperature on the flat plate was chosen as a test case. Different turbulent models, based on the Reynolds-Averaged Navier-Stokes (RANS) method and transition options such as γ-GEKO k-ω, γ-SST k-ω and transitional shear stress transport (SST) are compared to find out the suitable turbulent model. The advantages and limitations of each model are explored, considering their computational requirements and accuracy in predicting flow features. Furthermore, this abstract presents key findings from recent studies that have utilized turbulent models to investigate impinging slot jets. The Reynolds number of 20,000 with the jet to surface ratio H/B = 4 served as a test case. The results show the γ-GEKO-k-ω model has the good agreement with the experimental data. The γ-SST k-ω turbulence model fails to accurately predict the second peak in Nusselt number values.

Keywords: Jet impingement, Heat Transfer, Computational fluid dynamics (CFD).

1. Introduction

Due to its effectiveness in concentrating mass, momentum and especially heat transfer in a localized area, slot jet impinging commonly employed in various industrial manufacturing components, such as drying paper, textile and food production materials, heat treating for metalworking and semiconductor manufacturing, surface coating and painting, plastic film extrusion, welding and brazing, and electronics manufacturing to increase product quality and reliability and to meet the high levels of manufacturing standards. These are just a few examples of how air slot jet impingement is applied in industrial manufacturing to improve efficiency, quality, and control in various processes. Using Computational Fluid Dynamics (CFD) for the study of impinging jet phenomena provides a multitude of advantages, including cost-effectiveness and time efficiency when compared to experimental setups. Moreover, CFD offers exceptional flexibility, enabling swift adjustments to parameters, boundary conditions, and geometries, thereby making it an adaptable tool for investigating diverse impinging jet configurations and scenarios. In the literature review, numerous experiments have been conducted to investigate heat transfer in impinging jets over the past few decades for both round and slot jet [1]. Despite its seemingly simple geometry, predicting jet impingement is challenging due to the complexity of strong pressure variations, flow separation, and the formation and dissipation of vortices. Numerous researchers are directed towards the exploration of diverse turbulent models, aiming to identify the most suitable one that balances accuracy with computational efficiency [2]. however, accurately predicting these flow patterns continues to be a complex challenge.

Some reports suggest that the Transition shear stress transport (SST) model struggles to accurately predict the Nusselt number, as it exhibits a notable disparity with experimental data [3]. Crucially, they also advocated for the utilization of the k-ω model in predicting jet impingement heat transfer. However, it was observed that this model tends to overestimate the skin frictions values. The objective is to employ an intermittency transition model, incorporating various transition options of the k-ω model to anticipate the heat transfer characteristics of a slot jet impingement. This prediction will be compared against experimental data to assess the model's accuracy and suitability for such applications.

This study is structured into four distinct sections, each serving a specific purpose in the investigation. The initial section provides a comprehensive description of the problem at hand, offering a clear overview of the impinging slot jet geometry. Following this, the mathematical formulation section delineates the theoretical framework and equations employed to model and analyze the heat transfer process. The parameter values along with problem conditions and specifications are provided in the Solution Method section. Moving forward, the results and discussion section presents the findings derived from the simulations and provides a thorough analysis of these results in relation to the established experimental data. Finally, the study concludes with a concise summary of the key insights garnered, along with implications and potential avenues for further research in this domain.

2. Problem Description

This study focused on an air slot jet impinging on a flat plate, constant temperature was chosen for the study. a configuration commonly employed in various industrial manufacturing components. Jet impingements on heated walls were investigated assuming air as Newtonian fluid behaviour. The slot nozzle width B = 40 mm. The distance from the slot nozzle exit to the impinging plate was fixed at H/B = 4, while H stands for the distance of impingement and the constant temperature wall dimension L = 50B. The computational domain for the case under study is depicted in Figure 1., also same as the experiment in the literature [4]. with the reference axes X and Y included, and due to symmetry considerations, only one-half of the domain is analysed. The mean inlet velocity profiles were applied for this study.

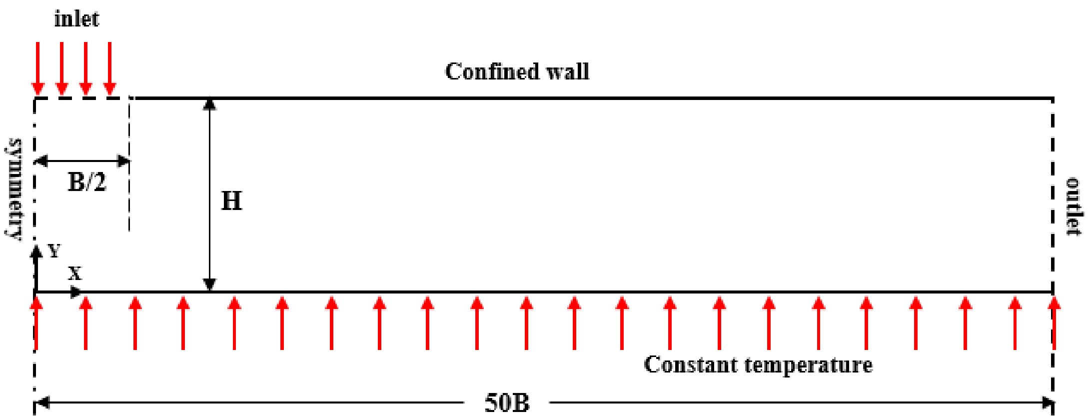

Figure 1. Computational domain geometry.

3. Mathematical formulation

To explain a localized transition at the outset, the intermittency (γ) model was incorporated into a transport equation along with the SST $k{-}\omega$ model. The transition model uses an intermittency factor to gradually introduce or reduce turbulence at the point of laminar-to-turbulent transition, affecting turbulent production. Ultimately, the model was fine-tuned using the standard transition onset equation to improve transition predictions by Langtry and Menter [6].

The intermittency factor influences the production term in the turbulent kinetic energy transport equation within the SST model, allowing for the simulation of both laminar and turbulent flows. introduced the transport equation for the intermittency (γ) as follows:

$$\frac{\partial(\rho\gamma)}{\partial t}+\frac{\partial(\rho U_j\gamma)}{\partial x_j}=\Upsilon_{\gamma 1}-\Gamma_{\gamma 1}-\Upsilon_{\gamma 2}-\Gamma_{\gamma 2}+\frac{\partial}{\partial x_j}\left[\left(\mu+\frac{\mu_t}{\sigma_y}\right)\frac{\rho\gamma}{\partial x_j}\right] \quad (1)$$

Both source term for the length of the transition region and the dissipation are introduced by:

$$\Upsilon_{\gamma 1}=2F_{length}\rho S[\gamma F_{onset}]^{0.5}, \qquad \Gamma_{\gamma 1}=\gamma\Upsilon_{\gamma 1}$$

$$\Upsilon_{\gamma 2}=0.06\rho\Omega\gamma F_{turb} \qquad , \qquad \Gamma_{\gamma 2}=50\gamma\Upsilon_{\gamma 2}$$

where S represents the strain rate magnitude, while F_{length} defines an empirical correlation that controls the length of the transition zones. The term Ω indicates the vorticity of flow fields. The set of equations the transition onsets can be found in the literature.

4. Solution Method

The downward jet impinging onto a flat confined surface at a Reynolds number of 20,000. These cases have been extensively employed for scrutinizing turbulence models in heat transfer predictions. The simulation in steady state was conducted using ANSYS-Fluent 2022R2, employing time-averaging techniques (RANS). Transition SST turbulence model is used to assess grid independence. Additionally, the coupled algorithm for pressure-velocity integration and the Green-Gauss cell-based scheme for gradients were implemented. The detailed boundary conditions are provided in Table 1. for inlet turbulent intensity I is 0.01 The characteristic turbulent length scale, denoted as l_c, is expressed as l_c= 0.015B. The inlet temperature T_{in} is set at 300 K, while the impinging surface temperature T_w is 310 K. Both the impinging and confined plates are treated as isothermal walls. The specific values for constant fluid properties are shown in Table 2.

Table 1. The boundary conditions.

	Inlet	**Outlet**	**Impinging plate**	**Confined wall**
k	$k_{in}=(u_{in}I)^2$	0		
μ	$u_{in}=\mathrm{Re}\mu_t/B$	Pressure outlet	No slip	No slip
ω	$\sqrt{k}/27l_c\beta^{*0.25}$	0		
T	300 K	300 K	310 K	300 K

The location of y+ is situated at a distance of y+ = 0.04 (which is less than or equal to 1), ensuring sufficient resolution of flow fields near the boundary layer of the wall. The investigation of grid independence relies on the Nusselt number, which is denoted as:

$$Nu=(\partial T/\partial y)_w/[(T_w-T_{in})/B] \quad (2)$$

Table 2. Fluid properties constant.

Density	1.1716	kg/m³
Dynamic viscosity	1.835×10^{-5}	kg/m·s
Thermal conductivity	0.0263	W/m·K
Specific heat capacity at constant pressure	1005.5	W/kg·K

4.1. Numerical setting

The simulation employed time-averaging techniques to analyze the flow field behavior using $\gamma - GEKO - k - \omega$, $\gamma - SST - k - \omega$ and transition SST model compared with the experiment data [4,5].

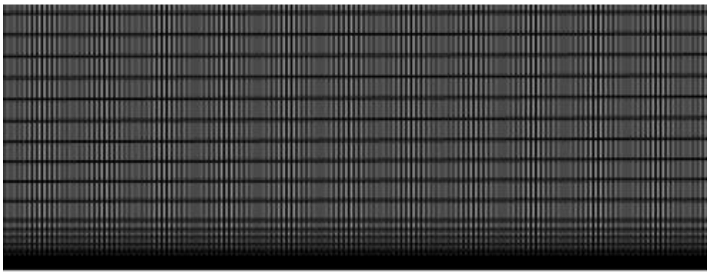

Figure 2. Cells distribution

4.2. Grid independence analysis

Time average technique simulations with transition SST models were used to simulate the flow field . We chose three cases with different numbers of cell for testing, there were 5.2, 6.2, 8.1 million total computational cells for testing case Mesh I, Mesh II and Mesh III and Fig. 2. Shows the cells distributions of Mesh II which refine mesh near the impinging surface to capture the boundary layer. As depicted in Fig. 3, It is observed that the Nusselt number distribution predicted by Mesh I has more error compare to the experimental data and the others meshes, where the results of Mesh II and Mesh III almost overlap with each other. To balance grid size-related errors with computational efficiency in the final solution, we consistently employed Case Mesh II for all simulations. It showed good agreement when compared with published data [4].

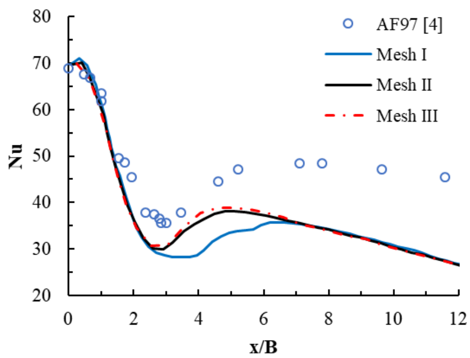

Figure 3. Grid independence analysis.

5. Results and Discussion

This section consists of four parts. The first part showing the mean Nusselt number on an impinging surface. Additionally, the experimental data [4] are included for comparison. The following part demonstrates the relationship between jet velocity and y-distance for each x position. Lastly, the comparison of dimensionless skin friction coefficient C_f is presented. The experimental data [5] is also plotted for comparison.

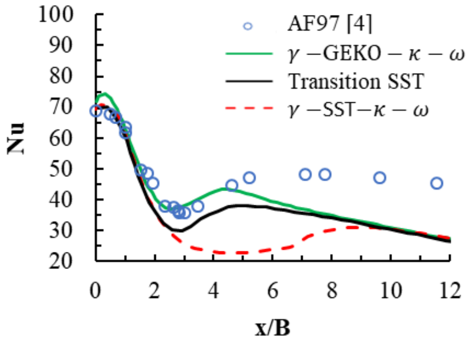

Figure 4. Comparisons between Nusselt number versus x-distance for different turbulence models.

At the stagnation point, the results demonstrate that all turbulence models have a good agreement with the experimental data, particularly γ-SST-k-ω and Transition SST model. The experimental results indicate that both γ-GEKO-k-ω and Transition SST turbulence models successfully capture the second peak of Nusselt number. Additionally, within the range of x/b < 5, the γ-GEKO-k-ω model exhibits a strong concordance with the available experimental data. Unlike the γ-SST-k-ω**,** this transition option does not align well with the experimental data, as shown in Figure 4. In contrast, the SST-k-ω model without the intermittency option shows a favorable trend of agreement, as substantiated by literature reviews for this study case [1].

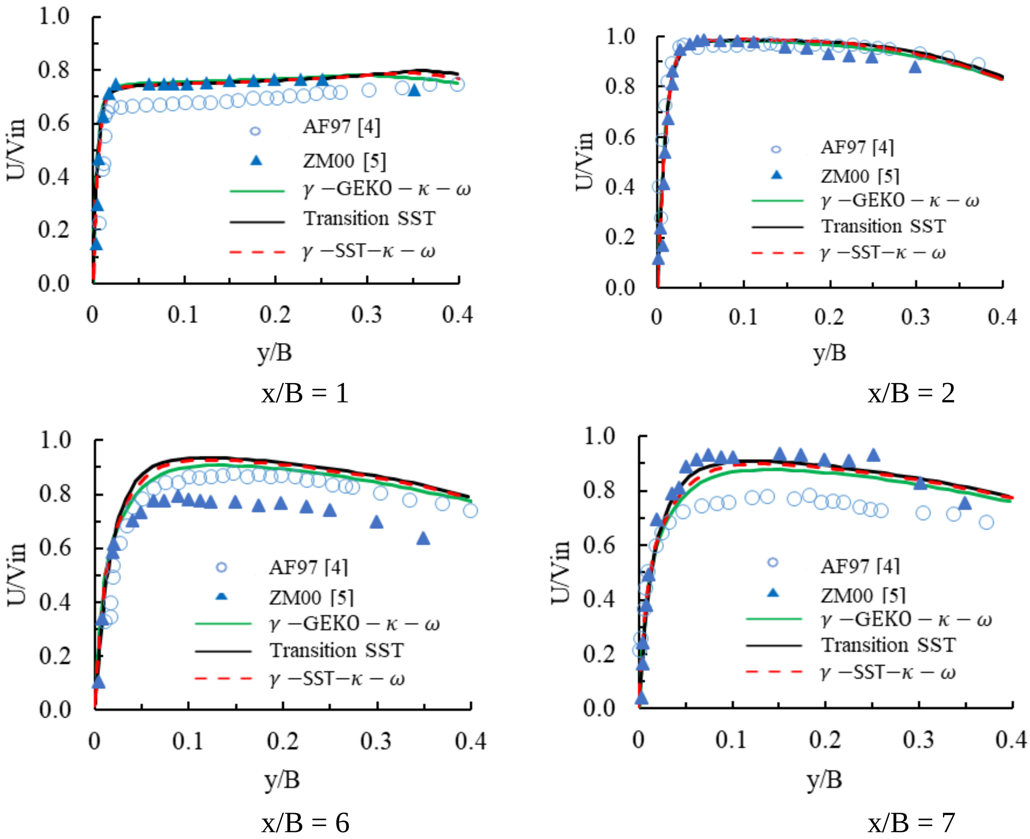

Figure 5. Velocity profiles along the y-position.

The impinging effect causes the jet to deflect in accordance with the streamline curvature. This induces a notable shear force, resulting in a pressure drop. As a result, velocities progressively increase as the flow moves away from the stagnation point. This leads to a higher maximum velocity at x/B = 2 compared to x/B = 1, as shown in Figure 5. All turbulent models exhibit a consistent alignment with the experimental data, following a similar trend at x/B = 1 and x/B = 2. As the flow moves away from the stagnation point, it decelerates as the jet spreads downstream. This deceleration gives rise to the generation of a vortex near the confinement area [7]. In this region, all turbulent models display a consistent profile and closely correspond to the experimental data. Nevertheless, at a significant x-direction distance (x/B = 7), the Transition SST model shows exceptional agreement with the experimental data [5].

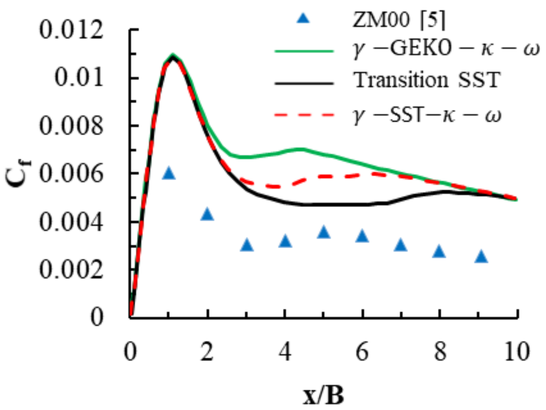

Figure 6. Results of skin friction distribution.

Since there is no streamwise flow on the impinging surface at the stagnation point, skin friction values are not applicable. The maximum streamwise velocity occurs near the stagnation point, resulting in the peak value of skin friction. Figure 6. Shows that the Transition SST model outperforms others in terms of capturing the dip value in skin friction at x/B = 3. Nevertheless, the skin friction coefficient also displays a second peak profile, which can be predicted by the γ-GEKO-k-ω and γ-SST-k-ω models. While the γ-GEKO-k-ω model can predict both the dip and second peak values, however the dip's position is higher compared to the γ-SST-k-ω models and transition SST model.

6. Conclusion

This study primarily focuses on conducting a numerical investigation to examine the heat transfer characteristics of slot jet impingement employing diverse turbulence models. The simulation was performed utilizing ANSYS FLUENT, with the application of RANS techniques to model the flow field. The obtained simulation results were subsequently compared with experimental data available in the literature. A Jet Reynolds number = 20,000 and a slot width to impinging surface ratio H/B = 4 were chosen as the test case. Based on these specified conditions, the summary is as follows:

- The γ-SST-k-ω model is unsuccessful in accurately capturing the second peak magnitude of Nusselt number.
- The γ-GEKO-k-ω model exhibits the closest alignment with the experimental data, indicating its superior predictive capability compared to other turbulence models considered in this study
- Across all evaluated turbulence models, the skin friction coefficient was consistently observed to be overestimated. This phenomenon underscores the need for further refinement and calibration of turbulence models to enhance their accuracy in predicting skin friction coefficients across a range of flow conditions and geometries.

7. References

[1] Zuckerman, N., & Lior, N. (2005). Impingement Heat Transfer: Correlations and Numerical Modeling. Journal of Heat Transfer, 127(5), 544-552. https://doi.org/10.1115/1.1861921

[2] Dewan, A., Dutta, R., & Srinivasan, B. (2012). Recent trends in computation of turbulent jet impingement heat transfer. Heat Transfer Engineering, 33(4-5), 447-460.

[3] Afroz, F., & Sharif, M. A. (2018). Numerical study of turbulent annular impinging jet flow and heat transfer from a flat surface. *Applied Thermal Engineering*, *138*, 154-172.

[4] Zhe, J., & Modi, V. (2001). Near Wall Measurements for a Turbulent Impinging Slot Jet (Data Bank Contribution. *J. Fluids Eng.*, *123*(1), 112-120.

[5] Huang, H., Sun, T., Zhang, G., Li, D., & Wei, H. (2019). Evaluation of a developed SST k-ω turbulence model for the prediction of turbulent slot jet impingement heat transfer. International Journal of Heat and Mass Transfer, 139, 700-712. https://doi.org/10.1016/j.ijheatmasstransfer.2019.05.058

[6] Menter, F. R., Langtry, R., & Völker, S. (2006). Transition modelling for general purpose CFD codes. Flow, turbulence and combustion, 77, 277-303.

[7] T.H. Park, H. G. C., J.Y. Yoo, S.J. Kim (2003). Streamline upwind numerical simulation of two-dimensional confined impinging slot jets. *International Journal of Heat and Mass Transfer*, *46*, 251-262.

CST0014

Bluff body design for vortex-induced vibration energy harvesting

N. Jankul, S. Supatheerawong, S. Yaiboontham, P. Chompamon, S. Songschon, S. Saimek, K. Septham, and T. Kamnerdtong*

Department of Mechanical Engineering, King Mongkut's University of Technology Thonburi, 126 Pracha Uthit Rd., Bang Mod, Thung Khru, Bangkok 10140, Thailand

* Corresponding Author: thoatsanope.kam@kmutt.ac.th

Abstract. This research utilizes Computational Fluid Dynamics (CFD) and Finite Element Method (FEM) to investigate the Fluid-Structure Interaction (FSI) problem of a Vortex-Induced Vibration (VIV) energy harvesting device from water flow. The aim of this work is to compare various bluff body shapes and determine the shape that offers high performance for energy harvesting. The shape models are generated using SolidWorks and then simulated using Altair HyperWorks (SimLab, AcuSolve, and OptiStruct). Water flows around bluff bodies at a free stream velocity of 1 m/s, with Reynolds number 35,000, causing vortex formation and flexible beam vibration behind. A frontal or projected area of bluff body is applied to all shapes with 35 and 30 mm in height and width, respectively. The streamwise length is 30 mm, which is equivalent to the diameter of the cylinder, and the flexible beam length is 1.2 times the streamwise length. The monitoring parameters are the displacement of the beam, the drag coefficient **(**C_D**)**, the lift coefficient **(**C_L**)**, and the Strouhal number **(**St**)**. Furthermore, velocity, pressure and vorticity contours are investigated. The simulation results have shown that the MGX-1 shape (magnet with sharp ends) has the highest equivalent power and beam displacement improvement, with values of 134.93% and 77.55% compared to the circular cylinder shape. The vorticity and pressure contours explain the physical phenomena, where the high vortex intensity region creates a significant pressure difference at the flexible beam, resulting in higher beam displacement.

Keywords: Bluff body, Computational fluid dynamics (CFD), Vortex - induced vibration (VIV), Fluid-Structure Interaction (FSI), Energy harvesting.

1. Introduction

Today, the world's human population is rapidly increasing, leading to a higher demand for energy consumption. This increased demand has led to a rise in energy production from non-renewable sources, particularly fossil fuels, which have significant negative environmental consequences. The consequences of their impact affect humans and animals in various ways, including health issues, economic challenges, and increased susceptibility to natural disasters. As a result, renewable energy has garnered greater interest as a choice to mitigate these problems. Renewable energy sources can be categorized into various types: wind, solar, biomass, hydropower, ocean, tidal, and current sea These forms of energy are considered clean sources because they contribute to zero or near-zero percent of greenhouse gas emissions and other air pollutants [1]. Their advantages lie in their inexhaustibility, as they can be utilized indefinitely [2.[

This study focuses on harnessing vibration energy generated by the flow of fluids past various shapes, commonly known as 'Bluff bodies.' These bodies act as vortex generators when fluids flow over them. The energy generated by the vibration of bluff bodies can be harvested and converted into various forms, including electrical energy. The primary objective of this study is to design a bluff body shape that enhances the efficiency of energy harvesting through the utilization of Computational Fluid Dynamics (CFD) simulations.

3. Methodology

3.1. Model Designs

The harvester mainly consists of a bluff body, a circular cylinder with a diameter of 35 mm, and a beam with a length of 42 mm and a thickness of 1 mm. as illustrate in Figure 1 [3,4].

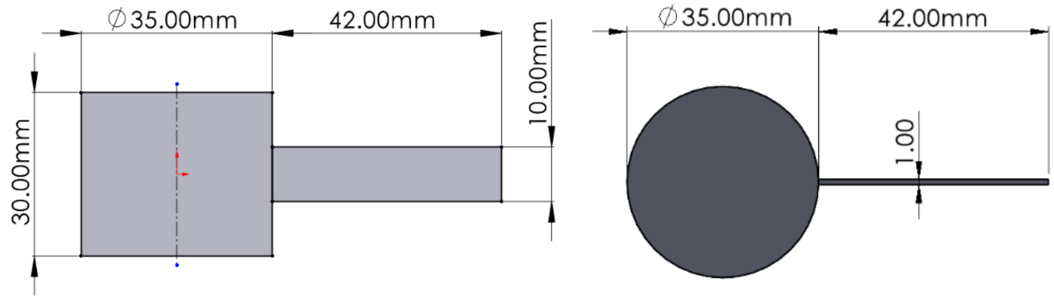

Figure 1. Model dimensions.

When designing the bluff body, various shapes are intentionally crafted to generate a large vortex emanating from the separation point, thereby enhancing its strength. The design also incorporates a specialized shape at the tip of the bluff body to facilitate and promote a higher-frequency flow [5, 6] as shown in Figure 2

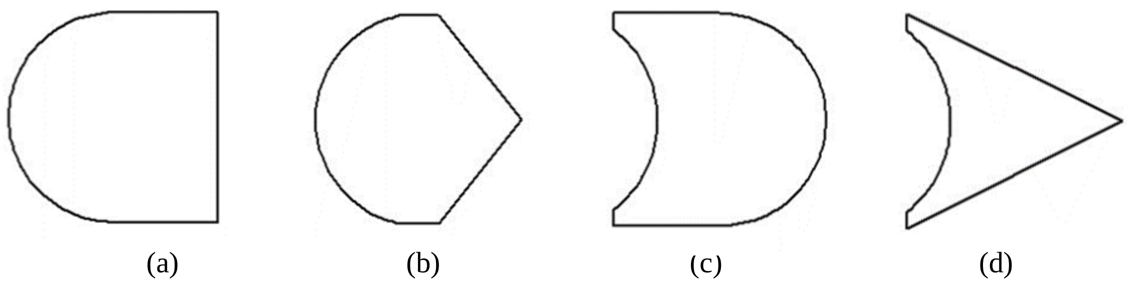

Figure 2. The bluff body model; Bread (a), Tri-O (b), Magnet (c), and Tri-mag (d).

To improve the efficiency of the bluff body shape, we made adjustments to specific shapes as illustrated in the figures. In Figure 2, shape (c) is referred to as 'Magnet,' and we modified one side of this shape from a curvature to a rectangle, naming it 'Magnet-SQ,' as depicted in Figure 3. Additionally, shape (d), known as 'Tri-mag,' underwent alterations in the curvature at the centerline of the front side. These variations are designated as T-series: Trimag-D0 with a curvature of 0 mm, Trimag-D10 with a curvature of 10 mm, Trimag-D20 with a curvature of 20 mm, and Trimag-D30 with a curvature of 30 mm, as illustrated in Figure 4.

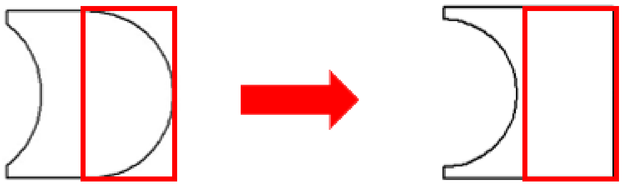

(a) (b)

Figure 3. The adjustment of Magnet (a) to Magnet-SQ (b).

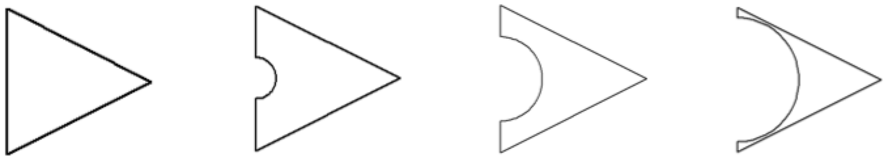

(a) (b) (c) (d)

Figure 4. The “T-series”; Trimag-D0 (a), Trimag-D10 (b), Trimag-D20 (c), Trimag-D30 (d).

As a result of adjusting “Magnet” and “Tri-mag”, we considered modifying the shapes to further improve their design and achieve greater efficiency. 'Magnet' was adjusted with more curvature at the centerline of the front side call “MGX-1”, as shown in Figure 5.

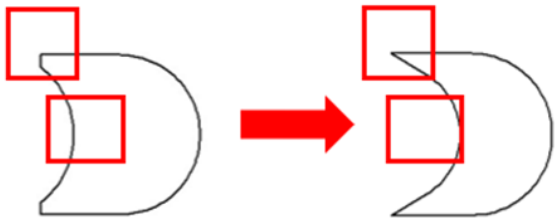

(a) (b)

Figure 5. The improvement of Magnet to be MGX-1.

Increasing the curvature in the T-series resulted in higher improvements. However, to enhance the efficiency of “Trimag-D30” from the T-series, we made further modifications. We adjusted the outer line of curvature at the front side to create a sharp edge, referred to as “Trimag-X.” Additionally, we adjusted the curvature at the trailing edge to create a more curved shape, known as “TSN” as illustrated in Figure 6.

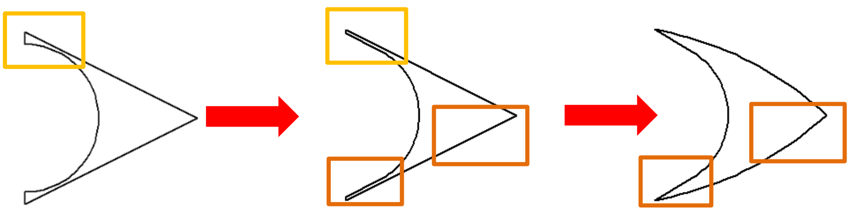

(a) (b) (c)

Figure 6. The improvement of Trimag-D30 (a) to Trimag-X (b), and Trimag-X (b) to TSN (c).

3.2. Simulation process

The three-dimensional simulation was conducted using the Computational Fluid Dynamics (CFD) technique with Altair HyperWorks, The simulation employed the Acusolve and Optistruct solvers, following the P-FSI (Fluid-Structure Interaction) approach. Initial setup included parameter configuration and mesh generation using Simlab.

The simulation aimed to solve the incompressible flow problem by applying the Reynolds-Averaged Navier-Stokes (RANS) equations. To predict flow characteristics affected by adverse pressure gradients resulting from shedding vortices within the boundary layer, the Spalart-Allmaras turbulent model [7] was employed.

Boundary conditions were crucial for solving the problem, including a free stream velocity of 1 m/s at the inlet and static pressure of 0 MPa at the outlet. A no-slip condition was applied to the main structures, namely the bluff body and beam, while a slipping condition was applied to the rest (see Figure 7). The Reynolds number was set at 35,000. The total number of element is about 500,000.

The CFL conditions were applied to control an appropriate time step with a CFL value of 1 [8]. The time step size was set at 0.005 seconds, and the desired y+ was set to 30 to accurately capture near-wall behavior [9].

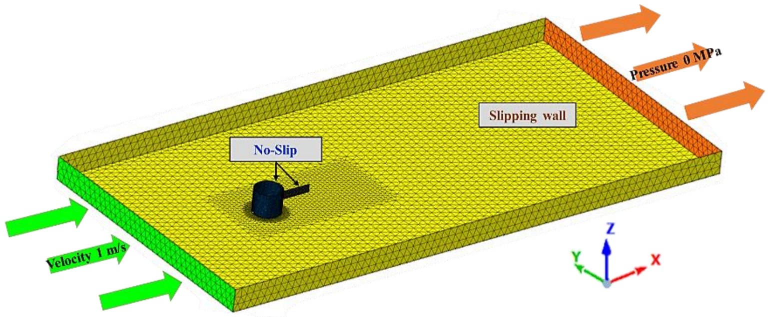

Figure 7. Simulation condition.

The computational domain had dimensions of 10D in width and 20D in length, as depicted in Figure 8, where D represents the cylinder diameter. The main structure was positioned 5D from the inlet, ensuring symmetry between the top and bottom walls.

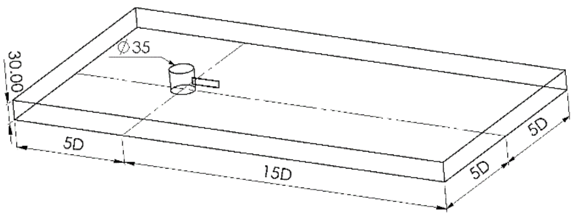

Figure 8. Computational domain.

In P-FSI method, Modal analysis was performed to investigate the deformation of the structure interacts with the fluid. The beam was discretized using hexahedral elements, with an average element size of 3 mm., as illustrated in Figure 9.

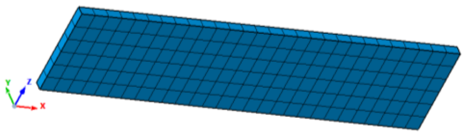

Figure 9. Beam meshing.

4. Results

This study divided the simulation into three cases, comparing various bluff body shapes with a circular cylinder as the standard.

4.1. Parameters monitoring

SET 1: Bread, Tri-o, Tri-mag and Magnet.

As shown in Figure 10, the "Magnet" shape demonstrated the most significant effect on the beam's displacement, with the "Tri-mag" shape showing comparable results.

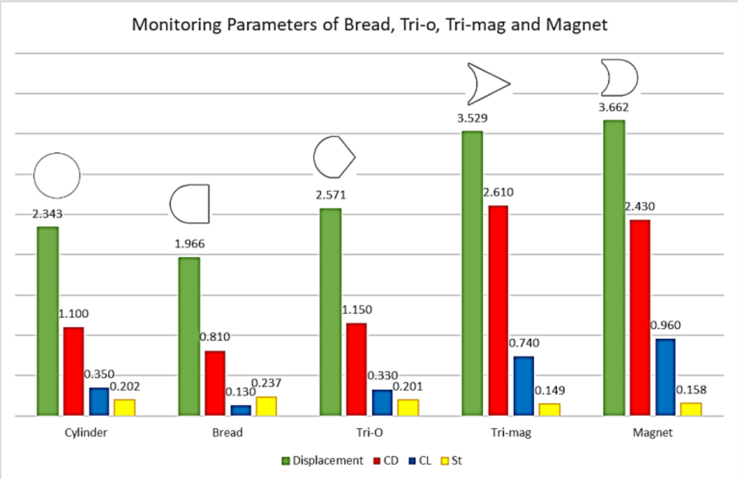

Figure 10. Displacement, C_D, C_L and Strouhal number of SET1.

SET 2: Trimag-D0, Trimag-D10, Trimag-D20 and Trimag-D30

Figure 11 presents a comparison of the T-series shapes with the cylinder. The results indicate that the "Trimag-D30" shape exhibited the greatest beam displacement among the T-series group. However, "Tri-mag" performed better than "Trimag-D30". Consequently, further adjustments were made to enhance the performance of "Trimag-D30".

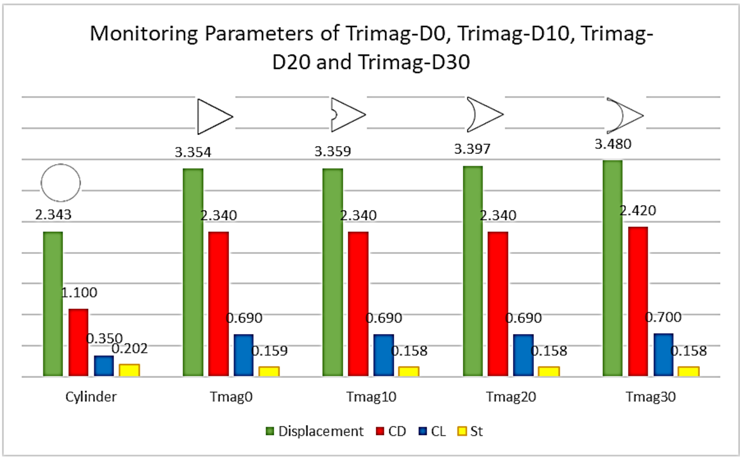

Figure 11. Displacement, C_D, C_L and Strouhal number of SET2.

SET 3: Magnet-SQ, Trimag-X, MGX-1 and TSN

Figure 12 presents the results of modified shapes, including "Magnet-SQ", "MGX-1", "Trimag-X", and "TSN", compared to the standard shape, the circular cylinder. In terms of displacement, "MGX-1" exhibited the highest beam displacement, followed by "TSN" and "Trimag-X".

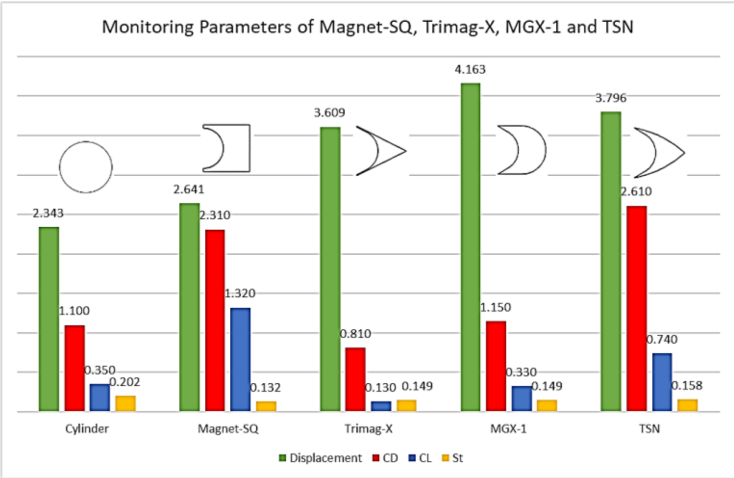

Figure 12. Displacement, C_D, C_L and Strouhal number of SET 3.

4.2. Visualisation

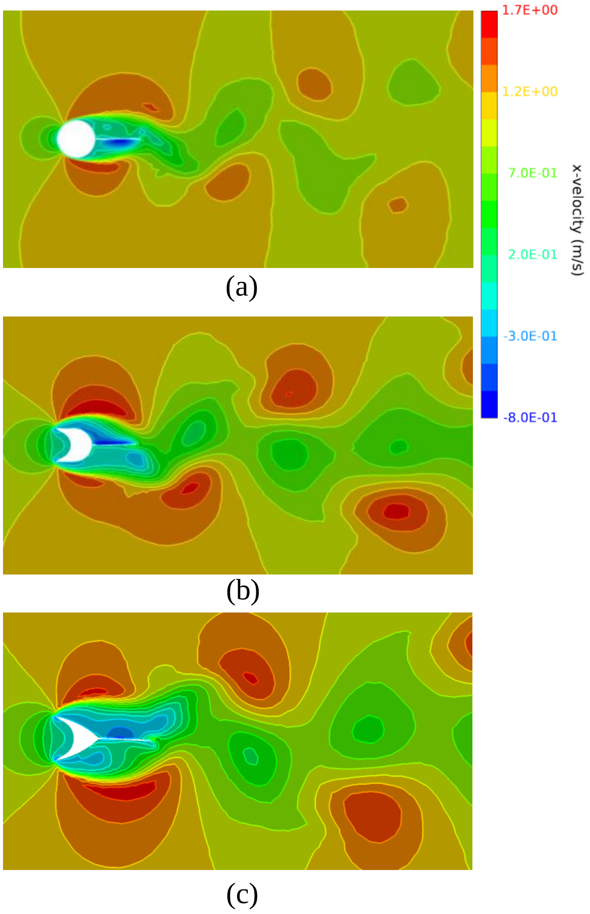

Figure 13. X-velocity contours of Cylinder (a), MGX-1 (b), and TSN (c).

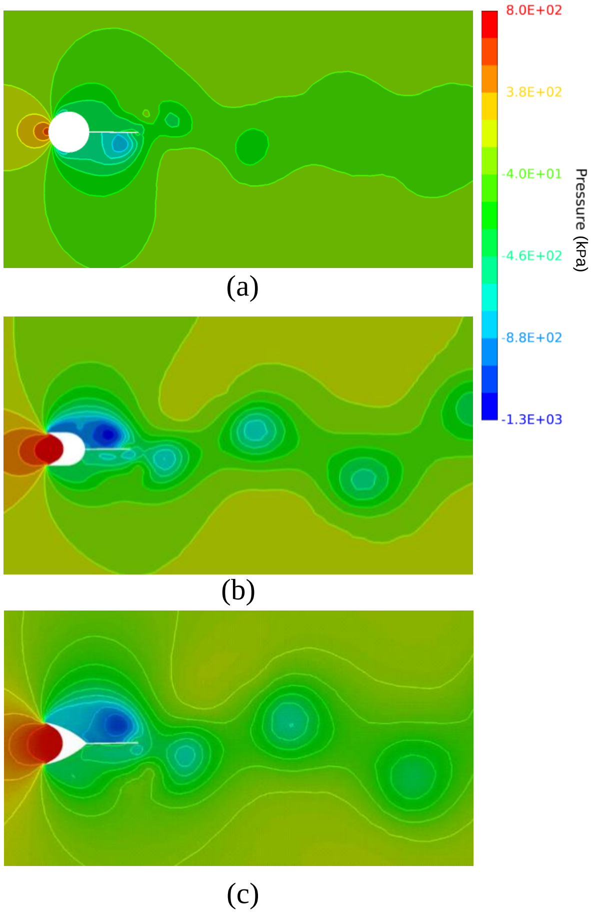

Figure 14. Pressure contours of Cylinder (a), MGX-1 (b), and TSN (c).

The presence of sharp edges in the 'MGX-1' and 'TSN' shapes creates higher-velocity regions, as illustrated in Figure 13. In Figure 14, it provides a visualization of the pressure distribution of “MGX-1” and “TSN” compared to the circular cylinder. It is evident that the pressure distribution on the beam of “MGX-1” and “TSN” demonstrates higher intensity compared to the circular cylinder, resulting in a greater pressure difference between the frontal and back sides of the bluff body shape. This difference leads to the higher displacement of the beam.

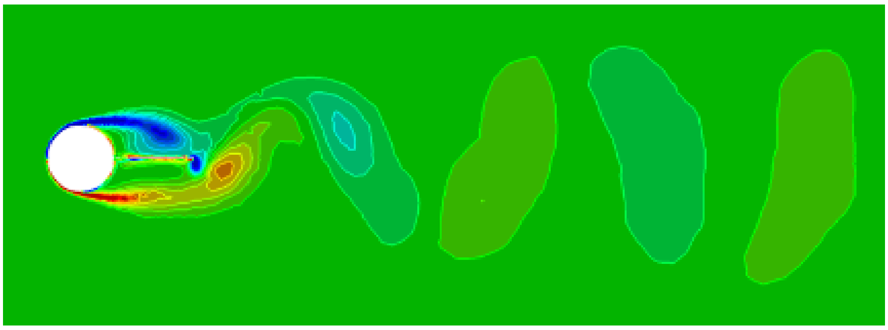

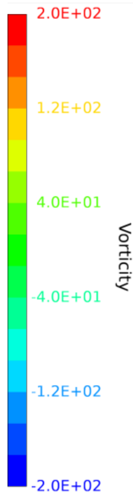

(a)

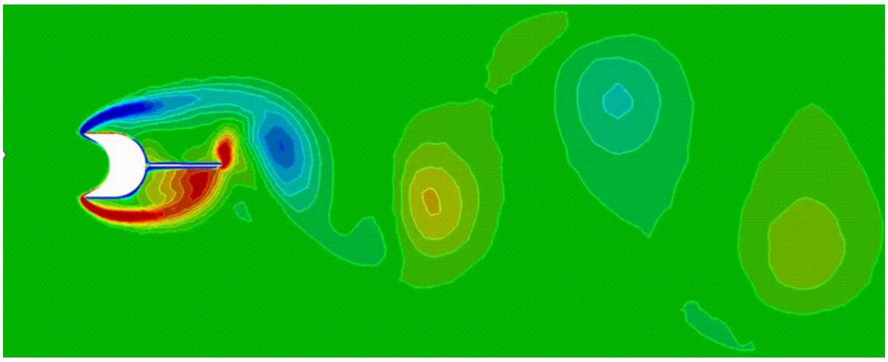

(b)

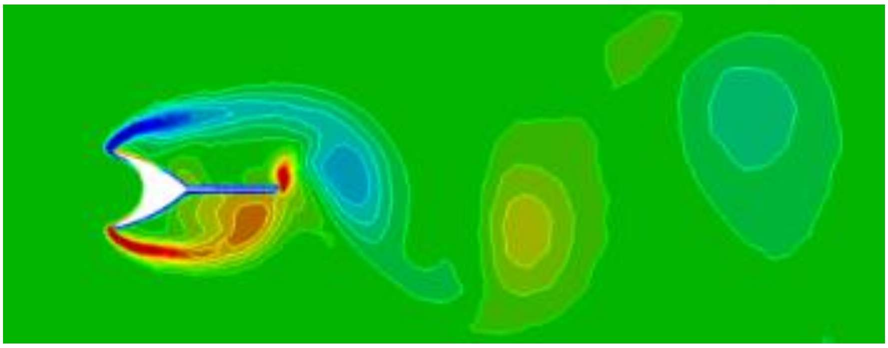

(c)

Figure 15. Vorticity contours of Cylinder (a), MGX-1 (b), and TSN (c).

The vorticity contour results clearly indicate that the separation point occurs at the sharp edges of “MGX-1”, and “TSN” resulting in higher vorticity intensity and larger size compared to the circular cylinder. Notably, in the case of "MGX-1" the vorticity is distributed from the middle towards the end of the beam (Figure 15(b)), which explains why "MGX-1" has a more pronounced effect on beam displacement compared to "TSN". These vortices exert a significant influence on both the beam's displacement and mechanical power.

4.3. Displacement and Power

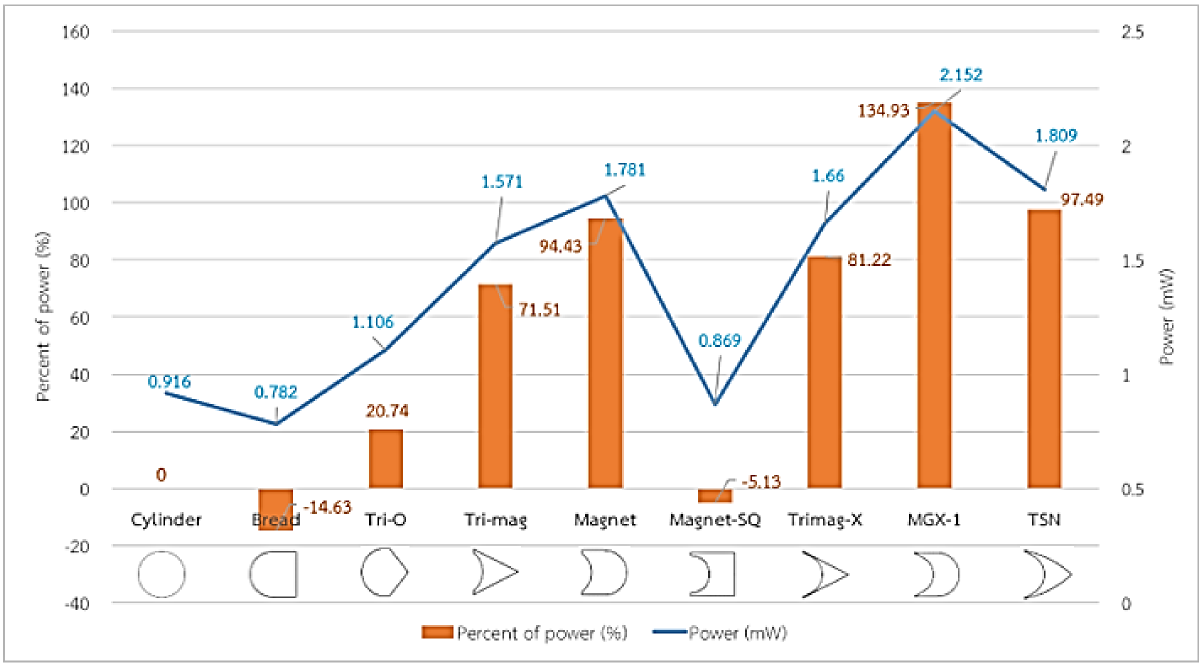

Figure 17. Power of bluff bodies when compare to the cylinder.

The mechanical power generation capabilities of eight bluff body shapes: Bread, Tri-O, Tri-mag, Magnet, Magnet-SQ, Trimag-X, MGX-1, and TSN shown in Figure 17. The results reveal that the "MGX-1" shape stands out, producing the highest mechanical power at 2.152 mW, representing a remarkable 134.93% improvement compared to the standard circular cylinder, which generated 0.916 mW. Among the other seven bluff body shapes, "Bread" generated 0.782 mW with a -14.63% improvement, "Magnet-SQ" produced 0.869 mW with a -5.13% improvement, "Tri-O" yielded 1.106 mW with a 20.74% improvement, "Tri-mag" generated 1.571 mW with a 71.51% improvement, "Trimag-X" produced 1.66 mW with an 81.22% improvement, "Magnet" yielded 1.781 mW with a 94.43% improvement, and "TSN" generated 1.809 mW with a 97.49% improvement.

6. Conclusion

To enhance the efficiency of energy harvesters by capitalizing on vortex-induced vibration phenomena in water flows, we conducted experiments using computational fluid dynamics simulations to design optimal bluff body shapes. In total, we designed 12 bluff body shapes, all sharing the same frontal dimensions of 35 mm in length, 30 mm in width, and 35 mm in height. Among these bluff body shapes, "MGX-1" emerged as the most efficient in improving harveste.r efficiency with 134.93% improvement. Notably, specific characteristics of bluff body shapes significantly influence harvester efficiency. These characteristics include the curvature and sharpness of the frontal area of the bluff body and the curvature at the backside.

7. References

[1] Demirbaş, A. (2006). Global renewable energy resources. *Energy sources, 28*(8), 779-792.

[2] Maradin, D. (2021). Advantages and disadvantages of renewable energy sources utilization. *International Journal of Energy Economics and Policy, 11(3),* 176-183.

[3] Chompamon, P., Tiansiri, R., Chularak, T., Kotwongsa, R., Songschon, S., Saimek, S., Septham, K., & Kamnerdtong, T. (2022). Performance improvement of caudal fin shapes for vortex-induced vibration energy harvesting. In *Proc. Int. Conf. of The 16th Asian Symposium on Visualization* (p 1-6).

[4] Chompamon, P., Tiansiri, R., Chularak, T., Kotwongsa, R., Songschon, S., Saimek, S Septham, K., Kamnerdtong, T. (2022). Performance evaluation of caudal fin shapes for vortex-induced vibration energy harvesting. In *Proc. Int. Conf. of The 12th TSME International Conference on Mechanical Engineering* (p 1-7)

[5] Zhao, D., Hu, X., Tan, T., Yan, Z., & Zhang, W. (2020). Piezoelectric galloping energy harvesting enhanced by topological equivalent aerodynamic design. *Energy Conversion and Management*, 222, 1-11.

[6] Mehdipour, I., Madaro, F., Rizzi, F., & De Vittorio, M. (2022). Comprehensive experimental study on bluff body shapes for vortex-induced vibration piezoelectric energy harvesting mechanisms. *Energy Conversion and Management: X*.

[7] Tarafder, M. S., & Bipul, M. S. I. (2023). Numerical Simulation of Turbulent Flow around Hydrofoil by Spalart-Allmaras Model, In *Proc. Int. Conf. of The 13th International Conference on Marine Technology* (pp. 7)

[8] Li, S., & Sun, Z. (2015). Harvesting vortex energy in the cylinder wake with a pivoting vane. *Energy, 88,* 783-792.

[9] George, W. K. (2013). *Lectures in Turbulence for the 21st Century*. Chalmers University of Technology.

CST0015

The heat distribution modeling on solar panels to develop cooling methods

Wiriya Borisut[1,*], Chamnan Pedchote[1], Prayoon Kunyoo[1], Supakan Keawleam[1], and Phongsakorn Thawonsatid[2]

[1]Navaminda Kasatriyadhiraj Royal Air Force Academy, 999 Midtrapab, Muak lak, Saraburi , 18180, Thailand
[2]GC Maintenance and Engineering company limited, 22/2 Maptaphut, Rayong, 21150, Thailand

* Corresponding author: wiriya.bori@rtaf.mi.th

Abstract. Recently, Computer aided design in engineering (CAE) is an important tools for many engineering design. Which the researchers apply CAE in the design of heat transfer. Finite Element analysis (FEA) is part of CAE. This FEA techniques was utilized to evaluate the heat dissipation on the solar cell panels which were used at NKRAFA in order to enhance heat dissipation efficiency. For this research, Ansys Stedy Stage Thermal program was used. The solar thermal energy is constant in boundary conditions. The results indicated that the heat dissipation type gap 2 mm. was the most suitable condition.

Keywords: FEA, CAE, Heat transfer, Simulation.

1. Introduction

A few years ago, the world has faced a crisis due to the COVID-19. Including the energy crisis resulting from the Ukraine-Russia war causing a direct impact on the ability to produce energy. By considering the cost of producing electricity. Coal is considered a cost-effective fuel. But the quantity available in that country has decreased. Moreover, the import of coal or building a coal-fired power plant, there is opposition from Independent agencies and citizens. If considering energy from natural gas which is a large amount of energy used in the country. There will be a risk of fluctuating price factors. According to world market prices. By producing electricity from the above. It is the main production method of the country.

Nowadays, the world's population has increasingly switched to using alternative energy. To help alleviate the burden of producing electricity. Whether it is solar energy, wind energy, geothermal energy, etc. As mentioned above, this alternative energy source has many limitations.

Geothermal energy, Use heat from beneath the ground from heat sources such as hot springs to bring heat to the working flued and used to produce electricity which has limitations on location Because it is close to tourist attractions and the production capacity rate is not very high.

For Thailand solar energy is glow up trend, in record since 2008 to 2018 solar energy is an upward trend. The government has a policy to promote the use of clean energy of which solar energy is one of them.

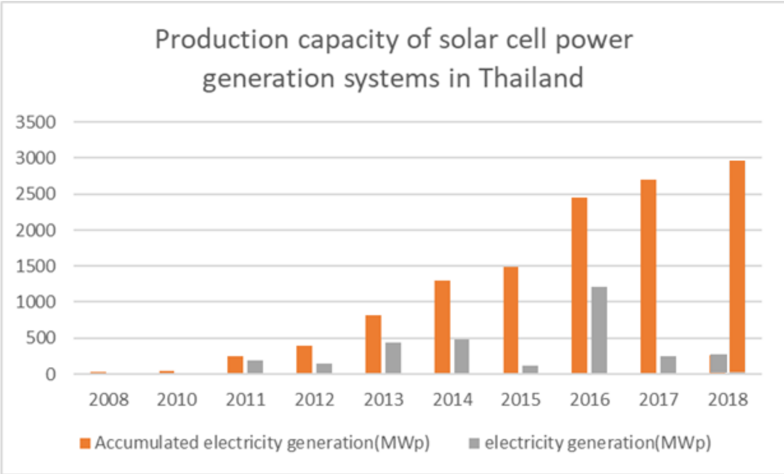

Figure 1. Production capacity of solar cell power generation systems in Thailand.

If the temperature rises, the heat must be reduced by using the active cooling method to make the solar cell have better performance. [2] Computational fluid dynamics (CFD) simulation and calculation of the cooling efficiency of the air ducts under the solar panels. As a result, solar cell performance increases by 12%-14% compared to solar cell panels without cooling. It will have an efficiency of only 8%-9%. [3]Experiments to increase work efficiency By spray cooling water on the PV module, the result is that it can reduce the temperature. and clean dust on the surface of the solar cell panel [4]

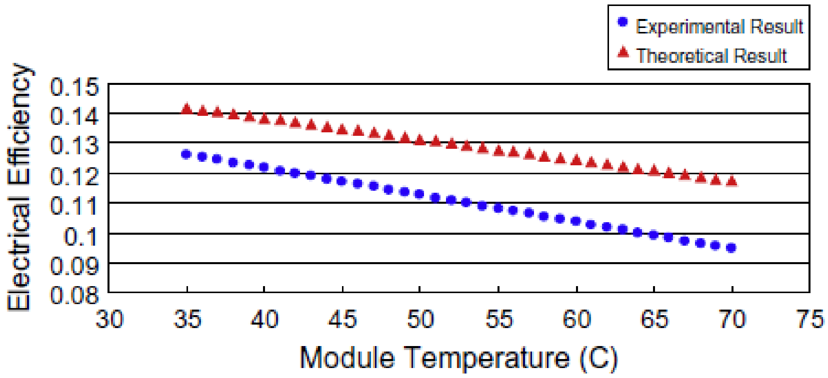

Figure 2. Compare temperature and electrical Efficiency [2].

2. Computational detail

2.1. CAD and Meshing

In this project presentation 5 cases of heat transfer models in different fin pattern layout. The fins geometry has Constance thickness 2 mm. and high 4 mm.

1. Solar panel stand alone
2. Solar panel with fin distance 2 cm.
3. Solar panel with fin distance 4 cm.
4. Solar panel pattern A (20 fin mid panel)
5. Solar panel pattern B (double fin distance 4 cm)

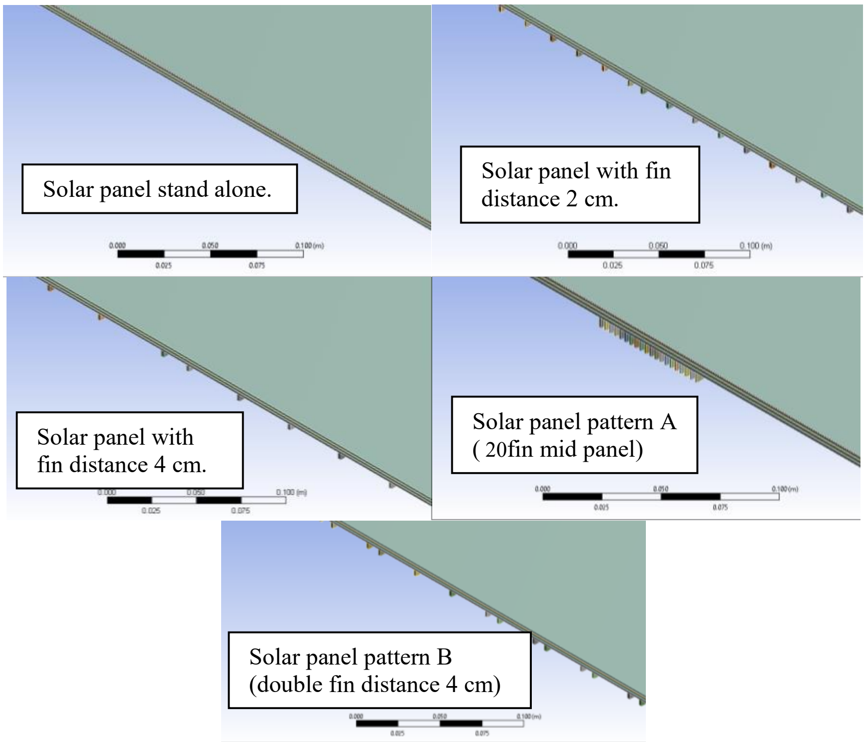

Figure 3. 3D model of fin arrangement on various types of solar panels.

In the solar panel have 5 layer The solar panel consists of The top layer is glass, the next layer is PVF, PV, PVF and back sheet. For this research have many fins under the solar panel show layout in figure 3.

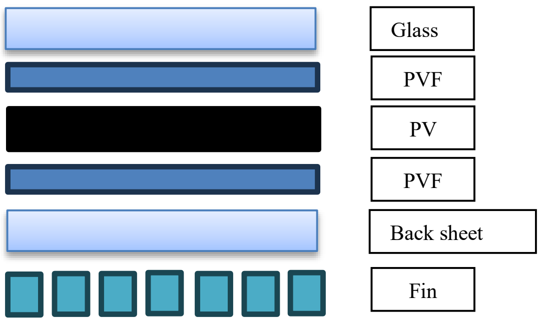

Figure 4. The placement of each layer within the solar panel.

For mesh detail show in Table 1.

Table 1. Mesh statistics.

Mesh	Non-Fin	Fin thick 2 mm. high 4 mm.			
		Gap 2 cm	Gap 4 cm	Pattern A	Pattern B
node	1618440	1783840	1704448	1684600	1777224
element	229625	243375	236775	235125	242825

The mesh is checked by grid independent the mesh resolution into fine mesh have 229,625 element the average temperature is 80.58 ºC, medium mesh have 129,375 the average temperature 80.64ºC and coarse mesh have 82,500 element the average temperature is 80.63ºC.

2.2. Boundary conditions

Assume that solar energy is constant and apply on the top layer 500 kJ/m^2 because this area has a lot of rain. And use convection coefficient constant 3 W/m^2 convection surface in top surface side surface bottom surface and fin surface. the heat transfer models assume steady state thermal. Material properties used constant value show in Table 2.

Table 2. Material properties [1].

Components	Thickness (mm)	Density (kg/m^3)	Thermal Conductivity	Heat Capacity
PV	1.5	2330	148	677
Back Sheet	1.5	960	2090	0.35
Glass	1.5	3000	500	1.8
PVF	0.5	1200	1250	0.2

3. Result

The study focuses on the fin pattern for cooling solar panel compare non-cooling solar panel. In the simulation based on finite element method (FEM) the temperature of all element calculate by Stedy-State Thermal in Ansys 18.1. The accuracy of the calculation results depends on the boundary condition settings.

3.1. Result non-cooling

In this simulation results in case non-cooling, the maximum and lower temperature on the top of glass were 81.05 C and 79.73 C. the average temperature was 80.82 C. The highest temperature is in the center of solar panel show in figure 5.

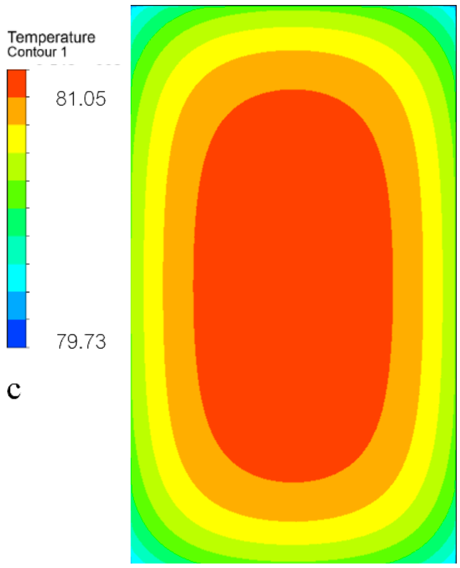

Figure 5. Show the temperature distribution on the non-cooling solar panel.

3.2. Result with-cooling
The simulation results show the fins effects of cooling and temperature distribution on the solar panel. the fin cooling can reduce temperature on the solar panel. show in the Table 3.

Table 3. The temperature of the solar panel with cooling

	non-fin	gap 2 cm	gap 4 cm	pattern A	pattern B
Temperature Max C	81.05	58.55	62.14	64.85	59.12
Temperature Min C	79.73	57.25	60.44	57.05	57.51
Temperature Average C	80.82	57.44	61.04	62.831	57.72

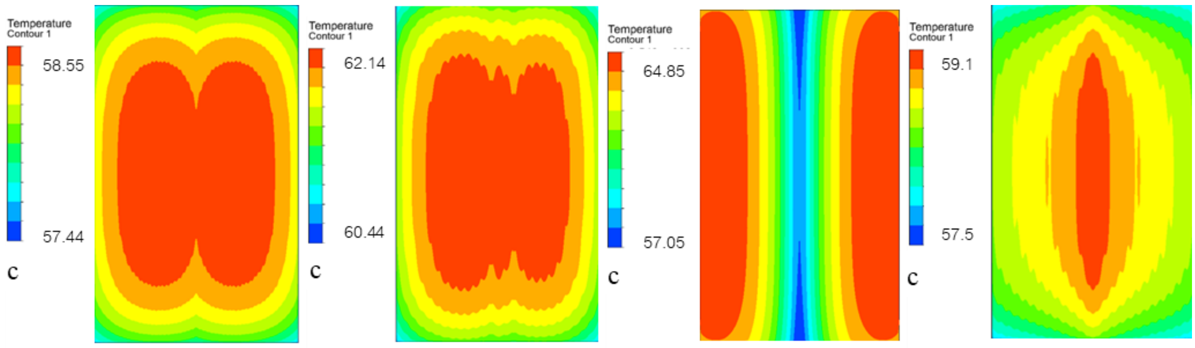

Figure 6. Show the temperature distribution on the cooling solar panel.

3.3. Validation with experiment
It is necessary to calibrate the modeling results with the experimental results. To increase the accuracy of modeling results. From the experimental results in the case of no cooling. It was found that the average temperature was degrees, the highest temperature was 70.25 °C , and the lowest temperature was 63.00°C .

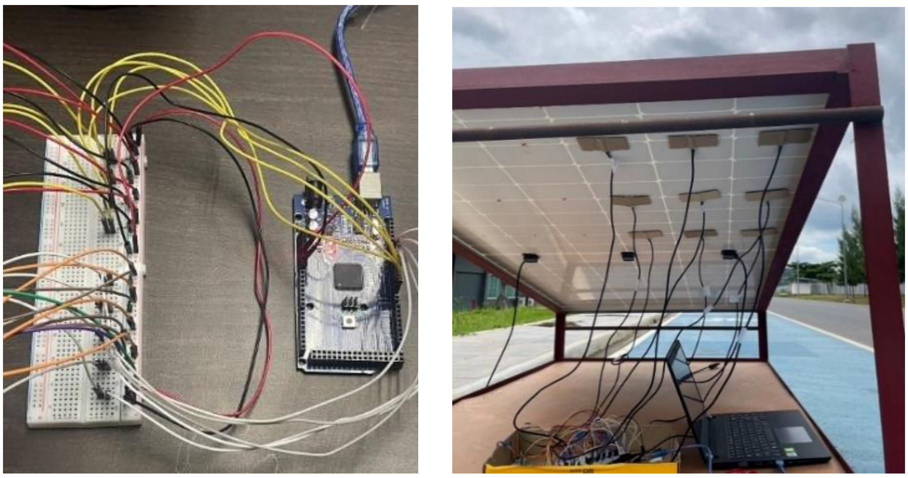

Figure 7. Installing the temperature data collection unit.

4. Conclusion

From the modeling results, it was found that the *2* cm orientation pattern was the best, which was able to reduce the average temperature to 57.44 degrees Celsius, accounting for 71.1% of the average temperature in the case without installing a cooling system. In this model, it is only an analysis to see the trend of temperature distribution. For higher accuracy is desired, it should be done with experimentation.

5. References

[1] Jaemin Kim and Yujin Nam. (2019). Study on the Cooling Effect of Attached Fins on PV Using CFD Simulation. *Energies 2019,12,758;doi:10.3390/en12040758*

[2] H.G. Teo,P.S Lee, M.N.A. Hawlader (2012). An active cooling system for photovotaic modules. *Applied Energy 90(2012)*,309-315

[3] Moharram, K.A.; Abd-Elhady, M.S.; Kandil, H.A.; El-Sherif, H. Enhancing the performance of photovoltaic panels by water cooling. Ain Shams Eng. J. 2013, 4, 869–877

[4] D'Angola, A.; Zaffina, R.; Emescu, D.; Di Loe, D.; Fracastoro, G.V.; Sperino, F. Best compromise of net power gain in a cooled photovolataic system. In Proceedings of the 2016 51st International Universities Power Engineering Conference, Coimbra, Portugal, 6–9 September 2016.

CST0016

Acoustic noise reduction using a set of circular arc splitter plates

P Pagdisongkram, J Tunkeaw, and W Rojanaratanangkule*

Department of Mechanical Engineering, Faculty of Engineering,
Chiang Mai University, Chiang Mai, Thailand

* Corresponding Author: watchapon.roj@eng.cmu.ac.th

Abstract. Acoustic noise is generated by a sound wave and is a variation from the ambient atmospheric pressure. The fluctuating density of the gas is the fundamental property of compressible flow. Through an equation of state, the density of the gas is proportional to its temperature and pressure. Direct computations of acoustic noise of flow across a circular cylinder are performed at a chord-based Reynolds number of 150 and a freestream Mach number of 0.2 by solving the compressible Navier-Stokes equations without the use of any modeling. To reduce noise across the cylinder, the splitter plates with a circular arc body are deployed concentrically near the top, middle, and bottom of the cylinder. The result of the installation of the additional splitter plate at the middle of the cylinder improves noise reduction from the radiated sound waves up to 11*dB*.

Keywords: Direct numerical simulation, Compressible flow, Splitter plate, Boundary data immersion method, Far-field noise, Cylinder flow.

1. Introduction

For the past several decades, flow past a bluff body has been interested by researchers due to flow separation and vortex shedding of the flow field leading to aerodynamic sound and fluctuating forces. Unsteady forces are crucial details for structural design because their amplitudes and frequencies could damage the structure through vortex-induced vibrations [1]. In aeroacoustics, noise is created primarily from surface pressure fluctuations [2] which could accumulate radiation and become unsafe if not properly controlled. Active or passive flow control techniques [3] can be applied to reduce the fluctuation from the vortex shedding. The vortex shedding correlates with unsteady aeroacoustic sound.

In this work, the Boundary Data Immersion Method (BDIM) is implemented. This extension of the virtual boundary method made for compressible viscous fluid flow which has the potential to simulate aeroacoustic sound and moving body in fluid flow [4]. Its predecessor, the immersed boundary method [5], was mainly used in a case where boundary conditions do not conform with the computational grid, yet itself and its extensions were made for incompressible cases rendering it inapplicable for this case.

In the aeroacoustic field, sound reduction is one of the main goals. Strouhal realized that aeolian tone is related to the frequency of radiated sound around the diameter of a cylinder to the freestream velocity [6]. Splitter plates are tools that have been used in many studies. You *et al.* [7] solved two-dimensional (2D) incompressible Navier-Stokes equations using Curle's solution [2] that was enhanced from Lighthill's acoustic analogy [8] to simulate the effect of solid boundaries on sound generation by inserting splitter plates and concluded that noise was mainly from dipole rather than quadrupole noise same as Curle [2] predicted that dipoles influence the sound field over quadrupoles in low-speed condition where Karman vortex street occurs. Curle predicted that sound linked to drag force gives twice the frequency of vortex shedding whereas lift force and sound share the same frequency.

2. Numerical Approach

2.1. Governing Equations

An acoustic noise of the flow over a two-dimensional cylinder was performed by using an in-house compressible Direct Numerical Simulation (DNS) code [9]. The code solves the full Navier-Stokes equations in a non-dimensional conservative form [10] in mapped computational space (ξ,η) as

$$\frac{\partial Q}{\partial t}+\frac{\partial E}{\partial \xi}+\frac{\partial F}{\partial \eta}=\frac{\partial E_v}{\partial \xi}+\frac{\partial F_v}{\partial \eta} \ , \tag{1}$$

where the conservative variable and the convective fluxes in generalized coordinates are given as

$$Q = JQ \quad \text{and} \quad E = y_\eta E - x_\eta F \quad , \quad F = -y_\xi E + x_\xi F \ , \tag{2}$$

and the viscous fluxes in generalized coordinates are

$$E_v = y_\eta E_v - x_\eta F_v \ \text{, and} \ F_v = -y_\xi E_v + x_\xi F_v \ . \tag{3}$$

The conservative variable, convective fluxes, and viscous fluxes in cartesian coordinates are

$$\begin{aligned} &Q=[\rho,\rho u,\rho v,E_T]^T \ , \\ &E=[\rho u,\rho uu+p,\rho uv,u\left(E_T+p\right)]^T \ , \\ &F=[\rho v,\rho uv,\rho vv+p,v\left(E_T+p\right)]^T \ , \\ &E_v=[0,\tau_{xx},\tau_{xy},-q_x+u\tau_{xx}+v\tau_{xy}]^T \ , \\ &F_v=[0,\tau_{yx},\tau_{yy},-q_y+u\tau_{yx}+v\tau_{yy}]^T \ , \end{aligned} \tag{4}$$

where J is the Jacobian matrix and, *e.g.*, $y_\eta = \partial y / \partial \eta$ is the transformation matrix. The quantity ρ fluid density, t is time, p is pressure, and $\tilde{I}$ is the identity tensor. The $u_i = (u_1, u_2) = (u, v)$ is the velocity vector in cartesian coordinates $x_i = (x_1, x_2) = (x, y)$ respectively. The viscous stress tensor τ_{ij} for the compressible flow [11] is given as

$$\tau_{ij} = \frac{\mu}{Re_\infty}\left(\frac{\partial u_i}{\partial x_j}+\frac{\partial u_j}{\partial x_i}-\frac{2}{3}\frac{\partial u_k}{\partial x_k}\tilde{I}\right) \ , \tag{5}$$

the total energy E_T and heat flux q_j [10, 12] are

$$E_t = \rho C_v T + \frac{1}{2}\rho u_i u_i \ \text{, and} \ q_j = -\frac{\mu}{Re_\infty}\left(\frac{\gamma}{Pr}C_v\frac{\partial T}{\partial x_j}\right) \tag{6}$$

To close the system of equations, the Equation of State (EOS) [10] is solved to obtain the pressure as

$$p = \rho\left(\gamma - 1\right)C_v T \tag{7}$$

where $\gamma = 1.4$ is the specific heat ratio, $Pr = 0.72$ is Prandtl number, T is temperature, and μ is the dynamic viscosity which is computed by using Sutherland's law with the Sutherland constant of about 0.36867 [13]. The freestream Reynolds number is $Re_\infty = \rho_\infty u_\infty D / \mu_\infty$ and the specific heat capacity at constant volume is $C_v = 1/\gamma(\gamma-1)M_\infty^2$ while the freestream Mach number and a cylinder diameter are M_∞ and D respectively.

2.2. Computational domain and meshing

The computational domain for simulating aerodynamic noise is separated into two zones, the physical and buffer zones, as shown in Figure 1 .The physical zone is identified as a sound zone which is in the range of radial $0.5 \le r/D \le 100$, while the rest is namely the buffer zone which is used to filter out acoustic disturbances [14]. The splitter plates inside the domain are represented by the BDIM. The length, thickness, and location of each plate are shown in Table 1.

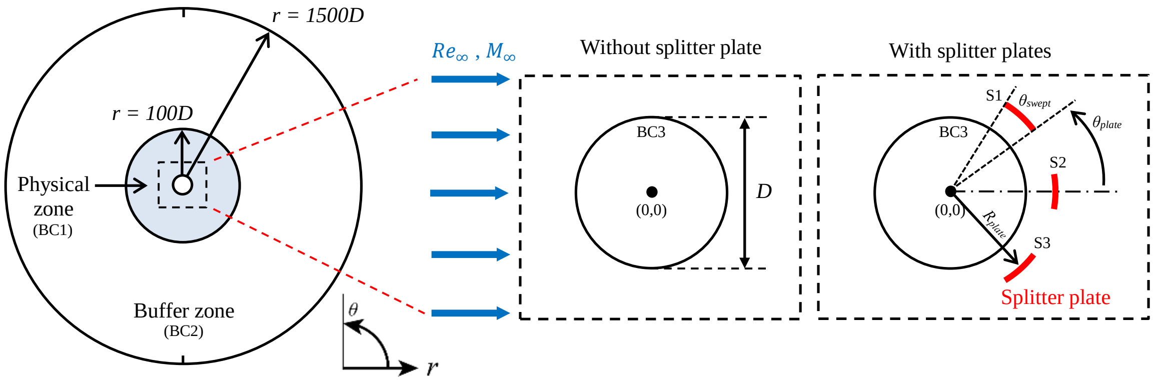

Figure 1. Schematic of the computational domain of flow past cylinder without splitter plate (NP0) and with splitter plates (NP2: with S1 and S3, NP3: with S1, S2, and S3).

Table 1. Location and sizing of each splitter plate.

Splitter plates	θ_{plate}	θ_{swept}	Thickness	R_{plate}
S1 (top)	60°	10°	0.005	0.84
S2 (middle)	0°	20°	0.005	0.84
S3 (bottom)	-60°	10°	0.005	0.84

Inside the physical zone, a very fine grid resolution was defined with the smallest grid spacing of about $\Delta r = 0.005D$ in the radial direction. This grid spacing was kept equidistant for about 101 grid points near the wall boundary condition to capture the pressure field. Then, it was gently stretched using polynomial stretching methodology [4] to $\Delta r = 0.02D$ at $r = 100D$. After that, it was greatly stretched to $\Delta r = 20D$ at the end of the buffer zone. As a result, the number of grid points in the radial direction is 871 (711 points in the physical zone and 160 points in the buffer zone). 513 grid points of grid spacing in the radial direction can be seen in Figure 2(b). For the azimuthal direction, a uniform grid spacing was applied over both zones. An example of this mesh can be seen in Figure 2(a).

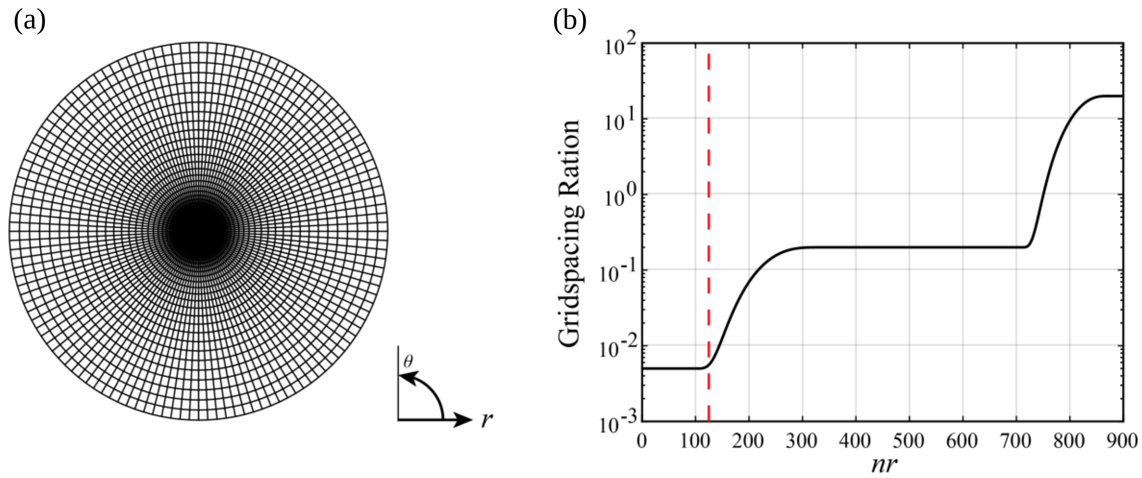

Figure 2. (a) Overall details of O-grid mesh used in this work and (b) Grid spacing in *x*-direction. The range of the physical zone is specified by the red dashed line.

2.3. Initial and boundary conditions

In this work, the simulations were divided into 3 cases, NP0: without a splitter plate, NP2 with top and bottom splitter plates (S1 and S3), and NP3 with top, middle, and bottom splitter plates (S1, S2, and S3). As seen in Figure 1, to study acoustic noise. The initial parameters for all cases are not different. The freestream density ρ_∞, velocity u_∞, temperature T_∞, and diameter D are equal to one. The freestream Reynolds number and Mach number are set to be and respectively [15]. For the boundary conditions, a uniform velocity was applied at the left side of the computational domain (BC1 side, as illustrated in Figure 1 and the no-slip condition on the wall boundary of a cylindrical (BC3 side). A Zonal Characteristic Boundary Condition (ZCBC) was applied to the buffer zone around the physical zone to prevent the reflected acoustic waves inside the computational domain [16].

2.4. Spatial and temporal discretization

The numerical simulations were performed by using an in-house DNS code. The code solves the governing equations in generalized coordinates. The temporal derivative term is solved by a five-step fourth-order accurate Runge-Kutta (RK45) scheme [17]. The spatial derivative terms are performed with a novel wavenumber-optimized Compact Finite Difference (CFD) scheme [18] near-spectral accuracy. This scheme offers low dispersion and dissipation errors. The time step for these schemes is set to be $\Delta t = 0.0025$ for all simulations and the maximum Courant-Friedrichs-Lewy (CFL) number is lower than 0.9 for all cases.

3. Simulation Results

3.1. Aerodynamic forces

Initially, the results were done with the case without a splitter plate as a validation study, the mean drag coefficient (C_D) and drag amplitude fluctuation of NP0 in Table 2 are comparable to Inoue and Hatakeyama's results (~1.34) and (~0.026) [14] and Mahato *et al.*'s results (~1.34) and (~0.0256) [15]. Whereas the lift fluctuation amplitude (0.51) is noticeably more compared to the drag fluctuation amplitude (0.026).

Table 2 shows that the drag reduction has been improved after splitter plates are added due to the flow separation delay similar to Mahato *et al.* [15] where the flow separation angle is also shifted from

NP0 at 113° to 123-124° which can be implied from where friction coefficient (C_f) values change its sign in Figure 3(b). The pressure coefficient (C_p) in Figure 3(a) indicates a severe pressure drop in NP0 explaining the cause of drag.

Table 2. Results of force coefficients and Strouhal number.

Cases	C_D	C_L	St
NP0	1.33 ± 0.026	0.0 ± 0.510	0.1824
NP2	1.20 ± 0.008	-0.00204 ± 0.31	0.1327
NP3	1.16 ± 0.006	0.00187 ± 0.14	0.1328
Inoue & Hatakeyama [14]	1.34 ± 0.026	0.0 ± 0.520	0.1830
Mahato *et al.* [15]	1.34 ± 0.025	0.0 ± 0.525	0.1824

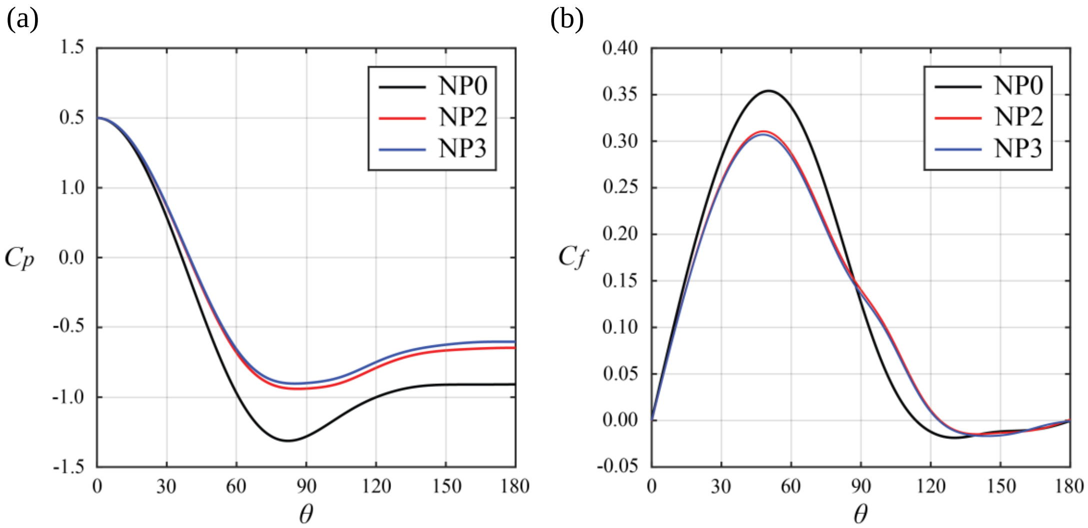

Figure 3. Variation of (a) time-averaged pressure coefficient and (b) friction coefficient with θ at Re = 150 and M = 0.2.

3.2. Vorticity of separated shear layers

Figure 4 shows vorticity contours of each case when the lift coefficient is at its peak value. The similarity of those results is the top part of vortex shedding covers the bottom part of vortex shedding while the lift is gained. NP0 has the shortest distance between the highest vorticity position of the soon-to-shed vortex and the cylinder's center whereas NP2 and NP3 have farther distance downstream due to the stretched separated shear layers in the freestream direction with NP3 having the farthest distance.

The backside of the cylinder region of NP0 is extremely contrasting between negative vorticity and positive vorticity creating higher lift fluctuation amplitude and higher vortex shedding frequency than other cases that have a vorticity cancellation effect [19]. The vorticity cancellations occur in NP2 and NP3 where both cases have splitter plates to create small separated shear layers that have opposite signed vorticity squeezing between larger separated shear layers with opposite signed vorticity with respect to the smaller one near the top and bottom of the cylinder simultaneously, causing them to interact among themselves and creating low vorticity zone further downstream directly after the small separated shear

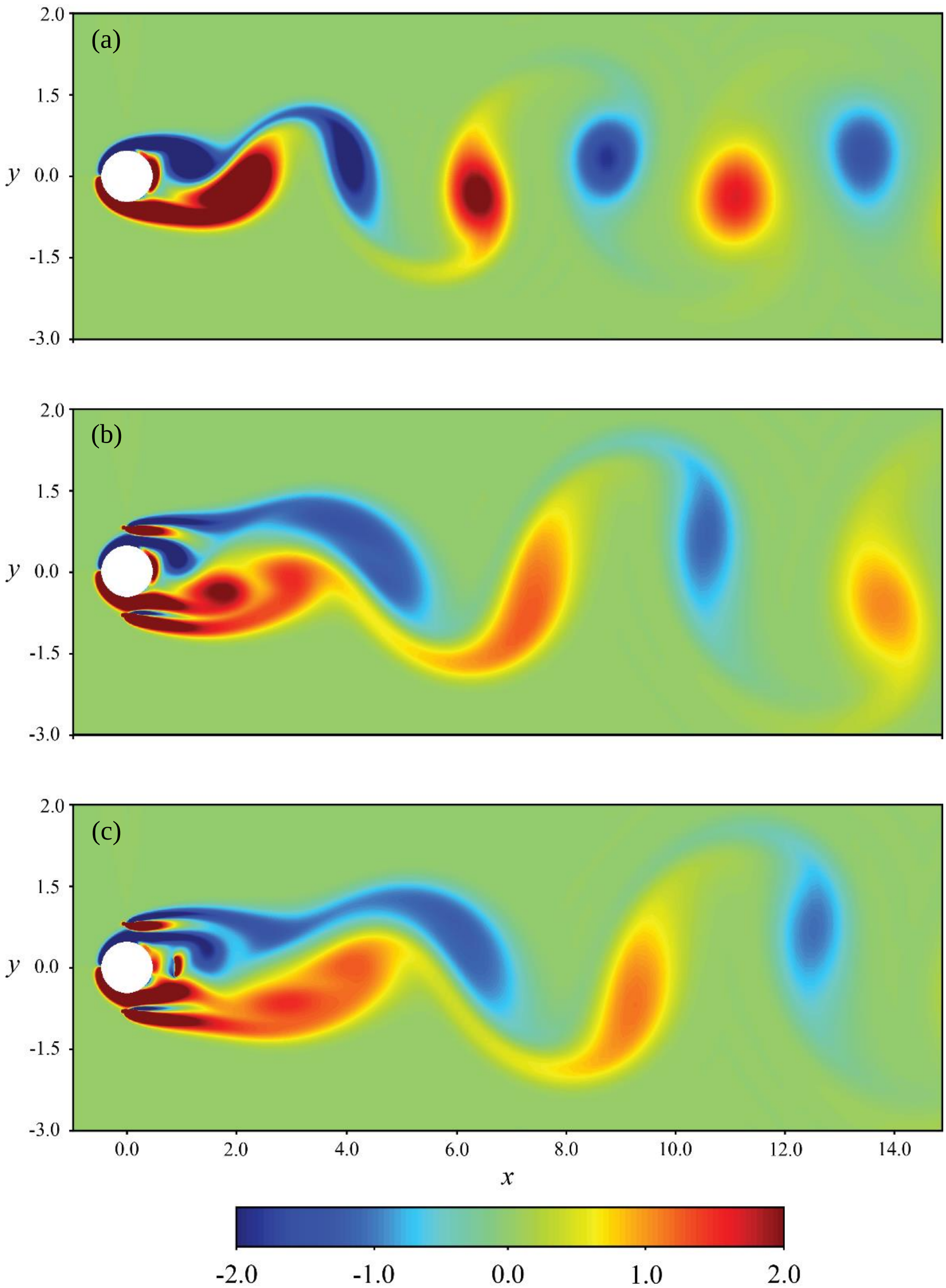

Figure 4. Vorticity contours of case (a) NP0, (b) NP2, and (c) NP3.

layers with opposite signed vorticity that are previously mentioned. This results in an overall weakened vorticity zone and stretched separated shear layers behind the cylinder. NP3 additionally negates vorticity within the gap between the cylinder and splitter plate resulting in weaker vorticity in the shear layer on the cylinder surface and then further reduces lift fluctuation. The greater shedding frequency of NP0 can be observed by the estimated number of vortices within the same streamwise direction of contour plots while NP2 and NP3 have more distance between each shedding vortices and hence the smaller Strouhal number than NP0.

3.3. Radiated sound fields

From the modified amplitudes of wave modes, Inoue and Hatakeyama showed that lift dipole has a control over the pressure field compared to drag dipole [14] where the pressure waves propagate perpendicularly to the freestream direction from the pressure fluctuations. Figure 5 shows the disturbance pressure field of all cases both without and with splitter plates. Both cases prove that the lift dipole has greater influence over the drag dipole and hydrodynamic disturbances are dominant in the wake region. The results are similar to the DNS results of Inoue and Hatakeyama [14] and Mahato *et al*. [15] for NP0. NP2 and NP3, also have similar pressure fields to Mahato *et al*.'s results [15] where the overall strength of the radiated sound field is reduced when splitter plates are added except for the strength in the perpendicular direction to the freestream is higher than the strength in the streamwise direction. With additional splitter plates, the overall strength of the radiated sound field is further reduced in all directions where the strength in perpendicular direction remains highest due to the lift dipole.

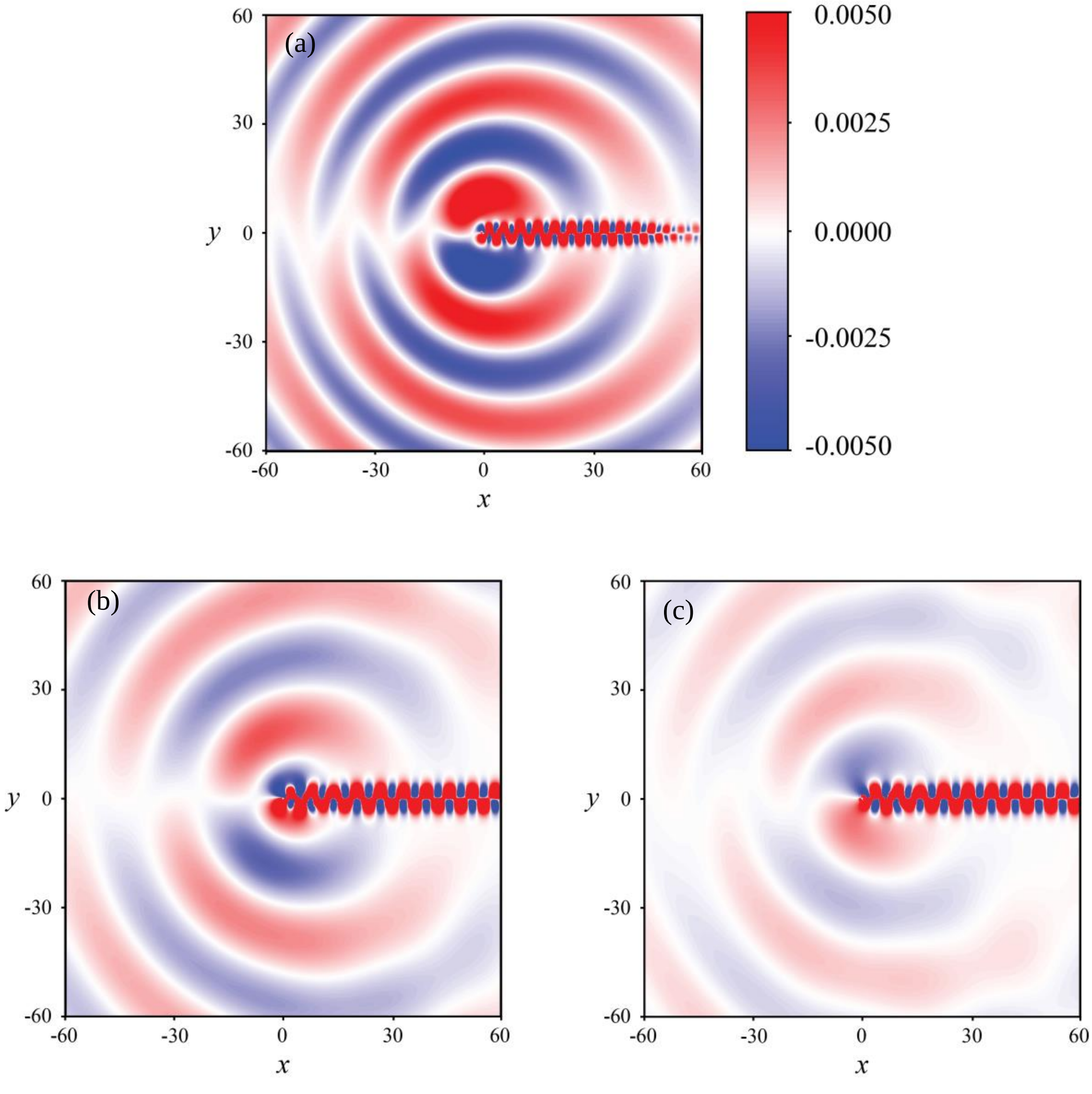

Figure 5. Disturbance pressure field contours of (a) NP0, (b) NP2, and (c) NP3.

The directivity plots (Figure 6(a)) of the disturbance pressure field's RMS value show a trace of dipole noise which is the main source of radiated sound from the flow. NP2 and NP3 share the same directivity pattern and seem to have noise interrupting in the perpendicular direction to the freestream causing the plots to be rippled unlike NP0, possibly from the results of lift dipole and sound waves reflecting from the splitter plates comparable to the effect in Figure 5 where it has higher strength in perpendicular direction. The splitter plates help reduce the RMS values of the disturbance pressure field and the additional plate further reduces it in NP3. Ultimately, the evidence is added up to the last results in Figure 6(b) on how the noise is reduced in each case with respect to NP0 where NP3 turns out to be the best setting of all the cases with the most noise reduction of 11.1dB followed by NP2 with 5.3dB noise reduction.

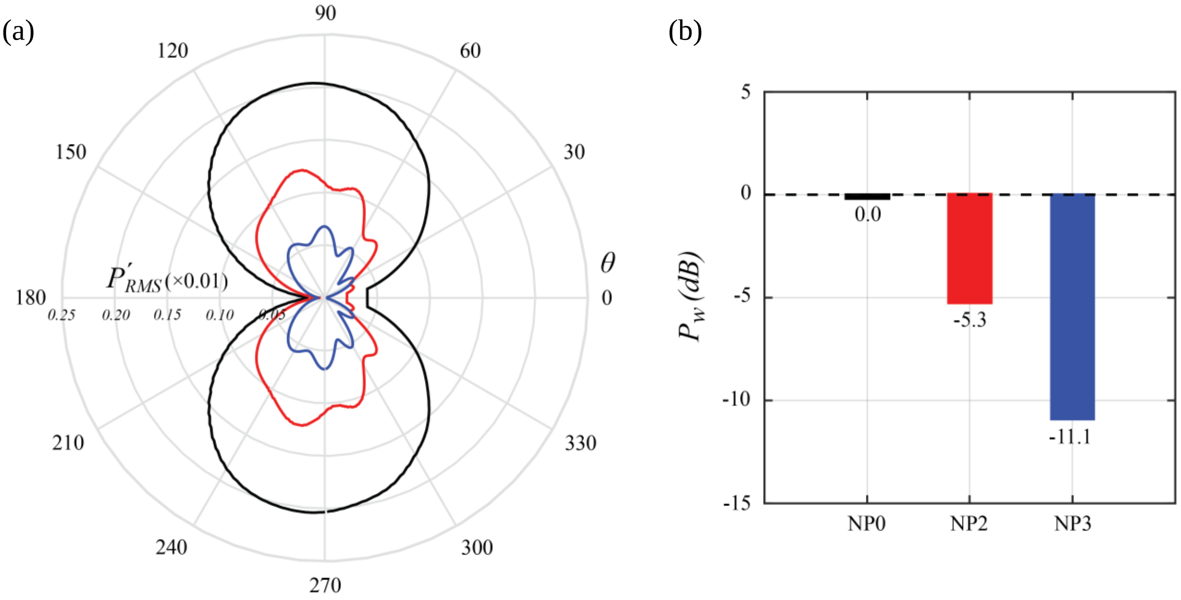

Figure 6. (a) Directivity patterns from RMS value of $p'(x, y, t)$ and (b) Net radiated sound power P_w with NP0 as reference.

4. Conclusions

The results of the simulation of flow past a cylinder with splitter plates at chord-based Raynolds number, $Re_\infty = 150$, and Mach number, $M_\infty = 0.2$, using in-house compressible DNS code have shown that splitter plates (NP2 and NP3) can help to reduce the flow and sound disturbances with maximum noise reduction of 11.1dB with respect to NP0. The lift and drag fluctuation amplitudes are greatly decreased from 0.51 to 0.14 in lift coefficient as well as the reduction in vortex shedding frequency from $St = 0.1824$ to 0.1328. These reduced values result in decreased strength of lift dipoles which are the main sources of noise and eventually significantly reduce the noise. The use of splitter plates diverts the separated shear layers from the cylinder surface and splitter plates into vortex cancellation creating a low vorticity zone, especially in NP3 where it negates the vorticity of shear layers on the cylinder surface and helps reduce additional noise.

5. Acknowledgments

This work was supported by the graduate school, the Department of Mechanical Engineering, Faculty of Engineering, Chiang Mai University, and the Royal Golden Jubilee (RGJ) Ph.D. program for the research grant and the Computational Turbulence and Aerodynamics Research (CTAR) lab for the High-Performance Computing (HPC) services.

6. References

[1] Williamson, C. H. K., & Govardhan, R. (2004). Vortex-induced vibrations. Annual Review of Fluid Mechanics, 36(1), 413–455.

[2] Curle, N. & Lighthill, M. J. (1955). The influence of solid boundaries upon aerodynamic sound. Proceedings of the Royal Society of London, 231(1187), 505–514.

[3] Choi, H., Jeon, W.-P., & Kim, J. (2008). Control of flow over a bluff body. Annual Review of Fluid Mechanics, 40(1), 113–139.

[4] Schlanderer, S. C., Weymouth, G. D., & Sandberg, R. D. (2017). The boundary data immersion method for compressible flows with application to aeroacoustics. Journal of Computational Physics, 333, 440–461.

[5] Mittal, R., & Iaccarino, G. (2005). Immersed boundary methods. Annual Review of Fluid Mechanics, 37(1), 239–261.

[6] Strouhal, V. (1878). Ueber eine besondere Art der Tonerregung. Annalen der Physik, 241(10), 216–251.

[7] You, D., Choi, H., Choi, M.-R., & Kang, S.-H. (1998). Control of flow-induced noise behind a circular cylinder using splitter plates. AIAA Journal, 36(11), 1961–1967.

[8] Lighthill, M. J. (1952). On sound generated aerodynamically I. General theory. (1952). Proceedings of the Royal Society of London, 211(1107), 564–587.

[9] Sandberg, R. D. (2013). Direct numerical simulations for flow and noise studies. Procedia Engineering, 61, 356–362.

[10] Tunkeaw, J., & Rojanaratanangkule, W. (2021). A discontinuity-capturing methodology for two-phase inviscid compressible flow. Warasan Witsawakamsat. Chulalongkorn University, 25(11), 45–56.

[11] Borvornsareepirom, N., & Rojanaratanangkule, W. (2022). A two-dimensional numerical investigation of aerodynamic noise from an inclined plate. Warasan Witsawakamsat. Chulalongkorn University, 26(6), 41–52.

[12] Beig, S. A., Aboulhasanzadeh, B., & Johnsen, E. (2018). Temperatures produced by inertially collapsing bubbles near rigid surfaces. Journal of Fluid Mechanics, 852, 105–125.

[13] White, F. M. (2006). Viscous Fluid Flow (3rd ed.). McGraw-Hill.

[14] Inoue, O., & Hatakeyama, N. (2002). Sound generation by a two-dimensional circular cylinder in a uniform flow. Journal of Fluid Mechanics, 471, 285–314.

[15] Mahato, B., Ganta, N., & Bhumkar, Y. G. (2021). Effective control of aeolian tone using a pair of splitter plates. Journal of Sound and Vibration, 494(115906), 115906.

[16] Sandberg, R. D., & Sandham, N. D. (2006). Nonreflecting zonal characteristic boundary condition for direct numerical simulation of aerodynamic sound. AIAA Journal, 44(2), 402–405.

[17] Kennedy, C. A., Carpenter, M. H., & Lewis, R. M. (2000). Low-storage, explicit Runge–Kutta schemes for the compressible Navier–Stokes equations. Applied Numerical Mathematics: Transactions of IMACS, 35(3), 177–219.

[18] Sandberg, R. D., Michelassi, V., Pichler, R., Chen, L., & Johnstone, R. (2015). Compressible direct numerical simulation of low-pressure turbines—part I: Methodology. Journal of Turbomachinery. Transactions of the ASME, 137(5).

[19] Buntine, J. D., & Pullin, D. I. (1989). Merger and cancellation of strained vortices. Journal of Fluid Mechanics, 205(1), 263.

The 13th TSME International Conference on Mechanical Engineering
12th – 15th December 2023
Chiang Mai, Thailand

DRC0001

Development of Four-Wheel Drive Skid-Steered Mobile Robot for Automated Hammering Inspection

Geunho Lee[1,*], Kaito Hirae[1], and Chunhe Li[1,*]

[1]University of Miyazaki, 1-1 Gakuen-Kibanadai Nishi, Miyazaki 8892192, Japan

* Corresponding Author: {geunho, lichunhe}@cc.miyazaki-u.ac.jp

Abstract.
This paper introduces the development of a four-wheel drive skid-steered mobile robot for realizing automatic hammering-inspection tasks in concrete infrastructure facilities. The developed mobile robot aims for supporting the following series of hammering-inspection process: moving to a desired hammering location, hammering after stop, collecting the hammering sounds, and moving the next location. In particular, to realize the hammering inspections by the mobile robot, it is necessary to achieve the two conditions of both the direct contact of a hammering-inspection unit with a desired hitting surface and the exactly recording of the hammering sounds. It means the importance of position control for the mobile robot equipped with the hammering unit to meet two conditions outdoors. For the purpose, the four-wheel drive skid-steered mechanism is adopted instead of complex steering mechanisms. Moreover, a PD controller based on the mathematical model of the mobile robot is employed to control accurate locations. The mathematical model and implementation of the mobile robot are explained in detail, and the effectiveness and the usability of the robot are verified through extensive simulations and experiments.

Keywords: hammering inspection, mobile robot, kinematic and dynamic model, PD controller.

1. Introduction

In Japan, social infrastructure has been rapidly aging. Since lots of bridges and tunnels were built for the period of rapid economic growth, the number of the infrastructure facilities that are now 50 years old has been increasing every year. To prevent accidents caused by these aging structures, periodic inspections should be strongly required. In detail, after the Sasago Tunnel collapse accident in Japan in 2012, the visual inspections of tunnels and other road facilities have been required every five years since 2014. However, it is local governments that are responsible for the maintenance and management of the social infrastructure, including inspections. In fact, the local governments do not have a very large budget for their maintenance and inspection activities.

Meanwhile, the number of engineers who can perform inspection and maintenance tasks in local governments continues to decline due to the outflow of population and the retirement of construction workers by the aging of the workforce. Moreover, there is a decrease in the number of working generations and a decline in tax revenues due to the outflow of population, resulting in financial difficulties. In addition to these social backgrounds above, there are lots of social infrastructure that are not fully maintained, and inspections are often done only by visual inspection. Therefore, to prevent accidents, regardless of a small number of people, there is a need for to provide accurate inspection results.

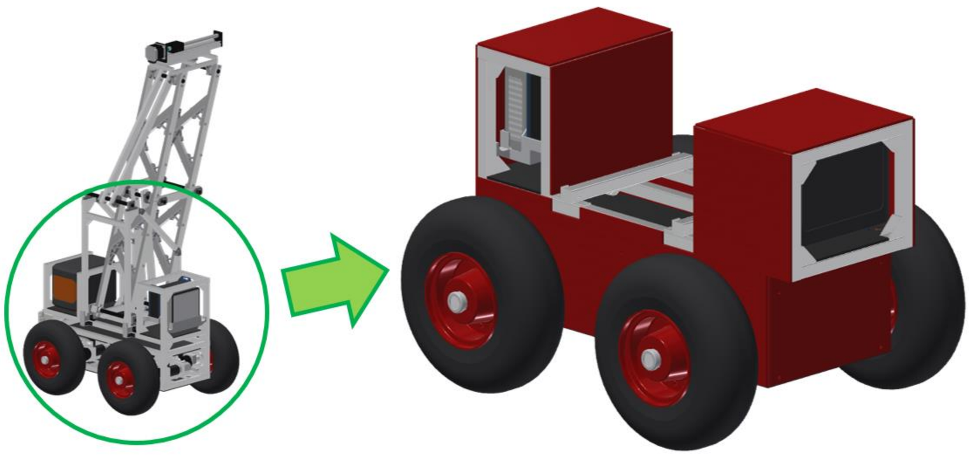

Figure 1. Conceptual illustration of a novel hammering-inspection robot and its mobile platform.

For the considerations above, we intend to eventually achieve a series of inspections for various concrete infrastructure facilities by using autonomous robots without the intervention of human workers. In detail, the hammering-inspection test, one among popular methods in infrastructure inspections, consists of four components: ‘movement to a desired place’, ‘hammering after stop at the location’, ‘signal acquisition’, and ‘analysis and determination’. Figure 1 shows the conceptual illustration of a novel hammering-inspection robot and its mobile platform. To implement the hammering-inspection robot, it is required of both the direct contact of a hammering-inspection unit with a desired hitting surface and the exactly recording of the hammering sounds. It means the importance of position control for the mobile robot equipped with the hammering unit to meet two conditions outdoors. As a first step, the mobile platform for the inspection robot equipped with a feedback controller is designed and developed.

2. Mobile Platform: Design and Implementation

2.1. Development Policy of Mobile Platform

The development policy of the mobile platform (for convenience, mobile robot, afterward) is to carry the hammering-inspection robot for the purpose of hitting tests in social infrastructure facilities such as tunnels while continuously examining. In general, mobile robots are often equipped with crawlers [1] and suspensions [2-3] to cope with uneven terrain. However, since the road condition of the tunnel to be inspected is basically a paved road, the robot allows to move on four wheels without a suspension. Instead of steering wheels, the four-wheel drive skid-steered unit of the mobile robot under the road environment is adopted such as crawler enabling the robot turning by sliding at different speeds between the left and right wheels. This consideration eliminates the need for a complex steering mechanism and allows the mobile robot to be compact and simplified while maintaining the rigidity of its platform [4].

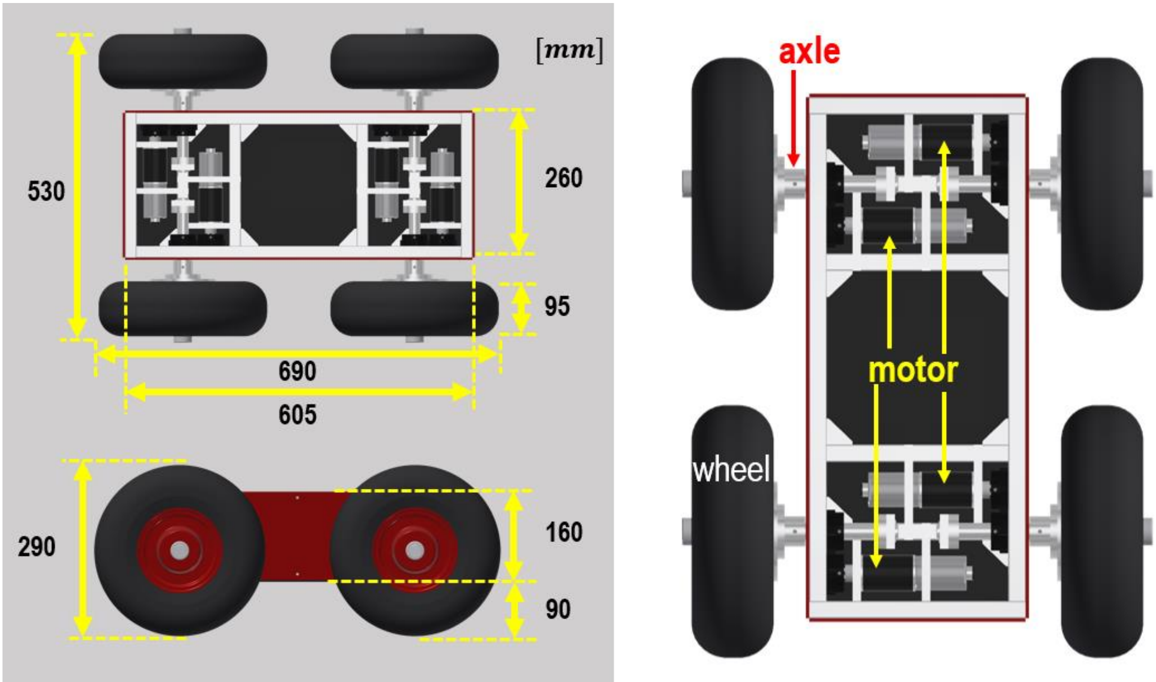

Figure 2. Specification (left) and three main parts (right) of mobile robot employing a four-wheeled drive skid-steered mechanism.

2.2. *Implementation of Mobile Platform*

Figure 2 shows the detailed specification of the mobile robot, and details three main parts such as motors, axles, and wheels. Extruded aluminum beams and acrylic plates are used for the outer fame of the mobile robot. Each wheel is rotated by a Maxon Motor GP42C gearhead and an EC-i 40, 100 W EC motor manufactured by the Maxon Motor Ltd. The robot is controlled by an Arduino Mega 2560 microcontroller and a MINISFORUM EliteMiNi TL50 PC as a main controller. To drive four motors, their power is provided a single Lipo battery. For the motor driver and the main controller, a Jackery Portable Power Supply 400 is used.

3. Mathematical Model: Kinematics and Dynamics

In this paper, the four-wheel drive skid-steered mobile robot (4WD SSMR) is considered as only planar motion. It is assumed that each wheel-ground contact is a single point and normal forces acting on the wheel-ground contact points are constant depending on the mass of robot and gravity. As shown in Figure 3, the mobile robot is represented with a point mass located at the center, near the front side of robot.

3.1. *Kinematics*

Figure 3-(a) illustrates the definitions and notations of kinematics of the mobile robot. The robot configuration vector q in global coordinate frames is $q = [X \quad Y \quad \theta]^T$ where X, Y, and θ are the position and orientation of the robot, respectively. Moreover, the local coordinate frames $[v_x \quad v_y \quad \omega]^T$ attached on the robot's center of mass (COM) is explained. The traveling direction of the robot is $\vec{x}$, and another axis counterclockwise perpendicular to $\vec{x}$ is represented by $\vec{y}$. The intersection of $\vec{x}$ and $\vec{y}$ is O. For the sake of convenience, O in this paper is represented by COM, hereafter. The opposite of the gravity direction $\vec{g}$ is defined as $+\vec{z}$.

Next, the transformation between the local velocities and the generalized velocities is given

$$\begin{bmatrix} \dot{X} \\ \dot{Y} \\ \dot{\theta} \end{bmatrix} = \begin{bmatrix} \cos\theta & -\sin\theta & 0 \\ \sin\theta & \cos\theta & 0 \\ 0 & 0 & 1 \end{bmatrix} \begin{bmatrix} v_x \\ v_y \\ \omega \end{bmatrix}. \tag{1}$$

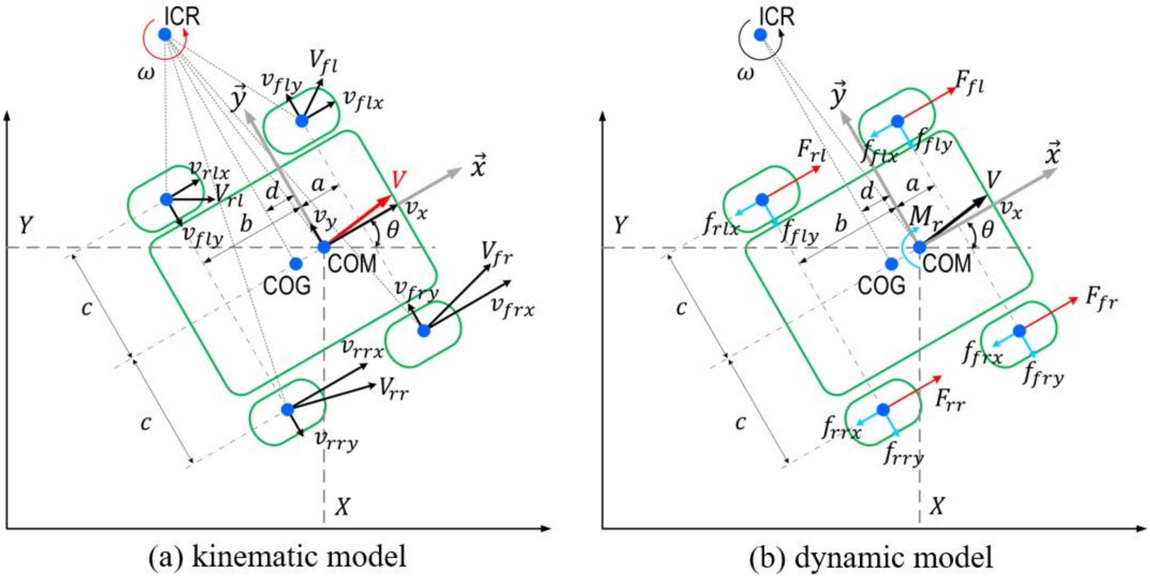

Figure 3. Definitions and notations of mathematical model for the mobile robot.

COM is a distance d away from the center of geometry (COG). ICR is located on the axis that intersects COG as shown in Figure 3. In this case the nonholonomic operational constraint that limits lateral skid is defined as [5]

$$v_y - d\omega = 0, \tag{2}$$

$$[-\sin\theta \quad \cos\theta \quad -d][\dot{X} \quad \dot{Y} \quad \dot{\theta}]^T = A(q)\dot{q} = 0. \tag{3}$$

Then Eq. (1) is rewritten

$$\dot{q} = S(q)\eta, \tag{4}$$

where $S(q)$ is

$$S(q) = \begin{bmatrix} \cos\theta & -d\sin\theta \\ \sin\theta & d\cos\theta \\ 0 & 1 \end{bmatrix}, \tag{5}$$

and, as the control input vector, η is

$$\eta = \begin{bmatrix} v_x \\ \omega \end{bmatrix}. \tag{6}$$

Since the columns of $S(q)$ are always in the null space of $A(q)$ [5-6], the following expression is satisfied

$$S^T(q)A^T(q) = 0. \tag{7}$$

3.2. Dynamics

The definitions and notations of dynamics in the mobile robot are illustrated in Figure 3-(b). First we introduce the left and right side forces then we describe the wheel dynamics

$$F_L/_2 = f_{fl} = f_{rl}, F_R/_2 = f_{fr} = f_{rr}, \tag{8}$$

$$I_w\dot{\omega}_w = \tau - DF, \tag{9}$$

where I_w is the wheel inertia, $\omega_w = [\omega_{fl} \quad \omega_{rl} \quad \omega_{fr} \quad \omega_{rr}]^T$ is the angular speeds vector of overall wheels, $\tau = [\tau_{fl} \quad \tau_{rl} \quad \tau_{fr} \quad \tau_{rr}]^T$ is the wheel torques' vector, $F = [F_L \quad F_R]^T$ is the force vector. Moreover, the force-torque conversion matrix D is defined

$$D = \frac{r}{2}\begin{bmatrix} 1 & 1 & 0 & 0 \\ 0 & 0 & 1 & 1 \end{bmatrix}^T. \tag{10}$$

where r is the wheel radius. Next the mathematical equations of robot motion in global coordinates is

$$m\ddot{X} = (F_L + F_R)\cos\theta - \left(f_x \cos\theta - f_y \sin\theta\right), \tag{11}$$

$$m\ddot{Y} = (F_L + F_R)\sin\theta - \left(f_x \sin\theta + f_y \cos\theta\right), \tag{12}$$

$$I\ddot{\theta} = c(-F_L + F_R) - M_r, \tag{13}$$

where m is the robot's mass and I is the robot's inertia about $\vec{z}$, f_x and f_y are the rolling and sliding friction forces, respectively, and M_r is the resistive moment about $\vec{z}$. The rolling-friction forces are too small when compared to sliding friction forces in the ideal case. A realistic model for rolling friction in case of slip can be found, for example in [7]. We assume the friction forces for only front-left wheel as follows

$$f_{flx} = \mu_x N_{fl} sgn\left(v_{flx}\right), f_{fly} = \mu_y N_{fl} sgn\left(v_{fly}\right), \tag{14}$$

where normal forces acting on the wheel-ground contact points due to gravity are calculated

$$N_{fl} = N_{fr} = \frac{b}{a+b}\frac{mg}{2}, N_{rl} = N_{rr} = \frac{a}{a+b}\frac{mg}{2}, \tag{15}$$

and finally the resistive moment is calculated

$$M_r = a\left[f_{fly} + f_{fry}\right] - b\left[f_{rly} + f_{rry}\right] + c\left[f_{frx} + f_{rrx} - f_{flx} - f_{rlx}\right]. \tag{16}$$

The general form of the robot dynamics including the nonholonomic constraint using the well-known Euler-Lagrange principle and introducing an additional vector for representing disturbances is

$$M(q)\ddot{q} + R(\dot{q}) + F_d = B(q)F + A^T(q)\lambda, \tag{17}$$

where $M(q) = \begin{bmatrix} m & 0 & 0 \\ 0 & m & 0 \\ 0 & 0 & I \end{bmatrix}$, $B(q) = \begin{bmatrix} \cos\theta & \cos\theta \\ \sin\theta & \sin\theta \\ -c & c \end{bmatrix}$, $R(\dot{q}) = \begin{bmatrix} f_x \cos\theta - f_y \sin\theta \\ f_x \sin\theta + f_y \cos\theta \\ M_r \end{bmatrix}$. (18)

$M(q)$ is the mass and inertia matrix, $R(\dot{q})$ is the vector of resistive forces and torques, F_d is the vector of disturbances, $B(q)$ is the input matrix, F is called as the control input at dynamic level previously defined, $A(q)$ is the constraint vector as in Eq. (3), and λ is the vector of Lagrange multipliers.

Taking the time derivative of Eq. (4) yields

$$\ddot{q} = S(q)\dot{\eta} + \dot{S}(q)\eta, \tag{19}$$

and using the relationships Eqs. (4), (7) and (19) one can convert the dynamic system in Eq. (17) to

$$\bar{M}\dot{\eta} + \bar{C}\eta + \bar{R} + \overline{F_d} = \bar{B}F, \tag{20}$$

where $\bar{M} = S^T M S$, $\bar{C} = S^T M \dot{S}$, $\bar{R} = S^T R$, $\overline{F_d} = S^T F_d$, and $\bar{B} = S^T B$.

4. Evaluation Results

Based on the mathematical model of the four-wheel drive skid-steered mobile robot, simulations were performed by using the MathWorks MATLAB program. According to a feedback controller, we compared trajectory results for path following. Figure 4 shows the comparison results for trajectories without controls, those with only the proportional (P) controller, and those with the proportional and differential (PD) controller, respectively. In these simulations, we had the mobile robot starting from the point (0,0) moves along the line $Y_{desired} = X + 1$. For the case without controls, the trajectory results plotted yellow solid line (labelled No controller) did not move toward $Y_{desired}$ at all. The line P controller employing the P controller follows the line $Y_{desired}$ while decreasing errors. Finally, the line PD controller performed under the PD controller quickly corrects the errors and follows $Y_{desired}$.

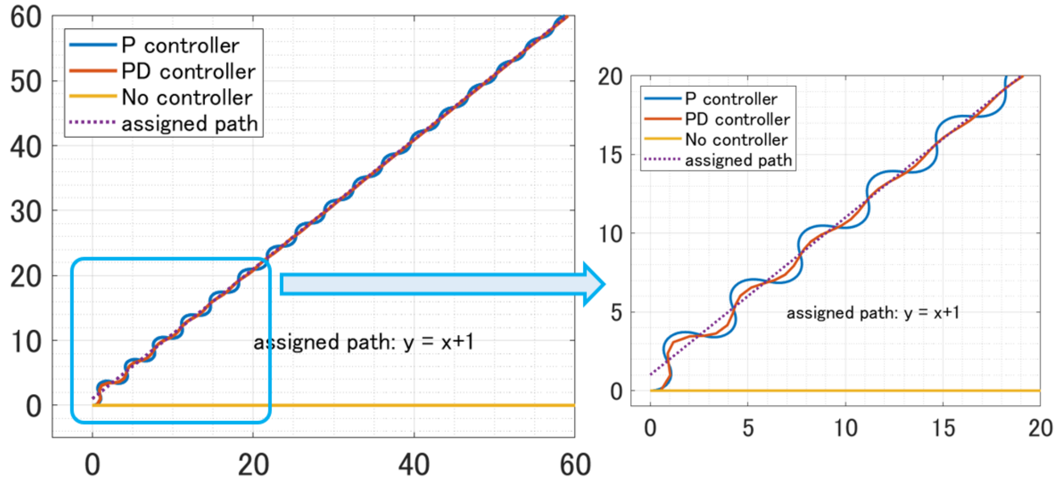

Figure 4. Comparison results for path following according to controllers.

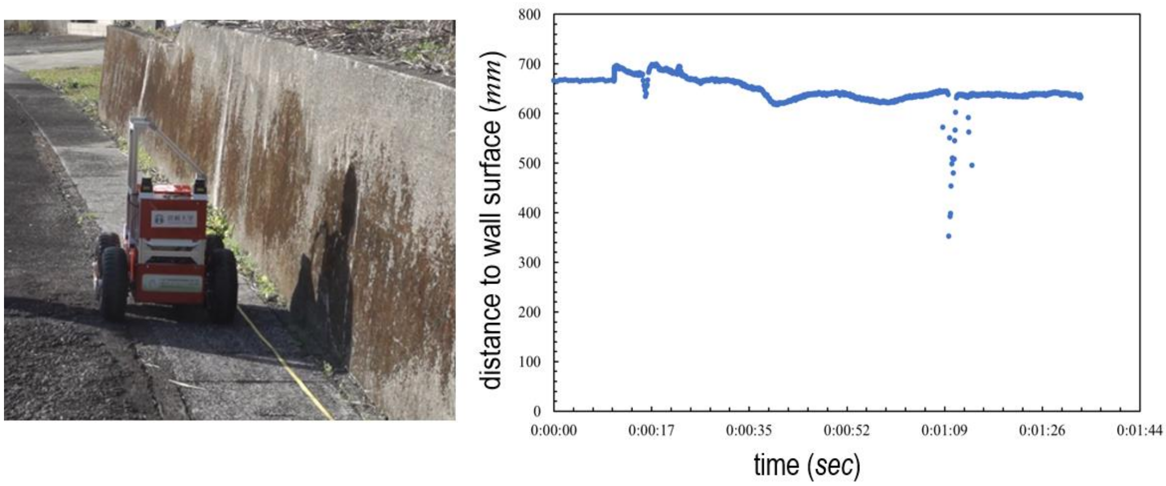

Figure 5. Experimental scene (left) and distance results to wall surface when moving (right).

Next, wall-following experiments were conducted outdoors to examine whether the feedback control implemented in the mobile robot worked properly. Figure 5 presents the experimental scene (left) and the results (right). To clearly evaluate the experimental results, we had the robot move while maintaining to a wall with an assigned distance 650 mm to the wall. The graph in Figure 5 shows the trajectory results by the mobile robot. Although there were the slight distance errors to the wall, it was confirmed that the robot could follow the constant assigned distance to the wall surface.

5. Conclusion

This paper introduced the development of a mobile platform for a hammering-inspection robot, allowing to automatically perform hammering tests in tunnels and other infrastructure facilities. The configuration, implementation, and mathematical model of the mobile robot were described. Simulations based on the mathematical model were conducted. Moreover, the four-wheel drive skid-steered mobile robot was implemented and evaluated whether the robot could be applied to real environments. From these results, this robot as shown in Figure 6 is expected to achieve the following process 'movement to a desired place', 'hammering', 'signal acquisition', and 'analysis and determination'. Finally, our presentation will detail on the realization of the proposed mobile robot and its control. The experimental video clips for the mobile robot and the inspection process will be introduced as our on-going studies. In the near future, we will develop and implement functions and mechanisms to realize the remaining three elements except the movements.

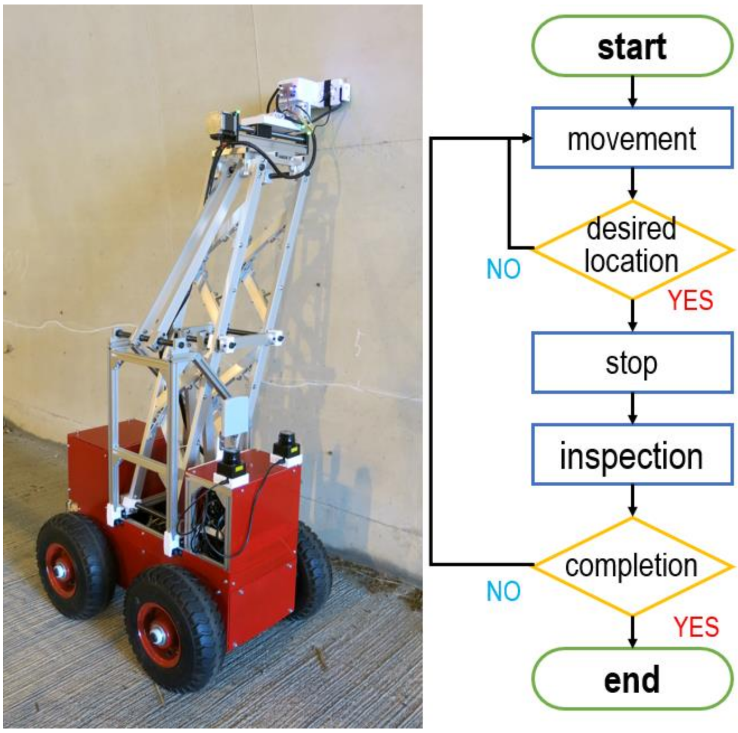

Figure 6. Hammering-inspection robot (left) and its inspection process (right).

6. Acknowledgments

This research was partially supported by grants from the KAJIMA Foundation.

7. References

[1] Lee, G., Ogata, O., & Li, C. (2022). Autonomous shape-variable crawler: One-dimensional displacement coordination for constant upper frame posture. *IEEE Transactions on Intelligent Transportation Systems*, 23(9), pp.14968-14977.
[2] Alipour, K. & Moosavian, S. A. A. (2009). Postural stability of wheeled mobile manipulators with flexible suspension considering tire friction model. In *Porc. 2009 IEEE/ASME International Conference on Advanced Intelligent Mechatronics*, pp.764-769.
[3] Lee, G., Togami, N., Hayakawa, Y., & Tamura, H. (2023). Two functional wheel mechanism capable of step ascending for personal mobility aids. *Electronics*, 12(6), pp.1-18.
[4] Ahmed, H., La, H. M., & Gucunski, N (2020). Review of non-destructive civil infrastructure evaluation for bridges: State-of-the-art robotic platforms, sensors and algorithms. *Sensors*, 20(14), pp.1-38.
[5] Caracciolo, L., de Luca, A., & Iannitti, S. (1999). Trajectory tracking control of a four-wheel differentially driven mobile robot. In *Proc. 1999 IEEE International Conference on Robotics and Automation*, pp.2632-2638.
[6] Kozłowski, K., & Pazderski, D. (2004). Modeling and control of a 4-wheel skid-steering mobile robot. *International Journal of Applied Mathematics and Computer Science*. 14(4), pp.477-496.
[7] Yi, J., Song, D., Zhang, J., & Goodwin, Z. (2007). Adaptive trajectory tracking control of Skid-steered mobile robots. In *Proc. 2007 IEEE International Conference on Robotics and Automation*, pp.2605-2610.

The 13th TSME International Conference on Mechanical Engineering
12th – 15th December 2023
Chiang Mai, Thailand

DRC0004

Dynamic Stability Analysis and Experiments of Self-Excited Vibration in a Flow Dynamics Conveying Machine

Masakazu Takeda[1,*], Yoshiki Sugawara[1], and Masahiro Watanabe[1]

[1]Aoyama Gakuin University, 5-10-1, Fuchinobe, Chuo-ku, Sagamihara-shi, Kanagawa-ken, 252-5258, Japan

* Corresponding Author: takeda@me.aoyama.ac.jp

Abstract. This work includes an examination of dynamic stability analysis and experimental investigations on self-excited vibrations seen in a flow dynamics conveying machine. The formulation of airflow between a plate emulating a conveying object and a levitation device in dynamic stability analysis is derived from the fundamental principles of two-dimensional leaky flow theory. The calculations for the fluid forces acting on the plate in an unstable manner are then performed. The current work conducts comprehensive calculations that consider the compressibility of air, a crucial element in the dynamic stability of the system. The coupled fluid-structure equations are produced by including the unsteady flow forces with the equations of motion of the plate. These equations yield the characteristic equations of the system, which provide the conditions necessary for the occurrence of self-excited vibration. This study elucidates the impact of airflow velocity, plate mass, and the width of the air supply slit, all of which are crucial factors in the system's design. The study involves the construction of an experimental apparatus that simulates a flow dynamics conveying machine. This apparatus is used to detect the displacement of a plate and the pressure fluctuation of the supplied air. The objective is to analysis the specific parameters that lead to the occurrence of self-excited vibration. In addition, the analysis is juxtaposed with empirical findings in order to authenticate the analytical framework. The investigation of the local work performed by the unsteady fluid force acting on the plate is employed to analysis the instability mechanism of self-excited vibration.

Keywords: Dynamic stability analysis, Plate, Self-excited vibration, Unsteady fluid force, Instability mechanism.

1. Introduction

Flow dynamics conveying devices are commonly employed in steel mills and liquid crystal panel production plants to facilitate the transportation of plates, such as steel sheets and glass, through the utilization of air pressure to levitate them. The flow dynamics conveying machine utilizes air pressure that is delivered through slits or holes on the surface of the chamber to achieve non-contact conveyance. As a result, this system offers advantages such as reduced power consumption and noise levels compared to traditional contact conveyance systems that rely on rollers. However, it should be noted that self-excited vibrations may arise on a plate that is supported by air pressure, leading to a decrease in productivity and the emergence of noise-related issues [1]. Hence, it is imperative to elucidate the vibration characteristics, generation conditions, and instability process pertaining to the self-excited vibration observed on a plate that is supported by air pressure.

Numerous investigations have been conducted thus far about a plate that is upheld by air pressure. The investigation conducted by Chang and Moretti [2] focused on the examination of the steady-state pressure resulting from airflow on the lower surface of the plate. This investigation focuses on the stability of floating plates in a steady state, with a notable absence of research on the dynamic stability of a plate that is supported by air pressure. Omori et al. [3] examined the properties of self-excited vibration in a belt that is supported by air pressure, employing both analytical and experimental approaches. Ishihara et al. [1, 4] conducted experiments on a flow dynamics conveyor that employs air pressure to suspend a belt for the purpose of load transportation. Their findings revealed the occurrence of self-excited vibration when the pressure fluctuations of the air passing through the gap beneath the belt were synchronized with the vibrational displacement of the belt. Moreover, a stability analysis was performed to assess the unsteady fluid force exerted on the lower surface of a plate that is supported by air pressure. The research revealed that the vibrations induced by the airflow beneath the plate, namely the crevice leakage-flow-induced vibrations [5], were identified as the primary source of excitation. Conversely, when considering gas bearings, wherein pressurized air is introduced into the bearing clearance to support the shaft through static pressure, existing research literature indicates that the compressibility of the air within the chamber located in the air supply section has an impact on the overall stability of the system [6, 7]. In the context of flow dynamics conveying machines, it is common practice to store the air supplied through the piping in a chamber prior to its distribution to the machine. This is done to achieve a consistent and uniform air supply across the entirety of the machine. Hence, similar to gas bearings, the impact of air compressibility within the chamber is deemed to influence the system's stability.

Hence, the researchers [8] developed a rudimentary analytical framework to study a plate that is upheld by air pressure, while considering the air compressibility air within the chamber. They proceeded to examine the stability of the system by both analysis and experimentation. Furthermore, the authors of this study examined the excitation mechanism and significant parameters of self-excited vibration, as outlined in the analytical model. The findings indicate that self-excited vibration is not solely attributed to vibrations created by leakage flow, as proposed by Ishihara et al [1, 4], but is also influenced by the compressibility of the air within the chamber. Nevertheless, the stability analysis conducted in this study made the assumption of a one-dimensional flow without considering fluid inertia. This assumption neglected the presence of a two-dimensional distribution of the air gap beneath the plate. Consequently, there exists a quantitative disparity between the analytical and experimental findings concerning the critical flow rate at which self-excited vibration is observed. Hence, in order to ascertain comprehensive criteria for the manifestation of self-excited vibration, it becomes imperative to do stability analysis of the air gap flow as a two-dimensional flow, incorporating the consideration of fluid inertia.

The present study involves the development of an analytical model that incorporates the effects of fluid inertia and air compressibility. This model is built upon the principles of two-dimensional leakage-flow-induced vibrations, as described in reference [9]. The objective of this investigation is to analyze the properties and circumstances under which self-excited vibrations occur in a plate that is supported by air pressure. The investigation involves the utilization of dynamic stability analysis and experimental methods. In this work, the analysis incorporates not only the compressibility of air in the chamber, as discussed in a prior report [8], but also accounts for fluid inertia and the compressibility of air in the gap. This study aims to elucidate the impact of key design elements, including the flow rate of supplied air, the mass of the plate, and the width of the air supply slit, on the occurrence circumstances of self-excited vibration. The obtained analytical results demonstrate a concurrence with the experimental findings, suggesting that an analytical model grounded on the principles of two-dimensional leakage-flow-induced vibrations, incorporating the effects of fluid inertia and air compressibility, can be effectively employed to quantitatively determine the conditions under which self-excited vibrations occur. Additionally, the intricate process of instability in self-excited vibration is examined by presenting the analysis of work distribution resulting from the fluid force acting on the surface of the plate.

2. Dynamic stability analysis

2.1. Model of Analysis

Figure 1 depicts a schematic representation of the analytical model. In the model, the *X*-axis is oriented horizontally, the *Y*-axis is oriented longitudinally (in the depth direction), and the *Z*-axis is oriented vertically. To elucidate the vibration characteristics and occurrence conditions in the translational vibration mode, we make the assumption that the plate undergoes vertical translation without any elastic deformation. In a flow dynamics conveying machine, a floating object exhibits spring and damper properties as a result of tension and damping effects throughout the conveyance process. Consequently, the structural model in this analysis include the inclusion of springs and dampers. The schematic illustration in Figure 2 depicts the surface of the chamber, featuring an air supply slit. The plate is buoyed by the air pressure that is delivered through the aperture located on the upper surface of the chamber. The quantity of slits pertains to a singular model with one slit (referred to as the "1-slit model"). The airflow within the space between the lower surface of the plate and the upper surface of the chamber is considered to be a two-dimensional flow occurring in both the *X* and *Y* directions. The flow path is discretized into N_X segments in the *X* direction and N_Y segments in the *Y* direction. The analysis of stability is conducted by taking into account the fluid inertia and compressibility of the air, utilizing the principles of the two-dimensional gap flow theory [9]. Furthermore, the analysis of stability in this study also included the consideration of air compressibility within the chamber. The procedure for dynamic stability analysis using this model is the same as previously reported [8].

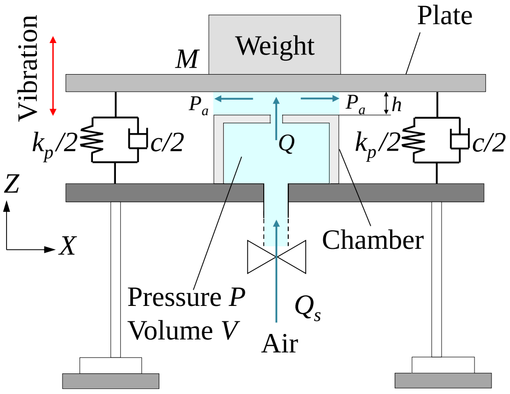

Figure 1. Schematic of the analytical model.

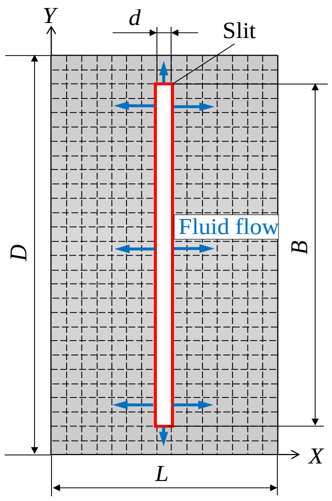

Figure 2. Schematic of chamber surface with slit.

2.2. Fundamental equations of fluid flow

The fundamental equation of gap flow passage is derived by extending the Navier-Stokes equations using the two-dimensional gap flow theory [9]. The equations governing the continuity of gap flow and the basic equations of gap flow in the *X* and *Y* directions are provided as follows:

$$\frac{\partial \rho Q_X}{\partial X} + \frac{\partial \rho Q_Y}{\partial Y} + \rho \frac{\partial h}{\partial t} = 0, \tag{1}$$

$$\frac{1}{\rho}\frac{\partial P_g}{\partial X} = -\frac{1}{h}\left\{\frac{\partial Q_X}{\partial t} + \frac{\partial}{\partial X}\left(\frac{Q_X^2}{h}\right) + \frac{\partial}{\partial Y}\left(\frac{Q_X Q_Y}{h}\right) + \frac{12\nu Q_X}{h^2}\right\}, \tag{2}$$

$$\frac{1}{\rho}\frac{\partial P_g}{\partial Y} = -\frac{1}{h}\left\{\frac{\partial Q_Y}{\partial t} + \frac{\partial}{\partial Y}\left(\frac{Q_Y^2}{h}\right) + \frac{\partial}{\partial X}\left(\frac{Q_X Q_Y}{h}\right) + \frac{12\nu Q_Y}{h^2}\right\}. \tag{3}$$

In this context, the variables h, P_g, Q_X , Q_Y, ρ and ν represent the floating displacement of the plate (i.e., the gap width), pressure within the gap, flow rate in the X direction across the gap, flow rate in the Y direction across the gap, air density within the gap, and the kinematic viscosity of air, respectively. The relationship between air density and pressure is defined by the following equation assuming isothermal change.

$$\rho = P_g \frac{\rho_a}{P_a}, \tag{4}$$

where P_a and ρ_a represent the atmospheric pressure and air density of the atmosphere, respectively.
The equation of continuity, which accounts for the influence of air compressibility within the chamber, is expressed as follows:

$$\frac{V}{K_e}\frac{dP}{dt} = Q_s - Q, \tag{5}$$

where the variables V, P, K_e, Q_s, and Q represent the following parameters: chamber volume, chamber internal pressure, modulus of elasticity of volume, flow rate entering the chamber, and flow rate exiting the chamber, respectively.
Figure 3 depicts a schematic representation of the airflow pattern as it passes through the apertures. Pressure drop is observed at the slit entry in Figure 3 of the red line segment. The mathematical expression that describes the relationship between the pressure differential between the internal pressure of the chamber (P) and the pressure above the slit (P_s), as influenced by the pressure drop and the flow rate (Q) going through the slits, can be expressed as follows:

$$Q = C_{ds} A_s \sqrt{2(P - P_s)/\rho_s}, \tag{6}$$

where the variables C_{ds} and ρ_s represent the flow coefficient of the entrance of the slits and the air density above the slit. The area of the slit entry, denoted as $A_s = d \cdot B$, is determined by the dimensions of the slit, specifically the width d and the length B. Furthermore, the gap entrance in figure 3 of the yellow part experiences a pressure reduction. In the region where air flows from the slit in the X direction, the pressure difference between the above slit pressure P_s and the gap inlet pressure $P_{g0}(j,k)$ caused by the pressure reduction is expressed by the following relational expression using the flow rate $Q_X(j,k)$.

$$Q_X(j,k) = C_{dg} h \sqrt{2\left\{P_s - P_{g0}(j+1,k)\right\}/\rho_s}, \tag{7}$$

where C_{dg} is the gap entrance's flow coefficient. A similar equation is also provided for the area where air flows from the slit in a Y direction.

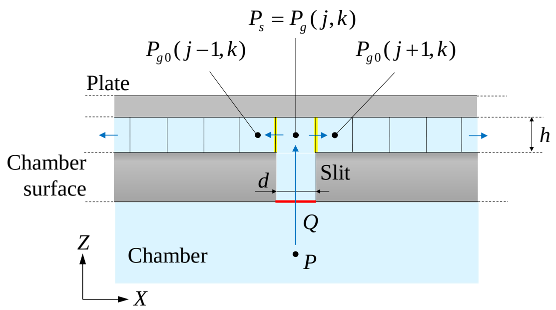

Figure 3. Schematic illustration of airflow through the slit.

2.3. Pressure distribution in the gap

The fundamental equation governing gap flow is discretized using a grid model. The pressure in the gap, Pg, is located at the grid point (j,k), while the flow rates in the gap, $Q_x(j,k)$ and $Q_y(j,k)$, are located at the grid points $(j+1/2,k)$ and $(j,k+1/2)$ respectively. In this context, the dimensionless coordinate axis is established as

$$x = X / L, \quad y = Y / D, \tag{8}$$

where L is the length of the plate and D is its width.
The pressure distribution in the gap is obtained by discretizing the fundamental equations of airflow (equations (1)-(4)) using the two-dimensional gap flow theory [9]. The equation representing the steady pressure distribution in the gap is provided as follows:

$$\bar{P}_g(j,k) = \left[b_1 \left\{ \bar{P}_g(j+1,k) + \bar{P}_g(j-1,k) \right\} + b_2 \left\{ \bar{P}_g(j,k+1) + \bar{P}_g(j,k-1) \right\} \right] / A_p, \tag{9}$$

$$b_1 = \ell_y{}^2 D^2, \quad b_2 = \ell_x{}^2 L^2, \quad A_p = 2(\ell_y{}^2 D^2 + \ell_x{}^2 L^2), \tag{10}$$

where "$^{-}$" displays the variables in the steady state and ℓ_x and ℓ_y are the lengths of the elements in the x and y directions, respectively. On the other hand, the following equation can be used to determine the unsteady pressure distribution in the gap:

$$\begin{aligned} \Delta\tilde{P}_g(j,k) &= \left[b_1 \left\{ \Delta\tilde{P}_g(j+1,k) + \Delta\tilde{P}_g(j-1,k) \right\} + b_2 \left\{ \Delta\tilde{P}_g(j,k+1) + \Delta\tilde{P}_g(j,k-1) \right\} \right] / A_p \\ &\quad - \frac{b_1 b_2}{A_p} \frac{\rho(j,k)}{\bar{h}^3} (\bar{h}^2 s + 12\nu) s \Delta\tilde{h}, \end{aligned} \tag{11}$$

where the variable s represents the Laplace variable, whereas the symbols "Δ" and "$^{\sim}$" indicate the variables in the unstable state and the Laplace converted variable, respectively.

2.4. *The plate's equation of motion*

The following is an expression for the equation of the plate's motion:

$$M\ddot{h} + c\dot{h} + k_p h + Mg = A_d \sum_{j=1}^{N_X} \sum_{k=1}^{N_Y} P_g(j,k), \tag{12}$$

where the variables M, c, k_p, and g represent the mass of the plate (including weight), the damping coefficient, the spring constant, and gravitational acceleration, respectively. Equation (12) represents the fluid force exerted on the surface of the plate, as demonstrated by the right-hand side. This force is determined by equations (9) and (11), whereas the area of the element, as depicted in Figure 2, is defined by

$$A_d = \ell_x L \ell_y D. \tag{13}$$

2.5. *The unsteady equations*

The method of perturbation is employed to linearize the variables in fundamental equations, while the state quantity is decomposed into a steady term and an unsteady term. Here, equations for unsteady states are given by

$$\begin{gathered} \frac{V}{K_e} \Delta\tilde{P} \cdot s = -\Delta\tilde{Q}, \quad \Delta\tilde{P}_s = \Delta\tilde{P} - \frac{\rho_s \bar{Q}}{C_{ds}^2 A_s^2} \Delta\tilde{Q}, \\ \Delta\tilde{P}_{g0}(j,k) = \Delta\tilde{P}_s - \frac{\rho_s \bar{Q}_x(j,k)}{C_{dg}^2 \bar{h}^2} \left\{ \Delta\tilde{Q}_x(j,k) - \frac{\bar{Q}_x(j,k)}{\bar{h}} \Delta\tilde{h} \right\}, \\ (M_s s^2 + cs + k_s) \Delta\tilde{h} = -A_d \sum_{j=1}^{N_X} \sum_{k=1}^{N_Y} \Delta\tilde{P}_g(j,k). \end{gathered} \tag{14}$$

2.6. Stability criterion

By organizing unsteady equations with respect to Laplace variable, the fluid force is expressed in a form that includes a second-order lag element due to fluid inertia and air compressibility factors. Therefore, deriving the coupled fluid-structure equation from the equation of motion of the plate shown in equation (14) (the right-hand side is the fluid force), a fourth-order characteristic equation about the vibration of the plate (Eq. (15)) can be derived by multiplying the second-order ODE of the structural system by the inverse of the second-order delay element of the fluid force.

$$a_4 s^4 + a_3 s^3 + a_2 s^2 + a_1 s + a_0 = 0, \tag{15}$$

where the coefficient a_i is determined by many physical features of the fluid flow in the gap and the chamber, as well as the mass of the plate, damping coefficient, spring constant, and the plate's floating gap. The stability of the system is compromised when at least one root of the characteristic equation has a positive real part. Additionally, the phenomenon of self-excited vibration is observed in scenario $\mathrm{Im}[s] \neq 0$.

2.7. Calculation parameters

Table 1 displays the principal parameters employed in the analysis. The values of the structural damping ratio Z, as well as the flow coefficients C_{ds} and C_{dg}, were found using experimental means. The values of division numbers N_X and N_Y were found by incrementing their respective values until the calculations yielded a constant value.

Table 1. Parameters in the calculation.

Spring constant k_p	[N/m]	4.97×10^4
Slit width d	[mm]	0.70 ～ 6.00
Slit length B	[mm]	360
Chamber volume V	[m$^{3]}$	5.6×10^{-3}
Chamber width L	[mm]	156
Chamber length D	[mm]	426
Air density ρ_a	[kg/m^3]	1.20
Kinematic viscosity ν	[m^2/s]	1.50×10^{-5}
Damping ratio ζ		0.07
Flow coefficient of gap entrance C_{dg}		0.85
Flow coefficient of slit C_{ds}		0.85
Division number N_X, N_Y		100
Gravity acceleration g	[m/s^2]	9.81

3. Experiment

Figure 4 depicts a schematic representation of the experimental setup. Figure 5 displays an image depicting the surface of the chamber, featuring a prominent slit. In the conducted experiment, the air emitted by the blower is collected within the chamber, and then exits through the aperture located on the upper surface of said chamber. The plate is buoyed by the force exerted by the air escaping from the aperture, which is facilitated by the introduction of air into the gap. The vertical movement of the plate is facilitated by the presence of a coil spring and a liner bearing. The measurement of the plate's displacement was conducted utilizing a gap sensor. The measurement of the air flow rate provided to the chamber, denoted as Q_s, was conducted using a flow meter. The mass M, which encompasses the combined mass of the plate and a weight placed upon it, was altered through the manipulation of the weight's dimensions on the plate. The remaining parameters and dimensions exhibit similarity to the analytical parameters.

This work investigates the unstable fluid force exerted on the plate's bottom surface. The instability mechanism is explored through the concurrent measurement of the plate's vibration displacement and the air pressure fluctuations in both the gap and the chamber. The pressure fluctuations within the gap were detected in the experiment by means of a pressure sensor, which was positioned through a hole on the surface of the plate. The pressure variation within the gap was assessed at several locations using a perforation. The pressure fluctuation seen in this study is a result of using the air pressure as a reference point. The fluctuation in pressure within the gap signifies the force exerted by the fluid per unit area on the plate's bottom surface. Hence, the calculation of the local work performed by the fluid force exerted on the plate within a certain time interval E_{local} can be expressed as follows:

$$E_{local} = \oint P_i \, \dot{X} dt = \overline{P}_i \cdot \overline{X} \cdot \pi \sin\phi \quad [\text{J/m}^2], \tag{16}$$

where $\overline{P}_i$, $\overline{X}$ and ϕ represent the amplitudes of pressure and vibration, respectively, and the phase difference between the displacement of vibration Δh and fluid pressure ΔP. The analysis involves an examination of the specific region where the local work performed by the fluid force, as indicated by equation (16), exhibits a positive value. This examination provides clarity regarding the location within the gap between the plate and the chamber surface where the pressure fluctuation responsible for the self-excited vibration is generated.

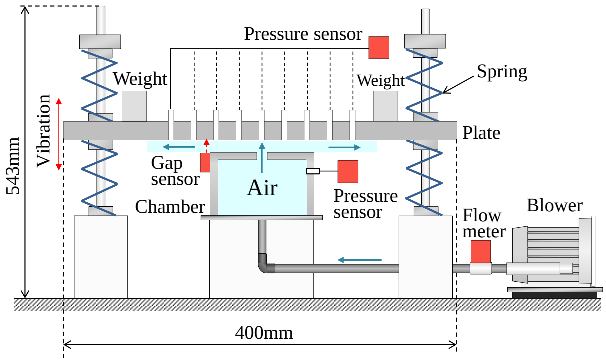

Figure 4. Schematic of the experimental setup.

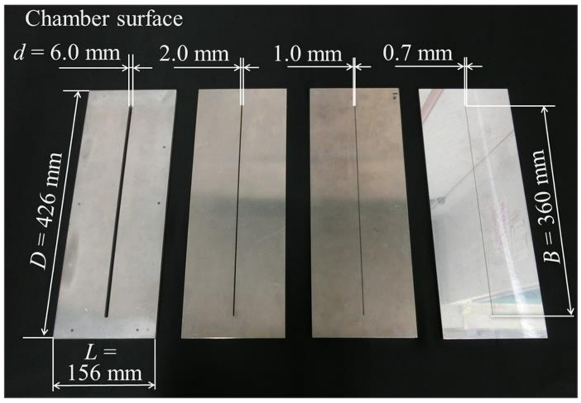

Figure 5. Image of the chamber surface.

4. Analysis and experimental results

4.1. Typical root locus

The results of the root locus computations for various airflow rates are depicted in Figure 6. This figure also illustrates the relationship between the airflow rate and the real component of the characteristic root, which represents the growth rate of the self-excited vibration. The presented data showcases representative findings obtained with a plate mass of 11.1 kg and a broad slit spacing of 6 mm. In instances where the airflow rate is diminished, it may be observed that the real component of the characteristic root assumes a negative value, so signifying the stability of the system. Nevertheless, when the rate of airflow is heightened, the positive real component of the characteristic root surpasses a specific critical flow rate, resulting in the occurrence of self-excited vibrations. The occurrence of self-excited vibration is contingent upon the mass of the plate and the width of the slit, as these determine the critical flow rate. The subsequent section, 4.2, delineates the circumstances in which self-excited vibration arises while manipulating the aforementioned parameters.

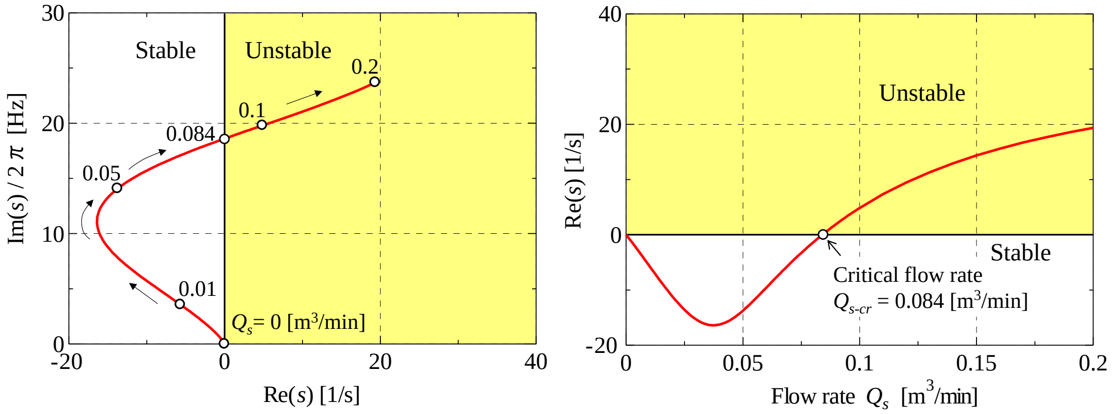

Figure 6. Root locus when flow rate increases for M=11.1kg, d = 6.0 mm.

4.2. *Instability conditions*

Figure 7 shows the conditions for the generation of self-excited vibration when the mass of the plate and the airflow rate are varied. The results for different slit width (Fig. 7(a)-7(d)) are shown here to clarify the effect of slit width on the conditions for generation of self-excited vibration. The figures show that the larger the slit width, the wider the area of self-excited vibration generation becomes, and self-excited vibration is generated in the area where the plate mass is small. On the other hand, as the slit width becomes smaller, the self-excited vibration generation region becomes narrower. However, care must be taken when designing a small slit width because clogging may occur in the slit.

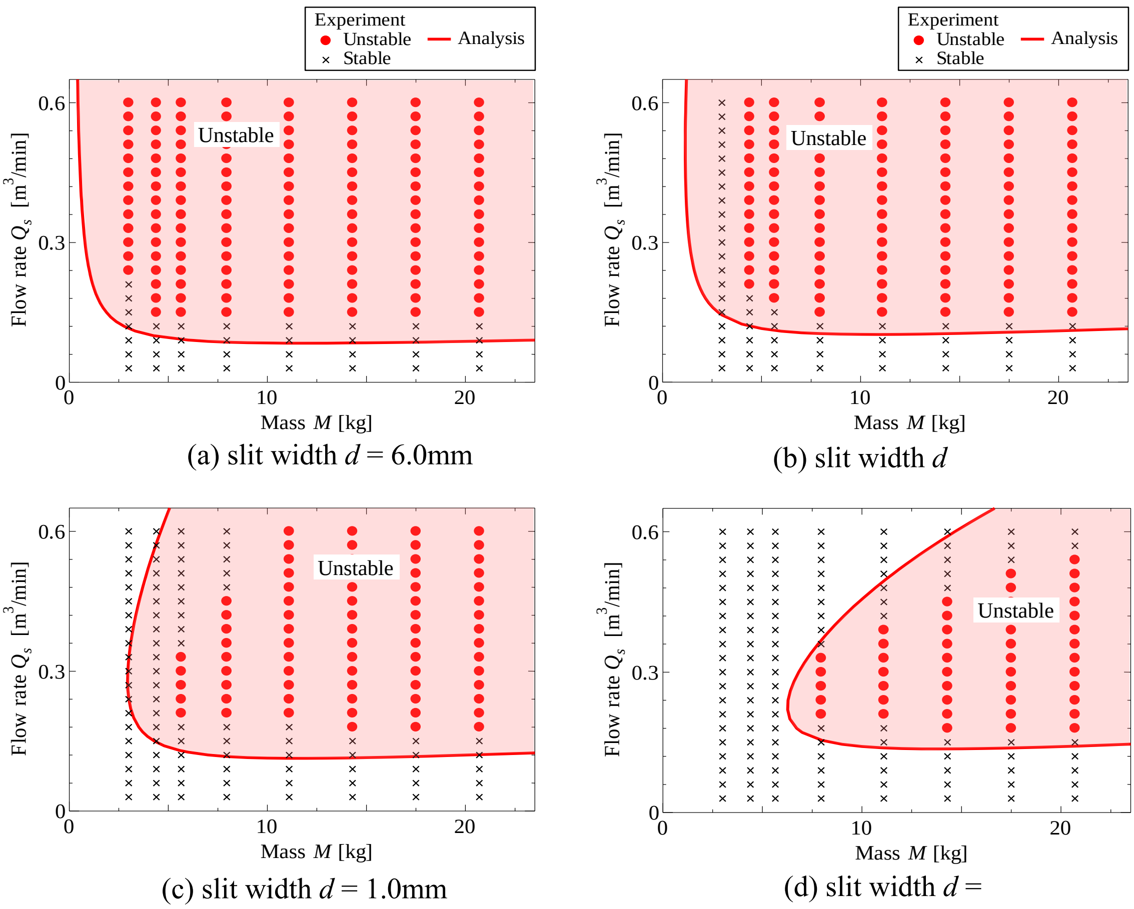

Figure 7. Critical flow rate $Q_{s\text{-}cr}$ for different slit widths d as a function of plate mass M.

4.3. Local work by the unsteady fluid force

Figure 8 illustrates the distribution of the unsteady fluid force obtained throughout the experimental procedure. The findings pertaining to various slit widths are presented herein to facilitate the examination of the underlying process responsible for the formation of a narrower region of self-excited vibration generation in cases where the slit widths are smaller, as depicted in Figure 7. The figure illustrates the maximum value of the work performed by the unstable fluid force, which is normalized with a maximum value of 1, as depicted in Fig. 8(a)-8(c). The red hue signifies the region in which the work resulting from fluid force is positive, while the blue hue signifies the region in which the work is negative. The depicted figure illustrates that irrespective of the width of the slit, the fluid force's work is consistently positive (indicated by the color red) in the vicinity of and above the slit, showing the presence of energy inflow. To clarify, self-excited vibration arises due to the exertion of positive work by the fluid force (namely, pressure fluctuation) on the plate's vibration in the vicinity and above the aperture. Prior research (Reference 11) has demonstrated that the generation of positive work resulting from fluid forces can be attributed to the compressibility of the air within the chamber. Conversely, in the spatial domain distant from the aperture, the fluid force exhibits negative work (shown by the color blue), whereas in the external region of the chamber, the fluid force does not do any work (indicated by the color green). In other words, the fluid force (pressure fluctuation) in these regions is not involved in the generation of self-excited vibration.

The results in Figure 7 shows that the critical flow rate at which self-excited vibration occurs decreases with increasing slit width, which is attributed to the increase in fluid force immediately above and near the slit. To discuss this in detail, Figure 9 shows the relationship between the pressure fluctuations in the chamber and above the slit. Figure 9(a) and (b) show the results for slit width of d = 6 mm and d = 1 mm, respectively. When the slit width is wide (Fig. 9 (a)), the pressure fluctuations above the slit and those in the chamber are almost in phase. However, when the slit width is small (Fig. 9 (b)), there is a phase difference in the pressure fluctuation. This is due to fluid resistance at the slit. This phase difference acts to reduce the positive work done by the excitation flow force, thus increasing the critical flow rate at which self-excited vibration occurs.

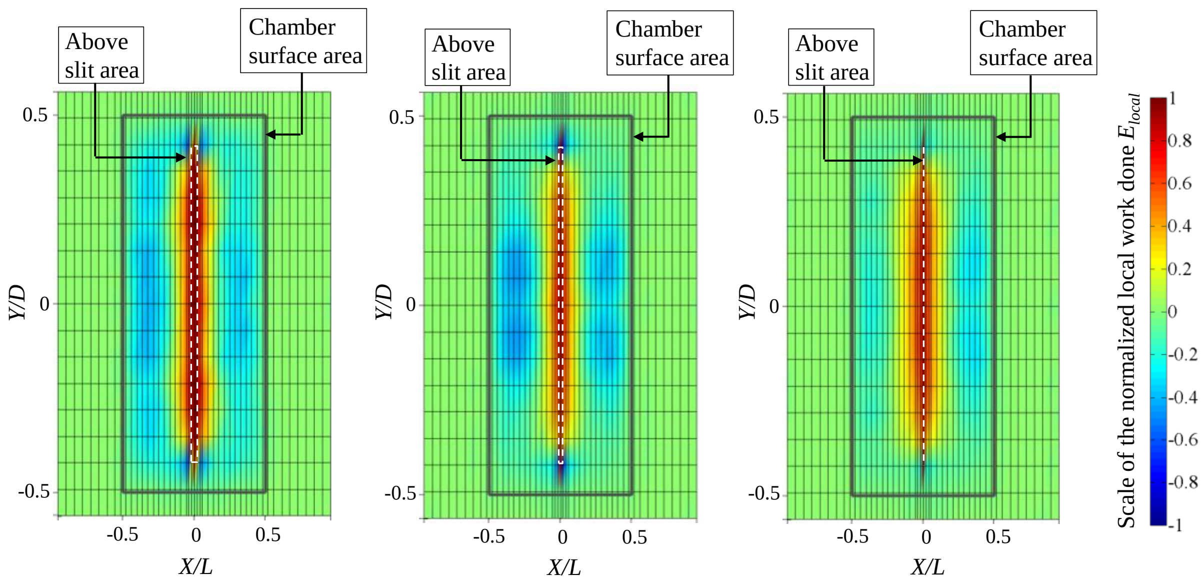

(a) d = 6.0mm (b) d = 2.0mm (c) d = 1.0mm

Figure 8. Normalized local work E_{local} by the fluid force in the of M = 5.65 kg, $Q_s = 1.2Q_{s\text{-}cr}$.

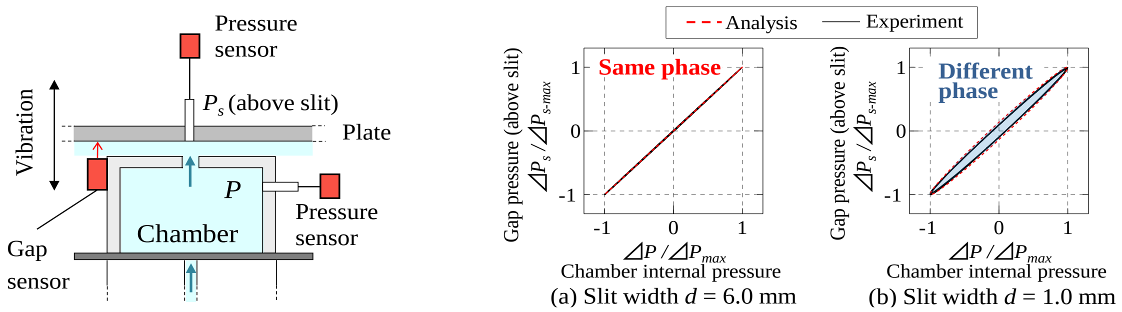

Figure 9. Relationship between the pressure fluctuations in the chamber ΔP and above the slit ΔP_s.

5. Conclusion

In this study, an analytical model that takes into account fluid inertia and compressibility of air was constructed based on the theory of two-dimensional leakage-flow-induced vibrations, and the occurrence conditions and characteristics of self-excited vibration generated by a plate supported by air pressure were investigated. The influence of important design parameters, such as airflow rate, the mass of the plate, and slit width, on the occurrence conditions of self-excited vibration was clarified. Furthermore, the detailed instability mechanism of the self-excited vibration was discussed by showing the work distribution due to the fluid force on the plate surface. The outcomes were summed up as follows:

(1) The analytical and experimental results generally agree well on the conditions for the occurrence of self-excited vibration. In other words, the analytical model developed in this study can be used to quantitatively calculate the conditions under which self-excited vibration occurs.

(2) As the slit width becomes wider, the critical flow rate at which self-excited vibration occurs decreases. This self-excited vibration occurs because the pressure fluctuation above and near the slit does positive work on the vibration of the plate.

(3) When the slit width is small, a phase difference is generated between the pressure fluctuation above the slit and the pressure fluctuation in the chamber due to fluid resistance at the slit. This phase difference acts to reduce the positive work done by the excitation flow force, thus increasing the critical flow rate at which self-excited vibration occurs.

6. Acknowledgments

This work was supported by JSPS KAKENHI Grant Number 20K14683.

7. References

[1] Ishihara, K. (2008). On Abnormal Vibration Generated in Flow Dynamic Conveyer. *Journal of System Design and Dynamics*, Vol. 2-2 , pp.550-560.

[2] Chang, Y.B. and Moretti, P.M. (2000). Aerodynamic Characteristics of Pressure-Pad Air Bars. *Journal of Applied Mechanics*, Vol. 67-1 , pp.177-182.

[3] Oomori, N. and Kobayashi, M. (2000). Stability Analysis of Flexible Belt floating on Air Flow. *Proc. of JSME Dynamics and Design Conference 2000*, No.342. (in Japanese)

[4] Ishihara, K. and Eto, D. (2011). Study on Generation Mechanism of Abnormal Vibration of Flow Dynamic Conveyer. *Journal of System Design and Dynamics*, Vol. 5-4, pp.589-602.

[5] Inada, F. and Hayama, S. (1988). A Study on leakage-flow- induced vibrations (Fluid-dynamic forces acting on the walls of a one-dimensional, narrow passage). *JSME Int. J.*, Series III 31, pp.39-47.

[6] Mori, H. and Mori, A. (1966). Stabilizing Element for Externally Pressurized Gas-Bearing (1st Report, Stabilizing Element Attached to Bearing Recess). *Trans. JSME*, Vol. 32-244, pp.1877-1882. (in Japanese)

[7] Licht, L. and Fuller, D.D. (1958). Self-Excited Vibrations of an Air-Lubricated Thrust Bearing. *Journal of Basic Engineering*, Vol.80-2, pp.411-414.

[8] Takeda, M. and Watanabe, M. (2017). Self-excited vibration of a plate supported by air pressure in a floating conveying machine. Proc. ASME PVP2017, No.PVP2017-65335.

[9] Li, D.-W., Kaneko, S. and Hayama, S. (2002). A study on annular leakage-flow-induced vibrations. *Journal of Fluids and Structures*, Vol.16, No.7, pp.909-930.

DRC0005

Autonomous Navigation without Sway for Overhead Crane through Warehouse Management System Integration

Tanatip Chunang[1], Nopparat Paomongkhon[1], Apitchaya Yimyeam[1], Nattapong Suksabai[2], and Ittichote Chuckpaiwong[1,*]

[1]Department of Mechanical Engineering, Faculty of Engineering, Mahidol University, 25/25 Phuttamonthon 4 Road, Salaya, Nakhon Pathom, 73170, Thailand
[2]Divison of Mechanical Engineering, Faculty of Engineering, Bangkok Thonburi University, Taweewattana, Bangkok, 10170, Thailand

* Corresponding Author: ittichote.chu@mahidol.ac.th

Abstract. In the warehouse where an overhead crane is used for material handling, a general warehouse system may not communicate data with the crane, which can reduce the efficiency of automatic material transfers. A crane system used in modern warehouses still employ the method of lifting the crane to its maximum heights and placing the goods in a desired position. However, raising a crane to its maximum height is not only inefficient but also can result in dangerous where the payload is above the head. This paper presents an automated crane system that integrates a navigation system and utilizes warehouse data, aiming to enhance both safety and efficiency in crane operations.

The proposed automated overhead crane navigation system is summarized as follows: The Warehouse Management System (WMS) can communicate with the overhead crane navigation system through a database that provides obstacle position data, which the path planning algorithm can be used. It was found that the A* Algorithm is not suitable for controlling overhead cranes, so a new algorithm called Improved Corner Algorithm was developed, which allows for easy speed control and precise navigation according to the objectives. As for the crane control, an input shaping technique was used to reduce sway effectively. A simulation was performed to demonstrate the capabilities of the overhead crane using a pendulum model that closely approximates a real-life application. The simulation result validated the functions of the proposed crane system including path planning, sway suppression, and warehouse management system. In conclusion, the automatic overhead crane navigation system increases the efficiency of the crane in terms of speed, reduce the number of personnel required for operation, and improve safety.

Keywords: Path Planning, Overhead Crane, Warehouse Management System, Sway Suppression, Input Shaping.

1. Introduction

The industrial realm extensively employed overhead cranes for the purpose of material handling within warehouse settings [1]. While the movement of goods in and out of a warehouse using an overhead crane was convenient, fast, and safe, it posed several challenges such as time management, warehouse design, and dynamic of the crane. Serving as integral components of material handling systems, the movement of goods to warehouses required internal management called Warehouse Management System (WMS) to increase efficiency in warehouse management [2] [3]. Another useful method is the layout design in warehouse using ABC analysis [4], which improves warehouse management efficiency. The method was used in sorting, arranging products, and designing the warehouse layout accordingly. While the management system and the design layout method are useful in designing the intelligent warehouse, another aspect that will complete the goods transferring process is designing the crane dynamics.

By knowing the start and end points, the next steps are to find the path and dynamics of the crane. Xin P, Wang X, Liu X, Wang Y, Zhai Z, and Ma X. [5 /presented a framework of path planning, which was to create waypoints from a starting point to a destination point and use various algorithms to find the shortest path without obstacles. The commonly used methods for path planning are as follows: RRT, RRT*, and A*. In brief, RRT and RRT* are quite attractive methods but there are still problems with both algorithms, such as excessive levels of randomness, low planning efficiency, and numerous sharp corners in the resulting paths. The general method called A* is still inconvenient in the real implementation where the resolution of the path depends on the number of the generated waypoints. Another method needs to be developed to minimize the number of waypoints and result in minimum path length.

The dynamic of the crane can be initially designed by selecting the trajectory generator for each crane axis. For example, the method for generating the movement of a robot or other devices using the technique of cubic spline interpolation to create a smooth and continuous curve between predetermined reference points can be found in [6] [7] [8]. Even though the crane can move according to the selected trajectory, the transferred object still oscillates according to the pendulum behavior, which may lead to unexpected situations. Several signal filtering techniques were developed, such as input shapers and command smoother [9]. One of these techniques can be used to smooth the desired trajectory for expecting no oscillation of the transferred object.

To address these challenges, the team conducted a project to develop an automated material handling system using an overhead crane with navigation capabilities to enhance efficiency and safety. In this work, Warehouse Management System (WMS) is applied to the overhead crane in simulation environment as the database for the path planning. The process that shows how to label the goods in warehouse is described. The path planning using the proposed waypoint selection will be described. The result shows that the proposed method is a superior technique compared to others. The cubic trajectory and input shaping was combined to use it as the velocity trajectory, which is the input to the overhead crane. The simulation of the proposed automated overhead crane with navigation capabilities will eliminate the need for manual movement of goods, which will reduce the likelihood of loss or damage of goods and improve customer satisfaction. Additionally, the system will reduce delays in production and eliminate the problems arising from human errors.

2. Modelling and Sway Suppression

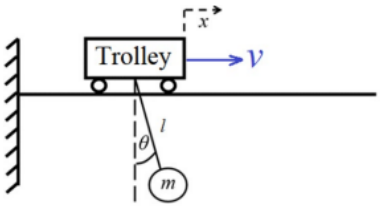

Figure 1. The coordinate system used to describe the motion of the overhead crane.

To create an automated crane that can accurately control the position and swing of the payload, the response of the speed of movement and the ability to control the swing when the load is moved up and down are considered. The swing can be suppressed by applying input shaping called Zero Vibration (ZV) to provide a constant level of anti-swing performance. To understand the behavior of the crane, a model of the crane is described by an equation of motion, using the 1-dimensional coordinate system in Figure 1. The trolley moves horizontally (x-axis), and the crane has a swing angle of θ. The payload has a mass of m, is hung under the trolley with a rope of length l, and moves with a velocity of v. The equation of motion for the oscillation of the hanging mass m is shown in equation (1). The full derivation of equation (1) can be seen in [10].

$$\ddot{\theta} + \left(\frac{b_{load}}{ml^2}\right)\dot{\theta} + \left(\frac{g}{l}\right)\theta = -\frac{1}{l}\dot{v} \qquad (1)$$

When b_{load} is set to a value that causes the pendulum to oscillate indefinitely, say 0 Ns/m (for the sake of explanation), and a mass of m = 100 kg is loaded onto a rope of length l = 3 meters. The natural frequency or frequency of oscillation in terms of angular velocity can be calculated using equation (2).

$$\omega_n = \sqrt{\frac{g}{l}} = \sqrt{\frac{9.81}{3}} = 1.808\ rad/\ s \qquad (2)$$

The natural frequency can be converted into the oscillation period of 3.48seconds. The Zero Vibration (ZV) input shaping was introduced based on the diagram shown in Figure 2, with the aim of eliminating the sway of the load. It involves combining two velocity signals: the first at *%50*velocity at initial time 1 second, and the second at *%50*velocity at the half oscillation period time lag of 1.74 seconds. The combined signal is shown in Figure 2 .As a result, no sway occurs from time 2.74seconds onward.

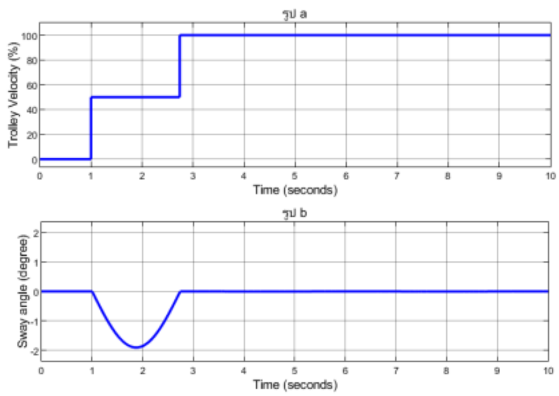

Figure 2. Show the sway suppression by combining velocity signals.

The above example specifies that there is no damping in the oscillation, resulting in continuous oscillation without stopping. The maximum oscillation angle has the same value throughout, while in a real crane system, there is some damping in the oscillation that reduces gradually, causing the maximum angle to reduce gradually until it finally stops oscillating, which may take several minutes. Therefore, the principle of suppressing the above-mentioned oscillation cannot be applied well when there is no damping. However, when there is damping, the maximum oscillation angle gradually decreases, so the first speed will be higher than 50%, while the second speed will be lower than 50%. Both speeds can be added up to 100%. In addition, the amplitude of the oscillation period from the natural frequency will also decrease slightly due to the impact of damping. However, this technique can be replaced with input shaping, which is widely used to suppress oscillations.

3. Design of the Control Scheme

The authors created a warehouse management system that can communicate with the crane navigation system and use the data obtained to integrate with the path planning and trajectory generation system. The data obtained from the navigation system were used to control the crane with a filter to eliminate oscillation. Finally, a 3D simulation was created to show the movement of the crane above the warehouse. The workflow of the crane control system is illustrated in Figure 3.

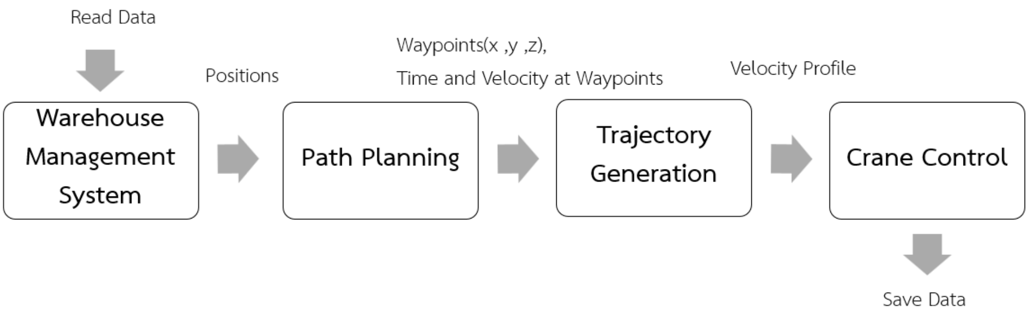

Figure 3. The workflow of the crane control system.

3.1. Warehouse Management System (WMS)

To make the overhead crane move automatically safely, in addition to the sensors currently used, the overhead crane in the warehouse management system should have a communication system to exchange data with the Warehouse Management System (WMS) so that the overhead crane can detect known obstacles or objects in the warehouse before using the sensors. The team therefore created a WMS as a database before used it in the path planning.

3.2. Path Planning

Path planning requires obtaining various position values such as the starting point, end point, and obstacles, using the database from the Warehouse Management System (WMS). The expected result of the path planning is the shortest path. The algorithms considered in this work are as follows:

- A* Algorithm: the authors used the A* Algorithm through the plannerAStarGrid function in MATLAB.
- Corner Algorithm (CA): this is an algorithm that the authors. A typical path planning algorithm involves randomly selected points around the area and connecting them together, much like a root of a tree. However, the problem is that the random points generated are too many. Therefore, the authors chose to use the corners of the product boxes as the waypoints to connect the paths.

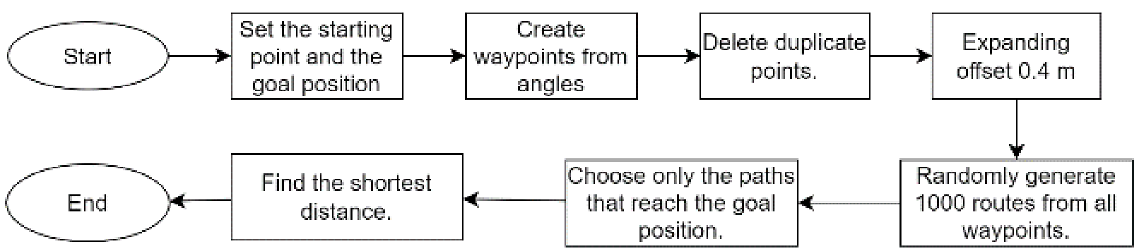

Figure 4. The diagram shows the calculation process of CA.

- Improved Corner Algorithm (ICA): the difference between the traditional CA method shown in Figure 4 and the improved method in Figure 5 is to reduce the number of times to randomly search for a path. Once the path is found, it will be optimized again to achieve the most efficient distance.

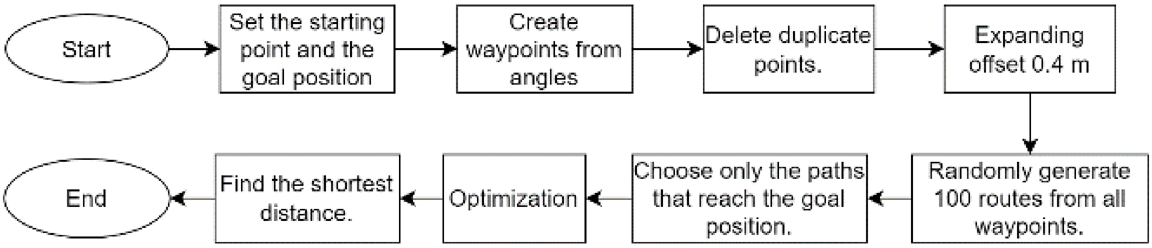

Figure 5. The diagram shows the calculation process of ICA.

3.3. Trajectory Generation
To create a path for movement, the following data are necessary: waypoints, time at each waypoint, and speed at each waypoint. The speed at each waypoint can be set to 0 to simplify the process of setting values. The resulting trajectory provided a speed profile which was used to control the movement of the crane.

3.4. Crane Control
When the overhead crane moves, the following payload sway can be dangerous. Therefore, controlling the crane to follow the path and to minimize the payload sway is necessary. To achieve this, data from the navigation system were used to control the crane and an input shaping is applied to eliminate the swing as shown in Figure 6. As described in section 2, input shaping uses 2 impulses to suppress the payload sway. The first half amplitude of the velocity input induces a payload sway for a certain frequency and the other half amplitude actuates the system precisely at the half system frequency from the first impulse. Thus, the 2 impulse obtains the half wave response of payload sway, which is no payload sway. Input shaping receives the velocity trajectory from the navigation system and outputs the shaped velocity, ready to transfer to the crane system in simulation. In general, an overhead crane is driven by three-phase inverters and motors, operated as the speed control mode. Therefore, in this work, the shaped velocity is assumed to be the actual velocity of the crane when the inverters have enough power to drive the crane toward the referent shaped velocity. In another word, the crane positioning control is a direct feedforward of the shaped velocity from input shaping. The payloads oscillation along the movement can be calculated by the pendulum model in section 2 and the crane position is simply obtained by time integral of the shaped velocity.

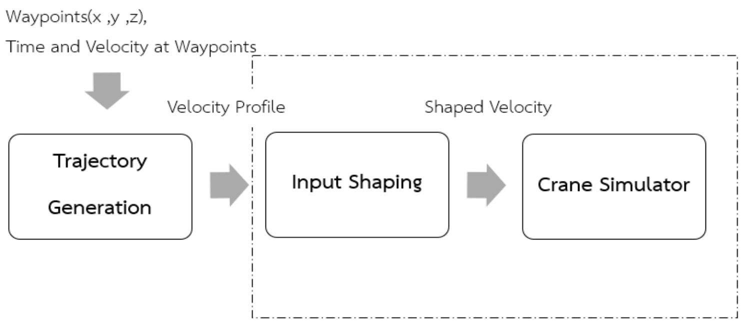

Figure 6. The process of the crane control system.

3.5. Simulation
Since the authors did not use an actual overhead crane in their testing, they created a simulation model of an overhead crane in a warehouse in MATLAB to demonstrate its movement, operation, obstacles, and sway. The simulation program is to provide a visualization of its operations, to facilitate study, and to allow for further development.

4. Results

This section will provide results of how the operations align with the ideas and theories presented in the previous section.

4.1. Labelling

The process of assigning codes to the product locations for ease of storage in a warehouse was adapted from the research work of Cuhanpet W. in] 20174 .[The code comprises of three digits as shown in Figure 7, with

- The first digit represents the y-axis (rack) position, denoted by A-Z.
- The second digit represents the x-axis (bay) position, denoted by *.99-01*
- The third digit represents the z-axis (level) position, denoted by A-Z.

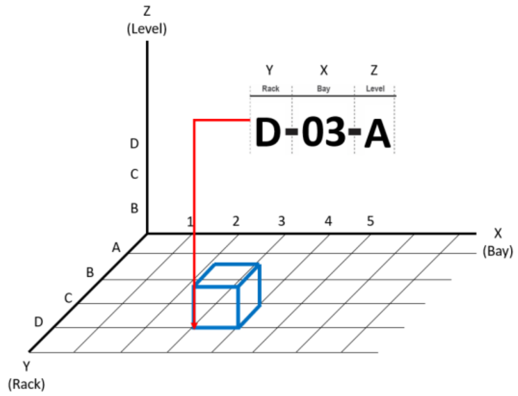

Figure 7. Labelling code for the product location.

4.2. Warehouse Management Program Development

The warehouse management program was written in MATLAB and involved creating a map of the warehouse and product locations based on WMS data. The program has three functions for operation, which are as follows:

- Function for incoming goods into the warehouse (move in)
- Function for removing goods from the warehouse (move out)
- Function for moving goods within the warehouse (transfer)

Figure 8 shows the move in function to receive goods into the warehouse with *2* options as follows: (1) manual location selection: a function in which users must specify the location they want to place, and (2) automatic location selection: a function in which the program automatically selects the location to place.

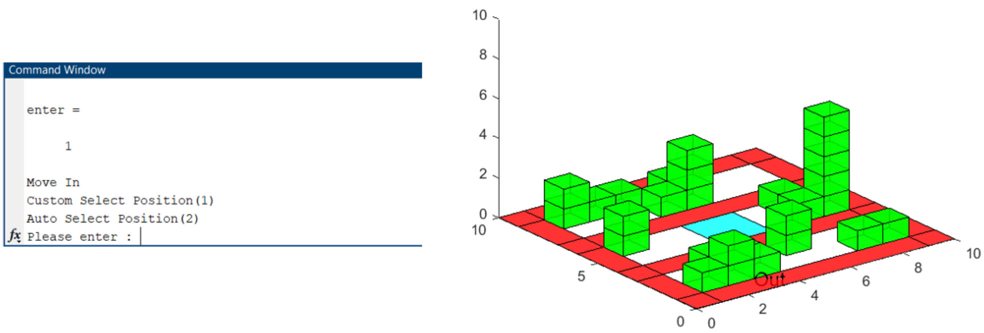

Figure 8. Function for incoming goods into the warehouse (move in).

Figure 9 show the move out function to export products from the warehouse, where the user must specify the product's location as a product label code. The program will then display the location of the desired product to be exported.

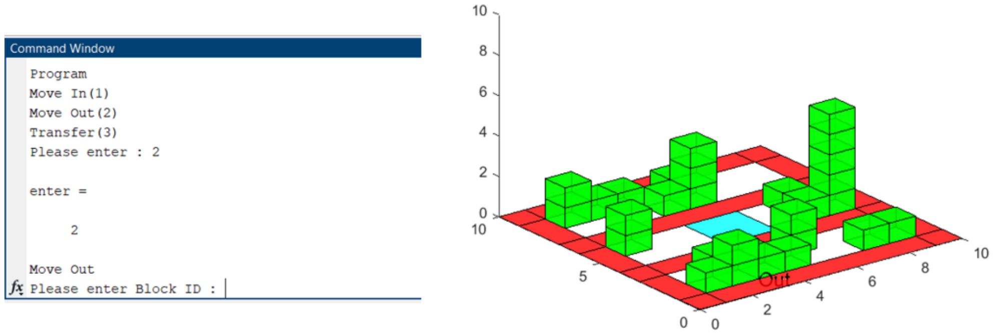

Figure 9. Function for removing goods from the warehouse (move out).

Figure 10 show the transfer function for moving products within a warehouse, where the user must input the product's label code and the label code of the destination location they want to move to. Then, the program will display the new location of the product.

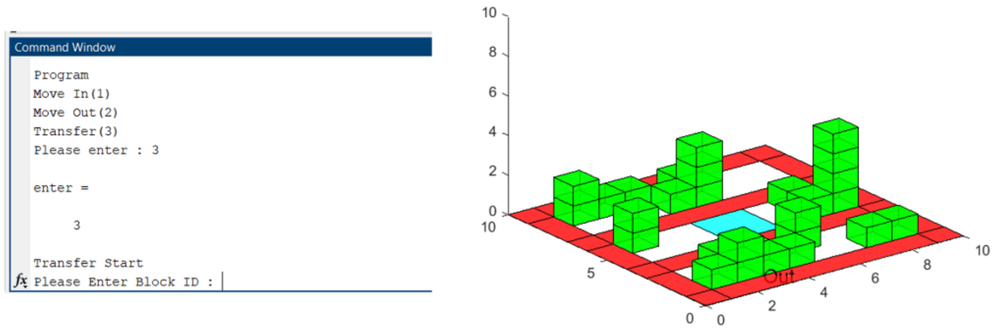

Figure 10. Function for moving goods within the warehouse (transfer).

4.3. Path Planning

Path planning used the warehouse database and commands obtained from the warehouse management program to create a route for movement. The selection criteria for algorithms are as follows:

- A small number of waypoints that can easily set the speed
- The shortest possible distance
- The shortest calculation time

Path planning results of the three algorithms are shown in Figure 11. The resulting performance are shown in the Table 1.

Table 1. The performance of the three algorithms: A*, CA, and ICA.

	A* Algorithm	CA	ICA
Shortest path (m)	11.71	11.28	11.09
Probability (%)	100	24	31
Average path (m)	11.71	12.38	11.55
Error (%)	0	9.75	4.15
Average calculation time (s)	1.37	11.86	1.64
Average number of waypoints	109	6	6

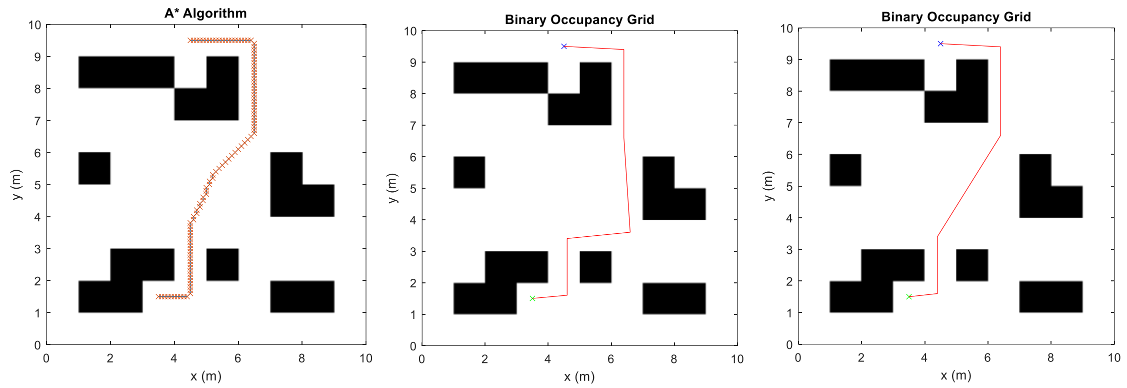

(a) (b) (c)

Figure 11. Path planning results of the three algorithms
(a) A* Algorithm, (b) Corner Algorithm, (c) Improved Corner Algorithm.

Based on the test results, Improved Corner Algorithm (ICA) worked best among the three because it has much less waypoints as compared with A*, making it easy to assign speeds. While the calculation time and path length of ICA are comparable to those of A*. The resulting path of ICA may be less optimal with respect to A*, but the path is straight making it easy to control. Therefore, the authors chose to use ICA for path planning and also the ICA resulting path for the trajectory generation.

4.4. *Trajectory Generation*

After taking the waypoints obtained from the ICA path planning method and assigning desired speeds to the waypoints, the cubic spline method, or the cubicpolytraj function in MATLAB was used to generate a smooth trajectory. Figure 12 shows the trajectory obtained from the proposed method. In the figure, the left is the position trajectory, and the right is the velocity trajectory.

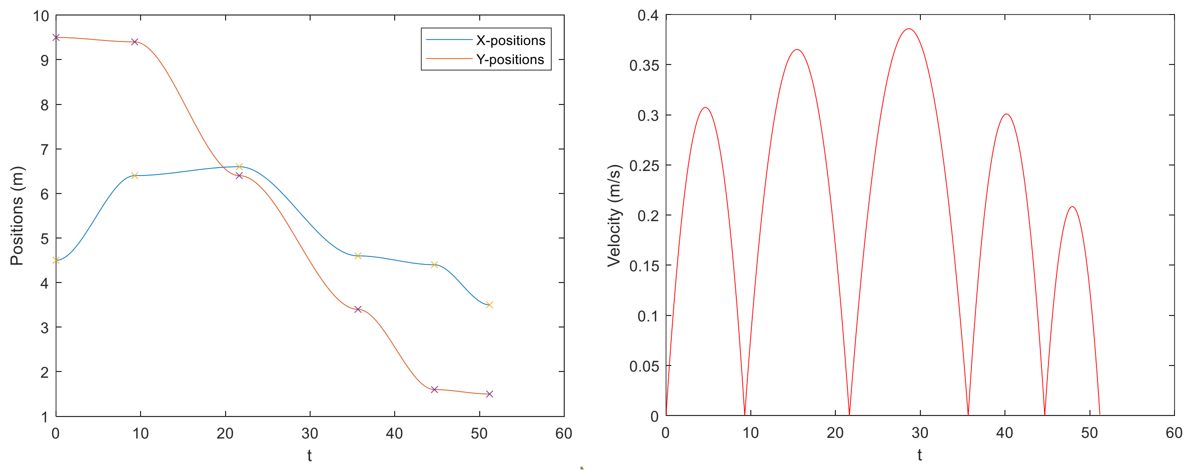

Figure 12. The trajectory obtained from the proposed algorithm
(left) position trajectory and (right) velocity trajectory.

4.5. *Crane Control*

Controlling the crane with sway suppression by adjusting the input velocity profile using input shaping was perform in MATLAB simulation. The velocity profiles with and without the input shaping are compared in the left of Figure 13. Because of the different velocity profiles, the resulting trolley position with input shaping slightly deviated from the original planned position especially at the corners, as seen in the right of Figure 13.

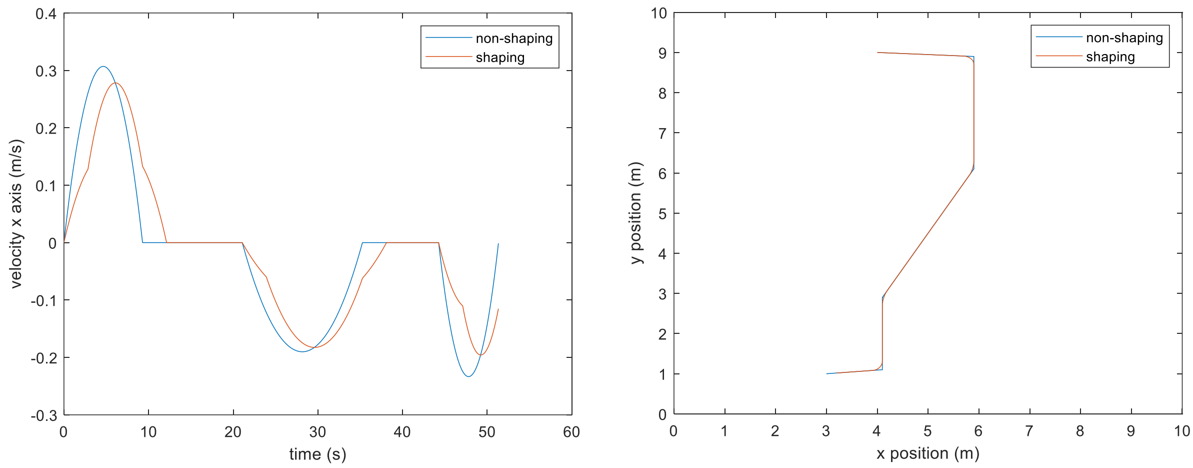

Figure 13. (Left) input velocity of non-shaping and shaping, and (right) the resulting position of the trolley when using non-shaping and shaping.

Even though the input shaper affects the crane position at corners, the sways caused by input shaping, as compared to non-input shaping, were significantly decreased, as shown in Figure 14.

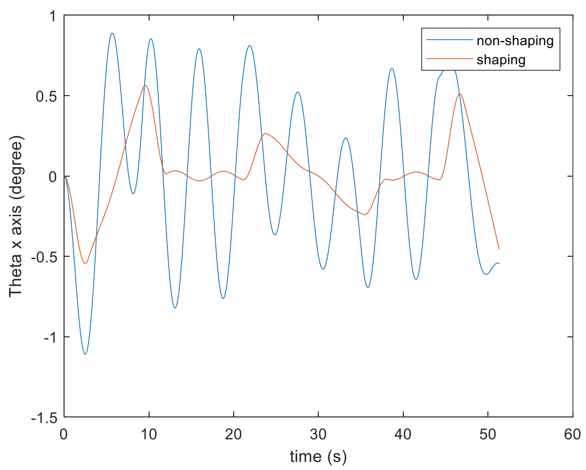

Figure 14. The sway angles when using the input shaping as compared to non-shaping.

With the WMS in conjunction to the navigation system, the simulation of the 3D movement of the crane was performed by using the velocity obtained from the trajectory generation to calculate the position of the crane over time. A screenshot of the 3D animated simulation workspace that displays obstacles, gripping, and movement of the crane are shown in Figure 15.

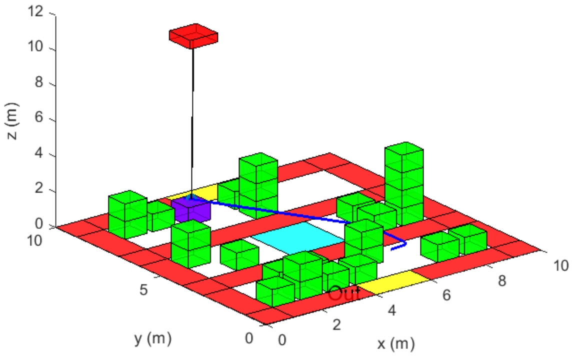

Figure 15. A screenshot of the 3D animated simulation.

5. Conclusions

The results were satisfactorily achieved according to the objectives and scope set. The proposed workflow can automatically guide the overhead crane based on the data from the warehouse management system, considering sway suppression. After that, the movements were simulated, and the results are as follows. Warehouse Management System (WMS) has various functions that can communicate with the overhead crane navigation system. This allows the navigation system to have a database that can indicate the position of obstacles. The authors proposed and tested the path planning algorithm, Improved Corner Algorithm (ICA), with the traditional A* algorithm. The ICA provided fewer waypoints than A*, which makes it easier to set the velocity for trajectory generation. Controlling sway using input shaping achieved the desired objective of reducing sway. From the simulation results, the design of the autonomous navigation can improve crane efficiency, speed, space utilization, reduce the number of workers needed, and increase safety.

6. References

[1] Suksabai N, Waikoonvet J, Chuckpaiwong I. (2020). Modelling Method Investigation of Drive and Motor for an Industrial Overhead Crane. *IOP Conference Series: Materials Science and Engineering*. 886, 012030.

[2] Kamnai A. (2007). "Warehouse Management" 2Nd ed. *Bangkok: Focus Media and Publishing Co., Ltd*.

[3] Pongchai A, Porapimol T. (2016). Special Characteristics of Education, Functions, and Factors Affecting Decision Making in Selecting Warehouse Management Software Systems. *Journal of Research and Development, KMUTT*. 39(3), 427-46.

[4] Cuhanpet W. (2017). *The layout design of finished goods in warehouse by ABC analysis case study of AAA company ltd.* [Master's thesis, Sripatum University]. College of Logistics and Supply Chain.

[5] Xin P, Wang X, Liu X, Wang Y, Zhai Z, Ma X. (2023). Improved Bidirectional RRT* Algorithm for Robot Path Planning. *Sensors*. 23(2),1041.

[6] Eslamiat H, Li Y, Wang N, Sanyal AK, Qiu Q, (2019). Autonomous waypoints planning, optimal trajectory generation and nonlinear tracking control for multi-rotor UAVs. *2019 18th European control conference (ECC)*: *IEEE*, 18906916.

[7] Wang H-J, Fu Y, Zhao Z-Q, Yue Y-J. (2019) An Improved Ant Colony Algorithm of Robot Path Planning for Obstacle Avoidance. *Journal of Robotics*. 6097591.

[8] Waikoonvet J, Suksabai N, Chuckpaiwong I, (2021). Collision-free Path Planning for Overhead Crane System Using Modified Ant Colony Algorithm. In *2021 9th International Electrical Engineering Congress (iEECON)*, 20656514.

[9] Suksabai N, Chuckpaiwong I (2023). The novel design of the command smoother for sway suppression of industrial overhead crane considering acceleration and deceleration limits. *International Journal of Dynamics and Control*. 11(2),1-19

[10] Suksabai N, Chuckpaiwong I. (2023). Input-Shaped Model Reference Control Using Sliding Mode Design for Sway Suppression of An Industrial Overhead Crane. *Engineering Journal*. 27(2),1-15.

DRC0006

System Parametric Study of Hunting Motion Stability of a Two-Axle Railway Bogie on Straight Track Via Hopf Bifurcation Analysis

Techit Sritrakul[1], Nattawoot Depaiwa[1], and Monsak Pimsarn[1,*]

[1]Department of Mechanical Engineering, School of Engineering, King Mongkut's Institute of Technology Ladkrabang, Bangkok 10520, Thailand.

* Corresponding Author: monsak.pi@kmitl.ac.th

Abstract. A railway vehicle running on a straight track has a stable motion at low speed. When it runs at higher speed, stability might change to an unstable form, significant lateral and yaw oscillations. This might lead to an accident due to wheel climb derailment. The objectives of this paper are to analyse the dynamic response of the railway bogie running on a straight track and to perform sensitivity analysis of system parameters on hunting motion stability using Hopf bifurcation analysis. The two-axle railway bogie model also takes into account of nonlinear yaw dampers and flange contact. The analysed results show that the front axle experiencing largest lateral displacement and the bogie lateral displacement is lowest when the rail vehicle speed is more than linear critical speed. For the sensitivity study, the results indicate that nonlinear critical speed has a considerable impact on wheel conicity. Simultaneously, the primary yaw stiffness is considerably altered. However, the secondary longitudinal stiffness is minimally affected.

Keywords: Railway bogie, railway vehicle dynamic, railway vehicle, hunting critical speed, Hopf bifurcation.

1. Introduction

Railway vehicle stability has been studied for more than two decades for increasing speed and improving riding comfort. One of the important factors for higher speed is stability. On one hand, a train moved at a lower speed. The train would have stable motion. On the other hand, the train moved higher speed. The train would become a hunting phenomenon or "Hunting motion" that is a source of significant lateral and yaw oscillations that contribute to vehicle instability, particularly at certain operating speeds [1] which a cause led to the derailment phenomenon. Furthermore, it affected the wheel-rail wear and made passengers uncomfortable.

Numerous studies have been conducted on the hunting dynamics in railway vehicles. Wickens analyzed the dynamics of existing railway vehicles on straight tracks and identified hunting as a self-excited oscillation in the lateral plane [2]. Yokose investigated the hunting stability of a bogie truck with small clearances and various factors affecting the limit cycle [3]. True and Jensen studied the dynamics of Cooperrider's bogie model and found speed ranges with stable forward motion, coexisting attractors, oscillations, and chaos [4]. Yabuno, Okamato, and Aoshima focused on the nonlinear characteristics of hunting in a wheelset model and proposed a method to determine the governing parameter [5]. Lee and Cheng derived coupled nonlinear differential equations for the motion of a two-axle bogie on curved tracks. They compared the influences of suspension parameters on the critical hunting speed [6].

The bifurcation method is a technique used to analyze the behavior of a system as parameters are varied in the dynamical system. It helps in identifying critical points where the system's behavior changes significantly. This method is applied in various fields, including hydraulic systems, impact systems, Van der Pol-Duffing oscillators, nonlinear and chaotic systems, and computer systems [7-11].

Furthermore, bifurcation analysis is well-known in hunting analysis because it allows for the investigation of the coupling effect of bogies on the hunting behavior of railway vehicles [12]. It helps to understand the stability and bifurcation types of the bogie, which directly affect the hunting stability of the entire vehicle system [13]. By analyzing the Hopf bifurcation behavior, it is possible to evaluate the critical hunting speeds and characterize the limit cycle oscillation behavior [14]. Bifurcation analysis also helps in determining the critical speed and limit cycle amplitude while considering nonlinearities such as yaw damping forces and friction creepage in the wheel-rail contact [15]. Additionally, it provides insights into the hysteresis phenomena of hunting motion and helps in determining outbreak velocities [16].

The nonlinearity of wheel-rail contact, the non-smoothness of the yaw damper, and the fluctuation of parameters such as the yaw damper and wheel tread shape are the key factors that determine the bifurcation and stability of railway systems [17]. Moreover, these factors can alter the bifurcation types of railway bogies, leading to changes in the behavior of the vehicle hunting stability [18]. The bifurcation behavior of limit cycles, which is affected by the nonlinear terms in the railway wheelset model, determines the occurrence of flange contact and derailment of high-speed railway vehicles [19]. Furthermore, the primary longitudinal stiffness and running velocity are bifurcation characteristics that can cause leaps in the lateral oscillation amplitude of the railway bogie system [20]. The yaw damper and its series stiffness value also play an important effect in railway bogie stability and bifurcation type. Nevertheless, most of the studies mentioned the variables that influence the critical speed. They did not clearly investigate the sensitivity of those parameters.

Therefore, the correctness of the equivalent function, the bifurcation behavior, the stability of the railway bogie on a straight track, and the sensitivity of system parameters on the critical speed are all represented in this work.

2. Bogie dynamical equations

The two-axle bogie model, 6-degree-of-freedom nonlinear system, is shown in Figure 1. The equations of lateral and yaw motion of both wheelsets are shown as the following [21]:

$$m_w \ddot{y}_i + \frac{2f_{11}}{V}\left[\left(1+\frac{r_0\lambda}{a}\right)\dot{y}_i - V\psi_i\right] + \frac{2f_{12}}{V}\dot{y}_i + W_A\frac{\lambda}{a} = F_{sys,yi} - F_{Ti} \tag{1}$$

$$\begin{aligned} &I_{wx}\ddot{\psi}_i + I_{wy}\frac{V}{r_0}\frac{\lambda}{a}\dot{y}_i + \frac{2af_{33}\lambda}{r_0}y_i - \frac{2f_{12}}{V}\left[\left(1+r_0\frac{\lambda}{a}\right)\dot{y}_i - V\psi_i\right] + \frac{2a^2f_{33}}{V}\dot{\psi}_i \\ &-aW_A\lambda\psi_i + \frac{2f_{22}}{V}\psi_i = M_{szi} - 2b_1F_{di} \end{aligned} \tag{2}$$

where the subscript i =1 identifies the rear wheelset and i =2 for the front wheelset. $f_{11}, f_{12}, f_{22}, f_{33}$ are the lateral creep force, lateral spin creep force, spin creep force, and longitudinal creep force. V, a, r_0, λ are the forward speed of the bogie, half of the track gauge, wheel radius, and wheel conicity. Furthermore, the equations of motion for the bogie frame are:

$$m_b\ddot{y}_b = -F_{sys,y1} - F_{sys,y2} - 2K_{sy}y_b - 2C_{sy}\dot{y}_b \tag{3}$$

$$I_{bz}\ddot{\psi}_b = -2K_{py}[y_1 - y_b + l_1\psi_b]l_1 + 2K_{py}[y_2 - y_b - l_1\psi_b]l_1$$
$$-2C_{py}[\dot{y}_1 - \dot{y}_1 + l_1\dot{\psi}_b]l_2 + 2C_{py}[\dot{y}_1 - \dot{y}_b - l_1\dot{\psi}_b]l_2 - 2K_{sx}b_2^2\psi_b \tag{4}$$
$$-2C_{sx}b_3^2\dot{\psi}_b + 2K_{px}b^2[\psi_1 - \psi_2 - 2\psi_b] + 2b_1[F_{d1} + F_{d2}]$$

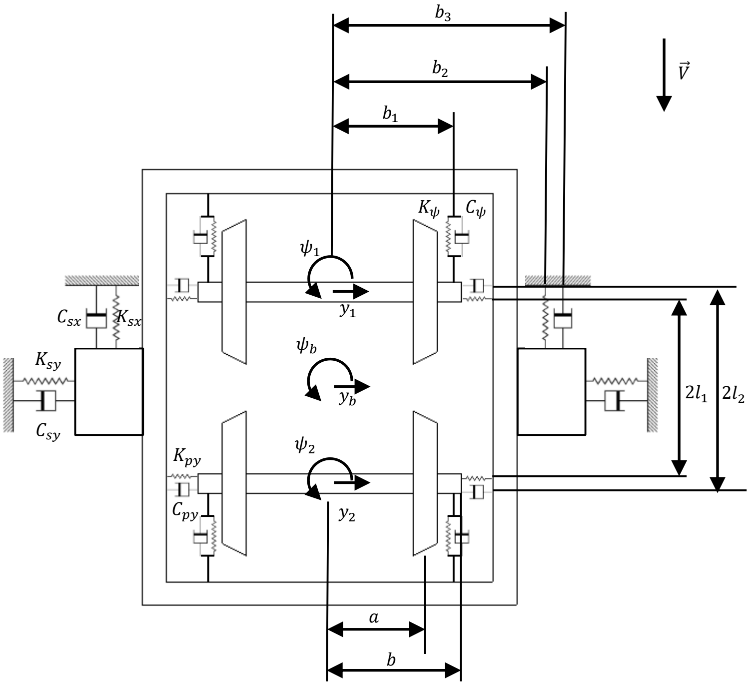

Figure 1. Two-wheelset bogie model.

where m_w, m_b, W_A are the wheelset mass, bogie frame mass, and axle load. I_{wx}, I_{wy}, I_{bz} are the roll moment and spin moment of inertia of wheelset, and yaw moment of inertia of bogie respectively. b, b_1, b_2, b_3 are the half of the primary yaw spring and damper arm, and the half of the secondary yaw spring and damper arm respectively. l_1, l_2 are the half of longitudinal distance of the secondary spring and the lateral secondary dampers. K_{px}, K_{py}, C_{py} are the primary yaw and lateral stiffness, and damping coefficient. $K_{sx}, K_{sy}, C_{sx}, C_{sy}$ are the secondary longitudinal and lateral stiffness and damping coefficient. $y_1, y_2, y_b, \psi_1, \psi_2, \psi_b$ represent the lateral and yaw displacement of the rear and front wheelsets and the bogie frame, and $\dot{y}_1, \dot{y}_2, \dot{y}_b, \dot{\psi}_1, \dot{\psi}_2, \dot{\psi}_b$ represent the lateral and yaw velocity of the rear and front wheelsets and the bogie frame, respectively.

Parameters $F_{sus,yi}$ and $M_{sus,zi}$ define the suspension force of the bogie and yaw moment of the wheelsets as Equation (5) and Equation (6):

$$F_{sys,yi} = -2K_{py}\left[y_i - y_b + (-1)^{i+1}l_1\psi_b\right] - 2C_{py}\left[\dot{y}_i - \dot{y}_b + (-1)^{i+1}l_2\dot{\psi}_b\right] \tag{5}$$

$$M_{sus,zi} = -2K_{px}b^2(\psi_i - \psi_b) \tag{6}$$

The nonlinear longitudinal yaw damping force F_{di} and flange contact force F_{Ti} are represented in Equation (7) and Equation (8):

$$F_{di} = \begin{cases} C_1V_{\psi i} + C_2V_{\psi i}^2 + C_3V_{\psi i}^3 + C_4V_{\psi i}^4 & V_{\psi i} > 0 \\ C_1V_{\psi i} - C_2V_{\psi i}^2 + C_3V_{\psi i}^3 - C_4V_{\psi i}^4 & V_{\psi i} < 0 \end{cases} \tag{7}$$

$$F_{Ti}=\begin{cases} K_r\left(y_i-\delta\right) & y_i>\delta \\ 0 & -\delta\le y_i\le\delta \\ K_r\left(y_i+\delta\right) & y_i<-\delta \end{cases} \tag{8}$$

where $V_{\psi i}=b_1(\dot{\psi}_i-\dot{\psi}_b)$ is the relative velocity of the longitudinal yaw damper. The yaw damper coefficients C_1 to C_4 are obtained from the experimental tests on the actual dampers. The constant K_r is the lateral rail stiffness and δ is the flange clearance. The lateral clearance model is illustrated in Figure 2 [22].

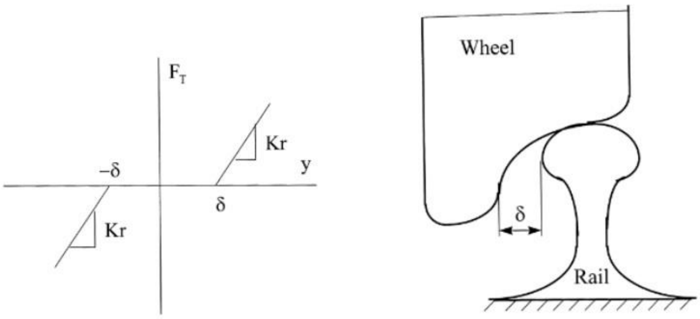

Figure 2. Flange force and lateral displacement between wheel and rail.

As it can be seen that numerous dynamical equations are employed in the bifurcation analysis which are complicated to calculate especially the nonlinear forces in Equation (7) and Equation (8). Sedighi and Shriazi [15] presented an equivalent function that simplifies the analytical investigation of the nonlinear problems to be easily estimated. However, this function was employed in the case of single wheelset. In the work, the equivalent function is rewritten and evaluated for the two-wheelset bogie instance:

$$\begin{aligned} F_{di}(V_{\psi i})=&\left(\frac{1}{2}+\frac{1}{2}\frac{\left|V_{\psi i}\right|}{V_{\psi i}}\right)\times\left(C_1V_{\psi i}+C_2V_{\psi i}^2+C_3V_{\psi i}^3+C_4V_{\psi i}^4\right) \\ &+\left(\frac{1}{2}-\frac{1}{2}\frac{\left|V_{\psi i}\right|}{V_{\psi i}}\right)\times\left(C_1V_{\psi i}-C_2V_{\psi i}^2+C_3V_{\psi i}^3-C_4V_{\psi i}^4\right) \end{aligned} \tag{9}$$

$$F_{Ti}=\frac{1}{2}K_r\left(2y_i+\left|y_i-\delta\right|-\left|y_i+\delta\right|\right) \tag{10}$$

3. The analytical-stability method

To get the result of the critical speed and the nonlinear behavior of the system, Equation (1) to Equation (4) can be written in the general form:

$$\dot{x}=f(x;V)=A(V)x+F(x) \tag{11}$$

where $A(V)$, a 12×12 system matrix, indicates the linear term that V is the control parameter, $F(x)$, an 12 element row vector, represents the nonlinear term which include nonlinear forces and x is state vector. The elements of the matrix $A(V)$ are described in [21] and the element of the vectors $F(x)$ and x are described following:

$$F(x)=\left\{0 \quad -\frac{1}{m_w}F_{T1} \quad 0 \quad -\frac{2b_1F_{d1}}{I_{wx}} \quad 0 \quad -\frac{1}{m_w}F_{T2} \quad 0 \quad -\frac{2b_2F_{d2}}{I_{wx}} \quad 0 \quad 0 \quad 0 \quad \frac{2b_1}{I_{bz}}(F_{d1}+F_{d2})\right\}^T$$

$$x = \{y_1 \quad \dot{y}_1 \quad \psi_1 \quad \dot{\psi}_1 \quad y_2 \quad \dot{y}_2 \quad \psi_2 \quad \dot{\psi}_2 \quad y_b \quad \dot{y}_b \quad \psi_b \quad \dot{\psi}_b\}^T$$

In steady state $(t \to \infty)$, the equilibrium point of the system is the nonlinear behavior of the system for the constant control parameter. Consequently, Equation (12) represents the equilibrium or fixed point response as:

$$\dot{x} = f(x;V) = 0 \tag{12}$$

4. Hopf bifurcation analysis

In nonlinear systems, when the curves of the frequency response of the system are plotted by manipulating parameters, the changes in the stability of the system or the fixed point are occurred. These points are called bifurcation points. For fixed point response, bifurcation points are classified according to the nature of the eigenvalues of the system. In the hunting phenomenon, Hopf bifurcation point is valid if $\dot{x} = f(x_0;V) = 0$ and all other eigenvalues of the Jacobian matrix have negative real part at $(x_0;V)$ and one pure imaginary eigenvalue pair $(\pm j\omega)$. Let the analytic extension of the imaginary eigenvalue pair $\lambda = \pm j\omega$ for $V = V_c$. In that instance, this condition is known as the condition of transversality, since the eigenvalue passes through the imaginary axis at non-zero speed. When the mentioned conditions are fulfilled, the periodic solution $(2\pi/\omega)$ is built at $(x_0;V)$. This type of bifurcation is called the Hopf bifurcation or the Poincaré–Adronov Hopf bifurcation [23].

As a velocity of the railway vehicle increases, it destabilizes and reveals onerous oscillations. According to bifurcation theory, hunting is a phenomenon known as Hopf bifurcation of a fixed point. The motion is steady (or exhibits a stable fixed point in phase space) below a certain "critical" forward velocity. Above the critical speed, hunting appears as undamped vehicle motion constrained between the wheel flange and the rail (or the fixed point loses stability and a limit cycle splits from it). The decay rate of the wheelset's phase portrait is determined by the control parameter V. When a stable spiral transforms into an unstable spiral surrounded by a tiny limit cycle, a supercritical Hopf bifurcation occurs. [24].

5. Parametric studies and results

The analysis of the influence of the system parameters on the hunting motion which the forward speed V is a control parameter, is calculated by solving Equation (11) using MATLAB software with the ode45 (Runge-Kutta (4,5)/ Dormand-Prince pair) command in the time domain. To ensure precise results, the maximum step time was set to 0.01. The system parameters are shown in Table 1.

Table 1. System parameters used for numerical simulation [15,21-22].

Parameters	Values	Parameters	Values	Parameters	Values
W_A	38,492.4 N	K_{sx}	2.189×10^5 N/m	b_3	0.889 m
m_b	4,255.6 kg	K_{sy}	1.532×10^5 N/m	l_1	1.295 m
m_w	1,800 kg	C_{sx}	6.129×10^5 N s/m	l_2	1.295 m
I_{wx}	625.7 kg m^2	C_{sy}	5.254×10^4 N s/m	f_{11}	6.728×10^6 N
I_{wy}	133.92 kg m^2	C_1	1.923×10^4 N s/m	f_{22}	1,000 N m^2
I_{bz}	10,314 kg m^2	C_2	5.14×10^5 N s/m	f_{12}	1,200 N m
r_0	0.533 m	C_3	-3.1127×10^6 N s/m	f_{33}	6.728×10^6 N
a	0.7176 m	C_4	5.14×10^6 N s/m	K_r	1.617×10^7 N/m
K_{py}	8.67×10^4 N/m	b	1 m	δ	9.23×10^{-3} m
K_{px}	8.67×10^4 N/m	b_1	1.27 m	λ	0.05
C_{py}	2.1×10^4 N s/m	b_2	0.794 m		

Figure 3 shows examples of the numerical simulation limit cycle, which demonstrates the validity and efficacy of the proposed equivalent function. As the result, the equivalent function is valid to be employed in the analysis section.

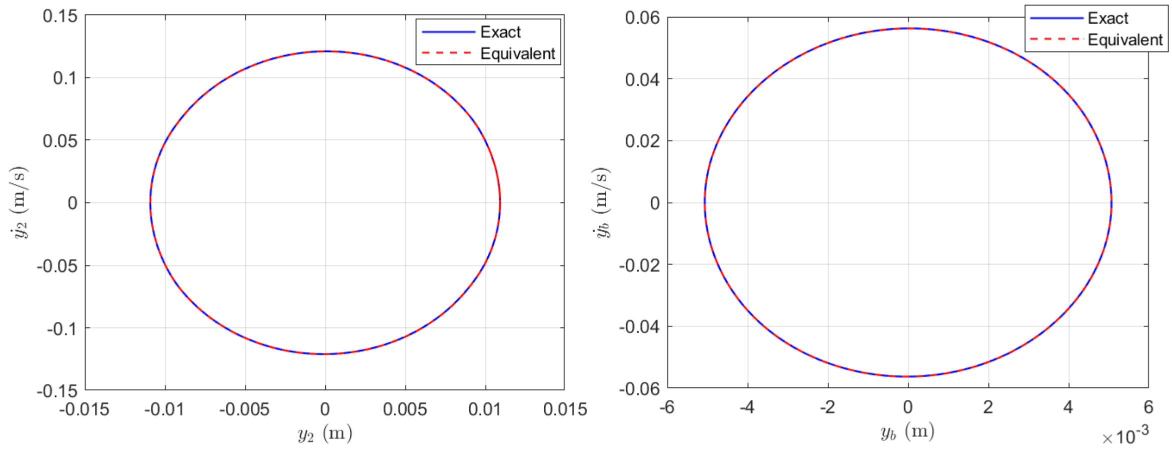

Figure 3. A comparison of the calculations for the limit cycles of lateral displacement of the front wheelset and bogie frame using the equivalent function and the exact formulae.

The bifurcation diagrams in Figures 4 exhibit an amplitude of the system response versus speed and a linear critical speed at $V_c = 32.8$ m/s. When V exceeds V_c, the amplitude of the system is higher, particularly the amplitude of front wheelset, which is above than the flange clearance, causing a derailment risk.

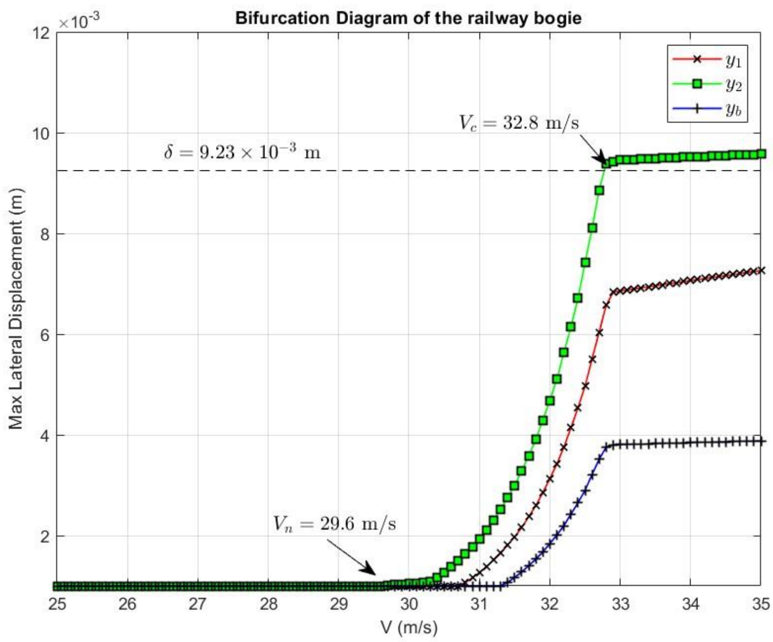

Figure 4. Bifurcation diagram of the railway bogie.

As it can be seen in Figure 4 that the bifurcation diagram of the front wheelset shows a nonlinear critical speed at $V_n = 29.6$ m/s, which differs by 9.69 percent from Yang's result [21]. The nonlinear behaviours of the railway bogie are represented in Figures 5-7. The phase portrait and the time dependence of lateral displacement at $V < V_n$ demonstrate that the stable state remains a stable fix point. For $V_n < V < V_c$, the system response and phase portrait change to unstable form in which the limit cycle expands. Because of the flange contact with the rail, the system response becomes stable for $V > V_c$, and the behaviour of the limit cycle significantly alters.

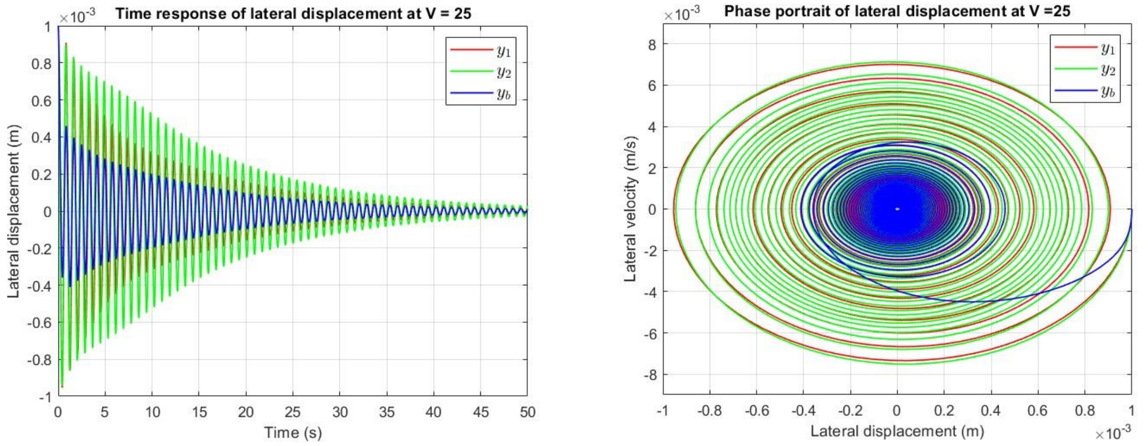

Figure 5. Time response and phase portrait of lateral displacement at V = 25 m/s.

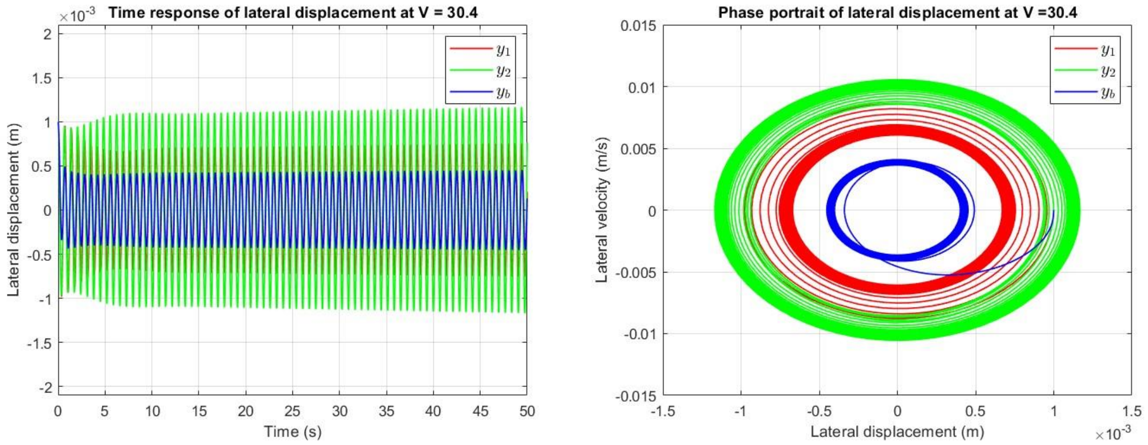

Figure 6. Time response and phase portrait of lateral displacement at V = 30.4 m/s.

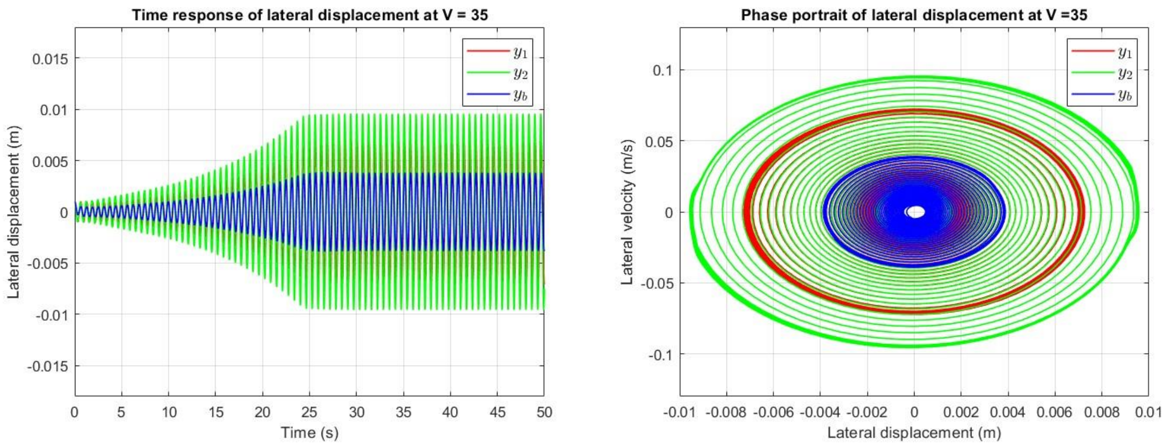

Figure 7. Time response and phase portrait of lateral displacement at V = 35 m/s.

Parametric studies with shifting values of the parameters and focusing on nonlinear critical speed change are depicted in Figures 8-10. As illustrated, the changes of the wheel radius r_0, wheel conicity λ and primary yaw stiffness K_{px} parameters are significantly affected an increasing nonlinear critical speed in every range of changes, with a decrease of 30% in wheel conicity increasing the nonlinear critical speed by 18.58% and an increase of 30% in both wheel radius and primary yaw stiffness increasing the nonlinear critical speed by 14.86% and 14.53% respectively. In other parameters, decreasing bogie mass m_b, wheelset mass m_w, primary lateral damper C_{py} and half of the longitudinal distance of the secondary spring and the lateral secondary dampers l_1, l_2 are influenced by an increasing critical speed, with a reducing wheelset mass being the most affected in terms of a reduced mass within 10.14% nonlinear critical speed increasing by reducing 30%, while others are only slightly affected. A change of primary lateral stiffness K_{py}, secondary longitudinal and lateral stiffness K_{sx}, K_{sy} and secondary longitudinal damping coefficient C_{sx}, C_{sy} has a slight impact on nonlinear critical speed by less than 5%. In contrast, a change in secondary longitudinal stiffness has a negligible impact on nonlinear critical speed by 0.33% in all ranges of changes.

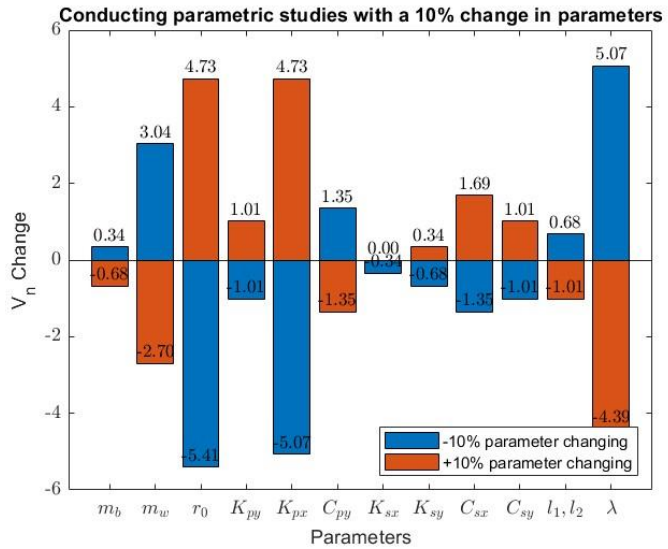

Figure 8. Bar chart of conducting parametric studies with a 10% change in parameters.

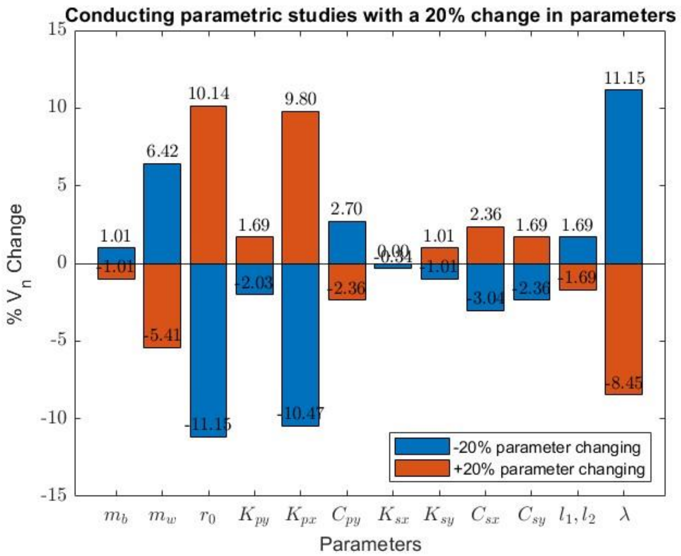

Figure 9. Bar chart of conducting parametric studies with a 20% change in parameters.

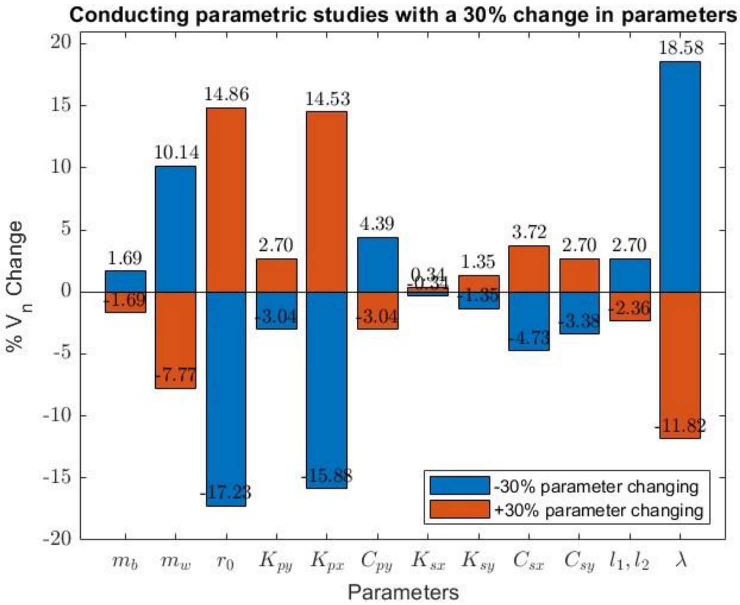

Figure 10. Bar chart of conducting parametric studies with a 30% change in parameters.

6. Conclusion

The analysis of bifurcation behavior, railway bogie stability on railway track, and the sensitivity of system parameters including bogie frame mass, wheelset mass, wheel radius, primary yaw and lateral stiffness, primary lateral damping coefficient, secondary longitudinal and lateral stiffness, secondary longitudinal and lateral damping coefficient, half of longitudinal distance of secondary spring and lateral secondary dampers, and wheel conicity on nonlinear critical speed are summarized:

1. Wheelset parameters including wheelset mass, wheel radius, and wheel conicity has a significant impact on changing nonlinear critical speed.
2. For the primary suspension parameters, the primary longitudinal stiffness is the most influencing parameter on nonlinear critical speed.
3. The changing of nonlinear critical speed is slightly affected by all secondary suspension parameters and bogie frame mass.
4. The results show that the secondary longitudinal stiffness has no impact on the nonlinear critical speed.

7. References

[1] Shabana, A.A., Zaazaa, K.E., & Sugiyama, H. (2007). *Railroad Vehicle Dynamics: A Computational Approach (1st ed.)*. CRC Press. https://doi.org/10.1201/9781420045857

[2] A., H., Wickens. (1965). Paper 1: *The Dynamics of Railway Vehicles on Straight Track: Fundamental Considerations of Lateral Stability*. 180(6):29-44. doi: 10.1243/PIME_CONF_1965_180_177_02

[3] Keiji, Yokose. (1988). *An analysis of running stability of high speed railway trucks connected in series with elastic and frictional forces working against truck turning*. Vehicle System Dynamics, 17:543-554. doi: 10.1080/00423118808969295

[4] Hans, True., Jens, Christian, Jensen. (1994). *Parameter study of hunting and chaos in railway vehicle dynamics*. Vehicle System Dynamics, 23:508-521. doi: 10.1080/00423119308969537

[5] Sen, Yung, Lee., Yung-Chang, Cheng. (2003). *Nonlinear hunting stability analysis of high-speed railway vehicles on curved tracks*. International Journal of Heavy Vehicle Systems, 10(4):344-361. doi: 10.1504/IJHVS.2003.003698

[6] Anant, Mohan. (2003). *Nonlinear Investigation of the Use of Controllable Primary Suspensions to Improve Hunting in Railway Vehicles*.
[7] Hao, Sun., Jianfeng, Tao., Chengjin, Qin., Honggan, Yu., Chengliang, Liu. (2021). *Dynamics Modeling and Bifurcation Analysis for Valve-Controlled Hydraulic Cylinder System Containing Counterbalance Valves*. Journal of Vibration Engineering, 1-17. doi: 10.1007/S42417-021-00342-6
[8] Hawraa., K., Mnahi. (2020). *Bifurcation Theory by Melnikov method in fast slow system*. 10(2):212-218.
[9] Lijuan, Ning. (2020). *Bifurcation analysis in the system with the existence of two stable limit cycles and a stable steady state*. Nonlinear Dynamics, 102(1):115-127. doi: 10.1007/S11071-020-05887-X
[10] Timur, I., Karimov., Olga, Druzhina., Valery, S., Andreev., Aleksandra, V., Tutueva., Ekaterina, E., Kopets. (2021). *Bifurcation Spectral Diagrams: a Tool for Nonlinear Dynamics Investigation*. doi: 10.1109/ELCONRUS51938.2021.9396657
[11] Nikola, Beneš., Luboš, Brim., Samuel, Pastva., David, Šafránek. (2019). *Digital Bifurcation Analysis of TCP Dynamics*. 339-356. doi: 10.1007/978-3-030-17465-1_19
[12] Pilkee, Kim., Jongwon, Seok. (2010). *Bifurcation analysis on the hunting behavior of a dual-bogie railway vehicle using the method of multiple scales*. Journal of Sound and Vibration, doi: 10.1016/J.JSV.2010.03.024
[13] Yong, Yan., Jing, Zeng. (2018). *Hopf bifurcation analysis of railway bogie*. Nonlinear Dynamics, doi: 10.1007/S11071-017-3634-7
[14] Caglar, Uyulan., Metin, Gokasan., Seta, Bogosyan. (2017). *Dynamic Investigation of the Hunting Motion of a Railway Bogie in a Curved Track via Bifurcation Analysis*. Mathematical Problems in Engineering, doi: 10.1155/2017/8276245
[15] Hamid, M., Sedighi., Kourosh, H., Shirazi. (2012). *Bifurcation analysis in hunting dynamical behavior in a railway bogie: Using novel exact equivalent functions for discontinuous nonlinearities*. Scientia Iranica, doi: 10.1016/J.SCIENT.2012.10.028
[16] U-Jin, Jeong., Seong-Won, Kim. (2000). *A Study on the Critical Speed of Railway Vehicles*. Transactions of The Korean Society of Mechanical Engineers A, doi: 10.22634/KSME-A.2000.24.8.1991
[17] Hao, Dong., Bin, Zhao., Yuanyuan, Deng. (2018). *Instability phenomenon associated with two typical high speed railway vehicles*. International Journal of Non-linear Mechanics, doi: 10.1016/J.IJNONLINMEC.2018.06.006
[18] Lifang, Cheng., Lifang, Cheng., Xiukun, Wei., Hongjun, Cao. (2018). *Two-parameter bifurcation analysis of limit cycles of a simplified railway wheelset model*. Nonlinear Dynamics, doi: 10.1007/S11071-018-4333-8
[19] Tingting, Zhang., Hans, True., Huanyun, Dai. (2018). *A codimension two bifurcation in a railway bogie system*. Archive of Applied Mechanics, doi: 10.1007/S00419-017-1314-1
[20] Yong, Yan., Jing, Zeng., Caihong, Huang., Tingting, Zhang. (2019). *Bifurcation analysis of railway bogie with yaw damper*. Archive of Applied Mechanics, doi: 10.1007/S00419-018-1475-6
[21] Ahmadian, M., & Yang, S.. (1998). *Effect of System Nonlinearities on Locomotive Bogie Hunting Stability*. 29(6), 365–384. https://doi.org/10.1080/00423119808969380
[22] Yang, S. and Ahmadian, M. *''The Hopf bifurcation in a rail wheelset with nonlinear damping''*, Proc. of Transportation Division, International Mechanical Engineering Congress and Exposition, Atlanta., pp. 112–135 (1996)
[23] Uyulan Ç, Gokasan M, Bogosyan S. *Stability and bifurcation analysis of the non-linear railway bogie dynamics*. Proceedings of the Institution of Mechanical Engineers, Part C: Journal of Mechanical Engineering Science. 2018;232(16):2787-2802. doi:10.1177/0954406217727304
[24] Strogatz, S.H., *Nonlinear Dynamics and Chaos, with Application to Physics, Biology, Chemistry and Engineering*, Perseus Books Publishing (1994)

BME0001

Design of Dynamic Stabilization System with Stiffness Similar to Normal Discs by Topology Optimization

Norravich Lertviriyachit[1,3], PairatTangpornprasert[1,2,3], ChanyaphanVirulsri[1,2,3,*]

[1]Center of Excellence for Prosthetic and Orthopedic Implant, Chulalongkorn University, Bangkok 10330, Thailand.
[2]Department of Mechanical Engineering, Faculty of Engineering, Chulalongkorn University, Bangkok 10330, Thailand.
[3]Biomedical Engineering Research Center, Faculty of Engineering, Chulalongkorn University, Bangkok 10330, Thailand.

* Corresponding Author: chanyaphan.v@eng.chula.ac.th

Abstract. Low back pain is undeniably a common spinal problem primarily caused by lumbar spine instability resulting from various disorders, ranging from tumors and herniated discs to spondylolisthesis. The gold standard treatment for this instability is the spinal fusion technique, which involves rigid fixation through pedicle screws and rods. This method allows patients to regain significant stability in their lumbar spines. However, it also carries a major drawback: the risk of adjacent segment degeneration (ASD) due to the necessary motion compensation from the adjacent spinal units. To address this issue, a dynamic stabilization system (DSS) was developed to help stabilize problematic segments while allowing motion, thus reducing the occurrence of ASD. Although state-of-the-art DSS focuses on enabling spinal motion within the neutral zone, further attention must be given to achieving a decent stiffness for the DSS. Existing DSS designs, such as Dynesys and Bioflex, mainly focused on providing motion but were too rigid to prevent ASD efficiently. Therefore, our research aimed to develop a DSS that can achieve a similar stiffness to normal lumbar discs by leveraging the advantages of carbon fiber-reinforced polyether-ether-ketone (CFR-PEEK), including strength, flexibility, and biocompatibility. Topology optimization as a tool in Ansys was utilized to obtain the initial shape of our DSS. During the optimization process, three types of moments—flexion-extension (FE), lateral bending (LB), and axial rotation (AR)—were applied as boundary conditions, with a magnitude of 6.6 Nm, to simulate physiological spinal movements. Subsequently, the initial shape underwent fine-tuned and validation to ensure that the final shape achieved the desired stiffness: k_{FE} = 1.8 Nm/°, k_{LB} = 2.3 Nm/°, and k_{AR} = 8.4 Nm/°. The resulting DSS exhibited stiffness values of k_{FE} = 2.10 Nm/°, k_{LB} = 2.66 Nm/°, and k_{AR} = 9.28 Nm/°, respectively. These outcomes deviated from the target of only 16.7%, 15.7%, and 10.5%, demonstrating the effectiveness of the design. However, the designed DSS manufacturing process remained challenging owing to its complicated shape.

Keywords: Dynamic stabilization system, Carbon-fiber reinforced polyether-ether-ketone (CFR-PEEK), Topology optimization.

1. Introduction

Low back pain is undoubtedly one of the most common spinal problems among all the pain caused in other spinal segments [1]. A report has demonstrated that about 70% of all back injuries that can cause work loss in the US occur in the lumbar region, especially in L4-5 [1]. Physicians typically decide to treat with non-surgical techniques, such as medication, and physical therapy, as the initial course of action. However, if the treatment outcomes show no improvement, they may turn to another technique called spinal fusion [2].

Spinal fusion is a surgical treatment considered the gold standard for addressing instability. This procedure involves the utilization of pedicle screw system, comprising pedicle screws and rods. Intraoperatively, patients are accessed to the problematic segments for treatment, and bone graft is implanted to replace the intervertebral discs. The pedicle screw system serves an essential role in rigidly stabilizing those segments while awaiting sufficient growth of bone graft to provide patients with adequate stability [2]. Despite the significant benefits of spinal fusion, this procedure also presents two major downsides. The first one involves long-term impact on patients. While the rigid fixation can provide stability to the spine, over time, the adjacent segments have to bear more loads and compensate for the restricted movements in the instrumented segments. This could lead to the risk of degeneration, known as adjacent segment degeneration (ASD) [3-5]. The second issue is related to the mechanical properties of Ti6Al4V, the medical-grade titanium alloy. In metastatic cases, titanium implants could interfere with radiography outcomes by generating artifacts, making it difficult to monitor complications, detect recurrent tumors, and proceed with radiotherapy [6, 7]. Its high Young's modulus could also lead to stress shielding, causing a reduction in bone density [7]. However, in the last few decades, carbon-fiber reinforced Poly-ether-ether-ketone (CFR-PEEK) has been introduced as a promising biocompatible material. The polymer composite properties of CFR-PEEK provide artifact-free radiography [6, 7] and prevent stress shielding due to the comparable Young's modulus to cortical bone [7].

To prevent or at least cut down the chances of developing ASD in patients undergoing spinal fusion, a dynamic stabilization system (DSS) was developed [3-5]. The principles behind the DSS closely resemble those of the pedicle screw system. The main difference between these two devices is that there is no need to perform spinal fusion as the DSS allows movements in the instrumented segments while providing stability and assists in transmitting excessive loads from the disc [3-5].

Despite the development of state-of-the-art DSS in various designs, such as Dynesys, Isobar, TOPS, and Accuflex, aimed at preserving motion by modifying the mechanisms in screws, rods, or both, they still exhibit certain limitations. To elaborate, the Dynesys (Dynamic Neutralization System), a pedicle screw based DSS, comprises titanium pedicle screws, polycarbonate urethane (PCU) spacers, and polyester (PET) cords. The PCU spacer functions as a stopper resisting spinal extension, whereas the PET cord resists spinal flexion [3]. However, numerous studies have indicated that the Dynesys did not demonstrate superiority in treating ASD when compared with traditional rigid fixation [3, 8]. The substantially decreased range of motion (ROM) in the operated segment reflected the high stiffness of the system. Another illustration is the Isobar, which uses damping rods as the DSS [3]. The study conducted by Y. Yang et al. [9] reported that the significant decreases in ROM of the treated level after the two years follow-up, and the rate of ASD compared with fusion was similar. The last example is TOPS device, a multiaxial DSS composed of two titanium plates placed together incorporating with PCU to form articulating core [3, 10], which acts like stoppers. Y. Anekstein et al. [10] reported that the TOPS device could restore the ROM of the instrumented level; anyway, the stiffness of the DSS is not mentioned despite the great clinical outcomes. These examples suggest that the suitable stiffness of the DSS, which might play a key role in minimizing ASD, is not given enough attention in previous research. For this reason, a novel DSS design with suitable stiffness is essential to effectively treat ASD.

Our research aimed to develop a DSS that can achieve similar stiffness to normal lumbar discs, including three types of motion: flexion-extension (FE), lateral bending (LB), and axial rotation (AR), from CFR-PEEK by utilizing topology optimization in Ansys.

2. Design specifications and conceptual design

2.1. Lumbar spinal motion segment stiffness

Schmidt et al. [11] conducted an in vitro experiment on cadaveric lumbar spines to measure and compare the stiffness of spinal motion segments between normal discs and discs with radial tear. In the testing process, torques were applied incrementally at each step, starting from 0, 0.5, 1.6, 3.6, 4.7, to 6.6 Nm, and the angular movement data for FE, LB, and AR were collected and used to calculate stiffness. The results showed that stiffness of normal discs for flexion, extension, LB, and AR were 1.8, 2.6, 2.3, and 8.4 Nm/°, respectively. Since the actual lumbar spine exhibits differences in stiffness between flexion and extension, we selected 1.8 Nm/° to represent the stiffness for FE due to the simplification in optimization process. Thus, for our DSS specifications, we decided to use k_{FE} = 1.8 Nm/°, k_{LB} = 2.3 Nm/°, and k_{AR} = 8.4 Nm/° as the targeted stiffness values.

2.2. Dynamic stabilization system size and rods configuration

The design region dimensions of the DSS had to be prescribed before initiating the topology optimization process. To define the reasonable boundary for designing the DSS, we referenced dimensions from the research carried out by S. H. Zhou et al. [12], which provided precise geometrical dimensions of the lumbar vertebrae and discs based on digitized CT images. The relevant parameters of the L4-5 vertebrae and disc, including spinal canal width, posterior vertebral height, and disc height, were used to determine the dimensions of the pre-optimized cuboid. The cuboid had dimensions of width x length x thickness equal to 28 x 50 x 14 mm^3 as illustrated in 'Figure 1'. Additionally, the DSS was designed to have horizontal rods configuration as displayed four imprinted surfaces on the sides of the pre-optimized cuboid. These surfaces would be further extended into rods after the optimized DSS structure is finalized. This design choice was chosen because horizontal rods distribute loads more evenly among individual pedicle screws, thereby minimizing the risk of screw loosening [4].

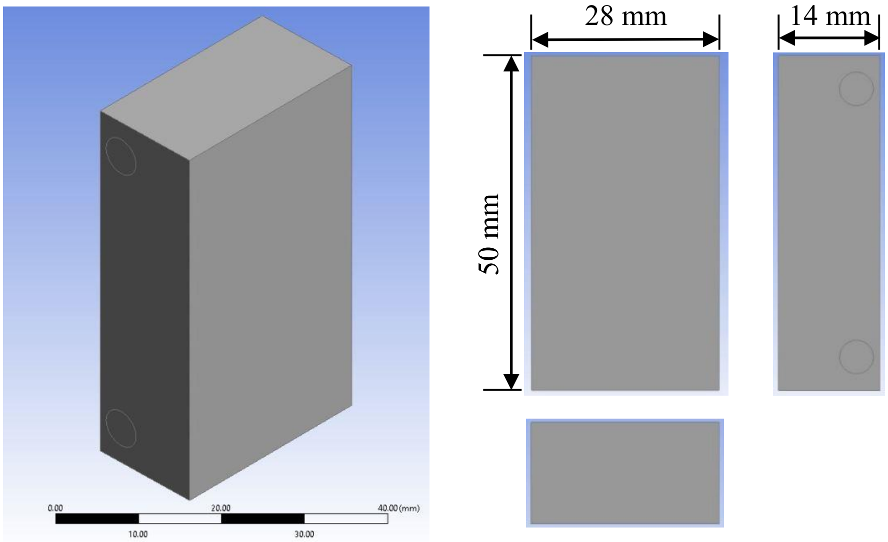

Figure 1. The pre-optimized cuboid in isometric, back, right, and bottom views.

2.3. Conceptual design of the DSS

In the field of mechanical engineering, the stiffness of an object under applied moments depends on the moment of inertia in its cross-sectional area [13]. Therefore, if we intend to adjust the stiffness of an object, we can simply modify it by removing or adding material into the cross-sectional area. However, since lumbar spines have three types of motion, namely FE, LB, and AR [1], it became highly intricate to manually design a DSS that achieves comparable stiffness across all these spinal movements. Hence, we proposed an alternative approach, utilizing topology optimization—a computational algorithm that aids in shaping the optimal profile of the DSS within a given material's design region to satisfy a specific constraint.

3. Dynamic stabilization system design

3.1. Finite element analysis

To achieve the DSS shape with the desired stiffness in three orientations, it was necessary to implement a multiple load cases topology optimization. Three 'static structural' toolboxes were integrated with 'topology optimization' toolbox. The simulation had to be executed for each scenario, including FE, LB, and AR, to get the initial simulation solutions. These solutions were then used as the input for the subsequent topology optimization process.

Initiating with FE simulation, the prepared pre-optimized cuboid underwent meshing into 1.0 mm hexahedral elements using the multi-zone method, resulting in a total of 94,427 nodes and 21,626 elements in the initial model. The bottom imprinted surfaces were assigned as fixed support, while a 6.6 Nm moment in FE direction was applied at the top imprinted surfaces as demonstrated in 'Figure 2'. The magnitude of applied moment was selected based on the maximum torque used in the experiment conducted by Schimidt et al. [11], aiming to mimic the same experimental setup.

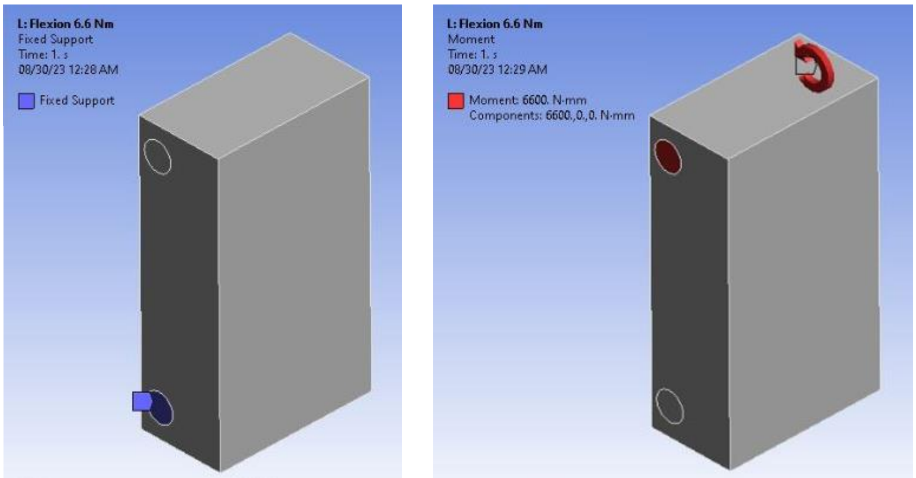

Figure 2. Boundary conditions for simulating FE.

For LB and AR simulations, we repeated the same setup and used the same meshed model as in the FE case. The only difference is the assigned direction of the applied moment which were aligned differently in each scenario.

3.2. Topology optimization

Our research has selected mass reduction as the response constraint and has set up the minimization of compliance as the primary objective. Optimization region was separately defined between a design region and an exclusion region. As shown in 'Figure 3', we selected the entire body of the cuboid as the design region, excluding all boundary conditions, to allow the algorithm to freely modify the optimal shape. In the objective setup, different weights were assigned to each 'static structural' environment based on the target stiffness value in each motion. To elaborate, in our optimization as depicted in 'Figure 4', 'static structural' simulated FE was assigned a weight of 1.8, 'static structural 2' simulated LB was assigned a weight of 2.3, and 'static structural 3' simulated AR was assigned a weight of 8.4. By doing so, the algorithm would prioritize maximizing the stiffness of FE:LB:AR in ratio of 1.8:2.3:8.4. Therefore, the effect of material properties was not of substantial importance and could be retained as default, which is structural steel. The mere drawback of this method is that the resulting stiffness in three directions would be proportional to the given ratio and might not exactly match the desired values. Thus, after obtaining the optimized shape, validation for the exact stiffness was required.

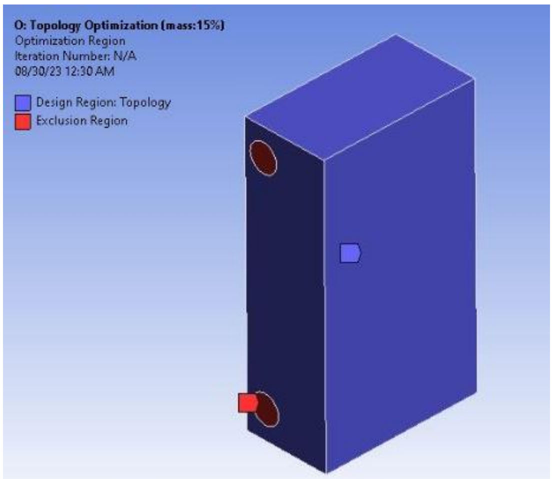

Figure 3. Optimization region.

Objective

Right click on the grid to add, modify and delete a row.

Enabled	Response Type	Goal	Criterion	Formulation	Environment Name	Weight
☑	Compliance	Minimize	N/A	Program Controlled	Static Structural	1.8
☑	Compliance	Minimize	N/A	Program Controlled	Static Structural 2	2.3
☑	Compliance	Minimize	N/A	Program Controlled	Static Structural 3	8.4

Figure 4. Assigned weight in topology optimization objective of each environment.

Although mass reduction was chosen as the response constraint, the suitable retained percentages of the material remained undefinable due to the fact that this approach returned the shape with stiffness in proportion. To achieve the intended stiffness more precisely, we should have conducted the topology optimization by varying the retained mass percentages then validated all optimized models. Nonetheless, for a more time-effective approach, we opted to initially perform topology optimize at the middle-retained percentages of 50%. By doing so, the impossible choices that could not achieve intended stiffness would be eliminated. In this research, the DSS with 50% retained mass showed excessive rigidity in all directions. To summarize the optimization workflow, the topology optimization was subsequently conducted with the retained mass percentages of 50%, 30%, and 15% to ascertain the effectiveness of this optimization approach.

4. Performance testing of the DSS

Before validation, fine-tuning of the optimized DSS was conducted due to complexity of the output shapes generated by the algorithm. To make them more manufacturable, the shapes were cleaned up and modified to the finalized configuration by eliminating some untidy parts and geometrizing the bodies.

4.1. Validating the stiffness of the optimized DSS

In the validation process, the finalized DSS would be ran in the simulation once again with same boundary conditions as before. However, the material properties were now assigned as CFR-PEEK. To simplify the simulation model, CFR-PEEK was assigned as an isotropic material with a Young's modulus (E) of 18 GPa [14] and a Poisson's ratio (v) of 0.44 [14].

The finalized shape with 50% retained percentages was meshed into 3.0104 mm element size using the hexahedral dominant method, resulting in a total of 99,105 nodes and 30,378 elements. Similarly, the finalized shape with 30% retained percentages was meshed into 3.0104 mm element size using the hexahedral dominant method, resulting in a total of 157,735 nodes and 40,552 elements. Lastly, the finalized shape with 15% retained percentage was meshed into 3.0104 mm element size using the hexahedral dominant method, resulting in a total of 189,680 nodes and 56,100 elements. The bottom imprinted surfaces of both models were assigned as fixed support, while the top imprinted surfaces were subjected to 6.6 Nm moments in each direction. Additionally, in the solution of each 'static structural' environment, the top imprinted surfaces were defined using element Euler angle tools to measure θ_{FE}, θ_{LB}, and θ_{AR} in each case. The stiffness in each orientation was calculated from the measured element Euler angle divided by magnitude of input moment (6.6 Nm).

5. Results

5.1. The topology optimized DSS

For the case of 50% retained percentages, the optimization needed 18 iterations to accomplish the objective of mass reduction. The optimization provided a hollow cuboid with two open holes on the bottom side. The resulting shape was then fine-tuned as shown in 'Figure 5'.

Figure 5. The optimized DSS with 50% retained mass: pre-adjusted (left) and adjusted (right).

For the case of 30% retained percentages, the optimization required 21 iterations to achieve the objective of mass reduction. The optimization resulted in a bottomless hollow cuboid with fillets on the sides. The resulting shape was further adjusted to be more geometrical as illustrated in 'Figure 6'.

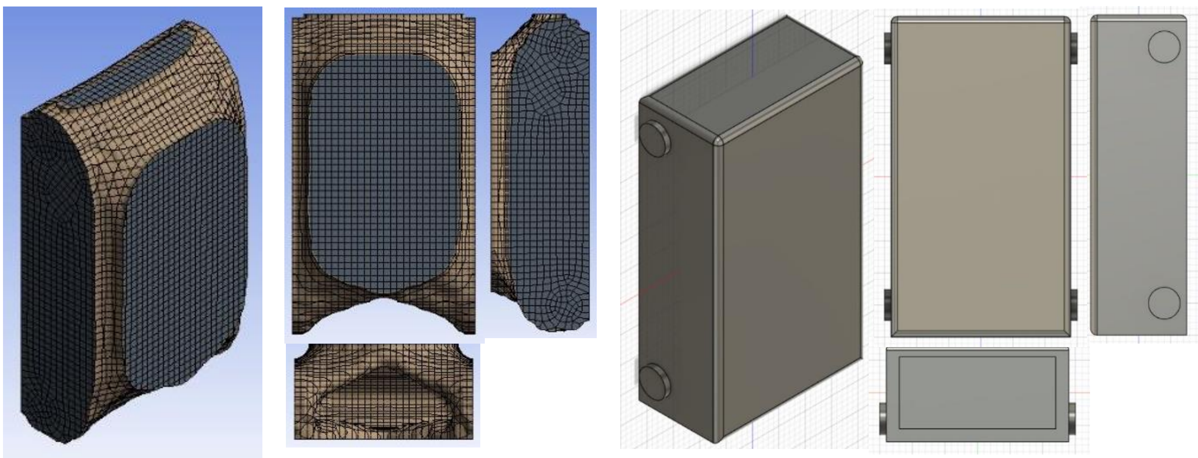

Figure 6. The optimized DSS with 30% retained mass: pre-adjusted (left) and adjusted (right).

For the case of 15% retained percentages, the optimization took 30 iterations to satisfy the objective of mass reduction. The optimization generated a shape without caps on either the top or bottom. The front side featured four holes and an X mark in the center, while the back side contained a hexagonal hole. The left and the right sides were penetrated with a slot shape which slightly positioned toward the top side. The resulting shape underwent additional refinement and modification as demonstrated in 'Figure 7'.

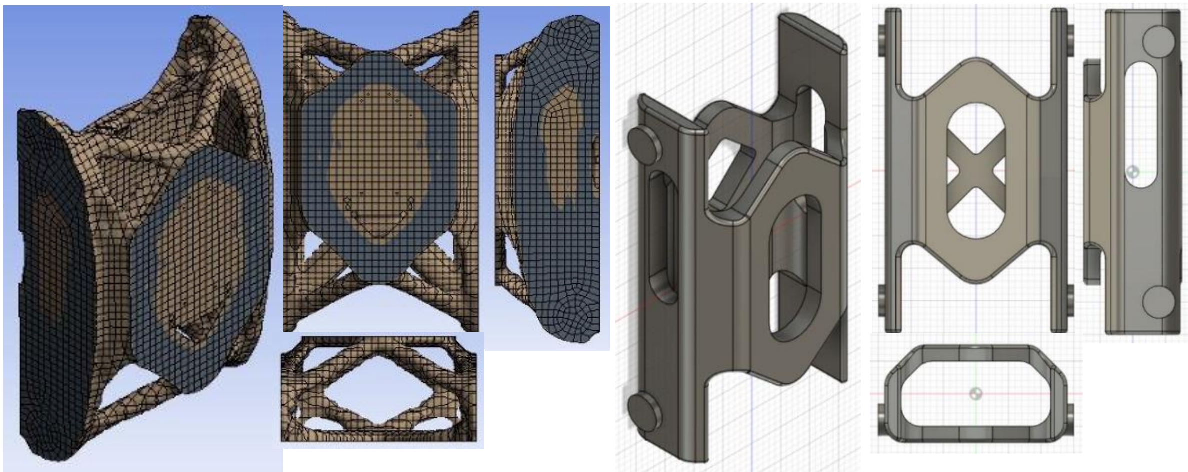

Figure 7. The optimized DSS with 15% retained mass: pre-adjusted (left) and adjusted (right).

5.2. Validation process

Table 1. Rotating angle and angular stiffness of the optimized DSS.

Design		DSS 50%			DSS 30%			DSS 15%		
k_{target} (Nm/°)		θ_{rot} (°)	k_{actual} (Nm/°)	Dev (%)	θ_{rot} (°)	k_{actual} (Nm/°)	Dev (%)	θ_{rot} (°)	k_{actual} (Nm/°)	Dev (%)
FE	1.8	1.813	3.64	102.2	1.996	3.31	83.8	3.148	2.1	16.7
LB	2.3	0.183	36.2	1473.9	0.246	26.8	1043.5	2.477	2.66	15.7
AR	8.4	0.274	24.1	186.9	0.526	12.5	48.8	0.711	9.28	10.5

From 'Table 1', the optimized DSS with 50% retained mass demonstrated rotating element Euler angles of 1.813°, 0.183°, and 0.274° for FE, LB, and AR, respectively. These angles were employed for calculating angular stiffness: k_{FE} = 3.64 Nm/°, k_{LB} = 36.2 Nm/°, and k_{AR} = 24.1Nm/°. Nevertheless, this DSS showed stiffness excessiveness in all motions, deviating from the target values of Dev_{FE} = 102.2%, Dev_{LB} = 1473.9%, and Dev_{AR} = 186.9%, with the most observed in the LB motion.

Meanwhile, the optimized DSS with 30% retained mass presented rotating element Euler angles of 1.996°, 0.246°, and 0.526° for FE, LB, and AR, respectively. These angles were then used to calculate angular stiffness: k_{FE} = 3.31 Nm/°, k_{LB} = 26.8 Nm/°, and k_{AR} = 12.5 Nm/°. Similar to the case with 50% retained mass, this DSS exhibited stiffness redundancy in all motions, deviating from the target values of Dev_{FE} = 83.8%, Dev_{LB} = 1043.5%, and Dev_{AR} = 48.8%, especially noticeable in the LB motion.

On the other hand, the optimized DSS with 15% retained mass displayed rotating element Euler angles of 3.148°, 2.477°, and 0.711° for FE, LB, and AR, respectively. These angles could be computed into angular stiffness: k_{FE} = 2.10 Nm/°, k_{LB} = 2.66 Nm/°, and k_{AR} = 9.28 Nm/°. This DSS showcased a decent level of stiffness, deviating from the target stiffness only by Dev_{FE} = 16.7%, Dev_{LB} = 15.7%, and Dev_{AR} = 10.5%. Normalizing the proportion of the target stiffness, $k_{FE} : k_{LB} : k_{AR}$ = 1.8 : 2.3 : 8.4, resulted in 1 : 1.28 : 4.67. Similarly, normalizing the proportion of the actual stiffness, $k_{FE} : k_{LB} : k_{AR}$ = 2.10 : 2.66 : 9.28, provided 1 : 1.27 : 4.42. Therefore, we concluded that the target stiffness and the actual stiffness of the optimized DSS with 15% retained mass closely resembled both in terms of amount and proportion.

6. Discussion

The target stiffness used in this research was referenced from a single study; however, numerous studies have explored lumbar spinal segment stiffness. S.J.P.M. van Engelen et al. [15] determined the distribution of stiffness values for each lumbar spinal segment in the neutral zone and found that the stiffness for L4-5 in FE, LB, and AR were 0.5, 0.8, and 2.4 Nm/°, respectively. S.A. Zirbel et al. [16] evaluated the effects of intervertebral disc degeneration on lumbar spinal segment stiffness in the neutral zone. Although this study did not provide stiffness values for intact lumbar models, they did have stiffness data for grade I intervertebral disc degeneration, which might somewhat reduce stiffness in the segments. The results showed that the lumbar stiffness for grade I in FE, LB, and AR were 0.24, 1.11, and 7.78 Nm/°, respectively. Despite the variation in stiffness values obtained from these studies due to individual patient conditions and testing protocols, it is noticeable that stiffness in FE and LB were close to each other and relatively small compared to AR. Therefore, we had to choose a specific stiffness to conduct the optimization.

According to ‘Table 1’, when considering the stiffness of both the optimized DSS with 50% and 30% retained mass, it becomes obvious that the resulting stiffness is not closely aligned with the assigned weight proportion. Particularly, the stiffness in the LB direction significantly deviates from the target LB stiffness, unlike the stiffness values in the other directions. To explain, it is necessary to reconsider the optimized shape generated by the algorithm with 50% and 30% retained mass. The DSS takes the based shape of a hollow cuboid, that is physically well-suited to resist torsional loads following the moment of inertia principle [13]. As the AR environment carries the most weight among all motion scenarios, the algorithm tends to prioritize stiffening this orientation over the others. Accordingly, to achieve the mass reduction, the optimizing program tends to eliminate the material from within the cuboid as the initial approach. However, this approach disputes with the objective of reducing stiffness in the LB direction, which could be effectively achieved by removing material along the left and right sides of the cuboid. Thus, this can be inferred that reducing mass to 30% retained mass might not be adequate to achieve the proper stiffness in all directions. This is supported by the case of 15% retained mass, which aligns more closely with the intended stiffness after optimization.

The pre-optimized used in the current study comprises only the main structure of the DSS, without the inclusion of the rods. The main reason behind this decision is that CFR-PEEK is a flexible material, unlike metal implants [7]. If the model included the horizontal rods made of CFR-PEEK, their flexibility could significantly alter the study’s results, particularly in term of LB stiffness. Thus, to mitigate the possibility of such errors, we decided to use titanium rods instead and assumed that these titanium bars would be rigid enough compared to the CFR-PEEK structure, allowing us to neglect the rods from the simulation model. In the case of the actual clinical uses, the presence of small titanium components within the overall implant did not interfere with the MRI outcomes [10], so we could still leverage the benefits of CFR-PEEK while incorporating titanium components. Currently, the wing parts of the designed DSS are relatively thin, resulting in difficulty in connecting to the titanium rods. Hence, the design needs to be further developed in the future.

There are several limitations in the study. The first one is the simplification in the simulation models, where we treated CFR-PEEK as an isotropic material. Since CFR-PEEK is a polymer composite which possesses orthotropic properties and its mechanical properties are influenced by the laying pattern of carbon fiber sheet, incorporating these factors into the simulation could potentially enhance the accuracy of the results in future research. Additionally, the small size of variation on retained percentages in the optimization, which was executed only 50%, 30%, and 15%, could reduce the opportunity to seek for the DSS shape with the most optimal stiffness. The last limitation involves the exclusion of a spinal model. Our simulations were conducted on bare DSS models. Subsequently, for future works, it is essential to either include the simulation of the entire lumbar spine or, if possible, conduct mechanical tests on our design in practice scenarios to validate the real model's performance.

7. Conclusion

Topology optimization is an effective tool that can be applied to facilitate the design of a complex shape for specific application of the DSS. Our design with 15% retained mass exhibits the stiffness in each motion: $k_{FE} = 2.10$ Nm/°, $k_{LB} = 2.66$ Nm/°, and $k_{AR} = 9.28$ Nm/°, which deviates from the intact lumbar spinal motion segment by only 16.7%, 15.7%, and 10.5%, respectively. These stiffness values closely resemble the assigned stiffness, $k_{FE} = 1.8$ Nm/°, $k_{LB} = 2.3$ Nm/°, and $k_{AR} = 8.4$ Nm/°, demonstrating the effectiveness of both the design and the application of topology optimization.

8. Acknowledgments

This work was supported by the Scholarship from the Graduate School, Chulalongkorn University to Commemorate the 72nd Anniversary of his Majesty King Bhumibol Adulyadej is gratefully acknowledged.

9. References

[1] Hall, S.J. and D. Lysell. (1995). *Basic biomechanics*.

[2] บุญมาประเสริฐ ต. (2014). *เอกสารคำสอน ปวดหลัง-ปวดคอ และ โรคข้อต่อกระดูกสันหลังเสื่อม*. คณะแพทย์ศาสตร์ มหาวิทยาลัยเชียงใหม่: ประเทศไทย.

[3] Gomleksiz, C., et al. (2012). A short history of posterior dynamic stabilization. *Advances in orthopedics*.

[4] Meyers, K., et al. (2008). Use of instrumented pedicle screws to evaluate load sharing in posterior dynamic stabilization systems. *The Spine Journal*, 8(6), p. 926-932.

[5] Nockels, R.P. (2005). Dynamic stabilization in the surgical management of painful lumbar spinal disorders. *Spine*, 30(16S), p. S68-S72.

[6] Boriani, S., et al. (2018). Carbon-fiber-reinforced PEEK fixation system in the treatment of spine tumors: a preliminary report. *European Spine Journal*, 27, p. 874-881.

[7] Kumar, N., et al. (2021). Can polyether ether ketone dethrone titanium as the choice implant material for metastatic spine tumor surgery? *World neurosurgery*, 148, p. 94-109.

[8] Lee, C.-H., et al. (2016). Dynamic stabilization using the Dynesys system versus posterior lumbar interbody fusion for the treatment of degenerative lumbar spinal disease: a clinical and radiological outcomes-based meta-analysis. *Neurosurgical focus*, 40(1), p. E7.

[9] Yang, Y., et al. (2015). Comparison of clinical and radiographic results between isobar posterior dynamic stabilization and posterior lumbar inter-body fusion for lumbar degenerative disease: a four-year retrospective study. *Clinical neurology and neurosurgery*, 136, p. 100-106.

[10] Anekstein, Y., et al. (2015). Seven years follow-up for total lumbar facet joint replacement (TOPS) in the management of lumbar spinal stenosis and degenerative spondylolisthesis. *European Spine Journal*, 24, p. 2306-2314.

[11] Schmidt, T.A., et al. (1998). The stiffness of lumbar spinal motion segments with a high-intensity zone in the anulus fibrosus. *Spine*, 23(20), p. 2167-2173.

[12] Zhou, S., et al. (2000). Geometrical dimensions of the lower lumbar vertebrae–analysis of data from digitised CT images. *European Spine Journal*, 9(3), p. 242-248.

[13] Hibbeler, R.C. (2006). *Mecánica de materiales*. Pearson educación.

[14] Becker, Y.N., et al. (2020). Hybrid composite pedicle screw-finite element modelling with parametric optimization. *Informatics in Medicine Unlocked*, 18, p. 100290.

[15] van Engelen, S.J., et al. (2015). The effect of neighboring segments on the measurement of segmental stiffness in the intact lumbar spine. *The spine journal*, 15(6), p. 1302-1309.

BME0002

Virtual Reality-Based Rehabilitation for Children with Cerebral Palsy

Jumana Ma'touq[1,*], Joseph Sweiss[1], Nasim Alnuman[1], Ibrahim Abuzer[1], and Muhannad Sabieleish[2]

[1] Department of Biomedical Engineering, German Jordanian University, Amman, 11180, Jordan
[2] Graduate of Department of Biomedical Engineering, German Jordanian University, Amman, 11180, Jordan

* Corresponding Author: jumana.matouq@gju.edu.jo, jumana.matouq@gmail.com

Abstract. Cerebral palsy (CP) is characterized by various impairments in muscle function, making it impossible for the affected person to carry out daily tasks. Virtual reality-based rehabilitation has been used as an alternative therapy for children with CP. The aim of this project was to develop a virtual environment to engage children with/without CP in an interactive therapeutic basketball game for upper limb rehabilitation. The game focuses on improving the patient's strength, range of motion, reaction time, and accuracy of placement. It consists of combining the virtual environment and the interface between the upper limb and the virtual environment. It has four levels, each with a predefined set of tasks and improvement goals. The subject throws the ball into the ring, and with each successful throw, the subject is progressed to the next level. An Inertial Measurement Unit (IMU) sensor and microcontroller were used to establish the interface between the user and the virtual environment. The first phase of the current project was conducted on four healthy subjects for the four levels to check applicability, interface reliability, flow, and completion time. Completion time and subject feedback were recorded. The Initial results provided benchmark data to test the game on CP subjects while monitoring brain and muscle activities to check neuromuscular progress and improvements. The second phase of the project is to test the virtual reality game on CP subjects and validate the adopted approach.

Keywords: Cerebral palsy, Virtual rehabilitation, Biomechanics, Rehabilitation games, Biomedical engineering.

1. Introduction

One of the most common causes of physical disability in children around the world is cerebral palsy (CP) [1, 2]. According to recent estimates of the regional and global prevalence of cerebral palsy (CP) from population-based research from all around the world, the prevalence of CP ranges from 1.5 to 3.4 per 1,000 live births [3]. Children with CP have impaired motor function and postural control, which are strongly associated with restrictions in activities of daily living [2]. A variety of management approaches are being used to improve and support the lives of the patients including physiotherapy, occupational therapy, orthopedic surgeries, adaptive equipment, assistive technologies, and rehabilitation [4].

Interventions based on virtual reality (VR) have been utilized to treat CP patients for the rehabilitation of upper and lower disorders [2]. VR can be defined as computer-generated settings with realistic-looking objects and scenes that give the user a sense of immersion in their surroundings. VR technologies have several advantages over traditional neuropsychological testing, including a more realistic and lifelike environment that may help participants to "forget" they are being tested, improved involvement, and increased learning generalization [5]. Burdea [6] pointed out that VR has significant advantages when used in the rehabilitation of patients with different conditions including adaptability and variability based on patient baseline, patient motivation, and reduced medical costs. VR-based therapy allows the practice at home independently or with interaction with others with/without the supervision of professionals [7, 8].

Some researchers have investigated VR for its effectiveness in the rehabilitation of children with CP. Chen et al. [9] studied the effectiveness of improving motor function in children with CP. They pointed out that using VR as a home training program can optimize the intervention and VR appears to be an effective intervention in improving motor function in children with CP. In another research, the performance of CP individuals in performing a real task was better after practicing a VR task [10]. A study by Leal et al. [7] concluded that better motor task was performed by CP subjects when the virtual environment interface was used compared to a realistic interface. The same finding was confirmed by Ökmen et al. [11] who concluded that using VR therapy in the rehabilitation of CP improves motor function and significantly impacts the treatment.

Based on previously published studies, game-based rehabilitation approaches have the potential to enhance clinical outcomes and help children with neuromotor deficits to participate actively. Despite the progress that has been made, there is weak exploratory evidence that using VR can improve hand function in children with CP in comparison to traditional physiotherapy [12]. Additionally, studies evaluating the effect of VR therapy on upper extremity function in children with CP are still limited [11, 13]. Thus, the aim of this project was to develop a virtual environment to engage children with/without CP in an interactive therapeutic basketball game for upper limb rehabilitation. The game focuses on improving the subject’s strength, range of motion, reaction time, and accuracy. The patient must throw the ball into the ring, and with each successful throw, the patient is advanced to the next level, with a total of four levels, each with its own predefined set of tasks and improvement goals. The second phase of the project, which is not included in this paper, is to test the virtual reality game on CP patients while monitoring brain and muscle activities in order to validate the adopted approach in comparison with traditional treatment.

2. Methods

The block diagram of the developed game is shown in Figure 1. It consists mainly of the virtual environment as well as the interface between the upper limb and the virtual environment. Each of these parts is explained as follows.

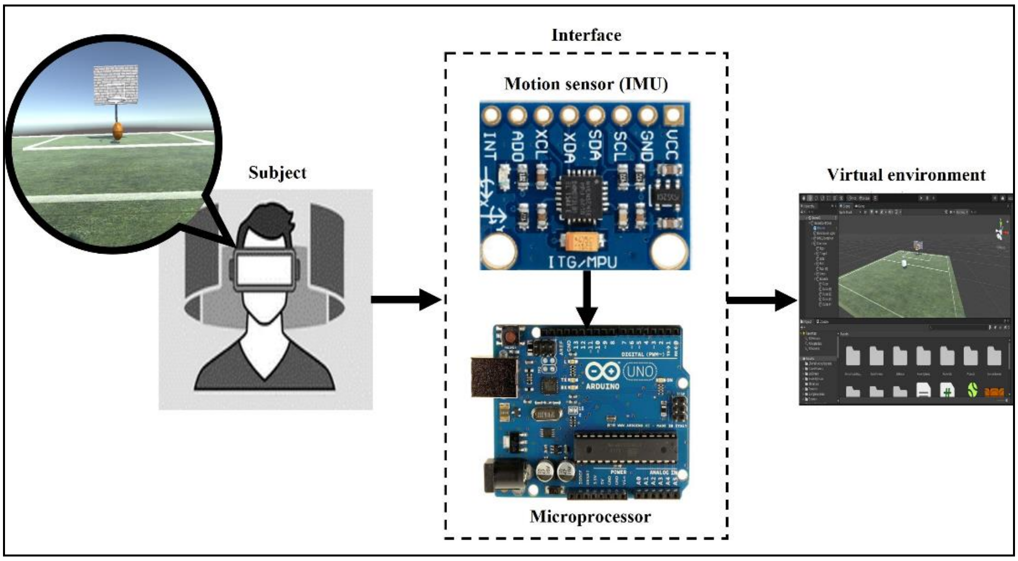

Figure 1. Block diagram of the developed game.

2.1. Game selection and rehabilitation goal

The CP in children is usually controlled by a classic physiotherapy plan that includes stretching, strengthening, positioning, splinting, casting, and the facilitation of movement [12]. Different physical games and exercises are used in the rehabilitation of CP patients [14]. These games aim to enhance specific upper-limb targets such as strength, range of motion, accuracy, and time based on physical rehabilitation rather than virtual rehabilitation. Among these games, basketball was chosen as it is simple, interesting for many kids, and can train shoulder, elbow, and wrist joints. Furthermore, different gaming challenges can be implemented for different CP patient levels.

The developed game aims to improve four rehabilitation goals, i.e., strength, range of motion, reaction time, and accuracy of placement. These goals can be improved using basketball games adjusted at different levels. Upper extremity muscular weakness in children with CP is clinically significant as it affects and lowers their ability to execute daily living activities [15]. Thus, studies have recommended strength training with intensive repetitions of the upper extremities in children with CP [15]. Strength training in CP patients leads to improved flexibility, muscle power, balance, posture, and activity level during daily living [16]. According to Pourazar et al., VR is a promising tool for the rehabilitation of children with CP and helps in improving their reaction time [5]. On the other hand, accuracy is a crucial task restriction for children with hemiplegic cerebral palsy (CP) that may affect how well the two hands work together when performing functional drawer-opening tasks [17].

2.2. The game levels

The game has four levels, each level targets specific rehabilitation goal(s), i.e., strength, range of motion, reaction time, and accuracy. The Level 1 challenge is to score the ball in the ring. In this level, the ring is fixed in one position at the end of the field. To score the ball inside the ring, it must be thrown in an angular motion like in real life. This level aims to improve the patient's upper limb in strength, range of motion, and accuracy. The second level (Level 2) challenge is to get the ball through the ring while the ring of the basket is rotating 360 degrees. The patient needs to choose the correct time to throw the ball to get it inside the basket. Thus, this level focuses on improving the reaction time along with improving strength, range of motion, and accuracy. The third level (Level 3) is similar to Level 1, however, the basket ring size is decreased to half. This level focuses on improving accuracy. In the last level (Level 4), the distance between the patient and the basket is doubled. This level focuses on improving the accuracy and strength needed to throw the ball.

2.3. The virtual environment

The developed basketball game was implemented in Unity (Unity Technologies, USA). Unity game engine is a platform for creating three-dimensional (3D) and two-dimensional (2D) interactive content and simulations such as real-time 3D animations, video games, and architectural visualizations. Different assets were used including the grass floor, basketball, ring, basketball board, and borders, see Figure 2. A physical material was attached to the basketball itself to bring a natural physical sense like the rubber in the real world.

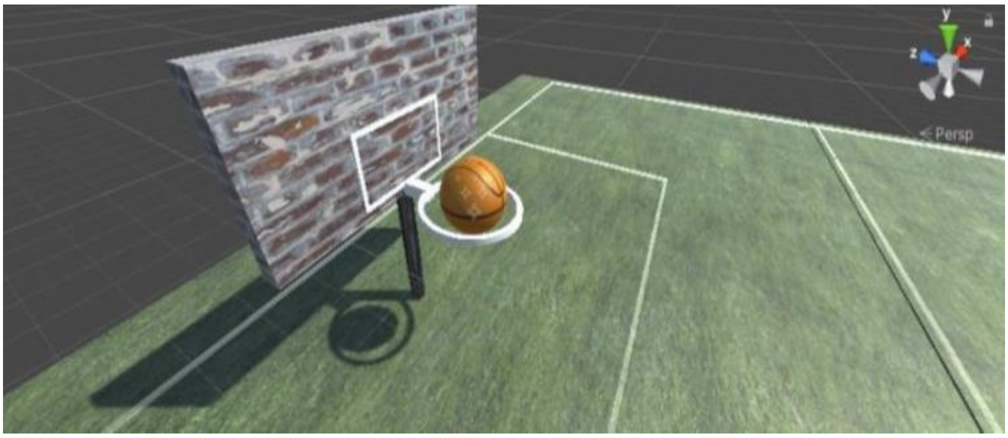

Figure 2. The grass floor, basketball, ring, and basketball board.

2.4. The interface between the subject and the virtual environment

In order to have an interactive game, an interface between the subject and the virtual environment is established. In order to track hand movement during playing, an Inertial Measurement Unit (IMU) motion sensor is connected to a microcontroller, i.e., Arduino UNO, see Figure 3. The IMU is a nine-axis motion sensor, i.e., it consists of a 3-axis accelerometer and a 3-axis gyroscope. It provides 2 to 6 Degrees of Freedom, which are associated with the different ways that an object can move in 3D space. The communication between the microcontroller and the virtual environment is established using Unity plugin, i.e., Uduino, which has all the mapping features needed for interactive communication.

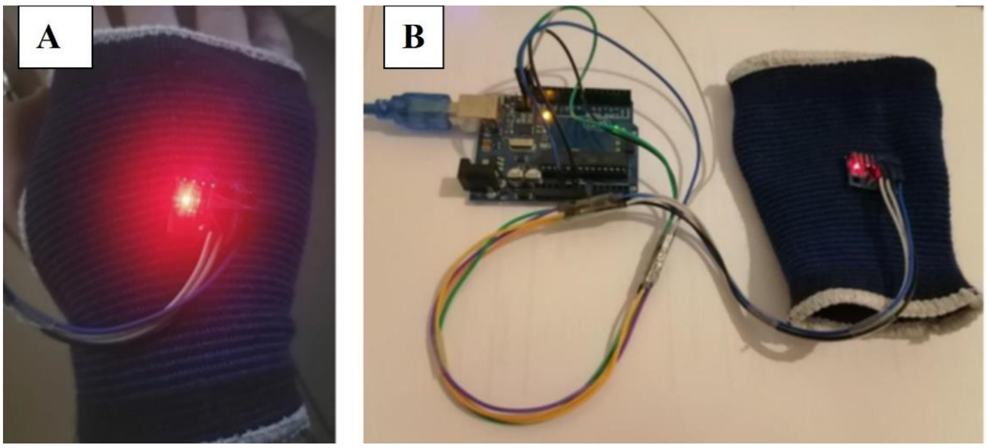

Figure 3. A) IMU sensor connected with a glove. B) IMU sensor connector to the microprocessor.

The sensor is attached to a glove so that whenever the patient moves his arm in any direction, the movements are mirrored onto the screen, generating a duplicate of his movements to play within the game. Changing the hand position also changes the viewing angle in the game. Figure 4 shows how a patient can play the game using the sensor attached to the glove and the changes in the viewing angle.

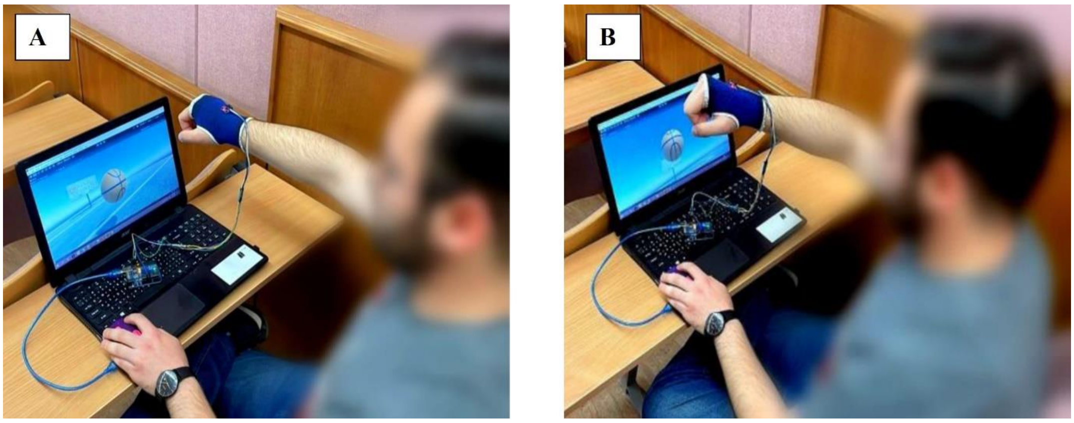

Figure 4. A) The hand is moved to the right and the software moves its camera angle to the right. B) The hand is moved to the middle and the software moves its camera angle to the middle.

2.5. Testing
The first phase of the current project was conducted on four healthy subjects for the four levels to evaluate applicability, interface, flow, and completion time. Each subject was asked to play the game with the four levels multiple times. The time and the number of trials needed to end each level was recorded for each subject. Subjects were asked about their feedback regarding the game.

3. Results and discussion
Table 1 shows the results of testing the game on four healthy subjects. In Level 1, subjects took 13.2 sec to 16.1 seconds to perform the task. Compared to the other levels, Level 2 took the longest time to complete the task. This might be explained due to the nature of the challenge in the task and the need to wait for the ring to fully rotate again if the user missed the proper position of the ring in the first round. At Level 2, the ring is rotating in a circular motion and the subject needs to find the exact time to throw the ball through the ring. All subjects completed the game comfortably and the feedback from the subjects indicated a smooth flow of the game with excellent progress.

Table 1. The results were collected for the four subjects at the four levels.

Subject	Level 1 (Trials = 2)	Level 2 (Trials = 2)	Level 3 (Trials = 3)	Level 4 (Trials = 4)
	Time (Sec)			
Subject 1	13.2	18.36	16.91	15.56
Subject 2	16.1	19.43	17.65	16.12
Subject 3	14.5	18.36	18.15	16.15
Subject 4	13.4	18.91	17.15	18.45

4. Conclusion

To conclude, this project was initially done to construct an environment for a virtual game, to prove the effectiveness of connecting the IMU sensor with the virtual environment and testing it on healthy subjects. The project is a basketball game, that helps the patient with mainly the motion and the strength of the muscles in the arms and hands. The subject needs to throw the ball into the ring, and with each scored shot, the subject is then taken to the next level being four levels in total while each level has its own set of objectives and improvements that are focused on.

The literature proved that virtual reality is efficient enough to be considered as a treatment method and is believed to be well suited for rehabilitation because it allows patients to interact in a safe and ecologically valid environment where exposure to sensorimotor possibilities can be controlled and modulated in a goal-oriented and autonomous manner. The four levels of the game required different competition times which adhere to the purpose of the system.

In the future, the system will be tested on CP patients while monitoring brain and muscle activities to compare their performance to the healthy subjects, study the improvement of performance over time to verify, and confirm the validity of the game to be used as a therapeutic approach for CP patients. Using more sensors can improve the following the progress of rehabilitation and the performance of the game.

5. References

[1] Rosenbaum, P., Paneth, N., Leviton, A., Goldstein, M., Bax, M., Damiano, D., … & Jacobsson, B. (2007). A report: the definition and classification of cerebral palsy April 2006. *Developmental Medicine & Child Neurology*. Supplement, 109, 8-14.

[2] Fandim, J. V., Saragiotto, B. T., Porfírio, G. J. M., & Santana, R. F. (2021). Effectiveness of virtual reality in children and young adults with cerebral palsy: a systematic review of randomized controlled trial. *Brazilian Journal of Physical Therapy*, 25(4), 369-386.

[3] McIntyre, S., Goldsmith, S., Webb, A., Ehlinger, V., Hollung, S. J., McConnell, K., … & Global CP Prevalence Group*. (2022). Global prevalence of cerebral palsy: A systematic analysis. *Developmental Medicine & Child Neurology*, 64(12), 1494-1506.

[4] Patel, D. R., Neelakantan, M., Pandher, K., & Merrick, J. (2020). Cerebral palsy in children: a clinical overview. *Translational Pediatrics*, 9(Suppl 1), S125-S135.

[5] Pourazar, M., Mirakhori, F., Hemayattalab, R., & Bagherzadeh, F. (2018). Use of virtual reality intervention to improve reaction time in children with cerebral palsy: A randomized controlled trial. *Developmental Neurorehabilitation*, 21(8), 515-520.

[6] Burdea, G. C. (2003). Virtual rehabilitation–benefits and challenges. *Methods of Information in Medicine*, 42(05), 519-523.

[7] Leal, A. F., da Silva, T. D., Lopes, P. B., Bahadori, S., de Araújo, L. V., da Costa, M. V. B., ... & Monteiro, C. B. D. M. (2020). The use of a task through virtual reality in cerebral palsy using two different interaction devices (concrete and abstract)–a cross-sectional randomized study. *Journal of NeuroEngineering and Rehabilitation*, 17(1), 1-10.

[8] de Mello Monteiro, C. B., Massetti, T., da Silva, T. D., van der Kamp, J., de Abreu, L. C., Leone, C., & Savelsbergh, G. J. (2014). Transfer of motor learning from virtual to natural environments in individuals with cerebral palsy. *Research in Developmental Disabilities*, 35(10), 2430-2437.

[9] Chen, Y., Fanchiang, H. D., & Howard, A. (2018). Effectiveness of virtual reality in children with cerebral palsy: a systematic review and meta-analysis of randomized controlled trials. *Physical Therapy*, 98(1), 63-77.

[10] Martins, F. P. A., Massetti, T., Crocetta, T. B., Lopes, P. B., da Silva, A. A., Figueiredo, E. F., ... & Monteiro, C. B. D. M. (2019). Analysis of motor performance in individuals with cerebral palsy using a non-immersive virtual reality task–a pilot study. *Neuropsychiatric Disease and Treatment*, 417-428.

[11] Ökmen, B. M., Aslan, M. D., Yüzer, G. F. N., & Özgirgin, N. (2019). Effect of virtual reality therapy on functional development in children with cerebral palsy: A single-blind, prospective, randomized-controlled study. *Turkish Journal of Physical Medicine and Rehabilitation*, 65(4), 371.

[12] Rathinam, C., Mohan, V., Peirson, J., Skinner, J., Nethaji, K. S., & Kuhn, I. (2019). Effectiveness of virtual reality in the treatment of hand function in children with cerebral palsy: a systematic review. *Journal of Hand Therapy*, 32(4), 426-434.

[13] Deutsch, J. E., Paserchia, C., Vecchione, C., Mirelman, A., Lewis, J. A., Boian, R., & Burdea, G. (2004). Improved gait and elevation speed of individuals post-stroke after lower extremity training in virtual environments. *Journal of Neurologic Physical Therapy*, 28(4), 185-186.
[14] Wulan, G. A. N., Deliana, S. M., & Pranoto, Y. K. S. (2021). Playing Percussion to Develop Physical-Motor and Emotional Skills of a Cerebral Palsy Child. *Journal of Primary Education*, 10(1), 19-26.
[15] Ozal, C., Türker, D., & Korkem, D. (2016). Strength training in people with cerebral palsy. Cerebral Palsy - Current Steps, InTech.
[16] McBurney, H., Taylor, N. F., Dodd, K. J., & Graham, H. K. (2003). A qualitative analysis of the benefits of strength training for young people with cerebral palsy. *Developmental Medicine and Child Neurology*, 45(10), 658-663.
[17] Hung, Y. C., Charles, J., & Gordon, A. M. (2010). Influence of accuracy constraints on bimanual coordination during a goal-directed task in children with hemiplegic cerebral palsy. *Experimental Brain Research*, 201, 421-428.

BME0003

Development of dynamic prosthetic foot for moderate active amputees using parametric optimization

Purin Piwat[1,2], Pairat Tangpornprasert[1,2], and Chanyaphan Virulsri[1,2,*]

[1] Center of Excellence for Prosthetic and Orthopedic Implant, Chulalongkorn University, Bangkok 10330, Thailand
[2] Department of Mechanical Engineering, Faculty of Engineering, Chulalongkorn University, Bangkok 10330, Thailand

* Corresponding Author: chanyaphan.v@eng.chula.ac.th

Abstract. The increasing number of leg amputees in Thailand, with approximately 40,000 individuals recorded in the year 2017[1], necessitates the development of affordable prosthetic solutions. However, while cost-effective, the commonly used Solid Ankle Cushion Heel (SACH) prosthetic feet hinder natural walking due to their stiff ankle. This makes them suitable for low activity level amputees but limited for those with moderate activity levels and higher, who possess the ability to utilize their remaining foot to release energy and walk naturally on various surfaces. However, designing prosthetic feet with the ideal stiffness for each group of amputees poses significant challenges. Achieving the appropriate foot thickness in various positions to attain ideal stiffness while maintaining high strength through a trial-and-error approach requires extensive iterative experimentation. This research aims to address this challenge by utilizing parametric optimization techniques to design a dynamic prosthetic foot with specific stiffness in both the heel and forefoot regions that are suitable for the weight range and the foot size of the amputee. The prosthetic foot structure is primarily constructed using carbon fiber composite material, ensuring high strength and lightweight characteristics. Finite Element Analysis (FEA) is employed to evaluate the deformation and stiffness of the designed prosthetic foot, following the international standard guideline ISO10328[7]. The research employs parametric optimization techniques to overcome the complexities of designing prosthetic feet with ideal stiffness for each group of amputees. The optimization process considers the carbon fiber thickness in the heel and forefoot regions, aiming to achieve tailored stiffness while ensuring structural integrity. The results of the FEA simulations, conducted following with ISO10328 guidelines, indicate that the designed prosthetic foot model, intended for amputees with a foot size of 26-27 cm and a weight range of 60 kg, exhibits suitable stiffness values of 9.70 Nm/degree in the forefoot area and 4.31 Nm/degree in the heel region, confirming its suitability for use by amputees with a moderate activity level within the specified weight range and foot size.

Keywords: Prosthetic foot, Stiffness, Parametric optimization.

1. Introduction

According to a 2017 survey conducted by the Thailand National Statistical Office, it was observed that among the total disabled population of 2,831,952 individuals, there existed a prevalence of lower limb amputee exceeding 1.4%, equating to approximately 39,600 individuals [1]. This also revealed a notable increase in the number of amputees compared to the previous survey. Notably, more than 91% of employed individuals with disabilities earned a monthly income below 15,000 Thai baht. In Thailand, the prevalent utilization of prosthetic feet among individuals with disabilities centers around the Solid Ankle Cushion Heel (SACH) prosthetic foot, primarily attributed to its cost-effectiveness. Characterized by a rigid ankle configuration and encased in rubber material for enhanced stability, the SACH prosthetic foot is particularly suitable for individuals with impaired balance who necessitate substantial support but limited for those with moderate activity amputees who possess the ability to utilize their remaining foot to release energy and walk naturally on various surfaces. Nonetheless, designing prosthetic feet with optimal stiffness corresponding to distinct amputee groups presents considerable high complexities due to the intricate interplay of numerous influencing parameters, such as the thickness of different parts of the workpiece, the type of material used, etc., while concerning the structural integrity of the prosthesis itself. If the design was done by trial-and-error methodology, the resultant computational requisites would be disproportionately extensive and have low accuracy. Presently, the ubiquity of multi-objective parametric optimization technology is evident within the landscape of design innovation. This research considers applying this methodology to prosthetic foot design. Therefore, the primary aim of this research is to address the challenge of designing a dynamic prosthetic foot specifically for amputees with a moderate activity level, with stiffness in both the heel and forefoot regions that are suitable for the weight range and the foot size of the amputee through utilizing parametric optimization techniques.

2. Method

2.1. Design sspecifications

Differing weights among individuals lead to varying reaction forces on the prosthetic foot. This necessitates the use of prosthetic feet with different levels of stiffness to ensure consistent flexion angles during the gait cycle. This study aims to design a prosthetic foot tailored for a 26 cm foot shell, optimized to support individuals weighing approximately 60 kg amputees. The prosthetic foot's stiffness for around 60 kg amputees during plantarflexion is estimated at approximately 4.3 Nm/deg, while dorsiflexion stiffness is around 9.6 Nm/deg, derived from angular spring stiffness measurements. For those classified under the K2-3 activity level, the ratios of plantarflexion and dorsiflexion stiffness to body weight are approximately 0.072 Nm/deg/kg and 0.16 Nm/deg/kg by order [2-5]. To simplify the design, the prosthetic foot that was designed in this study is defined as a passive prosthetic foot.

2.2. Preliminary design

After making a preliminary design according to the requirements using CAD program, the design will be as shown in 'Figure *1*'. From the figure, the designed prosthetic foot will consist of the following parts.

1. Forefoot is a part used to absorb force and restore energy to support user to progress from mid stance to toe off.
2. Heel is a part used to absorb force and restore energy to support user to progress from initial contact to mid-stance.
3. Connector is a piece used to attach the foot to the joint of the shank.

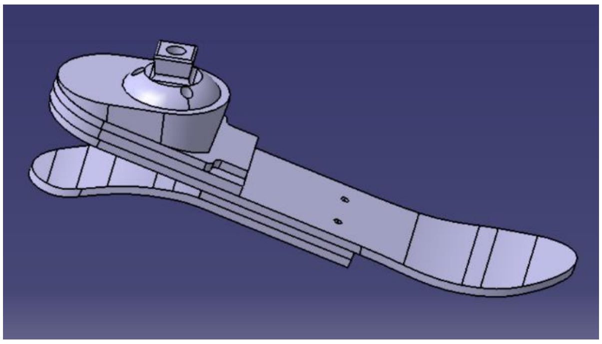

Figure 1. Preliminary design of prosthetic foot.

2.3. Detailed design

2.3.1 Design materials

Designed prosthetic foot requiring efficient energy transmission, carbon fiber/epoxy composites offer a compelling choice. These materials excel in their ability to withstand substantial bending forces along the fiber's direction while maintaining high flexibility and a lightweight profile. This makes them highly favored in the prosthetic foot industry. Within this study, the researcher favors the use of prepreg carbon fiber fabrics due to their ease of manufacturing. These fabrics come in different subtypes, unidirectional prepreg and woven prepreg. In this proposed prosthetic foot design, a hybrid approach is suggested. It involves combining the unidirectional fiber subtype with the woven fiber type. This choice is motivated by the recognition that forces acting on the prosthetic foot exhibit directional asymmetry during usage. This strategic fusion of fabric architectures addresses the distinct load-bearing demands of each aspect of the prosthetic foot. In this design, the properties of carbon fiber composite are used as shown in 'Table 1'.

Table 1. Properties of carbon fiber composite.

Properties	Unidirectional carbon fiber composite	Woven carbon fiber composite
Young's Modulus 0º (GPa)	135	66
Tensile Strength 0º (MPa)	2612	789
Young's Modulus 90º (GPa)	7.7	66
Tensile Strength 90º (MPa)	81.8	789
In-plane Shear Modulus (GPa)	3.55	19.5
In-plane Shear Strength (MPa)	54.3	125
Major Poisson's Ratio	0.27	0.3
Cured Ply Thickness (mm)	0.145	0.222

2.3.2 Determination of the optimum thickness of the prosthetic foot by parametric optimization method on finite element program

For the determination of optimal structural thickness within prosthetic foot designs, the utilization of finite element analysis employing the ANSYS software is deemed necessary because the structure of the prosthetic feet is complicated and difficult to directly calculate. Since the design consists of several composite materials with anisotropic material properties, the ACP (Ansys Composite Prep Post) module, a dedicated composite material computation module, was used for the calculation.

The approach begins by ascertaining the thickness for individual layers as well as the material properties inherent to the various types of carbon fiber composite employed. In pursuit of design precision, the structure is divided into two segments, delineated by the locations of applied forces—heel and forefoot. The calculations are executed at maximal loading conditions along gait cycle of 60 kg amputee. Computations are initiated from the forefoot region. This sequencing is rationalized by the understanding that forces applied to the forefoot do not typically induce deformation within the heel structure. However, deformations are observed in the forefoot when forces are exerted upon the heel. The process begins with the generation of a 2D representation of the forefoot, depicted without thickness as illustrated in Figure 2. Subsequently, the forefoot area is discretized into nine longitudinal sections, thus facilitating the calculation of distinct thickness values for each delineated region.

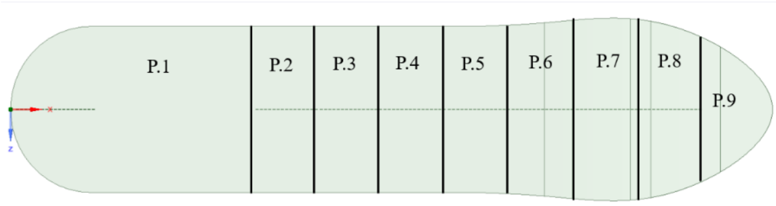

Figure 2. Preliminary design of prosthetic foot.

Subsequently, the forefoot structure was determined to consist of the following layers. The upper and lower layers were comprised of woven carbon fiber fabric, with two layers present on each lateral side. The intermediate layer was characterized by a unidirectional carbon fiber fabric layer, positioned longitudinally along the forefoot. This unidirectional layer was oriented at angles of 0, 45, and -45 degrees relative to the forefoot's longitudinal axis, taking the number of layers of 3 types of unidirectional carbon fiber fabrics of 9 areas as parameters. Later, the situation was designed to be used in the calculation. Reducing the structure to be calculated to only the forefoot, and buffer. Thereafter, external forces were applied via a plate set at a 20-degree inclination relative to the designated plane, constrained to motion only along the perpendicular plane. The magnitude of this external force, set at 670 N, was approximated to align with the force experienced during heel-off for an individual weighing 60 kg, which all 4 parts will be assembled with the following relationship.

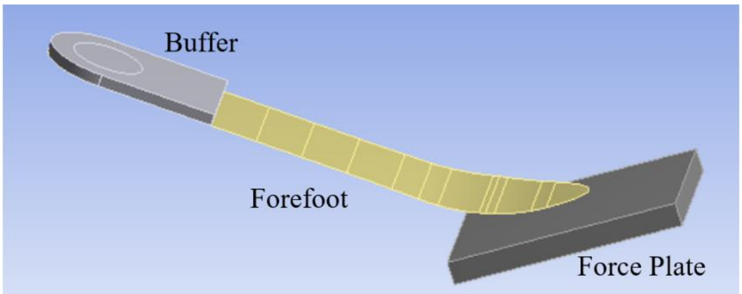

Figure 3. Preliminary design of prosthetic foot (fore foot).

1. Buffer was set as fixed support.
2. Force plate has frictionless contact with forefoot.
3. Forefoot has bonded contact with buffer.

After that, parametric optimization was calculated by assigning the number of carbon fiber layers that angled at 45 and -45 degrees to the longitudinal direction of the foot to be the same thickness to ensure symmetry within the foot structure. Additionally, a stipulation was introduced that the cumulative thickness of the anterior region must not exceed that of the posterior region. This provision was introduced with the intent of curbing the volume of samples necessitating computational evaluation, thereby enhancing the efficiency of the optimization process. In this optimization, MOGA (multi-objective genetic algorithm) technique was used with the configuration below. After that, objectives and parameters of this parametric optimization are defined as follows.

Configurations
1. 100 initial samples
2. 100 sample per iteration
3. Maximum 8 iterations
4. Maximum 10 candidates

Objectives
1. Minimize max stress in the structure.
2. Minimize the difference of max stress in each section along the longitudinal to make materials in all ranges bear similar loads.
3. Make the deformation value of the loaded part converge to 13.4 mm.

Variable Parameters
1. Number of 0° unidirectional carbon fiber layer in each section (9 parameters)
2. Number of 45° and -45° unidirectional carbon fiber layer in each section (9 parameters)

Total of 18 parameters.

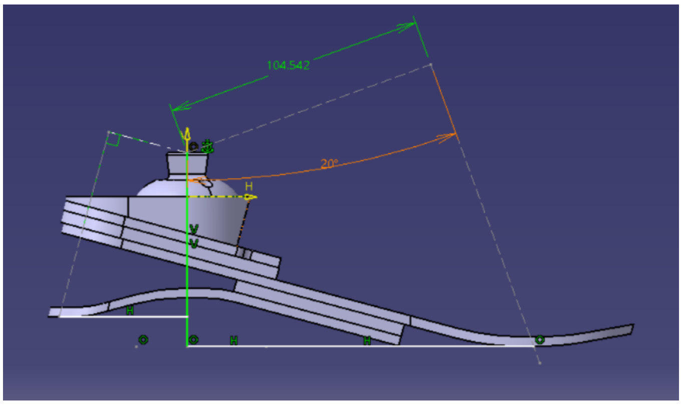

Figure 4. Preliminary design of prosthetic foot.

The specified deformation magnitude in the objective is obtained by calculating the required rotational stiffness value. From 'Figure 4', the distance that the force is applied around the ankle can be estimated as 104.5 mm can be substituted in equation (1) as follows [6].

$$k_{rot} \approx \frac{rF}{\frac{\delta}{r}} \approx \frac{F}{\delta} r^2 \approx k_l r^2$$

$$9.6\ N/deg = \frac{670N}{\delta\ mm} \times 0.105\ m^2 \times 1000 \times \frac{2\pi}{360} \tag{1}$$

$$\delta\ mm = 13.43\ \ mm$$

After determining the thickness of each section in the forefoot area, the researchers proceeded to develop a prosthetic foot model for the purpose of parametric optimization. This optimization aimed to identify the optimal thickness for the heel section of the prosthetic foot. The model employed in this optimization process was adjusted from the one utilized in the initial section test as ‘Figure 5’ by adding various parts that have relations connected to each other as follows.

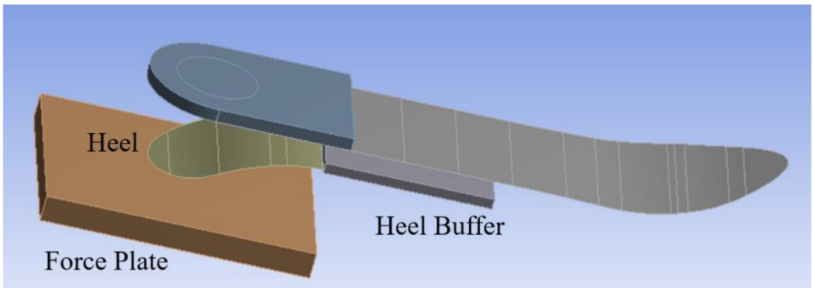

Figure 5. Preliminary design of prosthetic foot (heel).

1. Heel buffer has bonded contact with forefoot.
2. Heel buffer has bonded contact with heel.
3. Force plate has frictionless contact with heel.

As for the heel, similarly to the forefoot, the heel is divided into 10 longitudinal sections and is assigned taking the number of layers of 3 types of unidirectional carbon fiber fabrics of 10 areas as parameters, thereafter, changing the angle at which the force plate acts on it to 15 degrees relative to the horizontal. The force was 670 N and parametric optimization was performed with the following configurations, objectives, and parameters.

Configuration
1. 100 initial samples
2. 100 sample per iteration
3. Maximum 8 iterations
4. Maximum 10 candidates

Objectives
1. Minimized max stress in the structure.
2. Make the deformation value of the loaded part converge to 2.92 mm.

Variable Parameters
1. Number of 0^{o} unidirectional carbon fiber layer in each section (10 sections)
2. Number of 45^{o} and -45^{o} unidirectional carbon fiber layer in each section (10 sections)

Total of 20 parameters.

The deformation distance was obtained by estimating the applied force distance in 32.8 mm as in ‘Figure 6’ and substituting the value in equation (1) as follows.

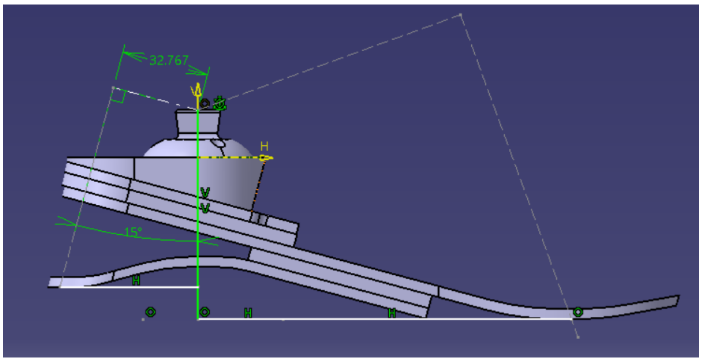

Figure 6. Preliminary design of prosthetic foot.

$$4.3\ N/deg = \frac{670N}{\delta\ mm} \times 0.0328\ m^2 \times 1000 \times \frac{2\pi}{360}$$

$$\delta\ mm = 2.92\ \ mm$$

3. Result

Candidate points of parametric optimization of the forefoot was obtained as shown in ‘Figure 7’, after the optimum point was selected from the candidate points the result was obtained as shown in Table 2 with a maximum stress occurring at 330.73 MPa and a deformation of 13.29 mm, as shown in ‘Figure 8’.

Name	P38 - Equivalent Stress Maximum (MPa)		P52 - diff stress (Pa)		P76 - Total Deformation 2 Maximum (mm)	
	Parameter Value	Variation from Reference	Parameter Value	Variation from Reference	Parameter Value	Variation from Reference
Candidate Point 1	330.73	0.00%	2.9548E+08	0.00%	13.289	0.00%
Candidate Point 2	329.59	-0.35%	2.9441E+08	-0.36%	13.187	-0.77%
Candidate Point 3	329.59	-0.35%	2.9441E+08	-0.36%	13.187	-0.77%
Candidate Point 4	329.59	-0.35%	2.9441E+08	-0.36%	13.187	-0.77%
Candidate Point 5	329.59	-0.35%	2.9441E+08	-0.36%	13.187	-0.77%
Candidate Point 6	330.52	-0.06%	2.9713E+08	0.56%	13.3	0.08%
Candidate Point 7	330.52	-0.06%	2.9713E+08	0.56%	13.3	0.08%
Candidate Point 8	330.52	-0.06%	2.9713E+08	0.56%	13.3	0.08%
Candidate Point 9	330.52	-0.06%	2.9713E+08	0.56%	13.3	0.08%
Candidate Point 10	330.52	-0.06%	2.9713E+08	0.56%	13.3	0.08%

Figure 7. Candidate points of forefoot from the simulation.

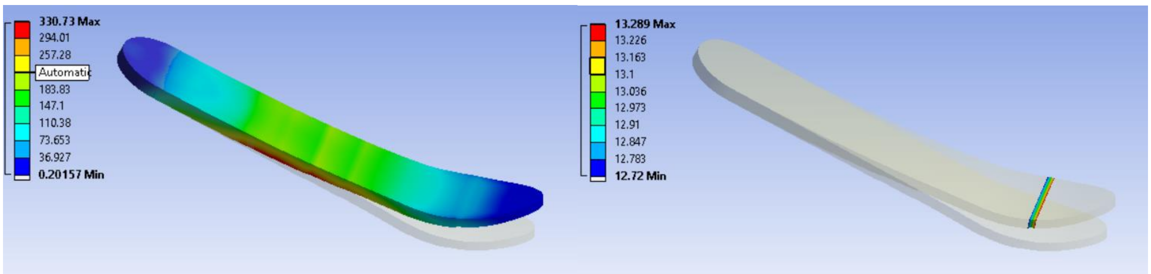

Figure 8. Stress generated and deformation in forefoot from the simulation.

Table 2. Result from parametric optimization in forefoot.

Type of carbon fiber	Section number								
	1	2	3	4	5	6	7	8	9
UD 0 deg	23	23	22	19	19	18	18	16	15
UD 45, -45 deg	8	7	7	6	5	5	5	4	4

Candidate points of parametric optimization of the heel was obtained as shown in ‘Figure 9’, after the optimum point was selected from the candidate points the result was obtained as shown in Table 3 with a maximum stress occurring at 153.98 MPa and a deformation of 2.92 mm, as shown in ‘Figure 10’ and ‘Figure 11’.

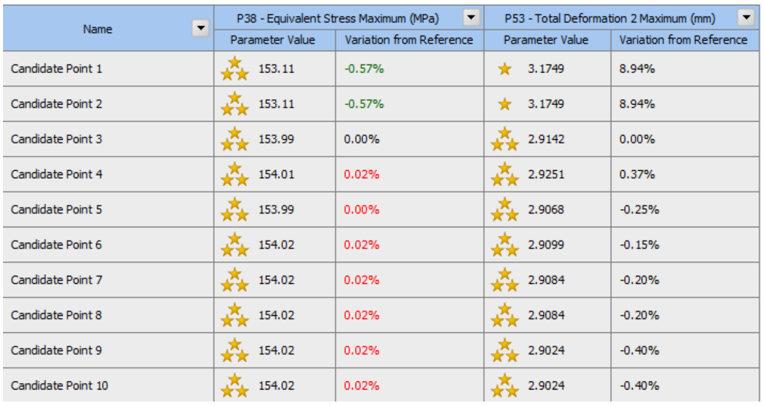

Name	P38 - Equivalent Stress Maximum (MPa)		P53 - Total Deformation 2 Maximum (mm)	
	Parameter Value	Variation from Reference	Parameter Value	Variation from Reference
Candidate Point 1	153.11	-0.57%	3.1749	8.94%
Candidate Point 2	153.11	-0.57%	3.1749	8.94%
Candidate Point 3	153.99	0.00%	2.9142	0.00%
Candidate Point 4	154.01	0.02%	2.9251	0.37%
Candidate Point 5	153.99	0.00%	2.9068	-0.25%
Candidate Point 6	154.02	0.02%	2.9099	-0.15%
Candidate Point 7	154.02	0.02%	2.9084	-0.20%
Candidate Point 8	154.02	0.02%	2.9084	-0.20%
Candidate Point 9	154.02	0.02%	2.9024	-0.40%
Candidate Point 10	154.02	0.02%	2.9024	-0.40%

Figure 9. Candidate points of heel from the simulation.

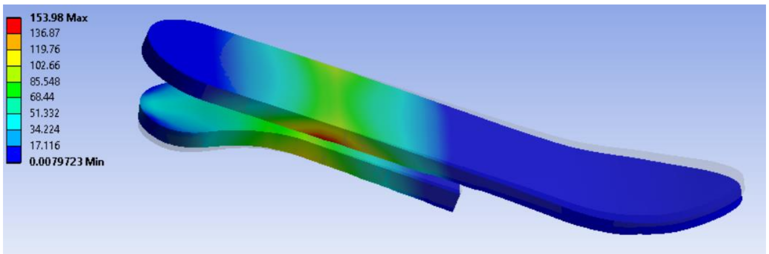

Figure 10. Stress generated in heel section from the simulation.

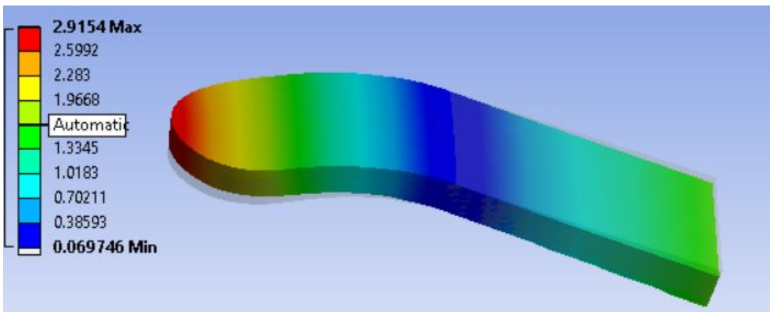

Figure 11. Deformation in heel section from the simulation.

Table 3. Result from parametric optimization in heel section.

Type of carbon fiber	Section number									
	1	2	3	4	5	6	7	8	9	10
UD 0 deg	29	28	28	28	28	28	27	27	26	26
UD 45, -45 deg	7	6	5	4	4	4	3	3	3	2

4. Discussion

As a result, in the forefoot section, 3 different candidate points are obtained, each with their own pros and cons. The researcher has chosen candidate point 1 to be further calculated. By considering candidate point 2 was excluded due to a 1.59% deformation difference from the set value, while candidate points 1 and 6 differed from the set value by 1.59%. Set only 0.83% and 0.75% respectively which stiffness is the most important objective. Thereafter, candidate point 1 was selected from the remaining 2 candidate points because of the smaller difference of max stress in each section along the longitudinal, while another objective was not significantly different. Next, in the result from heel section, 7 different candidate points were founded, when looking at the value of deformation that occurred only candidate points 3 and 4, which had the closest deformation values of -0.199% and 0.175%, respectively, were taken into consideration. While the difference in stress between those 2 candidate points was only 0.02%. Candidate point 3 was selected because excessive deformation of the prosthetic foot may cause the user to fall, whereas insufficient deformation only impairs gait without compromising the safety of the user. Therefore, from the selected thickness, the designed prosthetic foot will have plantarflexion and dorsiflexion stiffness values of 4.32 Nm/deg and 9.70 Nm/deg, respectively. Notably, these stiffness values were close to the predefined target values of 4.3 Nm/deg and 9.6 Nm/deg with only 0.47% and 1.04% stiffer for plantarflexion and dorsiflexion, respectively. Furthermore, the structural integrity analysis revealed that the resultant stress experienced by the prosthetic foot's components was limited to an insignificantly low value of 330.73 MPa.

5. Conclusions

The main objective of this study was the creation of a passive prosthetic foot tailored for an individual with a foot size of 26 cm and weighing 60 kg. The specific stiffness requirements were set at 4.3 Nm/deg for plantarflexion and 9.6 Nm/deg for dorsiflexion. The ultimate objective was to arrive at a prosthetic foot design that met these criteria while preserving strength. After the utilization of parametric optimization techniques, the resulting prosthetic foot not only achieved the targeted plantarflexion and dorsiflexion stiffness values of 4.32 Nm/deg and 9.70 Nm/deg respectively which mean only 0.47% and 1.04% different occur but also exhibited an advantageous attribute. Notably, the maximum stress experienced by the prosthetic foot component during operation was calculated at 330 MPa, which was much lower than the tensile strength of the material. This mean that the utilization of parametric optimization within the Finite Elements program yielded significant advantages in the development of prosthetic feet, specifically by facilitating the precise determination of optimal thickness in terms of stiffness and strength for the prosthetic foot during various phases.

6. References

[1] Thailand National Statistical Office (2017) , *Summary of important results of the disability survey*.

[2] Shepherd, M.K. and E.J. Rouse (2010). Comparing preference of ankle–foot stiffness in below- knee amputees and prosthetists. *Scientific reports*, 10(1), 16067.

[3] Shepherd, M.K., et al. (2018). Amputee perception of prosthetic ankle stiffness during locomotion. *Journal of neuroengineering and rehabilitation*, 15(1), 1-10.
[4] Clites, T.R., et al. (2021). Understanding patient preference in prosthetic ankle stiffness. *Journal of neuroengineering and rehabilitation*, 18(1), 1-16.
[5] Taboga, P. and A.M. Grabowski (2017). Axial and torsional stiffness of pediatric prosthetic feet. *Clinical Biomechanics*, 42, 47-54.
[6] Major, M.J. (2010). The influence of the mechanical properties of trans-tibial prostheses on amputee performance. *University of Salford (United Kingdom).*
[7] T.C.I.T. (2006). ISO 10328 Prosthetics - Structural Testing of Lower-limb Prostheses Requirements and Test Methods. *International Organization for Standardization: Geneva, Switzerland*, 168.
[8] Safaeepour, Z., et al. (2014). Quantitative analysis of human ankle characteristics at different gait phases and speeds for utilizing in ankle-foot prosthetic design. *Biomedical engineering online*,13(1), 1-8.
[9] Whittle, M.W. (2007). *Gait Analysis an Introduction*. Heidi Harrison.
[10] King, A.I. (2006). *Clinical Gait Analysis: Theory and Practice*. Chris Kirtley, Churchill Livingstone.
[11] Takahashi, K.Z. and S.J. Stanhope (2013). Mechanical energy profiles of the combined ankle–foot system in normal gait: Insights for prosthetic designs. *Gait & posture*, 38(4), 818-823.

The 13th TSME International Conference on Mechanical Engineering
12th – 15th December 2023
Chiang Mai, Thailand

BME0004

Double-Plate Arrayed EWOD Lab-on-a-Chip Platform for DNA Sequencing by LAMP Method

Apiporn Sangketdee[1], Nattapong Sikongplee[2], Chanchon Dhanaporn[3], and Wishsanuruk Wechsatol[1,*]

[1] Department of Mechanical Engineering, King Mongkut's University of TechnologyThonburi,126 Prachautid Rd,Bandmod,Thungkru,Bangkok 10140,THAILAND
[2] Department of Mechanical Engineering, King Mongkut's University of Technology Thonburi,126 Prachautid Rd,Bandmod,Thungkru,Bangkok 10140,THAILAND
[3] Department of Mechanical Engineering, King Mongkut's University of Technology Thonburi,126 Prachautid Rd,Bandmod,Thungkru,Bangkok 10140,THAILAND
[4] Department of Mechanical Engineering, King Mongkut's University of Technology Thonburi,126 Prachautid Rd,Bandmod,Thungkru,Bangkok 10140,THAILAND

* Corresponding Author: wishsanurak.wee@kmutt.ac.th

Abstract. This research is aimed to study the transport phenomena of viscous droplets under electrical field induced by the applied voltage between two parallel plates. The disturbance of electrical field causing the change of contact angle and thus moving the droplets in the direction of applied voltage accordingly is the so-called "electrowetting-on-dielectric (EWOD) phenomena". The 10 x 10 arrayed electrode layer was fabricated on printed circuit boards (PCB), while the Fluorine-doped Tin Oxide glasses (FTO glasses) were used as the parallel ground plates in order to create the electrical field for transporting droplets and for controlling the sizes of droplet samples in many electrochemical and biological detection processes such as DNA sequencing on the Lab-on-a-Chips. The heater plate was placed directly under the printed circuit boards to raise the temperature of the droplet samples on top of the printed circuit boards to be at the specific testing conditions for each electrochemical and biological detection. In this work, the temperature of droplets was controlled to be in the range between 62 – 65 °C, which is suitable for DNA sequencing by the loop-mediated isothermal amplification (LAMP) technique. Further study on the effects of viscosity to the responsive velocity of droplets were comparatively studied among pure DI water and syrup samples with the concentration of 10% 20% 30% 40% 50% 60% by weight. The droplets of DI water between two parallel plates reached the maximum velocity of 3.87 mm/s at 900 Volts. As the viscosity of syrup droplets increased with their concentrations, the responsive velocity of the syrup droplets deceased. The saturated syrup at the concentration of 60% could move at the velocity as low as 0.254 mm/s at 900 Volts. The studied results on the effects of viscosity on the EWOD performance for droplet transportation can be used to select suitable applied voltage for transporting viscous fluids with different dynamic viscosity on top of the EWOD platforms.

Keywords: Electrowetting on Dielectrics, Droplet manipulation, Lab-on-a-chip platform.

1. Introduction

Electrowetting on dielectric (EWOD) platforms are the device used to control movement of liquid droplets by applying an electric field. They operate on the principle of manipulating the forces generated by an electric field, which is the results from applying a voltage difference across the two parallel electrodes. This disruption on the surface tension of the liquid droplets causes an imbalance, prompting them to move in a specific direction. The movement of liquid droplets can be applied to various fundamental tasks as shown in Fig. 1 including dispensing, transporting, mixing, and splitting. EWOD devices can be found in many applications, particularly in the creation of the Lab-on-a-Chip platforms for electrochemical and biological detection as well as for the early syndrome diagnosis. These devices excel in managing and controlling tiny liquid droplets ranging from microliters to nano-litres with high precision.

Y. Mori and T. Notomi [1] developed the Lab-on-a-Chip platform to perform the loop-mediated isothermal amplification (LAMP) at 63°C – 65 °C for analysing pat hogens and detecting genetic structures within the samples. This platform is cost-effective and can be used in limited laboratory space. Kanchanaphum, P. [2] utilized the LAMP technique to identify eight different DNA species, simultaneously. The key aspect of this research involved the addition of CuSO4 to the sample and the detection using the LAMP technique, which allowed the visible infection detection with the naked eyes. One limitation of using CuSO4 is that it can detect DNA quantities lower than 10 picograms. J. Lee, H. Moon, J. Fowler, T. Schoellhammer, and Chang-Jin Kim [3] made the comparison on both aspects of the fundamental concept and the experimental verification on the electrowetting phenomena and the electrowetting on dielectrics phenomena and concluded that both methods control liquid droplets with different working principles. The electrowetting devices controls the wetting ability of certain dielectrics on metal surfaces by altering surface energy. While the electrowetting on dielectric devices are applicable to all types of aqueous liquids and are relied on the principle of changing electrical energy through dielectrics between the liquid and the electrical electrodes. The manipulation of droplets in both types of digital microfluidic devices depends on the surface tension force to disturb the equilibrium of water droplets.

Jain V. [4] developed an enclosed Electrowetting-on-Dielectric-(EWOD) device for controlling water droplets, while integrating the heating element with temperature control system and a digital microscope. The Fehling tests to detect glucose in a solution was conducted. Additionally, the device was used to demonstrate the transport of blood-like liquid droplets at relatively high temperatures of around 90°C. The developed system is reliable and proves the feasibility of creating an EWOD device with low cost using the real-time control concept.

W. Wang, J. Chen, and J. Zhou [5] studied the effects of electrode sizes and electrode geometry on the movement of droplets. The parameters influencing droplet movement are the width and length of the electrodes, as well as the gap between the electrodes. M. Abdelgawad and A. R. Wheeler [6] utilized the rapid prototyping approach for the creation of EWOD devices. The 3-D printing technology was used to create the copper electrodes on a Printed Circuit Board (PCB). Two fabrication methods were employed, -i.e., the creation of patterns using photolithography and wet etching, and the directly printed copper patterns on the surface using a laser printer. The appropriate design parameters such as the suitable thickness of insulation layers and hydrophobic layers, and the optimal electrode spacing were proposed. K. Sukthang et. al. [9] focused on designing an EWOD device for the early detection of diseases in shrimp using the LAMP-XO technique. In this study, the Printed Circuit Board (PCB) fabrication was chosen due to the cost-effectiveness and simplicity. The study results indicated that using the LAMP-XO technique on the EWOD device yields results consistent with those obtained in the conventional PCR laboratory.

In this paper, the focus is on developing an EWOD devices on printed circuit boards for simulating the preparation for droplet samples required in the LAMP sequencing technique. The 10 x 10 rectangular arrayed electrode layer with the width of 2.54 mm x 2.54 mm was fabricated for droplet manipulation involving dispensing, merging, and splitting processes to observe their functionality. Additionally, a heater with temperature feed-back controlled unit was installed to control the droplet temperature in the range between 63°C to 65°C, which is required to perform LAMP technique. This study also focuses on the effect of droplet viscosity on the responsive velocity of droplet movement on top of EWOD devices fabricated on printed circuit board.

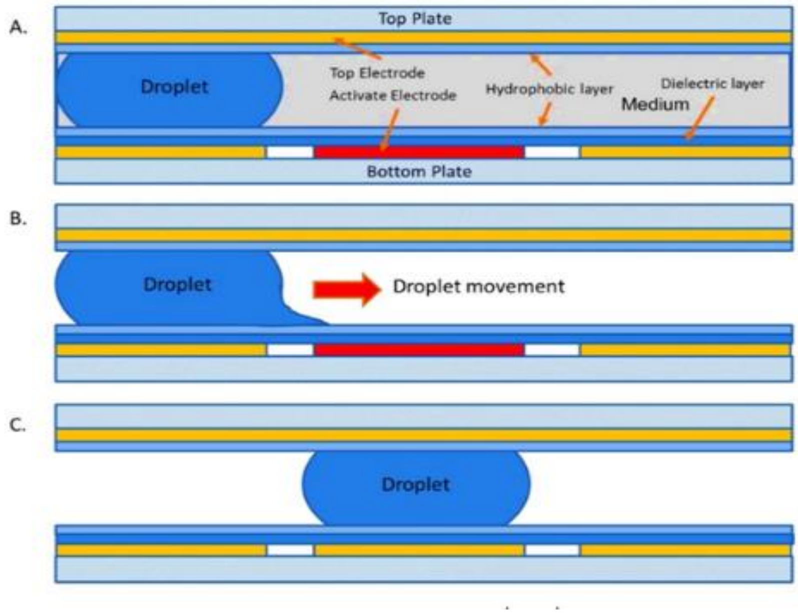

Figure 1. Configuration of a closed type EWOD device [9].

2. Suitable Electrode Geometry

The fabrication of closed type electrowetting on dielectric devices started from importing lower electrode layer on the substrates. The size of each electrode is important and directly related to the volume of controlled droplets. The smaller droplet requires the smaller size of electrode. The relation of droplet volume and the geometry of electrodes and void space in Fig. 2 can be described as Eq. (1) [9]. The droplet volumes according to electrode sizes at the width of void space equal to 1mm are reported in Table 1.

$$V_{full} = \frac{2L}{3}\pi(3w^2 + 2L^2) \quad (1)$$

where 2w is the width of each electrode [m]
2L is the width of the void space of EWOD device[m]

In this paper, the size of the bottom electrode is fixed at 2.54 mm x 2.54 mm and the width of the void space or the medium space is 1mm. When considering the corresponding droplet volume according to relation in Eq. (1) and the width of medium space at 1 mm, the suitable volume of droplets for 2.54 mm x 2.54 mm electrodes is 20.77 microlites. In this design, the gap space between two adjacent electrodes is 0.5mm as shown in Fig. 3.

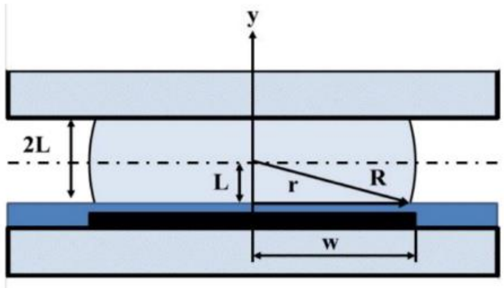

Figure 2. Geometry of a droplet situated inside a closed-type EWOD device [9].

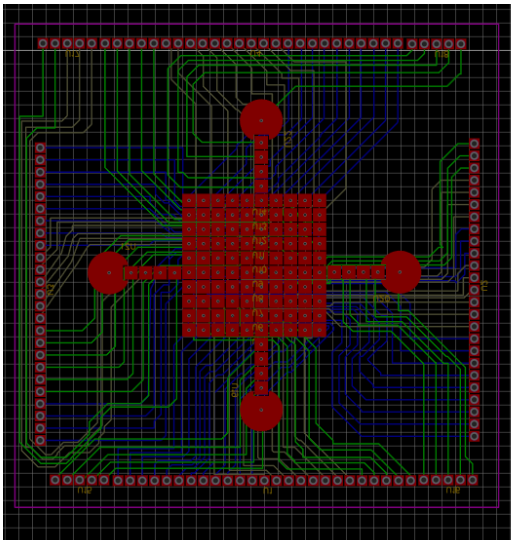

Figure 3. Bottom electrode size.

Table 1. The droplet volume according to electrode size at the width of medium space equal to 1mm [9].

W(mm)	Volume of Droplet (microliter)
1.00	3.64
1.25	5.41
1.50	7.57
1.75	10.12
2.00	13.07
2.54	20.77

3. Proposed Fabrication Procedure

This paper is aimed to propose the rapid fabrication produce of EWOD devices and their controller components. Let us start with the simple configuration of the controller components for controlling the discharging of applied voltage to each individual electrode in order to induce the droplet movement. The major control components are composed of

- *High Voltage Generator and Controller Board:* This circuit is responsible for the main control of the device for supplying and controlling the discharge electrical current, voltage, and frequency. Arduino microcontroller is used for programming the operational commands and transmitting control data for inducing droplet movement. The relevant equipment for high voltage generator is included of a step-up transformer, a function generator, and a power amplifier.

- *Node Selector Controller Board:* The node selector circuit is designed to control the delivery of high voltage received from the function generator. The electrical signal is undergone the transformation through the power amplifier and the transformer to achieve the desired high voltage. The node selector then distributes the voltage difference to each specific electrode on the printed circuit board. Arduino microprocessor is programmed to control the delivery of high voltage to each individual node on the PCB using a shift register as a signal receiver for commands from the Arduino microprocessor.

Unlike the previous work proposed by Sukthang et. al. [9] in Fig. 4, the designing of electrical terminals for closed-type EWOD devices using dual-array electrode configuration is proposed*:* In order to construct an EWOD device for controlling the movement of liquid droplets, the key aspect is to design electrical terminals that align with the desired objectives similar to the previous work by Sukthang [9]. In this work, we aimed to design a 10 x10 arrayed electrode layer as shown in Fig. 5, which has more adaptable capability to utilize in any specific desired objectives for Lab-on-a-Chip devices. We also chose to design the multi-layer PCBs to create the electrode layer substrate, so that the plane of 10 x 10 arrayed electrodes can be fabricated as shown in Fig. 5.

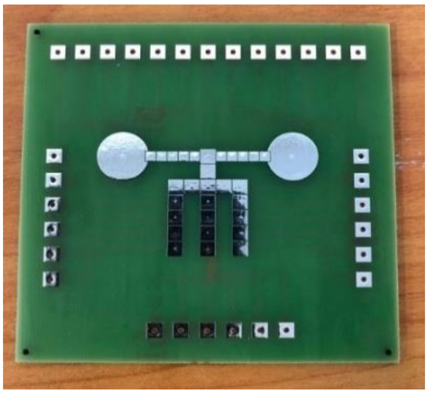

Figure 4. Print circuit board proposed by Suktang [9].

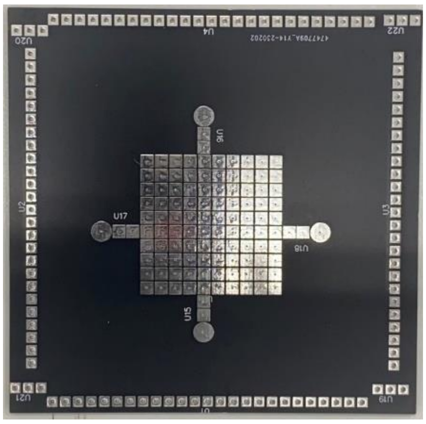

Figure 5. Print circuit board new design.

4. Experimental Methodology

In this research, the experimental tests are divided into four parts for simulating the testing conditions of LAMP detection processes on Lab-on-a-chip EWOD platforms as follows:

- Heating process test: A heater was installed to maintain a temperature range of 63 - 65 °C on the tested droplets. This is necessary to simulate the LAMP (Loop Isothermal Amplification) technique, which is used for DNA replication.
- Glass coating test: Coating to create the hydro-phobic condition is important to increase the droplet contact angle and to reduce the applied voltage required to move droplets. Three types of coated materials, Teflon film, PDMS and Teflon AF were tested by coating on glass surface to observe the contact angle. Coating process involves applying liquid form of coating substance on glass surfaces, removing trapped air bubbles, and baking at 120°C for PDMS and Teflon AF, while Teflon film is the most convenient for creating hydrophobic layers by simply placing on the substrate layers. Water droplets was placed on the coated surfaces to observe the contact angles for each coating materials.
- Droplet manipulation test: This test was designed for examining the movement of water droplets under transportation, separation and merging of DI water droplets.
- Viscous effect test: Viscosity of droplets has direct effects on the contact angle and ability to manipulate droplets. The syrup solutions with different concentration on sucrose were used to observe the effects of concentration on the transportation behavior of droplets on top of an Lab-on-a-Chip EWOD devices under specific applied voltages.

5. The Experimental Setup

The schematic diagram of the experimental setup was proposed as in Fig. 6 in order to supply and control applied voltage and electrical frequency. The specification of equipment is composed of

1. a step-up transformer with the discharge voltages in the range between 450 – 900 Volts,
2. a function generator for controlling the frequency of applied electrical field at 1000 Hz.
3. a power amplifier for controlling applied voltages in the range between 450-900 Volts,
4. a sequential controller (the Node Selector) for controlling the sequence of applying voltage on each specific electrode.

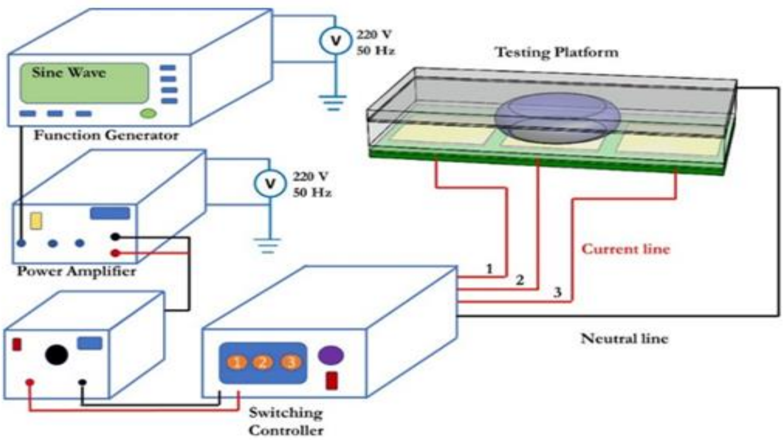

Figure 6. Diagram of control equipment setup and power supply for EWOD devices [9].

6. The Experimental Results

The first part involves testing the control of droplet temperature to verify that the liquid droplets are within the temperature range of 63 - 65 °C. The second part is measuring the contact angle to observe the highest contact angle due to the hydrophobic properties, which makes liquid droplets move easily. The third part is controlling the liquid droplets, combining them, and separating them to test the droplet manipulation capability. The fourth part involves testing the retention of values between DI water droplets and sucrose with varying concentrations by adjusting the applied voltages and observing the responsive velocity of the droplets.

6.1. Verification of the temperature control system for LAMP assay testing

The success of the lamp manufacturing process relies on several crucial variables, with the most important one being temperature control. To ensure the success of the LAMP DNA sequencing process, the temperature must remain constant within the range of 63 – 65 °C throughout the entire testing process. A 7 cm x 7 cm of heat flux plate with heating capacity of 200-watt with feedback temperature controller was placed under the PCB substrates. Temperature of droplets was monitored using a K-type thermocouples. The testing results confirms that the droplet temperature was well controlled in the range between 63 – 65 °C as shown in Fig. 7. The target temperate of droplet can be reached within less than 10 mins.

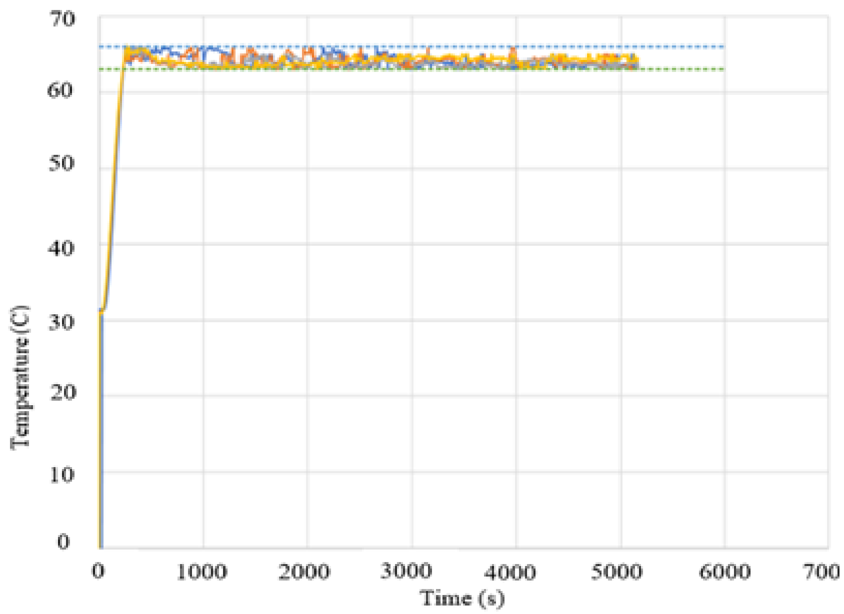

Figure 7. The droplet temperature being controlled at LAMP testing condition between 63 - 65°C.

6.2. Contact angles according to coating materials

The hydrophobic layer is an important part of a Lab-on-a-Chip EWOD platform. In this study, three different coating materials were applied to glass substrate to observe the effects of coating materials on the contact angle of DI water droplets, where the contact angles for each coating material in comparison to the untreated glass surface are reported in Table 2 and illustrated in Fig. 8. The Fluorine-doped tin oxide (Teflon-AF) provides the highest contact angle among the three tested coating materials. Therefore, the Teflon-AF was selected as the coated material for developing our Lab-on-a-Chip EWOD platform for LAMP testing.

Table 2. Contact angles for each type of coating materials.

Type of surface coating	Contact Angles
Untreated glass surfaces	35.525°
Glass surface wrapped with Teflon film	88.668°
Glass surface coasted with PDMS	112.041°
Glass surface coated with Fluorine-doped tin oxide (Teflon-AF)	119.625°

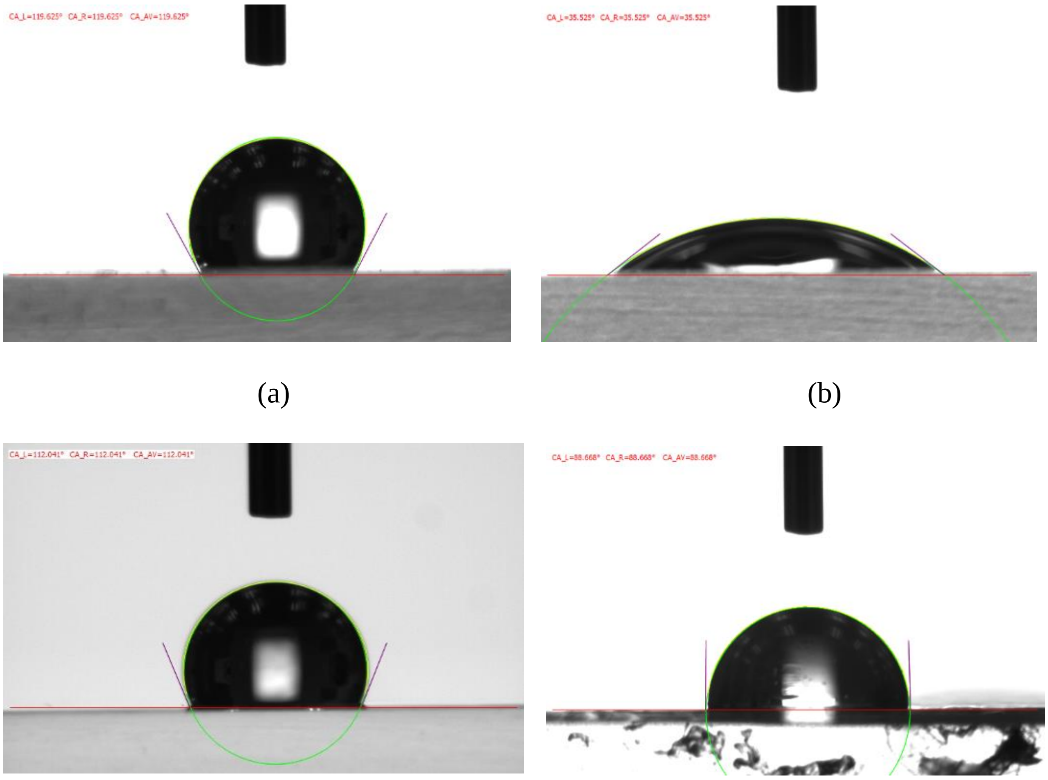

(a) (b) (c) (d)

Figure 8. Contact angle of (a) untreated glass surface, (b) Glass surface wrapped with Teflon film, (c) Glass surface coasted with PDMS, and (d) Glass surface coated with Fluorine-doped tin oxide (Teflon-AF).

6.3. Droplet manipulation test

In this test, the 2.54 mm x 2.54 mm electrodes were fabricated to create a 10 x 10 arrayed electrode layer on multilayer PCBs with capability to manipulate multiple droplets of the size 20.77 µL. Figure 9(a) shows the splitting capability that divides a droplet into two equal parts, while Fig. 9(b) shows the capability of EWOD devices to transport and to mix (to merge and to shake) two droplets together to create the homogenous mixing condition of the two droplet samples. The splitting process in Fig. 9(a) can be done by applying electrical voltage on the electrodes situated on both sides of the droplet sample, while holding the applied voltage on the electrode at the droplet position, and then switch off the applied voltage at the droplet position, while keep holing the applied voltage on both sided electrodes as shown in Fig. 9(a). The merging of droplets can be done simply by applying the electrical voltage voltages at the electrode in the middle between two droplets, and creating the homogeneous mixing condition can be done by moving the droplets back and forth at high switching speed to shake the mixed droplet.

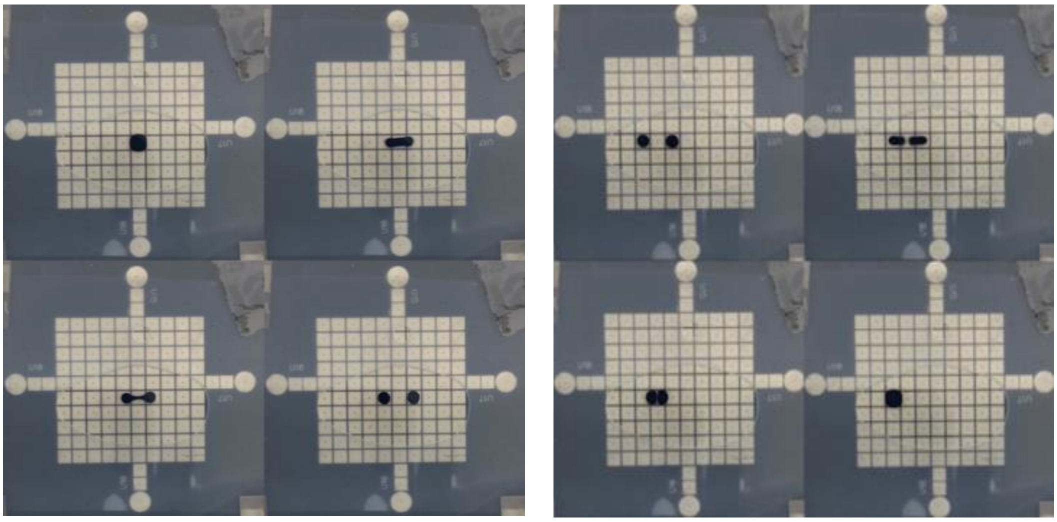

(a) (b)

Figure 9. Droplet manipulation (a) splitting process and (b) merging process.

6.4. The effects of viscosity on the responsive velocity of droplets

To study the effects of viscosity on the responsive velocity of droplet movement on top of an EWOD platform, the syrup solutions at concentration bay weight of 10%, 20%, 30%, 40%, 50%, and 60% were prepared by solute sucrose in DI water. The Rheometer was used to measure the dynamic viscosity of syrup solution with different concentration of sucrose and the respective dynamic viscosities are reported in Table 3, where the viscosity increases with the concentration of sucrose in syrup solutions.

Table 3. The viscosity values with different concentrations.

% Concentrations by w/w	Dynamic Viscosity [$N\text{-}s/m^2$]
10	0.001809
20	0.003401
30	0.009325
40	0.012198
50	0.032004

The responsive velocities of droplets were studied at the applied voltage between 400 – 900 Volts at the electrical frequency of 1,000 Hz, where the studied results are shown in Fig. 10. As the syrup concentration increases, the viscosity of the syrup solutions increasing, causing the responsive velocity of droplets to decrease under specific applied voltages. This implies that to preserve the responsive velocity of droplets as the viscosity increases, the higher amplitude of applied voltages is required. Note that all the experiments in this study were done at the controlled room temperature of 25 ± 2°C.

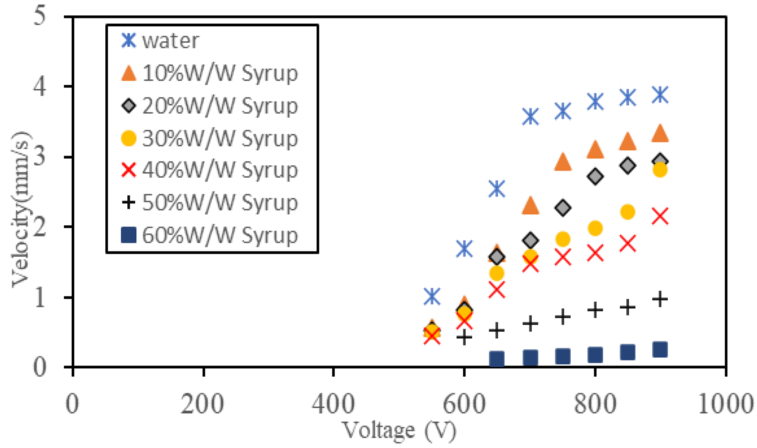

Figure 10. The responsive velocity of syrup droplets with different concentration of sucrose in DI water at various applied voltages and the fixed frequency of 1,000 Hz.

7. Conclusion
In this study, the design of 10 x 10 arrayed electrode layer was proposed. The Lab-on-a-Chip EWOD platform for LAMP (loop-mediated isothermal amplification) technique was fabricated. To ensure the performance of the proposed EWOD platform for LAMP testing, the transportation and droplet manipulation testes as well as the temperature control process were conducted. Further studied on the effects of viscosity on the responsive velocity of droplet movement were tested under the applied voltage between 400 – 900 Volts at the controlled electrical frequency of 1,000 Hz. The applied voltages required for maintain the responsive velocity at different concentration of syrup solutions and different viscosities were reported. Further investigation to develop the empirical formular governing the droplet movement behaviour of droplets on top of EWOD platform is recommended.

8. Acknowledgments

The author would like to express gratitude for the provided testing facility at the department of mechanical engineering, faculty of engineering, and the department of physics, faculty of sciences, King Mongkut's University of Technology Thonburi (KMUTT). The financial support from the National Science, Research and Innovation Fund (NSRF) via the Program Management Unit for Human Resources & Institutional Development, Research and Innovation [granted number B40G660039] and the Fundamental Fund [ID 4696540] are well acknowledged.

9. References

[1] Yasuyoshi Mori, Tsugunori Notomi, "Loop-mediated isothermal amplification (LAMP): a rapid, accurate, and cost-effective diagnostic method for infectious diseases" 2009 springer.com.

[2] Kanchanaphum, P. Identification of human DNA by loop-mediated isothermal amplification (LAMP) technique combined with white ring precipitation of $Cu(OH)_2$.

[3] Junghoon Lee, Hyejin Moon, Jesse Fowler, Thomas Schoellhammer, Chang-Jin Kim.Electrowetting and electrowetting-on-dielectric for microscale liquid handling.1 January 2002

[4] Jain, V., et al. (2015). "Design, fabrication and characterization of low cost printed circuit board based EWOD device for digital microfluidics applications." Microsystem Technologies 23(2): 389-397.

[5] Wei Wang, Jianfeng Chen, Jia Zhou, 2015, "DROPLET GENERATING WITH ACCURATE VOLUME FOR EWOD DIGITAL MICROFLUIDICS" 2015 IEEE

[6] Mohamed Abdelgawad and Aaron R. Wheeler, 2007, "Rapid Prototyping in Copper Substrates for Digital Microfluidics" Adv. Mater., vol.19, pp.133–137, 2007.

[7] Chatchawal Pongsumpun, 2012, "Control of Droplet Movement on a Surface," Master's Thesis in Mechanical Engineering, Faculty of Engineering, King Mongkut's University of Technology Thonburi, Thailand.

[8] Phantakan Jiaratwisin, 2015, "Fabrication of Electrowetting Devices on Dielectric Layers by Printing," Master's Thesis in Mechanical Engineering, Faculty of Engineering, King Mongkut's University of Technology Thonburi, Thailand.
[9] Sukthang, Kreeta, Jantana Kampeera, Chakrit Sriprachuabwong, Wansika Kiatpathomchai, Eakkachai Pengwang, Adisorn Tuantranont, and Wishsanuruk Wechsatol. 2021. "Sensitivity Validation of EWOD Devices for Diagnosis of Early Mortality Syndrome (EMS) in Shrimp Using Colorimetric LAMP–XO Technique.

BME0005

Effect of Curved Root Canal on Torsional Shear Stress of NiTi Rotary Files

Punyavud Tomeboon[1,*], Sirawut Hiran-us[2], Sarita Morakul[1], and Pairod Singhatanadgid[1]

[1] Department of Mechanical Engineering, Faculty of Engineering, Chulalongkorn University, Bangkok, 10330, Thailand
[2] Department of Operative Dentistry, Faculty of Dentistry, Chulalongkorn University, Bangkok, 10330, Thailand

* Corresponding Author: punyavud.t@gmail.com

Abstract. Rotating nickel-titanium (NiTi) dental files are widely used in endodontic treatments to shape and clean root canals. These instruments possess exceptional flexibility and cutting efficiency, which allows them to conform to the shape of the canal and return to their original straight configuration. Failures of rotary files often result from torsional load-induced fractures and flexural fatigue. This study aimed to investigate the torsional resistance of NiTi rotary files when operating in root canals with varying degrees of curvature. In such cases, the files experience a combined load of torsional and flexural forces due to the applied torque and bending caused by the curved root canal, respectively. Finite element analysis was employed to determine the torsional shear stress experienced by the rotary files subjected to torsional and flexural loads from the curved root canal. Solid models of dental files and artificial root canals were created using computer-aided design software and converted to finite element models. The finite element model of the files was then preloaded with the bending displacement (Setup I) and inserted into the root canal (Setup II) before applying the torsional load. Shear stress distribution and file deformation were thoroughly analyzed. The results of the finite element confirmed the previous experimental studies. For Setup II, maximum shear stress on the cross-section near the fixed support, i.e. 1 mm above the fixed support, decreased as the angle of curvature was increased. The difference in the methods used to create curved configuration of the files in both setups is the cause of conflicting conclusions in the previous experimental studies. The experiment in Setup II is closer simulate the real clinical situation than Setup I. Therefore, the curved root canal might have a positive effect on the torsional resistance of rotary files.

Keywords: endodontic rotary files; finite element analysis; torsional resistance; torsional shear stress; curved root canal.

1. Introduction

Root canal treatment is one of the most important processes for the endodontist to preserve a tooth that could have been removed completely. Root canal treatment simply consists of cleaning and filling the root canal with biocompatible material, namely gutta-percha. Root canal cleaning is a process to remove pulp and infected tissue within the root canal. The main equipment used to clean the root canal is endodontic files, which can be a hand file or a rotary file. Endodontic rotary files have been utilized for root canal treatment because of their efficiency, speed, and consistency. Rotary files are motor-driven instruments with cutting edge used to clean the root canal wall [1, 2]. They are usually manufactured from a nickel-titanium (Ni-Ti) alloy, which possesses superelasticity property. Because of this superior property, Ni-Ti alloys have been selected over stainless steel for rotary files. The Ni-Ti alloy can be bent into the root canal and returned to its original configuration after removal from the canal.

There are two modes of failure of the rotary file: bending fatigue and torsional fracture [3]. Failure due to fatigue from bending occurs when the instrument becomes bent upon insertion into a curved root canal. On alternately, a point in the file is subjected mainly to tensile and compressive bending stress. Teeth characterized by sharp curvatures in their root canals are at a higher risk of failure caused by bending stress compared to those with more standard root canal curvatures. Therefore, fatigue failure from bending load is a form of failure of rotary files. The other mode of failure is initiated by excessive torsional shear stress. Torsional fracture occurs when the file's tip or a section of the file becomes trapped within the root canal, while the file itself continues to rotate. The torsional force exceeds the file's threshold, leading to its fracture. The failure of the rotary file is directly related to the success of root canal treatment. Failure of the file during the root canal procedure is a significant complication that dentists must avoid [4]. Research in this field included clinical investigation, experimental research in a controlled environment, and computational techniques. Clinical studies are subject to ethical concerns and can require substantial costs, whether in terms of direct expenses or time requirements. Experimental studies offer a more manageable procedure but still require significant investment in terms of both cost and time for establishing testing facilities. A numerical approach presents a more cost-effective alternative, serving as an initial step preceding more comprehensive investigations. The finite element method (FEM), commonly utilized in engineering applications, is a numerical technique that is typically used to analyze the mechanical behavior of rotary files [5].

The mechanical behavior of rotary files has been studied using the FEM in several studies. These studies involved both commercially available rotary files [6-9] and files with an ideal cross-sectional configuration [10-12]. Typically, the finite element method was used to analyze the stress distribution within rotary files subjected to bending or torsional loads. The deformation of the files was investigated in terms of deflection and the torsional angle of rotation. Thus, both the strength and the flexibility of the files were examined. In practice, rotary files are subjected to complicated load conditions, the combination of both flexural and torsional loads. Jamleh et. al. [13] investigated the torsional resistance of rotary files under flexural load. Forty-eight commercial files were tested for torsional resistance in both straight and curved positions of 90° curvature. In this study, the specimens were bent into a curved configuration by rotate the handpiece 90° to form an experiment with 90° curvature canal. The applied torque was applied from the handpiece, but the torque was measured as the reaction torque at the 3-mm apical length using a torque gauge device. A significant decrease in torsional resistance was found in the files with a curved configuration compared to that of a straight configuration. However, another study by Seracchiani et. al. [14] reported a conflicting result. In the latter study, the experimental setup was slightly different from that of the former study. Sixty commercial files were inspected and categorized into 3 groups. Each group of files was preloaded by inserting into a stainless steel artificial curved canal with 60° and 90° curvature and a straight canal. The 2-mm apical length of the files was clamped to a specially designed device. The files were then loaded with the torsional moment and the torque to fracture and the time to fracture were recorded. It was found that the average torque to fracture on the files inserted into the 90° curvature canal was higher than that of the 60° curvature canal, which was higher than that of the straight canal. The study concluded that the flexural stresses in the curved canal specimen have a positive influence on the torsional resistance of instruments with a blocked tip.

Therefore, in this study, the effect of the curved root canal on induced torsional shear stress in the rotary files was investigated using FEM. The experiments in previous studies which have conflicting results were repeated numerically. The FEM solutions were compared with the experimental results. Recommendations for future studies regarding the torsional resistance of the rotary files operating in the curved canal will be given.

2. Rotary Files Operating in Root Canals

As mentioned previously, there are two major loads applied on the files during the operation in the root canal, the flexural and torsional loads. The flexural or bending load is the result from the curved root canal, while the torsional load is generated from the resistance between the file and root canal wall. Sometimes, the torsional load can be extremely high if the tip of file is adhered to the root canal wall. The rotary file's configuration operating inside the root canal is shown in Figure 1. Under flexural loading, an element on the file, especially on the surface of the file, is subjected to tensile stress and compressive stress, alternately. As a result, the file is subjected to bending fatigue and might fail after the file is operated for a certain number of cycles. Under torsional load, the file could fail due to excessive torsional shear stress. There are two studies that reported the effect of curved canal on the torsional shear resistance of the files. Both studies were experimental studies with different testing configurations. So, the objective of this study is to analyze the shear stress induced in the files operating in the straight and curved positions by utilizing the finite element method. The analysis would not only determine the torsional shear stress of the file operating in curved canal, but also validate the previous experimental studies which gave conflicting conclusions.

The finite element study was set up similar to the experimental studies by Jamleh et. al. [13] and Seracchiani et. al. [14]. Setup I, which simulated the experiment by Jamleh et. al. [13], had the rotary file fixed on the file's apical 3-mm. For the study of straight configuration, torque of 2 N-mm was applied on the other end. For the curved configuration, the file was bent by 30°, 60° and 90° before applied torque the shaft of the file, as shown in Figure 2. In the second setting, the file was inserted in a simulated root canal with an angle of 0°, 30°, 60°, and 90°. The apical 2-mm length of the file was then secured, and 2 N-mm torque was applied to the shaft of the file. With the insertion of the file into the simulated curved canal, the files were loaded with flexural load. The flexural load was higher in the set up with higher degree of curvature. The torsional shear stress was observed after the torsional load was applied. This setup, designated as "Setup II" in Figure 3, followed the experimental study by Seracchiani et. al. [14].

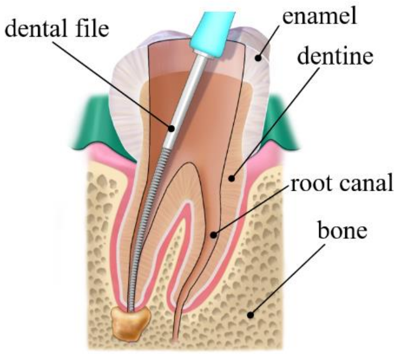

Figure 1. Dental file operating in the root canal.

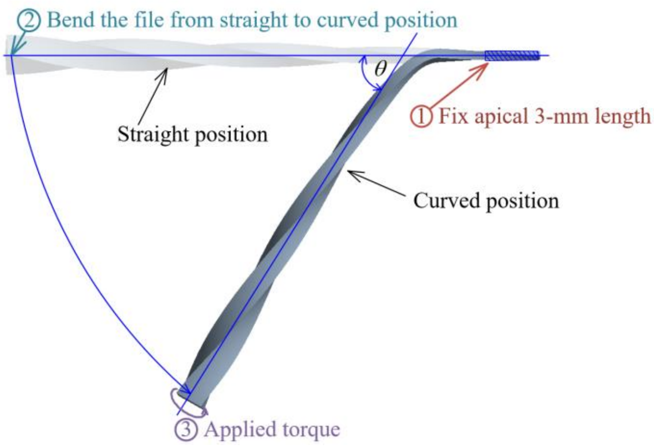

Figure 2. Loading of the file for Setup I.

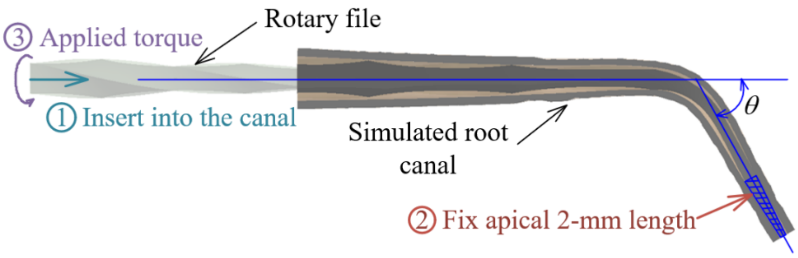

Figure 3. Loading of the file for Setup II.

3. Finite Element Analysis

Finite element method (FEM) is a numerical method which uses physical modeling and numerical calculation to predict mechanical behaviors and other phenomenon of a system under various physical conditions. This method is widely used in the engineering field since many engineering problems are complicated and cannot be solved using analytical methods. In this study, the shear stress on the rotary files subjected to both tortional and flexural load were investigated using the FEM. A commercial software "Ansys" was used in this study.

3.1. Finite Element Model

Before performing the finite element analysis, 3D solid models of rotary files were prepared by computer-aided design (CAD) software. Firstly, the 3D rotary files model with square cross-sectional configurations was created. The model was then exported as .step files and imported to ANSYS program. Next, the model was then meshed, and material properties were defined. The solid model of a file and the meshed model are shown in Figure 4. Mechanical properties of NiTi alloy used in the analysis are presented in Table 1 which are mechanical properties of superelastic materials modeled in Ansys. With these setups, the finite element model is ready to set up for load and boundary conditions.

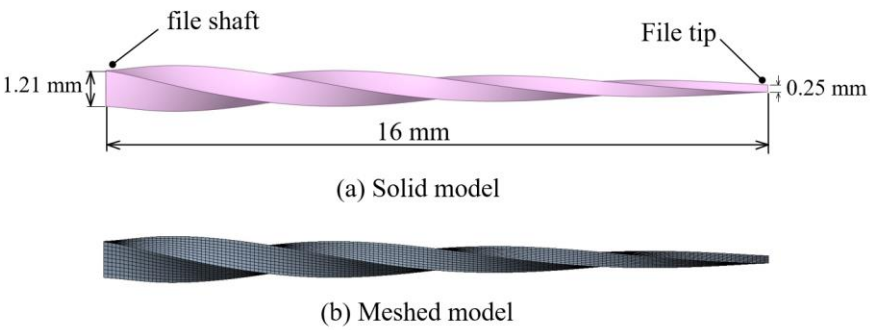

Figure 4. Solid and meshed model of a rectangular rotary file.

3.2 Load and Boundary Condition

To investigate the torsional resistance of NiTi rotary files when operating in root canals with varying degrees of curvature, two setups were investigated according to previous experiments. In the finite element analysis of Setup I as shown in Figure 5(a), the fixed support was applied to the surface of the file for the length of 3 mm from the tip of the file. Then, angular displacement which created an angle curvature of root canal was applied at the shaft of the file. Angular displacement of 30°, 60°, and 90° were applied for curved position and no angular displacement was applied for straight position. Then, a torque of 2 N-mm was applied at the shaft of the file. Shear stress was observed on the cross-section 1 mm, 2 mm, 3 mm, and 4 mm above the fixed support. In Setup II as shown in Figure 5(b), a linear displacement was applied axially of the shaft end of the file to move the file into an artificial root canal which has angle of curvature of 0°, 30°, 60° and 90°. After insertion into the root canal, the rotary file was fixed along the length of 2 mm from the tip. Finally, a 2 N-mm torque was applied at the file's shaft which is the same cross-section where the linear displacement was applied.

Table 1. Mechanical properties of nickel-titanium (NiTi) alloy [15].

Properties	Value
D (Density)	6.45 g/cm^3
E_A (Young's modulus of the full austenite phase)	42,530 MPa
ν (Poisson's Ratio)	0.3
σ_s^{AS} (Starting stress value for the forward phase transformation)	492 MPa
σ_f^{AS} (Final stress value for the forward phase transformation)	630 MPa
σ_s^{SA} (Starting stress value for the reverse phase transformation)	192 MPa
σ_f^{SA} (Final stress value for the reverse phase transformation)	97 MPa
$\bar{\varepsilon}_L$ (Maximum residual strain)	0.06
α (The difference between material responses in tension and compression)	0
E_s (Young's modulus of the full martensite phase)	12828 MPa

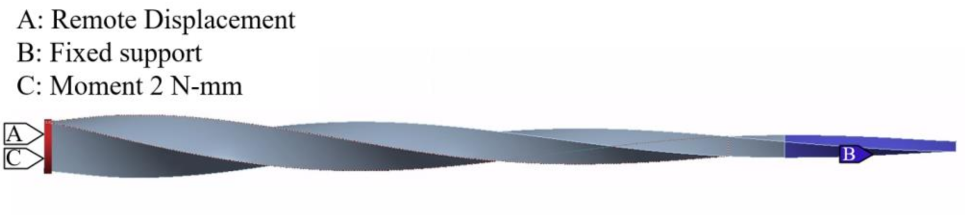

(a)

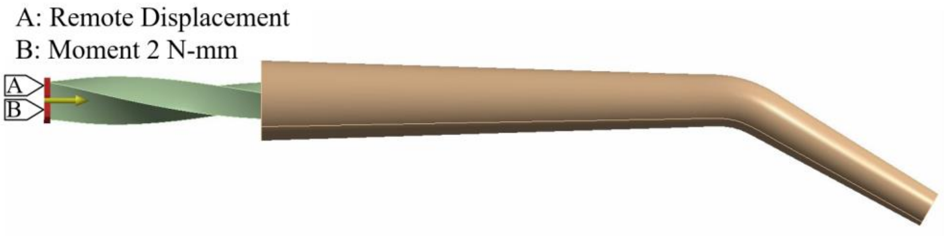

(b)

Figure 5. (a) Setup I with fixed support (blue) and a cross-section where displacement and torque were applied (red). (b) Setup II with a rotary file inserted in an artificial root canal.

4. Results

4.1. Convergence study

A convergence study was performed to ensure that element size used in the analysis was sufficient and the FEM solutions were accurate. To find the suitable element size, a triangle cross-sectional rotary file operating in Setup I with 0° angular displacement was used in the convergence study. The element sizes were set at 0.5 mm, 0.4 mm, 0.3 mm, 0.2 mm, 0.15 mm, 0.1 mm, 0.075 mm, and 0.05 mm. The convergence of the finite element model was considered from the contour of stress distribution, maximum equivalent (von-Mises) stress, and maximum shear stress on the file.

Equivalent stress distributions on the 4-mm cross-section from the tip of the file determined using different element sizes are presented in Figure 6. It was found that the stress distribution was practically constant when the element size used in the analysis was as low as 0.1 mm. Similarly, the maximum equivalent stress and the maximum shear stress in the cross-section can be considered as "converged" when the element size of 0.1 mm was used, as shown in Figure 7. Therefore, the element size of 0.1 mm was used in all the analyses in this study.

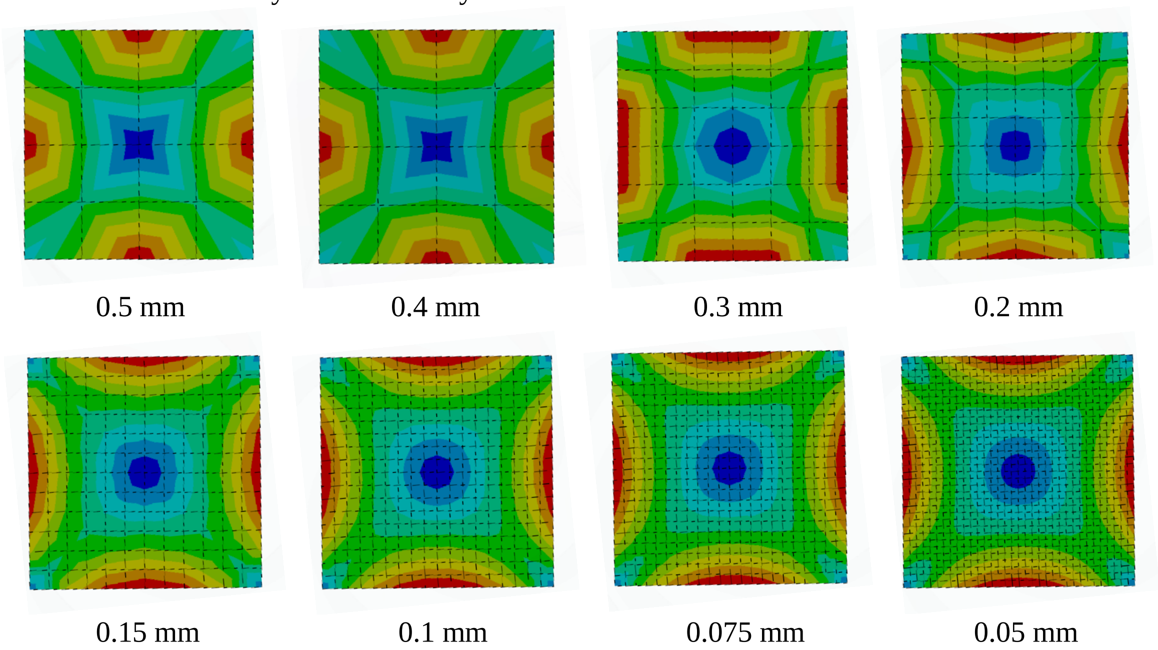

Figure 6. Contours of equivalent stress distribution on the cross section with element sizes of 0.5, 0.4, 0.3, 0.2, 0.15, 0.1, 0.075, and 0.05 mm.

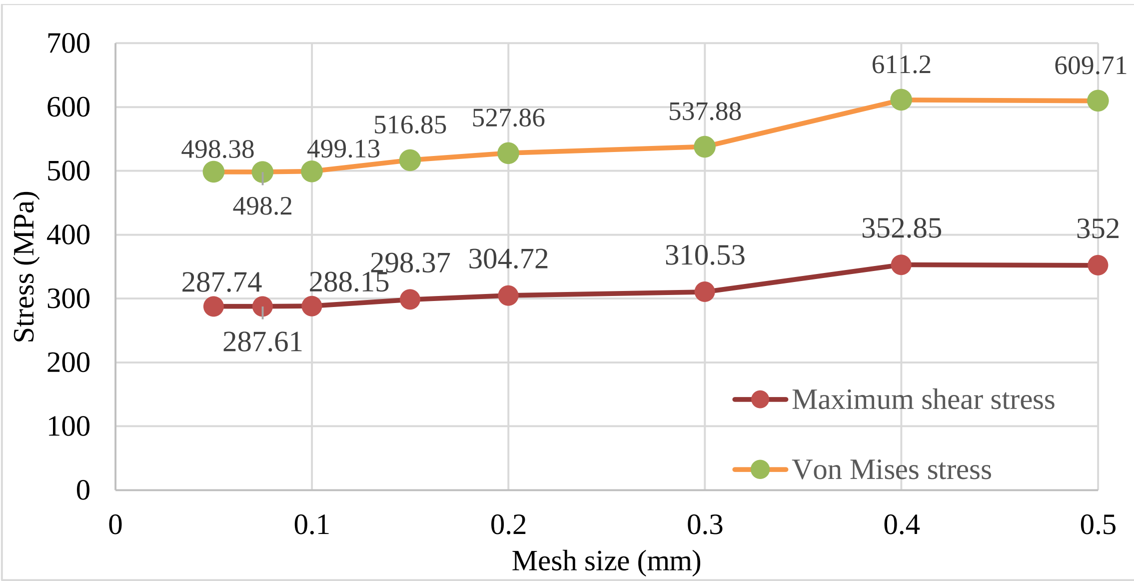

Figure 7. Equivalent stress and maximum shear stress values from different mesh size.

4.2. Shear stress distribution on the file

For the analysis with Setup I, shear stress distributions on the file oriented in a straight and different curved positions under the applied torsion of 2 N-mm are shown in Figure 8. A file in straight position is presented in Figure 8(a), while the file in curved positions of 30°, 60° and 90° are shown in Figure 8(b-d), respectively. For a straight file the maximum shear stress is observed on the cross-section 0.3 mm from the fixed support, approximately. For other curved positions, the maximum shear stress is detected at the inner curvature of the file and, approximately, at the same cross-section as the straight configuration, i.e. 0.1 mm for the file with 30° curvature, and 0.2 mm the files with 60° and 90° curvature.

Also, the shear stress detected in the specimens in Setup II is presented in Figure 9. The position of the maximum shear stress in case of straight and 30° curved positions are similar to the specimens in Setup I. The position of maximum shear stress is on the cross-section 0.1 mm and 0.3 mm above the fixed support for the case of straight and 30° curvature, respectively. On the other hand, the maximum shear stress for the case of 60° and 90° curved position is on the curved portion of the file. It should be noted that the length of fixed support for both setups is different, i.e. 3 mm for Setup I and 2 mm for Setup II.

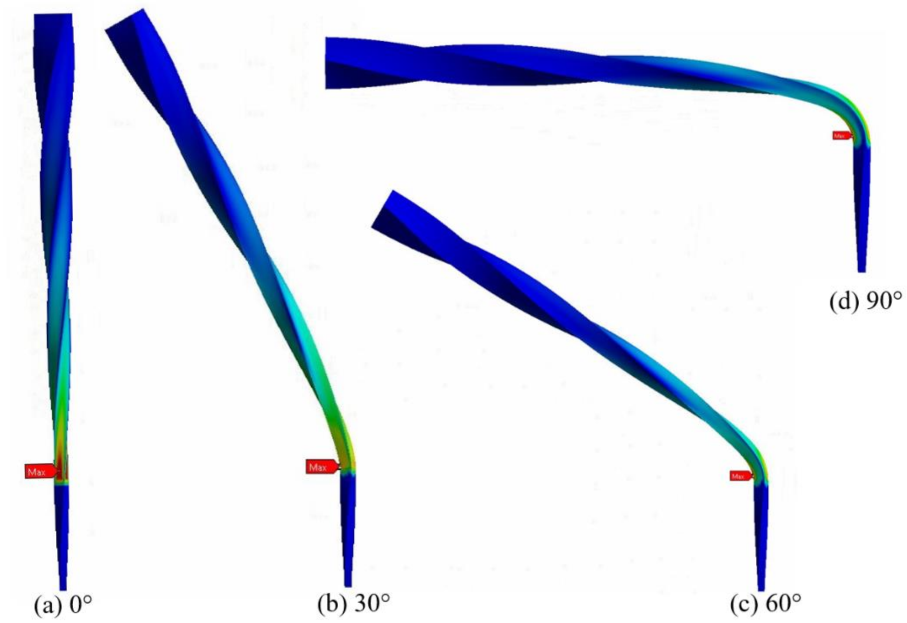

Figure 8. Shear stress distributions of a file in Setup I with (a) straight position (b-d) curved positions.

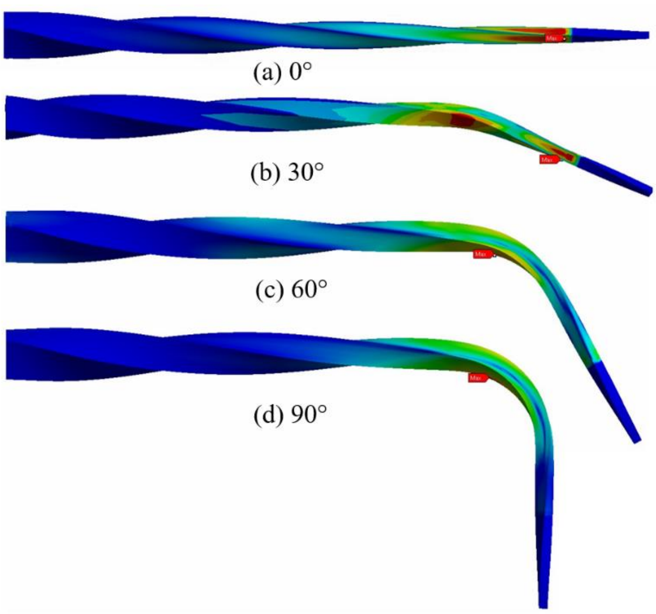

Figure 9. Shear stress distributions of a file in Setup II with (a) straight position (b-d) curved positions

4.3. Maximum shear stress on a specific cross-section

From the FEM results, the maximum shear stress on the cross-sections 1-mm, 2-mm, 3-mm and 4-mm above the fixed support was considered, as shown in Tables 2 and 3 for the cases of Setup I and Setup II, respectively. The maximum von Mises stress and the maximum shear stress on the body of the files are shown in the second and third columns of the tables. The last four columns present the maximum shear stress on the cross-sections 1-mm, 2-mm, 3-mm, and 4-mm above the edge of the fixed support. For the shear stress in the specimens loaded in Setup I, all stresses shown in Table 2 are higher if the files were preloaded to a higher curvature. In contrast, the stresses in the files loaded in Setup II do not have the same trend. For example, the maximum shear stress on the body in the case of 30° curvature is slightly lower than that of the case of the straight file. Similarly, shear stress at 1-mm cross-section above the fixed support is also lower in the case of files with higher curvature.

Table 2. Maximum stresses observed on the file loaded in Setup I.

Angle of curvature (Degree)	Max. von Mises stress on the body (MPa)	Max. shear stress on the body (MPa)	Max. shear stress on a cross-section above the fixed support (MPa)			
			1 mm	2 mm	3 mm	4 mm
0	499.13	288.15	230.90	160.64	118.55	89.159
30	847.37	426.24	272.67	259.58	208.22	159.53
60	1615.5	809.79	308.68	256.91	230.51	205.17
90	2124.7	1066.2	651.02	262.85	255.80	245.71

Table 3. Maximum stresses observed on the file loaded in Setup II.

Angle of curvature (Degree)	Max. von Mises stress on the body (MPa)	Max. shear stress on the body (MPa)	Max. shear stress on a cross-section above the fixed support (MPa)			
			1 mm	2 mm	3 mm	4 mm
0	549.36	317.17	290.46	230.40	160.31	118.25
30	583.24	315.08	256.15	280.97	311.27	253.23
60	750.45	386.90	127.27	231.04	307.88	279.48
90	999.19	502.1	68.036	245.15	413.75	427.88

5. Discussion

The results obtained from finite element analysis for specimens loaded in Setup I and II were consistent with the experimental studies by Jamleh et. al. [13] and Seracchiani et. al. [14], respectively. In Setup I, it is clearly seen that stresses induced in the files are higher if the specimens are pre-bent with higher curvature. These results agreed with the report in Ref. [13]. In the study by Jamleh et. al. [13], the file which is bent with a higher curvature can sustain a lower torsional moment than a file with a lower curvature. They also concluded that the torsional resistance of files operating in a curved root canal decreases compared to a file operating in a straight configuration or in a root canal with a lower curvature configuration.

For the simulation of the file loaded by inserting the file into the simulated canals, some stresses observed on the files in the case of straight root canals are higher than those of in the curved canals. Although not all the stresses obtained in case of straight root canal are higher than those of in the curved canal, the shear stress distribution in Setup II is different from that of Setup I. As shown in Figure 9(c), the position of maximum shear stress on case of 60° curvature is not on the cross-section near the fixed support, which is different from the cases of Setup I. This can be explained by considering the applied loads on the files before the applied torque of 2 N mm is applied. In Setup I, the applied load included the reaction force applied to bend the file to create the curvature and the reaction moment at the 3-mm apical of the file. The stresses observed after the applied torque of 2 N-mm on the file shaft are a combination of stress from the applied torque and from the forces to deform the file into a curved configuration. On the other hand, forces applied to the specimens in Setup II are probably lower than those of Setup II. In Setup II, the only force that bends the specimen is the reaction force of the simulated root canal. The reaction force from the 2-mm apical fixed support does not exist before the applied torque of 2 N-mm is applied. Therefore, it is reasonable to observe that the shear stress on the file in the cross-section near the fixed support is lower than that of the curved portion of the file (Figure 9 (c) and (d)). To confirm the hypothesis, the torsional moment reaction of the fixed support was determined and presented in Table 4. During the application of the torque, the torsional load applied on the file is mainly the 2 N-mm applied torque and the torsional moment reaction at the support, as shown in Figure 10. It is clearly seen that the torsional moment reaction on the support is lower in the specimen loaded into the root canals with higher curvature. In the straight configuration, the torsional moment reaction is almost equal to the applied torque of 2 N-mm. With the curved configuration, the internal torque at the apical part of the file is probably equal to the torsional moment reaction which is much lower than the applied torque of 2 N-mm.

Table 4. Moment reaction on the studied surface of the square rotary file in the root canal.

Angle of curvature (Degree)	Torsional moment reaction (N-mm)
0	1.996
30	1.461
60	0.585
90	0.204

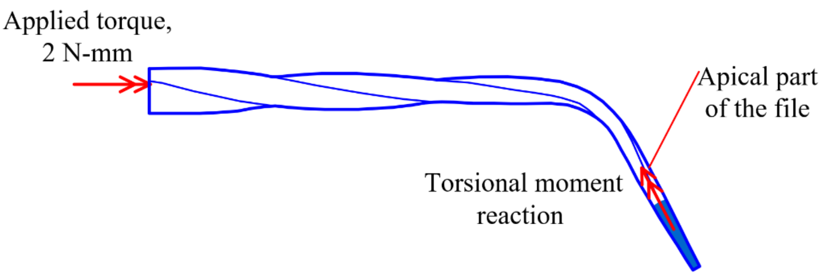

Figure 10. Applied torsional load and torsional moment reaction at the support.

6. Conclusion

This study investigated the torsional resistance of endodontic rotary files operating in a straight and curved root canal. Finite element analysis was utilized based on previous experimental studies which reported conflicting results. It is found that the experiment setups in the previous studies are different and are probably the cause of conflicting conclusions. In the experiment with Setup I, the specimen is bent and probably causing excessive loads to the file compared to the real clinical application. The experiment in Setup II probably resembles a more realistic clinical situation than that of the first setup. Therefore, it is possible that the resistance to torsional shear stress of the file is higher when it operates in a curved canal. This study utilized the finite element method to validate experimental studies. The finite element result served as a guide to assess the conflicting results of two studies. However, additional studies are required to investigate the parameters which may affect the torsional behavior of the file. The cross-sectional configuration, the position of the fixed support, and the location of the curved portion of the file are parameters that should be investigated.

7. References

[1] Liang, Y. & Yue, L. (2022). Evolution and development: engine-driven endodontic rotary nickel-titanium instruments. *International Journal of Oral Science*, *14*(1), 12.

[2] Dablanca-Blanco, A.B., Castelo-Baz, P., Miguéns-Vila, R., Álvarez-Novoa, P., & Martín-Biedma, B. (2022). Endodontic Rotary Files, What Should an Endodontist Know?. Medicina (Kaunas, Lithuania), *58*(6), 719.

[3] Sattapan, B., Nervo, G.J. , Palamara, J.E., & Messer, H.H. (2000). Defects in rotary nickel-titanium files after clinical use. *Journal of Endodontics*, *26*(3), 161-165.

[4] Gomes, M.S., Vieira, R.M., Böttcher, D.E., Plotino, G., Celeste, R.K., & Rossi-Fedele, G. (2021). Clinical fracture incidence of rotary and reciprocating NiTi files: A systematic review and meta-regression. *Australian endodontic journal*, *47*(2), 372–385.

[5] Chien, P.Y., Walsh, L.J., & Peters, O.A. (2021). Finite element analysis of rotary nickel-titanium endodontic instruments: A critical review of the methodology. *European journal of oral sciences*, *129*(5), e12802.

[6] Xu, X. & Zheng, Y. (2006). Comparative study of torsional and bending properties for six models of nickel-titanium root canal instruments with different cross-sections. *Journal of endodontics*, *32*(4), 372–375.

[7] Kim, H.C., Kim, H.J., Lee, C.J., Kim, B.M., Park, J.K., & Versluis, A. (2009). Mechanical response of nickel-titanium instruments with different cross-sectional designs during shaping of simulated curved canals. *International endodontic journal*, *42*(7), 593–602.

[8] Kim, T. O., Cheung, G. S., Lee, J. M., Kim, B. M., Hur, B., & Kim, H. C. (2009). Stress distribution of three NiTi rotary files under bending and torsional conditions using a mathematic analysis. *International endodontic journal*, *42*(1), 14–21.

[9] El-Anwar, M.I., Yousief, S.A., Kataia, E.M., & El-Wahab, T.M. (2016). Finite Element Study on Continuous Rotating versus Reciprocating Nickel-Titanium Instruments. *Brazilian dental journal*, *27*(4), 436–441.

[10] Zhang, E.W., Cheung, G.S., & Zheng, Y.F. (2010). Influence of cross-sectional design and dimension on mechanical behavior of nickel-titanium instruments under torsion and bending: a numerical analysis. *Journal of endodontics*, *36*(8), 1394–1398.

[11] Zanza, A., Seracchiani, M., Di Nardo, D., Reda, R., Gambarini, G., & Testarelli, L. (2021). A Paradigm Shift for Torsional Stiffness of Nickel-Titanium Rotary Instruments: A Finite Element Analysis. *Journal of endodontics*, *47*(7), 1149–1156.

[12] Versluis, A., Kim, H.C., Lee, W., Kim, B.M., & Lee, C.J. (2012). Flexural stiffness and stresses in nickel-titanium rotary files for various pitch and cross-sectional geometries. *Journal of endodontics*, *38*(10), 1399–1403.

[13] Jamleh, A., Almedlej, R., Alomar, R., Almayouf, N., Alfadley, A., & Alfouzan, K. (2021). Evidence for reduced torsional resistance of rotary files under curved position. *The Saudi dental journal*, *33*(7), 614–619.

[14] Seracchiani, M., Miccoli, G., Di Nardo, D., Zanza, A., Cantore, M., Gambarini, G., & Testarelli, L. (2021). Effect of Flexural Stress on Torsional Resistance of NiTi Instruments. *Journal of endodontics*, *47*(3), 472–476.

[15] Roda-Casanova, V., Antonio Pérez-González, A., Zubizarreta-Macho, A., & Faus-Matoses, V. (2022). Influence of Cross-Section and Pitch on the Mechanical Response of NiTi Endodontic Files under Bending and Torsional Conditions – Finite Element Analysis. *Journal of Clinical Medicine, 11(9), 2642.*

BME0006

Vibration of Degraded Human Knee Joint: Model and Simulation

N Ajavakom[1,*] and P Varopichetsan[1]

[1]Department of Mechanical Engineering, Chulalongkorn University, Bangkok 10330, Thailand

* Corresponding Author: nopdanai.a@chula.ac.th

Abstract. When a human knee joint degrades due to ageing, excessive use, an accident etc., it gives more difficulty to perform daily life activities like walking running sitting or squashing. To determine the severity of the degrade condition of the joint, the physician may use imaging techniques such as x-ray, CT scan, or magnetic resonance imaging (MRI). All of them need some high-technology equipment as well as specialized doctor to read the image results and thus it requires time and a lot of money for the patient. In addition to examination by using imaging techniques, in some current research, the measured vibration signals at the patella is used to indicate how much injured the knee joint is. In this study, we propose that patellofemoral joint degeneration can be identified by analysing vibrational signals obtained from an accelerometer attached to the patella while flexing and extending the knee joint. In addition, the physical factor related to the degradation of the knee joint that contributes most to the vibrating motion of the knee joint is determined. First, the model of a patella in motion is created and the vibration theory is applied to determine a mathematical model i.e. an equation of motion. Then friction induced vibration and roughness induced vibration are examined by collecting data varying the values of parameters: friction coefficient, normal force, quadriceps tendon elongation, angular velocity of a knee motion, cartilage surface roughness amplitude and roughness wavelength. The results, which are analysed in Matlab® simulation, show that the factor related to knee degradation that affects the vibration of the patella the most is the surface roughness of the knee's cartilage not the surface friction.

Keywords: Patellofemoral joint, Knee joint, Vibration, Patella.

1. Introduction

Ageing society becomes the topic of a lot of discussions and concerns in many countries including Thailand. People live longer due to better and highly advanced healthcare. However, when they get older, their joints including the knee joints deteriorate to the extent that it can cause joint pain or even inability to move at all. The knee joint degradation occurs due to not only ageing but also from everyday activities including walking, running, jumping, doing exercises, bearing too much body weight etc. Thus, knee joints should be well taken care of and gotten regular checkups. The examination of the knee joints currently used in hospitals and other healthcare facilities include the physical examination by an orthopedics, x-ray film reading, MRI (magnetic resonance imaging) reading by doctors etc. In addition, a new research topic in vibroarthographic signal (VAG) recorded on the patella while the patient is moving his/her knee is proposed to tell the grade of degradation of the knee joint [1-2]. Hence, understanding the vibration behavior of human knee joint would be of a great benefit to analyze the data collected from the patient's knee. The study herein is conducted to look into the horizontal and vertical vibrations of patella in the knee joint to determine its primary contributing factors: friction, normal force, muscle elongation, angular velocity of a knee motion, surface roughness amplitude or its wavelength. In addition, the study also investigate which degraded knee factors: friction, surface roughness amplitude or its wavelength contributes most to vibration of the knee. The study begins with friction induced vibration and roughness induced vibration [3-5] that are applied to create a dynamic model of a patella. Matlab® is then used to simulate the vibration signals of the patella when the parameters: friction coefficient between the cartilage of femur and patella, normal force on the patella, quadriceps tendon elongation when the knee joint moves, angular velocity of a knee motion, femur's cartilage surface roughness amplitude and its wavelength, are varied within normal human ranges.

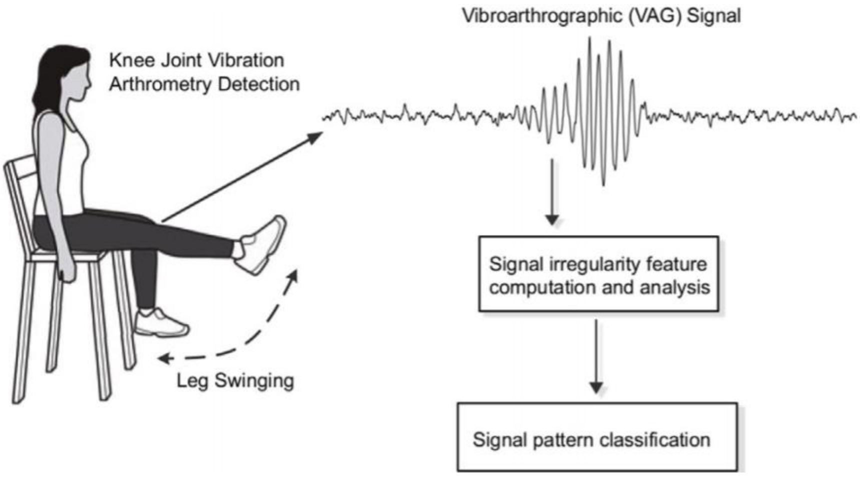

Figure 1. Vibroarthographic signal (VAG) recorded on the patella while moving his/her knee [2].

2. Motion of the Patello-Femoral Joint of Knee

Patella or kneecap is a sesamoid bone helping the muscles the quadriceps, which is a tendon connecting between a femur (thigh bone) to a tibia and the patellar ligament, bend the knee joints: extension as well as contraction. The forces in patello-femoral joint (PFJ) are from muscles especially quadriceps tendon and patellar ligament. The magnitudes and directions of these forces depend on the knee joint angle, distance between the body weight force and the joint's rotation point as well as others [6]. Shown in Figure 2, PRF (Patello-femoral reaction force) is the resultant force from the quadriceps force (QTF) and patellar tendon force (PTF). TRF is the force from patella on trochlear groove on the femur. ICR is the instantaneous center of rotation of the joint. PRF increases as the knee bends. PRF also depends on the activities: walking, running, jumping etc. It could be as much as 20 times of the body weight [6]. The motion of the PFJ when the knee is bent from no extension to full extension is shown in Figure 3. As the femur moves (tibia is fixed), it can be seen as if the patella moves on Trochlear groove on the femur.

Observing the knee joint motion in Figures 2 and 3, the dynamic model of the patella on the femur is set up to examine the motion of the patella subjected to the patella and the femur cartilage's surface roughness and friction. The motion of the patella is created from the flexion of the knee joint. It is assumed that when the knee is flexed the tibia is fixed vertically only the patella and the femur is in motion. The femur pulls the quadriceps and thus the patella moves on the femur's groove.

The dynamic model is shown in Figure 4 a), where the patella ligaments, the tendon, and the quadriceps muscles are assumed to act like a rubber band having both stiffness and damping like springs and dampers. The patella bone itself is considered a rigid body. The cartilage of the femur is quite soft, we can also modeled it with some elasticity and damping in radial direction. The friction of the cartilage surfaces is in the tangent direction. With some roughness of the surface, we can consider it as a base excitation with the given input functions. Figure 4 b) illustrates the free body diagram of the patella with four forces exerting on the patella: patellar ligament force F_p, quadriceps force F_q, cartilage friction force F_f and cartilage normal force F_3. The physical model can be simplified more for further motion analysis by eliminating the rotation of the patella and consider the motions in the horizontal x and vertical y directions as shown in Figure 5.

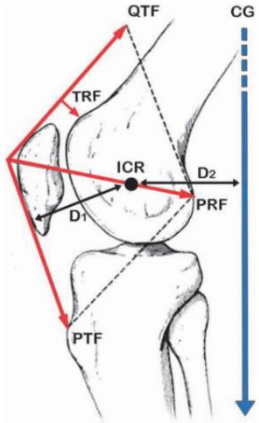

Figure 2. Forces on patella-femoral joint in sagittal plane [6].

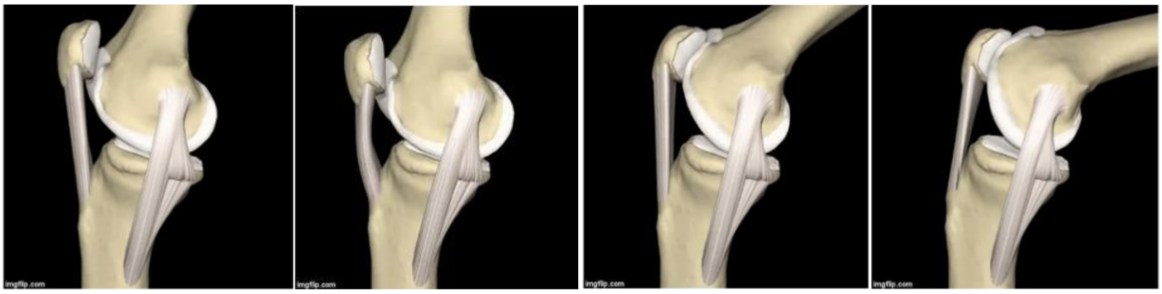

Figure 3. Motion of Patella on Trochlear groove at knee extension starting from no extension to full extension [7].

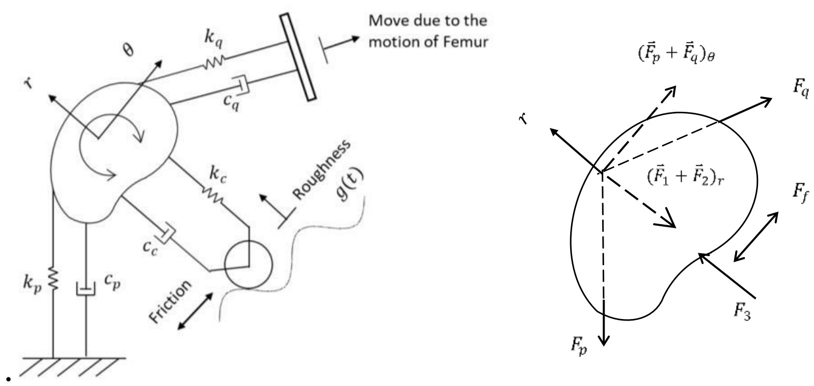

a) b)

Figure 4. a) Dynamic model and b) free body diagram of Patella in knee joint.

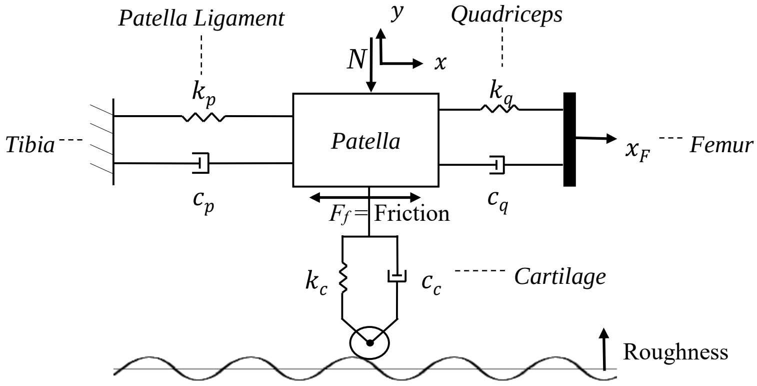

a)

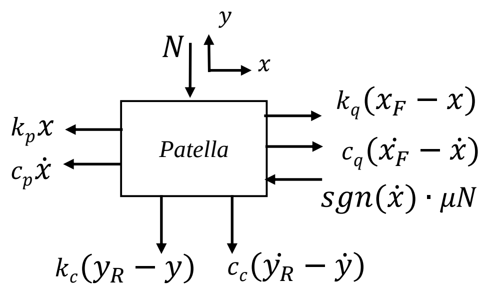

b)

Figure 5. a) Simple dynamic model and b) free body diagram of patella in knee joint.

Consider the dynamic model shown in Figure 5 a) and b). Applying the 2nd law of motion, the motion of the patella in the horizontal i.e. *x*-direction can be written as

$$\Sigma F_x = m a_x \tag{1}$$

The forces include the stiffness and damping forces from the patella ligament and the quadriceps and friction force between patella and femur:

$$-k_p x - c_p \dot{x} - f + k_q(x_F - x) + c_q(\dot{x}_F - \dot{x}) = m\ddot{x} \tag{2}$$

$$m\ddot{x} + (c_p + c_q)\dot{x} + (k_p + k_q)x = F_f + c_q \dot{x}_F + k_q x_F, \tag{3}$$

where m is the mass of patella,
c_p is the damping coefficient of patellar ligament,
c_q is the damping coefficient of quadriceps,
k_p is the stiffness of patellar ligament,
k_q is the stiffness of quadriceps,
x_F is the elongation of quadriceps,
F_f is the friction force between the patella and the femur cartilage surface,

Without loss of generality, we can first assume that the elongation of quadriceps input is harmonic as

$$x_F = X_F \sin(\omega_F t) \tag{4}$$

where X_F is the maximum elongation of quadriceps,
ω_F is the angular velocity of knee joint.

Let F_f be the kinetic coulomb friction force between patella and femur, i.e.

$$F_f = -\, sgn(\dot{x}) \cdot \mu N \quad (5)$$

where the signum function is

$$sgn(\dot{x}) = \begin{cases} 1 & \text{when} \quad \dot{x} > 0 \\ -1 & \text{when} \quad \dot{x} < 0 \end{cases} \quad (6)$$

where μ is the kinetic friction coefficient of cartilage,
N is the normal (compression) force on the patella.

Thus, the equation of motion in the *x*-direction is

$$m\ddot{x} + (c_p + c_q)\dot{x} + (k_p + k_q)x = -\, sgn(\dot{x}) \cdot \mu N + c_q \omega_F X_F \cos(\omega_F t) + k_q X_F \sin(\omega_F t) \quad (7)$$

In addition, the motion of the patella in the vertical i.e. *y*-direction can be written as

$$\Sigma F_y = m a_y \quad (8)$$

$$m\ddot{y} + c_c\dot{y} + k_c y = c_c \dot{y}_R + k_c y_R + N \quad (9)$$

where c_c is the damping coefficient of the cartilage,
k_c is the stiffness of cartilage,
y_R is the surface roughness function of the cartilage,

Let the surface roughness be harmonic

$$y_R = Y_R \sin(\omega_R t) \quad (10)$$

$$\omega_R = \frac{2\pi v}{\lambda_R} \quad (11)$$

where Y_R is the surface roughness amplitude of the cartilage,
v is the velocity of the patella in the *x*-direction,
λ_R is the surface roughness wavelength of cartilage.

Hence, the equation of motion in the *y*-direction is

$$m\ddot{y} + c_c\dot{y} + k_c y = c_c \omega_R Y_R \cos(\omega_R t) + k_c Y_R \sin(\omega_R t) + N \quad (12)$$

$$m\ddot{y} + c_c\dot{y} + k_c y = c_c \frac{2\pi\dot{x}}{\lambda_R} Y_R \cos(\frac{2\pi\dot{x}}{\lambda_R} t) \frac{2\pi\ddot{x}}{\lambda_R} + k_c Y_R \sin(\frac{2\pi\dot{x}}{\lambda_R} t) + N \quad (13)$$

From, equation (13), it can be observed that the vertical motion *y* of the patella depends on many parameters as well as the horizontal motion *x*. With equations (7) and (13), we can study the motion of human's patella on a rough femur's cartilage and the vibration characteristics of the patella as some of the physical parameters vary.

2.1. Knee Joint Dynamic Parameters

In the study of vibration characteristics of the patella, some of the parameters in determining the motion of patella are fixed and some are varied. The mass of patella is chosen to be fixed at 7.178 grams based on [8]. In addition, it is assumed that the coefficients of damping of the quadriceps and the patella tendon are equivalent at 1 Ns/mm [9] and the stiffness of both is 1000 N/mm [10]. It is also assumed that the cartilage of patella and femur has the damping coefficient of 5 Ns/mm [9] with stiffness of 2900 N/mm [11]. The variable parameters for our study are the friction coefficient between the patella and femur surfaces (0.01-0.03) [12], the normal force on the patella (100-7500 N) [6], quadriceps elongation (10-70 mm) [13], rotational speed of knee joint (0.5-12 rad/s) [14], surface roughness of the cartilage (1- 2 µm) and surface roughness wavelength (30-50 µm) [15]. The values of the parameters for calculations are summarized in Table 1.

Table 1. Physical properties for calculations.

Physical Parameter	Symbol	Value	Unit	Ref.
Patella mass	m	0.007178	kg	[8]
Damping coefficient of patellar ligament	c_p	1^*	Ns/mm	[9]
Damping coefficient of quadriceps tendon	c_q	1^*	Ns/mm	-
Damping coefficient on cartilage contact	c_c	5^*	Ns/mm	[9]
Stiffness of patellar ligament	k_p	1000^*	N/mm	-
Stiffness of quadriceps tendon	k_q	1000^*	N/mm	[10]
Stiffness on cartilage contact	k_c	2900^*	N/mm	[11]
Friction coefficient at patellofemoral contact	μ	0.01-0.03	-	[12]
Normal force on patella	N	100-7500	N	[6]
Quadriceps tendon elongation	X_F	10-70	mm	[13]
Angular velocity of the knee	ω_F	0.5-12	rad/s	[14]
Roughness amplitude of cartilage	Y_R	1-2	µm	[15]
Roughness wavelength of cartilage	λ_R	30-50	µm	[16]

* Approximate value

3. Matlab® simulation results and discussion

The motion of the patella is in both horizontal and vertical directions depends on many parameters as earlier mentioned and shown in Table 1. Note that the motion in the x and y directions are related as the motion in the y direction depends on the velocity of the patella in the x-direction seen in equations (7) and (13). Matlab® codes are written with ODE solvers to determine the motion when one or two parameters vary while the others are fixed. The calculated motion in the time domain results in vibration of the patella around the baseline motion (bending knee joint motion) in both the horizontal and the vertical directions. From the free body diagram, Figure 5 a), the motion in the horizontal direction should depend on the friction, the quadriceps, and the patella ligament forces. These forces are dependent on the friction coefficient at patellofemoral joint, the normal force on the patella, the quadriceps elongation and the angular velocity of knee joint. The results of how these parameters have effect on the horizontal motion of the patella are shown in the Section 3.1. Furthermore, from the same free body diagram, Figure 5 a), the vertical motion of the patella should be dependent on the exciting force from cartilage roughness, which are determined from the roughness amplitude and its wavelength. The study of this case is explained in Section 3.2.

3.1. Motions in the horizontal direction

3.1.1. Friction coefficient at patellofemoral joint

As the knee joint degrades, the friction coefficient at patellofemoral joint increases making the joint more stiff and harder to move. The friction coefficient is ranging from 0.1 to 0.3 while the normal force is kept constant at 350 N and the knee angular velocity is fixed at 1.75 rad/s (at a regular walking speed). It can be seen that the increase in friction reduces the motion amplitude in the horizontal direction quite linearly as depicted in Figure 6 a). Its slope, however, is quite small, hence it is expected that in a real experiment on human knee the increase in vibration cannot be detected much since there are other more significant factors, which will be shown in the upcoming sections.

3.1.2. Normal force on patella

In the simulations with the normal force is changing from 0 to 7500 N depicting the compressing force exerted on the patella by the connecting tendons and ligaments. It can be observed in Figure 6 b) that the horizontal displacement amplitude is decreasing linearly, however with somewhat low slope with not much variations. This result agree with the previous graph of friction coefficient Figure 6 a) as in Equation (5) the friction force depends on the friction coefficient and the normal force, i.e. more friction force means less displacement.

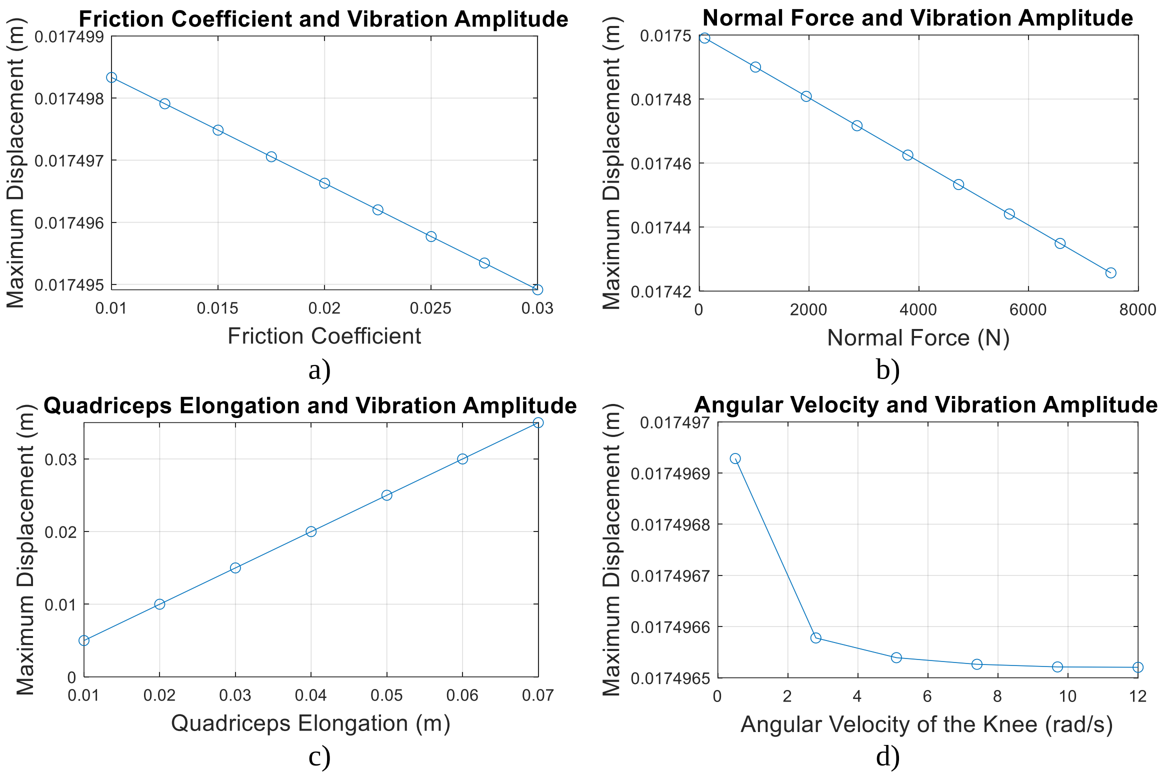

Figure 6. a) Friction coefficient b) normal force c) quadriceps elongation d) angular velocity inputs versus the amplitude of vibration in the *x*-direction of patella.

3.1.3. Quadriceps elongation

Based on [13], the quadriceps elongation due to knee bending while walking is chosen to vary from 10 to 70 mm while other parameters such as the normal force, the friction coefficient, the knee angular velocity are fixed. The elongation versus vibration amplitude plot illustrated in Figure 6 c) shows their strong and linear relationship. As we compare quadriceps elongation to other parameters in our study, the amplitude of motion of the patella depends on this parameter the most. That is more knee extension means more motion of the patella regardless of change in friction, normal force etc. Moreover, in body strength perspective, it points out that for a stronger quadriceps tendon, the elongation would be less resulting in a decrease in vibration of the patella.

3.1.4. Angular velocity of knee joint

Swinging the leg faster makes the knee joint rotate faster and the walking speed increases. However, from the results shown in Figure 6 d), the horizontal vibration displacement amplitudes of patella in all cases are not large. The change in the amplitudes is not much though it reduces a little as the angular velocity of the knee increases. Thus, in most cases of study done on the real human knee sample, the angular velocity of the knee joint is usually kept varying in a fixed range for examining effects of other parameters on vibration.

3.2. Motions in the vertical direction

3.2.1. Roughness amplitude and wavelength of cartilage

The simulations indicate that both the roughness amplitude and wavelength of the cartilage surface do have a significant effect on the vertical displacement of the patella as depicted in Figure 7 a) and b), respectively. When the surface roughness doubles in value, the maximum displacement almost doubles as well.

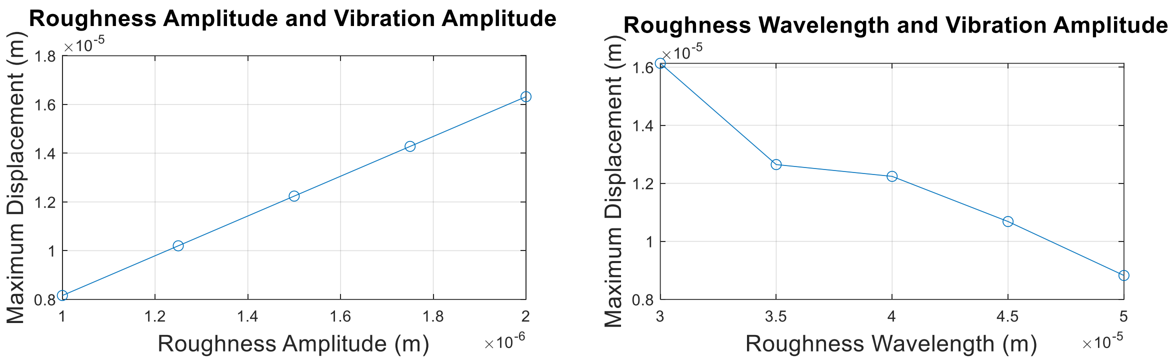

a) b)

Figure 7. a) Quadriceps elongation and roughness amplitude and b) quadriceps elongation and roughness wavelength vs the amplitude of vibration in the *y*-direction of patella.

3.3. Discussions on Motions in x and y directions

In summary, it can be observed from the results in Figure 6 that the quadriceps elongation has an effect on the horizontal motion of the patella than the other factors. Even more, it gives the higher amplitude of horizontal motion than the maximum vertical motion caused by other factors.

The vertical motion strongly depends on the femur's cartilage roughness and its wavelength. Since both of them are related to how much the knee degrades, the *y*-direction motion of the patella is much important in the real human knee test because it can reflect how much the knee joint damage actually is. In the examination, the vertical motion of the patella but not the horizontal motion should be the main focus if we want to determine how damage the knee joint is as it is directly related to the surface roughness and wavelength of the femur cartilage.

4. Conclusion

When a knee starts degrading due to any of various causes such as overuse, infection, accident etc., some vibrations are generated in knee joints, which can be detected by sensors attached on the patella as signals to indicate how much injured it is. Vibration theory is applied to build a mathematical model for assisting in fundamental medical diagnosis of knee joint problem. A simple dynamic model of patella is set up to examine the dependence of horizontal and vertical motion on the human knee's physical parameters of the cartilage, quadriceps tendon, and patellar ligaments. The Matlab simulations are performed to show how much varying friction coefficient of cartilage surface, normal force on the patella, quadriceps tendon elongation, knee joint angular velocity, cartilage's surface roughness and its wavelength affect the displacement amplitude of motion of the patella. The results show that the elongation of the quadriceps tendon is the most influence the horizontal motion of the patella. However, the knee degrading factors: the femur cartilage surface roughness and wavelength are important as the increase in surface roughness makes the vertical motion of the patella increase as much and the increase in wavelength reduces that motion directly as well. This study would share some fundamental knowledge for the further research on human knee joint degradation both simulations and experiments on factors and directions of motion to be observed that they should focus on.

5. References

[1] Wu, Y. (2015). *Knee joint vibroarthrograhic signal processing*. Springer.

[2] Wu, Y., Chen, P., Luo X., Huang, H., Liao, L., Yao, Y., Wu, M., & Rangayyan, RM. (2016). Quantification of knee vibroarthrographic signal irregularity associated with patellofemoral joint cartilage pathology based on entropy and envelope amplitude measures. *Computer Methods and Programs in Biomedicine*, 130, 1-12.

[3] Hinrichs, N., Oestreich, M, & Popp, K. (1998). On the modelling of friction oscillators. *Journal of Sound and Vibration*, 216**,** 435-459.

[4] Slavic, J., Bryant, M., & Boltezar, M. (2007). A new approach to roughness-induced vibrations on a slider. *Journal of Sound and Vibration*, 306, 732-750.

[5] Feldman, J. (2012). Roughness-induced vibration caused by a tangential oscillating mass on a plate, *Journal of Vibration and Acoustics*, 134**,** 21-29.

[6] Schindler, O. S., & Scott, W. N. (2011). Basic kinematics and biomechanics of the patello-femoral joint Part 1: The native patella. *Acta Orthopaedica Belgica*, 77, 421-431.

[7] *https://b-reddy.org/why-is-it-so-hard-to-straighten-your-knee-after-acl-surgery/* (access date August 30th, 2023)

[8] Al-Imam., A., & Al-Imam, M. L. (2016). Human patella morphometry and volumetry, an osteology-based study in the Japanese ethnicity. *European Journal of Pharmaceutical and Medical* Research, 3(10), 388-396.

[9] Prahlad, G. M., & Muller, J. H. (2014). *Computational modeling of objects presented in images: fundamentals, methods, and applications*, Springer, 188-203.

[10] O'Brien, T. D., Reeves, N. D., Baltzopoulos, V., Jonesa, D. A., & Maganaris, C. N. (2010). Mechanical properties of the patellar tendon in adults and children, 43, 1190-1195.

[11] Adamsa, M. A., Kerin, A. J., Bhatia, L. S., Chakrabartyb, G., & Dolan, P. (1999). Experimental determination of stress distributions in articular cartilage before and after sustained loading. *Clinical Biomechanics*, 14, 88-96.

[12] Woiczinski, M., Steinbrück, A., Weber, P., Müller, P. E., Jansson, V., & Schröder, C. (2016). Development and validation of a weight-bearing finite element model for total knee replacement. *Computer Methods in Biomechanics and Biomedical Engineering*, 19(10), 1033-45.

[13] Lindahl, O., & Movin, A. (1967). The Mechanics of Extension of the Knee-Joint. *Acta Orthopaedica Scandinavica*, 38, 226-234.

[14] Houston, M. E., Norman, R. W., & Froese, E. A., (1988). Mechanical measures during maximal velocity knee extension exercise and their relation to fibre composition of the human vastus lateralis muscle. *European Journal of Applied Physiology*, 58, 1-7.

[15] Ermakov, S., Beletskii, A., Eismont, O., & Nikolaev, V. (2015). *Liquid crystals in biotribology: Synovial joint treatment*. Springer.

[16] Murphy, E., Bresnihan, B., & FitzGerald, O. (2001). Validated measurement of periarticular bone mineral density at the knee joint by dual energy x ray absorptiometry. *Annals of the Rheumatic Diseases*, 60, 8–13.

[17] Lowrance, E. W., & Latimer, H. B., (1964). Measurements of Human Bones from Asia. *Transactions of the Kansas Academy of* Science, 67, 25-35.

BME0009

A Study of the Design Parameters of Supporting Rods for Posterior Leaf Spring Ankle Foot Orthosis (PLS-AFO)

P Sirilaophaisal[1] and A Wisessint[2,*]

[1]Graduate School, Department of Mechanical Engineering, Faculty of Engineering, Kasetsart University, 50 Ngam Wong Wan Road, Lad Yao, Chatuchak, Bangkok, 10900, Thailand
[2]Department of Mechanical Engineering, Faculty of Engineering, Kasetsart University, 50 Ngam Wong Wan Road, Lad Yao, Chatuchak, Bangkok, 10900, Thailand

* Corresponding Author: fengapw@ku.ac.th

Abstract. Posterior leaf spring ankle foot orthosis (PLS-AFO) is one of the choices for foot drop patients to improve their abnormal gait behavior. A certain part of the PLS-AFO plays a major role in supporting the forefoot so that it does not drop when patients walk. The diversity of human body types and gait characteristics would result in the different force values that apply pressure on the PLS-AFO device. Researchers have developed many types of supporting rods to apply with PLS-AFO, however, it can be difficult for medical specialists to determine the specifications of the device to be used for each patient. This work studies the material choices of PLS-AFO supporting rods to find suitable specifications for each type of foot drop patient. Three types of thermoplastic cylinders were selected for the static load testing. The results from nine pieces of the specimen were acquired, and a specification chart for material choices of the supporting rod was created.

Keywords: Ankle Foot Orthosis, Static Load Test, Fatigue Load Test, Posterior Leaf Spring AFO, Foot Drop Symptom.

1. Introduction

Ankle foot orthosis (AFO) is one of many options to treat foot drop patients [1]. Patients with foot drop symptoms cannot lift their forefoot up during the gait due to the damaged nerve or muscles that impair dorsiflexion ability [2]. The purpose of wearing AFO is to help maintain the ankle in a natural position. There are many types of AFO devices on the market [3] that could hold up the toe of the patient however most of them are expensive and difficult to adjust or repair by the patients themselves. May Su Khaing developed an adjustable posterior leaf spring (PLS) ankle foot orthosis which is affordable for low-income patients who cannot afford the conventional AFO [4]. In the mid and terminal stances, PLS-AFO offers a small amount of dorsiflexion. The elasticity of the spring-like mechanism would assist the push-off function during the gait cycle. There are choices of materials that researchers have used to fabricate PLS-AFO such as polypropylene, polyethylene, and nylon. Due to the fact that those materials are cheap, lightweight, and have high elasticity [5]. This research will study the material of the rod used in May Su Khaing’s design to determine the suitability of the rod material for the PLS-AFO.

2. Material

Following May Su Khaing's design of PLS-AFO which had been fabricated by an additive manufacturing process to be assembled with ready-made cylinder thermoplastics that are easy to acquire and cost less than conventional customized AFO. Thermoplastic is lightweight, durable, and physically suitable [6]. The three materials in this work all have spring-like properties that can absorb and desorb energy back to support the ankle after the push-off phase which is an essential characteristic of PLS-AFO as well as its supporting rod part since foot drop patients lack the force to perform dorsiflexion[7,8]. This research selected three thermoplastic materials, polypropylene, high-density polyethylene, and nylon. Each cylinder acts as a spring rod which is 10-millimeter diameter. These specific pieces of material can normally be found in any typical hardware store.

3. Experiment

This thermoplastic material comparison uses Instron 8801 series to do a static load test by the three-point bending technique. The experiment setting follows the flexural properties of the plastic standard test method, ASTM D790-03[9]. The span-to-depth ratio of the standard is 16:1, since the solid cylinders have a diameter, d = 10 mm, and therefore support span of this 3-point bending test, L = 160 mm. The calculation of the crosshead motion rate setting on the machine is followed as Equation (1):

$$R = ZL^2/6d \tag{1}$$

where:
R = rate of crosshead motion (mm/min)
L = support span (mm)
d = depth of beam (mm)
Z = rate of straining of the outer fiber (mm/mm/min)

Equation (1) has given a result of crosshead motion rate R = 4.2667 mm/min. This experiment used three different pieces for each type of material. The test begins when the test machine applies the load on the specimen simultaneously reaching the mid-span displacement of 40 mm. and then gradually unloads the force from the specimen until the loading nose is back at the starting point. The 40-millimeter mid-span displacement gives approximately a bending angle as the human ankle rotating angle of about 26 degrees[10,11]. All nine specimens were tested individually. Both loading force and displacement data can be obtained through the test machine

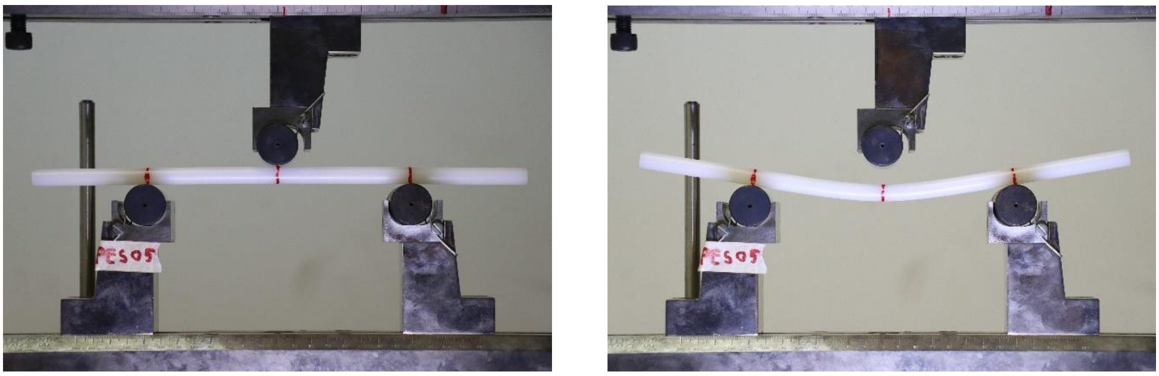

A) B)

Figure 1. Three-point bending static load-unload test setting, A) before testing, B) after testing.

4. Result

The three-point bending static load-unload test results are shown as follows:

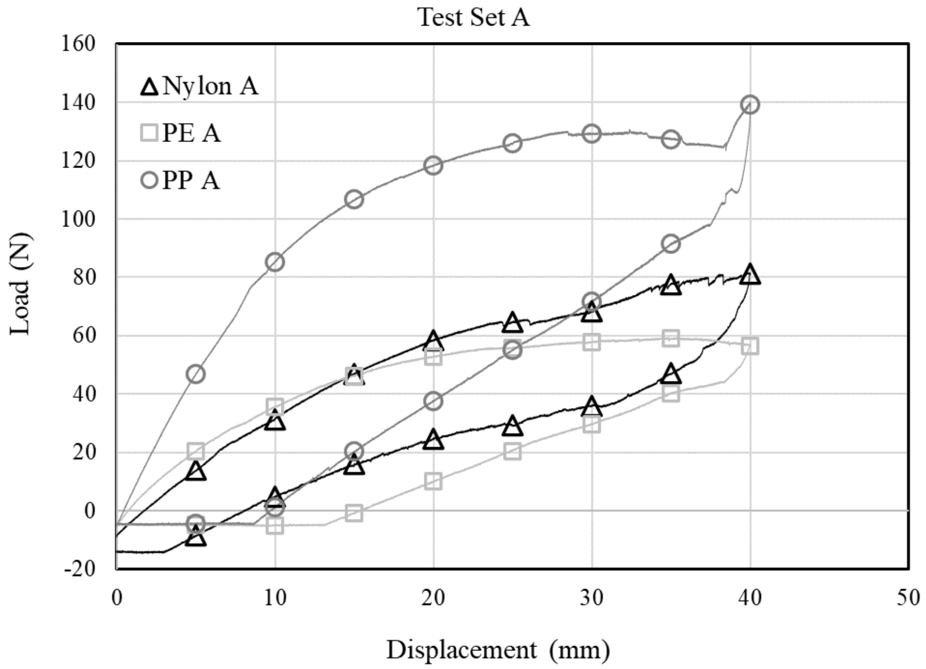

Figure 2. The three-point bending static load-unload test set A graph.

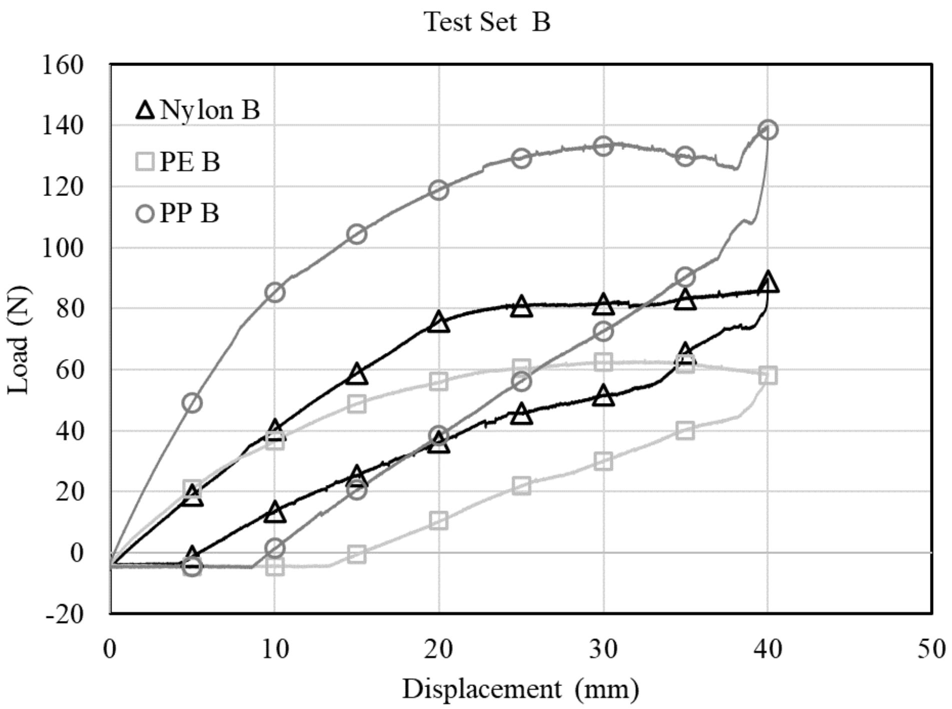

Figure 3. The three-point bending static load-unload test set B graph.

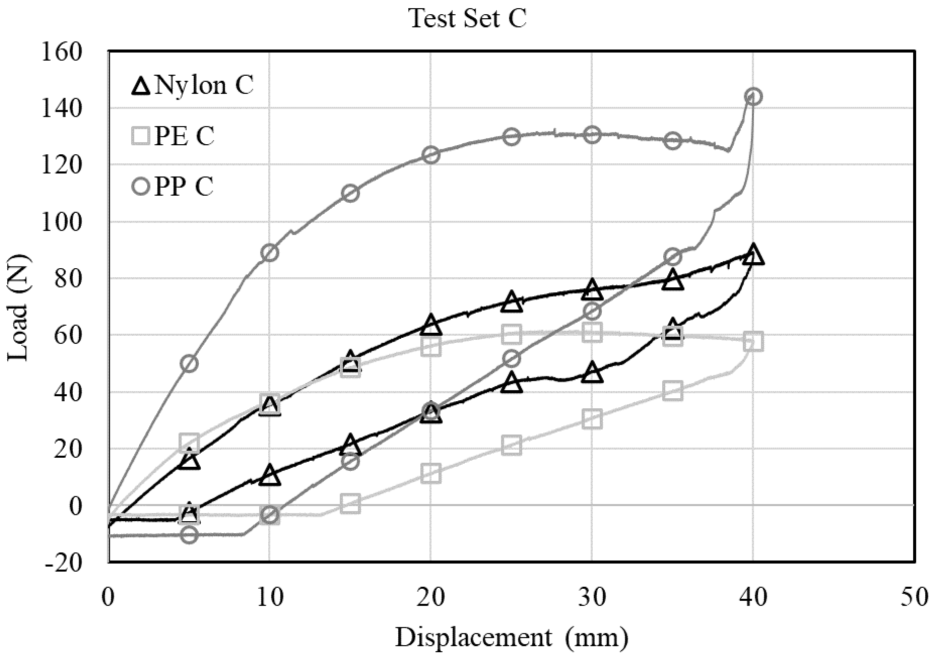

Figure 4. The three-point bending static load-unload test set C graph.

The result of plotting graphs from the three tests above has portrayed the unique characteristics of each thermoplastic. Each type of thermoplastic was tested individually in three different pieces of specimen to validate the accuracy of the experiment. The resulting trends of the same material type are analogous. The key data of static three-point bending test for material consideration was extracted from the plotting graphs are shown in the table below.

Table 1. Key data of static three-point bending test.

Material	Specimen	Slope (Elastic Region)	Maximum force (N)	δ (mm)
Nylon	A	2.81	81.71	3.0
	B	3.77	89.86	4.2
	C	3.32	89.28	4.1
PE	A	4.08	59.70	13.1
	B	4.19	63.18	13.3
	C	4.40	61.62	13.2
PP	A	9.41	140.15	8.7
	B	9.81	139.87	8.6
	C	9.98	145.28	8.4

When δ is the remaining deformation after the unloading process is completed.

According to Figure 1, the remaining deformation of the specimen after the unloading process(δ) refers to the distance between the mid-span contacting point before testing and after testing and had been monitored by the test machine. According to Table 1, the static three-point bending test has proven that polypropylene requires more force than nylon and polyethylene to bend. though it did not deform the least. On the contrary, polyethylene deforms the most, since it has the lowest maximum loading force. Nylon has the lowest remaining deformation and slope value in the elastic region which can be assumed that patients can use less muscle force with nylon on PLS-AFO. Although all three thermoplastics may deform permanently when undergoing cyclic loading force, all subjects can reform back closely to their original form. All tested specimens also reformed back to their original shape after being removed from the test machine for several minutes It can be assumed that these materials can be used repeatedly.

The static loading-unloading test has given the load force which loading nose press on the specimen and the midspan deflected distance. The two important data can provide the strain energy of the plastic rod as Equation (2):

$$U = \int_0^x P\,dx \tag{2}$$

The strain energy can be obtained by finding the area underneath the load and displacement graph [12,13]. The significance of the strain energy refers to the dissipated energy that permanently deforms the structure of the material. The method is to separate loading data from unloading data on the loading-unloading graph and find both strain energies separately, then subtract unloaded strain energy from loaded strain energy, the dissipated can be obtained as Equation (3)

$$\textit{Dissipated Energy} = \textit{Loaded strain energy} - \textit{Unloaded strain energy} \tag{3}$$

In iterated testing procedures such as this research, the average data value can be used as representative data for the subject to represent its value.

Table 2. Strain energy from the three-point bending test.

Material	Specimen	Dissipated energy (mJ)	Averaged (mJ)
Nylon	A	1,053.05	999.04
	B	1,033.20	
	C	910.87	
Polyethylene	A	1,164.68	1,214.18
	B	1,253.30	
	C	1,224.57	
Polypropylene	A	2,370.84	2,462.04
	B	2,418.34	
	C	2,596.95	

In Table 2, the result of finding the strain energy from the hysteresis graph has shown that nylon has the lowest energy dissipation throughout the entire cylinder. Polyethylene has slightly higher dissipated energy than nylon. However, polypropylene has the highest dissipated energy in this study.

The ability of the material to spring back when receiving input energy can be determined by the energy-returning ratio between the loading and unloading force as Equation (4)

$$Energy\ return\ ratio = \frac{Unloaded\ strain\ energy}{Loaded\ strain\ energy} \times 100\% \tag{4}$$

Table 3. Energy return ratio.

Material	Specimen	Energy return ratio	Average value
Nylon	A	43.86%	52.54%
	B	56.37%	
	]C	57.39%	
PE	A	31.15%	31.22%
	B	30.28%	
	C	32.22%	
PP	A	40.31%	38.51%
	B	40.03%	
	C	35.19%	

The calculated energy return ratio between loading and unloading process is shown in Table 3. According to this table, nylon evidently has the highest energy return ratio reflecting the spring-back capability to help patients lift their feet during the gait cycle after they exert ankle push-off.

Table 4. Material specification chart.

Material	Maximum loading force (N)	Dissipated energy (mJ)	Energy return ratio
Nylon	87	999	52.54%
PE	62	1214	31.22%
PP	142	2462	38.51%

Table 4 is the specification chart of the tested materials. Three parameters shown in Table 4 can help decide the appropriate material for the PLS-AFO supporting rod. They reflect the required force to bend the rod, the energy absorption ability, and the returning force to support the patient's gait cycle. Nylon requires less force to bend and springs back with greater force than the others. However, if the elasticity of nylon is insufficient, polypropylene can be considered.

5. Discussion

This research just provides some mechanical perspective assuming the basic situation of foot drop symptoms. Limitation details such as patient’s weight, activity level, and footwear type, are not included in this work. Medical professionals would use the information provided in this research to determine the patient’s criteria for the suitable application.

6. Conclusion

This study has successfully obtained a set of information that illustrates how three thermoplastic choices of materials in the shape of 10-millimeter cylinders are used to fabricate PLS-AFO. According to the information shown from the experiment, polypropylene requires the most amount of energy to bend, which means it is suitable for the patient who has stronger muscles. On the contrary, nylon requires less energy to deform so the patient would not need to put too much effort in order to do the plantarflexion and it also loses less shape. Polyethylene did not perform well and was not dominant in any factor, so it can be deduced that polyethylene is considered the least recommended choice. However, it is the medical professionals to determine which materials are suitable for each patient. This study is only one of the guidelines for material aspects.

7. References

[1] Kerr, E., Moyes, K., Arnold, G., & Drew, T. (2011, July). Permanent Deformation of Posterior Leaf-Spring Ankle-Foot Orthoses: A Comparison of Different Materials. JPO Journal of Prosthetics and Orthotics, 23(3), 144–148. https://doi.org/10.1097/jpo.0b013e3182272941

[2] Nori, S. L. (2022, June 25). Foot Drop. StatPearls - NCBI Bookshelf. https://www.ncbi.nlm.nih.gov/books/NBK554393/

[3] Choo, Y. J., & Chang, M. C. (2021, August 13). Commonly Used Types and Recent Development of Ankle-Foot Orthosis: A Narrative Review. Healthcare, 9(8), 1046. https://doi.org/10.3390/healthcare9081046

[4] Khaing, M. S., Samala, M., Guerra, G., & Wisessint, A. (2023, August 23). Design and mechanical testing of an adjustable posterior leaf spring ankle-foot orthosis for patients with drop foot. Prosthetics & Orthotics International. https://doi.org/10.1097/pxr.0000000000000278

[5] Bedard, G. G., Motylinski, J., Call, B., Gao, F., & Gray, L. (2016, January). Bench Test Validation of a Dynamic Posterior Leaf Spring Ankle-Foot Orthosis. JPO Journal of Prosthetics and Orthotics, 28(1), 30–37. https://doi.org/10.1097/jpo.0000000000000081

[6] Gao, F., Carlton, W., & Kapp, S. (2011, June). Effects of joint alignment and type on mechanical properties of thermoplastic articulated ankle-foot orthosis. Prosthetics & Orthotics International, 35(2), 181–189. https://doi.org/10.1177/0309364611409617

[7] Bregman, D., Harlaar, J., Meskers, C., & de Groot, V. (2012, January). Spring-like Ankle Foot Orthoses reduce the energy cost of walking by taking over ankle work. Gait & Posture, 35(1), 148–153. https://doi.org/10.1016/j.gaitpost.2011.08.026

[8] Kerkum, Y., Philippart, W., & Houdijk, H. (2021, August). The effects of footplate stiffness on push-off power when walking with posterior leaf spring ankle-foot orthoses. Clinical Biomechanics, 88, 105422. https://doi.org/10.1016/j.clinbiomech.2021.105422

[9] Standard Test Methods for Flexural Properties of Unreinforced and Reinforced Plastics and Electrical Insulating Materials. (n.d.). https://www.astm.org/d0790-17.html

[10] Levangie, P. K., & Norkin, C. C. (2011, March 9). Joint Structure and Function. F.A. Davis.

[11] Winter DA, Eng JJ, Isshac MG: A review of kinetic parameters in human walking. In Craik RL, Otis CA (eds): Gait Analysis: Theory and Application. St. Louis, MO, Mosby–Year Book, 1994.

[12] Yu, T., & Xue, P. (2022). Utilizing plastic deformation for energy absorption. Introduction to Engineering Plasticity, 293–326. https://doi.org/10.1016/b978-0-323-98981-7.00011-7

[13] Nurul Fazita, M., Abdul Khalil, H., Nor Amira Izzati, A., & Rizal, S. (2019). Effects of strain rate on failure mechanisms and energy absorption in polymer composites. Failure Analysis in Biocomposites, Fibre-Reinforced Composites and Hybrid Composites, 51–78. https://doi.org/10.1016/b978-0-08-102293-1.00003-6

ETM0003

Energy consumption of climate control system for bamboo moth mating

Thanakrit Maneerat[1], Yuttana Mona[2,*], Chatchawan Chaichana[2], and Nitthinan Borirak[3]

[1]Master's Degree Program in Energy Engineering, Faculty of Engineering, Chiang Mai University, Chiang Mai, 50200, Thailand
[2]Department of Mechanical Engineering, Chiang Mai University, Chiang Mai, 50200, Thailand
[3]Energy Technology for Environment Research Center, Chiang Mai University, Chiang Mai, 50200, Thailand

* Corresponding Author: yuttana.mona@cmu.ac.th

Abstract. This research aimed to evaluate the energy consumption of a climate control system designed for bamboo moth mating in Thailand. The system components, including: an air conditioner, heater, water spray, circulator fan, dehumidifier, thermally insulated breeding and spawning room, moth cage, and a microcontroller (WeMos D1 ESP8266 Wi-Fi). The study, conducted at Chiang Mai University, Thailand, involves monitoring the climate control system's operation for 20 days per testing batch. Within each group, moths were placed in cages, with each group consisting of one female and two male moths for mating. Three such groups were accommodated within one cage. The system maintained a temperature error of less than 0.50 °C and a relative humidity error of less than 5.00% RH. Data collection occurred daily at 10:00 a.m., including energy consumption data for calculating the cost of climate control in the moth breeding and spawning room for each batch. The research revealed that the system consumed approximately 28.12 kWh during a batch of female moths laying eggs, resulting in operating costs totalling 1320.96 Baht per batch for controlling temperature and humidity.

Keywords: Climate control systems, Bamboo moths, Microclimate, Energy consumption.

1. Introduction

The surging global demand for protein, propelled by the expanding world population, necessitates exploration of alternative protein sources to replace conventional animal-based proteins like pork, cattle, duck, chicken, fish, eggs, and milk [1]. This heightened need for animal-derived proteins is underlined by projections from the United Nations (UN), indicating an anticipated population surpassing 8 billion by mid-November 2022, with estimates pointing to approximately 8.5 billion by 2030 and a projected 9.7 billion by 2050, marked by an annual growth of 60 million individuals. Notably, guidelines from the U.S. Department of Agriculture and the U.S. Department of Health and Human Services in 2020 emphasizes that an optimal diet should consist of 10-35% of daily calories sourced from protein, implying an annual global protein intake increase of 1.12 billion kilograms. Consequently, considering the population of 8 billion people in 2022, accounting for demographic trends, the world would require roughly 150 billion kilograms of protein to meet dietary needs. This mounting demand for protein coincides with the challenge of depleting global resources, underscoring the urgency of exploring and adopting alternative protein sources to ensure sustainable nutrition amid rapid population growth [2].

At present, animal-derived proteins primarily exhibit three drawbacks. To begin, the environmental impact of livestock farming is notably detrimental, with one out of every four greenhouse gas emissions in the world's food production and agriculture sector attributed to this practice [11]. The second concern relates to the substantial land usage required by livestock in comparison to the resulting production output. Notably, broilers yield the most significant production per unit of body weight and land area, followed by chicken and milk cows [3]. Lastly, the consumption of meat elevates the risk of microbial infections and contributes to heightened concerns about mutation and the transmission of diseases originating from both livestock and animal products [5].

Currently, alternative sources of protein are required. These include plant-based options, cultured meat, and insect protein [15]. Insects have emerged as a noteworthy protein source [10], offering an environmentally friendly food source for both humans and animals that is cost-effective, sustainable, and relatively rich in protein and fats. This protein source also contains essential vitamins, dietary fiber, and minerals, including options like Coleoptera, crickets, grasshoppers (Orthoptera), moth caterpillars (Lepidoptera), and bamboo caterpillars (Omphisa fuscidentalis), providing consumers with a diverse array of choices.

The entire life cycle of a bamboo caterpillar, starting from an adult moth laying eggs, spans approximately one year. Consequently, an adult moth can only deposit eggs once annually, typically in July. During the period from August to May, the eggs undergo an approximately ten-month transformation into larvae [6,9]. The life cycle of a bamboo caterpillar initiates with female moths depositing their eggs onto the sheath of a bamboo shoot. Subsequently, the female moths spawn and die, the developing become caterpillar within the bamboo sheath for around 13-14 days. Following the hatching of the initial stage larvae, they burrow into the bamboo shoots for further growth. The transition from first instar larvae to the final stage of larvae takes nearly a month. By September, the head capsule width reaches 2.50 mm, and the larvae to be final stage for 270 days or nine months. In May, the head width increases to approximately 3.00 mm [6]. At this point, the bamboo caterpillar enters the pupal stage within a bamboo tube, undergoing a 45-day transformation to become a moth during the rainy season, and revert to the initial cycle [4]. Consequently, there has been development regarding research into insect hormones and physiology [4]. That discovered that the insect hormone juvenile hormone could expedite the maturation of final instar larvae, this reducing the bamboo larvae's life cycle from 1 year to approximately 6 months [16].

However, the use of insect hormones may result in moth maturation and egg laying during the rainy season (July) changing to summer (May). Moths born out of season are significantly affected by the summer conditions, which hinder their breeding and egg-laying. Moreover, bamboo moths can only lay eggs once a year due to the extended lifespan of bamboo larvae, which can live up to a year. Consequently, this knowledge spurred research into insect hormones and physiology, initiated [4]. That discovered that the juvenile hormone could expedite the maturation of 5th instar larvae, reducing the bamboo larvae's life cycle from 1 year to approximately 6 months [16].

For this reason, moths are exposed to unseasonal temperatures and humidity during their natural breeding season. Therefore, a humidity and temperature control system must be created for the moths to breed, lay eggs, and develop larvae. Even though it's out of season.

A need arises to establish optimal climatic conditions conducive to bamboo larvae farming, enabling the production of bamboo larvae consistently throughout the entire year, even beyond their typical breeding season. One approach involves creating a controlled microclimate, which refers to maintaining a stable climate within a specific area regardless of seasonal variations. This entails precise regulation of external climate chamber factors such as temperature, humidity, wind, and lighting, allowing for direct influence on the environmental conditions experienced by the organisms within that area. To facilitate year-round cultivation of bamboo larvae, a temperature-controlled chamber was designed for the purposes of breeding moths, facilitating egg-laying, and fostering the development of bamboo larvae, irrespective of the traditional breeding season.

Through the observation of moth behavior, it became evident that two primary factors, namely food and environmental conditions, significantly influence reproduction and spawning. This research specifically concentrated on the control of climate and energy usage to establish the optimal environmental conditions required for moths to breed and lay eggs. Table 1 provides the anticipated temperature and relative humidity levels essential for successful mating and spawning, as derived from references [6-8].

Table 1. Controlling climate conditions in the breed and spawn rooms.

Controlling climate conditions	Temperature (˚C)	Relative Humidity (%RH)
From 6:00 a.m. – 2:00 p.m.		73 – 80
From 2:00 p.m. – 6:00 p.m.	26 – 28	60 ± 5
From 6:00 p.m. – 6:00 a.m.		< 80

This research aimed to evaluate the energy consumption of a climate control system based on the previously mentioned data. Energy consumption data was systematically collected over the experimental period, and calculations were performed using the analyzed peak load, base load, and power factor information to determine the overall energy consumption.

2. Principles and Theory

2.1 Energy consumption measurement

Data collection and measurement of energy consumption inside the breeding and spawning room. energy consumption data compiles the overall amount of energy used by every appliance in the breeding and spawning room. Where this can be determined mathematically as in equation 1.

$$E(t) = E_1(t) + E_2(t) + \ldots + E_n(t) \tag{1}$$

where E is the Individual appliance electricity consumption contributing to the total measurement and n is the total number of active appliances within the time period t.

2.2 Peak load and base load defined

Peak load, also referred to as peak demand or peak load contribution, denotes a specific period during which there is a sustained and heightened requirement for electrical power due to increased demand. Conversely, base load, alternatively known as the minimum electrical demand, pertains to the lowest level of electrical demand needed throughout a 24-hour timeframe. This base load reflects the baseline requirement for electrical power during this extended period [13].

2.3 Load Factor (LF)

The Load Factor (LF) is defined as the ratio of the average load on the system in a certain period to the maximum load on the system during that period [14]. Where this can be determined mathematically as in equation 2.

$$LF = \frac{electricity\ energy\ consumption\ in\ a\ period}{peak\ load \times time\ period} \tag{2}$$

3. Method

3.1 Design the breed and spawn room

To climate control within the breed and spawn room, the design was conceived as a prototype featuring a steel structure with dimensions of approximately 1.50 m in width, 2.25 m in length, and 1.80 m in height, resulting in a total volume of 6.00 m^3. The walls are constructed from 6 mm thick transparent polycarbonate sheets, complemented by insulation lining, as shown in Figure 1 (A). Additionally, a window measuring 0.30 m in width and 0.60 m in length is incorporated, allowing natural light to penetrate the room. The interior space is versatile, accommodating two moth cages designated for breeding and spawning, as shown in Figure 1 (C).

The moth cage, which features a base area measuring 0.50 m by 0.50 m and a height of 0.50 m, ample room is provided for moths to fly and engage in breeding behaviors, while also offering support for the height of bamboo shoots. A rectangular cabinet with dimensions of 0.60 meters in width, 1.80 meters in length, and 0.60 meters in height is used to contain a moth cage. To effectively monitor conditions within the moth's cage, position the temperature and humidity sensor and data logger at its center, ensuring it is situated 1 cm. below the top of the cage, as shown in Figure 1 (B).

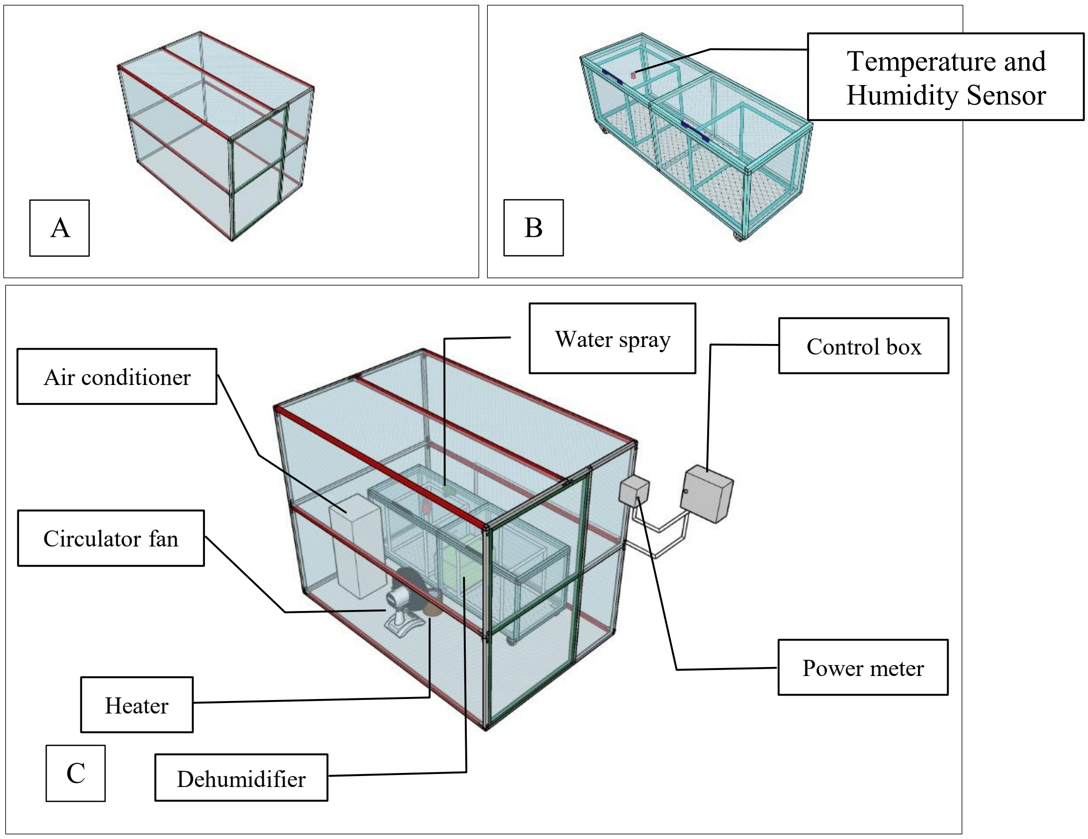

Figure 1. The breed and spawn room (A), Moth cage (B), Moth cage in the breed and spawn room (C).

Transparent polycarbonate sheets were employed as the inner wall to construct a chamber that closely simulates a natural environment suitable for moth breeding and egg laying. During daytime hours (from 8:00 a.m. to 6:00 p.m.), the inner wall is reinforced to support the polyethylene foam insulation and maintain its structural integrity as the external wall.

Because polycarbonate provides little protection from outside heat entering the room, it is essential to install polyethylene foam insulation as an external wall. This ensures that the desired temperature and relative humidity levels, falling within the range of 26-28°C and 70-90% RH, respectively, are effectively maintained.

Notably, polyethylene foam possesses a thermal conductivity range of 0.030-0.034 W/mK, rendering it an efficient insulation material for this specific purpose.

The heat load data considered six different heat sources, which include: 1) Heat load from all the walls, 2) Heat generated by moths, 3) Heat generated by bamboo shoots, 4) Heat produced by the circulating fan motor, 5) Heat emitted by the lights, and 6) Heat generated by the occupants in the room (further details are outlined in Table 1). The calculations revealed a daily heat load of 48,767.77 kJ/day, equivalent to 13.55 kWh/day. The total heat load is 3,851.91 BTU/hr. Consequently, an air conditioner was selected based on this calculated value. Based on the provided heat load data, it is necessary to determine the appropriate air conditioner capacity. There are air conditioning units available on the market that closely match the required cooling capacity, and a selection of air conditioners with a 6,000 BTU/hr. capacity has been made.

3.2 Measurement devices

Within the breeding and spawning room, sensors and data loggers have been installed to monitor air conditions, including parameters like temperature, humidity, and energy consumption. Additionally, the room is equipped with CCTV cameras that have the capability to record the behavior of moths within the chamber continuously, 24-hours a day.

Energy consumption data was gathered using the PZEM-004T V3 device and stored in the database. This data was collected at intervals of every 10 minutes, and it pertains to all the appliances located within the breeding and spawning room. These appliances typically operate in two states, either ON or OFF, and include items such as the fan (75 W), heater (300 W), and spray water system. It's worth noting that the air conditioner represents an exception to this pattern. The electricity consumption data from these appliances can be utilized to analyze various parameters, including peak load, base load, and load factor, by examining the load curve and daily data patterns.

The SHT20 sensor is encapsulated within a reflow solderable Dual Flat No leads (DFN) package, measuring 3 x 3 mm in footprint and 1.1mm in height. This sensor delivers calibrated and linearized sensor data in a digital format via the I2C communication protocol. In the context of the research, the SHT20 sensor played a crucial role in regulating temperature and humidity levels within the breeding and spawning room, serving as a feedback control mechanism to maintain the desired environmental conditions.

Temperature and humidity data were collected using the Elitech brand GSP-6 / Elitech Temperature and Humidity Data Logger. This data logger has the capability to record up to 16,000 data points for temperature and 16,000 data points for humidity. The temperature measurement range spans from -40°C to 85°C, while the humidity measurement range covers 10% to 99% RH (Relative Humidity). The data logger is configured to continuously record temperature and humidity within the room, operating 24 hours a day, and capturing data at 10-minute intervals.

3.3 Climate control system unit

The breeding and spawning room’s climate control unit is centered around a microcontroller, a compact control device with capabilities resembling those of a computer system. This microcontroller integrates CPU, memory, and ports and operates by interpreting commands written in the C language, facilitating control of Input and Output functions in accordance with user requirements. In the context of this project, a NodeMCU ESP8266 V3 board was carefully selected to acquire temperature and humidity data from the breeding room, serving as crucial feedback. Subsequently, the microcontroller utilizes this data to direct the temperature and humidity control devices, ensuring they adjust their settings according to pre-defined parameters. The schematic diagram of the climate control system for the breeding and spawning room is shown in Figure 2.

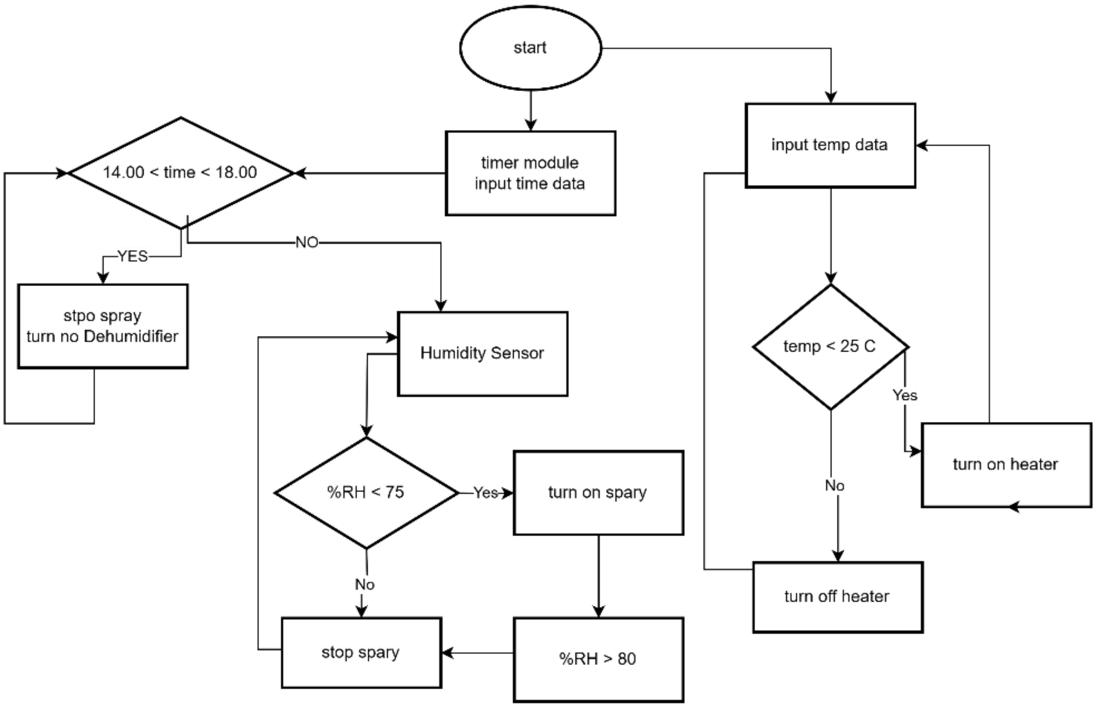

Figure 2. Schematic diagram of the climate control system for the breed and spawn room.

4. Results

4.1 Temperature and humidity in the breeding and spawning room of moths

According to the conditions outlined in the hypothesis, The temperature and relative humidity can be controlled in a range according to hypotheses based on the time of day, which increases the chance of moths breeding and depositing eggs. The error between setting relative humidity and actual relative humidity is less than 5.00%RH. As shown in Fig. 3, the period of time of a day is displayed on the horizontal axis. The relative humidity value is displayed on the vertical axis. The temperature can be maintained within the range of 26 to 28°C, as shown in Figure 4. That shows the climate control system can be carried out as the hypotheses.

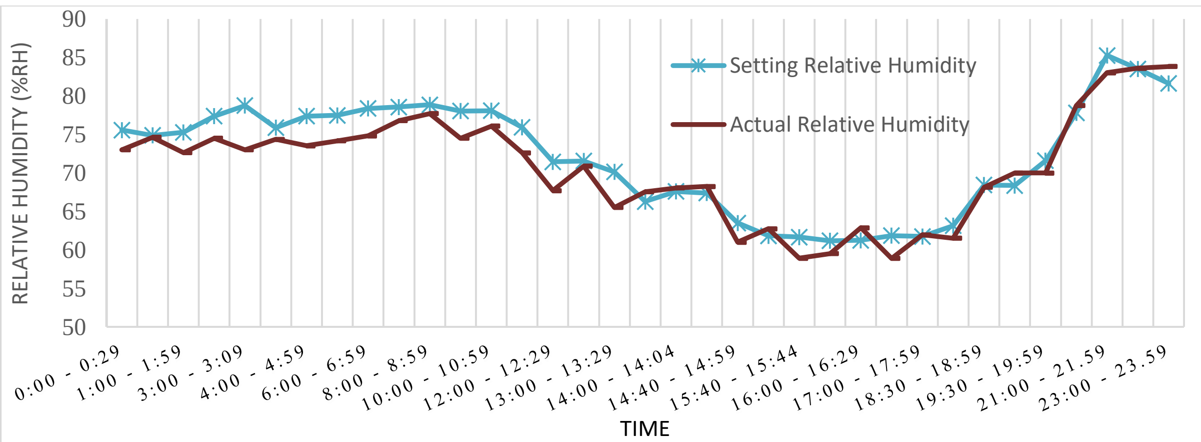

Figure 3. Setting Relative Humidity (Blue line) and Actual Relative Humidity (Brown line) compare inside moths' breeding and spawning room.

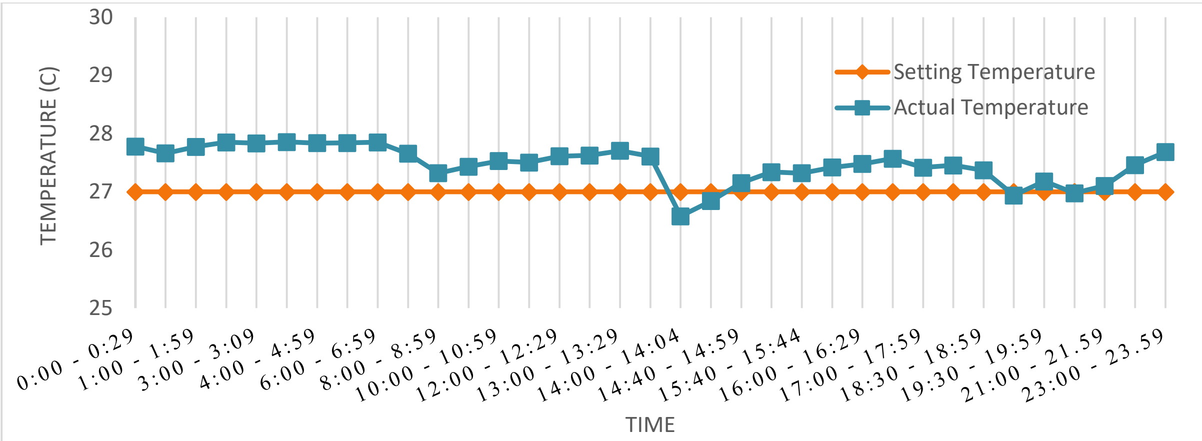

Figure 4. Setting Temperature (Orange line) and Actual Temperature (Blue line) compare inside moths' breeding and spawning room.

4.2 peak load, base load, and load factor

In Figure 5, The daily load curve provides insights into both peak load and base load analysis. Additionally, it allows for a rough estimation of load distribution from the total electricity consumption of the measured appliances over a specific time period. The horizontal axis represents time over the course of one day, with day and night details indicated at the top of the figure. The vertical axis displays the load demand in units of watts (W).

From the load curve, it is evident that peak loads occur when all appliances are active, resulting in a load demand ranging from 1,800 to 1,900 W. In contrast, the base load is consistently at 75 W, attributed to the continuous operation of the fan. This load curve illustrates the load states and variations throughout the day and night.

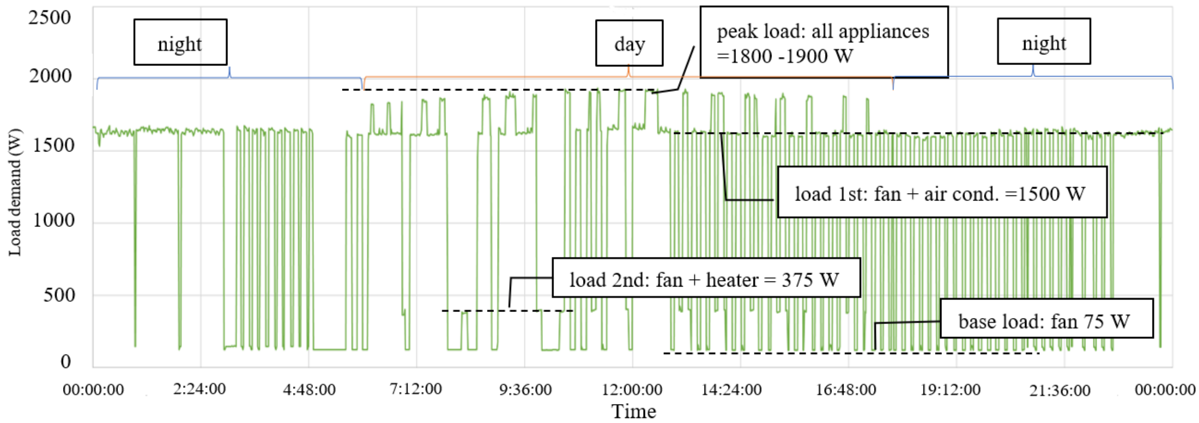

Figure 5. Load demand data in breeding and spawning room in 1 day (5 July 2022).

From equation (2), The Load Factor (LF) can be calculated as:

$$LF = 0.60$$

The climate control system has a load factor of 0.6 or 60%, which is higher than 50%. A high load factor signifies that the facility or system is operating efficiently because it consistently operates near its maximum capacity. This results in more efficient energy use.

Based on Figure 6, the ambient temperature and humidity of breeding and egg-laying areas as of July 5, 2022, when electricity consumption was recorded. It is assumed that in the 20-day experiment, or 1 batch of the experiment, the weather conditions will be the same as on July 5, 2022. Data on energy consumption and power usage during these periods were recorded.

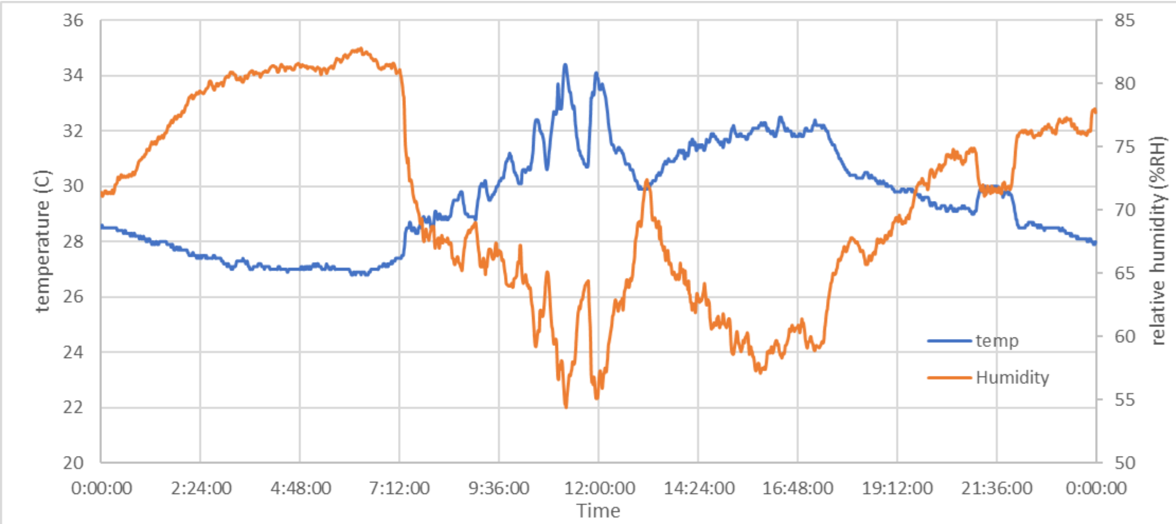

Figure 6. The ambient breeding and spawning room's temperature and relative humidity on July 5, 2022.

The total energy consumption is recorded at 28.12 units. To assess the cost of this energy consumption in terms of electricity tariffs [12], which were determined by the Provincial Electricity Authority in November 2018, can calculate the Energy cost per batch as follows:

$$\text{Energy cost per batch} = 20\ day \times 28.12\ \frac{kWh}{day} \times 2.3488\frac{Baht}{kWh} = 1{,}320.96 \text{ Baht.}$$

This represents the total cost associated with regulating temperature and humidity in the moth breeding and spawning room, amounting to 1,320.96 Baht per batch, which is dedicated to maintaining optimal conditions.

During one production batch lasting around 20 days, each cage can produce at least 500 off-season larvae. With two cages in the room, a total of at least 1000 off-season larvae can be produced in a single production cycle. The estimated energy usage per off-season larvae is approximately 0.56 kWh. Further research and development are necessary to achieve reduced energy consumption in out-of-season bamboo larvae production, With the goal of decreasing energy usage and increasing the production of bamboo larvae farming.

5. Conclusion

This research aimed to evaluate the energy utilization of climate control systems during the bamboo moth mating process, which spans approximately a year and includes stages from caterpillar to pupa, adult moth, and egg-laying. Female moths lay eggs only once annually, and the larval stage extends for 10 months. The moth cycle encompasses phases of pupation, adult moth emergence, mating, and egg-laying, which, on its own, isn't sufficient for commercial purposes. To address this limitation, a climate control system was developed to maintain a consistent environment by regulating factors such as air conditioning, heaters, and water spray, ensuring stability despite external seasonal variations influenced by variables like temperature, humidity, airflow, and light. Continuous temperature and humidity monitoring was carried out using the Elitech brand GSP-6 at 10-minute intervals. The energy consumption for one batch amounted to 28.12 kWh, resulting in operating costs of approximately

1,320.96 Baht per batch for temperature and humidity regulation in the breeding and spawning room. Furthermore, the energy consumption per off-season larvae was estimated at 0.56 kWh per larvae.

6. References

[1] Ismail, B. P., & others. (2020). Protein demand: review of plant and animal proteins used in alternative protein product development and production. Animal Frontiers, 10(4), 53–63. https://doi.org/10.1093/af/vfaa040

[2] Henchion, M., Hayes, M., Mullen, A. M., Fenelon, M., & Tiwari, B. (2017). Future Protein Supply and Demand: Strategies and Factors Influencing a Sustainable Equilibrium. Foods (Basel, Switzerland), 6(7), 53. https://doi.org/10.3390/foods6070053

[3] Flachowsky, G., Meyer, U., & Südekum, K.-H. (2017). Land Use for Edible Protein of Animal Origin—A Review. Animals, 7(12), 25. https://doi.org/10.3390/ani7030025

[4] Chiang Mai University, Faculty of Science. (2019). Researcher invents new technology from basic research to cultivate bamboo worms during off-season, creating community opportunities and commercial prospects. Retrieved from https://www.cmu.ac.th/th//3a49a2

[5] Sangwongdee, P. (2020). Global Crisis in the Outbreak of Emerging Infectious Diseases: The Role of the World Health Organization, a Situation in Thailand and a New Normal. Journal of Social Synergy, 11(1), 88–108. Retrieved from https://so04.tci-thaijo.org/index.php/thaijss/article/view/242124

[6] Singtripop, T., Wanichacheewa, S., Tsuzuki, S., & Sakurai, S. (1999). Larval Growth and Diapause in a Tropical Moth, Omphisa fuscidentalis Hampson. Zoological Science, 16(5), 725–733. doi:10.2108/zsj.16.725

[7] Li, L.-T., Wang, Y.-Q., Ma, J.-F., Liu, L., Hao, Y.-T., Dong, C., Gan, Y.-J., Dong, Z.-P., & Wang, Q.-Y. (2013). The effects of temperature on the development of the moth Athetis lepigone, and a prediction of field occurrence. Journal of Insect Science, 13(1).

[8] Thapa, R. (2008). Mass Rearing of Bamboo Borer; Omphisa fuscidentalis (Lepidoptera; Pyralidae) for Eggs and Larvae Production for Sustainable Management and Utilization of the Species. Archives of Mae Fah Luang University. Retrieved from http://archives.mfu.ac.th/database/items/show/1484

[9] Cunningham, R. (2000). Omphisa fuscidentalis. https://www.dnp.go.th/FOREMIC/NForemic/this_month/Omphisa/omphisa.htm

[10] Gahukar, R. T. (2016). Chapter 4 - Edible Insects Farming: Efficiency and Impact on Family Livelihood, Food Security, and Environment Compared With Livestock and Crops. In A. T. Dossey (Ed.), Insects as Sustainable Food Ingredients (pp. 85-111). Academic P

[11] Hannah Ritchie (2019) - "Food production is responsible for one-quarter of the world’s greenhouse gas emissions". Published online at OurWorldInData.org. Retrieved from: https://ourworldindata.org/food-ghg-emissions

[12] Thailand ETbpea. (2023). Electricity Reconsider. https://www.pea.co.th/Portals/0/demand_response/Electricity%20Reconsider.pdf?ver=2018-10-01-155123-370

[13] watchwire (2017). Peak Load & Base Electricity - Understand Differences. https://watchwire.ai/peak-load-base-load-electricity/

[14] Gotham, D., Muthuraman, K., Preckel, P., Rardin, R., & Ruangpattana, S. (2009). A load factor based mean–variance analysis for fuel diversification. Energy Economics, 31(2), 249–256. doi:10.1016/j.eneco.2008.10.004

[15] Hadi, J., & Brightwell, G. (2021). Safety of Alternative Proteins: Technological, Environmental and Regulatory Aspects of Cultured Meat, Plant-Based Meat, Insect Protein and Single-Cell Protein. Foods, 10(6), 1226. https://doi.org/10.3390/foods10061226

[16] Singtripop, T., Wanichacheewa, S., Sakurai, S. 2000. Juvenile hormone-mediated termination of larva diapause in the bamboo borer, Omphisa fuscidentalis. Insect Biochemistry and Molecular Biology, 30: 847-854.

ETM0005

A Study of microclimate designation in near equatorial climate condition: A case study in university building

Ekarin S.[1] and Chokchai C.[1,*]

[1]Faculy of Mechanical Engineering, Mahidol University, Salaya, Nakronpathom, 73170, Thailand

* Corresponding Author: chokchai.chu@mahidol.ac.th

Abstract. The objective of this study aims to analyse the factor of microclimate designation in order to reduce the energy consumption in the building. In this study, there are 3 different microclimate conditions (4x7 perennial tree, 2x5 perennial tree, 1m Shrub) had been set up in order to analyse the optimum condition to be used to gather with the experiment had been conducted in order to verify the simulation result. Whereas the studied building is located on laboratory building (1 level building), faculty of engineering, Mahidol University, Salaya, Nakornprathom. The verification of simulation result and the experiment had been analysed by using statistical method (Reliability, and independent T-Test). The results from simulation is shown that for 4x7 perennial tree is the best case in temperature reduction (when compare with the base line in 1st scenario with no tree) following by 1 m. shrub and 2x5 perennial tree consecutively.

Keywords: Microclimate, Energy Saving, Heat Transfer.

1. Introduction

The Microclimate is a local set of atmospheric conditions that differ from those in the surrounding areas, often slightly but sometimes substantially. Microclimatic conditions depend on such factors as temperature, humidity, wind and turbulence, dew, frost, heat balance, and evaporation [1]. The effect of soil type on microclimates is considerable. Sandy soils and other coarse, loose, and dry soils, for example, are subject to high maximum and low minimum surface temperatures [2]. The microclimates of a region are defined by the moisture, temperature, and winds of the atmosphere near the ground, the vegetation, soil, and the latitude, elevation, and season and many more related parameters. Near ground weather is also influenced by microclimatic conditions like wet ground impact to evaporation and atmospheric humidity increment. Bare soil dryness creates a surface crust that inhibits ground moisture from diffusing upward, which impact to the persistence of the dry of atmospheric. [3]

Cities are both the primary source of energy, carbon, pollution and waste problems facing the world as well as potential wellsprings of solutions in our anthropogenic age. The urban climate anomaly exemplifies this duality of unintended climate, comfort and energetic consequences of urbanization on the one hand, and the potential offered by its mitigation to act as a framework for the wider societal, environmental and well-being benefits on the other [4]. For the city in tropical climate which falls between the Tropic of Cancer and the Tropic of Capricorn. The Tropic of Cancer situated at the 23.5°N latitude forms the northern limit of the region, and the southern limit falls on the Tropic of Capricorn situated at 23.5°S latitude. However equatorial climate is stated to be the climatic type extending from 10–12°N and 10–12°S of the equator. So Equatorial Climate is a subtype of Tropical Climate [5]. For this near equatorial climate the temperatures is around over 18 °C throughout the year. There is not much temperature difference between the seasons. The equator falls into the Intertropical Convergence zone while the Subtropical Regions experience the Subtropical anticyclones. This is the convergence of the Northeast trade winds and the Southeast trades. Monsoon is a seasonal wind reversal experienced in many locations on Earth. Monsoons are best developed in southern and eastern Asia, especially over the Indian Ocean and the westernmost Pacific. Monsoons are directed from ocean to land. Winters are usually much drier. Inversion of trade winds is the most crucial factor influencing the thermal structure of the Tropical oceanic atmosphere [6]. However, one major factor for microclimate study is tree sizes and species [7]. In the previous study of tree types which impact to microclimate found that evapotranspiration of well-watered trees alone can decrease local 2 m air temperature at maximum by 3.1 – 5.8 °C during summer. While shading reduces surface temperatures, the interaction of a non-transpiring tree with radiation can increase 2 m air temperature by up to 1.6 – 2.1 °C in certain hours of the day at local scale [8]. This Study focus on the impact of tree sizes and species to the reduction of surrounding temperature and energy saving possibility when applying microclimate concept to energy consumption in Mahidol University Building, Salaya, Nakornprathom by using Rhinoceros software together with plugin like Glasshopper, Honey bee, Ladybug.

2. Data Analysis Technique

2.1. T-Test

A t test is a statistical test that is used to compare the means of two groups. It is often used in hypothesis testing to determine whether a process or treatment actually has an effect on the population of interest, or whether two groups are different from one another. The t test estimates the true difference between two group means using the ratio of the difference in group means over the pooled standard error of both groups as shown in equation 1.

$$\mathrm{t} = \frac{\chi_1 - \chi_2}{\sqrt{\left(s^2\left(\frac{1}{n_1} + \frac{1}{n_2}\right)\right)}} \tag{1}$$

where

t is the t value,

x_1 and x_2 are the means of the two groups being compared,

s^2 is the pooled standard error of the two groups,

n_1 and n_2 are the number of observations in each of the groups.

2.2. Pearson Correlation (R_{xy})

Pearson Correlation is a measure of linear correlation between two sets of data. It is the ratio between the covariance of two variables and the product of their standard deviations; thus, it is essentially a normalized measurement of the covariance, such that the result always has a value between −1 and 1. As with covariance itself, the measure can only reflect a linear correlation of variables, and ignores many other types of relationships or correlations.

The Pearson Correlation coefficient formula is shown in following

$$r_{xy} = \frac{N\sum XY - \sum X \sum Y}{\sqrt{\left(N\sum X^2 - \left(\sum X\right)^2\right)\cdot\left(N\sum Y^2 - \left(\sum Y\right)^2\right)}} \tag{2}$$

Correlation coefficient (R^2) is also applied to verify the correction of the calculation and experiment data [7].

Table 2. The Interpretation of the size (strength) of Correlation coefficient

Size of Correlation	Interpretation
0.90 to 1.00 or -0.90 to -1.00	Very high positive (negative) correlation
0.70 to 0.90 or -0.70 to -0.90	High positive (negative) correlation
0.50 to 0.70 or -0.50 to -0.70	Moderate positive (negative) correlation
0.30 to 0.50 or -0.30 to -0.50	Low positive (negative) correlation
0.00 to 0.30 or 0.00 to -0.30	Negligible correlation

2.3. Energy Saving calculation

The energy saving in the building from ambient temperature reduction can be determined from equation 3.

$$\Delta Q = \rho V C_p \Delta T \tag{3}$$

where

ΔQ = Change in Thermal Energy (kW)
ρ = Air Density (kg/m^3)
V = Room Air Volume (m^3)
Cp = Specific heat Capacity (kJ/kg.C)
ΔT = Temperature Difference in Celsius

3. Research Methodology

In order to achieve the objective of this study, the process of this research has been developed into 3 stages (Data preparation and verification, Data Simulation, Result Discussion) as shown in figure 1.

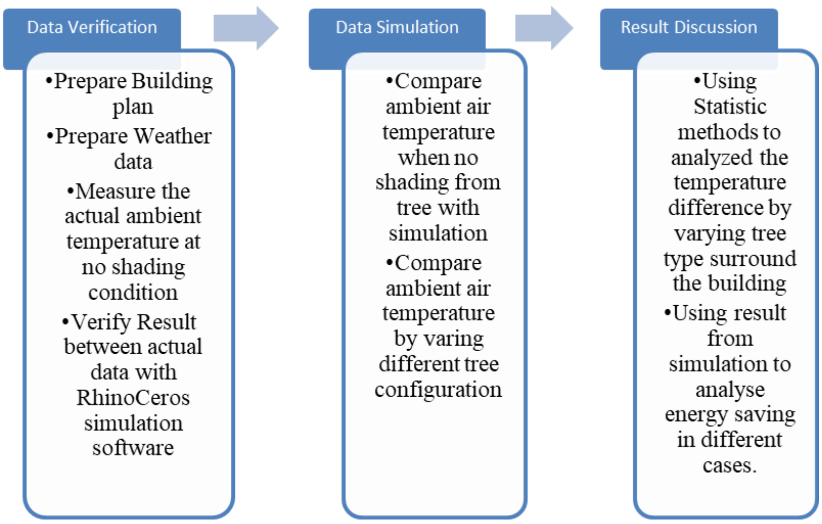

Figure 1. The Research Process.

4. Experimental Setup and Data Verification

4.1. Experimental Setup

In this research, the software Rhinoceros® version 7 (Trial version) had been used to simulate the ambient temperature in different condition. The software calibration had been done in order to verify the software. The experiment had been conducted in Mahidol University, Salaya by measuring the ambient air temperature for 1 week in same location without any shading from tree. The results from measurement had been recorded every 15 minutes during daytime (9.00-18.00) for 7 days. The measuring location is shown in figure 2. The data for each day had been averaged as represented temperature and brought to compare in simulation software. The building is Laboratory building which have 1 level. This building located at faculty of engineering, Mahidol University, Salaya, Nakornprathom (Lat.13.79597, Long.100.32456). The operating hour is office hour (8.00-17.00). The surrounding of building is covered by large tree and scrub as shown in figure 2.

Figure 2. Experimental Site for measuring ambient air temperature.

4.2. Data Simulation and Verification tools

In order to calibrate the software, the building model has been setup in Rhinoceros® version 7. All of building structure and shape has been setup in the software, which is similar to the real building together with the temperature and humidity measurement by using multi-meter at the building manually for 7 days.

In this research, the simulation model had been generated in order to verify the reliability of measured data. There are 3 major applications to be used, Rhinoceros® version 7, Grasshopper, Honey bee, and Ladybug plugin. Rhinoceros is used for design the building, tree and surrounding environment, Grasshopper as a plugin is used for setting up simulation script like selection of weather data, the parameter to be considered, building materials, etc. and Honey bee plugin is used for solar simulation, and Lady Bug plugin is used to visualize and analyse weather data in Grasshopper. After all of The simulation tools is completed. The data from simulation has been compared with actual data. The comparison result is shown in figure3.

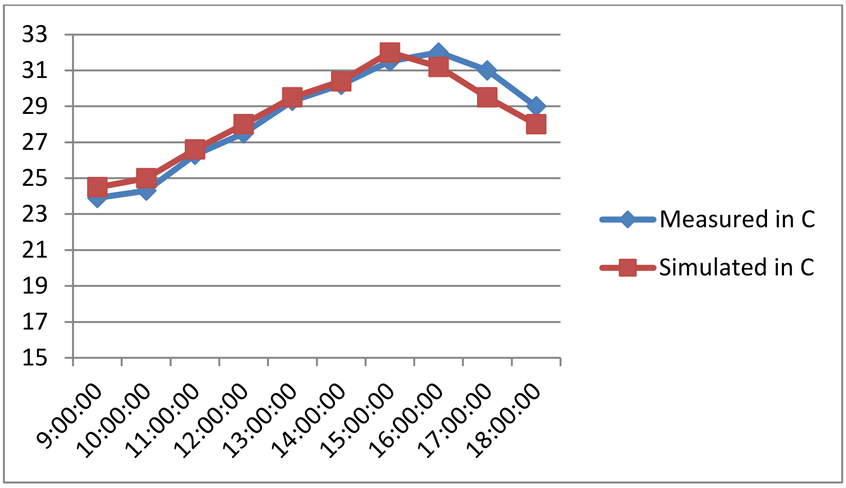

Figure 3. The Comparison between measured temperature and simulated temperature.

The comparison results is after the software is calibrated with the real measurement by adjusting the calculation function of software and recalculate for the selected day and then determine the correlation between measurement and simulation. However, The data comparison between measured and simulated temperature is further developed in order to determine the data correlation (R^2) to be 0.997 or 99.7%. The results imply that this simulation software can be used to predict temperature simulation in other difference cases.

5. Simulation setup

This research tools used Rhinoceros® together with grasshopper plugin to setup simulation model relation and honey bee plugin to simulate solar radiation and lady bugs plugin to visualize and analyse weather data in Grasshopper. The simulation script model is shown in figure 4.

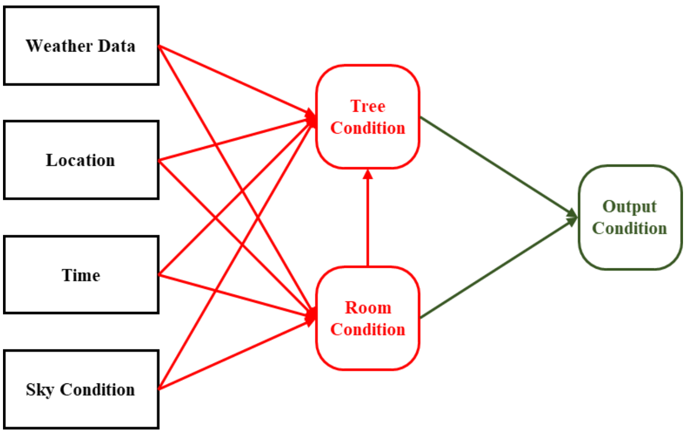

Figure 4. Grasshopper script model.

6. Research Framework

This research objective is to analyze the impact of tree sizes and species as a microclimate condition to energy saving in building. In order to reach the objective this research had setup the variation of tree sizes and species into 3 different conditions. (a perennial with size of 4x7 m, 2x5 m, and 1 m of shrub). The research framework can be shown in figure 5

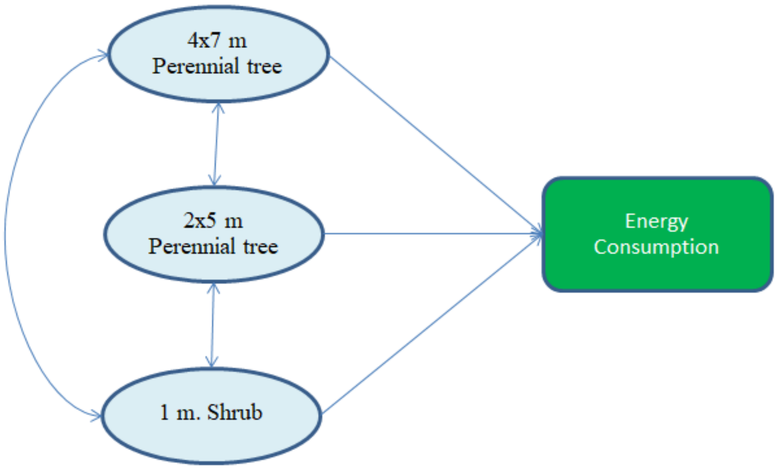

Figure 5. The Research Framework.

The environmental condition had been simulated in 4 conditions as shown in figure 6.

1. Non-tree surround
2. 4x7 m. of perennial tree (4 m. width and 7 m. height)
3. 2x5 m. of perennial tree (2 m. width and 5 m. height)
4. 1m. Shrub (1 m. height)

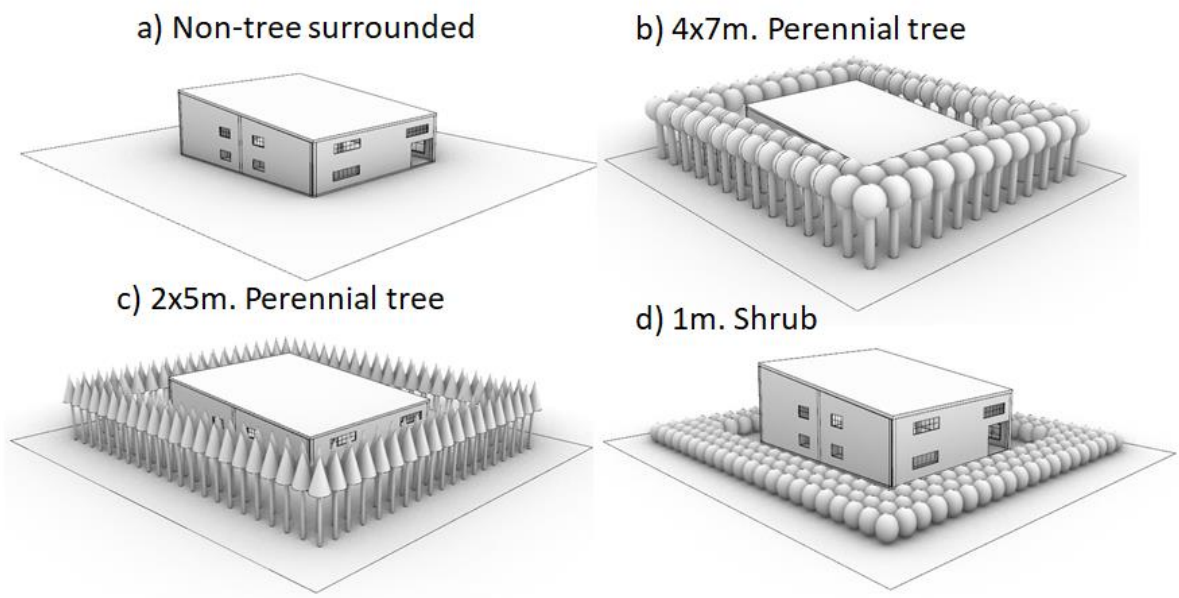

Figure 6. Simulation scenarios set up cases.

7. Results and Discussion

This research set up hypothesis interpretation into Null hypothesis (Ho) which definition to no difference between group and Alternate hypothesis (Ha) which definition difference between group.

The Energy saving in the room can be considered by changing of ambient temperature due to changing microclimate condition. This simulation used 1st scenario as the based case to be compared with other cases. The ambient air temperature had been set up as a result from simulation in order to use as a comparing parameter with each scenario. The results from simulation is shown in figure 8.

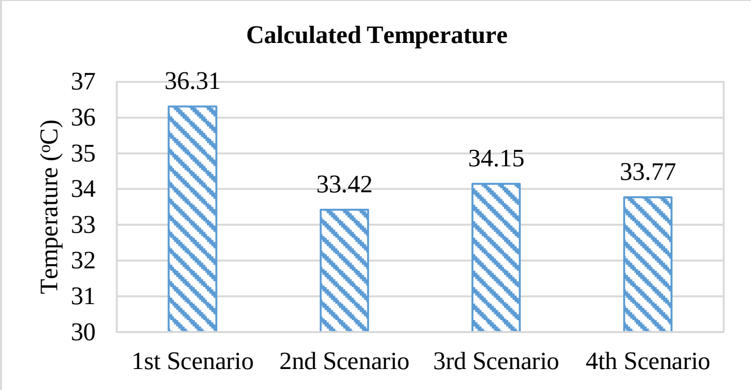

Figure 7. Ambient air temperatures from simulation.

The simulation results revealed that the lowest to highest temperature is 2nd scenario, 4th scenario, 3rd scenario and 1st scenario consecutively. The 1st scenario have no shading, all of heat from solar energy had been absorbed to the surrounding air. While other scenarios had shading from tree, the more shading the lower solar energy absorption. When energy has been absorbed at lower rate, it will impact to lowering of energy consumption rate. However, the simulation results revealed that 4th condition was better than 3rd condition because in this simulation the considered temperature position had been set up at the ground. 4th scenario was shrub which short trunk near ground when compared with 3rd condition which their leaves was farther than 4th scenario however their leave length was shorter than 2nd scenario.

Regarding to the result of temperature simulation, the energy saving equation from (3) is applied to calculate energy saving by temperature reduction comparing to each scenario. The comparison of energy reduction had been conducted by applying the 1st scenario as a base line then compared the base line with other scenarios. The comparison results are shown in figure 8. 2nd scenario compared with 1st scenario, 3rd scenario compared with 1st scenario and 4th scenario compared with 1st scenario consecutively.

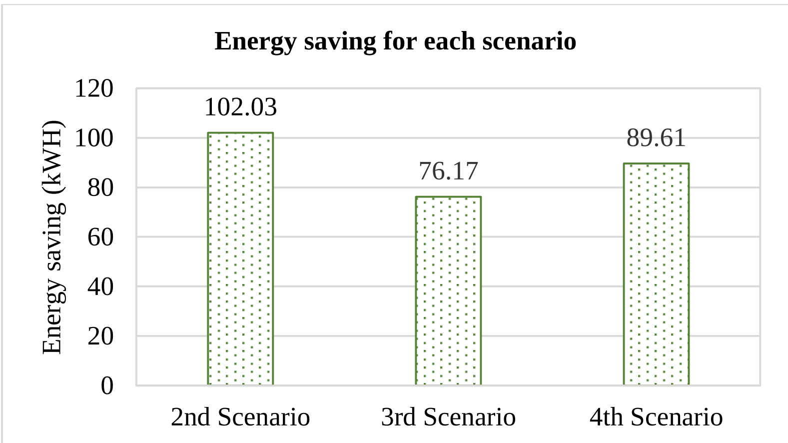

Figure 8. Energy Saving result from simulation.

The energy saving result revealed the most energy saving scenario is 2nd scenario, 4th scenario, and 3rd scenario consecutively. Regarding to electrical energy conversion from room thermal energy, the reduction of room temperature from ambient air temperature was impacted to lowering of electrical energy consumption from air condition as shown in figure 9.

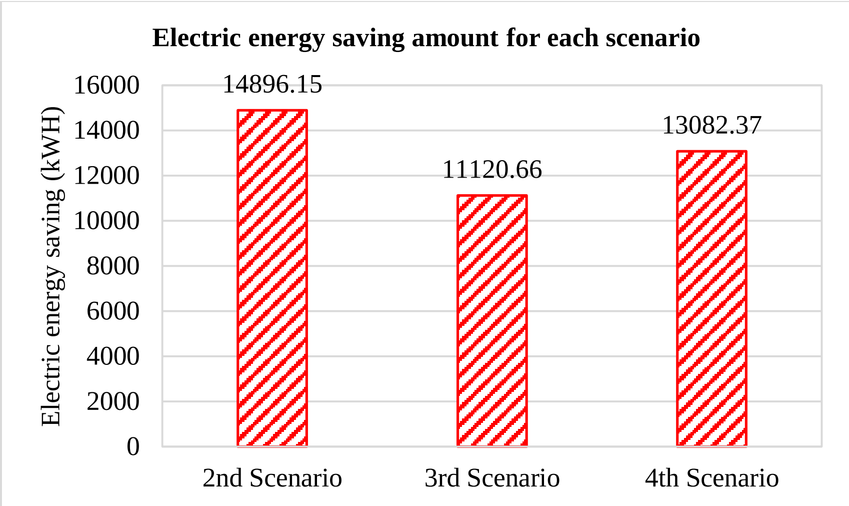

Figure 9. Electrical energy saving from reduction of ambient temperature.

The electrical energy consumption reduction results had been shown that the most electrical energy saving was 2nd scenario, 4th scenario and 3rd scenario consecutively.

8. Conclusion

Regarding to the result of microclimate simulation scenario comparison in different condition in this study, the results reveals that 4x7m perennial tree is in best condition in order to reduce the ambient temperature when compare with 2x5m perennial tree for 25% and 1m. shrub for 12%. The simulation results shown that shrub resulted in lower ground temperature than 2x5m perennial tree. When lowering ambient temperature, the energy consumption had been reduced automatically by reduction of sensible heat. However, this study considers only temperature reduction, which impacted to energy consumption only. This study is still not including the impact for convection heat transfer and radiation heat transfer from tree surround the building.

For the conclusion on this study, the microclimate parameter in this study was only temperature. For the furthermore research, other parameter like relative humidity, air flow, and other related parameter should be studied.

9. References

[1] T. Ahmed, D.Zhang (2020): a review. *Journal of Energy Report: A critical review of comparative global historical energy consumption and future demand: The story told so far, 10(6), 1973-1991.*

[2] Britannica (2023), Science&Tech 2023: https://www.britannica.com/science/microclimate

[3] World population review (2023), https://worldpopulationreview.com/country-rankings/energy-consumption-by-country

[4] Urban Microclimate Modelling for Comfort and energy studies (2020), Massimo Palme, Springer Link

[5] Samiran Das, M Kamruzzaman, Abu Resa Md.(2022), Assessment of characteristic changes of regional estimation of extreme rainfall under climate change: A case study in a tropical monsoon region with the climate projections from CMIP6 model, Journal of Hydrology, Elsevier

[6] Geiger, Rudolf (1954). "Klassifikation der Klimate nach W. Köppen" [Classification of climates after W. Köppen]. Landolt-Börnstein – Zahlenwerte und Funktionen aus Physik, Chemie, Astronomie, Geophysik und Technik, alte Serie. Berlin: Springer. Vol. 3. pp. 603–607.
[7] Wenjie Wang, Bo Zhang,Wei Zhou, Hailian Lv(2019),The effect of urbanization gradients and forest types on microclimatic regulation by trees, in association with climate, tree sizes and species compositions in Harbin city, northeastern China, Urban Ecosystem, Springer
[8] Naika Meili, Gabriele Manoli, Paolo Burlando, Jan Carmeliet, Winston T.L. Chow (2021), Tree effects on urban microclimate: Diurnal, seasonal, and climatic temperature differences explained separating radiation, evapotranspiration, and roughness effects: Elsevier, Vol.58.

ETM0006

Comparison study of building energy consumption in near equatorial climate condition: A Simulation case

Ekarin S.[1] and Chokchai C.[1,*]

[1]Faculy of Mechanical Engineering, Mahidol University, Salaya, Nakronpathom, 73170, Thailand

* Corresponding Author: ekarins2002@hotmail.com

Abstract. The objective this study aims to compare the energy consumption in the building located near the equatorial and analyse the factor that effected to energy consumption and to compare the difference of weather for the country near to equator. This research use energy plus simulation software as a tool to analyse energy consumption. The considered factor taken into accounted is continent, country which upper and lower latitude, distance from equator, distance from sea level, amount of forest in country. In order to verify the software reliability, energy audit had been conducted at faculty of information and communication technology building, Mahidol University, Salaya, Nakornprathom to verify from simulation result with the measurement from energy audit. The research parameter can be classified into 4 different parameters, location in different continents, location in different sea levels, location in different forest area, location in different latitude. The research result have been analysed by using ANOVA test, T-Test and Correlation. The comparison result of this study can be found that only distance from equator parameter is impacted to energy consumption difference. All other parameters are not impacted to energy consumption differentiation. This result of simulation can be implied that weather data of the area near to equator is not difference.

Keywords: Energy Simulation, Energy plus, Weather data, Statistic.

1. Introduction

The annual global energy consumption is estimated to 580 million terajoules. That's 580 million trillion joules or about 13865 million tons of oil equivalents [1]. However The world's electricity consumption has continuously grown over the past half a century, reaching approximately 25,300 terawatt-hours in 2021. Between 1980 and 2021, electricity consumption more than tripled, while the global population increased by roughly 75 percent. Growth in industrialization and electricity access across the globe has further boosted electricity demand [2]. In order to determine overall energy consumption, it is necessary to combine consumption data for many energy sources like electric consumption by country, fuel consumption by country. From top 5 energy consumption country recorded in year 2020 shown that china consume 145.46 billion kWh, united state (87.79 B. kwh), India (31.98 B.kWh), Russia (28.31 B.kWh), and Japan (17.03 B.kWh) consecutively. Energy in building for operating systems such as air conditioning, heating, ventilation, lighting and vertical transportation, which are essential for ensuring the safety and comfort of the building's occupants.

These systems account for 70 to 80 percent of the total energy consumed in buildings. Energy costs roughly account for about 30 to 40 percent of the total operating cost of a typical building [3]. However air-conditioning systems used in commercial and institutional building can account for more than 50 percent of total electricity consumed especially when the building located in hot and humid climates [4]. From the study of effect of weather on electric consumption [5], shown that temperature has robust and flat effects on electricity demand across all periods and Rain and sunshine have greater potential to affect people's consumption behavior Sunshine sensitivity increases from late afternoon and peaks in early evening [6]. In order to design building before construction, one of the most importance design phase is to simulate energy consumption in building. There are a lot of energy simulation software in the market (i.e. EnergyPlus, TRNSYS, Simulink libraries CarnotUIBK and ALMABuild, IDA ICE , Rhino Ceros (climate model)) to simulate energy consumption in variant condition. The objective of this study is to determine the different of energy consumption of country in near equator area and to compare the weather data for each area near to equator by changing 4 parameter (location in different continents, location in different sea levels, location in different forest area, location in different latitude). In this research, the reference building is located at Mahidol University, Salaya. This reference building is applied to another location in near equator area in different country, and then compares the energy consumption by using statistic methods. However, this comparison result for this research uses SPSS Software to analysis the data to determine what is the major factor that impact to energy consumption when the building location is in similar latitude (near equator) and the weather data for near equator area is different or not?

2. Data Analysis Technique

2.1. T-Test

A t test is a statistical test that is used to compare the means of two groups. It is often used in hypothesis testing to determine whether a process or treatment actually has an effect on the population of interest, or whether two groups are different from one another. The t test estimates the true difference between two group means using the ratio of the difference in group means over the pooled standard error of both groups as shown in equation 1

$$t = \frac{\chi_1 - \chi_2}{\sqrt{\left(s^2\left(\frac{1}{n_1} + \frac{1}{n_2}\right)\right)}} \tag{1}$$

where

t is the t value,

x_1 and x_2 are the means of the two groups being compared,

s^2 is the pooled standard error of the two groups,

n_1 and n_2 are the number of observations in each of the groups.

2.2. Analysis of Variance (ANOVA)

ANOVA, which stands for Analysis of Variance, is a statistical test used to analyze the difference between the means of more than two groups. ANOVA determines whether the groups created by the levels of the independent variable are statistically different by calculating whether the means of the treatment levels are different from the overall mean of the dependent variable. The assumptions of the ANOVA test are following, 1. Normally distributed response variable 2. Homogeneity of variance 3.Independence of observation.

The Anova test is performed by comparing two types of variation, the variation between the sample means, as well as the variation within each of the samples. Table 1 mentioned formula represents one-way Anova test statistics:

Table 1. The formulation of ANAVA test equation.

Source of Variation	Sum of Squares	Degrees of Freedom	Mean Squares (MS)	F
Within	$SSW = \sum_{j=1}^{k}\sum_{j=1}^{l}(X-\bar{X}_j)^2$	$df_w = k - 1$	$MSW = \frac{SSW}{df_w}$	$F = \frac{MSB}{MSW}$
Between	$SSB = \sum_{j=1}^{k}(\bar{X}_j - \bar{X})^2$	$df_b = n - k$	$MSB = \frac{SSB}{df_b}$	
Total	$SST = \sum_{j=1}^{n}(\bar{X}_j - \bar{X})^2$	$df_t = n - 1$		

where F = Anova Coefficient
MSB = Mean sum of squares between the groups
MSW = Mean sum of squares within the groups
MSE = Mean sum of squares due to error
SST = total Sum of squares
p = Total number of populations
n = The total number of samples in a population
SSW = Sum of squares within the groups
SSB = Sum of squares between the groups
SSE = Sum of squares due to error
s = Standard deviation of the samples
N = Total number of observations

2.3. Pearson Correlation (R_{xy})

Pearson Correlation is a measure of linear correlation between two sets of data. It is the ratio between the covariance of two variables and the product of their standard deviations; thus, it is essentially a normalized measurement of the covariance, such that the result always has a value between −1 and 1. As with covariance itself, the measure can only reflect a linear correlation of variables, and ignores many other types of relationships or correlations.

The pearson correlation coefficient formula is shown in following

$$r_{xy} = \frac{N\sum XY - \sum X \sum Y}{\sqrt{\left(N\sum X^2 - \left(\sum X\right)^2\right)\cdot\left(N\sum Y^2 - \left(\sum Y\right)^2\right)}} \quad (2)$$

Correlation coefficient (R^2) is also applied to verify the correction of the calculation and experiment data [7].

Table 2. The Interpretation of the size (strength) of Correlation coefficient.

Size of Correlation	Interpretation
0.90 to 1.00 or -0.90 to -1.00	Very high positive (negative) correlation
0.70 to 0.90 or -0.70 to -0.90	High positive (negative) correlation
0.50 to 0.70 or -0.50 to -0.70	Moderate positive (negative) correlation
0.30 to 0.50 or -0.30 to -0.50	Low positive (negative) correlation
0.00 to 0.30 or 0.00 to -0.30	Negligible correlation

3. Research Methodology

In order to achieve the objective of this study, the process of this research has been developed into 3 stages (Data preparation and verification, Data Simulation, Result Discussion) as shown in figure 1.

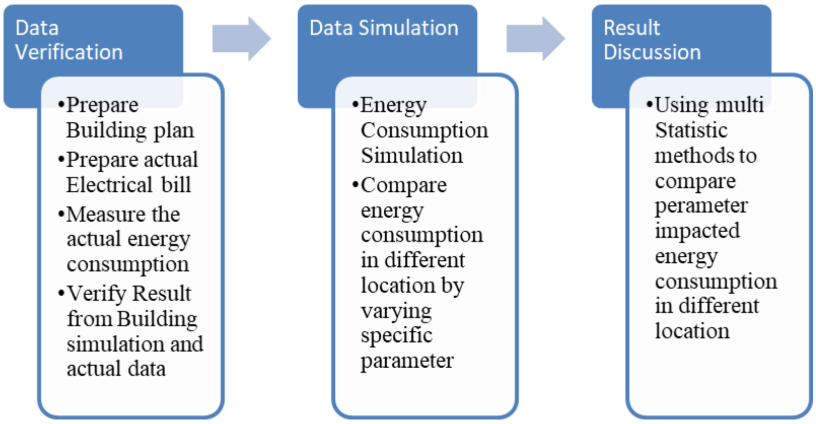

Figure 1. The Research Process.

4. Experimental Setup and Data Verification

4.1. Experimental Setup

In this research, the software Energy Plus had been used to simulate the result. However, The software calibration must firstly be done. In order to verify the software tools, The actual data from the experiment had been measured and recorded. The experimental site is located at Faculty of Information and communication technology which have 4 levels, Mahidol University, Salaya (13.7959, 100.3247). This building is educational building which normally operate from 8.00am to 5.00pm , Mon-Fri. The building are stand-alone building which no connection to other building. The building energy consumption data has been recorded for 7 days continuously. The actual electric bill (of last year) had also been collected to compare with the result from simulation.

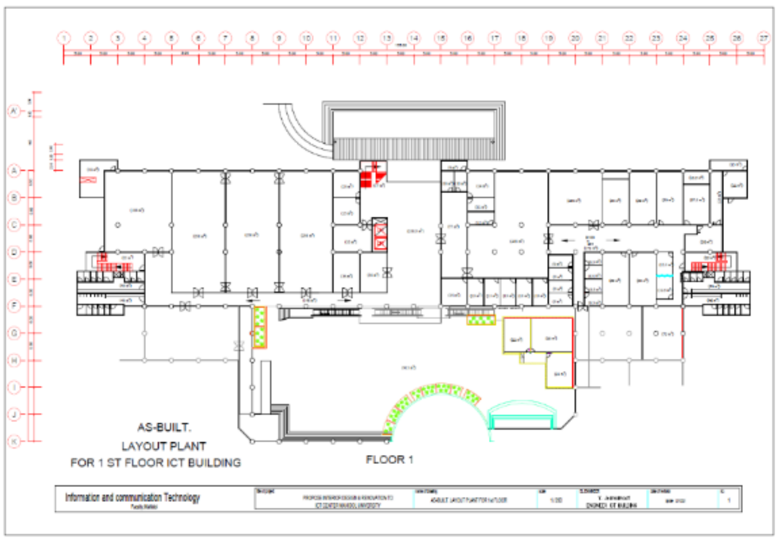

Figure 2. Floor plan for Information and communication technology Building, Mahidol University Salaya.

4.2. Data Simulation and Verification tools
In this research, there are 3 major application to be used, google sketch up, open studio, energy plus software. Google Sketch up is used for design the building, Open studio is used for setting up the building environment like weather data, building materials, etc. and energy plus is used for energy simulation [7]. After The simulation tools are well developed. The data from simulation has been compared with actual data. The comparison result is shown in figure3 and summary in table 3

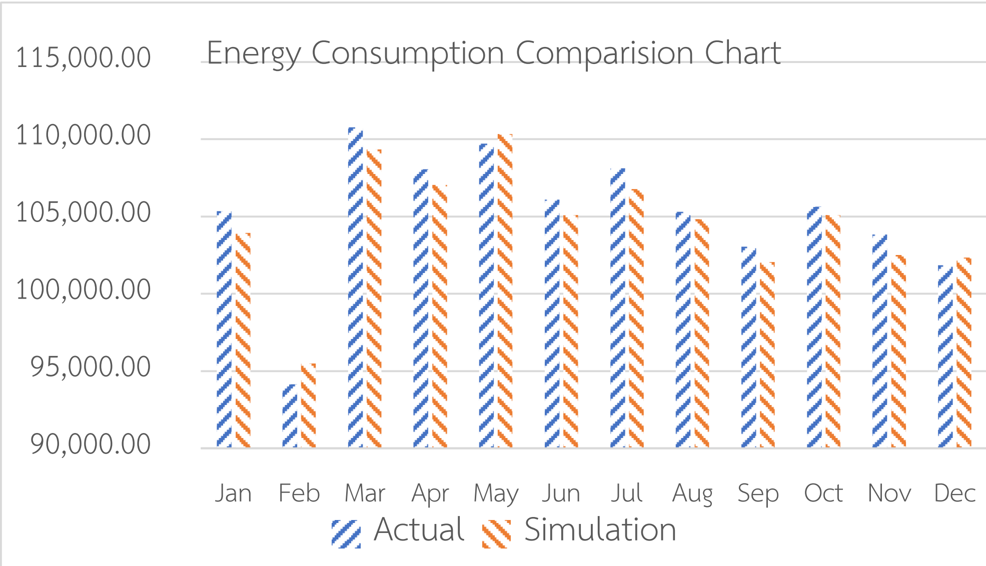

Figure 3. The Comparison between Actual Energy consumption and Simulation Result.

Table 3. The Energy consumption comparison between actual and simulation.

Energy Consumption comparison			
Actual (kWh)	Simulation (kWh)	Percent Error	Sig.
1,261,914.37	1,254,848.67	0.56%	0.01

From table3, the simulation result reveals the accuracy of simulation when compare with actual measurement have only 0.56% error. And signification level at 99.98% reliability. The results imply that this simulation software can be used to predict energy consumption simulation in other difference cases.

5. Simulation setup
This Research use sample from the country in near equatorial climate in different continent eg., Asia (Thailand, Malaysia , Indonesia (Maldives) , Sri Lanka, Vietnam), Africa (Yemen, Ethiopia, Ghana, Kenya, Senegal, Sudan), Central America(Belize, Cuba, Matinik Island, Nicaragua, El Salvador, Honduras, Vergin Island), Oceania (Fiji Island, Marshall Island, Palau Island, Philippines, Singapore), Latin America (Brazil, Ecuador, Peru, Venezuela, Nicaragua).

The simulation software used in this research is Energy plus simulation software together with open studio and google Sketch up as shown in figure 4.

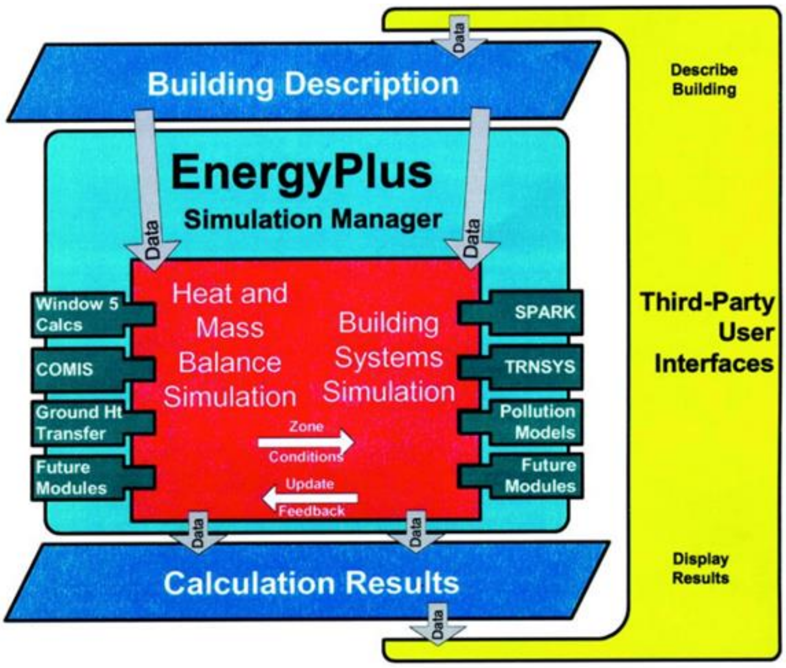

Figure 4. Energy Plus System Overview.

6. Research Framework

This simulation considers a country located in near equatorial which can be categorized into group of following parameter, Continental, Distance from equator, Direction from equator (due south or north), height from sea levels, Country Forest Area. The research framework can be illustrated in figure 5.

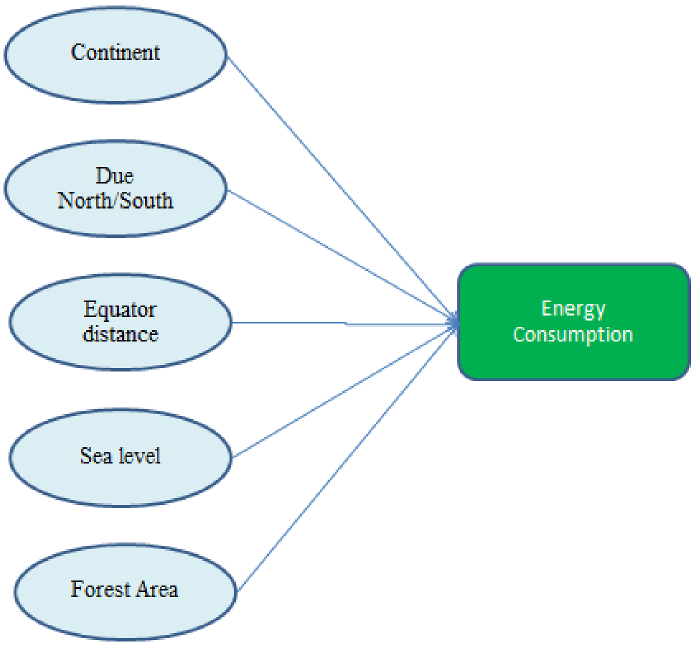

Figure 5. The Research Framework.

7. Results and Discussion

This research set up hypothesis interpretation into Null hypothesis (Ho) which definition to no difference between group and Alternate hypothesis (Ha) which definition difference between group.

7.1. The Energy consumption Between Continent

In order to verify energy consumption differentiation between the continents, the energy consumption within the continents must be verify the different first. ANOVA analysis has been applied in order to determine the energy consumption data within the group and between group as shown in table 4.

Table 4. ANOVA Analysis of Energy consumption between continents.

	Sum of Squares	df	Mean Square	F	Sig.
Between Groups	506,331,300,541.304	4	126,582,825,135.326	1.617	.204
Within Groups	1,800,280,221,729.642	23	78,273,053,118.680		
Total	2,306,611,522,270.946	27			

From Table 4, the results reveals that there are no different energy consumption with in the continent and between continents. This result can be explained that in near equator area, the energy consumption of country between continents is similar.

7.2. The energy consumption between north and south

Independent T-Test has been applied in order to determine the different between north and south as shown in table 5.

Table 5. Independent Samples Test.

	Levene's Test for Equality of Variances		t-test for Equality of Means					
							95% Confidence Interval of the Difference	
	F	Sig.	t	df	Sig. (2-tailed)	Mean Difference	Lower	Upper
Equal variances assumed	10.672	.003	1.333	26	.194	148,595.4358	-80,615.9078	377,806.7795
Equal variances not assumed			1.088	10.749	.300	148,595.4358	-152,783.1264	449,973.9981

From Table 5, the result reveals that there are no different energy consumption between Country in north and south latitude. This result can be explained that in near equator area, the energy consumption of country due north and due south is similar.

7.3. The Energy consumption when consider the distance from equator

Correlation Test has been applied in order to determine the different of distance to energy consumption as shown in table 6.

Table 6. Correlations test for distance from equator and energy consumption.

		Energy consumption	Distance
Energy consumption	Pearson Correlation	1	-.397*
	Sig. (2-tailed)		.037
	N	28	28
Distance from equator (km)	Pearson Correlation	-.397*	1
	Sig. (2-tailed)	.037	
	N	28	28

From Table 6, the result reveals that there are the energy consumption varied due to distance from equator in reverse direction (higher level of latitude, lower energy consumption). This result can be explained that in near equator area, the energy consumption of country in higher latitude is lower energy consumption when compare to lower latitude country.

7.4. The Energy consumption when consider the distance from sea levels

Correlation Test has been applied in order to determine the different of height from sea level to energy consumption as shown in Table 7.

Table 7. Correlations test for height from sea level to energy consumption.

		Energy consumption	height
Energy consumption	Pearson Correlation	1	-.287*
	Sig. (2-tailed)		.037
	N	28	28
Height (km)	Pearson Correlation	-.287*	1
	Sig. (2-tailed)	.037	
	N	28	28

From Table 7, the result reveals that there are no different between height from sea level and energy consumption. This result can be explained that in near equator area, the energy consumption of country which higher altitude is similar to lower altitude.

7.5. The Energy consumption when consider forest area in the country

Correlation Test has been applied in order to determine the different of forest area in the country to energy consumption as shown in table 8.

Table 8. Correlations test for forest area and energy consumption.

		Energy consumption	Forest Area
Energy consumption	Pearson Correlation	1	-.007*
	Sig. (2-tailed)		.973
	N	28	28
Forest Area (km)	Pearson Correlation	-.007*	1
	Sig. (2-tailed)	.973	
	N	28	28

From Table 8, the result reveals that there are no different between countries with different forest area to energy consumption. This result can be explained that in near equator area, the energy consumption of country which higher forest area is similar to lower of forest area.

8. Conclusion

Regarding to the result of comparison for energy consumption simulation in different condition in this study. When consider the country is in near equatorial area, the continent, due north / south, sea level altitude and forest area parameters are not impact to energy consumption differentiation. Only one factor that impact to energy consumption is “Distance from equator” (the longer distance, the less energy consumption)

For the conclusion on this study, the simulation varied weather data from energy plus software for each location. After the energy simulation comparison has been done, the result is shown that distance from equator is the only one parameter that impacted the energy consumption differentiation while other parameters are similar. This simulation result can implied that weather data for the country in near equator zone is not significantly difference. Therefore, from result of the study, found that the weather in near equator area is similar for all over the world. In order to reduce the energy consumption by adjusting the environment, microclimate design concepts must be applied to the building in near equator area.

9. References

[1] T. Ahmed, D.Zhang (2020): a review. *Journal of Energy Report: A critical review of comparative global historical energy consumption and future demand: The story told so far, 10(6), 1973-1991.*

[2] Enerdata (2023), Global Energy trends 2023: https://yearbook.enerdata.net/total-energy/world-consumption-statistics.html,

[3] World population review (2023), https://worldpopulationreview.com/country-rankings/energy-consumption-by-country

[4] Energy-Efficient Building Systems, Green Strategies for operation and maintenance (2006), Dr. Lal Jayamaha, McGraw Hill

[5] What is the effect of weather on household electricity consumption? Empirical evidence from Ireland, Jieyi Kang, Energy Economics, Vol 111, July 2022

[6] Cherry L. Jackson 2015, *Research Methods and Statistics: A Critical Thinking Approach* (Cengage Learning)

[7] Larry B., Andrew P., Daniel M. 2018 *Building Energy Modeling with Open Studio: A Practical Guide for Students and Professionals* (Springer)

ETM0009

Parametric Study of Induction Heating System for Hot-air Generator Application

P. Wongphetsakun[1], A. Kaewpradap[2], and W. Onreabrooy[1,*]

[1]Department of Physics, Faculty of Science, 126 Prachauthit Bangmod Thung Khru, Bangkok, 10140, Thailand
[2]Department of Mechanical Engineering, Faculty of Engineering, 126 Prachauthit Bangmod Thung Khru, Bangkok, 10140, Thailand

* Corresponding Author: wandee.onr@kmutt.ac.th

Abstract. This study focused on the influenced parameters of the induction heating model for hot-air generator. Instead of ohmic heating, the hot-air generator on the induction heating as the new energy resource was studied. The hot air bulb on induction cooker was applied as a numerical model to achieve the air temperature of 250°C with 1,000 watts. As the hot-air generator with induction heating model, the air velocity, bulb geometry, bulb inlet diameter and bulb outlet diameter were conducted to investigate the air temperature and velocity profile. The numerical results showed that the air temperature and air velocity significantly affected by bulb geometry, bulb inlet and bulb outlet diameter. This research shows that induction heating can be applied to a hot air generator with a temperature of more than 250°C within 13 minutes at a power of 1,000 watts. Induction heating can also be used as a method for creating hot fluids.

Keywords: Hot air, Induction heating, Air temperature, Air velocity, Numerical study.

1. Introduction

Nowadays, electromagnetic principles are applied to various devices in everyday life. Examples include wireless chargers, electromagnetic door locks, sensors, aluminum lid sealers and induction cookers [1]. This technology has a good performance with the main energy source, the electricity, that people use. Therefore, it tends to see more of its application in many devices. One of the applications that most people think of is the heat generation; the heat can be generated quickly and has more generation patterns than other methods. Induction heating relies on the principle of electromagnetic induction according to Faraday's law (Michael Faraday 1791-1867) [2]. When the magnetic flux on a conductor changes, an electromotive force is induced in the conductor. If an induced electromagnetic force (EMF) occurs in a closed-circuit coil, then an induced current occurs in that circuit. If an induced EMF occurs on a bulk or sheet conductor, there is an eddy current. Since the induction heating relies on eddy currents to heat the conductor, the heat generated by this method is relatively limited to the material itself. Currently, there are two types of devices using the induction heating technology [3]. The first type is an induction furnace, and the second is an induction cooker [4]. Researchers have studied induction heating in other heating devices such as automatic magnetic pulses [5], thus the generating efficient hot air is a reason to look for new applications with dispensers. Hot air obtained by electromagnetic induction technology is heated quickly compared to a heating coil electricity. The efficient heat generation is the reason to look for new applications. Commercially available hot air distributors today can be roughly divided into two types. The first type uses a heating lamp as the heat generator, which is commonly found in a closed convection oven [6]. The second type uses heating wires (heating coils and heating elements). In the past research, induction heating for pans and woks using planar cooktops were investigated [7]. In general, the hot air supply via the heating coils can achieve higher temperatures than that via the heating lamps, depending on the power and the shape of the device [8]. An example of a hot air device that uses the heating wire is a hot air blower. Despite different heat generators, the principle of hot air supply is the same; the air is blown through the heating element. It is interesting to provide another way to efficiently create hot air, the induction heating technology is investigated to apply for hot-air generators. As the hot-air generation application, the progressive collapse of buildings under high temperatures using successive approximation technique was analyzed [9]. In order to apply the induction technology for hot-air generation, the parameters related to the air temperature and velocity should be considered. Consequently, the parameters of conduction bulb geometry, height, outlet diameter and inlet air velocity were investigated which influenced the outlet air velocity and outlet air temperature including the velocity and temperature distribution in conduction bulb. The effects of parameters investigated in this study could be more valuable for hot-air generator technology.

2. Methodology

Magnetic field induction involves applying an electric current to an induction coil to create a high frequency magnetic field on the metal. This magnetic field energy causes electric charges in the metal to move and as a result, eddy currents occur, which results in direct heat generation in that area. If used in heating to create hot water, hot oil, hot gas, and hot air, it will result in a new technology with less energy loss than traditional heating methods from heating coils. The innovative induction heating system directly heats the metal bulb as a hot air heater. This makes energy efficiency more cost-effective and reduces energy loss significantly. This design can be used in various processes that use hot air in the future. Magnetic induction heating uses heat generated by eddy currents within a conductive material under an alternating magnetic field generated by an alternating current of frequency approximately 30 kHz flowing in an induction coil. The main advantage of this heating process is the transmission of electromagnetic energy from the inductor to the conductor material without direct contact and rapid heating. In this study, the hot air is generated by induction coil which is investigated by experiment and simulation study. In order to generate hot air by induction coil, the theory of heat transfer such a heat conduction and heat convection including induction and fluid flow theory are considered. Convection conduction and radiation of induction heating sources is made to have a further understanding of the mechanism of heat transfer for hot air generator application. Modelling heat transfer and air flow at various speeds are important factors in the design of hot air generating equipment. In this research, a metal bulb was designed to be used as a source for heating air under a magnetic field using an induction cooker with a power of 1,000watts. The heat conduction, heat convection and radiation through conduction is given by Eq. (1), (2) and (3), respectively.

$$Q_{cond} = -kA\frac{dx}{dT} \tag{1}$$

$$Q_{conv} = hA_S(T_S - T_f) \tag{2}$$

$$Q_{rad} = \varepsilon\sigma A_S(T_s^4 - T_f^4) \tag{3}$$

Q_{cond} Conduction heat transfer (W)

K Thermal Conductivity of material (W/m K or W/m °C)
dx Material thickness (m)
A Heat transfer area (m^2)
dT Temperature difference (K or °C)
Q_{conv} Convection heat transferred (W)
A_S Surface area (m^2)
h Heat transfer coefficient
T_S Surface temperature (K or °C)
T_f Fluid temperature (K or °C)
Q_{conv} Heat radiation (W)
σ Stefan–Boltzmann constant ($J/s \cdot m^2 \cdot K^4$)
ε Emissivity

Conductive materials can be heated by induction. To calculate the distribution of heat sources in metals. It can be shown that the heat arising in the metallic conductor is equal to the energy conversion at this point. The energy can be calculated using Eq. (4)

$$q = \frac{|\vec{J}|^2}{\sigma} \tag{4}$$

q Energy density (J/m^3)
$\vec{J}$ Electrical current density (A/m^2)
σ Electrical conductivity (S.m)

The change in eddy current density from the surface to the conductor can calculate the standard depth of penetration. The penetration depth δ is calculated using Eq. (5).

$$\delta = \sqrt{\frac{1}{\pi f \sigma \mu}} \tag{5}$$

μ Magnetic permeability (H/m)
f Magnetic field frequency (Hz)

3. Experimental setups

In this study, the simulation was applied to investigate the parametric study effects on induction hot-air generator. In order to study the simulation model, the basic condition of induction hot-air generator was experimented. The metal bulb model is designed and studied by Ansys fluent program. As the basic condition, the circle bulb with h 30 mm, d_{out}= ½ inch, the simulation results were performed to validate with experiment results obtained by experimental apparatus as shown in Figure 1(a). The metal bulb model is designed and studied by Ansys Fluent 2021 R2. The experimental section of induction hot-air generator consists of a heat generation part and a heat distribution part (conduction bulb). Firstly, the 1000 W of induction cooker was applied as the heat generation part, which supplied a high-frequency electromagnetic field and a material used in induction unit was induced to generate eddy current. Not only the induction cooker, a flat cylinder shape of conduction bulb with a diameter of 15 cm was applied in the heat generation part due to same size of diameter coil inside the induction cooker. The same size of diameter coil of induction cooker used in conduction bulb was expected to obtain a high flux density and a lot of energy or electrical power. Secondly, hot air distribution part consisted of a 530 W of blower with Teflon cable to act as a path for air from the blower into the induction unit. The generated hot-air could be distributed by blower and passed through the outlet of conduction bulb. The entire experiment is divided into two periods: The first period in which the induction unit has not been induced or cold test and the second period in which the induction unit has already been induced or hot test. The dimension of heat distribution part such a diameter (D_{out}), height (h) and wall thickness (t_w) are shown in Figure 1(b). In this work, the heat transfer factors of the induction heating hot air generator were studied using various models, as follows: bulb geometry, air velocity, and bulb outlet diameter, as shown in Table 1 and Figure 2 to determine air temperature and velocity profiles.

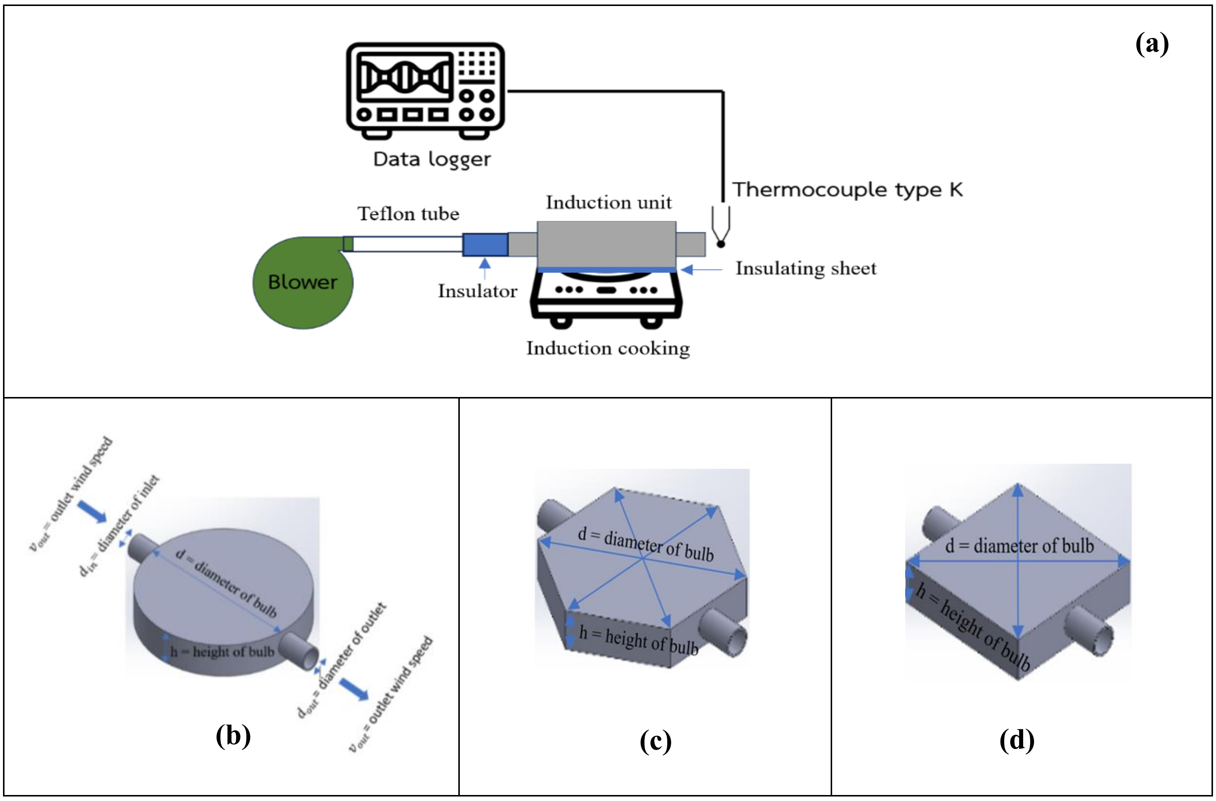

Figure 1. (a) Experimental apparatus of induction hot-air generator. (b), (c), (d) Dimension of hot air bulb.

Table 1. Parametric study conditions investigated by simulation model.

Geometry of bulb	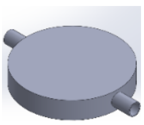 Circle	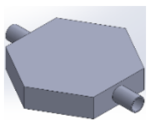 Hexagon	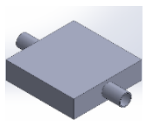 Rectangular
Height, h (cm)	3.0, 6.0, 9.0	3.0, 6.0, 9.0	3.0, 6.0, 9.0
Diameter, d (cm)	16	16	16
Outlet diameter, D_{out} (inch)	1/2, 3/4, 1.0	1/2, 3/4, 1.0	1/2, 3/4, 1.0
Inlet velocity, V_{in} (m/s)	4.8, 5.4, 6.3, 7.5, 8.3, 10.2		

4. Result and discussion

4.1. Validation of simulation model

4.1.1. Cold test

Experimental and simulation results measured the outlet air velocity at blower speed level 5 of a circular bulb with diameter (d) = 16 cm, h = 3.5 cm, and D_{out} = 3/4. The simulation outlet air average velocity was measured and calculated at distances 1, 2, 3, 4 and 5 mm from the conduction bulb exit as shown in Figure 3. The outlet air velocity (V_{out}) of each blower level was obtained, and the results are shown in Table 2. The comparison of outlet air velocity between experiment and simulation were different less 6.0%. The experimental results in Table 2 in this section show that the computer simulation model can determine the average wind speed at distances between 1-6 at each level of the blower. The results of calculating the average wind speed are as follows: Close to the measurement with an anemometer.

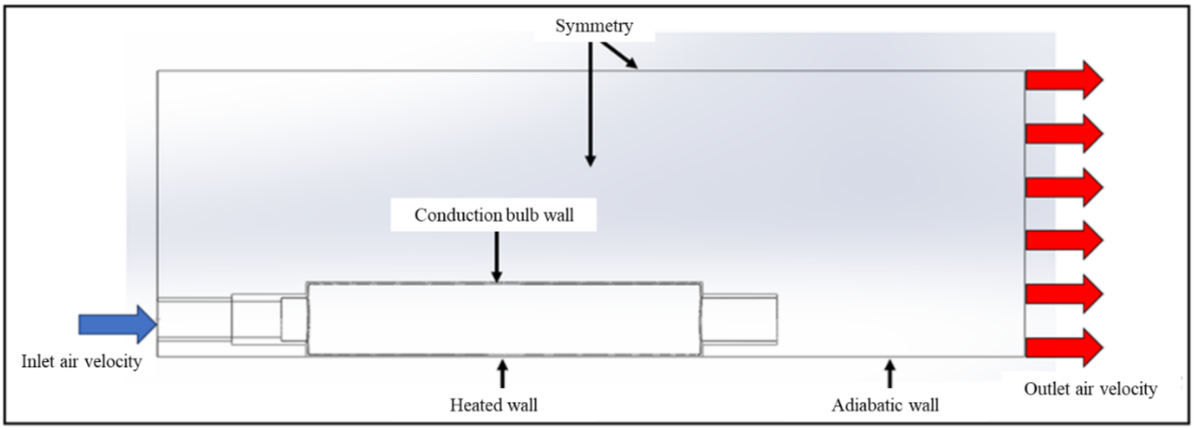

Figure 2 Simulation model of induction hot-air generator.

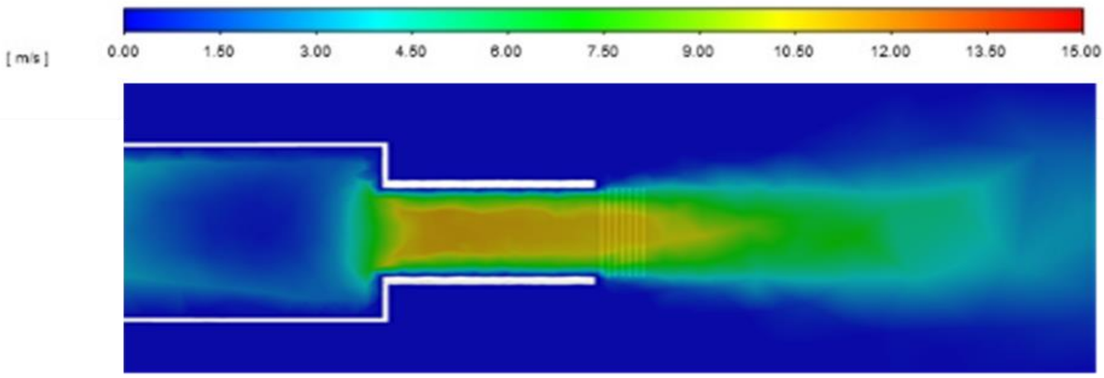

Figure 3. Simulation of outlet air velocity at blower speed level 5.

Table 2. Comparison of outlet air velocity between experiment and simulation.

Blower level	Experimental results		Simulation results	% Error
	V_{in} (m/s)	V_{out} (m/s)	V_{out} (m/s)	
1	4.8	4.2	4.2±0.1	0±0.1
2	5.4	4.8	4.9±0.1	2.1±0.1
3	6.3	5.7	5.7±0.2	0±0.2
4	7.5	6.5	6.8±0.2	4.6±0.2
5	8.3	7.2	7.6±0.3	5.6±0.3
6	10.2	8.9	9.3±0.3	4.5±0.3

4.1.2. Hot test

Following the hot test process, the time series of outlet air temperature (T_{out}) at conduction bulb exit related to variations of blower level were measured as shown in Figure 4. As the higher blow level, the inlet air velocity increase affected lower outlet air temperature. The T_{out} measured from the experiment at blower level 1, 2, 3, 4, 5 and 6 were compared to the simulation as illustrated in Figure 5(a). According to the comparison, the T_{out} measured from the experiment were same trends and closed to simulation results with less 11.0% of difference. Thus, the induction hot-air generator model is verified to investigate the parametric study in further steps.

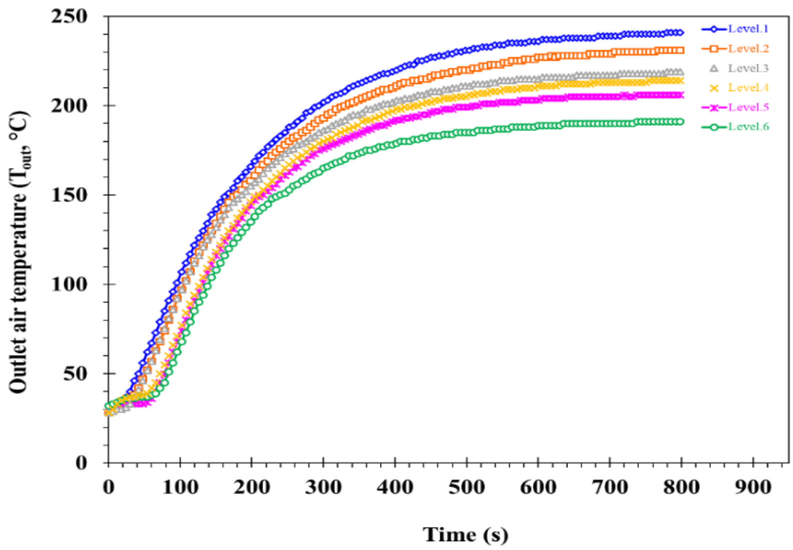

Figure 4. Experimental results of the increase in outlet air temperature (Tout) versus time at blower levels 1, 2, 3, 4, 5 and 6.

In this research, there are limitations of the instrument that cannot measure the wind speed of hot air. In this research, wind speed at room temperature was used as the primary data to find the relationship in Figure 5(b).

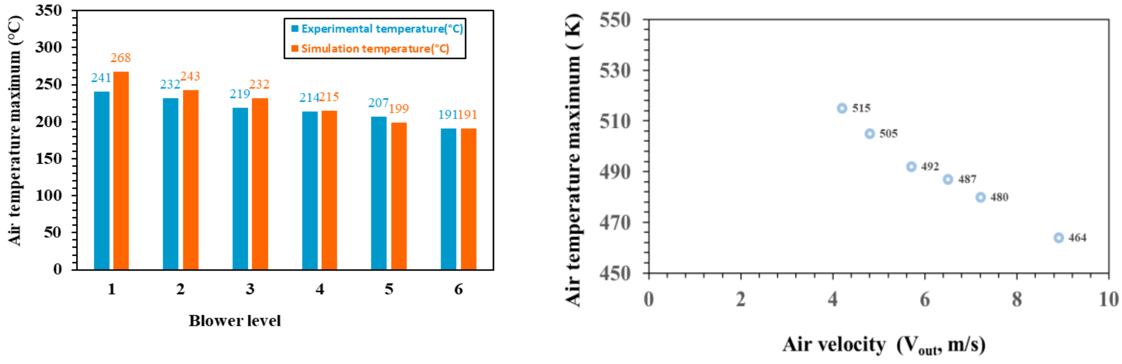

(a) (b)

Figure 5. (a) Comparison of outlet air temperature maximum (T_{out}) between experimental and simulation results and (b) Relationship between air speed and outlet air temperature maximum (T_{out}) at blower levels 1,2,3,4,5 and 6.

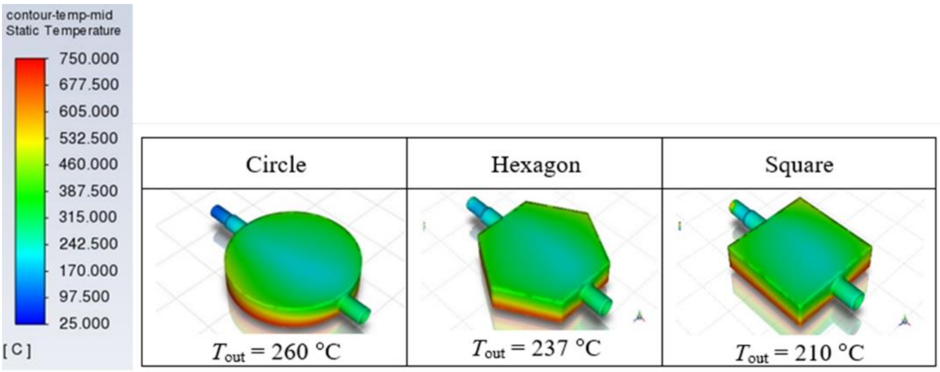

Figure 6. Outlet temperature distribution with variation of conduction bulb geometry of circle, hexagon and square at h =3.0 cm, D_{out}=1/2 inch and V_{in}= 4.8 m/s.

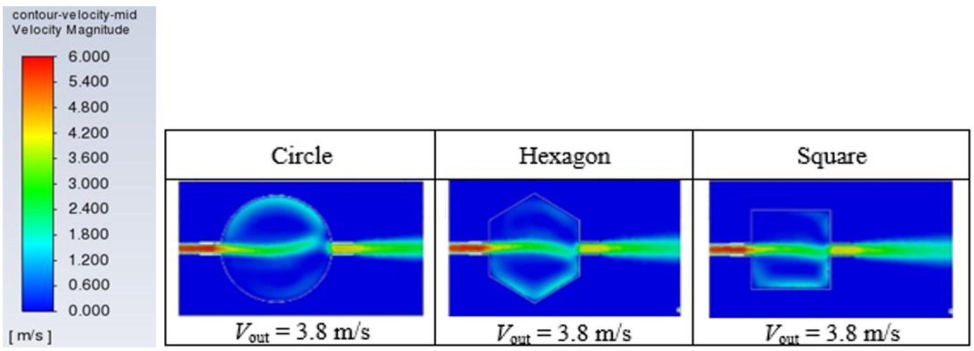

Figure 7. Outlet velocity (V_{out}) with variation of conduction bulb geometry of circle, hexagon and square at h =3.0 cm, D_{out}=1/2 inch and V_{in}= 4.8 m/s.

4.2. Parametric study

4.2.1. Geometry effect

As the parametric study of induction hot-air generator, the geometry and height of conduction bulb, inlet diameter and inlet velocity were examined. Firstly, the variations of geometry with same surface area, height of conduction bulb, inlet velocity affected the outlet air velocity (V_{out}) and temperature (T_{out}) were investigated. The results show the outlet air velocity of all geometries are almost same however, the outlet air temperature of circle and hexagon geometry are higher compared to rectangular geometry as shown in Figure 6 and 7. As the results, the circle geometry is more suitable for air flow and heat convection affected higher outlet air temperature.

4.2.2. Height effect

The variations of conduction bulb, 3.0, 6.0 and 9.0 cm of bulb height were studied, and the outlet air velocity (V_{out}) and temperature (T_{out}) were resulted as shown in Table 3.

Table 3. Simulation results of average outlet velocity and outlet temperature effected by the height of conduction bulb.

Geometry	h (cm)	V_{in} (m/s)	V_{out} (m/s)	T_{out} °C (K)
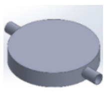	3.0	5.6	3.8	260 (533.0)
	6.0	5.6	3.8	273 (545.8)
	9.0	5.6	3.6	237 (510.6)
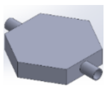	3.0	5.6	3.6	237 (510.6)
	6.0	5.6	3.8	273 (546.4)
	9.0	5.6	3.7	-
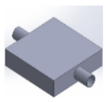	3.0	5.6	3.7	210 (438.4)
	6.0	5.6	3.8	254 (527.2)
	9.0	5.6	-	-

When the conduction bulb height was higher, lower outlet velocity and lower temperature were observed. At the same inlet velocity, the increase of volume affected the lower velocity inside the bulb and lower outlet velocity. Moreover, the lower temperature was obtained when the conduction bulb volume increased due to the heat convection. Figure 8 shows Outlet temperature distribution with variation of circle conduction bulb height, h = 3.0, 6.0, and 9.0 cm at D_{out} = 1/2 inch and V_{in}= 4.8 m/s. The result shows the maximum outlet temperature at h = 6.0 for circle and hexagon conduction bulb because the properly lower air velocity and greater volume enhanced the heating duration and heat convection.

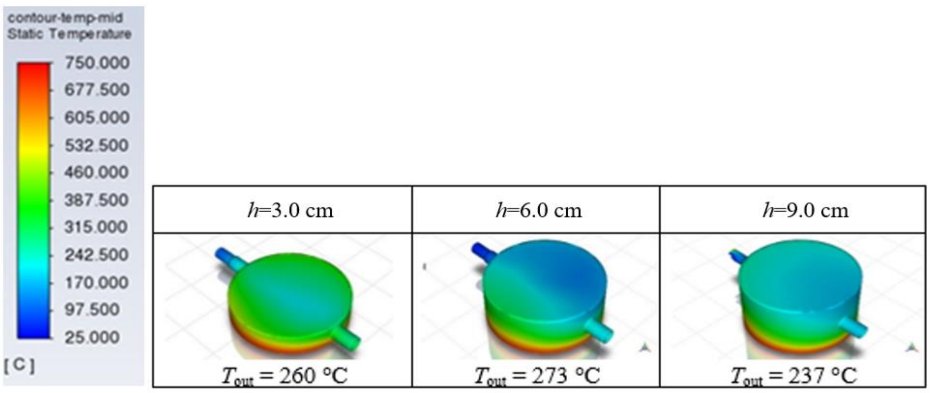

Figure 8. Outlet temperature distribution with variation of circle conduction bulb height, h = 3.0, 6.0, and 9.0 cm at D_{out}=1/2 inch and V_{in}= 4.8 m/s.

4.2.3. Outlet diameter effects

The outlet diameter of conduction bulb is an important parameter to investigate the effects on outlet velocity and temperature. As the previous results, the maximum outlet temperature was obtained by circle and hexagon geometry with 6.0 cm of bulb height, thus the outlet diameter of 1/2, 3/4 and 1.0 inch of conduction bulb were applied continuously from the mentioned conditions. Figure 9 shows the comparison of T_{out} with variation of D_{out} = 1/2, 3/4 and 1.0 inch between circle and hexagon conduction bulb at h = 6.0 cm and V_{in} = 4.8 m/s. The maximum outlet temperature at D_{out} = 1/2 inch from circle (273°C) and hexagon (263°C) geometry were obtained. It was because of less cross-section area affected higher pressure difference and longer air-heating duration, then higher outlet temperature was observed.

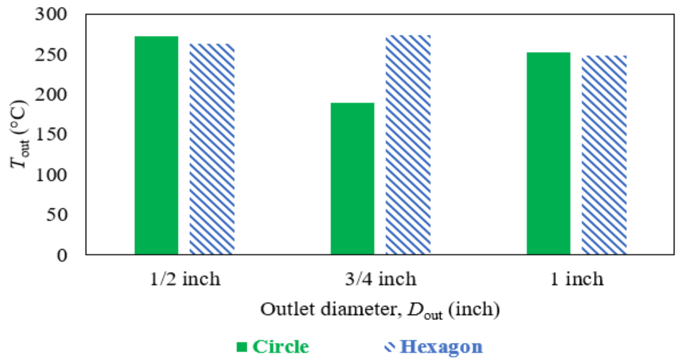

Figure 9. Comparison of T_{out} with variation of D_{out}=1/2, 3/4 and 1.0 inch between circle and hexagon conduction bulb at h =6.0 cm and V_{in}= 4.8 m/s.

4.2.4. Inlet air velocity effects

The inlet air velocity (V_{in}) is one of parameters which affected the air velocity inside the bulb and outlet air velocity. The variations of inlet air velocity applied by blower level 1-6 in this simulation model for V_{in}=4.8-10.2 m/s. As the highest outlet temperature of both circle (273°C) and hexagon (263°C) obtained from D_{out}=1/2 inch, the inlet air velocity of circle and hexagon were investigated continuously at h =6.0 cm and D_{out}=1/2 inch. Figure 10 shows the comparison of T_{out} with variation of V_{in}=4.8, 5.4, 6.3, 7.5, 8.3 and 10.2 m/s in hexagon conduction bulb at h =6.0 cm and D_{out}=1/2 inch. According to increase of inlet air velocity, the outlet temperature of both circle and hexagon conduction bulb decrease owing to heat convection and shorten heating duration. The results show the maximum outlet temperature of 263°C and 273°C were observed at V_{in}= 4.8 m/s for hexagon and circle conduction bulb, respectively.

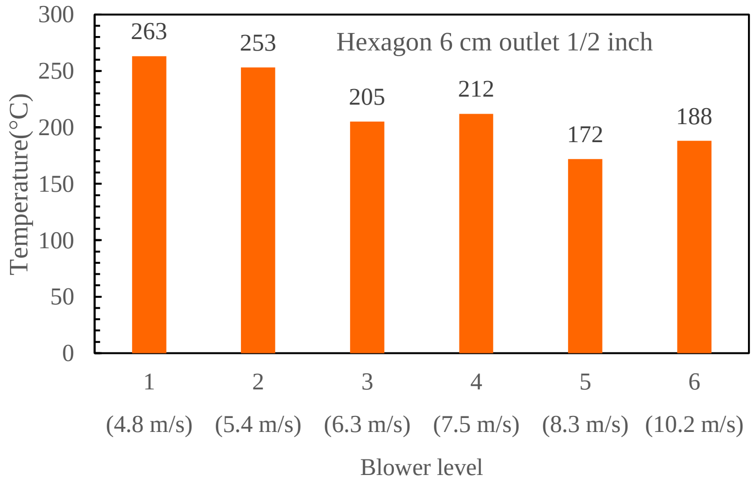

Figure 10. Comparison of T_{out} with variation of V_{in}=4.8, 5.4, 6.3, 7.5, 8.3 and 10.2 m/s for hexagon conduction bulb at h =6.0 cm and V_{in}= 4.8 m/s.

5. Conclusion

In this study of induction hot-air generator, parameters of conduction bulb geometry, height, outlet diameter and inlet air velocity were investigated which influenced the outlet air velocity and outlet air temperature including the velocity and temperature distribution in conduction bulb. As the parametric study, the circle and hexagon geometry with 6.0 height of conduction bulb at D_{out} =1/2 inch and V_{in}= 4.8 m/s could enhance the heat circulation and convection heat transfer and shorten heating duration affected the higher outlet temperature. This research has resulted in the creation of a prototype device for producing induction hot air with a metal bulb combined with an induction cooker at 1,000 watts, which can produce hot air at a temperature of 273°C in no more than 13 minutes.

6. Acknowledgement

The authors thank to Department of Physics, Faculty of Science, and Department of Mechanical Engineering, Faculty of Engineering, King Mongkut's University of Technology Thonburi for financial support and experimental facility. The authors also thank to Asst.Prof. Dr. Wittaya Kanchanapusakit and Mr. Chanawee Chantang for technical and data support.

7. References

[1] Sweeney M., Dols J., Fortenbery B., & Sharp F. (2014). Induction cooking technology design and assessment. *ACEEE Summer Study on Energy Efficiency in Buildings*, 9, 370-379.

[2] Liu H., Chang Y., Lin C., Chen Y., Lin C., Lin Y., Huang M., *&* Hsu H. (2022). Experimental and numerical multidisciplinary methodology to investigate the thermal efficiency of boiling pot on induction system. *Case Studies in Thermal Engineering*, 36 (102199) 1-13.

[3] Landi D., Cicconi P., Germani M., &Russo A. C. *(2016).* A Methodological approach to support the design of induction hobs. *Proc. of the ASME 2016 Int. Mechanical Engineering Congress & Exposition,* 1-10.

[4] Sanz-Serrano F., Sagues C., & Llorente S. (2016). Inverse modelling of pan heating in domestic cookers. *Applied Thermal Engineering*. 92, 137-148.

[5] *D.* Khort, *I.* Smirnov, *A.* Kutyrev, *& R.* Filippov. (2020). Device for automated magnetic pulse stimulation of plant production processes. *E3S Web of Conferences*, 161, (01064)1-5.

[6] Han W., Chau K.T., Jiang C., & Ching T. W. (2018). Comparison of induction heating for pans and woks using planar cooktops. *IEEE*, 358-365.

[7] Cabeza-Gila I., Calvo B., Grasa J., Franco C., Llorente S., & Martínez M.A. (2020). Thermal analysis of a cooking pan with a power control induction system. *Applied Thermal Engineering*, 180, (1157899) 1-10.

[8] Abraham J.P., & Sparrow E.M. (2004). A simple model and validating experiments for predicting the heat transfer to a load situated in an electrically heated oven. *Journal of Food Engineering,* 62, 409-415.

[9] Vieira L.L., Bezerra L.M., Yure R.S., Silva R.C., Silva W.V., Barbosa E.G., & Paula V.F. (2020). Analysis of the progressive collapse of buildings under high temperatures using successive approximation technique. *Journal of Civil Engineering and Architecture* 14, 46-60.

ETM0010

Understanding of Biosolids Transformation under Pyrolysis and Gasification Conditions

San Shwe Hla[1,*], Alex Ilyushechkin[1], Nuttaphol Sujarittam[2], and Chatchawan Chaichana[2]

[1]Energy Business Unit, Commonwealth Scientific and Industrial Research Organisation, 1 Technology Court, Pullenvale, Brisbane, Queensland 4069, Australia
[2]Department of Mechanical Engineering, Faculty of Engineering, Chiang Mai University, 239 Huay Kaew Rd., Muang District, Chiang Mai, Thailand 50200

* Corresponding Author: san.hla@csiro.au

Abstract. Biosolids derived from wastewater treatment plants are carbon containing, nutrient-rich, organic materials. Conventional disposal methods of biosolids in landfills and farms are no longer sustainable due to stricter environmental regulations and the need for costly, long-distance transportation. Biosolids have a large concentration of inorganic elements, with up to 50% by weight in dry basis, including valuable elements such as phosphorus. Phosphorous recovery from biosolids ash produced from combustion processes is increasing as the world seeks more circularity in waste management, yet little is known regarding the chemistry of biosolids conversion under pyrolysis and gasification conditions. The primary objective of this study was to explore how various thermochemical conversion processes and how operating conditions influence the gasification properties of biosolids and the transformation of mineral matter during conversion.

In this study, the thermochemical conversion characteristics of biosolids samples collected from a wastewater treatment plant in Brisbane were investigated. The study shows that gasification reactivity of biosolids chars align closely with chars from various waste types like wood, paper, plastic, and garden waste. Phosphorus was found in different forms and compounds in biosolid chars and ashes under various pyrolysis and gasification conditions. During gasification, all crystalline phases in chars/ash were observed as oxide forms, and their crystallinity increased in the presence of CO_2, indicating more oxidised conditions. Processing chars at temperatures exceeding 900°C led to the loss of certain inorganic elements, particularly P, Zn and Mg, as they bonded with volatile phases. Inorganic matter in chars pyrolysed at temperatures below 600°C appeared in an amorphous form, while at higher temperatures, it transformed into crystalline phases as oxides and phosphides. The findings of this study highlighted the importance of operational parameters and conditions affecting properties of biosolid chars and ashes produced during the thermochemical conversion process.

Keywords: biochars, inorganic matter, ash characteristics, pyrolysis; gasification.

1. Introduction

Biosolids refer to the remnants produced during the treatment of municipal wastewater, constituting mostly water, often exceeding 99% in content. These biosolids take the form of semi-liquid waste, composed of 75–85% water, while the residual solids predominantly consist of organic substances, macro-nutrients such as nitrogen, phosphorus, potassium, sulfur, micro-nutrients like copper, zinc, calcium, magnesium, iron, and a portion of inert materials [1, 2]. The conventional agricultural uses of biosolids are diminishing due to concerns about possible pollution stemming from their heavy metal content [1], along with the substantial expenses linked to transporting biosolids to remote agricultural sites approved for their application [3, 4]. In this context, thermal treatment of biosolids is regarded as a viable and eco-friendly alternative strategy for transforming substantial volumes of biosolids into useful energy and value-added products. Biosolids contains a significant proportion of mineral content rich in nutrients, particularly phosphorus (P), which holds potential for agricultural applications. According to Tyagi et al. [5], apatite mines are projected to be depleted of P within the next 150 years. Given the finite nature and non-renewable resource of global phosphate rock reserves essential for phosphorus fertilizer production, the retrieval of phosphorus from biosolids gains importance to preserve scarce phosphorus resources and mitigate the carbon footprint linked to the production and importation of phosphate fertilizers.

In their comprehensive analysis, Raheem et al. [1] classify existing methods for recovering P from biosolids into three main categories: 1) direct utilisation in agriculture, 2) treatment of sewage sludge and leachates through the precipitation of P in the forms of struvite and hydroxyapatite, and 3) utilisation as incinerated ashes. As previously indicated, employing biosolids directly in agricultural fields carries the potential for environmental contamination from pathogens, parasites, aromatic hydrocarbons, and heavy metals. Despite the presence of non-expensive stabilisation technologies, transportation expenses can become substantial, particularly based on the distance between authorised agricultural lands and wastewater facilities. For instance, on a daily basis, Logan City Council in Queensland state incurs a significant operational expense of approximately $1.8 million per year, accounting for 30% of the total operating costs of the wastewater treatment plant. This expense is associated with the transportation of six trucks loaded with biosolids, covering a distance of 300 kilometres to the Darling Downs agricultural region, where these biosolids are utilised to enhance soil quality. Extraction techniques for P through the precipitation of struvite and hydroxyapatite offer benefits like effective nitrogen removal and a reduced likelihood of heavy metal emissions. However, this approach requires high operational expenses, falls short in achieving complete P recovery, and still presents potential risks of environmental pollution through elevated levels of pathogens and parasites.

Employing thermochemical methods such as incineration/combustion offers a range of benefits, including effective P recovery, concurrent treatment of heavy substances, minimised odour during processing, and harnessing energy from biosolids. Nevertheless, there exist certain constraints with incineration/combustion techniques, notably high operational expenses, the potential for environmental contamination through flue gases, complexity of procedures, and economic viability only for large-scale facilities dealing with substantial amounts of biosolids. While the pursuit of greater waste management circularity drives the increasing retrieval of phosphorous from biosolids ash generated through combustion processes, our understanding of biosolids conversion chemistry remains limited in alternative thermochemical conversion methods specifically pyrolysis and gasification conditions.

Differing from combustion, pyrolysis constitutes a thermal conversion method executed within an environment lacking in oxygen, within a temperature range of 350 to 900 °C, resulting in the creation of vapours or pyrolytic gases. Unlike combustion, pyrolysis predominantly produces substantial quantities of char (roughly 50% of the biosolids' mass). These char by-products have the potential to serve as solid fuel sources for generating heat, or they can be harnessed for the purpose of adsorbing hazardous metals (HMs) or organic pollutants [6]. Gasification is a thermochemical process that converts biosolids into a combustible syngas, primarily composed of combustible gases like H_2, CO, and CH_4. This conversion occurs within a constrained oxygen environment and operates at elevated temperatures ranging from 700 to 1000 °C. While the implementation of biosolids gasification faces multiple several obstacles, particularly the significant moisture content of approximately 80% by weight and the relatively lower heating value (LHV), along with the elevated mineral matter content within the biosolids, these substantial challenges ultimately result in reduced gasification efficiency [1]. However, despite these challenges, the generation of syngas rich in considerable hydrogen becomes achievable [7-9].

While numerous international researchers have examined the behaviour of biosolids under various thermal circumstances and methods, research in this field remains relatively limited within Australia. This limitation is possibly attributable to the insufficient industrial applications aimed at converting biosolids into valuable energy using thermochemical conversion methods. In the current research, we explore the impact of different thermochemical conversion techniques and operational parameters on the gasification characteristics of biosolids. Furthermore, we investigate transformations of mineral matter components, including trace elements, during the conversion processes.

2. Experimental

2.1. Materials

Biosolid samples were collected from the endpoint of the entire treatment processes at the Oxley Creek WWT plant, a significant wastewater treatment facility managed by Queensland Urban Utilities in Brisbane, Australia. Following collection, these samples were dried inside a laboratory oven. Subsequently, they were crushed and sieved using a mortar and pestle to ensure uniform particle sizing, ranging from 0.43 mm to 1 mm. Once the samples were sized, they were suitable for various analyses, including pyrolysis experiments, as well as proximate and ultimate chemical analyses, and determination of their energy content.

2.2. Char & ash producing under different thermochemical conversion processes

Char samples were generated through pyrolysis conditions employing a horizontal tube furnace (HTF) capable of reaching temperatures as high as 1100°C. Inside the HTF, two crucibles, each containing dried biosolids, were carefully positioned, as illustrated in Figure 1.

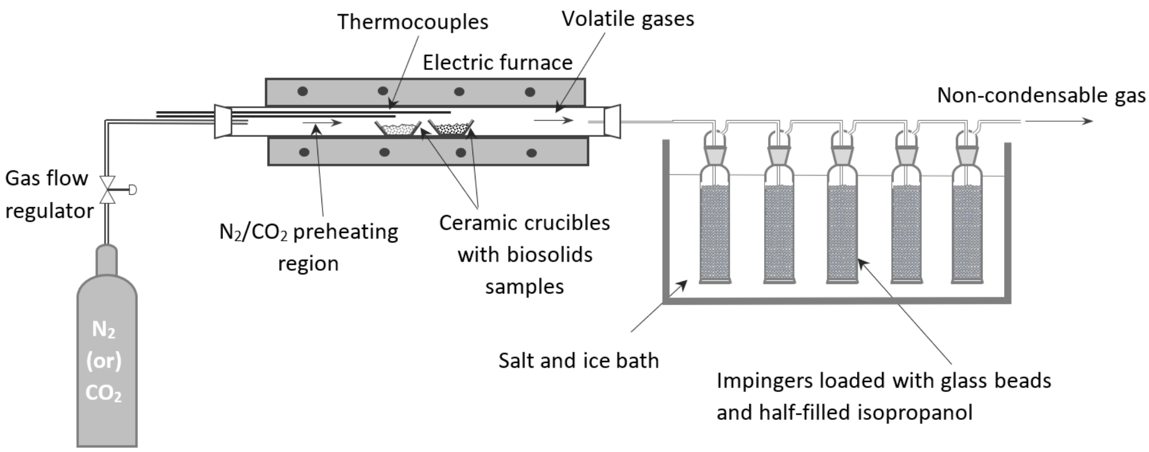

Figure 1. Schematic diagram of experimental set up of a horizontal tube furnace used to produce biosolids chars under pyrolysis and gasification conditions.

The reactor was then electrically heated from ambient temperature to the desired range of 300−1000°C at a controlled heating rate of 15°C per minute. Once the target temperature was achieved, it was held for a duration of 1 hour to ensure thorough elimination of devolatilisation by-products from the biosolids samples. Throughout this entire process, a continuous flow of nitrogen at atmospheric pressure was maintained, with a flow rate of 1 L per minute.

For the production of ash samples under gasification conditions, the same procedure was followed, but instead of N_2, CO_2 with a flow rate of 1 L per minute was employed as the reactant gas. This was carried out at target operating temperatures of 850°C and 950°C for a duration of over 24 hours.

To produce ash samples under combustion conditions, biosolids samples were subjected to oxidation in a high-temperature muffle furnace at temperatures of 580°C and 850°C for a period of 6 hours.

2.3. Char gasification test

Char samples obtained from pyrolysis experiments were used to investigate the CO_2-gasification characteristics of biosolids. Gasification reactivity measurements were conducted using a fixed-bed reactor under atmospheric pressure condition. Detailed information of experimental apparatus, the procedures and formulas used to estimate the reaction rates can be found in our previous publication [10].

2.4. Analysis of mineral matter

The bulk composition of biosolids ashes was assessed through X-ray fluorescence, following the ASTM D3174-12 standard [11]. To identify mineral phases present in dry biosolids, biosolid-derived chars under various pyrolysis conditions, and the ultimate ash samples, X-ray powder diffraction employing copper Kα radiation (λ=1.5406 Å) was utilised. Phase compositions in the powder diffraction patterns and phase content in the samples were identified using HighScore Plus software. Additionally, a separate calculation of phase content was carried out based on peak ratios only, and these results were subsequently compared.

3. Results and discussion

3.1. Pyrolysis behaviour of biosolids

Dried samples of biosolids were first analysed to determine their mineral matter/ash content, following the guidelines of an international standard (EN 14775:2009). The examination of biosolids samples using this standard method revealed an ash content of 39.8%. This figure is significantly greater than the ash content found in other types of agriculture-derived biomass known for their high ash content, such as rice husks [12-14] and green waste [15, 16]. The high ash content of biosolids could cause significant obstacles when considering their utilisation in thermochemical conversion systems, such as combustion and gasification processes. These challenges arise from the necessity for frequent ash removal and the potential issues related to sintering and clinker formation within high-temperature combustion zones [17, 18].

Solid yields of the biosolids tested under a large range of temperature are shown in Figure 2. The pyrolysis characteristics of biosolids can be described through a three-stage process: Initially, there is a significant reduction in solid yield between 250 and 400 °C. Subsequently, there are minor observed within the 400–800 °C range, succeeded by another significant drop between 800–1000 °C (refer to Figure 2). In the initial and intermediate stages of pyrolysis, the decrease in solid yield can be attributed to the release of total volatiles from biosolids, primarily originating from organic matter. However, the decline in solids beyond 800°C can be attributed to the release of volatiles, which can be traced back to both organic and inorganic matter.

This assertion is confirmed by measuring the ash contents of biosolids char samples generated at a range of pyrolysis temperature. Figure 2 indicates that the ash yields remained relatively stable for biosolid chars generated through pyrolysis temperatures ranging from 300 to 800 °C. However, a significant reduction in ash yields was observed for biosolid chars produced at pyrolysis temperatures exceeding 800°C.

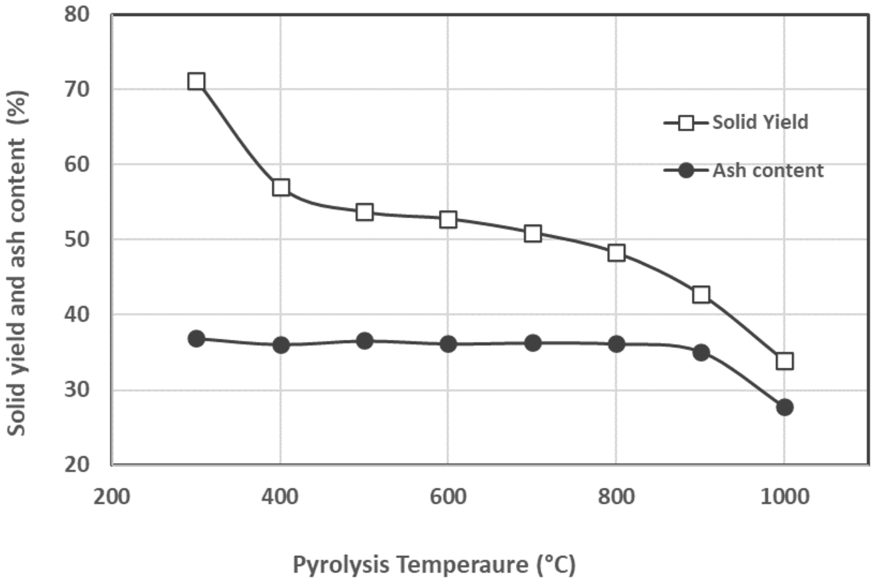

Figure 2. Solid yield of biosolids and their respective ash content tested under different pyrolysis temperatures.

The chemical composition of ashes from untreated biosolids and biosolid-derived chars generated over a range of pyrolysis temperatures is presented in Table 1. It is apparent from the table that there was a substantial reduction in the relative proportions of P_2O_5, SO_3, and ZnO (particularly Phosphor pentoxide) in the chars produced at higher operating temperatures. This phenomenon of mineral matter transitioning into gaseous phases during thermochemical processes has been documented in other research studies [9, 19]. The loss of mineral matter during high-temperature pyrolysis is connected to volatilisation of certain elements under reducing conditions, which will be explored further in the context of XRD analysis.

Table 1. The oxide-based chemical composition (in weight %) of ash derived from untreated biosolids (BS-01) and biosolid chars (BSC) generated through pyrolysis at 300°C, 800°C, 900°C and 1000°C.

	BS- 01	**BSC @ 300°C**	**BSC@800°C**	**BSC@900°C**	**BSC@1000°C**
SiO_2	15.6	16.7	17.0	18.1	21.7
Fe_2O_3	12.1	12.7	12.9	13.7	16.4
Al_2O_3	11.1	12.1	12.3	13.2	15.7
CaO	9.9	9.7	10.9	11.6	13.9
MgO	8.8	5.8	5.6	6.0	7.2
Na_2O	0.65	0.62	0.64	0.71	0.71
K_2O	1.94	1.91	2.0	2.1	2.24
TiO_2	1.1	1.18	1.16	1.31	1.5
P_2O_5	36.9	33.2	33.4	32.4	17.4
Mn_3O_4	0.12	0.12	0.11	0.13	0.15
BaO	0.11	0.11	0.12	0.13	0.16
ZnO	0.28	0.31	0.29	0.07	nd
SO_3	1.32	1.93	1.04	0.27	1.14

Within the initial dried biosolids, much like other biomass types, most inorganic components consist of amorphous inorganic phases and inadequately crystallised mineraloids from diverse groups and classes [20]. As volatiles are released during biosolid pyrolysis reactions, numerous crystalline phases emerge within biosolid chars due to the decomposition of salts and hydrocarbons, especially at elevated temperatures. The XRD spectra of chars produced at varying pyrolysis temperatures are presented in Figure 3.

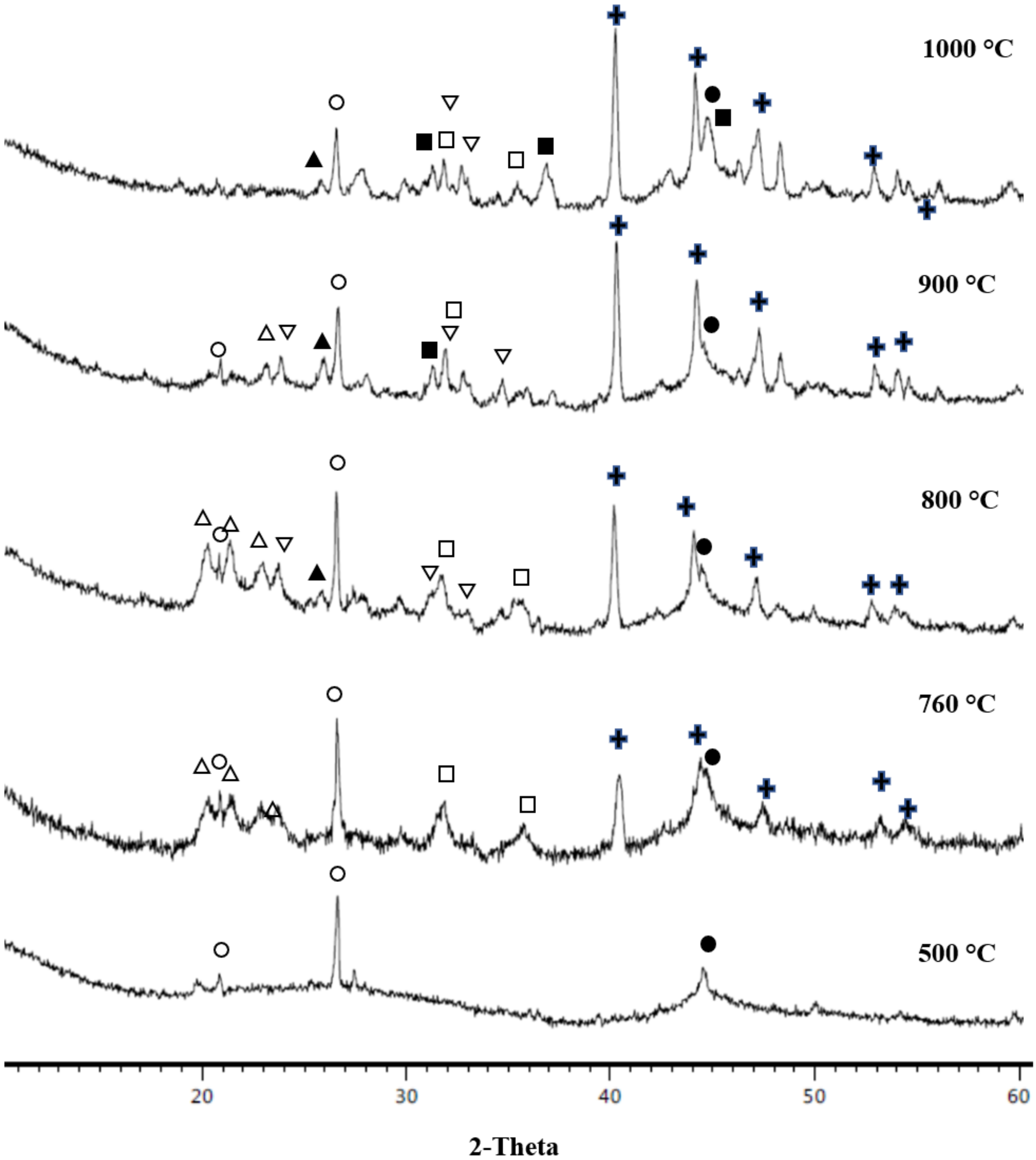

Figure 3. X-ray diffraction patterns of chars processed at different pyrolysis temperatures. Legend: ● - C, ○ - SiO_2, ✚ - Fe_2P, △ - $AlPO_4$, □ - $Al_2CaSi_2O_8$, ▽ - stanfieldite $Ca_4Mg_5(PO_4)_6$, ■ - spinel, $Mg_xFe_{1-x}Al_2O_4$, ▲ - Fe_2O_3.

At relatively lower temperatures, mineral mater in the chars exists predominantly in an amorphous form. For temperatures below 600 °C, only SiO_2 is found in its crystalline form as quartz. As pyrolysis temperatures reach 600 °C and beyond, the growth of $AlPO_4$ and $Al_2CaSi_2O_8$ phases becomes evident. The formation of Fe_2P initiates above 700 °C and prevails as a dominant phase at higher temperatures. At temperatures of 900 °C and above, some phosphorus appears in oxide form as stanfieldite. During this range of high temperatures, spinel and possibly hematite develop, while $AlPO_4$ diminishes within the char produced at 1000 °C of pyrolysis temperature.

3.2. Gasification behaviour of biosolids

The gasification characteristics of biosolid chars, generated at three distinct pyrolysis temperatures (800°C, 900°C, and 1000°C), were examined using a fixed-bed reactor with CO_2 as the reactant gas. To ensure that the effects of devolatilisation during gasification reactions were eliminated, all experiments were conducted at temperatures well below 800 °C. Arrhenius plots were constructed using rate data obtained by cooling the samples at the end of each run. Figure 4 illustrates the reactivity profiles of biosolids chars alongside gasification reactivity rates for different types of urban waste tested under similar range of gasification temperatures [10]. The results of this study indicate that the reactivity data for biosolids are generally consistent with the values found in the existing literature. Specifically, they align closely with data reported for chars produced from wood waste, paper waste, plastic waste, and garden waste.

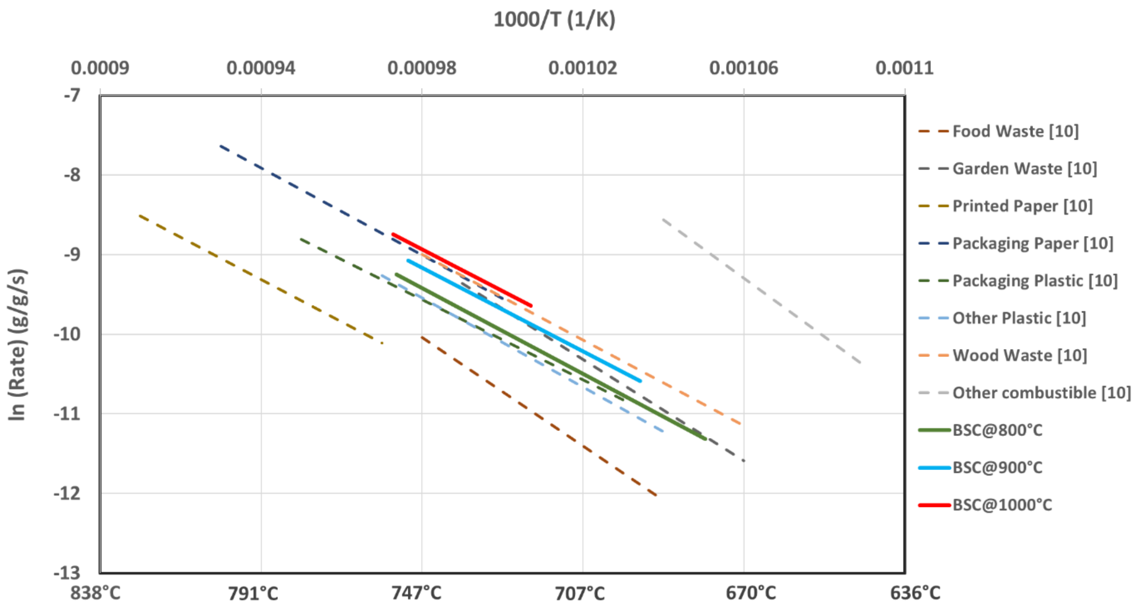

Figure 4. Comparison of Arrhenius plots representing specific reaction rates data for biosolids char with data for urban waste chars available in the literature.

When comparing the gasification reaction rates of biosolid chars produced at various pyrolysis temperatures, it was observed that the gasification rates were lower for samples generated at higher pyrolysis temperatures. This phenomenon is likely attributed to changes in the crystalline structure of the chars produced at elevated pyrolysis temperatures, which supports a catalytic effect favouring metal oxidation reactions that compete with char gasification reactions. As previously discussed, certain crystalline structures form in chars produced at pyrolysis temperatures of 760 °C and above. The gasification reactant gases may thus preferentially react with these crystalline structures, not solely with the carbon within the chars. Consequently, this effect tends to slow the gasification reactions, particularly for chars produced at higher temperatures (900 and 1000 °C).

Figure 5 shows the phase compositions of ash samples prepared at 850°C and 950°C in a CO_2 atmosphere using a horizontal tube furnace. In the process of pyrolysis, there is a lack of gaseous oxygen, and the available oxygen from volatile substances is insufficient to produce all minerals in their crystalline oxide state. Consequently, only a portion of the Si, Al, or Ca elements begins to transform into fine particles of calcium-alumino silicate, alumino, or alumino-magnesium phosphate. This transformation is evident from the broad X-ray diffraction (XRD) peaks illustrated in Figure 3.

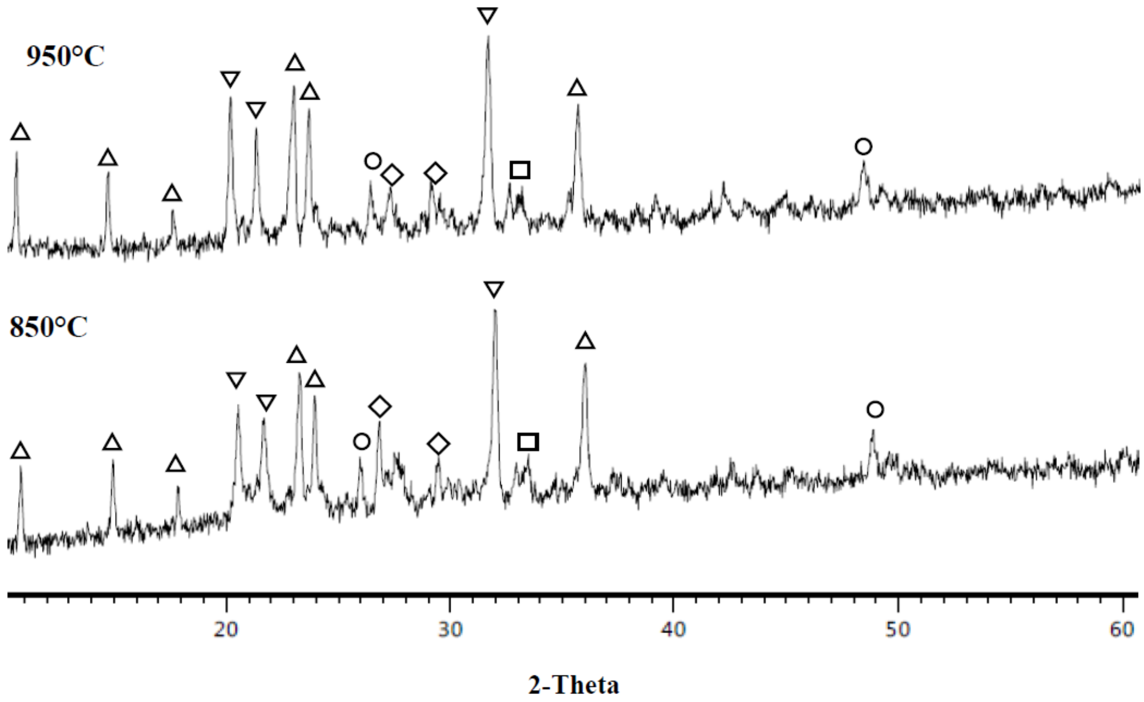

Figure 5. X-ray diffraction patterns of char samples processed in tube furnace with CO_2 at 850°C and 950°C. Legend: ▽ = stanfieldite, $Ca_4Mg_5(PO_4)_6$, △ = aluminium phosphate, $AlPO_4$, □ = spinel, $Mg_xFe_{1-x}Al_2O_4$, ○ = silica, SiO_2, ◇ = silicon diphosphate, SiP_2O_7.

As gasification reactions initiate, a certain amount of oxygen becomes accessible for oxidizing phosphides and facilitating the transformation of minerals into the $Ca_4Mg(Fe)_5(PO_4)_6$, SiP_2O_7 and $AlPO_4$ phases as shown in Figure 5. This occurs through reactions with calcium (Ca), silicon (Si) and magnesium (Mg) sourced from amorphous phases, and potentially from pre-existing crystalline phases. In the context of gasification reactions, the degree of crystallinity in the $Ca_4Mg(Fe)_5(PO_4)_6$ and $AlPO_4$ phases exhibits a slight increase compared to other crystalline phases. This phenomenon suggests that a greater quantity of cations becomes accessible from the amorphous phase as chars/ash undergo processing under gasification conditions.

3.3. Analysis of trace elements in biosolids ash produced under combustion and gasification conditions
Concentrations of trace elements were determined by inductively coupled plasma-atomic emission spectroscopy and inductively coupled plasma-mass spectrometry according to ASAS1038.10.0, (for Hg by Combustion/CVAAS), AS1038.10.4 (for F by Pyrohydrolysis/ISE), and NQ939 (for Cl by Eschka Fusion/UVVIS) standards. The phase composition of ash samples was identified using X-ray diffraction (XRD). The High Score Plus software package was used to identify mineral species.

Concentrations of trace elements in biosolid ashes produced under combustion (580°C and 850°C) and gasification conditions (850°C and 950°C) are listed in Table 2 and compared with trace elements in municipal solid waste (combined all waste streams) [21] and local regulations (QLD) [22].

As, Cd and Pb were found more volatile at gasification conditions, while Mo concentration in gasification ashes is twice higher than that one in combustion ashes. Fluorine is highly volatile in combustion ashes processed at 850°C than at 580°C, but less volatile at gasification at 850°C.

Concentrations of Sb and Se also decrease with processing temperature, and less volatile at gasification atmosphere. Zinc became partially volatile only at 950°C gasification.

Comparing with MSW biosolid ashes have much lower concentrations of Cr, Zn, but higher Ba and Pb (only ashes from combustion). Due to high Pb and Ni levels, biosolids ash may be categorised as Class V (Intractable). However, if its leachability is below the ASLP4 limit, it can be classified as Class IV (secure) [22].

Table 2. Comparison of Concentrations of trace elements in biosolid ashes generated under combustions and gasification conditions at different operating temperatures

	As	**B**	**Sb**	**Se**	**F(db)**	**Hg**	**Ba**	**Be**	**Cr**	**Cu**	**Mo**	**Ni**	**V**	**Zn**	**Ag**	**Cd**	**Pb**
BSA_C580°C	15.8	136	7.1	1.1	1103	nd	980	0.12	**197**	1280	48.2	98.4	52.5	**2360**	9.8	5.03	**108.4**
BSA_C850°C	13.1	93	3	0	39	nd	1000	0	**273**	1290	46.2	**256**	74.9	**2380**	10	3.91	**101**
BSA_G850°C	2.1	124	5.1	0.5	254	nd	997	0	**202**	1290	82.7	**162**	57.4	**2300**	10.2	0.03	19.87
BSA_G950°C	0.5	142	3.5	0.3	0	nd	1020	0.13	**208**	1400	61.5	**203**	63.9	**1620**	9	0	3.43
MSW [21]	169.7	176	70	0.2	210	0.0	491	0.5	**944**	483	39.2	62	22.4	**5159**	0.2	0.6	47
QLD not Reg	<200	<3700	<60	<110	<30000	<6	<40000	<1200	<10 (hex.)	-	<1100	<110	<172	<30	<1	<2	<34
QLD Reg	>200	>3700	>60	>110	>30000	>6	>40000	>1200	>10	-	>1100	>110	>172	>30	>1	>2	>34

BSA_C580°C = Biosolids ash produced at combustion at 580°C; BSA_C850°C = Biosolids ash produced at combustion at 850°C BSA_G850°C = Biosolids ash produced at gasification at 850°C; BSA_G950°C = Biosolids ash produced at gasification at 950°C

4. Summary and conclusion

This study examined the gasification characteristics of biosolids chars and how thermochemical processes and conditions impact mineral matter transformation. We produced char and ash samples from biosolids under various conditions and found that pyrolysis solid yield drops significantly at 300−500 °C and 800−1000 °C. Pyrolysis temperature influenced organic and inorganic matter release; below 800 °C released mainly organic species, whereas higher temperatures led to losses of phosphorus, magnesium, and zinc.

Mineral matter in chars produced at temperatures below 600 °C exhibited an amorphous structure, but at higher temperatures, it transformed into crystalline phases, primarily as oxides and phosphides. Under gasification conditions, all crystalline phases within the chars/ash appear in oxide forms. The study also compared trace element (TE) levels in biosolids chars with Queensland state environmental regulations. Due to elevated levels of lead (Pb) and nickel (Ni), biosolids ash may fall under Class V (Intractable) categorization unless its leachability remains below the ASLP4 limit, in which case it can be classified as Class IV (secure).

In conclusion, the study showed that mineral matter forms in biosolids chars and ashes are significantly influenced by varying operating temperature and processing conditions in different thermochemical processes.

5. References

[1] Raheem, A., Sikarwar, V. S., He, J., Dastyar, W., Dionysiou, D. D., Wang, W., & Zhao, M. (2018). Opportunities and challenges in sustainable treatment and resource reuse of sewage sludge: A review. *Chemical Engineering Journal*, *337*, 616-641.

[2] Kim, K. R., & Owens, G. (2011). 6.21 - Potential for Enhanced Phytoremediation of Landfills Using Biosolids – A Review. In M. Moo-Young (Ed.), *Comprehensive Biotechnology (Third Edition)* (pp. 276-284). Pergamon.

[3] Darvodelsky, P. (2011). *Biosolids snapshot*, Department of Sustainability, Environment, Water, Population and Communities, 2011.

[4] Fenwick, G. (2016, 31 August - 1 September, 2016). Achiving the biosolids strategy at Sandgate Sewage Treatment Plant. 79th Annual WIOA Victorian Water Industry Operations Conference and Exhibition, Bendigo, VIC, Australia.

[5] Tyagi, V. K., & Lo, S.-L. (2013). Sludge: A waste or renewable source for energy and resources recovery? *Renewable and Sustainable Energy Reviews*, *25*(Supplement C), 708-728.

[6] Gao, N., Quan, C., Liu, B., Li, Z., Wu, C., & Li, A. (2017). Continuous Pyrolysis of Sewage Sludge in a Screw-Feeding Reactor: Products Characterization and Ecological Risk Assessment of Heavy Metals. *Energy & Fuels*, *31*(5), 5063-5072.

[7] Choi, Y.-K., Ko, J.-H., & Kim, J.-S. (2017). A new type three-stage gasification of dried sewage sludge: Effects of equivalence ratio, weight ratio of activated carbon to feed, and feed rate on gas composition and tar, NH 3 , and H 2 S removal and results of approximately 5 h gasification. *Energy*, *118*, 139-146.

[8] Roche, E., de Andrés, J. M., Narros, A., & Rodríguez, M. E. (2014). Air and air-steam gasification of sewage sludge. The influence of dolomite and throughput in tar production and composition. *Fuel*, *115*(Supplement C), 54-61.

[9] Gil-Lalaguna, N., Sánchez, J. L., Murillo, M. B., Rodríguez, E., & Gea, G. (2014). Air–steam gasification of sewage sludge in a fluidized bed. Influence of some operating conditions. *Chemical Engineering Journal*, *248*, 373-382.

[10] Hla, S. S., Lopes, R., & Roberts, D. (2016). The CO_2 gasification reactivity of chars produced from Australian municipal solid waste. *Fuel*, *185*, 847-854.

[11] ASTM International. (2019). ASTM D3174-12: Standard Test Method for Ash in the Analysis Sample of Coal and Coke from Coal. In (pp. 1-6). West Conshohocken, PA: American Society for Testing and Materials.

[12] Liu, H., Wang, Y., Hu, H., Fu, B., Yao, H., & Wendt, J. O. L. (2020). Enrichment mechanism of arsenic in fine ash deposits during co-combustion of rice husk and coal. *Fuel*, *281*, 118712.

[13] Zheng, S., Yang, Y., Li, X., Liu, H., Yan, W., Sui, R., & Lu, Q. (2020). Temperature and emissivity measurements from combustion of pine wood, rice husk and fir wood using flame emission spectrum. *Fuel Processing Technology*, *204*, 106423.

[14] Zulqar Nain, M., & Kasilingam, S. (2023). Influence of rice husk ash and bagasse ash on durability of concrete. *Materials Today: Proceedings*.

[15] Hla, S. S., & Roberts, D. (2015). Characterisation of chemical composition and energy content of green waste and municipal solid waste from Greater Brisbane, Australia. *Waste Management*, *41*, 12-19.

[16] Ipiales, R. P., Mohedano, A. F., Diaz, E., & de la Rubia, M. A. (2022). Energy recovery from garden and park waste by hydrothermal carbonisation and anaerobic digestion. *Waste Management*, *140*, 100-109.

[17] Skoglund, N., Bäfver, L., Fahlström, J., Holmén, E., & Renström, C. (2016). Fuel design in co-combustion of demolition wood chips and municipal sewage sludge. *Fuel Processing Technology*, *141*, 196-201.

[18] Gao, N., Kamran, K., Quan, C., & Williams, P. T. (2020). Thermochemical conversion of sewage sludge: A critical review. *Progress in Energy and Combustion Science*, *79*, 100843.

[19] Bläsing, M., & Müller, M. (2013). Release of alkali metal, sulphur, and chlorine species from high temperature gasification of high- and low-rank coals. *Fuel Processing Technology*, *106*, 289-294.

[20] Vassilev, S. V., Baxter, D., Andersen, L. K., Vassileva, C. G., & Morgan, T. J. (2012). An overview of the organic and inorganic phase composition of biomass. *Fuel*, *94*, 1-33.

[21] Ilyushechkin, A., He, C., & Hla, S. S. (2020). Characteristics of inorganic matter from Australian municipal solid waste processed under combustion and gasification conditions. *Waste Manag Res*, *39*(7), 928-936.

[22] Department of Water and Environmental Regulations. (2019). *Landfill Waste Classification and Waste Definitions 1996 (as amended 2019)*. https://www.der.wa.gov.au/images/documents/our-work/licences-and-works-approvals/WasteDefinitions-revised.pdf

ETM0012

An Alternative Approach for Determining Charge Storage Mechanisms of Supercapacitors Using Sinusoidal Potential Scan

W Pholauyphon[1], K Nantasaksiri[2], T Suzuki[3], S Tsushima[3], and P Charoen-amornkitt[1,*]

[1]Electrochemical Energy Storage and Conversion Laboratory, Department of Mechanical Engineering, Faculty of Engineering, King Mongkut's University of Technology Thonburi, 126 Pracha Uthit Rd., Bang Mod, Thung Khru, Bangkok 10140, Thailand
[2]Mobility & Vehicle Technology Research Center, King Mongkut's University of Technology Thonburi, 126 Pracha Uthit Rd., Bang Mod, Thung Khru, Bangkok, 10140, Thailand
[3]Department of Mechanical Engineering, Graduate School of Engineering, Osaka University, Suita, Osaka 565-0871, Japan

* Corresponding Author: patcharawat.cha@kmutt.ac.th (P.Charoen-amornkitt)

Abstract. While the progress in novel designs of electrode materials has significantly improved energy storage device performance, particularly supercapacitors, understanding their impact on charge storage mechanisms remains uncertain. Moreover, the diversity of analytical techniques used for investigating these mechanisms often yields markedly different results, hindering effective comparison and comprehension of the underlying processes. To address these challenges, this work focuses on proposing an alternative approach to determine the contribution of charge storage. The results will be assessed in a similar manner to the conventional methods such as Trasatti's and Dunn's methods, which are typically employed in cyclic voltammetry (CV) measurements. Conventionally, CV measurements utilize cyclic triangular potential scans to investigate current responses. In this work, we specifically propose voltammetric measurements using a sinusoidal potential scan. Not only is this approach simple and easy to employ, but its responses can be conveniently utilized for further characterization, providing consistent results regardless of the analytical approaches. Thus, this approach enables a comprehensive understanding of the fundamental aspects of charge storage mechanisms. This research thus holds significant value for those involved in the development of supercapacitors, as it paves the way for advancements in future supercapacitors.

Keywords: Cyclic voltammetry, Modeling, Sinusoidal potential signal, Charge storage mechanism.

1. Introduction

Amidst rapid societal evolution and increasing demand for renewable and green energy, the generation of this energy depends on the variability of energy sources based on location and time. Consequently, there has been a significant surge of interest in energy storage devices [1]. Fuel cells, batteries, and electrochemical supercapacitors play pivotal roles in electrochemical energy storage systems, serving as essential components for enabling sustainable energy conversion and storage from renewable sources. However, special attention has been directed towards supercapacitors as pioneering solutions for advanced energy storage devices. These technologies [2] find extensive applications in automotive systems, backup power systems, etc. Supercapacitors, in particular, possess the unique capability to complete charging or discharging within seconds [3, 4]. Thanks to their remarkable power density, supercapacitors are poised to overcome the limitations posed by traditional energy storage devices, such as lithium-ion batteries [5]. Their rapid response and impressive performance make them a promising candidate for addressing the evolving energy storage landscape. However, their energy density is relatively poor, making it challenging for widespread commercialization.

To address the issue of low energy density in supercapacitors, numerous researchers have been engaged in the development of advanced electrode materials aimed at achieving high-performance supercapacitors [6-11]. However, recent efforts have not solely focused on novel materials and architectures, they have also been oriented toward comprehending the fundamental physical mechanisms that underlie charge storage within these materials. To this end, electrochemical characterization remains indispensable for comprehending and optimizing supercapacitor performance. Cyclic voltammetry (CV) is an electroanalytical method typically used for identifying charge storage mechanisms [12-14]. Conventionally, the cyclic triangular potential scan is used as an input and the total current is measured as an output. Previous studies [15-18] derived analytical and numerical correlations to provide insight into the relationship between the experimental conditions and the measured current. As of now, researchers have a consensus that interpreting CV data is a challenging task, and those correlations can be used in a very limited case [19].

Trasatti's [20] and Dunn's [21] approaches, which are the approaches typically used to characterize charge storage mechanisms, were developed based on such understanding where the diffusion-controlled contribution (response from a redox reaction) is a function of the scan rate to the power of 1/2 and the surface-controlled contribution (response from electric double layer) is a function of the scan rate to the power of 1. This is because they assumed that the diffusion-controlled process should follow the Randles-Sevcik equation. However, in practice, it is widely known that the response of the electric double layer does not follow the function of the scan rate to the power of 1, as shown in our previous study [22]. The response of an electric double layer will follow such a function only if it behaves as a pure capacitor. However, the electric double layer often behaves similarly to the constant phase element (CPE) in a practical situation [13, 22]. As Trasatti's and Dunn's methods rely on assumptions and simplifications, their accuracy hinges on specific conditions, and in many circumstances, the outcomes of these two methods differ, posing challenges in precisely identifying charge storage mechanisms and developing high-performance electrode materials.

However, our recent study carefully investigated the effects of different input waveforms and analytical methods on capacitance measurement in electric double layer capacitor applications [22]. The results revealed that the difference in capacitance often found in literature arises due to the cyclic triangular potential waveform. We then proposed an alternative approach to estimate the capacitance of a CPE using a sinusoidal potential scan in voltammetric measurements to unify the measured capacitance analyzed by different approaches. This gives rise to the question of what if such a sinusoidal potential scan was used in the analysis that carries out a similar manner to Trasatti's and Dunn's approaches. Therefore, in the study, we employed a well-established model developed by Charoen-amornkitt et al. [23] to simulate voltammetric behaviors using sinusoidal potential scans. This model incorporates resistances and a CPE into the physiochemical transport model, with a CPE representing the electric double layer. Trasatti's and Dunn's approaches were modified to fit with the sinusoidal potential scans and the results from both approaches were compared. Therefore, the objective of this study is to propose an alternative approach to unify charge storage mechanism characterization. The study seeks a way to make researchers be able to compare their results and communicate new research findings so that supercapacitor technology can be progressed. The findings of this study hold great significance for the advancement of charge storage mechanism characterization and pave the way for future research breakthroughs in the realm of high-performance energy storage materials.

2. Modified Trasatti's and Dunn's methods

2.1. Trasatti's method

The total capacitance (C_T) can be determined by combining diffusion-controlled capacitance (C_i) and surface-controlled capacitance (C_o) through the utilization of Eq. (1) [20].

$$C_T = C_i + C_o \tag{1}$$

Assuming the semi-infinite linear diffusion, the capacitance as a function of scan rate ($C(v)$) is inversely proportional to $v^{1/2}$, according to Eq. (2) [20]:

$$C(v) = \frac{Slope}{v^{1/2}} + C_o \tag{2}$$

In the scenario of an infinitely high scan rate ($v \rightarrow \infty$), the capacitance converges to C_o, given the hindrance of inner material diffusion. Utilizing the aforementioned equation, determining C_o is as straightforward as identifying the y-intercept on the plot correlating $C(v)$ and $v^{-1/2}$. Conversely, as the scan rate approaches zero, the capacitance reaches its peak, owing to the elimination of diffusion constraints. In this case, C_T can be obtained by getting the y-intercept of the $1/(C(v))$ vs $v^{1/2}$ plot, corresponding to Eq. (3) [20].

$$\frac{1}{C(v)} = slope \times v^{1/2} + \frac{1}{C_T} \tag{3}$$

By employing Eq. (1), the C_T and C_o discrepancy can be utilized to derive C_i. In the context of voltammetry using a sinusoidal potential scan, Equation (1) was adapted by replacing the parameter '*C*' with 'accumulated charge (*Q*).' Consequently, the total accumulated charge (Q_T) is a sum of both outer (Q_o) and inner (Q_i) surface charges, as described in Eq. (4).

$$Q_T = Q_i + Q_o \tag{4}$$

Furthermore, Eqs. (2) and (3) were adjusted to incorporate the applied frequency (*f*, Hz) in place of '*v*,' as illustrated below:

$$Q(v) = \frac{Slope}{f^{1/2}} + Q_o \tag{5}$$

$$\frac{1}{Q(f)} = slope \times f^{1/2} + \frac{1}{Q_T} \tag{6}$$

2.2. Dunn's method

In accordance with Dunn's approach [21], the current response noted at a consistent potential is ascribable to two discrete mechanisms: surface-controlled and diffusion-controlled mechanisms. Considering that the diffusion-controlled current adheres to $v^{1/2}$, while the surface-controlled current is contingent upon *v*, the association between current response ($i(v)$) at a constant potential is expressed as detailed in Eq. (7) [21].

$$i(v) = k_1 v + k_2 v^{1/2} \tag{7}$$

where $i(v)$ refers to the current response at a fixed potential, while k_1 and k_2 represent the coefficients for surface-controlled and diffusion-controlled processes, respectively. In the context of voltammetry involving a sinusoidal potential scan, the scan rate is adjusted in response to changes in potential voltage by using Eq. (8).

$$v = 2\pi f(\Delta V / 2)\sin(2\pi f t_{\Delta V}) \tag{8}$$

where Δv represents window voltage (V), and $t_{\Delta V}$ represents the time for applying one cycle of window voltage (s). Furthermore, the equation was additionally modified by dividing it by $v^{1/2}$ and is demonstrated as follows [21]:

$$\frac{i(v)}{v^{1/2}} = k_1 v^{1/2} + k_2 \tag{9}$$

Therefore, the slope and y-intercept extracted from the plot of $i(v)/v^{1/2}$ vs $v^{1/2}$ yield k_1, and k_2, respectively. These derived constants enable the computation of capacitive and diffusion-controlled contributions at each measured potential of the CV scan, as outlined in Eq. (5).

Typically, when exploring models to predict the responses of experimental voltammetric measurements, simpler reactions are often considered. In this study, we conducted a numerical simulation of voltammetric behavior using Charoen-amornkitt's model [23], which incorporates resistances and CPEs into the conventional physicochemical transport model through circuit analysis. This model is capable of predicting the response of a system that includes both faradaic and capacitive currents. Additionally, we adapted our developed model from Charoen-amornkitt et al.'s model [23] by replacing the triangular potential scan with a sinusoidal potential waveform function. This modification results in the expression of the time-dependent electric potential (V_{app}) at the electrode, as demonstrated in Eq. (10).

$$V_{app} = V_0 \sin(\omega t) \tag{10}$$

where V_0 represents the magnitude of the electric potential.

3. Results and discussions

In this study, we employed our developed model to simulate voltammetric measurements using a sinusoidal potential scan at various applied frequencies. This approach aims to investigate the identification of charge storage mechanisms through traditional analysis. To gain deeper insights into the impact of transitioning from a triangular to a sinusoidal potential waveform on the outcomes derived

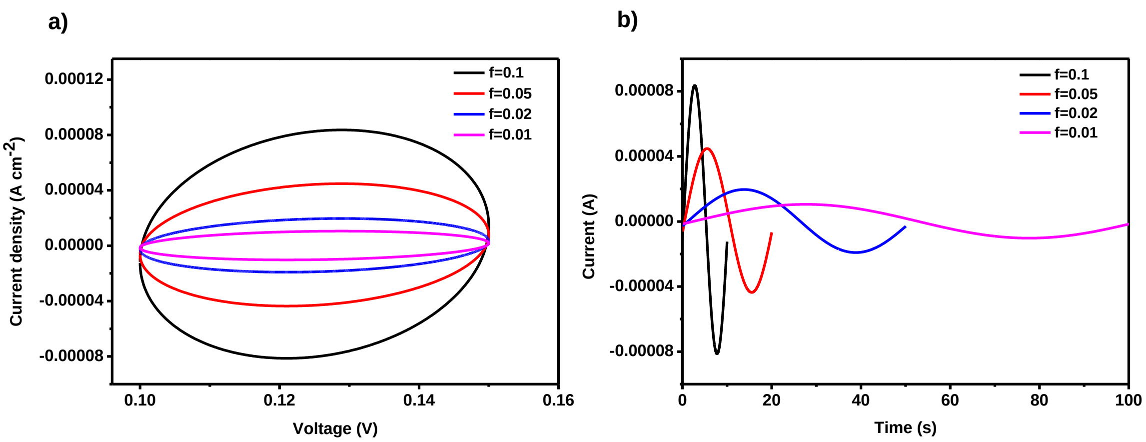

Figure 1. The illustrations of (a) voltammetric measurements conducted using a sinusoidal potential scan at different frequencies (f = 0.01, 0.02, 0.05, 0.1 Hz), and (b) the plot of current (i) as a function of time (t) across these various frequencies.

from Trasatti's and Dunn's methods, we utilized the simulated voltammetric data (see Figure 1a) as a sample dataset to investigate the identification of charge storage mechanisms.

Trasatti's method can be adapted to accommodate sinusoidal potential scans, enabling the quantitative determination of the percentage contribution from both diffusion-controlled and surface-controlled effects, as illustrated in Eq. (4). Figure 1(b) illustrates the relationship between current (i) and time (t, seconds) at different applied frequencies, corresponding to their volumetric behaviors. Integration of the i vs. t plots yields the accumulated charge at each frequency ($Q(f)$). Subsequently, the $Q(f)$ was used to create linear fits, as depicted in Figures 2(a) and (b), based on Eqs. (5) and (6), respectively. Moreover, the y-intercepts obtained from Eq. (5) and (6) allow for the determination of Q_o and Q_T, respectively. The Q_i was consequently calculated using Eq. (4). In order to investigate the influence of frequency on the charge storage mechanism, we employed the slope derived from the linear fit of the plot correlating $Q(f)$ with $Q(f)$ *vs.* $1/f^{1/2}$ to calculate the percentage of charge storage contribution, as illustrated in Figure 2(d).

Dunn's [14] approach was adjusted to accommodate sinusoidal potential scans by modifying the frequency to be scan rate as a function of time, which significantly differs from the scan rate applied in the case of the triangular potential waveform that maintains a constant scan rate throughout the entire voltage window. Furthermore, we collected the current data at a voltage of 0.025V, which corresponds to the midpoint of the voltammetric curves, and utilized it in Eq. (9). Figure 2(c) depicts the relationship between $i(v)/v^{1/2}$ and $v^{1/2}$, from which the slope (k_1) and the y-intercept (k_2) were extracted, representing surface-controlled and diffusion-controlled mechanisms, respectively. Subsequently, we utilized the

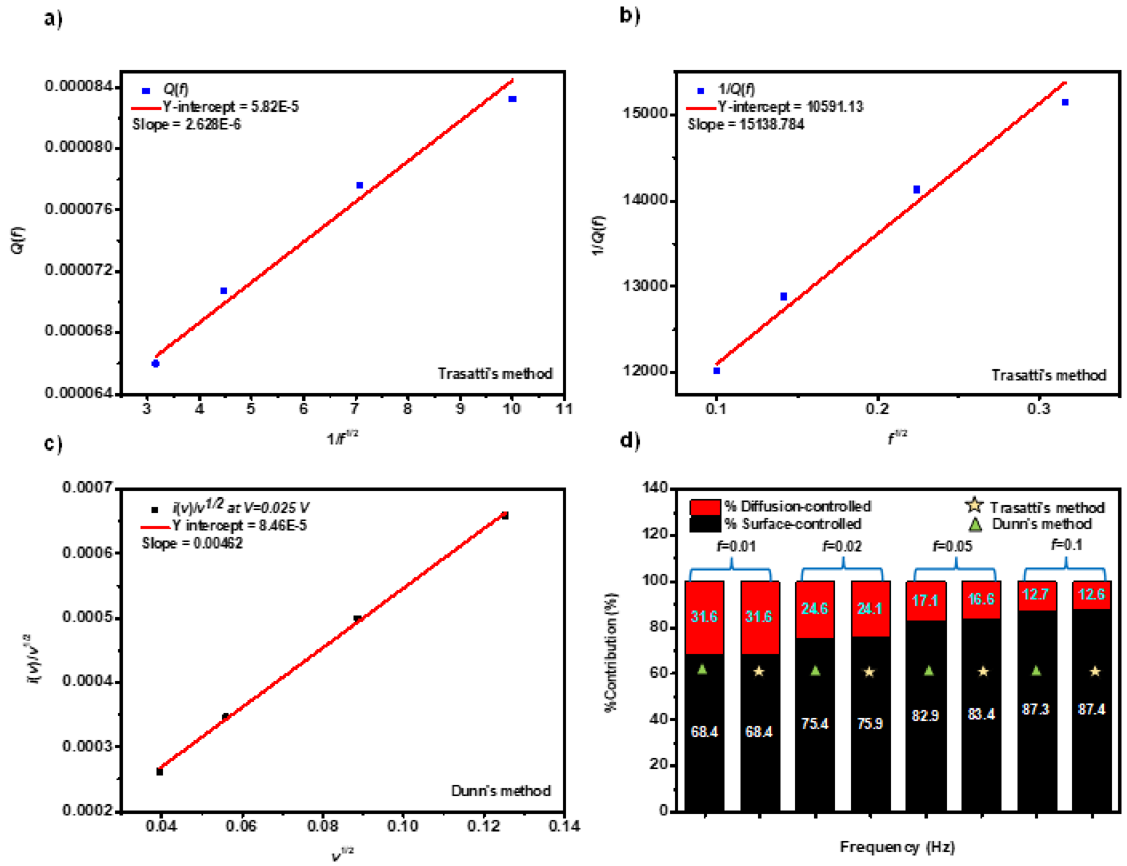

Figure 2. Plots illustrating the correlation between the following parameters: (a) $Q(f)$ *vs.* $1/f^{1/2}$, (b) $1/Q(f)$ *vs.* $f^{1/2}$, (c) $i(v)/v^{1/2}$ *vs.* $v^{1/2}$, and (d) the calculated percentage of charge storage contribution using Dunn's and Trasatti's methods at various applied frequencies.

values of k_1 and k_2 in Eq. (7) to establish the charge storage contributions attributed to surface-controlled and diffusion-controlled mechanisms as functions of frequency (Figure 2(d)).

Figure 2(d) presents a comparison of the calculated results obtained from both approaches. Notably, the results indicate that the calculated percentage of charge storage contribution, as determined by Trasatti's [20] and Dunn's [21] methods, does not exhibit significant differences across all frequencies. Given that Trasatti's and Dunn's methods are reliant on assumptions and simplifications, their accuracy is contingent upon specific conditions. Consequently, in numerous scenarios, disparities arise between the results obtained using these two methods. However, this study can prove that one vital key to the difference in results from both methods can be attributed to the applied triangular scan. These results can be explained by CPE behavior applied in our developed model [22, 23].

Hence, this study presents an alternative method aimed at standardizing the characterization of charge storage mechanisms from both approaches. This endeavour seeks to provide researchers with a means to compare their results and share new findings, thereby fostering progress in supercapacitor technology. The outcomes of this study bear significant importance for advancing the field of charge storage mechanism characterization, paving the path for potential breakthroughs in research concerning high-performance energy storage materials.

4. Conclusion

In this study, we introduce a sinusoidal potential scan-based voltammetric measurement method. This approach is not only straightforward and convenient to implement but also serves as a practical tool for characterizing charge storage mechanisms, producing consistent experimental results across different analytical techniques, including Trasatti’s and Dunn’s method. As a result, this study highlights that the transition from a triangular to a sinusoidal potential waveform in applied experiments can reconcile the calculated results obtained through Trasatti's and Dunn's methods. Such reconciliation has not been previously observed in prior research. This finding indicates that the variations in charge storage contribution, as frequently observed in the literature, can be attributed to the use of cyclic triangular potential waveforms. Moreover, these results suggest that the fluctuations in charge storage contributions, commonly noted in the literature, may be attributed to the utilization of cyclic triangular potential waveforms. Consequently, this study introduces an alternative approach to unify the calculated charge storage mechanisms analyzed by Trasatti's and Dunn's methods, leading to prevent misunderstanding and confusion in the characterization of electrode materials' charge storage properties in future research. As such, this study holds substantial significance for individuals engaged in supercapacitor development, laying the groundwork for future advancements in the field.

5. Acknowledgment

Dr. Wasinee Pholauyphon would like to express her sincere appreciation for the Postdoctoral Fellowship from King Mongkut’s University of Technology Thonburi. The authors would like to extend their heartfelt appreciation to Thailand Science Research and Innovation (TSRI).

6. References

[1] Arunachalam, S., B. Kirubasankar, D. Pan, H. Liu, C. Yan, Z. Guo, and S. Angaiah. (2020). Research progress in rare earths and their composites based electrode materials for supercapacitors. *Green Energy & Environment, 5*(3), 259-273. doi: https://doi.org/10.1016/j.gee.2020.07.021

[2] Rahman, M.M., P.M. Joy, M.N. Uddin, M.Z.B. Mukhlish, and M.M.R. Khan. (2021). Improvement of capacitive performance of polyaniline based hybrid supercapacitor. *Heliyon, 7*(7), e07407. doi: https://doi.org/10.1016/j.heliyon.2021.e07407

[3] He, X. and X. Zhang. (2022). A comprehensive review of supercapacitors: Properties, electrodes, electrolytes and thermal management systems based on phase change materials. *Journal of Energy Storage, 56*, 106023. doi: https://doi.org/10.1016/j.est.2022.106023

[4] Samantaray, S., D. Mohanty, I.M. Hung, M. Moniruzzaman, and S.K. Satpathy. (2023). Unleashing recent electrolyte materials for next-generation supercapacitor applications: A comprehensive review. *Journal of Energy Storage, 72*, 108352. doi: https://doi.org/10.1016/j.est.2023.108352

[5] El Issmaeli, Y., A. Lahrichi, S.S. Kalanur, S.K. Natarajan, and B.G. Pollet. (2023). Recent Advances and Prospects of FeOOH-Based Electrode Materials for Supercapacitors. *Batteries, 9*(5), 259.
[6] Dong, W., M. Xie, S. Zhao, Q. Qin, and F. Huang. (2023). Materials design and preparation for high energy density and high power density electrochemical supercapacitors. *Materials Science and Engineering: R: Reports, 152*, 100713. doi: https://doi.org/10.1016/j.mser.2022.100713
[7] Sammed, K.A., A. Farid, S. Mustafa, A. Kumar, M. Tabish, A.A. Khan, S. Ajmal, Z. Mo, A.R. Akbar, G. Yasin, Y.-j. Zeng, and W. Zhao. (2023). Developing next-generation supercapacitor electrodes by coordination chemistry-based advanced functional carbon nanostructures: Progress, Current challenges and prospects. *Fuel Processing Technology, 250*, 107896. doi: https://doi.org/10.1016/j.fuproc.2023.107896
[8] Cui, D., R. Wang, C. Qian, H. Shen, J. Xia, K. Sun, H. Liu, C. Guo, J. Li, F. Yu, and W. Bao. (2023). Achieving High Performance Electrode for Energy Storage with Advanced Prussian Blue-Drived Nanocomposites—A Review. *Materials, 16*(4), 1430.
[9] Forouzandeh, P., V. Kumaravel, and S.C. Pillai. (2020). Electrode Materials for Supercapacitors: A Review of Recent Advances. *Catalysts, 10*(9), 969.
[10] Pholauyphon, W., R.N. Bulakhe, J. Praneerad, R. Attajak, J. Manyam, I. In, and P. Paoprasert. (2021). Ultrahigh-performance titanium dioxide-based supercapacitors using sodium polyacrylate-derived carbon dots as simultaneous and synergistic electrode/electrolyte additives. *Electrochimica Acta, 390*, 138805. doi: https://doi.org/10.1016/j.electacta.2021.138805
[11] Pholauyphon, W., R.N. Bulakhe, J. Manyam, I. In, and P. Paoprasert. (2022). Enhancing Supercapacitor Performance Using Carbon Dots as Versatile Additives in Both Titanium Dioxide-Based Electrodes and Sodium Sulfate Electrolytes. *Energy & Fuels, 36*(8), 4564-4576. doi: 10.1021/acs.energyfuels.2c00060
[12] Charoen-Amornkitt, P., T. Suzuki, and S. Tsushima. (2019). Determination of Constant Phase Element Parameters under Cyclic Voltammetry Conditions Using a Semi-theoretical Equation. *Electrochemistry, 87*(4), 204-213. doi: 10.5796/electrochemistry.18-00082
[13] Charoen-amornkitt, P., T. Suzuki, and S. Tsushima. (2017). Ohmic resistance and constant phase element effects on cyclic voltammograms using a combined model of mass transport and equivalent circuits. *Electrochimica Acta, 258*, 433-441. doi: https://doi.org/10.1016/j.electacta.2017.11.079
[14] Gharbi, O., M.T.T. Tran, B. Tribollet, M. Turmine, and V. Vivier. (2020). Revisiting cyclic voltammetry and electrochemical impedance spectroscopy analysis for capacitance measurements. *Electrochimica Acta, 343*, 136109. doi: https://doi.org/10.1016/j.electacta.2020.136109
[15] Aristov, N. and A. Habekost. (2015). Cyclic Voltammetry - a versatile electrochemical method investigating electron transfer processes. *World J. Chem. Educ., 3*(5), 115-119. doi: 10.12691/wjce-3-5-2
[16] Liu, J., J. Wang, C. Xu, H. Jiang, C. Li, L. Zhang, J. Lin, and Z.X. Shen. (2018). Advanced energy storage devices: Basic principles, analytical methods, and rational materials design. *Adv. Sci., 5*(1), 1700322. doi: 10.1002/advs.201700322
[17] Sathiya, M., A.S. Prakash, K. Ramesha, J.M. Tarascon, and A.K. Shukla. (2011). V2O5-Anchored Carbon Nanotubes for Enhanced Electrochemical Energy Storage. *J. Am. Chem. Soc., 133*(40), 16291-16299. doi: https://doi.org/10.1021/ja207285b
[18] Lindström, H., S. Södergren, A. Solbrand, H. Rensmo, J. Hjelm, A. Hagfeldt, and S.-E. Lindquist. (1997). Li+ Ion Insertion in TiO2 (Anatase). 2. Voltammetry on Nanoporous Films. *The Journal of Physical Chemistry B, 101*(39), 7717-7722. doi: 10.1021/jp970490q
[19] Mathis, T.S., N. Kurra, X. Wang, D. Pinto, P. Simon, and Y. Gogotsi. (2019). Energy Storage Data Reporting in Perspective—Guidelines for Interpreting the Performance of Electrochemical Energy Storage Systems. *Advanced Energy Materials, 9*(39), 1902007. doi: https://doi.org/10.1002/aenm.201902007
[20] Ardizzone, S., G. Fregonara, and S. Trasatti. (1990). “Inner” and “outer” active surface of RuO_2 electrodes. *Electrochimica Acta, 35*(1), 263-267. doi: https://doi.org/10.1016/0013-4686(90)85068-X
[21] Wang, J., J. Polleux, J. Lim, and B. Dunn. (2007). Pseudocapacitive Contributions to Electrochemical Energy Storage in TiO2 (Anatase) Nanoparticles. *The Journal of Physical Chemistry C, 111*(40), 14925-14931. doi: 10.1021/jp074464w
[22] Charoen-amornkitt, P., W. Pholauyphon, T. Suzuki, and S. Tsushima. (2023). An approach to unify capacitance measurements of electric double layer capacitors using sinusoidal potential scan. *Journal of Energy Storage, 66*, 107522. doi: https://doi.org/10.1016/j.est.2023.107522
[23] Charoen-amornkitt, P., T. Suzuki, and S. Tsushima. (2020). Effects of voltage-dependence of the constant phase element and ohmic parameters in the modeling and simulation of cyclic voltammograms. *Journal of The Electrochemical Society, 167*(16), 166506. doi: 10.1149/1945-7111/abbe5d

ETM0013

Powertrain Modeling and Implementation of Energy Management Strategy for Plug-in Hybrid Motorcycle

S. Lin[1], P. Karin[1], M. Yamakita[2], B. Kerdsup[3], P. Saisirirat[4], and M. Masomtob[4,*]

[1]School of Engineering, King Mongkut's Institute of Technology Ladkrabang, Bangkok, 10250, Thailand
[2]School of Engineering, Tokyo Institute of Technology, 152-8550, Japan
[3]National Electronics and Computer Technology Center (NECTEC), National Science and Technology Development Agency (NSTDA), Pathum Thani, 12120, Thailand
[4]National Energy and Technology Center (ENTEC), National Science and Technology Development Agency (NSTDA), Pathum Thani, 12120, Thailand

* Corresponding Author: manop.mas@entec.or.th

Abstract. This paper presents the vehicle dynamic model for optimizing the plug-in hybrid motorcycle converted from commercial ICE motorcycle. The hybrid motorcycle still uses the original 250 cc internal combustion engine and adds 3kW electric in-wheel motor. They are connected in parallel hybrid configuration. Both engine and motor behaviors are created as mathematical models in MATLAB/Simulink and used to size the powertrain components to predict the fuel economy. All dynamic models of the hybrid vehicle including the lithium-ion battery pack, transmission, wheels, and vehicle dynamic model are created with MATLAB/Simulink while implementing the Equivalent Consumption Minimization Strategy (ECMS) for optimizing engine power as well as motor power demands and fuel consumption. In this study, Artemis urban and WMTC drive cycles are used for optimization. The results show that the performance of the hybrid motorcycle in terms of acceleration and fuel consumption is improved compared to the commercial ICE motorcycle.

Keywords: Plug-in hybrid motorcycle, vehicle dynamic, MATLAB/Simulink, fuel consumption.

1. Introduction

Recently, two-wheeled vehicles such as motorcycles and scooters contribute to a major part of air pollution, especially in the Asia region [1]. In 2021, the number of registered motorcycles totaling over 21 million vehicles which is twice the number of registered cars in Thailand according to the Thailand Automotive Institute. Motorcycles play an important part in a large group of people including students and commuters. They are popular because of their small size, and their convenience for short daily trips both in rural and urban areas. However, they cause severe impact to the environment and the interest has shifted to hybrid motorcycles [1].

Plug-in hybrid motorcycles can be a compelling option for riders who are interested in reducing their environmental impact while still enjoying the performance and versatility of a traditional motorcycle. The conversion process typically involves retrofitting the motorcycle with a battery pack, electric motor, and other components that allow it to operate on both electricity and gasoline. Despite the initial cost, converting an ICE motorcycle to a plug-in hybrid motorcycle can be a cost-effective choice over the long term. Plug-in hybrid motorcycles can achieve significantly better fuel efficiency than traditional ICE motorcycles, which means that riders can save money on fuel costs over time.

Energy management strategies are necessary to achieve the full potential of hybrid electric vehicles, which can reduce fuel consumption and emissions in comparison to conventional vehicles. Therefore, the vehicle model of the parallel hybrid powertrain and model-based hybrid controller are developed to minimize the fuel consumption. The hybrid control module (HCM) does not consider other cost functions, such as pollutant emissions or battery aging. Drivability issues such as noise, harshness, and vibrations are neglected as well. This research aims to investigate the simulation-based results of a hybrid two-wheeler powertrain for two different drive cycles and comparing with the results of the conventional ICE vehicle.

2. System Configuration and Vehicle Model

The hybrid electric motorcycle power train integrates both internal combustion engine (ICE) and electric motor to provide propulsion. The system configuration and vehicle model encompass several key components, including the power sources, the control unit, the transmission, and the energy storage system.

2.1. System Configuration

The vehicle for this study is a plug-in hybrid motorcycle with a parallel hybrid configuration which includes HEV model with 250 cc internal combustion engine, transmission, battery, motor, wheels, and associated powertrain control algorithms. The Yamaha YZ250F engine is modelled as a map-based engine using efficiency maps generated by a two-zone numerical model developed at the University of Idaho [2]. The electric motor efficiency map is generated from electric scooter testing on the dynamometer.

Figure 1 shows the mechanical and electrical power flow of the powertrain model used in the simulation. The internal combustion engine and electric machine are mechanically connected for the simplicity of the simulation, and their torque outputs are summed to provide traction to the wheels. In real-life scenarios for hybrid motorcycles, the electric machine is usually a hub wheel motor installed either at the front or rear wheels. The transmission consists of a chain drive and a gearbox which introduces two gear ratios: the transmission ratio $g_{tr}(i_{tr})$, which is a function of the selected gear i_{tr}, and the chain drive ratio g_{cd} as shown in Equation (1) and (2) in which the value of chain drive ratio is equals to 3. In this case, electric-only mode is not available due to the powertrain limitations of the motorcycle. To activate the electric-only mode in urban drive situations, a mechanical clutch is necessary to decouple the engine from the powertrain and the vehicle also needs a relatively bigger electric motor and battery size which increases the cost of the vehicle.

$$T_{pwt} = g_{tr}\left(i_{tr}\right) g_{cd}\left(T_{eng} + T_{mot}\right) \tag{1}$$

The speed of the engine and motor is expressed as

$$\omega_{eng} = \omega_{mot} = \frac{v_{veh}}{R_{wh}} g_{tr}\left(i_{tr}\right) g_{cd} \tag{2}$$

where v_{veh} is the vehicle speed and R_{wh} is the wheel radius. In this simulation, the bi-directional DC-DC inverter is excluded in the electric plant because the battery can be recharged from external electrical input. Charge-depletion is desired in this case because of the plug-in capability.

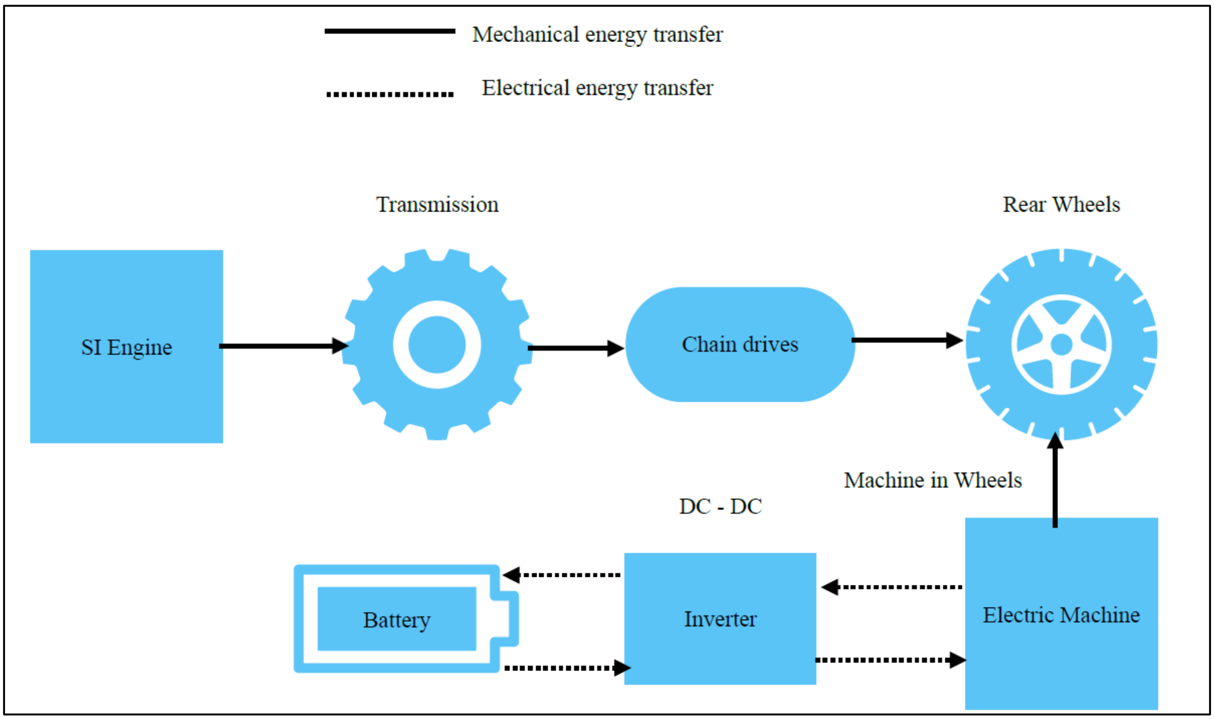

Figure 1. Powertrain configuration of the plug-in hybrid motorcycle.

The torque curves and efficiency maps of the engine and the electric machine are shown in Figure 2. And the battery parameters used in the simulation are shown in Table 1.

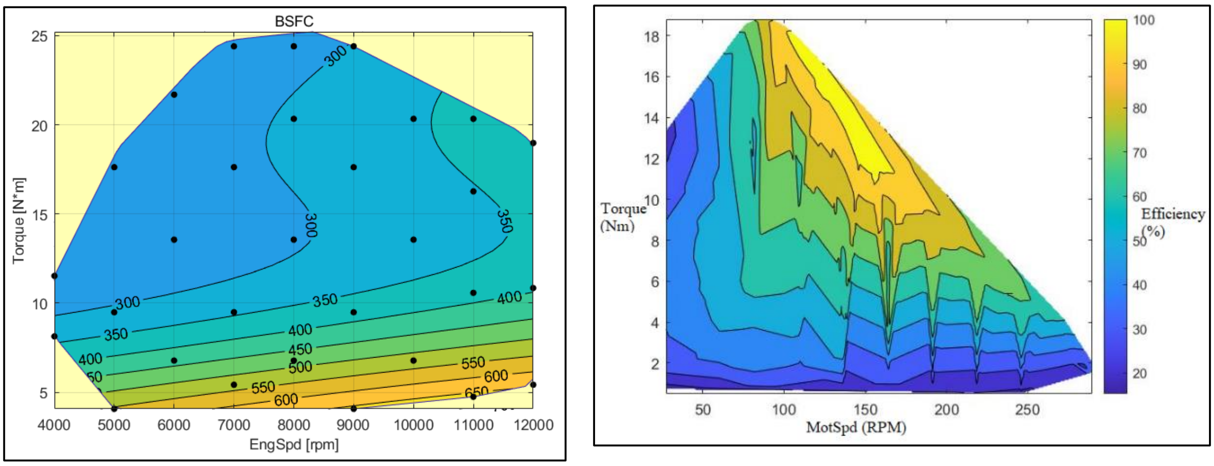

Figure 2. Engine efficiency map (YZ250f) and electric machine efficiency map.

Table 1. Battery Parameters.

Type	LiFePo4
Rated Capacity	40 Ah
Rated Voltage	72 V
Max Charge Current	15 A
Internal Resistance	≤70mΩ

2.2. Simulation Model

For vehicle-level analysis, MATLAB/ Simulink model has been developed to minimize fuel consumption. Figure 3 shows the implementation of the vehicle-level simulator which includes the main model blocks: drive cycle source, longitudinal rider, controllers, motorcycle vehicle and visualization. Input is the desired drive cycle that generates the sequence of setpoints for speed, acceleration, and slope that the vehicle should follow. The input is provided to the driver block which contains a PID controller to match the vehicle velocity with the desired drive cycle continuously.

The controller block performs essentially two sets of tasks. One is low-level or component-level control task, where each powertrain component is controlled by using feedback control methods. The second task or high-level or supervisory control is responsible for the optimization of energy flow. When designing the control system, the separation of the two controllers allows to consider only the battery state of charge dynamics as the system state and neglect the vehicle speed, since this is controlled directly by driver. The value of engine and motor torque must remain within their respective limitations called control constraints.

$$T_{mot,min}\left(\omega_{mot}\right) \le T_{mot} \le T_{mot,max}\left(\omega_{mot}\right) \quad (3)$$

$$T_{ice,min}\left(\omega_{eng}\right) \le T_{eng} \le T_{ice,max}\left(\omega_{eng}\right) \quad (4)$$

The electric motor power is also constrained by minimum and maximum available electric power.

$$P_{batt,min}(SOC) \le P_{mot,e} \le P_{batt,max}(SOC) \quad (5)$$

The above equation is then translated into an additional constraint on the control variable T_{mot},

$$T'_{mot,min}\left(\omega_{mot}, P_{batt,min}\right) \le T_{mot} \le T'_{mot,max}\left(\omega_{mot}, P_{batt,max}\right) \quad (6)$$

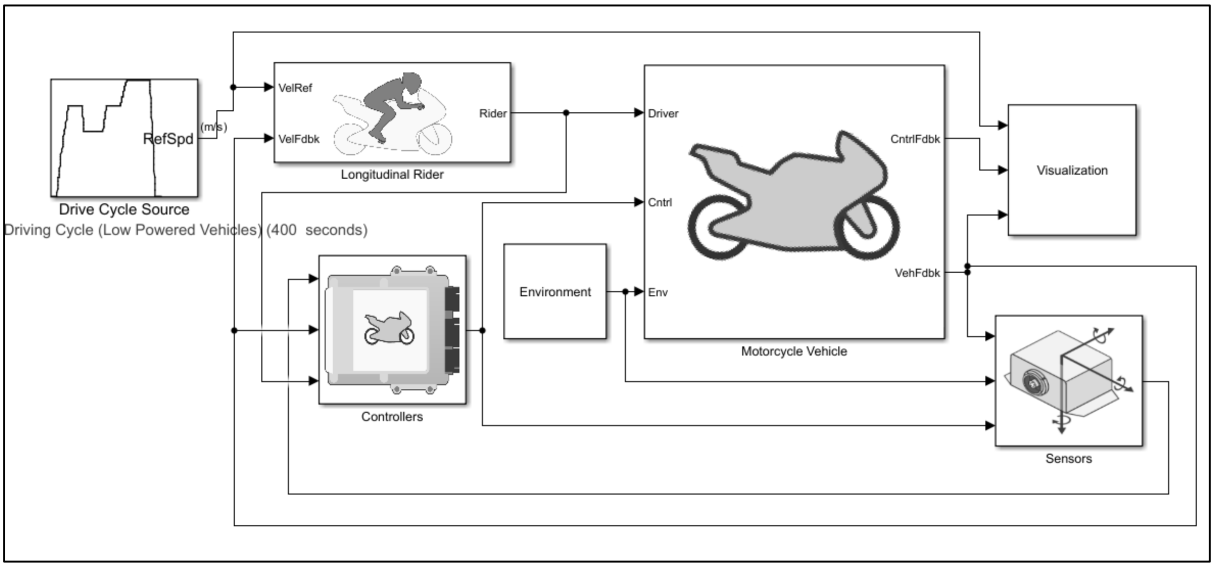

Figure 3. Top-level view of the vehicle simulator.

2.2.1. Equations of motion.

The vehicle is considered as a point mass and its interaction with the external environment is studied as shown in Figure 4 to compute the amount of power and energy needed to move it with specified speed. This high-level approach is useful to develop an understanding of the vehicle longitudinal dynamics and of the energy characteristics of hybrid vehicles [3].

The total energy consumption of the vehicle model can be derived from the traction force and vehicle speed as shown in Equation (7) and (8).

$$P_{traction} = F_{traction} v \tag{7}$$

$$F_{trac} = F_{pwt} - F_{brake} \tag{8}$$

If a vehicle is considered as a mass point, its motion equation, as shown in Equation (9), can be written from the equilibrium of forces shown in Figure 5.

$$M_{veh} \frac{dv_{veh}}{dt} = F_{inertia} = F_{trac} - F_{roll} - F_{areo} - F_{grade} \tag{9}$$

where M_{veh} is the vehicle mass, v_{veh} is the longitudinal vehicle velocity, $F_{inertia}$ is the inertial force, F_{trac} is the traction force acting on the wheels, F_{roll} is the rolling resistance, F_{aero} is the aerodynamic resistance, F_{grade} is the force due to road slope.

The aerodynamic resistance is expressed as

$$F_{aero} = \frac{1}{2} \varrho_{air} A_f C_d v^2_{veh} \tag{10}$$

where ρ_{air} is the air density which is 1.25 kg/m^3 in normal conditions. A_f is the vehicle frontal area, C_d is the aerodynamic drag coefficient.

The rolling resistance is expressed as

$$F_{roll} = c_{roll} M_{veh} g \cos\delta \tag{11}$$

where g is the gravity, δ is the road slope angle and c_{roll} is the rolling resistance coefficient.

The grade resistance is expressed as

$$F_{grade} = M_{veh} g \sin\delta \tag{12}$$

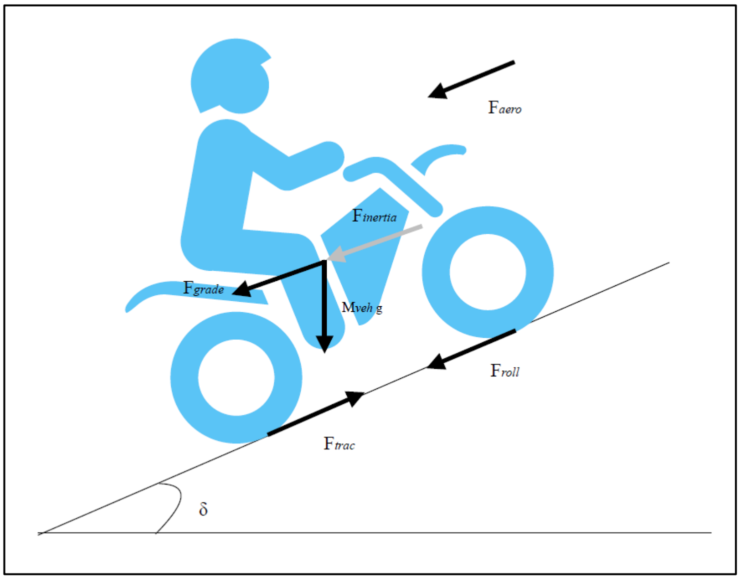

Figure 4. Forces acting on a motorcycle.

The simulation parameters for the vehicle dynamics of the plug-in hybrid motorcycle are shown in Table 2.

Table 2. Simulation parameters for the plug-in hybrid motorcycle.

Frontal area, A_f	2 m^2
Drag coefficient, C_d	0.2
Air density, ρ_{air}	1.22 kg/m^3
Rolling resistance coefficient, c_{roll}	0.1
Vehicle mass, M_{veh}	201 kg
Driver mass, M_{drv}	65 kg
Front wheel radius, R_{fwh}	0.2846 m
Rear wheel radius, R_{rwh}	0.3022 m
Chain drive ratio, g_{cd}	3
Engine	250 cc liquid-cooled DOHC 4-stroke (Yamaha YZ250f)
Motor	3000W Brushless DC motor (BENLG Falcon One)
Battery type	72V 40Ah Lithium iron phosphate
Fuel lower heating value, Q_{lhv}	46 J/kg

2.2.2. Equivalent Consumption Minimization Strategy (ECMS)

The Equivalent Consumption Minimization Strategy (ECMS) is a heuristic method to address the optimal control problem and has been shown to provide an effective solution to the HEV energy management problem. ECMS is an instantaneous approach derived from the Pontryagin's minimum principle. ECMS formulates a cost function for the equivalent fuel consumption to be optimized. In the power-based PMP formulation, the Hamiltonian is

$$H=P_{fuel}(t) + \lambda(t)\, P_{ech}(t) \tag{13}$$

where λ (t) is a weighting factor that transforms the battery power into fuel power and P_{ech} represents the electrochemical power.

The key idea of ECMS is that an equivalent fuel consumption can be associated with the use of electrical energy.

$$\dot{m}_{f,eqv}(t) = \dot{m}_f(t) + \dot{m}_{batt}(t) \tag{14}$$

where $\dot{m}_{f,eqv}(t)$ is the instantaneous equivalent fuel consumption, $\dot{m}_f(t)$ fuel mass flow rate from engine and $\dot{m}_{batt}(t)$ is the instantaneous equivalent fuel consumption from the battery.

The real fuel consumption from the engine is given as

$$\dot{m}_f(t) = \frac{P_{eng}(t)}{\eta_{eng}(t)Q_{lhv}} \tag{15}$$

where Q_{lhv} is the fuel lower heating value, $\eta_{eng}(t)$ is the engine efficiency and P_{eng} is the power produced by the engine. The virtual fuel consumption from the electric motor is given by

$$\dot{m}_{batt}(t) = \frac{s(t)}{Q_{lhv}}P_{batt}(t) \tag{16}$$

where the virtual specific fuel consumption is proportional to the equivalence factor s(t) which is a vector of values, one for charge and one for discharge, s(t)= [s_{chg}(t),s_{dis}(t)]. Its task is to assign a cost to the use of electricity, converting electrical power into equivalent fuel consumption. In this case, non-adaptive ECMS is used for the simulation which means constant s(t) value is used which can be properly tuned for minimum fuel consumption and charge sustenance over different drive cycles which include regenerative braking and bi-directional DC flow.

While implementing the ECMS, a penalty function is often used to guarantee that the SOC does not exceeds the admissible limits, $SOC_{max} \leq SOC \leq SOC_{min}$. In this simulation, the maximum value is set to 80% and the minimum value is set to 30% for longer battery life. Therefore, the Equation (14) is modified by using the penalty function as shown in Equation (17) and the penalty function is shown in Equation (18).

$$\dot{m}_{f,eqv}(t)=\dot{m}_f(t)+\frac{s(t)}{Q_{lhv}}P_{batt}(t)\,p(SOC) \tag{17}$$

$$p(SOC)=1-\left(\frac{SOC(t)-SOC_{target}}{\left(SOC_{max}-SOC_{min}\right)/2}\right)^a \tag{18}$$

For plug-in hybrids, the SOC target value should be lower than the initial one, i.e., $SOC_{target} < SOC(t_0)$. In practical vehicle applications, it is sufficient to keep the SOC between a range of values. The value of exponent (a) in Equation (18) allows for some difference between the desired and the actual SOC and it does not affect the vehicle functionality. In practice, the penalty function prevents the battery to be discharged when the battery SOC is too low by increasing the cost of P_{batt} and it facilitates the battery to be discharged when the SOC is too high by decreasing the cost of P_{batt}. In this simulation, the exponent value, a=3 is used for the penalty function.

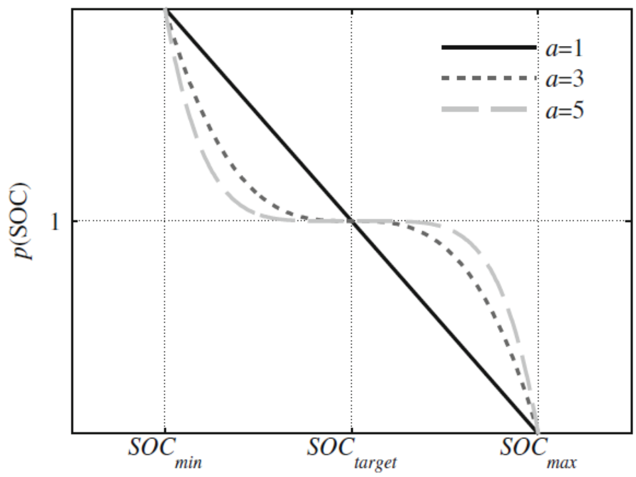

Figure 5. Penalty function used in the ECMS to correct for SOC deviation [3].

If the Equations (14) and (17) are rewritten in the form of power, multiplying all terms by Q_{lhv}, the instantaneous cost becomes

$$P_{eqv}(t)=P_{fuel}(t)+s(t)P_{batt}(t) \tag{19}$$

where the fuel power P_{fuel} is a function of engine speed and torque. It is computed as a function of vehicle speed, total torque request and motor torque as shown in Equation (20).

$$P_{fuel}=Q_{lhv}\dot{m}_f\left(T_{eng},\omega_{eng}\right)=P_{fuel}(T_{pwt},T_{mot},v_{veh}) \tag{20}$$

To minimize the fuel consumption, the standard degree of freedom for the optimization problem is the battery power P_{batt}. And the battery power is

$$P_{batt}=P_{em,e}(T_{mot},\omega_{mot}) \tag{21}$$

where $P_{em,e}(T_{mot},\omega_{mot})$ is the electrical power required by the electric machine to produce the torque T_{mot} at the speed ω_{mot}.

From the above equation, it can be observed that P_{batt} is directly related to the motor torque, T_{mot}, because the motor speed is imposed by external inputs from the battery. This allows using the motor torque as the control variable, which is more immediate for this powertrain architecture. The constraints for the control input, T_{mot} is shown in Equation (6).

The similarities between Equations (13) and (19) is clearly showing how the Hmaniltonian H of the optimization problem can be regarded as an equivalent fuel consumption P_{eqv} [3]. At each instant of time, the optimal solution $T_{mot}(t)$ is the one that minimizes the Hamiltonian function. One approach to minimization is to evaluate the function H for the complete set of admissible control values $T_{mot}(t)$ which is applied to the system. The Hamiltonian computation and minimization is done by the ECMS block included in the powertrain blockset library in MATLAB/ Simulink.

2.2.3. Drive cycles

Artemis urban drive cycle and WMTC (World Motorcycle Test Cycle) are both important methods used to assess the performance and fuel efficiency of vehicles in urban driving conditions. The Artemis urban drive cycles specifically focus on simulating real-world urban driving scenarios, considering factors such as stop-and-go traffic, varying speeds, and idling periods. These drive cycles are designed to mimic the typical driving patterns observed in urban areas, thereby providing a more accurate representation of a vehicle's fuel consumption and emissions in such settings. Overall, both Artemis urban drive cycle and WMTC play a crucial role in assessing the performance and efficiency of vehicles in urban driving conditions.

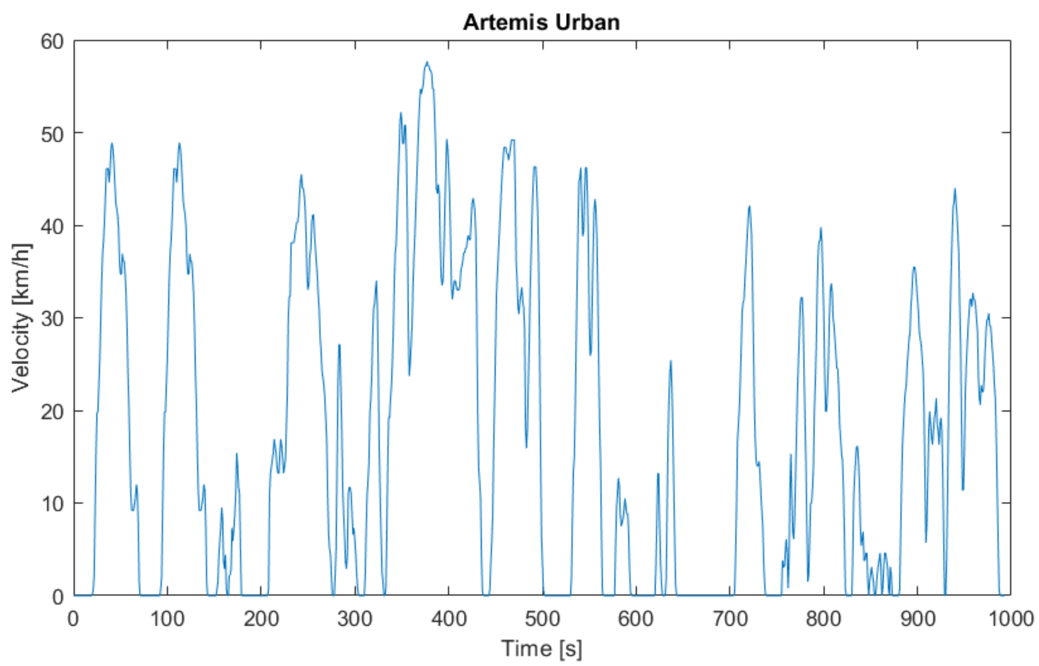

Figure 6. Artemis urban drive cycle.

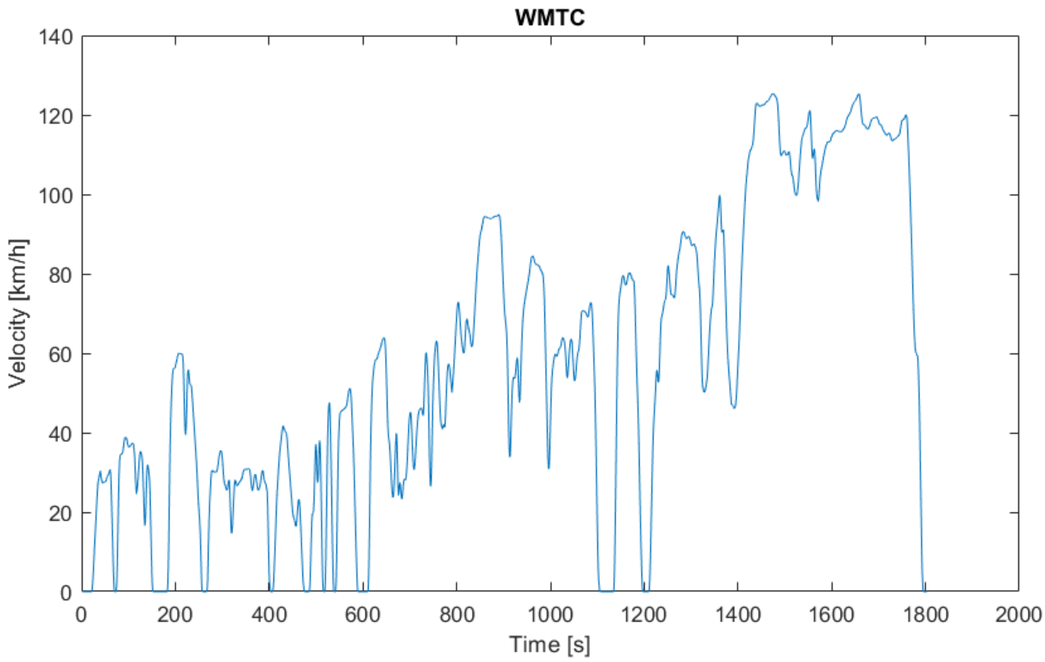

Figure 7. WMTC (World Motorcycle Test Cycle).

3. Simulation results and discussion

The simulation results of the plug-in hybrid motorcycle, using two different drive cycles and implementing the ECMS, provide valuable insights into the vehicle's performance and fuel consumption. The simulation takes into account various factors such as vehicle dynamics, engine, electric drivetrain, road conditions, traffic patterns, and driver behaviour, allowing for a realistic representation of real-world scenarios. The results show that the vehicle can exactly follow the target velocity and the highest fuel economy achieved by the plug-in hybrid motorcycle is over 220 MPG (US fuel economy) and the average fuel economy is 189 MPG over Artemis urban drive cycle as shown in Figure 8.

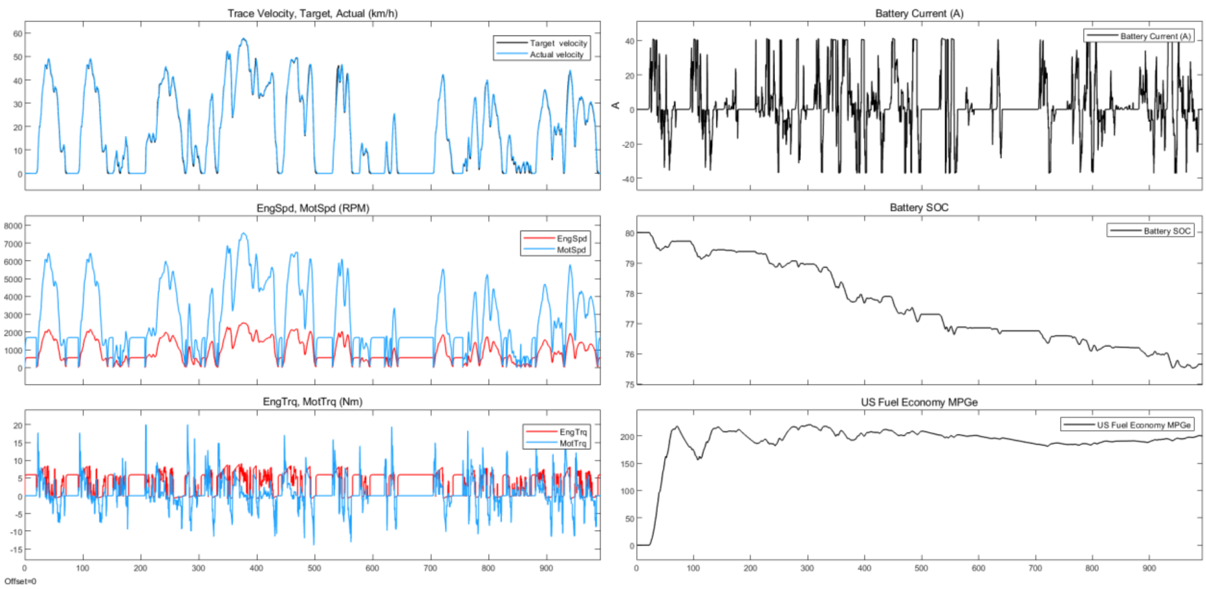

Figure 8. Vehicle performance over Artemis Urban drive cycle.

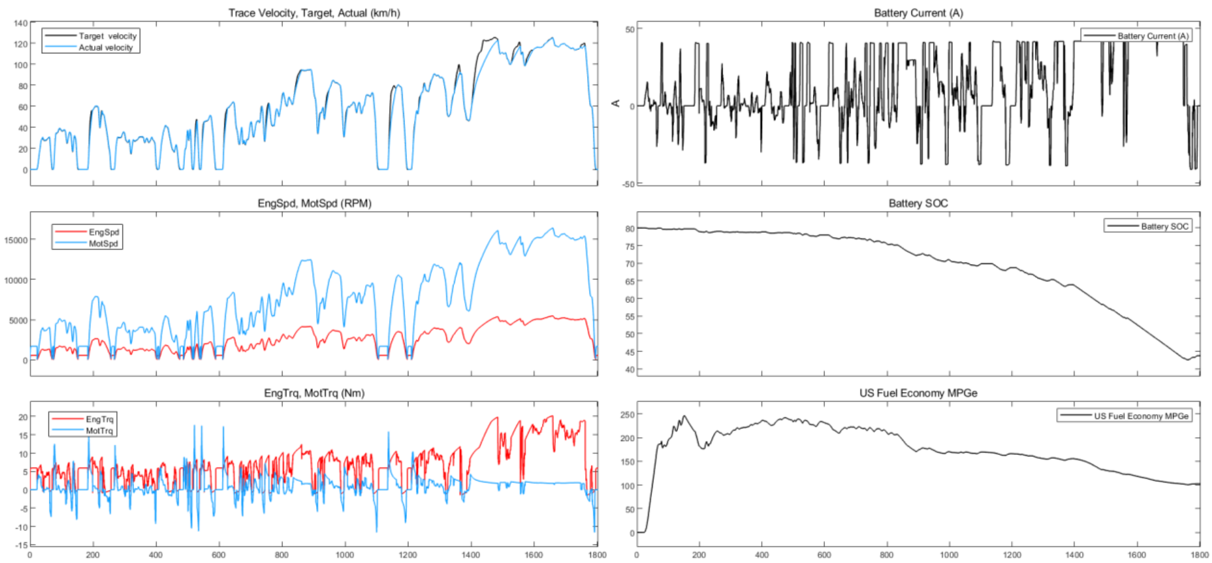

Figure 9. Vehicle performance over WMTC.

By analysing the simulation results, the electric machine provides as a buffer in speed and traction of the vehicle and battery SOC stays between the predefined values. The highest fuel economy achieved by the vehicle, over WMTC in Figure 9, is 246 MPG and the average value is 174 MPG. The engine model in a conventional vehicle achieved only 29 MPG over a certain drive cycle [2]. The simulation achieved remarkable performance although the real-world conditions might differ depending on the weather conditions, road conditions and vehicle dynamics. Different hybrid drivetrain configurations can be explored by using different parameters and including energy management strategies.

4. Conclusion

Fuel economy is a critical factor in the design and optimization of plug-in hybrid motorcycles. By incorporating both the internal combustion engine and the electric in-wheel motor, significant improvements in acceleration and fuel consumption can be achieved. However, there are still limitations in existing research, particularly in the area of energy management systems. Further investigation is needed, including the use of adaptive ECMS methods and improved energy management strategies. In conclusion, the potential benefits of plug-in hybrid motorcycles are significant, including reduced environmental impact and cost savings over time. Future research in this area focuses on improving energy management systems and exploring new approaches to optimizing hybrid powertrains. Therefore, the key findings of this research can be used in the development and refinement of plug-in hybrid motorcycle technology, as it enables engineers to make informed decisions regarding design, powertrain configuration, and energy management strategies to achieve enhanced fuel economy.

5. References

[1] Nguyen, Van-Trang & Pyung, Hwang & Huynh, Thinh. (2017). Computational analysis on Hybrid Electric Motorcycle with front wheel electric motor using Lithium Ion battery. 355-359. 10.1109/ICSSE.2017.8030896.

[2] Asfoor, Mostafa & Beyerlein, Steven & Lilley, Rory & Santora, Michael. (2015). Discrete Grid Optimization of a Rule-Based Energy Management Strategy for a Formula Hybrid Electric Vehicle. 10.4271/2015-01-1212.

[3] Simona Onori, Lorenzo Serrao, Giorgio Rizzoni (2016). *Hybrid electric vehicles energy management strategies*. Springer.

[4] Kommuri, N., McGordon, A., Allen, A., & Dinh, T. Q. (2020). Evaluation of a Modified Equivalent Fuel-Consumption Minimization Strategy Considering Engine Start Frequency and Battery Parameters for a Plugin Hybrid Two-Wheeler. Energies, 13(12), 3122.

The 13th TSME International Conference on Mechanical Engineering
12th – 15th December 2023
Chiang Mai, Thailand

ETM0017

Investigation of electrochemical reaction and transport properties of a rotating cylinder electrode with surface modification

T Suzuki[1,*], P Charoen-amornkitt[2], T Suzuki[1], and S Tsushima[1]

[1]Department of Mechanical Engineering, Graduate School of Engineering, Osaka University, Suita, Osaka 565-0871, Japan
[2]Electrochemical Energy Storage and Conversion Laboratory, Department of Mechanical Engineering, Faculty of Engineering, King Mongkut's University of Technology Thonburi, 126 Pracha Uthit Rd., Bang Mod, Thung Khru, Bangkok 10140, Thailand

* Corresponding Author: suzuki_t@ene.mech.eng.osaka-u.ac.jp

Abstract. There is a pressing need to understand the transport resistance at and near the electrode surface for electrochemical reaction systems with flow. In this study, we investigated effects of surface modification of a cylindrical electrode on its electrochemical and transport properties by using electrochemical measurements and numerical analysis. An electrochemical deposition process was applied to a platinum cylinder for modification of the surface structure of the electrode. Surface geometrical properties of the electrode was controlled by applied duration time of the deposition and was characterized by scanning electron microscopy and white light confocal microscopy. The cylindrical electrode was rotated in aqueous solutions with reactant metal ions and its reaction and transport properties were characterized. Electrochemical impedance spectroscopy and cyclic voltammetry in assistance with numerical analysis were used to determine electrochemical surface area, electrical double layer capacitance and reaction rate constant of the electrochemical system. Mass transport coefficients depending on rotating velocity was then obtained by measuring limiting currents in linear sweep voltammograms.

Keywords: Electrode, Electrodeposition, Surface structure, Rotating cylinder, Electrochemical reaction and transport.

1. Introduction

Understanding of electrochemical reaction systems with flow will lead to significant developments in the field of electrochemistry. There is a pressing need to understand transport resistance near electrode surfaces. The electrode's surface morphology significantly impacts the enhancement, given its role in providing a large surface area for the electrode, ensuring sufficient supply of reactants, and facilitating efficient removal of products. The electrode surface structure influences the formation of the concentration boundary layer and the electrochemical surface area, but the quantitative contribution to the reaction transport properties is not yet fully clarified.

To address this issue, in previous studies, electrochemical surface area, reaction rate constant, and mass transport coefficient, which are parameters of electrode performance, were successfully derived for carbon electrodes [1-4]. However, the surface geometrical properties of carbon are complex due to its functional groups, making it difficult to evaluate the effect of surface morphology on electrode performance. We presumed that the use of a stable platinum electrode with a well-defined surface structure instead of a carbon electrode will enable us to evaluate electrode performance focusing on the surface geometrical properties.

Therefore, in this study, we investigated effects of surface modification of a cylindrical electrode on its electrochemical and transport properties by using electrochemical measurements and numerical analysis. We utilized platinum cylinders that underwent surface modification via electrochemical deposition, varying the duration of deposition to yield distinct surface geometries. The model introduced by Charoen-amornkitt et al. [1] was applied to quantitatively assess how surface modification influenced parameters such as electrochemical surface area, reaction rate constant, and mass transport coefficient. By attaining a more profound comprehension of surface modification effects, researchers can engineer and optimize electrodes to elevate their performance, ultimately leading to the creation of efficient and economical energy storage devices.

2. Experimental

2.1. Platinum electrode

An electrochemical deposition process was applied to a platinum cylinder for modification of the surface structure of the electrode. In this experiment, a three-electrode method was used, with a platinum cylinder electrode (Figure 1) as the working electrode, a silver-silver chloride electrode as the reference electrode, and a platinum wire as the counter electrode. The solution was 5 mM Hydrogen Hexachloroplatinate(IV) Hexahydrate. Nitrogen was supplied to the solution for 15 minutes before the experiment, and a constant potential electrolysis was performed at an applied voltage of -0.255 V vs. Ag/AgCl. After applying the voltage for the specified time to a single platinum electrode, the electrode surface was characterized by scanning electron microscopy (SEM) and white light confocal microscopy, and electrochemical measurements were performed to determine the electrode surface area, etc.

After a series of measurements, electrodeposition was performed again on the same platinum electrode. Surface geometrical properties of the electrode was controlled by applied duration time of the deposition. The process was repeated for 100 s, 300 s, and 400 s on a single electrode, and the electrodes obtained at each stage were named as Pre-Deposition, Deposition 1, 2, and 3.

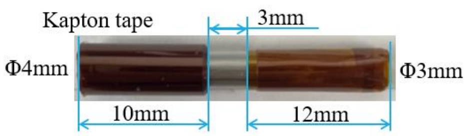

Figure 1. A platinum cylinder electrode.

2.2. Electrochemical impedance spectroscopy (EIS)

In this study, the electrode characterization model established by Charoen-amornkitt et al. [1] was employed. The model incorporated a constant phase element (CPE) to accommodate non-faradaic effects, while the conventional continuum model was used to replicate the faradaic processes taking place on the cylinder's surface. More details regarding the model can be found elsewhere [1-4]. To determine the CPE parameters, EIS measurements were conducted with an AC signal of 10 mV from 20 kHz to 0.1 Hz at 10 points per decade in the potential window of interest. 1.0 M potassium chloride (KCl) was used as the electrolyte. A linear Kronig–Kramers transform test was also performed to ensure that the experimental data were of good quality. The equivalent circuit used for evaluating the CPE parameters was the Modified Randles circuit [1]. The non-faradaic current generated by an electrical double layer is governed by a CPE. The impedance of the CPE in the Laplace domain can be expressed as

$$Z_{CPE}(s) = \frac{1}{Y_0 s^{\gamma}} \tag{1}$$

where Y_0 is the CPE parameter ($F \cdot s^{\gamma-1}$), s is the Laplace variable, and superscript γ is the CPE exponent.

Figure 2 illustrates a sample of EIS plots for the platinum electrode, each taken at a different DC biased potential. Notably, the EIS plots exhibit variations corresponding to the altered DC biased potentials, providing concrete evidence that both the CPE and ohmic characteristics underwent significant changes within the relevant potential range. These potential-dependent effects were duly incorporated into the model employed for this investigation.

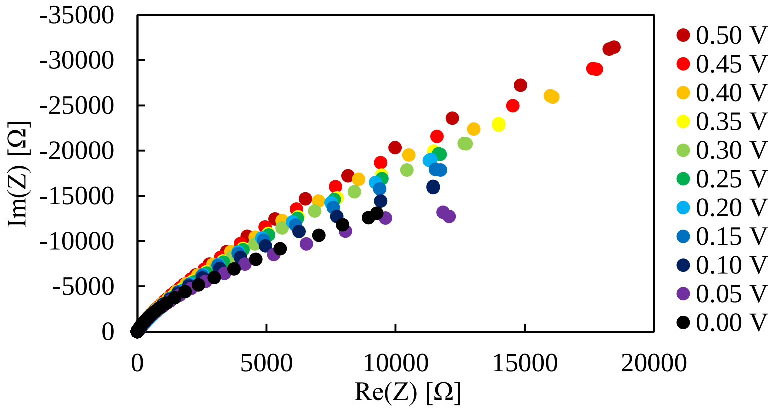

Figure 2. Sample of EIS plots for the Pt electrode.

2.3. Cyclic voltammetry (CV)

CV measurements were performed to determine the electrochemical surface area and reaction rate constants of the electrodes. The currents obtained from the measurements include faradaic current generated by the chemical reaction of the active material and non-faradaic current generated by the electrical double layer. The measurements were conducted at several scan rate of 10, 20, 30, 40, and 50 mV/s. The initial potential was 0.5 V, and the switching potential was 0 V. 1 mM ferri/ferrocyanide solution in 1.0 M potassium chloride (KCl) was used as the electrolyte. The diffusion coefficient of ferri/ferrocyanide was assumed to be 7×10^{-10} m^2/s during the calculations [5].

The electrochemical surface area and reaction rate constant were determined by fitting the numerical analysis to data obtained from CV measurements. The model used in the numerical analysis was proposed by Charoen-amornkitt et al [1]. The faradaic current was obtained from the Butler-Volmer equation and Fick's second law. The non-faradaic current was calculated using the time–domain response of the CPE. The total current can be expressed as a combination of these two currents using an equivalent circuit. A brief description of the model is presented below. For a detailed explanation, please refer to the paper [1].

For the faradaic part, an electrochemical system of interest is the simple redox reaction, $Red \rightleftarrows Ox + ne^{-}$, at the surface of the cylindrical electrode. The diffusion of active species is governed by Fick's second law, which can be expressed as

$$\frac{\partial c_j}{\partial t} = \nabla \cdot \left(D_j \nabla c_j\right) \tag{2}$$

where subscript j indicates the electroactive species Red or Ox, c_j is the species concentration ($\mathrm{mol/m^3}$), and D_j is the diffusivity of the species ($\mathrm{m^2/s}$).

The Butler-Volmer equation is used to describe the rate of an electrochemical reaction (Equation (3)).

$$\frac{j}{nF} = k_0(c_{Red})_s \exp\left(\frac{\alpha_a nF\eta}{RT}\right) - k_0(c_{Ox})_s \exp\left(\frac{-\alpha_c nF\eta}{RT}\right) \tag{3}$$

where j is the current density from the reaction of interest ($\mathrm{A/m^2}$), n is the electron transferred, F is the Faraday constant ($\mathrm{C/mol}$), k_0 is the reaction rate constant ($\mathrm{m/s}$), subscript s indicates the electrode surface, α_a is the anodic transfer coefficient, α_c is the cathodic transfer coefficient, R is the universal gas constant ($\mathrm{kg \cdot m^2/(s^2 \cdot K \cdot mol)}$), T is the temperature (K), and η is the overpotential (V). The current density at the electrode surface can also be expressed by the diffusion flux as

$$\frac{j}{nF} = D_{Red}\nabla(c_{Red})_s = -D_{Ox}\nabla(c_{Ox})_s \tag{4}$$

In cyclic voltammetry modeling, the total Faradaic current is expressed by the following equation (5) using the electrochemical surface area ($\mathrm{m^2}$), A_{act}.

$$I_f = jA_{act} \tag{5}$$

For the non-faradaic current, applying Equation (1), the capacitive current can be expressed as

$$I_c(s) = \frac{\bar{V}(s)}{Z_{CPE}(s)} = Y_0 s^\gamma \bar{V}(s) \tag{6}$$

where $\bar{V}$ is the voltage deviation from the initial condition (V). The current in the time domain can be obtained by taking the inverse Laplace transform and is expressed as

$$I_c(t) = \frac{d\bar{V}(t)}{dt} * A(t) + \bar{V}(0)A(t) \tag{7}$$

with

$$A(t) = \frac{Y_0 t^{-\gamma}}{\Gamma(1-\gamma)} \tag{8}$$

where the $*$ symbol denotes the convolution operation, and Γ represents the gamma function.

The total current can be expressed as

$$I_{total} = I_f + I_c \tag{9}$$

It is noteworthy that quantifying electrochemical surface area is often a challenging task. However, through the utilization of the model [1], it becomes possible to accurately characterize both the electrochemical surface area and reaction rate constants of the electrodes.

2.4. Linear sweep voltammetry (LSV)

LSV measurements were performed to derive the mass transfer coefficient. Unlike CV measurements, in the measurements, the electrode was rotated in the electrolyte, so that mass transport by convection took place. Ferri/Ferrocyanide solution was used as the electrolyte as in the CV measurements. LSV measurements were conducted at 50 mV/s and the initial potential was 0.5 V, and the final potential was 0 V. Since the axial length of a cylindrical electrode was longer than its radius, the effect of the top and bottom ends could be ignored, and only the circumferential component of the flow was assumed. From the measurements, the limiting current was obtained, and the mass transfer coefficient was derived using Equation (10).

$$h_m = \frac{I_L}{zFcA_{act}} \tag{10}$$

where h_m is the mass transfer coefficient (m/s), I_L is the limiting current (A), z is the number of exchange electrons, F is Faraday constant (C/mol), c is the concentration of active material ($\mathrm{mol/m^3}$), and A_{act} is the electrochemical surface area ($\mathrm{m^2}$). The electrochemical surface area determined by fitting the numerical analysis to data obtained from CV measurements is employed in equations to calculate the mass transfer coefficient.

3. Results and Discussion

3.1. Observation of electrode surface

Figure 3 shows the electrode surface structure at different electrodeposition times. It is clear that a thin layer of Pt was deposited covering the surface at 100 s of electrodeposition (Deposition 1), and a spherical structure with a diameter of about 1 μm appeared after 300 s (Deposition 2) and 400 s (Deposition 3) of electrodeposition.

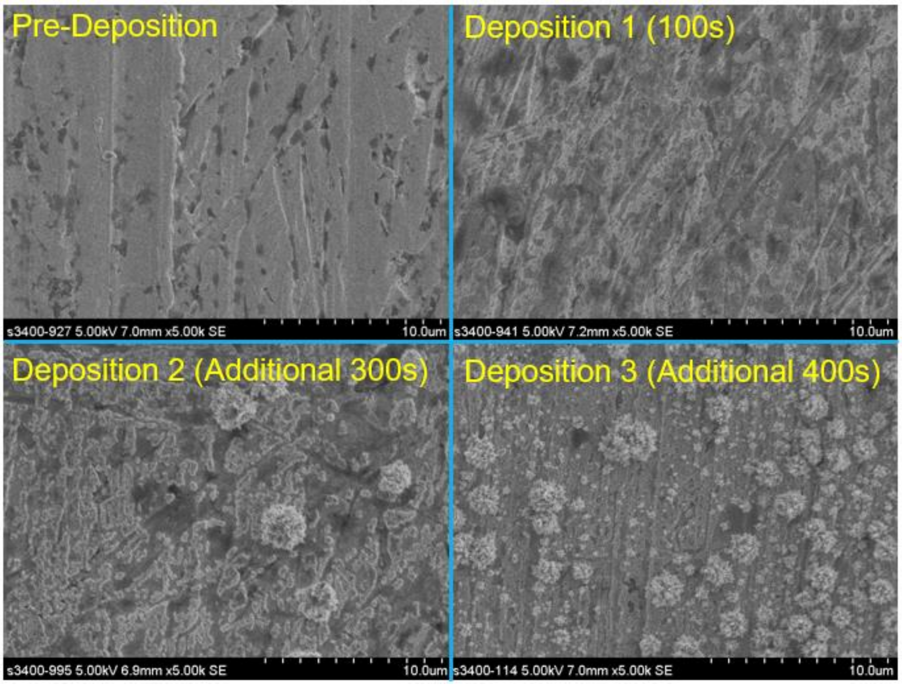

Figure 3. SEM images of electrode surface with different electrodeposition times.

3.2. Evaluation of electrode performance

CV measurements (Figure 4) showed that the total current was larger. Traditionally, this would indicate a greater electrochemical surface area. However, the model utilized in this investigation is capable of distinguishing between the influence of the electrochemical surface area and the electrical double layer. The characterization revealed that the increase is due to the influence of the electrical double layer increased through electrodeposition. This can be due to the increased non-smoothness of the electrode surface. Also, LSV measurements (Figure 5) indicated that the mass transfer coefficient increased with increasing electrodeposition time. The electrochemical surface area and reaction rate constant were obtained by fitting the experimental data and numerical analysis (Table 1), and were found to be the smallest at Deposition 2 and the largest at Deposition 3. It is considered that the electrode performance was improved by Deposition 3 because the spherical structure appeared widely on the electrode surface through electrodeposition.

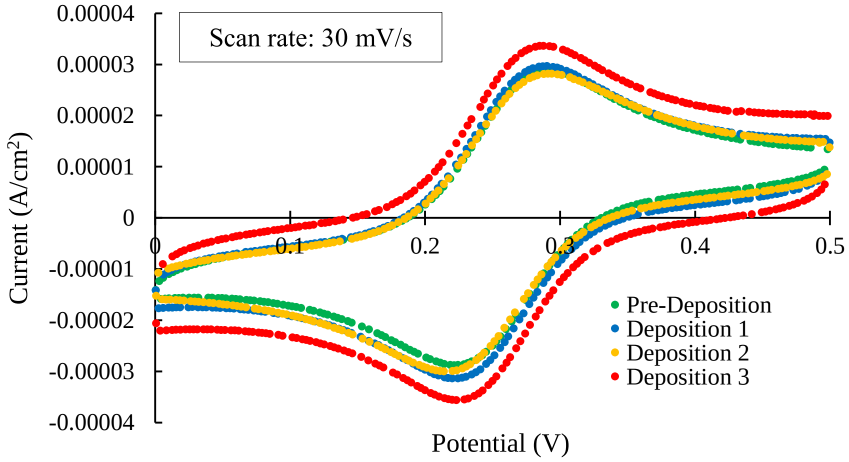

Figure 4. CV measurement results of Pt electrode at each electrodeposition time.

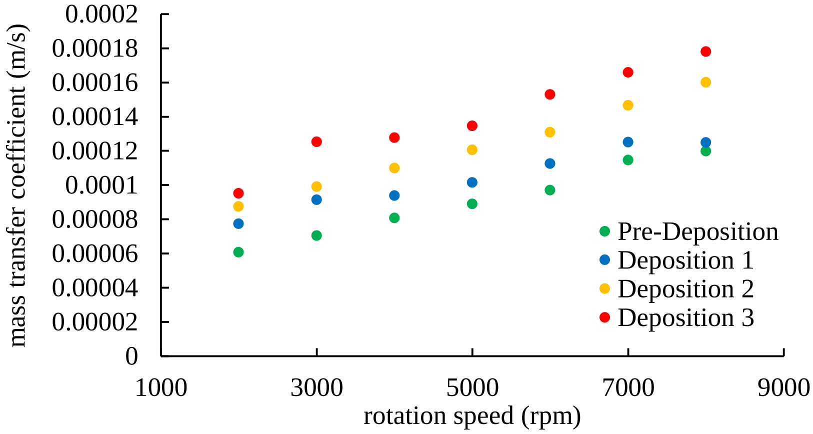

Figure 5. LSV measurement results of Pt electrode at each electrodeposition time.

Table 1. Parameters obtained from Experiments and Fittings.

	Pre-Deposition	Deposition 1	Deposition 2	Deposition 3
Electrochemical surface area (mm^2)	27.84	27.36	26.96	28.14
Reaction rate constant (10^{-4} m/s)	2.91	4.22	1.18	6.58
Mass transfer coefficient (10^{-5} m/s)	9.12	10.59	12.28	14.03

Since the quantitative contribution to the reaction transport dynamics was not yet fully clarified due to the difficulty in interpreting the complex signal, this study is among the first to successfully characterize effects of surface modification. The results from this study provided an idea that It is necessary to improve the control and observation of the electrode surface.

4. Conclusion

It was found that electrodeposition on Pt electrodes can give different surface structures. The initial stage of electrodeposition resulted in a thin surface covering, and further electrodeposition resulted in a spherical structure. Electrochemical measurements of Pt electrodes with different surface structures in a rotating cylinder field revealed changed in electrochemical surface area, electrical layer capacitance, reaction rate constant and mass transfer coefficient. It was confirmed that the surface geometrical properties affect the electrode performance. These findings hold valuable insights for future study to focus on enhancing the surface modification of fibrous electrodes.

5. Acknowledgments

The authors also would like to acknowledge the financial support by JSPS KAKENHI Grant Number 21H04540.

6. References

[1] Charoen-amornkitt P., Suzuki T. and Tsushima S. (2020). *J. Electrochem. Soc.*, 167, 166506.
[2] Charoen-amornkitt P., Suzuki T. and Tsushima S. (2019). *Electrochemistry,* 87, 204.
[3] Charoen-amornkitt P., Suzuki T. and Tsushima S. (2017). *Electrochim. Acta,* 258, 433.
[4] Charoen-amornkitt P., Pholauyphon W., Suzuki T. and Tsushima S. (2023). *J. Energy Storage,* 66, 107522.
[5] S. J. Konopka and B. Mcduffie (1970). *Analytical Chem.,* 42, 14, 1741.

ETM0019

Effect of Multiple V-Baffles on Thermal Enhancement Characteristics in a Channel

P Samruaisin[1], P Kaewkosum[2], A Phila[1], S Eiamsa-ard[1], S Bhattacharyya[3], V Chuwattanakul[2,*], and C Thianpong[2]

[1]Department of Mechanical Engineering, School of Engineering and Industrial Technology, Mahanakorn University of Technology, Bangkok, Thailand
[2]School of Engineering, King Mongkut's Institute of Technology Ladkrabang, Bangkok, Thailand
[3]Department of Mechanical Engineering, Birla Institute of Technology and Science Pilani, India

* Corresponding Author: varesa.ch@kmitl.ac.th

Abstract. In this paper, an experimental investigation of the heat transfer and friction behavior of a channel with multiple V-shaped baffles (oriented upward and downward) is described. The baffle turbulators were mounted on the heated bottom wall of a rectangular channel with a 3.75:1 aspect ratio. In the experiments, the pitch ratio (p/H) is 1.5, baffle height ratio (e/H) is 0.3, attack angle (θ) is 45°, baffle height (e) is 12 mm, and the Reynolds numbers (Re) from 6,000 to 24,000 were tested. The present findings demonstrate that all baffles significantly increased heat transfer by 2.35 to 3.77% compared to a smooth channel. The heat transfer rates generated by the multiple V-shaped baffles with an upward orientation were 4.55 to 9.85% higher than those obtained by the multiple V-shaped baffles with downward orientation under the same conditions. The greatest thermal performance factor for the range of conditions evaluated was 1.32 when multiple V-shaped baffles were utilized, oriented upward, at a Reynolds number of 6,000.

Keywords: Channel, Heat transfer, Multiple V-shaped baffles, Thermal performance.

1. Introduction

Solar energy, frequently harvested using a solar air heater (SAH), is a cost-free, clean source of energy. Techniques for enhancing heat transfer have been developed to enhance the thermal performance of solar collectors. These methods have been employed in a variety of industrial applications such as drying and heating water. A baffle or rib design can increase the heat transfer rate in a channel. In a survey of the literature [1-5], V-shaped shapes have been demonstrated to greatly enhance the heat transfer rate. Han and Zhang [1] examined the heat transfer rate of a duct with 45°/60° V-broken ribs installed in an channel on two opposing sides. According to their study, a broken rib with a 60° angle boosts heat transfer to a greater degree than at 45°. As a result, heat transfer is intensified more strongly than with a broken transverse rib. A V-shaped broken rib offers 2.5-4 times greater heat transfer compared to a solid V-shaped rib, which presents 2-3 times increased heat transfer with a 7-8 times larger pressure drop penalty. Promvonge *et al*. [2] described the thermal performance properties of a channel fitted with V-ribs having 45° and 60° attack angles with delta grooves. They found that combined devices had better thermal performance than a single device at relative pitch and blockage ratios of 1.0 and 0.108, respectively. Promvonge and Skullong [3] studied how different pitch ratios (*P/D*) and blockage ratios (*b/D*) of V-shaped baffles affected heat transfer performance. With an optimal thermal performance augmentation of 2.34 at respective pitch and blockage ratios of 1.0 and 0.15, their findings showed that a V-baffle with P/D=0.5 and b/D=0.2 produces a heat transfer rate that is roughly 4.46 times greater than a plain tube alone. Promvonge and Skullong [4] evaluated the thermal performance factor of a duct with chamfered V-grooves and punched holes. Three rib-pitch ratios (1.0, 1.5, and 2.0) and three inclination angles (45°, 0°, and -45°) were studied as rib parameters. According to their findings, compound turbulators with a 45° inclination angle provide the best heat transfer, especially for the V-up configurations. Hoonpong and Skullong [5] assessed the effectiveness of a solar air heater that had V-baffles inserted at various pitch ratios (0.1-0.3). Using V-baffles increases heat transfer up to 4.3 times higher than for a smooth channel, while also increasing friction losses by up to 37 times, according to their experimental results. The maximum thermal performance factor for the V-baffle is approximately 1.6 for baffle height and pitch ratios of 0.2 and 0.1, respectively. Jaytanaiwachira *et al.* [6] studied an experiment using turbulators and an inclined chamfered groove in a solar receiver duct. Reynolds numbers ranging from 5,300 to 24,000 were calculated. The experiment's findings showed that the highest heat transfer rate and friction loss were obtained when rib-groove turbulators were combined at inclined angles (β) of 0° and PR=1, while the highest thermal enhancement factor of 2.1 was discovered at β=45° and PR=1. Bohra *et al.* [7] investigated the Z-shaped baffles on the absorber plate in order to roughen it. The MATLAB program was utilized to estimate various performance characteristics. The impact of the blockage height ratio for a design with a relative pitch ratio of 1.5 and an attack angle of 45° under 1100 W/m^2 of insolation during operation. It is determined that the current configuration's optimum effective efficiency occurs at Reynold numbers between 5,000 and 10,000. With a blockage ratio of 0.3, the best performance was obtained. Jin *et al.* [8] showed the effect of several V-shaped ribs. The conditions are as follows the attack angles (α=30°, 45°, and 60°), thermohydraulic performance factor (n=4-14), pitch and high baffle ratio (P/e=10), and within *Re* at 10,000. A simulation within the parameter range of the study yields the following results Nu/Nu_s=3.28-4.02, f/f_s=3.26-6.13, and TPF=1.65-2.35. Investigating the effect of transverse baffles and multiple V-shaped baffle configurations (V-upstream baffles and V-downstream baffles) is the main goal of the current study. This study used V-shaped baffles to create a large longitudinal vortex flow and several impinging jets around the baffles, which increased the rate of heat transfer in the channel. Air was used as the working fluid with Reynolds numbers between 6,000 and 24,000.

2. Theoretical Aspects

The gathered data was utilized to calculate the Reynolds number (*Re*), Nusselt number (*N*u), friction factor (*f*), and thermal performance factor (*TPF*) values. The following section contains pertinent expressions for computing the aforementioned parameters as well as a few intermediate parameters. The investigation was performed under steady-state conditions. Wall and exit temperatures were monitored for at least two hours to ensure that steady-state conditions were achieved when monitoring pressure losses, thermal-hydraulic performance, and heat flow.

The Reynolds number is assessed using the diameter (D_h) as [9]

$$\mathrm{Re} = \frac{\rho U D_h}{\mu} \tag{1}$$

where k is the thermal conductivity of the working fluid (Air), D_h is the equivalent channel diameter determined from the flow cross-section (A) and perimeter (P).

$$D_h = \frac{4A}{P} = \frac{4(WH)}{2(W+H)} \tag{2}$$

The following formulas are used to calculate the average heat transfer coefficient (h) under a uniform heat flux condition using experimental data.

$$h = \frac{Q_{\text{conv}}}{A(T_{\text{w}} - T_{\text{b}})} \tag{3}$$

As shown below, the rate of convection heat transfer (Q_{conv}) is derived from the rate of air heat transfer (Q_{air}).

$$Q_{\text{conv}} = Q_{\text{air}} = \dot{m}C_{\text{p}}(T_{\text{o}} - T_{\text{i}}) \tag{4}$$

The average channel wall temperature (T_{w}) can be estimated, while thermochromic liquid crystal (TLC) sheet colors can be used to measure the average bulk air temperature (T_{b}).

$$T_{\text{b}} = \frac{(T_{\text{o}} + T_{\text{i}})}{2} \tag{5}$$

Air flow causes convection heat transfer. The following formula is used to describe the dimensionless Nusselt number [10], which is used to assess total heat transfer:

$$Nu = \frac{hD_{\text{h}}}{k} \tag{6}$$

The friction factor [9] is expressed using Eq. (7).

$$f = \frac{2}{(L / D_{\text{h}})} \frac{\Delta P}{(\rho U^2)} \tag{7}$$

The Nusselt number and friction factor are then used to determine the thermal performance factor (TPF) under a constant pumping power [11].

$$TPF = \left(\frac{Nu}{Nu_{\text{s}}}\right)\left(\frac{f}{f_{\text{s}}}\right)^{-\frac{1}{3}} \tag{8}$$

3. Experimental details

3.1. Experimental setup

Three sections of the experimental setup include an entering section (also known as the calm portion), a test section, and an outflow section. They were created within a rectangular heat exchanger channel that had a cross-sectional width and height of 150 mm and 40 mm (an aspect ratio of 3.75) and a length of 3500 mm. Figure 1 shows a schematic representation of the experimental setup. The channel walls of the system were effectively insulated to reduce heat losses. The airflow rate was modulated using an inverter, and air was introduced using a 2.2 kW fan. An orifice pressure loss across a plate was measured with a digital pressure gauge and then calculated using the airflow rate. A 600 W/m^2 uniform heat flux was delivered into the channel's bottom using a power supply controlled with a voltage-rectifying transformer. Eight RTD Pt100 thermocouples were positioned upstream and downstream of the test section to collect the data that was used to calculate the fluid's overall temperature. The channel wall temperatures were determined using TLC sheets that change color with temperature fluctuations. Images of the TLC were recorded using a high-resolution digital camera. The pressure losses across the test portion were also measured using a digital pressure gauge to calculate the friction factors. All data were gathered under steady-state conditions. The channel wall temperature was determined from the colours of the TLC sheet.

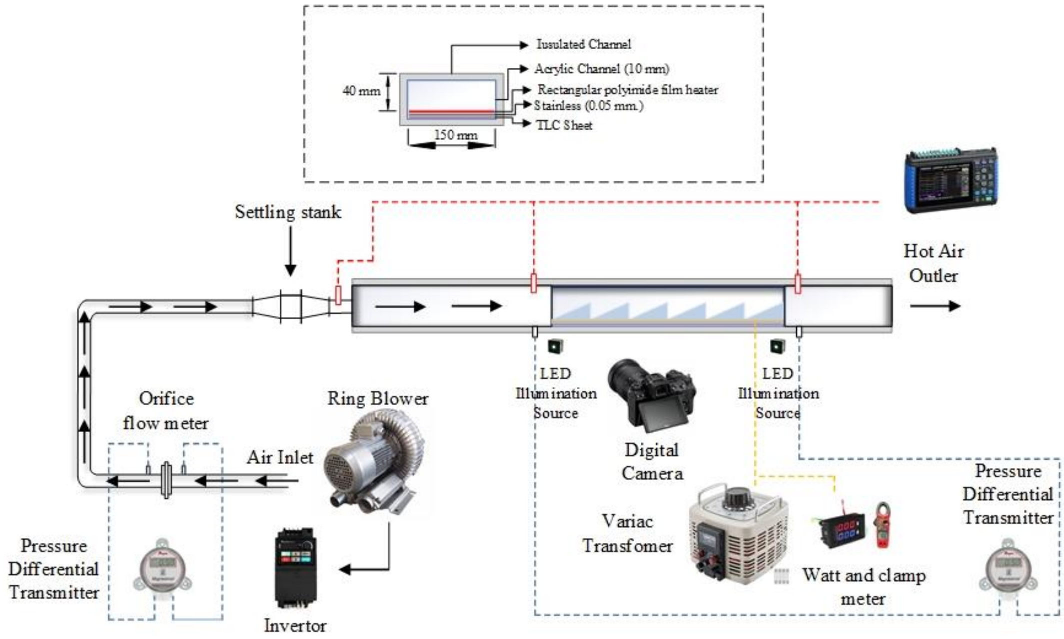

Figure 1. Schematic diagram of channel heat exchanger mounted with multiple V-shaped baffles.

3.2. Baffle geometries and operating conditions

Figures 2 and 3 depict the geometry of transverse baffles (TB) with multiple V-shaped baffles (M-VB) at an attack angle (θ) of 45^o arranged in upstream (V-up) and downstream (V-down) configurations on the inner lower surfaces of the channels. In the rectangular channel, baffle height (e) of 12 mm, pitch ratio (p/H) of 1.5, pitch (p) of 60 mm, and the height baffle ratio (e/H) of 0.3. Experimental research in the 6,000-24,000 Reynolds number range of rectangular baffled channels' thermal characteristics was done. The rectangular channel has a 3.75 aspect ratio. Table 1 presents an overview of the channel, baffle, and operating parameters.

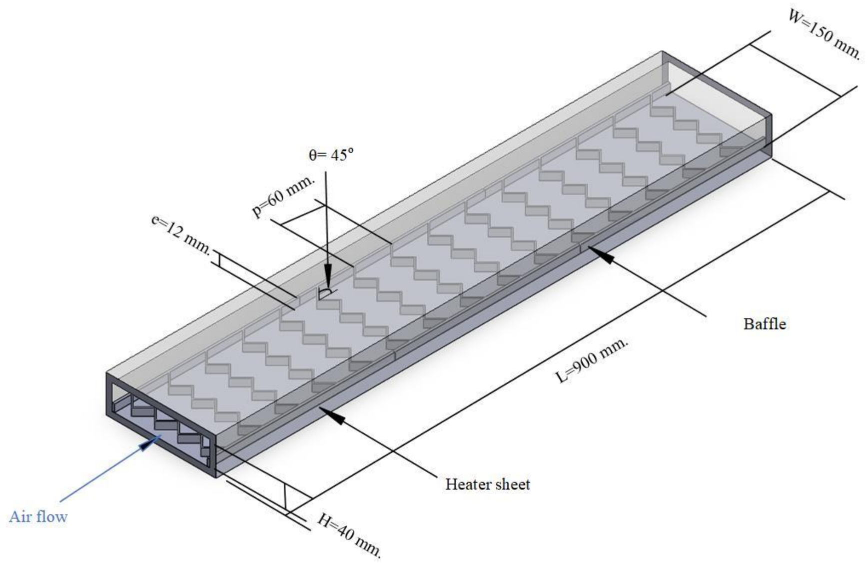

Figure 2. Channel installed with multiple V-baffles.

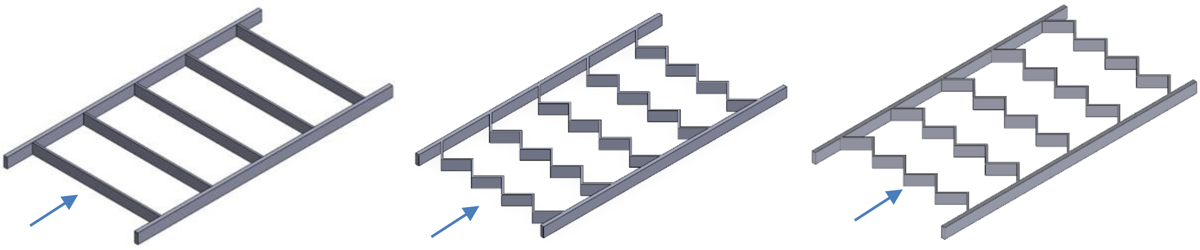

Figure 3. Transverse baffle configurations with several multiple V-baffles in upstream and downstream configurations.

Table 1. Transverse baffle geometries with notched baffles in inline and staggered arrangements, as well as operating conditions.

Test section	
Channel (Height, Width, Length; $H \times W \times L$)	40 mm ×150 mm ×900 mm
Channel aspect ratio (W/H)	3.75
Baffle material	Polylactic acid plastic (*PLA*)
Baffle height (e)	12 mm
Attack angle (θ)	45^o
Pitch ratio (p/H)	1.5
Baffle/height ratio (e/H)	0.3
Working fluid	Air
Reynolds number (Re)	6,000-24,000
Prandtl number (Pr)	0.7

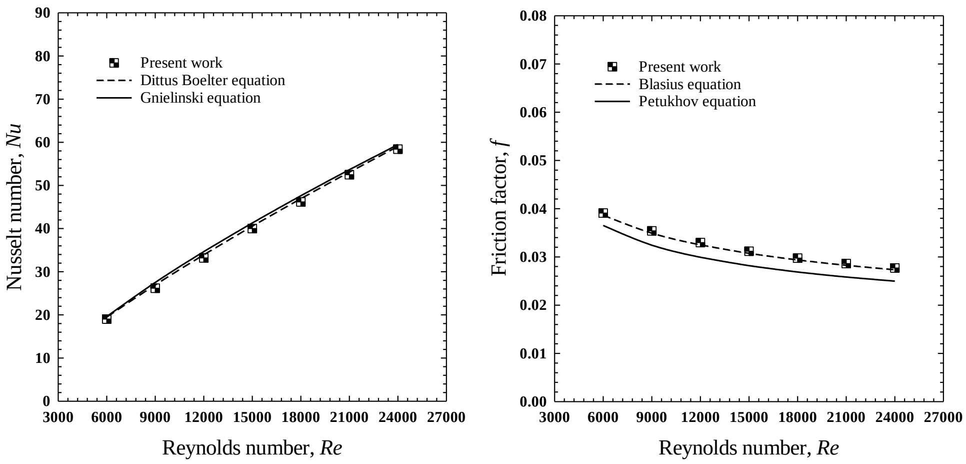

(a) *Nu* (b) *f*

Figure 4. Validation of the smooth channel.

4. Discussion of Experiment Results

A validation test is performed by comparing experimental data from the current smooth channel to data that were previously assessed using conventional correlations. A test was conducted to ascertain the dependability of the current experimental setup. Dittus-Boelter and Gnielinski correlations as well as Petukhov and Blasius correlations are representative and accepted correlations for the Nusselt number and friction factor, respectively. Figure 4 shows their similarity. It is clear that the results of the established correlations and our experimental findings agree. Friction factor and Nusselt number variations were ±1.81%, ±3.26%, ±1.36%, and ±9.01%, respectively.

4.1. Heat transfer

The Nusselt number (*Nu*) and Nusselt number ratio (Nu/Nu_s) on the inner bottom surfaces of the channel equipped with multiple V-shaped baffles upstream and downstream configurations are impacted by the Reynolds number (*Re*), as shown in Figures 5 and 6.

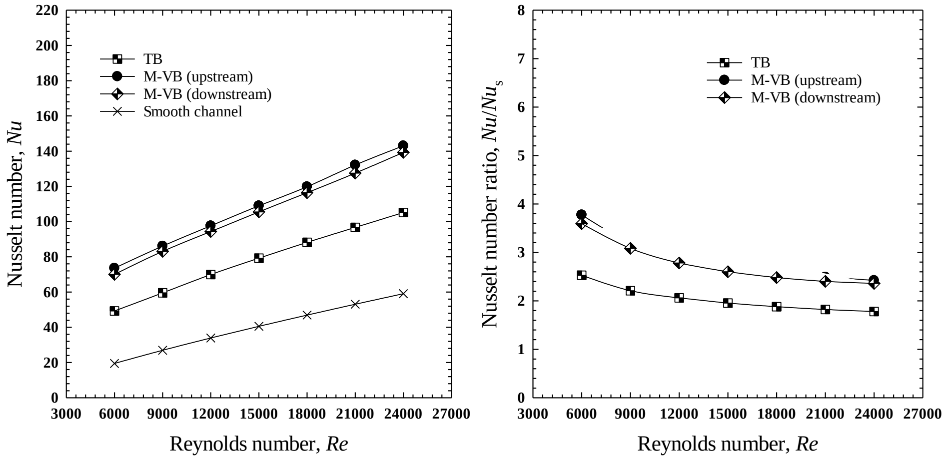

(a) (*Nu*) (b) Nu/Nu_s

Figure 5. Effects of multiple V-shaped baffles upstream and downstream on the average Nusselt number at various Reynolds numbers (*Re*).

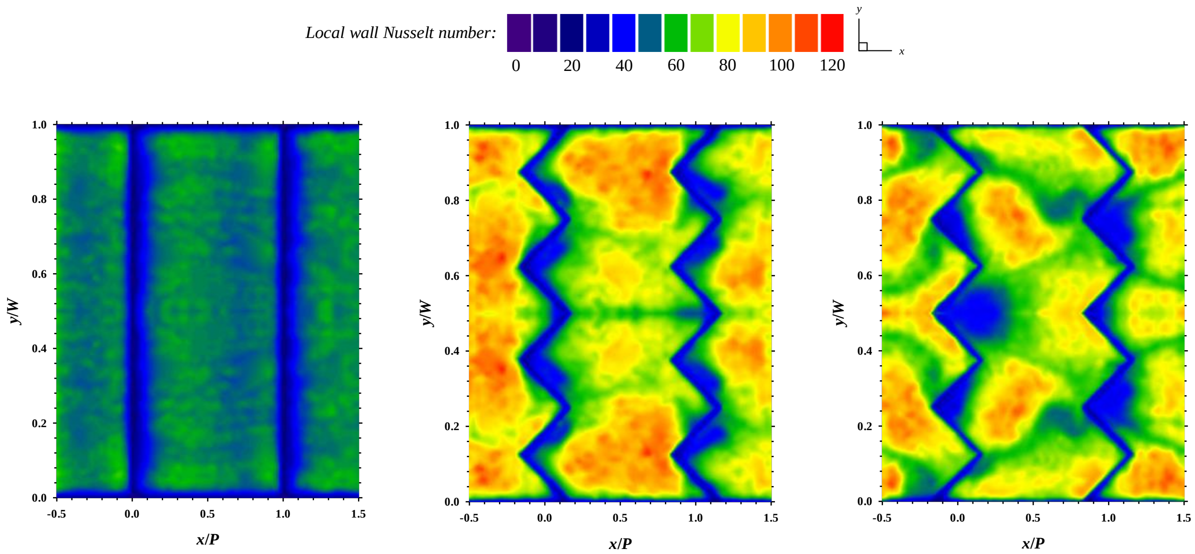

TB Multiple V-Shaped (Upstream direction) Multiple V-Shaped (Downstream direction)

Figure 6. Effects of multiple V-shaped baffles upstream and downstream on the local Nusselt number.

The Nusselt number (*Nu*) increased because turbulence intensifies with increasing Reynolds numbers. The Nusselt number ratio, however, decreased as the Reynolds number rose. This could be attributed to the system's thermal boundary layer being already thin at high Reynolds numbers in the absence of a baffle or smooth channel. Baffles therefore had less effect. The inner bottom surfaces of the channels were fitted with transverse baffles (TB) rather than multiple V-shaped baffles (M-VB) in the case of V-upstream baffles and V-downstream baffles with a baffle height ratio, *e/H*=0.30, as seen in Fig. 6. According to the experimental results, the baffled channel performed Nusselt number ratio (Nu/Nu_s) between 2.52 and 3.59 better in terms of heat transfer than a smooth channel. According to the study results, the multiple V-upstream baffle Nusselt number was marginally higher than the multiple V-downstream baffle. The present research is similar to that of Amnart *et al.* [12], which investigated simulation using a combined V-shaped baffle. It was discovered that the air stream produces a swirl and lengthens the amount of time during heat exchange when it flows across a V-shaped baffle, reducing the pressure loss values.

4.2. Pressure loss

The effects of multiple V-shaped baffles (M-VB) upstream and downstream on the friction factor are reported in Fig. 7. The friction factor (*f*) and friction factor ratio (f/f_s) trends, as well as the effects of the Reynolds number (*Re*), were examined. The friction factor and average friction factor consistently decrease with increasing Reynolds numbers. The findings imply that baffles that produce more turbulence will also result in a higher pressure drop and greater frictional losses. The use of transverse baffles (TB) at a Reynolds number of 6,000 causes the maximum friction factor, which is as high as 12.9 times that of the smooth channel.

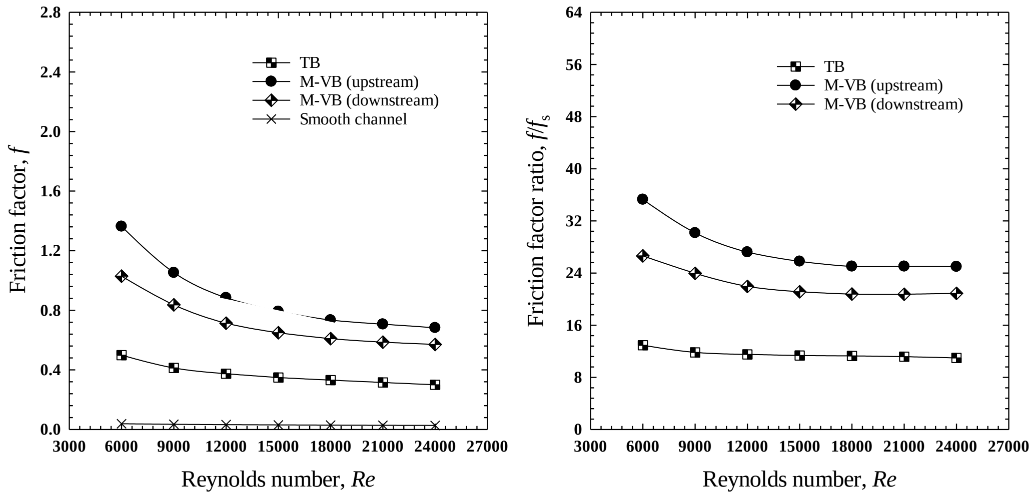

(a) (*f*) (b) f/f_s

Figure 7. Effects of multiple V-shaped baffles upstream and downstream on the average friction factor and friction factor ratio at different Reynolds numbers (*Re*).

4.3. Thermal performance factor

Figure 8 displays the channel with three alternative baffle layouts along with their thermal performance factor (*TPF*) results. In every scenario, as the Reynolds number increases, the thermal performance factor (*TPF*) decreases. According to these research findings, multiple V-shaped baffles (M-VB) downstream provide a higher thermal performance factor (*TPF*) than other baffles. The M-VB upstream thermal performance factor is up to 1.2 times that of a smooth channel. Some research suggests that adding roughness to a heat transfer surface can increase the heat transfer coefficient. However, the friction factor is increased by roughness. It follows such a system requires additional pumping power. The major goal of thermal design is to save energy in all forms, which is shown by higher thermal performance factors. Hence, the channel of the current study should be built to run at low Reynolds numbers with minor blockages.

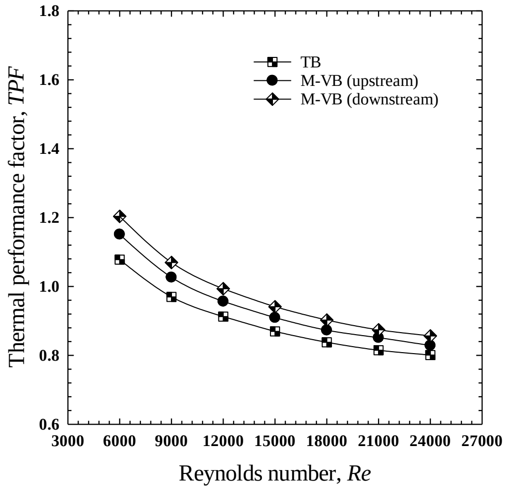

Figure 8. Effects of multiple V-shaped baffles upstream and downstream on the average thermal performance factor at various Reynolds numbers (*Re*).

5. Conclusions

Application was done of the two types baffles. For Reynolds numbers ranging from 6,000 to 24,000, the effectiveness of various V-shaped baffles (V-upstream and V-downstream) in comparison to the standard baffle (TB) was evaluated. According to our experimental findings, the conclusion can be summarized as follows:

5.1 Multiple V-upstream baffles provide superior heat transfer due to the major impact of higher heat transfer in the reattachment region. Other baffles were less effective for boosting heat transfer.

5.2 Multiple V-upstream and multiple V-downstream baffles produced less frictional losses than a typical baffle (TB).

5.3 Multiple V-upstream baffles offer a maximum thermal performance of 1.2 compared to a smooth channel. Heat transfer (Nu/Nu_s) is increase by 3.77 times that of a smooth channel. This is due to the dominant influence of higher heat transfer.

5.4 Another performance consideration is finding an optimal balance between enhanced heat transfer and the friction loss penalty. One of the primary factors in the best performance was the increased heat transfer brought on by the use of V-downstream baffles.

6. References

[1] Han, JC, & Zhang, YM. (1992). High-performance heat transfer ducts with parallel broken and V-shaped broken ribs. *International Journal of Heat and Mass Transfer*, *35*, 513-23.

[2] Promvonge, P., Khanoknaiyakarn, C., Sripattanapipat, S. & Skullong, S. (2021). Heat transfer in a solar air duct with multi-V-ribbed absorber and grooved back-plate. *Chemical Engineering Research and Design*, *168*, 84-95.

[3] Promvonge, P. & Skullong, S. (2021). Enhanced thermal performance in tubular heat exchanger contained with V-shaped baffles. *Applied Thermal Engineering*, *18*5, 116307.

[4] Promvonge, P. & Skullong, S. (2019). Heat transfer in solar receiver heat exchanger with combined punched-V-ribs and chamfer-V-grooves. *International Journal of Heat and Mass Transfer*, *143*, 118486.

[5] Hoonpong P. & Skullong, S. (2018). Performance improvement of solar air heater with V-baffles on absorber plate. *Journal of Research and Applications in Mechanical Engineering*, *6(1)*, 29-39.

[6] Jaytanaiwachira, N., Promvonge, P., Thianpong, C., & Skullong, S. (2022). Thermal-hydraulic performance of solar receiver duct with inclined punched-ribs and grooves. *Case Studies in Thermal Engineering*, *39*, 102437.
[7] Bohra, J., Bisht. S.V., Bhandari, P., Rawat, S.K., Singh, J., Kumar, K. & Rawat, B. (2022). Effect of variable blockage height ratio on performance for solar air heater roughened with 45° Z-shaped baffles. *Materialstoday:Proceeding*, *69(2)*, 153-157.
[8] Jin, D., Quan, S., Zuo, J .& Xu, S.,) 2019(. Numerical investigation of heat transfer enhancement in a solar air heater roughened by multiple V-shaped ribs, *Renewable Energy*, *134*, 78-88.
[9] White, F.M. (2021). *Fluid Mechanics*. 9th edition, McGraw Hill, New York.
[10] Cengel, Y.A. & Ghajar, A.J. (2015). *Heat and mass transfer: fundamentals & applications*, 5th edition, Mc Graw-Hill New York
[11] Webb, R.L. & Kim, N.H. (2005). *Principles of Enhanced Heat Transfer*. 2nd edition, John Wiley & Sons, New York.
[12] Boonloi, A. & Jedsadaratanachai, W. (2016). Numerical investigation on turbulent forced convection and heat transfer characteristic in a square channel with discrete combined V-baffle and V-orifice. *Case Studies in Thermal Engineering*, *8*, 226-235.

ETM0020

Experimental Investigation of Heat Transfer and Pressure Loss in a Channel Installed with Wave-Sine Shaped Baffles

W Keaitnukul[1], M Phumkaew[2], A Phila[2], K Wongcharee[1], V Chuwattanakul[3], N Maruyama[4,5], M Hirota[6], S Eiamsa-ard[2], and K Buanak[7,*]

[1]Department of Process and Industrial Engineering, School of Engineering and Industrial Technology, Mahanakorn University of Technology, Bangkok, Thailand.
[2]Department of Mechanical Engineering, School of Engineering and Industrial Technology, Mahanakorn University of Technology, Nongchok, Bangkok, Thailand.
[3]School of Engineering, King Mongkut's Institute of Technology Ladkrabang, Ladkrabang, Bangkok, Thailand.
[4]Engineering Innovation Unit, Graduate School of Regional Innovation Studies, Mie University, Tsu, Mie, 514-8507, Japan.
[5]Department of Mechanical Engineering, Faculty of Engineering, Mie University, Tsu, Mie, 514-8507, Japan.
[6]Department of Mechanical Engineering, Faculty of Engineering, Aichi Institute of Technology, Toyota, Aichi, 470-0392, Japan.
[7]Department of Automotive-Mechanical Engineering, Faculty of Industrial Technology, Rajabhat Rajanagarindra University, Mueang Chachoengsao, Thailand.

* Corresponding Author: kalong@techno.rru.ac.th

Abstract. An experimental study of heat transfer and pressure loss of channels with wave-sine shaped baffles (WSB) and the transverse baffle (TB) is presented in the current paper. The effects of geometric parameters: pitch ratio (p/H=1.5), blockage ratio (e/H=0.3), peak amplitude ratio (a/w=0.067), and four wavelength ratios (b/w=0.25, 0.33, 0.5, and 1.0) were studied in the following turbulent region of 6,000 ≤ Re ≤ 24,000). The results have shown that the WSB with a wavelength ratio of (b/w=0.5) resulted in the greatest heat transfer rate of up to 3.17-4.87 times than that of a smooth channel. The WSB provided a better thermal performance factor by around 57.62–78.11% over the TB. For the range of investigated parameters, it was discovered that the smallest wavelength ratio of (b/w=0.25) resulted in the greatest thermal performance factor of 0.91 to 1.28.

Keywords: Nusselt number, Pressure losses, Wave-sine shaped, Thermal performance.

1. Introduction

Energy conservation for thermal systems, including heat exchangers among many others, is crucial due to the rising demand for energy. Therefore, it is necessary to develop advanced equipment for the thermal system required in various industries for efficiency and cost-effective energy use. Passive heat transfer does not require external energy, while active heat transfer techniques require energy to increase the heat transfer rate. A smooth channel's low convection heat transfer coefficient is primarily caused by the creation of a boundary layer, together with insufficient flow mixing between the core and wall zones. Methods for accelerating heat transfer in channels include: generating vortices that disturb thermal boundary layers, and boosting turbulence. In addition, utilizing vortex flow devices to promote heat transfer leads to smaller, yet more efficient heat exchanger systems. Certain components, such as twisted tapes, baffles, ribs, dimples, and grooves, are widely used in both heating and cooling systems.

Compared to that of regular ribs, Tanda [1] indicated that V-broken ribs offer better heat transfer. From then on, ribs or baffles added or inserted into ducts for the increase of turbulence close to duct walls have been the subject of various research. It has been discovered that taller ribs of (e=5 mm, p/e=4 and 8) performed noticeably better in terms of heat transfer than lower ribs of (e=3 mm, p/e=13.3). The maximum heat transfer rate is provided by transversely fractured ribs. Transverse *solid* ribs of (p/e=4 and 8) have lesser heat transfer rate than that of transverse fractured ribs of (p/e=4 and 8) and V-shaped ribs of (p/e=8). When p/e was set to the value of 13.3, transverse solid ribs have proved, as a repetition, to produce lower heat transfer rates than those of cracked transverse ribs, despite these values being higher than those produced by V-shaped ribs. The angle of inclination of V-shaped ribs was also shown to have a few to no impact on the rate of heat transfer for both p/e values. Momin *et al*. [2] had meticulously examined the impacts of relative roughness height and attack angle at a fixed relative roughness pitch of 10 with Reynolds numbers ranging from 2500 to 18,000, on V-shaped ribs. It has been observed that the increase in Nusselt number alongside Reynolds number was present. Consequently, as Reynolds number decreases, the friction factor, on the other hand, increases in response. With a roughness height of 0.034, V-shaped ribs have resulted in the increase in Nusselt number that was 1.14 and 2.30 times greater, respectively, than that of the transverse ribs and smooth surface channels. Skullong *et al*. [3] used three wing porosity area ratios: (A_h/A_w=0.031, 0.085, and 0.167) and four groove-wing distance ratios of (g/H=0.4, 0.5, and 1.0) to examine the thermal performance of a solar air heater channel with compound wavy groove and delta-wing vortex generators positioned on the absorber plate. The highest heat transfer rate and friction factor are both produced by a lowered wing porosity area ratio of (A_h/A_w) at a groove-wing distance ratio of g/H=0.5, which is roughly 6 and 30 times of that of a plain channel. However, the wing porosity area ratio of A_h/A_w=0.085 and the groove-wing distance ratio of g/H=0.5 are the ones that produce the best thermal performance. The compound devices' thermal performance was roughly 46.3% better than that of the groove alone. According to Jaber *et al*. [4], experimental research has been conducted on turbulent heat transfer and friction within a corrugated square duct with different baffle geometries added. On the top and bottom walls of the duct, there are five different types of baffles that are attached to the duct, of which include: flat, rectangular, semi-circular, triangular, and trapezoidal baffles. The impacts of the duct's wavy surface, each baffle's distinct geometry, positioning, flow, and Reynolds number are examined. Under the state of continuous wall heat flux, air is used as the working fluid with Reynolds numbers ranging from 3,442 to 17,213 to result in a steady heat flux from the walls. The average Nusselt numbers and friction factors that were obtained during the experiment are present; according to the results, the trapezoidal baffle offers superior thermal performance compared to that of other baffles with different geometry. Thus, the current study has proved that the greatest thermal performance factor obtained from the experiment conducted under similar pumping power, has resulted in heat transfer of approximately 2.26 times more than that of the simple duct. Additionally, it was discovered that the baffles attached to the bottom wall of the duct function thermally superior than that of other baffles attached to the duct’s upper wall.

In this study, the effects of sine wave-shaped baffles on fluid properties, including Reynolds number (Re), Nusselt number (Nu), friction factor (f), and thermal performance factor (TPF) in a rectangular channel, are to be examined. In comparison to the transverse baffle, four different types of wave-sine baffles (b/w=0.25, 0.33, 0.5, and 1.0) were utilized, where the differentiation of each insert must be done to find an ideal baffle geometry.

2. Theoretical Aspects

The Reynolds number (*Re*), Nusselt number (*Nu*), friction factor (*f*), and thermal performance factor (*TPF*) were then calculated using gathered data. The relevant expressions for calculating the aforementioned parameters, as well as a few intermediate parameters, are provided in the following section. The experiment was conducted in a steady-state environment, with the wall and exit temperatures checked for at least two hours alongside heat flow, thermal-hydraulic performance, and pressure losses, to ensure uniformity.

The Reynolds number is calculated using the equivalent diameter (D_h) as follows:

$$Re = \frac{\rho U D_h}{\mu} \tag{1}$$

where ρ is the density of the working fluid, D_h is the equivalent channel diameter determined from the flow's cross-section (*A*) and perimeter (*P*).

The heat flux (*q*), average wall temperature along the *y*-axis at any *x*-position (T_{wx}), and the local characteristics fluid temperature (T_{bx}) can all be used to calculate the local heat transfer coefficient (h_x). This was done by using a linear interpolation method between the test section's inlet and outlet air temperatures as follows:

$$h_x = \frac{q}{(T_{wx} - T_{bx})} \tag{2}$$

The formula illustrated below is used to calculate the average heat transfer coefficient (*h*) under the uniform heat flux condition using experimental data

$$h = \frac{Q_{conv}}{A_s (T_w - T_b)} \tag{3}$$

The average channel wall temperature (T_w) can be estimated; while the thermochromic liquid crystal (TLC) sheet can be used to get the average bulk air temperature (T_b) illustrated as follows:

$$T_b = (T_i + T_o) / 2 \tag{4}$$

The convection process is what causes convection heat transfer. The following formula is used to describe the dimensionless Nusselt number (*Nu*), which is used to evaluate total heat transfer [6].

$$Nu = \frac{h D_h}{k} \tag{5}$$

The friction factor can be expressed using Eq. (6).

$$f = \frac{2}{(L / D_h)} \frac{\Delta P}{(\rho U^2)} \tag{6}$$

The Nusselt number and friction factor are then used to determine the thermal performance factor (TPF) as follows [7-8]:

$$TPF = \left(Nu / Nu_s\right)\left(f / f_s\right)^{-\frac{1}{3}} \tag{7}$$

3. Experimental Information

3.1. Experimental apparatus

Figure 1 depicts the rectangular channel that was utilized for this experiment and the wave-sine shaped baffles that were built on it. The test section was made out of a 10 mm thick acrylic material, with a cross-sectional area of 150 mm (*W*) and 40 mm (*H*). The wave-sine shaped baffles used in the experiment were made of polylactic acid (PLA). The 900 mm long test section wall was covered with a heating sheet, while a thin sheet of thermochromic liquid crystal (TLC) is as well attached to a stainless-steel sheet. The thickness of wave-sine shaped baffles is 1.5 mm, while the height is 12 mm. In Figure 2, four distinct types of sine wave-shaped baffles are displayed.

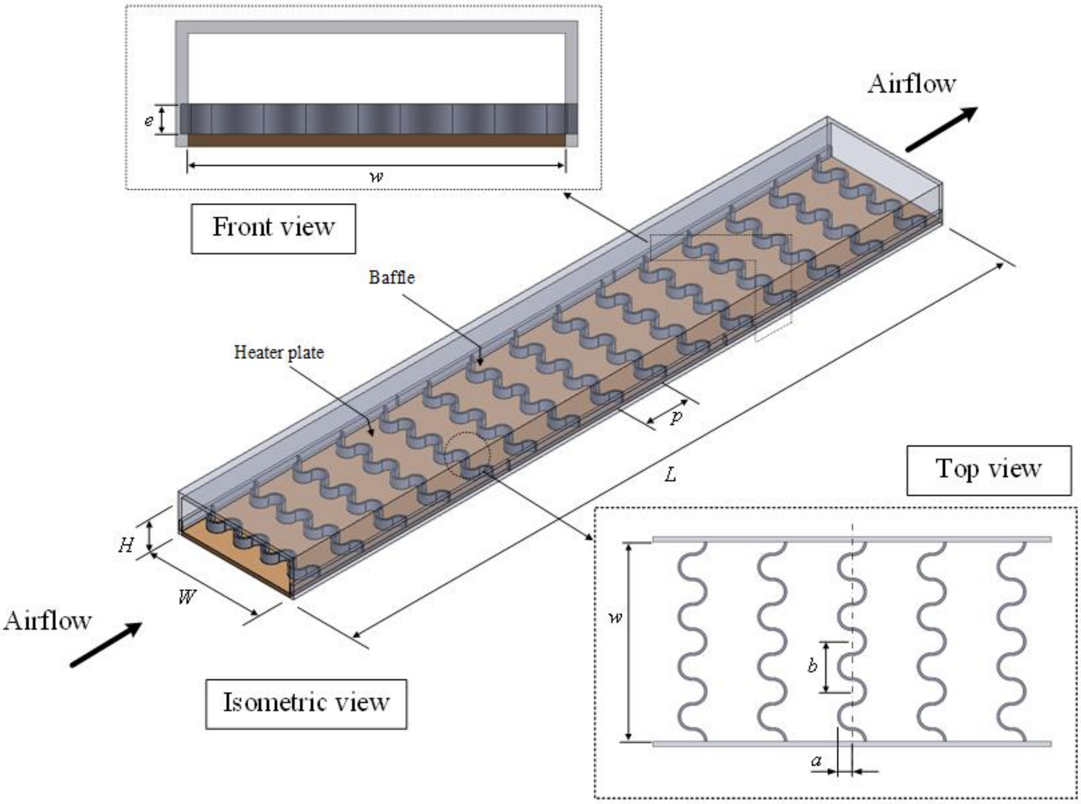

Figure 1. The structure of a rectangular channel mounted with wave-sine shaped baffles.

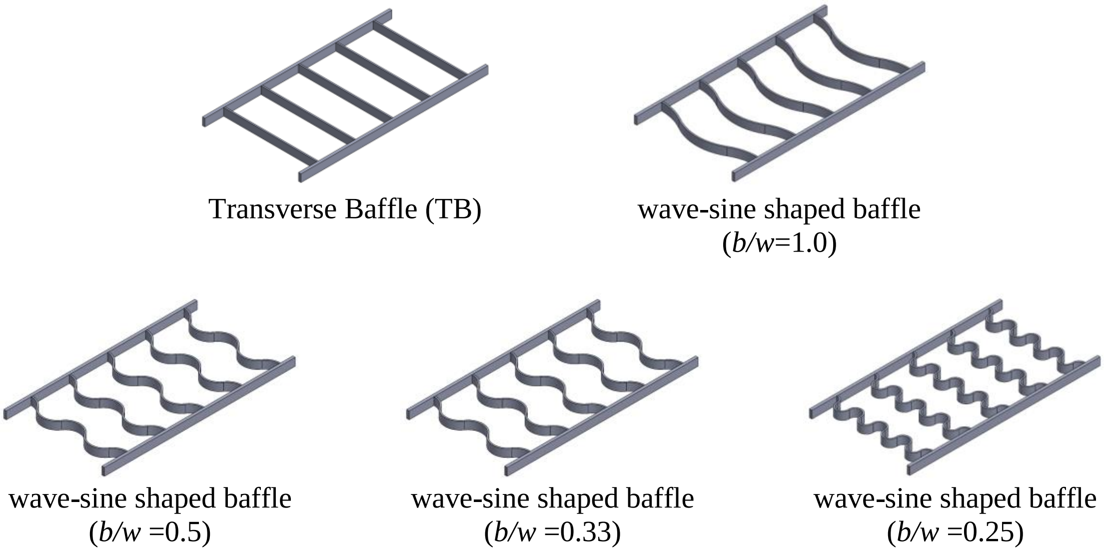

Figure 2. Configurations of the transverse baffle with wave-sine shaped baffles.

3.2. Operating parameters and baffle geometries
Figure 3 illustrates a panoramic view of the experimental setup. After the settling chamber, a rectangular channel with a test section and clam section was connected to a high-pressure fan, alongside an orifice flowmeter placed directly in this channel. For clarity and accuracy, the channel test component is depicted in Figure 1. The alternating current source was used to power a thin thermal sheet, which was principally responsible for maintaining a constant rate of surface heat release on the test area's lower plate. Specialized acrylic bars with low heat conductivity have been installed as thermal barriers at the intake and exit extremities of the upper area.

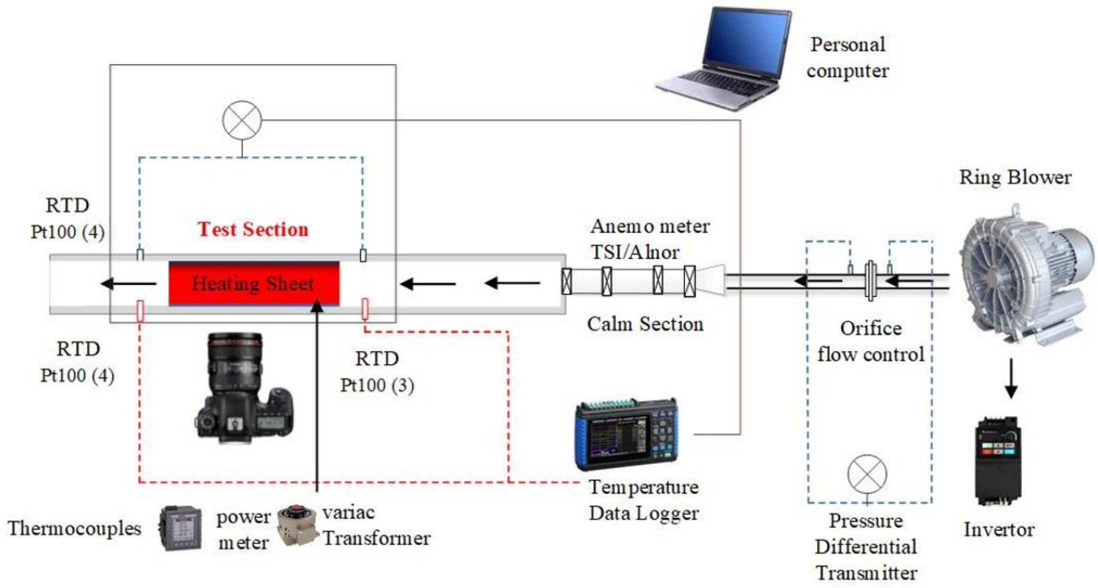

Figure 3. An illustration of the experimental setup.

A high-pressure fan was utilized to introduce the testing medium (air) into the system. To create effective air flow rates, an inverter was installed to alter the fan's working speed. An orifice plate that was calibrated using heated wire anemometers was used to monitor the airflow rate in the system, where the pressure over the orifice plate can be calculated using a digital pressure gauge. A thermochromic liquid crystal (TLC) sheet has been put predominantly on the bottom wall to determine temperature distributions, while two resistance-to-temperature detectors were positioned upstream (towards the higher part) of the channel entry to monitor the temperature of inflow collection. Two static pressure probes were inserted at the head of the main channel, which was subjected to an analysis of the average friction factor, to measure the axial pressure decrease throughout the experiment. The first tap is positioned 300 mm upstream of the leading edge of the channel, while the second is positioned 300 mm downstream of the trailing edge.

4. Experimental Results and Discussion
A validation test is performed by comparing experimental data from the current smooth channel to data that were previously evaluated using conventional correlations. To ascertain the dependability of the current experimental setup, a test was conducted, with 'Dittus-Boelter and Gnielinski' correlations and the 'Petukhov and Blasius' correlations as the typical correlations using Nusselt number and friction factor as factors, illustrated in Figure 4. It was evident that the current findings and the outcomes of the traditional correlations match, where the actual values of Nusselt number and friction factor deviates from the anticipated correlations by 1.81%, 3.26%, 1.36%, and 9.01%, respectively.

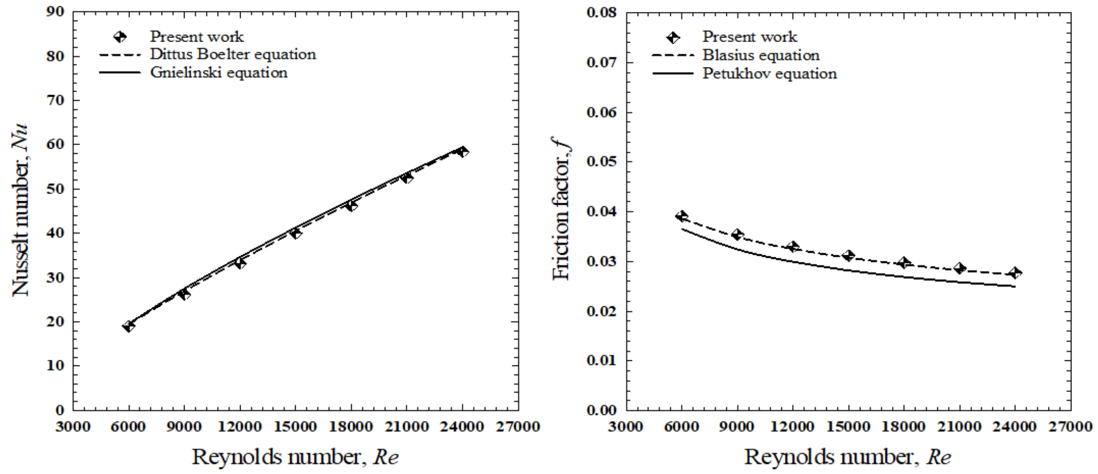

Figure 4. A validation test conducted in the current smooth channel.

4.1. Results of heat transfer

The Nusselt number (*Nu*) and Nusselt number ratio (Nu/Nu_s) obtained from the inner bottom surfaces of the channels equipped with the wave-sine shaped baffles (WSB) and the transverse baffle (TB) designs are shown in Figure 5 as values affected by the Reynolds number (*Re*). The Nusselt number (*Nu*) frequently increased due to turbulence which intensifies as the Reynolds number increases. The Nusselt number ratio, however, decreases as the Reynolds number increases; this might be attributed to the system's thermal boundary layer being already thin at a point where the Reynolds number is high, in the absence of a baffle or a smooth channel. The modification of baffles, therefore, had less of an effect on the alterations.

Compared to the transverse baffle (TB), wave sine-shaped baffles of (*b/w*=0.25, 0.33, 0.5, and 1.0) were attached to the inner bottom surfaces of the channels. When compared to the transverse baffle (TB), wave sine-shaped baffles (*b/w*=0.5) provided the maximum Nusselt number by enhancing heat transfer by around 78.29–92.63%.

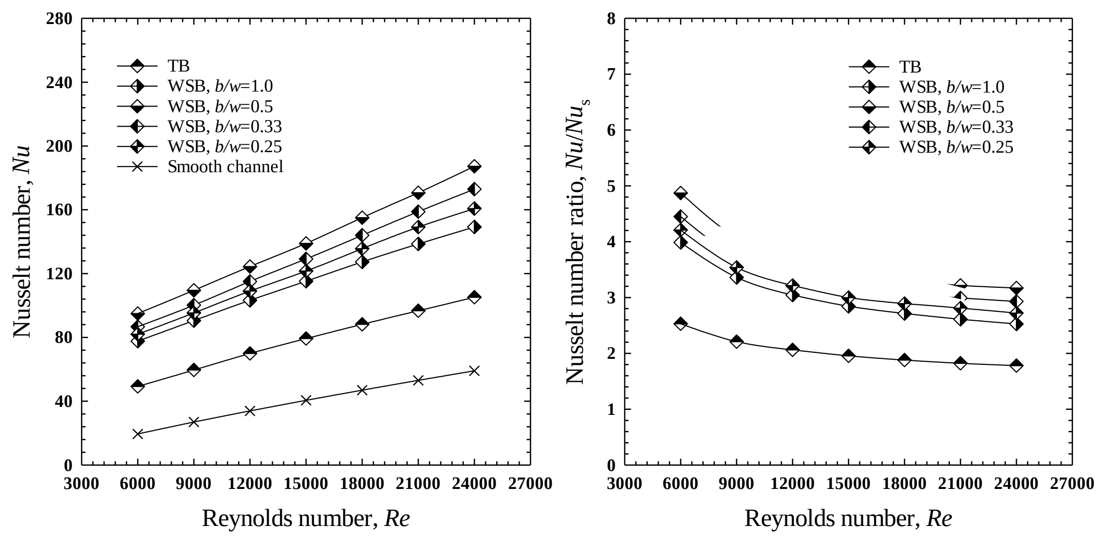

Figure 5. Effects of Reynolds number and wavelength ratio on Nusselt number and Nusselt number ratio.

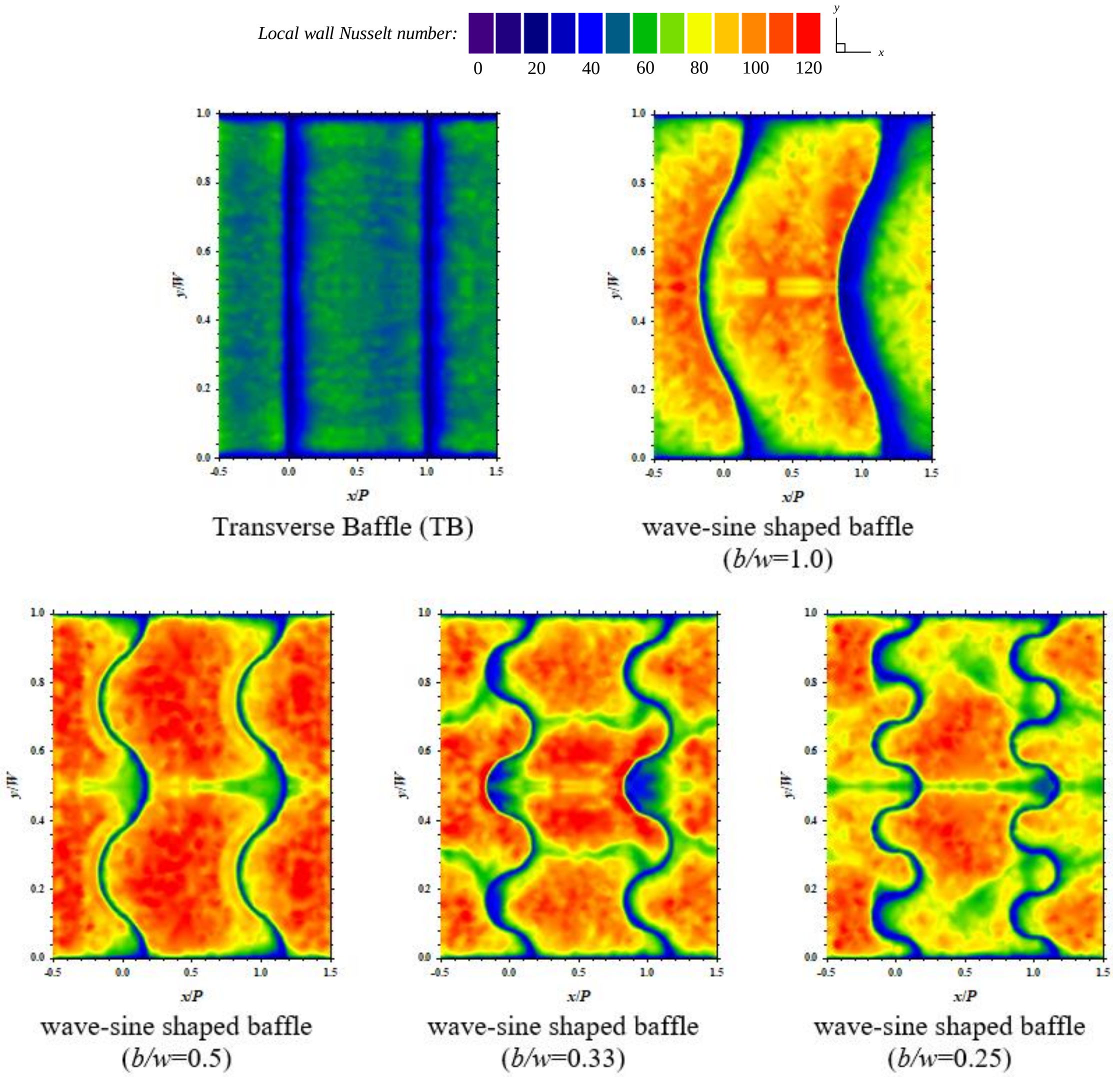

Figure 6. Nusselt number obtained on the surface installed with the transverse baffle and wave-sine shaped baffles of (b/w=0.25, 0.33, 0.5, and 1) at the Reynolds number of 6,000.

The results shown above are in alignment with the obtained Nusselt number illustrated in Figure 6. Increased reattachment is introduced by the wave sine-shaped baffle of (b/w=0.5), which increases the effectiveness of thermal boundary layer disruption. The lowest Nusselt number is produced by the transverse baffle (TB). At a given Reynolds number, Nusselt numbers of the channel with baffles are invariably higher than those obtained from smooth channels (Nu/Nu_s is greater than 1). The highest increase of the Nusselt number ratio (Nu/Nu_s), which is approximately 4.87 times, is achieved with the utilization of a wave-sine shaped baffle of (b/w=0.5) at the Reynolds number of 6,000.

4.2. Results of the Pressure loss

Figure 7 illustrated the trends of friction factor (f) and friction factor ratio (f/f_S) along with the impacts of Reynolds number (Re) on the latter two values. The average friction factor and friction factor ratio constantly rise along with the decreasing Reynolds number at the same Reynolds number value. The findings suggested that baffles that produce higher levels of turbulence will also result in a greater pressure drop and a greater friction loss. When a wave-sine shaped baffle of (b/w=0.5) is used in the range under consideration at Reynolds number of 6,000, the resulting maximum friction factor value can reach up to 67.22 times of that obtained in a smooth channel, which, correspondingly, would be similar for wave-sine shaped baffles of (*b/w*=0.33, 0.25, 1.0) and the transverse baffle (TB).

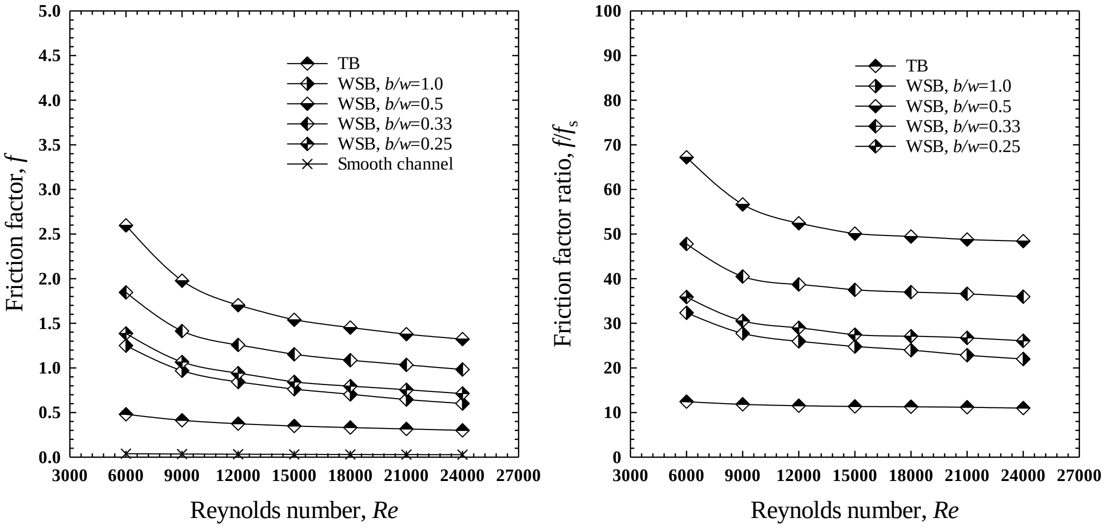

Figure 7. Effects of Reynolds number and wavelength ratio on friction factor and friction factor ratio.

4.3 Results of the thermal performance factor

With its four separate wave-sine shaped baffles (WSB) and the transverse baffle (TB), the channel's thermal performance values are shown in Figure 8. In every scenario, as the Reynolds number increases, the thermal performance factor decreases consequently. The wave-sine shaped baffle of (*b/w*=0.25) offers highest thermal performance factor, according to the research results. At the Reynolds number of 6,000, thermal performance factor is at its maximum value, which is 1.28 times more than that of the smooth channel, followed by wave-sine shaped baffles of (*b/w*=0.25, 1, 0.33, and 0.5), respectively.

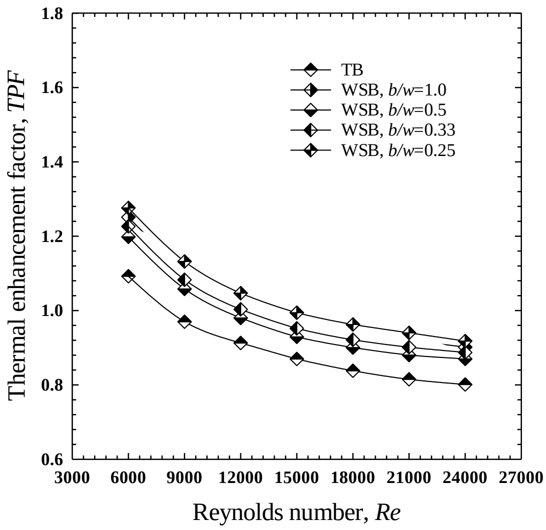

Figure 8. Effects of Reynolds number and wavelength ratio on thermal performance factor.

According to numerous studies, the heat transfer coefficient may be increased by roughening heat transfer surface. Roughness, on the other hand, makes friction more of a factor. Consequently, the system demands additional pumping power. The fundamental goal of the design is to minimize obstruction and operate the channel at low Reynolds numbers in order to save energy, as evidenced by a high thermal performance factor.

5. Conclusions

For Reynolds numbers ranging from 6,000 to 24,000, the usage of four different wave-sine shaped baffles (WSB) and the transverse baffle (TB) was examined. The experimental results have shown that the Nusselt numbers increase, while friction values, on the other hand, decrease when the Reynolds number rise.

- The wave-sine shaped baffle of (b/w=0.5) increased heat transfer by about 78.29-92.63%, resulting in the highest Nusselt number value.

- The friction factor for the wave-sine shaped baffle of (b/w=0.5) was 48.41-67.22 times more than that of a smooth channel.

- The wave-sine shaped baffle of (b/w=0.25) provided the highest thermal performance of 1.28 in comparison to the smooth channel, due to the dominating influence of increased heat transfer.

- Additional efficiency is the optimal trade-off between improved heat transfer and reduced friction loss. Thus, among the baffles with maximal performances, the wave-sine shaped baffle of (b/w=0.25) resulted in the highest thermal performance.

6. References

[1] Tanda G. (2004). Heat transfer in rectangular channels with transverse and V-shaped broken ribs. *International Journal of Heat and Mass Transfer*, 47(2), 229-243.

[2] Momin, A. M. E., Saini, J. S. & Solanki, S. C. (2002) Heat transfer and friction in solar air heater duct with V-shaped rib roughness on absorber plate. *International Journal of Heat and Mass Transfer*, 45(16), 3383–3396.

[3] Skullong S., Promvonge P., Thianpong C. & Pimsarn M. (2016). Thermal performance in solar air heater channel with combined wavy-groove and perforated-delta wing vortex generators. *Applied Thermal Engineering*, 100, 611-620.

[4] Abdulhameed, J. J., Khudhur, D. S. & Kassim, M.S. (2019). Effect of baffles geometry on heat transfer enhancement inside corrugated duct. *International Journal of Mechanical Engineering and Technology*, 10, 555-556.

[5] Cengel Y.A., & Ghajar A.J. (2015). *Heat and mass transfer: fundamentals & applications*. 5th edition, McGraw Hill New York.

[6] White F. M. (2021). *Fluid Mechanics*. 9th edition, McGraw Hill, New York.

[7] Webb R. L. & Kim N. H. (2005). *Principles of Enhanced Heat Transfer*. 2th edition, John Wiley & Sons, New York.

The 13th TSME International Conference on Mechanical Engineering
12th – 15th December 2023
Chiang Mai, Thailand

ETM0022

Experimental Investigation of Heat Transfer and Friction Loss in Two-pass Rectangular Channels with Ribbed Walls

P Thapmanee[1], S Pingta[2], A Phila[2], K Srisathit[2], K Wongcharee[1], N Maruyama[3,4], M Hirota[5], and S Eiamsa-ard[2,*]

[1]Department of Process and Industrial Engineering, School of Engineering and Industrial Technology, Mahanakorn University of Technology, Bangkok, Thailand
[2]Department of Mechanical Engineering, School of Engineering and Industrial Technology, Mahanakorn University of Technology, Bangkok, Thailand
[3]Engineering Innovation Unit, Graduate School of Regional Innovation Studies, Mie University, Tsu, Mie, 514-8507, Japan
[4]Department of Mechanical Engineering, Faculty of Engineering, Mie University, Tsu, Mie, 514-8507, Japan
[5]Department of Mechanical Engineering, Faculty of Engineering, Aichi Institute of Technology, Toyota, Aichi, 470-0392, Japan
[6]Division of System Engineering, Graduate School of Engineering, Mie University, Tsu, Mie, 514-8507, Japan.

* Corresponding Author: smith@mut.ac.th

Abstract. This article describes the heat transfer and friction factor characteristics in two-pass rectangular channels with sine wave ribs. The ribs employed in the current study had two different peak amplitudes (a) of 1 and 2 mm and a constant wave period (b) of 2π. Experiments encompassed Reynolds numbers (Re) ranging from 10,000 to 34,000. Results of the channels with ribbed walls are reported along with those of a smooth channel. Evidently, the Nusselt numbers of the channels with ribbed walls were enhanced by 1.07-1.24 times as compared to those of the smooth channel. The ribs with a larger wave amplitude gave superior heat transfer augmentation (beneficial effect) and also caused higher friction loss (drawback). An overall performance was evaluated in term of a thermal performance factor (*TPF*) which was determined from both heat transfer and friction loss results. The maximum *TPF* of the enhanced channel was found to be 1.03 (or 3% higher than that of the smooth channel) at a wave amplitude of 2 mm and Re of 10,000.

Keywords: Gas turbine, Ribbed turbulator, Thermal performance, Two-pass channel.

1. Introduction

Heat exchangers are utilized in vast applications including the automotive industry, internal cooling for gas turbine blades, air conditioning and refrigerant applications, electrical circuits in electronic chipsets, etc. [1]. Gas turbine blade is an essential part of aircraft propulsion and power generation. The basic requirements for turbine operation are high output power and thermal efficiency. Thus, working fluids are utilized at extremely high temperatures which may be beyond the operating temperature limit of materials [2-3]. To meet the output and safety standards, efficient heat transfer enhancement is necessary. In recent years, active and passive heat transfer enhancement techniques have been intensively developed in order to improve heat transfer rate and reduce heat exchanger size and hence a cost of heat exchanger. The most popular technique to enhance heat transfer in the internal serpentine cooling channels is the employment of rib turbulators. In gas turbine airfoils, ribs are commonly cast on two opposite walls of the cooling tunnel to facilitate heat transfer from the pressure and suction surfaces of the blade walls. However, one, two, three, or all four rib-roughened walls may be utilized in other applications such as electronic equipment, and nuclear reactors. In common turbulators simultaneously enhance heat transfer (a desired effect) and friction loss (an undesired effect). A thermal performance factor (*TPF*) is formulated to assess an overall performance of the system with turbulators by taking both heat transfer and friction loss results into account. A greater thermal performance factor reflects a better tradeoff between the enhanced heat transfer and increased friction loss. The challenge in designing ribs is to gain a reasonable tradeoff between both factors.

Studies of the influences of rib geometry (height, spacing, angle-of-attack, cross-section, and configuration) on heat transfer and flow characteristics. An early work by Han *et al.* [4] revealed that ribs at a 45° angle of attack were more efficient for heat transfer enhancement than the ones at a 90° angle of attack. At a given angle of attack, the ribs in a symmetrical arrangement showed comparable performance to the ones in a staggered arrangement. Chandra *et al.* [5] compared heat transfer in the channels with different numbers (one, two, three, and four) of ribbed walls. Experiments were performed at a pitch-to-rib height (P/e) ratio of 8, a rib-height-to-channel hydraulic diameter (e/D_h) ratio of 0.0625, and a hydraulic diameter-to-channel length ratio (L/D_h) of 20 for Reynolds numbers ranging from 10,000 to 80,000. Their results demonstrated that heat transfer rate and friction factor monotonically increased with an increasing number of rib walls. However, heat transfer performance dropped with increasing Reynolds number and the number of ribbed walls.

Wen-Lung Fu *et al.* [6] investigated the influence of channel aspect ratio (W/H = 0.25, 0.5, 1, 2, and 4) on heat transfer in two-pass rotating rectangular channels with smooth walls and 45-degree ribbed walls for Reynolds numbers of 5000, 10,000, 25,000, and 40,000. Evidently, all the ribbed channels gave comparable heat transfer enhancement. Nevertheless, the channel with an aspect ratio of 1:4 possessed the maximum thermal performance since it caused the lowest pressure penalty. It was also observed that at the inlet of the 180-degree turn, the heat transfer increased on both the leading and trailing surfaces.

Most previous studies focused on enhancing heat transfer by installing turbulators on heated channel walls. However, heat transfer augmentation of side walls has been rarely reported. Hence, this study is to provide additional heat transfer behaviors results of the side channel walls equipped with rib turbulators as compared to that of smooth ones in order to gain a better understanding on heat transfer of augmented channels. Furthermore, the current work also seeks conditions to improve thermal performance factor by comparing the results obtained by using the sine wave ribs with two different peak amplitudes (a) of 1 and 2 mm for Reynolds numbers (Re) ranging from 10,000 to 34,000.

2. Data reduction

In the present work, it is assumed that heat convection is solely responsible for total heat transfer. Therefore, air heat transfer (Q_{air}) is evaluated from convection heat transfer (Q_{conv}), which is expressed below.

$$Q_{air} = Q_{conv} = \dot{m}C_p\left(T_o - T_i\right) \quad (1)$$

Under the uniform heat flux condition, the following formulas are used to calculate the heat transfer coefficient (h).

$$h = \frac{Q_{\mathrm{conv}}}{A(T_{\mathrm{w}} - T_{\mathrm{b}})} \tag{2}$$

The Nusselt number (Nu) [7] is a dimensionless parameter used to assess total heat transfer, and it can be written as

$$Nu = \frac{hD_{\mathrm{h}}}{k} \tag{3}$$

where h is the convective heat transfer coefficient, k is the thermal conductivity of air (the working fluid) and D_{h} is the equivalent diameter of the channel, which can be calculated from

$$D_{\mathrm{h}} = \frac{2(WH)}{(W+H)} \tag{4}$$

The average wall temperature (T_{w}) can be evaluated from the temperature distribution acquired via the thermochromic liquid crystal (TLC) sheet. The average bulk air temperature (T_{b}) can be determined from

$$T_{\mathrm{b}} = \frac{(T_{\mathrm{i}} + T_{\mathrm{o}})}{2} \tag{5}$$

The equivalent diameter (D_{h}), air velocity (U) and the kinematic viscosity of air (ν) are substituted to calculate the Reynolds number from

$$Re = \frac{UD_{\mathrm{h}}}{\nu} \tag{6}$$

Friction factor (f) reflecting the required pumping power can be expressed as

$$f = \frac{2}{(L/D_{\mathrm{h}})} \frac{\Delta P}{\rho U^2)} \tag{7}$$

Finally, the Nusselt number ratio (Nu/Nu_{s}) and friction factor ratio (f/f_{s}) are applied to calculate the thermal performance factor (TPF) from

$$TPF = \left(\frac{Nu}{Nu_{\mathrm{s}}}\right)\left(\frac{f}{f_{\mathrm{s}}}\right)^{-\frac{1}{3}} \tag{8}$$

where the subscript "s" refers to a smooth channel (or a channel without rib).

3. Experimental Details

3.1. Experimental setup

The schematic diagram of an experimental facility is shown in Figure 1. A rectangular heat exchanger channel with a cross-section width and height of 40 mm and 20 mm (AR=2) and a length of 576 mm was divided into an inlet section (also known as the calm section), a test section, and an outlet section. The channel walls were well-insulated to prevent heat loss. An inverter was used to control the airflow rate, and a 2.55 kW fan was used to draw in air. Under the control of a voltage-rectifying transformer, the power supply unit heated the channel bottom with a constant heat flux of 600 W/m^2. The air temperature at the inlet and outlet was measured using eight RTD Pt100 thermocouples. The surface temperatures were evaluated from the colors of the *TLC* sheet which were recorded by a high-resolution digital camera. The pressure loss across the test tube with a pressure gauge was subjected to the calculation of a friction factor.

3.2. Ribbed walls and operating conditions

Table 1. shows the details of geometric parameters of a ribbed channel and operating conditions in the current work. Figure 2 depicts the configuration of the ribbed walls inside the rectangular channel. The ribs had two different wave amplitudes of *y*=sin(*x*) and *y*=2sin(*x*) referred to the heights of 1 mm and 2 mm, respectively.

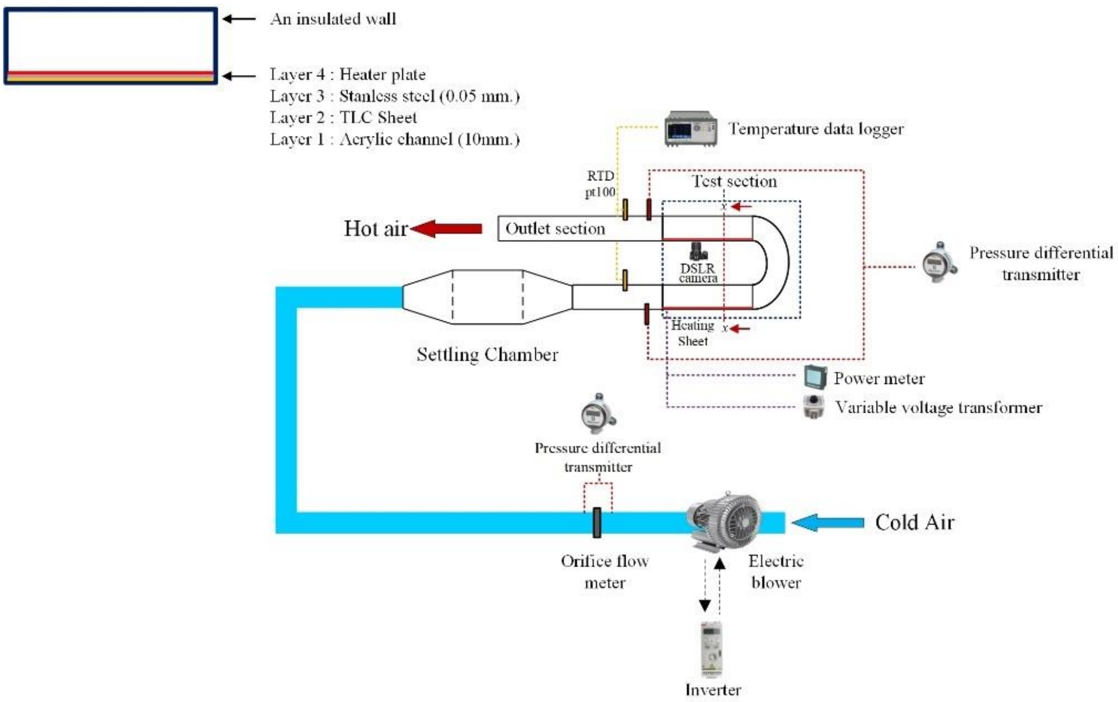

Figure 1. Schematic diagram of the experimental setup.

Table 1. Characteristics of the geometric parameters a ribbed channel and operating conditions.

Channel height, *H* (mm)	20
Channel, width, *W* (mm)	40
Channel length, *L* (mm)	576
Aspect ratio (*AR*)	2
Ribbed material	Polylactic acid plastic (PLA)
Wave period, *b* (mm)	2π
Wave amplitude, *a* (mm)	1-2 (*y*=sin(*x*), *y*=2sin(*x*))
Working fluid	Air
Reynolds number, *Re*	10,000 to 34,000
Prandtl number, *Pr*	0.7

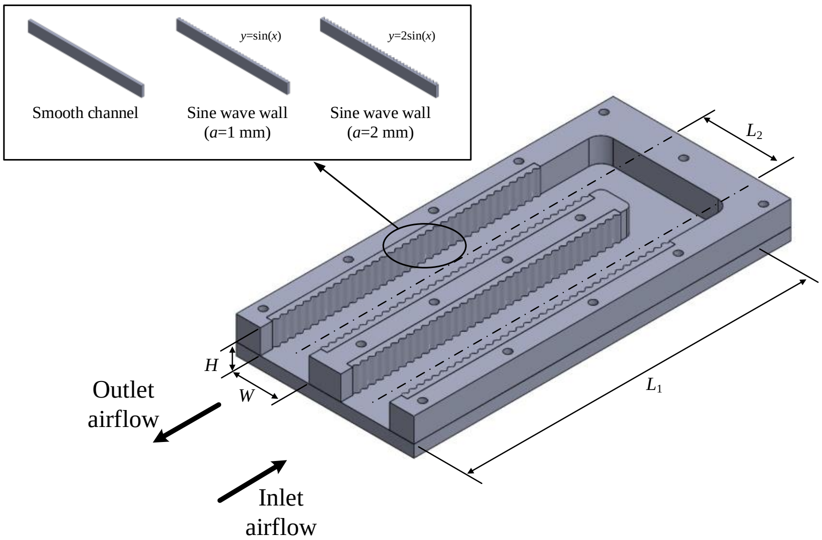

Figure 2. Configuration of ribbed walls with varied wave amplitudes.

4. Experimental Results and Discussion

The results of the experiment of the current smooth channel were validated by comparing the present results to those obtained from well-known correlations, such as the Dittus-Boelter correlations for Nusselt numbers and the Blasius correlations for friction factor. As shown in Fig. 3, the present results exhibited insignificant deviations within 7.22% and 4.32%, for Nusselt numbers and friction factors, respectively. Therefore, the existing facility and the methodology are applicable for further study.

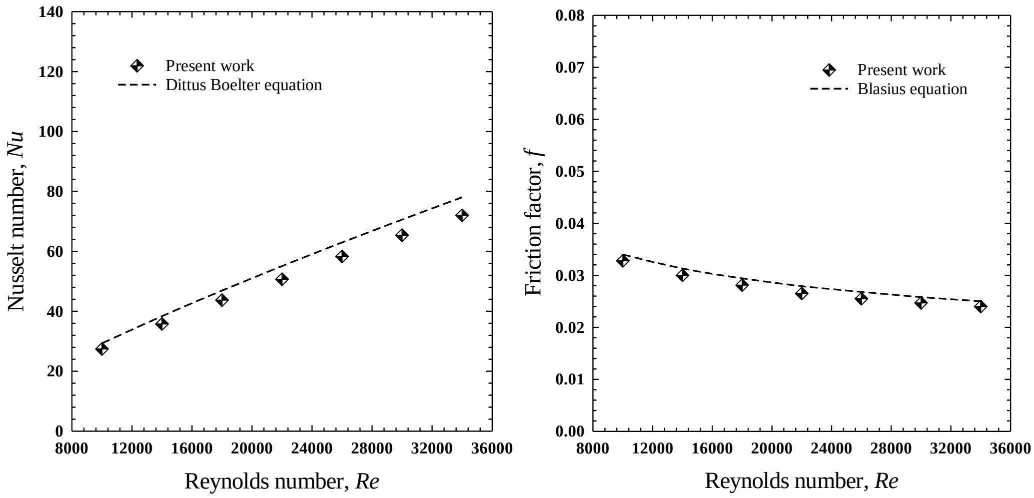

Figure 3. Validation test for the current smooth channel.

4.1. Results of heat transfer

Figure 4 shows the influences of Reynolds number (*Re*) and rib amplitudes on Nusselt number (*Nu*) and Nusselt number ratio (Nu/Nu_s). The rise of Reynolds number (*Re*) promoted Nusselt number (*Nu*) owing to turbulence intensification while Nusselt number ratio, decreased as the Reynolds number increased. This is basically attributed to the fact that the thermal boundary layer in the smooth channel is already thin at high Reynolds numbers. Thus, the role of the ribs in improving heat transfer becomes less important at higher Reynolds numbers.

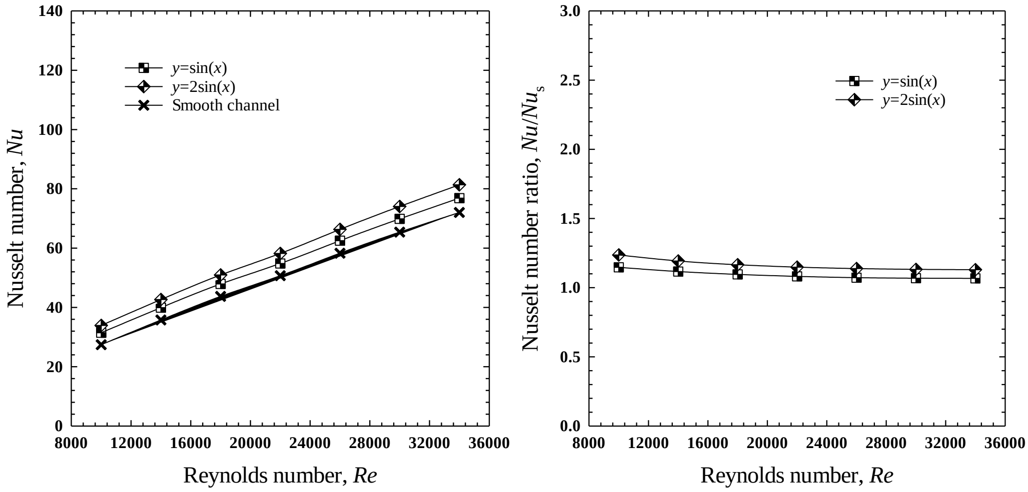

Figure 4. Effects of Reynolds number and the wave amplitudes of ribs on Nusselt number (*Nu*) and Nusselt number ratio (Nu/Nu_s).

Figure 4 demonstrates that at an identical Reynolds number, the heat transfer in the channels with ribs was superior to that of the smooth channel. Consequently, Nusselt number ratios (Nu/Nu_s) were consistently above unity. According to the research results, the channel installed with the ribbed walls having a sine wave shape improved heat transfer by about 12.95-14.68% in comparison to the smooth channel.

The ribbed channel with the larger wave amplitude (2 mm) yielded greater Nusselt number (*Nu*) and Nusselt number ratio (Nu/Nu_s) than the one with a smaller wave amplitude (1 mm.). The more chaotic fluid mixing and intensified turbulence, introduced by the ribs with the larger amplitude is responsible for the better heat transfer. For the examined range, the maximum enhancement of the Nusselt number ratio (Nu/Nu_0) of 1.24 times was obtained by the utilization of the ribs having a wave amplitude of 2.00 at a Reynolds number of 10,000.

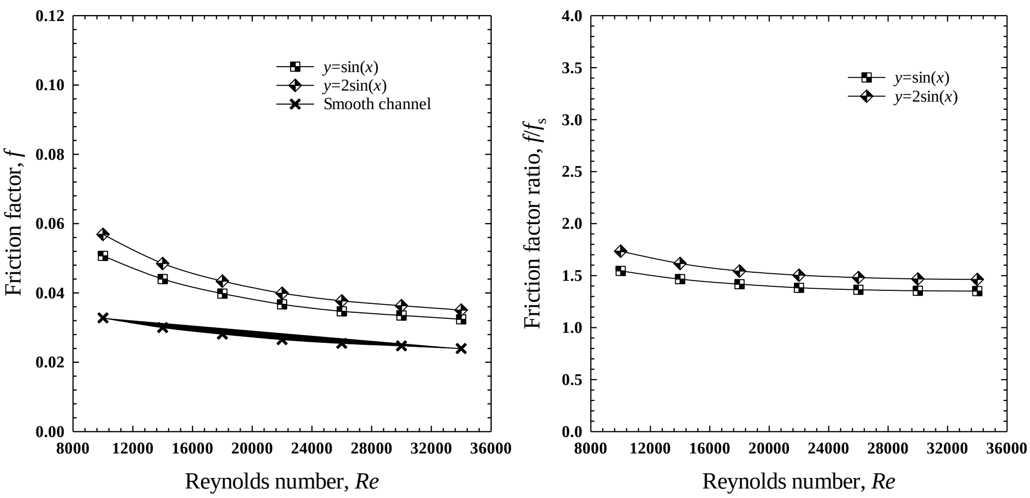

Figure 7. Effects of v Reynolds number and the wave amplitudes of ribs on friction factor (*f*) and friction factor ratio (f/f_s).

4.2. Results of the pressure loss

Figure 7 displays the friction factor (f) and friction factor ratio (f/f_s) results at various Reynolds numbers (Re). Both the average friction factor and friction factor consistently increase as the Reynolds Number decreases. At a given Reynolds number, the ribs with a wave amplitude of 2 mm caused a higher friction factor than the ones with a wave amplitude of 1 mm. The results suggested that the ribs having the larger amplitude generate stronger turbulence, subsequently causing higher pressure drop and thus friction loss. The application of the ribbed walls with wave amplitude at 2 mm caused a maximum friction factor of 1.73 times that of the smooth channel in the range under consideration.

4.3. Results of the thermal performance factor

The Nusselt number ratio and friction factor results reported in sections 4.2 and 4.3 were subjected to the evaluation of thermal performance factor (*TPF*) via Eq. (8). The resultant factors are shown in Fig. 8. Generally, as the Reynolds number increased, thermal performance factor slightly dropped. The ribbed channel with a wave amplitude of 2 mm yielded thermal performance factors in the range 0.99-1.03 while the one with a wave amplitude of 1 mm yielded thermal performance factors below unity (0.96-0.99) for the whole Reynolds number range. The better thermal performance factors were attributed to the dominant effect of enhanced heat transfer over the increased friction loss. Thus, the use of the former channels potentially saves overall energy as compared to the use of the smooth channel while the latter does not. In other words, the amplitude or height of ribs has an important role in controlling the trade-off between the enhanced heat transfer (advantage) and increased friction loss (drawback). Relying on the experimental results, the ribs with a wave amplitude of 2 mm yielded the maximum thermal performance factor of 1.03 at Reynolds number of 10,000. Therefore, it is recommended to use the ribs with a wave amplitude of 2 mm at low Reynolds numbers for energy-saving purpose.

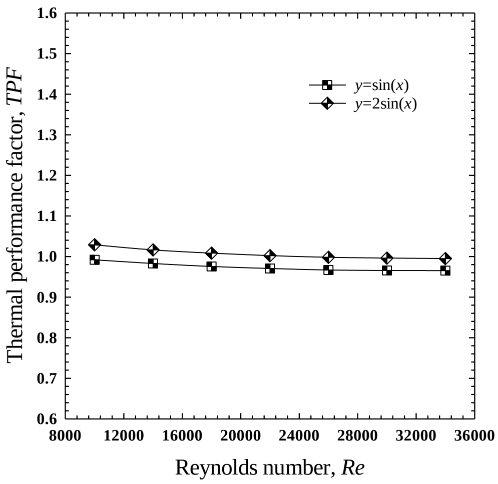

Figure 8. Effects of Reynolds number and the wave amplitudes of ribs on thermal performance factor

5. Conclusions

For Reynolds numbers ranging from 10,000 to 32,000, the use of ribbed channels having different wave amplitudes or heights (1 and 2 mm.) was investigated. The major findings are listed below.

1. The channel installed with the ribbed walls having a sine wave shape improved heat transfer by about 12.95-14.68% in comparison to the smooth channel.
2. The ribs with a larger wave amplitude gave superior heat transfer augmentation and also caused higher friction loss.

3. Thermal performance factors yielded by ribbed walls with a wave amplitude of 2 mm. were higher than those yielded by the ones with a wave amplitude of 1 mm due to the dominant effect of enhanced heat transfer.

4. For the examined range, the ribs with a wave amplitude of 2 mm yielded the maximum thermal performance factor of 1.03 at Reynolds number of 10,000.

6. References

[1] Budania, B. & Shergill, H. (2012). Simulation heat transfer enhancement in a laminar channel flow with built-in triangular prism. *International Journal on Emerging Technologies*, 3(1), 92-96.

[2] Liu, J., Wang, J. & Yang, K. (2023). Heat transfer enhancement by employing inserted plate in turbine blade internal cooling channel. *Case Studies in Thermal Engineering*, 45, 1-14.

[3] Han, J. C. (2006). Turbine blade cooling studies at Texas A&M University: 1980–2004. *Journal of Thermophysics and Heat Transfer*, 20(2), 161-187.

[4] Han, J. C., Glicksman, L. R. & Rohsenow, W. M. (1978). An investigation of heat transfer and friction for rib-roughened surfaces. *International Journal of Heat and Mass Transfer*, 21(8), 1143-1156.

[5] Chandra, P. R., Alexander, C. R. & Han. J. C. (2003). Heat transfer and friction behaviors in rectangular channels with varying numbers of ribbed walls. *International Journal of Heat and Mass Transfer*, 46, 481-495.

[6] Fu, W. L., Lesley Wrigh, M. & Han, J. C. (2006). Rotational buoyancy effects on heat Transfer in five different aspect-ratio rectangular channels with smooth walls and 45-degree ribbed walls. *Transactions of the ASME*, 128, 1130-1141.

[7] Cengel Y. A., & Ghajar A. J. (2015). *Heat and mass transfer: fundamentals & applications*. 5th edition, Mc Graw-Hill New York.

ETM0023

Thermal Characteristics of Rectangular Channels with Inline/Staggered Notched Baffles

A Phila[1], W Keaitnukul[1], M Phumkaew[2], S Jiragraivutidej[2], N Maruyama[3,4], M Hirota[5], S Eiamsa-ard[1], and K Buanak[6,*]

[1]Department of Mechanical Engineering, School of Engineering and Industrial Technology, Mahanakorn University of Technology, Bangkok, Thailand
[2]Department of Mechanical Engineering, Faculty of Engineering, Rajapark Institute, Wang Thonglang, Bangkok, Thailand
[3]Engineering Innovation Unit, Graduate School of Regional Innovation Studies, Mie University, Tsu, Mie, 514-8507, Japan
[4]Department of Mechanical Engineering, Faculty of Engineering, Mie University, Tsu, Mie, 514-8507, Japan
[5]Department of Mechanical Engineering, Faculty of Engineering, Aichi Institute of Technology, Toyota, Aichi, 470-0392, Japan
[6]Department of Automotive-Mechanical Engineering, Faculty of Industrial Technology, Rajabhat Rajanagarindra University, Mueang Chachoengsao, Thailand

* Corresponding Author: kalong@techno.rru.ac.th

Abstract. Thermal characteristics of baffled rectangular channel has been investigated experimentally over the range of Reynolds numbers of 6000 to 24,000. The aspect ratio of rectangular channels was 3.75. The inner surfaces of the lower plates of channels were installed with the notched baffles in inline and staggered arrangements. The notch height-to-baffle height ratio (*a*/*e*), space between adjacent notches (*b*), and roughness pitch ratio (*P*/*e*) were fixed at 0.125, 10, and 8, respectively. Local Nusselt number, average Nusselt number, friction factor, and thermal performance factor results are reported and discussed. The results of a smooth channel and the channel with typical baffles (TB) are also given for assessment. Experimental results suggested that the application of the staggered notched baffles (S-NB), inline notched baffles (I-NB), and typical baffles (TB) resulted in the increases of Nusselt numbers by approximately 48.0-66.6%, 44.3-63.1%, and 43.9 - 62.8%, respectively as compared to those of the smooth channel (SC). At a given Reynolds number, the notched baffles with staggered arrangement caused considerably greater Nusselt numbers accompanied by slightly higher friction losses than the ones with inline arrangement. Accordingly, the staggered notched baffles yielded superior thermal performance factor (*TPF*) to the inline ones. The greatest *TPF* of 1.28 was found by utilizing the staggered notched baffles at *Re* = 6000.

Keywords: Inline and staggered arrangements, Notched baffles, Thermal performance.

1. Introduction

There are numerous heat transfer enhancement techniques applied in thermal systems such as using inserts to promote turbulence or to generate swirl/vortex flow, modifying heat transfer surface to enlarge heat transfer areas and intensify turbulence, and utilizing nanofluids to enhance fluid conductivity and thus heat transfer by the working fluids. Among the techniques, surface modification through artificial roughness is one of the most effective ways to increase turbulence in air channels employed in heat exchangers, vortex combustors, and solar air heaters. [1]. Yang *et al*. [2] investigated the pressure loss and heat transfer characteristics of a square channel with opposing sides roughened by ribs with symmetric and staggered arrangements. Experiments encompassed rib height to the height of ribbed channel (e/H) ratios of 0.2 and 0.33, rib spacing to height ratio (S/e) ranged from 5 to 15, and Reynolds numbers from 1400 to 9000. At similar operating conditions, the symmetric ribs gave higher heat transfer coefficients and also caused higher pressure losses than the staggered ones. The maximum heat transfer coefficient was obtained at a moderate rib spacing to height ratio (S/e = 10). Habet *et al*. [3] installed inline and staggered baffles having perforation ratios varied from β=0% (solid baffle) to 40% for enhancing heat transfer of a rectangular channel for $12{,}000 \le Re \le 32{,}000$. At comparable conditions, the staggered baffles caused a lower friction loss penalty than the inline ones. At larger perforation ratios (β=20-40%), the staggered baffles outperformed the inline ones in heat transfer augmentation. For both inline and staggered baffles, thermal performance increased with decreasing perforation ratio. The largest *TPF* was achieved by the use of the staggered baffles with β of 0% (solid baffles) at Re=12,000. On the other hand, the minimum *TPF* was found in the case of the inline baffles with β of 30% at Re=32,000. Habet *et al*. [3] also investigated the effect of tilting angles (degree θ= 0º, 30º, 45º, and 60º) and perforation ratios (from 10% to 40%) of baffles heat transfer and flow resistance in a rectangular channel with an aspect ratio of 3:1. Manifestly, baffles with θ = 0º and β=10% yielded the highest heat transfer enhancement and caused the greatest friction loss since the baffles with lower tilting angles and smaller perforation ratios offered better reattachment and recirculating flow on the heating surfaces. In contrast, baffles with θ = 60º and β =40% caused the poorest heat transfer enhancement and the lowest friction factor. The best tradeoff between the enhanced heat transfer and the increased friction loss penalty relating to the maximum TPF was found at tilting angle (θ= 60º), perforation ratio (β=10%), and Re=12,000. Promvonge *et al*. [5] numerically investigated flow and heat transfer characteristics in a square channel equipped with 45° baffles. The baffles were installed in tandem and inline on the lower and upper channel walls. The results of the 90° transverse baffles were also reported for comparison. Numerical results revealed that two stream wise twisted vortex (*P*-vortex) flows were generated by the 45° baffles. The P-vortex flows consequently induced impinging flows which significantly promoted heat transfer across the channel. However, the heat transfer augmentation by the inline and staggered baffles are comparable. The optimal baffle height to channel height was 0.2, indicated by the highest *TPF* which was as high as 2.6 (twice as high as that of the 90° transverse baffles). Tanda [6] employed liquid crystal thermography to acquire the detailed distributions of the heat transfer coefficient in the channels installed with transverse continuous, transverse broken and V-shaped broken ribs. Experiments were carried out at attack angles (α) of 45°, 60, and 90°, rib height to channel diameter ratios (e/D) of 0.09 and 0.15, rib pitch to rib height ratios (p/e) of 4, 8, and 13.3, rib height to channel height ratios (e/H) of 0.15 and 0.25. Experimental results suggested that the transverse broken ribs with p/e = 4 and 13.3 have the best thermal performance, whereas transverse continuous ribs (again with p/e = 4 and 8) provide a little heat transfer augmentation or even a reduction (relative to the reference smooth channel).

The present work aims to extend the scope of the study on the effects of baffle geometry on heat transfer and friction loss characteristics in rectangular channels. The inline and staggered notched baffles were installed on the inner lower surfaces of the channels having an aspect ratio 3.75. The notch height-to-baffle height ratio (a/e), a space between adjacent notches (b), and a roughness pitch ratio were kept constant at 0.125, 10, and 8, respectively. Typical transverse baffles were also tested as a reference case. The main objective is to determine optimum heat transfer conditions for the Reynolds numbers ranging from 6000 to 24,000.

2. Theoretical Aspects

Nusselt number (Nu) is an important parameter that can contribute to a better heat transfer rate. The dimensionless Nusselt number is defined as

$$Nu = \frac{hD_\mathrm{h}}{k} \tag{1}$$

where D_h is the equivalent channel diameter calculated from the cross-sectional area of flow (A) and perimeter (P), and k is the thermal conductivity of the working fluid (Air), h is the convective heat transfer coefficient.

$$D_h = \frac{4A}{2P} = \frac{4(WH)}{2(W+H)} \tag{2}$$

The average heat transfer coefficient (h) under the uniform heat flux condition is calculated from the following equation.

$$h = Q_{conv} \big/ A\left(T_w - T_b\right) \tag{3}$$

The rate of convection heat transfer (Q_{cov}) is evaluated from the experimental data of air as

$$Q_{conv} = Q_{air} = \dot{m}C_p(T_o - T_i) \tag{4}$$

The average bulk air temperature (T_b) can be determined via thermochromic liquid crystal (TLC) sheet colors, whereas the average channel wall temperature (T_w) can be calculated from

$$T_b = \left(T_o - T_i\right)\big/2 \tag{5}$$

The Reynolds number based on the equivalent diameter (D_h) can be expressed as

$$Re = UD_\mathrm{h} \big/ v \tag{6}$$

The friction factor is defined as [8]

$$f = \frac{2}{(L/D_h)} \frac{\Delta P}{\rho U^2)} \tag{7}$$

Finally, the thermal performance factor (TPF) [9] is calculated from the Nusselt number and friction factor ratios as

$$\mathrm{TPF} = \left(\frac{Nu}{Nu_0}\right)\left(\frac{f}{f_0}\right)^{-\frac{1}{3}} \tag{8}$$

3. Experimental Details

3.1. Experimental setup

A rectangular heat exchanger channel with a width of 150 mm, a height of 40 mm (an aspect ratio of 3.75), and a length of 3500 mm was divided into three sections: an entering section (also known as the calm portion), a test section, and an outflow section. The schematic design of an experimental setup is shown in Figure. 1. The channel wall was well-insulated to minimize heat loss. Air was fed into the channel by a 2.2 kW fan. The airflow rate was controlled via an inverter. Airflow rates were measured using an orifice coupled with a digital pressure gauge. A power supply unit supplied heat to the bottom of the channel with a uniform heat flux of 600 W/m^2. Eight RTD Pt100 thermocouples which were located upstream and downstream of the test section were used to collect temperature data to evaluate a bulk temperature. The colors of the TLC sheet, which were captured by a high-resolution digital camera, were used as a guide for evaluating channel wall temperatures. In addition, a digital pressure gauge was used to measure the pressure loss across the test section for calculating the friction factor. All data were recorded at steady state conditions for the Reynolds numbers ranging from 6000 to 24,000.

3.2. Baffle geometries and operating conditions

The configurations of typical transverse baffles and notched baffles with inline and staggered arrays are shown in Fig. 2. The notched baffles were located on the inner surfaces of the lower plates of channels. The notch height-to-baffle height ratio (*a/e*), a space between adjacent notches (*b*), and a roughness pitch ratio were kept constant at 0.125, 10, and 8, respectively.

Figure 3 demonstrates the manner in which the typical transverse baffles are placed. Table 1 presents an overview of the channel, baffle, and operating parameters.

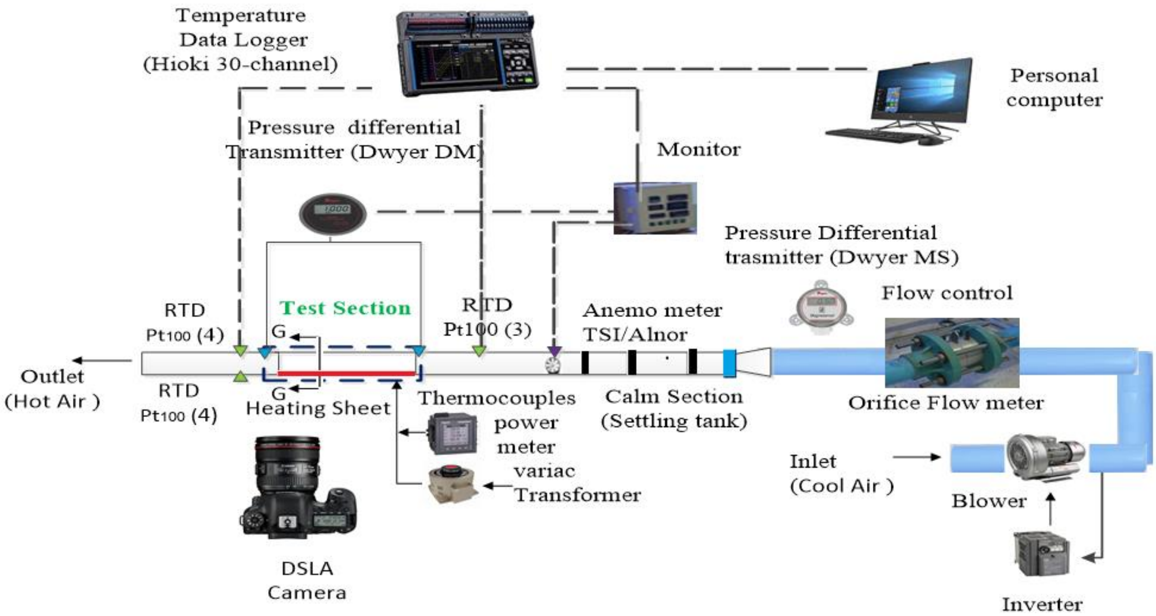

Figure 1. The experimental setup.

Table 1. Geometries of typical transverse baffles and notched baffles with inline and staggered configurations and operating conditions.

Test section	
Channel (Height, Width, Length; $H \times W \times L$)	40 mm ×150 mm ×900 mm
Channel aspect ratio (W/H)	3.75
Baffle material	Polylactic acid plastic (*PLA*)
Space between adjacent notches (b)	10
Roughness pitch ratio (P/e)	8
notch height-to-baffle height ratio (a/e)	0.125
Working fluid	Air
Reynolds number	6,000-24,000
Prandtl number	0.7

(a) transverse baffles (TB) (b) inline notched baffles (c) staggered notched baffles

Figure 2. Configurations of typical transverse baffles and notched baffles with inline and staggered arrays.

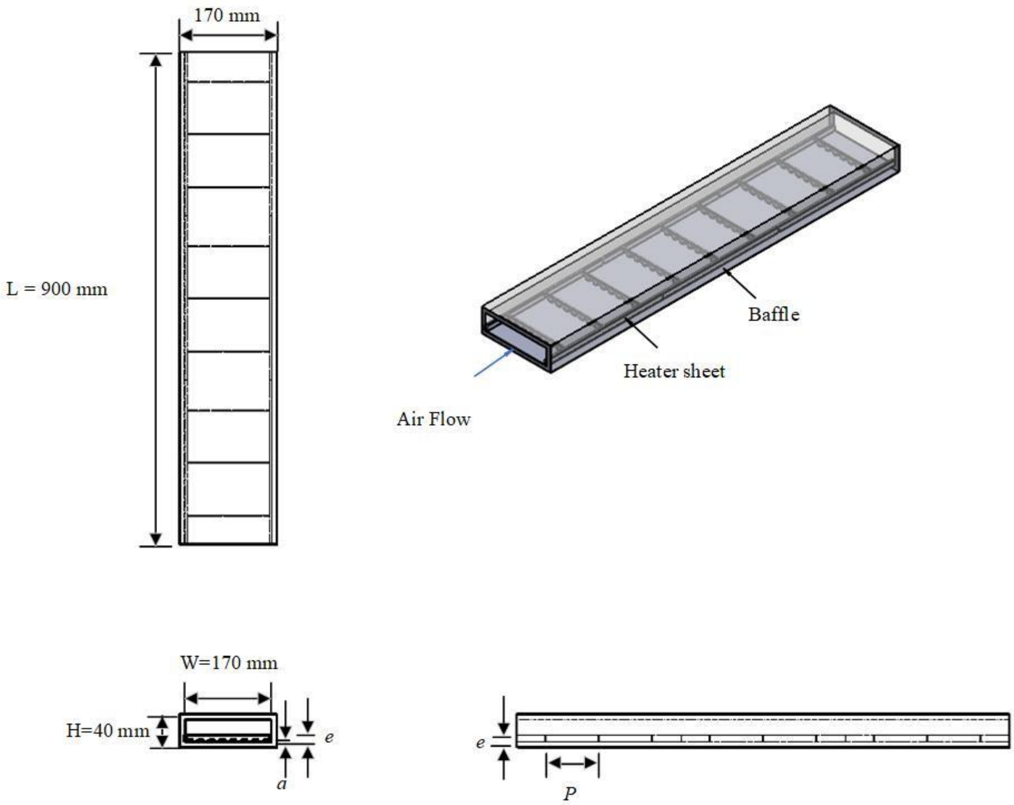

Figure 3. The arrangement of baffles.

4. Experimental Results and Discussion

In order to verify the reliability of the experimental setup and procedure, heat transfer and friction loss results from the current smooth channel are compared to data from well-known correlations which are Dittus-Boelter and Gnielinski correlations (Nusselt number) and Petukhov and Blasius correlations (friction factor). The comparison of the present results and those from the correlations is displayed in Figure 4. Obviously, the data from different sources were in good agreement. The deviations of the current Nusselt numbers and friction factors from the correlations within the ranges of 1.81%, 3.26%, 1.36%, and 9.01%, respectively.

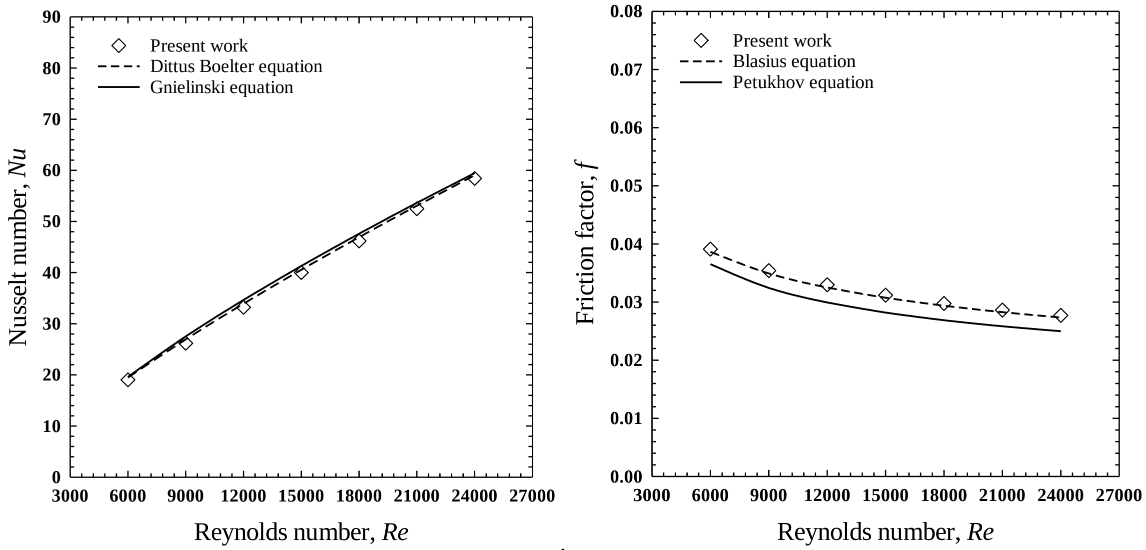

Figure 4. Validation test for the current smooth channel.

4.1. Heat transfer

Figure 5 illustrates the influence of Reynolds number (*Re*) on Nusselt number (*Nu*) and Nusselt number ratio (Nu/Nu_s). The Nusselt numbers of the channel with baffles were consistently greater than those of the smooth channel at a given Reynolds number (all Nu/Nu_s were above unity). Clearly, Nusselt number (*Nu*) increased as Reynolds number rose because turbulence was promoted. However, Nusselt number ratio dropped with increasing Reynolds number. This may be explained by the fact that the thermal boundary layer in the smooth channel is already thin at a high Reynolds number. Consequently, the presence of baffles possessed an insignificant effect on heat transfer enhancement.

Experimental results also showed that the application of the staggered notched baffles (S-NB), inline notched baffles (I-NB), and typical baffles (TB) resulted in the increases of Nusselt numbers by approximately 48.0-66.6%, 44.3-63.1%, and 43.9 - 62.8%, respectively as compared to those of the smooth channel (SC).

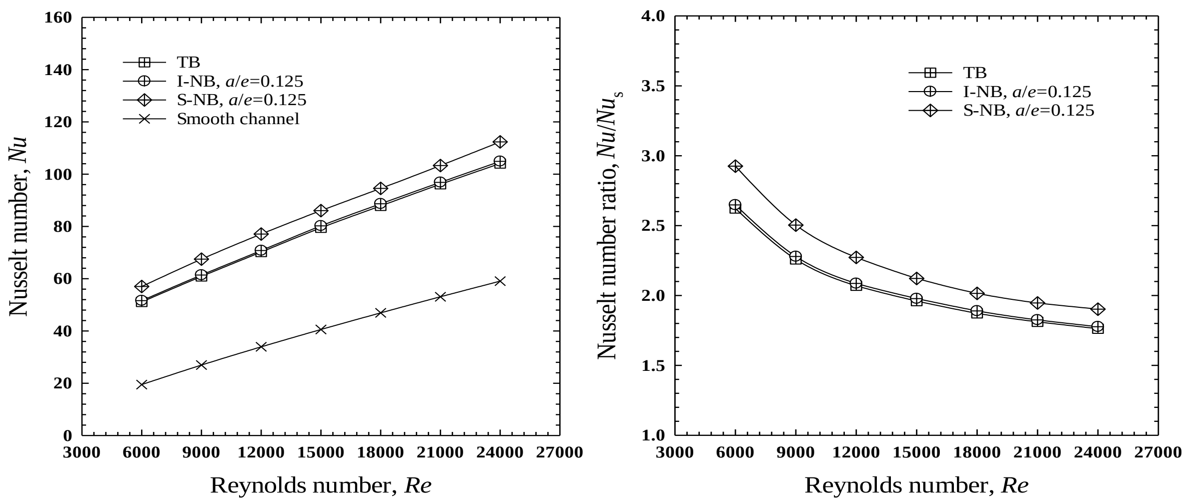

Figure 5. Effects of Reynolds number (*Re*) on Nusselt number (*Nu*) and Nusselt number ratio (Nu/Nu_s).

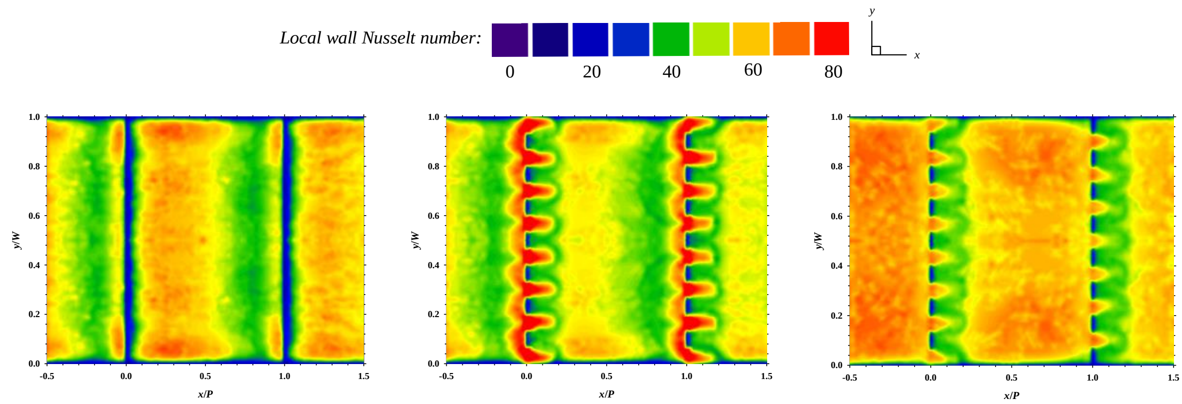

Typical Baffle (TB), P/e=8 I-NB (a/e)=0.125, P/e=8 S-NB (a/e)=0.125, P/e=8

Figure 6. Nusselt number contours on the surfaces installed with the typical baffle (TB), inline baffle (I-NB) and staggered notched baffles (S-NB) with a/*e of* 0.125, *b* of 10, *P/e* of 8, and Reynold number of 6,000.

The details of heat transfer behavior are presented in the form of Nusselt number contours as displayed in Figure 6. Obviously, the staggered notched baffles (S-NB) introduced larger high Nusselt number area than the staggered notched baffles (S-NB) and typical baffles (TB). Relying on the report by Habet *et al.* [3], the staggered perforated baffles showed higher heat transfer augmentation than the inline ones at higher perforation ratios (β=20–40%). Therefore, the presence of the spaces (notches) on the baffles together with the staggered arrangement in the current study may be the synergy factor in heat transfer enhancement. For the examined range, the staggered notched baffles (S-NB) yielded the maximum Nusselt number ratio (Nu/Nu_s) as high as 2.93 at a Reynolds number of 6,000.

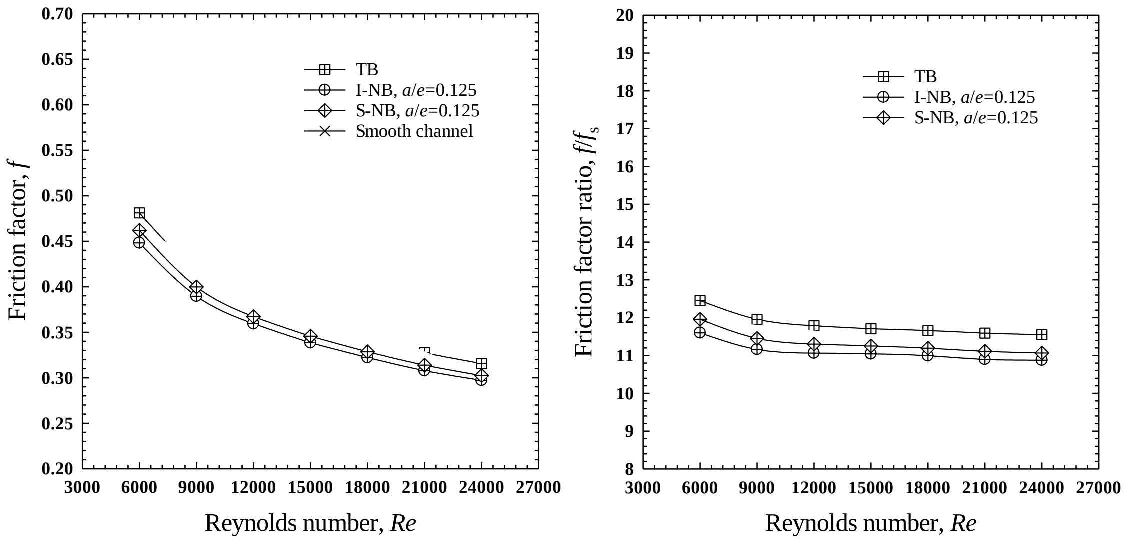

Figure 7. Friction factor & Friction factor ratio VS Reynolds number.

4.2. Friction loss

Figure 7 shows friction factor (f) and friction factor ratio (f/f_s) results at the Reynolds numbers ranging from 6000 to 24,000. Both the average friction factor and friction factor consistently increased as the

Reynolds Number decreased. In general, all channels equipped with baffles showed higher friction factors than the smooth channel. The results can be simply explained that the presence of baffles caused flow disturbance, resulting in higher pressure drop and thus friction loss. At a given Reynolds number, the staggered notched baffles (S-NB) and the inline notched baffle (I-NB) caused lower friction losses than the typical baffles (TB) attributed to the facilitated fluid flow through notches. Friction losses caused by staggered notched baffles (S-NB) were slightly higher than the inline notched baffle (I-NB) by around 1.75-3.09 %.

4.3. Thermal performance factor

Figure 8 shows the relationship between the thermal performance factor (*TPF*) at constant pumping power and Reynolds number. In all cases, thermal performance factors decreased as the Reynolds number rose. The results indicated that the application of the baffles was more favorable for energy saving at lower Reynolds numbers. At an identical Reynolds number, the staggered notched baffles (S-NB) yielded the highest thermal performance factor followed by the inline notched baffle (I-NB) and the typical baffle (TB). The staggered notched baffles (S-NB) outperformed the other baffles primarily attributed to their great heat transfer enhancement with moderate friction losses. In the examined range, the thermal performance factor reached the maximum value of 1.28 times at a Reynolds number of 6000.

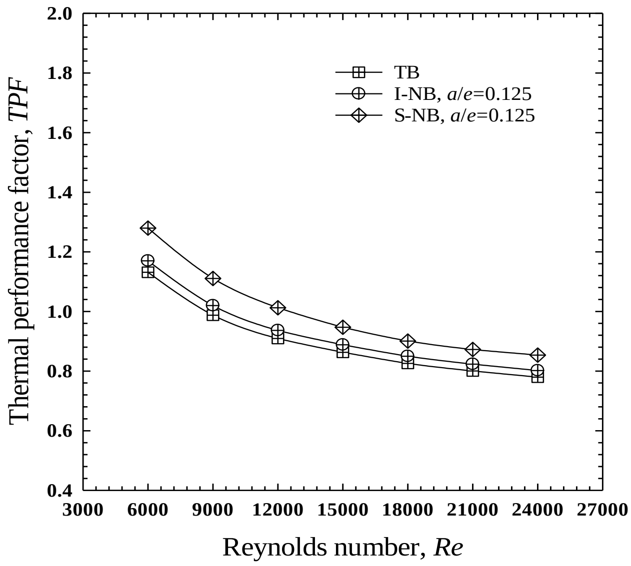

Figure 8. Thermal performance factor versus Reynolds number.

5. Conclusions

The use of the two different type baffles (staggered notched baffles (S-NB), and inline notched baffles (I-NB)) in comparison to the typical baffle (TB) was investigated for Reynolds numbers ranging from 6,000 to 24,000. The major findings are listed below.

- As Reynolds number increased, Nusselt numbers increased while the friction value declined.
- At a given Reynolds number, the staggered notched baffles (S-NB) yielded the highest Nusselt number (up to 2.92 times of the smooth channel) followed by the inline notched baffles (I-NB), and typical baffles (TB).
- The staggered notched baffles (S-NB) caused moderate friction losses which were slightly higher than those caused by the inline notched baffle (I-NB) but lower than those caused by the typical baffles.
- Among the tested baffles, the staggered notched baffles (S-NB) yielded the highest thermal

performance factor of 1.28, primarily attributed to their great heat transfer enhancement with moderate friction losses.

6. References

[1] Maradiya C., Vadher J., Agarwal R. (2018). The heat transfer enhancement techniques and their ThermalPerformance Factor. *Journal of Basic and Applied Sciencesfer*, (7), 1-21.

[2] Yang W., Xue S., He Y., Li W. (2017). Experimental study on the heat transfer characteristics of high blockage ribs channel. *Experimental Thermal and Fluid Science*, (83), 248-259.

[3] Habet M. A. E., Ahmed S. A., Saleh M. A. (2021). Thermal/hydraulic characteristics of a rectangular channel with inline/staggered perforated baffles. *International Communications in Heat and Mass Transfer*, (128), 105591.

[4] Habet M. A. E., Ahmed S. A., Saleh M. A. (2022). The effect of using staggered and partially tilted perforated baffles on heat transfer and flow characteristics in a rectangular channel. *International Journal of Thermal Sciences*, (174), 107422.

[5] Promvonge P., Sripattanapipat S., Kwankaomeng S. (2010). Laminar periodic flow and heat transfer in square channel with 45° inline baffles on two opposite walls. *International Journal of Thermal Sciences*, (49), 963-975.

[6] Tanda G. (2004). Heat transfer in rectangular channels with transverse and V-shaped broken ribs, *International Journal of Heat and Mass Transfe*r, (47), 229-243.

[7] Cengel Y.A., and Ghajar A.J. (2015). *Heat and mass transfer: fundamentals & applications*, 5th edition, Mc Graw-Hill New York.

[8] White F. M. (2021). *Fluid Mechanics*. 9th edition, Mc Graw Hill, New York.

[9] Webb R. L, Kim N. H. (2005). *Principles of Enhanced Heat Transfer*. 2th edition, John Wiley & Sons, New York.

ETM0024

Influence of Relative Baffle Heights on Heat Transfer Performance of Airflow in a Rectangular Channel with Discrete V-Pattern Baffles

S Pingta[1], P Thapmanee[2], A Phila[2], K Wongcharee[1], N Maruyama[3,4], M Hirota[5], S Eiamsa-ard[2], and P Promvonge[6,*]

[1]Department of Process and Industrial Engineering, School of Engineering and Industrial Technology, Mahanakorn University of Technology, Bangkok, Thailand.
[2]Department of Mechanical Engineering, School of Engineering and Industrial Technology, Mahanakorn University of Technology, Bangkok, Thailand
[3]Engineering Innovation Unit, Graduate School of Regional Innovation Studies, Mie University, Tsu, Mie, 514-8507, Japan
[4]Department of Mechanical Engineering, Faculty of Engineering, Mie University, Tsu, Mie, 514-8507, Japan
[5]Department of Mechanical Engineering, Faculty of Engineering, Aichi Institute of Technology, Toyota, Aichi, 470-0392, Japan
[6]Department of Mechanical Engineering, School of Engineering, King Mongkut's Institute of Technology Ladkrabang, Bangkok, Thailand

* Corresponding Author: pongjet.pr@kmitl.ac.th

Abstract. This experimental study aimed to investigate the influence of discrete V-shaped baffles with varying relative baffle heights (e/H = 0.1, 0.2, 0.3, 0.4) on the Nusselt number (Nu), friction factor (f), and thermal performance factor (TPF) of a rectangular channel. The channel had a fixed height (H) of 40 mm, while the height of the baffles (e) was altered to 4, 8, 12, and 16 mm, respectively. The baffle wall was maintained at a constant temperature, while the remaining three walls of the channel were thermally insulated. The study covered the Reynolds numbers (Re) in the range of 6,000-24,000 and the angle of attack (α) of 45 degrees. The relative pitch ratio (P/H) was held constant at 1.5 throughout the investigations. Comparative analyses against a smooth wall configuration revealed substantial enhancements in the Nusselt number (Nu) and friction factor (f) due to the incorporation of V-patterned baffles in the channel. Specifically, the Nusselt number exhibited a remarkable increase of 1.90-5.30 times for smooth channels, while the friction factor experienced a significant enhancement of 3.56-35.91 times of smooth channels. Among the different relative baffle heights tested, the discrete V-patterned baffles with a relative baffle height of 0.1 offered the best thermal performance at 2.63 times. This research contributes valuable insights into the positive impact of employing discrete V-shaped baffles with specific height ratios within a rectangular channel, thereby offering potential advancements in heat transfer enhancement.

Keywords: Discrete V-pattern baffles, rectangular channel, thermal performance.

1. Introduction

Renewable energy from the sun, in the form of solar radiation, is a renewable and environmentally friendly energy source. Solar collectors convert solar energy into thermal power for use in a variety of technical applications. Several heat transfer techniques have been developed to improve the thermal performance of solar collectors, and these approaches have been used in a variety of industrial applications. According to the literature, the application of baffles can increase the thermal performance of solar energy. Baffles inside the channel are utilized to produce turbulence to supplement the *Nu*. The baffles are inserted into a driven flow to generate turbulence within the channel and induce turbulence flow. Adding various types of baffles to the channel is another method for increasing *Nu* [1–8]. For an in-depth review of different experimental baffles of various shapes, dimensions, ranges, and angles, the researcher might be referring to Dutta and Hossain [9] evaluated the *Nu* and *f* in a solar channel with sloped solid and perforated baffles. Through the experiments, they figured out that the local *Nu* distribution is greatly affected by the perforation, orientation, and relative position of the second baffle plate, and *Nu* was 5.0 times higher than flat channel. Straight cooling channels with inclined ribs on two opposing walls were shown by Iacovides et al. [10] in turbulent forced convection. They proposed that turbulence's substantial impact on flow and heat development can be reduced by the considerable influence of rib-induced secondary motion. In a channel with an inclined or angled baffle, Lu and Jiang [11] investigated turbulent convection heat transfer both experimentally and numerically. Promvonge and Thianpong [12] investigated the effect of thermal performance assessment in a baffled channel (containing triangular, wedge, and rectangular rib-shapes) by heating just the top wall of the channel to create a constant heat-fluxed wall. According to their findings, the triangular rib offers the best thermal performance, while the triangular shape produces the highest increase in Nusselt number and friction factor. Promvonge et al. [13] investigated the effects of combined ribs and winglet-typed vortex generators (WVGs) on turbulence convection heat exchange in a channel and found that using ribs and winglet-typed vortex generators can increase heat exchange more than using only rib or winglet-typed vortex generators alone. The multidimensional flow and heat transmission in a channel with crossed discrete double-inclined ribs were investigated by Song et al. [14]. They demonstrated that the 45-attack angle has a larger Nusselt number than the 30 and 60. According to Prasad [15], which examined the thermal performance of a solar air heater duct accompanied by small wires, artificially modified solar air heaters showed stronger thermal performance than the smooth duct alone.

Based on the findings presented above, it is evident that the use of V-shaped baffles has a positive impact on enhancing heat transfer performance. However, it is noteworthy that there has been limited research conducted thus far to establish the optimal relative V-baffle height (the height of the V-shaped baffle in relation to the channel) for conducting experiments. In light of this, our current investigation seeks to ascertain the ideal baffle height while assessing heat transfer performance within a solar air channel by adding V-shaped baffles, spanning a range of Reynolds numbers from 6,000 to 24,000. Additionally-shaped baffles were investigated via varying relative baffle heights (e/h = 0.1, 0.2, 0.3, 0.4) on heat transfer (*Nu*), friction loss (*f*), and thermal performance factor (*TPF*) in a rectangular channel with a fixed height (*H*) of 40 mm while systematically altering the baffles' heights (*e*) to 4, 8, 12, and 16 mm.

2. Theoretical Aspects

Convection transfer of heat is carried out through the process of convection. One of the essential dimensionless parameters in the explanation of convective heat transfer is the Nusselt number (*Nu*). The following formula is employed for calculating the entire heat transfer [16]:

$$Nu = \frac{hD_\mathrm{h}}{k} \tag{1}$$

where *h* is the convective heat transfer coefficient, k is the thermal conductivity of the working fluid (air), D_h is the equivalent channel diameter derived from the flow's cross-section (*A*), and *P* is the channel's perimeter.

$$D_\mathrm{h} = \frac{4A}{P} = \frac{4WH}{2(W+H)} \tag{2}$$

The average heat transfer coefficient (*h*) under the uniform heat flux condition can be calculated from experimental data by using the formulas provided below.

$$h = \frac{Q_\mathrm{conv}}{A(T_\mathrm{w} - T_\mathrm{b})} \tag{3}$$

The rate of air heat transfer (Q_{air}) is taken into account to determine the rate of convection heat transfer (Q_{cov}), as shown below.

$$Q_\mathrm{conv} = Q_\mathrm{air} = \dot{m}c_\mathrm{p}(T_\mathrm{o} - T_\mathrm{i}) \tag{4}$$

The average bulk air temperature (T_b) could be determined with thermochromic liquid crystal (TLC) sheet colors, while the average channel wall temperature (T_w) can be calculated using;

$$T_\mathrm{b} = \frac{T_\mathrm{i} + T_\mathrm{o}}{2} \tag{5}$$

The equivalent diameter (D_h) is used to calculate the Reynolds number.

$$Re = \frac{UD_\mathrm{h}}{\nu} \tag{6}$$

Equation (7) could be used to express the friction factor.

$$f = \frac{2}{(L/D_\mathrm{h})}\frac{\Delta P}{(\rho U^2)} \tag{7}$$

Finally, considering the Nusselt number and friction factor, the thermal performance factor (*TPF*) is determined.

$$TPF = \left(\frac{Nu}{Nu_s}\right)\left(\frac{f}{f_s}\right)^{-\frac{1}{3}} \tag{8}$$

3. Experimental Details

3.1. Experimental setup

A rectangular heat exchanger channel with a cross-sectional width and height of 150 mm and 40 mm (an aspect ratio of 3.75), respectively, and a length of 3500 mm was separated into three sections: an entrance section (also known as the calm section), a test section, and an outflow section. Figure 1 shows the schematic design of an experimental setup. The channel wall of the system was carefully sealed to minimize heat loss. The airflow rate was controlled by an inverter, and a 2.2 kW fan was employed to bring in air. The pressure loss across the plate of an orifice was calculated using the airflow rate after measuring it using a digital pressure gauge. The power supply unit gives heat to the bottom of the channel with a uniform heat flux of 600 W/m^2 under the influence of a voltage-rectifying transformer. Eight RTD Pt100 sensors were placed upstream and downstream of the test section to collect data that was used for determining the temperature of the entire fluid. The colors of the TLC sheet were used as a reference for evaluating channel wall temperatures following the time they were taken by a high-resolution digital camera. A digital pressure gauge was also utilized to quantify the pressure loss over the test section in order to calculate the friction factor. All data were collected in steady-state situations. The colors of the TLC sheet were used to determine the temperature of the channel wall.

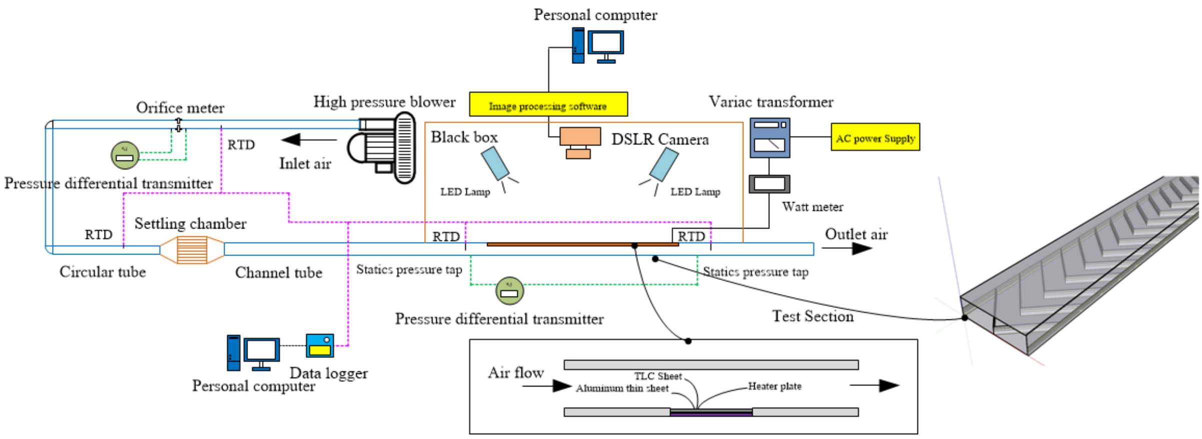

Figure 1. The experimental setup depicted in a schematic figure.

3.2. V-shaped Baffle geometries and operating conditions

Figure 2 shows the geometry of discrete V-shaped baffles with various relative baffle heights (*e/H* = 0.1, 0.2, 0.3, 0.4). On the inner lower surfaces of the channels, individual V-shaped baffles have been inserted. The relative baffle heights (*e/H* = 0.1, 0.2, 0.3 and 0.4), baffle heights (*e*) of 4, 8, 12, and 16 mm, angle of attack (α) of 45 degrees, and relative pitch ratio (*P/H*) were set to 1.5. The thermal properties of rectangular baffled channels were investigated empirically in the Reynolds number range of 6000 to 24,000. The aspect ratio of rectangular channels is 3.75. Figure 3 shows how the separate V-shaped baffles are installed. Table 1 provides a summary of the channel, baffle, and functional indicator characteristics.

Table 1. Geometries and operating conditions of discrete V-shaped baffles patterns.

Test section	
Channel (Height, Width, Length; $H\times W\times L$)	40 mm ×150 mm ×900 mm
Channel aspect ratio (*W/H*)	3.75
Baffle material	Polylactic acid plastic (*PLA*)
baffle heights (*e*)	4, 8, 12 and 16 mm
The relative baffle heights (*e/H*)	0.1, 0.2, 0.3 and 0.4
The angle of attack (α)	45 degrees
The relative pitch ratio (*P/H: 60/40 mm)*	1.5
Working fluid	Air
Reynolds number (*Re*)	6,000-24,000
Prandtl number	0.7

Figure 2 shows the geometry of discrete V-shaped baffles with various relative baffle heights (*e/H* = 0.1, 0.2, 0.3, and 0.4). On the inner lower surfaces of the channels, individual V-shaped baffles have been inserted. The relative baffle heights (*e/H* = 0.1, 0.2, 0.3, and 0.4), baffle heights (*e*) of 4, 8, 12, and 16 mm, angle of attack (α) of 45 degrees, and relative pitch ratio (*P/H*) were set to 1.5. The thermal properties of rectangular baffled channels were investigated empirically in the Reynolds number range of 6000 to 24,000. The aspect ratio of rectangular channels is 3.75. shows the geometry of discrete V-shaped baffles with various relative baffle heights (*e/H* = 0.1, 0.2, 0.3, and 0.4). On the inner lower surfaces of the channels, individual V-shaped baffles have been inserted. The relative baffle heights (*e/H* = 0.1, 0.2, 0.3, 0.4), baffle heights (*e*) of 4, 8, 12, and 16 mm, angle of attack (α) of 45 degrees, and relative pitch ratio (*P/H*) were set to 1.5. The thermal properties of rectangular baffled channels were investigated empirically in the Reynolds number range of 6000 to 24,000. The aspect ratio of rectangular channels is 3.75.

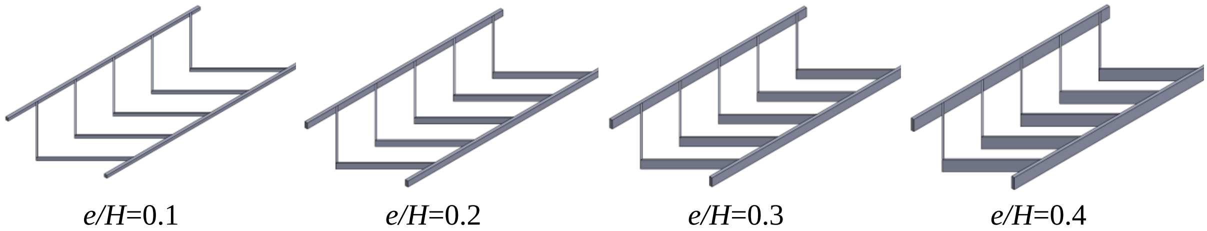

Figure 2. Configurations of discrete V-shaped baffles.

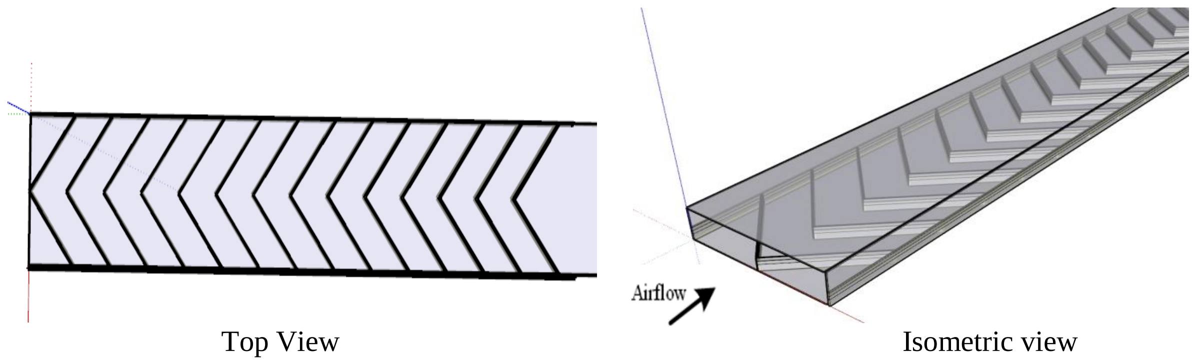

Figure 3. The arrangement of V-shaped baffle.

4. Experimental Results and Discussion

A validation test is performed by comparing experimental data from the current smooth channel to data determined using conventional correlations. A test was carried out to assess the validity of the current setup for experimentation. The traditional correlations for the Nusselt number and friction factor are the Dittus-Boelter and Gnielinski correlations and the Petukhov and Blasius correlations, respectively. Figure 4 shows the comparison. The latest findings significantly accorded with the established relations. The friction factor and Nusselt number are the correlations at the 3.2% and 10.4% levels, respectively.

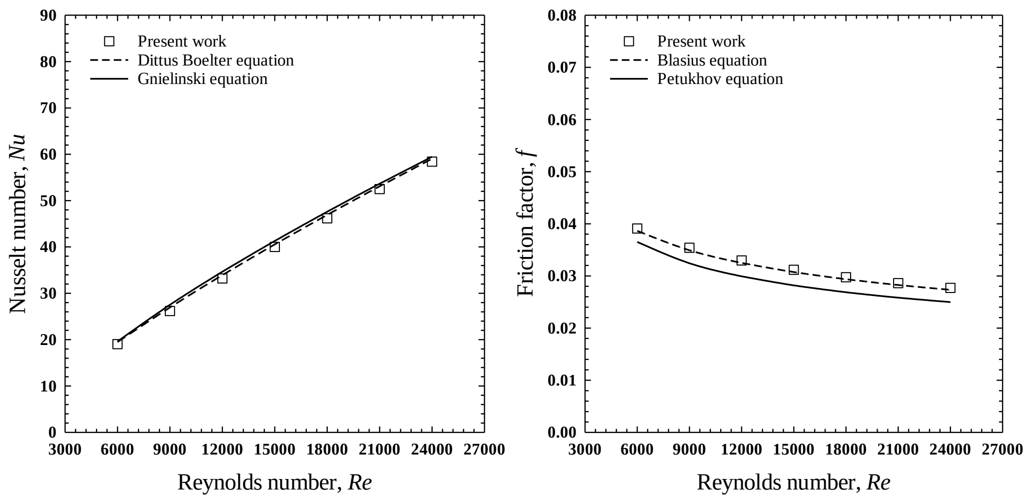

Figure 4. Validation test for the current smooth channel.

4.1. Results of heat transfer

Figure 5 shows whether the Reynolds number (*Re*) affects the Nusselt number (*Nu*) and Nusselt number ratio (*Nu/Nus*) on the lower bottom surfaces of the channels installed with the discrete V-shaped baffle layouts. In general, the Nusselt number (*Nu*) increases when the Reynolds number rises due to increased turbulence. However, when the Reynolds number increases, the Nusselt number ratio decreases. This is because the thermal boundary layer in the system without a baffle (the smooth channel) is already smaller at high Reynolds numbers. As a result, the effect of baffle placement on thermal boundary disruption becomes less important. At a given Reynolds number, the channel with baffles has larger Nusselt numbers than the smooth channel (Nusselt number ratios are greater than unity). It can also be demonstrated that baffles with higher blockage height ratios have higher Nusselt numbers. The maximum augmentation of the Nusselt number ratio is roughly 5.30 times at a relative roughness height (*e/H*) of 0.4 and a Reynolds number of 24,000.

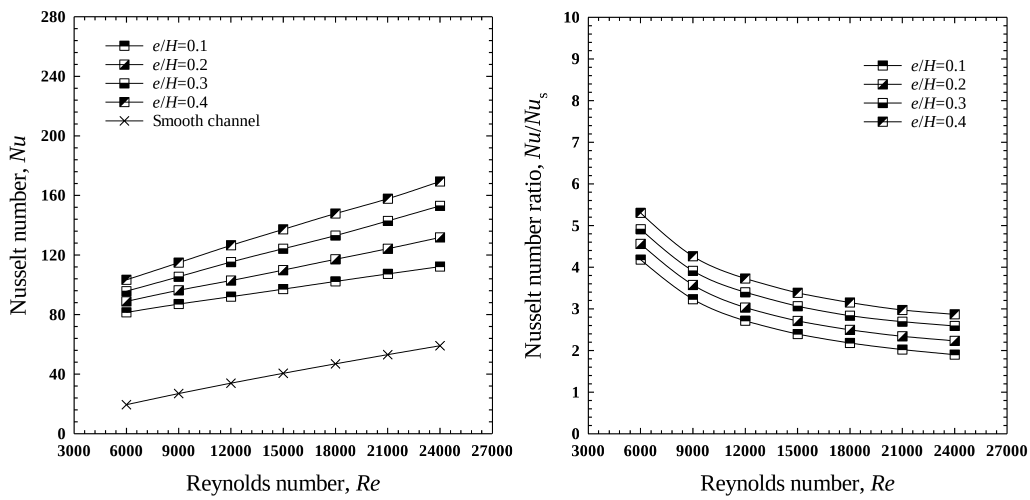

Figure 5. Effects of Reynolds number (*Re*) and a/*e* ratio on Nusselt number (*Nu*) and Nusselt number ratio (Nu/Nu_s).

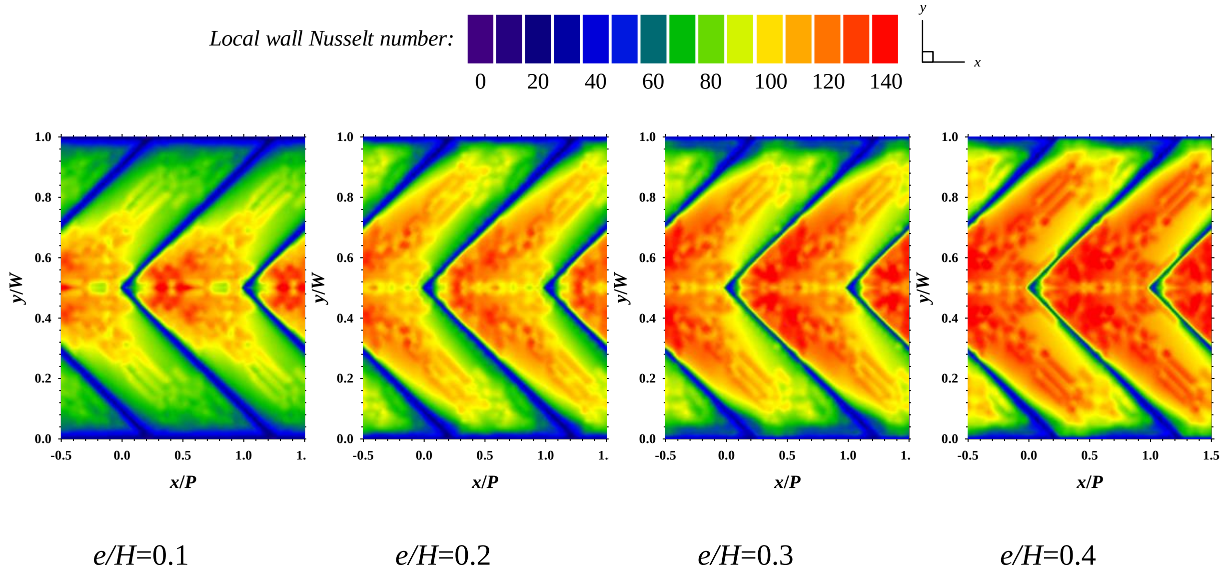

Figure 6. Nusselt number contours on the surface installed with the discrete V-shaped baffles with various relative baffle heights (*e/H* = 0.1, 0.2, 0.3, 0.4).

Figure 6 shows the Nusselt number contours, and the results revealed above are consistent. Discrete V-shaped baffles with greater *e/H* result in a higher Nusselt number, especially behind each baffle where flow reattachment occurs. Higher relative blockage height ratio baffles introduce more reattachment, which is more effective for thermal boundary layer disruption. The highest augmentation of the Nusselt number ratio (Nu/Nu_s) is roughly 5.30 times for V-shaped baffles (*e/H*) of 0.4 and a Reynolds number of 6,000.

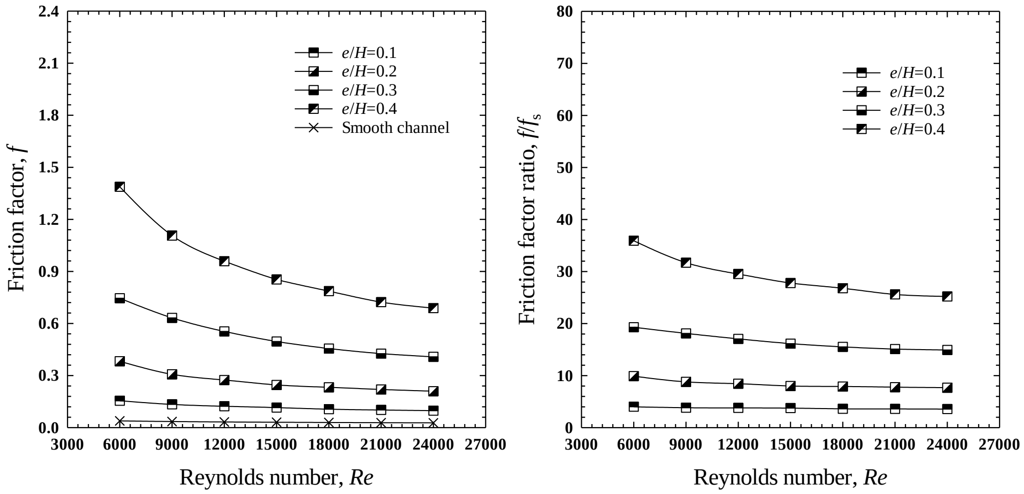

Figure 7. Friction factor & Friction factor ratio VS Reynolds number.

4.2. Results of the Pressure loss

Figure 7 illustrates the effects of Reynolds number (*Re*) on the friction factor (*f*) and friction factor ratio (f/f_s). At the same Reynolds number, both the average friction factor and the friction factor rise as the Reynolds number decreases. According to the results, the baffles that generate more turbulence create more pressure drop as a result of friction loss. According to the results, the baffles that generate more turbulence create more pressure drop and, consequently, friction loss. The placement of baffles with an *e/H* of 0.4 at a Reynolds number of 6,000 results in a maximum friction factor of 35.91 times that of the smooth channel in the considered range.

4.3. Results of the thermal performance factor

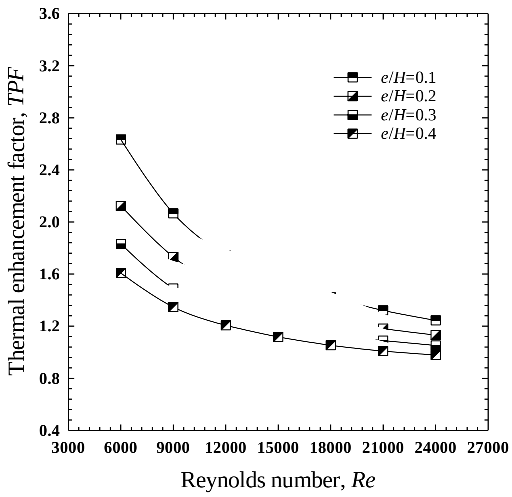

Figure 8. Thermal performance factor versus Reynolds number.

According to several studies, rough surface improves the heat transfer coefficient. Roughness, on the other hand, raises the friction factor. As a result, the system demands more pumping energy. The main objective of the design is for the channel to function at low Reynolds numbers and with little obstruction in order to save all of the energy, as evidenced by a high thermal performance factor. Figure 8 illustrates the thermal performance values for the channel with its four distinguished discrete V-shaped baffle arrangements. The thermal performance factor depends on how the Reynolds number rises in all instances. The thermal performance factor reaches its maximum value of *e/H* = 0.1 and a Reynolds number of 6000, indicating that the examined range has reached its optimal state. Heat transfer improves by 2.63 times when compared to the case without the baffle.

5. Conclusion

The heat transfer and friction loss of a channel with discrete V-shaped baffles are explained. Experiments contain baffles with *e/H* ratios of 0.10, 0.20, 0.3, and 0.40, as well as Reynolds numbers ranging from 6,000 to 24,000. The experimental results revealed that when the Reynolds number increases, Nusselt numbers increase while friction values drop. Discrete V-shaped baffles with a higher *e/H* ratio increase heat transfer rate while increasing friction loss. When compared to the smooth channel, discrete V-shaped baffles with an *e/H* of 0.40 increase heat transfer and friction loss up to 5.30 and 35.91 times, respectively, for the specified range. However, due to the significant impact of low friction loss, V-shaped baffles with an *e/H* of 0.10 give the best thermal performance of 2.63.

6. References

[1] Zhang F., Wang X., Li J. (2017). Flow and heat transfer characteristics in rectangular channels using combination of convex-dimples with grooves. *Applied Thermal Engineering*, (113), 926-936.

[2] Liu J., Xie G., Simon, T.W. (2014). Turbulent flow and heat transfer enhancement in rectangular channels. *International Journal of Heat and Mass Transfer*, (81), 563-577.

[3] Chamoli S., Lu R., Xu D., Yu P.(2018). Thermal performance improvement of a solar air heater fitted with winglet vortex generators. *Solar Energy*, (159), 966-983.

[4] Skullong S., Promthaisong P., Promvonge P.,Thianpong C., Pimsarn M.(2018). Thermal performance in solar air heater with perforated-winglet-type vortex generator. *Solar Energy*, (170), 1101-1117.

[5] Tamma S., Skullong S., Thianpong C., Promvonge P.(2014). Heat transfer behaviors in a solar air heater channel with multiple V-baffle vortex generators. *Solar Energy*, (110), 720-735.

[6] Baissi M.T., Brima A., Aoues K., Khanniche R., Moummi N.(2020). Thermal behavior in a solar air heater channel roughened with delta-shaped vortex generators. *Applied Thermal Engineering*, (165), 113563.

[7] Layek A., Saini J.S., Solanki S.C. (2007). Heat transfer and friction characteristics for artificially roughened ducts with compound turbulators. *International Journal of Heat and Mass Transfer*, (50), 4845-4854.

[8] Promvonge P., Skullong S.(2019). Heat transfer in solar receiver heat exchanger with combined punched-V-ribs and chamfer-V-grooves. *International Journal of Heat and Mass Transfer*, (143), 118486

[9] Dutta P., Hossain A. (2005). Internal cooling augmentation in rectangular duct using two inclined *baffles,International Journal of Heat and Fluid Flow*, (26), 223–232.

[10] Iacovides H., Kelemenis G., M. Raisee. (2003). Flow and heat transfer in straight cooling passages with inclined ribs on opposite walls: an experimental and computational study, *Experimental Thermal and Fluid Science*, (27), 283–294.

[11] Lu B., Jiang P.X.(2006). Experimental and numerical investigation of convection heat transfer in a rectangular channel with angled ribs, *Experimental Thermal and Fluid Science*, (30), 513–521.

[12] Promvonge P., Thianpong C. (2008). Thermal performance assessment of turbulent channel flows over different shaped ribs, *International Communications in Heat and Mass Transfer*, (35), 1327–1334.

[13] Promvonge P., Chompookham T., Kwankaomeng S., Thianpong C.(2010). Enhanced heat transfer in a triangular ribbed channel with longitudinal vortex generators. *Energy Conversion and Management*, (51), 1242–1249.

[14] Song W.M., Meng J.A., Li Z.X. (2010). Numerical study of air-side performance of a finned flat tube heat exchanger with crossed discrete double inclined ribs. *Applied Thermal Engineering*, (30), 1797–1804.

[15] Prasad B.N. (2013). Thermal performance of artificially roughened solar air heaters. *Solar Energy*, (91), 59–67.

[16] Webb, R.L., Kim. N.H. Principles of Enhanced Heat Transfer, 2nd ed., Taylor & Francis, New York, 785 pages (2005).

ETM0026

Deep learning-Based NSGA-II method for Achieving the Optimal Spiral Fin Geometry in a Crimped Spiral Fin-and-Tube Heat Exchanger

Mehrdad Mesgarpour[1, 2,*], Thawatchai Kaewkamrop[1], Shahab Goodarzi[3], Omid Mahian[4], Mostafa Safdari Shadloo[5], Sara Gholami[6], Somchai Wongwises[1,7]

[1] Fluid Mechanics, Thermal Engineering and Multiphase Flow Research Lab. (FUTURE), Department of Mechanical Engineering, Faculty of Engineering, King Mongkut's University of Technology Thonburi, Bangmod, Bangkok 10140, Thailand
[2] Department of Sustainable Energy Systems, Mälardalen University, Västerås, SE 72123, Sweden
[3] The Joint Graduate School of Energy and Environment, King Mongkut's University of Technology Thonburi, Bangkok, Thailand.
[4] Department of Chemical Engineering, Imperial College London, London SW7 2AZ, UK
[5] CORIA-UMR 6614, CNRS-University & INSA, Normandie University, 76000, Rouen, France
[6] Department of Architecture, Tabriz Islamic Art University, Tabriz, Iran
[7] National Science and Technology Development Agency (NSTDA), Pathum Thani 12120, Thailand

* Corresponding Author: Mehrdad.mes@kmutt.ac.th

Abstract. In this study, an optimisation approach was introduced to ascertain the optimal amalgamation of crimped spiral fin attributes, encompassing pitch, fin height, and the Reynolds number of airflow. These attributes were meticulously treated as variables, subjected to comprehensive scrutiny for their influence on the heat exchanger's performance. Substantial volumes of empirical data were generated through computational fluid dynamics (CFD) simulations and experimental investigations across three distinct scenarios. The range of boundary conditions was meticulously confined within the scope of $1{,}500 < Re_{inlet} < 6{,}400$. Upon stringent validation against experimental data, a deep neural network (DNN) was meticulously developed, boasting six strategically designed layers. This DNN ingeniously incorporated five pertinent inputs, comprising two geometrical parameters, air velocity, and two unvarying parameters, $T_{w,in}$ and $T_{air,in}$. The DNN outputted two critical targets: pressure drop and air-side heat transfer coefficient. Through comprehensive analysis of the DNN outputs, the optimal configuration of geometrical attributes was unveiled, a process aptly guided by the Non-dominated Sorting Genetic Algorithm (NSGA-II) methodology. Subsequently, an exhaustive CFD exploration was conducted, meticulously considering the optimal geometrical attributes pinpointed earlier. The outcomes presented a notable enhancement in effectiveness, showcasing improvements of up to 8% in comparison to experimental data. Notably, a holistic optimization approach that accounted for both optimization objectives yielded substantial benefits, exemplified by an impressive 8.4% reduction in air-side pressure drop, further reinforcing the empirical data. The results highlighted a convection heat transfer coefficient augmentation of 2.36% based on the parameter (fp/L), which aligns with the nearest experimental findings.

Keywords: Effectiveness, DL, Crimped spiral fin, Optimisation, NSGA-II.

1. Introduction

In recent times, the utilisation of deep learning (DL) methodologies has brought about a transformative impact across diverse domains, encompassing fields like engineering and the optimisation of heat transfer processes. One noteworthy area that has experienced substantial advancements due to this progress is the realm of heat exchanger design. These devices hold a critical role in various industrial operations and energy-conserving systems. Among the configurations within heat exchangers, one that has garnered significant focus is the spiral fin and tube structure. Finned tubes are widely employed in various thermal applications, including heat recovery steam generators, air heaters, air coolers, economizers, preheaters, and condensers. These tubes possess an extended heat transfer surface compared to their primary surface, leading to an augmentation in the heat transfer rate. The addition of a metal sheet, referred to as a "fin," to the tube's base surface serves to enhance heat dissipation. Primary thermal apparatuses, recognised as heat exchangers with a finned and spiral tube configuration, play a pivotal role in recuperating high-temperature flue gases. The standard operation of such a finned and spiral tube heat exchanger involves the exchange of heat between fluids characterised by different temperatures. Fluids traverse through the inner pipes while gases flow on the exterior[1-3].

In a comprehensive numerical investigation conducted by Saeedi et al. [4], an in-depth analysis of heat transfer within a horizontal ground heat exchanger featuring cylindrical fins was undertaken. The research highlighted a notable advantage conferred by the fins: a substantial augmentation in the contact area with the surrounding soil. Remarkably, the introduction of a 1-metre-long fin resulted in an impressive 20.7% enhancement in heat transfer efficiency along the entire length of the pipe. Furthermore, the study unveiled a distinctive performance disparity when contrasting the heat transfer characteristics of a vertical spiral tube—equipped with an equivalent fin count—to those of a horizontal tube configuration in the heat exchanger. Notably, the horizontal tube configuration exhibited approximately 3% superior heat transfer performance, showcasing its superior suitability for this specific thermal application. Liu et al. [5] conducted a numerical investigation into the heat transfer characteristics of a heat exchanger featuring trapezoidal fins with both variable fin lengths and variable angles. Employing the RNG k-ε model for turbulence. The results indicated that augmenting the angle of the trapezoidal fins led to an increase in the Nusselt number and pressure drop. Conversely, the elongation of the fin length resulted in an elevated Nusselt number and a simultaneous reduction in pressure drop.

Analysis of heat transfer performance in plate-fin heat exchangers for hydrogen liquefaction through a numerical model was carried out by Xu et al.[6] In this study, fins were selected in two forms, serrated and wavy fins. The results of their study showed that the problem conditions with high pressure and low temperature lead to a decrease in the velocity of fluid flow in the channel, as a result, serrated fins and wavy fins have a great effect on improving heat transfer performance. Also, the obtained results show new correlations for hydrogen liquefaction with high pressure. Under identical test conditions, Kawaguchi et al. [3] explored the influence of fin height, tube arrangement, and segmented fin height on heat transfer. This investigation encompassed a comparison between plain and serrated welded spiral fin-and-tube heat exchangers. Experimental outcomes highlighted the considerable impact of fin height on heat transfer traits. Notably, for serrated welded spiral fin-and-tube heat exchangers, elevating fin height led to an increase in the air-side heat transfer coefficient. Tube arrangement, however, exerted minimal influence on heat transfer features. Additionally, the researchers formulated a predictive correlation for the Nusselt number.

In an experimental study of the characteristics of heat transfer and fluid flow in a heat exchanger with an annular tube, Bai et al.[7] showed in one of their results in this study that with the increase in the length of the fins due to the larger area of the heat transfer, the average convection heat transfer coefficient and friction factor are improved by 20 and 28%, respectively, compared to shorter fins.

In an experimental study, Batista et al. [8] validated three numerical methods for accurate modeling of heat transfer in a finned heat exchanger with air-to-water crossflow tubes. They used several numerical models to analyse fluid flow and compared the results with experimental data.

In a numerical study, Prabakaran et al. [9] investigated the use of plate heat exchangers with diagonal fins in car air conditioning systems using flammable refrigerant R1234. This study yielded novel correlations for estimating the Nusselt number and friction coefficient through rigorous validation under defined conditions. The research findings have resulted in the development of fresh correlations for predicting the Nusselt number and friction coefficient of R1234. These predictive models offer highly accurate forecasts, boasting average absolute errors of only ±12% and ±15%, respectively.

DL-based optimization is a cutting-edge approach that leverages the power of artificial neural networks to optimize complex systems and processes efficiently. This revolutionary technique has gained significant traction across various domains, including engineering, finance, healthcare, and more. At its core, DL-based optimization involves training deep neural networks on large datasets to learn the underlying patterns and relationships within the data. These networks, often referred to as "black-box" models, can then be used to predict optimal solutions to complex problems that may be challenging to solve using traditional methods. One of the key advantages of DL-based optimization is its ability to handle high-dimensional and non-linear optimization problems with a level of accuracy and speed previously unattainable.

This study introduces an optimization approach for determining the optimal crimped spiral fin attributes, including pitch, fin height, and Reynolds number, impacting heat exchanger performance. Empirical data is gathered through computational fluid dynamics simulations and precise experiments, with boundary conditions within $1{,}500 < Re_{inlet} < 6{,}400$. After validation, a deep neural network (DNN) is developed with six layers, ingeniously incorporating five key inputs geometrical parameters, air velocity, $T_{w,in}$, and $T_{air,in}$. The DNN yields critical pressure drop and air-side heat transfer coefficient outputs. NSGA-II guides optimal attribute configuration, followed by a thorough CFD exploration.

2. Methodology

2.1. Experiment

The present study is developed based on an experimental study (Keawkamrop et al. [10]). An experimental study utilizes a wind tunnel setup with ambient air and hot water. The tunnel is insulated and has a cross-section of 0.43 × 0.48 m. Airflow is controlled by a 2.2 kW fan, and temperatures are monitored using thermocouples. The airflow rate is gauged through a digital manometer. The water loop involves a pump, heater, and flow meter. Water is pumped, heated, and then returned to the tank. Different fin types are tested under specific conditions outlined in Table 1. The study explores inlet water temperatures ranging from 55 to 70°C and flow rates between 6 and 14 LPM. Figures 1a and 1b presents a graphical illustration of crimped fin tube’s cross section and real photo of it.

Table 1. Test conditions.

Parameter	Crimped spiral fin
Inlet air dry bulb temperature, (˚C)	31.5±0.5
Inlet water temperature, (˚C)	55, 60, 65, and 70
Water volume flow rate, (LPM)	6 and 8
Frontal air velocity, (m/s)	2.0-8.0
d_f , (mm)	28.5
f_h , (mm)	Variable
d_o , (mm)	9.53
d_i , (mm)	7.53
f_t , (mm)	0.5
f_p , (mm)	3.18~6.35

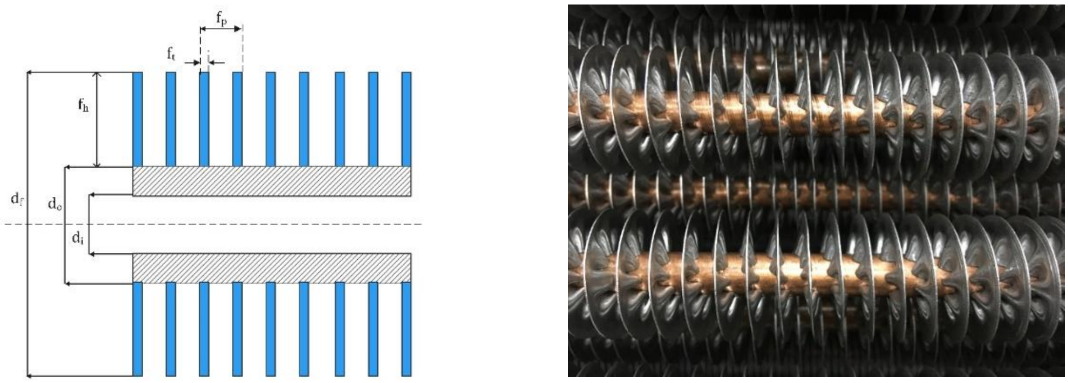

(a) (b)

Figure 1. Graphical illustration of crimped fin tube's cross-section.

The measurement accuracies are shown in Table 2.

Table 2. Measurement accuracies.

Parameter	Accuracy
Air-side thermocouple probes, ˚C	±0.1
Water-side thermocouple probes, ˚C	±0.1
Water flow meter, LPM	±0.4 (±0.02 of full scale)
Digital manometer, Pa	±0.5

2.2. Computational fluid dynamic

In the present study, we delve into a significant aspect of thermal dynamics by examining a 3D channel with dimensions akin to those in the experimental setup. This channel serves as a conduit for directing airflow through the heat exchanger, enabling us to explore its performance under controlled conditions. To accurately capture the intricacies of this airflow behaviour, a steady-state approach is employed, considering the inherent turbulence present in such scenarios. For this purpose, the k-w turbulence model is chosen, known for its effectiveness in predicting turbulent flows with boundary layer separation. The simulation of this complex scenario is facilitated through the utilisation of Ansys Fluent, a powerful CFD solver. Its advanced algorithms and robust capabilities allow us to intricately model the intricate interplay between fluid dynamics and heat transfer within the 3D channel. This simulation endeavour provides us with a virtual representation of how the airflow interacts with the heat exchanger, offering insights that would be challenging to obtain through conventional experimentation alone. The seamless transfer of data between Ansys Fluent and Python is facilitated through a combination of file formats, APIs (application programming interfaces), and scripting. This data exchange enables users to bridge the gap between simulation results generated in Ansys Fluent and the analysis, visualisation, or optimisation processes performed in Python. Pyfluent is an open-source technology that provides APIs to interface with Ansys Fluent, a CFD software. The other is a Python client library for Fluent, an open-source data collector and aggregator. The PyFluent that interfaces with Ansys Fluent is part of the PyAnsys ecosystem. It allows users to create customised workspaces and automate repetitive tasks using Python scripting. With PyFluent, you can access Ansys Fluent capabilities from pre-processing, setting up physics, and solving to post-processing. PyFluent, which is a client library for Fluent, is simple, fast, and reliable. It provides a Pythonic way to transmit JSON messages to Fluent. For better performance, it connects to Fluent's in-forward plugin and transmits messages that are serialised by MessagePack.

2.3. DL and optimization method

In the present study, we delve into a significant aspect of thermal dynamics by examining a 3D channel with dimensions akin to those in the experimental setup. This channel serves as a conduit for directing airflow through the heat exchanger, enabling us to explore its performance under controlled conditions. To accurately capture the intricacies of this airflow behaviour, a steady-state approach is employed, considering the inherent turbulence present in such scenarios. For this purpose, the k-w turbulence model is chosen, known for its effectiveness in predicting turbulent flows with boundary layer separation. The simulation of this complex scenario is facilitated through the use of Ansys Fluent, a powerful CFD solver. Its advanced algorithms and robust capabilities allow us to intricately model the intricate interplay between fluid dynamics and heat transfer within the 3D channel. This simulation endeavour provides us with a virtual representation of how the airflow interacts with the heat exchanger, offering insights that would be challenging to obtain through conventional experimentation alone. The seamless transfer of data between Ansys Fluent and Python is facilitated through a combination of file formats, APIs (application programming interfaces), and scripting. This data exchange enables users to bridge the gap between simulation results generated in Ansys Fluent and the analysis, visualisation, or optimisation processes performed in Python. Pyfluent is an open-source technology that provides APIs to interface with Ansys Fluent, a CFD software. The other is a Python client library for Fluent, an open-source data collector and aggregator. The PyFluent that interfaces with Ansys Fluent is part of the PyAnsys ecosystem. It allows users to create customised workspaces and automate repetitive tasks using Python scripting. With PyFluent, you can access Ansys Fluent capabilities from pre-processing, setting up physics, and solving to post-processing. PyFluent, which is a client library for Fluent, is simple, fast, and reliable. It provides a Pythonic way to transmit JSON messages to Fluent. For better performance, it connects to Fluent's in-forward plugin and transmits messages that are serialised by MessagePack.

Table 3. Deign parameters.

Design parameter	Range (Exp.)	Sample	Range (CFD)	Sample	Range of Re	$T_{w,in}$(°C)	$\dot{m}_{w,in}$ (0.1kg.s^{-1})
$\frac{f_p}{L}$	0.00935~0.01867	6	0.0029~0.86	20	1,500 < Re_{inlet} < 6,400	60	0.1
$\frac{d_i}{d_f}$	0.264	1	0.1~0.8	20			

To optimise the inter-fin spacing, the initial step entails conducting a comprehensive experiment simulation. Once the accuracy of this simulation is verified, the resulting CFD data is harnessed to train a foundational DL (DL) network. This principal network is comprised of ten deeply layered hidden structures, accepting inputs encompassing five distinct design parameters, the Reynolds number (Re), and two constants (Tw,in, and mass flow rate). As its outputs, this network generates two essential metrics: pressure drop and heat transfer coefficient. Subsequently, the foundational DL network serves as the input for a secondary DL network. This secondary network holds the responsibility of extrapolating values that fall within the bounds of the CFD dataset range. Furthermore, the optimisation layers are subsequently applied to the outcomes of this second network. This procedural arrangement effectively facilitates the attainment of optimal outcomes for the designated inter-fin spacing, leveraging the power of DL and surrogate modelling to streamline the optimisation process.

Combining DL with NSGA-II presents a powerful strategy for tackling complex optimisation problems. This approach aims to harness the predictive capabilities of DL while leveraging the search and selection mechanisms of NSGA-II. The strategic integration can be broken down into several key steps. Firstly, data collection and preprocessing are crucial. Gather a comprehensive dataset containing input parameters and their corresponding objective values. Train the model on the prepared dataset, allowing it to learn the underlying patterns. The trained DL model acts as a surrogate, offering rapid and accurate predictions of objective values without the need for costly function evaluations. Thirdly, integrate the DL model into NSGA-II. Replace the traditional objective function evaluations in NSGA-II with predictions from the DL model. Use the surrogate model to guide the selection of promising solutions, thereby reducing the computational burden. This step offers a balance between exploration and exploitation as NSGA-II evolves the population based on the surrogate's insights. Lastly, maintain a continuous feedback loop for model refinement.

3. Governing Equations

The air-side heat transfer rate is calculated from:

$$\dot{Q}_a = \dot{m}_a\, c_{p,a}\, \Delta T_a \tag{1}$$

The air-side heat transfer coefficient is determined from:

$$h_o = \frac{\dot{Q}_a}{A_o(T_{s,ave} - T_{a,ave})} \tag{2}$$

The air-side heat transfer rate ($\dot{Q}_a$) is determined from:

$$\dot{Q}_a = \dot{m}_a\, c_{p,a}\, (T_{a,\mathrm{out}} - T_{a,in}) \tag{3}$$

The total surface area (A_o) is the sum of the surface area of the fin (A_f) and the surface area of the un-finned base (A_b), which can be determined as follows:

$$A_o = A_f + A_b \tag{4}$$

The average surface temperature of spiral finned tube ($T_{s,\mathrm{ave}}$) is determined from:

$$T_{s,ave} = \frac{1}{A_o}\sum_{i=1}^{n} T_{s,i} A_i \tag{5}$$

The average air temperature ($T_{a,\mathrm{ave}}$) is determined from:

$$T_{a,\mathrm{ave}} = (T_{a,\mathrm{out}} + T_{a,in})/2 \tag{6}$$

The air-side pressure drop is determined from:

$$\Delta P = P_{a,in} - P_{a,out} \tag{7}$$

Here's a basic outline of the NSGA-II algorithm in mathematical terms:

- *Initialization:*
    - Randomly generate an initial population: P = {p_1, p_2, ..., p_N}[11].
- *Fitness Evaluation:*
    - Evaluate the fitness of each individual with respect to the M objectives: f(p_i) = (f_1(p_i), f_2(p_i), ..., f_M(p_i)) for i = 1 to N.
- *Non-Dominated Sorting:*
    - Categorize individuals into fronts based on dominance relationships.
    - Define a dominance relation: p_i dominates p_j (denoted as p_i ≺ p_j) if ∀m ∈ {1, 2, M}, f_m(p_i) ≤ f_m(p_j) and ∃m ∈ {1, 2, ..., M} such that f_m(p_i) < f_m(p_j).

- Assign a rank R(p_i) to each individual, where R(p_i) is the front to which p_i belongs.
- *Crowding Distance Calculation:*
    - Calculate crowding distance for individuals within each front.
    - For each objective m ∈ {1, 2, ... , M}, sort individuals based on their fitness values in that objective.
    - Calculate crowding distance D(p_i) for each individual p_i as the sum of the differences in fitness values with adjacent individuals in each objective.
- *Selection:*
    - Select individuals for the next generation based on fronts and crowding distances.
    - Start with the first front (F = 1) and fill S with individuals from the front until the total size exceeds N.
    - If the size of S is still less than N, move to the next front and add individuals until N is reached.
    - If S still has space, select individuals from the current front based on higher crowding distances to ensure diversity.
- *Crossover and Mutation:*
    - Apply genetic operators to the selected individuals in S to generate offspring Q.
- *Next Generation:*
    - Form the next generation population as the union of S and Q.
- *Termination:*
    - Repeat the above steps for a specified number of generations or until a termination criterion is met (e.g., a maximum number of generations reached).

where:
- **P**: Population of individuals.
- **N**: Number of individuals in the population.
- **M**: Number of objectives.
- **F**: Number of fronts after non-dominated sorting.
- **S**: Selected individuals for the next generation.
- **Q**: Offspring generated through crossover and mutation.
- **D**: Crowding distance calculated for individuals within a front.

In present study, we utilized a Cartesian mesh structure comprising a total of 865,844 meshes. To ensure the reliability of our results, we conducted a grid independency test to validate the appropriateness of the chosen mesh size. Our criteria for convergence were set at a threshold of 0.000001 for continuity and 0.00000001 for energy. These stringent convergence criteria were implemented to ensure that the solution reached a stable and reliable state, allowing for accurate analysis and interpretation of the results.

4. Validation

Validation in numerical simulation refers to the process of assessing the accuracy and reliability of a simulation model by comparing its predictions to experimental or real-world data. Referring to Figure 2, the investigation involves analysing and comparing convection heat transfer coefficients and pressure drops with experimental data. The outcomes of this analysis reveal that the highest discrepancy observed is 12.96% for convection heat transfer, while for pressure drop, it amounts to 13.95%.

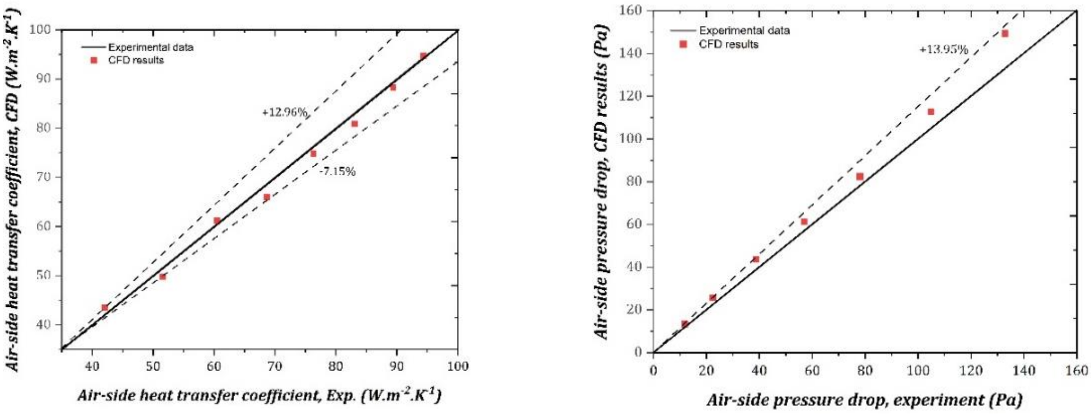

Figure 1. Verification of the results of CFD and experimental data for a) air-side heat transfer coefficient and b) pressure drop, when d_f=28.5 mm, f_p=3.18, $T_{W,in}$=60ºC, Mass flow rate$_{water,\ in}$=0.1kg/s.

5. Results and discussion

The number of parameters required for optimising geometrical parameters using a multi-objective method depends on the complexity of the problem and the specific design space being considered. In multi-objective optimization, there are typically multiple design variables (geometrical parameters in this case) that can be adjusted to find the best compromise between conflicting objectives. The number of parameters can vary widely based on the system being optimized. For instance, if you're optimising a simple geometrical shape, you might have just a few parameters like length, width, and height. Optimisation plays a crucial role in enhancing heat exchanger efficiency by fine-tuning design parameters and operational conditions to achieve the best possible performance. Optimising the number of fins and their geometry in a heat exchanger can significantly impact both pressure drop and heat transfer coefficient. Figure 3 presents the variation of dimensionless heat transfer coefficient and pressure drop based on f_p/L when Re = 1,500, df = 28.5 mm, fp = 3.18, TW = 60 oC, mass flow rate = 0.1 kg/s. The findings revealed a gradual decrease in the heat transfer coefficient after its initial sharp increase. As the number of fins along the length of the tube increased, the overall heat transfer improved while the pressure drop decreased. The experimental data contrasts the air-side performance of plain welded spiral fin-and-tube heat exchangers and serrated welded spiral fin-and-tube heat exchangers through parameters like the Nusselt number and Euler number. This comparison is aligned with prior research. To relate our findings to existing studies, we establish a ratio between the segmented fin height and the overall fin height. In this investigation, the ratio of segmented fin height to fin height ranges from 20.3% to 52.8%. Notably, this ratio escalates as the segmented fin height (h_s/f_h) increases. The Nusselt number demonstrates an upward trend as air-side Reynolds numbers climb, whereas the Euler number experiences a decline with increasing air-side Reynolds numbers. Remarkably, the heat exchanger with a h_s/f_h ratio of 62.5%, as per Ma et al. [12] work in 2012, exhibits a greater Nusselt number than what's indicated by the h_s/f_h ratio in our current study.

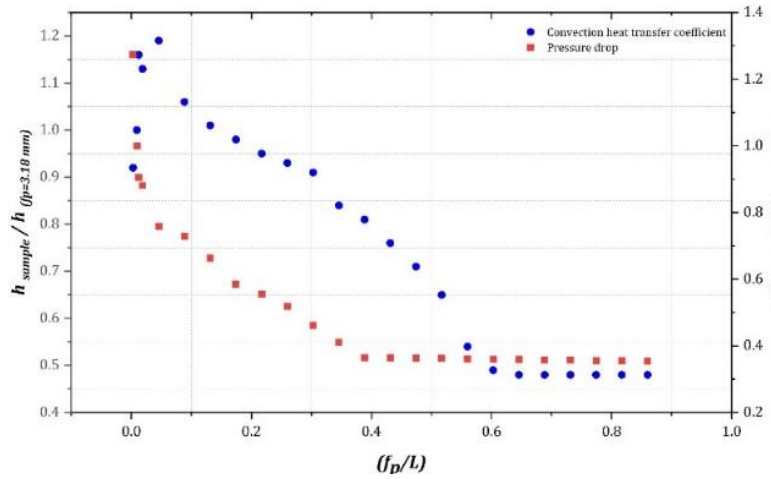

Figure 2. Variation of dimensionless convection heat transfer coefficient and pressure drop based on f_p/L, when d_f=28.5 mm, f_p=3.18, $T_{W,in}$=60ºC, Mass flow $rate_{water,\ in}$=0.1kg.s^{-1}.

Figures 4a and 4b present a comprehensive comparison between the experimental data and the optimised model across a broad range of frontal air velocities. These figures illustrate the improvements in air-side pressure drop and heat transfer coefficient achieved through multi-objective optimisation techniques. The cost function, a pivotal element of multi-objective optimisation, facilitates the pursuit of solutions that strike an optimal balance among conflicting objectives. In the context of multi-objective optimisation, the primary aim is to identify a collection of solutions that yield the most favourable compromise among multiple objectives. As shown in Figure 4a, the results show that optimising both parameters can cut the air-side pressure drop by as much as 8.4% compared to the experimental data. On the other hand, Figure 4b shows that optimising based on the parameter (fp/L) leads to a significant increase of 2.36 percent in the convection heat transfer coefficient, which is in line with the most recent experimental data.

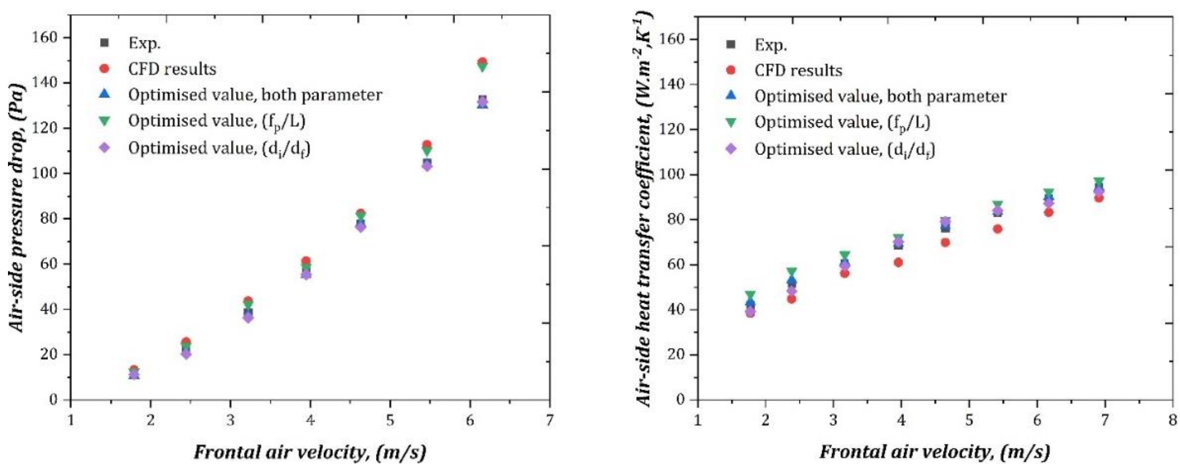

(a) (b)

Figure 3. A comparison between exp. data, CFD results and optimized results based on both functions for a) air-side pressure drop and b) heat transfer coefficient, when d_f=28.5 mm, f_p=3.18, $T_{W,in}$=60ºC, Mass flow $rate_{water,\ in}$=0.1kg/s.

6. Conclusion

In this study, an innovative optimisation methodology is introduced, focusing on determining the optimal combination of crimped spiral fin attributes. These attributes include pitch and fin height, considered in conjunction with the Reynolds number of the airflow. This methodology's principal aim is to enhance a heat exchanger's operational efficiency. These identifiable attributes are regarded as variable entities, with their discernible impacts on the thermodynamic efficiency of the heat exchanger undergoing thorough examination. The investigation generates substantial amounts of empirical data through computational fluid dynamics simulations and empirical experiments conducted across three distinct scenarios. The boundary conditions governing these efforts are meticulously calibrated within the 1,500 < Re_{inlet} < 6,400 range. A novel deep neural network (DNN) is employed to pursue the designated objective. The DNN features a layered architecture consisting of six carefully designed layers. Within this DNN architecture, five inputs are utilised, encompassing the geometrical parameters and the air velocity. These inputs collectively interact with two specified targets: the pressure drop and the thermal efficiency of the system. The results indicated that:

1. Optimization considering both parameters can lead to a significant reduction of up to 8.4% in air-side pressure drop when compared to the experimental data. Also, the results show that, based on the parameter (fp/L), yields a noteworthy enhancement of 2.36% in convection heat transfer coefficient, as aligned with the nearest experimental data.
2. The outcomes demonstrate that optimization considering both parameters can lead to a significant reduction of up to 8.4% in air-side pressure drop when compared to the experimental data.

7. References

[1] Nuntaphan, A., T. Kiatsiriroat, and C.C. Wang, *Air side performance at low Reynolds number of cross-flow heat exchanger using crimped spiral fins.* International Communications in Heat and Mass Transfer, 2005. **32**(1): p. 151-165.

[2] Nuntaphan, A., T. Kiatsiriroat, and C.C. Wang, *Heat transfer and friction characteristics of crimped spiral finned heat exchangers with dehumidification.* Applied Thermal Engineering, 2005. **25**(2): p. 327-340.

[3] Kawaguchi, K., K. Okui, T. Asai, and Y. Hasegawa, *The heat transfer and pressure drop characteristics of the finned tube banks in forced convection (effects of fin height on heat transfer characteristics).* Heat Transfer—Asian Research: Co‐sponsored by the Society of Chemical Engineers of Japan and the Heat Transfer Division of ASME, 2006. **35**(3): p. 194-208.

[4] Saeidi, R., Y. Noorollahi, S. Chang, and H. Yousefi, *A comprehensive study of Fin-Assisted horizontal ground heat exchanger for enhancing the heat transfer performance.* Energy Conversion and Management: X, 2023. **18**: p. 100359.

[5] Liu, M. and J.K. Calautit, *A parametric investigation of the heat transfer enhancement of tube bank heat exchanger with reversed trapezoidal profile fins.* Thermal Science and Engineering Progress, 2023. **42**: p. 101914.

[6] Xu, P., J. Wen, S. Wang, Q. Chen, and Y. Li, *Numerical simulation on flow and heat transfer performances of serrated and wavy fins in plate-fin heat exchanger for hydrogen liquefaction.* International Journal of Hydrogen Energy, 2023. **48**(54): p. 20680-20693.

[7] Bai, W., W. Chen, C. Zeng, G. Wu, and X. Chai, *Heat transfer and eccentric effect investigation on heat pipe used annular heat exchangers with densely longitudinal fins.* International Journal of Thermal Sciences, 2022. **179**: p. 107658.

[8] Batista, J., A. Trp, and K. Lenic, *Experimentally validated numerical modeling of heat transfer in crossflow air-to-water fin-and-tube heat exchanger.* Applied Thermal Engineering, 2022. **212**: p. 118528.

[9] Prabakaran, R., M. Salman, P.G. Kumar, D. Lee, and S.C. Kim, *Heat transfer and pressure drop characteristics of R1234yf during evaporation in a plate heat exchanger with offset strip fins: An experimental study.* International Journal of Heat and Mass Transfer, 2022. **194**: p. 123091.

[10] Keawkamrop, T., L.G. Asirvatham, A.S. Dalkılıç, H.S. Ahn, O. Mahian, and S. Wongwises, *An experimental investigation of the air-side performance of crimped spiral fin-and-tube heat exchangers with a small tube diameter.* International Journal of Heat and Mass Transfer, 2021. **178**: p. 121571.

[11] Sun, X., M. Xie, F. Zhou, J. Fu, and J. Liu, *Multi-objective optimization for combustion, thermodynamic and emission characteristics of Atkinson cycle engine using tree-based machine learning and the NSGA II algorithm.* Fuel, 2023. **342**: p. 127839.

[12] Ma, Y., Y. Yuan, Y. Liu, X. Hu, and Y. Huang, *Experimental investigation of heat transfer and pressure drop in serrated finned tube banks with staggered layouts.* Applied Thermal Engineering, 2012. **37**: p. 314-323.

The 13th TSME International Conference on Mechanical Engineering
12th – 15th December 2023
Chiang Mai, Thailand

ETM0027

Highly effective conversion of green ammonia to electricity in TURBO Fuel Cell systems (MGT-SOFC) for the future transportation sector with a focus on marine applications

H. P. Berg[1, *], R. Dückershoff[2], M. Kleissl[1], F. Mauss[1], A. Himmelberg[1], K. Blumenröder[3] and Chr. Rex[4]
[1]Brandenburg University of Technology CS, Cottbus, Germany
[2]THM – Technische Hochschule Mittelhessen, Friedeberg-Hessen, Germany
[3]T-CELL Aktiengesellschaft, Germany
[4]Euro-K GmbH, Germany

* Corresponding Author: peter.berg@b-tu.de

Abstract. With the term "TURBO Fuel Cell (TFC)", a very compact and highly efficient MGT-SOFC hybrid system was described in 2017 (by Berg et.al.) and validated in further research projects. The system is a recuperated micro gas turbine (MGT) process with an embedded solid oxide fuel cell (SOFC) subsystem with high temperature (HEX) and redox heat exchanger. For the ammonia fuel feed, the redox heat exchanger consists of a post-oxidation module with integrated heat exchange to the cracker. In the oxidation module, the anode exhaust gas is exothermically converted with the oxygen of the cathode exhaust gas of the SOFC. The heat from the fuel cell and from this post-reaction is used by the endothermic cracking process. Due to the high temperature, the catalyst and the nickel mesh of the anode side, ideal conditions for ammonia cracking exist. This paper describes the effect of the high heat integration of the Turbo Fuel Cell design and the thermodynamic background. Electrical efficiencies of more than 70% and the high-power density show very clearly the advantages of pressurized charging compared to atmospheric SOFC systems. Thanks to its highly compact design, the TFC system can compete with conventional diesel engines in terms of size. It is shown that a future use as a maritime auxiliary power unit (APU) and in the field of railroad propulsion technology is reasonable if green ammonia and other green fuels are used. Furthermore, it is shown that with a further adaptation and weight reduction of the SOFC cells, the TURBO Fuel Cell technology will have high significance as a future alternative drive-in mobility. In addition to the advantage of using ammonia as hydrogen storage, the article also points out the superiority of the TURBO Fuel Cell compared to other fuel cell systems and fuels with a special focus on marine applications.

Keywords: Ammonia Fuel Cell, SOFC, TURBO Fuel Cell, Green marine application.

1. Introduction

The engines of cruise and container ships as well as large freighters and ferries run on heavy oil and diesel. They are responsible for 3% of annual global CO_2 emissions (approx. 1 billion tons of CO_2) from fossil fuels. To support global climate goals despite increasing world trade, the International Maritime Organization [1] is working on a decarbonization strategy. By 2045, the shipping industry is expected to reduce emissions by 50% - 60%. In addition to improving classic energy efficiency measures, improving logistical processes, and optimizing ship propulsion, clean ship propulsion represents a competitive advantage. The greatest effect in reducing CO_2 emissions comes from changing fuels. A sensible long-term change even offers the potential of emission-free operation. This affects most ships that have combustion engines. These are currently powered by heavy oil, diesel, gasoline, or gas. A small group consists of ships with fuel cells (submarines), electric motors (small boats and ships), sail drives (sailboats and sailing ships) and nuclear drives (only in the military sector / e.g., aircraft carriers). These can be classified as unproblematic.

Sailing ships and ships with nuclear propulsion do not require chemical or electrochemical storage for the propulsion task. Pure electric propulsion systems are unsuitable for large ships as a conversion measure. This is due to their low energy density, durability, and robustness. For coastal shipping, small ships and short-range ferries, battery-based systems are conceivable and, in isolated cases, even sensible. Serial hybrid propulsion systems make sense for larger ships and are already in use on modern cruise ships (Fig. 1b). A combination of parallel-serial hybrid propulsion systems makes sense for yachts (Fig. 1a).

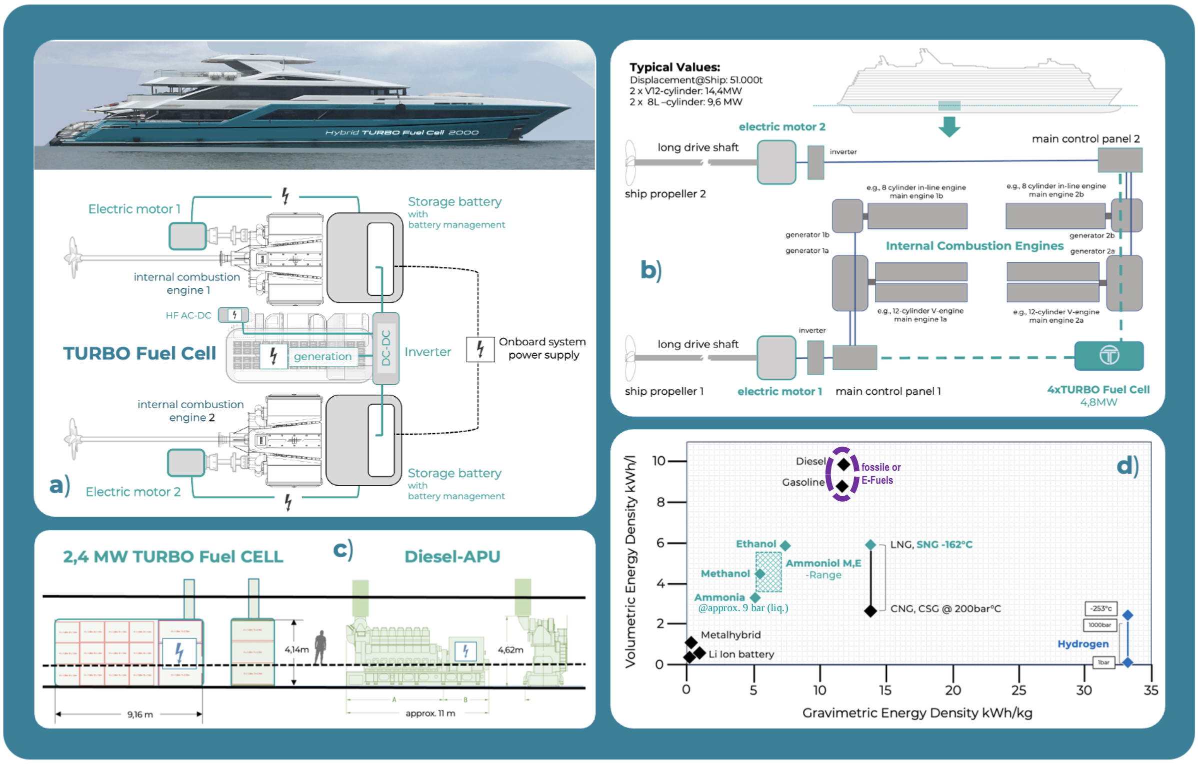

Figure 1. a) Hybrid Super Yacht with a parallel-serial 2MW hybrid propulsion system [3] with TURBO Fuel Cell, b) typical serial hybrid system of a cruise ship with 4,8MW TURBO Fuel Cell, c) comparison the proportions of a powerful 2,4MW TURBO Fuel Cell APU with a conventional diesel APU, d) gravimetric and volumetric energy properties of the fuels examined (capital 2).

Here and in the other areas, large two-stroke-, and four-stroke- engines in combination with CO_2-reduced (short to medium term) CO_2-neutral or CO_2-free (medium to long term) fuels should be aimed for. For this purpose, the refueling, fuel storage and fuel supply in the port as well as on the ship must be adapted and, of course, also comply with all legal safety requirements (the same applies to the hybrid propulsion systems). For the marine engines, the combustion processes must be adapted to the new fuels and the safety standards on the ship must be met. In addition to the large engines, the Auxiliary Power Unit must ideally also be converted to the main fuel, or the energy converters (chemical energy - to electrical energy) must be replaced. Therefore, it makes sense to introduce energy converters such as fuel cells into the Auxiliary Power Unit. Projected TURBO fuel cell systems (see also [2], [3], [4]) are already on a par with diesel generators in terms of installation space and weight and have a significantly higher electrical efficiency of over 70%. They are at the beginning of their product life cycle. This article describes the own research and development work in the field of multi-fuel TURBO Fuel Cell with a view to future fuel for the ship transport sector.

2. Energy carriers and energy converters for shipping.

Future fuel cell systems must be fuel-flexible for the reasons mentioned above. This is necessary because the following future fuels for ship engines are currently being discussed:

Hydrogen, E-Ammonia, E-Methanol, E-SNG (LNG), E-Ammoniol [5]

Figure 1d shows the different energy densities and Figure 2a shows the fuel-air-mixture heat value as a fuel comparison depending on the stoichiometric air demand (λ=1). Since engine application is of high importance for ships, this comparison makes sense. In principle, these fuels can all be used with the adaptation of the engine combustion process and in TURBO Fuel Cell – Systems. With this basis, the use of fuel cell systems of the TURBO Fuel Cell type can be prepared promptly for marine pilot applications.

Technologies for this use can be derived from the research described in this article. Below is a brief overview of the TURBO Fuel Cell energy converter and the interesting green fuels of the future.

2.1. TURBO Fuel Cell

The TURBO Fuel Cell was presented in 2017 (by Berg et.al.) as a compact hybrid design between a micro gas turbine and a SOFC (Solid Oxide Fuel Cell). In the presented research and development work, all essential components of the circular process were validated. This development phase focused on the stationary TURBO Fuel Cell for the living spaces of tomorrow. This design was thermodynamically optimized. For example, heat loss is minimal because the system has layered flow channels (MLC - Multi Layer Containment). The external container temperature is therefore below 50°C. An outer shell with ambient temperature enables the design to be adapted e.g. to the city architecture. The design of this type has a vertical axis (figure 2 shows the basic structure), while the application for the rail or ship mobility sector has a horizontal axis with a SOFC stack grape clustered more compactly. The basic research work is shown here for understanding based on stationary application.

Figure 3 shows the basic principle of the hybrid MGT-SOFC process. The air is compressed (component A) and preheated by the recuperator (component B). Heat is then supplied to the fluid through the fuel cell module (component C, instead of a combustion chamber). The hot gas then flows to the turbine (component A) and is expanded. It then flows out via the recuperator and exchanges heat with the compressed air. The turbine drives the compressor and the generator. Turbine, compressor and generator (power head A/ TURBO system) sit on one shaft with air bearings.

During the research work, the cycle components were validated experimentally and computationally. The component interconnection can be seen in principle in Figure 3 and in more detail in Figure 6 and 7. Figure 7 also shows the parameters of the cycle points on which the experiments were based. During the tests, individual components and subsystems were examined and the results were used for comparison and as a specification for the cycle calculation. The research was carried out iteratively through calculation methods, construction, and testing. A small insight into the component tests can be obtained from Figure 4.

Figure 4 F shows, for example, the pre-reformer, which is connected to the post-oxidation (after-combustion chamber) and is tested under real pressure conditions with a CH_4 steam mixture in the test setup 4G. This setup can also be used (as described in Chapter 3) for cracker tests (without steam) for ammonia application. The thermodynamically sensible positioning of this component is constructively between the SOFC stack grape and the turbo system (see figure 2). Since this module is used for pre-reforming or pre-cracking, it is called RC (Reformer-Craker). The following functional assignments result for the fuels: hydrogen (R=0, C=0), ammonia (R=0, C=+), methanol (R=+, C=0), natural gas/methane (R=+, C=0), ammoniol (R=+, C=+).

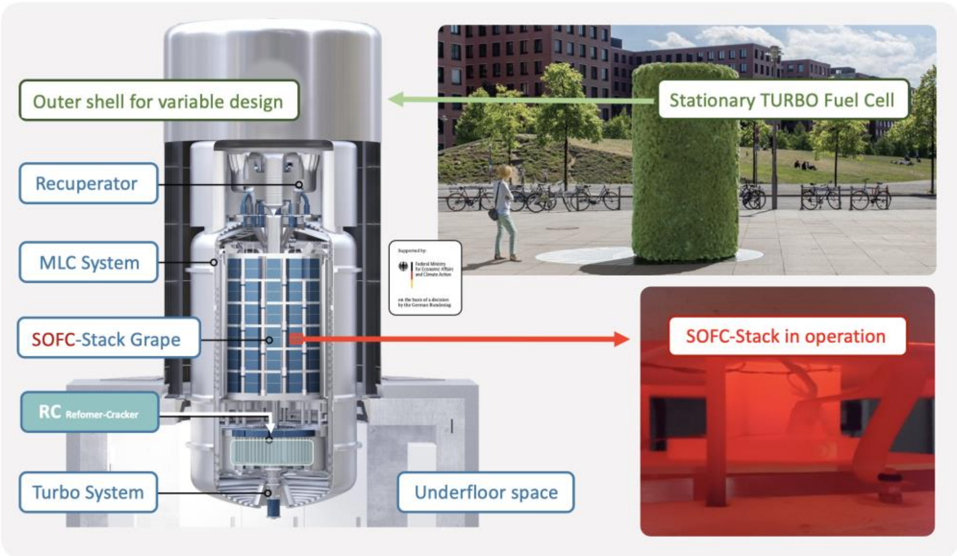

Figure 2. Design of a stationary TURBO fuel cell system (research funding from the Federal Ministry for Economic Affairs and Climate Protection, BMWK), view of a SOFC in test operation under operating conditions (bottom left).

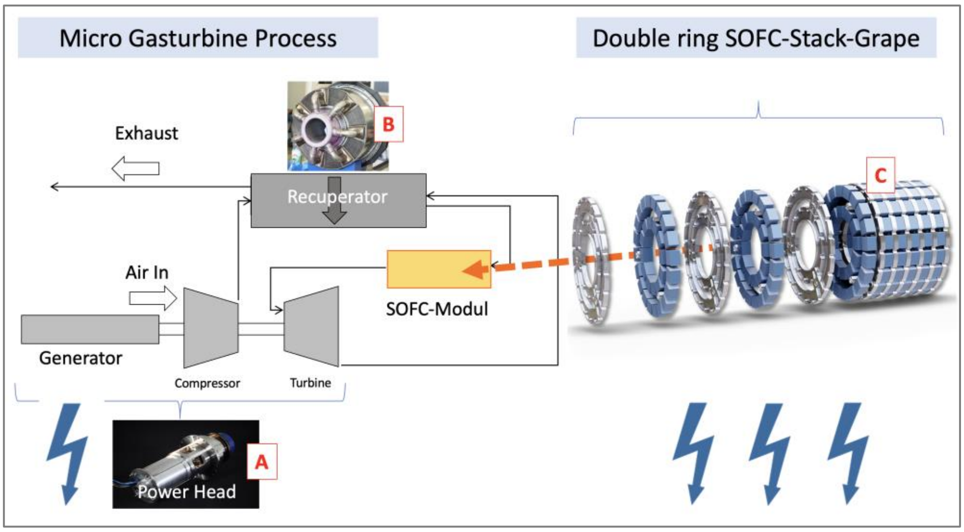

Figure 3. Simplified representation of a TURBO Fuel Cell- (MGT-SOFC hybrid-) process with important components. A = air-bearing turbo set with generator, compressor and turbine (power head), B = recuperator (with 91.5% effectiveness and 4.3% total pressure drop) [9]. C = SOFC stack grape with MK- SOFC type (see Figure 4E) from the research partner Fraunhofer Institute for Ceramic Technologies and Systems IKTS [15].

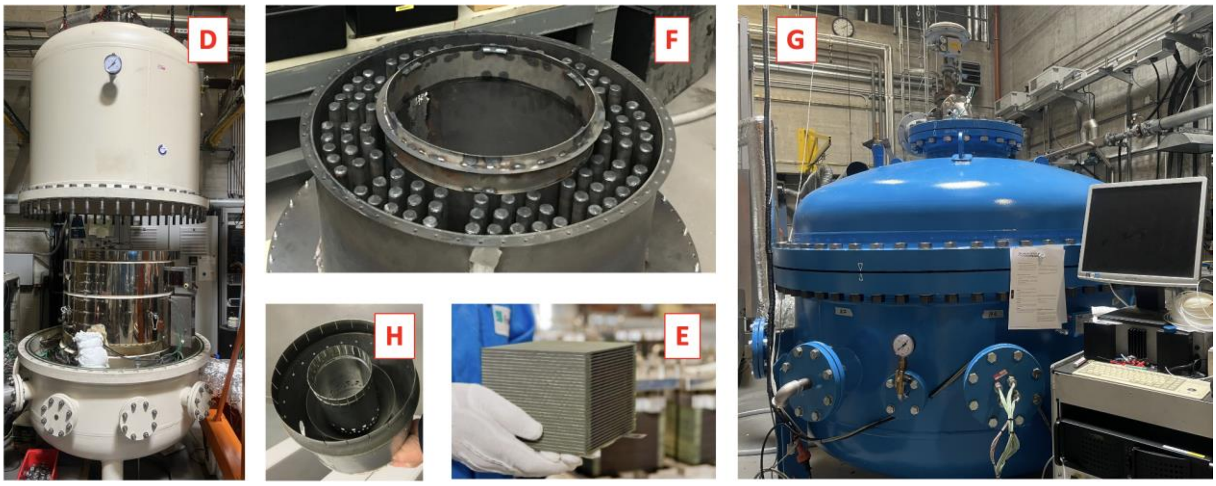

Figure 4. D = test facility for testing SOFC stacks up to 8 bar (typical TURBO Fuel Cell System nominal pressure 3,5 to 4.8 bar), E = SOFC stack (type MK, performance information see [15]), F = reformer (predecessor of the RC design, see Chapter 3), G = pressure test stand up to 6 bar (nominal pressure 3,5 to 4.8 bar), for testing of RC units including afterburner, H = starting and control combustion chamber, this component sits between the turbine and the RC unit (see Figure 6 and 7).

Many cycle calculations were carried out for all fuels (Figure 7) and results on electrical efficiency were presented in a dimensionless format (figure 8). With the development of a cracker nomogram, the design of an ammonia turbo fuel cell was also possible (figure 9). Below these fuels are described and evaluated for future marine application in combination with the highly efficient TURBO Fuel Cell.

2.2. Hydrogen

The Combustion only produces water vapor and low NO_X emissions, which are technologically easy to control. Hydrogen could be used in coastal and ferry operations. Here the conditions are like those with electric drives. Hydrogen is not suitable for merchant ships, although direct combustion in piston engines is possible. The high flammability is a safety factor. Furthermore, the volumetric energy density is 4.5 times higher than that of heavy oil. Furthermore, hydrogen must be liquefied, i.e., it must be cooled down to minus 253 °C. Due to the disadvantages mentioned and the high transport costs, it makes sense to store hydrogen in fuels in which carbon or nitrogen is used as a carrier via the chemical compounds. Some possible future green E-Fuels, Methane (SNG), Methanol, Ammonia and Ammoniol (mixture of E-Ammonia with E-Methanol, Bioethanol), are listed below. A power-to-fuel-to-power (PFP) index defined by [6] was used to compare the fuels regarding their energy efficiency. In the refence, the authors energetically compare carbon- and nitrogen-based fuels in terms of their potential as chemical hydrogen storage for stationary energy applications. The PFP index is calculated from the ratio of the energy available from the combustion of the fuel to the energy that flowed into the overall chain of producing the fuel (water splitting, air splitting, CO_2 splitting, manufacturing, transport).

2.3. Ammonia

By weight, ammonia is twice as energetic as hydrogen. A temperature of -33°C is required for liquefaction. Storage and transport are therefore less complicated compared to hydrogen. Ammonia is toxic and safety requirements are relatively high. However, there is a lot of experience in transporting ammonia and a basic infrastructure already exists. When combustion in piston engines, an appropriate combustion process is required because ammonia-air mixtures have a flame speed that is too low. In practice, ammonia is broken down and the flame speed is increased with the hydrogen. PFP - index of 35% [6].

2.4. Methanol

Methanol is a chemical that is already traded in many seaports. Methanol can be produced from hydrogen and CO_2 in a climate-neutral manner. It is liquid at room temperature and can be easily transported. Marine engines have already been developed as dual-fuel engines and can therefore burn diesel and methanol. Greenhouse gas emissions from ships can be reduced by around 20% using methanol. Methanol is considered a so-called transition fuel. Methanol has a PFP-index of 32% [6].

2.5. Methan/ SNG (LNG)

Methane/SNG (LNG): Synthetic methane can be produced from hydrogen using CO_2, which can be used in liquefied form SNG (Synthetic Natural Gas / CH_4). SNG is deep cold (cryogenic). It becomes liquid at atmospheric pressure at a temperature of approximately -161 °C. The expansion ratio of liquid to gaseous is 1:600. The gravimetric energy density of SNG is 50 MJ/kg, higher than the value of 43.13 MJ/kg for diesel. Furthermore, it has a volumetric advantage over diesel. However, this is offset by the more complicated tank structure, which means a higher volume requirement. SNG/Methane has a PFP-index of 31% [6].

2.6. Ammoniol [5]

Ammoniol is a made-up word formed from ammonia (Ammoni-) and alcohol (-ol). This fuel is a carbon-nitrogen based mixed fuel consisting of one or two alcohols and ammonia (see [6] and first experimental investigation by Tanner [7]). The designation M and/or E stands for the solvent liquids methanol (M) and ethanol (E) - carbon based. Ammoniol can be produced from hydrogen and CO_2 in a climate-neutral manner. Via the H_2-ammonia path (nitrogen-based) and the H_2-methanol path (carbon-based) and ethanol components (E), e.g. via biomass. The CO_2 requirement is significantly lower than for the fuels methanol and SNG. This fuel is liquid like methanol at ambient temperature and can be transported very easily. The octane number is 110 ROZ. Ship engines that have a dual-fuel process can be operated with it. The mixture calorific value is between ammonia and methanol (fig.: 1d). Greenhouse gas emissions from ships can be reduced immediately by 28% using Ammoniol. Like methanol, ammoniol could represent a transition fuel. Ammoniol has a PFP-index of approx. 33% (calculated from above values at [6]). For transport areas where no water can be obtained for the steam reforming process during the mission (e.g. in the railway sector), a mixed fuel with a high water content was also considered (fig.: 5). This allows the ammonia content in the solvent to be further increased. The PFP-index is skewed more towards ammonia (PFP - index of 35%). This stable carbon-nitrogen based mixed fuel can be prepared with different water contents, ethanol, methanol, other alcohols ($C_nH_{2n+2}O$), and dissolved ammonia. If water is added to increase the amount of ammonia, the term Hydro-Ammoniol was introduced by [6]. Figure 5 shows the solubility of ammonia at atmospheric pressure using the example of solvents consisting of two substances (water-methanol 0 to 4 o'clock, methanol-ethanol 4 to 8 o'clock, ethanol-water 8 to 12 o'clock). The dimensionless values (solubility coefficients) on the circles indicate how many grams (g) of NH_3 are stably soluble in 100g of solvent. The values are based on measurements by Tanner [7] including own tests and apply to 1.01325 bar at 14°C. They can easily be converted to Tanner for small pressure differences. The partial pressure of the ammonia over the mixture can be easily determined via the vapor pressure and the total pressure using the following ratio equation:

$$\frac{\textbf{Partial pressure} \text{ of } NH_3 \text{ at total pressure p}}{\textbf{Partial pressure} \text{ of } NH_3 \text{ @ 1,01325 bar, 14°C}} = \frac{\textbf{Dissolved amount} \text{ of } NH_3 \text{ (g) @ total pressure p}}{\textbf{Dissolved amount} \text{ of } NH_3 \text{ (g) @ 1,01325 bar, 14°C}}$$

NH_3 mixtures with the solvent's ethanol, methanol and ethanol-methanol are interesting for motor applications. Figure 5 shows the maximum solubility coefficients in the lower segment (4 to 8 o'clock). From the left 100% solvent ethanol (8 o'clock) with a solubility coefficient of 15.9 gNH_3/ 100g and to the right 100% solvent methanol with a solubility coefficient of 29.0 gNH_3/ 100g (4 o'clock) and the solubility coefficients with any mixed ethanol-methanol solvent in between. The background to this is that it could be of interest, for example, to bind NH_3 in bio alcohol and climate-neutrally produced e-methanol. This liquid fuel can be used very easily in gasoline combustion engines. Since the use of NH_3-$C_nH_{2n+2}O$ mixtures in SOFC systems requires a steam reforming process of the fuel, the H_2O can already be mixed into the fuel and thus the NH_3 content can be increased. For this reason, the areas of Hydro-Ammoniol E (left) and M (right) are shown in the segments on the left and right. 100% water with 61.4g NH_3 / 100g is at the "12 o'clock" position. The diagram can also be used to determine NH_3-ethanol-methanol-water mixtures that were not shown. The proportions can be increased significantly by increasing the pressure.

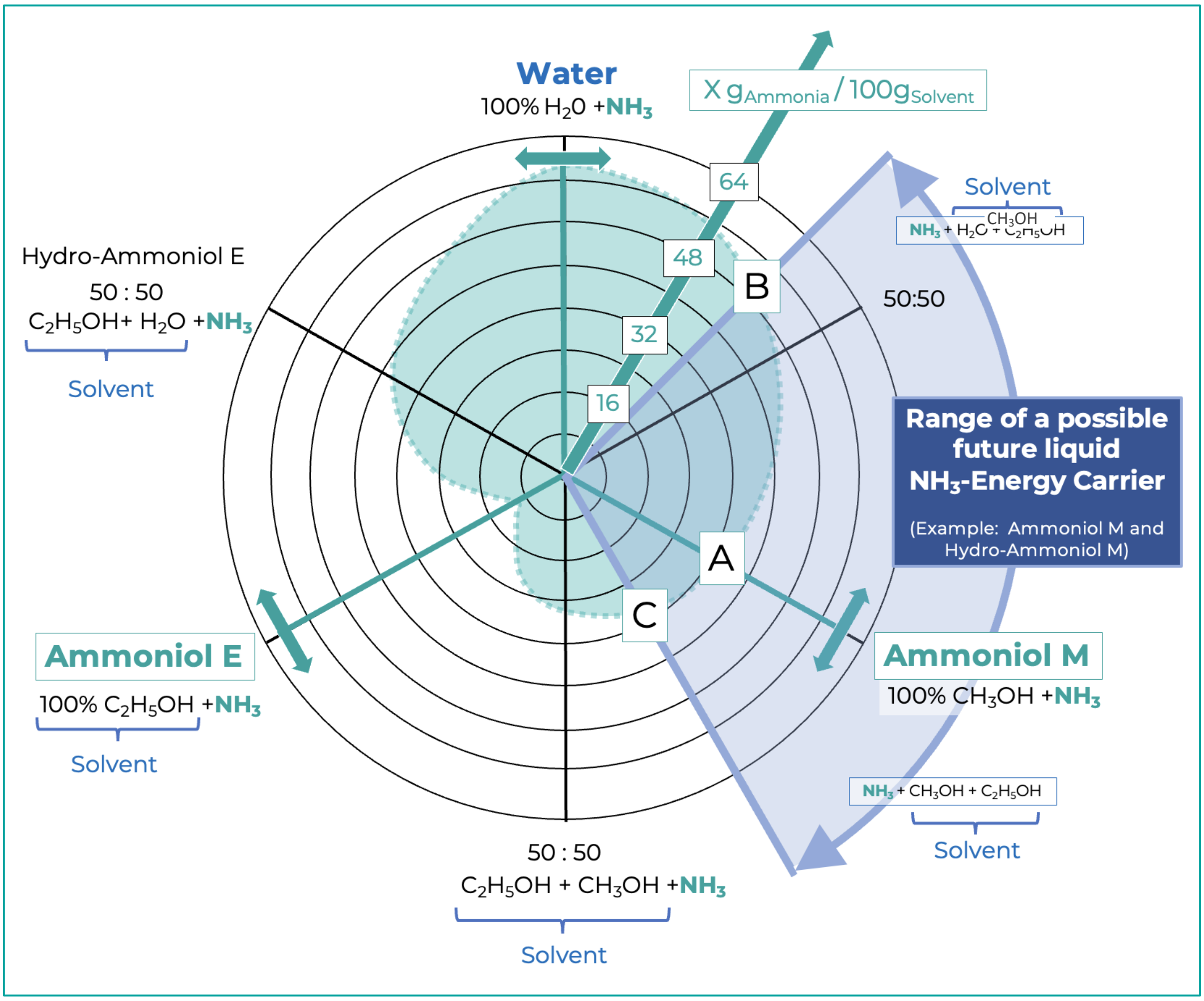

Figure 5. Ammoniol and its solubility of NH_3 at 1.01325 bar at 14°C in the solvents: water-ethanol (E), water-methanol (M), and methanol-ethanol.

For ship applications with hybrid combination systems, the fuel range C to A makes sense because water is available for the TURBO Fuel Cell and the ship engines with Ammoniol ME would have a high-performance fuel with the appropriate flame speed, excellent filling, and high-octane number. This would make an optimal combination of TURBO Fuel Cell and combustion engine possible. For example, for pure TURBO Fuel Cell railway applications, the range A to B (Hydro-Ammoniol M) could be interesting, as an even higher proportion of NH_3 could be transported.

3. TURBO Fuel Cell energy converter in the marine sector

Internal combustion engines (two-stroke engines and four-stroke engines) are largely used to convert the chemically bound energy of the fuels mentioned and the traditionally used energy sources (diesel, heavy oil, gasoline). Gas turbines and fuel cell drives (e.g., in submarines) are also used. Because of their high-power density, gas turbines are primarily used in the military sector at full load. Most ship gas turbines are aero derivatives, i.e., based on powerful aircraft engines. In combination with SOFC generator units (like the one shown here), very effective high-performance propulsion can be achieved. Diesel engines with generators are primarily used as Auxiliary Power Units. They are used to supply the ship with electricity, for example during port times. In the case of hybrid electric systems, these producers work in the electric system network (Figure 1a and b). Traditional Auxiliary Power Unit (APU) can therefore be viewed from a new perspective. An APU-System based on a TURBO Fuel CELL architecture could be an important pioneer for a generally new drive system technology. Systems of this type were already described in 2017 (by Berg et.al. [2]) as a very compact and highly efficient MGT-SOFC hybrid system and validated in further research and development projects [6]. A TURBO Fuel Cell is a recuperated micro gas turbine (MGT) with an embedded solid oxide fuel cell (SOFC) subsystem with high temperature heat exchanger (HEX) and redox heat exchanger (Reformer-Cracker Modul RC). This RC-redox heat exchanger for ammonia fuel use (or for steam reformation of C_xH_y or $C_nH_{2n+2}O$ - fuels) consists of a post-oxidation module with integrated heat exchange to the ammonia cracker (or C_xH_y - or $C_nH_{2n+2}O$ reformer). In the oxidation module, the anode exhaust gas is exothermically reacted with the oxygen from the cathode exhaust gas of the SOFC. The heat from the fuel cell and from this post-reaction is used for these endothermic processes (ammonia cracker or reforming process). Figure 6 shows the schematic structure of the system.

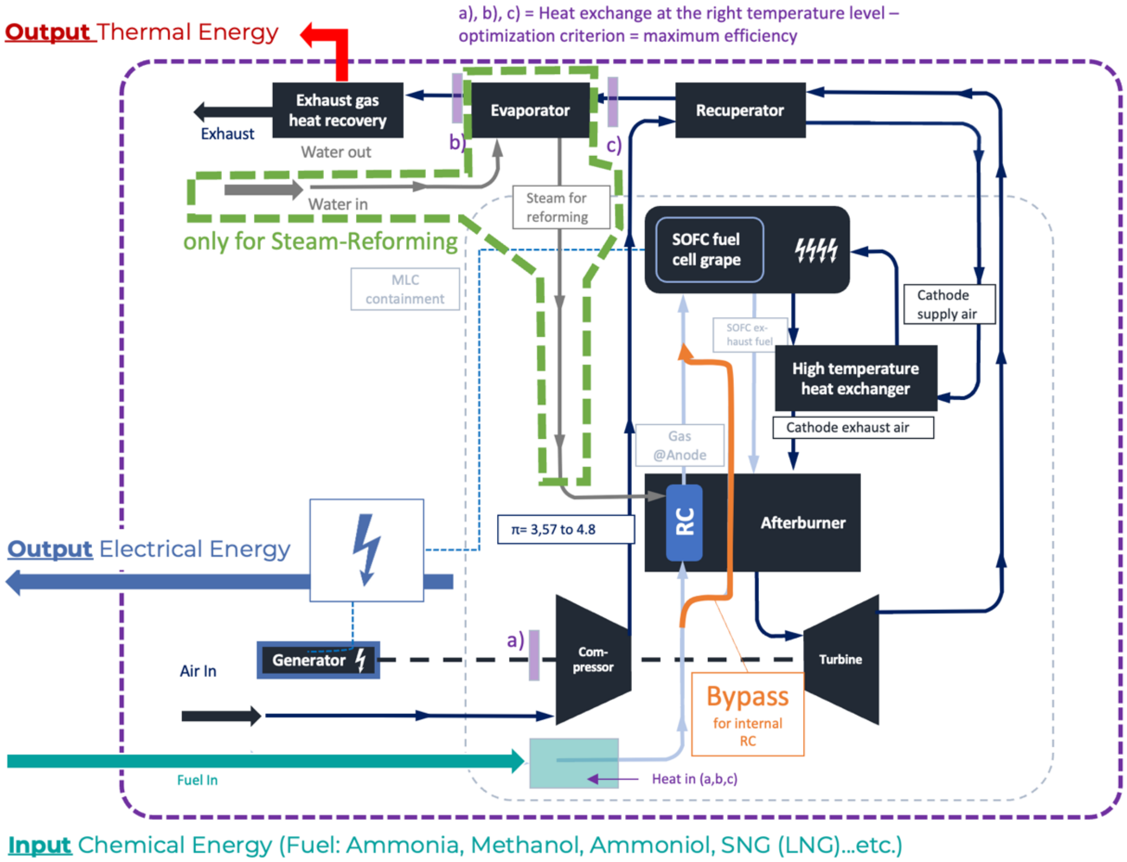

Figure 6. Sketch of the TURBO Fuel Cell cycle architecture. A further refinement can be found in Figure 7.

The advantage of the TURBO Fuel Cell System is the high fuel flexibility and the direct use of the fuel in the SOFC (incl. RC-module). This is possible because in SOFC fuel cells the oxygen ions migrate through the solid oxide electrolyte from the cathode side to the anode side. In a PEM fuel cell system, however, protons migrate from the anode to the cathode side. Pure hydrogen is needed here at low temperatures. After the cracking process, ammonia would therefore have to be cleaned of nitrogen and the temperature would have to be adjusted to the operating temperature of the PEM-fuel cell. This is more cumbersome and reduces the efficiency.

SOFC systems do not have this problem. Cracked ammonia ($2NH_3 = N_2 + 3H_2$) or the reformate in the case of a C_xH_y- or $C_nH_{2n+2}O$ - fuel (or a combination of both, e.g., Ammoniol) can be fed directly (with RC-Bypass split, fig.: 6 and 7) to the anode side. The high temperature in the SOFC system favors the cracking and reforming process. For strain decoupling and contacting, the SOFC cell contains a nickel mesh on the anode side, which is advantageous for internal reforming and internal cracking. The pre-reformer or pre-cracker (RC, fig.:6) convert heat into an increase in the enthalpy of formation of the supplied gas.

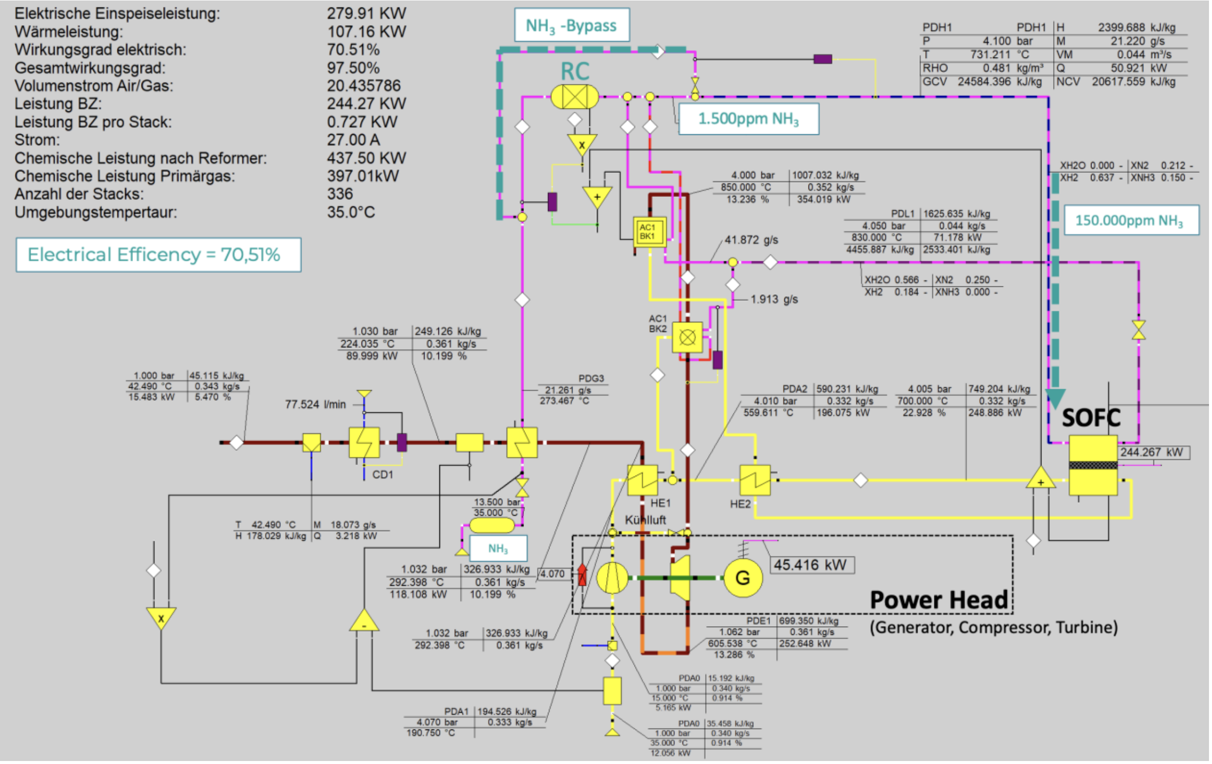

Figure 7. Example of a typical TURBO Fuel Cell cycle architecture. A number of calculations were carried out with EBSILON Professional v16, which are summarized in Figure 9. The circuit structure essentially corresponds to the figure shown here.

The same happens on the anode side due to the nickel content (nickel mesh) and the high temperatures (internal reforming or internal cracking). From a thermodynamic point of view, low-value heat is converted into high-quality enthalpy of formation, which is converted into electricity in the SOFC - in addition to the high efficiency of the galvanic conversion (first effect), the efficiency is further significantly increased (second effect). By removing heat from the internal reforming or internal cracking at the anode, heat is removed from the SOFC stack and the resulting reduction in the cooling cathode air contributes to a further increase in efficiency through the turbomachine.

The authors refer to RC as “material-chemical recuperation of heat”. In the case of a C_xH_y fuel, the same functionality is achieved by the steam reformer (R) as in the cracker (C), which is attached to the same cycle position. For this reason, a standard component RC-module for the TURBO Fuel Cell is currently under development (by Euro-K GmbH [9] and T-CELL AG [10]). In the first development phase (start 2019) of the TURBO Fuel Cell, the steam reforming (R) of natural gas/methane was carried out using a reformer with a nickel-based catalyst. Since the cracking process can also be carried out with Ni-based catalysts, a universal design for a pre-reformer/cracker (RC) was defined. Due to the high conversion quality of the RC unit, the concentrations of the educt (C_xH_y, $C_nH_{2n+2}O$…etc. and/or NH_3) in the SOFC feed must be increased by a bypass. The composition of the anode gas can thus be adjusted to optimize efficiency.

In contrast to the positive thermodynamic effect described above, there is further heat recovery in the recuperator, which increases the efficiency of the system (assigned to the MGT process share). Since the SOFC is embedded in this MGT process like a combustion chamber, the non-convertible heat is converted into work by the MGT cycle and converted into electricity via the generator (third effect). As a further effect, the pressure charging increases the efficiency of the SOFC (fourth effect). The combination of all these effects results in a very high system electrical efficiency of more than 70% $_{el.}$ up to 75% $_{el}$.

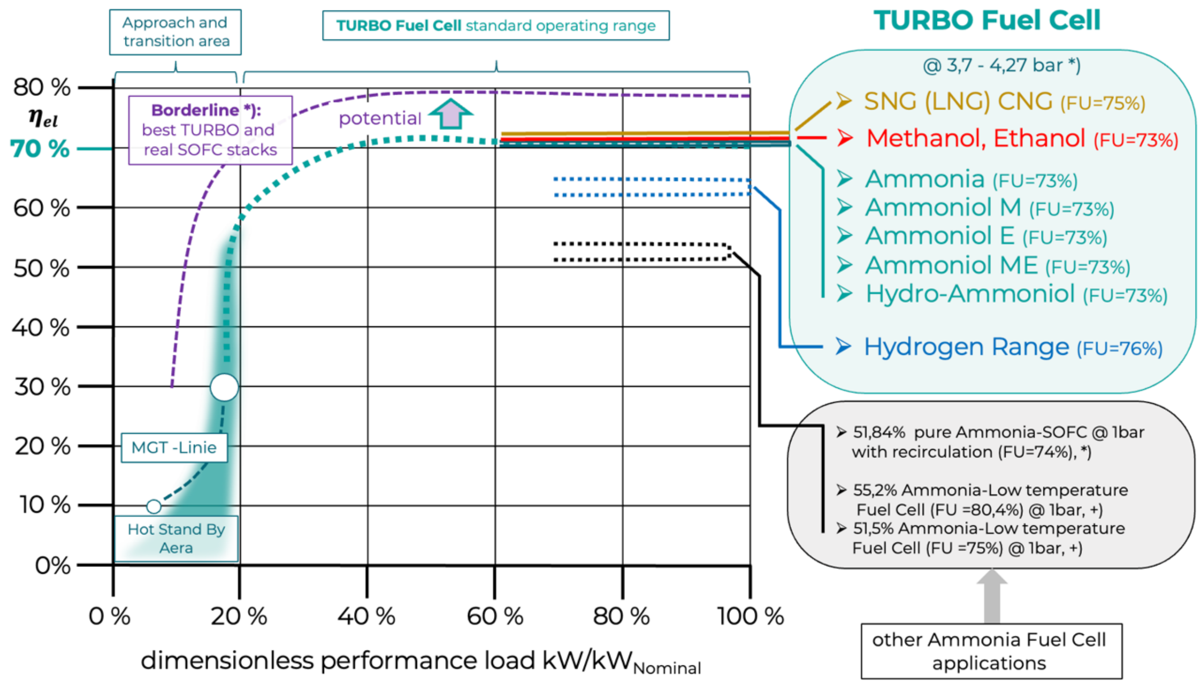

Figure 8. All green fuels (e-ammonia, e-Ammoniol, e-methanol, SNG) can be converted in a TURBO Fuel Cell with very high levels of efficiency / *) own results. Ammonia-low-temperature fuel cell systems have a significantly lower efficiency, compare: +) [12]. FU = fuel utilization

This generally applies to all C_xH_y or $C_nH_{2n+2}O$ - fuels, ammonia and mixtures (such as Ammoniol). In the case of C_xH_y fuels and some mixtures, the system must be equipped with an additional steam generator due to the steam reforming process (figure 7).

Various fuels were analysed for comparison. Different mixing ratios of fuel gases and liquids were defined as substitute fuels. This fuel was then fed into the model for a TURBO Fuel Cell system and analysed in terms of fuel conversion and efficiency using an SOFC model implemented in EBSILON Professional v16. The model used corresponds to the fuel cell stacks and peripheral components analysed at BTU (Brandenburg University of Technology CS, Chair of Prof. Berg). Electrical efficiencies and fuel conversions have now been developed for various power consumption levels. Fig. 8 shows efficiency curves and lines of maximum fuel conversion. A curve with maximum fuel to electricity conversion was also plotted (Borderline). It turns out that TURBO Fuel Cell systems also have the highest efficiency potential for ammonia reconversion into electricity. The exact calculation is carried out by simulating the entire TURBO Fuel Cell cycle (see also [11]). Figure 8 shows the results using different fuels. The efficiency of all C and N based fuels (including mixed fuels, e.g., Ammoniol) is always above 70%. The second effect does not exist with hydrogen (H_2) so the electrical efficiencies in this application are in the range between 60% to 70%. Figure 8 also shows the efficiencies of other fuel cell systems. The TURBO Fuel Cell clearly sets itself apart from the other systems with the highest efficiency, and that with maximum multi-fuel suitability.

Research shows that the TURBO Fuel Cell has further potential in optimizing the turbo system up to electrical system efficiency of 78%. The figure shows the boundary line (purple), which was calculated using real SOFC system values. The operating range below 20% is also visualized in the figure. In this area, the efficiency drops significantly as the system works more and more in pure MGT operation before finally reaching hot standby. There is a lack of clarity in the investigations in this area because accurate thermal tuning (bypass controls, etc.) requires system experimentation. In the operating range above 20% to 100%, the research results are very clear. The partial load range could be increased through optimization. Since the SOFC has higher values in this area than in the full load range, the increase in efficiency of the SOFC outweighs the decrease in efficiency of the turbo system (MGT system).

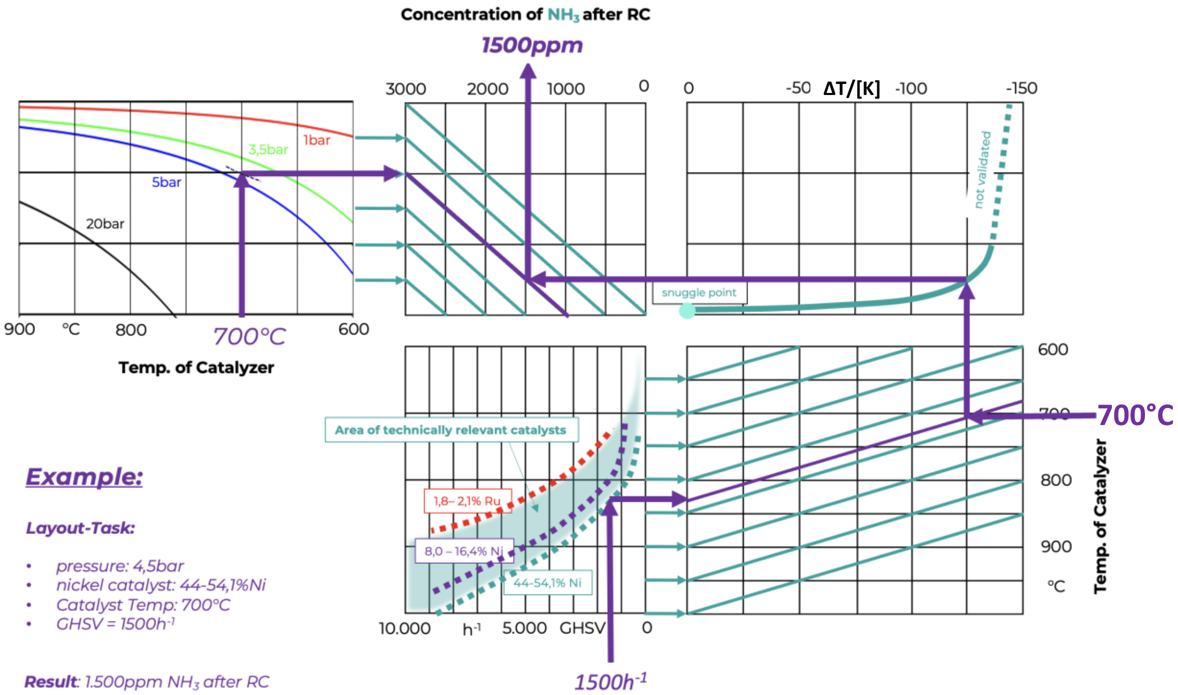

Figure 9. Nomogram-Example GHSV = 1.500h^{-1}, catalyst temperature = 700°C, nickel catalyst (44.54,1% Ni), pressure = 4.5 bar.

Calculations of atmospheric SOFC systems and fuel cells for ammonia use (according to [12]) show significantly poorer efficiencies. The highest efficiency of the TURBO Fuel Cell is because of the effects described above. If there is no carbon in the fuel (e.g., NH_3), no water needs to be added for the catalytic conversion. In contrast, the Steam/Carbon ratios range between 2 to 3 depending on the application for C_xH_y etc. This is necessary so that the carbon formation limit is not reached.

In the case of ammonia application, as already mentioned, the cracked gas is enriched with ammonia again before the SOFC stack so that the internal cracking achieves the best effect. This means that an ideal cracker is not technologically desirable (same applies analogously to the reforming process). Designing a machine, it is therefore important to build the cracker “not too big” and “not too small”. The nomogram developed in Figure 9 is used to optimize this in advance. It is based on exact validated measured values from [12] in the 1 bar range and has been extended to higher pressures with calculations from [14] and own calculations of the equilibrium curves (nomogram partial image at the top left). Figure 6 shows an example of the design of an RC (in cracker operation) with a gas hourly space velocity (GHSV) of 1,500 h^{-1}, a catalyst temperature of 700 °C, a nickel catalyst, and a pressure of 4.5 bar. With an ammonia (NH_3) concentration required from the process calculation (SOFC anode entry), the design chosen in the example would be sufficiently low. The concentration is significantly increased via the bypass line (see Fig. 7). Due to the high RC capability of NH_3 cracking, the system has sufficient operational reliability during cold starts.

4. Summery and Outlook

With the TURBO fuel cell, the fuel is converted into electricity with good SOFC efficiency and additional electricity is generated from the SOFC exhaust gas by embedding it in the thermal MGT cycle. This charging of the SOFC further increases the fuel cell efficiency. Through the chemical recuperation of heat by the RC (reformer/cracker) and through the internal conversion in the fuel cell, the efficiency is further increased by the chemical fuel energy supplied to the SOFC. The cooling effect caused by the internal exothermic conversion in the SOFC (less compressed air is required) leads to a further increase in efficiency. As described in this publication, there are 4 effects that increase efficiency. That is why the electrical efficiencies of the TURBO fuel cell systems are always above 70 percent for all fuels (except pure hydrogen). The system is multi-fuel capable and therefore ideally suited to converting the investigated fuels for maritime applications. TURBO fuel cell systems in the range from 1600 kW to 1.2 MW can currently be implemented. This publication can provide a recommendation regarding the fuel and the TURBO Fuel Cell energy converter. The following fuel-ranking results (No. 1 = “greenest fuel”): Ammonia, Ammoniol, Methanol, SNG/LNG. Hydrogen is not an option for the maritime sector. Carrying out a ranking based on the existing technologies and the rapidness of technology introduction, the result is: Methanol, Ammoniol, ammonia, SNG/LNG. In the authors' opinion, the technological transition to fuel cell technology (in the marine and railway sectors) is well achieved by TURBO Fuel Cell technology.

5. Acknowledgments

The inspiration for the present study came from the TURBO FUEL CELL FuE Project at Brandenburg University of Technology CS, funded by the Federal Ministry for Economic Affairs and Climate Action (BMWK).

6. References

[1] IMO, *International Maritime Organization*, https://www.imo.org/, retrieved 2023/08/28

[2] Berg H.P., Himmelberg A., Lehmann M., Dückershoff R., Neumann M., *The Turbo-Fuel-Cell 1.0 – family concept, Compact Micro Gas Turbine (MGT) – Solid Oxide Fuel Cell (SOFC) energy converters in the 100-500 kW electrical power range for the future*; 8th TSME-International Conference on Mechanical Engineering (TSME-ICoME 2017); IOP Conf. Series: Materials Science and Engineering 297 (2018) 012004

[3] Berg H.P., *Innovative high-performance hybrid propulsion systems as TURBO Fuel Cell – Combustion Engine combination for superyachts.* Conceptual designs from the Berg Design and Engineering Group. Information requestable via www.by-berg.de , 2022.

[4] Berg H.P., Dückershoff R., Lehmann M., Prechavut N., *MICRO TURBO-FUEL-CELL-TECHNOLOGY - Hybrid compact turbo machinery technology and thermodynamic aspects regarding design parameters of a high efficient MGT-SOFC-system*; Proceedings of 12th European Conference on Turbomachinery Fluid dynamics & Thermodynamics ETC12, April 3-7, 2017; Stockholm, Sweden; Paper ID: ETC2017-266

[5] Berg H.P., *Ammoniol - High Performance Fuel as ammonia-alcohol mixture for use in gasoline engines with easy refueling*. Study by TIB-Technology and Engineering Office Berg on behalf of Prof. Dr. Berg Holding. Can be procured via www.berg-germany.com , 2023.
[6] Dana, A.G., Elishav, O., Bardow A., Shter G.E., Grader G.S., *Stickstoffbasierte Kraftstoffe: eine "Power-to-Fuel-to-Power"* - Angewandte Chemie 2016 https://doi.org/10.1002/ange.201510618
[7] Tanner R., *Ueber die Verwendung von Ammoniak als Treibstoff (On the use of ammonia as fuel)*, Doctoral Thesis, ETH- Zurich, Switzerland, 1945 https://doi.org/10.3929/ethz-a-000097159
[8] BTU Cottbus-Senftenberg, *TurboFuelCellFuE* https://www.b-tu.de/t-cell/ retrieved 2023 /08 /28
[9] Euro-K GmbH, https://euro-k.de/ retrieved 2023 /08 /28
[10] T-Cell AG, https://www.t-cell.ag/ retrieved 2023 /08 /28
[11] Dückerhoff R., Berg H.P., Kleissl M., Walther A., Himmelberg A., *Flexibilization of an MGT-SOFC hybrid system for electricity and hydrogen production for the realization of a sustainable hydrogen economy* (TSME-ICOME 2022)
[12] Nigbur F.E., *Ammoniak-Cracker zur Brenngasversorgung von Brennstoffzellen - Experimentelle und simulative Untersuchung* , Doctoral Thesis, University Duisburg-Essen, Germany, eISBN 978-3-7369-7497-6, Cuviller Verlag Göttingen, 2021, www.cuvillier.de
[14] Loge Deutschland GmbH, https://logesoft.com/de/ retrieved 2023 /08 /28
[15] Research Partner: Fraunhofer Institute for Ceramic Technologies and Systems IKTS, Germany https://www.ikts.fraunhofer.de/en/departments/energy_systems/materials_and_components/ceramic_energy_converters/sofc_stack_development.html retrieved 2023 /08 /28

TSF0001

Effect of inlet condition on flow distribution in a Water-Cooling Plates of 18650 Li-ion Battery pack

R. Nanthatanti[1], J. Charoensuk[1,*], M. Masomtob[2], and S. Hirai[3]

[1]Department of Mechanical Engineering, School of Engineering, King Mongkut's Institute of Technology Ladkrabang, Bangkok 10520, Thailand
[2]Energy Innovation Research Group (EIRG), National Energy Technology Centre (ENTEC), National Science and Technology Development Agency (NSTDA), Pathum Thani 12120, Thailand
[3]Department of Mechanical Engineering, Tokyo Institute of Technology, Tokyo, Japan

* Corresponding Author: jarruwat.ch@kmitl.ac.th

Abstract. The flow distribution inside the liquid-cooling plate located in the middle of lithium-ion battery modules was investigated. Under steady-state circumstances, the most crucial parameters evaluated were the inlet temperature and the inlet velocity of cooling water. The variation in the inlet velocity [0.5, 1.0, 2.0 and 3.0 m/s] and the inlet temperature [25°C, 30°C, 35°C and 40°C] were conducted in a steady-state simulation. As a result, the inlet velocity of cooling water has a great impact on water flow distribution and temperature differences. However, the inlet temperature of cooling water does not have a significant effect on them. The standard deviation of the cooling water velocity when increasing the water speed was lowest at around 0.0096 by using an inlet water velocity of 0.5 m/s with an Inlet temperature of 40°C. It was seen that when the inlet temperature increased, the standard deviation would decrease. On the other hand, the result of this value varies with the same trend as the inlet water velocity.

Keywords: Liquid-cooling plate, flow distribution, the standard deviation.

1. Introduction

Now a day,Enhancing the capacity and power density of batteries is required for the current development of electric vehicles. It is commonly considered that the number of battery cells should be packed as densely as possible to maximize output capacity and power density. On the other hand, high-power usage creates a significant thermal problem due to heat generation inside the battery cell. Maximum temperature also has an impact on battery performance and lifetime. Battery performance degrades as temperatures rise because, at higher temperatures, the battery can accelerate the chemical reaction inside beyond the set limit value. According to A. Greco, X. et al. [1], the battery temperature should be kept constant in the range of 20–40°C with a maximum temperature differential of less than 5°C.

1.1. Battery life
As we know that higher temperatures can shorten the battery life, which is the most crucial factor influencing battery aging and causing early battery failure because higher temperatures can accelerate the chemical reaction in the battery and also increase water leakage with corrosion. The temperature of the battery should be less than 33 °C, as indicated by [1], to extend battery life to more than 10 years, as the current projection is that an electric car battery could last between 10 and 20 years before needing to be replaced.

1.2. Battery thermal management system
There are different forms of thermal management for battery packs. They are mainly divided into three categories: Liquid cooling [8–10], phase change materials (PCM) cooling, and air cooling [2-4]. These techniques have advantages and disadvantages. According to D. Chen et al. [11], air cooling is simple to build but has poor cooling effectiveness and is insufficient to maintain temperature under adverse conditions. PCM cooling can efficiently lower temperatures in battery modules and reduce temperature differences, but it was limited by phase changes in volume and encapsulation. Liquid cooling systems can also remove heat from batteries. Compared to other fluids with the same flow rate, this method is quite capable of reducing a significant amount of heat[5]. Due to its practical design and efficient cooling, it is mainly used in the cooling system. However, the liquid cooling system requires more attention because of liquid leakage and corrosion[6]. It is expected that the design would be better suited for battery heat management systems that use the liquid cooling method and water as the coolant.

1.3. The 10S36P battery module
The 10S36P battery module is divided into numerous sections. The first is the busbar, a copper strip with terminals for connecting to the negative terminal of a battery. It is designed to limit possible negative differences and reduce repeat connections to certain terminals. The second one is the plastic housing, which serves as insulation on both sides of the battery pack. If you focus only on one battery module, there are three components inside: the nickel plating, which results in higher energy density, greater storage capacity, and improved electrical conductivity. The anodized aluminium plate provides a durable oxide layer that is fully integrated. This was used as a liquid cooling plate, as shown in Figure 2, that can protect the dielectric substrates from damage during heat transfer of battery cells, and finally, a negative 36P terminal plate that can hold the 18650 li-ion battery to be fixed in the centre[12-15]. It has many advantages, as explained before. There are one hundred eighty Li-ion battery cells in the battery pack. Five battery modules are packed with aluminium cooling plates in the middle, and each battery module has thirty-six cells, as shown in Figure 1.

1.4. Problem simplification of 10S36P battery module
While keeping the essential components for thermal analysis, the cooling pad and flow channel of a battery module was modelled. Following are the rationales of the problem specification.

- 1ststep: Discard the upper case and positive plate because they are not considered for cooling in the positive terminal.
- 2nd step: Neglect the ohmic heating on the busbar that conducts the heat to the positive terminal. So, the bus bar will be removed.
- 3rd step: Discard all of the insulation parts [the bushes and all connectors] that can fasten the battery module.
- 4th step: Discard the plastic base because it is an insulation part and has lower thermal conductivity.
- 5th step: Using the x-z plane to show half the cooling module because the cooling system is symmetric. A submodule of the battery cooling system that contains the negative terminal plate, anodized aluminium plate, and nickel plate was found and the liquid cooling plate will be further investigated.

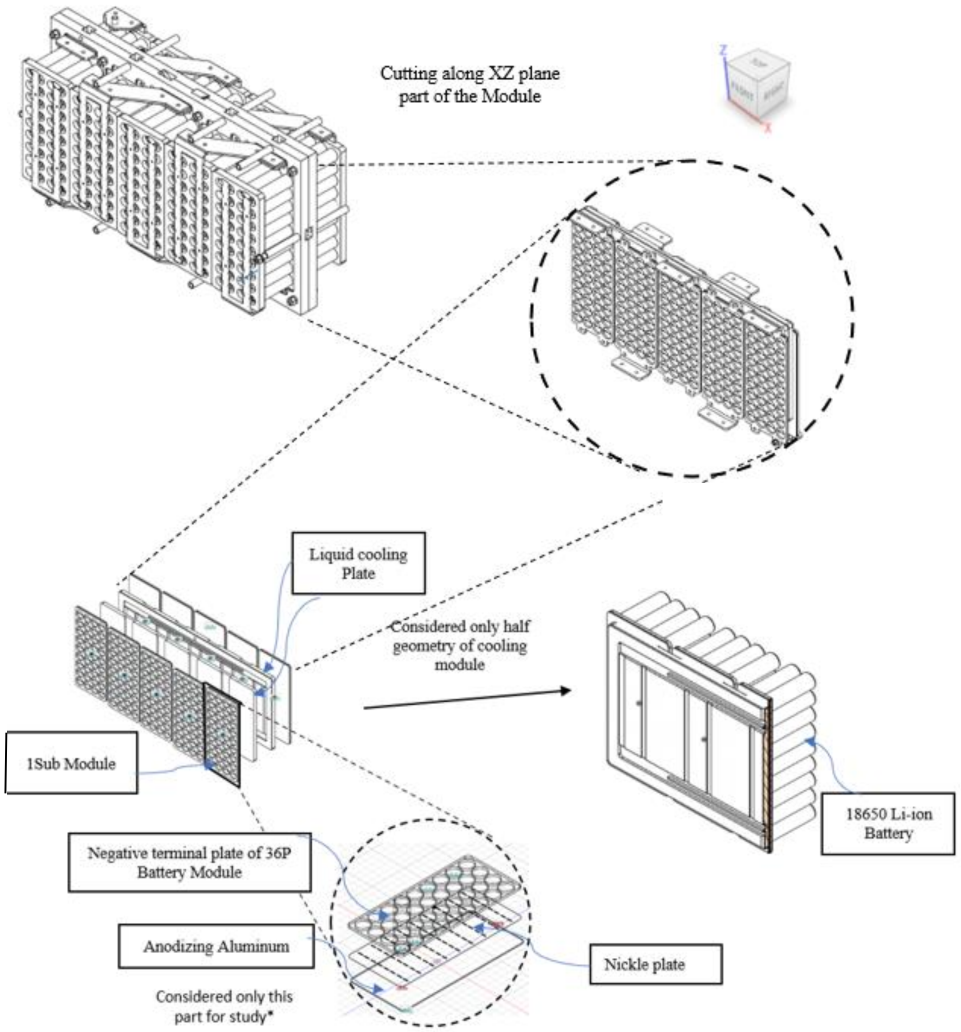

Figure 1. Explode View of 18650 Li-ion battery module with cooling channel configuration.

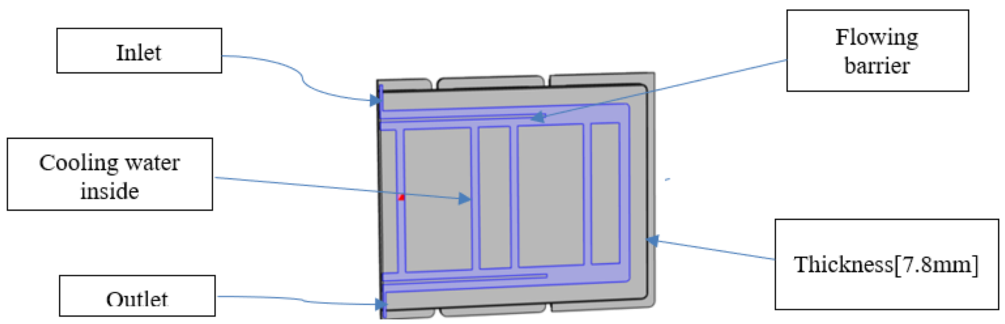

Figure 2. The configuration of liquid cooling plates with two flow channel per base.

2. The effect of flowing parameters and properties of the material

The model was made by using Autodesk Fusion 360 [CAD software] and COMSOL Multiphysics® 6.0 to design 3D modeling of the battery module with cooling channel and explore steady-state simulation to see the uniform flow channel distribution inside the mesh model of the channel inside the liquid cooling plate when using various inlet conditions of cooling inlet temperature and cooling water velocity, respectively. The simulation steps are computational domain, setting boundary conditions in the steady state model, and finally, mesh independence of the cooling channel model for solver setting.

2.1. Geometry and Materials

The 3D-model-CAD file in this work includes solid and fluid elements. 1 submodule contains 36 battery cells; 1 nickel plate, 1 insulation layer, and 1 anodized aluminum plate make up the work's solid components. Because of their poor heat transmission, some solid components, including the battery module housing, the positive common plate, and aluminum wire, are not considered in the model.

Table 1. The battery's thermophysical parameters and properties of the material.

Material	Phase	Thermal Conductivity [W/(m.K)]	Heat Capacity [J/(kg.K)]	Density [kg/m^3]	Heat Ratio	Viscosity [Pa.s]
Battery Cell	Solid $[k_x, k_y, k_z]$	{1.01,30.22, 1.01}	750	2690	-	-
Aluminum	Solid	155	893	2730	-	-
Coolant	Liquid	0.405	3300	1078	1	0.00429

The geometry influences the average velocity in the cooling channel, which can influence the boundary layers created by the fluid flowing along with the bounding surfaces. This research aims to focus on flowing parameters such as mass flow rate, pressure drop, and temperature differences between the inlet and outlet of the liquid cooling plate that's composed of material and battery cell properties from Table1. As the flow distribution of cooling water increases inside the cooling channel, the heating value that is evacuated from the 18650 Li-ion battery by the aluminum cooling plate will be enhanced, resulting in better cooling performance. The maximum permissible battery temperature is 33°C, even though the desired difference in temperature between battery packs should be less than 5°C, which might improve the cooling effectiveness of the battery cell [16].

2.2. The Cooling Strategy used in Cooling channel simulation

2.2.1Choosing the inlet velocity of cooling water

The influence of flow rate on cooling performance is investigated using steady-state modelling. Flow rates of 50 L/h (0.5 m/s), 100 L/h (1.0 m/s), 200 L/h (2.0 m/s), and 300 L/h (3.0 m/s) were simulated.

2.2.2 Choosing the inlet temperature of cooling water

As the temperature of the coolant had an influence on the thermal properties of lithium-ion batteries, the simulation started with a small water velocity set at 0.5 m/s, and with the temperature at 25 °C, followed by 30°C, 35°C, and 40°C respectively.

2.3. Governing equation of the water-cooling system

Each battery is assumed to be identical, considering changes in geometry and chemical composition. The basic governing equations of 2D steady flow in the cooling channel of Battery cooling Plate, such as the continuity equation, momentum equation, and energy equations[5-7] will be shown below:

Continuity equation
$\nabla(\vec{v}) = 0$ (1)
Momentum conservation equation
$\frac{\partial \vec{v}}{\partial t} + (\vec{v}\nabla)\vec{v} = -\frac{\nabla\rho}{\rho} + \frac{\mu}{\rho}\nabla^2\vec{v}$ (2)

where ∇ = the divergence
ρ = the cooling water density =998 [kg/m^3]
μ = the dynamic viscosity coefficient of cooling water (Pa·s)
$\frac{\partial \vec{v}}{\partial t}$ = the partial derivative of velocity vector
$\vec{v}$ = the velocity vector of the cooling water

Energy conservation equation
$\rho C_P\left(v_x\frac{\partial E}{\partial x} + v_y\frac{\partial E}{\partial y}\right) = k_T\left(\frac{\partial^2 E}{\partial x^2} + \frac{\partial^2 E}{\partial y^2}\right)$ (3)

where ∇ = the divergence)the partial derivative(
C_P = the specific heat capacity of cooling water= 4.187 [kJ/kg·K]
v_x = the velocity of cooling water in x direction (m/s)
v_y = the velocity of cooling water in y direction (m/s)
$\frac{\partial E}{\partial x}$ = the partial derivative of thermal energy per unit pathlength in x direction
$\frac{\partial E}{\partial y}$ = the partial derivative of thermal energy per unit pathlength in y direction
k_T = the thermal conductivity (W/m·°C)
E = the thermal energy (J)

The steady flow energy equation has shown below in eq(4)

$mC_p\frac{\partial T_0}{\partial t} = \dot{m}_w C_P(T_o - T_i) + \dot{Q}$;$\dot{m}_w = \rho_\omega \dot{v}_w$; $\dot{Q} = \dot{q}_b\forall$ but $\frac{\partial T_0}{\partial t}$ at initial boundary in steady state = 0
then $\dot{m}_w C_P(T_o - T_i) = -\dot{Q}$ and $\dot{m}_w C_P(T_i - T_o) = \dot{Q}$ (4)

where $\dot{Q}$ =Heat removal rate to the liquid in the cooling channel [kW]
$\dot{q}_b$= Volumetric heat generation rate inside battery [W/ m^3]
$\dot{v}_w$ =Volumetric flowrate of inlet water [m^3/s]
ρ_ω =Density of cooling water [998 kg/m^3]
C_P =Heat capacity of cooling water[4.187 kJ/kg·°C]
T_i = Inlet temperature [°C]
T_o= Outlet temperature [°C]
$\forall$ = The entire volume of 18650 Li-ion Battery[m^3]
m = Fluid mass within the cooling channel [kg]

3. The step for numerical methodology of steady state model

3.1. Computational domain

The geometry of the liquid cooling plate with cooling channels inside focused only on flow parameters, temperature differences between inlet and outlet, and pressure drops across the cooling plate that affect cooling performance. Secondly, the cooling channel model was performed using steady state to investigate the channel velocity and find the standard deviation to perform flow distribution for the result. However, in order to reduce computational time due to the large number of mesh elements, the half-symmetric cooling channel model was used to reduce the complexity of the previous model. as shown in Figure 3.

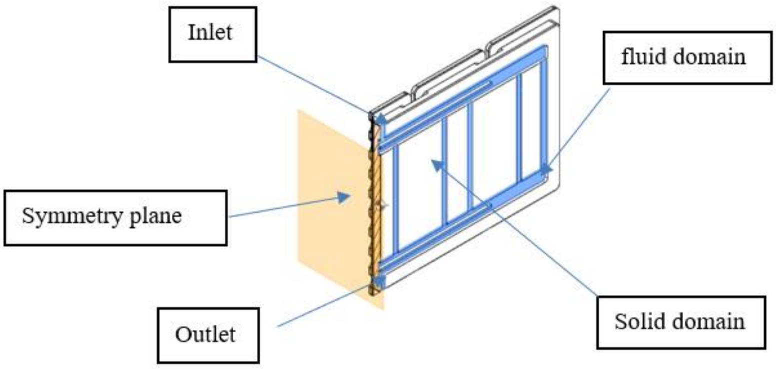

Figure 3. The computational domain of the half geometry for cooling channel configurations.

3.2. Setting boundary condition in steady state model

For the study of the maximum temperature at the outlet ($T_{out,max}$)and the distribution of the water by considering the channel velocity, the flow rate and the coolant inlet temperature are considered boundary conditions within the steady-state model, as shown in Table 2. The flow velocity is the first parameter to be set [0.5, 1, 2, and 3 m/s], and the inlet temperature is set as the second parameter [25, 30, 35, and 40 °C].

Table 2. The boundary inlet parameters of steady state circumstances.

Inlet velocity of water (m/s)	Inlet temperature of water (°C)
0.5	25
1.0	30
2.0	35
3.0	40

3.3. The mesh independence of the cooling channel model

Figure 4 depicts the multizone split. A meshing component has been built up for the fluid region to give the best simulation quality. The typical size was around 0.25 mm. When volume meshing is started, the base size is usually the size of the biggest components in the fluid domain. The mesh would be coarser if the base size was large, whereas the mesh would be finer if the base size was small. The simulations were performed with various mesh sizes until insignificant changed of the temperature difference and pressure drop were noticed.

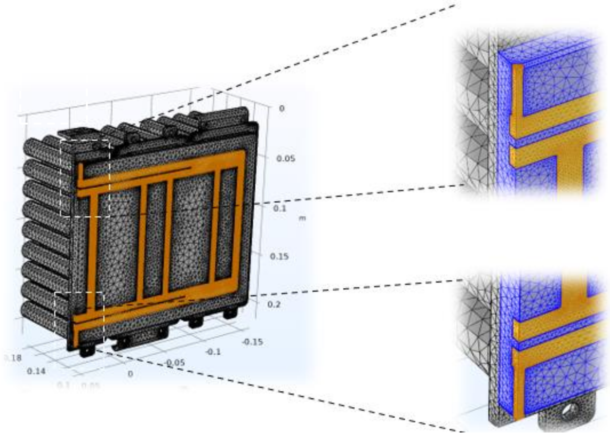

Figure 4. Mesh independence with sizes.

The simulation of flow in the water channel was performed with different mesh sizes until insignificance change was observed and after the number of grids reached $8*10^5$, the calculating results did not significantly change with the variation of the meshes. The essential feature of the independence mesh statistics was displayed below in Table 3.

Table 3. The mesh statistics inside mesh model.

Description	Value
Average element quality	0.6574
Tetrahedron	670752
Pyramid	514
Prism	21018
Triangle	208732
Quad	2664
Edge element	23704
Vertex element	1107

4. Steady state Simulation Result

4.1. Temperature difference and pressure drop between inlet and outlet of cooling channel

The pressure drop increased significantly as the amount of water in the inlet rose sharply; however, when using just a bit of inlet velocity, the pressure of water inside the cooling channel appeared to be the smallest, with a slight effect at an inlet velocity of 0.5 m/s due to the inlet temperatures of cooling water. Furthermore, temperature differences climbed to 3°C.When using the maximum incoming water flow rate of 3 m/s, a considerable pressure drop is generated reaching its maximum at 12000 Pa. The pressure drop is considerably influenced by the high flow rate and the temperature difference. Finally, the temperature difference and pressure drop did not vary significantly while raising the inlet temperatures of the fluid; results were significantly influenced when increasing the inlet velocity was utilized for the boundary circumstances.

4.2 Flow Visualization of the cooling channel

Considering an inlet velocity of 0.5 m/s and an inlet temperature of 30 °C, the maximum velocity inside the channel is 0.042 m/s, the minimum is 0.031 m/s, and the average velocity is 0.037 m/s. Then increase the inlet velocity to 3 m/s and use the same temperature inlet. The maximum velocity will be increased to 0.234 m/s, and the minimum is 0.165 m/s. Then find the relative between the inlet velocity of cooling water and Standard deviation

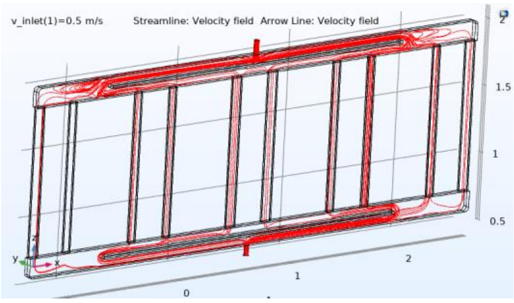

Figure 5. Inlet Velocity = 0.5m/s

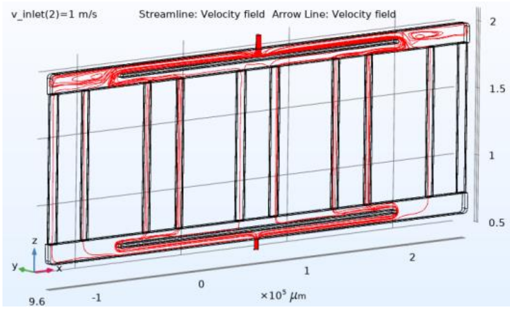

Figure 6. Inlet Velocity = 1.0m/s

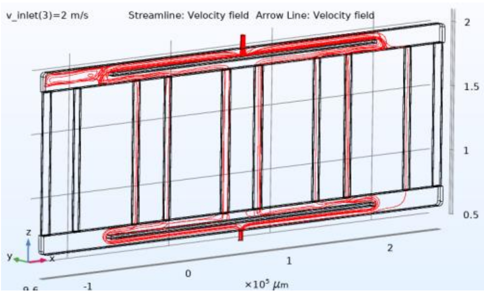

Figure 7. Inlet Velocity = 2.0m/s

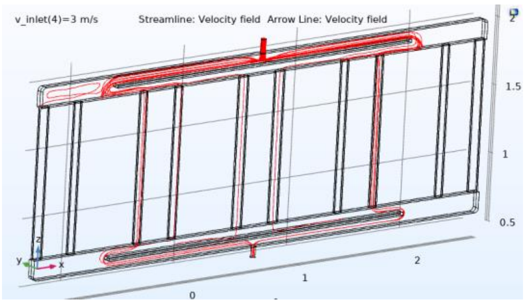

Figure 8. Inlet Velocity = 3.0m/s

Figures 5, 6, 7, and 8 show the velocity streamline inside the cooling channel while varying the water inlet velocity at 0.5, 1, 2, and 3 m/s. This design produced the best velocity uniformity and more water distribution when using the lowest inlet velocity. However, when enhancing the inlet velocity, the distribution of water in the channel is quite bad. This causes the speed of the water flowing through the cooling channel to become more turbulent. Regarding the impact of the inlet temperature of the water.

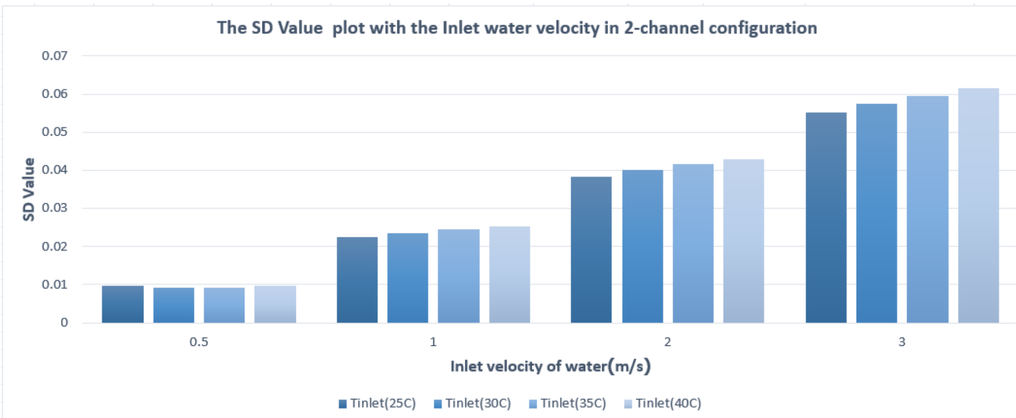

Figure 9. Result of the standard deviation with the inlet water velocity started from inlet temperature 25 °C to 40 °C.

According to Figure 9, the standard deviation of the cooling water velocity when increasing the water speed was lowest at around 0.0096 by using an inlet water velocity of 0.5 m/s with an inlet temperature of 40 °C, and the least amount of velocity inside the cooling channel was around 0.0309 m/s. It was seen from the chart that when the inlet temperature increased, the Standard deviation would be quite stable when using a low Inlet velocity of water but slightly increase when using an inlet velocity of cooling water> 1 m/s. Moreover, the result of the standard deviation value plot has a more significant effect on the increasing inlet velocity of water that distributes inside the cooling channel than the influence of the inlet temperature parameters.

4.3. Removed heat rate (kW) plot with inlet velocity of cooling water (m/s)

While comparing different inlet temperature values, the capability to remove heat from the battery appeared to be consistent at roughly 0.060 kW as inlet velocity increased. [Error 3.25% from the exact value] According to the chart, increasing the inlet temperature of cooling water within the cooling plate has an insignificant effect on the heat removal rate, regardless of how much the inlet velocity changes. The precise value of heat removal rate obtained from eq(4) is 0.0553 kW, which is very close to the simulation result that was explained before and has an inaccuracy percentage of approximately 16.58% when using inlet velocity at 2 m/s.

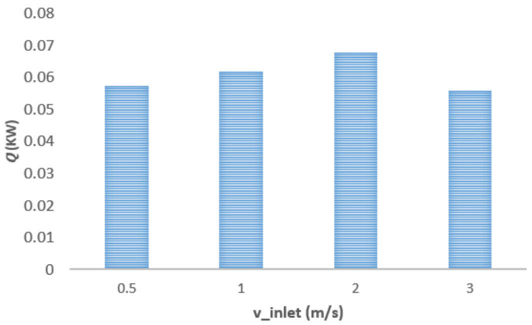

Figure 10.

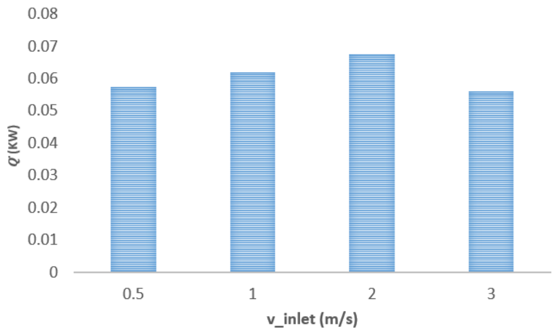

Figure 11.

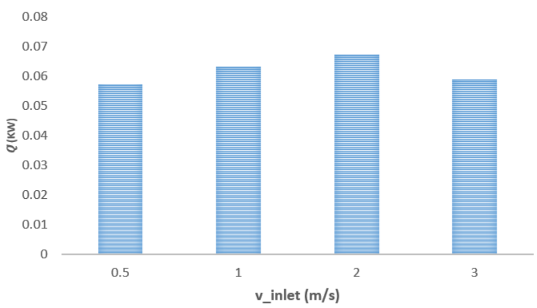

Figure 12.

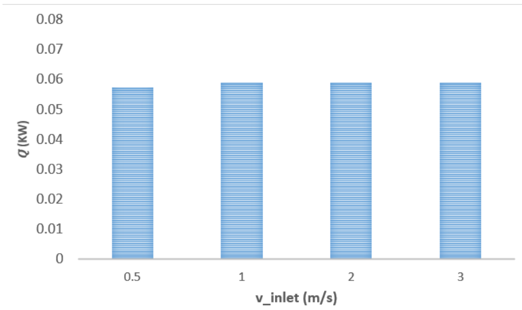

Figure 13.

Figures. 10,11,12 and 13 show the relationship between heat removed rate (kW) and inlet velocity of water (m/s) compared at various inlet temperatures of 25°C, 30°C, 35°C, and 40°C respectively.

5. Conclusion

Employing the lowest inflow velocity can produce the best velocity consistency along with enhanced water dispersion. When inflow velocity increases, water distribution in the channel becomes relatively poor compared to the standard deviation trend, which increases the water flowrate when passing through the cooling channel. The standard deviation of the cooling water velocity when increasing the water speed was lowest at around 0.0096 by using an inlet water velocity of 0.5 m/s with an inlet temperature of 40 °C, and the least amount of velocity inside the cooling channel was around 0.0309 m/s.The capability to remove heat from the battery appeared to be consistent at roughly 0.060 kW as inlet velocity increased.

6. Acknowledgment

The author would like to thank you for the research facilities from National Science and Technology Development Agency (NSTDA), National Energy Technology Centre (ENTEC), Department of Mechanical Engineering, Faculty of Engineering and King Mongkut's University of Technology Ladkrabang (KMITL)

7. References

[1] A. Greco, X. Jiang, and D. Cao, "An investigation of lithium-ion battery thermal management using paraffin/porous-graphite-matrix composite," J. Power Sources, vol. 278, pp. 50–68, 2015.

[2] L. H. Saw, Y. Ye, A. A. O. Tay, W. T. Chong, S. H. Kuan, and M. C. Yew, "Computational fluid dynamic and thermal analysis of Lithium-ion battery pack with air cooling," Appl. Energy, vol. 177, pp. 783–792, 2016

[3] H. Wang, W. Xu, and L. Ma, "Actively controlled thermal management of prismatic. Li-ion cells under elevated temperatures," Int. J. Heat Mass Transf., vol. 102, pp. 315–322, 2016

[4] Z. Lu, X. Z. Meng, L. C. Wei, W. Y. Hu, L. Y. Zhang, and L. W. Jin, "Thermal Management of Densely packed EV Battery with Forced Air-Cooling Strategies," Energy Procedia, vol. 88, pp. 682–688, 2016

[5] Z. Qian, Y. Li, and Z. Rao, "Thermal performance of lithium-ion battery thermal management system by using mini-channel cooling," Energy Convers. Manag., vol.126, pp. 622–631, 2016

[6] C. Lan, J. Xu, Y. Qiao, and Y. Ma, "Thermal management for high power lithium-ion battery by mini channel aluminum tubes," Appl. Therm. Eng., vol. 101, pp. 284–292, 2016

[7] X.-H. Yang, S.-C. Tan, and J. Liu, "Thermal management of Li-ion battery with liquid metal," Energy Convers. Manag., vol. 117, pp. 577–585, 2016

[8] M. Alipanah and X. Li, "Numerical studies of lithium-ion battery thermal management systems using phase change materials and metal foams," Int. J. Heat Mass Transf., vol. 102, pp. 1159–1168, 2016

[9] J. Yan, Q. Wang, K. Li, and J. Sun, "Numerical study on the thermal performance of a composite board in battery thermal management system," Appl. Therm. Eng., vol.106, pp. 131–140, 2016

[10] Y. Azizi and S. M. Sadrameli, "Thermal management of a LiFePO4 battery pack at high-temperature environment using a composite of phase change materials and aluminum wire mesh plates," Energy Convers. Manag., vol. 128, pp. 294–302, 2016

[11] D. Chen, J. Jiang, G.-H. Kim, C. Yang, and A. Pesaran, "Comparison of different cooling methods for lithium-ion battery cells," Appl. Therm. Eng., vol. 94, pp. 846–854, 2016

[12] Barbir, F., 2005, PEM Fuel Cells, Elsevier Inc., pp. 33-72

[13] Bernardi, D., Pawlikowski, E. and Newman, J., 1984, "General energy balance for battery systems", Journal of the Electrochemical Society, Vol. 84-2, No. 1, pp. 164-165.

[14] Incropera, F.P. and De Witt, D.P., 1990, Introduction to Heat Transfer, 2nd ed., John Wiley & Sons, Inc., PP. 1-9.

[15] Chantheve P., Laoonual Y., Masomtob M., Hirai S., Lailuck V., Rompho S., Sriram P., and Chanurai N., "A Simplified Approach for Heat Generation due to Entropy Change in Cylindrical LCO Battery', 2018 IEEE Transportation Electrification Conference & Expo Asia-Pacific, June 6h - 9th, 2018, Bangkok, Thailand

[16] Y. Huang, P. Mei, Y. Lu, R. Huang, X. Yu, Z. Chen, A.P. Roskilly, A novel approach for Lithium-ion battery thermal management with streamline shape mini channel cooling plates

TSF0004

Flow Simulation of Noodle Pot Porous Cover

P Phon[1], J Tawatchai[1], A Wiwat[2], P Tinnakorn[2], and K Preecha[2,*]

[1]Department of Energy and Air Conditioning Engineering,
[2]Department of Mechanical Engineering,
Faculty of Engineering and Technology, Rajamangala University of Technology Isan,
744 Suranarai Rd., Muang, Nakhonratchasima, 30000, Thailand

* Corresponding Author: preecha@rmuti.ac.th

Abstract. This research article aims to analyze the phenomenon of exhaust gas flow through a porous cover on a noodle pot. The flow of gas was studied using Computational Fluid Dynamics (CFD) to investigate changes in velocity along the cover. To validate the simulation model, experimental data was compared with the simulation results, which had previously been used to examine another case study. A stainless-steel wire mesh with a pore per inch (PPI) of 10 was used to create the noodle pot cover. The impact of cover thickness and height was taken into consideration. The results indicated that the velocity distribution at the bottom of the pot, without a cover, was higher than when the cover was installed. When the cover was in place, the air flowed along the height of the noodle pot, and the velocity distribution at the sides of the pot was relatively high. The thickness and height of the cover had a significant effect on the exhaust gas discharge.

Keywords: Flow simulation, Noodle pot cover, Porous media, Stainless steel wire net.

1. Introduction

In recent years, there has been a growing interest in the efficient utilization of exhaust gases from various industrial processes, as a means to reduce environmental pollution and enhance energy recovery [1]. In this context, the study of gas flow phenomena through porous structures has gained significant attention due to its potential applications in exhaust gas treatment and heat transfer enhancement [2-5]. The present research article focuses on the analysis of exhaust gas flow through a noodle pot's porous cover, with the aim of understanding how the flow velocity changes along the cover.

The initial concept of a flow insulation system utilizing highly porous materials with high porosity was originally introduced by Echigo [6]. This innovative concept has found application in enhancing the performance of various systems, including radiation burners and heat exchangers, among others. Building upon Echigo's pioneering work, Tien et al. [7] introduced a concept of thermal insulation within a flow system. This concept has extended investigation for many applications to improve the heat transfer in porous media applications both experiment and simulation [8-10].

To protect the energy loss due to flue gas from the cooking gas stove, the wind shield gas stove cover (WS cover) was the closed cover that protect the energy loss from the stove to the moving air (wind) by convection. Energy losses, on the other hand, are also carried away by the exhaust gas, with some losses occurring due to heat radiation. Subsequently, advancements in gas stove design led to the development of stove covers that incorporated the concept of air preheating [11-13]. These covers employed stainless-steel wire net porous materials. It was observed that the presence of such a cover significantly elevated the temperatures at the bottom of the cooking pot and in the surrounding area. This, in turn, resulted in a notable increase in the thermal efficiency of the gas stove. This improvement stemmed from both enhanced heat radiation and the preheating of air. However, these porous covers operated as closed systems and featured rather complex structures, necessitating modifications to the stove's original design.

To improve the heat transfer from the gas burner to the noodle pot, the basic concept should be investigated. Therefore, an flue gas distribution at bottom and side of the noodle pot were investigate in term of flue gas velocity distribution along the height of the cover and determine how its flow characteristics are affected by the cover's thickness. Additionally, this investigation explores the influence of the cover's height on the gas flow pattern within the noodle pot. The findings from this study have the potential to enhance exhaust gas management and contribute to the development of more effective and efficient exhaust gas treatment systems.

In the subsequent sections of this article, we will present the methodology employed for conducting the experiments and CFD simulations. Furthermore, the results obtained from both the experimental and computational analyses will be thoroughly examined and compared. Ultimately, the implications of these findings will be discussed, shedding light on the impact of cover thickness and height on exhaust gas flow dynamics within the noodle pot.

2. Experimental setup

To validate the simulation of fluid flow through the noodle pot, experimental data were collected. Figure 1 presents a schematic diagram of the experimental setup, which includes a noodle pot with a 45 cm inner diameter, a cover constructed from a 10 pores-per-inch stainless steel (using 304 stainless steel grade) with a wire diameter of 0.5 mm, and a blower for air intake. The cover was designed using the stainless-steel wire mesh formed into a porous medium with 1 mm gaps (achieving a porosity of 0.90), 15 mm thickness, and 20 cm height. The gap between the noodle pot and the cover is 10 mm. Air was introduced beneath the pot at its center at a velocity of 12 m/s. During testing, a hot wire anemometer was employed to measure air velocities at the pot's base, both inside and outside the porous medium.

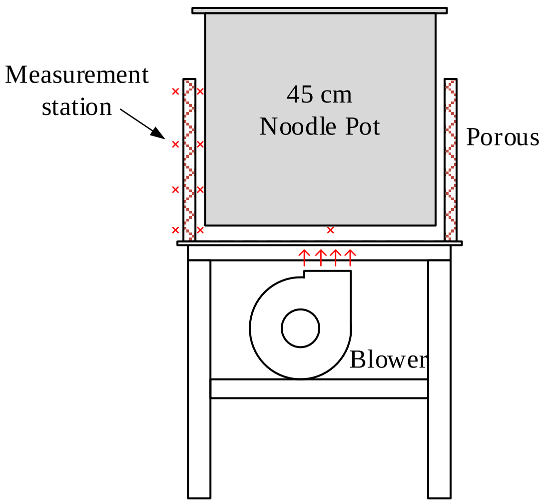

Figure 1. Schematic diagram of the experimental apparatus.

3. CFD Simulation Model

A study was conducted to simulate the flow through a lid covering a gas stove noodle pot with a diameter of 45 cm, both with and without the installation of the cover. Th cover model made of stainless-steel wire net porous media with a size of 10 meshes per inch, achieving a porosity of 0.90. Three thicknesses were considered: 15, 20, and 25 mm, and five heights: 20, 25, 30, 35, and 40 cm. Air was introduced beneath the pot, which had a base diameter of 35 cm, positioned over the gas stove burner. SolidWorks 2021was utilized for modeling this flow process. The study set air speeds at the pot's base at 8, 10 and 12 m/s for simulation purposes. Following this, the simulation outcomes were benchmarked against actual experimental results to verify accuracy and consistency. This approach aims to bridge computational predictions with real-world fluid dynamics in culinary applications. The model and meshing of the examined noodle port with the cover made of the stainless-steel porous media by SolidWorks 2021 are shown in figure 2.

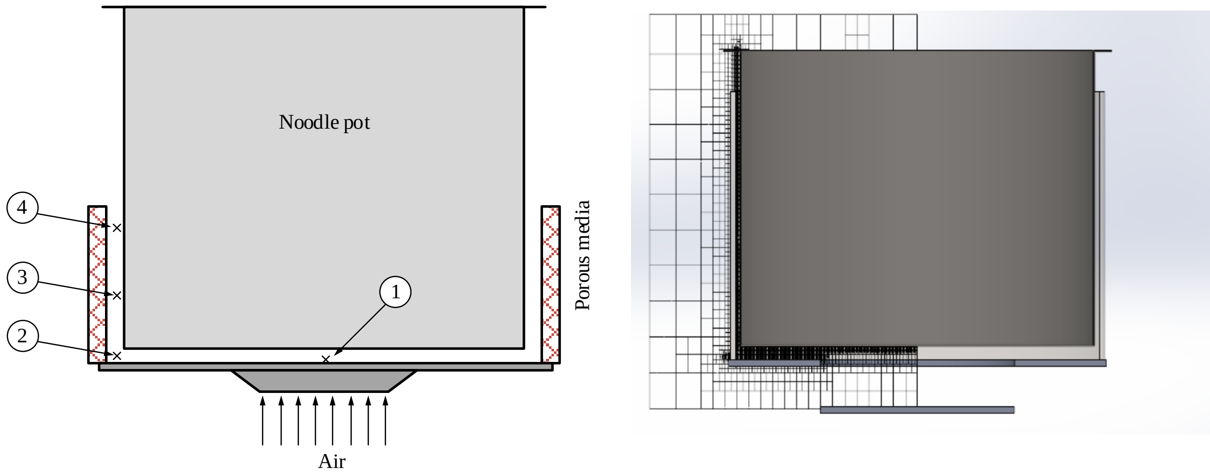

(a) (b)

Figure 2. Simulation model and meshing by SolidWorks 2021.

4. Results and Discussions

A study was conducted to simulate the airflow through a noodle pot. Experimental data were collected and compared to the results from the flow simulation under identical conditions to validate the accuracy of the model. After validation, the model was used to study other conditions. The airflow through the noodle pot was examined in scenarios both with and without the installation of a lid made of a porous stainless steel mesh material.

4.1. Validation the accuracy of the simulation model

Figure 3 indicates the simulation results of an air flowing on noodle pot cover made of stainless-steel porous media: (a) velocity vector and (b) velocity contour. It illustrates that the porous media could control the direction of an air flowing along the surface of the noodle pot. This means that it could affect to increase convection heat transfer.

Figures 4 shows a comparison of experimental results with those from the simulation by measuring at the same points, namely the position under the noodle pot's bottom (measurement station 1) and positions inside and outside the porous material, which are measurement stations 1 to 4 as shown in Figure 2 (a). From the comparison, it could be seen that the results from the simulation are close to the experimental results, confirming that the simulation with SolidWorks Simulation is acceptable. Therefore, this simulation can be reliably used to study other conditions in the future.

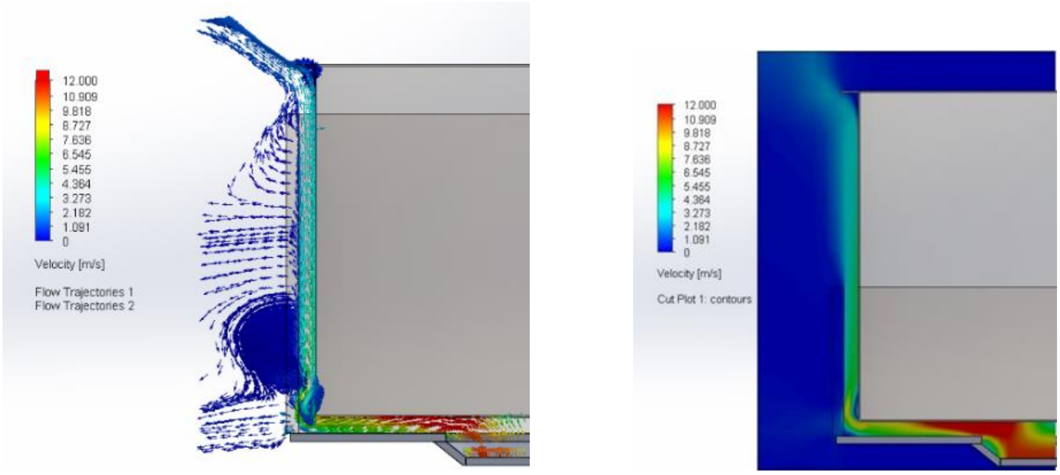

(a) (b)

Figure 3. Velocity profile and velocity contour of and air flowing on noodle pot cover made of porous media 15 mm thick, 20 cm height, and initial velocity 12 m/s.

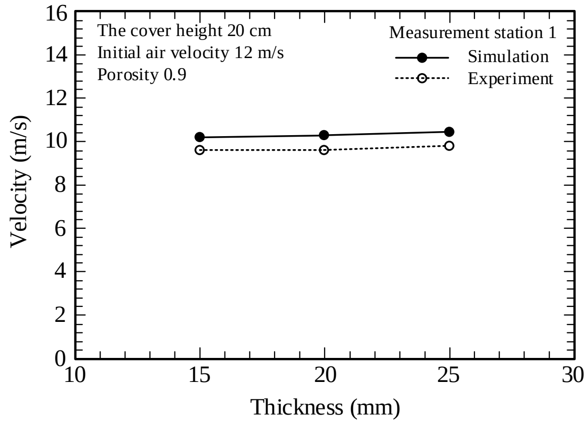

(a)

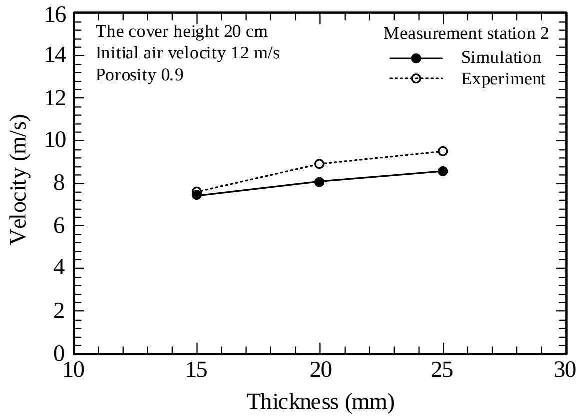

(b)

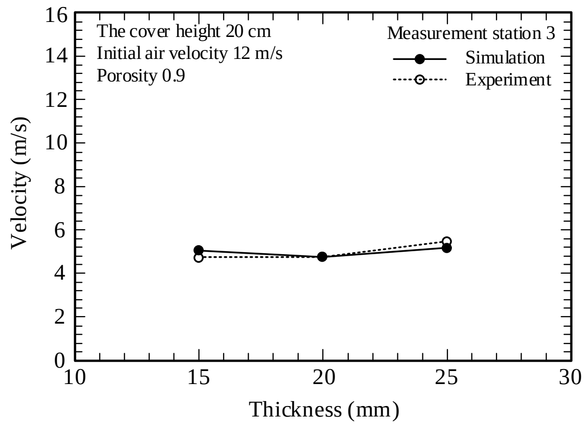

(c)

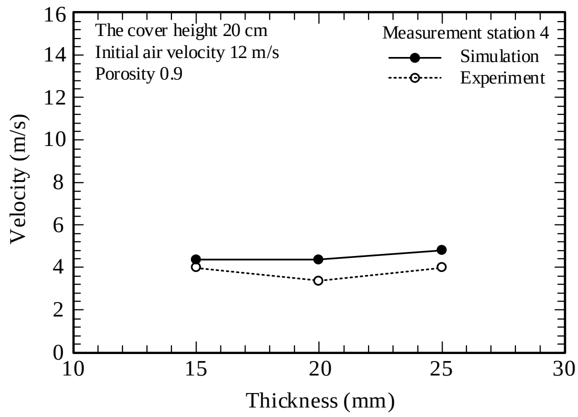

(d)

Figure 4. Comparison of the experimental and simulation data at measurement stations 1, 2, 3, and 4.

4.2. Flow Simulation Results

Figure 5 (a) shows the influence of inlet velocity to the velocity along the noodle pot radius. It seems that air velocity at central of the port is nearly zero due to the flow direction change along to the port radius. The air velocity increases to its maximum at a position one-fourth of the radius of the noodle pot due to the occurrence of a constriction, which results in the smallest cross-sectional flow area. The velocity then gradually decreases along the radius until it reaches the side of the pot. However, the decrease in velocity is not significant, indicating satisfactory velocity distribution. When considering the impact of velocity, it was found that the air speed beneath the pot's bottom increases in line with the initial velocity throughout the radius of the pot's bottom. This behavior aligns with the fundamental principles of fluid mechanics.

When examining the air velocity along the vertical side of the pot as illustrated in Figure 5 (b), it was observed that in the case without an installed porous noodle pot cover, the velocity is high for the first quarter of the pot's height and then decreases to zero. However, when a porous noodle pot cover is installed, it can maintain approximately half of the initial velocity almost up to the pot's maximum height. This indicates that in terms of heat transfer, the heat can be conveyed more effectively mode of convection heat transfer the heat with the cover compared to the case without the cover.

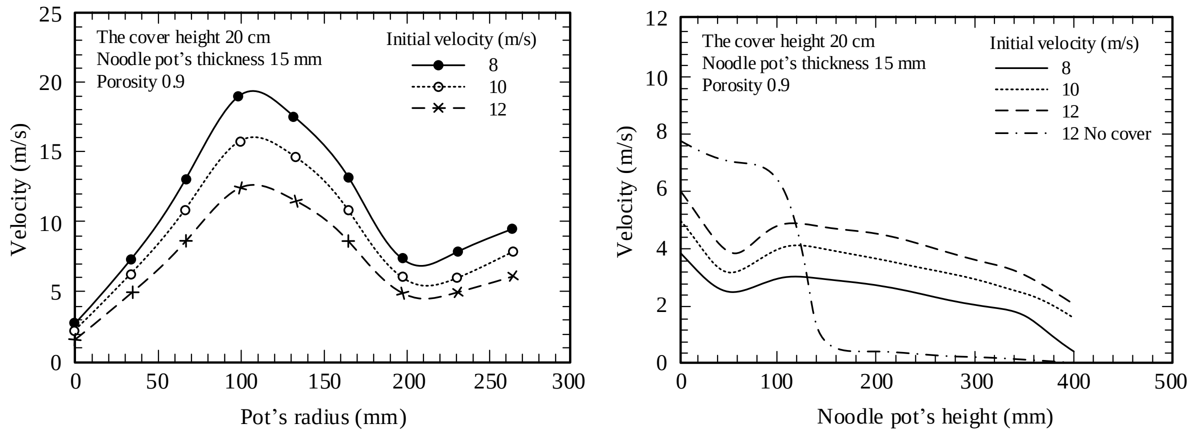

(a) (b)

Figure 5. Influence of inlet air velocity to the velocity along (a) the noodle pot radius and (b) the side of noodle pot height, in the case of installing a cover with a height of 20 cm and a thickness of 15 mm compared to the case of without cover.

In comparison of velocity along the port radius in case with and without installing the porous port cover as shown in figure 6 (a), it seems that in case of without installing the cover, the air velocity is always higher than the case installing the cover. However, for the side of the port, the air velocity in case of installing the port cover is higher (figure 6 (b)) than the case of without the cover. In considering of influence of the cover height, the results showed that the cover height does not effectively to the velocity distribution.

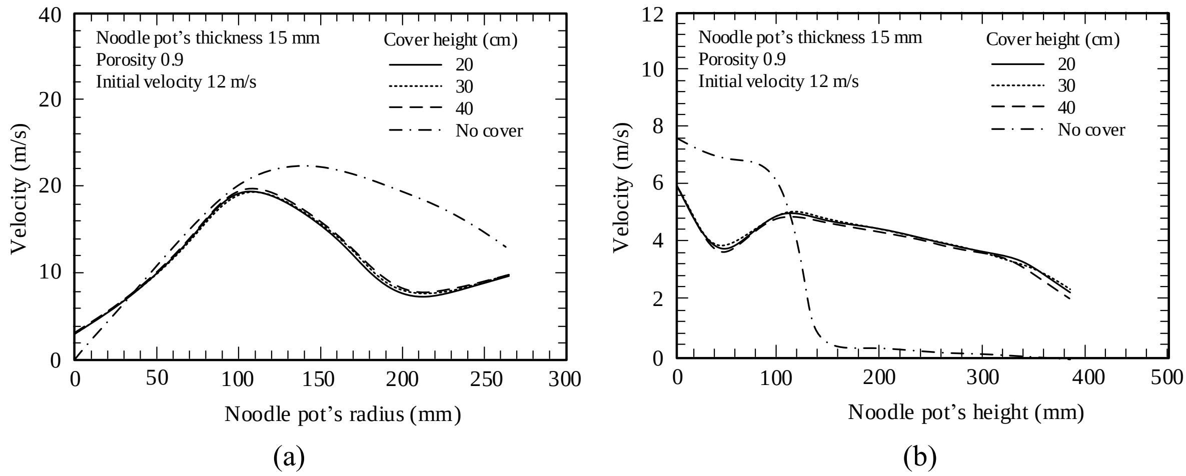

Figure 6. Influence of height of porous noodle pot over to the velocity along (a) the noodle pot radius and (b) the side of noodle pot height, compared to the case of without cover.

Figures 7 shows the influence of thickness of porous noodle pot cover. The study found that the thickness of the port cover significantly affects the changes in air velocity beneath the pot's bottom and along its sides, with the trends being consistent. This indicates that the pot cover for noodles made of meshed stainless porous material influences air distribution. This air velocity, in turn, impacts heat convection or heat transfer.

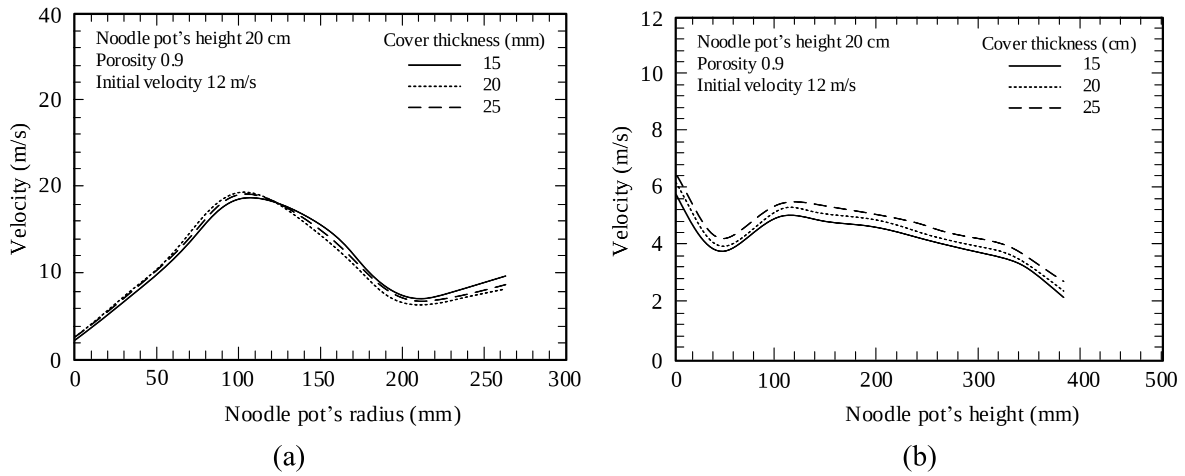

Figure 7. Influence of thickness of porous noodle pot over to the velocity along (a) the noodle pot radius and (b) the side of noodle pot height, compared to the case of without cover.

5. Conclusion

In study of the flow simulation of noodle pot that installing the cover made of stainless-steel porous media, the results from experiment were used to cross-check the outcomes from software-based simulations. Then, the flow simulation was used explored several other variables. The main conclusions drawn from the research are as follows:

5.1 The simulation results of airflow on a noodle pot cover made of stainless-steel porous media, showing both velocity vectors and contours. The porous media directs the airflow on the noodle pot's surface, which can enhance convection heat transfer.

5.2 In comparison of experimental and simulated data, measurements were taken at identical points, both under the pot's base and at eight positions in and around the porous material. The closeness between the two data sets underscores the reliability of the SolidWorks Simulation.

5.3 The velocity patterns in and around the noodle pot, focusing on the impact of inlet velocity and the presence (or absence) of a porous cover. Specifically, the velocity follows fluid mechanics principles, being almost zero at the pot's center and peaking at a quarter of the pot's radius. The porous cover's presence results in better heat convection, particularly along the pot's height, suggesting a more effective convective heat transfer mode when using the cover.

5.4 Consistent trend exists where the thickness plays a pivotal role in airflow patterns, which subsequently impacts the heat convection process.

6. References

[1] Gamrat, S., Poraj, J., Bodys, J., Smolka, J., & Adamczyk, W. (2016). Influence of external flue gas recirculation on gas combustion in a coke oven heating system. *Fuel Processing Technology*, 152, 430-437.

[2] Boggavarapu, P., Ray, B., & Ravikrishna, R. V. (2014). Thermal Efficiency of LPG and PNG-fired burners: Experimental and numerical studies. *Fuel*, 116, 709-715.

[3] Saetta, A. V., Schrefler, B. A., & Vitaliani, R. V. (1995). 2—D model for carbonation and moisture/heat flow in porous materials. *Cement and Concrete research*, 25(8), 1703-1712.

[4] Yoshino, M., & Inamuro, T. (2003). Lattice Boltzmann simulations for flow and heat/mass transfer problems in a three-dimensional porous structure. *International Journal for Numerical Methods in Fluids*, 43(2), 183-198.

[5] Yi, D., He, L., Lv, L., & Gao, J. (2020). Study on the Influence of Different Positions of the Air Inlets in the Kitchen on the Air Supplement Effect. *In Proceedings of the 11th International Symposium on Heating, Ventilation and Air Conditioning* (ISHVAC 2019) Volume III: Buildings and Energy 11 (pp. 1473-1481). Springer Singapore.

[6] Echigo, R. (1982). Effective Energy Conversion Method between Gas Enthalpy and Thermal Radiation and Application to Industrial Furnaces. *Proc.7th Int. Heat Transfer Conf*., Vol.6, pp.361-366.

[7] Wang, K. Y. and Tien C. L. (1984). Thermal insulation in flow system: Combined radiation and convection through a porous segment, *ASME. J. Heat Transfer*., Vol. 106, pp. 453-459.

[8] Khantikomol, P., Saito, S., and Yokomine, T. (2009). Study of Multilayer Flow Insulation utilizing Open-Cellular Porous Plates, Proc. *Int. Conf. Power Engineering* (ICOPE-09), Vol.3, pp.37-42.

[9] Kamiuto, K. (1999). Modeling of elementary transport processes and composite heat transfer in open-cellular porous materials, *Trends in Heat, Mass & Momentum Transfer*, Vol. 5, pp.141-161.

[10] Kamiuto, K. and Matsushita, T. (1998). High-temperature radiative properties of open-cellular porous materials, *Proc. 11th Int. Heat Transfer Conf*., Vol. 7, pp. 385-390.

[11] Nutthawut Rungsimuntuchat. (2001). Application of Porous Medium for Energy Saving in Gas Cooker. Thesis of Master. Engineering (Mechanical Engineering). *King Mongkut University of Technology Thonburi.*

[12] Jugjai, S. and Sanijai, S. (1996). Parametric Studies of Thermal Efficiency in a Proposed Porous Radiant Recirculated Burner : *A Design Concept for the Future Burner Proceedings of RERIC International Energy Journa*l, Vol. 18, pp. 97-11

[13] Dong, L.L., Cheung, C.S. and Leung, C.W. (2002). Heat transfer from an impinging premixed butane air slot flame jets. *International Journal of Heat and Mass Transfer*, Vol.45, pp. 979-992.

TSF0005

Effect of heat transfer from variation of cross-sectional area in helical coil heat exchanger manufacturing process

Suriya Sukarin, Manusak Janthong, and Sathaporn Thongwik*
Department of Mechanical Engineering, Faculty of Engineering, Rajamangala University of Technology Thanyaburi Thailand

* Corresponding Author: sathaporn.th@en.rmutt.ac.th

Abstract. This paper explores the relationship between percent ovality (ω) caused by increasing heat transfer area of the helical coil in coil connect shell helical heat exchanger (CCS) manufacturing process. The percent ovality (ω) increase is caused by the helical coil forming process by copper tube rolling, resulting in the tube cross-section having an oval shape (FC). An increase in ω directly affects the Critical Reynolds number, causing the transition point of the working fluid from laminar to turbulent flow to change. In addition, an increase in ω results in a decrease in the Nusselt number and heat transfer coefficient compared to circular tubes (OC). This test also provides insight into the flow characteristics within helical coils with elliptical tube cross-sections, which are further useful for CCS design.

Keywords: helical coil heat exchanger, percent ovality, Heat transfer, heat recovery, renewable energy.

1. Introduction

A heat exchanger is a main device in industrial work which heat is transferred from one medium to another, widely used in various industries such as automobile, refrigeration and air conditioning, and energy conservation. A.Mahmoudi et al. [1] states that 50% of world energy loss was caused by heat. Provided that the energy loss could be reduced and the heat could be recycled, the air pollution would be considerably reduced. Hence, heat exchangers have been developed and applied for energy conservation by recovering waste heat from industrial production process or machines the most cost-effectively such as drawing heat energy from waste water [2].

The application of heat exchangers for energy conservation in this paper presents its co-working with the heat pump system. The heat pump system generates heat by drawing heat from machinery working process and transferring it through working fluid, and the heat can then be used in different forms like washing, reheating, or air conditioning where it needs heating in winter [3, 4]. The major devices of the heat pump system consist of a compressor, evaporator, condenser, and pipe line [5]; these can be found in normal refrigeration system. Different renewable energy systems may occasionally be designed for co-working with heat pump system to enhance its efficiency such as solar system in which more devices need to be added like flat plate solar collectors or PV modules [6], and photovoltaic/thermal (PV/T) may sometimes be used to co-work with heat pump system [7]. However, it is undeniable that the heat exchanger is the main factor to help increase or decrease performance of heat pump system (COP) [8] whether it co-works with any system.

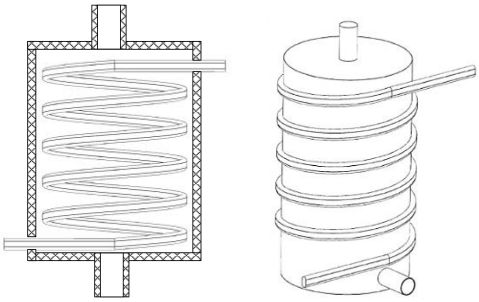

Figure 1. Helical Heat exchanger a) Coil in shell helical heat exchanger (CNS) b) Coil connect shell helical heat exchanger (CCS).

Different types of heat exchangers are popularly used with heat pump system depending on the suitability of use and purposes of design. In this paper, only helical heat exchanger (HHE) will be presented since it is popularly used to co-work with the heat pump system and easy to produce and install. The study of AP Sasmito et al. [9] revealed that internal flow of helical coil was more effective on heat transfer than that on straight tubes according to the principle of working fluid flowing in helical coil in which heat exchange occurs on the surface of working fluid tube. Blanco et al. [10] studied HHE which was double helical coil with one wall contacting each other and found that heat transfer occurred at the contacting area. Moreover, the study of N. Ghorbani et al. [11] showed that the whole surface of helical coil affected heat exchange of HHE. One of HHE widely used is the coil in shell helical heat exchanger (CNS).This heat exchanger with working fluid flowing in helical coil is put into conductor storage which the CNS is generally found in heat storage including heating substances in chemical production process. Besides, several pieces of research on CNS development were conducted by many researchers such as AK Solanki et al. [12] whose study dealt with the comparison of pressure drop in CNS with different surface of helical coil. AD Tuncer et al. [13] also investigated the effectiveness of CNS in different conditions by comparing the experimental results with those drawn from CFD. Furthermore, AD Tuncer et al. [14] studied the use of fins to increase the effectiveness of CNS, and HM Maghrabie et al. [15] evaluated the effectiveness of CNS using Nano fluids as working fluid. However, when CNS has been used for a long time, leakage and combustibility of working fluid may be occurred. The CNS used in heat pump system has refrigerant as its working fluid [16] [17] which could lead to contamination or burst of working fluid [18]; therefore, coil connect shell helical heat exchanger (CCS) is designed to reduce danger of working fluid by not putting helical coil in conductor storage, but by winding helical coil around conductor storage in which heat is transferred from the surface between helical coil wall and conductor storage wall. Since helical coil is produced from circular tube – having quite less contacting area for heat transfer, this affects the reduction of heat transfer. Hence, the wider area of heat transfer, the more effective the CCS is – the main focus of this paper to explore the effect of widening area of helical coil.

Bending pipes is a main process in helical coil production of HHE as found in the study that curve bending caused the change in cross sectional area of the pipe from circular tube helical coil (OC) into flat tube helical coil (FC) [19] [20]as seen in figure 2. Although such change widened contacting area of helical coil and that of conductor storage, its deformation affected the flow in the tube as well as heat transfer that could be different from the flow in the OC. This can be found in AM Hussein's experiment [21] showing different forms of cross sectional tube affecting the flow in the tube including its heat transfer, but excluding bent tubes like helical coil. Thus, this problem will mainly be discussed in this paper. Provided that understanding of flow behavior and heat transfer process in FC is drawn, effectiveness of CCS and overall effectiveness of heat pump system will be enhanced.

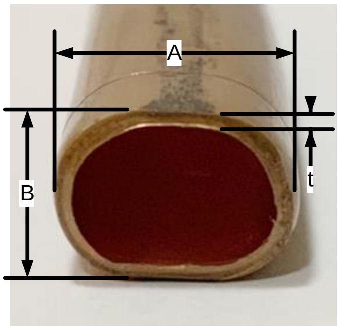

Figure 2. Cross section of helical coil after rolling.

2. System testing

2.1. FC formation

The experiment focuses on the effect of thermal energy change resulting from internal flow in the tube of FC due to deformation of the cross sectional area of helical coil in the production process. This deformation is caused by the bending moment in the curve bending of copper tube with a diameter of 10.5 and thickness of 1 mm. in helical coil forming. The FC samples with an equal diameter and pitch are tested and their percent ovality (ω) shown in Table 1 is calculated by Equation 1 [20]. An increase of percent ovality (ω) results in an increase in surface of heat transfer on the wall (A_{wall}). Each FC sample is then coiled into 5 turns (C) with a pitch (P) of 50 mm. and coiled diameter (D) of 180 mm. as shown in figure 3.

$$\omega = \frac{(A+B)}{\varphi} \times 100 \qquad (1)$$

By which $$\varphi = \frac{A+B}{2}$$

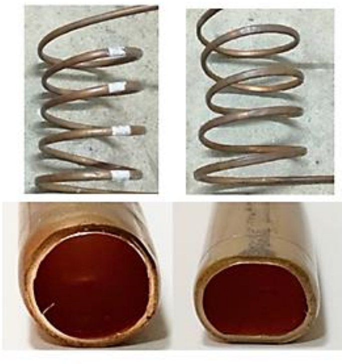

Figure 3. Two variations of the helical coil.

The test is carried out under the condition of constant surface heat flux [22] in which the working fluid (water) at the constant temperature of 50±1℃ flowing in the FC; the flow rate ($\dot{m}$) is controlled at a range from 0.2 to 2.0 l/min throughout the test. Thermocouple type K is used to collect temperature data of FC wall which is divided into 2 groups. Group 1 is installed along the twist of FC at 360°, 720°, 1080°, and 1440° whereas Group 2 is installed at the inlet and outlet of FC. The thermocouple of the two groups is connected to the data acquisition for recording the result. After that, the FC samples are soaked in the water basin at a constant temperature of 30±2°C. In this paper, a cooling unit is a device used to help control the temperature as shown in Figure 4.

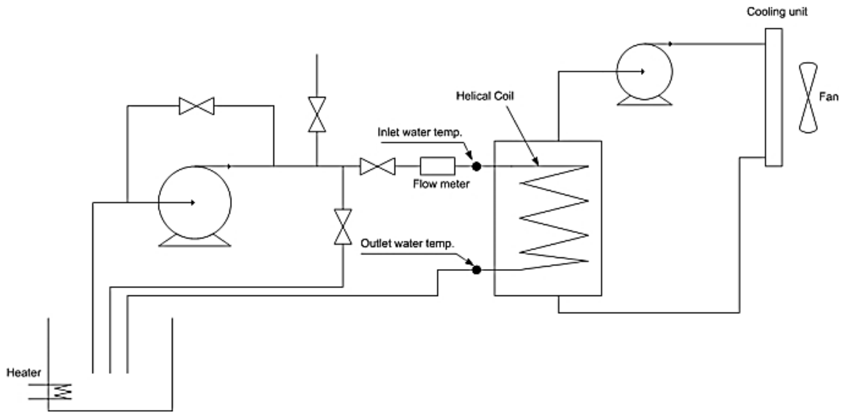

Figure 4. System diagram of the test.

Table 1. Different sizes of FC samples in the test.

Samples	**A (mm.)**	**B (mm.)**	**ω**	**D_h (mm.)**
FC-1	14.00	10.00	33	12.03
FC-2	15.00	9.00	50	11.68

2.2. Thermal process analysis

The overall thermal analysis$(\dot{Q}_{all})$ is analyzed on the surface of all FCs (A_{all}) based on Equations 2–5 as follows:

$$\dot{Q}_{all} = \dot{m}c_p(T_{oc} - T_{ic}) \quad (2)$$

$$\Delta T_{LM,all} = T_s - \frac{T_i + T_e}{2} \quad (3)$$

$$h = -\frac{\dot{Q}_{all}}{A_{all}\,\Delta T_{LM,all}} \quad (4)$$

$$\dot{q}_{all} = \frac{\dot{Q}_{all}}{A_{all}} \quad (5)$$

Where

T_{oc} is an outlet water temperature of FC (°C)

T_{ic} is an inlet water temperature of FC (°C)

T_s is an average surface temperature of FC (°C)

T_i is an inlet working fluid temperature of FC (°C)

T_i is an outlet working fluid temperature of FC (°C)

$\dot{q}_{all}$ is an overall thermal flux (W/m^2)

h is heat transfer coefficient (W/m^2 ·°C)

The internal flow of FC, Nusselt number (Nu), and Reynolds number (Re) is analyzed as shown in Equations 6 and 7:

$$Nu = \frac{hD_h}{k} \tag{6}$$

$$Re = \frac{\rho D_h u}{\mu} \tag{7}$$

Where D_h is a hydraulic meter,

$$D_h = 4\left[\frac{\frac{\pi d^2}{4}+B(A-B)}{\pi B+2(A-B)}\right] \tag{8}$$

Critical Reynolds number (Re_{cr}) which is a turning point from Laminar flow to turbulent flow is considered as shown in Equation 9 [23]:

$$Re_{cr} = 2100\left[1+12\left[\frac{d}{D}\right]^{0.5}\right] \tag{9}$$

3. Test results

According to the physical characteristics, FC-1 (ω=33%) and FC-2 (ω=50%) are different hydraulic meters. In this article, the hydraulic meter of the FC-2 is 2.98% higher than FC-1, resulting in the Critical Reynolds number (Re_{cr}) of the FC-1 being 3.22% higher than the FC-2. Compared to the OC tube, the critical Reynolds number of OC was 7.90% and 11.38% lower than those of FC-1 and FC-2, respectively.

Consider the relationship between Nusselt number and Reynolds number, as shown in Figure 5. The test results showed that the two variables were directly correlated. Over the entire testing period, the OC based on the S. S. Pawar et al [24]. Test result had a higher Nusselt number than FC-1 and FC-2 by 1.22%, 9.72% respectively. When comparing FC-1 (ω=33%) and FC-2 (ω=50%), the Nusselt number of FC-1 was on average 5% higher than that of FC-2.

This comparison assumes that ω is equal, which the authors refer to the straight pipe test results of Abdolbaqi et al [25] (FSS-1 and FSS-2). From the results, it was found that the Nusselt number in straight pipes was higher than that of helical coil pipes. Because of comparison, the Nusselt number of FSS-1 was 60.27% higher on average than FC-1 and FSS-2 was on average 76.12% higher than FC-2 Nusselt number.

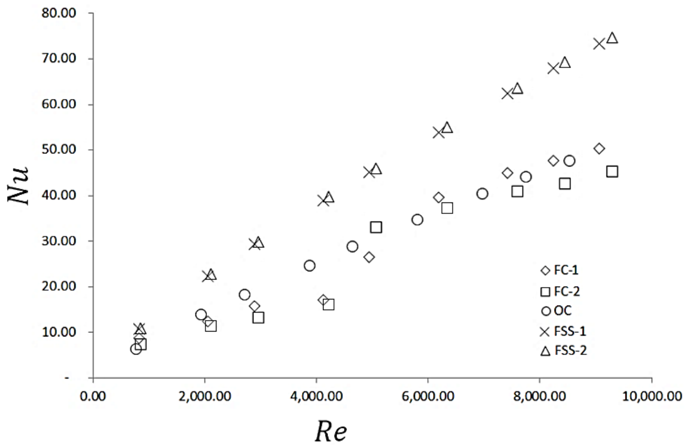

Figure 5. Correlation between Reynolds number (Re) and Nusselt number (Nu).

Consider the relationship between the flow rate and the heat transfer coefficient of each type of pipe. As shown in Figure 6. The relationship between these two variables is in direct proportion. The test results in the first group, the OC-type helical coil, had the highest heat transfer coefficient, 22.59% higher than FC-1 and FC-2, 28.18% respectively. A subsequent group of comparisons between FSS, FC-1 and FC-2 showed that the heat transfer coefficient of FSS-1, ω=33% was 60.27% higher than that of FC-1, ω=33% on average, and that of FSS-2, ω=50%. Than FC-2 76.12%

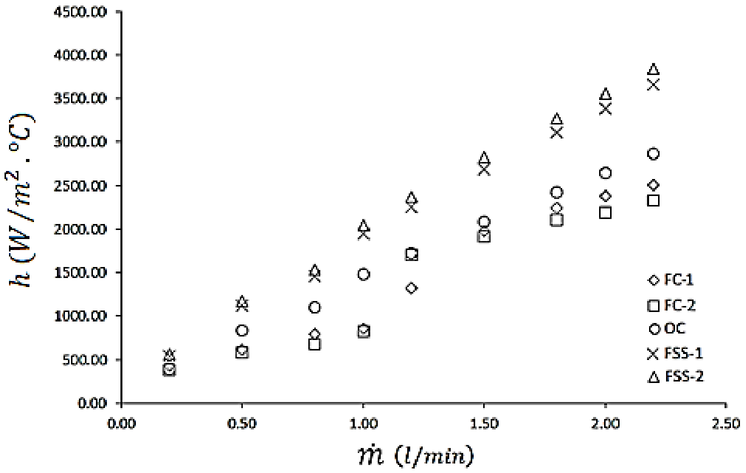

Figure 6. Correlation between flow rate ($\dot{m}$) and Overall heat transfer coefficient (h).

4. Conclusion

A method for increasing the heat transfer area of the helical coil for use with CCS by rolling a circular cross-section tube into a FC-cross section. The change in pipe cross-section in this manner is determined by ω. The increase of ω directly affects the critical Reynolds number of the working fluid is higher. As a result, the working fluid flowing within the FC changes its flow from laminar flow to turbulent flow at a higher Reynolds number. An increase in ω also decreases the Nusselt number of FC. Another factor contributing to the decrease in the Nusselt number is the nature of the pipe. The results of the comparison between FC and FSS show that straight tubes have higher Nusselt numbers than helical coil tubes. This test found that increasing ω resulted in a decrease in the heat transfer coefficient. All these conclusions will help designers of CCS heat exchangers to understand the relationship between ω and the internal flow of the helical coil. The authors hope this article will be useful for the design of CCS with higher thermal efficiency for heat pump systems.

5. References

[1] A. Mahmoudi, M. Fazli, and M. R. Morad, "A recent review of waste heat recovery by Organic Rankine Cycle," *Applied Thermal Engineering,* vol. 143, pp. 660-675, 2018, doi: 10.1016/j.applthermaleng.2018.07.136.

[2] A. H. Cahya and R. Permatasari, "Design of Shell and Tube Heat Exchanger for Waste Water Using Heat Transfer Research Inc," *International Journal of Advanced Science and Technology,* vol. 29(05), pp. 611 - 622, 2020.

[3] L. Yang, H. Yuan, J.-W. Peng, and C.-L. Zhang, "Performance modeling of air cycle heat pump water heater in cold climate," *Renewable Energy,* vol. 87, pp. 1067-1075, 2016, doi: 10.1016/j.renene.2015.08.055.

[4] S. Ramaraj, J. E. Braun, E. A. Groll, and W. T. Horton, "Performance analysis of liquid flooded compression with regeneration for cold climate heat pumps," *International Journal of Refrigeration,* vol. 68, pp. 50-58, 2016, doi: 10.1016/j.ijrefrig.2016.04.017.

[5] C. Arpagaus, F. Bless, J. Schiffmann, and S. S. Bertsch, "Multi-temperature heat pumps: A literature review," *International Journal of Refrigeration,* vol. 69, pp. 437-465, 2016, doi: 10.1016/j.ijrefrig.2016.05.014.

[6] E. Bellos, C. Tzivanidis, K. Moschos, and K. A. Antonopoulos, "Energetic and financial evaluation of solar assisted heat pump space heating systems," *Energy Conversion and Management,* vol. 120, pp. 306-319, 2016, doi: 10.1016/j.enconman.2016.05.004.

[7] R. Kong, T. Deethayat, A. Asanakham, and T. Kiatsiriroat, "Performance and economic evaluation of a photovoltaic/thermal (PV/T)-cascade heat pump for combined cooling, heat and power in tropical climate area," *Journal of Energy Storage,* vol. 30, 2020, doi: 10.1016/j.est.2020.101507.

[8] I. Ortega, J. Sieres, F. Cerdeira, E. Álvarez, and J. Rodríguez, "Performance analysis of a R407C liquid-to-water heat pump: Effect of a liquid–vapor heat exchanger and domestic hot water production," *International Journal of Refrigeration,* vol. 101, pp. 125-135, 2019, doi: 10.1016/j.ijrefrig.2019.02.024.

[9] A. P. Sasmito, J. C. Kurnia, W. Wang, S. V. Jangam, and A. S. Mujumdar, "Numerical analysis of laminar heat transfer performance of in-plane spiral ducts with various cross-sections at fixed cross-section area," *International Journal of Heat and Mass Transfer,* vol. 55, no. 21-22, pp. 5882-5890, 2012, doi: 10.1016/j.ijheatmasstransfer.2012.05.085.

[10] D. L. Blanco, K. Nagano, and M. Morimoto, "Experimental study on a monovalent inverter-driven water-to-water heat pump with a desuperheater for low energy houses," *Applied Thermal Engineering,* vol. 50, no. 1, pp. 826-836, 2013, doi: 10.1016/j.applthermaleng.2012.07.008.

[11] N. Ghorbani, H. Taherian, M. Gorji, and H. Mirgolbabaei, "An experimental study of thermal performance of shell-and-coil heat exchangers," *International Communications in Heat and Mass Transfer,* vol. 37, no. 7, pp. 775-781, 2010, doi: 10.1016/j.icheatmasstransfer.2010.02.001.

[12] A. K. Solanki and R. J. I. J. o. T. S. Kumar, "Condensation frictional pressure drop characteristic of R-600a inside the horizontal smooth and dimpled helical coiled tube in shell type heat exchanger," vol. 154, p. 106406, 2020.

[13] A. D. Tuncer, A. Sözen, A. Khanlari, E. Y. Gürbüz, and H. İ. Variyenli, "Analysis of thermal performance of an improved shell and helically coiled heat exchanger," *Applied Thermal Engineering,* vol. 184, 2021, doi: 10.1016/j.applthermaleng.2020.116272.

[14] A. D. Tuncer, A. Sözen, A. Khanlari, E. Y. Gürbüz, and H. İ. Variyenli, "Upgrading the performance of a new shell and helically coiled heat exchanger by using longitudinal fins," *Applied Thermal Engineering,* vol. 191, 2021, doi: 10.1016/j.applthermaleng.2021.116876.

[15] H. M. Maghrabie, M. Attalla, and A. A. A. Mohsen, "Performance assessment of a shell and helically coiled tube heat exchanger with variable orientations utilizing different nanofluids," *Applied Thermal Engineering,* vol. 182, 2021, doi: 10.1016/j.applthermaleng.2020.116013.

[16] D. Colbourne and K. J. I. j. o. r. Suen, "Equipment design and installation features to disperse refrigerant releases in rooms—part I: experiments and analysis," vol. 26, no. 6, pp. 667-673, 2003.

[17] D. Colbourne and K. J. I. j. o. r. Suen, "Equipment design and installation features to disperse refrigerant releases in rooms—part II: determination of procedures," vol. 26, no. 6, pp. 674-680, 2003.

[18] W. Zhang, Z. Yang, X. Zhang, D. Lv, and N. Jiang, "Experimental research on the explosion characteristics in the indoor and outdoor units of a split air conditioner using the R290 refrigerant," *International Journal of Refrigeration,* vol. 67, pp. 408-417, 2016, doi: 10.1016/j.ijrefrig.2016.03.018.

[19] P. S. ES, "Pipe bending methods, tolerances, process and material requirements," 1987.

[20] S. Sumesh, A. R. Veerappan, and S. Shanmugam, "Evaluation of postulated cross sections with ovality and thinning for 90° pipe bends with circumferential throughwall cracks subjected to in-plane closing bending," *Engineering Failure Analysis,* vol. 75, pp. 82-91, 2017, doi: 10.1016/j.engfailanal.2016.12.021.

[21] A. M. Hussein, K. V. Sharma, R. A. Bakar, and K. Kadirgama, "The effect of cross sectional area of tube on friction factor and heat transfer nanofluid turbulent flow," *International Communications in Heat and Mass Transfer,* vol. 47, pp. 49-55, 2013, doi: 10.1016/j.icheatmasstransfer.2013.06.007.

[22] A. C. Yunus, *Heat and mass transfer: fundamentals and applications*. McGraw-Hill Education, 2019.

[23] P. Srinivasan, S. Nandapurkar, F. J. T. o. t. I. o. C. E. Holland, and t. C. Engineer, "Friction factors for coils," vol. 48, no. 4-6, pp. T156-+, 1970.

[24] S. S. Pawar and V. K. Sunnapwar, "Experimental studies on heat transfer to Newtonian and non-Newtonian fluids in helical coils with laminar and turbulent flow," *Experimental Thermal and Fluid Science,* vol. 44, pp. 792-804, 2013, doi: 10.1016/j.expthermflusci.2012.09.024.

[25] M. K. Abdolbaqi, W. H. Azmi, R. Mamat, N. M. Z. N. Mohamed, and G. Najafi, "Experimental investigation of turbulent heat transfer by counter and co-swirling flow in a flat tube fitted with twin twisted tapes," *International Communications in Heat and Mass Transfer,* vol. 75, pp. 295-302, 2016, doi: 10.1016/j.icheatmasstransfer.2016.04.021.

TSF0009

Airflow Analysis based on the Location of Air Conditioning in Negative Pressure Room

Ghaim Man Oo[1], Komsilp Kotmool[2], and Mongkol Mongkolwongrojn[1,*]

[1, 2, 1*] College of Advanced Manufacturing Innovation, King Mongkut's Institute of Technology Latkrabang, 1 Soi Chalongkrung 1, Latkrabang, 10520, Bangkok, Thailand

* Corresponding Author: mongkol.mo@kmitl.ac.th

Abstract. Negative pressure rooms are typically used for highly infectious patients, such as tuberculosis or COVID-19. This research aims to control the airborne particles from the patient on the various airflow distributions due to the three different locations of air conditioning (AC) such as case_1, case_2, and case_3 inside the negative pressure room. The main objective is to choose the best location among the three cases for air conditioning depending on the airflow distribution, velocity, and temperature. Transient numerical simulations are carried out by using ANSYS-Fluent, standard k-ε turbulent model, and discrete phase model with the Lagrangian method. In this work, the negative pressure room is considered together with the buffer room and exhaust hood for the contaminant extraction as the mechanical ventilation. According to the numerical results, the air velocity variations from the air conditioning cause more turbulent effects that tend to complex particle extraction processes. It is observed that case_2 is the best location compared with case_1 and case_3 based on the dispersion of coughed droplet particles from the patient. This work will help to protect both patients and healthcare workers from the spread of disease.

Keywords: Negative pressure room, Locations of air conditioning, Discrete phase model.

1. Introduction

The negative pressure room is a key component of the arsenal of infection prevention and control methods in this era of rapidly spreading infectious diseases like COVID-19. The transmission of the COVID-19 virus has contributed to the pandemic's intensity and speed, which has resulted in major morbidity and mortality worldwide [1]. Therefore, the design and functionality of the negative pressure room are instrumental in limiting the spread of airborne pathogens and ensuring the well-being of individuals within healthcare facilities and research environments.

In a negative pressure room, the air pressure is maintained at a lower level compared to the adjacent spaces. This pressure differential ensures that air flows from the surrounding areas into the negative pressure room, preventing potentially contaminated air from exiting and dispersing into other parts of the building. This controlled airflow helps minimize the risk of transmitting infectious agents to healthcare workers, patients, and visitors. Its main purpose is to prevent hazardous airborne organisms, such as viruses, bacteria, or fungi, from fleeing the room and infecting the surroundings. Design standards for negative pressure rooms can vary from country to country based on local regulations, guidelines, and healthcare practices [2]. It's important to consult the relevant desired negative pressure in the specific country because pressure differential values and air change rate vary based on the design standards. As an achievement, the optimum design of the negative pressure room has been analyzed for any desired negative pressure without considering the air conditioning (AC) model. In this design, the aerosol particles can be extracted only 98% and 2% trapped near the patient's head [3]. Therefore, in the current work, three different cases with various air conditioning locations are numerically investigated with the help of ANSYS-Fluent to modify the previous design of a negative pressure room and choose the best location of air-conditioning based on human comfort. As shown in Figure 1, these three situations are referred to as cases_1 through 3: case_1 is where the AC is mounted on the wall on the patient's left side, case_2 is where it is mounted on the wall on the patient's right side, and case_3 is where it is mounted on the wall opposite the exhaust hood.

According to literature surveys on interior air conditioning, it is crucial to examine how variations in airflow and temperature affect human comfort. Adnan Memom and Balkrushna Shah studied the mixing airflow effect of a central and split air conditioning system in the classroom depending on the aerosol-based disinfectant machine to minimize the spread of the COVID-19 virus by numerical method. They found that the high turbulent zone inside the room is the efficient way to distribute disinfectant to every corner of the classroom by analyzing various parameters with a velocity of air conditioning, 3.9 m/s [4]. Sudhangshu Sarma, O. P. Jakhar, and George Pichurov numerically analyzed the impact of the air conditioner locations on temperature and velocity distribution in an office room. They considered four different locations of air conditioners that are mounted on the wall of the north, east, south, and west of the office room with inlet velocity, 2 m/s, and 4 m/s, and suggested that the relationship between the position of air conditioner and thermal environment in the room [5, 6]. A. Sarkar, M. S. Khan, Abhinandan Kumar and V. N. Bartaria investigated the effect of different locations of single and double duct AC model with air inlet velocity, 4m/s and 0.19 m/s for single and double duct by numerical method. The authors emphasized mainly the parameter of temperature and the double duct AC model can give a little high room pressure with a small velocity amount compared with single duct AC without considering the effect of return air in the room [7, 8].

Jahar Sarkar and Soumen Mandal carried out experimental and numerical work for the airflow and temperature distribution of air conditioning space with three different turbulent models and AC inlet velocity, 2.13 m/s, and 3.13 m/s. They revealed that k-ε and k-ω can give the most relevant results compared with experiment data based on velocity and temperature distribution [9]. Manoj Kumar Gopaliya and Neha Kumari reported that the positioning of an air conditioner in a room with four different locations is analyzed on the effects of thermos-fluid characteristics. They considered the heat source as a spherical model to be the equivalent amount of two persons and AC inlet velocity, 3.5 m/s for overall thermal fluid flow performance. They chose one of the mounting positions with the lowest temperature among all mounting positions of their study [10]. Although many previous studies have looked into the locations of AC in normal pressure rooms, it is very rare for information on the negative pressure room together with the AC model. Therefore, the objective of this present work is to choose the best AC position inside the negative pressure room from three different cases based on the parameters of velocity, pressure, temperature, and aerosol particle tracking with the help of computational fluid dynamics (CFD). Additionally, contrary to earlier research, the AC geometry is modeled to have an inclined inlet velocity surface of 45 degrees, as seen in Figure 1.

2. Methodology

2.1. Physical Model and Boundary Conditions

In this study, the negative pressure room together with the buffer room is simulated and reported with desired pressure ≥ –5 Pa and air change rate (ACH) ≥ 10 based on the design standards of airborne infection isolation room [2]. As the ventilation system, the supply air is designed to get the desired negative pressure based on the Bernoulli theorem, the exhaust hood is placed near the patient's head to extract the aerosol particles, and the air conditioning is installed for human comfort. The idea of area changes according to the Bernoulli theorem for the desired negative pressure conditions is specially modified in this system and this concept can maintain any desired negative pressure even if the AC inlet velocity is very high. For the clean air supply, it is considered that a HEPA filter is used in front of the supply fan and in the exhaust outlet to protect against the dispersion of contaminated air. The detailed dimensions of the negative pressure room and AC model are illustrated as shown in Figure 1. In this computational domain, the patient's body is considered rectangular and the door_1 is assumed fully opened throughout the calculation.

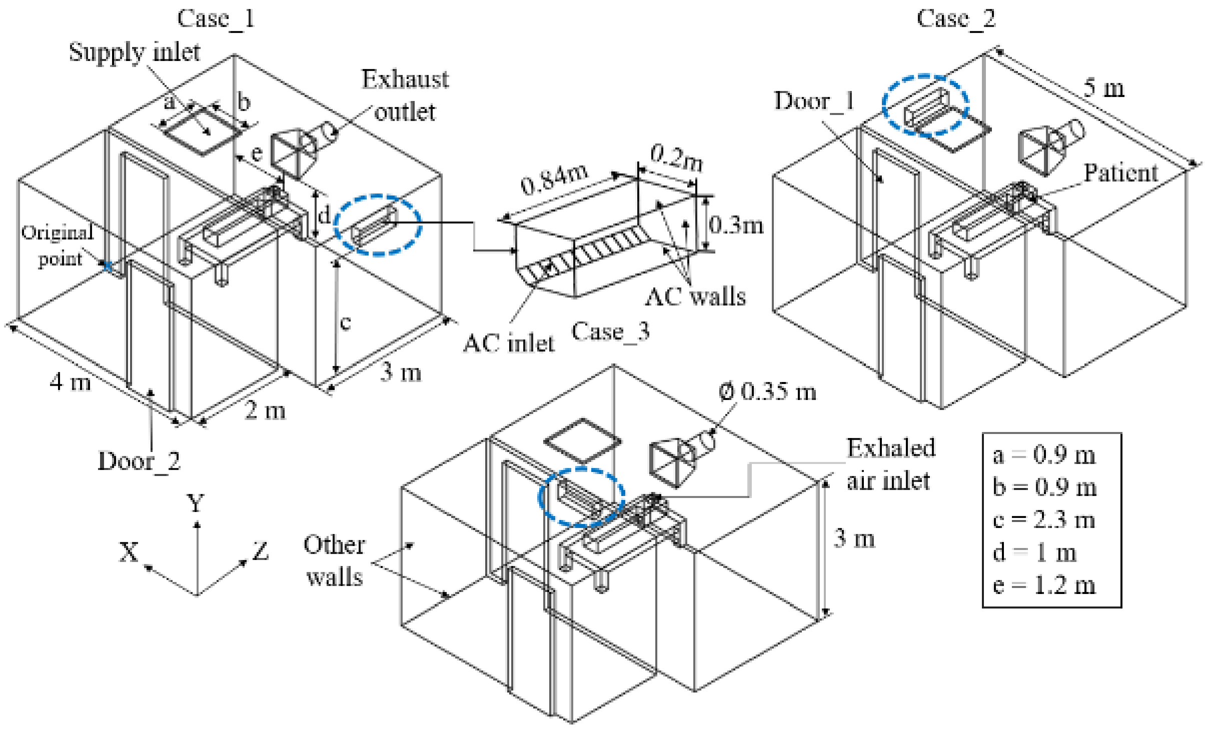

Figure 1. The geometry of a negative pressure room with different AC locations.

Table 1. Boundary conditions for CFD simulation.

Item	Type	Value
AC inlet	Velocity inlet	Velocity = 3-5 m/s, Temperature = 22˚C
Supply inlet	Pressure inlet	Pressure = –10 Pa, Temperature = 22˚C
Breathing and coughing particles from the patient	Velocity inlet	Exhaled velocity = 0.18 m/s Particle velocity = 10 m/s Temperature = 37˚C, Flow rate = 2.4e-9 kg/s Density = 998 kg/m^3, Diameter = 10-100 µm
Exhaust outlet	Velocity inlet	Velocity = –3 m/s, Temperature = 24˚C
Other room walls	wall	h = 14.7 W/m^{2}K
Patient body	wall	Heat flux = 32 W/m^2

After considering the first step of the computational domain for simulation, it is essential to ensure that the boundary conditions are based on genuine data from real-world settings. As the previous literature, although the AC inlet velocity is considered between 2 m/s and 4 m/s in indoor air ventilation systems, it is taken into account as 3 m/s to 5 m/s of the current simulation based on the actual measurement. Additionally, the remaining detailed boundary conditions are unique for the optimum design as in Table 1, which are successfully confirmed with the relevant references in the previous research work [3].

2.2. Meshing and Grid Independence

Meshing is the important grid generation step, which divides the computational domain into finite volumes or elements. In this calculation, the unstructured mesh of tetrahedron type is mainly applied due to the complex structure of the geometry, and refinement mesh is considered in the surface of the main supply inlet and exhaust outlet. The standard wall function is also applied to investigate the near-wall effects. Moreover, a grid-independent test is performed, which means that the solution does not significantly change when the elements are increased in the computation. This test is also a necessary point to get the actuate solution from numerical investigations. Therefore, Element size 6,116,980 is used through all the future computations to save the computation time and the error percentage of velocity, pressure, and temperature is less than the acceptable error percent, 5% as shown in Figure 2.

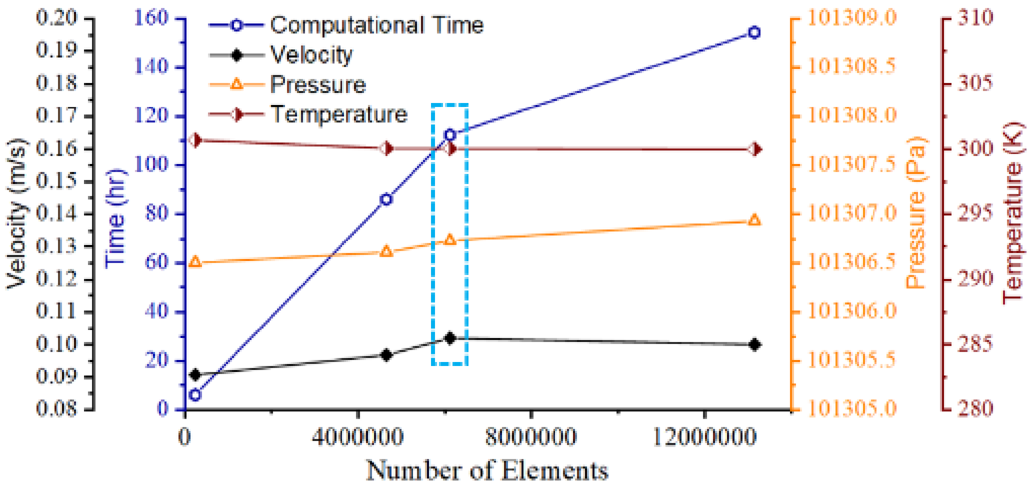

Figure 2. Grid independence study for simulation.

2.3. Governing Equations

The airflow inside the room is assumed as incompressible flow and a SIMPLE algorithm of velocity-pressure coupling to solve the pressure correction equation in ANSYS-Fluent. The three-dimensional negative pressure room for transient flow simulations is carried out for up to 30 minutes by using the governing equations of continuity, momentum, and energy equations [11]:

$$\frac{\partial \rho}{\partial t} + \nabla.(\rho u) = 0 \tag{1}$$

$$\frac{\partial (\rho u)}{\partial t} + \nabla.(\rho u u) = -\nabla P + \nabla.(\mu \nabla u) + \nabla.\tau_t + \rho g \tag{2}$$

$$\frac{\partial}{\partial t}(\rho E) + \frac{\partial}{\partial x_i}\left[u_i(\rho E + P)\right] = \frac{\partial}{\partial x_j}\left[\left(k + \frac{c_p \mu_t}{Pr_t}\right)\frac{\partial T}{\partial x_j} + u_i(\tau_{ij})_{eff}\right] + S_h \tag{3}$$

For the ventilation airflow systems, the standard k-ε turbulent model is the most suitable model due to its accuracy and low computational cost [10, 12]. The following are the transport equations for turbulence's kinetic energy, k, and dissipation rate, ε respectively:

$$\frac{\partial}{\partial t}(\rho k)+\frac{\partial}{\partial x_i}(\rho k u_i)=\frac{\partial}{\partial x_j}\left[\left(\mu+\frac{\mu_t}{\sigma_k}\right)\frac{\partial k}{\partial x_j}\right]+G_k+G_b-\rho\varepsilon-Y_M+S_k \tag{4}$$

$$\frac{\partial}{\partial t}(\rho\varepsilon)+\frac{\partial}{\partial x_i}(\rho\varepsilon u_i)=\frac{\partial}{\partial x_j}\left[\left(\mu+\frac{\mu_t}{\sigma_\varepsilon}\right)\frac{\partial \varepsilon}{\partial x_j}\right]+C_{1\varepsilon}\frac{\varepsilon}{k}\left(G_k+C_{3\varepsilon}G_b\right)-C_{2\varepsilon}\rho\frac{\varepsilon^2}{k}+S_E \tag{5}$$

In addition, a discrete phase model is applied to track the moving particles and investigate the percentage of particles trapped and escaped inside the negative pressure room by the Lagrangian method. In this study, gravity, drag force, Brownian force, and Staffman's force are mainly considered for the floating particle transfer to the air, and the corresponding equation of motion is as follows [11, 13]:

$$\frac{d\vec{u}_p}{dt}=F_D\left(\vec{u}-\vec{u}_p\right)+\frac{\vec{g}\left(\rho_p-\rho\right)}{\rho_p}+\vec{F} \tag{6}$$

3. Validation for CFD Calculation

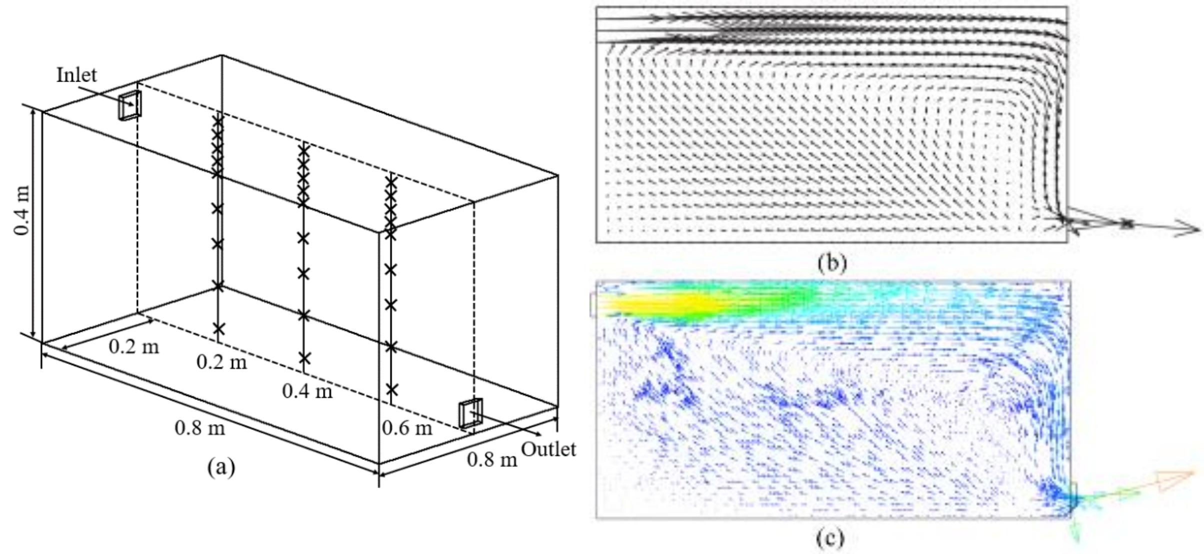

Figure 3. (a) Geometry of the ventilation chamber; Typical airflow distribution at the middle plane with 0.225 m/s: (b) previous study [14]; (c) current study

An experimental work of the ventilation chamber was chosen as the validation model for the airflow distribution, and the detailed geometry dimensions and measuring points are shown in Figure 3. (a) [14]. In this study, the published model was modeled with similar geometrical parameters, and the structured mesh size, 178, 642 is used for simulation prediction. The results of middle plane typical airflow velocity vectors from the validation model are compared to F. Chen et al. experimental results showed the same airflow pattern as described in Figure 3. (b) and (c). Moreover, velocity magnitude variations at three different locations, X = 0.2m, 0.4m, 0.6m are validated in good agreement with the experiment study as compared in Figure 4.

For the particle dispersion validation, the previous study investigated on the aerosol flow path in the negative pressure room [3], which adopted the same methods and boundary conditions. In this study, the modified model with air conditioning in different locations was analyzed to approach the best particle controllable effect for a safe environment.

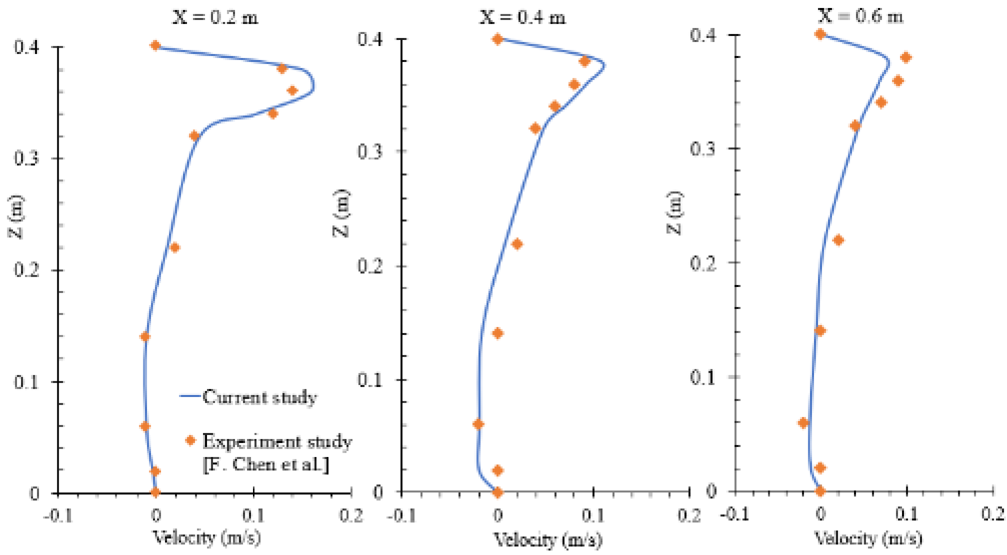

Figure 4. Validation of measurement and numerical velocities at three different locations as x direction; 0.2m, 0.4m, and 0.6m.

4. Results and Discussions

Depending on the previous study, Ratio (9) which is the area ratio of supply and exhaust area is continued to modify the particle settling effect by considering the AC model of three different cases inside the negative pressure room. The room pressure can maintain an absolute pressure of 101315.88 Pa with an AC inlet velocity, of 3 m/s although there is a little negative pressure reduction due to the increasing AC inlet velocity. When the previous model is modified with the AC model, the particle trapped percentage can reduce from 2% to 0.27% and 0% at AC velocity 3 m/s and higher. Through the discussion, the particle trapped percentage and particle stuck mean the percentage of some particles settling near the patient's head and the particle escaped means particles can move out from the negative pressure room to outside.

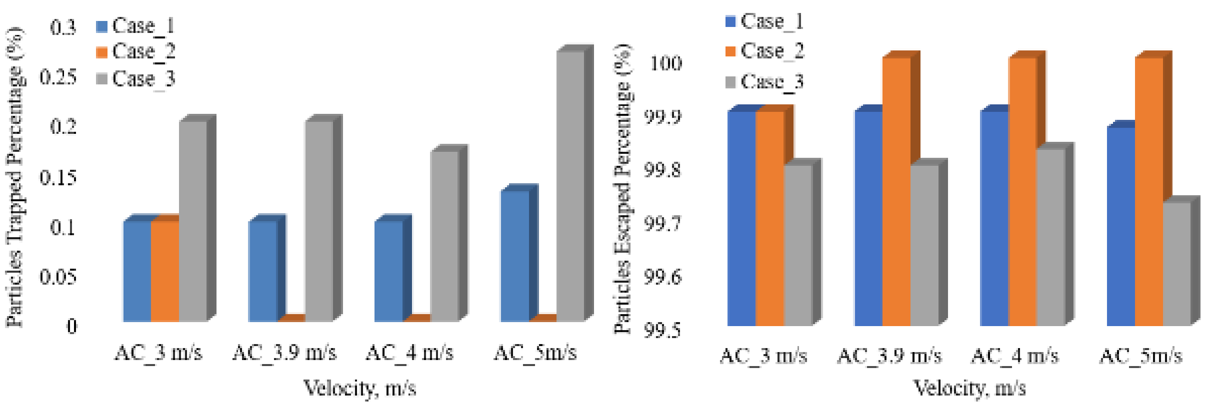

(a) (b)

Figure 5. Percentage of aerosol particles; (a) Trapped inside the negative pressure room, (b) Escaped from the negative pressure room.

In Figure 5. (a) and (b) compares the percentage of trapped and escaped particles in three cases according to the AC velocity range of 3 m/s to 5 m/s. It has been noted that cases_1 and 3 show particles stuck by roughly 0.13% and 0.27%, respectively, and cases_1 and 3 only allow 99.87% and 99.73% of the particles to escape. Although case_2 can efficiently perform a 100% particle escaping effect at an AC velocity of 3.9 to 5 m/s, there is about 0.13 % cannot be extracted at an AC velocity, of 3 m/s as shown in Figure 5. (b). In summary, case_2 can extract all the aerosol particles up to 100% in many conditions but case_1 and 3 retain 0.13% and 0.27% of the particles trapping effect. For future discussion, all the cases with AC inlet velocity, of 3.9 m/s are reported.

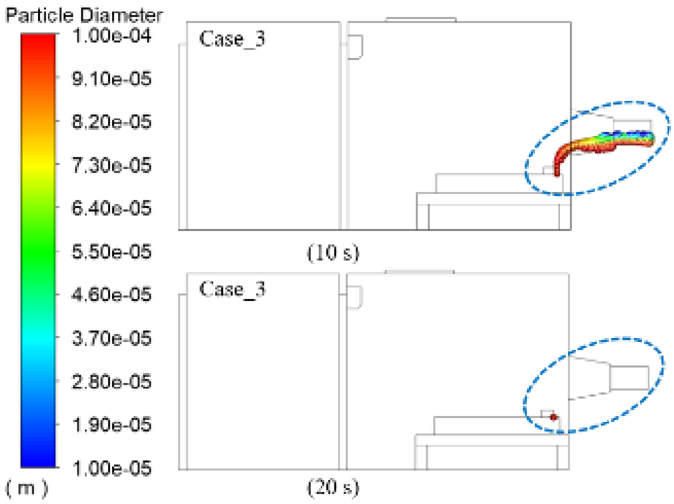

Figure 6. Dispersion of aerosol particles at different time 10 sec and 20 sec.

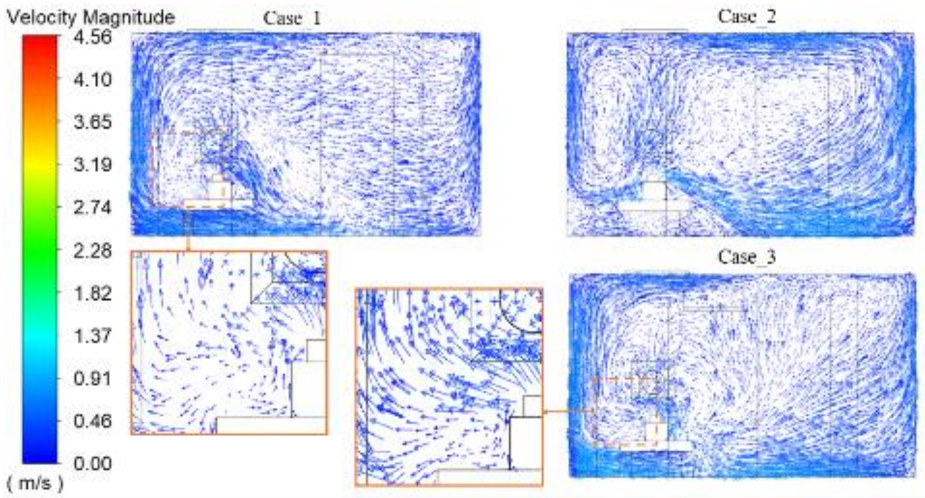

Figure 7. Comparison of Velocity vector distributions in three different cases at XY plane, Z = 2.6m.

For the study on particle movement, it is assumed that the patient was coughing 3000 particles each time in a second, with a diameter of 10–100 µm [15]. As can be seen in Figure 6, the aerosol particles from the human mouth can move out without dispersion inside the room at 10s and some particles are settling near the patient's head at 20s. Therefore, it is necessary to find the settling problem in case_1 and 3 like a similar particle-trapped effect. Figure 7 shows the velocity vector variations in case_1, 2, and 3 at XY plane, X = 2.6m, and there is no turbulence occurring in case_2 near the patient’s head. In case_1 and case_3 can be seen that small turbulence is occurring near the left-hand side of the patient's head. This small turbulent flow can cause the particles to settle and trap problems in case_1 and 3 configurations.

Additionally, the majority of velocity magnitude values are lower than the maximum tolerable human speed of 1.5 m/s. As indicated in Figure 8, pathlines dispersion is examined to analyze the airflow distributions from the primary negative pressure chamber to the buffer room. Comparing the streamlines of the three examples reveals that case_2 is more expandable than the other two.

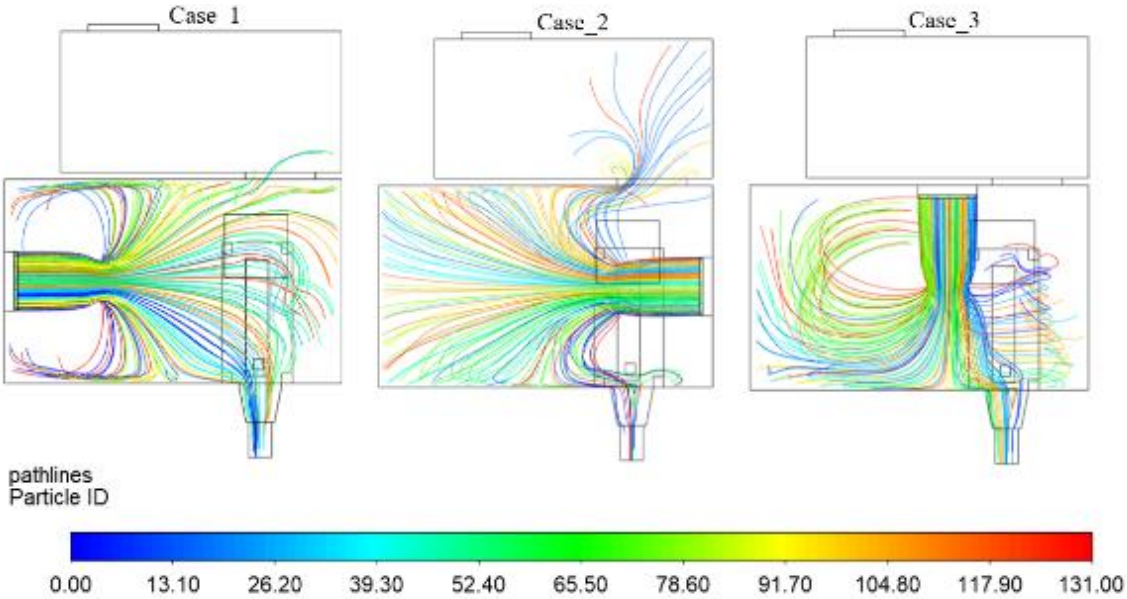

Figure 8. Comparison of Pathlines formation in three different cases at 20 sec.

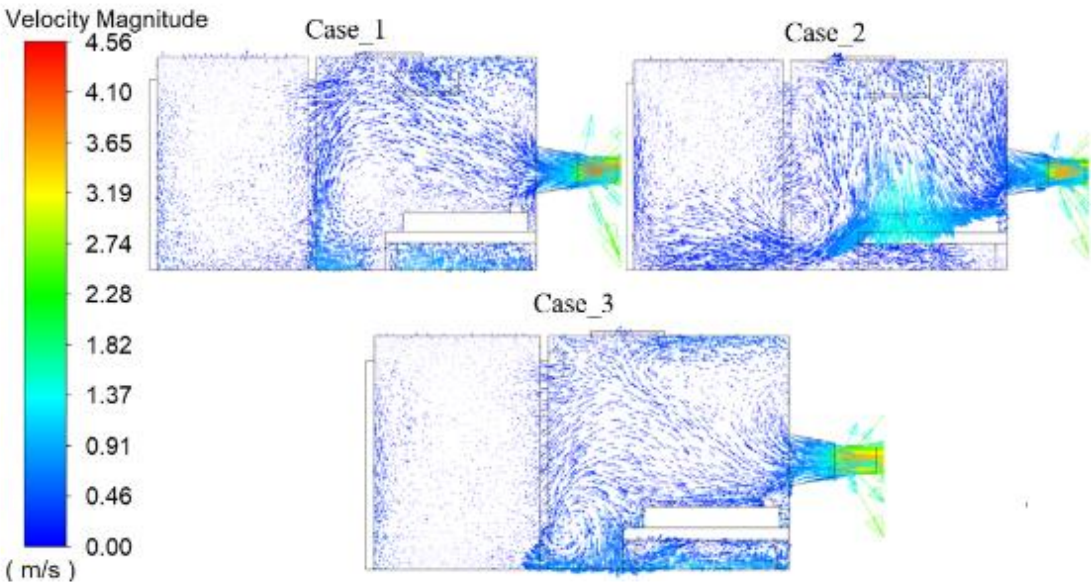

Figure 9. Comparison of airflow distribution in three different cases at YZ plane, X = 1.3m.

Figure 9 shows the three different airflow cases at the YZ plane, X = 1.3m, and case_2 can give a cooler environment around the patient compared with the other two cases. Although a little high velocity strikes the patient from the AC inlet, this velocity magnitude is still under the maximum comfortable velocity. Similar airflow patterns can be seen in Cases_1 and 3 where the strong turbulent airflow occurs close to Door 1 and flows over the patient's body and out the exhaust hood.

Finally, to investigate the thermal comfort, temperature contours of three cases are stated in Figure 10. It can be observed that the same temperature contours inside the negative pressure room of case_1 and 3 can be caused due to the similar airflow pattern as mentioned in the previous Figure 9. Likewise, the cold environment near the patient can give due to the high air velocity variation in case_2. The maximum temperature of case_2, 33.6˙Cis the lowest temperature compared with the remaining two cases 1 and 3, 37.55˙C and 36.95˙C although case_1 and 3 seem to be wide areas of thermal comfort.

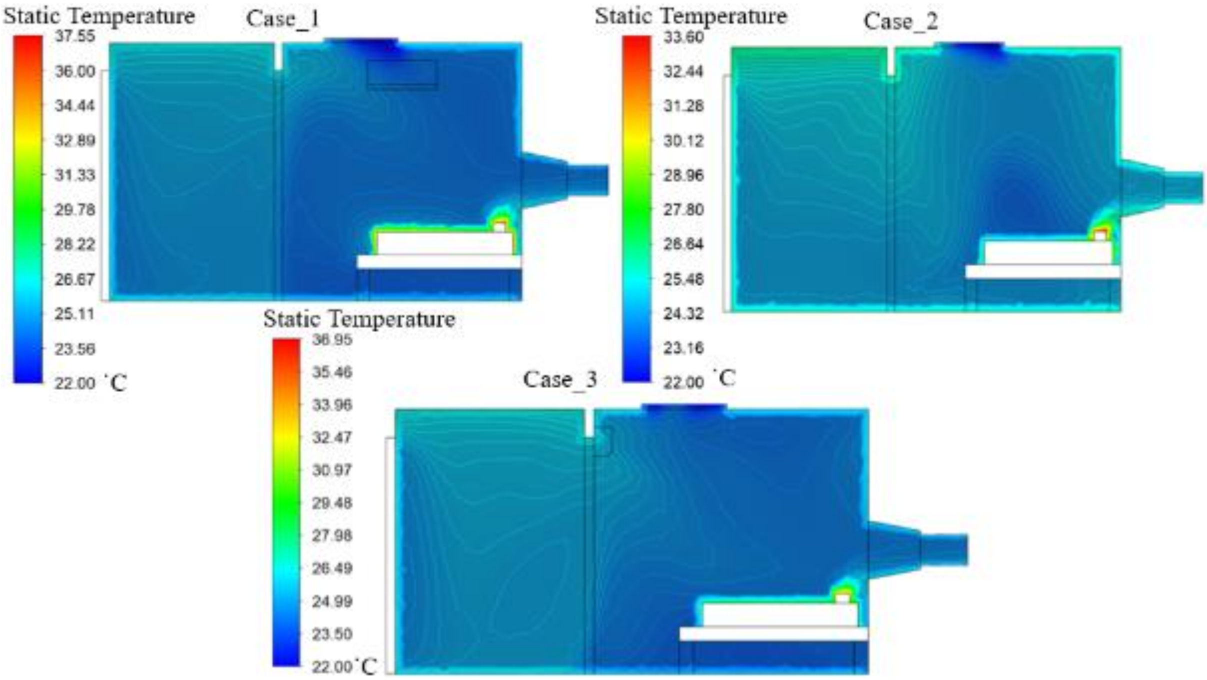

Figure 10. Comparison of temperature contours in three cases at YZ plane, X = 1.3m.

5. Conclusions

The flow dynamics and dispersion of aerosol particles by coughing of a COVID-19 infected patient in the three cases with various locations of the air conditioning inside the negative pressure room were studied. The 3D simulations were carried out for different ventilation airflow velocities from the AC inlet. Following are the conclusions that can be made based on the results that have been presented:

1. The modified configuration together with the air conditioning model can improve the aerosol particle extraction efficiency from 98% up to 99.87%.
2. Case_1 and case_3 have particle trapped percent of 0.13% and 0.27% respectively due to the small turbulent airflow occurrence near the patient's head. Therefore, case_2 can give no particle settling effect and 100% extraction.
3. According to the streamlines analysis, case_2 showed the pathlines can move toward the buffer room compared with the other two.
4. The velocity magnitude variations in three cases revealed that the inside velocities are under the maximum acceptable velocity for human comfort.
5. Case_2 can maintain a cooler environment for the patient with the lowest maximum temperature, 33.6˙C.

As a summary, case_2 is the best location for the air conditioning inside the negative pressure room for both 100% prevention of aerosol particle effect and human comfort compared with the other cases, case_1 and case_3. These findings might be applied to any negative pressure room design that includes a development strategy for the efficient removal of aerosol particles.

6. Nomenclature

ρ	Density of fluid, air	Y_M	Contribution of the fluctuating dilatation in compressible turbulence to the overall dissipation rate
t	Time	$\mathrm{Pr_t}$	Prandtl number
u	Velocity magnitude in x direction	$C_{1\varepsilon}, C_{2\varepsilon}, C_{3\varepsilon}$	Constants used in the turbulent model
v	Velocity magnitude in y direction	σ_k	Turbulent Prandtl numbers for k
w	Velocity magnitude in z direction	σ_ε	Turbulent Prandtl numbers for ε
$\boldsymbol{\tau}$	Shear stress	S_k, S_ε, S_h	Source terms
$\mathbf{u}$	Fluid velocity vector	c_p	Specific heat capacity at constant pressure
P	Pressure	T	Temperature
E	Total energy	μ	Dynamic viscosity
g	Gravitational acceleration	u_p	Velocity of particle
k	Turbulent kinetic energy	ρ_p	Density of particle
ε	Rate of dissipation	F_D	Drag force
G_k	Generation of turbulent kinetic energy due to the mean velocity gradients	$\vec{F}$	Additional forces acting on the unit mass
G_b	Generation of turbulent kinetic energy due to buoyancy		

7. Acknowledgments

This work was supported by King Mongkut’s Institute of Technology Latkrabang. The authors would like to acknowledge the Computer Simulation Engineering Laboratory, College of Advanced Manufacturing Innovation, KMITL for providing the computational facilities.

8. References

[1] Zhang G-Q, Pan H-Q, Hu X-X, He S-J, Chen Y-F, Wei C-J, et al. The role of isolation rooms, facemasks and intensified hand hygiene in the prevention of nosocomial COVID-19 transmission in a pulmonary clinical setting. Infectious Diseases of Poverty. 2020;9:1-6.

[2] Ruikar A. Designing effective ventilation strategy for an Airborne infection isolation room (AIIR) using CFD. simulationHub; 2021.

[3] Oo GM, Kotmool K, Mongkolwongrojn M. Analysis of parametric optimization on the design of negative pressure room. Advances in Building Energy Research. 2023;17:412-39.

[4] Memon A, Shah B. CFD Analysis to Minimize the Spread of COVID-19 Virus in Air-Conditioned Classroom. Applications of Computation in Mechanical Engineering: Select Proceedings of 3rd International Conference on Computing in Mechanical Engineering (ICCME 2021): Springer; 2022. p. 121-36.

[5] Pichurov G, Stankov P, Markov D. Hvac control based on CFD analysis of room airflow. IFAC Proceedings Volumes. 2006;39:213-8.

[6] Sarma S, Jakhar O. Computational Analysis of Impact of The Air-Conditioner Location On Temperature And Velocity Distribution In An Office-Room. International Research Journal of Engineering and Technology (IRJET). 2016;3.

[7] Abhinandan Kumar1 VNB. CFD ANALYSIS OF ROOM WITH AIR CONDITIONER BY USING ANSYS WORKBENCH. Journal of Emerging Technologies and Innovative Research, (JETIR). 2018;5:99-104.

[8] Sarkar A. Analysis of Room with Single Duct Air Conditioner using Computational Fluid Dynamics. Available at SSRN 4104196. 2021.
[9] Sarkar J, Mandal S. CFD modeling and validation of temperature and flow distribution in air-conditioned space. 2008.
[10] Gopaliya MK, Reddy Pulagam MK, Kumari N. Comparative Study of Positioning of Air Conditioner in a Room Using CFD. Advances in Air Conditioning and Refrigeration: Select Proceedings of RAAR 2019: Springer; 2020. p. 161-76.
[11] Fluent A. Theory guide. ANSYS Canonsburg; 2015.
[12] Laubi R, Abbood N. CFD analysis of the classroom thermal conditions built from the sandwich panel. Journal of Physics: Conference Series: IOP Publishing; 2021. p. 012019.
[13] Farouk MI, Nassar AF, Elgamal MH. Numerical study of the transmission of exhaled droplets between the instructor and students in a typical classroom. Applied Sciences. 2021;11:9767.
[14] Chen F, Simon C, Lai AC. Modeling particle distribution and deposition in indoor environments with a new drift–flux model. Atmospheric Environment. 2006;40:357-67.
[15] Gorbunov B. Aerosol particles generated by coughing and sneezing of a SARS-CoV-2 (COVID-19) host travel over 30 m distance. Aerosol Air Qual. Res. 21, 200468. 2021.

TSF0010

Operating characteristics of a miniature swing rotary expander for a Rankine cycle regenerative system using waste heat

Daiki Makino[1,*] and Toshio Otaka[1]

[1]Kokushikan University, 4-28-1, Setagaya, Setagaya-ku, Tokyo, 154-0023, Japan

* Corresponding Author: s2me001h@kokushikan.ac.jp

Abstract. Greenhouse gases are major international problem to be solved. Therefore, it is important to use efficiency, and high energy conservation measures are needed. For the reason, waste heat regeneration systems that utilize low temperature waste heat from hot springs and factories are attracting attention. There has been limited search Rankine cycle as a highly efficient miniature regenerative system using low temperature waste heat. Most of the currently practical use regeneration systems using waste heat are in over the 1kW class. Although there have been reported case of thermoelectric power generation using low temperature heat sources, there are no practical example of high efficiency systems. The authors have therefore designed and developed a 300W class swing rotary expander (hereafter referred to as "Prototype") for use miniature regeneration systems. This Prototype is installed to a flange case for convenient experimentation. The design specifications of the Prototype are shaft output of 300W, expansion unit inlet temperature of 353K expansion unit outlet temperature of 323K, and HFC 134a as the working fluid. HFC13a is for experimental convenience. The mechanism part uses a swing rotary with 2 cylinders. The intake does not use valve. This paper compares Prototype with an already developed 1 kW class expander for vehicle waste heat and presents the shaft power analysis and thermodynamic characteristics. These results reveal the usefulness of the miniature low temperature waste heat regeneration system. Furthermore, these results demonstrate that the system containing a swing rotary expander is one of the promising candidates as a new waste heat regeneration system.

Keywords: Regeneration system, Low temperature waste heat, Rankine cycle, Swing rotary expander.

1. Introduction

In recent years, interest in global environmental issue such as the SDGs has increased internationally. There are many environmental problems represented by global warming, and improvements are required. The Japanese government has set an ambitious goal in the Paris Agreement to reduce Japan's greenhouse gas emissions by 46% from 2013 levels by 2030. Additionally, the Japanese government has declared that it will achieve carbon neutrality by 2050.

Currently, power generation in Japan is performed by large-scale energy systems such as thermal power generation. Large-scale energy systems have the disadvantage of producing large amounts of greenhouse gas emissions. In addition, nuclear power generation requires countermeasures against accidents, and advanced safety measures are needed. Large-scale energy systems may experience unstable energy supply during disasters such as earthquakes. Therefore, rather than relying solely on large-scale energy systems, the introduction of distributed energy systems that utilize renewable energies such as wind power generation and solar power generation is progressing worldwide. However, most of the thermal energy such as household waste heat, industrial waste heat, and power generation waste heat is not utilized. Regenerating such discarded unused energy will improve the effectiveness of distributed energy systems that do not depend on large-scale energy systems. Research on highly efficient large-scale power generation systems that use high-temperature heat sources such as geothermal power generation and thermal power generation is progressing, but research on highly efficient small-scale regeneration systems that use low-temperature waste heat below 373K is limited. The Rankine cycle is one example of a power generation system using waste heat, but there are few studies on small-scale regeneration systems using low-temperature waste heat. Most of the waste heat regeneration systems currently in practical use are over 1kW. Although examples of thermoelectric power generation using low-temperature heat sources have been reported, there are no examples of highly efficient practical use.

The authors designed and developed a 300W class swing rotary expander for miniature regeneration systems. In addition, we introduced some thermodynamic characteristics shown by shaft power analysis and experiments of the expander compared with the 1000W class swing rotary expander that we were designing and developing earlier. These results demonstrate the usefulness of a miniature low-temperature waste heat regeneration system. Furthermore, these results indicate that the system containing the swing rotary expander is one of the more promising candidates for the new waste heat recovery system.

2. Swing rotary expander

A regeneration system that uses low-temperature waste heat as a heat source is expected to fluctuate in the amount of heat from the heat source. Therefore, it is necessary to design an expander that functions well against load fluctuations. In addition, in order to increase the effectiveness of the compact regeneration system, it is necessary to downsize the expander and make it maintenance-free. Therefore, a swing rotary mechanism was adopted for the expander.

2.1. Specification of "Prototype"

Table 1 shows the design specifications of the swing rotary expander designed and developed by the authors (hereafter referred to as the "Prototype") [1].

Table 1. Design specifications of the prototype.

Shaft power	0.3kW
Mechanism	Swing rotary (2 cylinders)
Pressure ratio	2
Refrigerant	HFC134a
Lubrication	POE
Temperature Inlet/Outlet	353K/223K
Pressure Inlet/outlet	2.63MPa/1.32MPa

The prototype is designed to have 2 cylinders and a shaft output of 0.3kW. HFC134a is used as the refrigerant, which was selected in consideration of the ease of experimentation. Eventually, we will replace it with a refrigerant with a lower global warming potential. The structure of the prototype is shown in figure 1. The expander is sealed, and a portion of the shaft is exposed outside the case. Torque is measured by connecting the shaft directly to a torque meter. We also installed a sight glass so that you can see inside the case. A positive displacement oil pump is built into the sub-bearing to reliably supply oil to each sliding part. The shaft has an introduction hole for introducing high pressure gas into the cylinder. There is an intake groove in the crank part of the shaft, and this intake groove communicates with the roller, allowing high-pressure gas to be introduced. This is a mechanism that controls intake timing by rotating the shaft.

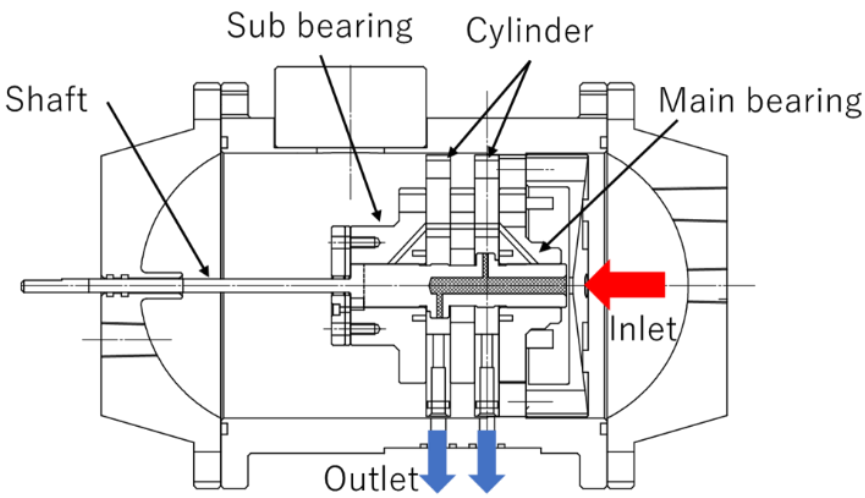

Figure 1. Schematic view of the prototype.

2.2. Specification of "EX01"

The EX01[2] is designed to have 2 cylinders and a shaft output of 1kW. Like the prototype it has 2 cylinders structure. In EX02, the design specifications are shown in table.2. The structure of the EX02 is shown in figure 2.

Table 2. Design specifications of the EX01.

Shaft power	1kW
Mechanism	Swing rotary (2 cylinders)
Pressure ratio	2
Refrigerant	HFC134a
Lubrication	POE
Temperature Inlet/Outlet	353K/223K
Pressure Inlet/outlet	2.63MPa/1.32MPa

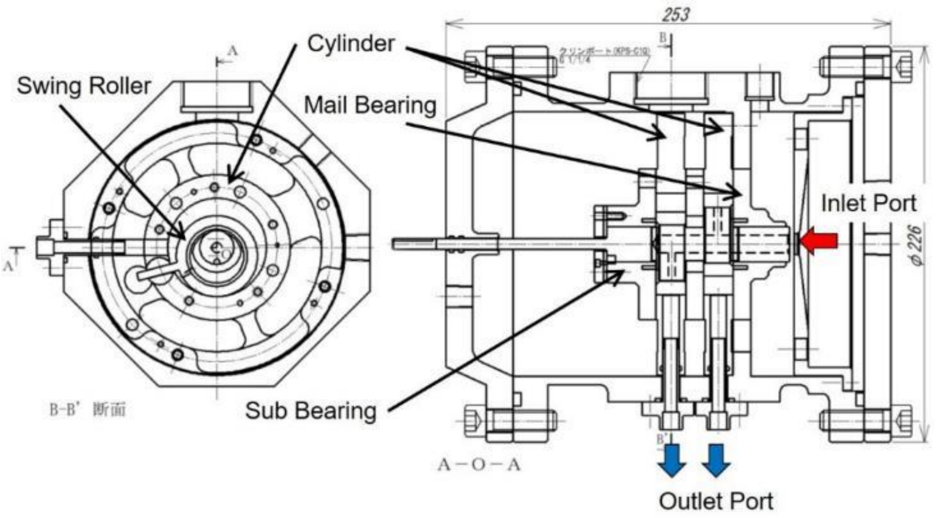

Figure 2. Schematic view of the EX01.

3. Result of functional evaluation experiments

As an experiment to confirm the performance of the expander, we conducted an experiment using dry air as the working fluid [1], [2]. The two expanders used in this experiment require oil seals in the operating space and sliding parts. An optimal oil seal is required to improve the efficiency of the expander, so by using dry air as the working fluid, it is possible to evaluate performance under the most severe oil seal conditions, where no oil flows into the expander inlet. Figure 3 shows an overview of the expander evaluation method. A torque meter and an electromagnetic brake are connected to the expander. It is possible to apply a constant load to the expander by applying voltage to the electromagnetic brake. The rotation speed at this time was recorded by a torque meter.

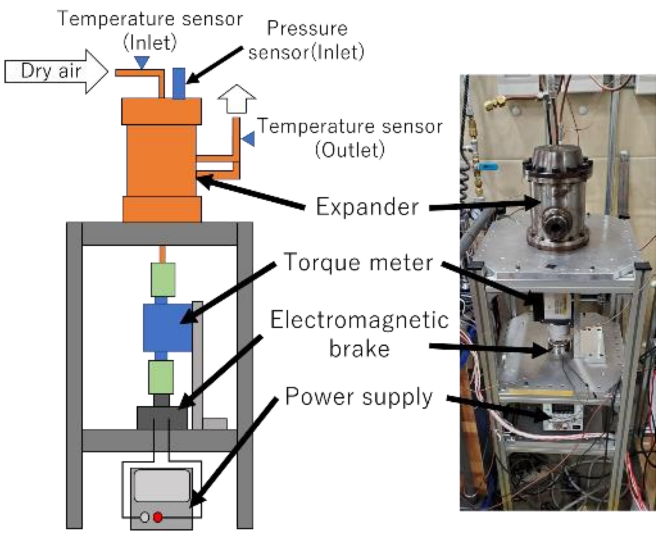

Figure 3. Experimental apparatus.

3.1 Dimensionless of the shaft power

Figure 4 shows the dimensionless of the expander to the rotation speed of the expander when dry air is used as the working fluid. The dimensionless shaft power ratio decreases as the effect of mechanical loss increases with increasing rotational speed. The reason why the dimensionless shaft output of the Prototype is lower than that of the EX01 is that the working space is smaller when the suction starts due to the smaller eccentricity, and the pressure drop of the working fluid has a greater effect. In addition, because of its miniature size, the effect of clearance is also significant, resulting in increased mechanical losses. In this research, dry air is used as the working fluid, which is the most severe oil seal condition. By using the working fluid as a refrigerant according to design specifications, oil flows into the expander inlet, reducing mechanical losses.

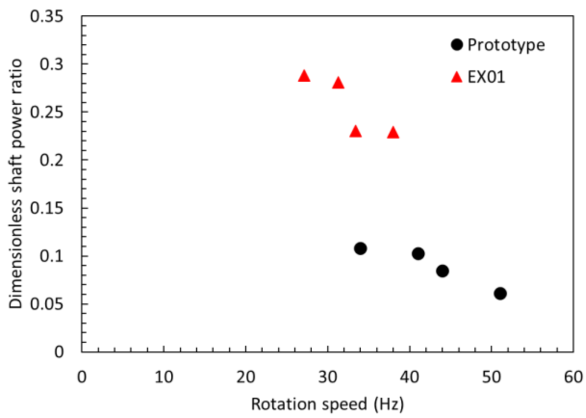

Figure 4. Dimensionless shaft power ratio to rotational speed.

$$\boldsymbol{N} = \frac{\boldsymbol{W_{exp}}}{\boldsymbol{W_{pre}}} \tag{1}$$

$$\boldsymbol{W_{pre}} = \boldsymbol{nP_1V} \tag{2}$$

where $\boldsymbol{N}$ is Dimensionless number of the expander. $\boldsymbol{W_{exp}}$ (W) is the experimental shaft power. $\boldsymbol{W_{pre}}$ (W) is the predicted shaft power. $\boldsymbol{n}$ (Hz) is the rotation speed. $\boldsymbol{P_1}$ (Pa) is the expander inlet pressure. $\boldsymbol{V}$ ($\boldsymbol{m^3}$) is the expander scavenging volume.

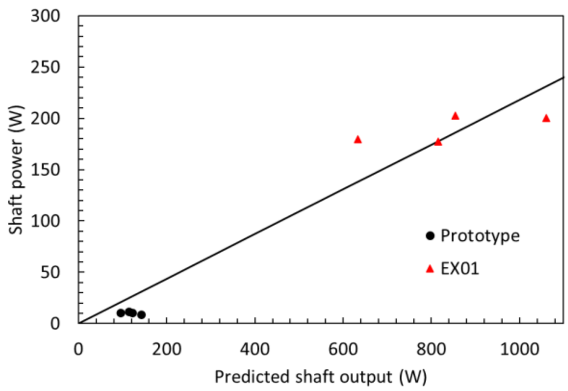

Figure 5. Comparison Predicted shaft power and experimental results.

Figure 5 shows the predicted shaft power versus the shaft power. The trend was obtained by comparing two expanders with different specifications using the least-squares method. The results are useful for determining the specification of the expander. One of the reasons for the low shaft power of the prototype is the increased mechanical losses due to the small-excluded volume.

3.2 The expander efficiency

Figure 6 shows the expander efficiency versus rotation speed. The prototype has a small eccentricity due to its small size, and the effect of the pressure drop in the cylinder is significant. Dry air also reduces volumetric efficiency. Therefore, when the excluded volume is small, it is important to optimize the eccentricity and cylinder height.

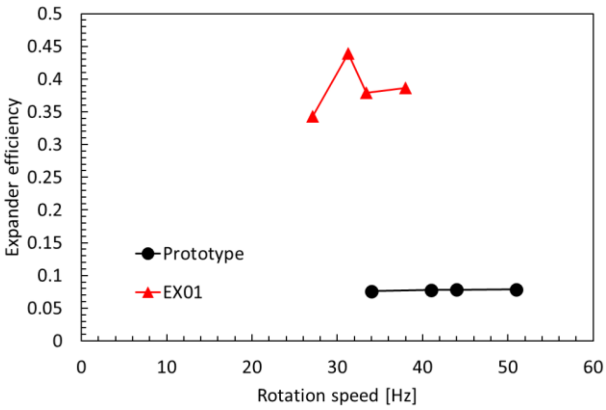

Figure 6. The efficiency of the expander.

4. Conclusion

The authors evaluated the results of experiments using dry air as the working fluid for both the Prototype and EX01. In this research, the following results were obtained.

(1) By making the experimental results dimensionless, it became possible to compare the differences in the specifications of each expander. Therefore, certain trends useful for specification determination were obtained.

(2) The maximum expander efficiency of 0.08 and 0.44 were obtained for the prototype and EX01 expanders, respectively.

This study shows the performance under the most severe oil seal condition with dry air as the working fluid. Therefore, the influence of mechanical losses is significant, and the prototype has a small exclusion volume, which significantly reduces the volumetric efficiency. In addition, the small eccentricity results in a large pressure drop in the cylinder. The eccentricity and cylinder height must be optimized for a miniature-sized expander. These results enhance the usefulness for miniature low-temperature waste heat regeneration system.

5. Acknowledgments

I would like to express my gratitude to Prof. Otaka. I want to thank Students of Otaka Laboratory of Kokushikan University.

6. References

[1] Daiki, M. Toshio, O. (2023). Operating characteristics of a swing rotary expander for a miniature power generating system using waste heat energy for local production for local consumption. Proc. Int. Conf. on Power Engineering. Kyoto. Japan

[2] Toshio, O. Makoto, A. (2022). Fundamental study on a swing rotary expander for a small-sized regenerative device using the engine waste heat of a vehicle. Proc. TSME Int Conf. on Mechanical Engineering. Phuket. Thailand.

TSF0011

A Numerical Investigation of Evaporation Process in a Minichannel of Printed Circuit Heat Exchanger

Nyein Nyein Aye[1], Withun Hemsuwan[2], and Chalothorn Thumthae[1,*]

[1,2,1*] School of Mechanical Engineering, Suranaree University of Technology, Muang District, Nakhon Ratchasima 30000, Thailand

* Corresponding Author: chalothorn@sut.ac.th

Abstract. Numerous studies have been carried out on printed circuit heat exchangers (PCHEs) with mini/microchannel cores, but few works have investigated two-phase flow. This study was investigated the heat transfer and evaporation flow performance of a minichannel PCHE. A three-dimensional model of a semicircular minichannel with a hydraulic diameter of 0.884 mm and a total length of 446 mm was utilized as the numerical model for initial validation purposes. The numerical simulation of the phase-change mass and heat transfer in a minichannel channel was modelled using ANSYS Fluent software. The VOF method with the SST k-ω model and a user-defined function (UDF) code based on the Lee model was used to illustrate the behaviour of the vapour distinct from the liquid. The numerical results were employed to understand the reasons for the changes in physical properties during the evaporation process. This investigation showed that complex two-phase heat transfer mechanisms can be successfully modelled using the CFD technique.

Keywords: minichannel, VOF method, evaporation.

1. Introduction

The concept of a mini/microchannel heat exchanger, Printed Circuit Heat Exchanger (PCHE), originated in Australia in 1980 and was further developed by Heatric in England during the same year. PCHE is a compact and efficient device. Flow paths are formed through photochemical etching on metal plates, which are subsequently bonded and diffusion to create the core. PCHE stands out with its excellent properties including a small hydraulic diameter, efficient heat exchange, and ability to withstand varying temperatures and pressures. Researchers have extensively investigated PCHE's thermal-hydraulic performance using both experimental and numerical methods [1] .

Jiang et al. [2] conducted a study on the impact of structural channel parameters on the thermal-hydraulic performance of an airfoil PCHE using CFD simulations with supercritical carbon dioxide (S-CO_2) as the working fluid. Oleiwi Samarmad et al. [3] carried out both numerical and experimental investigations to analyse the impact of corrugated wavy channel amplitude on the thermal-hydraulic performance of PCHE using liquid water as the working fluid. Their findings indicated that higher amplitudes resulted in improved heat transfer performance in the PCHE. Zhou et al. [4] conducted a numerical simulation of a straight semi-circular channel PCHE to investigate the heat transfer and flow characteristics of molten salt and CO_2-based mixtures under various operating conditions. Safari et al. [5] using CFD, they investigated the thermal performance of PCHE in three different channel cross sections. The trapezoidal wave channel achieved better heat transfer than the rectangle and triangular channels. Jin et al.[6] derived the new correlations of heat transfer applied in zigzag channel PCHE by experiment and investigated the effects of mass flux, inlet temperature, and system pressure on the heat transfer performance. While PCHEs have been extensively studied, the majority of research has focused on single-phase working fluids with no phase transition processes. Consequently, the investigation of two-phase flow in minichannels of PCHE has received further attention.

For the advancement of PCHEs in two-phase cryogenic applications, it is crucial to know the condensation and evaporation heat transfer characteristics of natural gas (NG). Goto et al. [7] conducted experimental research to explore the impact of channel geometry on condensation flow visualization, heat transfer, and pressure drop within straight and wavy minichannel PCHEs. Their findings indicated that wavy minichannels demonstrated enhanced heat transfer and pressure drop performance in comparison to straight channels. Hu et al. [8] conducted flow boiling characteristics experiments of R22 in zigzag channels, heat transfer coefficient correlation was developed to reflect the effects of sloshing conditions. Yoo et al. [9]examined condensation heat transfer and pressure drop in PCHEs with semicircular channels using propane. Thirty experimental cases explored different mass fluxes, saturation pressures, and vapour quality to derive correlations for the two-phase heat transfer and pressure drop. Shin et.al. [10] carried out experimental investigations on the use of zigzag channels in a 200 kW PCHE, capable of operating with liquid nitrogen below -170 ˚C. Liu et al. [11] explored an experimental investigation of flow instability, two-phase flow patterns, and performance analysis within a microchannel co- and counter-current heat exchanger. The heat exchanger, measuring 20 mm by 20 mm, featured 18 parallel microchannel on both sides. They recommended the use of the counter-current configuration due to its remarkable efficiency enhancement at higher mass fluxes compared to its co-current counterpart.

While research on two-phase PCHE experiments is ongoing, much of the data available from previous studies is constrained in terms of the scale and application of PCHE. When designing a PCHE for Floating Storage Recirculation Unit (FSRU) applications and Liquefied Natural Gas (LNG) transfers, it becomes crucial to thoroughly assess the heat transfer performance under two-phase conditions. The literature studies showed that two-phase localized heat transfer within PCHEs proves to be a challenging task. Therefore, it is necessary to study the two-phase heat transfer through CFD simulation, which can possibly decrease energy consumption and manufacturing costs. This study aimed to gain insights into the behaviour of two-phase flow during flow vaporization in a straight channel by combining experimental observations with numerical simulations. The simulations focused on a horizontal channel, using nitrogen as the working fluid. Particular attention was given to the evolution of the flow modes, and the local flow and transport phenomena were analysed. In addition, the accuracy of the simulations was validated with experimental data.

2. Methodology

2.1. A PCHE model preparation and boundary conditions

This study conducted the experimental parameters of straight channel PCHE using two-phase nitrogen working fluid [12]. The experiment used different inlet conditions for the hot and cold sides: two-phase for the cold and gas phase for the hot. The hot and cold sides had distinct plates, with straight-channel and N-type-channel designs, respectively. Both sides featured aligned channels within the core, with a 446 mm length for core heat transfer. Therefore, the two-phase flow numerical 3D model channel length was considered 446 mm, and the semi-circular channel diameter was 0.884 mm. Real PCHE systems use a single inlet and outlet nozzle to distribute fluid across multiple microchannel. Inlet and outlet header designs, fluid states, and channel patterns can lead to misdistribution [12]. Simulations based on a single channel may not reflect actual outcomes due to these complexities. Performing simulations for all channel is very time-consuming, especially for diverse cases. Software limitations exist for simulating the nitrogen phase change from liquid to gas. PCHE's alternating cold and hot layer arrangement leads to a periodic boundary condition. Assuming uniform heat loss, the majority of heat from hot-side channels transfers to cold-side channels. Therefore, the present simulation was considered a single-channel PCHE, as shown in Figure 1. For the boundary condition, the computational model set three types of surfaces: inlet mass flowrate, outlet pressure drop, and heat wall. In simulation, a single-straight channel geometry was tested for model verification and evaporation flow visualization. The model was verified by using both cold (liquid) nitrogen and hot (vapour) nitrogen. Therefore, the heat wall boundary conditions were a heat source wall used on the cold side and a heat sink wall used on the hot side.

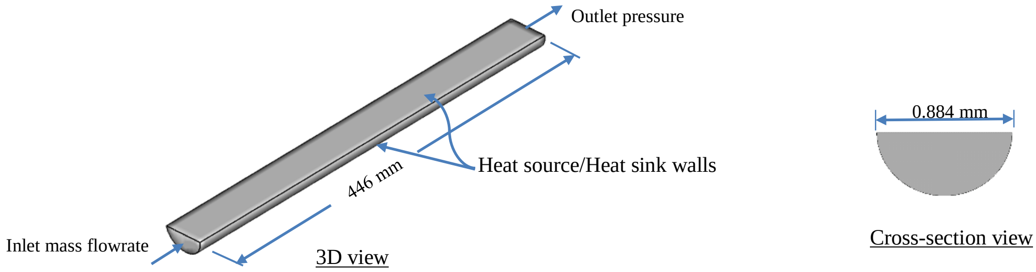

Figure 1. A single-channel PCHE geometry and boundary conditions.

2.2. Numerical simulation method of multiphase flows

This paper utilizes the Volume of Fluid (VOF) model to analyse phase-to-phase interactions between fluids, including mass, momentum, and energy transfers at the interphase. In the VOF model, computational cell of volume fractions for each phase are recorded. All phases of volume fractions sum to unity [13].

$$\alpha_l + \alpha_g = 1 \tag{1}$$

where α_l represents the volume fraction of the liquid phase and α_g is for vapor phase, respectively. The conservation equations are employed to track the surface between these phases, and the equations are computed for the volume fraction of each phase. The continuity equations for each phase can be understood as:

$$\frac{\partial \alpha_l}{\partial t} + \nabla.(u\alpha_l) = \frac{-S}{\rho_l} \tag{2}$$

$$\frac{\partial \alpha_v}{\partial t} + \nabla.(u\alpha_v) = \frac{-S}{\rho_v} \tag{3}$$

where S represents the mass transfer rates due to phase change, expressed in kg/(m^3·s). Based on the Navier-Stokes formulations and the interfacial two-phase flow, a momentum transport equation is present in cells for the two phases. This equation depends on the volume fractions of all phases, and it must also consider the force caused by surface tension at the interface.

$$\frac{\partial}{\partial t}(\rho \vec{u}) + \nabla.(\rho \vec{u}\,\vec{u}) = -\nabla p + \nabla.\left[\mu\left(\nabla\vec{u} + \nabla\vec{u}\right)\right] + \rho\vec{g} + \vec{F}_\sigma \tag{4}$$

In this context, $\vec{F}_\sigma$ defines the volumetric surface tension force, applying the Continuum Surface Force (CSF) model introduced by Brackbill et al. [14]. Here, $\vec{u}$ is the shared velocity field, p stands for pressure, and F represents the gravitational force.

$$F_\sigma = \sigma\frac{\alpha_l\rho_l k_g \nabla\alpha_g + \alpha_g\rho_g k_l \nabla\alpha_l}{0.5\left(\rho_l + \rho_g\right)} \tag{5}$$

where the interfacial surface tension between the phases symbols as σ (N/m) which can be expressed in terms of the pressure jump across the surface, acting as the source term in the momentum equation. ρ_l and ρ_g denote the liquid density and vapour density, while k_l and k_g represent the curvatures of the liquid and vapour phases, respectively. To adjust the body force term in the surface tension, the curvatures of the phases use in calculation which can be defined as,

$$k_l = \frac{\nabla\alpha_l}{|\nabla\alpha_l|}, k_g = \frac{\nabla\alpha_g}{|\nabla\alpha_g|} \tag{6}$$

As the previous discussion, the VOF model simulates the movement of distinct phases by tracing the interface's motion across the entire solution domain. The continuity equation is employed to solve for the volume fraction of each phase, thereby tracking the interface between the phases. This approach accounts for situations where a control volume is not entirely occupied by a single phase.

The energy equation, shared between the liquid and vapour phases can be defined as follows:

$$\frac{\partial}{\partial \mathrm{t}}(\rho E) + \nabla.\left[\vec{u}\left(\rho E + p\right)\right] = \nabla.\left(k_e \nabla T\right) + \dot{Q} \tag{7}$$

The equation involves the shared temperature field, denoted as *T*, along with the enthalpy represented by *E*. And the effective thermal conductivity, k_e , plays a crucial role in the equation. Additionally, the term $\dot{Q}$ (W/m^3) incorporates the heat transfer rates occurring through the interface.

$$E = \frac{\left(\alpha_l \rho_l E_l + (1\text{-}\alpha_l)\rho_g E_g\right)}{\left(\alpha_l \rho_l + (1\text{-}\alpha_l)\rho_g\right)} \tag{8}$$

$$k_e = \alpha_1 k_{e,l} + (1-\alpha_l) k_{e,g} \tag{9}$$

In which the values of E_l and E_g are determined based on the specific heat of liquid and vapor phases demonstrated by:

$$E_l = C_l\left(T - 298.15\right), E_g = C_g\left(T - 298.15\right) \tag{10}$$

2.2.1 Mass source term

To simulate the evaporation and condensation processes, a mass transfer model based on Lee (1980) and is adapted. In this model, the phase change is represented by a mass source term, which is primarily influenced by constant pressure and the saturation temperature. If the saturation occurs at $T \geq T_{sat}$, the evaporation process takes place. During this process, the mass of the liquid phase decreases, while the mass of the vapour phase increases within the control volume. The magnitudes of mass source term are:

$$S = c_l \alpha_l \rho_1 \frac{T\text{ - }T_{sat}}{T_{sat}} \tag{11}$$

$$S = c_g \alpha_g \rho_g \frac{T\text{ - }T_{sat}}{T_{sat}} \tag{12}$$

When the saturation occurs at $T < T_{sat}$, it occurs the condensation process meanwhile the mass of the liquid phase increases and the mass of vapor phase decreases in the control volume respectively.

To ensure a satisfactory numerical convergence of the interfacial temperature at T_{sat}, the empirical coefficients c_l and c_g are needed to be fine-tuned and can be expressed as a time relaxation parameter with unit l/sec. Large c_l and c_v values cause convergence issues, while small values lead to a significant deviation between the interfacial temperature and the saturation temperature. In this study, the value of c_l and c_g are set equal to 10 s^{-1} which has the best convergences solution of continuity and energy equations with the minimum deviation from saturation temperature at the interface.

2.2.2 Heat source term

The evaporation and condensation mass transfer source terms are developed from the heat transfer source term. This enables the direct definition of the heat transfer source as:

$$\dot{Q} = h_{lg}.S \tag{13}$$

where h_{lg} represents the latent heat, J/kg.

3. Results and discussion

3.1. Mesh grid sensitivity test

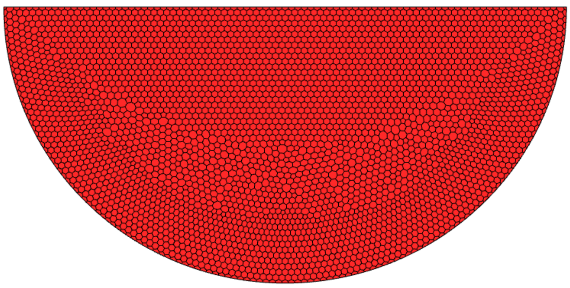

Figure 2. A cross-sectional view of the channel's polyhedral mesh for the PCHE model.

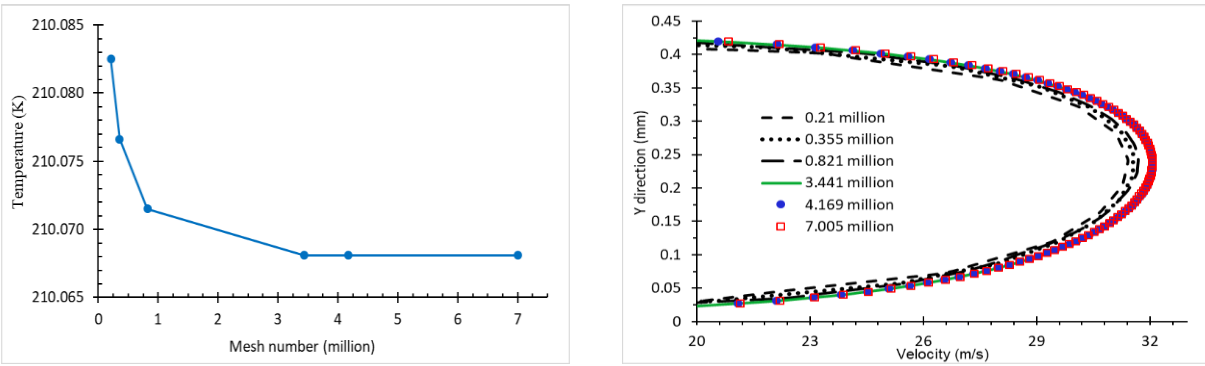

Outlet temperature

Velocity profile at centre of outlet

Figure 3. Shows the grid sensitivity test for CFD simulation convergence.

The 3D numerical simulation was carried out using the ANSYS Fluent program. A mesh grid convergence study was conducted under steady-state conditions vapor nitrogen. Polyhedral elements were used to mesh the numerical model, as shown in Figure 2. Six sets of grid numbers were simulated and compared, considering an inlet mass flowrate of 1001.5 kg/hr, inlet temperature of 288.45 K, inlet fluid pressure of 0.82 MPa and a heat sink of -25.6 kW of the entire PCHE channels. The continuity, momentum, and energy governing equations were solved using the SST k-omega turbulence model and the Semi-Implicit Method for Pressure-Linked Equations (SIMPLE). Thermo-physical properties, influenced by temperature and pressure, were sourced from NIST chemistry webbook and implemented in the program using a piecewise-linear approach. The outlet temperatures and velocity profiles from the numerical simulations using six different grid numbers were compared, as depicted in Figure 3. Ultimately, a grid with over 3 million elements was chosen for its accuracy and efficiency in the subsequent study. The decision on the optimal number of elements was based on 3.441 million the element size.

3.2. Numerical model verification

An experimental data was carried out to verify the numerical model PCHE, using nitrogen (N_2) as liquid fluid and gas fluid, respectively [12]. The verification considered both steady and transient experimental conditions. The experimental PCHE was designed for industrial-scale use with a capacity of up to 50 kW as a recuperator on a floating storage regasification unit (FSRU). This experiment analysed the flow rate effect of the hot side on the PCHE, which holds particular importance in the thermal and hydraulic analysis of the PCHE. Moreover, in an effort to minimize heat loss or gain, the experiment included three additional cases under single-phase conditions. The recorded data on outlet pressure and temperature was used to calculate the effective heat transfer. In the present study, steady-state numerical analysis was employed to investigate the impact of flow rate variations on the hot side. Additionally, heat loss experiments were conducted as part of the current numerical evaporation transient analysis. The experimental data used for the verification of the numerical model through the equation below [12]:

$$\textit{Absolute percent error} = \left| \frac{(T_{CFD} + 273.15) - (T_{Exp} + 273.15)}{(T_{Exp} + 273.15)} \times 100\% \right| \qquad [14]$$

3.2.1. Steady state condition

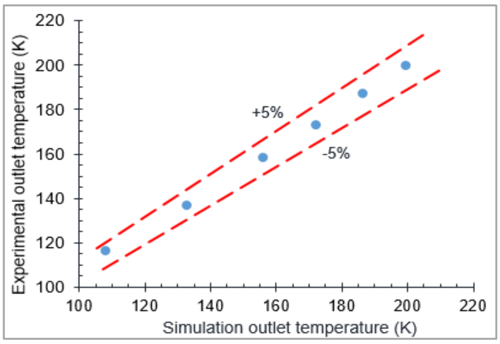

Figure 4. Comparison between experimental and simulation results under steady state condition (hot side).

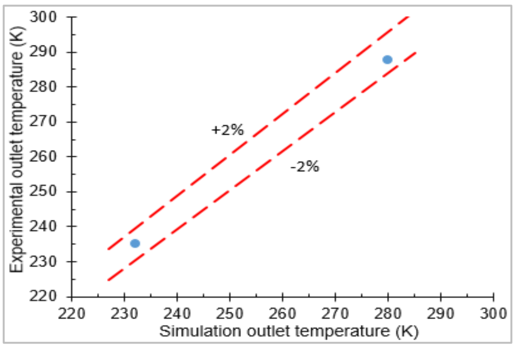

Figure 5. Comparison between experimental and simulation results under transient condition (cold side).

To validate the simulation, outlet temperatures were measured. The hot side operated under steady-state vapour conditions. The inlet mass flowrate of the entire PCHE model varied from 531.5 kg/h to 1001.5 kg/h. The inlet temperatures and pressures are 288.45–288.95 K and 0.82-0.83 MPa. The heat sink ranged from -25.6 kW to -27.5 kW. The present results showed good agreement, as shown in figure 4, compared with experimental results [12].

3.2.2. Transient state condition

The cold side simulated for analysis of transient two-phase (vapour-liquid) conditions. For case 1, the inlet mass flowrate of the entire PCHE model, temperature, pressure, and heat source were 213 kg/hr, 102.05 K, 1.35 MPa, and 18.2 kW. In case 2, these values were 205.1 kg/hr, 102.85 K, 1.59 MPa, and 20.6 kW. The time step was chosen to ensure a Courant number lower than 1 and ranged from 0.01 to 0.00001 seconds. The numerical simulation presented in this study exhibited excellent agreement with experiments, with an absolute error of less than 2% in Figure 5. Thus, the outcomes of this study can be validated.

3.3. Two-phase flow analysis

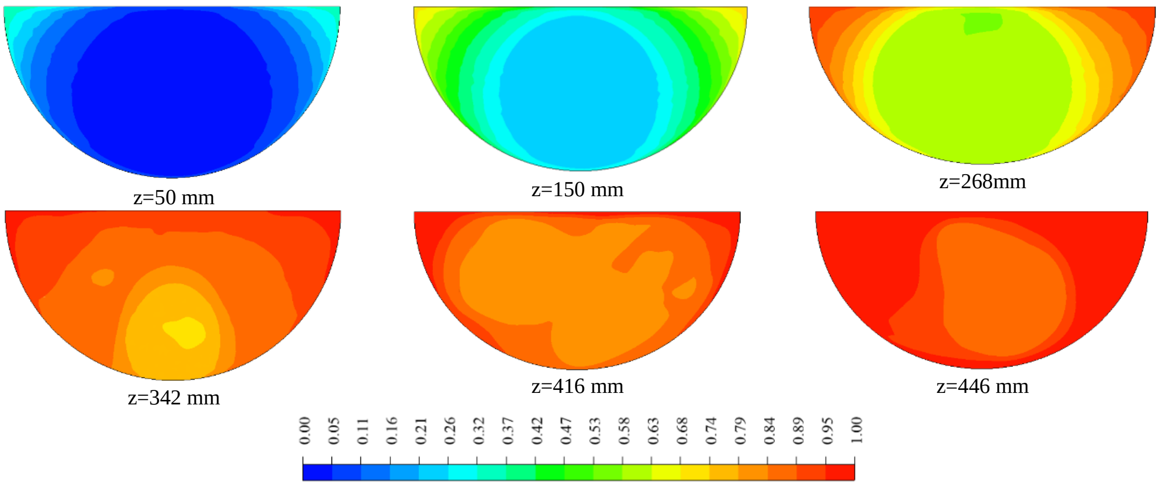

Figure 6. Illustrates vapour-phase distribution at different cross-sectional views (a number of 0 represents the liquid phase, while a number of 1 corresponds to the fully vapor phase).

The validated model was used to simulate nitrogen evaporation flow patterns in PCHE minichannels. The analysis focused on the second case of a transient test. Cross-sectional views were taken at different vapour qualities to analyse the distribution of two-phase flow along the channel, as shown in Figure 6. Initially, the gas phase at the sharp corners emerged where the lower and upper surfaces of the channel intersected in the flow direction. Subsequently, it extended towards the middle of the channel surface. The liquid phase from the heated wall evaporated and transitioned into the gas phase. The observation revealed an increasing vapour presence along the upper channel and a decrease in liquid nitrogen content along the lower channel due to gravity effects.

Figure 7 illustrates the velocity vectors representing the vapour phase pattern within the cross-sections. Flow velocity was significantly low at the sharp corners, corresponding to the initial emergence of the vapour phase. The application of heat flux to the fluid from the upper and lower surfaces led to earlier vaporization near these surfaces compared to the central region. The study revealed the emergence of multiple vortices near the phase transition interface. This occurrence was prompted by the rapid convection of nitrogen from the vapour to the liquid-vapour interface, a result of the preferential evaporation of nitrogen, which is not uniform. As a result, the liquid-vapour flow exhibited vortex flow, resulting in improved heat exchange efficiency. The interface tension between phases depends on their composition, resulting in attraction or repulsion. Particularly, the non-uniform evaporation rate drives movement from the side with high evaporation flux to that with low evaporation flux. This process reduced energy dissipation linked to the inherent fluid flow caused by evaporation. Over long distances, the vapour field undergoes substantial changes due to increased evaporation. Although the radial velocity component increases, vortices are still present. Due to strong convection, a wake region with a recirculation vortex becomes noticeable.

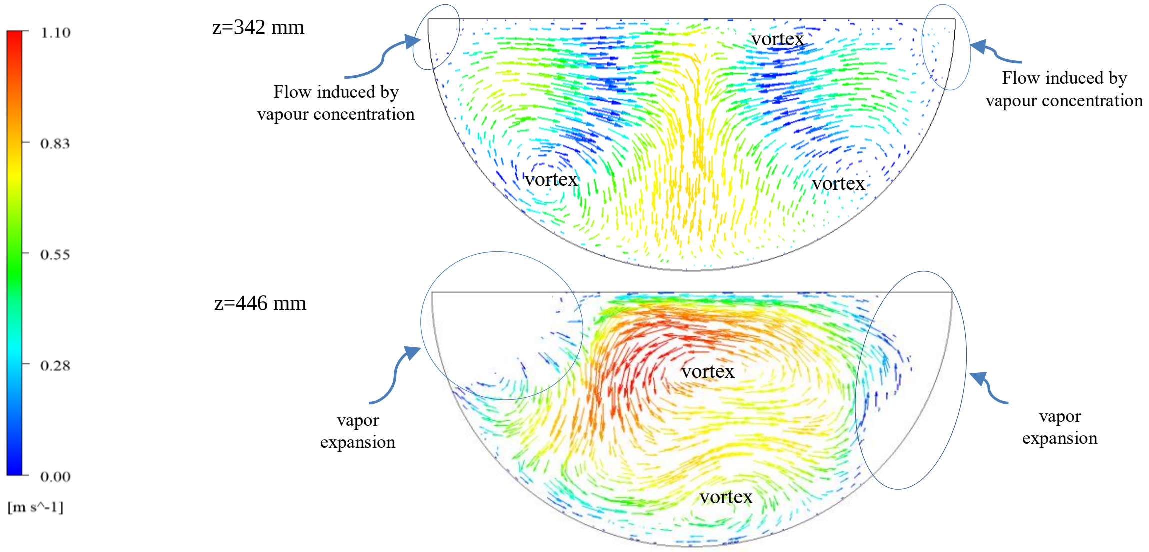

Figure 7. Behaviours velocity of a vapour phase pattern inside undergoing evaporation.

This study examines the interesting dynamics of evaporation processes, interpreting how and why flow patterns transition from symmetry to asymmetry. Initially, under uniform conditions, symmetric flow structures emerge due to consistent droplet shapes and substrate properties at z = 50–268 mm in Figure 6. As the evaporation process progresses, it becomes influenced by external factors and property gradients, leading to the development of complex and asymmetric flow structures. These asymmetrical flow fields are, in part, attributed to non-uniform heat distribution, fluid property variations, and channel geometry effects, causing non-uniform evaporation rates and differences in evaporation mass flux, as shown in Figure 7. At z = 342-446 mm in Figure 6, the vapor-mediated interactions further contribute to the asymmetry by introducing concentration gradients within the liquid phase, leading to long-range attraction or repulsion forces and shifts in flow patterns. The introduction of a volatile liquid phase disrupts the existing symmetry, initiating significant changes in the vapor field dynamics and further accentuating the asymmetry. In essence, the complex interplay of external influences and vapor-mediated interactions throughout the evaporation process accounts for the transition from initial symmetry to asymmetry in flow patterns.

4. Conclusion

The study focused on nitrogen evaporation in PCHE minichannels. A simplified model was used for the numerical analysis of evaporation flow and characteristics under different conditions. Numerical results aligned well with experimental data. During evaporation, the gas phase initially emerged at the sharp corners where the channel's upper and lower surfaces met in the flow direction. It then extended along the surface towards the middle. Non-uniform vortex flow patterns were identified at various locations and depicted as flow pattern maps. With increasing flow distance, forced convective effects became prominent, marked by high velocities and improved vapour quality. This study introduced the fundamentals of flow evaporation, particularly in the context of cryogenic applications. This knowledge provides a reliable tool that can be effectively applied in various two-phase scenarios within the field of computational fluid dynamics (CFD) analysis. Future work will analysis the flow patterns, regimes, and distributions within channels in order to understand the complex mechanisms underlying the flow evaporation heat transfer process. Additionally, there is a need to develop more appropriate transition criteria to define whether the heat transfer process is primarily governed by two-phase forced convection.

5. Acknowledgments

The authors express their gratitude for the support received from the Mechanical and Process System Engineering Program and the Vithedbundit Scholarship at the Institute of Engineering, Suranaree University of Technology (Thailand).

6. References

[1] Nikitin K, Kato Y, Ngo L. (2006). Printed circuit heat exchanger thermal–hydraulic performance in supercritical CO2 experimental loop. *International Journal of Refrigeration*, 29:807-14.

[2] Jiang T, Li M-J, Yang J-Q. (2023). Research on optimization of structural parameters for airfoil fin PCHE based on machine learning. *Applied Thermal Engineering*, 229.

[3] Oleiwi Samarmad A, Mohammad Jaffal H. (2023). Performance evaluation of a printed circuit heat exchanger with a novel two-way corrugated channel. *Results in Engineering*, 19.

[4] Zhou Y, Yin D, Guo X. (2023). Flow and heat transfer performance of molten salt and CO2-based mixtures in printed circuit heat exchangers. *Applied Thermal Engineering*, 224.

[5] Safari Y, Abdollahi SA, Mahmoudi M, Safaei M, Taghinia F, Pasha P, et al. (2023). Numerical study of heat transfer of wavy channel supercritical CO_2 PCHE with various channel geometries. *International Journal of Thermofluids*, 18.

[6] Jin F, Yuan D, Chen D, Hu L, Huang Y, Bu S. (2023). Experimental study on cooling heat transfer performance of supercritical CO_2 in zigzag printed circuit heat exchanger. *International Journal of Heat and Mass Transfer*, 215.

[7] Goto T, Jige D, Inoue N, Sagawa K. (2023). Condensation flow visualization, heat transfer, and pressure drop in printed circuit heat exchangers with straight and wavy microchannels. *International Journal of Refrigeration*.

[8] Hu H, Li Y, Li J. (2023). Experimental investigation on flow boiling characteristics in zigzag channels under different sloshing conditions. *Applied Thermal Engineering*, 230.

[9] Yoo JW, Nam CW, Yoon SH. (2022). Experimental study of propane condensation heat transfer and pressure drop in semicircular channel printed circuit heat exchanger. *International Journal of Heat and Mass Transfer*, 182.

[10] Shin J-H, Lee KH, Yoon SH. (2022). Experimental work for the performance of a printed circuit heat exchanger (PCHE) using nitrogen under trans-critical states. *Energy Reports*, 8, 12765-75.

[11] Liu T-L, Fu B-R, Pan C. (2012). Boiling two-phase flow and efficiency of co- and counter-current microchannel heat exchangers with gas heating. *International Journal of Heat and Mass Transfer*, 55, 6130-41.

[12] Shin J-H, Yoon SH. (2020). Thermal and hydraulic performance of a printed circuit heat exchanger using two-phase nitrogen. *Applied Thermal Engineering*, 168.

[13] Hasanpour B, Irandoost MS, Hassani M, Kouhikamali R. (2018). Numerical investigation of saturated upward flow boiling of water in a vertical tube using VOF model: effect of different boundary conditions. *Heat and Mass Transfer*, 54, 1925-36.

[14] Brackbill J KD, Zemach C. (1992). A continuum method for modeling surface tension. *Journal of Computational Physics*, 100, 335–354.

The 13th TSME International Conference on Mechanical Engineering
12th – 15th December 2023
Chiang Mai, Thailand

TSF0013

Extrusion Flow of Concentrated Particle Suspensions in Abrupt Contraction Channel

T Koshiba[1,*] and T Yamamoto[2]

[1] National Institute of Technology, Nara College,
22 Yatacho, Yamatokoriyama, Nara, 639-1080, Japan
[2] Osaka Electro-Communication University,
18-8, Hatsucho, Neyagawa, Osaka, 572-8530, Japan

* Corresponding Author: koshiba@mech.nara-k.ac.jp

Abstract. In this study, we experimentally examined the extrusion flow of a concentrated particle suspension in an abrupt contraction channel. We discussed the particle behavior from the results in the flow resistance and flow visualization. The fluid used in the experiment was three kinds of mixtures of transparent acrylic spherical particles with glycerine which is a dispersion medium. In measurement of flow resistance, we confirmed that the flow resistance increases with increasing of particle concentration. In addition, in the flow visualization, we found that the particle concentration was higher at the corners near the abrupt contraction part. The particle concentration distribution in this channel was caused by the flow velocity distribution. Furthermore, separately, in the experiment using a squeezing flow, it was found that there is a correlation between particle concentration changes and flow resistance.

Keywords: Particle suspension, Extrusion flow, Abrupt contraction channel, Particle aggregation.

1. Introduction

Particle suspensions, which are mixtures of solid particles and liquids, can be found in many fields. For example, there are raw materials for composite materials, drug development, food industry, and geotechnical engineering. In general, particle suspensions are characterized by many factors such as particle shape, particle size, particle properties, particle concentration, and dispersion medium properties. In particular, the flow of concentrated suspensions is non-Newtonian and contains many interesting phenomena in the view points of rheology [1-3]. For example, it is reported that the jamming effect and dilatant behavior caused by particle aggregation during flow are related to the shear-thickening property in the shear viscosity of concentrated particle suspensions [4-6]. The shear-thickening property practically appears as an increase in flow resistance. The increase in flow resistance is a significant technical problem from the viewpoint of energy consumption and facility design in fields that handle concentrated particle suspensions, and efforts are being made to suppress the increase in flow resistance. On the other hand, the particle aggregation in particle suspensions is caused by interactions between particles during flow, and experimental and numerical studies have been conducted to clarify the occurrence mechanism. In particular, such interaction between particles depends on the particle size, and in case of colloidal size below 10 μm, the colloidal chemical interactions are considered to be dominant. Furthermore, in research on such size, noting surface properties of particle and statical/dynamical interaction between particles, the particle behavior is considered from a relatively microscopic point of view. On the other hand, in the case of particle size beyond 10 μm or more, since the hydrodynamic interaction becomes more remarkable than the colloidal chemical action, the subjects of research focus on a macroscopic behavior observed in various flow regimes such as a simple shear flow and a contraction flow. In particular, because the velocity profile of bulk flow gives the change in velocity among individual particles, the particle migration along the velocity gradient is induced [7]. Such particle migration induced by shear flow is interesting phenomena, and numerical and experimental studies have been carried out by many researchers.

Under such background, we noted the effect of flow geometry on the behavior of particle suspension and aimed to experimentally clarify the flow of particle suspensions with thick concentration having the particle of relatively large size (>100 μm), where hydrodynamic interactions are considered to be dominant. We focus on the extrusion flow using an abrupt contraction channel, and carried out the experiment for the measurement of flow resistance and flow visualization. Furthermore, the effect of particle concentration to flow resistance and flow patterns were discussed.

2. Experiments

2.1. Experimental apparatus

Figure 1 shows the schematic view of the experimental apparatus. The test fluid enclosed in the test section is given a flow by a drive piston that moves at a constant speed. Movement of the drive piston takes place via a direct drive rail that is directly connected to a servo motor. Speed control of the drive piston is performed by rotation control of the servomotor and monitored by a displacement sensor attached to the linear guide rail. The flow resistance is evaluated by the torque output of the servo motor. In the experiment of flow visualization, an LED light source was used and flow images are taken with a video camera installed at the top of test section. Although not shown in the figure, two polarizing plates are provided on the light incident side and the light emitting side, respectively, and the flow visualization is performed under a state of crossed nicols.

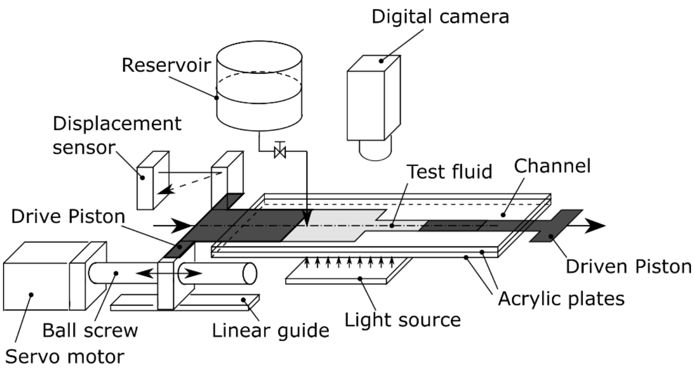

Figure 1. Schematic view of experimental apparatus.

Figure 2 shows the details of the test section. The channel size is shown in the same figure. The stroke of the drive piston is 25 mm. The abrupt contraction channel is made of stainless steel with a thickness of 1 mm and is constructed by sandwiching between two acrylic plates with a thickness of 5 mm. The contraction ratio of the channel is 4:1. In addition, the driven piston having a width of the flow channel is provided on the outlet side of the flow channel, and a constant volume condition is maintained in the flow channel.

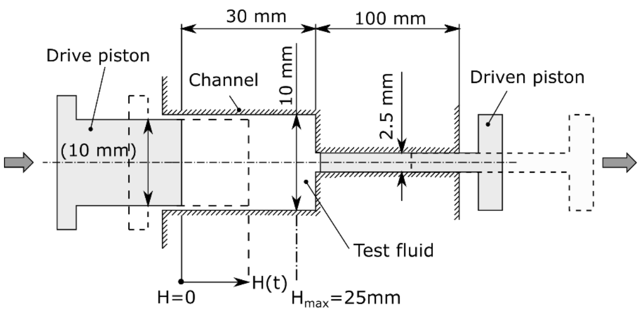

Figure 2. Details of test section.

2.2. Test Fluid

In this experiment, as test fluids, three kinds of suspensions with different particle concentrations were used. In common for each fluid, the dispersoids (solid particles) are spherical particles (φ125-150 μm) made of transparent acrylic resin, and the dispersion medium (liquid) is glycerin. In addition, such particle size was selected to facilitate visualization of change in particle concentration during flow. The details of test fluids are shown in Table 1.

Table 1. Test fluids.

Fluid	Concentration (vol.%)
A	30
B	40
C	50

Figure 3 shows the property of steady shear viscosity with regard to test fluids. The measurement of steady shear viscosity was carried out using a rotational rheometer with the concentric Couette fixture. In addition, as the reference, the viscosity of glycerin which is the dispersion medium is also shown in the same figure. From Figure 3, it can be seen that the shear viscosities of particle suspension are non-Newtonian and show the shear-thinning of shear viscosity. The shear thinning of shear viscosity becomes remarkable with increasing of particle concentration. Furthermore, for all suspensions, as the shear rate increases, the shear-thinning property becomes gentler and shows a tendency to approach a constant value.

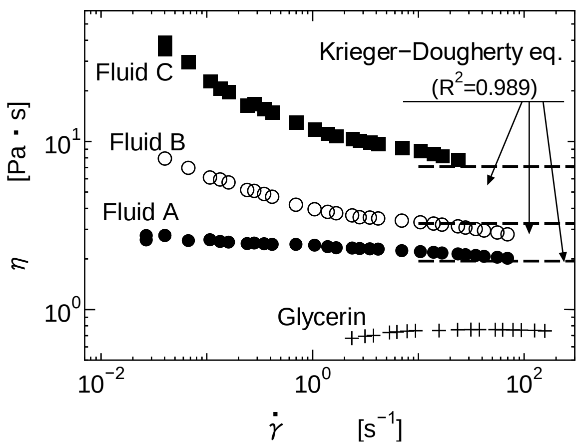

Figure 3. Steady shear viscosities η versus shear rate $\dot{\gamma}$ for test fluids.

Regarding to the shear viscosity of particle suspension, various models have been proposed until now. Among these models, it is known that the Krieger-Dougherty's semi-theoretical Equation [8] is valid for the wide range of volume fraction, relatively. Therefore, we tried to fit Krieger-Dougherty's Equation (Equation (1)) with the shear viscosity of suspension in the high shear rate range.

$$\mu = \mu_f \left[1 - \frac{\varphi}{\varphi_m}\right]^{-a\varphi_m} \tag{1}$$

Here, μ is the suspension viscosity, μ_f the viscosity of glycerin which is the dispersion medium, φ the volume fraction of particle. Besides, a, φ_m are the fitting parameters. In particular, φ_m corresponds to the maximum packing fraction of particle. In this experiment, a, φ_m were set to 2.35 and 0.65, respectively.

In Figure 3, we found that the shear viscosity of particle suspension in the range of high shear rate was roughly consistent with Krieger-Dougherty's Equation. The value of R^2 between the Krieger-Dougherty Equation and viscosity data is shown in Figure 3.

3. Results and Discussion

3.1. Flow resistance

Figure 4 shows the change in flow resistance for each fluid at the piston speed of 7.0 mm/s and the difference in the piston speed with regard to the flow resistance for Fluid B. In Figure 4(a), in the case of Fluid C with a high particle concentration, the increase in flow resistance appears immediately after the movement of drive piston. On the other hand, in Fluid A having a low concentration, the change in the flow resistance is not clearly observed during the moving process of the driving piston. In the case of Fluid B, although the flow resistance is not as remarkable as that of Fluid C, the gentle increase in the resistance can be confirmed until the halfway point of piston stroke. However, passing the halfway point of piston stroke, the flow resistance shows a steep increase. Defining the point showing the steep increase in resistance as H_c, the magnitude of H_c depends on the piston speed and approaches to the right side with increasing in piston speed. However, the increment tendency of resistance beyond H_c has almost the same slope regardless of piston speed. Therefore, regarding Fluid B, we examined the critical point H_c of resistance increase with respect to the piston speed.

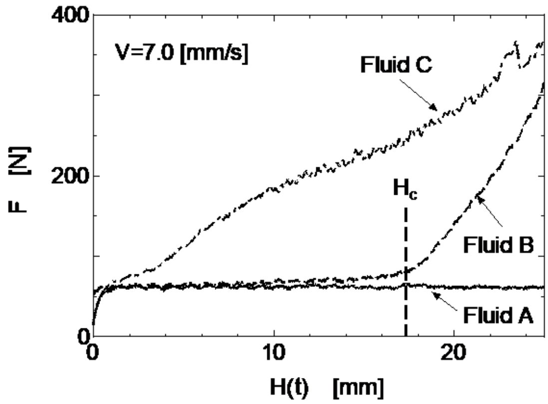

(a)

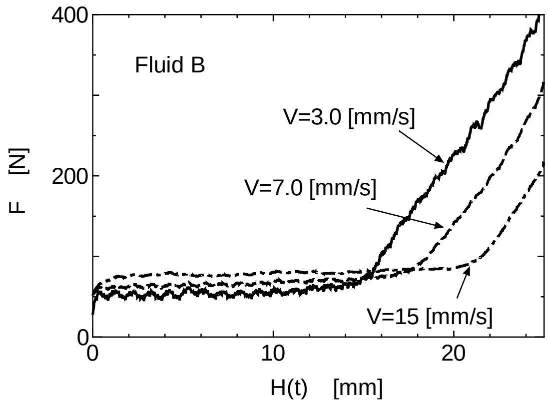

(b)

Figure 4. Change in the flow resistance during extrusion flow: (a) difference in the particle concentration on the flow resistance, (b) the effect of piston speed on the flow resistance.

Figure 5 shows the results. From Figure 5, it was found that the position of the critical point moved to the contraction part (H=25 mm) as the piston speed increased. This increase in the flow resistance is expected to be due to the particle aggregation at this stage, but its occurrence was expected to be transited the downstream side due to inertial force effects.

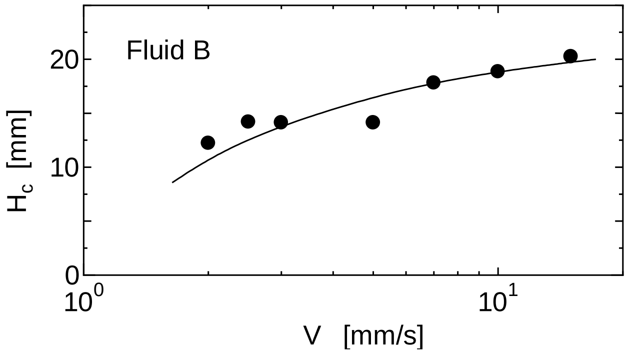

Figure 5. Relationship between the piston position at the increment of flow resistance and the piston velocity.

3.2. Flow visualization

Figure 6 shows the flow visualization results. These images shows the difference depending on the fluid at the piston speed of 3mm/s. In all images, the moving direction of the piston is to the right, and the fluid is pushed out to the right. From Figure 6, for Fluid A, there are almost no difference between the images during flow and that for the static state. On the other hand, in Fluids B and C, when the tip of piston approaches to the contraction part, the images gradually becomes whitish. In particular, for Fluid C, the overall brightness increases when the piston position is H = 15.5 mm, and becomes even more noticeable when the piston position is H = 22.8 mm.

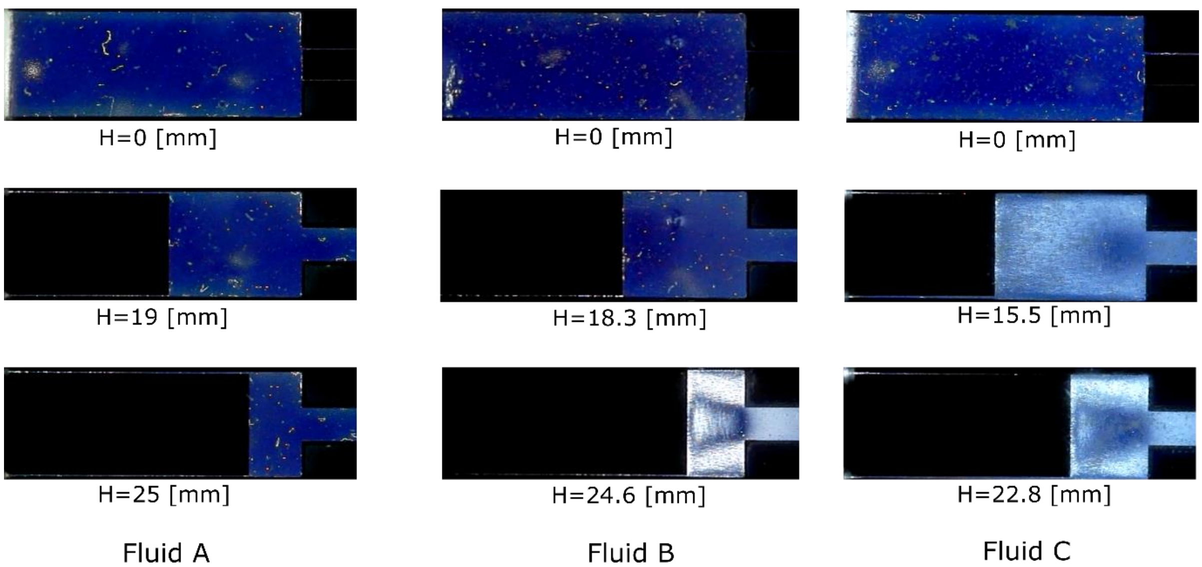

Figure 6. Flow images for each fluid at the piston speed of 3 mm/s. The flow direction is from left to right.

The change in brightness means a change in the polarization state of transmitted light in the polarized observation field, and in the case of a particle suspension, it is thought to be due to a change in the particle concentration in the fluid. Also, the area near the corner of the channel is brighter than the center of the channel, but these facts suggest that the particle migration relating to the velocity distribution in the channel during the movement of the piston is induced. In other words, since the flow velocity near the corners becomes slow, the movement of particles is also slow. Therefore, because the spacing between particles is dense, the particles begin to aggregate and the particle concentration becomes large.

3.3. Relationship between flow resistance and change in brightness

Examining the relationship between the results of the flow resistance shown in Figure 4 and the brightness distribution in Figure 6 is of important to clarify the extrusion flow of concentrated particle suspension. However, as shown in Figure 6, the distribution of particle concentration covers in the whole of flow channel and there are locally large differences in the concentration. Besides, the suspension particles used in this experiment are transparent particles, and the change in the brightness of fluid with accompanying the increment of flow resistance includes the effect of the polarization state of the transmitted light. The change in brightness seen in Figure 6 is similar to the phenomenon called "force chain" reported in powder engineering [6,9]. The force chain appears in applying the squeezing force to transparent grains packed in the container and means the propagation path for force associated with grain contact. In the large size of particles, many short paths connecting particles overlap, and these paths are observed as the bright streak-like pattern. Therefore, we tried to find the correlation between the pushing force of piston and particle concentration using a squeezing flow as other method. The schematic view of squeezing flow is inserted in Figure 7. The squeezing flow is arisen out by pushing the piston to the dense suspension in a container. The channel using in the experiment of squeezing flow is the same channel as the extrusion experiment, but the driven piston is fixed. In addition, to emphasize the change in the particle concentration during a squeezing process, the volume fraction of particle was set to 60 vol.%, which was higher than test fluids in Table 1. The relation of the pushing force of piston with the brightness in squeezing flow are shown in Figure 7. Additionally, the relationship between the volume fraction and the brightness at the rest state is also shown in Figure 7.

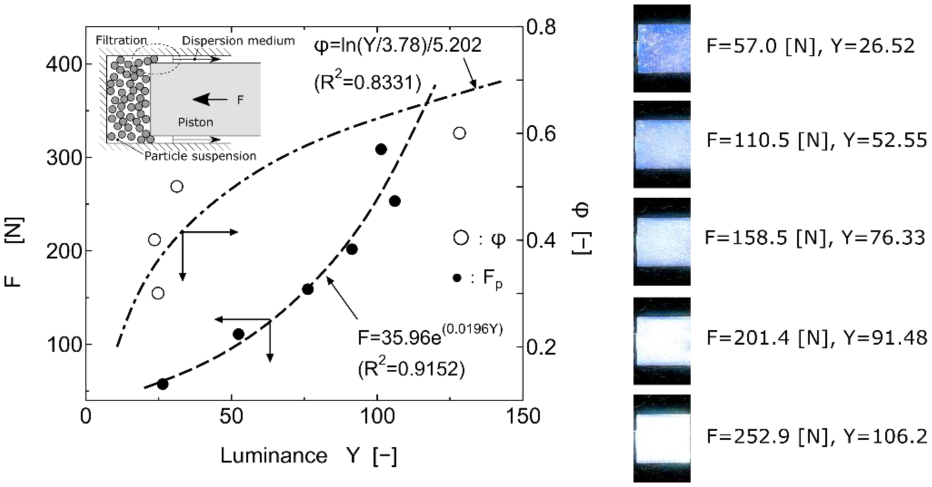

Figure 7. Relationship between the pushing force of piston and the luminance of image in experiments of a squeezing flow.

In Figure 7, the brightness for each image is evaluated by the luminance Y (Equation (2)) in YIQ color space converted from the RGB color space. As a result, we can find that both the volume fraction in suspension and the pushing load of piston are proportional to the luminance.

$$\begin{bmatrix} Y \\ I \\ Q \end{bmatrix} = \begin{bmatrix} 0.299 & 0.587 & 0.114 \\ 0.596 & -0.274 & -0.332 \\ 0.211 & -0.523 & 0.312 \end{bmatrix} \begin{bmatrix} R \\ G \\ B \end{bmatrix} \tag{2}$$

Therefore, we estimated the relation of the brightness of suspension with the volume fraction and the pushing load of the piston using the approximating curves. The approximating curves for the volume fraction and the pushing load are shown in Figure 7, respectively. From these curves, eliminating the luminance, we obtained the relation between the pushing load of the piston (F) and the particle concentration (φ) in fluids such as Equation (3).

$$\varphi = \frac{1}{5.202} \ln \left[\frac{1}{0.07409} \ln \left(\frac{F}{35.96} \right) \right] \tag{3}$$

Figure 8 shows the change in particle concentration with increasing in flow resistance. Figure 8 is based on the results of Figure 4(a). Comparing of Figure 8 with Figure 6, it seems that the prediction of particle concentration using Equation (3) relatively agrees with the brightness of images. In particular, as the piston position approaches 25 mm, the particle concentration for Fluid A and C converges to about 65 vol.%. This convergence value of volume fraction is almost the same as the $\varphi_m = 0.65$ in the Krieger-Dougherty Equation, described in Section 2.2. Accordingly, it is considered that Equation (3) represents the change in particle concentration with accompanying the insertion of piston, qualitatively. However, noting the onset of insertion of piston, we find that there is the difference between the prediction and the volume fraction in real. We guess that these differences relate to the accuracy of approximating curve regarding the luminance and particle concentration.

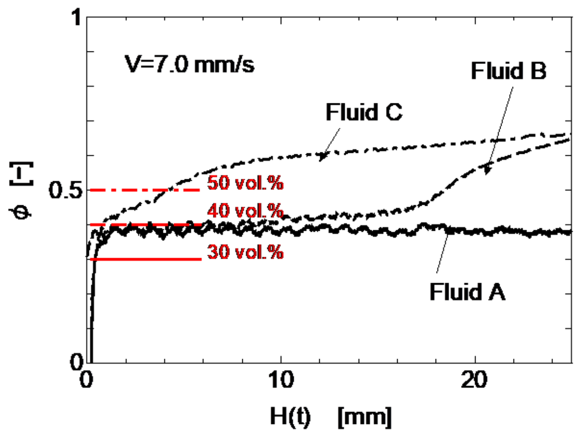

Figure 8. Change in particle concentration estimated from the luminance of flow images and the pushing force in a squeezing experiment.

4. Conclusion

In this study, the extrusion flow of particle suspension with dense concentration was experimentally examined using an abrupt contraction channel. In particular, the effect of the particle concentration to the flow resistance and flow pattern was discussed. In the measurement of the flow resistance, it was found that the flow resistance for suspension with higher concentration of particle increases with accompanying the insertion of drive piston. The piston position showing the increment of the flow resistance depends on the piston speed and approaches near the contraction part with increasing of piston speed. From results in flow visualization, we confirmed that the brightness of fluid flowing the abrupt channel, changes with accompanying the insertion of piston. It is predicted that the change in brightness is caused by particle migration due to the velocity distribution. Therefore, separately, examining the relationship between the flow resistance and flow image using the squeezing flow, we found that there is the correlation between both increment tendencies. Furthermore, estimating the change in particle concentration with accompanying the insertion of piston, we confirmed that the change in brightness shown in flow images is qualitatively represented by the correlated Equation obtained in the squeezing experiments. In this experiment, however, although we did not discuss on the particle size much more, it will be expected that more interesting phenomena occurs as the particle size became smaller. In future, we think that it is necessary to carry out the experiment targeting particle suspension with a smaller size below 100 μm.

5. References

[1] Otsubo, Y. (2003). The present status and prospect of suspension rheology. *Journal of the Society of Rheology, Japan*, 31(1), 15-22.

[2] Haw, M.D. (2004). Jamming, two-fluid behavior, and ”self-filtration” in concentrated particulate suspensions, *Physical Review Letters*, 92(18), 185506-1-185506-4.

[3] Kim, J., Xu, F., & Lee, S., (2017) Formation and destabilization of the particle band on the fluid-fluid interface, *Physical Review Letters*, 118, 074501-1-074501-6.

[4] Wagner, N.J., & Brady, J.F., (2009), Shear thickening in collodal dispersions, *Physics Today*, 62(10), 27-32.

[5] Kmibayashi, M., Ogura, H., & Otsubo, Y., (2008), Shear-thickening flow of nanoparticle suspensions flocculated by polyme bridging, *Journal of Colloid and Interface Science*, 321, 294-301.

[6] Cates, M.E., Wittmer, J.P. Bouchaud, J.-P. & Claudin, P., (1998), Jamming, force chains, and fragile matter, *Physical Review Letters*, 81(9), 1841-1844.

[7] Dbouk, T., Lemaire, E., Lobry, L., & Moukalled, F., (2013), Shear-induced particle migration: Predictions from experimental evaluation of the particle stress tensor, *Journal of Non-Newtonian Flud Mechanics*, 198, 78-95.

[8] Wilms, P., Hinrichs, J., & Kohlus, R., (2022), Macroscopic rheology of non-Brawnian suspensions at high shear rates: the influence of solid volume fraction and non-Newtonian behaviour of the liquid, *Rheologica Acta*, 61,123-138.

[9] Peters, J.F., Muthuswamy, M., Wibono, J., & Tordesillas, A., (2005), Chracterization of force chains in granular materials, *Physical Review E*, 72, 041307-1-041307-8.

The 13th TSME International Conference on Mechanical Engineering
12th – 15th December 2023
Chiang Mai, Thailand

TSF0015

Fundamental Flow Characteristics of Impinging Synthetic Jets

Michiya Yasumiba[1,*], Koichi Nishibe[2], Donghyuk Kang[3], and Kotaro Sato[4]

[1]Mechanical Engineering Program in the Graduate School of Engineering, Kogakuin University, 2665-1 Nakano-cho, Hachioji-shi, Tokyo, 192-0015, Japan
[2]Department of Mechanical Engineering, Tokyo City University, 1-28-1 Tamatsutsumi, Setagaya-ku, Tokyo, 158-8557, Japan
[3]Department of Mechanical Engineering, Saitama University, 255 Shimo-Okubo, Sakura-ku, Saitama-shi, Saitama, 338-8570, Japan
[4]Department of Mechanical System Engineering, Kogakuin University, 2665-1 Nakano-cho, Hachioji-shi, Tokyo 192-0015, Japan

* Corresponding Author: am22068@ns.kogakuin.ac.jp

Abstract. Research on impinging jets has proven valuable in several industrial sectors, including the cooling of high-temperature objects, cleaning object surfaces, and drying paint films. Moreover, impinging jets deliver exceptional cooling capabilities for mechanical components and electronic devices with high heat loads. Recently, synthetic jets have emerged as a potential solution for cooling ultra-compact devices, such as CPUs, owing to their simple driving principle and suitability for miniaturization and weight reduction. However, majority of these studies have primarily focused on temperature control, such as object cooling, with limited reports on the effects of the geometry and position of the collision object on the flow field. This study aims to address this gap by investigating the co-relation between the plate-to-slot distance and the dimensionless stroke through the placement of a constant length plate downstream of the synthetic jet. Moreover, the alternation in the vortex structure of the synthetic jet between the plate and the slot was observed by varying the length of the side surface of the slot. The main results are that the flow field of the impinging synthetic jet depends on the plate-to-slot distance, the dimensionless stroke, and the slot-side wall length. When the slot-side wall length is large and a certain value of plate-to-slot distance, the flow field was observed to differ from that of a continuous impinging jet depending on the dimensionless stroke.

Keywords: Impinging jets, Synthetic jets, Dimensionless stroke, Plate-to-slot distance.

1. Introduction

Impinging jets[1],[2] are often employed for localized cooling inside electronic devices because of their excellent heat dissipation effect. Recently, as the competition for the miniaturization of electronic devices has intensified, further space savings in cooling devices are required. Therefore, there is a growing trend in the application of synthetic jets[3]-[33], which have a simple driving principle and are suitable for miniaturization and weight reduction[3]-[11], instead of conventional small fans. For example, Gopal et al.[3] reported a six-fold increase in the life of light-emitting diode (LED) products compared with conventional small fans by implementing synthetic jets for LED cooling. Bazdidi-Therani et al.[4] observed that high-frequency synthetic jets have higher heat transfer rates than steady jets. However, because these studies focused on temperature control but did not examine the flow field in detail, the cooling mechanism remains unclear. In particular, the relationship between the basic flow characteristics of the jet and the position and geometry of the impinging object has not been discussed, and the optimal cooling conditions when a synthetic jet is applied remain unresolved.

In this study, a target flat plate of fixed length was placed downstream of a planar synthetic jet, and the behavior of the impinging jet was investigated numerically. In particular, the effects of the plate-slot distance and dimensionless stroke on the flow characteristics were analyzed. In addition, the behavior of the vortex structure formed between the plate and slot and the wall jet on the target plate, owing to the presence or absence of sidewalls parallel to the plate on the slot side, were observed.

2. Nomenclature

b_0	:	Slot width [m] ($= 5.0 \times 10^{-3}$ m)
x_w	:	Plate-to-slot distance [m]
X_w	:	Dimensionless plate-to-slot distance ($= x_w/b_0$)
s_w	:	Plate length [m]
S_w	:	Dimensionless plate length ($= s_w/b_0$)
U_{s0}	:	Characteristic velocity in synthetic jets [m/s] ($= \frac{1}{T}\int_0^{\frac{T}{2}} u_0(t)dt$)
γ	:	Kinematic viscosity coefficient
R_e	:	Reynolds number ($= U_{s0}b_0/\gamma = 1.49 \times 10^3$)
U_{c0}	:	Characteristic velocity in continuous jet [m/s]
u	:	Velocity along *x*-axis [m/s]
u_0	:	Velocity along *x*-axis at slot exit [m/s]
v	:	Velocity along *y*-axis [m/s]
t	:	Time [s]
T	:	Period of velocity oscillation at slot exit [s]
f	:	Frequency [Hz]
f^*	:	Dimensionless frequency ($= fb_0/U_{s0} = 1/L_0$)
l_0	:	Stroke length [m] ($= U_{s0}/f$)
L_0	:	Dimensionless stroke length ($= U_{s0}/fb_0$)

Figure 1 shows an enlarged view of the area near the slot exit. The position and length of the target plate are indicated by the symbols in the figure A comparison is made between the cases (a) where the slot side surface length is $30b_0$ and (b) where there is no wall parallel to the plate on the slot side to investigate the effect of the slot side surface owing to the plate–slot interaction.

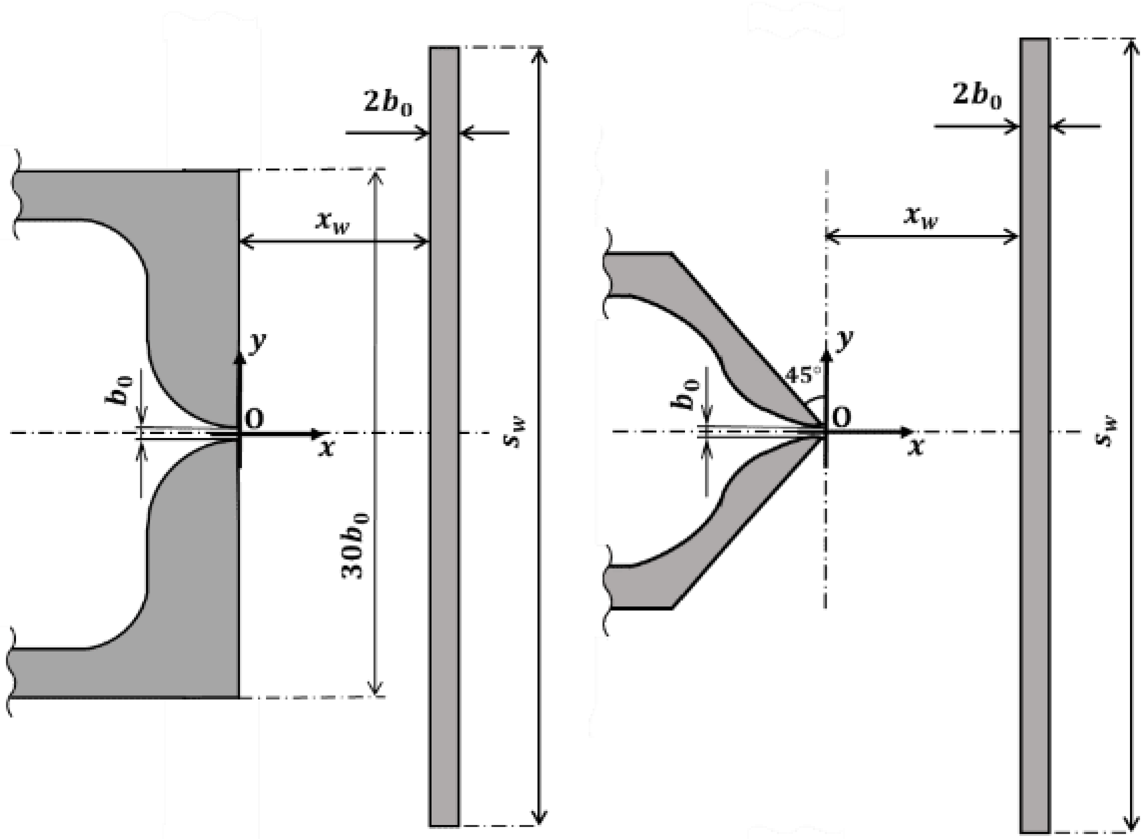

(a) Surface length of slot side is $30b_0$ (b) No wall parallel to plate on slot side

Figure 1. Diagram of slot exit.

3. Numerical Simulation

Ansys Fluent (ver. 2021 R1) was used for the numerical calculations. Because the validity of the numerical method has been confirmed by Yasumiba et al.[31], a two-dimensional incompressible viscous fluid was assumed and the standard k-ϵ model was applied to the turbulence model, following their method. Figure 2 shows the computational domain of the numerical simulation, using Figure 1(b) as an example. The boundary conditions were defined as the velocity at the slot inlet, static pressure at the outlet of the computational domain (top, bottom, left, and right), and non-slip conditions at the sides of the slot and on the surface of the target plate. Figure 3 shows an example mesh with a dimensionless plate-to-slot distance of $X_w = 10$, using Figure 1(b) as an example. The mesh was a tetramesh with approximately 120,000 elements. The unsteady Navier-Stokes equations are solved by the finite volume method (FVM), for example, the continuity equation holds for the inlet and slot exit in Figure 2 in the manuscript.

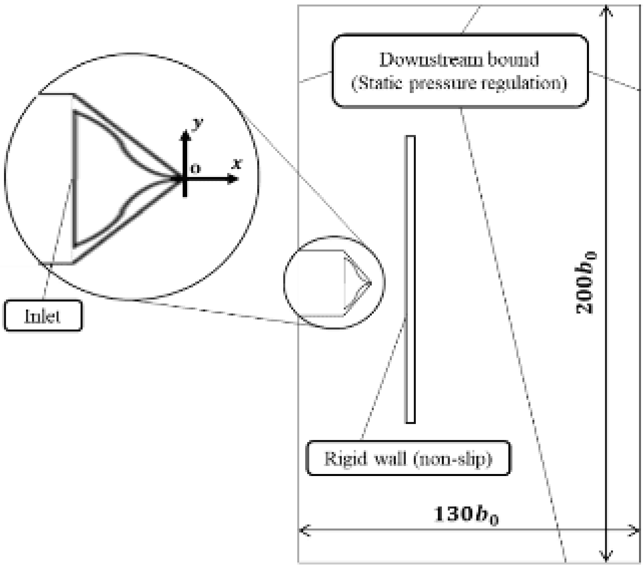

Figure 2. Domain and boundary conditions in numerical analysis.

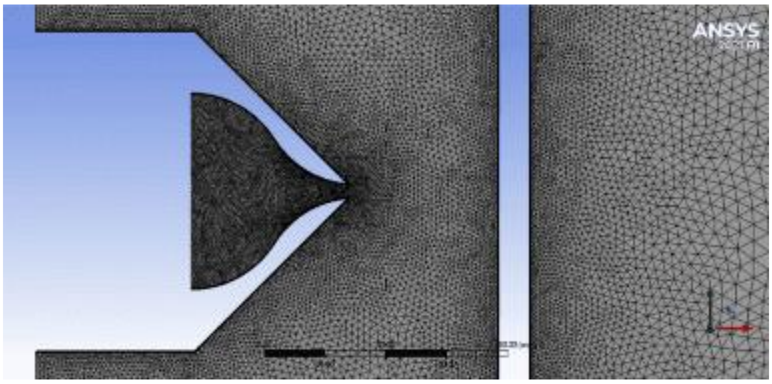

Figure 3. Typical mesh near slot in case of $X_w = 10$.

4. Results and Discussion

Figures 4–6 show the contour plots of the numerically computed time-averaged nondimensional velocity. A case with a slot-side wall length of $30b_0$ is shown in (a), and a case with no wall on the slot side is shown in (b). Results for $L_0 = 90$ $(f = 10\,Hz,\ f^* = 1.11 \times 10^{-2})$ and $L_0 = 15$ $(f = 60\,Hz,\ f^* = 6.67 \times 10^{-2})$ are shown for (i) a continuous jet and (ii) and (iii) for a synthetic jet, respectively. In this study, the representative velocity of the continuous and synthetic jets was $U_{c0} = U_{s0} = 4.5\ \mathrm{m/s}$. The slot width, which is the representative length, was $b_0 = 5.0 \times 10^{-3}$ m, and the dimensionless target plate length was constant at $S_w = 100$. The Reynolds number was $R_e = 1.49 \times 10^3$.

Figure 4 shows the calculation results for $X_w = 30$ as an example of a large target plate-to-slot distance. For all conditions (i), (ii), and (iii) in (a) and (b), the jet lost most of its velocity in the x-direction after impacting the target plate and proceeds in the y-direction as an adherent jet on the plate surface. No significant difference was observed between the (a) slot sidewall length 30b0 and (b) no-slot sidewall owing to the extended distance between the target plate and the slot. Nishibe et al.[13] reported that a flow similar to that of a continuous jet is formed sufficiently downstream of the synthetic jet, including the fluctuation characteristics. Under conditions where X_w is relatively large, the impingement by the synthetic jet is expected to behave in almost the same manner as that of a continuous jet.

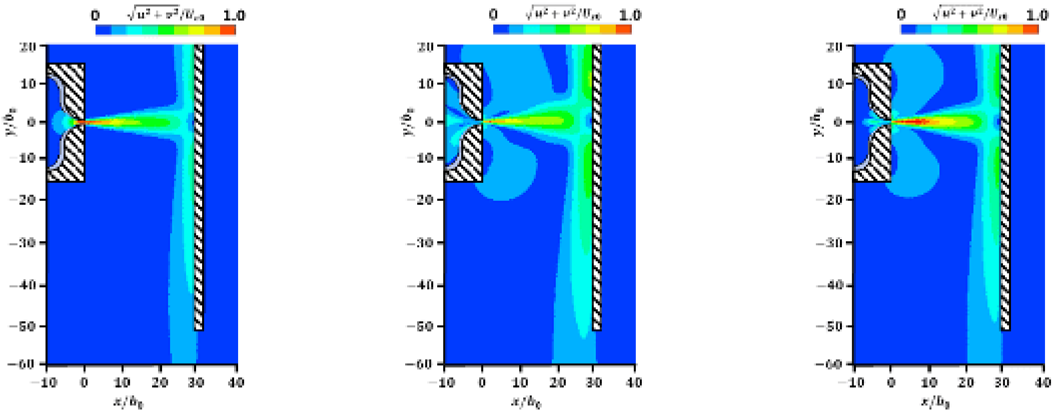

(i) Continuous jets (ii) $L_0 = 90$ ($f = 10$ Hz, $f^* = 1.11 \times 10^{-2}$) (iii) $L_0 = 15$ ($f = 60$ Hz, $f^* = 6.67 \times 10^{-2}$)

(a) Slot side wall length = $30b_0$

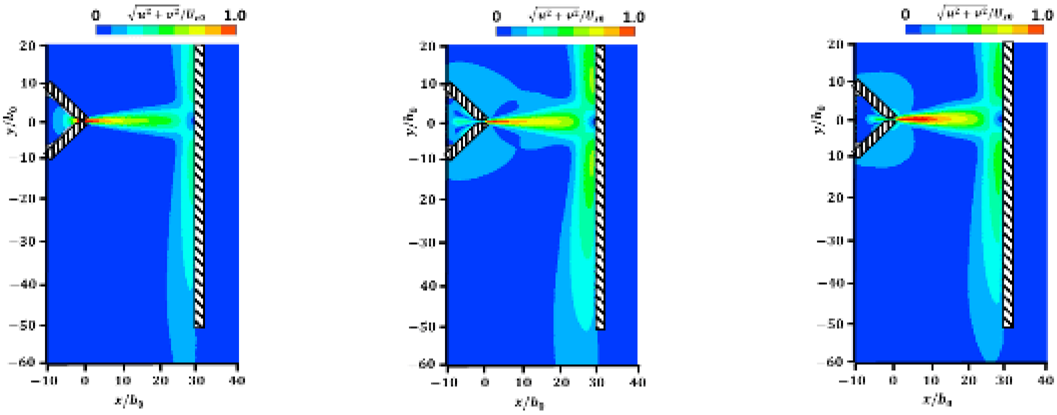

(i) Continuous jets (ii) $L_0 = 90$ ($f = 10$ Hz, $f^* = 1.11 \times 10^{-2}$) (iii) $L_0 = 15$ ($f = 60$ Hz, $f^* = 6.67 \times 10^{-2}$)

(b) No wall parallel to plate on slot side

Figure 4. Flow field of continuous and synthetic jets from computational fluid dynamics (CFD). [$U_{c0} = U_{s0} = 4.5$ m/s, $b_0 = 5.0 \times 10^{-3}$ m, $R_e = 1.49 \times 10^3$, $S_w = 100$, $\boldsymbol{X_w = 30}$]

Figure 5 shows the calculation results for $X_w = 15$ as an example of a medium target plate-to-slot distance. First, focusing on (a), (i) continuous jets and (iii) $L_0 = 15$ formed wall-attached jets in the y-direction, as in Figure 4, but (ii) $L_0 = 90$ did not form a wall-attached jet, and a recirculation region was formed between the target plate and the slot. In contrast, in (b), a wall-attached jet similar to that shown in Figure 4 was formed for all conditions (i), (ii), and (iii), and no difference in behavior owing to dimensionless strokes was observed. The reason for the difference in the flow field under condition (ii) in (a) and (b) is that in (a), the dimensionless stroke is relatively large, but in (ii), vortices with a large circulation volume are formed at significant time intervals. Under significant spatial restriction conditions, backflow occurred during the entrainment and suction processes, which might be why the target, in the case of (ii), vortices with a large circulation volume formed over an extended time interval. Under these conditions, the flow field depends on the dimensionless stroke and the slot sidewall length.

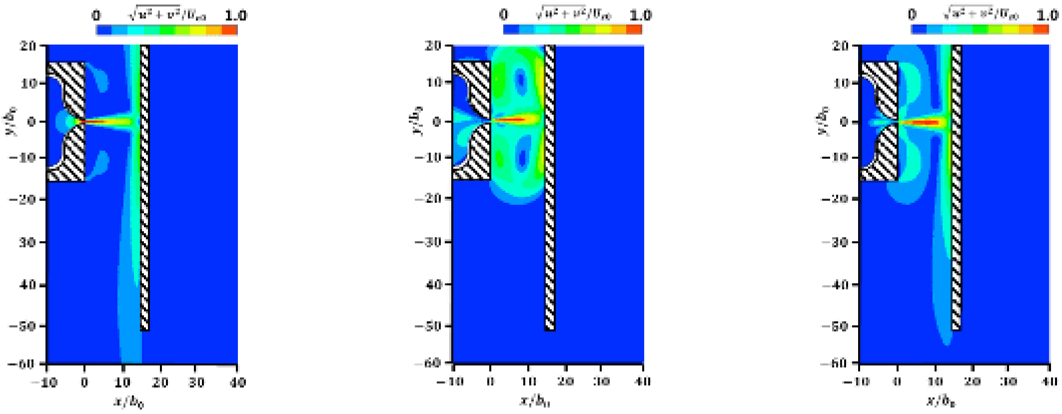

(i) Continuous jets

(ii) $L_0 = 90$
($f = 10$ Hz, $f^* = 1.11 \times 10^{-2}$)

(iii) $L_0 = 15$
($f = 60$ Hz, $f^* = 6.67 \times 10^{-2}$)

(a) Slot side surface length = $30b_0$

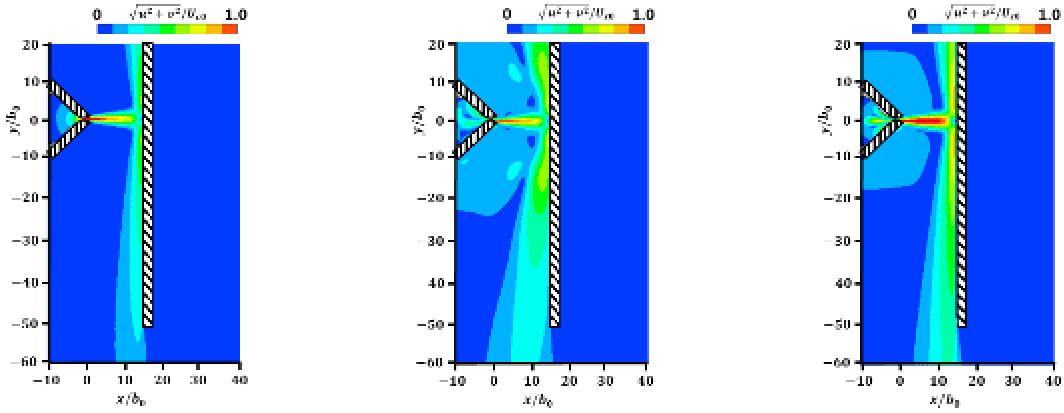

(i) Continuous jets

(ii) $L_0 = 90$
($f = 10$ Hz, $f^* = 1.11 \times 10^{-2}$)

(iii) $L_0 = 15$
($f = 60$ Hz, $f^* = 6.67 \times 10^{-2}$)

(b) No wall parallel to plate on slot side

Figure 5. Flow field of continuous and synthetic jets from CFD.
[$U_{c0} = U_{s0} = 4.5$ m/s, $b_0 = 5.0 \times 10^{-3}$ m, $R_e = 1.49 \times 10^3$, $S_w = 100$, $\boldsymbol{X_w} = \mathbf{15}$]

Figure 6 shows the calculation results for $X_w = 10$ as an example of a small target plate-to-slot distance. In (a) and (i), the continuous jet formed a wall-attached jet, whereas in (ii) and (iii), the synthetic jet formed a recirculation region under both conditions. Under this condition, where the distance between the target plate and the slot is small, the synthetic jet with a zero-net flow suppressed entrainment, making it difficult to form a wall-attached jet at a real flow rate. However, in case (b), wall-attached jets was formed, as in Figures 4 and 5, because of the small spatial restriction. The results for (b) in Figs. 4–6 do not depend on the dimensionless frequency, suggesting that the vortex pair maintained symmetry and translated in the y-direction as a mirror image of the target plate surface, even after collision. In the flow field under this condition, no difference was observed owing to the dimensionless strokes in (ii) and (iii), and only a difference owing to the presence or absence of the slot side wall in (a) and (b) was observed. Therefore, when the distance between the target plate and slot was relatively small, the flow field appeared to depend on the length of the slot-side surface. In addition, when the slot-side wall was present, flow field was not dependent on the dimensionless stroke and the jet continued to adhere to the wall surface after impact. That is capable of proper mass transport as an impinging jet. Therefore, the impinging synthetic jet is a promising alternative to continuous jets, and could be applied to the miniaturization and weight reduction of cooling devices for electronic devices.

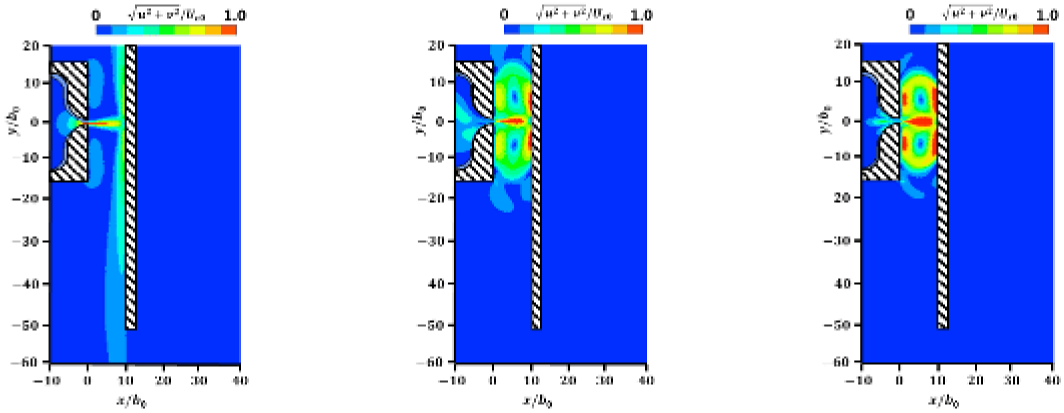

(i) Continuous jets

(ii) $L_0 = 90$ ($f = 10$ Hz, $f^* = 1.11 \times 10^{-2}$)

(iii) $L_0 = 15$ ($f = 60$ Hz, $f^* = 6.67 \times 10^{-2}$)

(a) Slot side surface length = $30b_0$

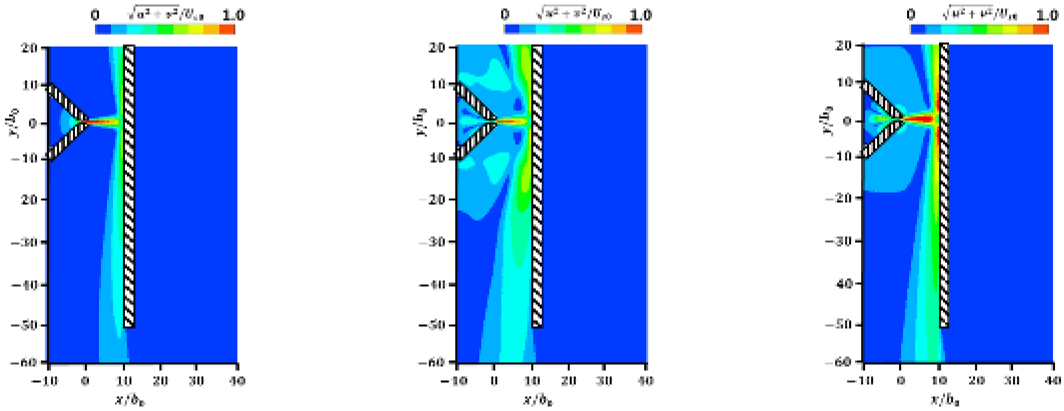

(i) Continuous jets

(ii) $L_0 = 90$ ($f = 10$ Hz, $f^* = 1.11 \times 10^{-2}$)

(iii) $L_0 = 15$ ($f = 60$ Hz, $f^* = 6.67 \times 10^{-2}$)

(b) No wall parallel to plate on slot side

Figure 6. Flow field of continuous and synthetic jets from CFD.
[$U_{c0} = U_{s0} = 4.5$ m/s, $b_0 = 5.0 \times 10^{-3}$ m, $R_e = 1.49 \times 10^3$, $S_w = 100$, $\boldsymbol{X_w} = \mathbf{10}$]

5. Conclusions

In this study, numerical calculations of colliding synthetic jets were performed for various target plate-to-slot distances. The velocity fields are presented as parameters of dimensionless stroke length and the presence or absence of slot side walls. The main conclusions are as follows. The flow characteristics of the colliding synthetic jet depend on the target plate–slot distance, dimensionless stroke, and slot-side wall length. However, when the target plate–slot distance is small, the flow field generally depends only on the length of the slot-side wall. In addition, when the certain value of plate-to-slot distance, the flow field depends on the dimensionless stroke. When the dimensionless stroke is large, a large recirculating vortex is formed between the plate-to-slot; when the dimensionless stroke is small, a wall-attached jet is formed, similar to the flow field of impinging continuous jet.

6. Acknowledgments

This work was supported by JSPS KAKENHI Grant Number 23K17731 and Hatakeyama Research Grant of Turbomachinery Society of Japan. We would like to thank Editage (www.editage.jp) for English language editing.

7. References

[1] Tsujimoto, K., Ao, K., Shakouchi, T. and Ando, T. (2011). Numerical Investigation on Flow Structures and Mixing Performances of Vector-Controlled Free Jet using DNS. *Journal of Fluid Science and Technology*, 6-4, pp. 401–411.

[2] Kanamori, A, Hiwada, M, Senaha, I, Oyakawa, K. (2011). Effect of orifice configuration on flow behavior and impingement heat transfer. *The Japan Society of Mechanical Engineers Essay Collection (Part B)*, *77*(775), pp.456-464 (in Japanese).

[3] Gopal, K., Kean, C. A., Rajnish, N. S: a review. *Contents lists available at ScienceDirect: Synthetic jet impingement heat transfer enhancement, Applied Thermal Engineering* 149 (2019) 1305–1323.

[4] Bazdidi-Tehrani, F., Karami, M., Jahromi, M., (2011). Unsteady flow and heat transfer analysis of an impinging synthetic jet. *Springer*, *Heat Mass Transfer*, 47:1363–1373.

[5] Malingham, R, Glezer, A. (2005). Design and thermal characteristics of a synthetic jet ejector heat sink. *Journal of Electronic Packaging*, *127*, pp.172-177.

[6] Pavlova, A, Amitay, M. (2006): “Electronic cooling with synthetic jet impingement”. *ASME Journal of Heat and Mass Transfer*, *128*(9), pp.897-907.

[7] Chaudhari, M, Puranik, B, Agrawal, A. (2010). Effect of orifice shape in synthetic jet based impingement cooling. *Experimental Thermal and Fluid Science*, *34*(2), pp.246-256.

[8] Wang, L, Feng, LH, Xu, Y, Xu, Y, Wang, JJ. (2022). Experimental investigation on flow characteristics and unsteady heat transfer of noncircular impinging synthetic jets. *International Journal of Heat and Mass Transfer*, *190*, 122760.

[9] Xu, Y, Moon, C, Wang, JJ, Penyazkov, OG, Kim, KC. (2019). An experimental study on the flow and heat transfer of an impinging synthetic jet. *International Journal of Heat and Mass Transfer*, *144*, 118626.

[10] Silva-Llanca, L, Ortega, A, Rose, I. (2015). Experimental convective heat transfer in a geometrically large two-dimensional impinging synthetic jet. *International Journal of Thermal Sciences*, *90*, pp.339-350.

[11] Trávníček, Z, Vít, T. (2015). Impingement heat/mass transfer to hybrid synthetic jets and other reversible pulsating jets. *International Journal of Heat and Mass Transfer*, *85*, pp.473-487.

[12] Kobayashi, R, Terakado, H, Sato, K, Taniguchi, J, Nishibe, K, Yokota, K. (2020). Behavior of plane synthetic jets generated by an asymmetric stepped slot. *International Journal of Fluid Machinery and Systems*, *13*(1), pp.253-265.

[13] Nishibe, K, Fujita, Y, Sato, K, Yokota, K, Koso, T. (2011). Experimental and numerical study on the flow characteristics of synthetic jets. *Journal of Fluid Science and Technology*, *6*(4), pp.425-436.

[14] Glezer, A., Amitay, M. (2002). Synthetic jets. *Annual Review of Fluid Mechanics*, *34*(1), pp.503-529.

[15] Holman, R, Utturkar, Y, Mittal, R, Smith, BL, Cattafesta, L. (2005). Formation criterion for synthetic jets. *AIAA Journal*, *43*(10), pp.2110-2116.

[16] Smith, BL, Swift, GW. (2003). A comparison between synthetic jets and continuous jets. *Experiments in Fluids*, *34*(4), pp.467-472.

[17] Tang, H, Zhong, S. (2005). 2D numerical study of circular synthetic jets in quiescent flows. *Aeronautical Journal*, *109*(1092), pp.89-97.

[18] Koso, T, Morita, M. (2014). Effects of stroke and Reynolds number on characteristics of circular synthetic jets. *Journal of Fluid Science and Technology*, *9*(2), JFST0021.

[19] Koso, T, Matsuda, S, Masuda, H, Akahoshi, T. (2014). Effect of stroke on structure of vortex ring array in circular synthetic jets. *Journal of Fluid Science and Technolog*, *9*(3), JFST0034.

[20] Nishibe, K, Fujiwara, T, Ohue, H, Takezawa, H, Sato, K, Yokota, K. (2014). Synthetic jet actuator using bubbles produced by electric discharge. *Journal of Fluid Science and Technology*, *9*(3), JFST0033.

[21] Smith, BL, Glezer, A. (2002). Jet vectoring using synthetic jets. *Journal of Fluid Mechanics*, *458*, pp.1-34.

[22] Kobayashi, R, Nishibe, K, Watabe, Y, Sato, K, Yokota, K. (2018). Vector control of synthetic jets using an asymmetric slot”. *Journal of Fluids Engineering*, *140*(5), 051102.

[23] Kobayashi, R, Watabe, Y, Tamanoi, Y, Nishibe, K, Kang, D, Sato, K. (2020). Jet vectoring using secondary Coanda synthetic jets. *Mechanical Engineering Journal*, *7*(5), 20-00215.

[24] Zhang, Q, Tamanoi, Y, Kang, D, Nishibe, K, Yokota, K, Sato, K. (2023). Influence of amplitude of excited secondary flow on the direction of jets. *Transactions of the Japan Society for Aeronautical and Space Sciences*, *66*(2), pp.37-45.
[25] Amitay, M, Smith, DR, Kibens, V, Parekh, DE, Glezer, A. (2001). Aerodynamic flow control over an unconventional airfoil using synthetic jet actuators. *AIAA Journal*, *39*(3), pp.361-370.
[26] Haider, BA, Durrani, N, Aizud, N, Zahir, S. (2010). Aerodynamic stall control of a generic airfoil using synthetic jet actuator. *International Journal of Aerospace and Mechanical Engineering*, *4*(9), pp.788-793.
[27] Yen, J, Ahmed, NA. (2012). Parametric study of dynamic stall flow field with synthetic jet actuation. *Journal of Fluids Engineering*, *134*(7), 071106.
[28] Duvigneau, R, Hay, A, Visonneau, M. (2007). Optimal location of a synthetic jet on an airfoil for stall control. *Journal of Fluids Engineering*, *129*(7), pp.825-833.
[29] Nishibe, K, Nomura, Y, Noda, K, Ohue, H, Sato, K. (2018). Influence of stroke on performance characteristics of synthetic jet fan. *Journal of Applied Fluid Mechanics*, *11*(4), pp.945-956.
[30] Yasumiba, M., Sato, K., Ito, T., Kawahara, R. and Yokota, K. (2022). Flow around bluff body downstream of synthetic jets. *Proceedings of the 28th Annual Meeting of the Kanto Branch of the Japan Society of Mechanical Engineers* (in Japanese).
[31] Yasumiba, M., Nishibe, K., Kang, D., Sato, K. (2022). Flow Characteristics of Two-Dimensional Plane Impinging Synthetic Jets. *Interdisciplinary Conference on Mechanics, Computers and Electrics (ICMECE 2022).*
[32] Watabe, Y, Sato, K, Nishibe, K, Yokota, K. (2016). The influence of an asymmetric slot on the flow characteristics of synthetic jets. *In: Proceedings of the 5th International Conference on Jets, Wakes and Separated Flows (ICJWSF2015) Springer International Publishing*, pp. 101-107.
[33] Ishizawa, T, Sato, K, Nishibe, K, Yokota, K. (2016). Performance characteristics of a fan using synthetic jets. *In: Proceedings of the 5th International Conference on Jets, Wakes and Separated Flows (ICJWSF2015)*, *Springer International Publishing*, pp. 109-115.
[34] Shakouchi, T. (2004). Jet Flow Engineering. *Tokyo, JAPAN: Morikita Publishing.*

TSF0016

Numerical study of fluid behaviors in fibrous porous electrodes and optimization of electrode structure using lattice Boltzmann simulation

Daiki Tanaka[1,*], Takahiro Suzuki[1], and Shohji Tsushima[1]

[1]Department of Mechanical Engineering, Osaka University, Suita, Osaka 565-0871, Japan

* Corresponding Author: tanaka_d@ene.mech.eng.osaka-u.ac.jp

Abstract. Decarbonization has become an international challenge, especially in the power sector, where a massive introduction of renewable energy is urgently needed. Solar and wind power, in general, require the use of large-scale energy storage systems for leveling their fluctuating nature of power generation. Vanadium redox flow batteries (VRFBs) are promising devices for large-scale energy storage systems. The engineered design of the fibrous electrodes and the embedded flow fields in VRFBs is a crucial factor that enhances charge and discharge efficiency. In this study, we developed a three-dimensional mathematical model based on the lattice Boltzmann method to calculate the flow, concentration, and potential fields in carbon fiber electrodes. Lattice Boltzmann simulations were developed that fully consider activation, ohmic, and concentration overpotentials with variation of open circuit potential attributed to local reactant concentration. LBM simulation showed that the vanadium ion was inhomogeneously consumed due to both penetration and stagnation behaviors of the supplying electrolyte in the porous electrodes, resulting in the overvoltage of VRFBs. The LBM model was also utilized to compare the effects of electrode structure on irreversibility loss of energy in VRFBs for pore-scale optimization of the fibrous electrodes.

Keywords: Lattice Boltzmann method, Fibrous media, Electrochemical Reaction, Transport Processes.

1. Introduction

The lattice Boltzmann method is a CFD technique that uses gas molecular kinetics as an analogy and is widely used in engineering. Recent years have seen a surge of interest in enhancing Vanadium Redox Flow Batteries (VRFBs) through research on various aspects, including components, channel structures, and electrode configurations. In particular, the electrode structure is closely related to the flow, active material, and chemical reaction distribution, and has been shown to have a significant impact on the reaction transport properties of VRFBs, necessitating optimization of the electrode structure [1]. In VRFBs, fibrous electrodes have been widely applied presumably due to their large specific surface area and better electric conductance. However, experimental data is difficult to obtain for carbon electrodes because of their microscopic and porous structure. Therefore, employing the lattice Boltzmann method for numerical analysis at the pore-scale proves effective. The objective of this study is to develop a 3D mathematical model based on the lattice Boltzmann method to calculate the flow, concentration, and potential fields in carbon fiber electrodes, and to develop it into the adjoint-sate lattice Boltzmann method to optimize the electrode structure and elucidate the electrode structure that maximizes the performance of VRFBs.

2. Theory

2.1. The lattice Boltzmann Method

The lattice Boltzmann method (LBM) approximates the fluid with a large number of virtual particles with finite velocities. The particle distribution functions assigned to the corresponding directions experience "collision" and "translation" at each time step based on the lattice Boltzmann equation, satisfying macroscopic fluid behaviors, i.e. mass and momentum conservation. The moments of the velocity distribution function in the obtained time series are used to calculate the macroscopic density and velocity of the fluid in a calculation domain [2]. The lattice used in LBM is regular, and in three dimensions, the cubic lattice shown in Figure 1 is commonly used. In this study, the D3Q15 model is used for the fluid field, and the D3Q7 model is used for the concentration and potential field.

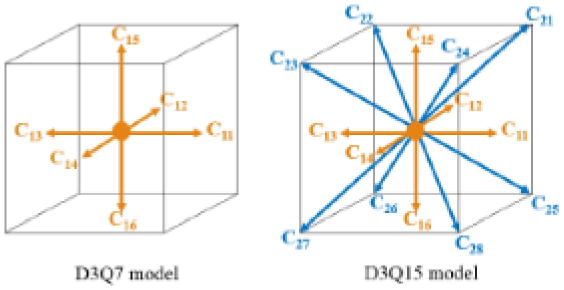

Figure 1. Three-dimensional lattice models.

2.1.1. The lattice Boltzmann Equation for Flow field

The velocity distribution function of the flow field is determined such that the lattice Boltzmann equation and the local parallel distribution function follow the governing equations of the fluid field. Based on the model of He, Luo [3], it is written as

$$f_i(\boldsymbol{x}+\boldsymbol{c}_i\Delta t, t+\Delta t) - f_i(\boldsymbol{x},t) = -\frac{1}{\tau_f}\left[f_i(\boldsymbol{x},t) - f_i^{eq}(\boldsymbol{x},t)\right] \tag{1}$$

$$f_i^{eq}(\boldsymbol{x},t) = w_i\left[\rho + \rho\left[3\frac{\boldsymbol{c}_i\cdot\boldsymbol{v}}{c^2} + \frac{9}{2}\frac{(\boldsymbol{c}_i\cdot\boldsymbol{v})^2}{c^4} - \frac{3}{2}\frac{\boldsymbol{v}\cdot\boldsymbol{v}}{2}\right]\right] \tag{2}$$

with

$$\rho(\boldsymbol{x},t) = \sum_i f_i(\boldsymbol{x},t) \tag{3}$$

$$\boldsymbol{v}(\boldsymbol{x},t) = \frac{\sum f_i(\boldsymbol{x},t)\boldsymbol{c}_i}{\rho(\boldsymbol{x},t)} \tag{4}$$

$$p(\boldsymbol{x},t) = \frac{1}{3}\rho(\boldsymbol{x},t)\,c^2 \tag{5}$$

$$w_i = \begin{cases} \dfrac{2}{9} & (i=0) \\ \dfrac{1}{9} & (i=11\sim16) \\ \dfrac{1}{72} & (i=21\sim28) \end{cases} \tag{6}$$

2.1.2 The lattice Boltzmann Equation for concentration field

The governing equation for the concentration field is the advection-diffusion equation, and electrophoresis is considered in this study. The lattice Boltzmann equation and the local equilibrium distribution function were determined to satisfy the governing equations. Based on the model of Sullivan, Sani, Johns, and Gladden [4] and He, Li [5], the distribution function and the local equilibrium distribution function are written as

$$g_{i,s}(\boldsymbol{x}+\boldsymbol{c}_i\Delta t, t+\Delta t) - g_{i,s}(\boldsymbol{x},t) = -\frac{1}{\tau_g}\left[g_{i,s}(\boldsymbol{x},t) - g_{i,s}^{\mathrm{eq}}(\boldsymbol{x},t)\right] - \left(1-\frac{1}{2\tau_g}\right)\frac{z_s F}{RT}(\boldsymbol{c}_i - \boldsymbol{v})\cdot\nabla\phi_1 g_{i,s}^{\mathrm{eq}}(\boldsymbol{x},t)\Delta t_g + s_{\mathrm{V}_s^+}\Delta t_g \tag{7}$$

$$g_{i,s}^{\mathrm{eq}}(\boldsymbol{x},t) = C_s\left(J_{i,s} + K_i \boldsymbol{c}_i\cdot\boldsymbol{v}\right) \tag{8}$$

with

$$C_s(\boldsymbol{x},t) = \sum_i g_{i,s}(\boldsymbol{x},t) \tag{9}$$

$$J_{i,s} = \begin{cases} J_{0,s} & (i=0) \\ \dfrac{1-J_{0,s}}{6} & (i = 11\sim 16) \end{cases} \tag{10}$$

$$K_i = \frac{1}{2c^2} \tag{11}$$

$s_{\mathrm{V}_s^+}$ in equation (7) is the generation annihilation term described below.

2.1.3 The lattice Boltzmann Equation for potential field

The governing equations for the potential field are charge conservation equations. The lattice Boltzmann equation and the local equilibrium distribution function were determined to satisfy the governing equations. Based on the model of Guo, Zhao, and Shi [6], the distribution function and the local equilibrium distribution function are written as

$$h_i(\boldsymbol{x}+\boldsymbol{c}_i\Delta t, t+\Delta t) - h_i(\boldsymbol{x},t) = -\frac{1}{\tau_h}\left[h_i(\boldsymbol{x},t) - h_i^{\mathrm{eq}}(\boldsymbol{x},t)\right] + s_{e^-}\Delta t_h \tag{12}$$

$$h_i^{\mathrm{eq}}(\boldsymbol{x},t) = \frac{\phi}{6} \tag{13}$$

with

$$\phi(\boldsymbol{x},t) = \sum_i h_i(\boldsymbol{x},t) \tag{14}$$

s_{e^-} in equation (12) is the generation annihilation term described below.

2.1.4. Methods for analyzing electrochemical reaction field

The current density at the electrode reaction surface of VRFBs is determined by the Butler-Volmer equation when considering the positive and negative electrode. In this study, the current density i is determined by the Tafel equation (Equation (15)), since the reaction is considered on the anode side of the VRFBs during charging.

$$i = -i_0 \frac{C_{\mathrm{V}^{3+}}}{C_{\mathrm{V}^{3+}}^{\mathrm{ref}}} \exp\left(-\frac{\alpha_c F}{RT}\eta_{\mathrm{act}}\right) \tag{15}$$

where η_{act} is the activation overvoltage.

To consider the distribution of the electrochemical reaction and overvoltage, the potential difference between the current collector and the electrolyte membrane is defined as the total overvoltage η_{all}. Considering the Nernst equation, the activated overvoltage η_{act} can be written as

$$\eta_{\mathrm{act}} = \eta_{\mathrm{all}} + \phi_s - \phi_1 + \frac{RT}{F}\ln\left(\frac{C_{\mathrm{V}^{3+}}}{C_{\mathrm{V}^{3+}}^{\mathrm{ref}}}\right) \tag{16}$$

where ϕ_l is the electrolyte potential and ϕ_s is the electrode potential.

The local current density i_{loc} resulting from the electrochemical reaction at the interface between the electrode and the electrolyte can then be written as

$$i_{loc} = i_0 \frac{C_{V^{3+}}}{C_{V^{3+}}^{ref}} \exp\left[-\frac{\alpha_c F}{RT}\left(\eta_{all} + \phi_s - \phi_l + \frac{RT}{F}\ln\left(\frac{C_{V^{3+}}}{C_{V^{3+}}^{ref}}\right)\right)\right] \tag{17}$$

Assuming that the sum of the local current densities is equal to the macroscopic current, the total overvoltage can be written as

$$\eta_{all} = -\frac{RT}{\alpha_c F}\ln\left[\frac{AI}{\sum a_{loc} i_0 \frac{C_{V^{3+}}}{C_{V^{3+}}^{ref}}\left[\exp\left[\frac{\alpha_c F}{RT}\left(-\phi_s + \phi_l - \frac{RT}{F}\ln\left(\frac{C_{V^{3+}}}{C_{V^{3+}}^{ref}}\right)\right)\right]\right]}\right] \tag{18}$$

Using the calculated local current density i_{loc}, the local production and annihilation rates of V3+ ions $s_{V^{3+}}$ and electrons consumed by the electrochemical reaction s_{e^-} can be determined by Equations (19) and (20), respectively.

$$s_{V^{3+}} = -\frac{a_{loc} i_{loc}}{F} \tag{19}$$

$$s_{e^-} = -a_{loc} i_{loc} \tag{20}$$

2.2. Adjoint-sate lattice Boltzmann Method

There are various methods for structural optimization, and the most efficient material distribution can be found by using topology optimization, which offers more degrees of freedom than dimensional or shape optimization. Topology optimization with respect to LBM has been studied using various methods. Tekitek [7] first proposed Adjoint-state lattice Boltzmann equation limited to a parameter identification problem. Topology optimization was also performed in this study using the accompanying variable method.

Defined as the state ϕ, the design parameter α, the constraint equations $F(\phi,\alpha)$, and the cost function $\mathcal{J}(\phi)$ to be minimized by optimization, the optimization problem is "to find the controls α and the state ϕ such that $\mathcal{J}(\phi)$ is minimized under the constraint $F(\phi,\alpha) = 0$. For this purpose, it is effective to use the Lagrange multiplier method. Assuming that the accompanying variable is ϕ, the Lagrangian function is defined as

$$\mathcal{L}(\phi,\alpha,\phi^*) = \mathcal{J}(\phi) + \langle F(\phi,\alpha),\phi^*\rangle \tag{21}$$

where the state ϕ is a collection of f_i, g_i, and h_i, and the constraint function $F(\phi,\alpha)$ is the lattice Boltzmann equation described above.

The adjoint-state ϕ^* consists of f_i^*, g_i^*, and h_i^*l as well as f_i, g_i, and h_i. The cost function can be minimized by searching for α, ϕ, and ϕ^* where the Lagrangian function $\mathcal{L}$ is a stationary point. The following equation holds at the stationary point.

$$\delta\mathcal{L} = \frac{\partial\mathcal{L}}{\partial\xi}\delta\xi + \frac{\partial\mathcal{L}}{\partial\phi}\delta\phi + \frac{\partial\mathcal{L}}{\partial\alpha}\delta\alpha \tag{22}$$

We derived the Adjoint-state lattice Boltzmann equations to obtain the adjoint-state based on the method of Florian, Yann and Christophe [8].

$$-\frac{\partial f_i^*}{\partial t} - \boldsymbol{c}_i\cdot\nabla f_i^* + \frac{1}{\tau_f}\left(f_i^*(\boldsymbol{x},t) - \sum_j \frac{\partial f_j^{eq}}{\partial f_i} f_j^*\right) + Q_i^f = 0 \tag{23}$$

$$-\frac{\partial g_i^*}{\partial t} - \boldsymbol{c}_i\cdot\nabla g_i^* + \frac{1}{\tau_g}\left(g_i^*(\boldsymbol{x},t) - \sum_j \frac{\partial g_j^{eq}}{\partial g_i} g_j^*\right) + Q_i^g = 0 \tag{24}$$

$$-\frac{\partial h_i^*}{\partial t} - \boldsymbol{c}_i \cdot \nabla h_i^* + \frac{1}{\tau_h}\left(h_i^*(\boldsymbol{x},t) - \sum_j \frac{\partial h_j^{eq}}{\partial h_i} h_j^* \right) + Q_i^h = 0 \tag{25}$$

with

$$Q_i^f = \sum_j g_j^* \left[C_s K_i \boldsymbol{c}_j \cdot \boldsymbol{c}_i \left\{ -\frac{1}{\tau_g} + \left(1 - \frac{1}{2\tau_g}\right) \frac{z_s F}{RT} (\boldsymbol{c}_j - \boldsymbol{v}) \cdot \boldsymbol{\nabla}\phi_1 \Delta t \right\} + \left(1 - \frac{1}{2\tau_g}\right) \frac{z_s F}{RT} \frac{\partial \boldsymbol{u}}{\partial f_i} \cdot \boldsymbol{\nabla}\phi_1 g_j^{eq} \Delta t \right] \tag{26}$$

$$Q_i^g = \sum_j \left[\left\{ \left(1 - \frac{1}{2\tau_g}\right) \frac{z_s F}{RT} (\boldsymbol{c}_j - \boldsymbol{v}) \cdot \boldsymbol{\nabla}\phi_1 \frac{\partial g_{j,s}^{\mathrm{eq}}}{\partial g_i} \Delta t_g - \frac{\partial s_{\mathrm{V}^{3+}}}{\partial g_i} \right\} g_j^* - \frac{\partial s_{\mathrm{e}^-}}{\partial g_i} h_j^* \right] \tag{27}$$

$$Q_i^h = \sum_j \left(-\frac{\partial s_{\mathrm{V}^{3+}}}{\partial h_i} g_j^* - \frac{\partial s_{\mathrm{e}^-}}{\partial h_i} h_j^* \right) \tag{28}$$

2.3. The update of the solid/fluid distribution and Optimization

In this study, the design parameter α is the solid/fluid distribution. To clarify the interface between fluid and solid, α is represented by a level-set function (LSF) $\Phi(\boldsymbol{x})$. The LSF is used to delimit the solid/liquid interface as

$$\alpha(\boldsymbol{x}) = \begin{cases} 1 & \text{if } \Phi(\boldsymbol{x}) \geq 0 \\ 0 & \text{if } \Phi(\boldsymbol{x}) < 0 \end{cases} \tag{29}$$

The cost function gradient $\nabla \mathcal{J}$ is computed in Equation (30) using the adjoint variables derived in the Adjoint-sate lattice Boltzmann functions and the solution of the forward LBF. The cost function affects only a part of the Adjoint-sate lattice Boltzmann functions, so it can be easily rewritten for various minimization problems. In this study, the cost function is the concentration flowrate at the outlet of the domain expressed in Equation (31).

$$\nabla \mathcal{J} = \sum_i \frac{w_i f_i^*}{\tau_f} \left[3\frac{\boldsymbol{c}_i \cdot \boldsymbol{v}}{c^2} + \frac{9}{2}\frac{(\boldsymbol{c}_i \cdot \boldsymbol{v})^2}{c^4} - \frac{3}{2}\frac{\boldsymbol{v} \cdot \boldsymbol{v}}{2} \right] + \sum_i g_i^* \left[\frac{C_s K_i}{\tau_g} \boldsymbol{c}_i \cdot \boldsymbol{v} - \left(1 - \frac{1}{2\tau_g}\right) \frac{z_s F}{RT} (\boldsymbol{c}_i - \boldsymbol{v}) \cdot \boldsymbol{\nabla}\phi_1 \left(g_{i,s}^{\mathrm{eq}}(\boldsymbol{x},t) + \frac{C_s K_i}{\tau_g} \boldsymbol{c}_i \cdot \boldsymbol{v} \right) \Delta t_g \right] \tag{30}$$

$$\mathcal{J} = \frac{1}{|\partial \mathrm{X_{OUT}}|} \int_{\partial \mathrm{X_{OUT}}} \boldsymbol{v} \cdot \boldsymbol{n}\, C_s \, \mathrm{d}\boldsymbol{x} \tag{31}$$

The update of the solid/fluid distribution α is performed via the evolution of the LSF $\Phi(\boldsymbol{x})$, such as:

$$\Phi^{n+1}(\boldsymbol{x}) = \Phi^{n}(\boldsymbol{x}) - \nabla \mathcal{J} \tag{32}$$

3. Test cases and Results

The test case is shown in Figure 2 and the calculation parameters in Table 1. Concentration and pressure drop at the inlet are given. The boundary face between the fluid and the electrode is the HHBB boundary condition. The range of electrodes generated by the topology optimization is restricted to near the centre of the computational domain.

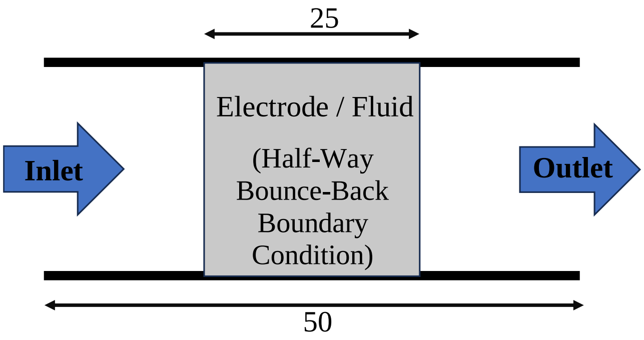

Figure 2. Schematic diagram of test cases.

Table 1. Calculation parameters.

Calc. domain [μm^3]	$50 \times 24 \times 25$
Grid resolution [μm/voxel]	1.0
Diff. coeff. [m^2/s]	2.4×10^{-10}
Applied Pres. drop [Pa]	20
Inflow V^{3+}conc. [M]	0.5
Current density [A/cm^2]	0.1
Shumidt number [-]	1.82×10^4

For the topology optimization calculations, the initial structure was set up as shown in Figure 3. For comparison, a regular structure with fibrous porosity was created and the forward LBM and cost function were calculated. The structures and concentration distributions of the initial, optimized, and regular structures are shown in Figure 3.

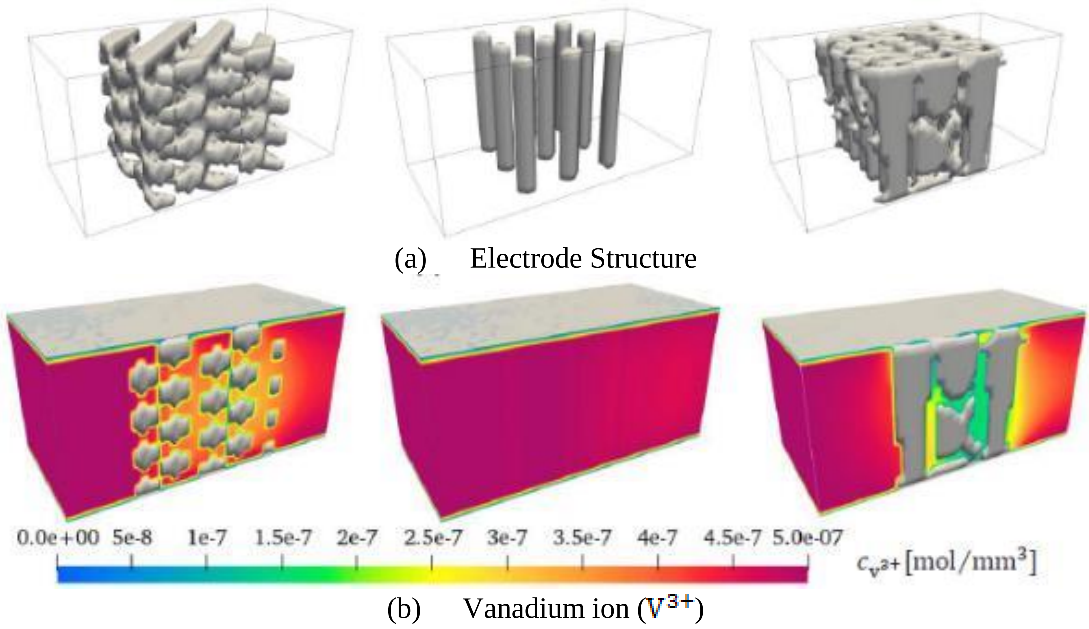

Figure 3. Fiber-scale simulation results of the negative electrode in the vanadium redox flow battery under the charge. (Left: Ordered structure [diameter of fiber is 4.0 μm], Center: Initial Structure, Right: Optimized structure).

A fibrous structure is generated and the concentration near the outlet is decreasing. In fact, the outlet flow concentration (Equation (31)) was observed to decrease and converge with the structure update (Figure 4). The cost function of the updated structure was smaller than that of the ordered structure.

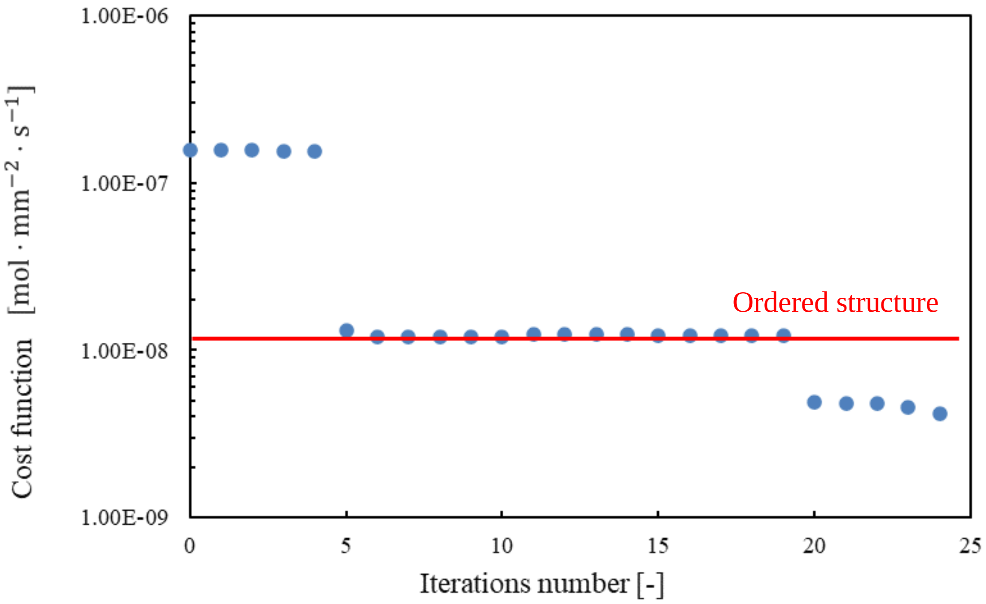

Figure 4. Evolution of the cost function with the iteration count.

4. Conclusions

We developed our three-dimensional mathematical model based on the lattice Boltzmann method, which calculates the flow, concentration, and potential field, and further developed it into an adjoint-sate Lattice Boltzmann Function to optimize the electrode structure. As a result, it was confirmed that the cost function decreases with time as the structure is updated to a fiber-like structure.

5. Acknowledgments

This work was partially supported by JSPS KAKENHI Grant Number 21H04540**.**

6. References

[1] Tsushima, S., Suzuki, T., (2016). *Nagare*. 35. 27.
[2] Chen, S., Doolen, GD. (1998). *Annu Rev Fluid Mech*. 30. 329.
[3] He, X., Luo, L. S., (1997). *Journal of Statistical Physics*. 88. 927.
[4] Sullivan, S. P., Sani, F. M., Johns, M. L., Gladden, L. F. (2005). *Chemical Engineering Science*. 60. 3405.
[5] He, X., Li, N. (2000). *Computer Physics Communications*. 129. 158.
[6] Guo, Z., Zhao, T. S., Shi, Y. (2005). *The Journal of Chemical Physics*. 122. 144907.
[7] M. Tekitek, M. Bouzidi, F. Dubois, P. Lallemand (2006). *Comput. Fluids*. 35. 805.
[8] Florian, D., Yann, F., Christophe, J., (2018). *Journal of Computational Physics*. 365. 376.

TSF0022

Effect of Open Elliptical Reflector Shape on Pressure Gradient during Shock Wave Focusing

Masaya Taniguchi[1], Tetsuro Nitta[1], Hiroshi Fukuoka[1,*], Atsushi Suda[1], Kazuki Hiro[1], and Keiichi Nakagawa[2]

[1]National Institute of Technology, Nara College, 22 Yata-cho, Yamatokoriyama, Nara, 639-1080, Japan
[2]University of Tokyo, 7-3-1 Hongo, Bunkyo-ku, Tokyo, 113-8656, Japan

* Corresponding Author: fukuoka@mech.nara-k.ac.jp

Abstract. Optogenetics is a technology to study brain cell function by irradiating light directly onto specific brain cells and partially controlling neurons' activity. However, the ability to deliver light into deep brain structures is limited due to absorption in the surrounding tissue. To solve this problem, we propose a novel approach to use focused underwater shock waves as pseudo-optical fibers. Underwater shock waves are focused by open elliptical reflectors, which have one of their focal points open. The elliptical reflector must be cut to place the focal point inside the brain. In this study, we investigated the relationship between the pressure gradient generated by the focusing of the underwater shock waves and the shape of the open elliptical reflectors. As its numerical experimental tool, ANSYS AUTODYN, was used to calculate the pressure gradient for different shapes of open elliptical reflectors. The parameters used in the calculations were the flatness of the reflector and the open ratio of the reflector. We found that for open elliptical vessels with the open ratio of 0.2, 0.3, 0.4, 0.5, and 0.6, decreasing the flatness from 0.5 to 0.1 increased the pressure gradient by a maximum of 15.2 MPa/mm. Similarly, decreasing the open ratio from 0.6 to 0.2 increased the pressure gradient by a maximum of 12.5 MPa/mm. Our results provide a basis for the design of open elliptical reflectors for use in optogenetics.

Keywords: Underwater shock wave, Focusing shock wave, Open elliptical reflector, Numerical calculation, Optical waveguide.

1. Introduction

Optogenetics is attracting attention for its ability to elucidate the mechanisms of brain cells. Optogenetics is a technology that activates brain cells by directly irradiating specific brain cells with light, thereby partially controlling the activity of neurons. Many studies using this technology have been reported. Shimoda et al. reported a method to reduce the symptoms of epileptic seizures [1]. Khabou et al. reported that applying optogenetics to patients with inherited retinal dystrophies is an effective means of restoring retinal vision [2]. Thus, optogenetics contributes significantly to the elucidation of the brain function.

It is difficult for light to penetrate deep into light-scattering materials such as the brain. The brains of primates are enormous compared to those of rats and other animals. Therefore, it is difficult to deliver light to deep brain cells of large primates in optogenetics. It is necessary to develop a technology to deliver light to target cells less invasively to the brain to advance optogenetics for primates.

We propose to use a focused underwater shock wave as a pseudo-optical fiber. The underwater shock wave is focused by using an elliptical reflector. If the underwater shock wave is generated at the focal point of the reflector, it is focused at another focal point. The focused underwater shock wave can obtain a high-pressure, high-density region. A pressure gradient is generated in this region. This gradient is considered to be usable as the optical fiber.

An open elliptical reflector must be used to form the optical fiber in the brain, with one end of the elliptical reflector being cut off. Open elliptical reflectors reduce the reflective wall of it. This reduction is expected to affect the shock wave focusing phenomena. There are many studies on the focusing of shock waves. Yang et al. experimentally and numerically confirmed ignition behaviors induced by focused shock waves with wedges of different angles and reflectors of various shapes [3],[4]. Several studies on the shock wave focusing phenomena use the open elliptical reflectors. Hasebe et al. reported on applying the underwater shock waves focused by the open elliptical reflectors to bulging [5]. Most of these reports do not discuss the pressure gradient because they are aimed at utilizing the pressure and energy obtained by the focused shock wave.

The objective of this study is to derive the shape of the open elliptical reflector that can obtain a high-pressure gradient. In order to achieve this objective, numerical analyses of the pressure field of the open elliptical reflectors were conducted. In this report, the open elliptical reflectors were evaluated from the numerical analysis results regarding the qualitative pressure field and quantitative pressure distribution. These evaluations discuss the shape of the open elliptical reflectors required to obtain the high-pressure gradient.

2. Computational Method

Figure 1 shows the computational area and the boundary conditions. Numerical calculations were performed using ANSYS AUTODYN. In the numerical calculations, the axisymmetric two-dimensional unsteady compressible Lagrange equation and the Mie-Gruneisen equation of state were solved using the finite volume method. Time progression was explicit and discretized by a second-order central difference scheme using the Leapfrog method. The computational domain used in this numerical calculation was divided by hexahedral elements with a maximum length of 0.1 mm. In Figure 1, the boxed lines in the model represent the boundary conditions. The blue, red, and green lines represent the wall, transmission, and axial symmetry conditions. The open elliptical reflector is represented in the present numerical calculation using the wall boundary condition. In the experiments in this study, the high-pressure region was induced by the laser irradiation to generate the underwater shock wave. In general, the high-pressure region induced by the laser irradiation is known to have a Gaussian distribution. Therefore, in the calculation, an initial pressure to induce the underwater shock wave was given in the Gaussian distribution, as shown in Figure 2. Each divided initial pressure was 1.00, 0.32, and 0.01 GPa from the center of the first focal point.

As one of the calculation parameters, we introduced the flatness of the open elliptical reflectors, $F = (L_L - L_S)/L_L$, where L_L and L_S were the long and short radii of the ellipse, respectively. L_L was fixed at 15 mm, and by varying L_S, F varied from 0.1, 0.2, 0.3, 0.4 and 0.5. As another calculation parameter, we introduced the open ratio $O = L_O/2L_L$ for the open elliptical reflectors, where L_O was the open length of the open elliptical reflectors. O was varied from 0.2, 0.3, 0.4, 0.5 and 0.6. As shown in Figure 3, this numerical code was verified using the pressure decrease due to the propagation of the plane shock waves. Equation (1), derived from the Sedov-Taylor solution and the Rankine-Hugoniot equation, was used to compare the numerical result. In Equation (1), P, A, and D were pressure, constant determined by initial conditions and propagation distance. As shown in Figure 4, this numerical calculation was validated by a qualitative comparison of the numerical results of underwater shock wave focusing phenomena using an elliptical reflector with the experimental results [6].

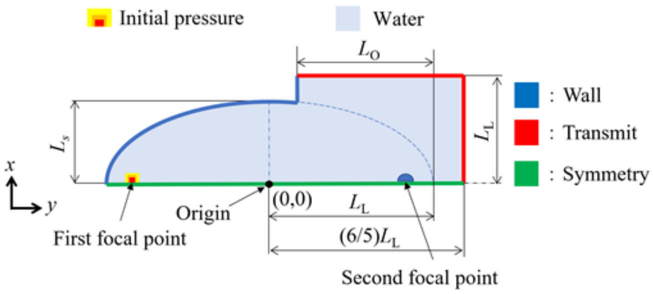

Figure 1. Computational area and boundary conditions.

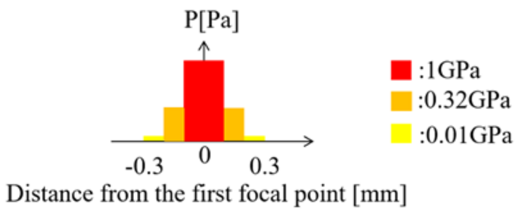

Figure 2. Initial pressure.

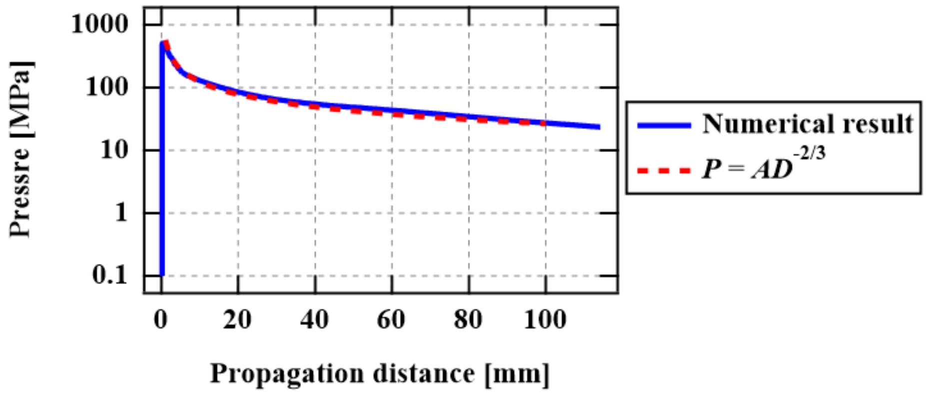

Figure 3. Calculation results of pressure decrease due to plane shock wave propagation using numerical simulation and Equation (1).

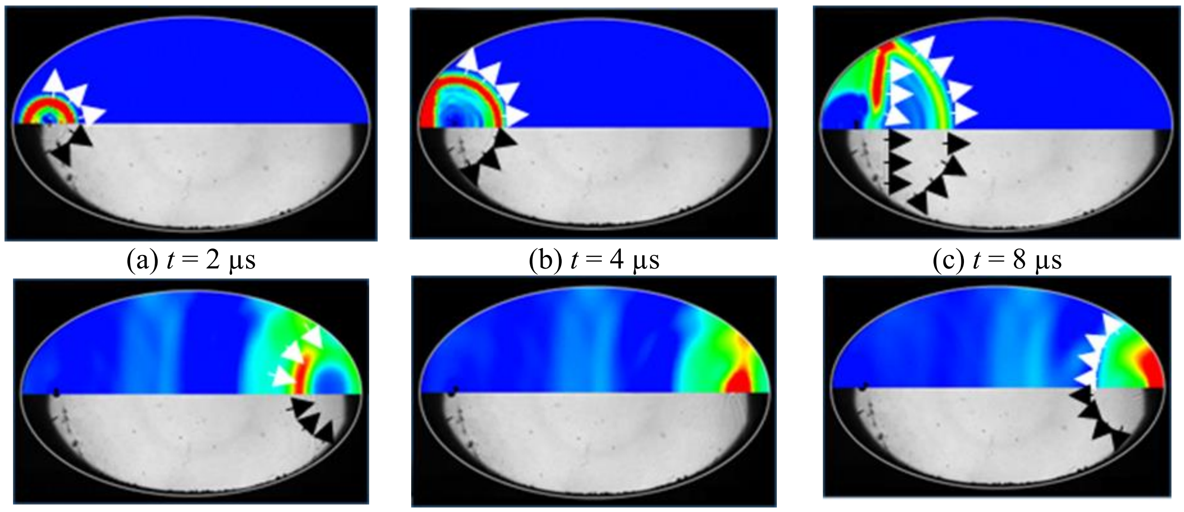

(a) $t = 2$ μs (b) $t = 4$ μs (c) $t = 8$ μs

(d) $t = 29$ μs (e) $t = 31.5$ μs (a) $t = 35$ μs

Figure 4. Qualitative comparison of density fields obtained from numerical calculations and shadowgraph images obtained from experiments. The figure is adapted from our previous work [6].

$$P = AD^{-\frac{2}{3}} \tag{1}$$

3. Results and Discussion

3.1. Typical pressure field

Figure 5 shows the time history of the pressure field in the open elliptical reflector for flatness $F = 0.1$ and open ratio $O = 0.5$, where t is the time elapsed from the moment the calculation is started. The arrows in Figure 5 indicate the propagation direction of the shock wave. Figures 5(a)-(b) show that the shock wave generated at the first focal point propagates in a circular direction. Figure 5(b) shows when the shock wave reaches the wall. The shock wave is then reflected by the wall, as shown in Figures 5(b)-(c). Since the open elliptical reflector is not perfectly elliptical, only a portion of the shock wave is reflected. Therefore, as shown in Figure 5(c), the shock wave is divided into a reflected shock wave (RSW) and a non-reflected shock wave (FSW). The FSW spreads circularly and diffuses. On the other hand, RSW propagates toward the second focal point while focusing due to the reflective property of the ellipses. Figure 5(d) shows when the RSW reaches the second focal point. It can be confirmed that a high-pressure region is formed around the second focal point due to the focusing of RSW.

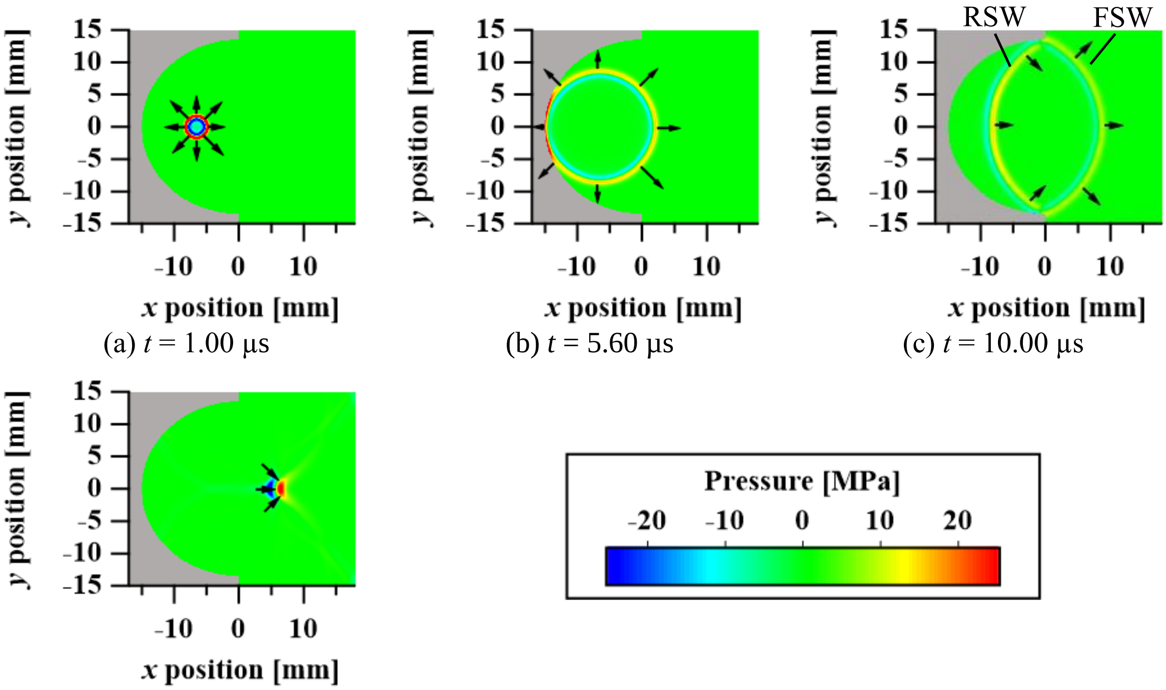

(a) $t = 1.00$ µs (b) $t = 5.60$ µs (c) $t = 10.00$ µs (d) $t = 19.50$ µs

Figure 5. Time history of the pressure field for $F = 0.1$, and $O = 0.5$.

3.2. Effect of flatness F of open elliptical reflector on shock wave focusing phenomena

In the case that the flatness of the open elliptical reflector is changed, the direction of incidence of the shock wave toward the second focal point changes. To investigate the effect of the change in the direction of incidence on the shock wave focusing phenomenon, Figure 6 shows the pressure field during shock wave focusing for flatness $F = 0.1$, 0.3, and 0.5. Figure 6 shows that as F increases, the shape of the high-pressure region around the second focal point expands vertically. The difference between these shapes is thought to be caused by nonlinear reflections of the shock wave. Generally, when a shock wave reflects, it is not linear [7]. The reflection angle of the shock wave is determined by parameters such as the angle of incidence. The angle of incidence on a wall depends on the flattening ratio. Therefore, the reflection angle differs for each flatness, which may explain the difference in the way the shock waves focusing.

It was confirmed that changes in the flatness affect the shock wave focusing region. Figures 7(a) and (b) show the pressure distributions on the x and y direction at the moment of shock wave focusing using the open elliptical reflector for F = 0.1, 0.3, and 0.5. The horizontal axis in Figure 7 is the distance from the second focal point. Figure 7(a) shows that the high-pressure region is formed from -1mm to 1mm for all flatness in the *x* direction. On the other hand, Figure 7(b) shows that the width of the high-pressure focusing region increases with increasing flatness in the *y* direction. This increase in width indicates the expansion of the shape of the high-pressure region due to the increase in the flattening ratio, as described above. Figures 7 (a)-(b) confirmed that the shock wave focusing region is nearly circular on the second focal point as the flatness is decreased.

To quantitatively evaluate the pressure gradient at the shock wave focusing by changing the flatness, the relationship between the flatness and the pressure gradient at the moment of the shock wave focusing is shown in Figure 8. The pressure gradient was defined as the slope of the line connecting the peak pressure and its half value. Figure 8 shows that the pressure gradients in the *x* and *y* direction increase as the flatness decreases. From the above, it is confirmed that as the shape of the open elliptical reflector becomes closer to a circle, the high-pressure region formed at the second focal point becomes localized.

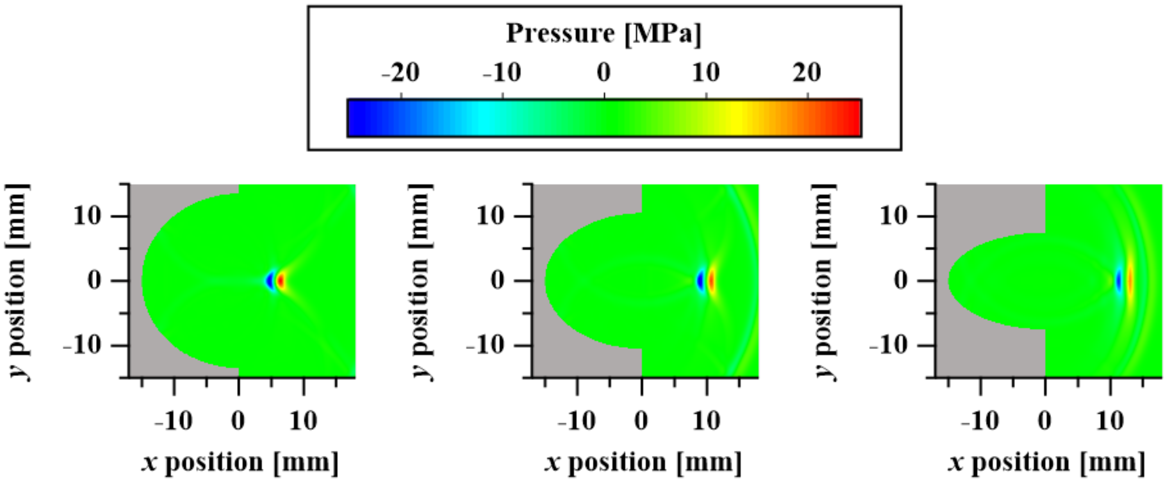

(a) $F = 0.1$ (b) $F = 0.3$ (c) $F = 0.5$

Figure 6. Pressure field at the moment of shock wave focusing for O = 0.5.

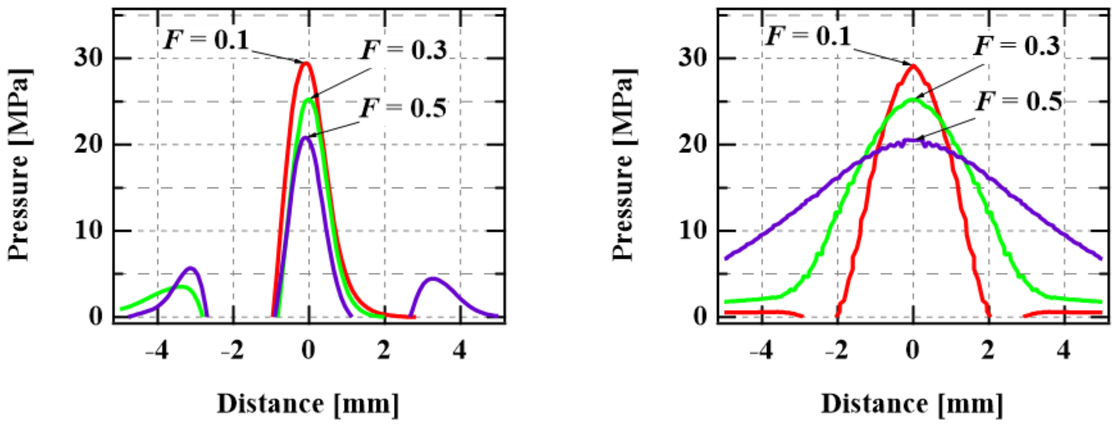

(a) x direction (b) y direction

Figure 7. Pressure distribution at the moment of shock wave focusing around the second focal point for O = 0.5.

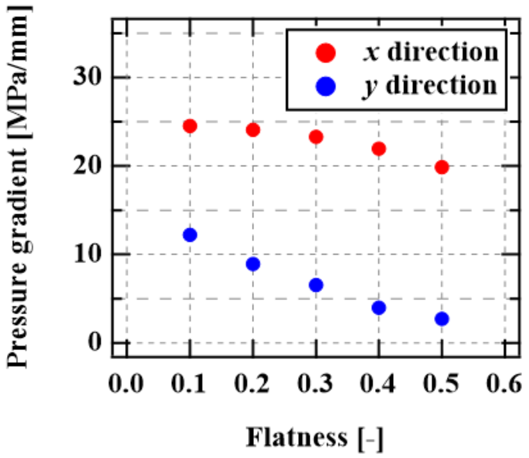

Figure 8. Relationship between flatness and pressure gradient at the moment of shock wave focusing for O = 0.5.

3.3. Effect of open ratio O of open elliptical reflector on shock wave focusing phenomena

In section 3.1, it was confirmed that the shock wave focusing region is formed by the RSW. The RSW is formed due to the reflection of the shock wave by the wall of the open elliptical reflector. Therefore, changes in the length of the reflecting wall are expected to affect the shock wave focusing phenomenon. Figures 9(a) and (b) show the pressure distributions on the x and y direction at the moment of shock wave focusing using the open elliptical reflector for O = 0.2, 0.4, and 0.6. The horizontal axis in Figure 9 is the distance from the second focal point. As shown in Figures 9(a) and (b), it can be confirmed that the pressure in the shock wave focusing region at the second focal point increases as the open ratio is decreased. This increase in pressure is likely due to the increase in the amount of the RSW caused by the make longer the reflective wall.

Figure 10 shows the relationship between the pressure gradient and the open ratio for F = 0.1, 0.3, and 0.5. Figure 10 shows that the pressure gradients in the x and y direction increase with decreasing the open ratio. These results suggest that using an open elliptical reflector with low flatness and open ratio is desirable for obtaining high-pressure gradients. This high-pressure gradient is thought to alter the refractive index and prevent light scattering. Using the shock wave focusing areas with the high-pressure gradients as an alternative to optical fibers is expected to expand the range of photomedicine applications to cells in the deep brain.

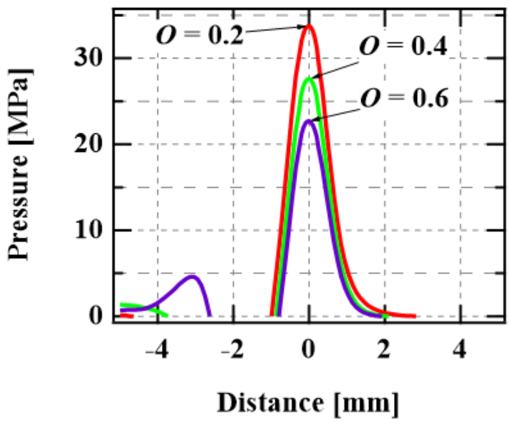

(a) x direction

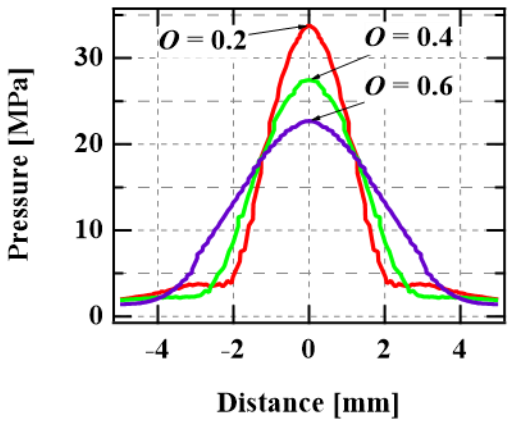

(b) y direction

Figure 9. Pressure distribution at the moment of shock wave focusing around the second focal point for F = 0.3.

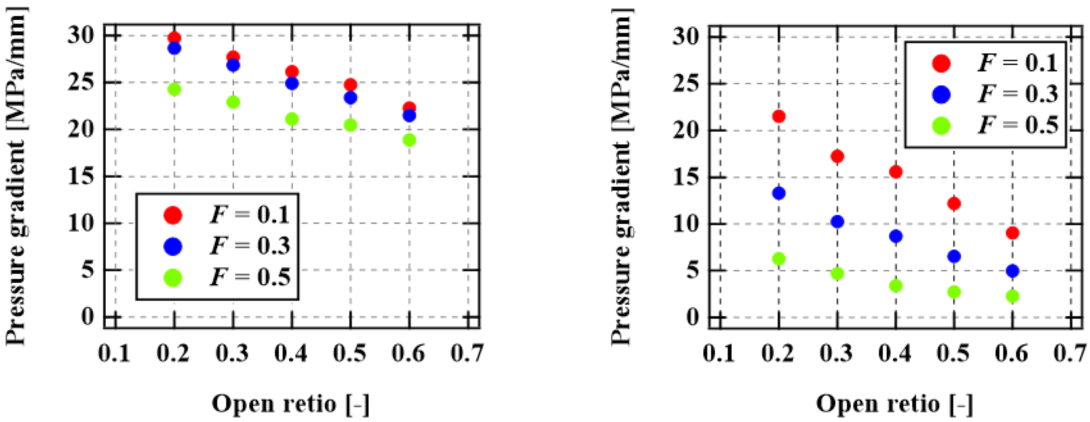

(a) *x* direction (b) *y* direction

Figure 10. Relationship between flatness and pressure gradient at the moment of shock wave focusing for *F* = 0.1, 0.3, and 0.5.

4. Conclusion

The objective of this study is to derive the shape of an open elliptical reflector required for high-pressure gradients based on numerical results. The calculation parameters are the flatness *F* and the open ratio *O* of the open elliptical reflector. For *O* = 0.2, 0.3, 0.4, 0.5, and 0.6, the pressure gradient at the moment when the shock wave focusing increased as the flatness decreased from 0.5 to 0.1. This is thought to be due to a nonlinear reflection of the shock wave. Similarly, the pressure gradient at the moment of the shock wave focusing increased as the open ratio decreased from 0.6 to 0.2. This is likely due to the increase in the amount of a reflected shock wave caused by the make longer the reflective wall. These results suggest that the open elliptical reflector with low flatness and open ratio should be used to obtain the high-pressure gradient.

5. Acknowledgments

This study was supported by the Japan Agency for Medical Research and Development (JP21dm0207076h033), “Brain Mapping by Integrated Neurotechnologies for Disease Studies.” I would like to express my deepest gratitude to Mr. Naruki Tomioka and Mr. Tetsuro Ikeyama for their guidance during this research.

6. References

[1] Shimoda, Y., Beppu, K., Ikoma, Y., Morizawa, M. Y., Zuguchi, S., Hino, U., Yano, R., Sugiura, Y., Moritoh, S., Fukazawa, Y., Suematsu, M., Mushiake, H., Nakasato, N., Iwasaki, M., Tanaka, F. K., Tominaga, T., & Matsui, K. (2022). Optogenetic stimulus-triggered acquisition of seizure resistance. *Neurobiology of Disease* (Vol. 163, p. 105602).

[2] Khabou, H., Orendorff, E., Trapani, F., Rucli, M., Desrosiers, M., Yger, P., Dalkara, D., & Marre, O. (2023). Optogenetic targeting of AII amacrine cells restores retinal computations performed by the inner retina. *Molecular Therapy - Methods & Clinical Development* (Vol. 31, p.101107).

[3] Zezhong, Y., Jun, C., & Bo, Z. (2023). Deflagration and detonation induced by shock wave focusing at different Mach numbers. *Chinese Journal of Aeronautics*.

[4] Zezhong, Y., & Bo, Z. (2023). Numerical and experimental analysis of detonation induced by shock wave focusing. *Combustion and Flame* (Vol. 251, p. 112691).

[5] Hasebe, T., Takenaga, Y., Kakimoto, H., & Imaida, Y. (1999). High strain rate forming using an underwater shock wave focusing technique. *Journal of Materials Processing Technology* (Vol. 85, No. 1-3, pp. 194-197).

[6] Ito, S., & Fukuoka, H. (2020). Behavior of Underwater Shock Wave in Ellipticall Cell. In *Yellow Sea Rim Workshop on Explosion, Combustion and Other Energetic Phenomena for Various Environmental Issues: YSR2020* (p. 25).

[7] Ben-Dor., G. (1992). *Shock Wave Reflection Phenomena*. Springer Verlag.

TSF0024

Evaluation of Sap Flow Rates in Tomato by Stem Heat Balance Method Using Infrared Thermography

Taro Nishimae[1], Hiroshi Fukuoka[1,*], Atsushi Suda[1], and Kenichi Iida[1]
[1] National Institute of Technology, Nara college, 22 Yata-cho, Yamatokoriyama,Nara, 639-1080, Japan

* Corresponding Author: fukuoka@mech.nara-k.ac.jp

Abstract. Quantifying plant growth conditions is essential for plant growth management. A sap flow is one of the most effective indicators of plant growth conditions. A Stem Heat Balance (SHB) method is used to measure the sap flow. The SHB method is a non-destructive method for measuring a sap flow rate by calculating a heat balance from the surface temperature of a heated stem. A previous study confirmed that a temperature measurement position significantly influences the accuracy of a sap flow calculation in the SHB method. However, finding an optimum temperature measurement position with conventional discrete temperature measurement using thermocouples is difficult. As a solution, we propose measuring temperature using infrared thermography. This study aims to establish the SHB method using infrared thermography. In this report, we confirm the influence of the temperature measurement position on the accuracy of the sap flow calculation. We experimented in a laboratory to evaluate the accuracy of our method. We used hydroponically grown tomatoes as an experimental target. The sap flow rates were evaluated by measuring transpiration rates using a weighing method. The transpiration rate was varied by changing the irradiation time of an artificial light source (LED), which was used to simulate sunlight. As a result, the accuracy of the sap flow calculation converged at positions away from the heater. It was also found that the temperature measurement position close to the heater was unsuitable for calculating the sap flow rate.

Keywords: Sap flow rate, Stem Heat Balance method, Infrared thermography, Transpiration, Herbaceous plant.

Nomenclature

Q	Heating value, W
Q_d	Heat conduction downstream, W
Q_u	Heat conduction upstream, W
Q_r	Heat dissipation to atmosphere, W
Q_f	Heat transport by sap convection, W
T	Measuring temperature, °C
λ	Thermal conductivity, $\mathrm{W/m \cdot K}$

A	Stem cross-sectional area, m^2
Δx	Distance between the two thermocouples used to measure, m
k	Sheath conductance, $\mathrm{W/K}$
F	Sap flow rate, g/min
C_W	Specific heat of water, $\mathrm{J/kg \cdot K}$
F_T	Transpiration rate, g/min
P_G	Average distance from the heater center to the two temperature measurement points, mm
d	Stem diameter, mm

1. Introduction

The number of farmers and new farmers in Japan is seriously decreasing. As a countermeasure for this problem, the management of plant growth using plant and growth condition data as an indicator is useful. This topic has been studied extensively. Xingchang et al. proposed a method to estimate nutrient resorption compromised by leaf mass loss and area[1]. Sugita et al. evaluated the optimal irrigation frequency for pineapples in the greenhouse based on growth variables and water status[2].

Among plant growth indicators, many studies have focused on sap flow, which provides information on plant water use. Enrique et al. detected water stress in olive trees based on the sap flow and trunk diameter[3]. Fu et al. studied the effects of several fertilizers and water on a grapevine sap flow[4].

A Stem Heat Balance (SHB) method, non-invasive, is a typical method for measuring sap flow. The SHB method calculates the sap flow by heating the stem and calculating the heat balance consisting of convection by the sap flow, heat conduction in the stem, and heat radiation to an atmosphere[5]. The heat balance is obtained from the stem surface temperature measured by thermocouples. The SHB method is a non-destructive method for calculating the sap flow rate, making it an ideal method for plant growth.

Numerous studies have been conducted on the SHB methods to measure the sap flow non-invasive. Nishioka et al. proposed an improved calibration-free SHB method using four thin-film heaters[6]. Baker et al. compared the accuracy of sap flow measurement between monocotyledonous and dicotyledonous plants in the SHB method[7].

In a previous study, Suenaga et al. investigated the effect of temperature measurement position on sap flow calculation results using highly reproducible model equipment that imitate a plant[8]. As a result, Suenaga et al. clarified the appropriate temperature measurement position under arbitrary experimental conditions. However, it is difficult to find the appropriate temperature measurement position using conventional discrete temperatures by thermocouples, and continuous temperature measurement is necessary. We propose an improvement using infrared thermography, a continuous temperature measurement device.

This study aims to establish the SHB method using infrared thermography. In this report, we investigate the effect of temperature measurement position on the accuracy of the sap flow calculation by the SHB method using infrared thermography. The influence of the transpiration rate and the temperature measurement position on the heat rate in the SHB method is also confirmed. The sap flow rate of a tomato was calculated using the SHB method with infrared thermography. The temperature measurement position using thermocouples is referred to as the sap flow calculation position in the case of using infrared thermography.

2. Theory of the SHB Method

Figure 1 shows the heat distribution for the SHB method. As shown in Figure 1, the heating quantity Q to the stem is distributed between the upper and lower heat conduction Q_d and Q_u, the heat radiation to the atmosphere Q_r, and the heat transport by convection of sap Q_f. The distribution of the heating quantity is represented by Equation (1).

$$Q = Q_{\mathrm{d}} + Q_{\mathrm{u}} + Q_{\mathrm{r}} + Q_{\mathrm{f}} \tag{1}$$

Q_{d}, Q_{u}, Q_{r} and Q_{f} in Equation (1) are calculated using the same formula as Sakuratani[5], respectively:

$$Q_{\mathrm{d}} = \lambda A \frac{T_{\mathrm{d}} - T_{\mathrm{d}}'}{\Delta x} \tag{2}$$

$$Q_{\mathrm{u}} = \lambda A \frac{T_{\mathrm{u}} - T_{\mathrm{u}}'}{\Delta x} \tag{3}$$

$$Q_{\mathrm{r}} = k(T_{\mathrm{c}} - T_{\mathrm{c}}') \tag{4}$$

$$Q_{\mathrm{f}} = F C_{\mathrm{w}}(T_{\mathrm{u}} - T_{\mathrm{d}}) \tag{5}$$

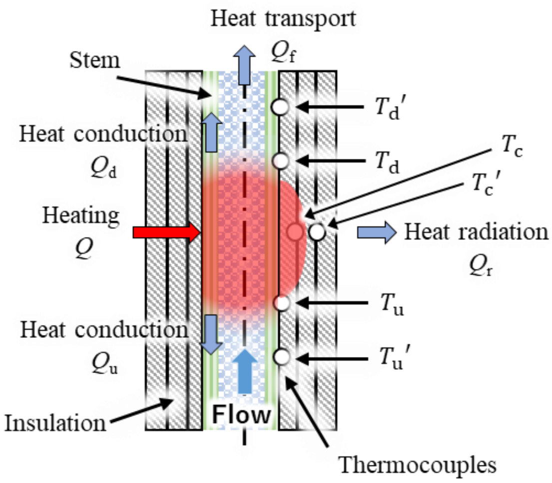

Figure 1. Heat distribution for SHB method.

3. Experimental method

Figure 2 shows a schematic diagram of the experiment. The sap flow rate was calculated using an infrared thermography (InfReC R550) and an infrared-SHB (I-SHB) gauge attached to the stem. Sap flow calculation is done on hydroponically grown tomatoes. The calculated sap flow rate was evaluated by comparing it with the transpiration rate. Transpiration is measured by the weighing method.

The I-SHB gauge consists of a thin-film heater, insulation, and thermocouples. The thin-film heaters, insulation, and thermocouples are responsible for heating the stem, insulating the stem from the outside air, and measuring the radial heat radiation of the stem, respectively. The thin-film heater comprises a nichrome wire, a copper sheet, and a polyimide seal. The thin-film heater is connected to a regulated DC power supply and generates heat when voltage is applied. Temperatures measured with thermocouples were recorded using a data logger. Infrared thermography was used to measure the stem surface temperature.

The tomato variety was Frutica. Tomato was grown by irradiating them with an artificial light source (LED) every 12 hours to reproduce daytime and nighttime conditions. The temperature was fixed at 26°C throughout the year. Tomato stem diameter and height were 6 mm and 1100 mm, respectively.

The SHB method was calculated using the same physical properties as Sakuratani[5]. The sheath conductance k was set to 0.00492 W/K based on the equation for one-dimensional steady-state heat conduction in a cylinder. In the SHB method, the stem surface temperatures at two points above and below the heater center and the temperature between the insulation behind the heater were used to calculate the sap flow rate. The distance between the two sap flow calculation points on the stem surface is 5 mm. The arrangement of the two points was symmetrical, with the heater at the center. P_G/d ranges from 1.35 to 3.75. There are 39 patterns of P_G/d in total. P_G is the average distance from the heater center to the two temperature measurement points. d is the tomato stem diameter. In other words, when sap flow was calculated from two points 10 and 15 mm from the heater center, the average distance P_G was 12.5 mm, and when divided by the stem diameter of 6 mm, P_G/d = 2.08.

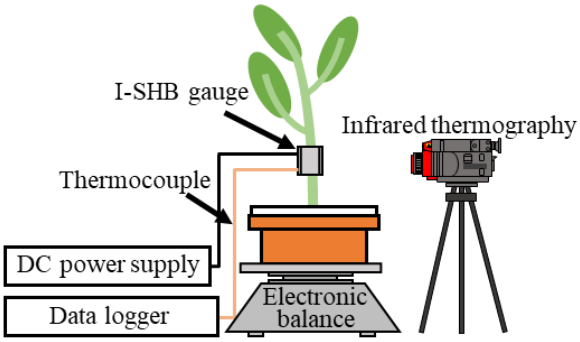

Figure 2. Diagram of experiment.

4. Results and discussion

4.1. Validity of temperature measurements by infrared thermography

Figure 3 shows the infrared thermography and the thermocouples temperature measurements on the heated stem surface to confirm the validity of the infrared thermography temperature measurements. The vertical and horizontal axes are the measured temperature and the distance from the heater center, with the downstream side positive and the upstream side negative, respectively. The red and blue plots show the measured temperatures of the infrared thermography and the thermocouples, respectively. The thermocouples were positioned 10 and 20 mm above and below the heater center, respectively. In this experiment, the stems were 6 mm in diameter. It can be seen from Figure 3 that the measured temperatures of the infrared thermography and thermocouples are almost equal. The average relative error between the temperatures measured by the infrared thermography and the thermocouples was 4.5 %. Therefore, the temperature measurement of the stem surface by infrared thermography is effective.

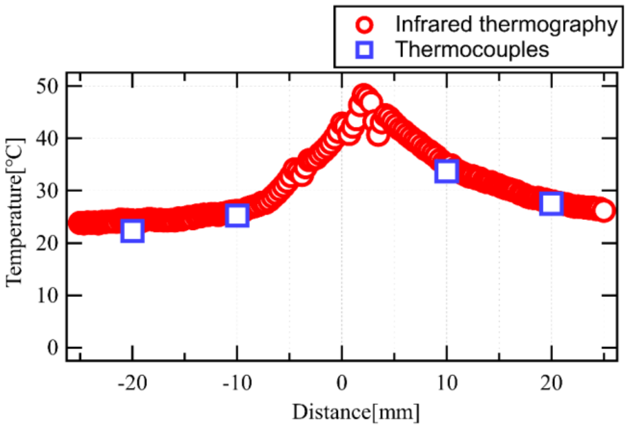

Figure 3. Comparison of temperatures measured by infrared thermography and thermocouples.

4.2. *Thermal image of stem surface*

Figures 4(a) and (b) show thermal images of the stem surface at F_T = 0.08 g/min and 0.2 g/min, respectively. The downstream and upstream sides in the figures have positive and negative coordinates, respectively. In Figure 4(a), the temperature increases in the range of -5~25 mm. This is because the heater is installed in the -5~5 mm range. The temperature increase in the -5 to 25 mm range is attributed to the convection of the sap, which transports heat to the downstream side. The same phenomenon can be observed in Figure 4(b) at F_T = 0.2 g/min. Figure 4(b) shows a decrease in temperature in the range of -5~25 mm compared to Figure 4(a). The reason for this is that the effect of convection by the sap increased as the amount of transpiration increased. The increased convective influence is expected to transport more heat downstream.

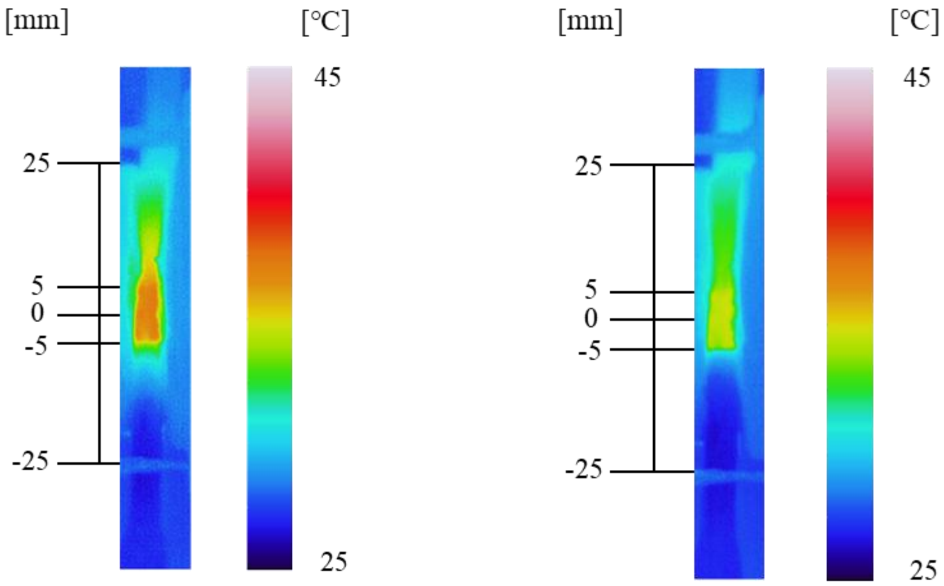

(a) F_T = 0.08 g/min (b) F_T = 0.2 g/min

Figure 4. Thermal image of stem surface.

4.3. *Effect of transpiration rate on heat balance*

From the above, it was confirmed that the effect of convection increased as the transpiration rate increased. To quantitatively confirm the effect of changes in transpiration on convection, Figure 5 shows the relationship between the transpiration rate and the heating rate for P_G/d=2.08 (heat conduction to the stem surface downstream Q_d, heat conduction to the stem surface upstream Q_u, heat radiation from the back of the heater Q_r, and heat transport by convection of sap Q_f). In Figure 5, the horizontal and vertical axes are the transpiration rate and the ratio of each heat quantity in the SHB method, respectively. In Figure, the blue, red, green, and yellow areas represent Q_d, Q_u, Q_r, and Q_f, respectively. The highest Q_f in the heat balance of the SHB method is 80% for FT=0.08. The lowest Q_f is 65% for F_T=0.20. Therefore, the ratio of Q_f is the highest in the heat balance of the SHB method. The increase in the transpiration rate confirms the increase in Q_f. The Q_d, Q_u, and Q_r decrease can also be seen as Q_f increases. The effect of the change in transpiration on the heat balance was quantitatively confirmed.

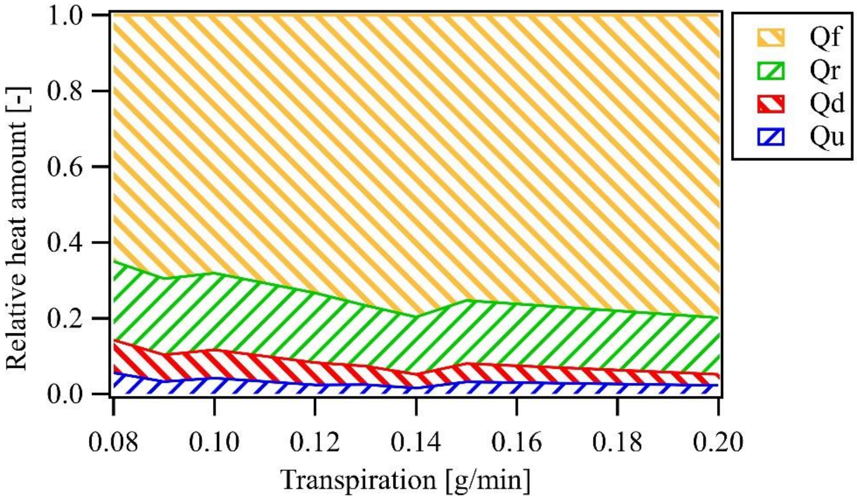

Figure 5. Relationship between transpiration rate and heating rate for P_G/d=2.08.

4.4. Effect of P_G/d on heat balance

In our previous study, we confirmed that the sap flow calculation position influences the accuracy of the sap flow calculation by using model equipment. Therefore, it is very important to investigate the effect of the sap flow calculation position on the heat balance in plants. To investigate the effect of changes in the sap flow calculation position on the heat balance, Figure 6 shows the relationship between P_G/d and each heat rate (Q_d, Q_u, Q_r, and Q_f) for F_T = 0.12 g/min. In Figure 6, the horizontal and vertical axes are the P_G/d and the percentage of each heat quantity in the SHB method. Figure 6 shows that Q_f has the highest ratio for all P_G/d. In the range of P_G/d = 1.25-2.0, Q_f increases as P_G/d increases. The decrease in Q_u is also observed with the increase in the Q_f. This means that Q_f increased despite a constant transpiration rate. In other words, changes in the sap flow calculation position affect the accuracy of the sap flow calculation.

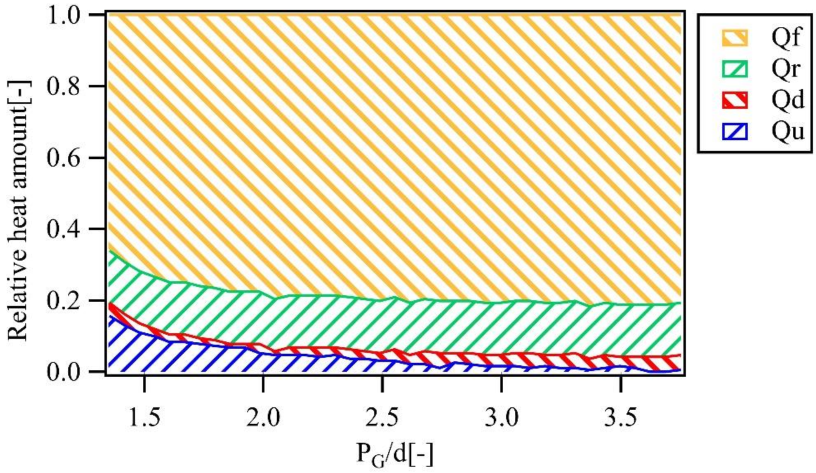

Figure 6. Relationship between P_G/d and heat balance for F_T = 0.12 g/min.

4.5. Sap Flow Rate Calculation Results

Figure 7 shows the relationship between P_G/d and sap flow calculation accuracy for F_T = 0.12 g/min to investigate the effect of sap flow calculation position on accuracy. The horizontal and vertical axes are the relative error of the calculated sap flow rate to P_G/d and transpiration rate, respectively. In Figure 7, the relative error of the calculated sap flow rate is negative with increasing P_G/d in the range of P_G/d

= 1.25-2.25. Furthermore, the relative error of the calculated sap flow rate is almost constant and converged for P_G/d = 2.25-3.75. The reason for convergence is the difference between the stem surface temperature and the mixed-mean temperature within the stem. Q_f in the SHB method represents the heat transport by the sap flow. Theoretically, the mixed-mean temperature is used to calculate Q_f. However, the stem surface temperature is used to calculate Q_f because the SHB method is a non-invasive inspection method. The stem surface near the heater is susceptible to heat conduction by the heater heat. Therefore, the temperature difference between the stem surface temperature and the mixed-mean temperature in the stem is larger the closer it is to the heater. On the other hand, the position away from the heater is not affected by the heat conduction of the heater heat, so the temperature difference between the surface temperature and the mixed-mean temperature in the stem becomes small. Therefore, the accuracy of sap flow calculation converged. The accuracy of sap flow calculation increased with decreasing P_G/d in the range of P_G/d = 1.25-2.25. On the other hand, the relative error of calculated sap flow for P_G/d = 2.25-3.75 was within 10% in all cases. Therefore, the position close to the heater is unsuitable for the sap flow calculation.

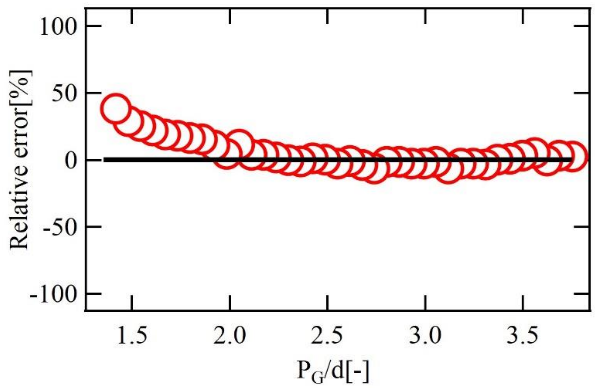

Figure 7. Relationship between P_G/d and accuracy of sap flow calculation.

5. Conclusion

This report aims to investigate the effect of a temperature measurement position on the accuracy of a sap flow calculation by an SHB method using infrared thermography. For this purpose, the sap flow rate of tomatoes was calculated by the SHB method using infrared thermography. The parameters used were transpiration rate F_T and the distance from the heater center to the sap flow calculation position P_G/d. The ratio of heat transport by sap convection, Q_f, was the highest for all transpiration rates in this experiment. The ratio of Q_f increased with increasing the transpiration rate. Furthermore, the ratio of Q_f increased as P_G/d increased. This means that changes in the P_G/d affect the accuracy of the sap flow calculation. An Error in the sap flow calculation increased with decreasing P_G/d in the range of P_G/d = 1.25-2.25. The error in the sap flow calculation for P_G/d = 2.25-3.75 was all within 10%. Therefore, the range P_G/d = 1.25-2.25, which is closer to the heater, is unsuitable for sap flow calculation.

6. Acknowledgments

This study was supported by The Foundation for Applied Research and Technological Uniqueness at Nagaoka University of Technology.

7. References

[1] Wang, X., Chen, Y., Liu, F., Zhao, R., & Quan, X. (2020). Nutrient resorption estimation compromised by leaf mass loss and area shrinkage. *Forest Ecology and Management: Variations and solutions*,472, 118232.

[2] Sugita, N, H., Herrera, M., Marano, R., & Luaces, P. (2022). Evaluation of irrigation frequency on pineapple plants grown in greenhouse conditions. *Scientia Horticulturae*, 302, 111186.

[3] Fernández, E, J., Moreno, F., Martín-Palomo, J, M., Cuevas, V, M., Torres-Ruiz, M, J., & Moriana, A. (2011). Combining sap flow and trunk diameter measurements to assess water needs in mature olive orchards. *Environmental and Experimental Botany*, 72(2), 330-338.
[4] Fu, S., Wei, X., Wang, T., & Bai, Y. (2022). Effects of different water and fertilizer treatments on grapevine sap flow and water consumption characteristics. *Scientia Horticulturae*, 304, 111317.
[5] Sakuratani, T. (1989). A Heat Balance Method for Measuring Water Flux in the Stem of Intact Plants. *Agric Meteorol*, 37(1), 9-17.
[6] Nishioka, K., Tsunoda, Y., & Mizunaga, H. (2012). An Improved Design of Sap Flow Gauge without Calibration Using Quad Thin Film Heater. *The society of instrument and control engineers*, *48*(12), 800-808.
[7] Baker, M, J., Moreno, & Nieber, L, J.. (1989). An analysis of the steady-state heat balance method for measuring sap flow in plants. *Agricultural and Forest Meteorology*, *48*, 93-109.
[8] Suenaga, K.,Fukuoka, H., Suda, A., Nakamura, S., & Iida, K. (2021). positioning improvement of temperature measurement for flow rate measurement system based on stem heat balance method, *The 32nd International Symposium on Transport Phenomena*.

TSF0025

Physical factors of fabric duct that influence on occupant thermal comfort

S Boonpaijit[1], S Panjapisutsri[1], T Prunkyangyuen[1], and K Khaothong[1,*]

[1]Department of Mechanical Engineering, Faculty of Engineering at Kamphaeng Saen, Kasetsart University Kamphaeng Saen Campus, Nakhon Pathom, 73140, Thailand.

* Corresponding Author: fengkkk@ku.ac.th

Abstract. This study investigates the physical characteristics of fabric ducts with holes that directly affect the supply and distribution of air factors and the thermal comfort of occupants in air-conditioned rooms following the ASHRAE 55 standard by computational fluid dynamics (CFD). The results show the fabric duct size, hole size, and the angle of holes influence the thermal comfort factors at the ankle region more than the neck region of the occupants in the air-conditioned room.

Keywords: fabric duct, supply air, taguchi method, and air conditioning.

1. Introduction

The air conditioning system has revolutionized indoor environments. Its primary function is to condition the air, making it suitable for human comfort by controlling temperature, humidity, and air quality in regulating weather conditions within enclosed spaces. Thailand's favor of air-cooled air conditioning systems reflects their effectiveness in providing comfort amidst a tropical climate. The choice of materials for manufacturing air ducts is vital in ensuring efficient cooling while considering factors like durability and energy efficiency. Furthermore, understanding how different air ducts affect system layout helps optimize airflow distribution and overall performance. Galvanized steel sheets, canvas, pre-insulated air ducts, and PVC-coated polyester fiber fabric have unique properties that contribute to durability, insulation capabilities, cost-effectiveness, and ease of installation. In the tropical country of Thailand, Air conditioning system designers must consider three main factors [1-2].

1. The temperature of the exposed air, commonly referred to as the dry bulb temperature, is within the comfort range for occupants, typically between 24 °C and 27 °C.

2. The comfort range for Thai occupants between 6:00 p.m. and 10:00 a.m. typically falls within a wind speed range of 0.2 m/s to 0.4 m/s.

3. In Thailand, 50% to 60% relative humidity is optimal for human comfort. This range allows for efficient evaporation while minimizing excessive water loss from our bodies. It enables sweat to evaporate adequately without causing excessive drying or dehydration.

According to the Ashrae-55 standard, the predicted mean vote (PMV) index quantifies the level of thermal comfort experienced by individuals based on their subjective feedback. Using Equation (1) to calculate PMV values and refer to Table 1 for categorization, designers can determine whether an indoor environment is within the acceptable range of occupant comfort. The predicted percentage dissatisfaction (PPD) index provides further insight into occupant comfort levels. Equation (2) allows for calculating PPD values based on PMV data. Table 2 then categorizes PPD values to indicate the percentage of occupants likely to be dissatisfied with their thermal conditions [3].

$$PMV = 0.303[3.155e^{-0.114M} + 0.028]L \quad (1)$$

$$PPD = 100 - 95 \times e^{-(0.03353PMV4 + 0.2179PMV2)} \quad (2)$$

M is metabolic rate(W/ m^2, Btu/h×ft^2, met), and L is thermal load (W/ m^2).

Table 1. PMV index scale

PMV value	Feeling
-3	cold
-2	cool
-1	slightly cool
0	neutral
1	slightly warm
2	warm
3	hot

Table 2. Acceptable Thermal Comfort

PPD	PMV range
PPD < 10%	-0.5 < PMV < 0.5

Equations (3) represent the conservation equations and are fundamental to understanding flow behavior, providing insight into how fluids move, mix, and interact with their surroundings. The parameter includes information about velocity fields, pressure distributions, and other essential flow properties by solving these equations numerically using the k-ε turbulence model, as shown in Equations (4), which are solved by computational fluid dynamic methods.

$$\frac{\partial M_{cv}}{\partial t} = \sum M^{\bullet}_{in} - M^{\bullet}_{out} \quad (3)$$

M is mass flow rate (kg/s) in Control volume.

$$\frac{\partial \rho \varepsilon}{\partial t} + \frac{\partial \rho \varepsilon u_i}{\partial x_i} = \frac{\partial}{\partial x_i}\left(\left(\mu + \frac{\mu_t}{\sigma_\varepsilon}\right)\frac{\partial \varepsilon}{\partial x_i}\right) + C_{\varepsilon 1}\frac{\varepsilon}{k}\left(f_1 \tau^R_{ij}\frac{\partial u_i}{\partial x_j} + C_B u_t P_B\right) - f_2 C_{\varepsilon 2} \quad (4)$$

Human comfort can be controlled by cold air generation and air transmission and distribution from the duct. Therefore, the air conditioning system designer must consider the air duct's type and the space's size. Comparing the performance of conventional ductwork with recent advancements in fabric duct that the results conclusively show that fabric ducting systems heat the room faster, more uniformly, and more efficiently [4]. Energy savings in air-conditioning systems are paramount to energy conservation in buildings. The selection of air duct type depends on the usage characteristics. The different types of air ducts cause various energy losses, directly affecting energy costs [5]. This research is on the physical factors of modern fabric air ducts woven from polyester fibers along warp and weft, allowing for good tensile strength. The pre-outermost layer is acrylic coated to make it strong and flexible, and the outermost layer is PVDF coated to prevent mold formation [6].

2. Methodology

This research study investigates air distribution in a small air-conditioned room (5 m in width, 6 in length, and 4 in height). The distribution of air was achieved through the use of PVC-coated polyester fabric ducts, considering five physical factors: duct diameter (D), duct bore diameter (D_i), bore degree (degree), duct internal temperature (T_{dis}), and room temperature(T_{inr}). Each factor has been analyzed at five different levels, as shown in Table 3, corresponding to the Taguchi L25 experimental design.

Table 3. Taguchi L25 experimental design.

Experiment	D (mm)	D_i (mm)	Degree	T_{dis} (°C)	T_{inr} (°C)	Experiment	D (mm)	D_i (mm)	Degree	T_{dis} (°C)
1	200	10	30	8	28	14	240	40	30	12
2	200	20	60	10	30	15	240	50	60	14
3	200	30	90	12	32	16	260	10	120	10
4	200	40	120	14	34	17	260	20	150	12
5	200	50	150	16	36	18	260	30	30	14
6	220	10	60	12	34	19	260	40	60	16
7	220	20	90	14	36	20	260	50	90	8
8	220	30	120	16	28	21	280	10	150	14
9	220	40	150	8	30	22	280	20	30	16
10	220	50	30	10	32	23	280	30	60	8
11	240	10	90	12	30	24	280	40	90	10
12	240	20	120	8	32	25	280	50	120	12
13	240	30	150	10	34	14	240	40	30	12

Investigate the 3D air-conditioned room model in Figure 1. The boundary condition is consonant with red shading, and the initial condition is consonant with black shading, as shown in Figure 2. Using the SolidWorks flow simulation software to solve the PPD and PMV index on the Neck (19 red color points) and ankles (19 white color points) shown in Fig 3, following the recommendations provided by ASHRAE-55.

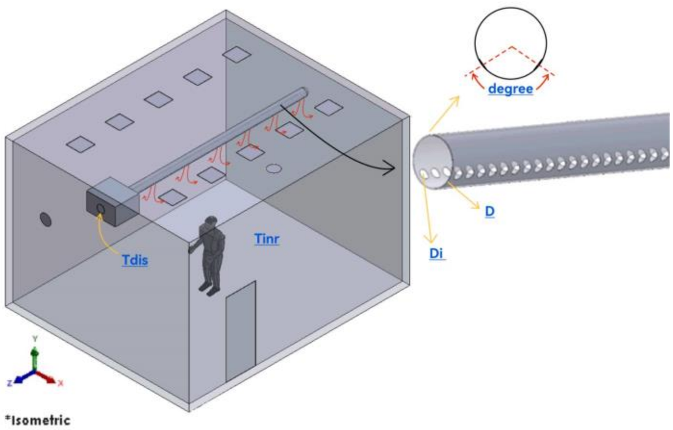

Figure 1. The 3D air-conditioned room model.

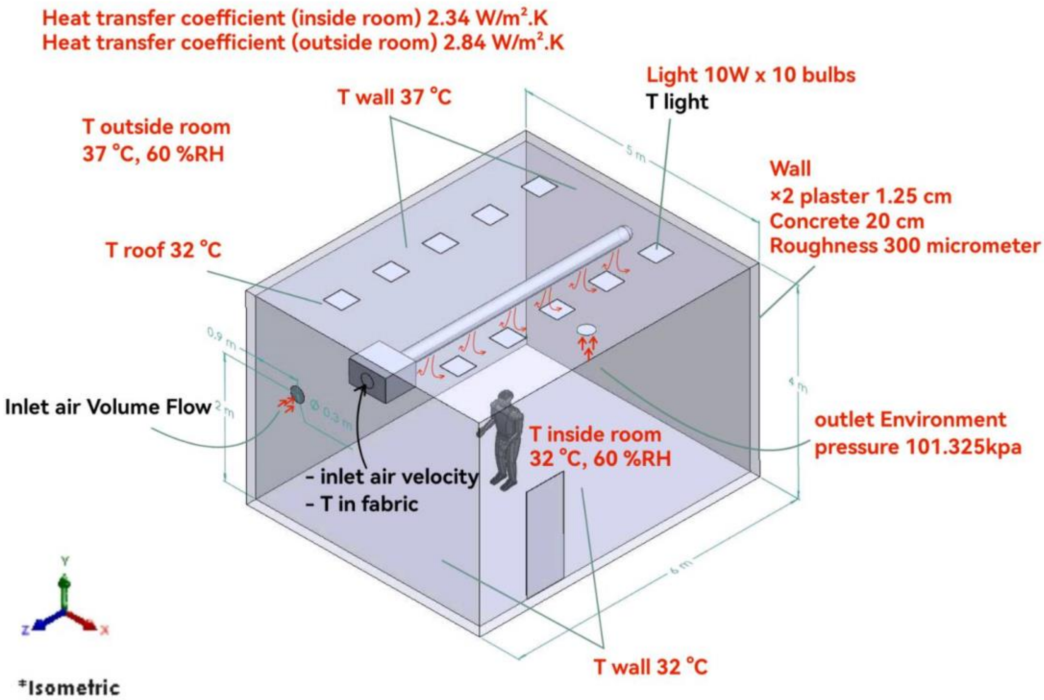

Figure 2. Boundary condition and Initial condition.

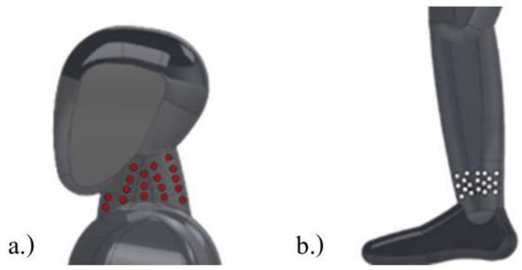

Figure 3. a.) Neck (19 red point) and b.) Ankle (19 white point).

3. Results

Results of 25 simulation results and validation of the simulation using with the CBE Thermal Comfort Tool.

3.1 Results

Experimental 4, Varying PMV values and PPD are acceptable Thermal comfort according to ASHRAE-55 cause the difference in body heat at the ankle and neck, as shown in Figures 4a and 4b. The ankle region's lower metabolic activity and reduced blood circulation contribute to a cooler sensation, making it more comfortable than the neck region. These findings on the intricate dynamics of thermal comfort within different anatomical zones emphasize the importance of localized analysis when assessing overall human well-being in various environmental conditions.

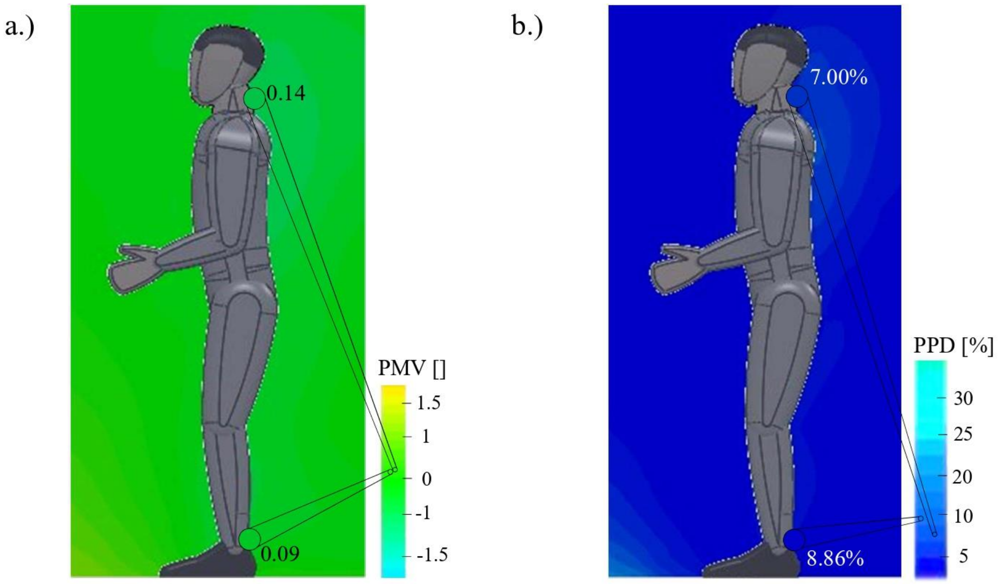

Figure 4. XY Plane a.) PMV and b.) PPD.

The contour of PMV and PPD at the neck and ankle inside the room in the XZ plan of experiment 4, as shown in Figures 5 and 6. The airflow at the end of the room and the amount of heat on the left, front and the end walls are higher than the other walls, causing the PMV and PPD indexes to have different values from other areas within the room. The temperature at the end of the room was cool, and the left wall area was somewhat warmer than the other areas. and the temperature in the ankle plane is higher than in the neck plane.

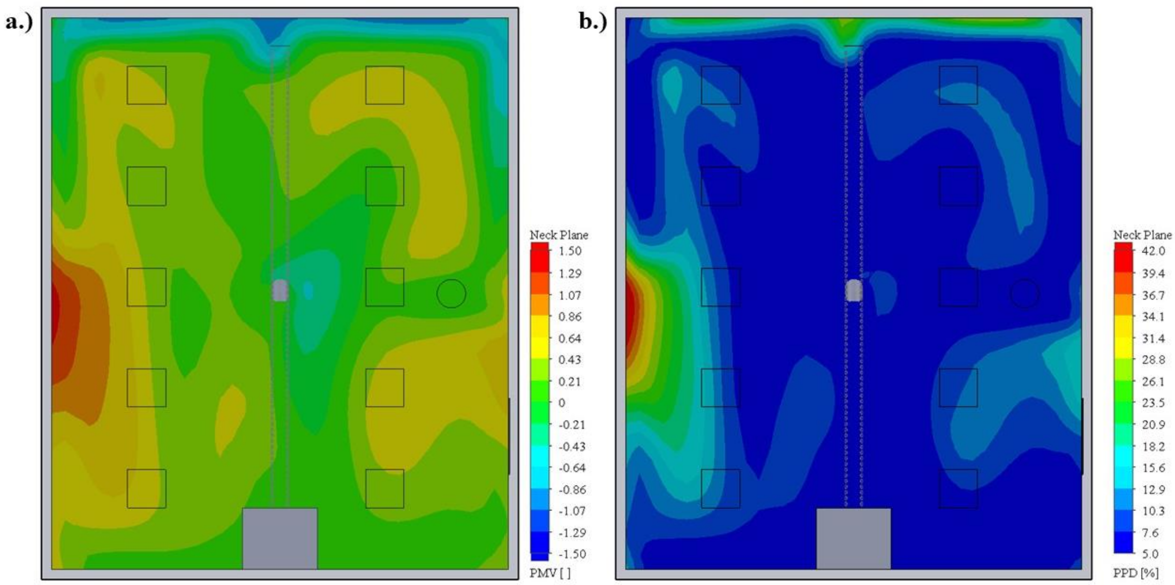

Figure 5. XZ Plane at the neck. a.) PMV and b.) PPD.

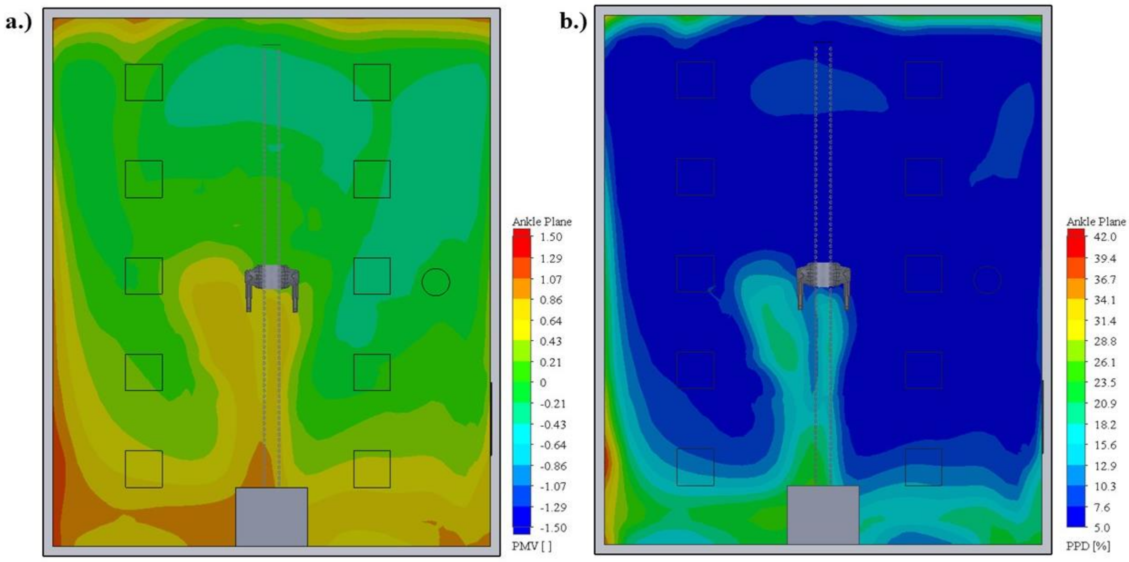

Figure 6. XZ Plane at the ankle. a.) PMV and b.) PPD.

Figure 7 shows valuable insights into different body regions' thermal comfort levels. The results comprehensively understand the neck and ankle area's PMV and PPD index values. The green line signifies the values at the neck region, while the orange line represents those at the ankle area. This differentiation helps identify potential variations in thermal comfort experienced by individuals across different body parts. Referring to Ashrae-55 guidelines, it becomes evident that simulations 4, 5, 9, and 10 show the specified comfort zone that these simulations successfully maintain acceptable thermal comfort levels for occupants.

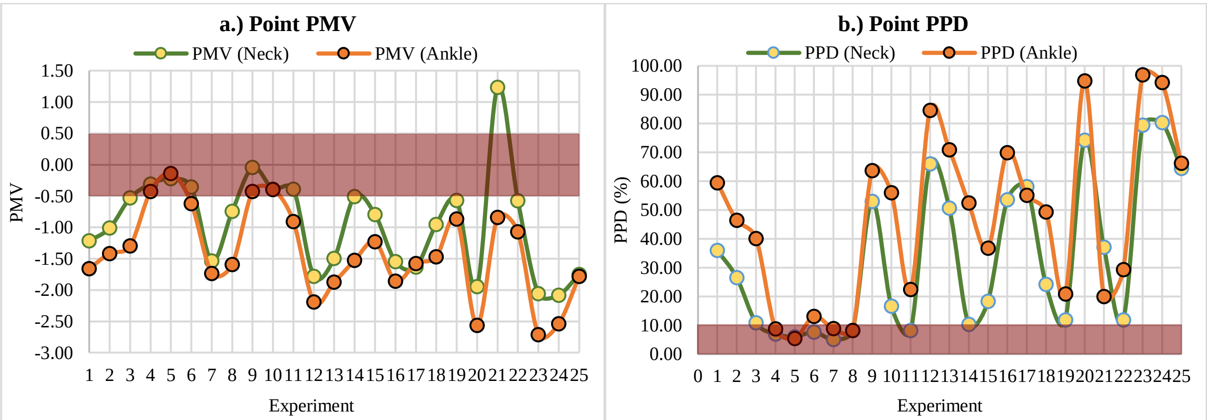

Figure 7. Point of a.) PMV and b.) PPD.

The XZ plane simulation results of the PMV and PPD index on the neck and ankle shown in Figure 8 offer a comprehensive understanding of the thermal conditions of individuals in different parts of their bodies. Duct diameter of 200 mm ensures air can flow through it, allowing for efficient cooling. Similarly, the 40 mm size of duct bore diameter facilitates the smooth release of cool air into the room. Furthermore, air holes are distributed 96 into two rows with an angle of 120 degrees so that cool air is distributed throughout the room.

Finally, the conditioning effect on air temperature creates a pleasant indoor environment with a room temperature of 34 ºC and duct internal temperature of 14 ºC. This substantial cooling relieves hot weather conditions and creates a comfortable setting for occupants.

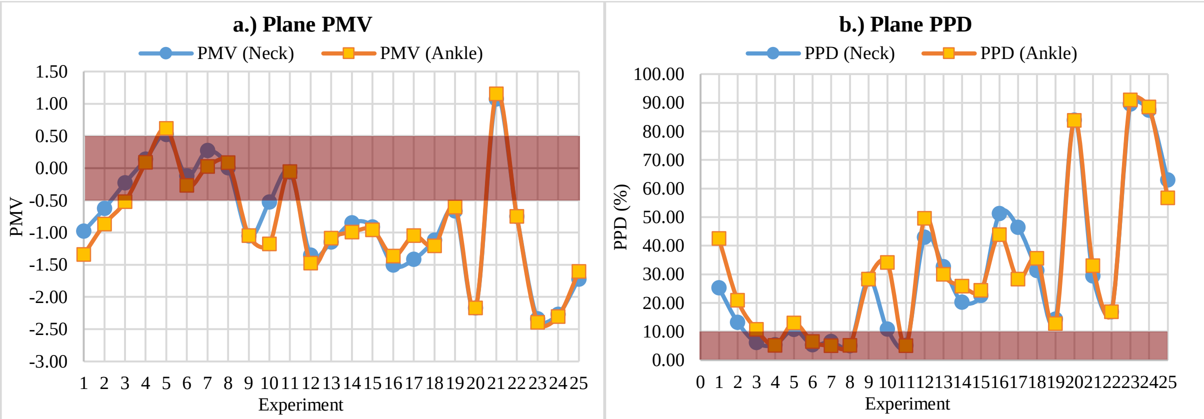

Figure 8. Plane XZ of a.) PMV and b.) PPD

3.2 *Validation*

The Ashrae-55 Standard is the accuracy of all 25 models assessed using simulation with the CBE Thermal Comfort Tool [7], as shown in Figure 9. The evaluation results from simulation 4, the simulation with an acceptable index. and found that when compared with the simulation results, there was an acceptable error, which is an acceptable average error percentage in the research not exceeding 10% [8]. When analyzing the simulation results, it was found that all 25 cases showed 7.70 percent—the research acceptable average percentage error not exceeding 10% [8]. Upon analyzing the simulation results, it was observed that all 25 cases exhibited 7.70%.

Figure 9. CBE Thermal Comfort Tool

4. Conclusion

Computational fluid dynamics methods can explain how air delivery affects occupant comfort as recommended by the ASHRAE-55 standard in small air-conditioned rooms. The designer must specify a duct diameter of 200 mm. Similarly, the 40 mm size of duct bore diameter facilitates the smooth release of cool air into the room. Furthermore, air holes are distributed 96 into two rows with an angle of 120 degrees so that cool air is distributed throughout the room. Finally, the conditioning effect on air temperature creates a pleasant indoor environment with a room temperature of 34 ^{o}C and a duct internal temperature of 14 ^{o}C.

5. Acknowledgments

This research is funded by Kasetsart University through the Graduate School Fellowship Program**.**

6. References

[1] Buranasompob, T. (1996). *Design of energy-efficient buildings*. Bangkok: Amarin Printing and Plublishing co.ltd.
[2] Taweekun, J., & Tantiwichien, A. (2013). Thermal Comfort Zone for Thai People. *Journal of Scientific Research*, *5*(5), 525-529.
[3] ASHRAE, A. (2017). Thermal environmental conditions for human occupancy. American Society of Heating, Refrigerating and Air-Conditioning Engineers. *ANSI/ASHRAE Standard 55-2017*, 39-53.
[4] Fontanini, A., Olsen, M. G., & Ganapathysubramanian, B. (2011). Thermal comparison between ceiling diffusers and fabric ductwork diffusers for green buildings. *Journal of Energy and Buildings*, 43(11), 2973-2987.
[5] Tanadecha, P., & Khaothong, K. (2023). Thermoeconomic analysis of duct works for air-conditioned building in Thailand. *Journal of Energy and Built Environment*.
[6] Khaothong, K., Chaiworapuek, W., & Priyadumkol, J. (2019). Pressure Loss Diagram of Air Flow in Polyester Fabric Duct Acrylic PVC Coated. *Journal of KMUTNB.*, 29(3), 448-449.
[7] Tartarini, F., Schiavon, S., Cheung, T., & Hoyt, T. (2020). CBE Thermal Comfort Tool: Online tool for thermal comfort calculations and visualizations. *Jounal of SoftwareX*, 12, 3.
[8] Dutt, N., Binjola, A., Hedau, A. J., Kumar, A., Singh, V. P., & Meena, C. H. (2022). Comparison of CFD Results of Smooth Air Duct with Experimental and Available Equations in Literature. *International Journal of Energy Resources Applications (IJERA)*, 1(1), 40-47.

The 13th TSME International Conference on Mechanical Engineering
12th – 15th December 2023
Chiang Mai, Thailand

TSF0027

Dependence of Inlet Flow Condition on Heat Transfer around the Flat Plate in a Pulsating Duct Flow

Hironori SAITOH[1,*] and Raiki KATOH[2]

[1]Departmet of Mechanical Engineering, Sojo University
Ikeda 4-22-1, West Ward, Kumamoto City, 860-0082, Japan
[2]Graduate School of Mechanical Engineering, Sojo University
Ikeda 4-22-1, West Ward, Kumamoto City, 860-0082, Japan

* Corresponding Author: saitoh@mec.sojo-u.ac.jp

Abstract. This study deals with the performance improvement with active temperature control of thermal devices, heat engines, and process engineering such as metal casting and injection molding by resin injection. We focus on the pulsating flow in sort of higher controllability of flow behaviour in comparison with steady flow. The objective of this study is to make clear the effect of velocity distribution at inlet on heat transfer characteristics around the flat plate installed in a pulsating duct flow. The result showed that no impact of flow pulsation on heat transfer around the flat plate was obtained in the case with uniform velocity distribution at inlet, on the other hand, heat transfer enhancement by flow pulsation was indicated when non-uniform velocity distribution was supplied at the inlet of the duct.

Keywords: Heat transfer, Flow pulsation, Pulsating frequency and amplitude, Inlet velocity profile.

1. Introduction

This research is a fundamental study in the interdisciplinary field of mechanical engineering and life sciences, aiming to the application of "active temperature control of various mechanical devices through pulsating flow" based on the "temperature regulation mechanism by blood flow in living organisms." Temperature control is important in various industrial devices. However, many modern industrial devices have been designed under steady-state operation with their constant temperature, and passive control of their temperature such as cooling is typically employed in sort of thermal-endurance of their materials. For example, cooling losses in reciprocating internal combustion engines can account for about 30%, although it depends on the operating conditions. Excessive cooling of cylinder liner and block occurs except for the expansion stroke when it is exposed to high-temperature combustion gases. Therefore, such heat loss can be reduced by active temperature control of cylinder liner with precise control of cooling water flow. On the other hand, living organisms have evolved over a long period of time and efficiently regulate body temperature through blood flow (pulsating flow) and perspiration. In addition, living organisms exhibit high responsiveness in temperature regulation. This study aims to quantitatively elucidate the heat and mass transfer/transport characteristics of pulsating flow using flow rate modulation modes, time-averaged flow rate, pulsation frequency, and amplitude as parameters. This study also explores the potential of active temperature control by convection heat transfer with pulsating flow for improving the efficiency of industrial equipment operating under unsteady state conditions, which is introduced at the beginning of the abstract.

Research on pulsating flow has been the subject of numerous experimental and numerical analysis reports. Shiibara [1] et al. extensively surveyed earlier studies (1988-2017). They summarized and classified the results regarding the heat transfer characteristics on the wall in contact with pulsating flow and reported conflicting findings among researchers regarding the effects of imparting pulsation (temporal flow rate modulation) on heat transfer enhancement. One of the reasons for the lack of a unified understanding is pointed out as the localized nature of measurements and the discussion of flow fields and accompanying heat transfer characteristics based on their time-averaged values. To address this issue, they discussed phenomena based on measurements using infrared thermography for fully developed flows. Most recent review on pulsating flow was reported by Ye [2] et al. (2021) for the wide range of pulsating flow with 182 references. They also concluded that the heat transfer effect of pulsating flow is unstable, sometimes the heat transfer is enhanced and sometimes the heat transfer is weakened due to the complex phenomenon of pulsating flow and the differences in experimental geometric models, operating conditions and waveform. Finally, they summarized that there is still no widely accepted explanation on the mechanism of pulsating flow, therefore, the study of pulsating flow is still very worthy of attention, and the mechanism of pulsating flow has yet to be further studied even for the single-phase flow. As the latest report in the turbulent region, Yamazaki [3] and Oda [4] focused on the transient non-similarity in momentum and heat transport and conducted validation through phenomenological predictions using direct numerical simulation (DNS) and experiments using hot and cold wires for the fully developed region. On the other hand, this study targets relatively short flow paths and focuses on flow and heat transfer in the inlet region not developed flow region. The authors [5-6] have previously investigated the heat transfer characteristics on a flat plate set in a rectangular duct under continuous sinusoidal flow rate fluctuation and intermittent pulse wave fluctuation as pulsation modes. The results showed significant differences in heat transfer characteristics around the flat plate, which depends on the inlet flow condition with and without a screen mesh at an upstream side of the flow passage regardless the pulsation modes (waveforms). The screen mesh was equipped aiming for uniform velocity distribution at inlet of the flow passage.

The objective of this study is to make clear the effect of inlet velocity distribution in the direction of the channel width on heat transfer around the flat plate installed in a pulsating duct flow. Local velocity measurements at the inlet of the flow path were conducted as well as the experiments that evaluated heat transfer characteristics.

2. Experimental Setup and Method

2.1. Test Section

The structure of the test section is shown in Figure 1. The test section consists of a rectangular duct with a square cross section of 100 mm x 100 mm and a heating flat plate placed to delimit the duct at its center. Stainless-steel foil, 0.02mm in thickness, was attached on both surfaces of the flat plate as a heater. On the assumption that the flow in the rectangular duct is symmetrical with the heating flat plate as the boundary, one of the two heaters was used as a heat transfer surface to investigate heat transfer characteristics, while the other was a guard heater to achieve negligible small heat loss across the plate. Each heater on the both sides of the flat plate was attached in a form of four 15 mm x 300 mm (width x length) strips of stainless-steel foil connected in series. The front and back side heaters were also connected in series to achieve an electrical resistance of 6.4 Ω. This value of electrical resistance was calculated by designing the heater to achieve a heat flux corresponding to the experiments in the mixed (forced/natural) convection region using an AC power supply (100 V) and wiring with a general parallel cord with its current capacity around 4 A.

The heating flat plate was constructed from two plates. Thermocouples were attached at 14 locations (7 points x 2 rows in the flow direction) on the back side of the heat transfer surface. Thermocouple bundles were extracted to the outside of the test section through the space formed between two plates.

The duct has a pair of transparent Plexiglas windows for carrying out the visualization of thermal boundary layer formed on the heating surfaces by color Schlieren method. Details of the thermocouple mounting locations are shown in Figure 2.

2.2. Heat Transfer Experiment

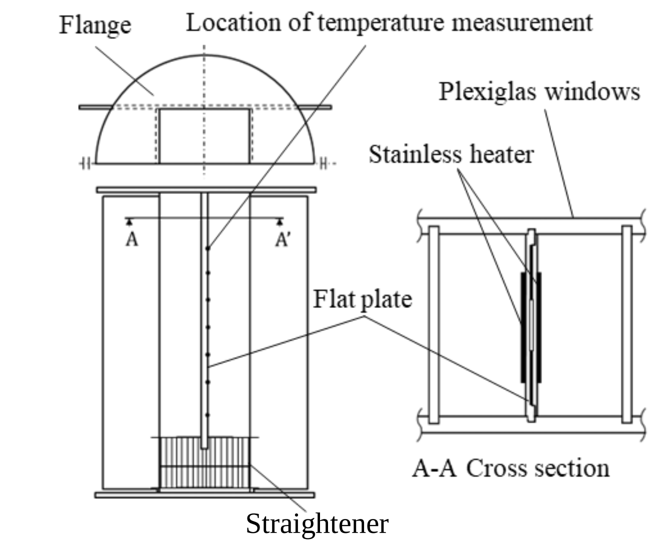

Figure 1. Test Section.

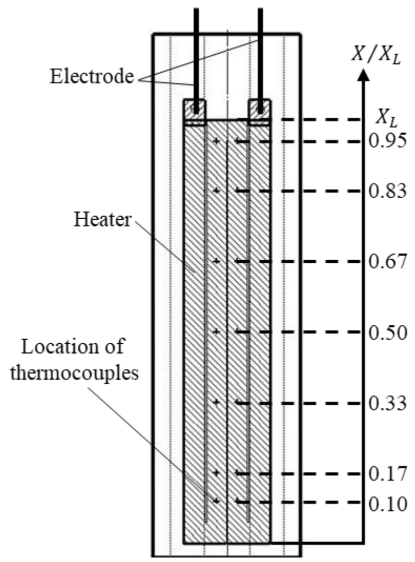

Figure 2. Heat transfer surface.

A schematic diagram of the Experimental equipment is shown in Figure 3. The test fluid was air and was driven by a sirocco fan. Temporal flow fluctuations were achieved by providing flow resistance through the reciprocating movement of a valve installed at an upstream side of the test section. Air passing through the test section was released from a surge tank into the atmosphere as a steady flow. The velocity of the released air was measured with a hot-wire anemometer. Experiments were conducted under uniform heat flux conditions by electric heating of the stainless heater. The heat flux was determined by dividing the supplied electrical power by the heat transfer area, expressed as Equation (1).

$$\dot{q} = I \cdot V / A_{hs} \tag{1}$$

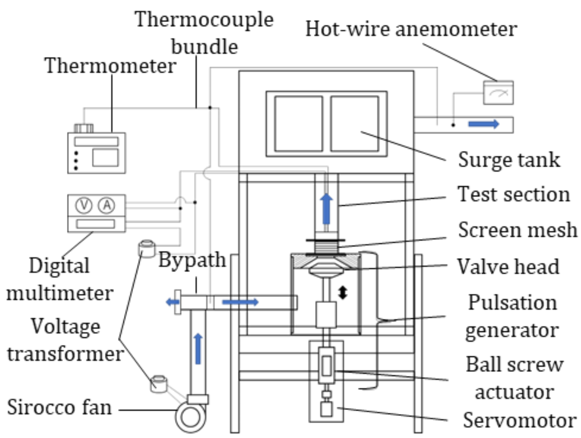

Figure 3. Experimental apparatus.

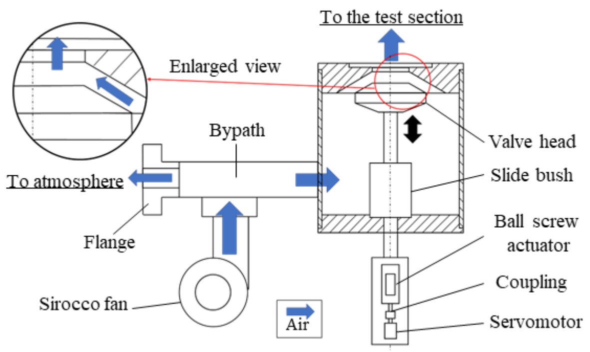

Figure 4. General view of the pulsation generator.

Temperature field in its steady state is yielded because the flat plate with the heat transfer surface has its own heat capacity, even if the flow rate temporally fluctuates. Therefore, the heat transfer characteristics can be quantitatively evaluated by taking temperature measurements and calculating the time-averaged local heat transfer coefficient and local Nusselt number after the thermal steady state has been reached. The time-averaged local heat transfer coefficient was calculated from Equation (2).

$$h(x) = \dot{q}/\{t_W(x) - t_b(x)\} \tag{2}$$

In Equation (2) $t_W(x)$ and $t_b(x)$ indicates respectively, measured local temperature of the heat transfer surface and the local mixing average temperature (bulk temperature) of the working fluid, air. Bulk temperature was defined as Equation (3) by using heat flux ($\dot{q}$), inlet air temperature (t_{in}), width of heat transfer surface (w), length of heat transfer surface (x), specific heat at constant pressure (c_p) and volume flow rate ($\dot{V}$). Local Nusselt number was defined as Equation (4) using the local heat transfer coefficient and equivalent diameter of the duct (d_e) as the representative length.

$$t_b(x) = t_{in} + (\dot{q} \cdot w \cdot x)/(\rho \cdot c_p \cdot \dot{V}) \tag{3}$$

$$Nu(x) = h(x) \cdot d_e/k \tag{4}$$

2.3. Pulsation Generator

A sketch of the pulsation generator is shown in Figure 4, and a photograph of it is shown in Figure 5. That consists of a servomotor, coupling and a ball screw actuator (20 mm in screw pitch). The reciprocating motion of the valve was achieved by repeated forward and reverse rotation of the servomotor connected to the ball screw actuator. Frequency, stroke and pulsation mode can be set by electronic control of the servomotor. In this experiment, the pulsation mode with sinusoidal flow rate fluctuation was only tested.

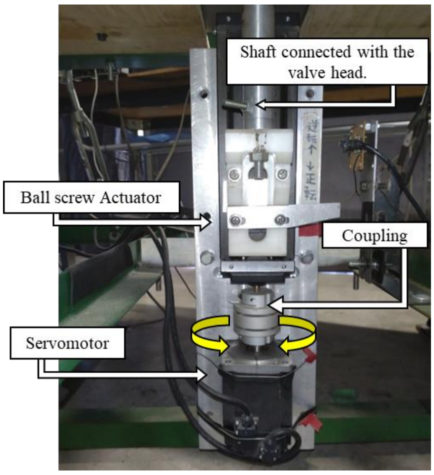

Figure 5. A photograph of the pulsation generator.

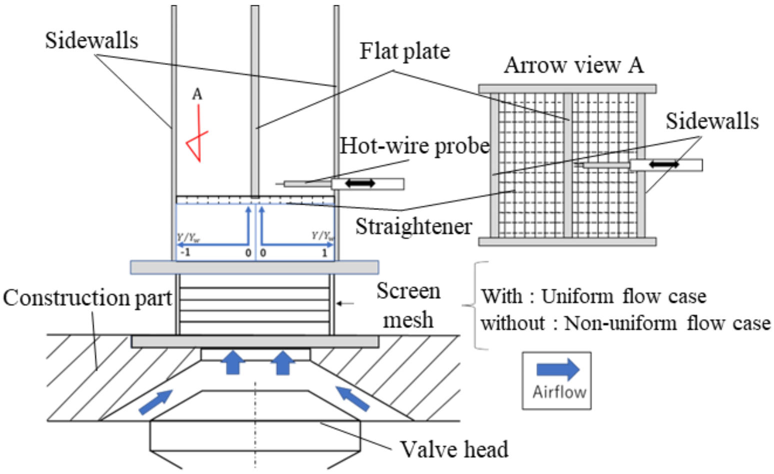

Figure 6. Local velocity measurement in the direction of channel width at the inlet. ($X/X_L = 0$)

2.4. Equipment and Method of Inlet Velocity Measurement

A general view of the experimental setup for inlet flow velocity measurement is shown in Figure 6. Inlet velocity distribution in the direction of the channel width and their temporal variations were investigated. Local velocities were measured by traversing a hot wire probe inserted in the test section from the sidewall. As shown in Figure 6, the measurement range was $-1 \leqq Y/Y_W \leqq 1$, where Y_W was the distance between the heating surface of the flat plate and the side wall, and Y was coordinate in the direction of channel width. The origin of Y was the heating surface, therefore, the range of measurement in a form of a dimensionless location in channel width direction was expressed as $-1 \leqq Y/Y_W \leqq 1$. The uniform inflow and non-uniform inflow conditions were examined by existence or absence of a screen mesh at the inlet of the test section.

3. Experimental Conditions

Two different types of Reynolds numbers were employed in the experiment. They were distinguished by two types of representative velocity: time-averaged velocity and velocity amplitude. Equations (5) and (6) show the respective definitions. The velocity amplitude (u_f) in Equation (6) was defined as Equation (7).

$$Re_m = u_m \cdot d_e/\nu \ \ (u_m{:}\,Mean\ Velocity) \tag{5}$$

$$Re_f = u_f \cdot d_e/\nu \ \ \left(u_f{:}\,Velocity\ amplitude\right) \tag{6}$$

$$u_f = \{(A_{max} - A_{min})/(A_{max} + A_{min})\} \cdot u_m \tag{7}$$

In Equation (7), A_{max} and A_{min} respectively mean maximum and minimum cross section area formed by the reciprocating valve and the contraction parts at the top of the pulsation generator. Dimensionless pulsating amplitude was defined as the ratio of two different Reynolds numbers. In the experiments, TDC position of the valve (2 mm below fully closed) was fixed, and the amount of descent varied for 5 mm, 10 mm, and 20 mm. The dimensionless amplitudes of the respective amount of descent correspond to 0.56, 0.72, and 0.85. The dimensionless angular frequency and Womersley number were defined as Equations (8) and (9).

$$\omega' = R^2\omega/\nu \tag{8}$$

$$Wo = \sqrt{\omega'} \tag{9}$$

The range of each parameter as experimental conditions is shown in Table 1.

Table 1. Experimental conditions.

Time-averaged Reynolds Number Re_m	Dimensionless Amplitude Re_f/Re_m	Frequency f[Hz]	Angular Frequency ω[rad/s]	Dimensionless Angular Frequency ω'	Womersley Number Wo
1000~8000	0.56	1	6.28	394.7	19.87
(Interval:1000)	0.72	2	12.57	789.4	28.10
	0.85	3	18.85	1184	34.41
		4	25.13	1579	39.73
		5	31.42	1974	44.42

4. Result and Discussion

4.1. Heat Transfer Characteristics in Laminar Flow Region

Figure 7 shows local Nusselt number distributions on the heat transfer surface in the flow direction ($Nu(X)$) under the flow rate condition of Re_m=2000, laminar flow case. Left and right side figures indexed as (a) and (b) correspond to the results obtained with and without the screen mesh at the upstream of the test section, respectively. In the case with the screen mesh, uniform velocity distribution at the inlet seemed to be achieved, on the other hand, in the case without the screen mesh, non-uniform velocity distribution in the direction of the channel width seemed to be expected. For each figure (a) and (b), results under pulsating amplitude conditions of Re_f/Re_m=0.56, 0.72, and 0.85 are presented from top to bottom. Larger amplitude means longer stroke of valve oscillation as illustrated between the graphs of (a) and (b). There was no significant difference in $Nu(X)$ between steady flow and pulsating flow cases regardless the pulsation frequency as shown in Figure 7 (a) for the inlet condition as uniform velocity distribution. In addition, the tendency of monotonous decrease of $Nu(X)$ was indicated in the flow direction. Contrary, with the inlet condition of non-uniform velocity distribution as shown in Figure 7 (b), heat transfer enhancement by flow pulsation was indicated. In addition, $Nu(X)$ showed an extreme maximum value in the range around $0.2 < X/X_L < 0.6$ and decreased thereafter in the flow direction. A tendency for $Nu(X)$ to increase with increasing frequency was also observed. This heat transfer characteristic as introduced the above were confirmed for all the examined pulsating amplitude (Re_f/Re_m) conditions as shown in Figure 7 (b), although the dependence of pulsating frequency on heat transfer became weak with increasing of pulsating amplitude (Re_f/Re_m).

In order to reveal these heat transfer characteristics on the flat plate were attributed to what sort of velocity profile at the inlet of the test section, we measured the inlet velocity distribution in the direction of the channel width by traversing a hot wire probe as previously represented in Figure 6.

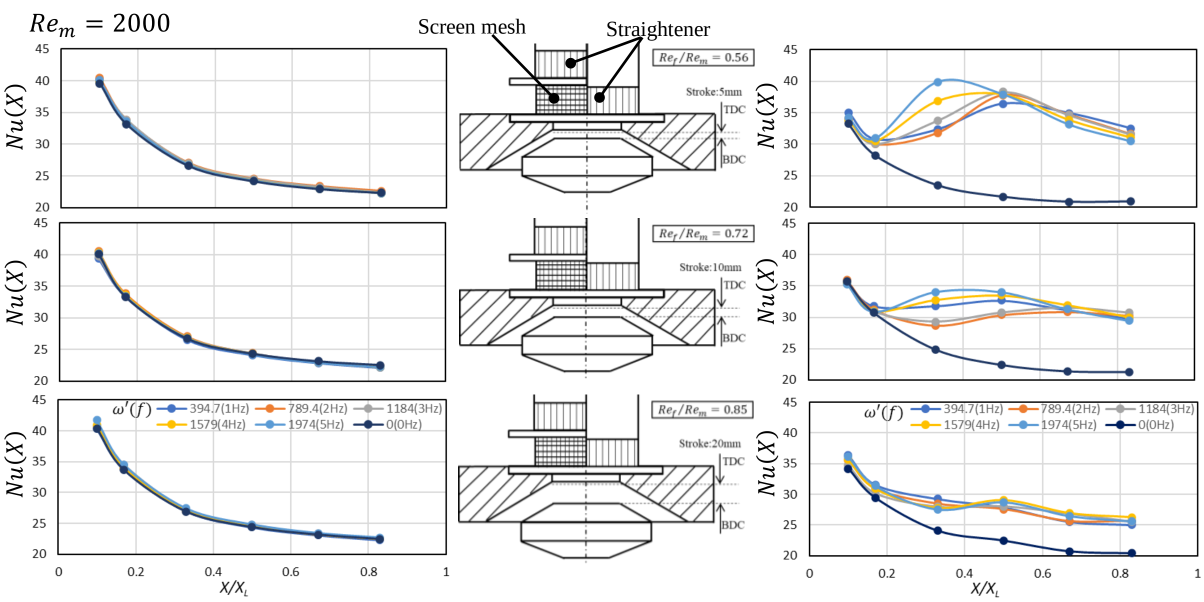

(a) with a screen mesh at inlet (b) without a screen mesh at inlet

Figure 7. Local Nusselt number distribution in the cases with and without a screen mesh at inlet (Re_m=2000).

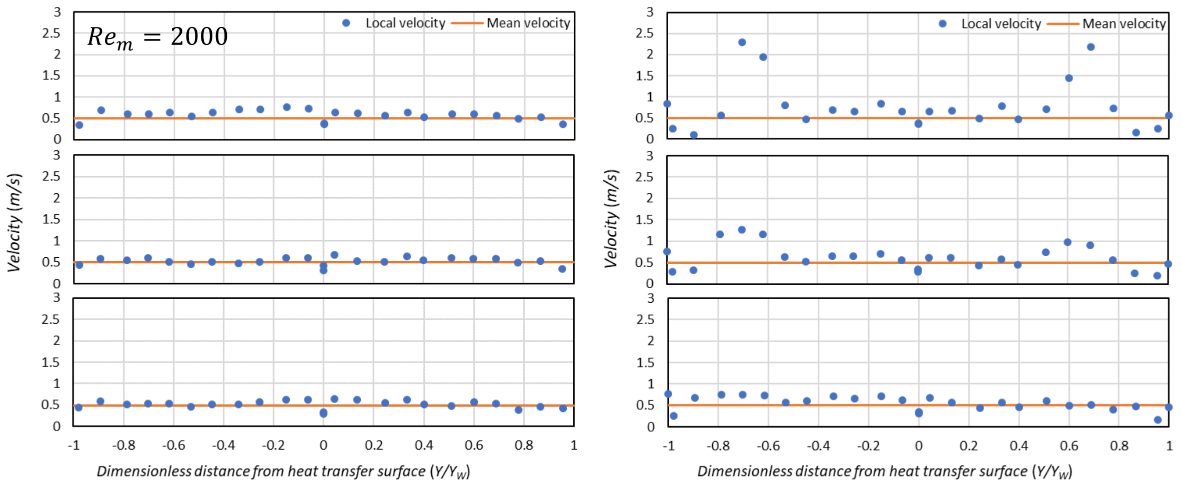

(a) with a screen mesh at inlet (b) without a screen mesh at inlet

Figure 8. Velocity profile at inlet in the cases with and without a screen mesh (Steady flow: Re_m=2000)

Figure 8 shows the velocity distribution in span-wise direction under steady state conditions of Re_m=2000, and the experimental conditions of each figure (a) and (b) correspond to those of Figures 7 (a) and (b). Different pulsating amplitude conditions of Re_f/Re_m=0.56, 0.72, and 0.85 for the steady flow mean the different valve position of each BDC (Bottom Dead Centre) as illustrated in Figure 7. Approximate uniform velocity distribution regardless of valve BDC position was confirmed as expected in the case with the screen mesh (See Figure 8 (a)). The same tendency in velocity distribution was observed also for the time-averaged velocity in the case of pulsating flow. On the other hand, in the case without the screen mesh as shown in Figure 8 (b), non-uniform velocity distribution was clearly observed when Re_f/Re_m=0.56 in amplitude condition (See most upper figure of Figure 8 (b)). Velocities around five times higher than the time-averaged velocity(u_m) which was calculated from the mean flow rate were resulted around the location of $Y/Y_w = \pm 0.7$. Contrary, velocities lower than u_m were observed in the regions of $Y/Y_w < -0.8$ and $0.8 < Y/Y_w$. This tendency was also confirmed for the time-averaged velocity in the case of pulsating flow. Such velocity profile may cause inclined mainstream due to stronger shearing force acted on the fluid particles by flow rate fluctuation. As the result of such large-scale fluid motion may induce the increase of local flow rate at the region close to the heat transfer surface around $X/X_L = 0.3 - 0.4$ stream-wise location in comparison with steady flow case. This can be one of the reasons of heat transfer enhancement by flow pulsation under non-uniform inflow condition as shown in the most upper figure of Figure 7 (b). Although the same characteristic of inlet velocity profile was confirmed also when Re_f/Re_m=0.72 in amplitude condition (See middle figure of Figure 8 (b)), non-uniformity of velocity distribution was smaller than that of Re_f/Re_m=0.56 amplitude case. In addition such characteristics of non-uniform velocity profile almost disappeared when Re_f/Re_m=0.85 in amplitude condition (See the lowest figure of Figure 8 (b)).

We also focused on the temporal fluctuation of local velocity. Figures 9 (a) and (b) show measured data of different three locations of $Y/Y_w = 0.5, 0.6,$ and 0.9 in cases of uniform and non-uniform inlet velocity condition, respectively, under Re_m=2000 and Re_f/Re_m=0.72 conditions. Both figures of (a) and (b) from top to bottom of each correspond to the different frequency cases of ω' =394.7(1Hz), 798.4(2Hz), and 1974(5Hz). In the case of inflow with uniform velocity distribution as shown in Figure 9 (a), although

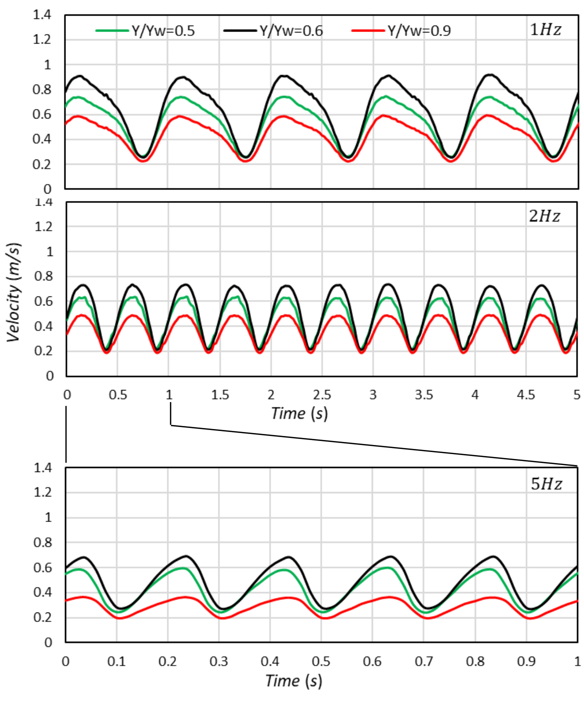

(a) uniform inflow condition

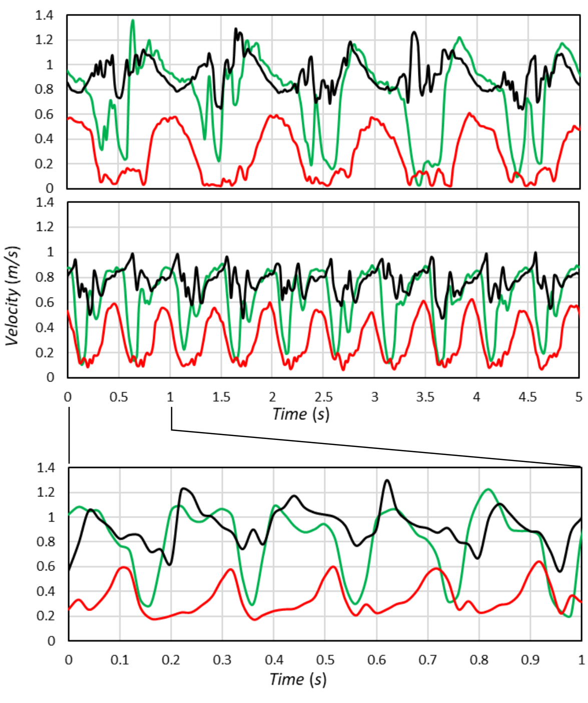

(b) non-uniform inflow condition

Figure 9. Temporal local velocity fluctuations (Re_m=2000, Re_f/Re_m=0.72).

the periodical maximum values for each velocity fluctuation showed a slight difference at each Y/Y_w location, the periodical minimum values approximately coincided each other. In addition, velocity fluctuations were completely synchronized with each other. Namely, no phase shift was observed under the uniform inflow condition. This fact allows us to have one finding: regular velocity fluctuation with maintaining the approximate uniform distribution occurs, therefore negligible small shearing force acts on the fluid particles between adjacent streamlines when the inflow with uniform velocity distribution is supplied to the duct. Contrary, for the case of inflow with non-uniform velocity distribution and their fluctuation represented in Figures 8 (b) and 9 (b), velocity fluctuation was not synchronized each other for different three Y/Y_w locations. Although no significant phase shift was observed, irregular turbulence was observed at $Y/Y_w = 0.6$. Based on the above introduced results of inlet velocity measurement as shown in Figures 8 and 9, the reason of heat transfer characteristics as shown in Figure 7 can be explained. No impact of flow pulsation on heat transfer around the flat plate under the uniform inflow condition seems to be yielded because the local time-averaged velocity/flow rate near heat-transfer-surface region is approximately the same as those of steady flow case. On the other hand, in case of the non-uniform inflow condition, heat transfer enhancement is achieved by the combined effects of large scale fluid motion such as inclined main-stream introduced the above and transition in flow regime up to turbulence in the region around $Y/Y_w = 0.6$ location in the direction of the channel width. Various scale of eddies seems to be created by turbulence, which can promote the mixing of the fluid. Heat transfer enhancement with increasing of pulsation frequency can be induced by such increased mixing action of the fluid.

4.2. Heat Transfer Characteristics in Turbulent Flow Region

Figure 10 shows local Nusselt number distributions on the heat transfer surface in the flow direction ($Nu(X)$) uunder the flow rate condition of Re_m=5000, turbulent flow case. Layout of each figure of (a) and (b) is the same as Figure 7 for laminar flow region of Re_m=2000 case. No impact of flow pulsation on heat transfer was also confirmed in case of uniform inflow condition, and heat transfer enhancement was indicated in case of non-uniform inflow condition, in turbulent flow. In case of (b), monotonous decrease of $Nu(X)$ was not observed in the case of Re_f/Re_m=0.56 amplitude condition even in the steady flow case. Although the same tendency of heat transfer enhancement introduced in the previous subsection for laminar flow region was obtained also in turbulent flow region, dependence of pulsating

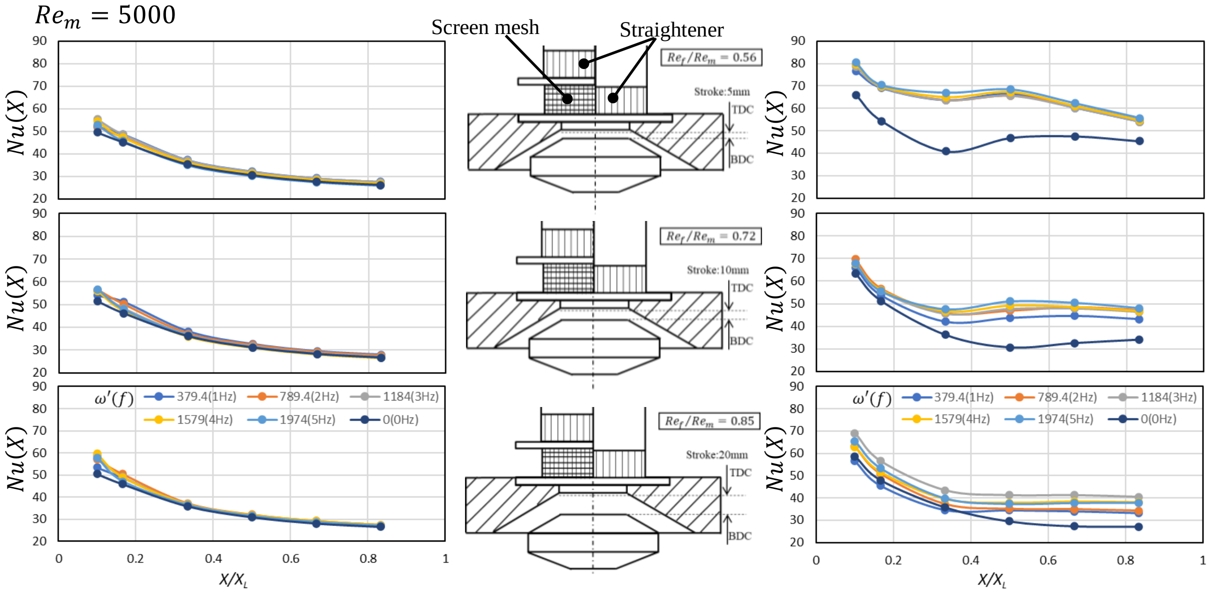

(a) uniform inflow condition (b) non-uniform inflow condition

Figure 10. Local Nusselt number distribution in the cases with and without a screen mesh at inlet (Re_m=5000).

frequency and amplitude on heat transfer in laminar flow region was stronger than that of one in turbulent region. This can be attributed to that the effect of inertia due to the momentum in flow direction is stronger than that of velocity fluctuation. Figure 11 shows the velocity distribution in span-wise direction under steady state conditions of Re_m=5000. Similar characteristic of velocity profile at the inlet in case of laminar flow region was observed also in turbulent flow region. The same tendency of velocity fluctuation in laminar flow region as shown in Figure 9 is also expected though the measurement of velocity fluctuation in turbulent flow region has not been completed yet.

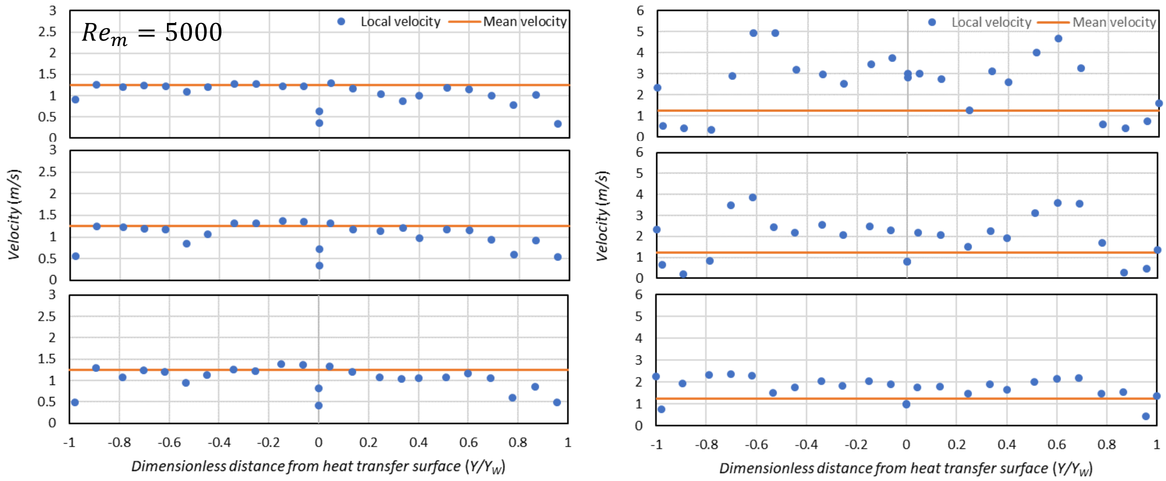

(a) uniform inflow condition (b) non-uniform inflow condition

Figure 11. Velocity profile at inlet in the cases with and without a screen mesh (Steady flow: Re_m=5000).

5. Conclusions

The following conclusions on heat transfer characteristic around the flat plate installed in a pulsating duct flow were obtained through the experiments under the conditions of $Re_m = 1000{\sim}8000$, $Re_f/Re_m = 0.56, 0.72$, and 0.85, ω' =394.7, 798.4, 1184, 1579, and 1974.

1. Heat transfer characteristics around the flat plate depend on the velocity distribution at the inlet of the duct.
2. The effect of flow pulsation on heat transfer around the flat plate is negligible small under uniform inflow condition (uniform velocity distribution at the inlet of the duct).
3. Heat transfer enhancement can be obtained under the non-uniform inflow conditions (non-uniform velocity distribution at the inlet of the duct).
4. Above introduced heat transfer characteristics are observed regardless of flow regimes (laminar or turbulent)

6. Future work

In order to make clear the mechanism of heat transfer enhancement under non-uniform inflow condition, measurement of velocity distribution in span-wise direction under steady and pulsating flow conditions is required also in the downstream region as well as inlet of the duct. Numerical prediction of flow and heat transfer and their verification with experimental results are also required for further investigation.

7. Nomenclature

A: cross sectional area	$[m^2]$
c_p: specific heat at constant pressure	$[J/(kg \cdot K)]$
d_e: equivalent diameter	$[m]$
f : pulsating frequency	$[Hz]$
h : heat transfer coefficient	$[W/(m^2 \cdot K)]$
I : current value	$[A]$
Nu: Nusselt number	$[-]$
t_b : bulk air temperature	$[K]$
t_{in}: inlet air temperature	$[K]$
t_w: wall temperature	$[K]$
$\dot{q}$: heat flux	$[W/m^2]$
R : Half of equivalent diameter	$[m]$
Re_f: velocity amplitude-based Reynolds number	$[-]$
Re_m: mean velocity-based Reynolds number	$[-]$
Re_f/Re_m: dimensionless pulsating amplitude	$[-]$
u_f : velocity amplitude	$[m/s]$
u_m: mean velocity	$[m/s]$
V : voltage value	$[V]$
$\dot{V}$: volume flow rate	$[m^3/s]$
x : heat transfer surface length	$[m]$
w : heat transfer surface width	$[m]$
Wo: Womersley number	$[-]$
κ : thermal conductivity of air	$[W/(m \cdot K)]$
ν : kinematic viscosity	$[m^2/s]$
ω : angular frequency	$[rad/s]$
ω': dimensionless angular frequency	$[-]$

8. Acknowledgements

The authors of this paper would like to express an appreciation to Mr. J. Inoue and Mr. T. Sakaue for their assistance in carrying out the experiments and data reductions.

9. References

[1] N.Shiibara et al. (2017). Unsteady characteristics of turbulent heat transfer in a circular pipe upon sudden acceleration and deceleration of flow. *Int. J. Heat Mass Transfer* 113, 490-501.

[2] Qianhao Ye, Yonghai Zhang, and Jinjia Wei (2021) A Comprehensive Review of Pulsating Flow on Heat Transfer Enhancement, *Applied Thermal Engineering, Volume 196, 117275* (https://doi.org/10.1016/j.applthermaleng.2021.117275)

[3] T. Yamazaki et al. (2021). Study on time-local dissimilarity of momentum and heat transfer based on energy redistribution in pulsating turbulent flows. *Proc of the 58th Japan Heat Transfer Symposium*.

[4] Y. Oda et al. (2021). Measurements of periodically fluctuating velocity and temperature with hot- and cold-wires in pulsating turbulent flows with heat transfer. *Proc of the 58th Japan Heat Transfer Symposium*.

[5] S. Matsuo & H. Saitoh. (2011). Heat and Mass Transport Characteristics of Pulsating Flow in a Rectangular Duct Part 2. Effect of Amplitude on Heat Transfer of a Flat Plate Installed in the Duct. *Thermal Science and Engineering*, Vol. 19, No. 1, pp. 25-35.

[6] M. Kotani & H. Saitoh. (2017) Flow and heat transfer around the flat plate installed in a pulsating duct flow with intermittent flow rate fluctuation. *Proc. of the 8th TSME International Conference on Mechanical Engineering* (Thailand).

TSF0029

Fluid-Structure-Acoustic Coupling Analysis for Articulation Process

Mei Matsubara[1], Hirotoshi Hasegawa[1], Takahisa Yamamoto[2,*], and Etsuji Nomura[3]

[1] Advanced Course of Interdisciplinary Technology Development, National Institute of Technology, Gifu College, 2236-2 Kamimakuwa, Motosu, 5010495, Japan
[2] Dept. Mech. Eng., National Institute of Technology, Gifu College, 2236-2 Kamimakuwa, Motosu, 5010495, Japan
[2] OCSE^2, Ichinomiya, Aichi, Japan

* Corresponding Author: ytaka@gifu-nct.ac.jp

Abstract. This study conducted a fluid-structure-acoustic coupling analysis method for the articulate process. The study uses preCICE, a coupling library that weakly couples two solvers. The radiative boundary method was used to map between the two solvers, and the force and displacement were coupled using the implicit method. This study calculated the "perpendicular flip," a benchmark problem for fluid-structure coupling, as the fundamental calculation. Air flows from the left into a 10 m-long two-dimensional duct. A rubber plate is installed in the central part, and its deformation due to the flow is analyzed. The sound pressure distribution shows a high value behind the rubber plate, confirming that it propagates backward. In this analysis condition, it was impossible to clarify the influence of the vibration of the rubber plate on the sound field. In the future, the study plans to adjust the analysis conditions and clarify the influence of the vibration of the fluid and the structure on the sound field.

Keywords: Fluid-Structure Interaction, Acoustic Analysis, Articulation.

1. Introduction

The symbiotic relationship between innovation and deep understanding often shapes scientific progress. A prime example of this is Computational Fluid Dynamics (CFD), which has evolved significantly over the past few decades to become an indispensable tool across various scientific domains [1]. This evolution is a byproduct of advancing computational power and is deeply rooted in the continuous refinement of algorithms and modeling techniques.

Today's multifaceted applications of CFD, ranging from aerospace engineering to biomedical research, underscore its relevance and versatility. One particularly compelling field of application lies in the intricate interplay between fluids and structures and the resulting acoustic phenomena. Whether it is the aerodynamics of advanced aviation technology, the acoustic nuances of cutting-edge underwater vehicles, or the profound complexity of human voice production, the boundaries of our knowledge are continuously being pushed and redefined. Innovative methodologies such as the fully coupled hybrid computational aeroacoustics approach on hierarchical Cartesian meshes [2] and the simultaneous analysis of noise source and propagation with acoustic radiation [3] are testaments to this evolution.

Phonation, the act of producing voice, is a marvel of biological engineering. Beyond mere communication, it represents a symphony of coordinated physiological actions encompassing airflow, structural dynamics, and acoustics. Through their seemingly simple mechanics, the human vocal cords house a world of intricate physical interactions that culminate in voice production. Research into the acoustic wave phenomena in combustion chambers [4] or the coupling of CFD with vibroacoustic finite element models for vehicle interior noise prediction [5] may seem distant, but they contribute to a deeper understanding that could radically transform various fields. For instance, such advances in CFD and acoustic simulations could lead to groundbreaking treatments for voice disorders.

On the technological front, integrating CFD-predicted loads with structural acoustic models and developing processes combining lattice Boltzmann simulations with statistical energy analysis hint at future enhancements in voice recognition systems [6]. In the performing arts, the lessons learned from the combined CFD and CAA simulations with impedance boundary conditions [7] and the investigation into flow acoustic coupling [8] could establish novel techniques for vocalist training paradigms.

With this context, our research aims to contribute and pioneer. By crafting a comprehensive fluid-structure-acoustic interaction analysis method, the authors hope to unlock more profound layers of understanding about voice production. This initiative, though contemporary in its approach, harbors potential for future advancements that could reshape both our understanding and application of voice.

2. Methods

2.1. Overview

The focal point of our research methodology was to accurately capture the interplay between fluid dynamics, structural behavior, and the resulting acoustic phenomena. Using a combination of advanced solvers and coupling strategies, this study constructed a computational model that closely mimics the real-world phenomena under study.

2.2. Structural Analysis

Solver: The CalculiX ver.2.20 was our choice due to its robust capabilities in handling nonlinear structural dynamics problems [9].

Governing Equations: The equilibrium of forces in structural dynamics is represented by:

$$MU'' + CU' + KU = F \tag{1}$$

where:

- *M* is the mass matrix
- *C* is the damping matrix
- *K* is the stiffness matrix
- *U* is the displacement vector
- *F* is the external force vector
- The dots represent time derivatives.

2.3. Fluid Analysis

Solver: OpenFOAM ver.2206 was utilized [10]. This study leaned on the “rhoPimpleAdiabaticFoam” module, specifically tailored for weakly compressible flows with provisions for both laminar and turbulent regimes.

Governing Equations: The Navier-Stokes equations describe the fluid motion:

$$\rho\left(\frac{\partial u}{\partial t}+u\cdot\nabla u\right)=-\nabla p+\mu\Delta u+F_{\mathrm{ext}} \tag{2}$$

where:

- ρ is the fluid density
- u is the fluid velocity vector
- p is the fluid pressure
- μ is the dynamic viscosity of the fluid
- F_{ext} represents external forces, such as those from the structure.

2.4. Acoustic Analysis

For acoustic perturbations, this study utilized the linearized Euler equations integrated with our in-house module:

$$\frac{\partial^2 p_a}{\partial t^2}-c_\infty^2\frac{\partial^2 p_a}{\partial x^2}=-\frac{\partial^2 p'}{\partial t^2} \tag{3}$$

where:

- p' refers to the fluctuation in pressure from CFD
- p_a is the acoustic pressure
- c_∞ is the speed of sound.

2.5. Solver Coupling with preCICE:

preCICE ver.2.5.0 provided the bridge between our structural and fluid solvers as shown in Figure 1 [11]. It enabled the iterative exchange of boundary conditions, ensuring that both solvers converged to a consistent solution.

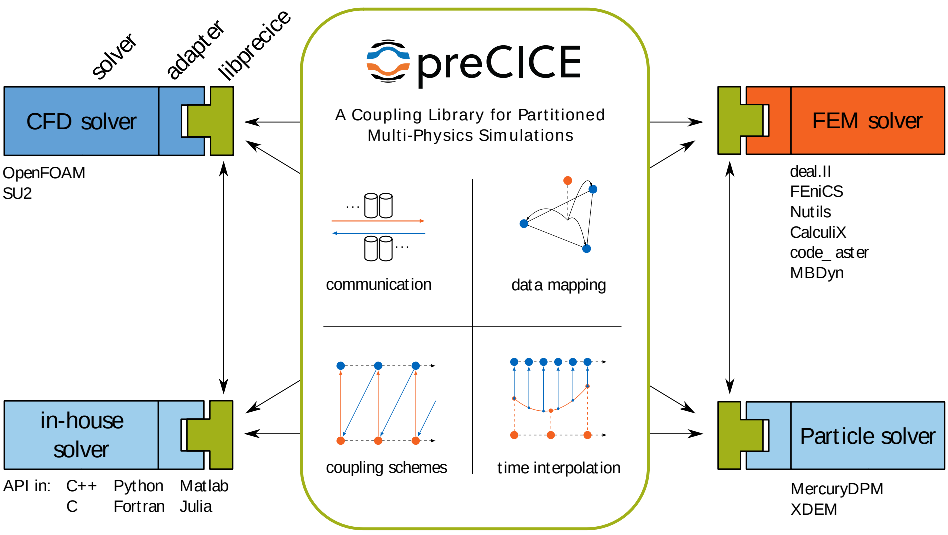

Figure 1. Schematics of preCICE and other solvers.

2.6. Data Mapping

This study utilized the Radial Basis Function (RBF) method to efficiently transfer data between the solvers. The RBF interpolates values based on:

$$f(r) = \sum_{i=1}^{n} \lambda_i \Phi(\|r - r_i\|) \tag{4}$$

where:

- Φ is a basis function
- r_i are the centers of the basis functions
- λ_i are the coefficients determined by the boundary conditions.

3. Results and Discussion

3.1. Fluid Flow Around Wedge-Shape Obstacle

3.1.1. Velocity Field and Characteristic Frequencies

This study calculated the flow field around a wedged-shaped obstacle, as shown in Figure 2. Standard condition is considered, and airflow is set at 95 m/s. The other boundaries are set as pressure boundary conditions (zero gradient condition for velocity and relative pressure is equal to zero). These analysis conditions are referred from the predecessor prior research [1] in order to check the validation of this calculation. The analysis began with examining the velocity field, presented as a contour diagram. Data were also collected from a fixed point located one meter behind the wedge. A Discrete Fourier Transform (DFT) analysis was subsequently conducted on this data to discern the characteristic frequencies intrinsic to the system.

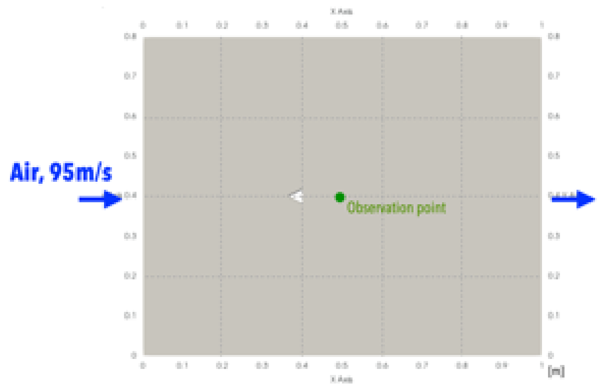

Figure 2. Test case geometry.

3.1.2. Sound Pressure Levels and Vibrational Flow

Figure 3 shows the contour maps of velocity and acoustic pressure. The series of Kalman vortex are observed after the wedged-shaped obstacle. Figures 4 and 5 illustrated significant findings regarding sound pressure levels. Vibrational flow, observed prominently in the wake of the wedge, was accompanied by noise generation. The correlation between these two phenomena warrants further exploration.

3.1.3. Strouhal Number and Frequency Predictions

A comparative study with literature revealed a Strouhal number approximation of 0.21. Based on this, the authors predicted a fluid vibration frequency of around 400 hertz. The empirical data supported this prediction, indicating a peak within this frequency range. Notably, the Sound Pressure Level (SPL) registered at approximately 300, a figure slightly exceeding the literature value. While this deviation was noted, the overarching trend remained consistent with theoretical predictions.

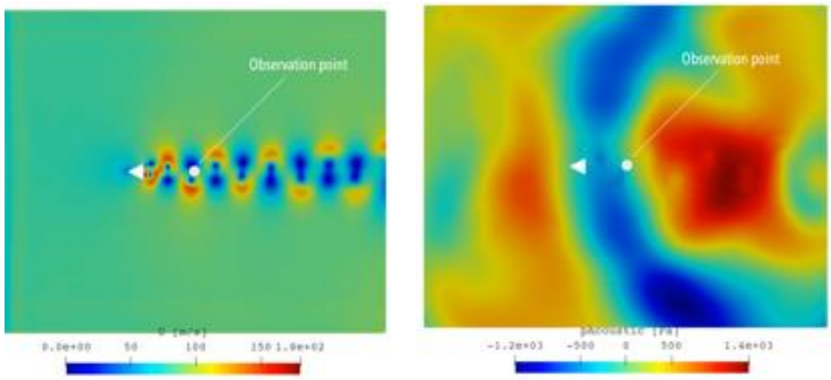

Figure 3. Contour maps of velocity and acoustic pressure.

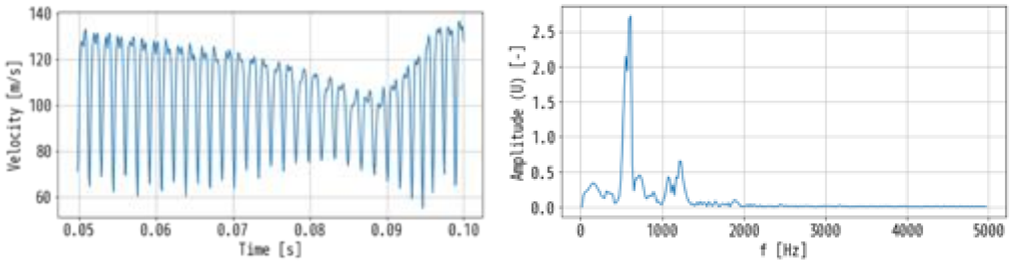

Figure 4. Velocity fluctuation and its frequency at the observation point.

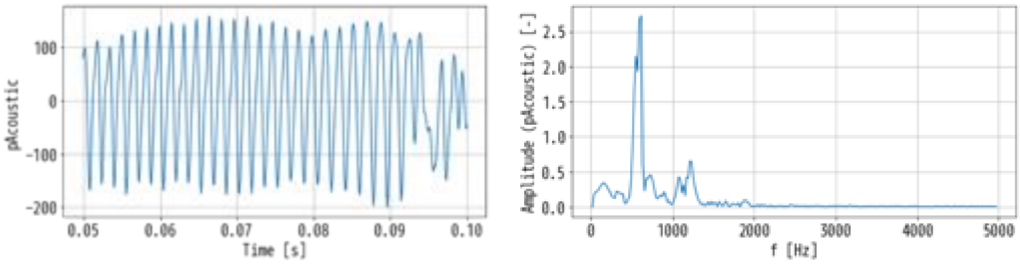

Figure 5. Acoustic pressure fluctuation and its frequency at the observation point.

3.1.4. Concluding Remarks of Acoustic Analysis Model

To summarize, our research results, in congruence with established literature, reinforce the validity of the fluid-acoustic model developed in this study. The findings resonate with existing knowledge and pave the way for deeper insights into the intricate dynamics of fluid-acoustic interactions. In fact, the numerical model indicates the interaction mechanism between the fluid flow field and the acoustic field, and the location of the sound source in the target system.

3.2. Perpendicular Flap Proble

In the calculation to offer a comprehensive analysis of fluid dynamics and acoustics, this study decided to incorporate structural calculations. One of the primary challenges this study tackled was the "Perpendicular Flap Problem," a model that, while seemingly simple, provides profound insights into fluid-structure interactions.

The flap was meticulously designed, taking both geometric and material considerations into account (Figure 6). The material chosen was reminiscent of rubber, with a Young's modulus of 90 MPa. Such a choice was made to simulate real-world applications where materials with such elasticity often come into play, especially in automotive and aerospace industries where noise and vibrations can be crucial factors.

3.2.1. Incorporating Structural Calculations:

To create a baseline, our first step involved observing the system without any flap deformation. Utilizing high-resolution contour diagrams, this study mapped the velocity and sound pressure levels (Figure 7). Furthermore, this study introduced measurement points at strategic locations to capture the nuanced velocity and acoustic pressure changes over time (Figures 8 and 9). The subsequent DFT analysis results were key in understanding the underlying frequency components.

This static scenario, where the flap remained undeformed, revealed intriguing patterns. The velocity fields displayed discernible periodic variations, predominantly peaking below 50Hz. In parallel, the sound pressure levels showcased similar fluctuations, suggesting a consistent behavior in this static environment.

Figure 6. Fluid flow analysis around deformable flap by Fluid-Structure-Acoustic analysis.

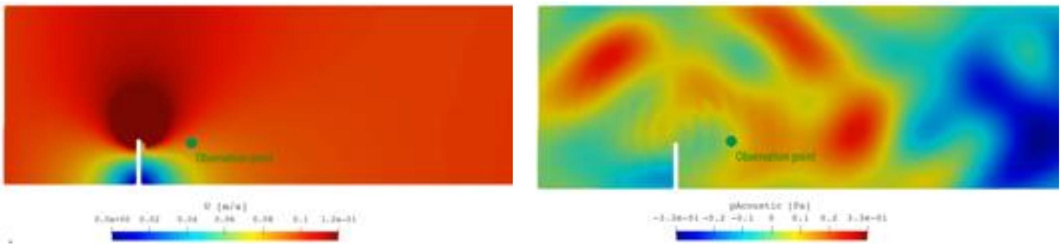

Figure 7. Contour maps of velocity and acoustic pressure (t=0.65s) (w/o FSI).

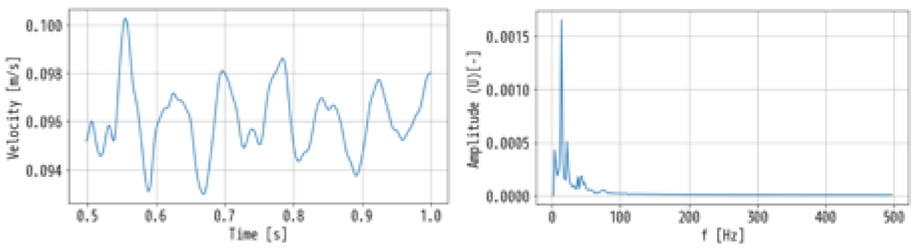

Figure 8. Velocity fluctuation (left) and its frequency (right) at the observation point (w/o FSI).

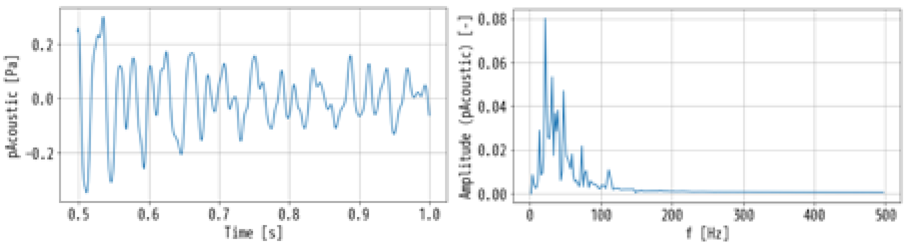

Figure 9. Acoustic pressure fluctuation (left) and its frequency (right) at the observation point (w/o FSI).

3.2.2 Dynamics with Flap Deformation

Transitioning to a more dynamic scenario, the authors introduced deformation into the flap and closely monitored the ensuing changes. In this scenario, the velocity fields began showcasing irregularities, breaking away from the previously observed periodic patterns (Figures 10 - 12).

One of the standout observations was in the sound pressure levels. A clear shift was noted as the peak frequency, initially at 50Hz, transitioned to a more elevated 200Hz. This raised intriguing questions about the nature of interactions at play. Upon conducting a separate frequency analysis focused solely on the flap, this study found its primary natural frequency to be around 164Hz. This frequency was pivotal in our understanding. It became evident that this inherent frequency was significantly influencing our observations, especially the altered sound pressure peak. This study deduced that such shifts were the direct results of the combined effects of fluid-acoustic dynamics and the flap's structural properties.

Figure 10. Contour maps of velocity and acoustic pressure (t=0.65s) (w FSI).

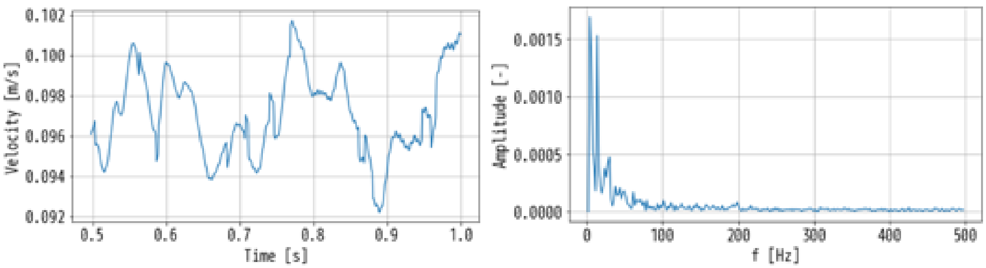

Figure 11. Velocity fluctuation and its frequency at the observation point (w FSI).

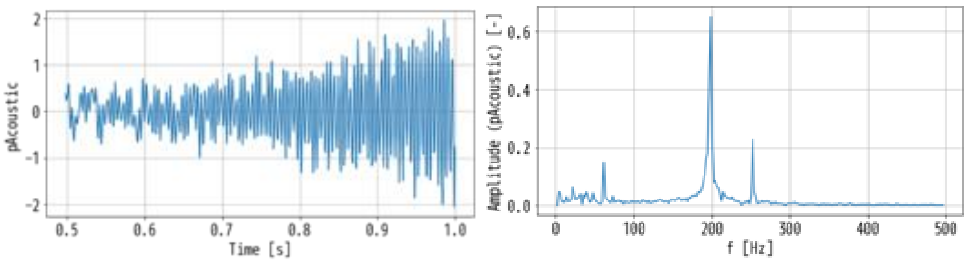

Figure 12. Acoustic pressure fluctuation and its frequency at the observation point (w FSI).

4. Conclusion

This study delved deep into the intricacies of fluid dynamics, acoustics, and their interplay with structural properties, using the "Perpendicular Flap Problem" as our primary model. The flap's meticulous design and material choice, simulating real-world applications, paved the way for enlightening observations, providing us a window into the multifaceted world of fluid-structure interactions.

The baseline scenario, where the flap remained static, offered consistent patterns in both velocity fields and sound pressure levels, emphasizing the importance of frequency components, particularly below 50Hz. This foundation proved invaluable when flap deformation was introduced, unveiling unobserved complexities. Upon flap deformation, the deviation in the sound pressure peak from 50Hz to 200Hz was an eye-opener, directing our attention to the flap's inherent natural frequency of 164Hz.

This shift demonstrated the fluid-acoustic dynamics and spotlighted the structure's intrinsic properties' crucial role in shaping these dynamics. Our observations underline the profound impact of combining fluid and structural dynamics, suggesting a need for further exploratory studies in this domain.

Ultimately, the results reiterate the importance of holistic studies, blending different physics to capture the complete picture. This manuscript bridges a knowledge gap and propels the understanding of fluid-acoustic-structural interactions, laying a foundation for future research endeavors.

5. Acknowledgments

This research was partially supported by the Mazda Foundation research grant 2022. The authors express our sincere gratitude for their assistance.

6. References

[1] Mani M., & Dorgan A (2023). A perspective on the state of aerospace computational fluid dynamics technology. *Annual Review of Fluid Mechanics 2023*, 55, 431-457.

[2] Schlottke-Lakemper M., Yu H., Berger S. et al. (2017). A fully coupled hybrid computational aeroacoustics method on hierarchical Cartesian meshes. *Computers & Fluids*, 144(2), 137-153.

[3] Ferrante P., Francescantonio P., Hoffer P-A. et al. (2014). Integrated “CFD-Acoustic” Computational Approach to the Simulation of Aircraft Fan Noise, *Proc. ASME Turbo Expo: Power for Land, Sea, and Air*, Paper No. GT2014-26429.

[4] Sankaran V., Xia G., Ellis M. & Merkle C. (2004). CFD Simulations of Acoustic Wave Phenomena in Combustion Chamber, *Proc. Computational Fluid Dynamics 2004*, 89-94.

[5] Glandier C., Eiselt M. & Bauer E. (2015). Coupling CFD with Vibroacoustic FE Models for Vehicle Interior Low-Frequency Wind Noise Prediction, *SAE Int. J. Passenger Cars*, doi: 10.4271/2015-01-2330.

[6] Martin S., Daniels H., Venor J. & Musser C. (2022). Validation of Combining Compressible CFD Results with Statistical Energy Analysis for Vehicle Interior Noise Simulation, *Proc. 12th Int. Styrian Noise, Vibration & Harshness Congress*, doi: 10.4271/2022-01-0936.

[7] Li, A., Chen, J., and Liu, Y. (2021). Combined CFD and CAA Simulations with Impedance Boundary Conditions, SAE Technical Paper 2021-01-1048, doi.org/10.4271/2021-01-1048.

[8] Ashoke D., Abhijit K., Sudharsan K. & GeethaSri K. (2016). CFD -CAA simulation of flow acoustic coupling in a half-dump combustor, *J. Propulsion and Power*, doi:10.2514/1.B35629.

[9] Dhondt, G. (2004). *The Finite Element Method for Three-Dimensional Thermomechanical Application*, Wiley, 2004.

[10] OpenFOAM ver.2206 (2022). https://openfoam.com, 2022.

[11] preCICE ver.2.5.0 (2022). https://precice.org, 2022.

TSF0030

Experimental Measurements of a Simplified Thermal Model for Surface Temperature Prediction of a Single Pouch Cell Li-ion Battery

May Thazin Oo[1,*], Chi-na Benyajati[2], Jenwit Soparat[2], and Preechar Karin[3]

[1] Faculty of Engineering, King Mongkut's Institute of Technology Ladkrabang, Bangkok 10520, Thailand
[2] National Metal and Materials Technology Center, National Science and Technology Development Agency, Pathumthani 12120, Thailand
[3] School of Engineering, King Mongkut's Institute of Technology Ladkrabang, Bangkok 10520, Thailand

* Corresponding Author: maythazin19920507@gmail.com

Abstract. In an electric vehicle, the battery energy capacity is an important factor for long-range operation. As the opposing operating temperature can affect battery performance, safety, and degradation, a thermal battery management system is required to provide a suitable ambient temperature environment for better battery functioning. To develop battery power systems, the thermal behaviours of lithium-ion batteries is increasingly becoming a key factor for electric vehicles in today's automotive industry. In this study, a simplified thermal model of a single Li-ion pouch cell focuses on predicting the temperature distribution over the surface of the battery. To investigate the temperature rise, a thermal model was considered using commercial CFD software to solve the heat-generation parameters of the 25Ah lithium-ion pouch cell, which has been tested under transient conditions according to experimental data. The important thermal simulation parameters are established based on the Joule heating effect and heat capacity equation while considering heat source domains with boundary conditions based on the results of the experiment. A scenario of a battery specimen located inside an enclosed space was simulated. Furthermore, the variation of experimental temperature measurements with respect to ambient temperature operation at 1 C and 1.5 C charge and discharge rate, 50% state of charge, and 4.2V, 3.0V, and 2.0V open-circuit voltage (OCV) was monitored by the Maccor battery testing machine that measured the battery testing equipment such as electrical loads, electronic sensors, and nine thermocouples on a battery surface. According to the result, the temperature distribution on the battery surface at different discharge rates would be compared between the experiment and simulation to determine the suitability of the battery thermal model setup employed in this study. The configuration presenting a small module inside a battery pack will be considered in future work.

Keywords: Battery, Lithium ion, Thermal simulation, Temperature prediction, Thermal Model.

1. Introduction

At present fossil fuel-based economy typically related to energy has brought in numerous challenges before the global community drawing several issues such as increasing oil demand, exhaustion of nonrenewable energy resource and political instability as well around the world that sometimes create unusual demand. Due to the random use of fossil fuel, excessive emission of carbon-di-oxide leading to global warming is also threatening our everyday life that should not be gone unnoticed. Taking all these into considerations, Electric Vehicles (EVs) and Hybrid Electric Vehicles (HEVs) usage have been deemed to be the most typical and promising replacement of traditional vehicles based on internal combustion (IC) engine.

The recent development of EVs and HEVs technologies in contemporary eras is the reflection of the ongoing demand and upcoming urgency. The main and important driving force of such electric vehicles are batteries used widely to supply power due to the advantage of lower environmental threat, high energy density and longer life span. At the same time, batteries are also required to have a particular focus in case of the application in EVs to get the maximum output with minimum effect. Batteries can also cause alarming safety issues such as fire or explosion due to excessive current, overheat, over voltage, over charging/ discharging or even the aging of batteries' life span.

In recent time, different technologies on Li-Ion batteries have been able to differentiate themselves for HEV and EV applications due to energy density, reduced cost, and life span [23,24]. For example, lithium titanate battery with LTO for anode material is one type of Li-ion battery that has been able to draw much more consideration due to its outstanding thermal stability. As conveyed in Ref. [21], the incorporation of cells built on LTO in a battery module, for HEV/EV applications in most Li-ion batteries, could be found to be an amazing resource due to its thermal steadiness and it could avoid security threats at the time of driving. In addition, the study of thermal behavior of LTO cells by Wang et al. [1] assured that Li-Ti batteries have recognized boarded energy and powerful thermal steadiness.

To deal with the safety issues and performance of batteries, Battery Management System (BMS) has been a great innovation that incorporates several key technologies within its capacity, such as monitoring battery state, protecting battery from operating beyond its safety area, secondary data calculation and reporting, authentication of battery and balancing it as well. For the analysis of battery behavior, monitoring its state, design of real-time controller, fault diagnosis and thermal management, there is always the need of an effective battery model. It is also required to use proper estimation methods to monitor several states that play crucial roles in managing the operation of batteries which includes, but not limited to, battery's health state, charging state and inner temperature which we cannot measure directly. Charging batteries too fast may lead to huge energy loss and rise of temperature adversely and slow charging also has negative effect on the availability of EVs usage. Furthermore, large temperature variations also lead to the aging of battery rapidly and causes overheating or supercooling, which ultimately will shorten the service life of batteries [3]. The extensive research on thermal behavior of Li-ion batteries carried out by some research groups [4-7] encompass a broader aspect of study from cell level to battery (cell stack) and battery pack stages as well. In some of their studies, 3D CFD modeling, impact of physical properties of materials [8,9] para paper, energetic power profiles and hypotheses based on geometry were studied. Moreover, including forced conduction in a battery pack or in a specific design [15], variable designs of forced conduction [16] and cooling methods, phase changing cooling materials usage in lieu of air [10-14] and thermal management have been superior issues of investigative research in contemporary periods [17-20]. This study, which is especially focused on the thermal experimentation of surface temperature distribution on heat generation, was modeled using the Maccor battery testing machine at different charge and discharge rates. In addition, temperature was performed as well, and thermocouples were used exclusively for the validation part as it was recommended by the surface structure of the positive and negative electrodes in the battery case, while another thermocouple arranged the ambient temperature. A comprehensive detail of the methodology for the determination of model parameters and model generation is provided as well. On the other hand, it will propose to upgrade the model to a battery pack in additional work after the validation of LTO battery's 3D thermal model. The simulation results will show results in respect of the competence of the developed modelling methodology and the temperature variations in a battery. However, Section 2 describes methodology, Section 3 arranges the model development combining theory and modeling, Section 4 portrays the experimental procedure for the calculation of parameter, Section 5 demonstrates the simulation results and validation of the model, and Section 6 ends with the conclusive judgement in this study.

2. Methodology

The objective of this study is to simplify a thermal model by exposing heat generation and heat transfer to predict surface temperature distribution of single pouch cell Li-Ion battery for large scale battery pack. This model integrates key parameters of the design of battery cell (for example dimensions, materials, and respective corporeal parameters) and related physics (computational fluid dynamics (CFD) and heat transfer). The modelling method consists of three phases: pre-operating, model's resolution, and post- operating respectively. At the pre-operating stage, geometry of the battery is evaluated and produced in an appropriate method for more analysis. As input parameters, corresponding physics determined values of parameters and operational settings are inserted. Hereafter, corresponding physics are specified over different substances. At model's resolution phase, the consideration of battery's heat generation as a mass heat source numerically solves the steady-state and thermal time-dependent difficulty with natural cooling phenomena. The battery cell has always the tendency to the direct exposure to a cooling ambient air condition. The cell combines the properties of anisotropy. As a result, the primary temperature with consistent definition is imposed on related demarcation lines. Different significant marginal conditions are established then. With the help of battery power charger and discharger machine (MACCOR), the volume of generation of the heat source is assessed (inside LTO cell corresponding to the current rate). Power electronic loader wire, thermocouple sensors, computer-controlled data acquisition system are used as an input to the thermal model. The battery in operational mode suddenly generates a uniform, finite, and steady quantity of heat energy in the surrounding air. An unobstructed heat energy is transmitted in the longitudinal (x), horizontal (y) and normal (z) directions. After that, the whole domain is broken down into a fitting mesh to be dissolved through finite volume method (FVM) technique in ANSYS CFD commercial software. The determination of spatial-temporal temperature distribution and heat generation amount of the battery cell under cycling state are the ultimate results of this model. At the post-processing phase, the results are evaluated with a series of related yields.

3. Model Development

3.1. Model

The picture of the battery cell is shown in Fig. 1, and a 3D thermal model was built to investigate the heat generation and surface temperature distribution of a LIB during the charge and discharge process at different C-rates using ANSYS CFD commercial software. The presented unit cell, a large pouch cell, has a 25Ah nominal capacity and is made up of several layers. The different parts of the cell geometry were designed as a negative current collector, a negative tab separator, a positive current collector, and a positive tab corresponding to the lithium-ion pouch cell battery. The explanation of the model's development is given below, including the geometry, model input parameters, mathematical description of the model, experimental procedure, and results.

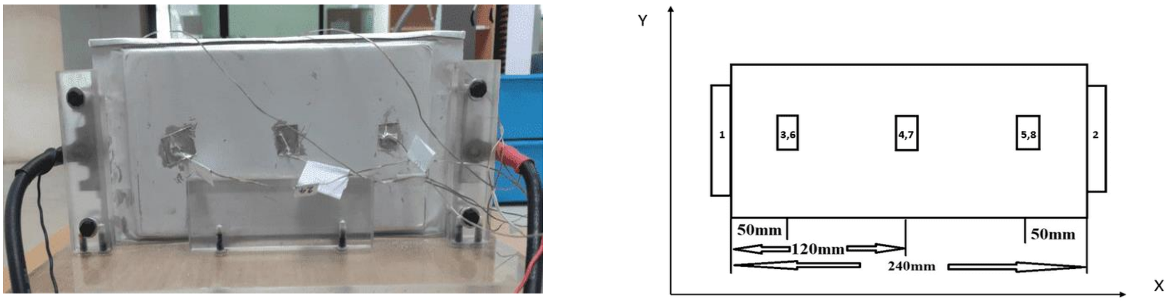

(a) (b)

Figure 1. (a) Lithium-ion battery cell (b) 2D Schematic Diagram of Thermocouple Sensor Location.

3.2. Geometry

A simplified 3D layered thermal model of a unit cell was designed to reduce computational time. The dimensions of the lithium-ion pouch cell were carefully measured at 105 mm width, 195 mm length, and 14mm thickness in the laboratory. The laminated structure of the battery case thickness is generally small and negligible to clarify the calculation of the thermal model. The cell assembly includes five components: negative tab, negative current collector, separator, positive tab, and positive current collector, which are illustrated by the actual battery layers in Figure 2.

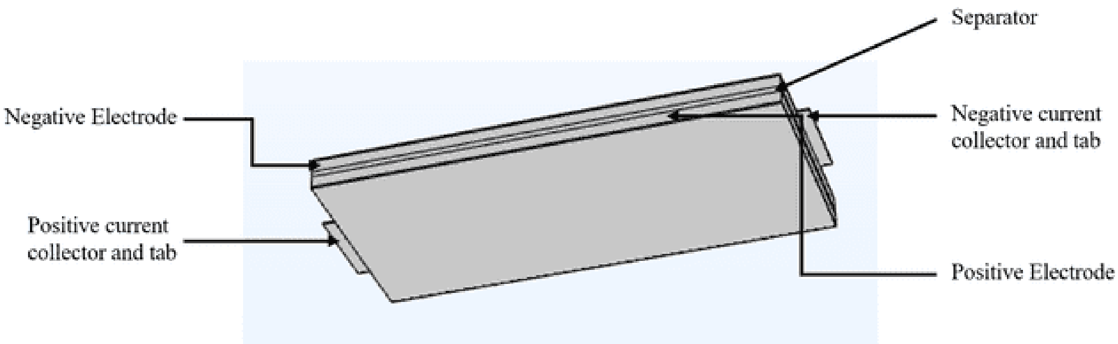

Figure 2. Schematic of a simplified 3D thermal model

3.3. Parameter and physical properties

The dynamic parameter of the lithium-ion cell required by the model calculations are listed in Table 1 [22,25,26]. The next step is to provide suitable validation and characterization according to the physical parameters presented in Table 2. Furthermore, the physical properties of the pouch cell are supposed to simplify calculations through the heat generation process inside the pouch cell, which is complicated. Fundamentally in the 3D CFD approach, internal heat generation can vary as the result of electrochemical reactions due to charge or discharge rate of the batteries.

3.4. Mathematical descriptions and boundary conditions

In a 3D model, the boundary conditions convincing the interface between the surrounding air and the battery surface were coupled at the boundary line. For the battery, heat transfer propagation, heat conduction, heat convection, and heat radiation are the three main parts within and outside the battery. Many methods and models are described in such a way that heat transfer models, heat generation models, data-driven models, etc. have been developed to catch up with the thermal behaviours of the batteries.

Assuming the material inside the cell and battery temperature distribution are considered uniform for each layer plan, there is negligible overall effect of internal radiation in the cell, and the model only considers heat conduction and heat convection for the cooling ambient air conditions. The incompressible flow of heat transfer fluid is proposed as laminar. The 3-D transient energy balance in

Eqn. (1) of a pouch cell is defined as the above assumption, which is described as based on Cartesian coordinates.

$$mCp\frac{\delta T}{\delta t} = Q + kx\frac{\delta T^2}{\delta x^2} + ky\frac{\delta T^2}{\delta y^2} + kz\frac{\delta T^2}{\delta z^2} - qconv \quad (1)$$

where T is the cell domain temperature (K), Cp is the specific heat capacity of the cell (J/kg/K), m is the mass of the cell (kg), Q is the internal generation or heat source (W), and kx, ky, and kz are the thermal conductivity (W· m −1 ·K −1) across the x-direction, y-direction, and z-direction, respectively.

$$qconv = hS(Tamb - T) \quad (2)$$

where h is the coefficient of heat transfer convection (W/m^2), and S is the area of the battery cell (m^2). The battery case is sealed by an aluminum sheet. In such a case, the convention boundary conditions are assumed to be the same as those with surrounding air, and kx is the thermal conductivity along the layers of the inner cell electrode. In this model, kz and ky are the surface thermal conductivity as reported in Ref [27], as assumed to be the same parameters as given in Table 1.

Table 1. Thermal parameters of the model.

Component	Cp	ρ	h	k
Positive tab and cc (aluminum)	903	2770	5	170
Negative tab and cc (copper)	385	8933	5	398
Anode	1437	3510	5	1.04
Separator	1978	1009	5	0.34
Cathode	700	1500	5	5
LTO full cell Ref. [2]	2662	845	5	kx = 0.23 ky = kz 19.1

Table 2. Characteristics of the LTO pouch cell.

Properties	LTO
Mechanical	
Length of the cell, mm	195
Width of the cell, mm	105
Thickness of the cell, mm	14
Length of the tabs, mm	35.5
Width of the tabs, mm	50
Electrical	
Nominal voltage, V	3.7
Nominal capacity, Ah	25

3.5. Experimental Procedure

The lithium-ion battery cell used in this investigation was a 25Ah DPME25N cell with a nominal voltage of 3.7 V. As shown in Figure 3, the experimental flow procedure was set up to measure the cell surface temperature distribution at 1 C, 1.5 C fully charged and discharged, and 50% state of charge.

1) A total of nine thermocouple sensors were used in the unit cell module, located (#3 to #6) on the battery cell, as shown in schematic diagram of Figure 1(b). Two cycler cables and thermocouple sensors at locations #1 and #2 were attached to positive and negative tabs, and #9 was kept free to test the environment temperature.

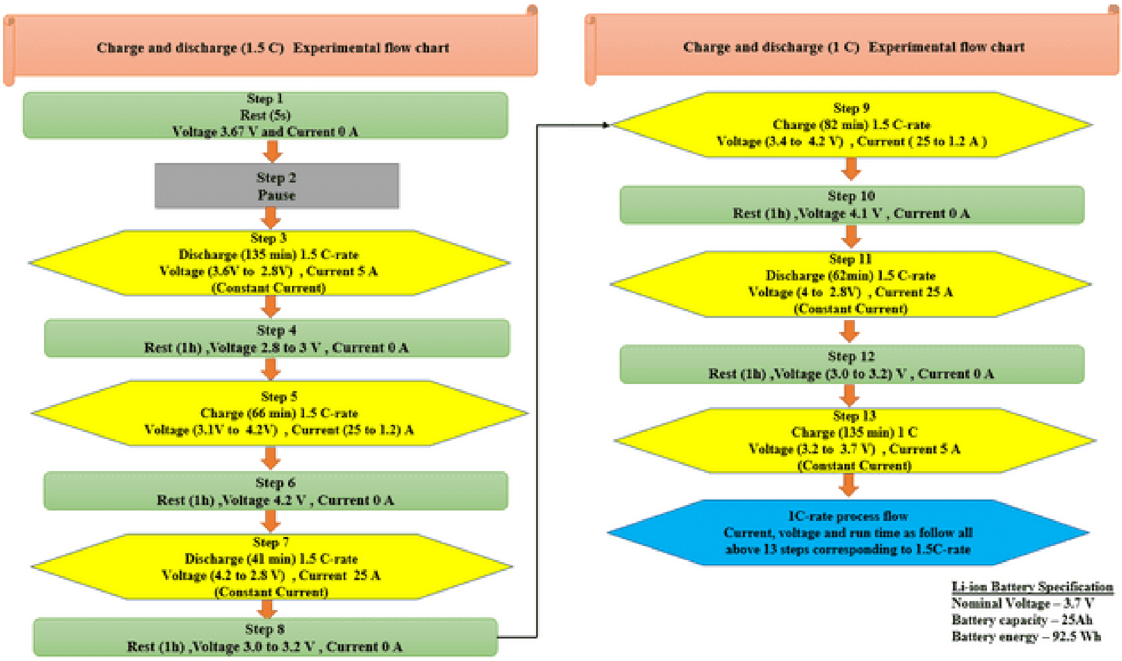

Figure 3. Power charger and discharger machine (MACCOR) experimental flow chart.

2) The picture in Figure 4 (a) and (b) shows that the thermocouples are connected to a power charger and discharger machine (MACCOR), the room temperature is maintained at 20–25˚C, and the cell is discharged, corresponding to the experimental flow chart at 3.6–2.8 volts with a constant current of 5A until 135 minutes, taking at 50% SOC. After the discharging, the cycler rests for one hour, the current is 0A, and the voltage reaches 2.8V to 3V.
3) 5 starts the charging process when the current decreases from 37.5 A to 1.2 A and the voltage reaches 4.2 V. The temperature data at all locations is recorded every 8 seconds.
4) Steps 6 and 7 are repeated for the rest time (Vmax = 4.2V) and discharge process (voltage 4.2 to 2.8V) with a constant current of 25A and a 41-minute discharge time. And the 1C rate charging and discharging process is repeated at 50% SOC as follows: the above flow chart in Figure 3.

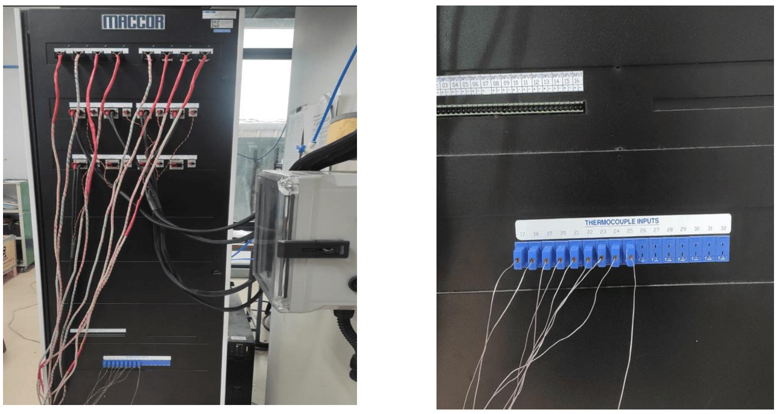

(a) (b)

Figure 4. (a) Maccor testing machine (b) 9 thermocouple sensor connecting at the battery and machine.

4. Test Results

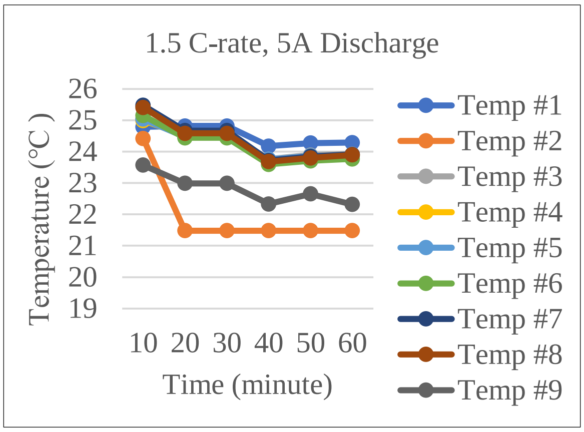

(a)

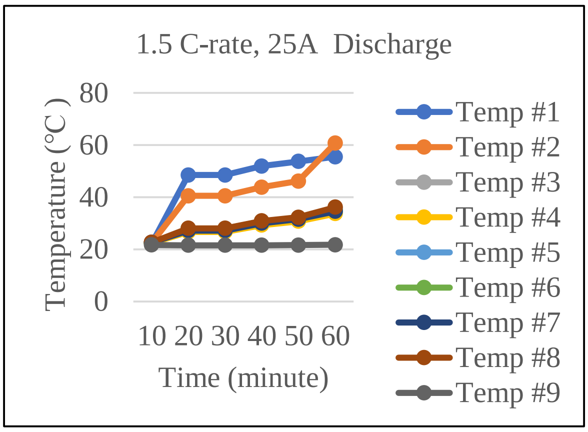

(b)

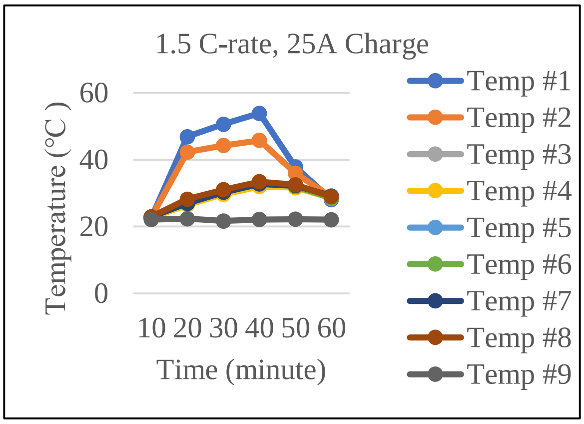

(c)

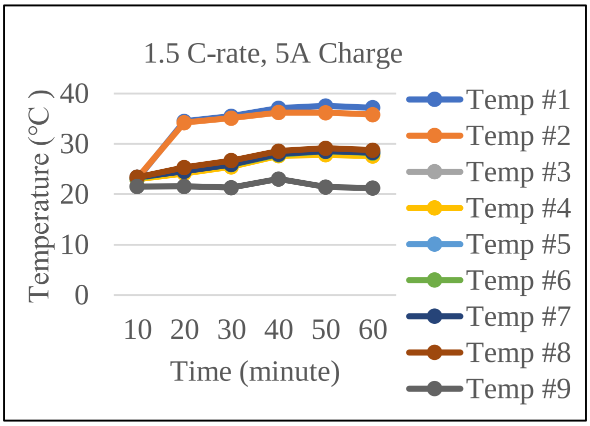

(d)

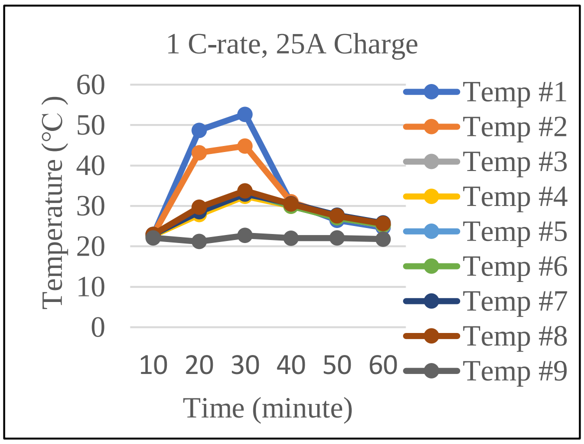

(e)

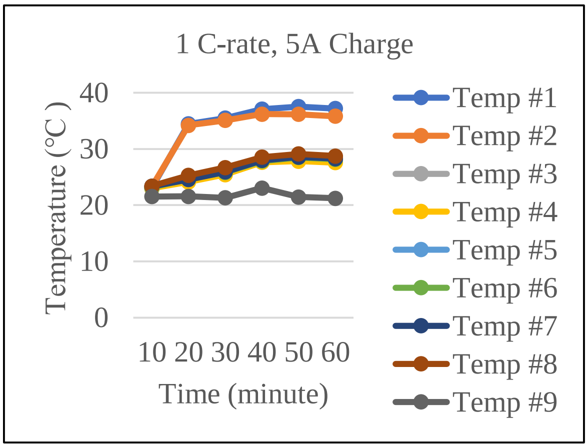

(f)

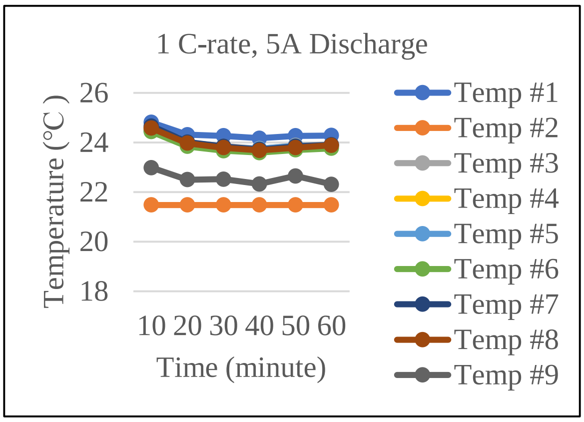

(g)

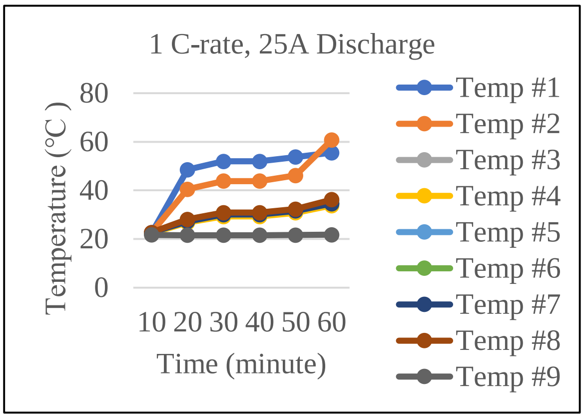

(h)

Figure 5. (a) and (b) show average surface temperature variation at 1.5C-rate, 5A, and 25A discharge. (c) and (d) show average surface temperature variation at 1.5 C-rate, 5A, and 25A charge. (e) and (f) show average surface temperature variation at 1 C-rate, 5A, and 25A charge. (g) and (h) show average surface temperature variation at 1C-rate, 5A, and 25A discharge.

Experiment results are carried out at 1.5 C-rate, the constant current 5A discharging test, and the average surface temperature (at all thermocouple locations) is not quite stable within 20–26 °C before 50% DOD in Figure 5(a). In Figure 5(b), at the locations of thermocouples #1 and #2, the temperature increased abruptly after 20 minutes while the current input was 25A. For 5A and 25A charging tests, the temperature increased until over 50 °C after 30 minutes of 20% SOC, as shown in Figure 5(c) and (d). The surface temperature is in a stable condition during constant current discharge test at all locations, and the temperature is 20–25 °C in Figure 5(g). The largest temperature gradient can be seen when the current increased 25A on both 1C and 1.5 C-rate charge and discharge progress. Locations #1 and #2 mostly have higher temperatures than others' locations, and location # 9 always has the lowest temperature especially obtained at room temperature. The peak surface temperature gradients are compared at 1C and 1.5C at charge and discharge with different voltages and currents, as described in Table 3. The comparison of experimental and simulation results can be seen in Table 4.

Table 3. Experimental measurements result of different current and voltage during discharge.

Cooling Type	Charge Current (A)		Charge Voltage (V)	Rest or Open Circuit Voltage (V)	Ambient Temperature (°C)	Peak Temperature (°C)	
						1.5C	1C
Natural Cooling	1.5C	25	4.1	4.2	25	60	60
	1C	25	3.9	4.1			
Cooling Type	**Charge Current (A)**		**Charge Voltage (V)**	**Rest or Open Circuit Voltage (V)**	**Ambient Temperature (°C)**	**Peak Temperature (°C)**	
						1.5C	**1C**
Natural Cooling	1.5C	5	3.1	3.2	25	25	25
	1C	5	3.1	3.2			

Table 4. Comparison between experimental and simulation results at 5 A and 25A current rate.

Current rate		Discharge		Charge			Temp: Difference (°C) Between Experiment & Simulation			
		1.5 C	1C	1.5C	1C		1.5C	1C	2C	3C
5A	Max Exp: Temp: (°C)	25	24.5	35.8	37.19	Discharge	0	0.5	-	-
	Max Simulation Temp: (°C)	25	25	-	-	Charge	-	-	-	-
25A	Max Exp: Temp: (°C)	61	60.7	53.8	52.64	Discharge	24	23.7	-	-
	Max Simulation Temp: (°C)	37	37	-	-	Charge	-	-	-	-

5. Simulation results

The current density of the 1.5 C discharge rate, the testing time in 45 minutes, the simulation model, which is set up as a user-defined function of the current discharge rate, is 25A, the temperature result is 310K as shown in Figure 6(a), and the thermocouple locations #3, #5, #4, and #7 are higher than others. According to Figure 6(b), the user-defined function for the current discharge rate is 5A, and the simulation result is 298K with a uniform surface temperature distribution. At a 1C discharge, the results are nearly like the 1.5C discharge temperature distribution when the current operation rate is 5A and 25A. Heat generation is being generated around the middle of the cell in Figures 6 (c) and (d). In summary, a high current rate means high heat generation and high temperature emissions in the battery cell.

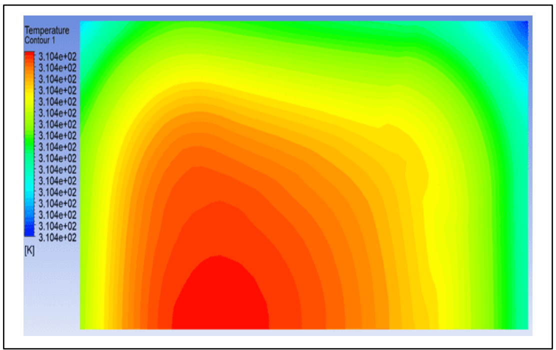

(b) 1.5C discharge, 25A user-defined
Max Surface Temp: is 310K.

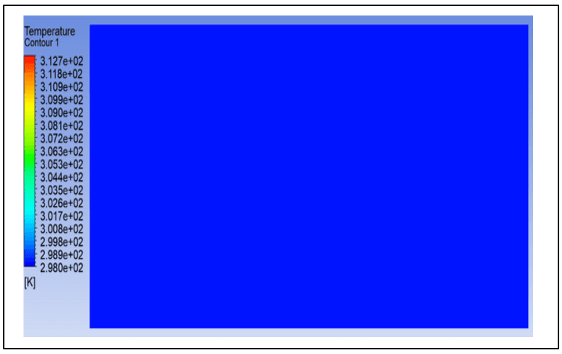

(a) 1.5C discharge, 5A user-defined
Max Surface Temp: is 298K.

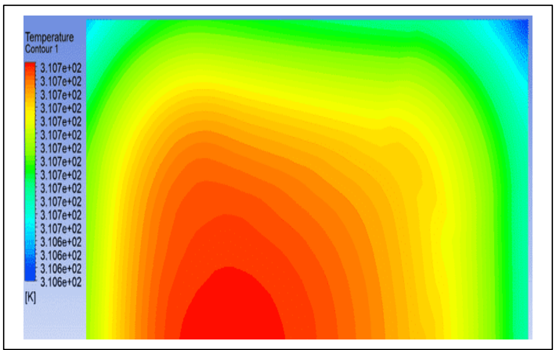

(d) 1C discharge, 25A user-defined
Max Surface Temp: is 310K.

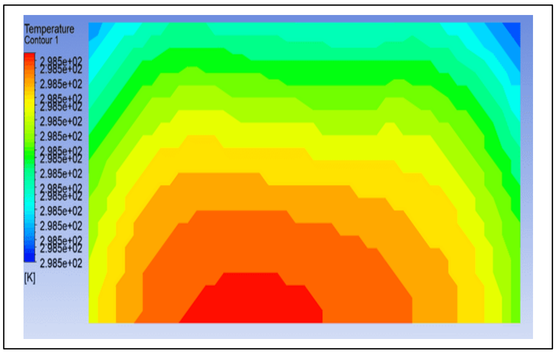

(c) 1C discharge, 5A user-defined
Max Surface Temp: is 298K.

Figure 6. Temperature description profile (K) during discharge.

6. Conclusion

A simplified unit cell's non-uniform surface temperature distribution was visually observed according to experiment results at different time states. The temperature gradient profile was simulated with ANSYS CFD software involving a finite volume method. The optimum temperature range of the lithium-ion battery must be between 20 °C and 40 °C. Otherwise, the test results established that high heat generation on the cell surface was carried out after the current state of 25A, 50% DOD, and SOC. The acceptable temperature range only can see that 5A current on each of the C-rates at 25°C at different 1C, 1.5C charge and discharge rates. As a comparison of surface temperature gradients between the simulation and experiment results, the temperature differences are thoroughly high, according to Table 4. In addition, the test results compared with the simulation model have an error of at least 20%, which is not good precision for electrified vehicles. In future work, the battery cooling strategy will be innovated for this model, and it can protect against the problem of thermal runaway or battery aging. To complete this study, the cooling system or electrochemical investigation will require more research and methods for further development. This thermal model proved that high current will be the result of high heat generation or high temperature distribution on the battery cell. In summary, the presented model methodology can be improved by the battery cooling system, which will give some idea of a better-designed single cell to pack-level model for BTMS.

7. Acknowledgment

National Metal and Materials Technology Center, National Science and Technology Development Agency, Pathumthani 12120, Thailand References

8. References

[1] Q. Wang, Q. Sun, P. Ping, X. Zhao, J. Sun, Z. Lin, *Heat transfer in the dynamic cycling of lithium-titanate batteries. Int. J. Heat. Mass Transf*. 93 (2016) 896-905

[2] Rao Z, Wang S. *A review of power battery thermal energy management. Renewable & Sustainable Energy Reviews, 2011,* 15 (9): 4554–4571

[3] R. Kizilel, R. Sabbah, J.R. Selman, S. Al-Hallaj, *An alternative cooling system to enhance the safety of Li-ion battery packs, J. Power Sources 194 (2009)* 1105– 1112.

[4] Park B, Lee C H, Xia C, et al. *Characterization of gel polymer electrolyte for suppressing deterioration of cathode electrodes of Li ion batteries on high rate cycling at elevated temperature. Electrochimica Acta*, 2016, 188: 78–84

[5] S. Al-Hallaj, H. Maleki, J.S. Hong, J.R. Selman, *Thermal modeling and design considerations of lithium-ion batteries, J. Power Sources 83* (1999) 1–8.

[6] Y. Chen, J.W. Evans, *Heat transfer phenomena in lithium/polymer-electrolyte batteries for electric vehicle application, J. Electrochem. Soc. 140* (1993) 1833– 1838.

[7] Y. Chen, J.W. Evans, *Thermal analysis of lithium polymer electrolyte batteries by a two-dimensional model-thermal behavior and design optimization 3, Electrochem. Acta 9* (1994) 517–526.

[8] Y. Chen, J.W. Evans, *Thermal analysis of lithium-ion batteries, J. Electrochem. Soc*. 143 (1996) 2708–2712.

[9] Y. Chen, J.W. Evans, *Three-dimensional thermal modeling of lithium-polymer batteries under galvanostatic discharge and dynamic power profile, J. Electrochem. Soc. 141* (1994) 2947–2955.

[10] T.I. Evans, R.E. White, *A thermal analysis of a spirally wound battery using a simple mathematical model, J. Electrochem. Soc. 136* (1989) 2145–2152.

[11] R. Sabbah, R. Kizilel, J.R. Selman, S. Al-Hallaj, *Active (air-cooled) vs. passive (phase change material) thermal management of high-power lithium-ion packs: limitation of temperature rise and uniformity of temperature distribution, J. Power Sources 182 (2008)* 630–638.

[12] A. Mills, S. Al-Hallaj, *Simulation of passive thermal management system for lithium-ion battery packs, J. Power Sources 141 (2005)* 307–315.

[13] S.A. Khateeb, M.M. Farid, J.R. Selman, S. Al-Hallaj, *Design and simulation of a lithium-ion battery with a phase change material thermal management system for an electric scooter, J. Power Sources 128 (2004)* 292–307.

[14] T. Wang, K.J. Tseng, J. Zhao, *Development of efficient air-cooling strategies for lithium-ion battery module based on empirical heat source model, Appl. Therm. Eng. 90 (2015)* 521–529.

[15] H. Sun, X. Wang, B. Tossan, R. Dixon, *Three-dimensional thermal modeling of a lithium-ion battery pack, J. Power Sources 206 (2012)* 349–356.
[16] D. Chen, J. Jiang, G.H. Kim, C. Yang, A. Pesaran, *Comparison of different cooling methods for lithium-ion battery cells, Appl. Therm. Eng. 94 (2016)* 846–854
[17] X. Li, F. He, L. Ma, *Thermal management of cylindrical batteries investigated using wind tunnel testing and computational fluid dynamics simulation, J. Power Sources 238 (2013)* 395–402.
[18] R. Mahamud, C. Park, *reciprocating air flow for Li-ion battery thermal management to improve temperature uniformity, J. Power Sources 196 (2011)* 5685–5696.
[19] J. Zhao, Z. Rao, Y. Huo, X. Liu, Y. Li, *Thermal management of cylindrical power battery module for extending the life of new energy electric vehicles, Appl. Therm. Eng. 85 (2015)* 33–43.
[20] N. Javani, I. Dincer, G.F. Naterer, G.L. Rohrauer, *Modeling of passive thermal management for electric vehicle battery packs with PCM between cells, Appl. Therm. Eng. 73 (2014)* 307–316.
[21] K.A. Murashko, A.V. Mityakov, J. Pyrhonen, V.Y. Mityakov, S.S. Sapozhnikov, *Thermal parameters determination of battery cells by local heat flux measurements, J. Power Sources 271 (2014)* 48e54.
[22] H. Maleki, S. Al Hallaj, J.R. Selman, Ralph B. Dinwiddie, H. Wang, *Thermal properties of lithium-ion battery and components, J. Electrochem. Soc.* 146 1999 947.
[23] N.Omar, P.V.D. Bossche, *Assessment of performance of lithium iron phosphate oxide, nickel manganese cobalt oxide and nickel cobalt aluminum oxide based cells for using in plug-in battery. Conf, 2011 electric vehicle applications, in: IEEE Veh. Power Propuls.*
[24] M. Hannan, F. Azidin, A. Mohamed, Hybrid electric vehicles and their challenges: a review, Renew. Sustain. Energy Rev. 29 (2014) 135e150.
[25] M. Chen, Q. Sun, Y. Li, K. Wu, B. Liu, P. Peng, Q. Wang, *A thermal runaway simulation on a lithium titanate battery and the battery module, Energies 8(2015)* 490-500
[26] W. Haynes, *CRC Handbook of Chemistry and Physics,* 90th ed., 2011.
[27] T.L. BergmanN, A.S. Lavine, F.P. Incropera, D.P. Dewitt, *Fundamentals of Heat and Mass Transfer,* 2007.

TSF0031

Hybrid thermal management system for cooling commercial Electric Vehicle Batteries – An overview

Kittinan Boonma, Napol Patimaporntap, Yossapong Laoonual, Stephen Manova, and Somchai Wongwises*

Department of Mechanical Engineering, Faculty of Engineering, King Mongkut's University of Technology Thonburi (KMUTT), Bang Mod, Bangkok 10140, Thailand

* Corresponding Author: Somchai.won@kmutt.ac.th

Abstract Li-ion batteries (LIBs) have been widely used as the primary power source in electric vehicles (EVs) due to their high energy density, long cycle life, and environmental friendliness. However, excessive heat generation in LIBs can adversely impact performance and safety. Effective cooling systems are essential to maintain the battery's temperature, and prevent thermal runaway, thereby ensuring optimal performance. Air and liquid are the currently employed media for active cooling system. Phase change materials and heat pipes are used in passive cooling systems. These systems have been employed separately or as combined cooling methods to control battery pack temperature. This review provides valuable information on various air flow channel designs, battery cell arrangements and spacing to cool battery pack/modules. Also, the review highlights the current state-of-the-art associated with the hybrid battery thermal management systems (HBTMSs) with air as a primary source for cooling the commercially used LIBs.

Keywords: Electric vehicle, Li-ion battery, Battery thermal management systems, Air cooling systems.

1. Introduction

Currently, electric vehicles (EVs) are one of the suitable alternatives for reducing air pollution [1]. The major source of power for these EVs is their battery system. Particularly, Li-ion batteries (LIBs) are commercially used in EVs as they possess high power and energy density, less weight and longer life cycle with no impact on battery memory. However, the primary issue with LIBs is high temperatures during the charging/discharging processes. Failing to monitor and control this heat can result in decreased capacity and increased possibilities for the battery pack's temperature to become unstable. Furthermore, in challenging operating conditions like quick charging and low temperatures, there are more chances for the deterioration in the battery's performance. Technical reports indicate that the optimal operating temperature of a LIB ranges from 25 to 40 ^{o}C [2-4]. The temperature difference (ΔT) between the cells, modules, and pack levels during working condition should be less than 5 ^{o}C [2-5]. Hence, to ensure consistent temperature distribution and maintain the ideal temperature range within an EV battery, it is essential to install an appropriate battery thermal management system (BTMS) [2].

2. Battery thermal management systems

BTMSs are designed to maintain LIBs within their optimal operating temperature range, ensuring not only optimum performance but also operational safety and a long-life span. These BTMSs must have increased dependability, cost-effectiveness, low energy consumption, and simple maintenance procedures. Additionally, it is also important to consider the physical arrangement of the cells while designing the thermal management system. LIBs are available in various configurations, including cylindrical, pouch, and prismatic designs, making them appropriate for a wide range of applications. Cylindrical-shaped batteries have the advantages of low cost and flexibility in system adoption. Also, it is simpler to control the temperature of cylindrically design batteries because of their compact size and thickness. However, they have low capacity. Li-ion batteries with prismatic designs have a high energy content and are fabricated similarly to cylindrical batteries. The pouch cell employs a flexible cell bag made of laminated aluminum or polymer rather than a rigid metal housing used for prismatic cells [5]. The heating location in Li-ion cells varies depending on the cell type. Cylindrical cells experience the highest temperature at their center and the lowest at their surface [6]. However, prismatic and pouch cells have high temperatures at the battery tabs [7].

Generally, BTMSs can be classified into four primary groups [2]. There is also a combined cooling system and these diverse systems come with their own advantages/drawbacks. Air-cooling is frequently employed due to its uncomplicated design, affordability, and lightweight nature. Nonetheless, under stressful conditions, there can be a significant ΔT within a battery module or pack [3]. A liquid cooling system works better than air cooling and can transfer heat from the battery more quickly. However, it is complicated to design and a liquid cooling system has higher installation costs and risks leakage [6]. A heat dissipation system with phase change material (PCM) integration has advantages of a simple design and cost-effectiveness. However, the currently available PCMs exhibit relatively low thermal conductivity, leading to limited heat dissipation rates [8]. Therefore, heat pipes (HPs) are suggested and are often referred to as superconductors because of their excellent heat transfer capabilities [2]. The advantages of HPs include their enhanced thermal conductivity, greater efficiency, and higher heat transfer capabilities. Furthermore, they are a hybrid BTMS (HBTMS) approach that involves a combination of the above-mentioned methods to enhance the heat rejection from the battery module/pack. The present review investigates the HBTMS with air as a primary cooling medium. Particularly, this review involves highlighting the significance of air-cooling systems in combination with three other cooling techniques, liquid cooling, PCM, and HP.

3. Air-cooled battery thermal management systems

Utilizing an air-cooled BTMS can enhance battery pack design by optimizing the cell arrangement and considering each pack's unique needs, aimed at achieving peak thermal performance, cost-effectiveness, and the highest possible specific energy.

3.1. Battery cell arrangement

This section discusses the organized arrangement of battery cells in various configurations. The shape of the battery module/pack affects the temperature distribution. Therefore, heat dissipation design must be taken into consideration as well. Sefidan *et al*. [9] compared nine different cell arrangements and reported that cooling using a combination of air and a nanofluid resulted in maximum temperature (T_{max}) reduction, from 16 to 24 ºC. Cell arrangements are shown in Figure 1 (II-XI). Wang *et al*. [10] conducted a study on cell configurations and forced air cooling techniques for battery modules used in high-power LIB packs. They examined the thermal behavior of modules in various cell arrangement structures, including rectangular arrangements such as 1x24 (Figure 1 (I)), 3x8 (Figure 1 (III)), and 5x5 arrays (Figure 1 (XI)), a hexagonal arrangement with 19 cells (Figure 1 (VI)), and a circular arrangement with 28 cells (Figure 1 (VII)). Furthermore, they investigated the efficiency of air-cooling by varying the placement of the cooling fan on the module. Optimal performance was observed for the cubic arrangement (5x5 array) when the fan was operated at an airspeed of 1 m/s and positioned at the top of the module. The corresponding T_{max} and ΔT were reported as 33.58 °C and 2.95 °C respectively, for the optimum conditions. Kang *et al*. [11] developed a model for battery packs based on battery cell test results, specifically comparing square and rectangular packs. For rectangular packs, the air layer inside the module maintains a lower temperature because it experiences a shorter path for heat transfer. The experimental and numerical results showed the T_{max} values for the rectangular pack were 38.08 °C and 38.66 °C, respectively. Similarly, the ΔT was reported as 17.57 °C and 13.16 °C, respectively. Yu *et al*. [12] examined battery pack temperature with a staggered cell arrangement. Each housing comprised 22 cells and had three modules in an analysis of their transient thermal behaviour when subjected to both natural and forced air cooling conditions. Based on the results, the T_{max} and ΔT of the battery were reduced to 30.1 °C and 2.2 °C for the highest ambient temperature (T_{amb}) of 25 °C and an air velocity of 1 m/s. Table 1 shows a summary of the existing works published on different battery cell arrangements.

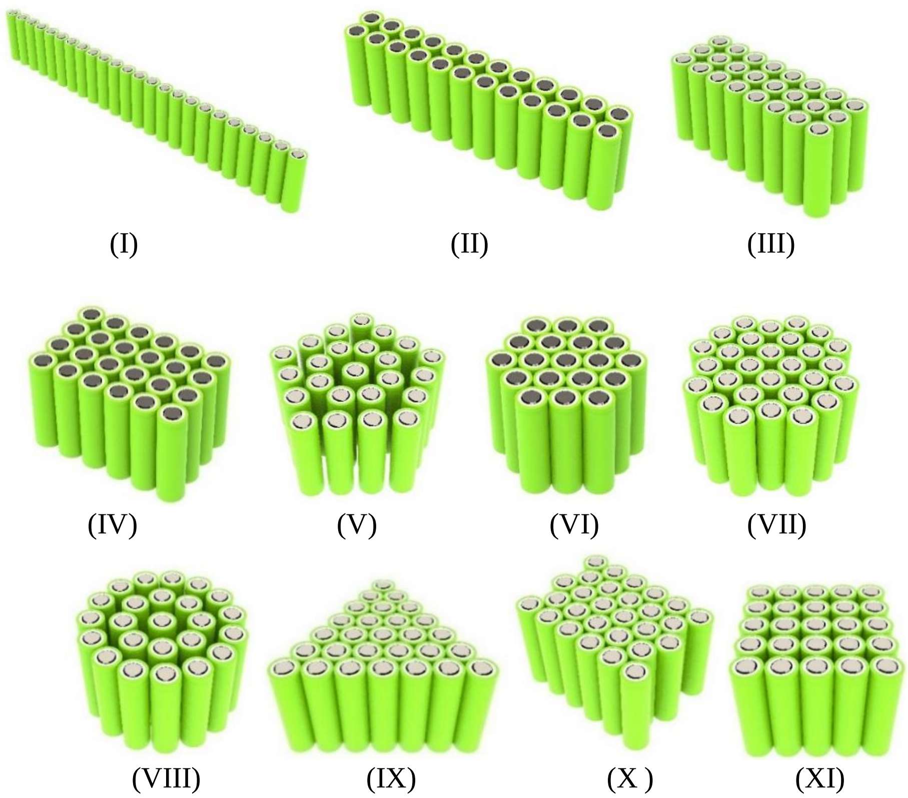

Figure 1. Cell arrangements for different battery modules [9,10].

Table 1. Summary of the existing literature published on battery cell arrangement.

Authors	Method(s)	Main point(s)	Load on battery	Air velocity (m/s)	T_{amb} (°C)	T_{max} (°C)	ΔT (°C)	Remark
Sefidan *et al.* [9]	Numerical	Cell arrangement and module structure	Discharge 3 C-rate	0.5	25	<40	>5	-
Wang *et al.* [10]	Experimental and Numerical	Cell arrangement and module structure	Discharge 3 C-rate	1	25	<40	<5	5x5 array
Kang *et al.* [11]	Experimental and Numerical	Cell arrangement	Discharge 1C-rate	5	25	<40	>5	Rectangle
Yu *et al.* [12]	Experimental	Cell arrangement	Charge/ Discharge 1C-rate	1	25	<40	>5	-

3.2. Module structure and cooling channel design

Modification in the module structure and cooling channel design are the other factors that can impact the performance of a battery module/pack. This section is dedicated to the design considerations concerning the different positions of air inlets and outlets for battery modules/packs. Sharma and Prabhakar [13] proposed that performance is significantly influenced by design, with superior results noted when the inlet and outlet are positioned at opposite ends of a battery pack. Additionally, baffles are also incorporated to minimize pressure drop. Addition of novel substructures, *e.g.*, fins or winglets, have also resulted in higher turbulence and improved convective cooling inside the channels. Wang *et al*. [14] investigated nine distinct BTMS configurations, each featuring a different air inlet and outlet, as shown in Figure 2 (III-VII), (X), and (XI). Detailed information on battery pack temperature based on various positions is given in Table 2. Altering the positions of the air inlet and outlet had a notable impact on the flow pattern and cooling performance of battery packs. Figures 2 (V) and (VII) exhibited the lowest temperatures, reduced by 2.90 °C and 4.96 °C in comparison to the conventional Z-type BTMS. Oyewola *et al*. [15] stated that the step quantity affects the battery pack's heat dissipation. A 7-step case model has the best system's T_{max}, 51.9 °C, and cell ΔT of 1 °C compared to the Z-type model. Furthermore, Shahid and Agelin-Chaab [16] reported that incorporating all three components (jet inlets, inlet plenum, and multiple vortex generators) in the pack leads to a significant improvement in cooling performance and temperature uniformity. These results showed an approximate 5% reduction in T_{max} and a 21.5% lower ΔT. Additionally, single cell temperature uniformity was improved by 16%.

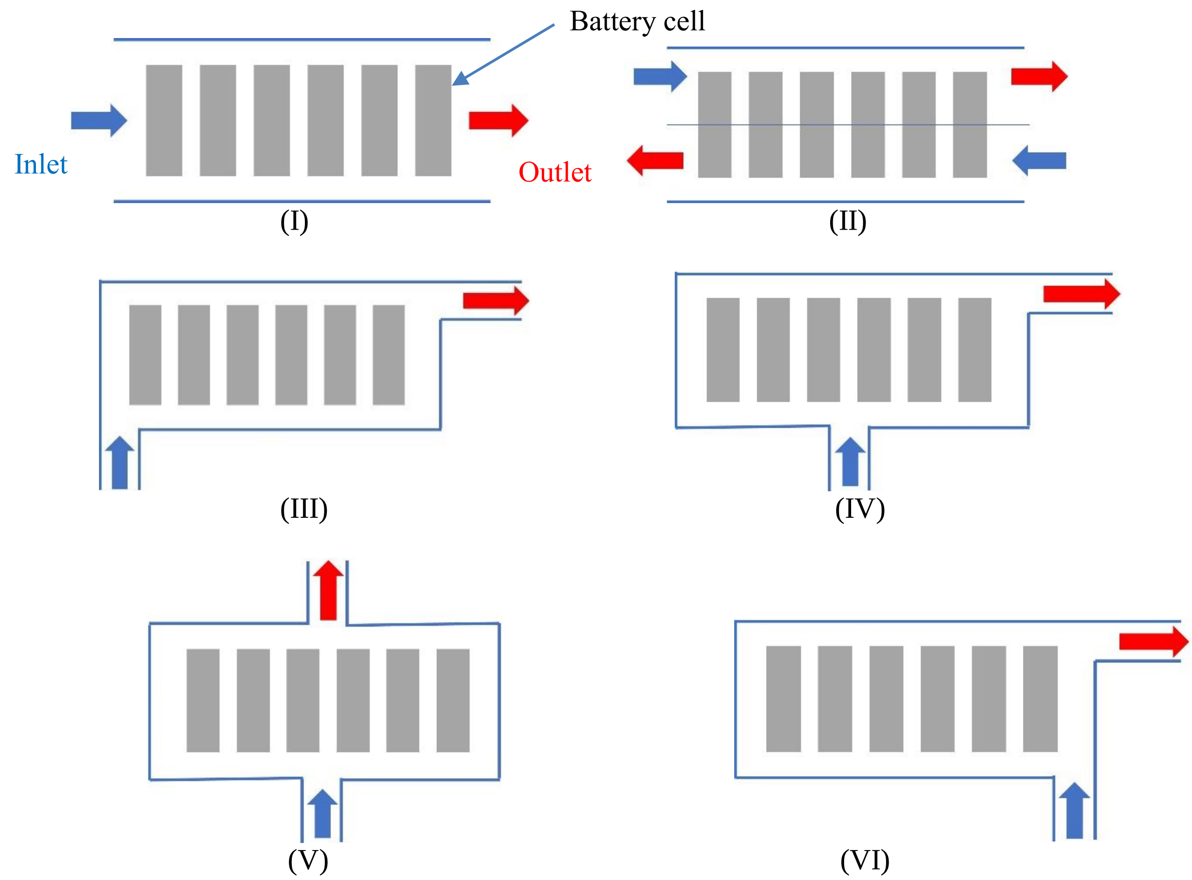

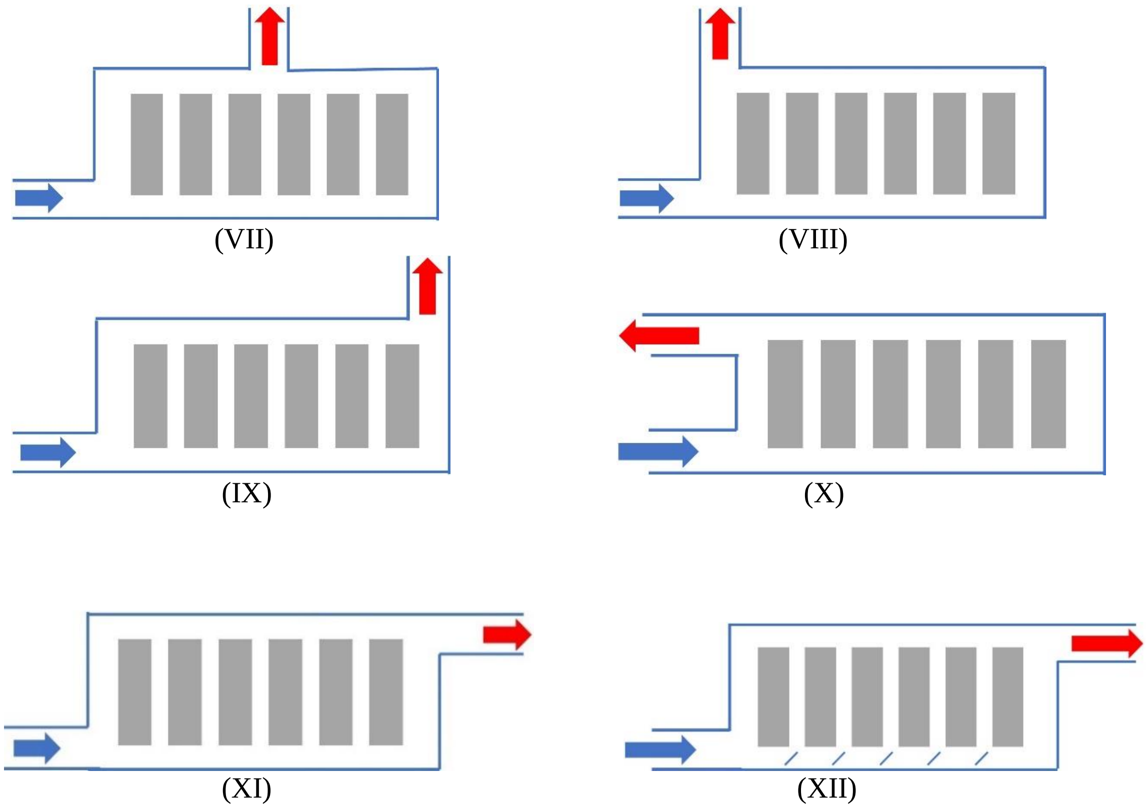

Figure 2. Different inlet/outlet flow arrangements used in an active air-cooled BTMS [15,16].

Table 2. Research on module structure and cell spacing.

Authors	Module structure(s)	Spacing (mm)	Load on battery	Air velocity (m/s)	T_{amb} (°C)	T_{max} (°C)	ΔT (°C)	Optimum condition
Wang *et al.* [14]	III	3	11.8 W	3.5	26.15	53.66	>5	Installed two parallel plates
	IV	3	11.8 W	3.5	26.15	51.86	<5	
	V	3	11.8 W	3.5	26.15	54.88	>5	
	VI	3	11.8 W	3.5	26.15	53.73	<5	
	VII	3	11.8 W	3.5	26.15	53.47	<5	
	VIII	3	11.8 W	3.5	26.15	54.97	>5	
	IX	3	11.8 W	3.5	26.15	53.36	<5	
	X	3	11.8 W	3.5	26.15	53.10	<5	
	XI	3	11.8 W	3.5	26.15	52.39	<5	
Oyewola *et al.* [15]	XI	3	11.8W	3.5	26.15	51.9	<5	Case 4 (7-step)
Behi *et al.* [17]	I	2	Discharge 1.5 C	2	26	37.1	<5	-
Na *et al.* [18]	II	8	Discharge 3 C rate	3	-	29.1	<5	Reverse layered air flow
Zhang *et al.* [19]	XII	3	11.8 W	4	26.15	47.76	<5	Case 6-6-7-13-9 (H1,H2,H3,H4,H5)

3.3. Cell spacing

One of the foremost design factors that has a significant impact on cooling performance is arrangement of battery cell spacing. Yang *et al*. [20] concluded that an appropriate design of the cooling system for aligned cell arrangements, with specific longitudinal and transverse intervals, can improve the temperature uniformity and reduce power requirements. Chen *et al*. [21] proposed a parallel BTMS and analyzed the effects of different cell spacings in the pack. A maximum reduction of 3 °C in T_{max} and 60% in ΔT were reported for the optimum cell spacing. Fan *et al*. [22] found that the aligned arrangements consumed 23% less power compared to the cross configurations. The aligned battery pack, despite requiring less space, resulted in the best performance with uniformity in the temperature distribution. This was followed by the staggered and cross packs. Increasing the air intake temperature from 20 to 30 °C enhances temperature uniformity. At a discharge rate of 1C, the maximum ΔT decreased by 12% at 0.6 m/s and 20% at 1 m/s. Moosavi *et al*. [23] did a numerical analysis that demonstrated a direct and positive relationship between the T_{max} within the cells and both transverse and longitudinal pitch ratios. Conversely, the analysis revealed a negative correlation between the ΔT and the pitch ratios. Gungor [4] reported that maintaining the ideal cell spacing can ensure that the ΔT within the air-cooled LIB module remains within the acceptable temperature limit of 5 °C, all while meeting the requirements for optimal operating conditions. The recommended range for cell spacing in air-cooled BTMS ranges from 3.5 to 5.8 mm, for Reynolds numbers ranging from 250 to 2000.

4. Hybrid battery thermal management systems

HBTMSs involve a combination of more than one BTMS, which exploits the advantages of the multiple systems while simultaneously reducing the negative aspects of each of the individual systems. HBTMSs combine methods to achieve higher thermal performance, such as coupling air and liquid cooling, air cooling with a PCM, air cooling with HPs, or coupling more than two of these methods.

4.1. Coupling air and liquid cooling

Yang *et al*. [24] integrated liquid and air cooling methods to reduce the T_{max} of the module and improve temperature uniformity. The authors reported that an increased inlet flow rate decreased the T_{max} and ΔT but increased power consumption. Additionally, adding extra cooling tubes and mini-channels enhanced cooling performance. Moreover, suitable tube spacing, flow direction, and spacer combinations also enabled maintenance of ΔT within 4.13 °C and lowered the T_{max} to 31.98 °C. Li *et al*. [25] presented a BTMS that integrates multi-channel parallel liquid cooling with air cooling. This approach was done to effectively address the heat dissipation and improve temperature distribution within battery modules. The direction of coolant flow reduces the ΔT of the module by 58% but does not effectively control the T_{max} of the battery. Xin *et al*. [26] introduced a compound cooling approach that combines liquid and air cooling. The objective of this method is to enhance uniformity in the temperature distribution throughout the battery module. Multiple heat-conducting blocks were uniformly distributed along the battery's longitudinal direction. Zhou *et al*. [27] explored the performance of a BTMS with the HBTMS method. Implementation of air jets at the cylinder ends reduces the maximum ΔT of batteries from 5.7 to 4.0 °C compared to liquid cooling. These authors reported 3.6 and 28.9 °C reductions in ΔT and T_{max}, respectively, when the coolant path is minimized, and a half-helical duct is reduced to two sections. The findings of this study contribute to enhancing the safety and dependability of battery operations and provide insights for the design of HBTMSs.

4.2. Coupling air cooling with a PCM

Ling *et al*. [28] discovered that by combining forced air convection with phase change materials (PCMs), they could maintain the battery pack's T_{max} below 50 °C under cycling conditions, regardless of a 7 °C increased T_{amb}. The PCMs are responsible for regulating both the T_{max} and the maximum ΔT inside the pack, while forced air convection cooled the battery pack during two cycle discharges at 1.5 and 2C rates. Nazar *et al*. [29] did a comparison of the ΔT values among cells with and without a BTMS. They found that using no thermal management resulted in a ΔT of about 10 °C, while an active cooling (air cooling) reduced the ΔT to about 6 °C, and passive cooling with PCM reduced it to about 3.5 °C. Ranjbaran *et al*. [30] found that increasing the air velocity or extending the cooling duct length inside the PCM can result in lower battery surface temperatures. Furthermore, the temperature distribution within the battery pack was maintained within 1.6 °C, confirming its uniform temperature distribution. However, it was observed that an augmented inlet air stream or longer cooling ducts also led to larger ΔT values.

4.3. Coupling air cooling with heat pipes

Feng *et al*. [31] investigated the thermal and strain management of a battery pack by employing a heat pipe with forced convection. As the discharge rate became higher, the temperature and strain on the battery also increased. The management system under consideration offers several advantages, including a compact design, low energy consumption, and a capacity to effectively mitigate temperature and strain induced in the battery. Behi *et al*. [17] revealed that the use of heat pipe copper sheets, HPs, and forced convection cooling strategies improved the uniformity of temperature distribution and reduced the T_{max} compared to natural convection. Temperature decreases of 42.7, 42.1, and 34.5 °C were respectively reported for forced convection, HP, and HPCS, compared to natural convection. Moreover, researchers [32-34] focused on air cooling and flat HP-assisted cooling by conducting a thermal analysis on a lithium titanate (LTO) cell to determine the position of maximum heat generation and enhance the performance of the LTO cell under various conditions.

4.4. Coupling air cooling with a PCM and a heat pipe

Wu *et al*. [35] proposed an HP-assisted PCM-based BTMS to effectively and feasibly cool EV batteries. Forced air convection can control T_{max}, keeping it below 50 °C even at a discharge rate of 5C, with greater stability and lower temperature fluctuation under cycling. Septiadi *et al*. [36] proposed an HP-BTMS and PCM, which showed better performance, reducing the temperature to 37 °C, when an electric bike was driven at high speeds, highlighting its potential for maintaining battery safety. Adding forced convection at 3 m/s reduced the temperature to 35.25 °C under high discharge rates. This resulted in an 87% reduced temperature differential and provided for a more uniform battery temperature distribution.

5. Conclusion

This paper provides a comprehensive review of BTMSs using an air-cooled approach. Discussion of various strategies for enhancing thermal performance, such as battery cell arrangement, module structure, cooling channel improvements, and cell spacing are presented. Moreover, this study explores combinations of HBTMS techniques, encompassing coupling air and liquid cooling, air cooling with use of a PCM, air cooling with HPs, and air cooling with a PCM and HPs. These solutions have the potential to increase the performance of cooling systems. However, air-cooling provide advantages due to their simplicity, safety, and cost-effectiveness. In the case of combining air cooling with other techniques, it becomes necessary to consider the compactness of the system, energy consumption, and maintenance requirements as well. Hence, the proposed review is expected to provide a comprehensive understanding of various strategies that can be used for cooling EV batteries.

6. References

[1] L. Yu and Y. P. Li, "A flexible-possibilistic stochastic programming method for planning municipal-scale energy system through introducing renewable energies and electric vehicles," *Journal of Cleaner Production*, vol. 207, pp. 772–787, Jan. 2019, doi: 10.1016/j.jclepro.2018.10.006.

[2] K. Boonma, Patimaporntap. N, H. Mbulu, P. Trinuruk, K. Ruangjirakit, Y. Laoonual, and S. Wongwises, "A Review of the Parameters Affecting a Heat Pipe Thermal Management System for Lithium-Ion Batteries," *Energies*, vol. 15, no. 22, Art. no. 22, Jan. 2022, doi: 10.3390/en15228534.

[3] H. Behi, M. Behi, D. Karimi, J. Jaguemont, and M. Ghanbarpour, "Heat pipe air-cooled thermal management system for lithium-ion batteries: High power applications," *Applied Thermal Engineering*, vol. 183, p. 116240, Jan. 2021, doi: 10.1016/j.applthermaleng.2020.116240.

[4] S. Gungor, “Analytical and numerical investigations on optimal cell spacing for air-cooled energy storage systems,” *International Journal of Thermal Sciences*, vol. 191, p. 108332, Sep. 2023, doi: 10.1016/j.ijthermalsci.2023.108332.
[5] M. M. Hamed, A. El-Tayeb, I. Moukhtar, A. Z. El Dein, and E. H. Abdelhameed, “A review on recent key technologies of lithium-ion battery thermal management: External cooling systems,” *Results in Engineering*, vol. 16, p. 100703, Dec. 2022, doi: 10.1016/j.rineng.2022.100703.
[6] M. Shahjalal, T. Shams, M. E. Islam, W. Alam, and M. Modak, “A review of thermal management for Li-ion batteries: Prospects, challenges, and issues,” *Journal of Energy Storage*, vol. 39, p. 102518, Jul. 2021, doi: 10.1016/j.est.2021.102518.
[7] B. Bose, A. Garg, B. K. Panigrahi, and J. Kim, “Study on Li-ion battery fast charging strategies: Review, challenges and proposed charging framework,” *Journal of Energy Storage*, vol. 55, p. 105507, Nov. 2022, doi: 10.1016/j.est.2022.105507.
[8] X. Wang, S. Liu, Y. Zhang, S. Lv, H. Ni, Y. Deng, and Y. Yuan, “A Review of the Power Battery Thermal Management System with Different Cooling, Heating and Coupling System,” *Energies*, vol. 15, no. 6, p. 1963, Mar. 2022, doi: 10.3390/en15061963.
[9] A. M. Sefidan, A. Sojoudi, and S. C. Saha, “Nanofluid-based cooling of cylindrical lithium-ion battery packs employing forced air flow,” *International Journal of Thermal Sciences*, vol. 117, pp. 44–58, Jul. 2017, doi: 10.1016/j.ijthermalsci.2017.03.006.
[10] T. Wang, K. J. Tseng, J. Zhao, and Z. Wei, “Thermal investigation of lithium-ion battery module with different cell arrangement structures and forced air-cooling strategies,” *Applied Energy*, vol. 134, pp. 229–238, Dec. 2014, doi: 10.1016/j.apenergy.2014.08.013.
[11] D. Kang, P.-Y. Lee, K. Yoo, and J. Kim, “Internal thermal network model-based inner temperature distribution of high-power lithium-ion battery packs with different shapes for thermal management,” *Journal of Energy Storage*, vol. 27, p. 101017, Feb. 2020, doi: 10.1016/j.est.2019.101017.
[12] X. Yu, Z. Lu, L. Zhang, L. Wei, X. Cui, and L. Jin, “Experimental study on transient thermal characteristics of stagger-arranged lithium-ion battery pack with air cooling strategy,” *International Journal of Heat and Mass Transfer*, vol. 143, p. 118576, Nov. 2019, doi: 10.1016/j.ijheatmasstransfer.2019.118576.
[13] D. K. Sharma and A. Prabhakar, “A review on air cooled and air centric hybrid thermal management techniques for Li-ion battery packs in electric vehicles,” *Journal of Energy Storage*, vol. 41, p. 102885, Sep. 2021, doi: 10.1016/j.est.2021.102885.
[14] M. Wang, S. Teng, H. Xi, and Y. Li, “Cooling performance optimization of air-cooled battery thermal management system,” *Applied Thermal Engineering*, vol. 195, p. 117242, Aug. 2021, doi: 10.1016/j.applthermaleng.2021.117242.
[15] O. M. Oyewola, A. A. Awonusi, and O. S. Ismail, “Design optimization of Air-Cooled Li-ion battery thermal management system with Step-like divergence plenum for electric vehicles,” *Alexandria Engineering Journal*, vol. 71, pp. 631–644, May 2023, doi: 10.1016/j.aej.2023.03.089.
[16] S. Shahid and M. Agelin-Chaab, “Analysis of Cooling Effectiveness and Temperature Uniformity in a Battery Pack for Cylindrical Batteries,” *Energies*, vol. 10, no. 8, p. 1157, Aug. 2017, doi: 10.3390/en10081157.
[17] H. Behi, D. Karimi, M. Behi, M. Ghanbarpour, and J. Jaguemont, “A new concept of thermal management system in Li-ion battery using air cooling and heat pipe for electric vehicles,” *Applied Thermal Engineering*, vol. 174, p. 115280, Jun. 2020, doi: 10.1016/j.applthermaleng.2020.115280.
[18] X. Na, H. Kang, T. Wang, and Y. Wang, “Reverse layered air flow for Li-ion battery thermal management,” *Applied Thermal Engineering*, vol. 143, pp. 257–262, Oct. 2018, doi: 10.1016/j.applthermaleng.2018.07.080.
[19] F. Zhang, A. Lin, P. Wang, and P. Liu, “Optimization design of a parallel air-cooled battery thermal management system with spoilers,” *Applied Thermal Engineering*, vol. 182, p. 116062, Jan. 2021, doi: 10.1016/j.applthermaleng.2020.116062.
[20] N. Yang, X. Zhang, G. Li, and D. Hua, “Assessment of the forced air-cooling performance for cylindrical lithium-ion battery packs: A comparative analysis between aligned and staggered cell arrangements,” *Applied Thermal Engineering*, vol. 80, pp. 55–65, Apr. 2015, doi: 10.1016/j.applthermaleng.2015.01.049.
[21] K. Chen, Y. Chen, Z. Li, F. Yuan, and S. Wang, “Design of the cell spacings of battery pack in parallel air-cooled battery thermal management system,” *International Journal of Heat and Mass Transfer*, vol. 127, pp. 393–401, Dec. 2018, doi: 10.1016/j.ijheatmasstransfer.2018.06.131.
[22] Y. Fan, Y. Bao, C. Ling, Y. Chu, X. Tan, and S. Yang, “Experimental study on the thermal management performance of air cooling for high energy density cylindrical lithium-ion batteries,” *Applied Thermal Engineering*, vol. 155, pp. 96–109, Jun. 2019, doi: 10.1016/j.applthermaleng.2019.03.157.

[23] A. Moosavi, A.-L. Ljung, and T. S. Lundström, “A study on the effect of cell spacing in large-scale air-cooled battery thermal management systems using a novel modeling approach,” *Journal of Energy Storage*, vol. 72, p. 108418, Nov. 2023, doi: 10.1016/j.est.2023.108418.
[24] W. Yang, F. Zhou, H. Zhou, Q. Wang, and J. Kong, “Thermal performance of cylindrical lithium-ion battery thermal management system integrated with mini-channel liquid cooling and air cooling,” *Applied Thermal Engineering*, vol. 175, p. 115331, Jul. 2020, doi: 10.1016/j.applthermaleng.2020.115331.
[25] M. Li, F. Liu, B. Han, J. Guo, and Y. Xu, “Research on temperature control performance of battery thermal management system composited with multi-channel parallel liquid cooling and air cooling,” *Ionics*, vol. 27, no. 6, pp. 2685–2695, Jun. 2021, doi: 10.1007/s11581-021-04033-w.
[26] S. Xin, C. Wang, and H. Xi, “Thermal management scheme and optimization of cylindrical lithium-ion battery pack based on air cooling and liquid cooling,” *Applied Thermal Engineering*, vol. 224, p. 120100, Apr. 2023, doi: 10.1016/j.applthermaleng.2023.120100.
[27] H. Zhou, J. Niu, X. Guo, L. Xu, Z. Song, and X. Yin, “Thermal performance of a hybrid thermal management system based on the half helical coil coupled with air jet cooling for cylindrical Lithium-ion battery,” *Applied Thermal Engineering*, vol. 225, p. 120231, May 2023, doi: 10.1016/j.applthermaleng.2023.120231.
[28] Z. Ling, F. Wang, X. Fang, X. Gao, and Z. Zhang, “A hybrid thermal management system for lithium ion batteries combining phase change materials with forced-air cooling,” *Applied Energy*, vol. 148, pp. 403–409, Jun. 2015, doi: 10.1016/j.apenergy.2015.03.080.
[29] M. W. Nazar, N. Iqbal, M. Ali, H. Nazir, and M. Z. B. Amjad, “Thermal management of Li-ion battery by using active and passive cooling method,” *Journal of Energy Storage*, vol. 61, p. 106800, May 2023, doi: 10.1016/j.est.2023.106800.
[30] Y. S. Ranjbaran, M. H. Shojaeefard, and G. R. Molaeimanesh, “Thermal performance enhancement of a passive battery thermal management system based on phase change material using cold air passageways for lithium batteries,” *Journal of Energy Storage*, vol. 68, p. 107744, Sep. 2023, doi: 10.1016/j.est.2023.107744.
[31] L. Feng, S. Zhou, Y. Li, Y. Wang, and Q. Zhao, “Experimental investigation of thermal and strain management for lithium-ion battery pack in heat pipe cooling,” *Journal of Energy Storage*, vol. 16, pp. 84–92, Apr. 2018, doi: 10.1016/j.est.2018.01.001.
[32] H. Behi, D. Karimi, M. Behi, J. Jaguemont, and M. Ghanbarpour,“Thermal management analysis using heat pipe in the high current discharging of lithium-ion battery in electric vehicles,” *Journal of Energy Storage*, vol. 32, p. 101893, Dec. 2020, doi: 10.1016/j.est.2020.101893.
[33] H. Behi, T. Kalogiannis, M. Suresh Patil, J. V. Mierlo, and M. Berecibar, “A New Concept of Air Cooling and Heat Pipe for Electric Vehicles in Fast Discharging,” *Energies*, vol. 14, no. 20, p. 6477, Oct. 2021, doi: 10.3390/en14206477.
[34] H. Behi, M. Behi, D. Karimi, J. Jaguemont, and M. Ghanbarpour, “Heat pipe air-cooled thermal management system for lithium-ion batteries: High power applications,” *Applied Thermal Engineering*, vol. 183, p. 116240, Jan. 2021, doi: 10.1016/j.applthermaleng.2020.116240.
[35] W. Wu, X. Yang, G. Zhang, K. Chen, and S. Wang, “Experimental investigation on the thermal performance of heat pipe-assisted phase change material based battery thermal management system,” *Energy Conversion and Management*, vol. 138, pp. 486–492, Apr. 2017, doi: 10.1016/j.enconman.2017.02.022.
[36] W. N. Septiadi, M. Alim, and M. N. P. Adi, “The application of battery thermal management system based on heat pipes and phase change materials in the electric bike,” *Journal of Energy Storage*, vol. 56, p. 106014, Dec. 2022, doi: 10.1016/j.est.2022.106014.

The 13th TSME International Conference on Mechanical Engineering
12th – 15th December 2023
Chiang Mai, Thailand

TSF0033

Enhanced Grid Generation Method with artificial intelligent for Accurate Tracking of Nanoparticles Using Birth/Death Cells Around Spherical Particles

Mehrdad Mesgarpour[1,2], Somchai Wongwises[1,3], Abdellah Hadjadj[4], Alias Jedi[5,6], Leyla Amiri[7], and Mostafa Safdari Shadloo[4,8,*]

[1]Fluid Mechanics, Thermal Engineering and Multiphase Flow Research Lab. (FUTURE), Department of Mechanical Engineering, Faculty of Engineering, King Mongkut's University of Technology Thonburi, Bangmod, Bangkok 10140, Thailand
[2]Malardalen University, Hogskoleplan 1, 72220 Vasteras, Sweden
[3]National Science and Technology Development Agency (NSTDA), Pathum Thani 12120, Thailand
[4]CORIA-UMR 6614, CNRS-University & INSA, Normandie University, 76000, Rouen, France
[5]Universiti Kebangsaan Malaysia, Dept of Mechanical and Manufacturing Engineering, Selangor, Malaysia
[6]Universiti Kebangsaan Malaysia, Centre for Automotive Research (CAR), Selangor, Malaysia
[7]Mechanical Engineering Department, Université de Sherbrooke, Sherbrooke, QC J1K 2R1, Canada
[8]Institut Universitaire de France, Rue Descartes, F-75231 Paris, France

* Corresponding Author: msshadloo@coria.fr

Abstract. Particle-fluid systems often face computational bottlenecks when regenerating grids for accurate particle tracing, especially when dealing with smaller particle sizes. In this study, we propose a novel grid generation method that integrates artificial intelligence techniques to enhance the efficiency and accuracy of grid regeneration based on the movement and position of particles over time. The method utilizes birth/death cells surrounding the particles within a Cartesian coordinate system. In this approach, the grid generated will be eliminated once a particle has passed a specific position, and cluster grids will be generated at the particle's front to reduce the computational load. A simulation is conducted in a square cross-section channel with laminar flow (Re = 50), consisting of 100 spherical nanoparticles with a diameter of 10 nm. The primary grid generation method focused on generating grids within a reference cube measuring 50 x 50 x 50 nm around each particle. In the current study, we employ a recurrent neural network approach to forecast particle positions and trajectory paths at each time step throughout the duration of the study. By identifying interaction points and predicting the path lines, the secondary grid generation loops efficiently generated cells in front of the particles while removing passed cells, thereby reducing computational costs and calculation load. The results of the study demonstrate that the proposed method significantly improves the accuracy and reduces the computational cost of grid generation in particle-fluid flows. The results indicate that including the ML method in the grid generation could reduce the grid generation time by up to 24% compared to the standard grid generation method. By integrating artificial intelligence techniques, the enhanced grid generation method enables precise tracking of nanoparticles, overcoming the challenges associated with smaller particle sizes.

Keywords: Grid generation method, birth/death cell method, computational fluid dynamics (CFD), artificial neural networks (ANN).

1. Introduction

Computational Fluid Dynamics (CFD) is a powerful tool used to analyse and simulate fluid flow in various engineering and scientific applications. From designing aircraft and cars to optimizing industrial processes and predicting weather patterns, CFD plays a vital role in solving complex fluid dynamics problems[1]. A well-structured and refined grid can capture fine details of the flow, such as boundary layers, vortices, and shocks, which are critical in many engineering applications. On the other hand, a coarse grid may overlook important features, leading to inaccurate results and potentially compromising the overall analysis.

The grid quality significantly effects CFD solver performance, impacting convergence and stability. A poorly generated grid leads to convergence difficulties and unstable simulations. An overly refined grid can improve accuracy but increases computational costs. Grid generation involves finding the right balance between accuracy and computational efficiency. Optimal grid design can reduce the computational time required to obtain accurate results. In many cases, solid particle positions and interactions with the fluid change over time in multiphase flow.

Nianhua et al. [2] provided a concise overview of the utilization of machine learning in the realm of unstructured mesh generation for CFD. They delve into an analysis of critical challenges inherent in mesh generation when leveraging machine learning techniques. Simultaneously, they introduce a structured approach to data handling, facilitating the automated extraction of unstructured mesh sample datasets. Furthermore, the research team introduces an innovative methodology that combines the Advancing Front (AFT) technique with artificial neural networks (ANN). This fusion results in the development of a novel two-dimensional triangular grid generation method that is grounded in machine learning principles. This advancement holds promise for more efficient and precise mesh generation in CFD simulations.

Huang and et al. [3] initially relied on goal-oriented adaptive mesh refinement to seek optimal meshes. Nevertheless, this approach is often computationally intensive and restricted to a limited set of software tools. In their research contribution, they pivot toward a machine-learning-based strategy to discern optimal mesh densities. Their methodology entails the generation of optimized meshes through traditional techniques, coupled with the development of a convolutional neural network. This neural network is designed to predict optimal mesh densities for diverse geometries.

Zhang and et al. [4] introduce an innovative approach to automated unstructured mesh generation, leveraging machine learning to predict an optimal finite element mesh for a new, previously unencountered problem. Their framework centre's around the training of an ANN to guide conventional mesh generation software by predicting the necessary local mesh density across the entire domain. The methodology they propose involves a training regimen based on a posteriori error estimation.

In this current study, we introduce an innovative approach aimed at reducing computational costs and improving the accuracy of grid generation for small particles, employing machine learning techniques. Our methodology involves training a neural network using the trajectory data of each particle over time. To achieve this goal, we are developing a recurrent neural network (RNN) specifically tailored for predicting the grid domain surrounding each particle in its new position. This prediction is made based on various particle parameters, including velocity, position, and trajectory line. By leveraging the RNN's capacity to capture temporal dependencies in the data, we anticipate achieving more efficient and precise grid generation for small particles. This novel method holds great promise for enhancing the computational efficiency and accuracy of simulations involving small particles within fluid dynamics or other fields where precise grid generation is crucial.

2. Methodology and problem statement

In the CFD, a trajectory line refers to the path that a particle or fluid element follows within a flow field over a certain period of time. It's essentially a continuous curve or line that traces the movement of a specific point in the fluid as it moves through the domain. Trajectory lines are used to visualize and analyse the behaviour of particles or fluid elements in a flow, helping to understand aspects like particle dispersion, mixing, and transport. To update the conventional grid generation approach, we are employing machine learning methods in the context of simulating laminar flow with a Reynolds Number (Re) of 50 within a tube with a pure water as a base containing 100 spherical nanoparticles with a diameter of 10 nm. Specifically, this study incorporates 1% Al_2O_3 nanoparticles into pure water, as shown in Figure 1. The focus of this work is to enhance the grid generation process within the fluid domain surrounding the particle. The methodology for this grid generation has been comprehensively outlined in a prior publication. In this approach, the trajectory of the particle is a crucial aspect. It serves as the path that the particle follows throughout its motion. These trajectory details are stored in a dedicated matrix. Simultaneously, particle-specific parameters, such as velocity, are recorded in a separate matrix. The trajectory matrix contains a comprehensive record of the trajectory vectors at each time step, providing valuable insights into the particle's movement within the fluid.

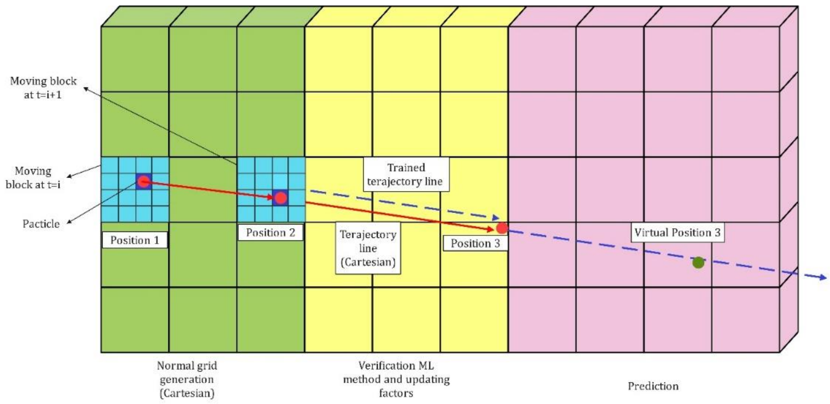

Figure 1. Incorporation of 1% Al2O3 Nanoparticles into Pure Water.

To save the trajectory line at each time step, position data (coordinates) of particles or fluid elements must be stored at that time step. This can be done by creating and updating a data structure, such as an array or a matrix, to store the trajectory information. The following code shows the trajectory saving method.

```
# Initialize variables
time_steps = N  # Number of time steps
particle_count = M  # Number of particles
# Create data structures to store trajectory data
trajectory_data = []
# Start time-stepping loop
for time_step in range(time_steps):
```

```
    # Calculate new positions of particles based on the fluid flow
    for particle in range(particle_count):
        # Calculate new position of particle based on velocity field
        new_position = calculate_new_position(particle)
            # Append the new position to the trajectory data
        trajectory_data[particle].append(new_position)
# Now, trajectory_data contains the trajectory of each particle at each time step
```

2.1. Grid Generation

Desecrating the computational field can be performed directly in physical space or in a transferred computational space. Its choice also depends on the numerical method employed and the geometry of the problem. If the network nodes are located at the intersection of lines, parallel and equidistantly spaced in a two-dimensional rectangular field or a three-dimensional cubic field, and the network points can be easily numbered, this type of network is called an organized network. In general, in an unorganized network, each network point is surrounded by a constant number of cells, and the number of cells around each point can be variable. Each polygon is considered as a "Tile" associated with a generating point. Each polygon or region around a point (center) includes an area that is closer to that point than any other point. In essence, Voronoi diagrams are a powerful geometric tool used to partition a space into regions based on the closest point from a given set of points. There are various methods for generating a Watson-type mesh [5], but they all produce the same Delaunay triangulation because the Delaunay triangulation generated by this method is unique. One of the properties of this method is that its data structure is based on cells, where each cell introduces three vertices of a triangle and three neighbouring triangles. The core of nanoparticle grid generation is presented in [6].

The trajectory of the particle can then be plotted by tracking its position over time. The trajectory can be used to study the motion of particles in fluid flows, such as the motion of pollutants in the atmosphere or the motion of droplets in a spray. Adaptive grid generation in CFD is a technique used to dynamically refine or coarsen the grid in specific regions of the simulation domain based on the solution's local characteristics. Fig 2 shows the results of following code on the case study boundary condition.

```
from fenics import *
# Define the mesh and function space
mesh = RectangleMesh(Point(0, 0), Point(1, 1), N, N)
V = FunctionSpace(mesh, 'P', 1)
# Define the solution variable
u = Function(V)
# Define the initial grid refinement level
refinement_level = 0
# Define the threshold for gradient-based refinement
gradient_threshold = 0.5 # 0.5 as sample
# Perform adaptive grid refinement loop
for i in range(5):  # 5 refinement steps
    # Solve the PDE with the current grid
    solve(pde, u)
        # Calculate the gradient of the solution
    gradient = project(grad(u), VectorFunctionSpace(mesh, 'P', 1))
        # Determine cells to refine based on gradient
    refine_cells = MeshFunction('bool', mesh, mesh.topology().dim())
    refine_cells.set_all(False)
        for cell in cells(mesh):
        if cell.hmax() > 0.1 and gradient(cell.midpoint()).norm() > gradient_threshold:
            refine_cells[cell] = True
        # Refine the mesh based on the criterion
```

```
    mesh = refine(mesh, refine_cells)
       # Update the function space
    V = FunctionSpace(mesh, 'P', 1)
       # Update the solution function
    u = Function(V)
       # Increase the refinement level
    refinement_level += 1
# Final solution after adaptive grid refinement
```

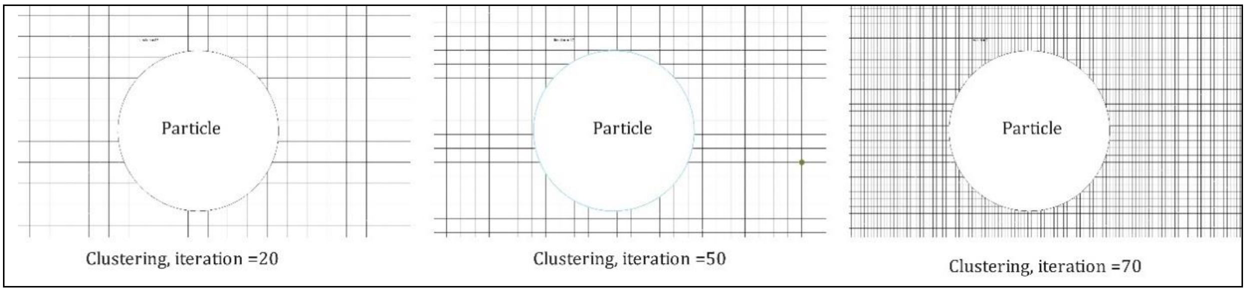

Figure 2. Creating a fine-grained structure around the block, encompassing spherical particles, involves three clustering iterations.

2.2. Recurrent neural network

Unlike feedforward neural networks, which process data in a single pass through the network, RNNs use the output from the previous step as input to the current step. This makes RNNs well-suited for tasks that involve sequences of data, such as language modelling, speech recognition, and time-series prediction. The basic building block of an RNN is the recurrent unit, which takes the current data point and the previous internal state as input, producing an output and an updated internal state. The output of each unit is then fed back into the next unit as input, allowing the network to maintain a memory of previous inputs. One of the challenges with RNNs is that the gradients can either vanish or explode over time, which can make it difficult to train the network effectively. To address this issue, several variants of RNNs have been developed, including Long Short-Term Memory (LSTM) networks and Gated Recurrent Units (GRUs) . These networks use specialized units that can selectively remember or forget information, making them more effective at processing long-term dependencies.

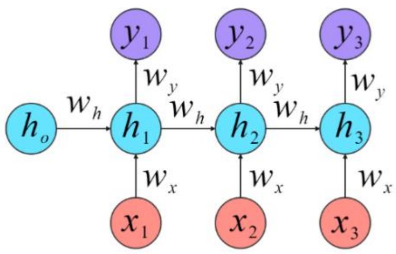

Figure 3. Graphical illustration of RNN model.

The most commonly used cost function for RNNs is Cross-entropy loss, which measures the difference between the predicted output and the true output. However, other cost functions can be used, depending on the specific problem being solved by the RNN. Overall, the cost of an RNN depends on several factors, including its size and complexity, the number of time steps being used during training, the algorithm used to train the network, and the cost function used to optimize it.

3. Governing equations

The mathematical model includes the conservation equations in the Eulerian framework for any m^* fluid, expressed by:

$$\frac{\partial(\alpha^{m^*}\rho^{m^*})}{\partial t}+\frac{\partial(\alpha^{m^*}\rho^{m^*}u^{m^*})}{\partial x}+\frac{\partial(\alpha^{m^*}\rho^{m^*}v^{m^*})}{\partial y}+\frac{\partial(\alpha^{m^*}\rho^{m^*}w^{m^*})}{\partial z}=S^{int}_{m^{m^*}} \quad (1)$$

Balance of momentum in *x, y* and *z* directions

$$\frac{\partial(\alpha^{m^*}\rho^{m^*}u^{m^*})}{\partial t}+\frac{\partial(\alpha^{m^*}\rho^{m^*}u^{m^*}u^{m^*})}{\partial x}+\frac{\partial(\alpha^{m^*}\rho^{m^*}v^{m^*}u^{m^*})}{\partial y}+\frac{\partial(\alpha^{m^*}\rho^{m^*}w^{m^*}u^{m^*})}{\partial z}=\frac{\partial}{\partial x}\left[\alpha^{m^*}(\mu^{m^*}+\mu_T^{m^*})\frac{\partial u^{m^*}}{\partial x}\right]+ \frac{\partial}{\partial y}\left[\alpha^{m^*}(\mu^{m^*}+\mu_T^{m^*})\frac{\partial u^{m^*}}{\partial y}\right]+\frac{\partial}{\partial z}\left[\alpha^{m^*}(\mu^{m^*}+\mu_T^{m^*})\frac{\partial u^{m^*}}{\partial z}\right]+S^{m^*}_{u^{m^*}} \quad (2)$$

$$\frac{\partial(\alpha^{m^*}\rho^{m^*}v^{m^*})}{\partial t}+\frac{\partial(\alpha^{m^*}\rho^{m^*}u^{m^*}v^{m^*})}{\partial x}+\frac{\partial(\alpha^{m^*}\rho^{m^*}v^{m^*}v^{m^*})}{\partial y}+\frac{\partial(\alpha^{m^*}\rho^{m^*}w^{m^*}v^{m^*})}{\partial z}=\frac{\partial}{\partial x}\left[\alpha^{m^*}(\mu^{m^*}+\mu_T^{m^*})\frac{\partial v^{m^*}}{\partial x}\right]+ \frac{\partial}{\partial y}\left[\alpha^{m^*}(\mu^{m^*}+\mu_T^{m^*})\frac{\partial v^{m^*}}{\partial y}\right]+\frac{\partial}{\partial z}\left[\alpha^{m^*}(\mu^{m^*}+\mu_T^{m^*})\frac{\partial v^{m^*}}{\partial z}\right]+S^{m^*}_{v^{m^*}} \quad (3)$$

$$\frac{\partial(\alpha^{m^*}\rho^{m^*}w^{m^*})}{\partial t}+\frac{\partial(\alpha^{m^*}\rho^{m^*}u^{m^*}w^{m^*})}{\partial x}+\frac{\partial(\alpha^{m^*}\rho^{m^*}v^{m^*}w^{m^*})}{\partial y}+\frac{\partial(\alpha^{m^*}\rho^{m^*}w^{m^*}w^{m^*})}{\partial z}=\frac{\partial}{\partial x}\left[\alpha^{m^*}(\mu^{m^*}+\mu_T^{m^*})\frac{\partial w^{m^*}}{\partial x}\right]+ \frac{\partial}{\partial y}\left[\alpha^{m^*}(\mu^{m^*}+\mu_T^{m^*})\frac{\partial w^{m^*}}{\partial y}\right]+\frac{\partial}{\partial z}\left[\alpha^{m^*}(\mu^{m^*}+\mu_T^{m^*})\frac{\partial w^{m^*}}{\partial z}\right]+S^{m^*}_{w^{m^*}} \quad (4)$$

The energy conservation equation for the mixture model in multiphase flow is expressed as follows [7]:

$$\frac{\partial(\rho^m H^m)}{\partial t}+\nabla.(\rho^m U^m w^m)=\nabla.(\lambda^m\Delta T^m)-\nabla.q_H^{\dot{m}}+\zeta-\nabla.\Sigma_{m^*=1}^{2}(\alpha^{m^*}\rho^{m^*}U^{dr,m^*}H^{m^*}) \quad (5)$$

$$\rho^m=\sum_{m^*=1}^{2}(\alpha^{m^*}\rho^{m^*}) \quad (6)$$

$$\lambda^m=\sum_{m^*=1}^{2}(\alpha^{m^*}\lambda^{m^*}) \quad (7)$$

3.1 Recurrent neural network

In the core of an RNN is the recurrent layer, which maintains a hidden state vector that is updated at each time step based on the current input and the previous hidden state. These equations can be written as:

$$h^t = f(W_x h_{xt} + W_{hht-1} + b_h) \quad (8)$$
$$y^t = g(W_h y_{ht} + b_y) \quad (9)$$

where h^t is the hidden state vector at time *t*, *xt* is the input vector at time *t*, y^t is the output vector at time *t*, *f* and g are non-linear activation functions, W_xh, W_{hh}, W_{hy}, b_h, and by are weight matrices and bias vectors that are learned during training. To train an RNN, we use a technique called backpropagation through time (BPTT), which involves computing the gradient of the loss function with respect to the network parameters at each time step and using gradient descent to update the parameters. The BPTT algorithm involves unfolding the recurrent layer into a feedforward network and applying the regular backpropagation algorithm to compute the gradients. The code then generates a hybrid training dataset consisting of random data and labels, with 80% of the samples used for training and 20% used for testing. The data is represented as a tensor of shape (num_samples, num_timesteps, 1) and the labels are integers in the range [0, num_classes). Finally, the model is trained on the training data for 10 epochs using a batch size of 32, and the testing set is used for validation.

4. Verification

A verification study in grid generation refers to the accuracy of results and mesh quality. In the present study, the results of simulation and grid generation are compared with the Soma et al. [8].

Table 1. A comparison between the results of present study and Soma et al. [8] in different number of grids.

Case	Number of grids	CFD results	Soma et al. [8]
1	15,639	1.141	1.214
2	18,966	1.186	
3	25,361	1.211	
4	37,714	1.211	

In the present study, the number of neurons and the required sample for training (number of generated grids) are also evaluated.

Table 2. Neuron sensetivity analysis.

Number of neurons	Number of samples	R^2	Maximum error with Soma et al. [8] for Nusselt number (%)
8	8,366	0.241	74
	9,955	0.362	56
	12,366	0.842	21
	25,361	0.863	18
9	8,366	0.147	96
	9,955	0.569	32
	12,366	0.959	15
	25,361	0.963	13
10	8,366	0.211	76
	9,955	0.478	37
	12,366	0.948	16
	25,361	0.963	13

5. Result and discussion

Grid generation is a critical but often time-consuming step in computational modeling. In Figure 4, a comparison is presented between a novel grid generation method and the traditional approach for generating fine grids. The results clearly demonstrate the advantages of the novel method, showcasing a remarkable 17% reduction in computational time when compared to the conventional method. This improvement in grid generation efficiency is of substantial significance in the realm of computational modeling. By significantly reducing the time required to create finely detailed grids, the novel method not only expedites the modeling process but also contributes to overall computational cost savings.

The accuracy of our prediction model is intricately tied to the effectiveness of the primary grid generation system. The quality of our predictions is notably influenced by various factors, including particle-particle interactions and fluctuations in fluid properties. At the commencement of our simulation, the particle distribution is relatively uniform, resulting in each particle having an initial trajectory matrix filled with zero values.

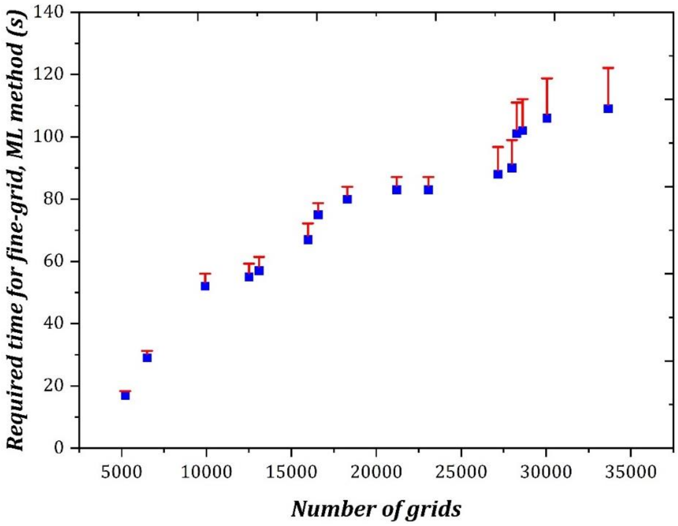

Figure 4. The impact of the grid generation method on creating a fine-grid.

Additional insights into this aspect are presented in Table 3. Our findings reveal that extending the training time step for the machine learning model can significantly diminish prediction errors. Furthermore, the number of training instances plays a pivotal role in fine-tuning the accuracy of simulation. The results indicated that, including ML method in the grid generation could reduce the grid generation time up to 24% in comparison standard grid generation method.

Table 3. Accuracy of prediction based on training time step and number of training data set.

Training time step (s)	Number of training data	Share of training to test (%)	ML training + prediction time (s)	Error (%)
2	8,963	85	25	51
	12,366		39	25
	21,699		61	16
4	14,632	84	42	41
	19,638		57	14
	24,969		64	12
5	17,204	85	55	25
	23,633		62	13
	28,041		71	10

Figure 5 presents a comparative analysis of ML and conventional methods for predicting particle positions and velocities. The results underscore a noteworthy trend: ML methods demonstrate initial accuracy in predicting particle positions and velocities, which gradually diminishes over time. This decline in accuracy can be attributed to the inherent stochastic nature of particle behavior and the limited information available during the training process, especially regarding particle velocities. In the realm of fluid dynamics, particle-particle interactions play a pivotal role.

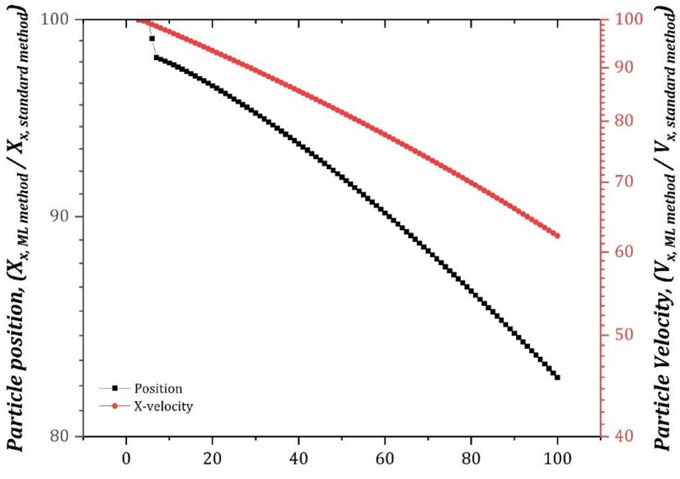

Figure 5. A comparison between dimensionless particle position in X direction and particle velocity over time.

The number of grids in a computational simulation has a significant impact on the computational cost, particularly in terms of both computational time and memory usage. This impact can vary depending on the type of simulation, the complexity of the problem, and the available computational resources. Increasing the number of grids typically leads to higher spatial resolution in the simulation. This means that you can capture finer details and variations in the physical phenomena being modelled. The demonstrated capability of ML across a wide range of grid densities further underscores its potential as a valuable tool in computational modelling and analysis.

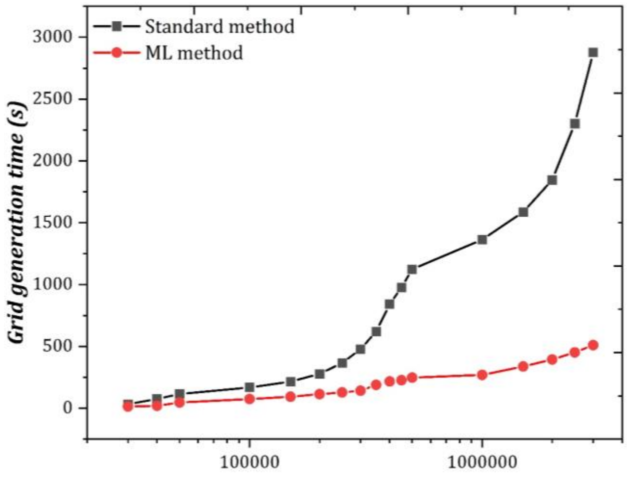

Figure 6. Performance of ML method compared to standard method for high resolution case study.

6. Conclusion

Grid generation is a pivotal phase in computational methods, and this study introduces an innovative approach by incorporating machine learning to streamline the computational cost. Specifically, this novel grid generation method is tailored for nanoparticle simulations. In the context of laminar flow with a Re of 50, the study involves a 1% volume fraction of Al_2O_3 nanoparticles dispersed in a pure fluid. The method employed here entails a two-step grid generation process in the forward direction for simulation purposes. During this process, grid networks are meticulously crafted, and particle trajectory data is concurrently stored in distinct matrices. This approach allows for a more efficient and accurate representation of the computational domain and the behaviour of nanoparticles within the fluid flow. By combining traditional grid generation techniques with machine learning, this study aims to significantly reduce the computational resources required for simulating complex fluid-particle interactions. The results indicated that:

1- The findings from this comparison reveal that ML approaches can substantially decrease the time needed for grid generation in simulations. Moreover, the results demonstrate that ML methods exhibit notable proficiency, even when dealing with a large number of grids in the simulation. This advancement in grid generation efficiency, as facilitated by ML, has far-reaching implications for computational simulations, enabling accelerated model setup and reducing the computational burden associated with generating complex grids.
2- The results indicate that including the ML method in the grid generation could reduce the grid generation time by up to 24% compared to the standard grid generation method.
3- The results clearly demonstrate the advantages of the novel proposed method, showcasing a remarkable 17% reduction in computational time compared to the conventional method. This improvement in grid generation efficiency is of substantial significance in the realm of computational modeling.

7. Acknowledgments

This work was conducted within the framework of ESP Carnot Institute (Energy and Propulsion Systems). The authors would like to express their gratitude and thanks to Malaysia-France Bilateral Collaboration (MATCH) research grant for funding this research under code MATCH-2021-001.

8. References

[1] Einarsrud, K.E., V. Loomba, and J.E. Olsen, *Applied Computational Fluid Dynamics (CFD)*. 2023, MDPI. p. 461.

[2] Nianhua, W., L. Peng, C. Xinghua, and Z. Laiping, *Preliminary investigation on unstructured mesh generation technique based on advancing front method and machine learning methods.* 力学学报, 2021. **53**(3): p. 740-751.

[3] Huang, K., M. Krügener, A. Brown, F. Menhorn, H.-J. Bungartz, and D. Hartmann, *Machine learning-based optimal mesh generation in computational fluid dynamics.* arXiv preprint arXiv:2102.12923, 2021.

[4] Zhang, Z., Y. Wang, P.K. Jimack, and H. Wang. *MeshingNet: A new mesh generation method based on deep learning*. in *International Conference on Computational Science*. 2020. Springer.

[5] Rebay, S., *Efficient unstructured mesh generation by means of Delaunay triangulation and Bowyer-Watson algorithm.* Journal of Computational Physics, 1993. **106**(1): p. 125-138.

[6] Mesgarpour, M., O. Mahian, P. Zhang, S. Wongwises, L.-P. Wang, G. Ahmadi, S. Nižetić, M. Sheremet, and M.S. Shadloo, *A hybrid deep learning-CFD approach for modeling nanoparticles' sedimentation processes for possible application in clean energy systems.* Journal of Cleaner Production, 2023. **399**: p. 136532.

[7] Yeoh, G.H. and J. Tu, *Computational techniques for multiphase flows*. 2019: Butterworth-Heinemann.

[8] Soma, N.A. and L.R. Jarif, *CFD analysis of laminar Heat Transfer in a Plane Backward Facing Step Using Nanofluid.* 2019.

EDU0001

The Use of DWSIM to Analyze and Optimize Steam Cycles

S Chantasiriwan[1,*] and S Charoenvai[2]

[1]Faculty of Engineering, Thammasat School of Engineering, Thammasat University, Rangsit Campus, Pathum Thani, 12121, Thailand
[2]No affiliation

*Corresponding Author: somchart@engr.tu.ac.th

Abstract. Traditionally, mechanical engineering students learn engineering cycles through manual or semi-manual calculations. There are downsides of this type of learning. An analysis of an engineering cycle requires material properties and balances of mass and energy. The determination of material properties using charts and tables may be time consuming. The derivation of mass and energy balances is prone to errors. More importantly, sensitivity and optimization analyses are too tedious if calculations are performed manually. It is suggested in this article that a process simulator should be used for the purpose of engineering education on steam cycles. Replacing manual calculations with computerized process simulations will enable students to have more time to learn about detailed analyses, and prepare students better for engineering jobs, in which computerized process simulators are invariably used. The process simulator recommended in this article is DWSIM, which is available at no cost. Examples of using DWSIM to analyse and optimize some steam cycles are provided in this article.

Keywords: Engineering education, Thermodynamics, Rankine cycle, Steam power plant, Optimization.

1. Introduction

In mechanical engineering education, the comprehension of engineering cycles has long been expected to be gained through manual or semi-manual calculations. Inspection of textbooks on engineering thermodynamics [1 - 4] confirms the above statement. This conventional approach may present several limitations that hinder students from achieving a comprehensive understanding of engineering cycles. The analysis of engineering cycles requires consideration of material properties, mass balance, and energy balance. However, using charts and tables for determining material properties is time consuming. In addition, the derivation of mass and energy balances is sometimes accompanied by the specter of human errors. A glaring issue arises when students delve into sensitivity and optimization analyses because manual or semi-manual calculations become unreasonably laborious. Acknowledging these challenges, it becomes evident that a paradigm shift is needed in mechanical engineering education – a shift towards harnessing the capabilities of computerized process simulations.

This article advocates for the incorporation of process simulators to elevate the pedagogical approach to understanding steam cycles. By replacing time-consuming manual calculations with the precision and efficiency of computerized simulations, students can dedicate more time to in-depth analyses and immersive learning experiences. Furthermore, such a transformation aligns seamlessly with the demands of the modern engineering landscape, where proficiency in utilizing computerized process simulators is a paramount skill. This approach has been a subject of considerable interest. Affandia et al. [5] developed a program written in MATLAB to assist the teaching of Rankine cycle. Gourde and Akih-Kumgeh [6] presented a MATLAB program with graphical user interface that could be used to determine thermodynamic properties of steam. Dumka et al. [7] developed Python models of air standard cycles. Aulicino and Bakrania [8] designed a Python-based lab activity for the parametric analysis of power and refrigeration cycles. Dominguez et al. [9] used MATLAB applications as tools for teaching thermodynamic cycles.

Although there are several commercial process simulators that may be used for this purpose, an open-source process simulator is recommended in this paper. Two open-source chemical process simulators have become popular in recent years: COCO (https://www.cocosimulator.org/) and DWSIM (https://dwsim.org/). Advantages of DWSIM include its capability to model more processes, its GUI superiority, and its more user-friendliness. Comparison between simulation results of DWSIM have been shown to be comparable with those of commercial process simulators [10, 11]. Furthermore, DWSIM has increasingly been used as a research tool [12 - 17]. It may be expected that DWSIM will gain more acceptance by the research community and the industry in the future. Therefore, it is appropriate to familiarize students with DWSIM.

It is an objective of this paper to demonstrate how DWSIM can help improve the teaching and learning of steam cycles. The following sections describe three typical steam cycles taught in mechanical engineering courses, explain the use of DWSIM to model these cycles, and show how sensitivity and optimization analyses can be performed using DWSIM.

2. Steam Cycles

Figure 1 shows three steam cycles. Basic Rankine cycle in Figure 1(a) consists of 4 processes: liquid pressure increase (1-2), heat addition (2-3), steam expansion (3-4), and heat rejection (4-1). An improved steam cycle is Rankine cycle with reheating in Figure 1(b). Steam expansion is divided into two processes (3-4 and 5-6). In addition, reheating process (4-5) is added. Another improved steam cycle is Rankine cycle with regeneration shown in Figure 1(c). Like Rankine cycle with reheating, there are also two steam expansion processes in this cycle. However, the steam flow rates in the two steam expansion processes are unequal. The steam flow rate is m_s in the 5-6 process. Steam is extracted from the steam turbine after the 5-6 process. The mass flow rate of extracted steam is ym_s so that the steam flow rate in the 6-7 process is $(1 - y)m_s$. Extracted steam is mixed with feed water in open feed water heater (OFH) in Figure 1(c) before heated feed water is sent to the boiler. Two pumps are used in Rankine cycle with regeneration. The first pump, located next to the condenser, increases water pressure from p_1 to p_2. The second pump, located next to the boiler, increases water pressure from p_3 to p_4.

The primary goal of an analysis of a steam cycle is to determine the net work output and the thermal efficiency. Knowledge of pump and turbine efficiencies is needed for this purpose. Details of analyses of the three cycles shown in Figure 1 are described in engineering thermodynamics textbooks [1 - 4]. Results of the analyses are summarized in Table 1.

3. DWSIM Models

DWSIM v.8.5.1 (released on 24 July 2023) is used in this paper. The first step in constructing DWSIM model of a steam cycle is selecting water as the working fluid in the model. Next, Steam Tables (IAPWS-IF97) is selected as the thermodynamics of water. This section provides steps of constructing and simulating the three steam cycles shown in Figure 1. It should be noted that although newer versions of DWSIM will be available in the future, simulation procedures described in this paper are expected to remain unchanged.

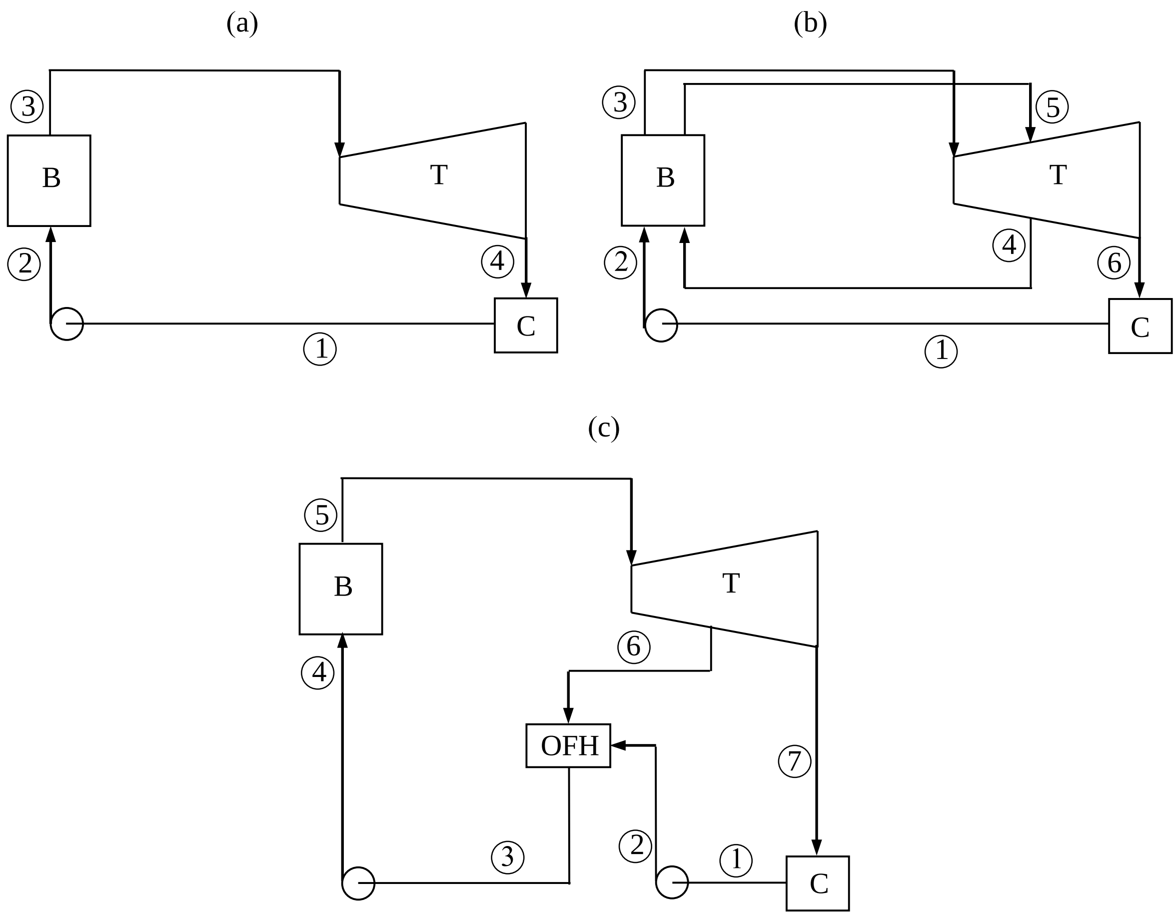

Figure 1. (a) Basic Rankine cycle, (b) Rankine cycle with reheating, and (c) Rankine cycle with regeneration.

Table 1. Network outputs (w_{net}) and thermal efficiencies (η_{th}) of steam cycles.

Steam cycle	w_{net}	η_{th}
Basic Rankine cycle	$h_3 - h_4 - h_2 + h_1$	$1 - \frac{h_4 - h_1}{h_3 - h_2}$
Rankine cycle with reheating	$h_3 - h_4 + h_5 - h_6 - h_2 + h_1$	$1 - \frac{h_6 - h_1}{h_3 - h_2 + h_5 - h_4}$
Rankine cycle with regeneration	$h_5 - h_6 - h_4 + h_3 + (1-y)(h_6 - h_7 - h_2 + h_1)$	$1 - \frac{(1-y)(h_7 - h_1)}{h_5 - h_4}$

A flowsheet of basic Rankine cycle is shown in Figure 2. Names of system components are default names provided by DWSIM. Pump is represented by PUMP-1. Material stream 1 is the input of PUMP-1, material stream 2 is the output, and E1 is the energy stream. Boiler is represented by HT-1. Material stream 2 is the input of HT-1, material stream 3 is the output, and E2 is the energy stream. Steam turbine is represented by X-1. Material stream 3 is the input of X-1, material stream 4 is the output, and E3 is the energy stream. Condenser is represented by CL-1. Material stream 4 is the input of CL-1, material stream 1′ is the output, and E4 is the energy stream. It should be noted that material stream 1 cannot be the output of CL-1 because DWSIM performs calculations in the forward direction. This means that properties of material stream 1 must be specified, and properties of material stream 1′ must be calculated. Initially, the resulting cycle appears to be an open cycle. A tool in DWSIM to convert in to a closed cycle is Recycle Block (R-1). The input of R-1 is material stream 1′, and the output is material stream 1.

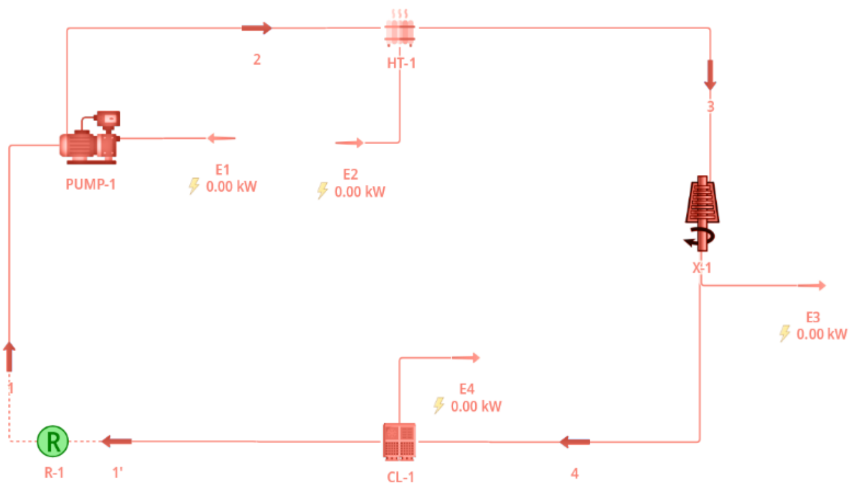

Figure 2. DWSIM flowsheet of basic Rankine cycle before simulation.

In order to simulate basic Rankine cycle in DWSIM, values of parameters are required as inputs. A procedure for the simulation consists of the following steps.

- Open the window of material stream 1.
- Select “Pressure and Vapor Fraction (PVF)” for Flash Spec.
- Specify 10 kPa for pressure, 1.0 kg/s for mass flow rate, and 0 for vapor phase mole fraction.
- Close the window.
- Open the window of PUMP-1.
- Select “Outlet Pressure” for Calculation Type.
- Specify 10 MPa for pressure and 80% for efficiency.
- Close the window.
- Open the window of HT-1.
- Select “Outlet Temperature” for Calculation Type.
- Specify 0 Pa for pressure drop, 100% for efficiency, and 500°C for outlet temperature.
- Close the window.
- Open the window of X-1.
- Select “Outlet Pressure” for Calculation Type.
- Specify 10 kPa for pressure and 85% for efficiency.
- Close the window.
- Open the window of CL-1.
- Select “Outlet Vapor Mole Fraction” for Calculation Type.
- Specify 0 Pa for pressure drop, 100% for efficiency, and 0 for outlet vapor fraction.
- Close the window.

Figure 3 shows the flowsheet of basic Rankine cycle after all required input parameters are specified. Since the mass flow rate is 1 kg/s, power equals specific work, and heat transfer rate equals specific heat transfer. It can be seen that the net work output for this cycle is 1079.99 kJ/kg, and the specific heat input is 3170.63 kJ/kg. Therefore, the thermal efficiency is 34.06%.

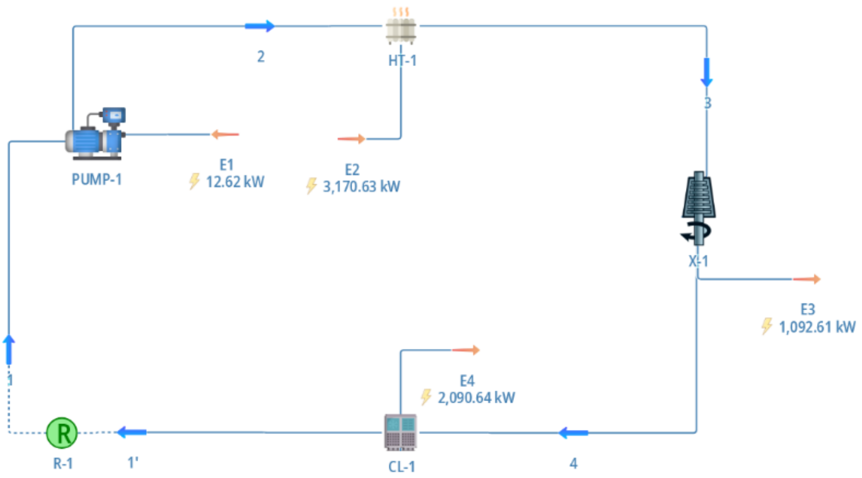

Figure 3. Simulation results of basic Rankine cycle.

To simulate Rankine cycle with reheating, the values of two additional parameters that need to be specified are reheat pressure and reheat temperature. Let the reheat pressure and temperature be 3 MPa and 500°C. Figure 4 shows the flowsheet of Rankine cycle with reheating after all required input parameters are specified. A procedure for simulating this cycle in DWSIM is similar to that of basic Rankine cycle. Additional steps of the simulation are listed below.

- Open the window of X-1.
- Select "Outlet Pressure" for Calculation Type.
- Specify 3 MPa for pressure and 85% for efficiency.
- Close the window.
- Open the window of HT-1.
- Select "Outlet Temperature" for Calculation Type.
- Specify 0 Pa for pressure drop, 100% for efficiency, and 500°C for outlet temperature.
- Close the window.
- Open the window of X-2.
- Select "Outlet Pressure" for Calculation Type.
- Specify 10 kPa for pressure and 85% for efficiency.
- Close the window.

It can be seen that the total specific work output is 1284.75 kJ/kg, and the specific work input is 12.62 kJ/kg. Therefore, the specific net work output is 1272.13 kJ/kg. The total specific heat input is 3547.57 kJ/kg. Thermal efficiency is 35.86%.

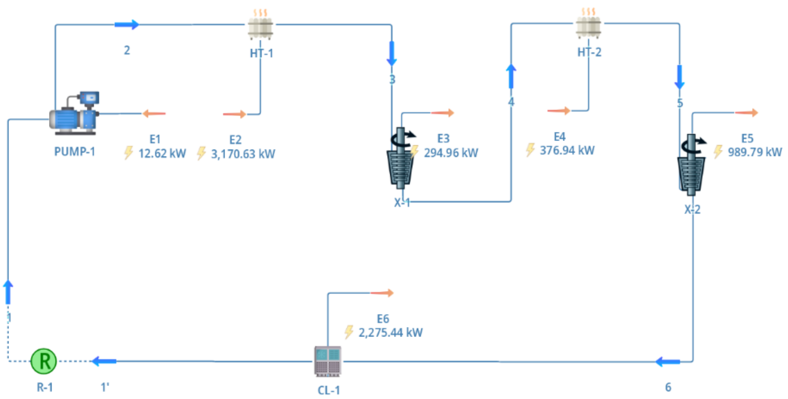

Figure 4. Simulation results of Rankine cycle with reheating.

A flowsheet of Rankine cycle with regeneration is shown in Figure 5. Because the steam flow rates in the two turbine stages (5-6 and 6-7) are unequal, Stream Splitter (SPL-1) is added between the two turbine stages. Material stream A is the input of SPL-1, and material streams B and 6 are the outputs. Actually, A and B may be considered as auxiliary states of steam, which are required for the construction of the DWSIM model. Intrinsic steam properties of A, B, and 6 are identical. However, the mass flow rate of A is the sum of the mass flow rates of B and 6. Open feed water heater is represented by Stream Mixer (MIX-1). Material streams B and 2 are the inputs of MIX-1, and material stream 3′ is the output. Material stream 3 is the input of PUMP-2. Material stream 3 cannot be the output of MIX-1 because of the forward computation performed by DWSIM. Recycle Block (R-1) is added to complete the cycle. The input of R-1 is material stream 3′, and the output is material stream 3.

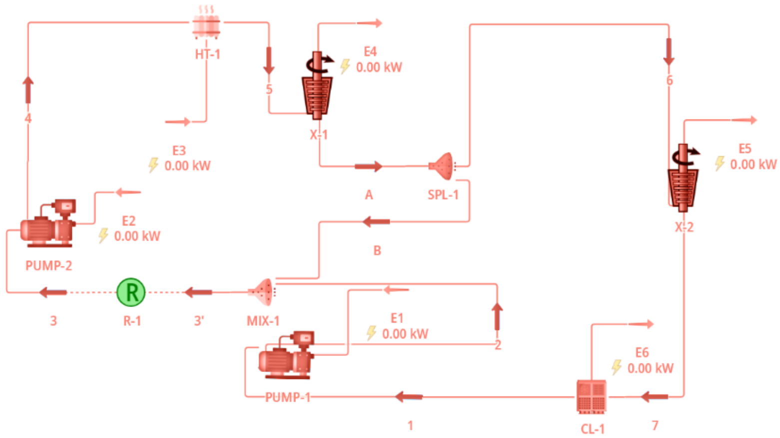

Figure 5. DWSIM flowsheet of Rankine cycle with regeneration before simulation.

A procedure for simulating Rankine cycle with regeneration consists of the following steps.

- Open the window of material stream 3.
- Select “Temperature and Pressure (TP)” for Flash Spec.
- Specify 455 K for temperature, 3 MPa for pressure, and 1.0 kg/s for mass flow rate.
- Close the window.
- Open the window of PUMP-2.
- Select “Outlet Pressure” for Calculation Type.
- Specify 10 MPa for pressure and 80% for efficiency.
- Close the window.
- Open the window of HT-1.
- Select “Outlet Temperature” for Calculation Type.
- Specify 0 Pa for pressure drop, 100% for efficiency, and 500°C for outlet temperature.
- Close the window.
- Open the window of X-1.
- Select “Outlet Pressure” for Calculation Type.
- Specify 3 MPa for pressure and 85% for efficiency.
- Close the window.
- Open the window of SPL-1.
- Select B for “Outlet Stream 1” and 6 for “Outlet Stream 2”.
- Select “Stream Split Ratios” for Calculation Type.
- Set “Stream 1 Split Ratio” to 0.2.
- Close the window.

- Open the window of X-2.
- Select “Outlet Pressure” for Calculation Type.
- Specify 10 kPa for pressure and 85% for efficiency.
- Close the window.
- Open the window of CL-1.
- Select “Outlet Vapor Mole Fraction” for Calculation Type.
- Specify 0 Pa for pressure drop, 100% for efficiency, and 0 for outlet vapor fraction.
- Close the window.
- Open the window of PUMP-1.
- Select “Outlet Pressure” for Calculation Type.
- Specify 3 MPa for pressure and 80% for efficiency.
- Close the window.

Figure 6 shows the flowsheet of Rankine cycle with regeneration after all required input parameters are specified. It can be seen that the total specific work output is 949.56 kJ/kg, the total specific work input is 12.89 kJ/kg. Therefore, the specific net work output is 936.67 kJ/kg. The specific heat input is 2592.70 kJ/kg. The thermal efficiency is 36.13%.

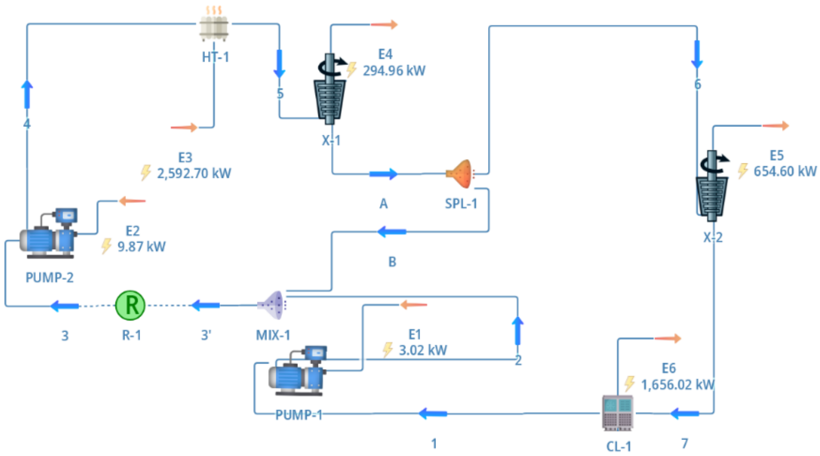

Figure 6. Simulation results of Rankine cycle with regeneration.

4. Sensitivity and Optimization Analyses

The thermal efficiency of a steam cycle is defined as

$$\eta_{th} = \frac{w_{net}}{q_{in}} \tag{1}$$

where w_{net} is specific net work output, and q_{in} is specific heat input. DWSIM does not calculate the thermal efficiency in the flowsheet. However, Spreadsheet is provided by the program for this purpose.

Three parameters that affect the thermal efficiency of the basic Rankine cycle are the maximum pressure, the maximum temperature, and the minimum pressure. The maximum pressure is specified as Outlet Pressure of PUMP-1 in Figure 3. The maximum temperature is specified as Outlet Temperature of HT-1. The minimum pressure is specified as Outlet Pressure of X-1. Figure 7 shows that the thermal efficiency increases with the maximum pressure and maximum temperature, and decreases as the minimum pressure increases.

For Rankine cycle with reheating, there are two additional parameters that affect the thermal efficiency: reheat temperature and reheat pressure. Thermal efficiency increases with reheat temperature if the other parameters are unchanged. The reheat pressure is specified as Outlet Pressure of X-1 in

Figure 4. Figure 8 shows that there is the optimum reheat pressure that results in the maximum thermal efficiency. The optimum pressure is 1.74 MPa, and the maximum thermal efficiency is 36.00%.

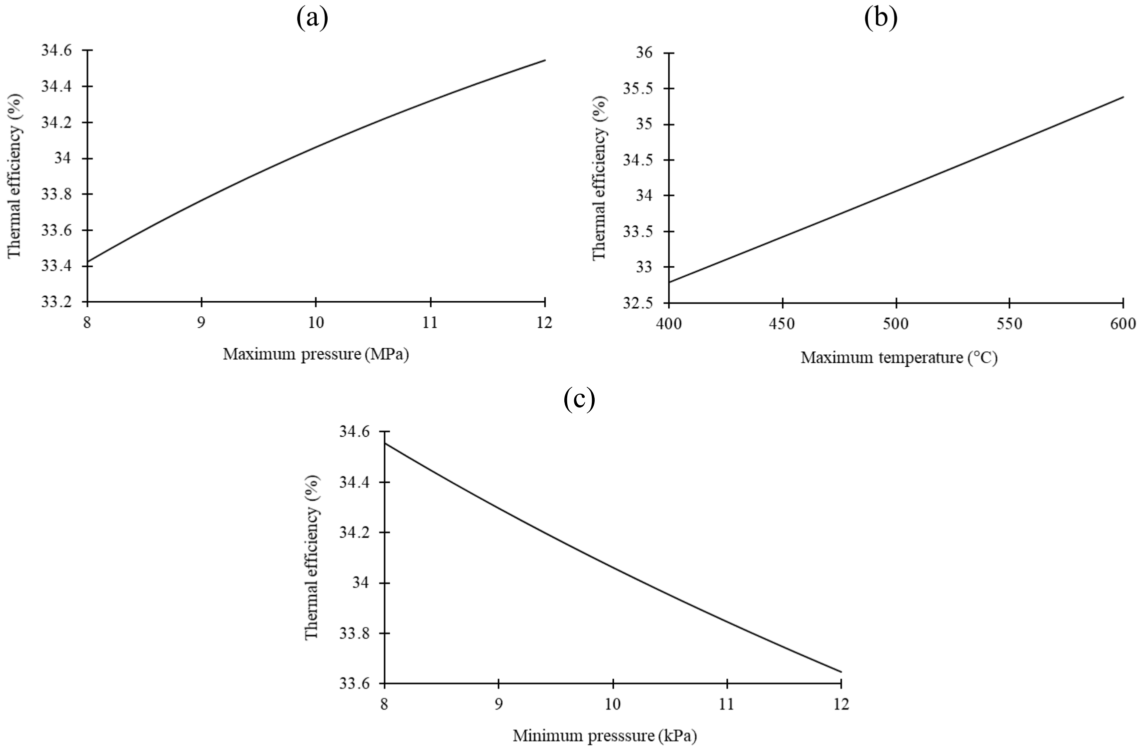

Figure 7. Effects on thermal efficiency of basic Rankine cycle of (a) maximum pressure, (b) maximum temperature, and (c) minimum pressure

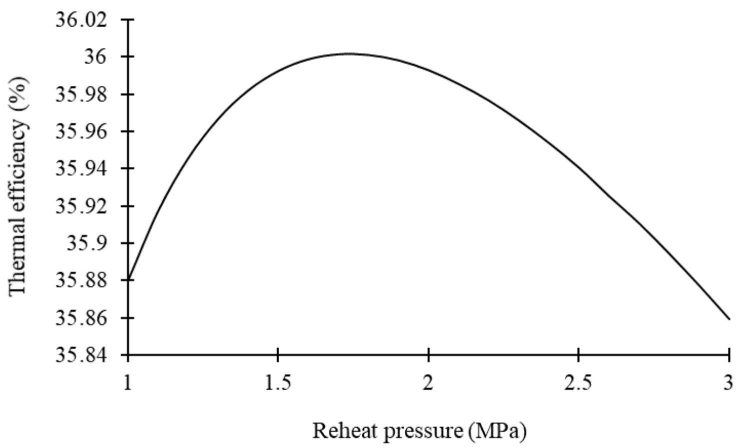

Figure 8. Effect of reheat pressure on thermal efficiency of Rankine cycle with reheating.

With the other parameters fixed, the thermal efficiency of Rankine cycle with regeneration depends on the extracted steam fraction and the extracted steam pressure. If the extracted steam pressure is kept fixed, the thermal efficiency increases with the extracted steam fraction. The upper limit of the extracted steam fraction is reached when the outlet of the open feed water heater is saturated liquid. To construct a DWSIM model of Rankine cycle with regeneration that has the maximum efficiency, material streams C and D are added, along with CL-2 and energy stream E7. These dummy components do not affect the cycle. Specify 0 kg/s for mass flow rate of C. Use Specification Block (SP-1) to set the pressure of C equal to the outlet pressure of X-1. Select "Outlet Vapor Mole Fraction" for Calculation Type of CL-2. Specify 0 for outlet vapor fraction. The next step is using Controller Block (C-1) to vary Stream 1 Split Ratio of SR1 so that the specific enthalpy of 3′ equals that of D. Figure 9 shows the flowsheet of Rankine cycle with regeneration that has the maximum extracted steam fraction. The thermal efficiency of this cycle is 36.90%.

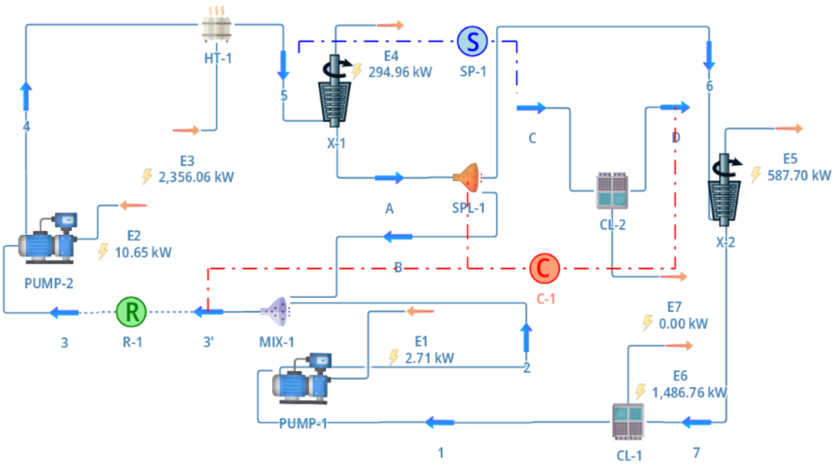

Figure 9. Simulation results of Rankine cycle with regeneration that has the maximum extracted steam fraction.

By setting the extracted steam fraction to the maximum value, the thermal efficiency of Rankine cycle with regeneration depends on only the extracted steam pressure, which is specified as Outlet Pressure of X-1 in Figure 9. A plot of thermal efficiency as a function of extracted steam pressure is shown in Figure 10. It can be seen that the optimum extracted steam pressure is 1.14 MPa, and the maximum thermal efficiency is 37.37%.

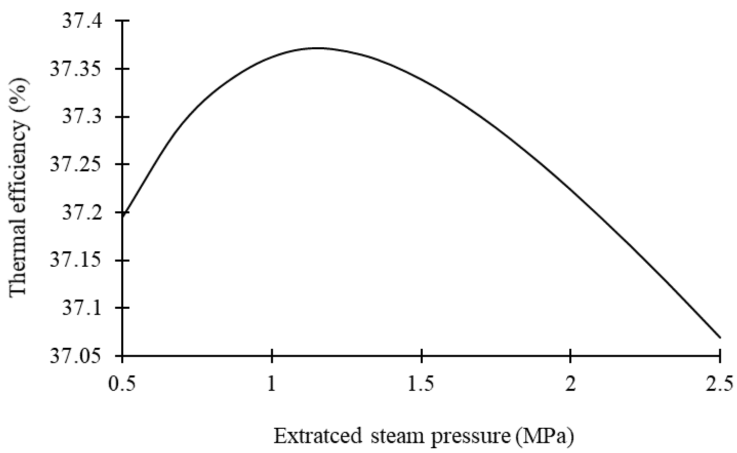

Figure 10. Effect of extracted steam pressure on thermal efficiency of Rankine cycle with reheating that has the maximum extracted steam fraction.

5. Conclusion

The modern trend of engineering education is the incorporation of the development in computer skills in classroom lessons. Traditional teaching of engineering thermodynamics, however, still relies on manual and semi-manual computations. This paper is aimed at introducing DWSIM, which is an open-source process simulator, for teaching and learning of steam cycles. Description of the construction of models of basic Rankine cycle, Rankine cycle with reheating, and Rankine cycle with regeneration is provided, and simulation results are obtained for these cycles. It is also shown that sensitivity and optimization analyses can be performed without much difficulty. More complex cycles can certainly be studied using DWSIM. Therefore, DWSIM is recommended as a promising tool for teaching engineering thermodynamics.

6. References

[1] Cengel, Y. A., & Boles, M. A. (2006). *Thermodynamics: An Engineering Approach*, *5th ed*. McGraw-Hill.

[2] Balmer, R. T. (2011). *Modern Engineering Thermodynamics*. Academic Press.

[3] Borgnakke, C., & Sonntag, R. E. (2013). *Fundamentals of Thermodynamics*, *8th ed*. John Wiley & Sons.

[4] Moran, M. J., Shapiro, H. N., Boettner, D. D., & Bailey, M. B. (2014). *Fundamentals of Engineering Thermo-dynamics*, *8th ed*. John Wiley & Sons.

[5] Affandia, M., Abdullahb, I., & Khalida, N. S. (2015). MATLAB as a tool for the teaching of Rankine cycle with simulation of simple steam power plant. *Jurnal Teknologi*. 77, 23-26.

[6] Gourde, R. M., & Akih-Kumgeh, B. (2017). A Matlab program for the determination of thermodynamic properties of steam. *International Journal of Mechanical Engineering Education*. 45, 228-244.

[7] Dumka, P., Rana, K., Tomar, S.P.S, Pawar, P.S., & Mishra, D.R. (2022). Modelling air standard thermodynamic cycles using python. *Advances in Engineering Software*. 172, 103186.

[8] Aulicino, A., & Bakrania, S. (2022). A Python-based lab module to conduct thermodynamic cycle analysis. In 2022 IEEE Frontiers in Education Conference, FIE 2022 (Uppsala). 8 – 11 October 2022, Code 184790.

[9] Dominguez, J. C., Lorenzo, D., García, J., Hopson, C., Rigual, V., Alonso, M. V., & Oliet, M. (2023). MATLAB applications for teaching Applied Thermodynamics: Thermodynamic cycles. *Computer Applications in Engineering Education*. 31, 900-915.

[10] Tangsriwong, K., Lapchit, P., Kittijungjit, T., Klamrassamee, T., Sukjai, Y., & Laoonual, Y. (2020). Modeling of chemical processes using commercial and open-source software: A comparison between Aspen plus and DWSIM. *IOP Conference Series: Earth and Environmental Science*. 463, 12057.

[11] Chantasiriwan, S. (2023). Simulation and optimization of vapor absorption refrigeration system using DWSIM. *Chemical Engineering Transactions*, 100, 613-618.

[12] Hassan, M. (2022). A simulation of energy generation from Jatropha solid residues in a power plant in Jazan city, KSA. *Heliyon*. 8, e09352

[13] Rao, N., Lele, A. K., & Patwardhan, A. W. (2022). Optimization of Liquid Organic Hydrogen Carrier (LOHC) dehydrogenation system. *International Journal of Hydrogen Energy*. 47, 28530-28547.

[14] Zaragoza, S., Muro, C., Hernandez, K., Diaz-Blancas, V., Sonia Martinez, M., & Francisco, R. (2023). Separation and phenol recovery from resin effluents by ultrafiltration. A proposal to use this method on an industrial scale. *Chemical Engineering Communications*. 210, 47-60.

[15] Sigue, S., Abderafi, S., Vaudreuil, S., & Bounahmidi, T. (2023). Design and steady-state simulation of a CSP-ORC power plant using an open-source co-simulation framework combining SAM and DWSIM. *Thermal Science and Engineering Progress*. 37, 101580.

[16] Biswas, A., & Mandal, B. K. (2023). Analysis of organic Rankine cycle using various working fluids for low-grade waste heat recovery. In *8th International Conference on Advances in Energy Research, ICAER 2022 (Mumbai).* 7 - 9 July 2022, Code 295319.

[17] Devkota, S., Ban, S., Shrestha, R., & Uprety, B. (2023). Techno-economic analysis of hydropower based green ammonia plant for urea production in Nepal. *International Journal of Hydrogen Energy*. 48, 21933–21945.


CAD-IT
Ansys
CERTIFIED ELITE CHANNEL PARTNER
CAD-IT assists and guides its customers to successful implementation of Industry 4.0 enablement technologies such as Additive Manufacturing, Augmented Reality, (AR) Industrial Internet of Things (IoT) and Engineering Simulation or Computer-Aided Engineering (CAE). Connect with us on your transformation journey to realize the potential and benefits of Digital Twin and the Digital Factory.
CAD-IT Consultants (Asia) Pte. Ltd. (Thailand Representative Office)
www.cadit.co.th
02 645 3127 to 9
thailand@caditglobal.com
Bringing you tomorrow's technology...Today!


บริษัท เอฟเวอร์เทค จำกัด
EVERTECH CO.,LTD.
ISO9001 : 2015
ISO 9001
BUREAU VERITAS Certification
UKAS
About Us
Evertech Co.,Ltd. We have been operating since 2007 as an importer and distributor of high quality measuring and testing equipment. From both Asia, Europe and America to hope that customers can choose to use quality products and services at reasonable prices.
Pure electric vehicle integrated training system
Motor, Transformer and Electrical Technology Trainer
Multifunction Installation Tester EV Charger
Solar Module Analyzer
Thermal Image Camera
Solar & Wind Hybrid Power Generation Trainer
www.evertech.co.th
บริษัท เอฟเวอร์เทค จำกัด EVERTECH CO.,LTD.
@evertech
(02)8702884-5,
(02)4289793-5


gerenga group
German Engineering & Automation
Markforged
AUBO
robot
ZIMMER
ARMOR
UR STATION
gerenga
Manufacturing
Solutions
Production Automation
Research & Development
Packaging, Transport & Storage
Production Management
Training Solutions
(+66)2 105 4519
sales-asia@gerenga.com
www.gerenga.co.th


About USE.FLO-LINE
We are leader of Hydraulic systems and Automation systems which was estabished in 1994 as a foreign joint venture company. Which was for med by a collaboration between a group of thai engineers and academics. To fix the problem and establish machine maintenance equipment that uses hydraulic and pneumatic systems to the facility operated in the country as Union Seki Engineering Co.,Ltd in 1991 , thenwas contacted to conduct business.
In 2021 USE.FLO-LINE has cooperated with KUKA robot set up training center for robotics which support to universities and industrials.
In 2015 we have started automation and robotics business for education. Included testing and training kit for universities.
111 Moo.1 347Rd. Chaing Rak Noi Samkhok
Pathumthani Thailand 12160
Didactic Products
ISDC
Automatic Control
Hydraulic System
Design & Structure
USE FLO-LINE
ISDC
: www.usefloline.com
: www.facebook.com/usefloline
: www.youtube.com/usefloline
Danfoss
atos
WC
VIBO
STAUFF
HYDRAFORCE
INOVANCE
ABB


Primacy
Distributor of products training for education
With over 40 years of experience
PRIMACY SUPPLY.,CO LTD.
Mechanical Engineering
gunt HAMBURG
Automotive Engineering
Training
FXB
Open wind tunnel
Heat conduction convection and radiation
Gasoline-Electricity Hybrid Section
Electric Vehicle Drive System Assembly and Connection Training
Torsion testing machine
Series and parallel configuration of pumps
L4 Level Low-speed Self-driving
Tel : 02-465-3440
Email : sales@primacy.co.th
https://www.primacy.co.th

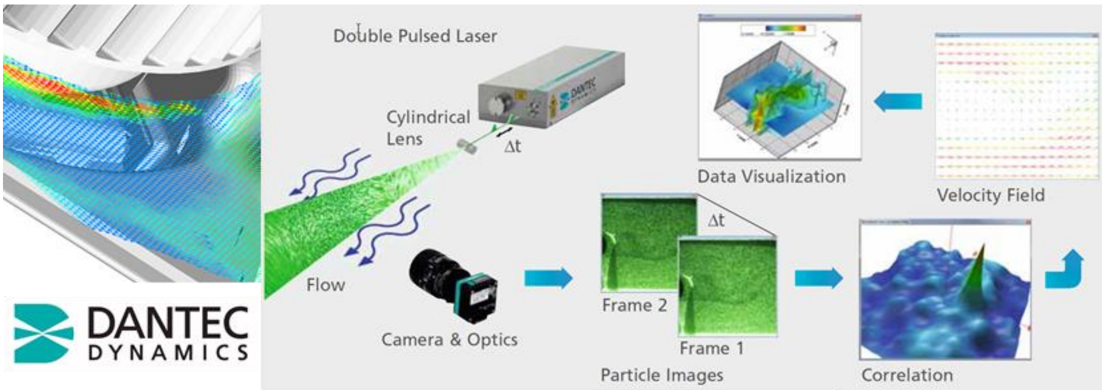
Double Pulsed Laser
Cylindrical Lens
Δt
Flow
Camera & Optics
Data Visualization
Velocity Field
Frame 2
Frame 1
Particle Images
Correlation
DANTEC DYNAMICS

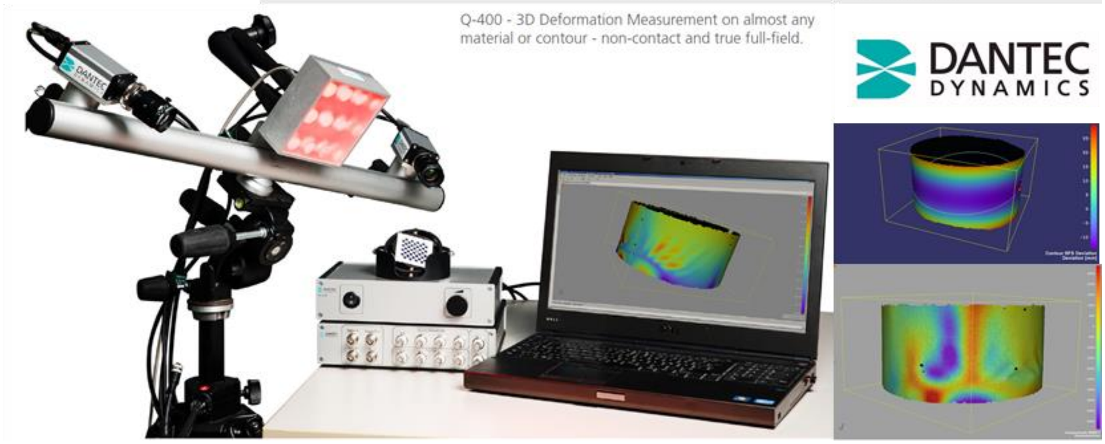
Q-400 - 3D Deformation Measurement on almost any material or contour - non-contact and true full-field.
DANTEC DYNAMICS


" BCG & Low Carbon "
Innovation Awards
Energy Saving & Low Carbon
IEEE Journal
AFEO
เจริญชัย
Low Carbon
ENERGY SAVING
SOLUTION

Department of Mechanical Engineering, Faculty of Engineering, Chiang Mai University
239 Huay Kaew Rd., Suthep, Muang District, Chiang Mai, 50200 Thailand

Tel. (+66) 53 94 2006 Ext. 417 Mobile (+66) 81 602 6431

https://me.eng.cmu.ac.th/

ISBN (e-book) 978-616-398-916-1

Department of Mechanical Engineering, Faculty of Engineering, Chiang Mai University
239 Huay Kaew Rd., Suthep, Muang District, Chiang Mai, 50200 Thailand

Tel. (+66) 53 94 2006 Ext. 417 Mobile (+66) 81 602 6431

https://me.eng.cmu.ac.th/

ISBN (e-book) 978-616-398-916-1